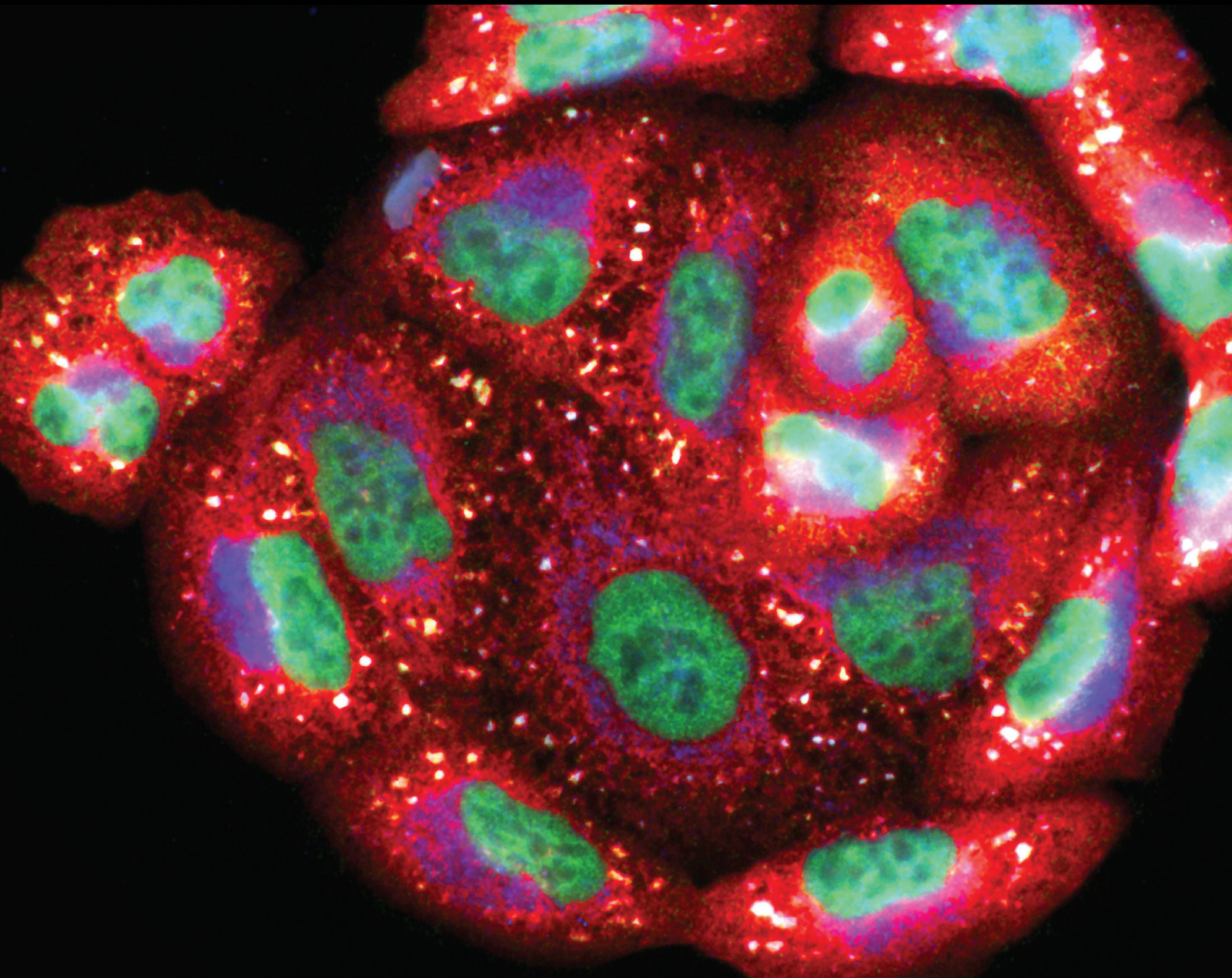


# The Role of Redox Homeostasis in Cancer Biology and Anticancer Therapy 2021

Lead Guest Editor: Qiang Tong

Guest Editors: Peichao Chen, Guoku Hu, Bin Duan, and Xiangpan Li





---

**The Role of Redox Homeostasis in Cancer  
Biology and Anticancer Therapy 2021**

Oxidative Medicine and Cellular Longevity

---

**The Role of Redox Homeostasis in  
Cancer Biology and Anticancer Therapy  
2021**

Lead Guest Editor: Qiang Tong

Guest Editors: Peichao Chen, Guoku Hu, Bin Duan,  
and Xiangpan Li



---

Copyright © 2022 Hindawi Limited. All rights reserved.

This is a special issue published in "Oxidative Medicine and Cellular Longevity" All articles are open access articles distributed under the Creative Commons Attribution License, which permits unrestricted use, distribution, and reproduction in any medium, provided the original work is properly cited.

# Chief Editor

Jeannette Vasquez-Vivar, USA

## Associate Editors

Amjad Islam Aqib, Pakistan  
Angel Catalá , Argentina  
Cinzia Domenicotti , Italy  
Janusz Gebicki , Australia  
Aldrin V. Gomes , USA  
Vladimir Jakovljevic , Serbia  
Thomas Kietzmann , Finland  
Juan C. Mayo , Spain  
Ryuichi Morishita , Japan  
Claudia Penna , Italy  
Sachchida Nand Rai , India  
Paola Rizzo , Italy  
Mithun Sinha , USA  
Daniele Vergara , Italy  
Victor M. Victor , Spain

## Academic Editors

Ammar AL-Farga , Saudi Arabia  
Mohd Adnan , Saudi Arabia  
Ivanov Alexander , Russia  
Fabio Altieri , Italy  
Daniel Dias Rufino Arcanjo , Brazil  
Peter Backx, Canada  
Amira Badr , Egypt  
Damian Bailey, United Kingdom  
Rengasamy Balakrishnan , Republic of Korea  
Jiaolin Bao, China  
Ji C. Bihl , USA  
Hareram Birla, India  
Abdelhakim Bouyahya, Morocco  
Ralf Braun , Austria  
Laura Bravo , Spain  
Matt Brody , USA  
Amadou Camara , USA  
Marcio Carcho , Portugal  
Peter Celec , Slovakia  
Giselle Cerchiaro , Brazil  
Arpita Chatterjee , USA  
Shao-Yu Chen , USA  
Yujie Chen, China  
Deepak Chhangani , USA  
Ferdinando Chiaradonna , Italy

Zhao Zhong Chong, USA  
Fabio Ciccarone, Italy  
Alin Ciobica , Romania  
Ana Cipak Gasparovic , Croatia  
Giuseppe Cirillo , Italy  
Maria R. Ciriolo , Italy  
Massimo Collino , Italy  
Manuela Corte-Real , Portugal  
Manuela Curcio, Italy  
Domenico D'Arca , Italy  
Francesca Danesi , Italy  
Claudio De Lucia , USA  
Damião De Sousa , Brazil  
Enrico Desideri, Italy  
Francesca Diomede , Italy  
Raul Dominguez-Perles, Spain  
Joël R. Drevet , France  
Grégory Durand , France  
Alessandra Durazzo , Italy  
Javier Egea , Spain  
Pablo A. Evelson , Argentina  
Mohd Farhan, USA  
Ioannis G. Fatouros , Greece  
Gianna Ferretti , Italy  
Swaran J. S. Flora , India  
Maurizio Forte , Italy  
Teresa I. Fortoul, Mexico  
Anna Fracassi , USA  
Rodrigo Franco , USA  
Juan Gambini , Spain  
Gerardo García-Rivas , Mexico  
Husam Ghanim, USA  
Jayeeta Ghose , USA  
Rajeshwary Ghosh , USA  
Lucia Gimeno-Mallench, Spain  
Anna M. Giudetti , Italy  
Daniela Giustarini , Italy  
José Rodrigo Godoy, USA  
Saeid Golbidi , Canada  
Guohua Gong , China  
Tilman Grune, Germany  
Solomon Habtemariam , United Kingdom  
Eva-Maria Hanschmann , Germany  
Md Saquib Hasnain , India  
Md Hassan , India

Tim Hofer , Norway  
John D. Horowitz, Australia  
Silvana Hrelia , Italy  
Dragan Hrnčić, Serbia  
Zebo Huang , China  
Zhao Huang , China  
Tarique Hussain , Pakistan  
Stephan Immenschuh , Germany  
Norsharina Ismail, Malaysia  
Franco J. L. , Brazil  
Sedat Kacar , USA  
Andleeb Khan , Saudi Arabia  
Kum Kum Khanna, Australia  
Neelam Khaper , Canada  
Ramoji Kosuru , USA  
Demetrios Kouretas , Greece  
Andrey V. Kozlov , Austria  
Chan-Yen Kuo, Taiwan  
Gaocai Li , China  
Guoping Li , USA  
Jin-Long Li , China  
Qiangqiang Li , China  
Xin-Feng Li , China  
Jialiang Liang , China  
Adam Lightfoot, United Kingdom  
Christopher Horst Lillig , Germany  
Paloma B. Liton , USA  
Ana Lloret , Spain  
Lorenzo Loffredo , Italy  
Camilo López-Alarcón , Chile  
Daniel Lopez-Malo , Spain  
Massimo Lucarini , Italy  
Hai-Chun Ma, China  
Nageswara Madamanchi , USA  
Kenneth Maiese , USA  
Marco Malaguti , Italy  
Steven McAnulty, USA  
Antonio Desmond McCarthy , Argentina  
Sonia Medina-Escudero , Spain  
Pedro Mena , Italy  
V́ctor M. Mendoza-Núñez , Mexico  
Lidija Milkovic , Croatia  
Alexandra Miller, USA  
Sara Missaglia , Italy

Premysl Mladenka , Czech Republic  
Sandra Moreno , Italy  
Trevor A. Mori , Australia  
Fabiana Morroni , Italy  
Ange Mouithys-Mickalad, Belgium  
Iordanis Mourouzis , Greece  
Ryoji Nagai , Japan  
Amit Kumar Nayak , India  
Abderrahim Nemmar , United Arab Emirates  
Xing Niu , China  
Cristina Nocella, Italy  
Susana Novella , Spain  
Hassan Obied , Australia  
Pál Pacher, USA  
Pasquale Pagliaro , Italy  
Dilipkumar Pal , India  
Valentina Pallottini , Italy  
Swapnil Pandey , USA  
Mayur Parmar , USA  
Vassilis Paschalis , Greece  
Keshav Raj Paudel, Australia  
Ilaria Peluso , Italy  
Tiziana Persichini , Italy  
Shazib Pervaiz , Singapore  
Abdul Rehman Phull, Republic of Korea  
Vincent Pialoux , France  
Alessandro Poggi , Italy  
Zsolt Radak , Hungary  
Dario C. Ramirez , Argentina  
Erika Ramos-Tovar , Mexico  
Sid D. Ray , USA  
Muneeb Rehman , Saudi Arabia  
Hamid Reza Rezvani , France  
Alessandra Ricelli, Italy  
Francisco J. Romero , Spain  
Joan Roselló-Catafau, Spain  
Subhadeep Roy , India  
Josep V. Rubert , The Netherlands  
Sumbal Saba , Brazil  
Kunihiro Sakuma, Japan  
Gabriele Saretzki , United Kingdom  
Luciano Saso , Italy  
Nadja Schroder , Brazil

Anwen Shao , China  
Iman Sherif, Egypt  
Salah A Sheweita, Saudi Arabia  
Xiaolei Shi, China  
Manjari Singh, India  
Giulia Sita , Italy  
Ramachandran Srinivasan , India  
Adrian Sturza , Romania  
Kuo-hui Su , United Kingdom  
Eisa Tahmasbpour Marzouni , Iran  
Hailiang Tang, China  
Carla Tatone , Italy  
Shane Thomas , Australia  
Carlo Gabriele Tocchetti , Italy  
Angela Trovato Salinaro, Italy  
Rosa Tundis , Italy  
Kai Wang , China  
Min-qi Wang , China  
Natalie Ward , Australia  
Grzegorz Wegrzyn, Poland  
Philip Wenzel , Germany  
Guangzhen Wu , China  
Jianbo Xiao , Spain  
Qiongming Xu , China  
Liang-Jun Yan , USA  
Guillermo Zalba , Spain  
Jia Zhang , China  
Junmin Zhang , China  
Junli Zhao , USA  
Chen-he Zhou , China  
Yong Zhou , China  
Mario Zoratti , Italy







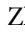






## Contents

### **DJ-1/FGFR-1 Signaling Pathway Contributes to Sorafenib Resistance in Hepatocellular Carcinoma**

Xin Chen , Guohua Yang, Xiaohong Guo, Jing Zhang, Wei Sun, Dongbo Liu, Hui Wang, and Shunfang Liu 

Research Article (20 pages), Article ID 2543220, Volume 2022 (2022)

### **ROS-Related miRNAs Regulate Immune Response and Chemoradiotherapy Sensitivity in Hepatocellular Carcinoma by Comprehensive Analysis and Experiment**

Yangtao Xu , Xiaoqin He , Junjian Deng , Lin Xiong , Biao Chen , Jiayu Chen , Xiaoyu Zhang , Wenliang Chen , Xin Liu, Xinyao Hu , Jiayi Li , Shan Jiang , Yang Shen , and Ximing Xu 


Research Article (27 pages), Article ID 4713518, Volume 2022 (2022)

### **The Prognostic Value and Immunological Role of STEAP1 in Pan-Cancer: A Result of Data-Based Analysis**

Chen Zhao , Kewei Xiong , Zhiqiang Ji , Fengming Liu, and Xiangpan Li 





Research Article (28 pages), Article ID 8297011, Volume 2022 (2022)

### **Therapy-resistant and -sensitive lncRNAs, SNHG1 and UBL7-AS1 promote glioblastoma cell proliferation**

Mei Cao, Rong Ma, Huaqing Li, Juan Cui, Chi Zhang, and Jian Zhao 


Research Article (15 pages), Article ID 2623599, Volume 2022 (2022)

### **Glycosylation-Related Genes Predict the Prognosis and Immune Fraction of Ovarian Cancer Patients Based on Weighted Gene Coexpression Network Analysis (WGCNA) and Machine Learning**

Chen Zhao , Kewei Xiong , Fangrui Zhao, Abdalla Adam , and Xiangpan Li 

Research Article (23 pages), Article ID 3665617, Volume 2022 (2022)

### **Quantitative Proteomics Analysis Expands the Roles of Lysine $\beta$ -Hydroxybutyrylation Pathway in Response to Environmental $\beta$ -Hydroxybutyrate**

Wanting Hou, Guobin Liu, Xuelian Ren, Xianming Liu, Lei He, and He Huang 

Research Article (15 pages), Article ID 4592170, Volume 2022 (2022)

### **Corrigendum to “System Analysis of ROS-Related Genes in the Prognosis, Immune Infiltration, and Drug Sensitivity in Hepatocellular Carcinoma”**

Jun Hui Xu , Yong Jun Guan , Zhen Dong Qiu , Xin Zhang , Liu Liu Zi , Yu Zhou , Chen Chen , Jia Yu , Yi Chao Zhang , and Wei Xing Wang 

Corrigendum (1 page), Article ID 9875295, Volume 2022 (2022)



### **Quantitative Proteomics Reveals the Role of Lysine 2-Hydroxyisobutyrylation Pathway Mediated by Tip60**

Ning Wang, Yue Jiang, Ping Peng, Guobin Liu, Shankang Qi , Kun Liu , Qi Mei , and Jian Li

Research Article (13 pages), Article ID 4571319, Volume 2022 (2022)








**Anlotinib Enhances the Antitumor Activity of High-Dose Irradiation Combined with Anti-PD-L1 by Potentiating the Tumor Immune Microenvironment in Murine Lung Cancer**

Meng Yuan , Yirui Zhai, Yu Men, Maoyuan Zhao, Xin Sun, Zeliang Ma, Yongxing Bao, Xu Yang, Shuang Sun, Yunsong Liu, Wanting Zhang, and Zhouguang Hui 




Research Article (11 pages), Article ID 5479491, Volume 2022 (2022)

**The ROS/GRK2/HIF-1 $\alpha$ /NLRP3 Pathway Mediates Pyroptosis of Fibroblast-Like Synoviocytes and the Regulation of Monomer Derivatives of Paeoniflorin**

Zhongyang Hong , Xianzheng Zhang , Tianjing Zhang , Ling Hu , Ruijin Liu , Pan Wang , Han Wang , Qianqian Yu , Dan Mei , Ziyang Xue , Feng Zhang , and Lingling Zhang 


Research Article (15 pages), Article ID 4566851, Volume 2022 (2022)

**HNF4A Regulates the Proliferation and Tumor Formation of Cervical Cancer Cells through the Wnt/ $\beta$ -Catenin Pathway**

Hong-Mei Ma , Qian Zhang, Xue-Mei Yang, Yan Hu, Juan Zhang, Lin Chen, Bin Zhao, Wen-ting Yang , and Rui Xu 




Research Article (17 pages), Article ID 8168988, Volume 2022 (2022)

**Liensinine Inhibits Osteosarcoma Growth by ROS-Mediated Suppression of the JAK2/STAT3 Signaling Pathway**

Fei Jia , Yu Liu, Xinyu Dou, Chuanchao Du, Tianli Mao, and Xiaoguang Liu 

Research Article (21 pages), Article ID 8245614, Volume 2022 (2022)

**The Effects of RBP4 and Vitamin D on the Proliferation and Migration of Vascular Smooth Muscle Cells via the JAK2/STAT3 Signaling Pathway**

Wan Zhou , Wei Wang, Xiao-Jing Yuan, Chun-Chun Xiao, Yan Xing, Shan-Dong Ye , and Qiang Liu 



Research Article (23 pages), Article ID 3046777, Volume 2022 (2022)

**The Hypoxia-Related Gene COL5A1 Is a Prognostic and Immunological Biomarker for Multiple Human Tumors**

Hua Zhu , Xinyao Hu , Shi Feng , Zhihong Jian , Ximing Xu , Lijuan Gu , and Xiaoxing Xiong 

Research Article (42 pages), Article ID 6419695, Volume 2022 (2022)

**lncRNA SNHG15 Induced by SOX12 Promotes the Tumorigenic Properties and Chemoresistance in Cervical Cancer via the miR-4735-3p/HIF1 $\alpha$  Pathway**

Jiang Yang, Mei Yang, Huabing Lv, Min Zhou, Xiaogang Mao, Xiaomin Qin, Ying Xu, Lin Li , and Hui Xing 

Research Article (15 pages), Article ID 8548461, Volume 2022 (2022)



**Signature Construction and Molecular Subtype Identification Based on Pyroptosis-Related Genes for Better Prediction of Prognosis in Hepatocellular Carcinoma**

Ji Chen , Qiqi Tao, Zhichao Lang, Yuxiang Gao, Yan Jin, Xiaoqi Li, Yajing Wang, Yuxiao Zhang, Suhui Yu, Boyu Lv , Zhengping Yu , and Changyong Lin 

Research Article (20 pages), Article ID 4494713, Volume 2022 (2022)

## Contents

### **Downregulation of CYP39A1 Serves as a Novel Biomarker in Hepatocellular Carcinoma with Worse Clinical Outcome**

Dan Li, Tao Yu, Junjie Hu, Jie Wu, Shi Feng, Qingxue Xu, Hua Zhu, Xu Zhang, Yonggang Zhang, BenHong Zhou, Lijuan Gu , and Zhi Zeng 





Research Article (18 pages), Article ID 5175581, Volume 2021 (2021)

### **Ionizing Radiation Upregulates Glutamine Metabolism and Induces Cell Death via Accumulation of Reactive Oxygen Species**

Pengfei Yang, Xiangxia Luo, Jin Li, Tianyi Zhang, Xiaoling Gao , Junrui Hua, Yonghong Li, Nan Ding, Jinpeng He, Yanan Zhang, Wenjun Wei, Jufang Wang , and Heng Zhou 








Research Article (22 pages), Article ID 5826932, Volume 2021 (2021)

### **The Synergistic Reducing Drug Resistance Effect of Cisplatin and Ursolic Acid on Osteosarcoma through a Multistep Mechanism Involving Ferritinophagy**

Zhen Tang, Hui Dong, Tian Li , Ning Wang, Xinghui Wei, Hao Wu, Yichao Liu, Wei Wang , Zheng Guo , and Xin Xiao 


Research Article (17 pages), Article ID 5192271, Volume 2021 (2021)

### **LINC00467, Driven by Copy Number Amplification and DNA Demethylation, Is Associated with Oxidative Lipid Metabolism and Immune Infiltration in Breast Cancer**

Hao Bo, Wancong Zhang , Xiaoping Zhong , Jiasheng Chen , Yang Liu , Kit-Leong Cheong , Pengju Fan , and Shijie Tang 


Research Article (27 pages), Article ID 4586319, Volume 2021 (2021)

### **Moderate Static Magnet Fields Suppress Ovarian Cancer Metastasis via ROS-Mediated Oxidative Stress**

Chao Song , Biao Yu , Junjun Wang , Xinmiao Ji , Lei Zhang , Xiaofei Tian , Xin Yu , Chuanlin Feng , Xinyu Wang , and Xin Zhang 



Research Article (18 pages), Article ID 7103345, Volume 2021 (2021)

### **Exploration of Redox-Related Molecular Patterns and the Redox Score for Prostate Cancer**

Yue Wu, Xi Zhang, Huan Feng, Bintao Hu, Zhiyao Deng, Chengwei Wang, Bo Liu, Yang Luan, Yajun Ruan, Xiaming Liu, Zhuo Liu, Jihong Liu, and Tao Wang 

Research Article (28 pages), Article ID 4548594, Volume 2021 (2021)

### **A Ferroptosis-Related Prognostic Risk Score Model to Predict Clinical Significance and Immunogenic Characteristics in Glioblastoma Multiforme**

Dongdong Xiao, Yujie Zhou , Xuan Wang , Hongyang Zhao , Chuansheng Nie , and Xiaobing Jiang 


Research Article (30 pages), Article ID 9107857, Volume 2021 (2021)

### **System Analysis of ROS-Related Genes in the Prognosis, Immune Infiltration, and Drug Sensitivity in Hepatocellular Carcinoma**

Jun Hui Xu , Yong Jun Guan, Zhen Dong Qiu, Xin Zhang , Liu Liu Zi , Yu Zhou, Chen Chen, Jia Yu, Yi Chao Zhang , and Wei Xing Wang 

Research Article (30 pages), Article ID 6485871, Volume 2021 (2021)

**Downregulation of the Proton-Activated Cl<sup>-</sup> Channel TMEM206 Inhibits Malignant Properties of Human Osteosarcoma Cells**

Fei Peng , Haohuan Li, Jianping Li, and Zhe Wang


Research Article (16 pages), Article ID 3672112, Volume 2021 (2021)

**ROS Pleiotropy in Melanoma and Local Therapy with Physical Modalities**

Sanjeev Kumar Sagwal  and Sander Bekeschus 

Review Article (21 pages), Article ID 6816214, Volume 2021 (2021)

**Interplay between Mitochondrial Metabolism and Cellular Redox State Dictates Cancer Cell Survival**

Brittney Joy-Anne Foo, Jie Qing Eu, Jayshree L. Hirpara, and Shazib Pervaiz 



Review Article (20 pages), Article ID 1341604, Volume 2021 (2021)

**Comprehensive Analysis of Ferroptosis-Related Markers for the Clinical and Biological Value in Gastric Cancer**

Yanfei Shao , Hongtao Jia , Shuchun Li , Ling Huang , Batuer Aikemu , Guang Yang , Sen Zhang , Jing Sun , and Minhua Zheng 




Research Article (29 pages), Article ID 7007933, Volume 2021 (2021)

**A Novel Systematic Oxidative Stress Score Predicts the Prognosis of Patients with Operable Breast Cancer**

Kaiming Zhang, Liqin Ping, Tian Du, Yan Wang, Ya Sun, Gehao Liang, Xi Wang, Xiaoming Xie, Weidong Wei, Xiangsheng Xiao , and Jun Tang 

Research Article (14 pages), Article ID 9441896, Volume 2021 (2021)

***Lactobacillus plantarum* and *Lactobacillus brevis* Alleviate Intestinal Inflammation and Microbial Disorder Induced by ETEC in a Murine Model**

Xuebing Han, Sujuan Ding , Yong Ma, Jun Fang , Hongmei Jiang, Yi Li, and Gang Liu 

Research Article (11 pages), Article ID 6867962, Volume 2021 (2021)

**Targeting Reactive Oxygen Species Capacity of Tumor Cells with Repurposed Drug as an Anticancer Therapy**

Jiabing Wang , Dongsheng Sun , Lili Huang , Shijian Wang , and Yong Jin 

Review Article (17 pages), Article ID 8532940, Volume 2021 (2021)

## Research Article

# DJ-1/FGFR-1 Signaling Pathway Contributes to Sorafenib Resistance in Hepatocellular Carcinoma

Xin Chen <sup>1</sup>, Guohua Yang,<sup>2</sup> Xiaohong Guo,<sup>3</sup> Jing Zhang,<sup>1</sup> Wei Sun,<sup>1</sup> Dongbo Liu,<sup>1</sup> Hui Wang,<sup>2</sup> and Shunfang Liu <sup>1</sup>

<sup>1</sup>Department of Oncology, Tongji Hospital, Tongji Medical College, Huazhong University of Science and Technology, Wuhan 430030, China

<sup>2</sup>Department of Medical Genetics, School of Basic Medical Science, Demonstration Center for Experimental Basic Medicine Education, Wuhan University, Wuhan 430071, China

<sup>3</sup>Department of Medical Biology, School of Basic Medical Sciences, Hubei University of Chinese Medicine, Wuhan 430065, China

Correspondence should be addressed to Shunfang Liu; [lsftj2011oncology@163.com](mailto:lsftj2011oncology@163.com)

Received 29 September 2021; Revised 3 May 2022; Accepted 13 May 2022; Published 20 June 2022

Academic Editor: Guoku Hu

Copyright © 2022 Xin Chen et al. This is an open access article distributed under the Creative Commons Attribution License, which permits unrestricted use, distribution, and reproduction in any medium, provided the original work is properly cited.

Sorafenib is the first-line therapeutic regimen targeting against advanced or metastatic stage of hepatocellular carcinoma (HCC). However, HCC patients at these stages will eventually fail sorafenib treatment due to the drug resistance. At present, molecular mechanisms underlying sorafenib resistance are not completely understood. Our past studies have shown that DJ-1 is upregulated in HCC, while DJ-1 knockdown inhibits HCC xenograft-induced tumor growth and regeneration, implying that DJ-1 may be a potential target in for HCC treatment. However, whether DJ-1 plays a regulatory role between tumor cells and vascular endothelial cells and whether DJ-1 contributes to sorafenib resistance in HCC cells are largely unclear. To address these questions, we have performed a series of experiments in the current study, and we found that (1) DJ-1, one of the molecules secreted from HCC cells, promoted angiogenesis and migration of vascular endothelial cells (i.e., ECDHCC-1), by inducing phosphorylation of fibroblast growth factor receptor-1 (FGFR-1), phosphorylation of mTOR, phosphorylation of ERK, and phosphorylation of STAT3; (2) downregulation of FGFR1 inhibited tube formation and migration of ECDHCC-1 cells stimulated by DJ-1; (3) FGFR1 knockdown attenuated the phosphorylation of FGFR1 and impaired the activity of Akt, ERK, and STAT3 signals induced by DJ-1 in ECDHCC-1 cells; (4) knocking down FGFR1 led to the elevated expression of proapoptotic molecules but decreased level of antiapoptotic molecules in sorafenib-resistant HCC cells; and (5) Downregulation of FGFR1 suppressed tumor growth and angiogenesis of sorafenib-resistant HCC cells *in vivo*. Altogether, our results hinted that DJ-1 plays vital roles in tumor microenvironment in HCC development, and DJ-1/FGFR1 signaling pathway may be a therapeutic target for overcoming sorafenib resistance in treating HCC patients at the late stage.

## 1. Introduction

Hepatocellular carcinoma (HCC) is the predominant type of liver cancer. At present, partial hepatectomy and liver transplantation offer the best prognosis for HCC patients when the tumor is <5 cm in diameter, limited to one lobe of the liver, without invasion of liver vasculature, and liver function is well preserved [1]. Unfortunately, a high postoperative

tumor recurrence rate significantly decreases long-term survival. Owing to the invasive growth and late symptom presentation, most patients are diagnosed at advanced stages and are not eligible for surgery [2]. Sorafenib, an orally available tyrosine kinase inhibitor, is the first-line drug against advanced HCC since 2008, which significantly improved the overall survival of unresectable HCC patients. However, the promising therapy has demonstrated limited clinical

efficacy, typically only extending patients' survival by about 3 months. Some patients with HCC initially respond well to sorafenib but will eventually fail due to cancer progression, indicating that there is an acquired resistance to sorafenib in HCC [3]. Up to now, the mechanism responsible for this acquired resistance of HCC to sorafenib is unclear, and we propose a possible means by which it is achieved.

As a novel oncogene, protein deglycase DJ-1 is a 20 kDa protein which is abundantly expressed in more than 22 human tissues, including the liver and vascular endothelium [4]. DJ-1 is associated with multiple biological functions, such as transcriptional regulation, chaperone activity regulation, protease function regulation, and mitochondrial regulation [5]. Meanwhile, it has been reported that DJ-1 is one of the regulators in tumorigenesis, invasion, and metastasis in various cancers, including HCC [6]. Our past research found that DJ-1 was upregulated in HCC. In addition, downregulation of DJ-1 resulted in decreased proliferation, adhesion and invasion of HepG2 cells *in vitro*, and inhibited the growth of HepG2-induced tumor *in vivo*, which implies its crucial role for DJ-1 in the oncogenesis of HCC [7, 8]. Meanwhile, DJ-1 has been found to promote angiogenesis during osteogenesis and has been identified as a communicating factor between osteoblasts and endothelial cells [9]. As it is well known that antiapoptosis of tumor cells and angiogenesis of vascular endothelial cells are both involved in sorafenib resistance, inhibition of angiogenesis in tumor is expected to overcome drug resistance to HCC. Whether DJ-1 plays a crucial role in angiogenesis of HCC vascular endothelial cells and acts as a cross-talk regulatory role between tumor cells and vascular endothelial cells in HCC sorafenib resistance is largely unclear.

Fibroblast growth factor receptor 1 (FGFR1), a tyrosine kinase receptor, is the predominant type of FGFR and plays a key role in promoting angiogenesis in endothelial cells. FGF induced the phosphorylation of FGFR1 and activated downstream signaling molecules, such as Src kinase, focal adhesion kinase (FAK), and extracellular signal-regulated kinase 1/2 (ERK1/2), which have been implicated in endothelial cell differentiation [10]. Meanwhile, sorafenib suppresses tumor angiogenesis and proliferation by inhibiting multikinases such as the serine/threonine kinase family (e.g., Raf-1, PI3K/Akt, ERK1/2, and STAT3) and the receptor tyrosine kinase family (e.g., FGFR, VEGFR, and PDGFR) [3]. Furthermore, the acquired resistance to sorafenib in HCC has been linked to the activation of FGF/FGFR1 signaling pathway [11]. Importantly, it has been reported that DJ-1 can induce the phosphorylation of FGFR1 and activate the FAK and ERK1/2 signal pathway, which result in the stimulation of migration and capillary formation of vascular endothelium [9]. Therefore, it is reasonable to suspect that the DJ-1/FGFR1 signaling pathway might contribute to sorafenib resistance in HCC, and the inhibition of DJ-1/FGFR1 pathway will benefit a subset of sorafenib resistant patients with high expression of DJ-1.

Here, DJ-1 was targeted as a cross-talk regulator between HCC cells and vascular endothelial cells, and the proangiogenic effect of DJ-1/FGFR1 signaling in ECDHCC cells was investigated. We also explored the underlying mechanisms

on the reversal effect of sorafenib resistance in HCC cells by downregulating FGFR1.

## 2. Materials and Methods

**2.1. Cell Culture and Establishment of Sorafenib Resistance in HCC Cell Lines.** The human hepatocellular carcinoma cell lines (HepG2 and HUH-7), endothelial cells derived from hepatocellular carcinoma (ECDHCC-1), THLE-2, and L02 cells derived from healthy liver cells were all obtained from American Type Culture Collection (ATCC; Manassas, VA, USA). Cells were cultured at 37°C with 5% CO<sub>2</sub> in Dulbecco's modified Eagle's medium (DMEM) high-glucose medium containing 10% fetal serum (Gibco-Life Technologies, Carlsbad, CA, USA) and 1% penicillin and streptomycin. To establish the sorafenib-resistant HCC cell lines, the half-maximal inhibitory concentration (IC<sub>50</sub>) of HCC cells to sorafenib was initially determined by incubating cells with different concentrations of sorafenib in 96-well plates, and cell viability was measured 3 days later as described below. The cells were cultured in 6-well plates at  $1 \times 10^4$  cells/well and incubated with sorafenib at a concentration just below their respective IC<sub>50</sub>. The concentration of sorafenib was slowly increased by 0.25 μM per week. After 6 to 7 months, sorafenib-resistant cell lines were obtained and continuously maintained in the presence of sorafenib. The resistance index (RI) was calculated as the ratio of IC<sub>50</sub> of sorafenib resistant cell line to IC<sub>50</sub> of corresponding control cell line.

**2.2. ELISA Assay of DJ-1.** DJ-1 level in the culture medium was assessed by enzyme-linked immunosorbent assay using a commercially available human protein DJ-1 (PARK7) ELISA kit (#CSB-E12024h, CUSABIO, Wuhan, China) according to the manufacturer's protocol.

**2.3. Expression and Purification of His-Tagged DJ-1 Protein.** Expression and purification of recombinant DJ-1 were carried out using the pET28a vector according to the supplier's protocols (EMD Millipore, Darmstadt, Germany). DJ-1 was cloned into the pET28a vector and sequenced. The DJ-1 construct was transformed into *Escherichia coli* BL21 (DE3) for expression of His-tagged DJ-1 (His DJ-1), and recombinant protein was purified on nickel-NTA agarose columns. Finally, the concentration and purity of His-tagged DJ-1 protein were determined using the Bradford assay (Bio-Rad), and the production was verified by western blotting analysis with anti-His tag and anti-DJ-1 specific antibody, respectively.

**2.4. Construction of FGFR1 shRNA Expression Plasmid.** The pLKO.1 lentiviral plasmid was selected to construct the shFGFR vector. Empty vector was used as a control group. To generate lentiviruses, HEK 293T cells were cotransfected with pLKO-shFGFR1 plasmid, psPAX2 packaging plasmid, and pMD2.G envelop plasmid using Lipofectamine 3000 (Invitrogen). Transduction of pLKO-shFGFR1 lentivirus and stable FGFR1 knock down was conducted according to the manufacturer's protocols. Short hairpin RNAs (shRNA) targeting FGFR1 (shFGFR1) were detailed as follows: FGFR1-Sh1: 5' - CCA CAG AAT TGG AGG CTA CAA-3'

, FGFR1-Sh2: 5'-GAT GGC ACC CGA GGC ATT ATT-3',  
FGFR1-Sh3: 5'-TGC CAC CTG GAG CAT CAT AAT-3'.

**2.5. Cell Proliferation Assay of CCK8.** Cell proliferation was evaluated through a colorimetric assay by using cell counting kit-8 (CCK-8, GLPBIO, USA) reagent following the manufacturer's protocol. Briefly, ECDHCC cells were seeded into 96-well plates at a density of  $5 \times 10^3$  cells/well in a medium with 10% FBS and allowed to adhere for 24 h. Next, cells were cultured in a medium with 1% FBS in the presence or absence of indicated medium or reagent (Sigma-Aldrich, St. Louis, MO, USA) for a further 24 h and/or 48 h. Afterwards, 10  $\mu$ L of CCK-8 reagent was added and maintained for 3 h. A microplate reader (Multiskan MK3, Thermo, Waltham, MA) was used to measure the optical density of 450 nm and 630 nm.

**2.6. Tube Formation Assay.** Matrigel (# K905-50, Biovision, Milpitas, USA) was dissolved at 4°C overnight, and 48-well plates were prepared with 100  $\mu$ L Matrigel in each well after coating and incubating at 37°C overnight. ECDHCC cells ( $1 \times 10^5$  cells/well) were plated and incubated for 6 h at 37°C. ECDHCC cell tube formation was assessed with a photomicroscope, where tube branches and total tube length were calculated using the angiogenesis plugin of Image J software (NIH, Bethesda, MD, USA).

**2.7. Wound Healing Assays.** Migration activity was measured using wound healing assays. ECDHCC cells were seeded into 6-well plates. After the cell density reached 80% confluence, a wound was created by scratching the cell monolayer with a 200  $\mu$ L pipette tip. Wound healing was monitored, and the migration distance was imaged at different time points. Experiments were repeated in triplicate.

**2.8. Flow Cytometry Assessment of Cell Apoptosis.** Cell apoptosis was analyzed by annexin-V/PI. In brief, cells were cultured in a 6-well plate at a density of  $1 \times 10^6$  cells/well and incubated with indicating reagent for 24 h. Cells were then trypsinized and harvested by centrifugation, washed with cold PBS, and resuspended in 200  $\mu$ L binding buffer. Then, cells were stained with annexin-V-fluorescein isothiocyanate (FITC, 0.5  $\mu$ g/mL) and PI (50  $\mu$ g/mL) in the dark for 15 min and analyzed using a flow cytometer (FACScan, Becton-Dickinson, NJ, USA).

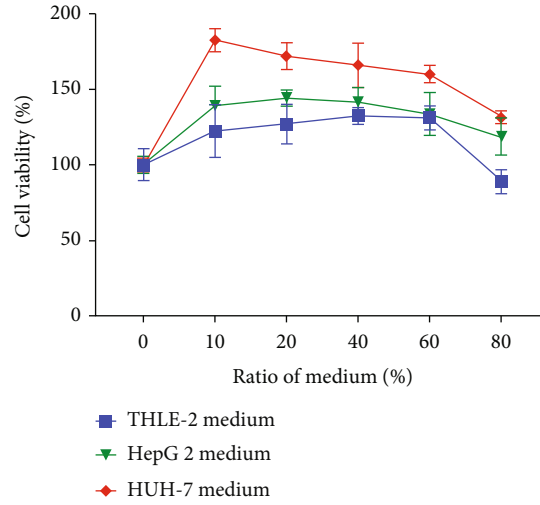
**2.9. Co-Immunoprecipitation (Co-IP).** Cells were washed twice in ice-cold PBS, harvested, and lysed with RIPA lysis buffer (#P0013D, Beyotime, Wuhan, China) for immunoprecipitation experiments. For each sample, 1.5 mg of protein was incubated with protein A+G agarose fast flow (#P2028, Beyotime, Wuhan, China) and anti-DJ-1 rabbit pAb (#382793, 1:1000, ZEN, Wuhan, China). After an overnight incubation at 4°C, the beads were washed, and the final pellet was suspended in RIPA buffer. Bound proteins were eluted from the beads by heating and centrifugation and then analyzed by western blotting analysis.

**2.10. Quantitative Real-Time Polymerase Chain Reaction (qRT-PCR).** Total RNA was extracted by using TRIzol

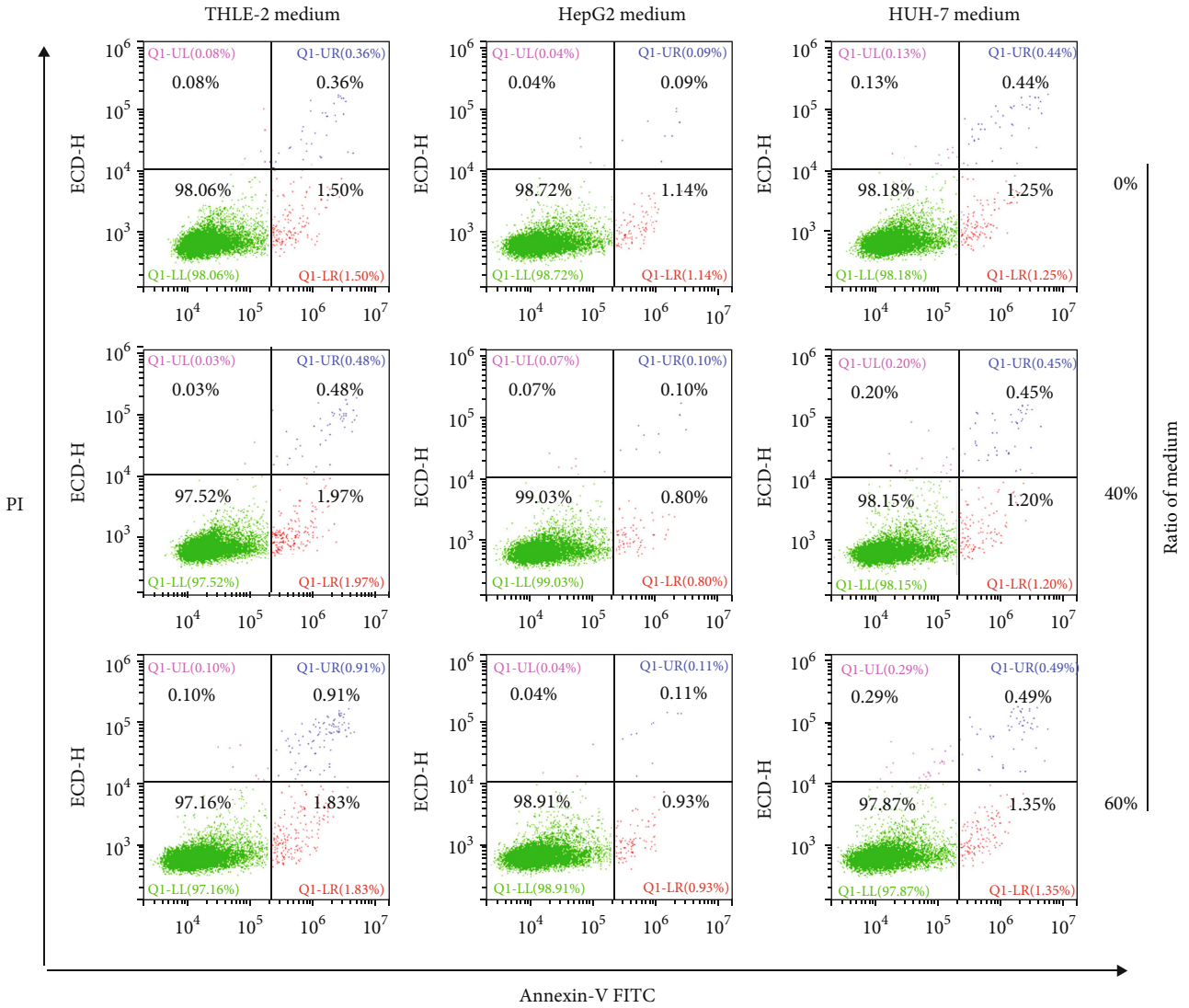
reagent (Takara, Japan). The reverse transcription reaction was performed using 1  $\mu$ g of total RNA that was reverse transcribed into cDNA using oligo(dT) primers. Real-time PCR was carried out using the SYBR Premix Ex Taq (Takara, Japan) according to the manufacturer's protocol with the ABI-7500 (ABI, USA). Briefly, 2  $\mu$ L cDNA template was added to each 20  $\mu$ L reaction with sequence-specific primers: FGFR1 F: 5'-CGG GAC ATT CAC all ATC GA-3', R: 5'-CCG CCC AGA GTG AAG ATC TC-3';  $\beta$ -Actin F: 5'-TGA CGT GGA CAT CCG CAA AG-3', R: 5'-CTG GAA GGT GGA CAG CGA GG-3'.  $\beta$ -Actin was used as an endogenous control to normalize expression data. The cycling conditions comprised initial 10 min polymerase activation at 95°C, followed by 40 cycles at 95°C for 15 s, 60°C for 60 s, and 72°C for 15 min. The FGFR1 transcript levels were quantified using  $2^{-\Delta\Delta CT}$  method [12].

**2.11. Western Blotting Analysis.** Total protein was extracted from cells using the RIPA buffer (PPLYGEN, C1053, China) supplemented with protease inhibitor cocktail (Roche, Switzerland). Western blotting was performed by SDS-PAGE gels and transferred onto polyvinylidene fluoride (PVDF) membranes. After blocking with 5% nonfat milk, membranes were separately probed with primary antibodies. Our primary antibodies are listed below: p-FGFR1-Tyr653/654 mouse mAb (#3476, 1:500, CST, USA), FGFR1 mouse mAb (#60325-1-Ig, 1:1000, Proteintech, USA), p-Akt-S473 rabbit pAb (#AP0140, 1:1000, ABclonal, China), Akt rabbit pAb (#11016, 1:1000, ABclonal, China), p-mTOR-S2448 rabbit pAb (#AP0094, 1:1000, ABclonal, China), mTOR rabbit pAb (#20657-1-AP, 1:1000, Proteintech, USA), p-ERK1/2 (ERK1-T202/Y204+ERK2-T185/Y187) rabbit pAb (#AP0472, 1:1000, ABclonal, China), ERK1/2 rabbit pAb (#16443-1-AP, 1:1000, Proteintech, USA), p-STAT3-Tyr705 rabbit pAb (#381552, 1:1000, ZEN, China), STAT3 rabbit pAb (#A11216, 1:1000, ABclonal, China), cleaved caspase 3 rabbit pAb (#A2156, 1:1000, ABclonal, China), cleaved caspase 9 rabbit pAb (#A2636, 1:1000, ABclonal, China), Bax rabbit pAb (#50599-2-Ig, 1:1000, Proteintech, USA), Bcl-2 rabbit pAb (#12789-1-AP, 1:1000, Proteintech, USA), and GAPDH rabbit mAb (#2118S, 1:1000, CST, USA). After incubation at 4°C overnight, membranes were washed and incubated with appropriate secondary antibody (1:3000, ABclonal, China). The proteins of interest were detected by SuperSignal™ West Pico PLUS Chemiluminescent Substrate (Thermo, USA) using a Gel Imaging System (GE Biosciences, Buckinghamshire, England).

**2.12. Animal Studies.** Nude male mice (5-week-old) were purchased from Beijing Vital River Laboratory Animal Technology Co., Ltd. Our animal studies were performed under the protocols approved by the IACUC of Huazhong University of Science and Technology. Basic procedures have been described previously [13]. In brief, we chose HUH-7/R cell line as our model and design the in vivo experiments with 3 groups: (1) HUH-7/R+control; (2) HUH-7/R+sorafenib+DJ-1; and (3) HUH-7/R+sorafenib+DJ-1+shFGFR1. Cells ( $5 \times 10^6$  cells/injection) were injected subcutaneously into nude mice. We measured tumor growth



(a)



(b)

FIGURE 1: Continued.

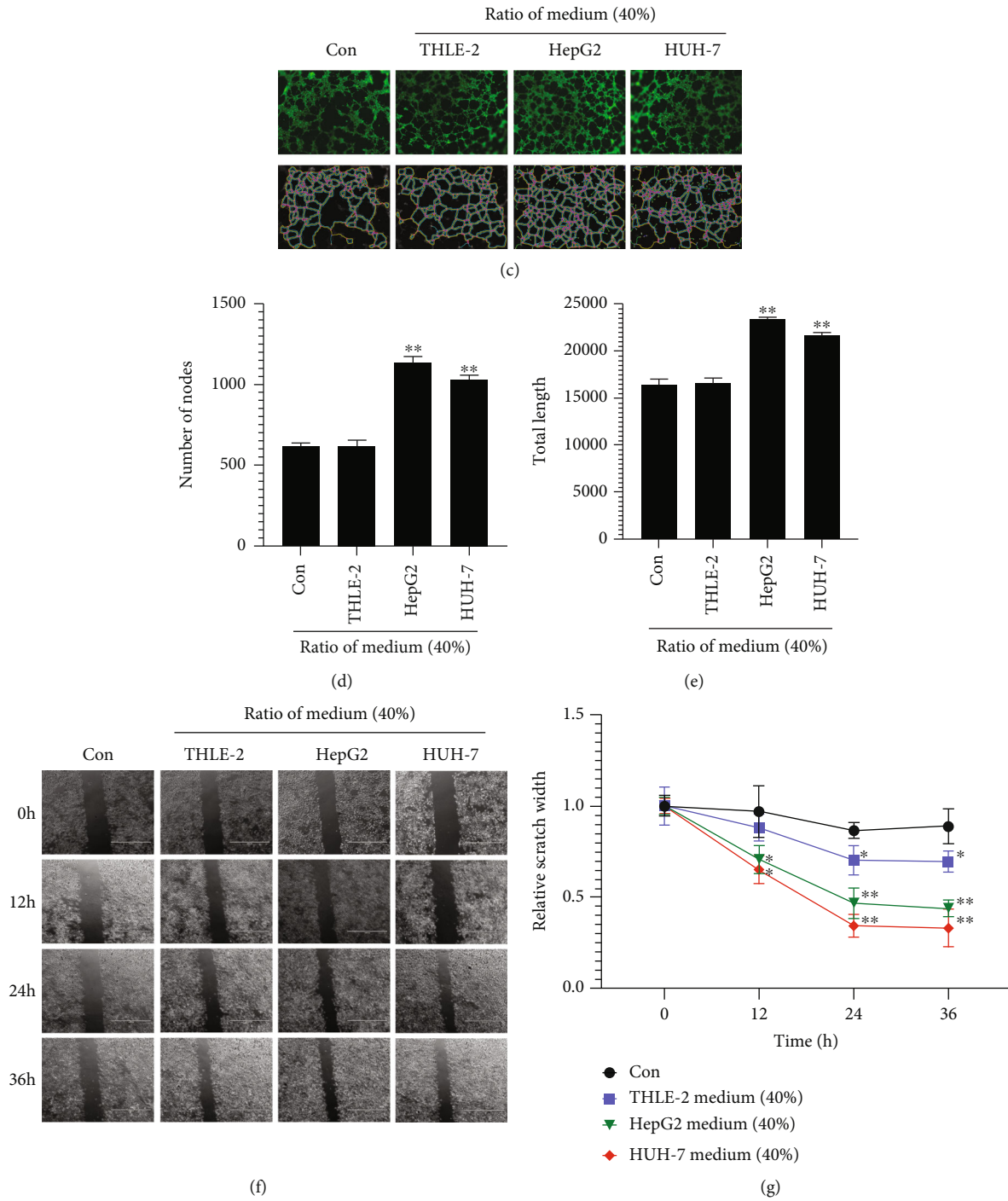


FIGURE 1: Effect of HCC culture medium on biological characteristics of ECDHCC-1 cells. (a and b) Cell viability (a) and cell apoptosis (b) of ECDHCC-1 cells were checked after incubation with HepG2-, HUH-7-, or THLE-2-conditioned media at the indicated ratio to ECDHCC-1 medium. (c–e) Fluorescence microscopy imaging of tube formation (c) and quantification of the number of nodes (d) and total tube length (e) by using tube formation assay utilizing the indicated medium with a 40% ratio to ECDHCC-1 medium were analyzed. (f and g) Wound healing (f) and quantification of the relative scratch width (g) of ECDHCC-1 cells treated with the indicated medium with a 40% ratio to ECDHCC-1 medium were performed. Con: Control group. \* $P < 0.05$  and \*\* $P < 0.01$  versus Con. (original magnifications:  $\times 200$  for fluorescence).



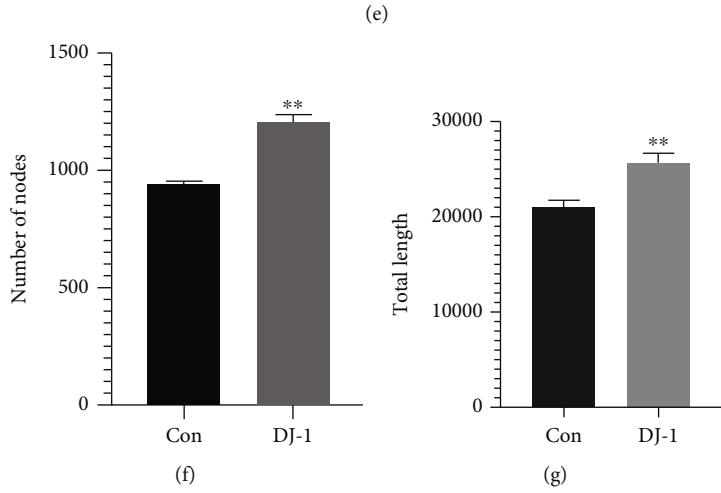
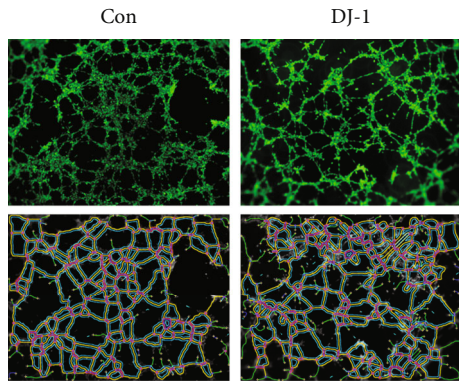
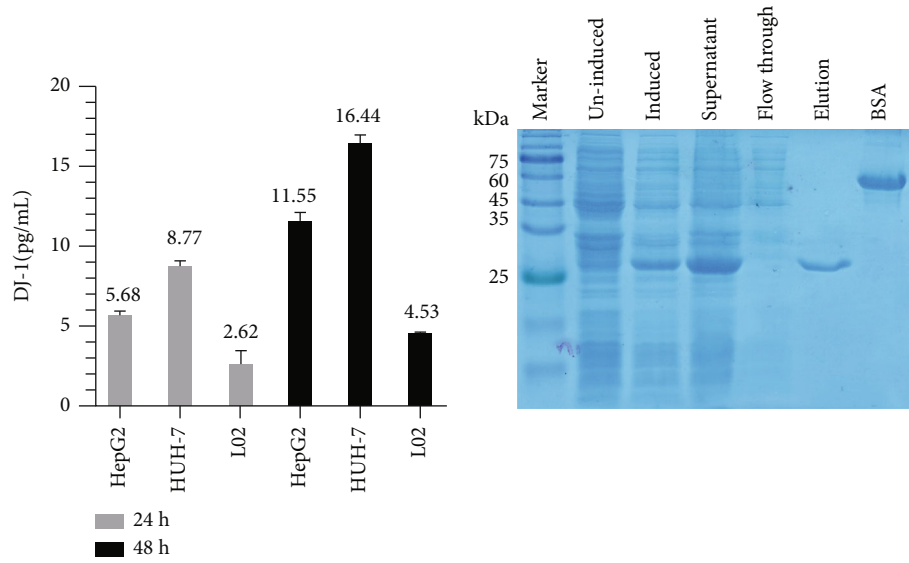


FIGURE 2: Continued.

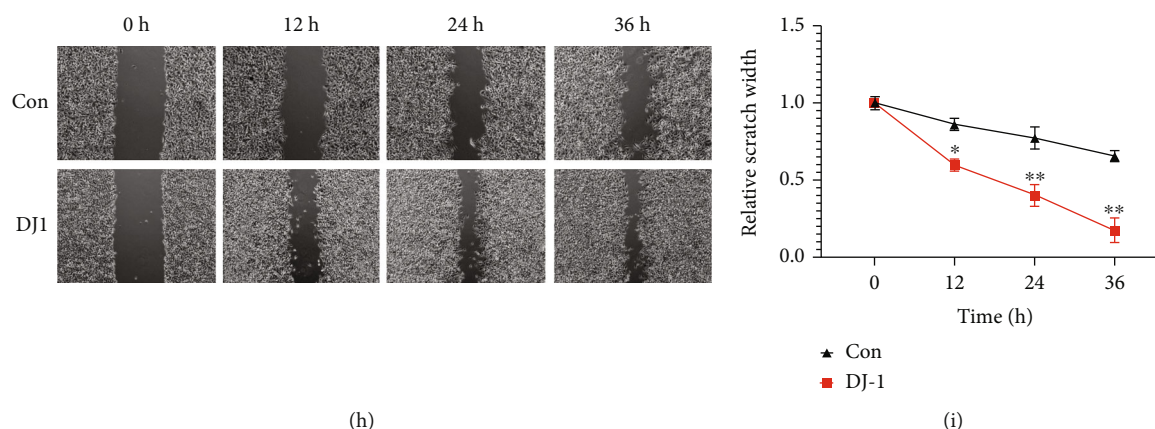


FIGURE 2: DJ-1 induced of angiogenesis and migration in ECDHCC-1 cells. (a) DJ-1 secretion in HCC cells. HepG2 and HUH-7 cells were seeded for culture medium (CM) collection. The CM was harvested and examined by ELISA for DJ-1 expression after 24 and 48 h. (b) Purification of DJ-1 as indicated in the elution lane. (c and d) Product verification of DJ-1 by western blotting analysis with anti-His tag (c) and anti-DJ-1 (d) specific antibody was performed, respectively. (e–g) Fluorescence microscopy imaging of capillary tube formation (e) and quantification of DJ-1 induced tube nodes (f) and tube length (g) using tube formation assay were conducted. (h and i) Wound healing image (h) and quantification of the relative scratch width (i) of ECDHCC-1 cells induced by DJ-1 were analyzed. Con: Control group. \* $P < 0.05$  and \*\* $P < 0.01$  versus Con. (original magnifications:  $\times 200$  for fluorescence).

twice to three times weekly in two dimensions using a digital caliper, and tumor volume was calculated using  $1/2$  (length  $\times$  width<sup>2</sup>). At the end of the experiments, xenograft tumors were harvested, and tumor weight, incidence, and tumor images were recorded.

**2.13. Chicken Chorioallantoic Membrane (CAM) Model.** Basic procedures were performed as previously described [14]. In brief, we used the fertilized chicken eggs that were incubated at 37°C, and the CAM membrane was scored on ~day 10 of embryonic development to remove the top layer of the CAM epithelium.  $2 \times 10^6$  HCC cells (i.e., HUH7 and HUH7/R) were mixed with  $2 \times 10^6$  ECDHCC-1 cells at the ratio of 1:1, which were treated and grouped as follows: (1) mixed cells+control; (2) mixed cells+DJ-1; (3) mixed cells+sorafenib; (4) mixed cells+sorafenib+DJ-1; and (5) mixed cells+sorafenib+DJ-1+shFGFR1. We added finally manipulated cells onto the scored CAM. Chicken embryos were then incubated and maintained at 37°C during the experiments.

**2.14. Statistical Analysis.** Data are presented as mean  $\pm$  SD. Differences were performed using the student's *t*-test for two groups or one-way ANOVA for multiple groups with Bonferroni's post hoc test by use of GraphPad 5.0 software (GraphPad Prism, CA, USA). In all cases,  $P < 0.05$  was considered significant.

### 3. Results

**3.1. HCC Culture Medium Promotes Angiogenesis and Migration of ECDHCC-1 Cells.** To test how HCC cells interact with vascular endothelial cells, we first collected the culture medium from HepG2, HUH-7, and THLE-2 cells, which was added to the culture medium of ECDHCC-1 cells at different ratios. CCK8 assays showed that ECDHCC-1 has

a better cellular growth behavior when HCC or THLE-2 cell culture medium was at 10–60% ratio of ECDHCC-1 cell culture medium (Figure 1(a)), and no apoptotic effect was observed in each culture medium at 40% and 60% ratio (Figure 1(b)). Thus, the conditioned medium was used at a ratio of 40% in the tube formation and wound healing experiments. Our results showed that the numbers of nodes and total tube length increased in the HepG2- and HUH-7-treated group (Figures 1(c)–1(e)), and the migration of ECDHCC-1 cells was increased in the HepG2 and HUH-7 group at 12, 24, and 36 h. There was also a slight increased trend observed in the THLE-2 group at 24 and 36 h (Figures 1(f) and 1(g)). These results suggested that secretory factors in the culture medium of HCC cells may promote angiogenesis and migration of vascular endothelial cells.

**3.2. DJ-1 Could Significantly Induced Angiogenesis and Migration of ECDHCC-1 Cells.** Previous studies have reported that DJ-1 is a soluble protein and may play important roles in neuronal maintenance and oxidative stress as well as cancer progression [15, 16]. To investigate if DJ-1 is one of the secretory factors in HCC cell culture medium and functions to help endothelial cells for their angiogenesis and migration, DJ-1 level in culture medium was assessed by ELISA, and the results showed that DJ-1 was secreted in HepG2, HUH-7, and L02 cells at an average of 5.68, 8.77, and 2.62 pg/mL in 24 h, respectively, and DJ-1 level increased to an average of 11.55, 16.44, and 4.53 pg/mL at 48 h, respectively (Figure 2(a)). Subsequently, the DJ-1 gene was cloned and expressed as a protein with the molecular weight at about 25 kDa. DJ-1 was then purified at a concentration of 0.758 mg/mL at a purity of above 85%, which was verified by western blotting of anti-His tag and anti-DJ-1 specific antibodies (Figures 2(b)–2(d)). Then, cell viability of ECDHCC-1 was assayed by CCK8 assay after treatment

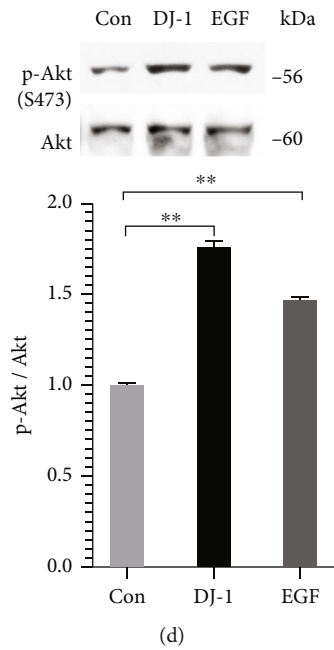
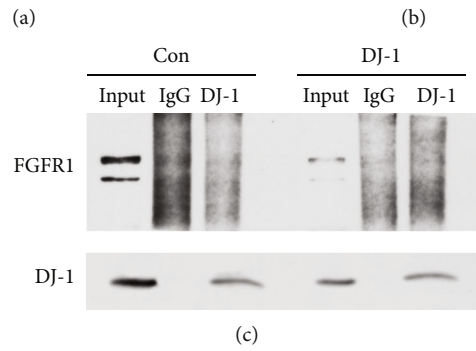
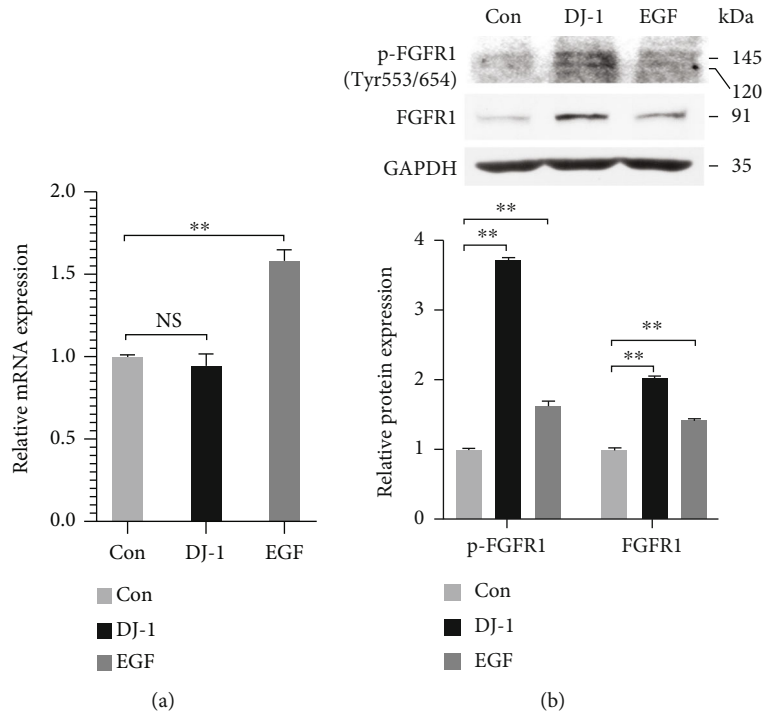


FIGURE 3: Continued.

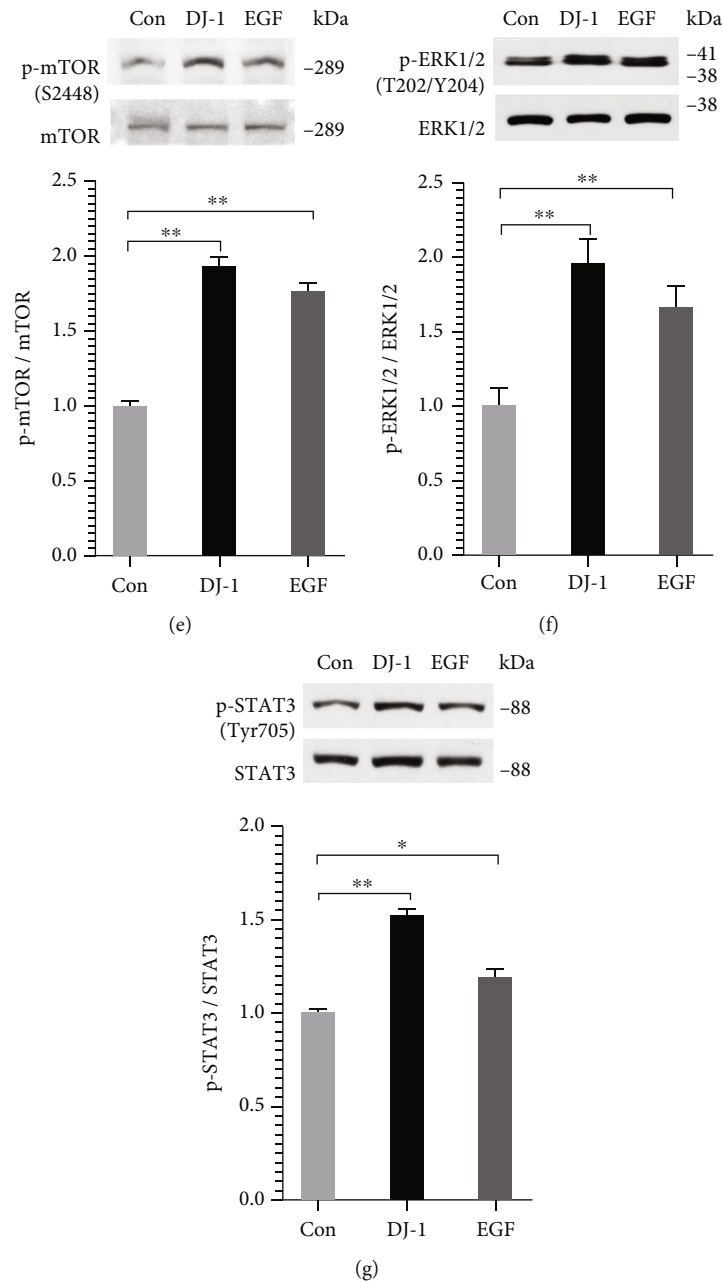


FIGURE 3: DJ-1 induced FGFR1 phosphorylation and activated the Akt, ERK, and STAT signaling pathways in ECDHCC-1 cells. (a and b) Cells were treated with DJ-1 (15  $\mu\text{g}/\text{mL}$ ) for 24 h, and then the mRNA expression of FGFR1 (a) and protein expression of phosphorylated FGFR1 (p-FGFR1) and total FGFR1 (b) were detected by qRT-PCR and western blotting analysis, respectively. The inducing activity of DJ-1 was compared with that of EGF (20  $\text{ng}/\text{mL}$ ). (c) Co-immunoprecipitation assay for FGFR1 and DJ-1 was performed. (d–g) Western blotting analysis of Akt, mTOR, ERK, and STAT3 phosphorylation was conducted. The inducing activity of DJ-1 was compared with that of EGF (20  $\text{ng}/\text{mL}$ ). \* $P < 0.05$  and \*\* $P < 0.01$  versus Con.

by purified DJ-1 at 5, 10, 15, and 20  $\mu\text{g}/\text{mL}$ , respectively, and no significant difference was detected between the treated and untreated groups (data not shown). Thus, purified DJ-1 at the concentration of 15  $\mu\text{g}/\text{mL}$  was used in the following experiments. Interestingly, the results of the tube formation assay revealed a significant induction of angiogenesis as determined by the increased number of nodes and total tube length (Figures 2(e)–2(g)). Meanwhile, cell migration was also enhanced significantly after DJ-1 treatment (Figures 2

(h) and 2(i)). These results suggested that DJ-1 might function as a proangiogenic factor and migration facilitator *in vitro*.

**3.3. The Effect of DJ-1 Is Involved in the Activation of the Akt/mTOR, ERK1/2, and STAT3 Signaling Pathways, Probably Mediated via FGFR1.** DJ-1 induces FGFR1 signaling, which results in angiogenesis in endothelial cells [9]. To explore whether the effect of DJ-1 on angiogenesis of ECDHCC-1

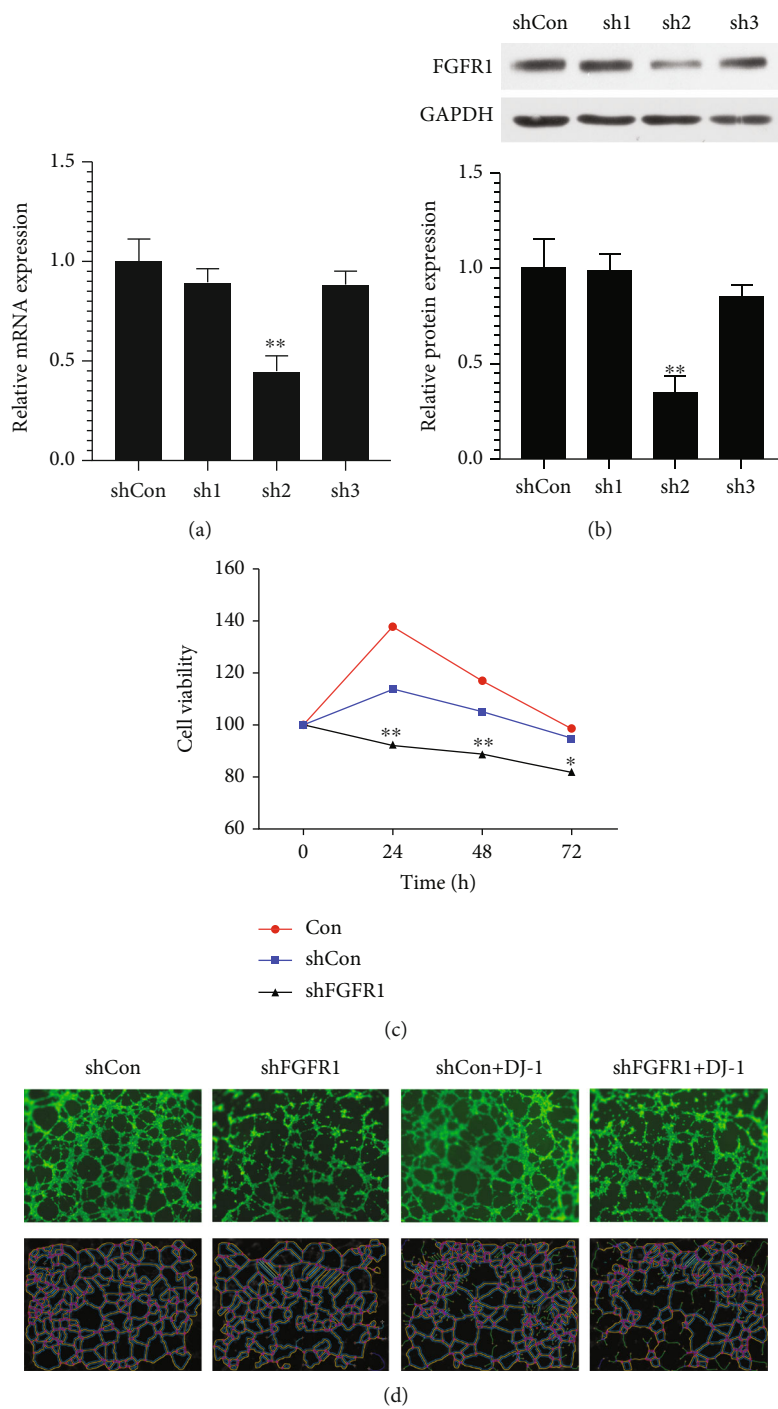


FIGURE 4: Continued.

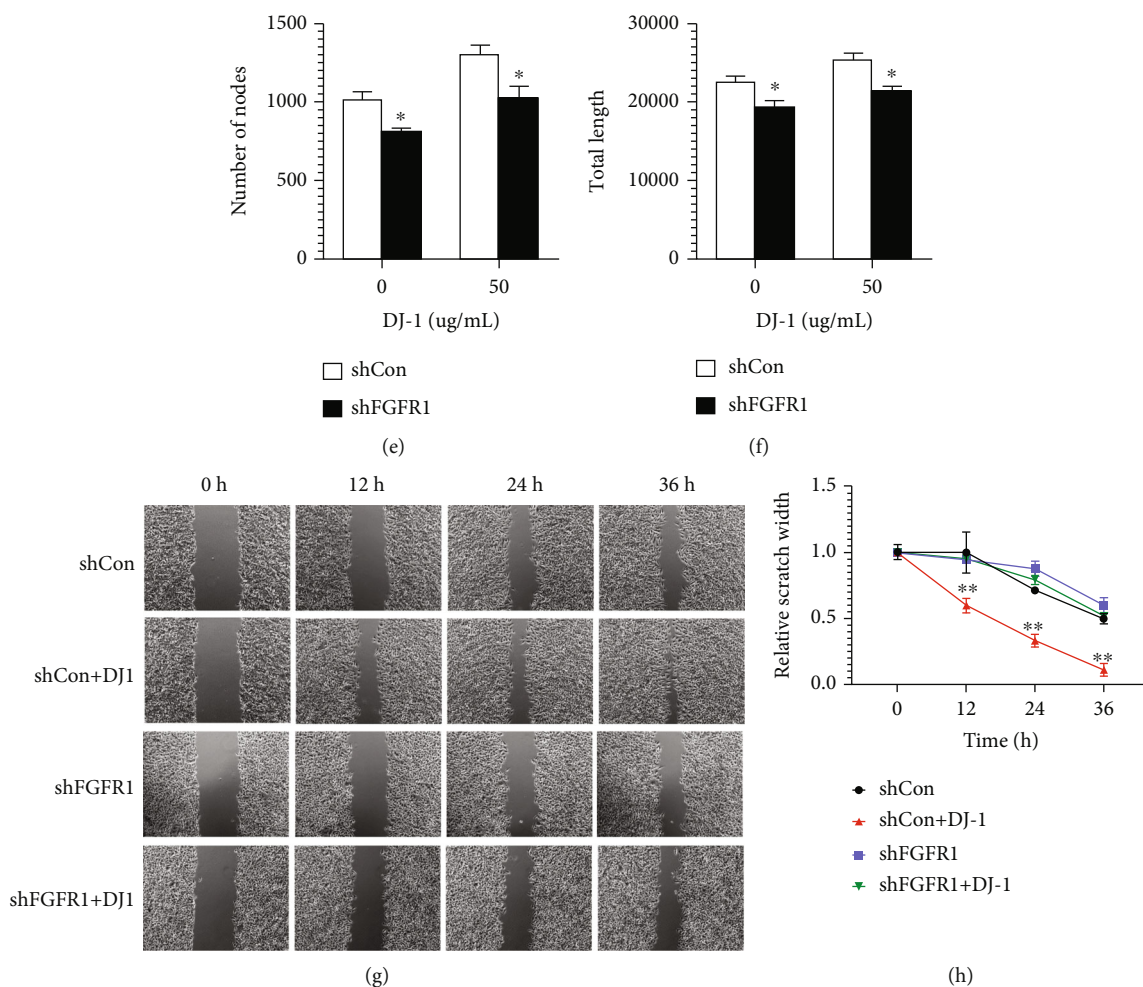


FIGURE 4: Downregulation of FGFR1 inhibited tube formation and migration of ECDHCC-1 cells stimulated by DJ-1. (a) and (b) Knockdown of FGFR1 by shRNA was confirmed by qRT-PCR and western blotting analysis. (c) Cell viability was analyzed by CCK8. (d–f) The effect of FGFR1 knockdown on DJ-1 inducing angiogenesis on ECDHCC-1 cells was assessed for tube formation assay (d), the number of nodes (e), and total length (f) of capillary tube.  $n = 3$  for all groups. (g) and (h) The effect of FGFR1 knockdown on DJ-1 inducing migration on ECDHCC-1 cells was examined. Photographs ( $\times 20$ ) were taken at 12, 24, and 36 h, respectively, after treatment with  $15 \mu\text{g}/\text{mL}$  DJ-1 (g). Relative scratch width was quantified by image J software (h). \* $P < 0.05$  and \*\* $P < 0.01$  versus Con. (original magnifications:  $\times 200$  for fluorescence).

cells was mediated by FGFR1 in our study, the mRNA and protein levels of FGFR1 were detected by qRT-PCR and western blotting, respectively. Our results showed that there was no significant difference in FGFR1 mRNA levels between the control and DJ-1 treatment groups (Figure 3 (a)). However, there was a significant upregulation of protein expression of both p-FGFR1 and total FGFR1 after DJ-1 treatment (Figure 3(b)). Subsequently, a co-immunoprecipitation assay was carried out, but the results showed that there was no direct interaction between DJ-1 and FGFR1 (Figure 3(c)). Moreover, western blotting of the downstream angiogenesis and migration signaling pathways showed that DJ-1 activated Akt/mTOR, ERK1/2, and STAT3 signaling pathways significantly (Figures 3(d)–3 (g)). These results suggested that the effect of DJ-1 on ECDHCC-1 involved activation of Akt/mTOR, ERK1/2,

and STAT3 signaling pathway, which might be mediated, at least partially, by FGFR1.

**3.4. Downregulation of FGFR1 Inhibited the Effect of DJ-1 through Inactivation of Akt/mTOR, ERK1/2, and STAT3 Signaling Pathways.** Furthermore, three FGFR1 shRNA plasmids named sh1, sh2, and sh3 were transfected into ECDHCC-1 cells, respectively. qRT-PCR and western blotting both verified effective downregulation of FGFR1 by the sh2 plasmid (Figures 4(a) and 4(b)). The following experiments were carried out using sh2, which was referred to shFGFR1. CCK8 assay showed that cell viability was decreased after downregulation of FGFR1 (Figure 4(c)). The increased number of nodes and total tube length, as well as migration ability observed after DJ-1 treatment, was all attenuated by knockdown of FGFR1 (Figures 4(d)–4(h)).

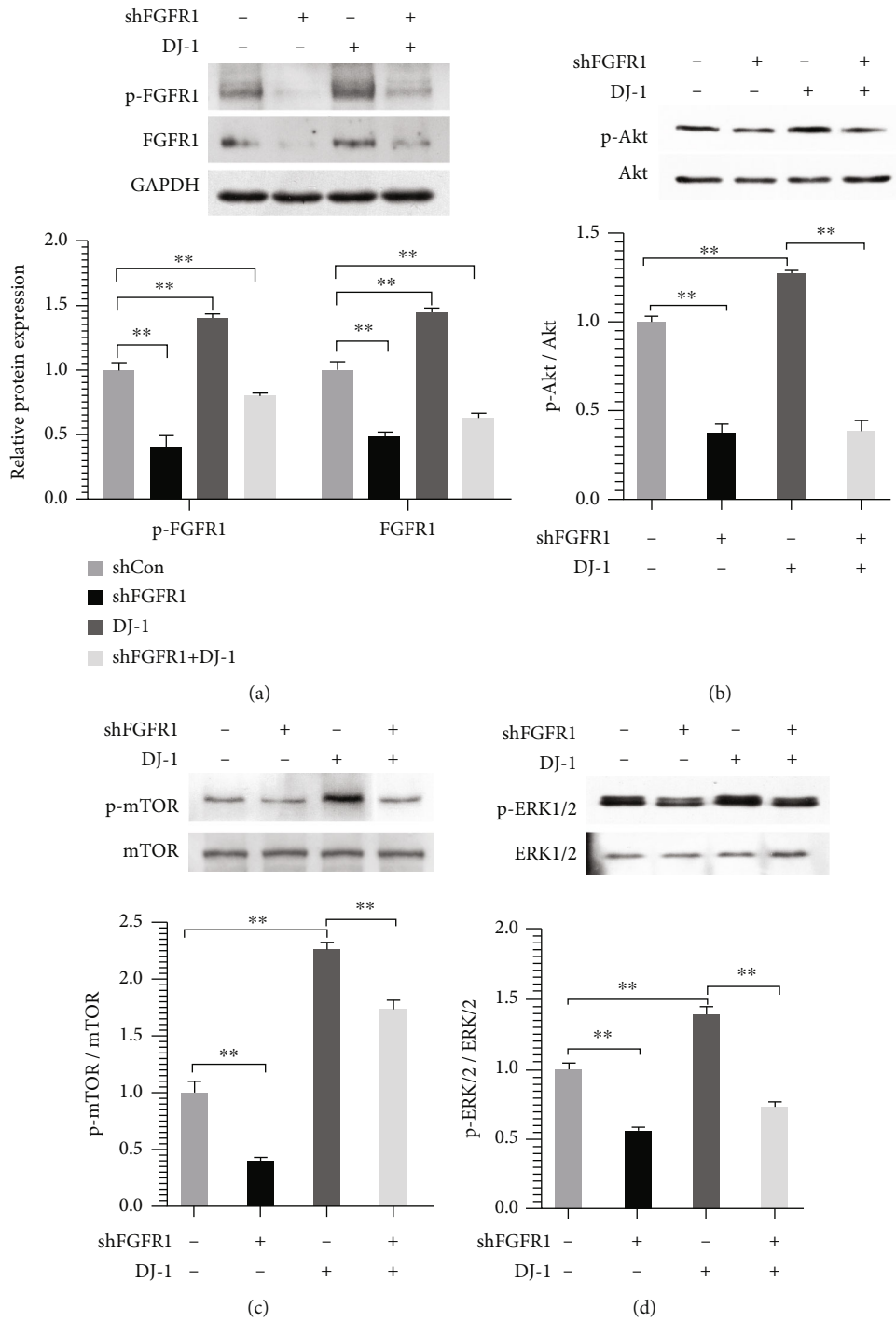


FIGURE 5: Continued.

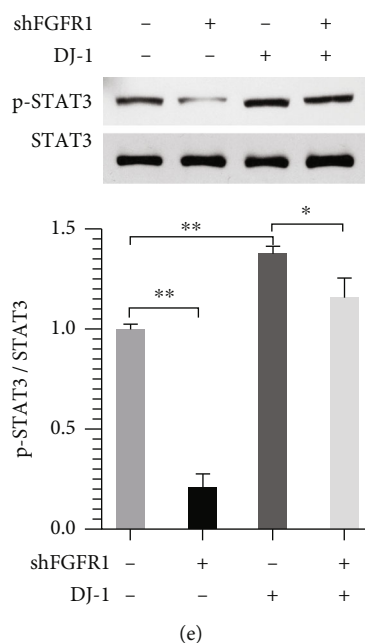


FIGURE 5: Downregulation of FGFR1 attenuated the phosphorylation of FGFR1 and reversed the activity of Akt, ERK, and STAT3 signal induced by DJ-1. Cells with stable knockdown of FGFR1 were treated with or without DJ-1 (15  $\mu\text{g}/\text{mL}$ ) for 24 h, and then, the protein expression of p-FGFR1/FGFR1 (a), p-Akt/Akt (b), p-mTOR/mTOR (c), p-ERK1/2/ERK1/2 (d), and p-STAT3/STAT3 (e) was examined by western blotting, respectively. The empty vector group was used as the control (Con). \* $P < 0.05$  and \*\* $P < 0.01$  versus Con.

Interestingly, while DJ-1 induced upregulation of FGFR1, phosphorylation of AKT/mTOR, ERK1/2, and STAT3 was also reversed after knockdown of FGFR1 (Figures 5(a)–5(e)). These results suggested that the DJ-1 induced angiogenesis and migration in ECDHCC-1, probably mediated via FGFR1.

**3.5. Downregulation of FGFR1 Could Impact on the Survival of Sorafenib-Resistant HCC Cells via Regulating Apoptosis-Associated Molecules.** Cellular sensitivity to sorafenib (1, 2, 5, 10, 20, 50, 100, and 150  $\mu\text{M}$ ) was measured by the CCK8 assay, and the  $\text{IC}_{50}$  was determined as 2.5  $\mu\text{M}$  for THLE-2 cells, 4  $\mu\text{M}$  for HepG2, and 3.5  $\mu\text{M}$  for HUH-7, respectively (Figure 6(a)). The sorafenib-resistant HUH-7 cell line (HUH-7/R) was constructed (Figure 6(b)), and the RI was 1.61. Moreover, the resistant characteristics were verified for the increased expression of P-gp and MRP1 (Figure 6(c)). Compared with HUH-7 cells, the apoptotic cells were decreased in the HUH-7/R group after sorafenib treatment, as well as in the condition treated with sorafenib and DJ-1. However, the apoptotic effect was enhanced in HUH-7/R cells after transient downregulation of FGFR1 after combined treatment with sorafenib and DJ-1, resembling the results observed following HUH-7 cell treatment with sorafenib and DJ-1 (Figures 6(d) and 6(e)). These results suggested that downregulation of FGFR1 could reverse HCC cell resistance to sorafenib to some extent. In addition, after transient downregulation of FGFR1 and combined treatment with sorafenib and DJ-1, the expression of proapoptotic markers, i.e., cleaved caspase 3, cleaved caspase 9, and Bax, was all increased (Figures 6(f)–6(l)), and the expression of the antiapoptotic marker (Bcl-2) was decreased (Figures 6(f)–6(l); Sup-

plementary Figure 1). These results together implied that FGFR1 could affect survival of sorafenib-resistant HCC cells via regulating apoptosis-associated molecules.

**3.6. Targeting FGFR1 Could Suppress Tumor Formation and Angiogenesis of the Sorafenib-Resistant HCC Cells In Vivo.** To further confirm if FGFR1 plays a vital role in sorafenib resistance in HCC cells, we first chose HUH-7/R cell line as our model and treated HUH-7/R cells at different conditions, i.e., vehicle control, sorafenib, sorafenib plus DJ-1, and sorafenib plus DJ-1 and FGFR1 knockdown, where were then injected subcutaneously into immunodeficient mice (i.e., nude mice). In our pilot study, we found that FGFR1 knockdown showed the trend of inhibiting tumor growth of sorafenib-resistant cells on the condition of sorafenib and DJ-1 treatment (Figures 7(a)–7(c)). In support, we applied the chicken chorioallantoic membrane (CAM) model, which has been widely used as an in vivo tool to study tumor angiogenesis and metastasis [17, 18]. In our study, we used HUH-7 cells and HUH-7/R cells and divided them into 5 groups: (a) cells + control treatment; (b) cells + DJ-1; (c) cells + sorafenib; (d) cells + sorafenib + DJ-1; and (e) cells + sorafenib + DJ-1 + shFGFR1. Compared to the control group, we found that (1) DJ-1 overexpression led to the increase of total vessel length and vessel density; (2) sorafenib inhibited angiogenesis of HUH-7 cells by shortening their vessel length, but not the HUH-7/R cells; and (3) FGFR1 knockdown dramatically inhibited angiogenesis of HUH-7/R cells with both sorafenib treatment and DJ-1 overexpression (Figures 7(d) and 7(e)).

At the end of this experiment, we harvested cells from tissues derived in CAM model and checked for their expression



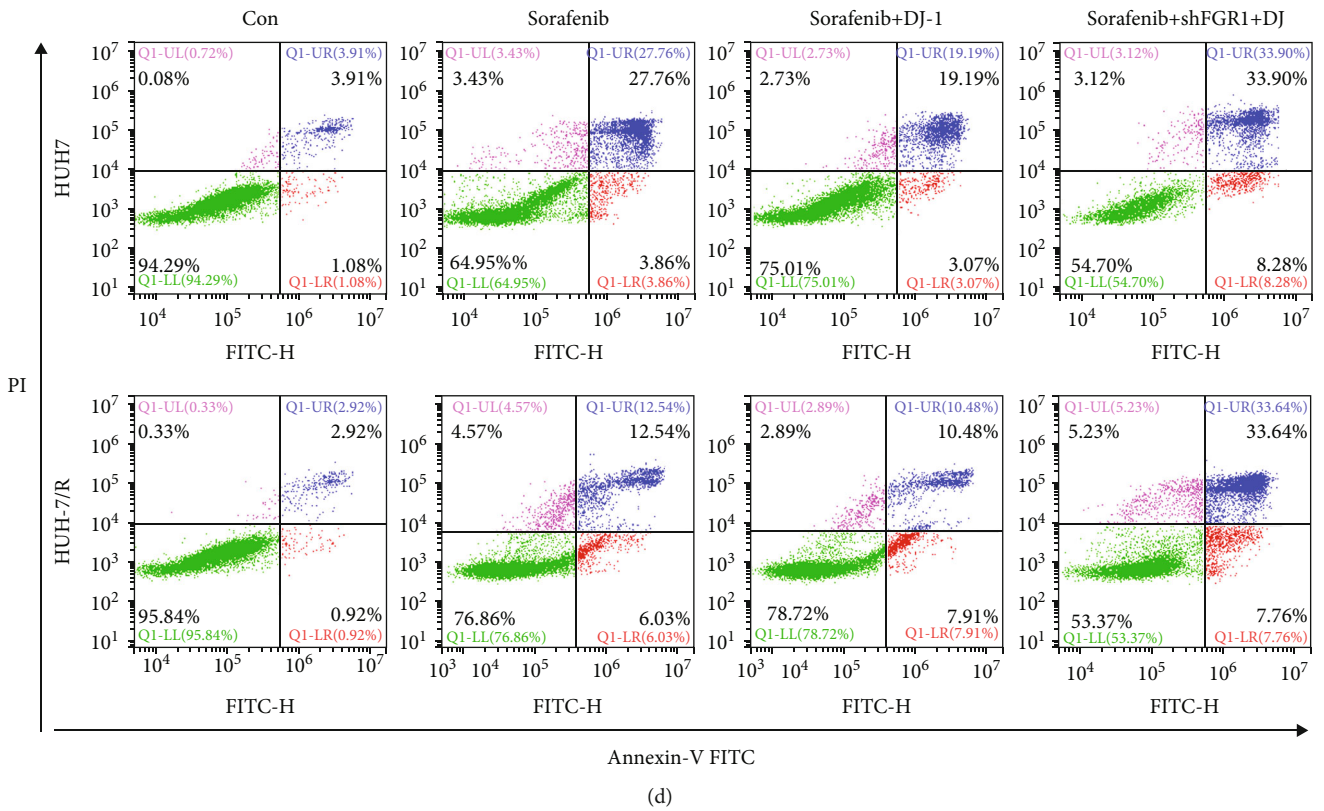
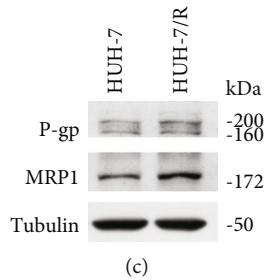
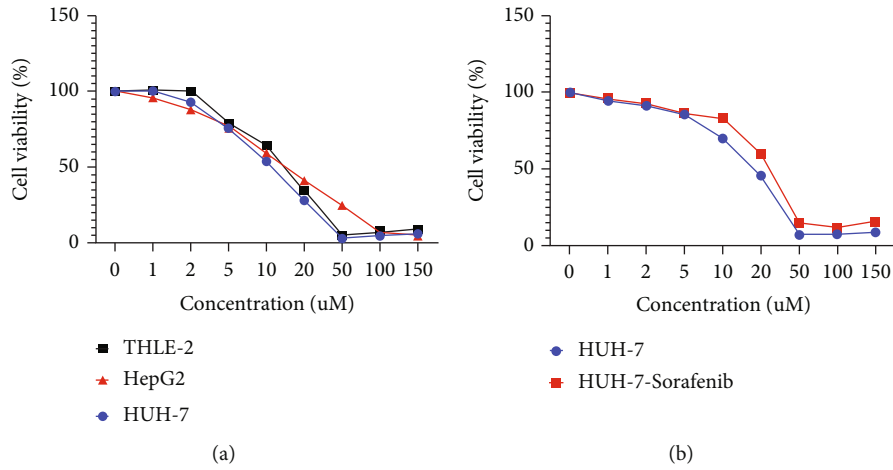


FIGURE 6: Continued.

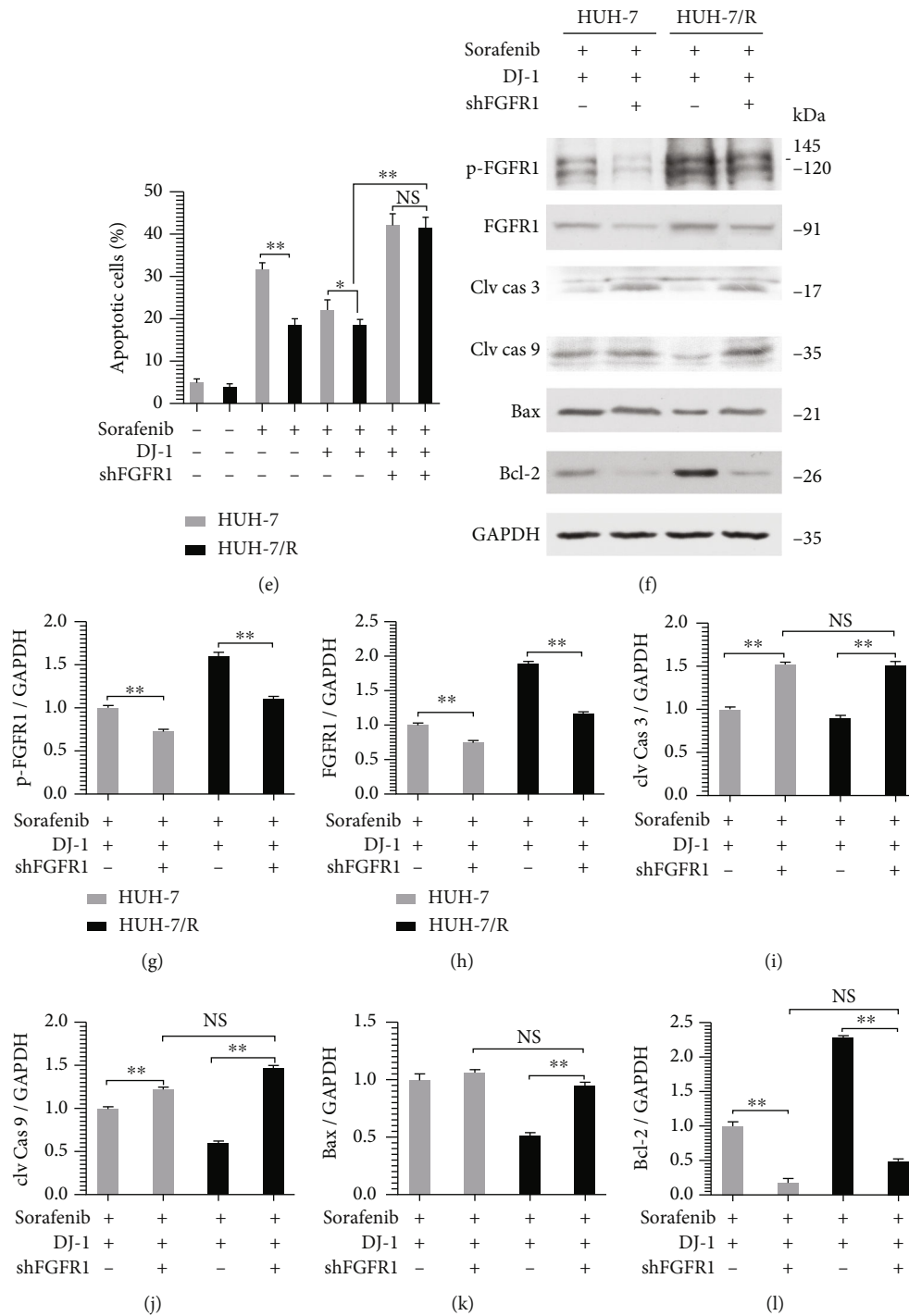
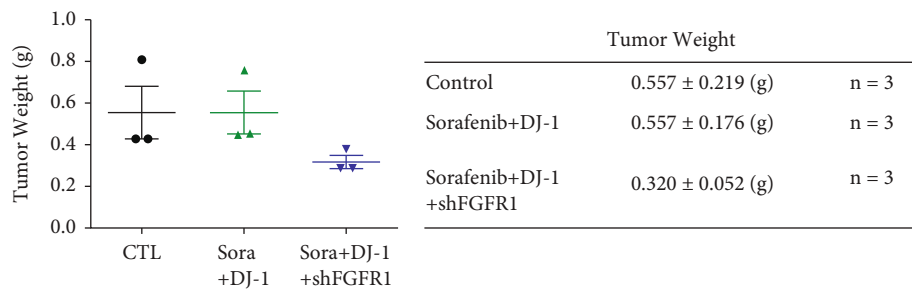
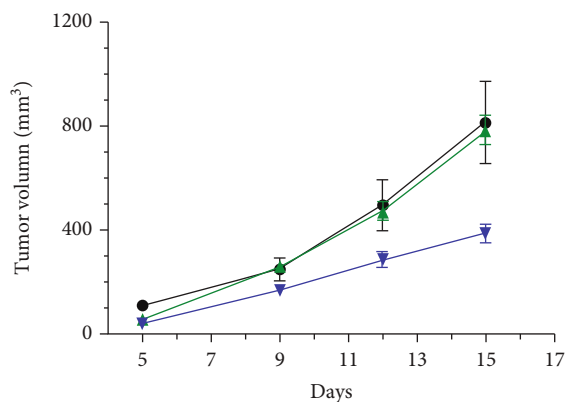


FIGURE 6: Downregulation of FGFR1 affected the apoptosis of sorafenib-resistant HCC cells. (a) Cell viability of THLE-2, HepG2, and HUH-7 after treatment with indicated concentration of sorafenib was assessed by CCK8 assay, and half-maximal inhibitory concentration (IC<sub>50</sub>) was calculated with a linear fit. (b) Sorafenib-resistant HUH-7 cell line (HUH-7/R) was constructed, and the cell viability was assessed to define the resistance index (RI) of the HUH-7/R cell line. (c) Western blotting analysis of multidrug resistance marker of P-gp and MRP1 was detected. (d and e) Flow cytometry assessment of cell apoptosis by annexin-V/PI (d) and two representative groups after transient knockdown of FGFR1 in HUH-7 and HUH-7/R cells was statistically analyzed (e). (f)–(l) Western blotting analysis of p-FGFR1/FGFR1, cleaved caspase 3, cleaved caspase 9, Bax, and Bcl-2 was carried out in HUH-7 and HUH-7/R cells after transient knockdown of FGFR1 and combined treatment with sorafenib and DJ-1. NS: Not significant, \**P* < 0.05 versus DJ-1 group, and \*\**P* < 0.01 versus the vehicle or DJ-1 alone.

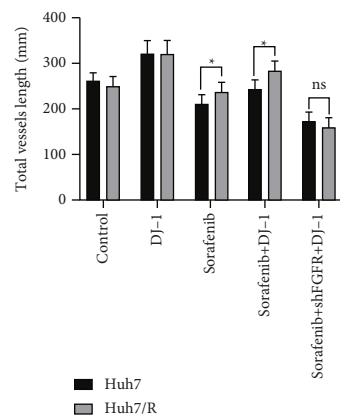
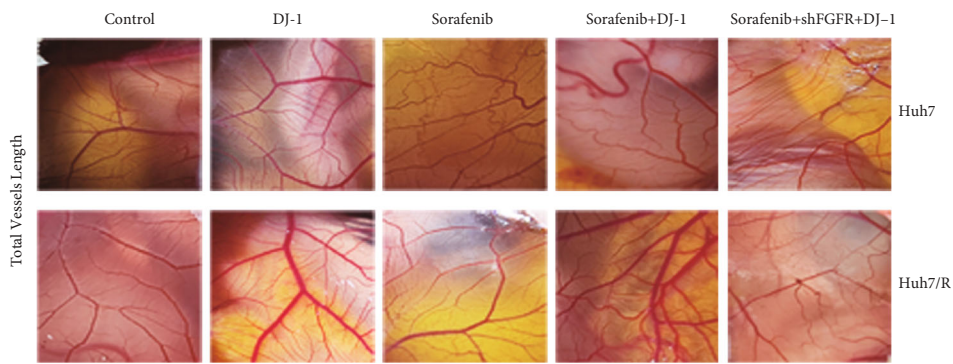


(a)



● Control  
 ▲ Sorafenib+DJ-1  
 ▼ Sorafenib+DJ-1+shFGFR1

(b)



(c)

FIGURE 7: Continued.

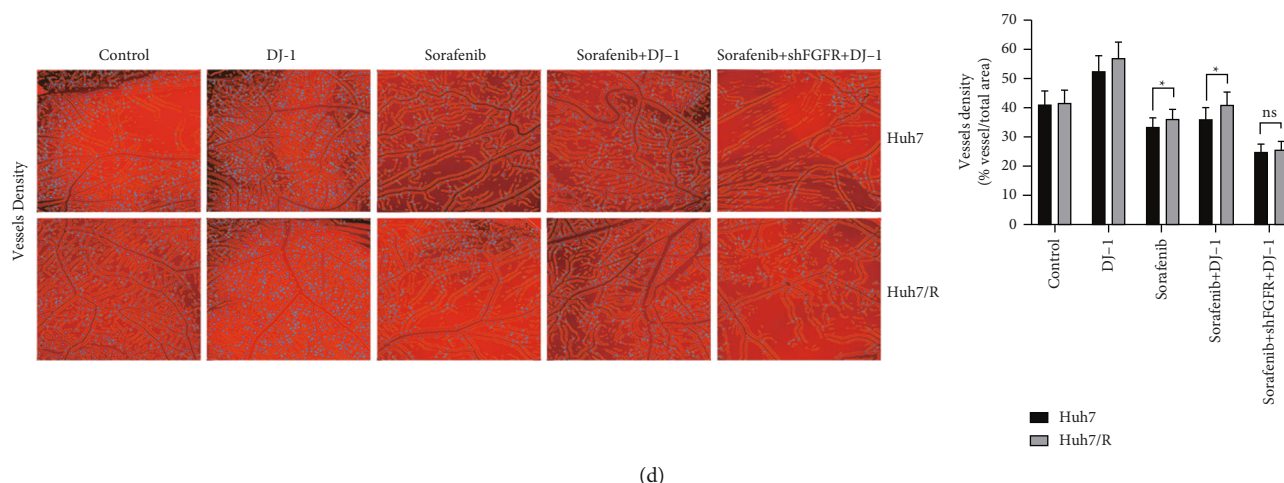


FIGURE 7: FGFR1 knockdown impairs tumor growth and angiogenesis of sorafenib-resistant HCC cells *in vivo*. (a and b) Pilot studies of tumor xenograft experiments were performed for HUH-7/R cells with 3 groups of treatment: i.e., vehicle control; sorafenib+DJ-1; and sorafenib+DJ-1+shFGFR1.  $5 \times 10^6$  cells per injection were injected subcutaneously into two flanks of nude mice ( $n=3$ ), and tumor weight (a) and tumor volume (b) were recorded. Tumor volume was checked twice to three times weekly using a digital caliper. (c and d) Tumor cell angiogenesis was examined in the chicken chorioallantoic membrane (CAM) model. Both HUH-7 and HUH-7/R cells were mixed with ECDHCC-1 cells at the ratio of 1:1 and then treated at different conditions: (1) cells+control; (2) cells+DJ-1; (3) cells+corafenib; (4) cells+sorafenib+DJ-1; and (5) cells+sorafenib+DJ-1+shFGFR1. In CAM model, total vessel length (c) and density (d) were measured at the end of the experiments.

of the FGFR1 and apoptosis-associated molecules (Supplementary Figure 2). Consistently, we found that FGFR1 knockdown could increase the expression of proapoptotic molecules and inhibit the expression of antiapoptotic molecules (Supplementary Figure 2). These data, altogether, suggested that FGFR1 knockdown can reverse sorafenib resistance in HCC *in vivo*.

#### 4. Discussion

In the present study, we isolated and purified DJ-1 secreted by HCC cells and found that DJ-1 could induce the phosphorylation of FGFR1 and promote angiogenesis and migration of ECDHCC-1 cells. The downstream mechanisms of DJ-1/FGFR1 involved the activation of the Akt/mTOR, ERK1/2, and STAT3 signaling pathways. Furthermore, knockdown of FGFR1 inhibited the tube formation and migration of ECDHCC-1 cells stimulated by DJ-1. It also displayed a significant proapoptotic effect comparable to that of sorafenib on nonresistant HCC cells in the presence of DJ-1, which may imply reversal of sorafenib resistance in HCC cells. These findings suggested that extracellular DJ-1 secreted by HCC cells might be a cross-talk regulator between tumor cells and vascular endothelial cells. The inhibition of DJ-1/FGFR1 signaling may be crucial to reverse the resistance of HCC to sorafenib, especially with tumors bearing high levels of DJ-1.

We have reported that DJ-1 expression was significantly upregulated in HCC, and the levels correlated with preoperative AFP, liver cirrhosis, vein invasion, differentiation, and Edmondson grade of HCC. Moreover, both tumor-free survival time and overall survival time in the DJ-1 high expres-

sion group were shorter than those in the low expression group. Hence, DJ-1 was proposed as an independent prognostic factor for overall survival of HCC patients [7]. Additionally, we verified that stable knockdown of DJ-1 decreased proliferation, adhesion, and invasion of HepG2 cells *in vitro* and inhibited the growth of HepG2-induced tumor *in vivo*, suggesting a crucial role for DJ-1 in the oncogenesis of HCC [8].

The curative treatment of resection or liver transplantation is usually applicable for patients diagnosed at an early-stage. For patients diagnosed at an advanced stage of HCC, sorafenib is the first-line choice of systemic therapy. However, almost all HCC patients at the late stages eventually fail in sorafenib treatment due to sorafenib resistance [19]. Our previous study suggested that DJ-1 shRNA effectively reversed the Adriamycin resistance of human breast cancer cells with a 2.68-fold increase in the sensitivity to the Adriamycin [20]. Meanwhile, FGFR, a receptor tyrosine kinase, has been identified as a critical regulator of vascular development, and the activation of FGF/FGFR signaling was considered as the driver of acquired resistance to sorafenib [11]. In the current study, we hypothesized DJ-1 as a cross-talk regulator between HCC cells and vascular endothelial cells. Interestingly, we found that DJ-1 could promote angiogenesis in HCC vascular endothelial cells via activation of FGFR1 in this study, suggesting an important role of DJ-1/FGFR1 signaling in the development of angiogenesis.

It has been reported that sorafenib suppresses tumor angiogenesis and proliferation by inhibiting the signals mediated by serine/threonine kinases, such as Raf/MEK/ERK1/2 cascade, as well as the signals mediated by receptor tyrosine kinases, such as FGFR, VEGFR, and PDGFR. These

kinases are involved in cell proliferation, angiogenesis, and apoptosis [21]. In details, the analysis of *in vitro* experiments reported that there was a strong correlation between the inhibition of the Raf/MEK/ERK1/2 cascade and the anticarcinogenic effect of sorafenib. Inhibition of the VEGFR accounts, at least in part, for the antiangiogenic effects of sorafenib [22]. Moreover, overexpression of FGFR1, the predominant FGFR in endothelial cells, stimulates endothelial cell proliferation [10]. In addition, other signaling pathways are implicated in the initiation and progression of HCC, such as PI3K/Akt/mTOR, JAK/STAT, and the Wnt/ $\beta$ -catenin cascade [23]. Results from previous studies suggested that DJ-1 induced phosphorylation of FGFR1 and activated the FAK and ERK1/2 signaling pathways and resulted in the stimulation of migration and capillary formation of vascular endothelium [9]. Furthermore, we have previously determined that the knockdown of DJ-1 inhibited human HepG2 cell growth and xenograft-induced tumor generation potentially through the Akt signaling pathway [8], and in the present study, we found that DJ-1 induced the activation of downstream Akt/mTOR, ERK1/2, and STAT3 in ECDHCC-1 cells via at least partially FGFR1, which suggested the important role of DJ-1/FGFR1 signaling pathway on the initiation, progression, proliferation, and angiogenesis in HCC vascular endothelium. Hence, DJ-1 antagonizes the therapeutic effect of sorafenib and may lead to therapy resistance. Our results are in the agreement with previous studies which showed that overexpression of DJ-1 can increase the drug resistance of cancer cells including pancreatic cancer [24], nonsmall cell lung cancer (NSCLC) [25], and leukemia [26].

The cytotoxic effect of sorafenib plays a crucial role in antitumor treatment. Generally, apoptosis is the major form of cytotoxicity and it is required for tumor regression and sustained clinical remissions [27–29]. Sorafenib downregulates the antiapoptotic molecules (such as Bcl-2) and increases the expression of proapoptotic molecules, such as Bax and p53-upregulated-modulator-of-apoptosis (PUMA) [29]. Conversely, the oncogenic effect of DJ-1 is mainly attributed to its antiapoptotic ability. In the present study, a sorafenib-resistant HCC cell line HUH-7/R was established. Treatment with DJ-1 inhibited the apoptotic effect of sorafenib in both HUH-7 and HUH-7/R cells. In addition, knockdown of FGFR1 could lead to a proapoptotic effect on HUH-7/R cell line after treatment of sorafenib and DJ-1, with significant upregulation of cleaved caspase 3/9 and Bax and an obvious downregulation of Bcl-2. Importantly, our pilot xenograft experiments showed the trend that FGFR1 knockdown could impair tumor growth of sorafenib-resistant HCC cells in the presence of DJ-1 treatment. Furthermore, our studies in the CAM model revealed that DJ-1 overexpression promoted angiogenesis of sorafenib-resistant HCC cells, but this phenotype could potentially be reversed by FGFR1 knockdown (Figure 7). Altogether, our results suggested that DJ-1/FGFR-1 signaling pathway contribute to sorafenib resistance in HCC, and downregulation of DJ-1/FGFR1 signaling might be a promising strategy to improve the curative effect of sorafenib, especially in those patients with high expression of DJ-1.

Nevertheless, our current studies have some limitations. For example, although our pilot xenograft studies displayed the trend of inhibiting tumorigenicity of sorafenib-resistant HCC cells via FGFR1 knockdown, a large cohort of mouse xenograft study may be needed to verify this phenotype. Also, we propose that DJ-1 is probably one of the factors secreted from culture medium of HCC cells, which may impact the biological features of endothelial cells. Future work involves of high-throughput screening is indispensable to uncover novel molecules that is potentially responsible for sorafenib resistance. Moreover, a genetically engineered model is required to specifically knock out DJ-1, using either DJ-1 conditional knockout mouse model [30] or establishing DJ-1-deleted sorafenib-resistant HCC cells via CRISPER, to provide the direct evidence that DJ-1 is vital in sorafenib resistance in HCC and DJ-1/FGFR1 signaling is a potent target. In addition, detailed mechanisms underlying sorafenib resistance via DJ-1/FGFR1 signaling shall be uncovered in the future directions.

## 5. Conclusion

In summary, the present study hinted that HCC cells may interact with vascular endothelial cells via DJ-1. Moreover, FGFR1 downregulation can impair angiogenesis and tumor growth of sorafenib-resistant HCC cells on the condition of DJ-1. Altogether, our data provide the evidence that DJ-1 and FGFR-1 signaling may be a potential target for treating patients with sorafenib resistance.

## Data Availability

The original contributions presented in the study are included in the article Material. Further inquiries can be directed to the corresponding author.

## Conflicts of Interest

The authors declare that the research was conducted in the absence of any commercial or financial relationships that could be construed as a potential conflict of interest.

## Authors' Contributions

Xiaohong Guo participates in performing the experiments and wrote the manuscript. Xin Chen and Guohua Yang designed the research, helped to interpret the data, and revised the manuscript. Jing Zhang, Wei Sun, Dongbo Liu and Hui Wang conducted the experiments and assisted with the analysis. Shunfang Liu supervised the research. All the authors have read and approved the final manuscript. Xin Chen and Guohua Yang contributed equally to this work.

## Acknowledgments

The present study was supported by the National Natural Science Foundation of China (81602626, 82174020, and 81602592), the Fundamental Research Funds for the Central Universities (2016YXMS111), and Chen Xiao-Ping

Foundation for The Development of Science and Technology of Hubei Province (CXPJH12000001-2020308).

## Supplementary Materials

Figure 1 FGFR1 knockdown increased the expression of proapoptotic markers but impairs the expression of antiapoptotic markers *in vitro*. Western blotting analysis of p-FGFR1/FGFR1, cleaved caspase 3, cleaved caspase 9, Bax, and Bcl-2 was performed for HUH-7/R cells after treatment of DJ-1 and FGFR1 in the presence of sorafenib. Downregulation of FGFR1 led to elevated level of proapoptotic molecules, including caspase 3, cleaved caspase 9, and Bax, but dampened level of antiapoptotic molecule, such as BCL-2. Supplementary Figure 2: knocking down of FGFR1 increased the expression of proapoptotic markers but impairs the expression of antiapoptotic markers in the CAM model. In the CAM model, tissues were harvested at the end of the experiments from each group, which were then checked for the expression of p-FGFR1/FGFR1, cleaved caspase 3, cleaved caspase 9, Bax, and Bcl-2 via western blotting analysis. Consistently, FGFR1 knockdown could induce the expression of proapoptotic molecules (caspase 3, cleaved caspase 9, and Bax) and decrease level of antiapoptotic molecule (BCL-2). (Supplementary Materials)

## References

- [1] N. N. Rahbari, A. Mehrabi, N. M. Mollberg et al., "Hepatocellular carcinoma," *Annals of Surgery*, vol. 253, no. 3, pp. 453–469, 2011.
- [2] E. Adachi, S. Maehara, E. Tsujita et al., "Clinicopathologic risk factors for recurrence after a curative hepatic resection for hepatocellular carcinoma," *Surgery*, vol. 131, no. 1, pp. S148–S152, 2002.
- [3] J. M. Llovet, S. Ricci, V. Mazzaferro et al., "Sorafenib in advanced hepatocellular carcinoma," *The New England Journal of Medicine*, vol. 359, no. 4, pp. 378–390, 2008.
- [4] Y. Hod, S. N. Pentylala, T. C. Whyard, and M. R. El-Maghrabi, "Identification and characterization of a novel protein that regulates RNA-protein interaction," *Journal of Cellular Biochemistry*, vol. 72, no. 3, pp. 435–444, 1999.
- [5] P. V. Raninga, G. D. Trapani, and K. F. Tonissen, "Cross talk between two antioxidant systems, thioredoxin and DJ-1: consequences for cancer," *Oncoscience*, vol. 1, no. 1, pp. 95–110, 2014.
- [6] J. Cao, S. Lou, M. Ying, and B. Yang, "DJ-1 as a human oncogene and potential therapeutic target," *Biochemical Pharmacology*, vol. 93, no. 3, pp. 241–250, 2015.
- [7] S. Liu, Z. Yang, H. Wei et al., "Increased DJ-1 and its prognostic significance in hepatocellular carcinoma," *Hepato-Gastroenterology*, vol. 57, no. 102-103, pp. 1247–1256, 2010.
- [8] S. Liu, G. Long, H. Wei et al., "DJ-1 knockdown inhibits growth and xenograft-induced tumor generation of human hepatocellular carcinoma cells," *Oncology Reports*, vol. 33, no. 1, pp. 201–206, 2015.
- [9] J. M. Kim, H. I. Shin, S. S. Cha et al., "DJ-1 promotes angiogenesis and osteogenesis by activating FGF receptor-1 signaling," *Nature Communications*, vol. 3, no. 1, p. 1296, 2012.
- [10] M. Antoine, W. Wirz, C. G. Tag et al., "Expression pattern of fibroblast growth factors (FGFs), their receptors and antagonists in primary endothelial cells and vascular smooth muscle cells," *Growth Factors*, vol. 23, no. 2, pp. 87–95, 2005.
- [11] V. Tovar, H. Cornella, A. Moeini et al., "Tumour initiating cells and IGF/FGF signalling contribute to sorafenib resistance in hepatocellular carcinoma," *Gut*, vol. 66, no. 3, pp. 530–540, 2017.
- [12] K. J. Livak and T. D. Schmittgen, "Analysis of relative gene expression data using real-time quantitative PCR and the  $2^{-\Delta\Delta C_T}$  method," *Methods*, vol. 25, no. 4, pp. 402–408, 2001.
- [13] X. Chen, Q. Li, X. Liu et al., "Defining a population of stem-like human prostate cancer cells that can generate and propagate castration-resistant prostate cancer," *Clinical Cancer Research*, vol. 22, no. 17, pp. 4505–4516, 2016.
- [14] M. Ishihara, J. Hu, A. Wong, C. Cano-Ruiz, and L. Wu, "Mouse- and patient-derived CAM xenografts for studying metastatic renal cell carcinoma," *Enzyme*, vol. 46, pp. 59–80, 2019.
- [15] S. S. Cha, H. I. Jung, H. Jeon et al., "Crystal structure of filamentous aggregates of human DJ-1 formed in an inorganic phosphate-dependent manner," *The Journal of Biological Chemistry*, vol. 283, no. 49, pp. 34069–34075, 2008.
- [16] J. Cao, X. Chen, L. Jiang et al., "DJ-1 suppresses ferroptosis through preserving the activity of S-adenosyl homocysteine hydrolase," *Nature Communications*, vol. 11, no. 1, p. 1251, 2020.
- [17] F. D. Victorelli, V. M. O. Cardoso, N. N. Ferreira et al., "Chick embryo chorioallantoic membrane as a suitable *in vivo* model to evaluate drug delivery systems for cancer treatment: a review," *European Journal of Pharmaceutics and Biopharmaceutics*, vol. 153, pp. 273–284, 2020.
- [18] S. H. Jiang, S. Zhang, H. Wang, J. L. Xue, and Z. G. Zhang, "Emerging experimental models for assessing perineural invasion in human cancers," *Cancer Letters*, vol. 535, article 215610, 2022.
- [19] J. Chen, R. Jin, J. Zhao et al., "Potential molecular, cellular and microenvironmental mechanism of sorafenib resistance in hepatocellular carcinoma," *Cancer Letters*, vol. 367, no. 1, pp. 1–11, 2015.
- [20] S. Liu, J. Liu, Z. Yang, Q. Yin, X. P. Ma, and J. L. Yi, "DJ-1 shRNA reverses multidrug resistance of human breast cancer Adriamycin resistant cell line MCF-7/ADM," *Chinese Journal of General Surgery*, vol. 19, pp. 1219–1222, 2010.
- [21] G. M. Keating, "Sorafenib: a review in hepatocellular carcinoma," *Targeted Oncology*, vol. 12, no. 2, pp. 243–253, 2017.
- [22] Z. Ezzoukhry, C. Louandre, E. Trécherel et al., "EGFR activation is a potential determinant of primary resistance of hepatocellular carcinoma cells to sorafenib," *International Journal of Cancer*, vol. 131, no. 12, pp. 2961–2969, 2012.
- [23] S. G. Swamy, V. H. Kameshwar, P. B. Shubha et al., "Targeting multiple oncogenic pathways for the treatment of hepatocellular carcinoma," *Targeted Oncology*, vol. 12, no. 1, pp. 1–10, 2017.
- [24] Y. Chen, M. Kang, W. Lu et al., "DJ-1, a novel biomarker and a selected target gene for overcoming chemoresistance in pancreatic cancer," *Journal of Cancer Research and Clinical Oncology*, vol. 138, no. 9, pp. 1463–1474, 2012.
- [25] H. Z. Zeng, Y. Q. Qu, W. J. Zhang, B. Xiu, A. M. Deng, and A. B. Liang, "Proteomic analysis identified DJ-1 as a cisplatin resistant marker in non-small cell lung cancer," *International Journal of Molecular Sciences*, vol. 12, no. 6, pp. 3489–3499, 2011.

- [26] H. Liu, M. Wang, M. Li et al., "Expression and role of DJ-1 in leukemia," *Biochemical and Biophysical Research Communications*, vol. 375, no. 3, pp. 477–483, 2008.
- [27] A. Galmiche, B. Chauffert, and J. C. Barbare, "New biological perspectives for the improvement of the efficacy of sorafenib in hepatocellular carcinoma," *Cancer Letters*, vol. 346, no. 2, pp. 159–162, 2014.
- [28] Z. Zeng, Q. Lu, Y. Liu et al., "Effect of the hypoxia inducible factor on sorafenib resistance of hepatocellular carcinoma," *Frontiers in Oncology*, vol. 11, article 641522, 2021.
- [29] R. Sonntag, N. Gassler, J. M. Bangen, C. Trautwein, and C. Liedtke, "Pro-apoptotic sorafenib signaling in murine hepatocytes depends on malignancy and is associated with PUMA expression \_in vitro\_ and \_in vivo\_," *Cell Death & Disease*, vol. 5, no. 1, article e1030, 2014.
- [30] B. Qiu, J. Wang, Y. Yu et al., "DJ-1 promotes development of DEN-induced hepatocellular carcinoma and proliferation of liver cancer cells," *Oncotarget*, vol. 8, no. 5, pp. 8499–8511, 2017.

## Research Article

# ROS-Related miRNAs Regulate Immune Response and Chemoradiotherapy Sensitivity in Hepatocellular Carcinoma by Comprehensive Analysis and Experiment

Yangtao Xu <sup>1</sup>, Xiaoqin He <sup>1</sup>, Junjian Deng <sup>1</sup>, Lin Xiong <sup>2</sup>, Biao Chen <sup>1</sup>, Jiayu Chen <sup>1</sup>, Xiaoyu Zhang <sup>1</sup>, Wenliang Chen <sup>1</sup>, Xin Liu <sup>1</sup>, Xinyao Hu <sup>1</sup>, Jiayi Li <sup>1</sup>, Shan Jiang <sup>1</sup>, Yang Shen <sup>1</sup> and Ximing Xu <sup>1</sup>

<sup>1</sup>Cancer Center, Renmin Hospital of Wuhan University, Wuhan, Hubei, China 430060

<sup>2</sup>Pathology Department, Renmin Hospital of Wuhan University, Wuhan, Hubei, China 430060

Correspondence should be addressed to Ximing Xu; [doctorxu120@aliyun.com](mailto:doctorxu120@aliyun.com)

Received 4 November 2021; Accepted 9 April 2022; Published 9 May 2022

Academic Editor: Cinzia Signorini

Copyright © 2022 Yangtao Xu et al. This is an open access article distributed under the Creative Commons Attribution License, which permits unrestricted use, distribution, and reproduction in any medium, provided the original work is properly cited.

Reactive oxygen species (ROS) plays an essential role in the development of cancer. Here, we chose ROS-related miRNAs for consensus clustering analysis and ROS score construction. We find that ROS is extremely associated with prognosis, tumor immune microenvironment (TIME), gene mutations, N6-methyladenosine (m6A) methylation, and chemotherapy sensitivity in hepatocellular carcinoma (HCC). Mechanistically, ROS may affect the prognosis of HCC patients in numerous ways. Moreover, miR-210-3p and miR-106a-5p significantly increased the ROS level and stagnated cell cycle at G2/M in HCC; the results were more obvious in cells after ionizing radiation (IR). Finally, the two miRNAs suppressed cell proliferation, migration, and invasion and promoted apoptosis in huh7 and smmc7721 cells. It indicated that ROS might affect the prognosis of HCC patients through immune response and increase the sensitivity of HCC patients to radiotherapy and chemotherapy.

## 1. Introduction

Hepatocellular carcinoma (HCC) is the sixth most frequently diagnosed cancer and the third leading cause of cancer death in the world in 2020 [1, 2]. The incidence of HCC is rising faster than other tumors, and the incidence of HCC in China is more than 10 times that of Europe and the United States, and its mortality rate ranks fifth among cancers [3]. There are many factors contributing to the high incidence of liver cancer, such as alcohol abuse, smoking, metabolic syndrome, and hepatitis virus. Especially in China, hepatitis B virus is the major risk factor for HCC [4]. Due to the insidiousness of the onset of HCC, patients are often diagnosed at an advanced stage. Although immunotherapy has developed rapidly in the past few years, improving the survival of patients with HCC, only a few patients with HCC could benefit from this treatment [5]. Therefore, novel molecular markers with more clinical util-

ity are needed to improve diagnostic and prognostic prediction and guide the clinical treatment of HCC patients.

miRNAs are a group of approximately 21–25 nucleotides length and small endogenous single-stranded noncoding RNAs, which can negatively regulate gene expression via binding to the 3'-untranslated region of messenger RNA (mRNA) [6]. miRNA profiling can be used to predict cancer diagnosis and prognosis, for the pattern of miRNA expression can be correlated with cancer type, stage, and other clinical variables [7].

Recently, reactive oxygen species (ROS) have been shown to promote metastasis in a variety of cancers and play important roles in tissue homeostasis, cellular signaling, differentiation, and survival [8–13]. ROS are pleiotropic molecules or free radicals produced by numerous complex mechanisms. Its excessive production, failure of clearance mechanisms, and even insufficient antioxidants may lead to the accumulation of ROS, ultimately leading to oxidative



stress [14]. Moreover, increasing evidence has suggested that numerous miRNAs have been linked to processes associated with ROS. Wang and colleagues find that significant increases in miR-34a-5p and miR-495-3p are consistent with ROS levels, but miR-34a-5p inhibition is reduced only in intestinal injury [15]. In addition, the research indicates that miR-15b inhibits ROS production by regulating SIRT4 [16]. However, studies of ROS-related miRNAs mainly focus on cardiac diseases, and the mechanism of hypoxia-induced miRNAs in tumors remains not clear.

In this research, we screened 36 ROS-related miRNAs from three reviews [14, 17, 18]. Then, 9 ROS-related miRNAs were selected and used for subsequent analysis. Through comprehensive analysis, ROS score was significantly corrected with prognosis, tumor immune microenvironment (TIME), gene mutations, m6A methylation, and chemotherapy sensitivity in HCC. In the experiments, miR-210-3p and miR-106a-5p extremely increased the ROS level and stagnated cell cycle at G2/M. Collectively, we confirmed the strong correlation between ROS and HCC through bioinformatics and experimental methods.

## 2. Materials and Methods

**2.1. Dataset Source.** The clinical data of HCC patients were downloaded from the University of California Santa Cruz (UCSC, <https://xenabrowser.net/datapages/>). The research included 374 tumor and 50 normal samples. The miRNA expression data of HCC patients were downloaded from the The Cancer Genome Atlas (TCGA) data portal by the “TCGAbiolinks” R package [19]. Furthermore, the mutation data of the TCGA-LIHC was downloaded from the websites (<https://portal.gdc.cancer.gov/>).

**2.2. Identification of Consensus Clustering and Prognosis for ROS-Related miRNAs.** According to the expression levels of 9 ROS-related miRNAs, HCC patients were clustered into different clusters by using R package “ConsensusCluster-Plus” (<http://www.bioconductor.org/>).

**2.3. The Calculation of ROS Scores.** 340 HCC patients were randomly divided into a validation dataset (170 patients) and training dataset (170 patients). Then, LASSO regression and univariate Cox analysis were used to identify five risk signatures, including miR-210-3p, miR-20b-5p, miR-144-5p, miR-106a-5p, and let-7a-5p. Then, the ROS scores were calculated by the formula:  $\text{Ros Score} = \sum_{i=1}^n \text{Coefficient}(\text{miRNA}_i) \times \text{Expression}(\text{miRNA}_i)$ .

**2.4. Cell Culture.** Human HCC huh7 and smmc7721 cell lines were purchased from Procell Life Science & Technology Co., Ltd. (Wuhan, China). The cells were cultured in high-glucose Dulbecco’s modified Eagle’s medium (DMEM) supplemented with 10% fetal bovine serum (FBS; Thermo Fisher Scientific, Inc., Waltham, MA, USA). All cells were cultured in a humidified incubator with 5% CO<sub>2</sub> at 37°C.

**2.5. Cell Transfection.** The minics of miR-210-3p (5’CUGU GCGUGUGACAGCGGCUGA), miR-106a-5p (5’AAAA GUGCUUACAGUGCAGGUAG), and NC (5’UUCUCC

GAACGUGUCACGUTT) were purchased from Suzhou GenePharma Co., Ltd. The Huh7 and Smmc7721 cells were seeded at  $8 \times 10^3$  cells/well in 96-well plates or  $7.5 \times 10^4$  cells/well in 6-well plates for 24 h, and then, the cells were transfected with MiR-210-3p/miR-106a-5p minics and NC minics for 48 h according to the Lipofectamine 3000 kit instructions.

**2.6. Ionizing Radiation.** The huh7 and smmc7721 cells were divided into normal and ionizing radiation groups. The ionizing radiation groups were exposed to 6 Gy X-ray.

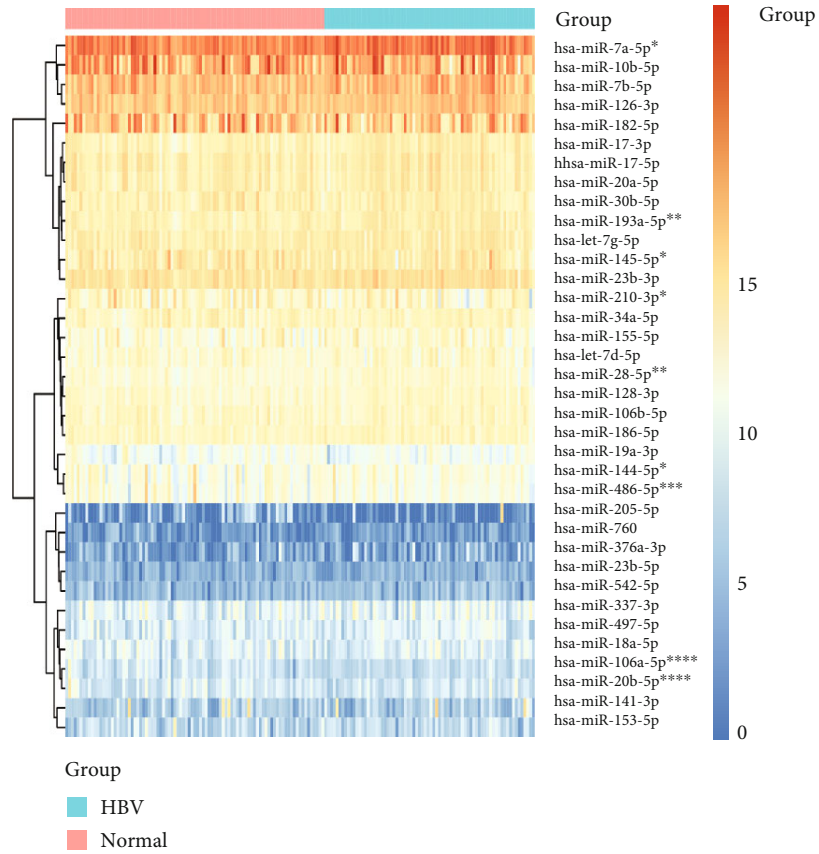
**2.7. qRT-PCR.** qRT-PCR was performed with Hairpin-it™ Real-Time PCR miRNAs (GenePharma). The specific primers, miR-106a-5p and miR-210-3p, were purchased from Suzhou GenePharma Co., Ltd. Thermal cycles were as follows: 95°C for 3 min and 40 cycles of 95°C for 15 s, 62°C for 40 s. Melting curve analysis was used to confirm the specificity of amplification. The relative expressions of miRNAs to SNORD44 were determined using the comparative  $2^{-\Delta\Delta C_t}$  method.

**2.8. Measurement of ROS Production.** Flow cytometry was used to assay ROS levels in Huh7 and Smmc7721 using a ROS assay kit (Shanghai Biyuntian Biological Co., Ltd.). Briefly, the cells were seeded in 6-well plates at a density of  $2.5 \times 10^5$  cells/well for 24 h. Next, the cells were incubated with 10 μM of 2’,7’-dichlorodihydrofluorescein diacetate (DCFH-DA) for 15 min at 37°C in a dark room. A Beckman cytoFLEX flow cytometer was used to detect ROS levels. The data was analyzed by using the CytExpert 2.3 software.

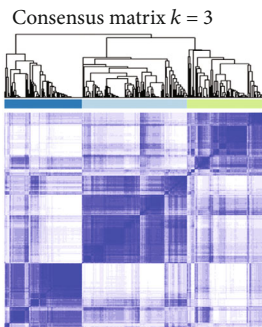
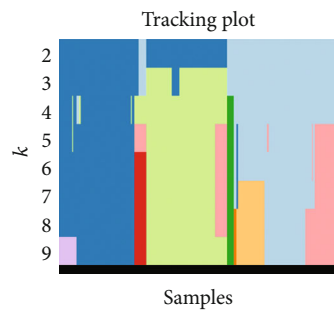
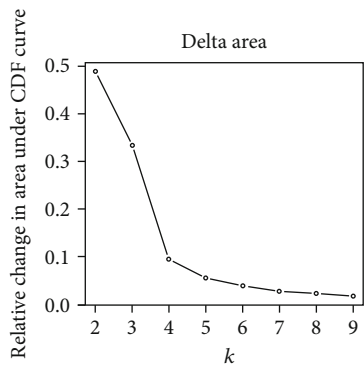
**2.9. Cell Cycle Analysis.** Cell cycle analysis was conducted with a cell cycle staining kit (MultiScience Biotech Co., Ltd.). The transfected cells were seeded in 6-well plates at a density of  $2.5 \times 10^5$  cells/well for 72 h. Then, the cells were collected and incubated with 1 mL of DNA Staining solution and 10 μM of permeabilization solution for 30 min in a dark room. A Beckman cytoFLEX flow cytometer was used to detect the cell cycle. The data was analyzed by using the CytExpert 2.3 software (Beckman Coulter, CA, USA).

**2.10. Transwell Assay.** Transwell assay was conducted to analyze the migrated and invasive abilities of cells. For cell migration, transfected SMMC-7721 and Huh7 cells ( $1 \times 10^4$  cells/well) in 100 μL serum-free DMEM medium were placed in the upper chambers (Costar, Corning, NY, USA), and 500 μL DMEM medium containing 10% FBS was added to the lower chambers. Cells remaining on the top surface were removed with a cotton swab after the incubation for 24 h, while migrated cells through the membranes were fixed with 4% paraformaldehyde and stained with 0.1% crystal violet (Sigma, St. Louis, MO, USA). The stained cells were counted from five random fields under a microscope. For cell invasion, the experiment was performed following the same approach using transwell chambers pretreated with Matrigel (BD, San Jose, CA, USA).

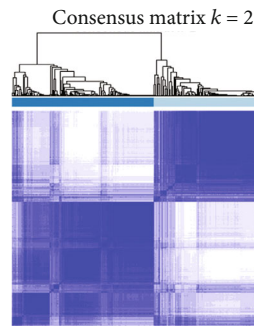
**2.11. Cell Proliferation Test.** The transfected cells ( $7 \times 10^3$ ) were seeded in 96-well plates; cell proliferation was assessed



(a)

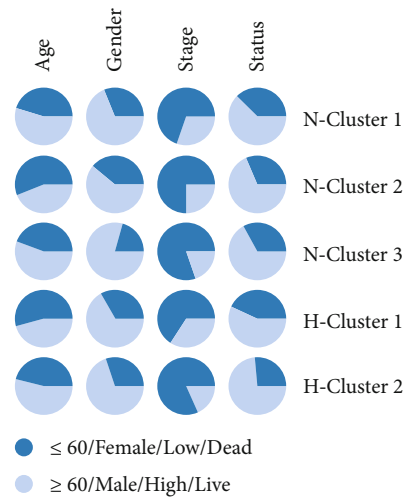


- 1
- 2
- 3



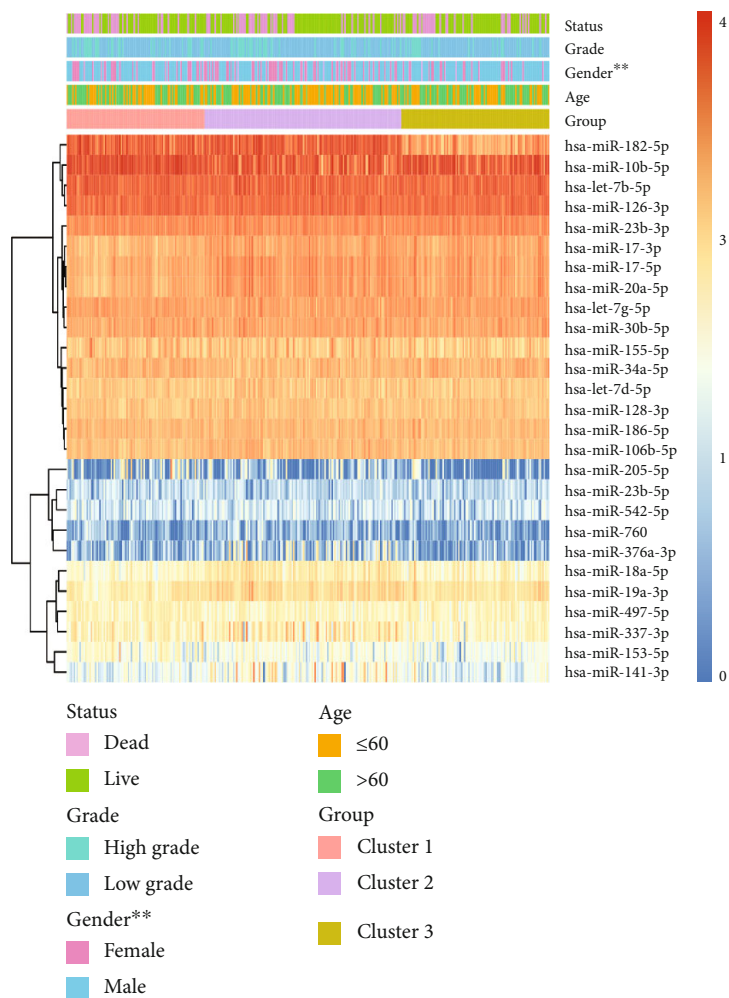
- 1
- 2

(b)



(c)

FIGURE 1: Continued.



(d)

FIGURE 1: Continued.

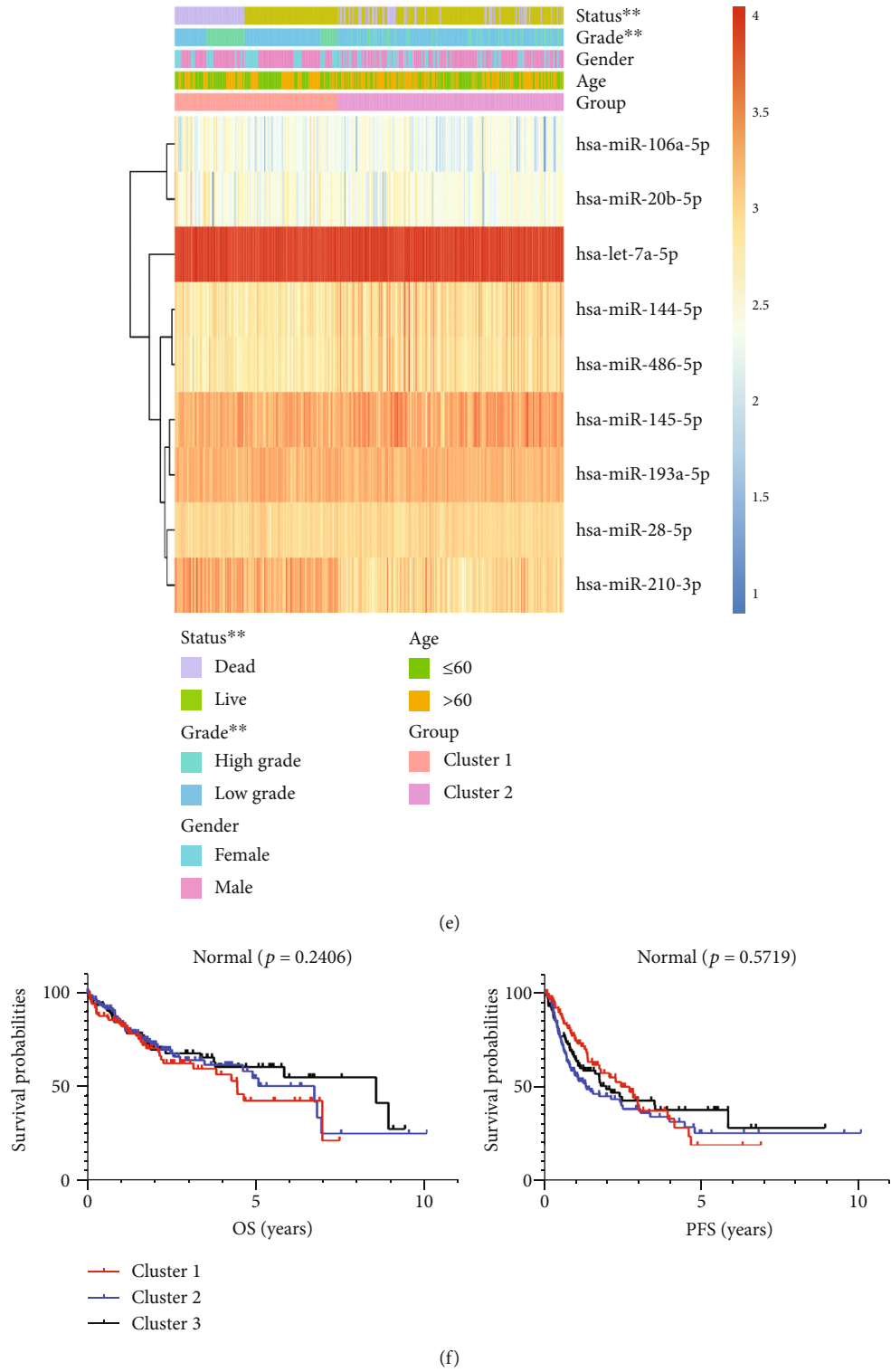


FIGURE 1: Continued.

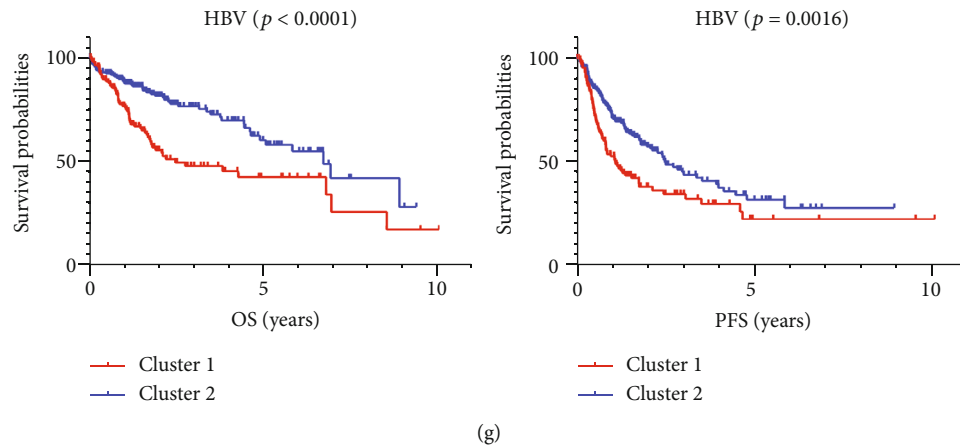


FIGURE 1: Consensus clustering for HBV- and none HBV-related ROS miRNAs with the clinical features and survival of HCC patients. (a) Expression levels of ROS-related miRNAs in HBV and normal samples. (b) Consensus clustering for HBV- and none HBV-related ROS miRNAs. (c) The proportion of clinical features in cluster types. (d) Clinical features in cluster1/2/3 for none HBV-related ROS miRNAs. (e) Clinical features in cluster1/2/3 for HBV-related ROS miRNAs. (f) Prognosis of cluster1/2/3. (g) Prognosis of cluster1/2. \* $p < 0.05$ , \*\* $p < 0.01$ , \*\*\* $p < 0.001$ , and \*\*\*\* $p < 0.0001$ .

by the CCK8 reagent (Sigma-Aldrich) which was read from culture media at 450 nm (ELx800 Microplate Reader, BioTek Instruments, Winooski, VT, USA) at 0, 24, 48, and 72 h. Cell proliferation was expressed relative to the corresponding control.

**2.12. Wound Healing Assay.** The transfected cells were seeded in 6-well plates at a density of  $2.5 \times 10^5$  cells/well for 72 h, then draw a wound between the dense cells with a 200  $\mu$ L gun head. The gap closure was monitored under the microscope and a digital camera (CK30-SLP; Olympus, Tokyo, Japan) at 0, 24, and 48 h. Images were analyzed using the ImageJ version 1.52a software (National Institute of Health, Bethesda, MD, USA).

**2.13. Cell Apoptosis Analysis.** Apoptosis was assayed using the annexin V–phycoerythrin (PE)/7-aminoactinomycin D (7-AAD) or annexin V–adenomatous polyposis coli (APC)/7-AAD kit (Becton-Dickinson). The transfected cells were rinsed with ice-cold PBS and resuspended in 100  $\mu$ L of  $1 \times$  binding buffer. Then, the liquid was stained with 5  $\mu$ L 7-AAD and 5  $\mu$ L annexin V–APC/PE and incubated for 15 min in the dark. Then, another 400  $\mu$ L binding buffer was added into the mixture before cell apoptosis was detected on a Beckman cytoFLEX flow cytometer. The analysis of the above data was carried out using the CytExpert 2.3 software (Beckman Coulter, CA, USA).

**2.14. Statistical Analysis.** Statistical tests were carried out using GraphPad Prism 8.0 (GraphPad Software Inc., San Diego, CA, USA) and R version 4.0.2 (version 4.0.2, <https://www.r-project.org/>). “TCGAbiolinks,” “ConsensusClusterPlus,” “survival,” “glmnet,” “estimate,” “pRRophetic,” “maftools,” “edgeR,” and “timeROC” R packages were used.

### 3. Results

**3.1. HBV-Related ROS miRNAs Were Significantly Associated with Clinical Features in HCC.** Experimental evidences indicate that HBV X protein could cause DNA mutation through ROS generation [20]. To optimize the 36 ROS-related miRNAs, the difference of miRNAs between HBV patients and normal patients was further analyzed. As showed in Figure 1(a), 9 ROS miRNAs were significantly correlated with HBV, including miR-210-3p, miR-20b-5p, miR-144-5p, miR-106a-5p, miR-486-5p, miR-28-5p, miR-139a-5p, miR-145-5p, and let-7a-5p. Furthermore, according to the similarity between the expression level of m6A regulators and the proportion of fuzzy clustering measures, it is determined that  $k = 2$  has the best clustering stability from  $k = 2$  to 9, (Figure 1(b) and S1). HCC patients were clustered into cluster1 ( $n = 142$ ) and cluster2 ( $n = 197$ ), based on the expression levels of 9 HBV-related ROS miRNAs. Interestingly, we found that cluster1 was significantly associated with high grade, dead patients, and bad prognosis (Figures 1(e) and 1(g)). Also, HCC patients were clustered into cluster1 ( $n = 97$ ), cluster2 ( $n = 138$ ), and cluster3 ( $n = 104$ ), according to the expression levels of 27 none HBV-related ROS miRNAs (Figure 1(b) and S2). However, the grade, status, and prognosis of HCC patients were not significantly different in cluster1/2/3 (Figures 1(c), 1(d), and 1(f)). The results showed that 9 HBV-related ROS miRNAs were more significant than to none HBV-related ROS miRNAs in HCC.

**3.2. Correction between ROS Score and Clinical Features in HCC.** Firstly, 340 HCC patients were randomly divided into a validation dataset (170 patients) and training dataset (170 patients). Then, 5 candidate HBV-related ROS miRNAs were selected to calculate ROS score by using LASSO regression in the training dataset (Figure 2(a)). According to the expression of the candidate HBV-related ROS miRNAs,

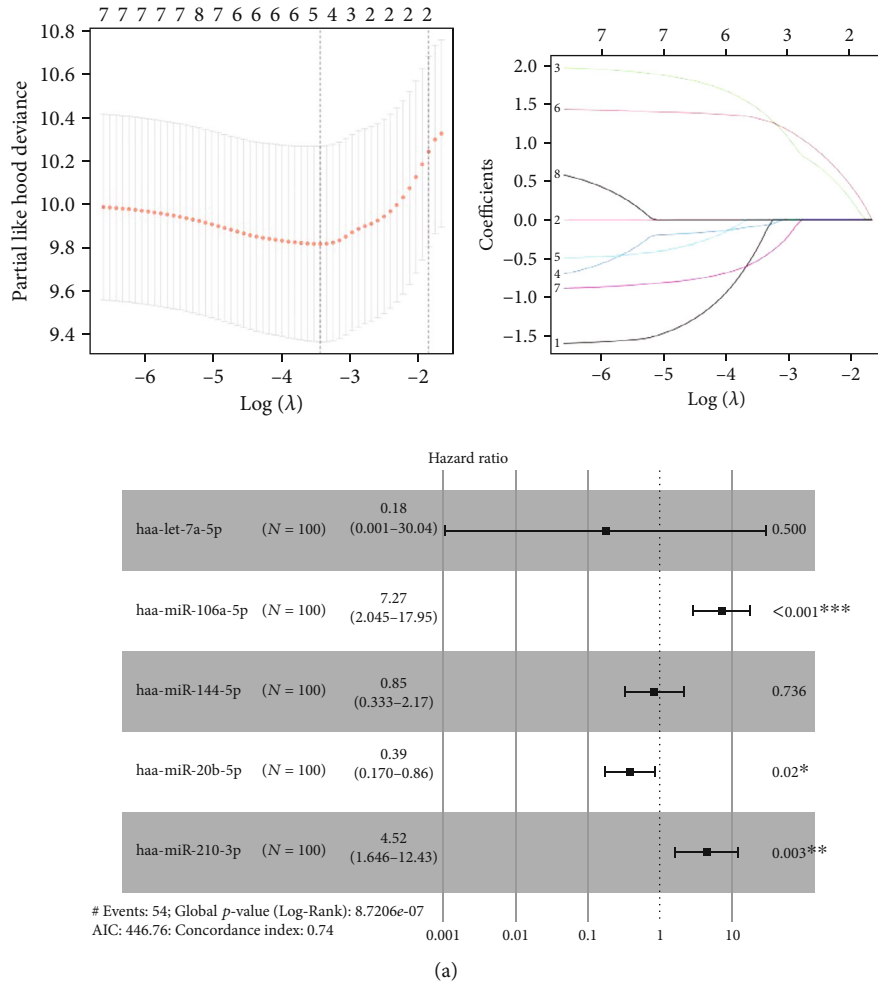


FIGURE 2: Continued.

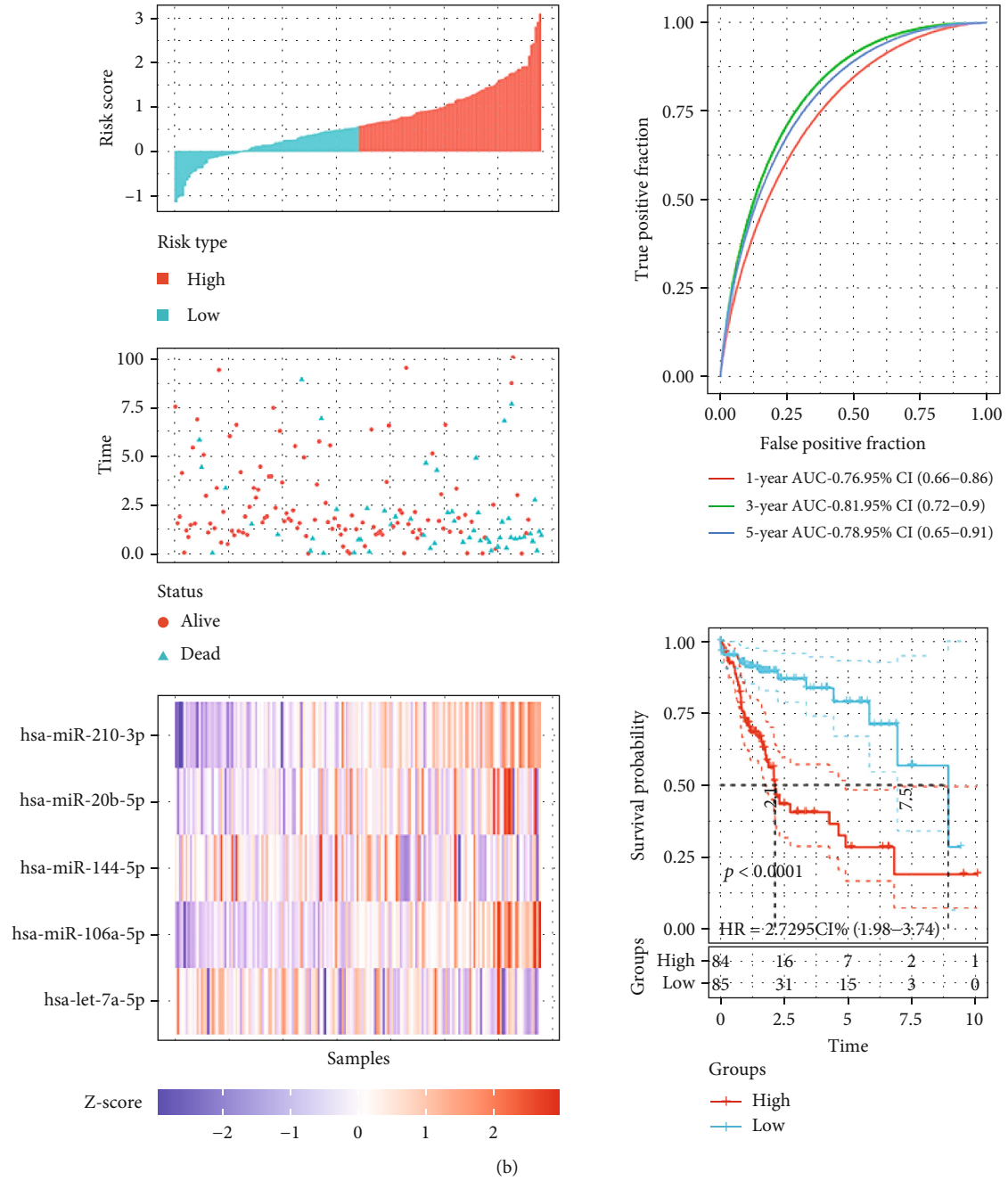


FIGURE 2: Continued.

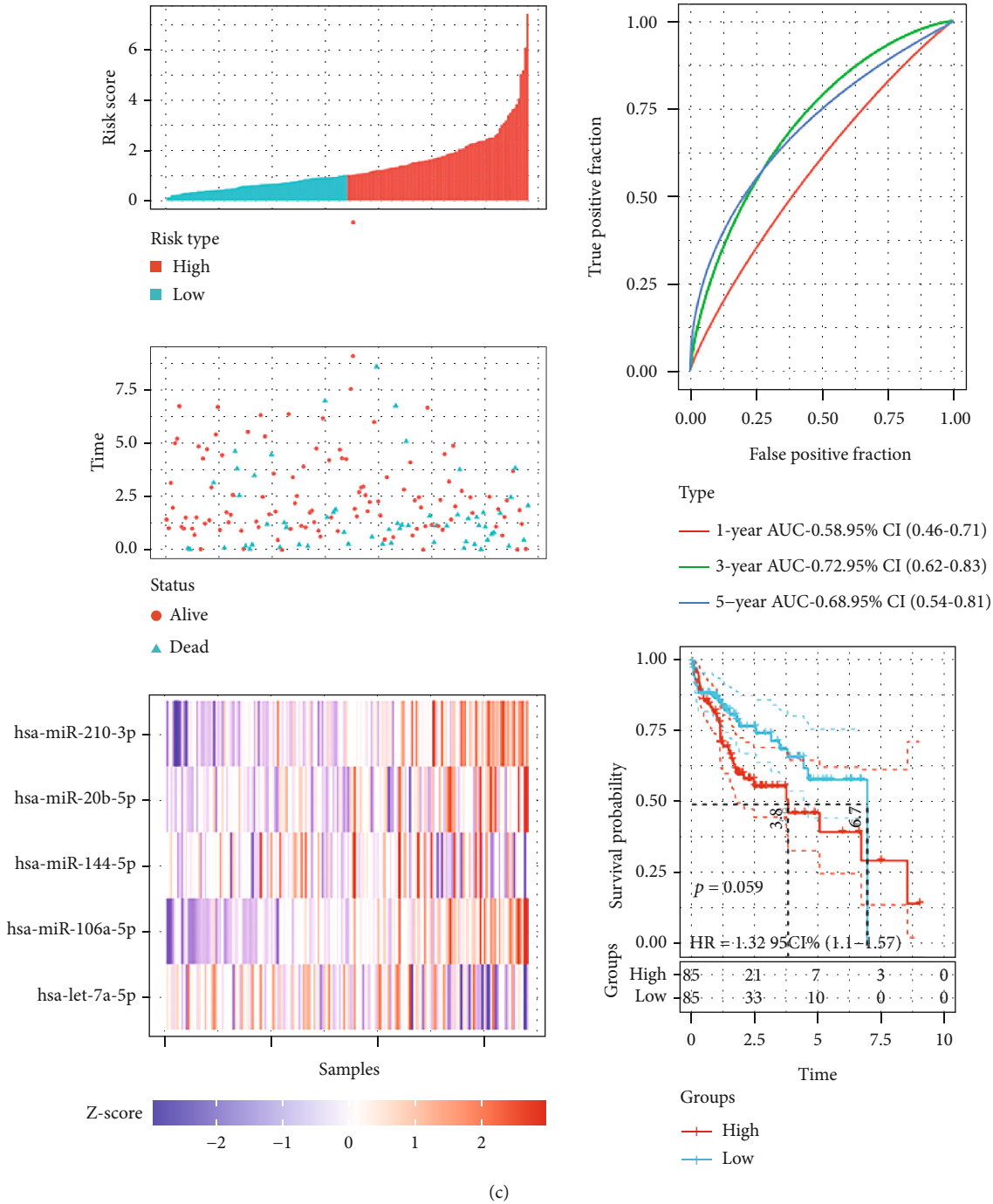


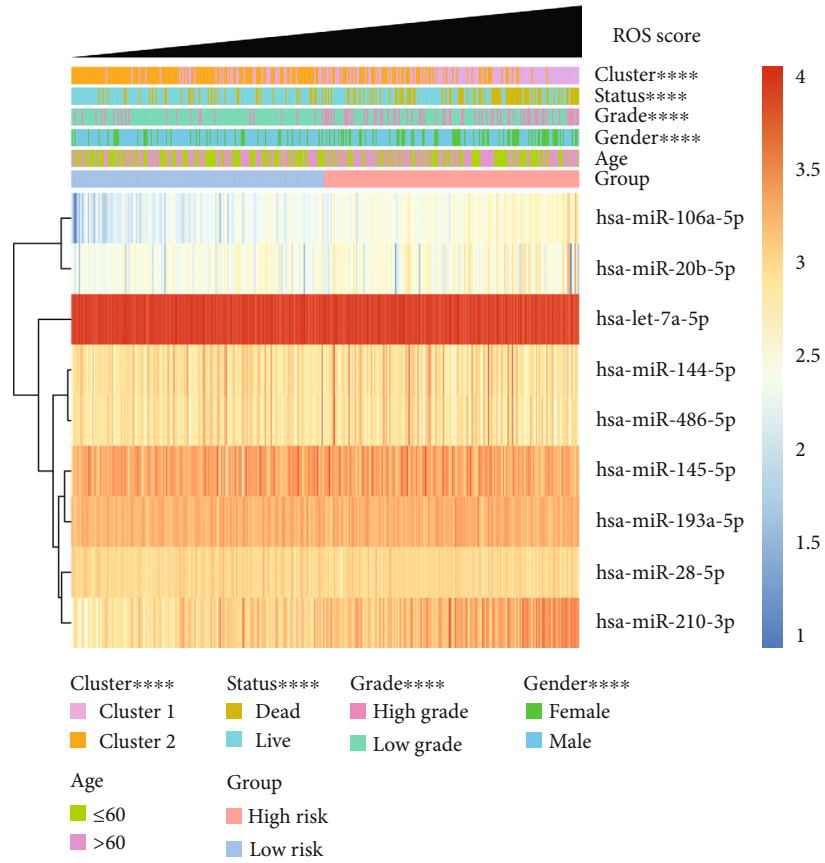
FIGURE 2: The construction of ROS score. (a) Five ROS-related miRNAs were selected through LASSO analysis. (b) The AUC of ROS score signature in training dataset. (c) The AUC of ROS score signature in validation dataset.

the formula went as follows: Ros Score =  $(2.3606 \times \text{let} - 7a - 5p \text{ Expression}) + (0.9226 \times \text{miR} - 106a - 5p \text{ Expression}) + (-0.3014 \times \text{miR} - 144 - 5p \text{ Expression}) + (-0.6911 \times \text{miR} - 20b - 5p \text{ Expression}) + (1.4139 \times \text{miR} - 210 - 3p \text{ Expression})$ . Furthermore, patients were divided into high- and low-risk groups, based on the median ROS score. The ROS score of high-risk group was higher, the low-risk group was instead. Interestingly, we found that high-risk groups were significantly associated with bad prognosis (Figure 2(b)). Moreover, the time-dependent receiver oper-

ating characteristic (ROC) curve was constructed. The time-dependent ROC curve (AUC) of five candidate HBV-related ROS miRNAs was 0.76, 0.81, and 0.78 at one year, three years, and five years (Figure 2(b)). With regard to the validation dataset, the AUC of the miRNAs was 0.58, 0.72, and 0.68 at one year, three years, and five years (Figure 2(c)). The results indicated that ROS score had a strong ability to predict prognosis in HCC.

Furthermore, clinical features between high- and low-risk groups were explored. We find that cluster1, high grade,





(a)

FIGURE 3: Continued.

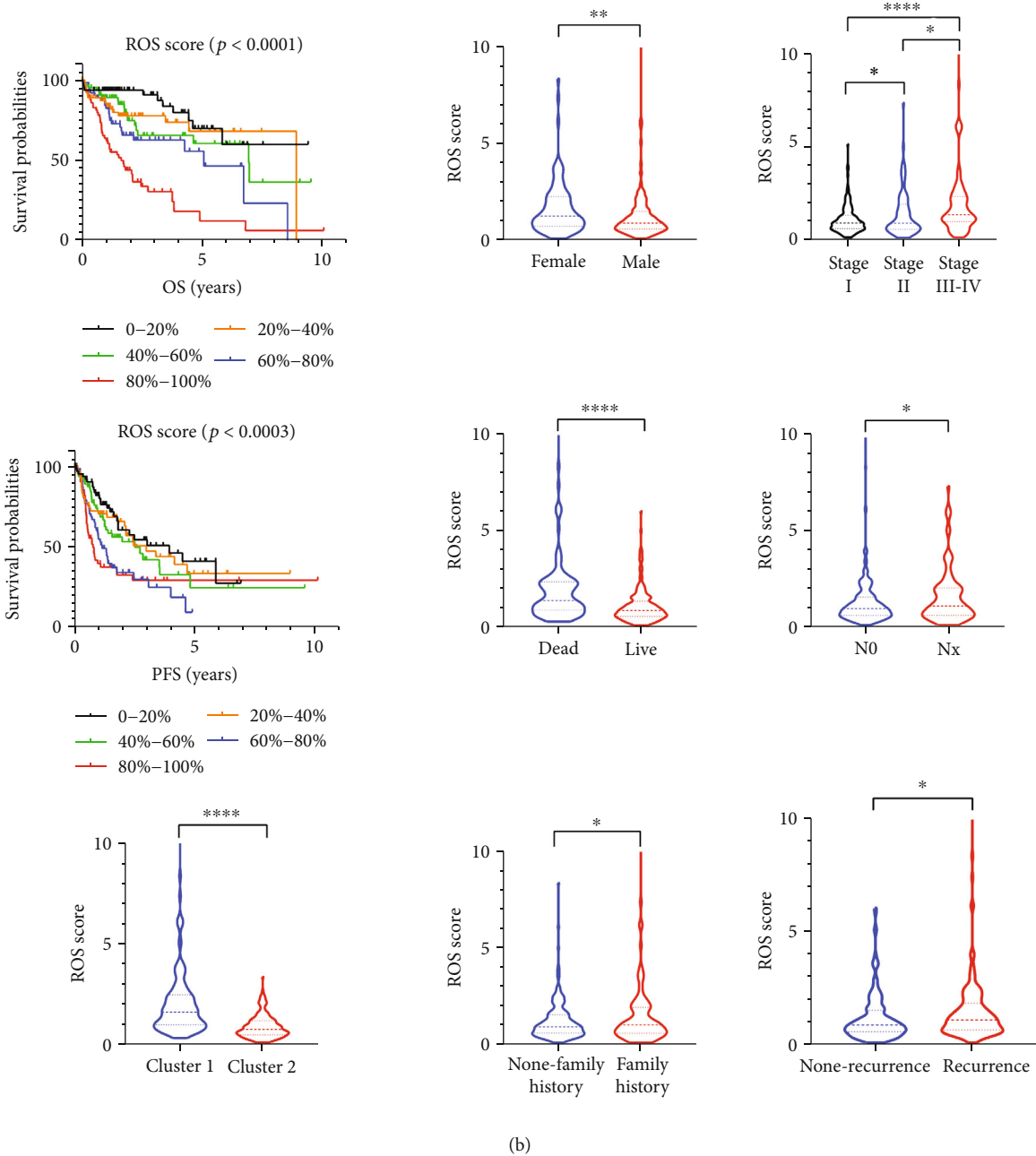


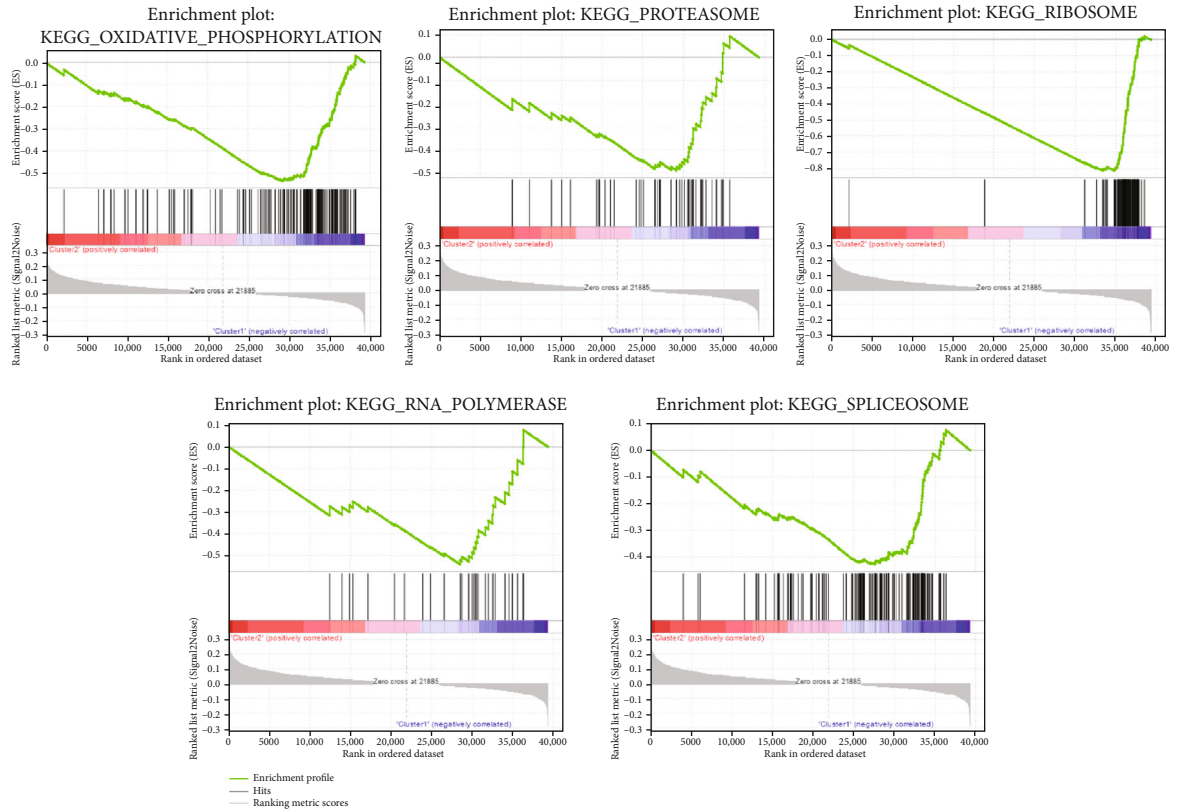
FIGURE 3: The correlation between clinical features and ROS score. (a) Clinical features in the high- and low-risk groups. (b) ROS score in patients with different clinical characteristics. \* $p < 0.05$ , \*\* $p < 0.01$ , \*\*\* $p < 0.001$ , and \*\*\*\* $p < 0.0001$ .

dead status, female, and worse prognosis were significantly enriched in high-risk group (Figure 3(a)). And the higher the ROS score, the more significant the correlation. Additionally, there were significant differences in tumor recurrence and lymph node metastasis between high- and low-risk groups (Figure 3(b)). The results showed that ROS score could effectively predict the clinical features of HCC patients.

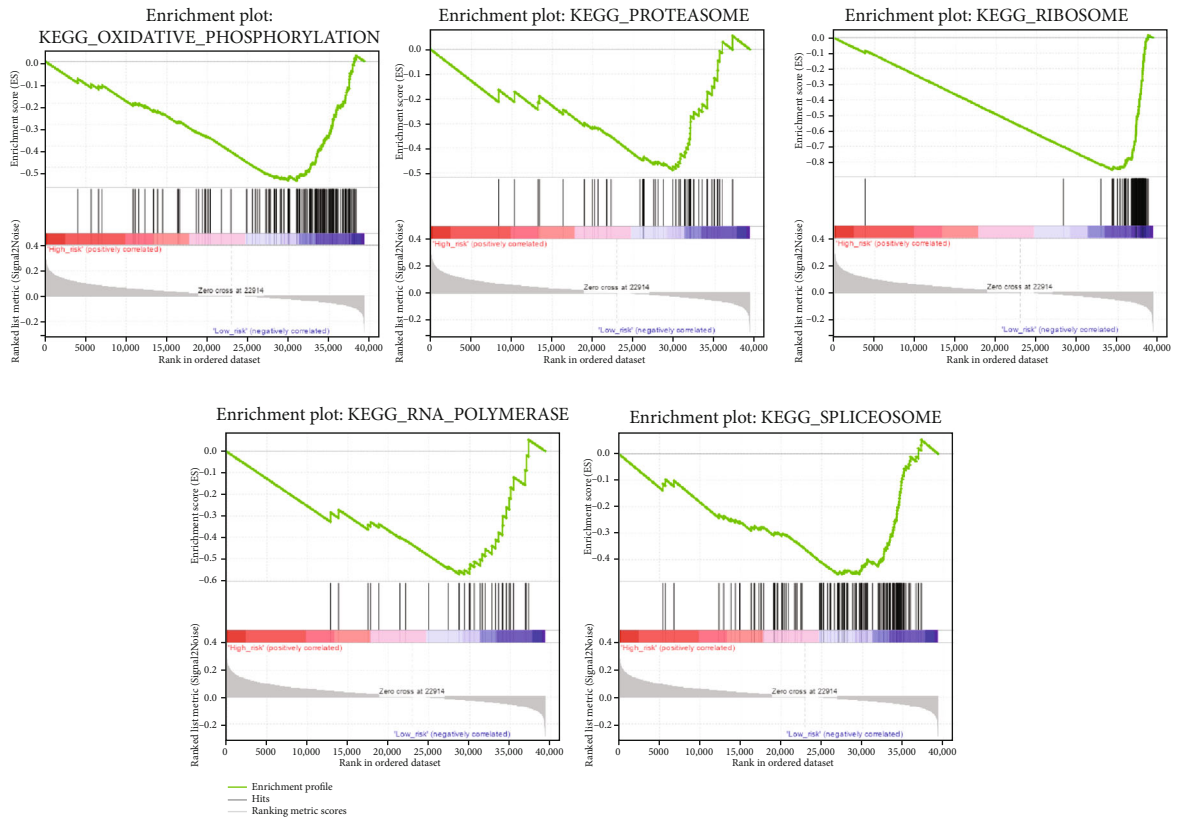
Additionally, GSEA was further analyzed in HCC. The pathways “oxidative\_phosphorylation,” “proteasome,” “ribosome,” “polymerase,” and “spliceosome” were rich in cluster1 (Figure 4(a)). There were similar results in the

high-risk group (Figure 4(b)). These pathways were directly or indirectly associated with cancers.

3.3. ROS Was Associated with TIME in HCC. Experimental evidences showed that the production of ROS in macrophages could affect both natural and acquired immunity and immune responses [21]. Therefore, the correlation between ROS score and TIME in HCC was analyzed. We found that half of the immune cells (11/22) were significantly different in cluster1/2, especially “T cell CD4 memory resting,” “T cell follicular helper,” “Macrophages M0,” and “Macrophages M2” (Figure 5(a)). Moreover, 9 of the 22 immune cells were



(a)



(b)

FIGURE 4: Continued.

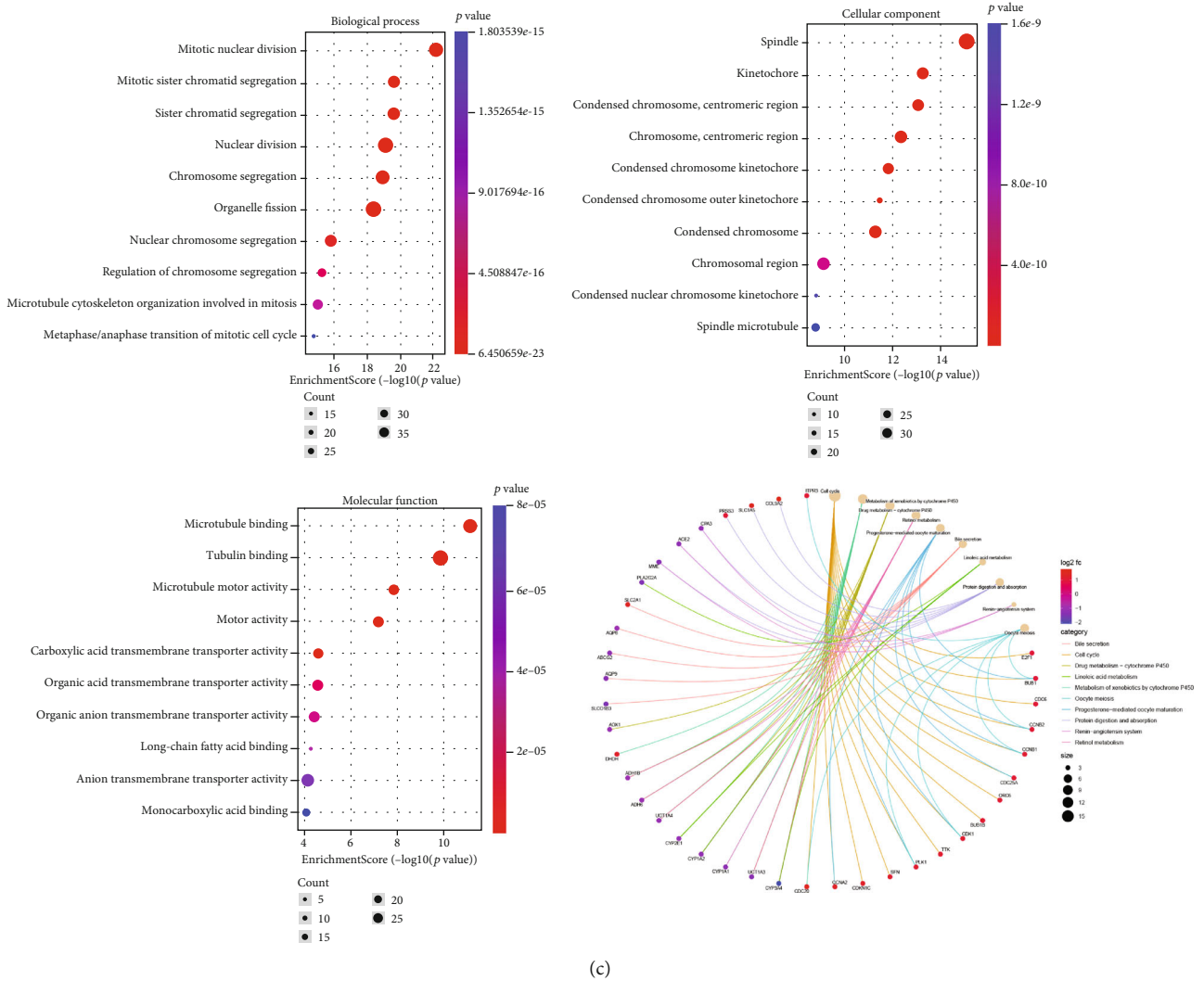


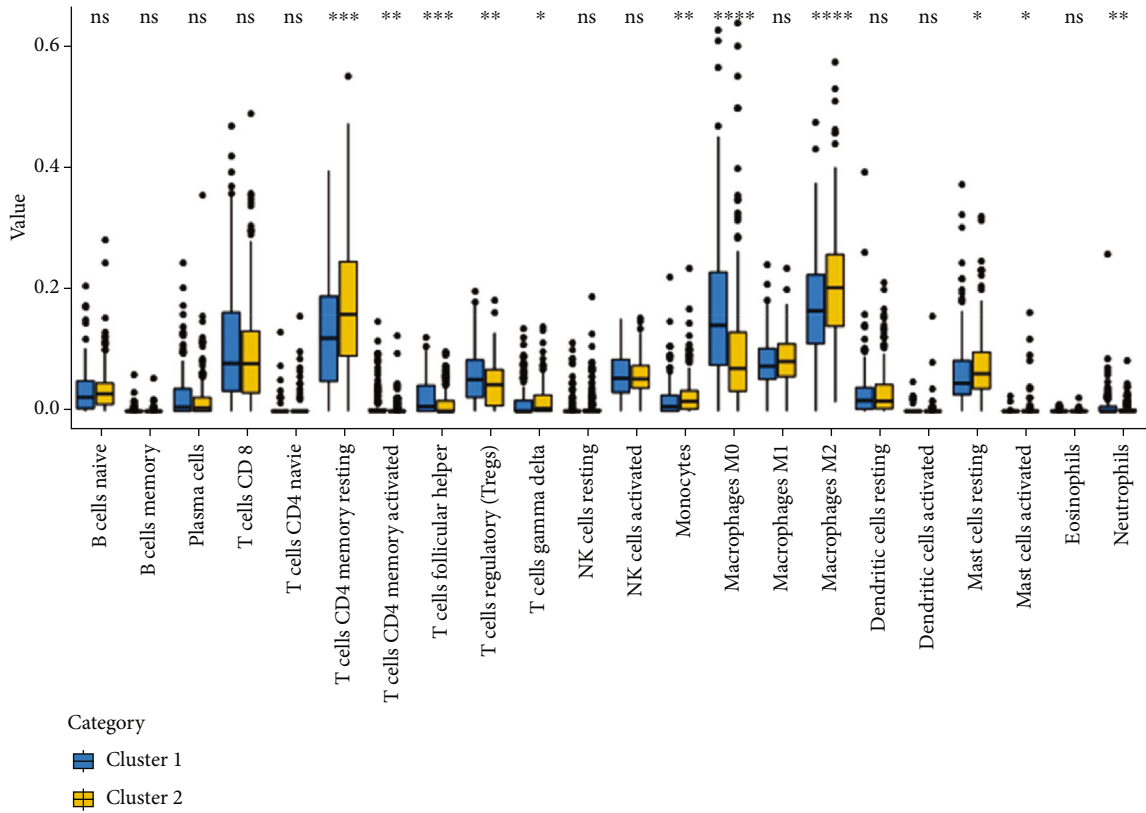
FIGURE 4: GSEA and GO enrichment analysis. (a) GSEA analysis in cluster1/2. (b) GSEA analysis for the high- and low-risk groups. (c) GO enrichment analysis for the common target genes of miR-210-3p and miR-106a-5p.

extremely different in the high- and low-risk groups, especially “T cells follicular helper,” “Macrophages M0,” “Mast cells resting,” and “Eosinophils” (Figure 5(b)). We further analyzed the effects of ROS on immune checkpoint inhibitors; six well-known immune markers were selected for analysis. We found that almost all markers (5/6) were distinct in cluster1/2 and high/low-risk groups (Figures 5(c) and 5(d)). All expression levels of six immune markers were higher in cluster1 and high-risk group, which were associated with worse prognosis in HCC patients. Furthermore, we analyzed the correction between immune cells/markers and ROS score. As showed in Figure 5(e), about one-third of the cells were significantly associated with ROS score. It indicated that ROS could affect the immune response and immunotherapy in HCC.

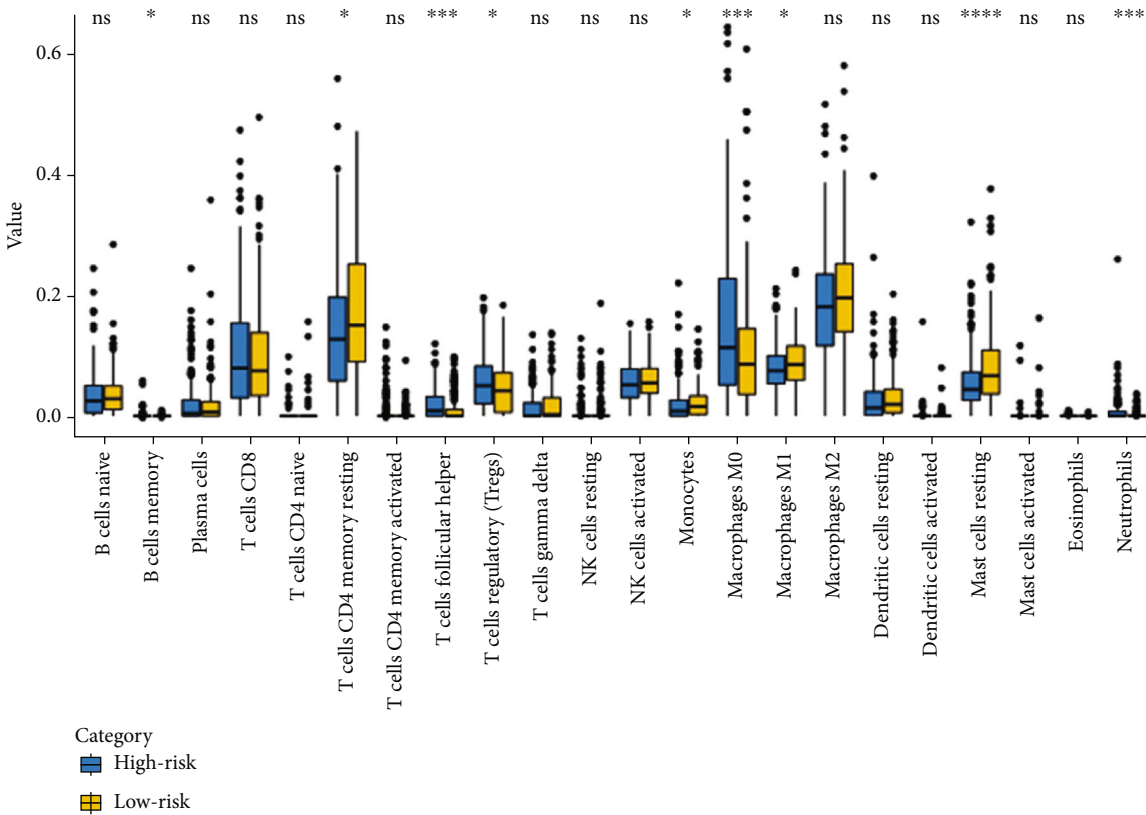
**3.4. The Correction between ROS and Gene Mutation in HCC.** ROS contributes to the accumulation of DNA mutations [22]. We further analyzed the effects of ROS on gene mutations in HCC patients. We found that the mutation rate of HCC patients was higher in cluster1 and high-risk group

than in cluster2 and low-risk group (Figures 6(a)–6(d)). The highest mutation rate was TP53 in cluster1 and high-risk group (Figures 6(a) and 6(b)). Moreover, the mutated genes were more in cluster1 and high-risk group than in cluster2 and low-risk group (Figures 6(e) and 6(f)). As showed in Figure 5(g), ROS score of HCC patients with TP53+ was higher than patients with TP53- (Figure 6(g)). The results indicated that ROS could effect gene mutations, especially TP53 in HCC patients.

**3.5. ROS Regulate m6A Methylation Level of HCC.** Alteration of N6-methyladenosine (m6A) levels participates in cancer pathogenesis and progression [23–25]. We further analyzed the correction between ROS and m6A levels. The results showed that most of the m6A RNA methylation regulators (14/19) were more highly expressed in the high-ROS score group than in the low-ROS score group (Figure 6(h)). In addition, ROS-related miRNAs were significantly correlated with m6A RNA methylation regulators (Figure 6(i)). We further found that ROS score was positively correlated with

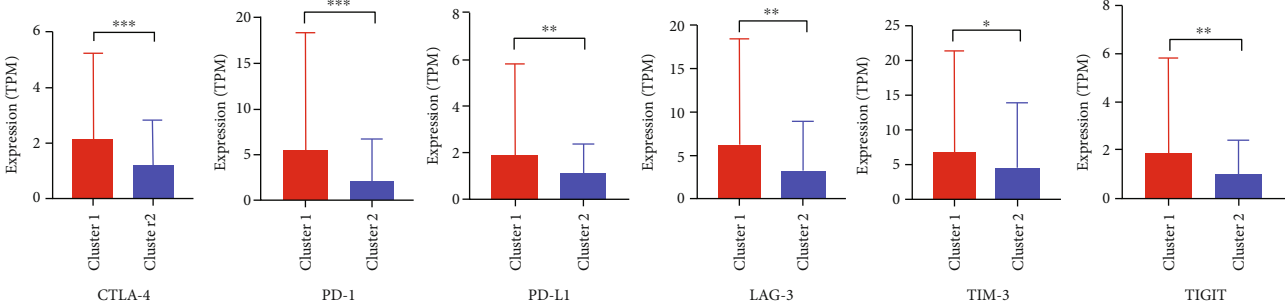


(a)

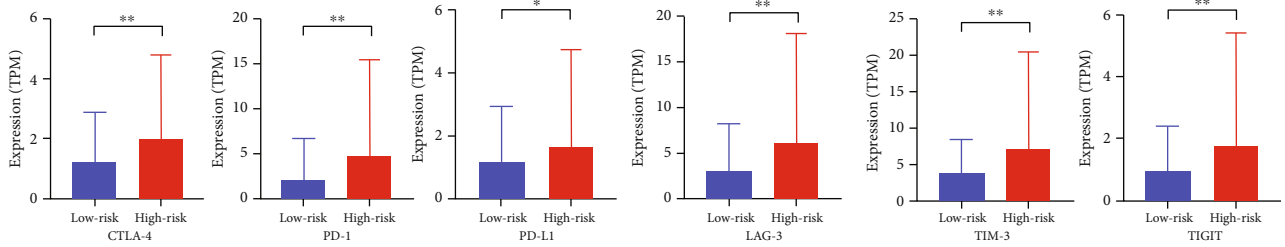


(b)

FIGURE 5: Continued.



(c)



(d)

FIGURE 5: Continued.

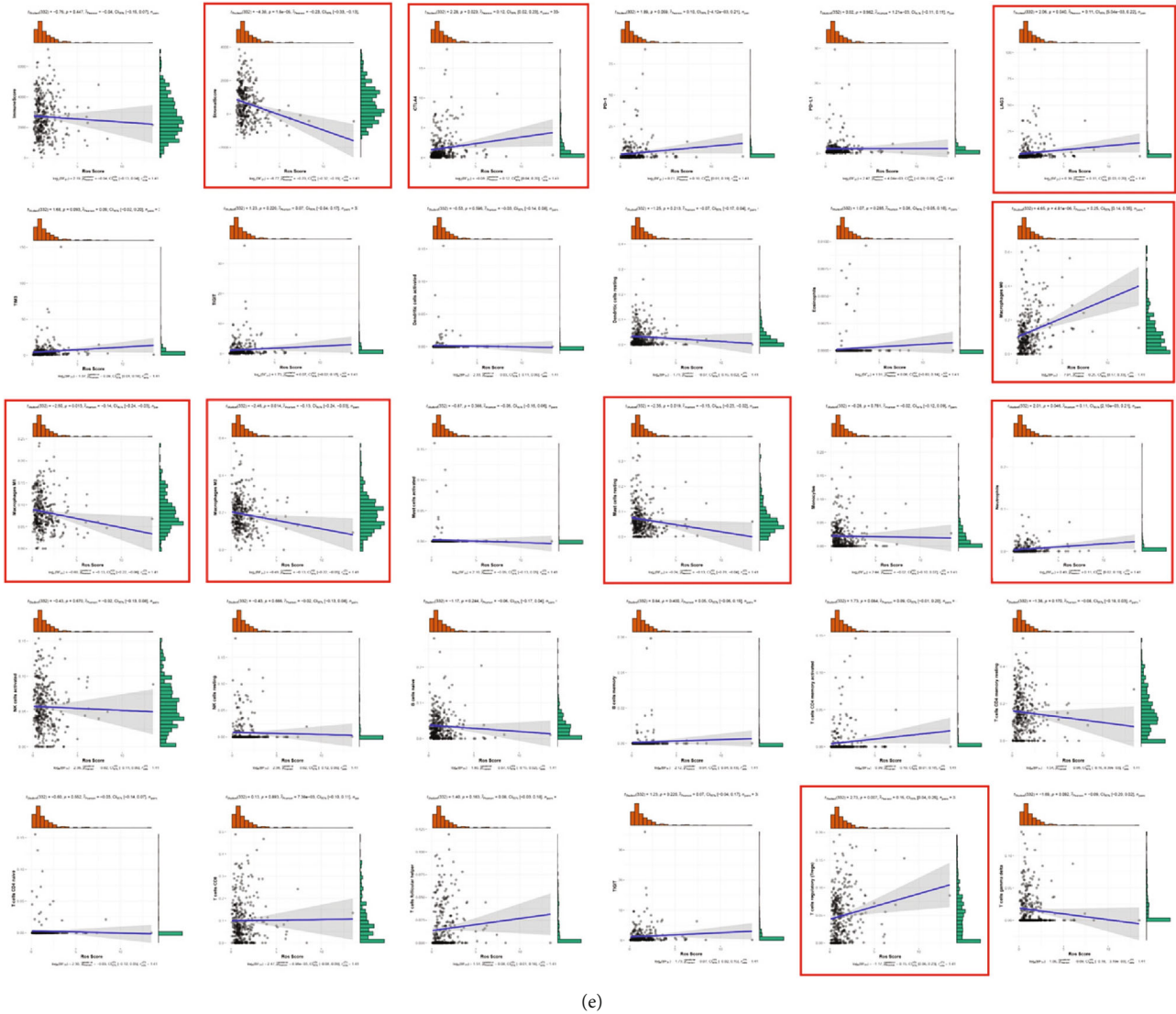


FIGURE 5: The correlation between TIME and ROS score. (a, b) The expression of 22 immune cells in cluster1/2 and high/low-risk groups. (c, d) The expression of six immune markers in cluster1/2 and high/low-risk groups. (e) The correlation between TIME and ROS score. \* $p < 0.05$ , \*\* $p < 0.01$ , \*\*\* $p < 0.001$ , and \*\*\*\* $p < 0.0001$ .

the m6A score (Figure 6(j)). The results indicated that ROS could promote m6A methylation level of HCC.

**3.6. ROS Induced Chemotherapy Sensitivity in HCC.** Many chemotherapeutic agents act on cancer through ROS production [26–28]. We further explored whether ROS could also affect the chemotherapy sensitivity in HCC. The correlation between chemotherapy drug and ROS score was analyzed by using R package “pRRophetic”. As showed in Figure 7, “Sorafenib,” “Gefitinib,” “Rapamycin,” and “Lapatinib” were more highly expressed in high-ROS score patients. It showed that ROS could increase the chemotherapy sensitivity in HCC.

**3.7. miR-210-3p and miR-106a-5p Were Associated with ROS and Cell Cycle.** We further analyzed the overall survival (OS) of the five ROS-related miRNAs in HCC, only the OS of

miR-210-3p and miR-106a-5p have statistical significance (Figure S3). We further find that miR-210-3p and miR-106a-5p increased ROS levels in huh7 and smcc7721 cells (Figure 8(a)). It is reported that ROS plays a role in radiation-induced cancer cell death [29]. Furthermore, we examined the effect of miRNAs on HCC cell cycle. Interestingly, miR-106a-5p and miR-210-3p stagnated the cell cycle at G2/M phases; the results were more obvious in cells after IR (Figures 8(b)–8(e)). It indicated that ROS-related miRNAs might improve the radiotherapy sensitivity of HCC. Additionally, GO enrichment analysis was performed for the common target genes of miR-210-3p and miR-106a-5p; the results were similar to GSEA analysis (Figure 4(c)).

**3.8. miR-210-3p and miR-106a-5p Suppressed HCC Cells.** We further analyzed the biological function of miR-210-3p and

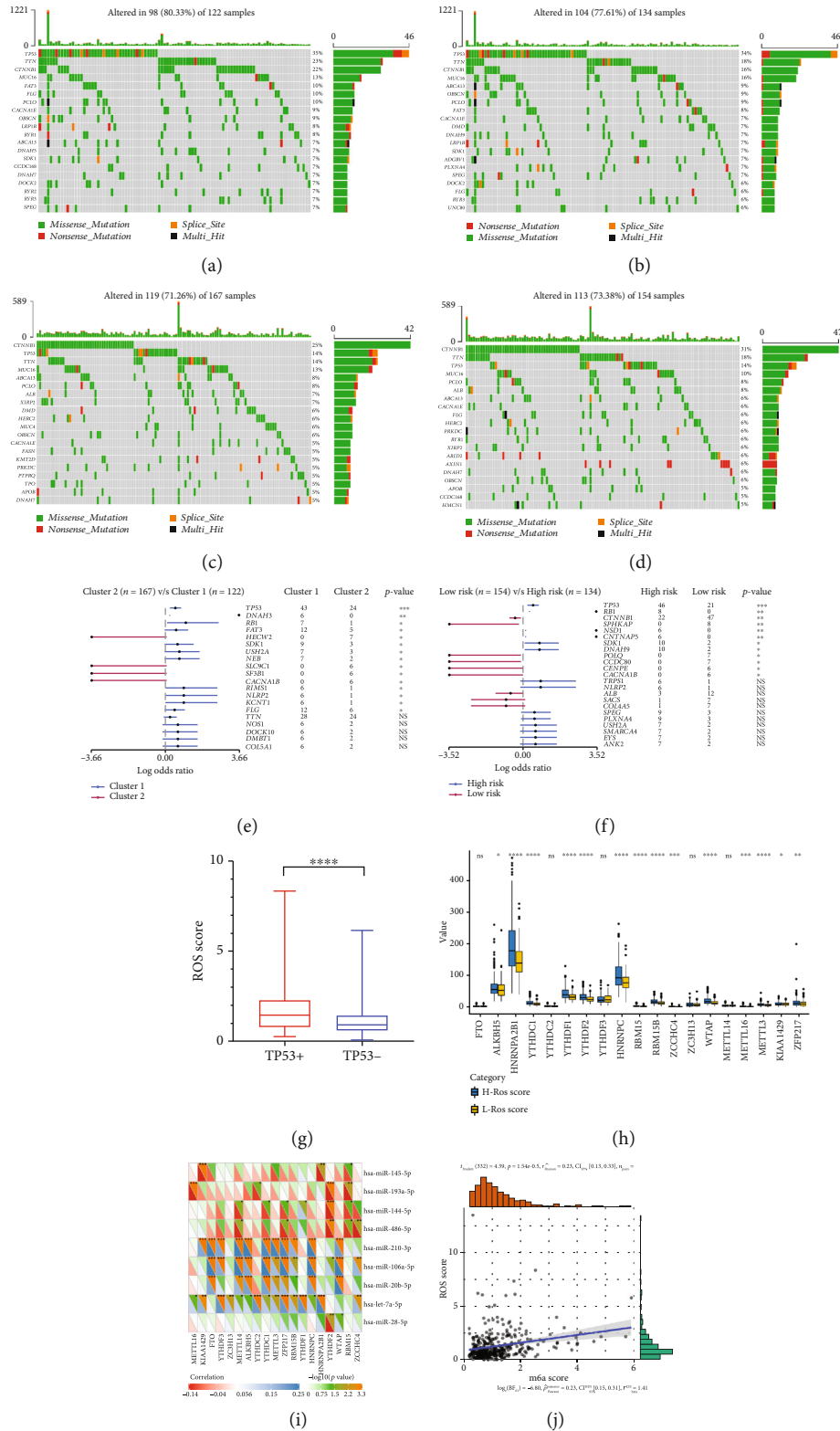


FIGURE 6: The correlation between gene mutation, m6A methylation, and ROS score. (a) Gene altered of cluster1. (b) Gene altered of the high-risk group. (c) Gene altered of cluster2. (d) Gene altered of the low-risk group. (e, f) Gene mutations in cluster1/2 and high/low-risk groups. (g) The expression of ROS score in HCC patients with TP53+/- . (h) The expression of 19 m6A methylation regulators in high- and low-ROS score patients. (i) The correlation between 19 m6A methylation regulators and 9 ROS-related miRNAs. (j) The correlation between m6A score and ROS score. \* $p < 0.05$ , \*\* $p < 0.01$ , \*\*\* $p < 0.001$ , and \*\*\*\* $p < 0.0001$ .



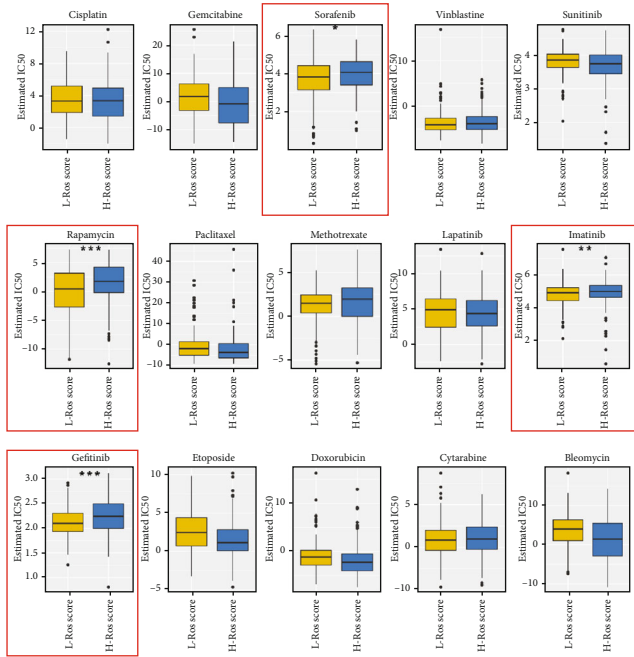


FIGURE 7: The correlation between chemotherapy agents and ROS score. \* $p < 0.05$ , \*\* $p < 0.01$ , \*\*\* $p < 0.001$ .

miR-106a-5p in HCC. We found that miR-210-3p and miR-106a-5p could suppress huh7 and smmc7721 cell proliferation (Figure 9(a)). Furthermore, two miRNAs inhibited cell migration and invasion (Figures 9(b)–9(e)). Additionally, two miRNAs promoted apoptosis of huh7 and smmc721 cells.

#### 4. Discussion

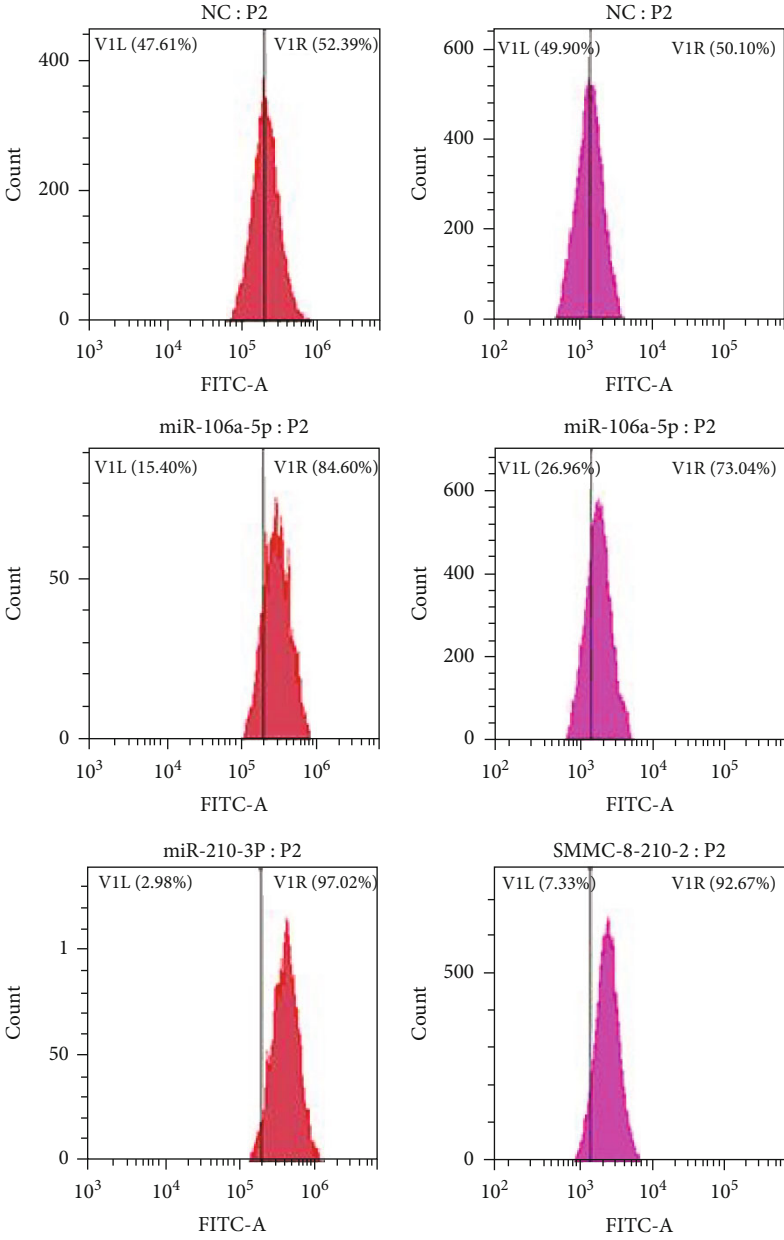
The mechanisms of ROS in cancer are complex for numerous reasons [29]. First, ROS play a key role in the development of cancer [30–33]. Second, ROS induced G2/M arrest leads to affect the cell-cycle progression [34–37]. Third, chronic inflammation is regulated by ROS, which promote tumorigenesis [38, 39]. Forth, the expression levels of various tumor-related genes are regulated by ROS, including p53 [40–42]. Fifth, ROS are associated with cell apoptosis [43, 44]. Sixth, lots of chemotherapeutic and radiotherapeutic agents kill cancer cells by increasing ROS levels [45, 46]. Although ROS act on tumors through numerous pathways, the specific mechanisms remain unclear. ROS have a dual effect on tumors [29]. For example, ROS can promote tumor cell proliferation, such as bladder, liver, breast, lung, and ovarian cancer cells [47–50]. However, ROS also inhibits tumor cell proliferation, including liver, prostate, and breast cancer cells [51–53]. According to these previous reports, the role of ROS in tumors is contradictory and complex. Therefore, the mechanism of ROS in tumors needs to be further investigated. Currently, the effect of ROS in HCC needs further analyzed.

In this research, 36 ROS-related miRNAs were screened and divided into HBV-related ROS miRNAs (9) and none HBV-related ROS miRNAs (27). Then, HCC patients were divided into cluster1 and cluster2, based on the expression

of the HBV-related ROS miRNAs. We found that cluster1 was significantly associated with high grade, dead patients, and bad prognosis. In addition, HCC patients were divided into cluster1, cluster2, and cluster3. However, the clinical features were not significantly different in cluster1/2/3. It indicated that HBV-related ROS miRNAs were more relevant to HCC patients. HBV can cause DNA mutation through ROS generation and is an important pathogenic factor of HCC [4, 20]. The miRNAs associated with both ROS and HBV are more relevant to HCC patients than mRNAs that are purely related to ROS. It was consistent with the above results. Additionally, HBV-related ROS miRNAs included miR-210-3p, miR-20b-5p, miR-144-5p, miR-106a-5p, miR-486-5p, miR-28-5p, miR-139a-5p, miR-145-5p, and let-7a-5p. Most of HBV-related miRNAs (6/9) were consistent with the previous reports [54–59].

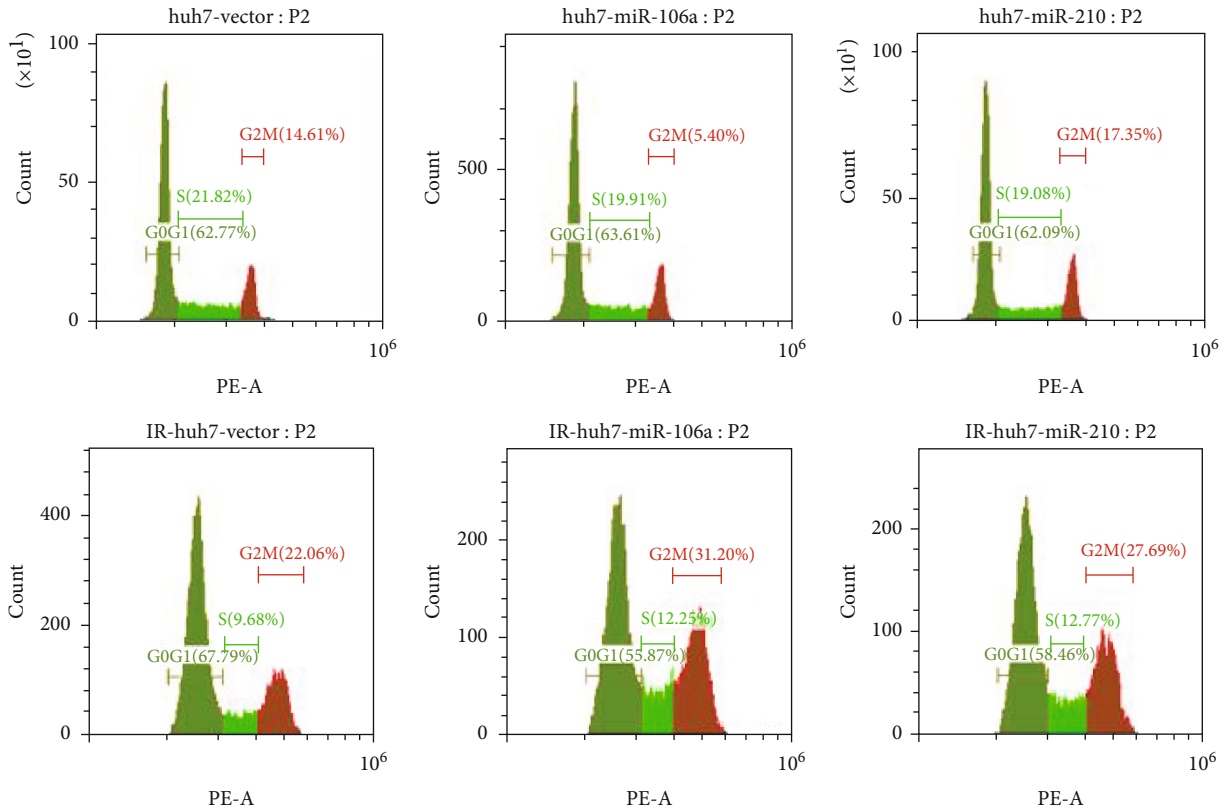
Furthermore, 340 HCC patients were randomly divided into a validation dataset (170 patients) and training dataset (170 patients). Five candidate HBV-related ROS miRNAs were selected to calculate ROS score by using LASSO regression in the training dataset, including let-7a-5p, miR-106a-5p, miR-144-5p, miR-20b-5p, and miR-210-3p. ROS score was calculated by using the formula. Patients were divided into high-risk (high ROS score) and low-risk groups (low ROS score), based on the median ROS score. The high-risk groups were significantly associated with bad prognosis in the training dataset. Also, the similar result occurred in the validation dataset. Moreover, the AUC of five candidate HBV-related ROS miRNAs was 0.76, 0.81, and 0.78 at one year, three years, and five years in training dataset. In regard to the validation dataset, the AUC of the miRNAs was 0.58, 0.72, and 0.68 at one year, three years, and five years. AUC > 0.5 indicated prognostic ability, while AUC > 0.7 indicated a strong prognostic ability. The results showed that five candidate HBV-related ROS miRNAs had a strong prognostic ability.

Furthermore, we analyzed the relationship of TIME, mutation, m6A methylation, chemotherapy sensitivity, and ROS score in HCC. Interestingly, half of the 22 immune cells were significantly different in cluster1/2, especially “T cells CD4 memory resting,” “T cells follicular helper,” “Macrophages M0,” and “Macrophages M2” ( $p < 0.001$ ). Moreover, ROS score was significantly corrected with immune checkpoint inhibitors; the expressions of CTLA-4, PD-1, LAG-3, TIM-3, and TIGIT were higher in the high-risk group. The results have also been verified in cluster1. Additionally, “StromalScore,” “CTLA-4,” “LAG-3,” “Macrophages M0,” “Macrophages M1,” “Macrophages M2,” “Neutrophils,” “Mast cells resting,” and “T cells regulatory (Tregs)” were extremely associated with ROS score ( $p < 0.05$ ). These results showed that ROS could affect the immune response and immunotherapy in HCC. The increase of NADPH oxidase-derived extracellular and intracellular ROS is a major cause of oxidative stress, which contributes to functional changes in immune cells [60]. Interestingly, macrophages M0/1/2 were all associated with ROS score, and it indicated that ROS regulated tumor cells through macrophages. Moreover, ROS production in macrophages affects

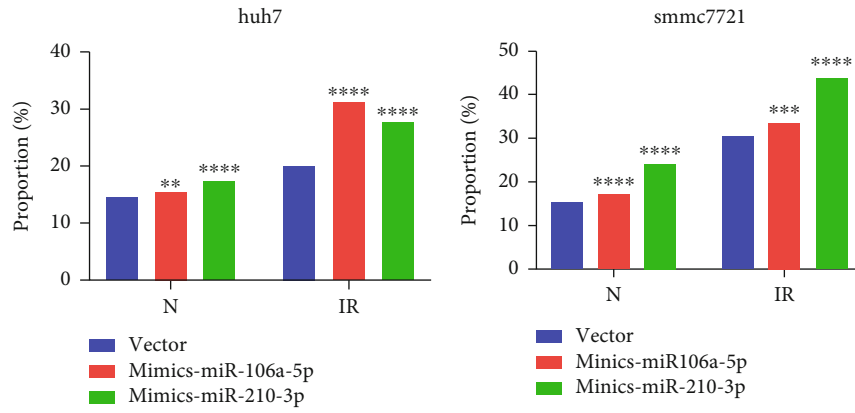


(a)

FIGURE 8: Continued.



(b)



(c)

(d)

FIGURE 8: Continued.

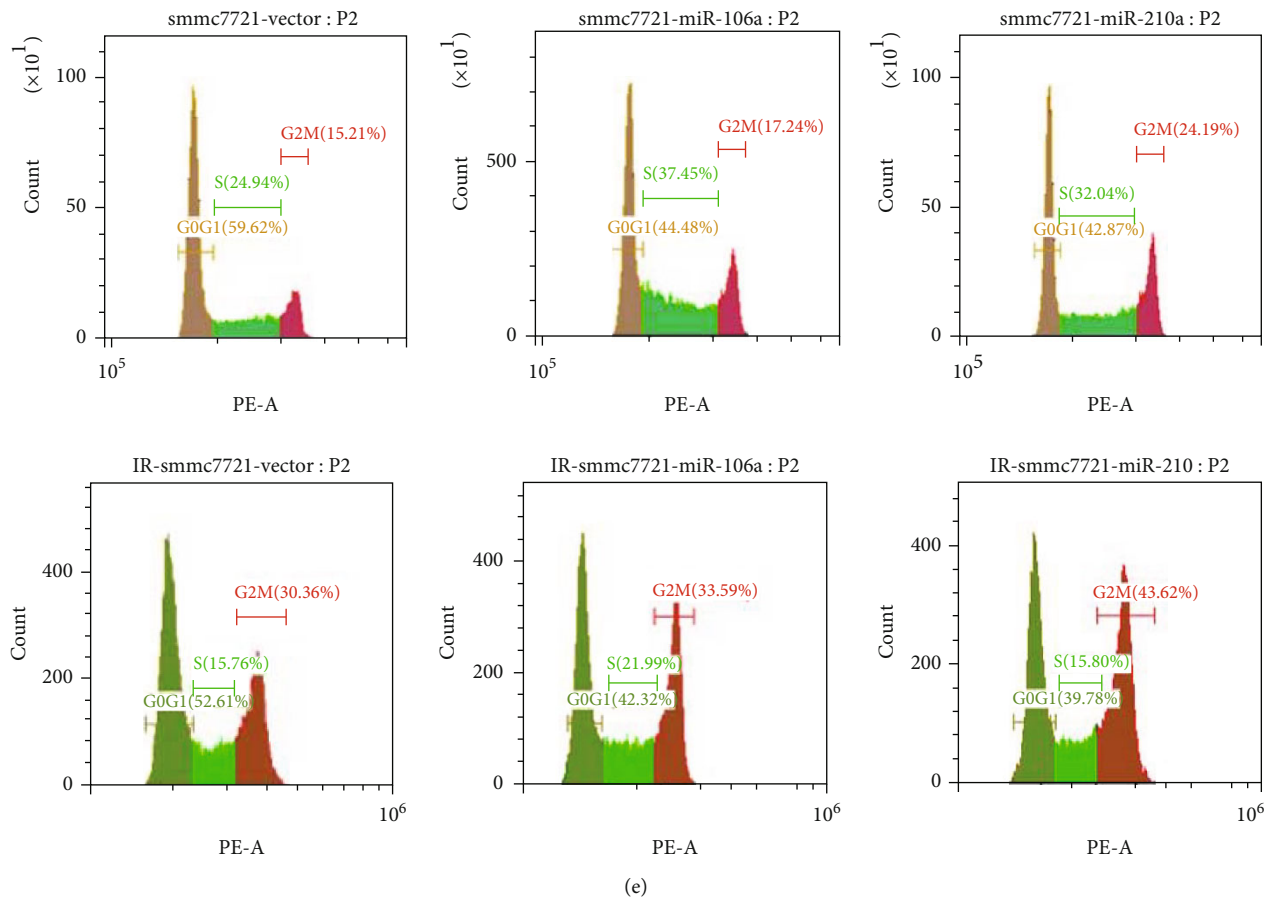


FIGURE 8: The ROS levels and cell cycle in HCC. (a) The ROS levels in huh7 and smmc7721 cells. (b) Cell cycle in huh7 cells. (c) The analysis of cell cycle in huh7 cells. (d) The analysis of cell cycle in smmc7721 cells. (e) Cell cycle in smmc7721 cells. IR: ionizing radiation; N: normal. \* $p < 0.05$ , \*\* $p < 0.01$ , \*\*\* $p < 0.001$ , and \*\*\*\* $p < 0.0001$ .

natural and acquired immunity and the immune response [21]. Thus, previous reports confirm our results.

In regard to gene mutation, the mutation rates of HCC patients with high ROS score were higher, and TP53 mutation rates were the highest among all genes in HCC patients with high ROS score. The results have also been verified in cluster1. Due to the lack of antioxidant damage repair system, mitochondria DNA (mtDNA) is more susceptible to ROS damage and mutation [61]. In turn, mtDNA mutations can increase ROS production, further aggravating the mutation effect and accumulating mutations, thus increasing the risk of tumor mutation [62]. What is more, ROS promote HCC cell survival by regulating TP53 degradation [63]. These researches confirm our results.

Regarding to m6A methylation, Zhuang and his colleagues find that m6A demethylase FTO could induce oxidative stress and ROS production and show impaired tumor growth [64]. Also, Yu and his colleagues find that ROS significantly induces global mRNA N6-methyladenosine (m6A) levels by modulating ALKBH5, to induce various biological processes quickly and effectively including DNA damage repair [65]. In this research, it is the first time to report that ROS is significantly associated with m6A in HCC. However, there are few reports about ROS and m6A; the mechanism of ROS and m6A needs further exploration.

Many chemotherapeutic agents kill tumor cells through ROS production [29]. For example, procarbazine is one of the first drugs to be developed based on its ROS-producing properties [45]. Until to now, the drug is approved to treat Hodgkin's lymphoma, non-Hodgkin's lymphoma, and primary brain tumors [66, 67]. In our research, we analyzed the difference of chemotherapy drugs between high-ROS score patients and low-ROS score patients. The results showed that "Sorafenib," "Gefitinib," "Rapamycin," and "Lapatinib" were more highly expressed in high-ROS score patients, which indicated that ROS could increase the chemotherapy sensitivity in HCC.

Finally, our experiments showed that ROS-related miRNAs miR-210-3p and miR-106a-5p could increase the ROS level of HCC. Moreover, these two miRNAs could stagnate HCC cell cycle at G2/M; the results were more obvious in cells after IR. The relative radiosensitivity of cells is determined by the cell cycle stage. Cells are most sensitive to radiation in G2/M phase, less sensitive in G1 phase, and least sensitive in late S phase [68].

Therefore, ROS-related miRNAs miR-210-3p and miR-106a-5p can increase the radiotherapy sensitivity of HCC cells. ROS play a role in radiation-induced cancer cell death, including lung cancer, prostate cancer, and breast cancer [69–71]. Our experimental results provide data support for

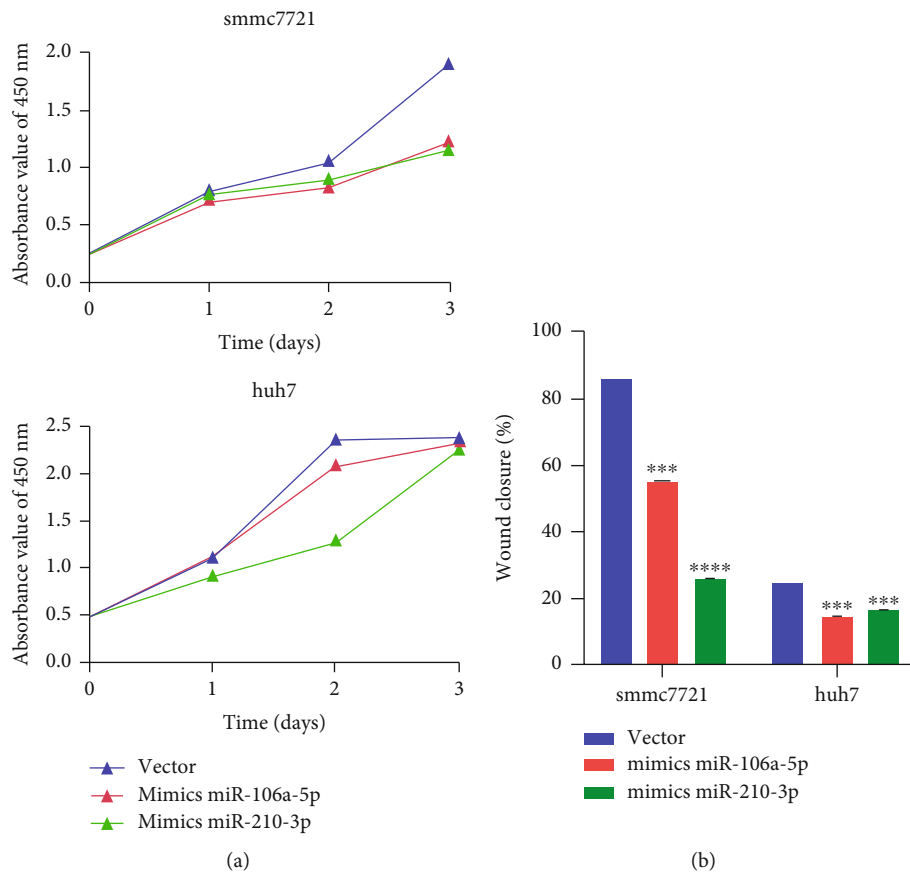


FIGURE 9: Continued.

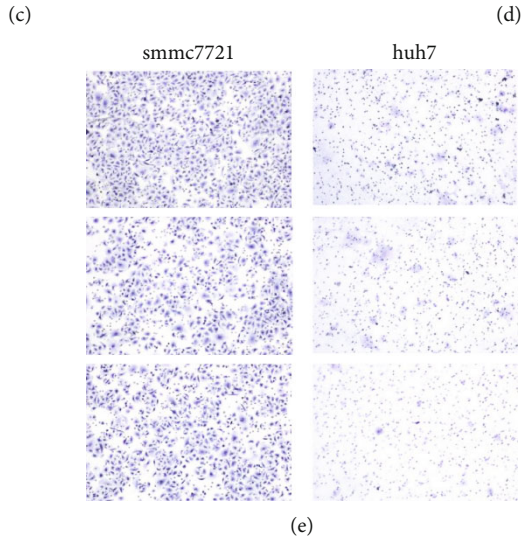
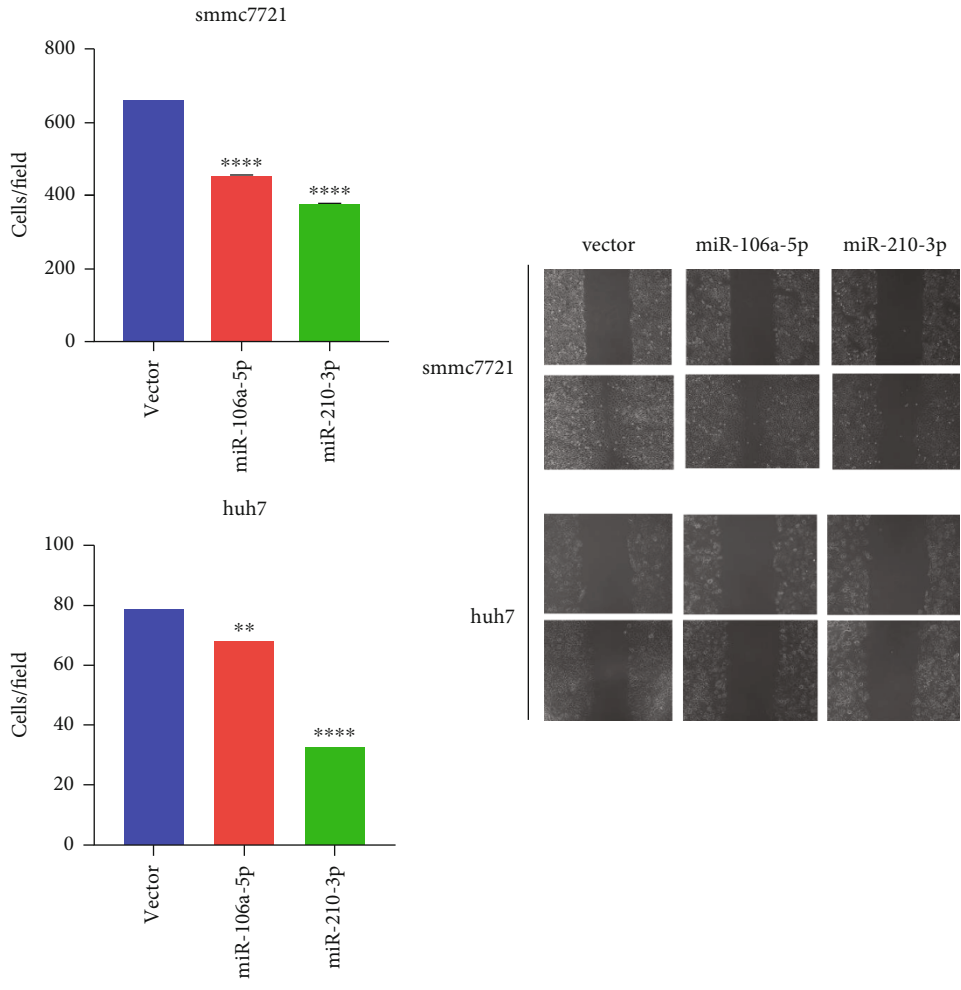


FIGURE 9: Continued.

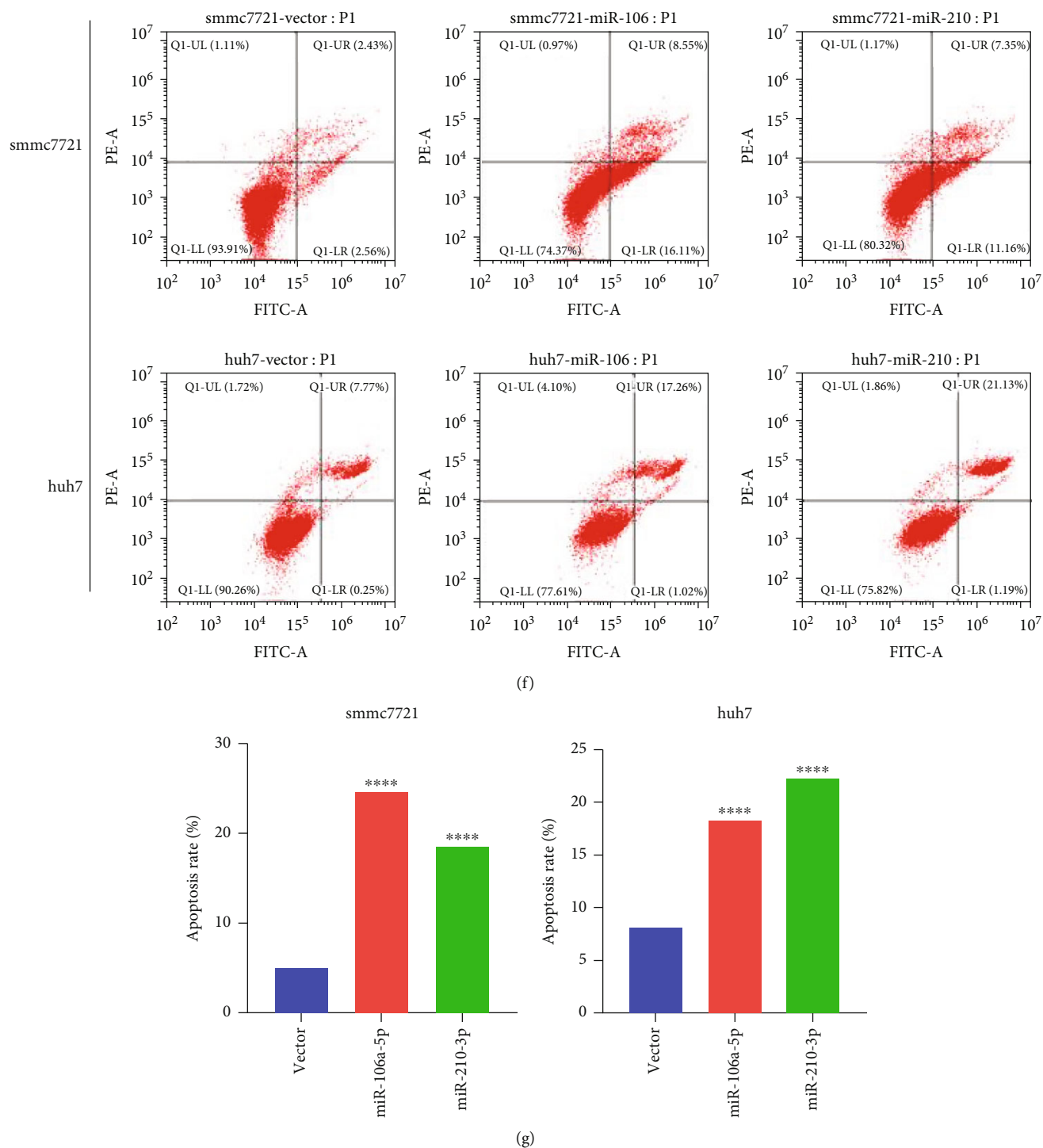


FIGURE 9: The biological function of miR-210-3p and miR-106a-5p in HCC. (a) The CCK8 value of miR-210-3p and miR-106a-5p in huh7 and smmc7721 cells. (b, d) miR-210-3p and miR-106a-5p inhibited huh7 and smmc7721 cell migration. (c, e) miR-210-3p and miR-106a-5p inhibited huh7 and smmc7721 cell invasion. (f, g) miR-210-3p and miR-106a-5p promoted apoptosis of huh7 and smmc721 cells. \*  $p < 0.05$ , \*\*  $p < 0.01$ , \*\*\*  $p < 0.001$ , and \*\*\*\*  $p < 0.0001$ .

the role of ROS in HCC radiotherapy. Moreover, the experimental results showed that miR-210-3p and miR-106a-5p suppressed HCC cell proliferation, migration, and invasion. And two miRNAs promoted apoptosis of huh7 and smmc721 cells. It indicated that miR-210-3p and miR-106a-5p played a key role in the biological function of HCC.

In summary, we systematically assessed the relationship of clinical features, TIME, mutation, m6A methylation, chemotherapy sensitivity, and ROS score in HCC. HCC patients were divided into cluster1/2 and high/low-risk groups, based on the expression of ROS-related miRNAs and ROS score. High ROS score was significantly with worse prognosis,

immune cells, and immune checkpoint inhibitors. High ROS score also regulated gene mutation, m6A methylation level, and increased chemotherapy sensitivity in HCC. These results were confirmed in both cluster1/2 and high/low-risk groups. Moreover, ROS-related miRNAs miR-210-3p and miR-106a-5p significantly increased the ROS level and radiotherapy sensitivity and played a key role in the biological function of HCC. Therefore, ROS might improve the radiotherapy sensitivity of HCC patients, which could provide a new treatment strategy for HCC patients.

### Data Availability

The clinical data of HCC patients were downloaded from the University of California Santa Cruz (UCSC, <https://xenabrowser.net/datapages/>). The research included 374 tumor and 50 normal samples. The miRNA expression data of HCC patients were downloaded from the The Cancer Genome Atlas (TCGA) data portal by the “TCGAbiolinks” R package. Furthermore, the mutation data of the TCGA-LIHC was downloaded from the websites (<https://portal.gdc.cancer.gov/>).

### Conflicts of Interest

The authors declare that the research was conducted in the absence of any commercial or financial relationships that could be construed as a potential conflict of interest.

### Authors' Contributions

Ximing Xu contributed to the conceptualization, methodology, and writing—review and editing. Yangtao Xu contributed to the methodology, resources, software, formal analysis, and writing—original draft. Xiaoqin He contributed to the methodology, resources, and formal analysis. Junjian Deng contributed to the methodology, resources, and software. Lin Xiong contributed to the validation and data curation. Xiaoyu Zhang contributed to the validation and data curation. Wenliang Chen contributed to the visualization and supervision. Xin Liu contributed to the visualization and supervision. Xinyao Hu contributed to the visualization. Jiayi Li contributed to the visualization. Shan Jiang contributed to the visualization. Yang Shen contributed to the supervision.

### Acknowledgments

This work was supported by funding from the National Natural Science Foundation of China (No. 31971166) and the National Key R&D Program of China (2019YFE0115900).

### Supplementary Materials

Figure S1: consensus clustering matrix from  $k = 2$  to 9 for 9 HBV-related ROS miRNAs. Figure S2: consensus clustering matrix from  $k = 2$  to 9 for 27 none HBV-related ROS miRNAs. Figure S3: the OS of miR-210-3p and miR-106a-5p in HCC. (*Supplementary Materials*)

### References

- [1] H. Sung, J. Ferlay, R. L. Siegel et al., “Global Cancer Statistics 2020: GLOBOCAN estimates of incidence and mortality worldwide for 36 cancers in 185 countries,” *CA: A Cancer Journal for Clinicians*, vol. 71, no. 3, pp. 209–249, 2021.
- [2] A. Forner, J. M. Llovet, and J. Bruix, “Hepatocellular carcinoma,” *Lancet*, vol. 379, no. 9822, pp. 1245–1255, 2012.
- [3] W. Chen, R. Zheng, P. D. Baade et al., “Cancer statistics in China, 2015,” *CA: A Cancer Journal for Clinicians*, vol. 66, no. 2, pp. 115–132, 2016.
- [4] H. B. El-Serag, “Epidemiology of viral hepatitis and hepatocellular carcinoma,” *Gastroenterology*, vol. 142, no. 6, article e1261, pp. 1264–1273, 2012.
- [5] C. Zhong, Y. Li, J. Yang et al., “Immunotherapy for hepatocellular carcinoma: current limits and prospects,” *Frontiers in Oncology*, vol. 11, article 589680, 2021.
- [6] D. P. Bartel, “MicroRNAs: target recognition and regulatory functions,” *Cell*, vol. 136, no. 2, pp. 215–233, 2009.
- [7] Y. S. Lee and A. Dutta, “MicroRNAs in cancer,” *Annual Review of Pathology*, vol. 4, pp. 199–227, 2009.
- [8] I. S. Harris and G. M. DeNicola, “The complex interplay between antioxidants and ROS in cancer,” *Trends in Cell Biology*, vol. 30, no. 6, pp. 440–451, 2020.
- [9] S. Arora, A. Bhardwaj, S. Singh et al., “An undesired effect of chemotherapy: gemcitabine promotes pancreatic cancer cell invasiveness through reactive oxygen species-dependent, nuclear factor  $\kappa$ B- and hypoxia-inducible factor 1 $\alpha$ -mediated up-regulation of CXCR4\*,” *Journal of Biological Chemistry*, vol. 288, no. 29, pp. 21197–21207, 2013.
- [10] J. Goh, L. Enns, S. Fatemie et al., “Mitochondrial targeted catalase suppresses invasive breast cancer in mice,” *BMC Cancer*, vol. 11, 2011.
- [11] K. Ishikawa, K. Takenaga, M. Akimoto et al., “ROS-generating mitochondrial DNA mutations can regulate tumor cell metastasis,” *Science*, vol. 320, no. 5876, pp. 661–664, 2008.
- [12] B. R. O’Leary, M. A. Fath, A. M. Bellizzi et al., “Loss of SOD3 (EcSOD) expression promotes an aggressive phenotype in human pancreatic ductal adenocarcinoma,” *Clinical Cancer Research*, vol. 21, no. 7, pp. 1741–1751, 2015.
- [13] D. C. Radisky, D. D. Levy, L. E. Littlepage et al., “Rac1b and reactive oxygen species mediate MMP-3-induced EMT and genomic instability,” *Nature*, vol. 436, no. 7047, pp. 123–127, 2005.
- [14] J. P. L. de Sá, D. A. D. Câmara, A. S. Porcacchia et al., “The roles of ROS in cancer heterogeneity and therapy,” *Oxidative Medicine and Cellular Longevity*, vol. 2017, Article ID 2467940, 2017.
- [15] G. Wang, J. Yao, Z. Li et al., “miR-34a-5p inhibition alleviates intestinal ischemia/reperfusion-induced reactive oxygen species accumulation and apoptosis via activation of SIRT1 signaling,” *Antioxidants & Redox Signaling*, vol. 24, no. 17, pp. 961–973, 2016.
- [16] A. Lang, S. Grether-Beck, M. Singh et al., “MicroRNA-15b regulates mitochondrial ROS production and the senescence-associated secretory phenotype through sirtuin 4/SIRT4,” *Aging (Albany NY)*, vol. 8, no. 3, pp. 484–505, 2016.
- [17] S. O. Ebrahimi, S. Reisi, and S. Shareef, “miRNAs, oxidative stress, and cancer: a comprehensive and updated review,” *Journal of Cellular Physiology*, vol. 235, no. 11, pp. 8812–8825, 2020.



- [18] F. Torma, Z. Gombos, M. Jokai et al., "The roles of microRNA in redox metabolism and exercise-mediated adaptation," *Journal of Sport and Health Science*, vol. 9, no. 5, pp. 405–414, 2020.
- [19] A. Colaprico, T. C. Silva, C. Olsen et al., "TCGAbiolinks: an R/Bioconductor package for integrative analysis of TCGA data," *Nucleic Acids Research*, vol. 44, no. 8, 2016.
- [20] K. Koike, "Hepatitis B virus X gene is implicated in liver carcinogenesis," *Cancer Letters*, vol. 286, no. 1, pp. 60–68, 2009.
- [21] J. Lloberas, J. P. Muñoz, M. I. Hernández-Álvarez, P. J. Cardona, A. Zorzano, and A. Celada, "Macrophage mitochondrial MFN2 (mitofusin 2) links immune stress and immune response through reactive oxygen species (ROS) production," *Autophagy*, vol. 16, no. 12, pp. 2307–2309, 2020.
- [22] M. Carbone, S. T. Arron, B. Beutler et al., "Tumour predisposition and cancer syndromes as models to study gene-environment interactions," *Nature Reviews Cancer*, vol. 20, no. 9, pp. 533–549, 2020.
- [23] L. He, H. Li, A. Wu, Y. Peng, G. Shu, and G. Yin, "Functions of N6-methyladenosine and its role in cancer," *Molecular Cancer*, vol. 18, no. 1, p. 176, 2019.
- [24] J. Y. Roignant and M. Soller, "m<sup>6</sup>A in mRNA: an ancient mechanism for fine-tuning gene expression," *Trends in Genetics*, vol. 33, no. 6, pp. 380–390, 2017.
- [25] J. Z. Ma, F. Yang, C. C. Zhou et al., "METTL14 suppresses the metastatic potential of hepatocellular carcinoma by modulating N(6)-methyladenosine-dependent primary microRNA processing," *Hepatology*, vol. 65, no. 2, pp. 529–543, 2017.
- [26] G. T. Wondrak, "Redox-directed cancer therapeutics: molecular mechanisms and opportunities," *Antioxidants & Redox Signaling*, vol. 11, no. 12, pp. 3013–3069, 2009.
- [27] N. A. Santos, C. S. Catão, N. M. Martins, C. Curti, M. L. P. Bianchi, and A. C. Santos, "Cisplatin-induced nephrotoxicity is associated with oxidative stress, redox state imbalance, impairment of energetic metabolism and apoptosis in rat kidney mitochondria," *Archives of Toxicology*, vol. 81, no. 7, pp. 495–504, 2007.
- [28] Y. Jiang, C. Guo, M. R. Vasko, and M. R. Kelley, "Implications of apurinic/apyrimidinic endonuclease in reactive oxygen signaling response after cisplatin treatment of dorsal root ganglion neurons," *Cancer Research*, vol. 68, no. 15, pp. 6425–6434, 2008.
- [29] S. C. Gupta, D. Hevia, S. Patchva, B. Park, W. Koh, and B. B. Aggarwal, "Upsides and downsides of reactive oxygen species for cancer: the roles of reactive oxygen species in tumorigenesis, prevention, and therapy," *Antioxidants & Redox Signaling*, vol. 16, no. 11, pp. 1295–1322, 2012.
- [30] J. Boonstra and J. A. Post, "Molecular events associated with reactive oxygen species and cell cycle progression in mammalian cells," *Gene*, vol. 337, pp. 1–13, 2004.
- [31] P. A. Cerutti, "Prooxidant states and tumor promotion," *Science*, vol. 227, no. 4685, pp. 375–381, 1985.
- [32] F. Q. Schafer and G. R. Buettner, "Redox environment of the cell as viewed through the redox state of the glutathione disulfide/glutathione couple," *Free Radical Biology & Medicine*, vol. 30, no. 11, pp. 1191–1212, 2001.
- [33] W. S. Wu, "The signaling mechanism of ROS in tumor progression," *Cancer Metastasis Reviews*, vol. 25, no. 4, pp. 695–705, 2006.
- [34] K. Irani, Y. Xia, J. L. Zweier et al., "Mitogenic signaling mediated by oxidants in Ras-transformed fibroblasts," *Science*, vol. 275, no. 5306, pp. 1649–1652, 1997.
- [35] L. He, M. H. Nan, H. C. Oh et al., "Asperlin induces G<sub>2</sub>/M arrest through ROS generation and ATM pathway in human cervical carcinoma cells," *Biochemical and Biophysical Research Communications*, vol. 409, no. 3, pp. 489–493, 2011.
- [36] S. Macip, A. Kosoy, S. W. Lee, M. J. O'Connell, and S. A. Aaronson, "Oxidative stress induces a prolonged but reversible arrest in p53-null cancer cells, involving a Chk1-dependent G<sub>2</sub> checkpoint," *Oncogene*, vol. 25, no. 45, pp. 6037–6047, 2006.
- [37] D. Xiao, A. Herman-Antosiewicz, J. Antosiewicz et al., "Diallyl trisulfide-induced G<sub>2</sub>-M phase cell cycle arrest in human prostate cancer cells is caused by reactive oxygen species-dependent destruction and hyperphosphorylation of Cdc25C," *Oncogene*, vol. 24, no. 41, pp. 6256–6268, 2005.
- [38] S. P. Hussain, L. J. Hofseth, and C. C. Harris, "Radical causes of cancer," *Nature Reviews Cancer*, vol. 3, no. 4, pp. 276–285, 2003.
- [39] S. Reuter, S. C. Gupta, M. M. Chaturvedi, and B. B. Aggarwal, "Oxidative stress, inflammation, and cancer: how are they linked?," *Free Radical Biology & Medicine*, vol. 49, no. 11, pp. 1603–1616, 2010.
- [40] N. S. Chandel, M. G. Vander Heiden, C. B. Thompson, and P. T. Schumacker, "Redox regulation of p53 during hypoxia," *Oncogene*, vol. 19, no. 34, pp. 3840–3848, 2000.
- [41] B. Liu, Y. Chen, and D. K. St Clair, "ROS and p53: a versatile partnership," *Free Radical Biology & Medicine*, vol. 44, no. 8, pp. 1529–1535, 2008.
- [42] Y. R. Seo, M. R. Kelley, and M. L. Smith, "Selenomethionine regulation of p53 by a ref1-dependent redox mechanism," *Proceedings of the National Academy of Sciences of the United States of America*, vol. 99, no. 22, pp. 14548–14553, 2002.
- [43] Z. Luo, X. Xu, T. Sho et al., "ROS-induced autophagy regulates porcine trophectoderm cell apoptosis, proliferation, and differentiation," *American Journal of Physiology Cell physiology*, vol. 316, no. 2, pp. C198–C209, 2019.
- [44] L. Tang, J. Li, W. Fu, W. Wu, and J. Xu, "Suppression of FADS1 induces ROS generation, cell cycle arrest, and apoptosis in melanocytes: implications for vitiligo," *Aging (Albany NY)*, vol. 11, no. 24, pp. 11829–11843, 2019.
- [45] M. F. Renschler, "The emerging role of reactive oxygen species in cancer therapy," *European Journal of Cancer*, vol. 40, no. 13, pp. 1934–1940, 2004.
- [46] S. M. Toler, D. Noe, and A. Sharma, "Selective enhancement of cellular oxidative stress by chloroquine: implications for the treatment of glioblastoma multiforme," *Neurosurgical Focus*, vol. 21, no. 6, 2006.
- [47] K. E. Eblin, T. J. Jensen, S. M. Wnek, S. E. Buffington, B. W. Futscher, and A. J. Gandolfi, "Reactive oxygen species regulate properties of transformation in UROtsa cells exposed to monomethylarsonous acid by modulating MAPK signaling," *Toxicology*, vol. 255, no. 1–2, pp. 107–114, 2009.
- [48] A. R. Na, Y. M. Chung, S. B. Lee, S. H. Park, M. S. Lee, and Y. D. Yoo, "A critical role for Romo1-derived ROS in cell proliferation," *Biochemical and Biophysical Research Communications*, vol. 369, no. 2, pp. 672–678, 2008.
- [49] A. De Luca, F. Sanna, M. Salles et al., "Methionine sulfoxide reductase A down-regulation in human breast cancer cells results in a more aggressive phenotype," *Proceedings of the*

- National Academy of Sciences of the United States of America*, vol. 107, no. 43, pp. 18628–18633, 2010.
- [50] Y. Qin, X. Pan, T. T. Tang, L. Zhou, and X. G. Gong, “Anti-proliferative effects of the novel squamosamide derivative (FLZ) on HepG2 human hepatoma cells by regulating the cell cycle-related proteins are associated with decreased  $\text{Ca}^{2+}$ /ROS levels,” *Chemico-Biological Interactions*, vol. 193, no. 3, pp. 246–253, 2011.
- [51] D. O. Moon, M. O. Kim, Y. H. Choi, J. W. Hyun, W. Y. Chang, and G. Y. Kim, “Butein induces  $\text{G}_2/\text{M}$  phase arrest and apoptosis in human hepatoma cancer cells through ROS generation,” *Cancer Letters*, vol. 288, no. 2, pp. 204–213, 2010.
- [52] P. S. Koka, D. Mondal, M. Schultz, A. B. Abdel-Mageed, and K. C. Agrawal, “Studies on molecular mechanisms of growth inhibitory effects of thymoquinone against prostate cancer cells: role of reactive oxygen species,” *Experimental Biology and Medicine (Maywood, N.J.)*, vol. 235, no. 6, pp. 751–760, 2010.
- [53] Y. Qu, J. Wang, P. S. Ray et al., “Thioredoxin-like 2 regulates human cancer cell growth and metastasis via redox homeostasis and NF- $\kappa$ B signaling,” *The Journal of Clinical Investigation*, vol. 121, no. 1, pp. 212–225, 2011.
- [54] A. Morishita, K. Fujita, H. Iwama et al., “Role of microRNA-210-3p in hepatitis B virus-related hepatocellular carcinoma,” *American Journal of Physiology Gastrointestinal and Liver Physiology*, vol. 318, no. 3, pp. G401–G409, 2020.
- [55] A. K. Singh, S. B. Rooge, A. Varshney et al., “Global microRNA expression profiling in the liver biopsies of hepatitis B virus-infected patients suggests specific microRNA signatures for viral persistence and hepatocellular injury,” *Hepatology*, vol. 67, no. 5, pp. 1695–1709, 2018.
- [56] Z. Z. Zhang, X. Liu, D. Q. Wang et al., “Hepatitis B virus and hepatocellular carcinoma at the miRNA level,” *World Journal of Gastroenterology*, vol. 17, no. 28, pp. 3353–3358, 2011.
- [57] Q. Q. Hao, Q. H. Wang, W. Xia, and H. Z. Qian, “Circulating miRNA expression profile and bioinformatics analysis in patients with occult hepatitis B virus infection,” *Journal of Medical Virology*, vol. 92, no. 2, pp. 191–200, 2020.
- [58] M. H. van der Ree, L. Jansen, Z. Kruize et al., “Plasma micro-RNA levels are associated with hepatitis B e antigen status and treatment response in chronic hepatitis B patients,” *The Journal of Infectious Diseases*, vol. 215, no. 9, pp. 1421–1429, 2017.
- [59] M. Deng, J. Hou, J. Hu et al., “Hepatitis B virus mRNAs functionally sequester let-7a and enhance hepatocellular carcinoma,” *Cancer Letters*, vol. 383, no. 1, pp. 62–72, 2016.
- [60] L. Sun, X. Wang, J. Saredy, Z. Yuan, X. Yang, and H. Wang, “Innate-adaptive immunity interplay and redox regulation in immune response,” *Redox biology*, vol. 37, article 101759, 2020.
- [61] M. Inoue, E. F. Sato, M. Nishikawa et al., “Mitochondrial generation of reactive oxygen species and its role in aerobic life,” *Current Medicinal Chemistry*, vol. 10, no. 23, pp. 2495–2505, 2003.
- [62] B. Bandy and A. J. Davison, “Mitochondrial mutations may increase oxidative stress: implications for carcinogenesis and aging?,” *Free Radical Biology & Medicine*, vol. 8, no. 6, pp. 523–539, 1990.
- [63] Q. Huang, L. Zhan, H. Cao et al., “Increased mitochondrial fission promotes autophagy and hepatocellular carcinoma cell survival through the ROS-modulated coordinated regulation of the NFKB and TP53 pathways,” *Autophagy*, vol. 12, no. 6, pp. 999–1014, 2016.
- [64] C. Zhuang, C. Zhuang, X. Luo et al., “N6-methyladenosine demethylase FTO suppresses clear cell renal cell carcinoma through a novel FTO-PGC-1 $\alpha$  signalling axis,” *Journal of Cellular and Molecular Medicine*, vol. 23, no. 3, pp. 2163–2173, 2019.
- [65] F. Yu, J. Wei, X. Cui et al., “Post-translational modification of RNA m6A demethylase ALKBH5 regulates ROS-induced DNA damage response,” *Nucleic Acids Research*, vol. 49, no. 10, pp. 5779–5797, 2021.
- [66] E. Bouffet, A. Jouvret, P. Thiesse, and M. Sindou, “Chemotherapy for aggressive or anaplastic high grade oligodendrogliomas and oligoastrocytomas: better than a salvage treatment,” *British Journal of Neurosurgery*, vol. 12, no. 3, pp. 217–222, 1998.
- [67] P. H. Gutin, C. B. Wilson, A. R. Kumar et al., “Phase II study of procarbazine, CCNU, and vincristine combination chemotherapy in the treatment of malignant brain tumors,” *Cancer*, vol. 35, no. 5, pp. 1398–1404, 1975.
- [68] T. M. Pawlik and K. Keyomarsi, “Role of cell cycle in mediating sensitivity to radiotherapy,” *International Journal of Radiation Oncology • Biology • Physics*, vol. 59, no. 4, pp. 928–942, 2004.
- [69] J. A. Bertout, A. J. Majmundar, J. D. Gordan et al., “HIF2 $\alpha$  inhibition promotes p53 pathway activity, tumor cell death, and radiation responses,” *Proceedings of the National Academy of Sciences of the United States of America*, vol. 106, no. 34, pp. 14391–14396, 2009.
- [70] E. K. Koh, B. K. Ryu, D. Y. Jeong, I. S. Bang, M. H. Nam, and K. S. Chae, “A 60-Hz sinusoidal magnetic field induces apoptosis of prostate cancer cells through reactive oxygen species,” *International Journal of Radiation Biology*, vol. 84, no. 11, pp. 945–955, 2008.
- [71] J. Ahn, C. B. Ambrosone, P. A. Kanetsky et al., “Polymorphisms in genes related to oxidative stress (CAT, MnSOD, MPO, and eNOS) and acute toxicities from radiation therapy following lumpectomy for breast cancer,” *Clinical Cancer Research*, vol. 12, no. 23, pp. 7063–7070, 2006.

## Research Article

# The Prognostic Value and Immunological Role of STEAP1 in Pan-Cancer: A Result of Data-Based Analysis

Chen Zhao <sup>1</sup>, Kewei Xiong <sup>2</sup>, Zhiqiang Ji <sup>3</sup>, Fengming Liu,<sup>2</sup> and Xiangpan Li <sup>1</sup>

<sup>1</sup>Department of Oncology, Renmin Hospital of Wuhan University, Wuhan 430060, China

<sup>2</sup>School of Mathematics and Statistics, Central China Normal University, Wuhan 430079, China

<sup>3</sup>School of Public Health, Cheeloo College of Medicine, Shandong University, Jinan 250012, China

Correspondence should be addressed to Chen Zhao; [chen\\_zhao@whu.edu.cn](mailto:chen_zhao@whu.edu.cn) and Xiangpan Li; [rm001227@whu.edu.cn](mailto:rm001227@whu.edu.cn)

Received 15 October 2021; Revised 1 December 2021; Accepted 9 December 2021; Published 11 March 2022

Academic Editor: Alessandro Poggi

Copyright © 2022 Chen Zhao et al. This is an open access article distributed under the Creative Commons Attribution License, which permits unrestricted use, distribution, and reproduction in any medium, provided the original work is properly cited.

**Purpose.** This study is aimed at systematically analyzing the expression, function, and prognostic value of six transmembrane epithelial antigen of the prostate 1 (STEAP1) in various cancers. **Methods.** The expressions of STEAP1 between normal and tumor tissues were analyzed using TCGA and GTEx. Clinicopathologic data was collected from GEPIA and TCGA. Prognostic analysis was conducted by Cox proportional hazard regression and Kaplan-Meier survival. DNA methylation, mutation features, and molecular subtypes of cancers were also investigated. The top-100 coexpressed genes with STEAP1 were involved in functional enrichment analysis. ESTIMATE algorithm was used to analyze the correlation between STEAP1 and immunity value. The relationships of STEAP1 and biomarkers including tumor mutational burden (TMB), microsatellite instability (MSI), and stemness score as well as chemosensitivity were also illustrated. **Results.** Among 33 cancers, STEAP1 was overexpressed in 19 cancers such as cervical squamous cell carcinoma and endocervical adenocarcinoma (CESC), colon adenocarcinoma, and lymphoid neoplasm diffuse large B cell lymphoma while was downregulated in 5 cancers such as adrenocortical carcinoma, breast invasive carcinoma (BRCA), and kidney chromophobe renal cell carcinoma. STEAP1 has significant prognostic relationships in multiple cancers. 15 cancers exhibited differences of DNA methylation including bladder urothelial carcinoma, BRCA, and CESC. STEAP1 expression was positively correlated to immune molecules especially in thyroid carcinoma and negatively especially in uveal melanoma. STEAP1 was associated with TMB and MSI in certain cancers. In addition, STEAP1 was connected with increased chemosensitivity of drugs such as trametinib and pimasertib. **Conclusions.** STEAP1 was an underlying target for prognostic prediction in different cancer types and a potential biomarker of TMB, MSI, tumor microenvironment, and chemosensitivity.

## 1. Introduction

Cancer is a global health issue of different genetic disorders and leads to a dominant cause of mortality worldwide [1, 2]. Carcinogenesis is dynamically driven by environmental selection forces, and tumor progression is triggered by regulation of gene expression such as DNA methylation, histone, and genome instability as well as alterations in transcriptome level between normal and tumor tissues [3–5].

Six transmembrane epithelial antigen of the prostate 1 (STEAP1) was firstly investigated as a potential biomarker in prostate cancer and has been identified to be overexpressed in several types of cancers [6]. STEAP1 locates at

the cell membrane, has been suggested a role in intercellular communication, modulating the transport of small molecules and ions such as  $\text{Na}^+$ ,  $\text{Ca}^{2+}$ , and  $\text{K}^+$ , and releasing soluble cytokines and chemokines [7, 8]. STEAP1 also has metal reductase activity capable of reducing metal ion complexes and oxygen [9, 10].

Moreover, STEAP1 is highly expressed in multiple cancer tissues such as bladder, colon cancer, ovarian, and prostate and has the role of promoting invasion of tumor cells [10, 11]. In addition, several studies exploring the role of STEAP1 in cancer cells showed that its overexpression inhibits apoptosis and induces epithelial to mesenchymal transition, ultimately contributing to tumor progression

and aggressiveness [12]. Although STEAP1 has been considered as an optimal target for T cell-based immunotherapy, with applications in a subset of cancer types nowadays [9], its expression and mutation landscape as well as prognostic value in many other cancers still remained to be investigated.

This study is aimed at systematically analyzing the expression, function, and prognostic value of STEAP1 in various cancers. The associations of STEAP1 with tumor microenvironment, immune-infiltrating, and other immune-related biomarkers in different cancer types were also investigated based on online web servers and R program.

## 2. Materials and Methods

**2.1. Data Collection and Statistical Analysis.** The workflow of this study is shown in Figure 1 with STEAP1 expression distribution in both tumor and healthy individuals. Transcriptional RNA sequencing (RNA-seq) data of 33 cancer types from The Cancer Genome Atlas (TCGA) and Genotype-Tissue Expression (GTEx) datasets from UCSC XENA [13] (<https://xenabrowser.net/datapages/>) were formatted in Transcripts Per Kilobase Million (TPM) according to Toil strategy [14] and transformed by  $\log_2$ . The 33 cancer types including in this study were as follows: adrenocortical carcinoma (ACC), bladder urothelial carcinoma (BLCA), breast invasive carcinoma (BRCA), cervical squamous cell carcinoma and endocervical adenocarcinoma (CESC), cholangiocarcinoma (CESC), colon adenocarcinoma (COAD), lymphoid neoplasm diffuse large B cell lymphoma (DLBC), esophageal carcinoma (ESCA), glioblastoma multiforme (GBM), head and neck squamous cell carcinoma (HNSC), kidney chromophobe renal cell carcinoma (KICH), kidney renal clear cell carcinoma (KIRC), kidney renal papillary cell carcinoma (KIRP), acute myeloid leukemia (LAML), brain lower grade glioma (LGG), liver hepatocellular carcinoma (LIHC), lung adenocarcinoma (LUAD), lung squamous cell carcinoma (LUSC), mesothelioma (MESO), ovarian serous cystadenocarcinoma (OV), pancreatic adenocarcinoma (PAAD), pheochromocytoma and paraganglioma (PCPG), prostate adenocarcinoma (PRAD), rectum adenocarcinoma (READ), sarcoma (SARC), skin cutaneous melanoma (SKCM), stomach adenocarcinoma (STAD), testicular germ cell tumors (TGCT), thyroid carcinoma (THCA), thymoma (THYM), uterine corpus endometrial carcinoma (UCEC), uterine carcinosarcoma (UCS), and uveal melanoma (UVM).

The differences of STEAP1 expression level between normal and tumor tissues in distinct cancer types were estimated by both nonpaired and paired statistical tests. To investigate the correlation between clinicopathologic features and STEAP1, Gene Expression Profiling Interactive Analysis [15] (GEPIA, <http://gepia.cancer-pku.cn/>) was used to analyze the STEAP1 expression differences among pathological stages in different cancer types. Furthermore, histological grades were also explored with clinical data downloaded from TCGA cohort (<https://portal.gdc.cancer.gov/>) where patients in G1 or G2 were stratified into an early-grade group whereas patients in G3 or G4 were stratified into an advanced-grade group. It should be noted that for BLCA with low and

high grades, LGG with WHO G2 and G3 were included for the missing distinct histological grades.

The prognostic value of STEAP1 was performed by univariate Cox proportional hazard regression and Kaplan-Meier (KM) survival analysis with high- and low-expression groups at the optimal cutoff determined by survival package in R (version 3.6.3) for overall survival (OS), disease specific survival (DSS), and progression-free interval (PFI).

**2.2. Biological Analysis and Tumor Microenvironment (TME).** Harmonizome [16] (<https://maayanlab.cloud/Harmonizome/>) is a web portal with a collection of information about 295496 attributes and 56720 genes from 114 datasets provided by 66 online resources. The top-100 coexpressed genes with STEAP1 were found in Harmonizome platform and were then validated in TCGA cohort of 33 cancer types. The genes were also included in the functional enrichment analysis regarding Gene Ontology (GO) and Kyoto Encyclopedia of Genes and Genomes (KEGG) for significant biological terms and pathway exploration in the clusterProfiler package (version 3.14.3) [17]. Patients were classified into high- and low-expression groups of STEAP1 at the median cutoff to calculate the logFoldChange (logFC) by the formula:  $\log_{FC} = \log_2(\text{high group}/\text{low group})$ . Then, Gene Set Enrichment Analysis (GSEA) was performed based on the logFC value in each cancer types.

UALCAN [18] (<http://ualcan.path.uab.edu/>) is a resource for omics data analysis, a protein expression which was retrieved from Clinical Proteomic Tumor Analysis Consortium (CPTAC) Confirmatory/Discovery dataset. The methylation difference of STEAP1 between normal and tumor samples was evaluated. DNA methylation interactive visualization database (DNMIVD, <http://119.3.41.228/dnmivd/index/>) was used to investigate the methylation of STEAP1 regarding the correlation between STEAP1 expression level in Fragments Per Kilobase Million (FPKM) form and the methylation level of its promoter [19–21]. The mutation exploration was carried out by cBioPortal (<https://www.cbioportal.org/>), an open-access resource for interactive analysis of all-round cancer genomics datasets. The statistics of mutation frequency and corresponding mutation types in different cancer types were also examined.

TIMER database [22, 23] (<https://cistrome.shinyapps.io/timer/>) was utilized to analyze the immune-infiltrating of B cell, CD8+ T cell, CD4+ T cell, macrophage, neutrophil, and dendritic cell. TISIDB [24] (<http://cis.hku.hk/TISIDB/index.php>) is an online platform for tumor and immune system interaction, which integrates multiple heterogeneous data types including resources from PubMed database, high-throughput screening data, exome and RNA sequencing dataset of patient cohorts with immunotherapy, and well-orchestrated data from TCGA. It was adopted to systematically analyze the correlation of STEAP1 expression and molecular subtypes, TME including immune-infiltrating of lymphocytes, immunomodulators with immunoinhibitors, immunostimulators and major histocompatibility complex (MHC) molecules in humans (human leukocyte antigen, HLA), chemokine, and receptors for different cancer types. To explore the characteristics of relationships between

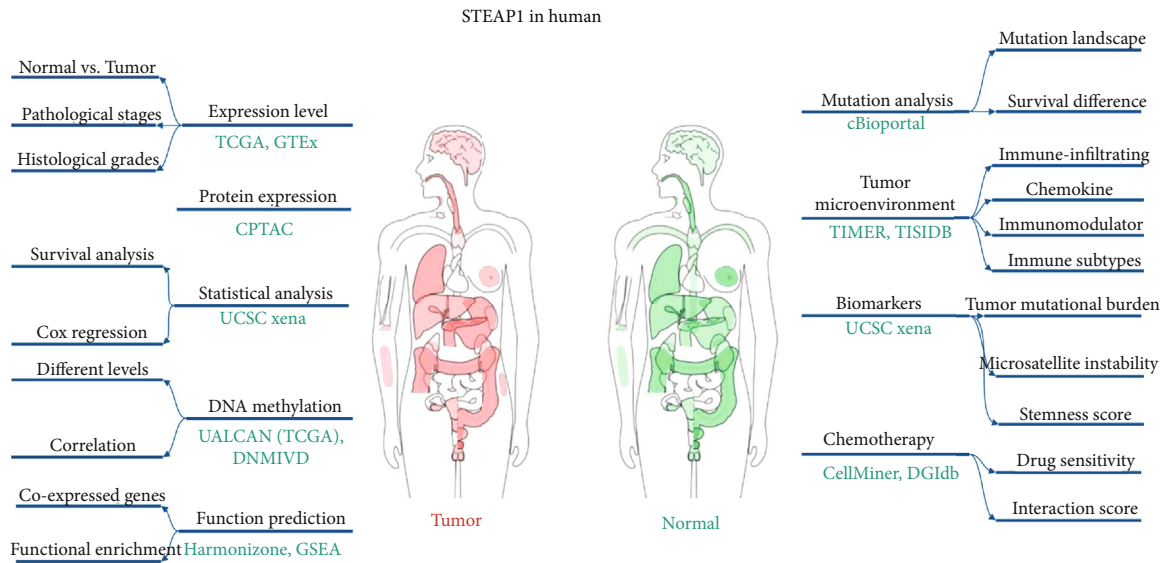


FIGURE 1: The workflow of this study and the distribution of STEAP1 expression level in human beings from GEPIA.

TME and STEAP1 expression level, ESTIMATE algorithm which is aimed at computing the scores of stromal cells and immune cells in malignant tumor tissues using expression data was applied to assess the correlations of STEAP1 and immune scores by Pearson correlation coefficients.

**2.3. Correlation of Biomarkers and STEAP1 Expression.** Single-nucleotide variant data of patients was employed to calculate tumor mutational burden (TMB), and another biomarker microsatellite instability (MSI) of patients in different cancer types was taken to estimate the STEAP1 expression correlation. Moreover, RNA-based and DNA methylation-based stemness scores (RNAss and DNAss) were retrieved to analyze the correlations.

**2.4. Drug Sensitivity and Interactions.** CellMiner [25, 26] (<https://discover.nci.nih.gov/cellminer/home.do>) is designed for study integration and research of molecular and pharmacological data for the NCI-60 cancerous cell lines. DTP NCI-60 with average z-score and the corresponding RNA-seq data were downloaded. The correlations of STEAP1 expression level and drug scores were measured by Pearson correlation coefficients. In addition, the Drug Gene Interaction Database [27] (DGIdb, [https://dgidb.genome.wustl.edu/search\\_interactions](https://dgidb.genome.wustl.edu/search_interactions)) providing connections between genes and the known or potential drug associations was used to study the interactions of top-100 coexpressed genes from Harmonizome with their target approved antineoplastics and immunotherapeutics.

### 3. Results

**3.1. STEAP1 Expression Levels among Clinicopathological Features.** Based on TCGA and GTEx cohorts, as shown in Figure 2(a), STEAP1 was significantly upregulated in CESC, COAD, DLBC, ESCA, GBM, HNSC, KIRC, LGG, LUAD, LUSC, OV, PAAD, PRAD, READ, SKCM, STAD, TGCT,

THYM, UCEC, and UCS whereas it was downregulated in ACC, BRCA, KICH, LAML, and THCA. It indicated that the expression of STEAP1 exhibited heterogeneity in urinary cancers such as renal cell carcinoma and female reproductive disorders such as breast invasive cancer, ovarian cancer, and endometrial carcinoma but consistency in digestive cancer types such as colorectal cancer and gastric cancer as well as respiratory cancers. Paired tests demonstrated STEAP1 had significant different expression on BRCA, ESCA, HNSC, KICH, KIRC, LUAD, LUSC, PRAD, READ, STAD, THCA, and UCEC between normal and tumor tissues (Figures 2(b)–2(m)).

The total protein expression of STEAP1 in breast cancer, colon cancer, lung adenocarcinoma, and UCEC samples was significantly higher than that in normal samples with  $p$  value less than 0.001 (Figure S1a–d) whereas primary ovarian tumor samples exhibited lower STEAP1 expression level than normal samples with  $p$  value less than 0.01 (Figure S1e). The promoter methylation levels of STEAP1 between normal and tumor tissues exerted significant differences in 15 cancers such as BLCA, BRCA, and CESC (Figure 3). According to DNMIIVD, STEAP1 expression levels were negatively correlated with methylation levels of its promoter calculated by Spearman correlation coefficients in BRCA ( $r = -0.11$ , Figure S2a), PRAD ( $r = -0.1$ , Figure S2d), SKCM ( $r = -0.14$ , Figure S2e), and UCEC ( $r = -0.52$ , Figure S2f) while having positive connections with the methylation of its promoter in COAD ( $r = 0.11$ , Figure S2b) and LUSC ( $r = 0.11$ , Figure S2c).

Kruskal-Wallis (KW) test performed on GEPIA website revealed that STEAP1 expression altered significantly with pathological stages in ACC, DLBC, KICH, LUAD, OV, PAAD, and THCA (Figures 4(a)–4(g)). In addition, patients with high grade or advanced-grade group in BLCA (Figure 4(h)), HNSC (Figure 4(i)), LGG (Figure 4(k)), and STAD (Figure 4(l)) had significant higher STEAP1 expression while individuals in high grade or advanced-grade

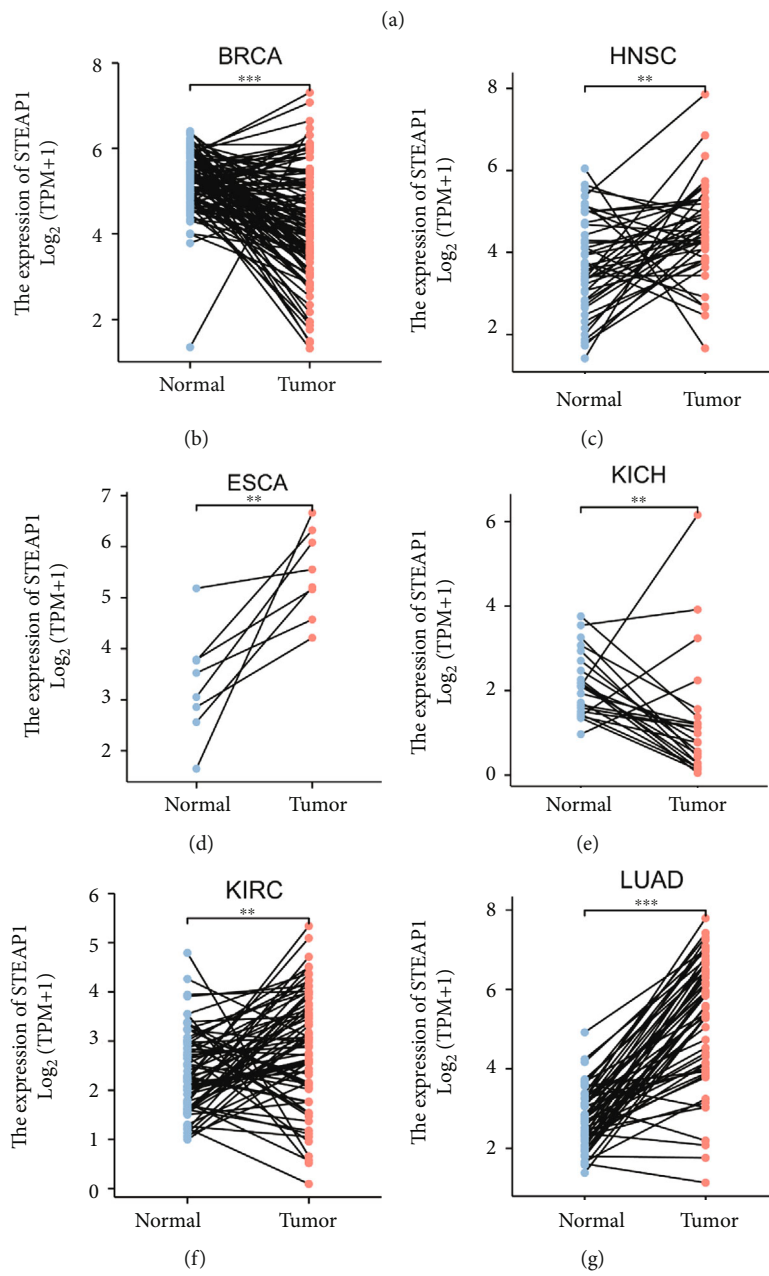
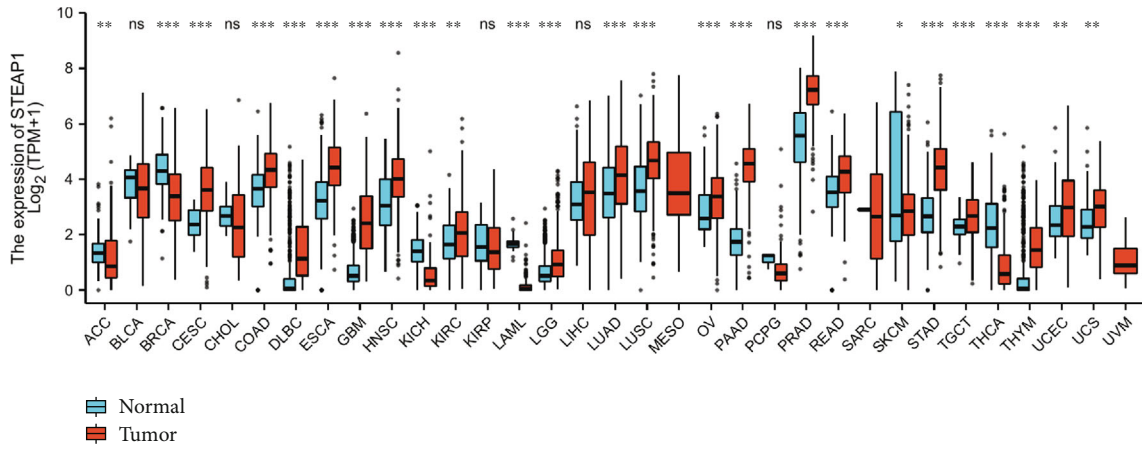


FIGURE 2: Continued.

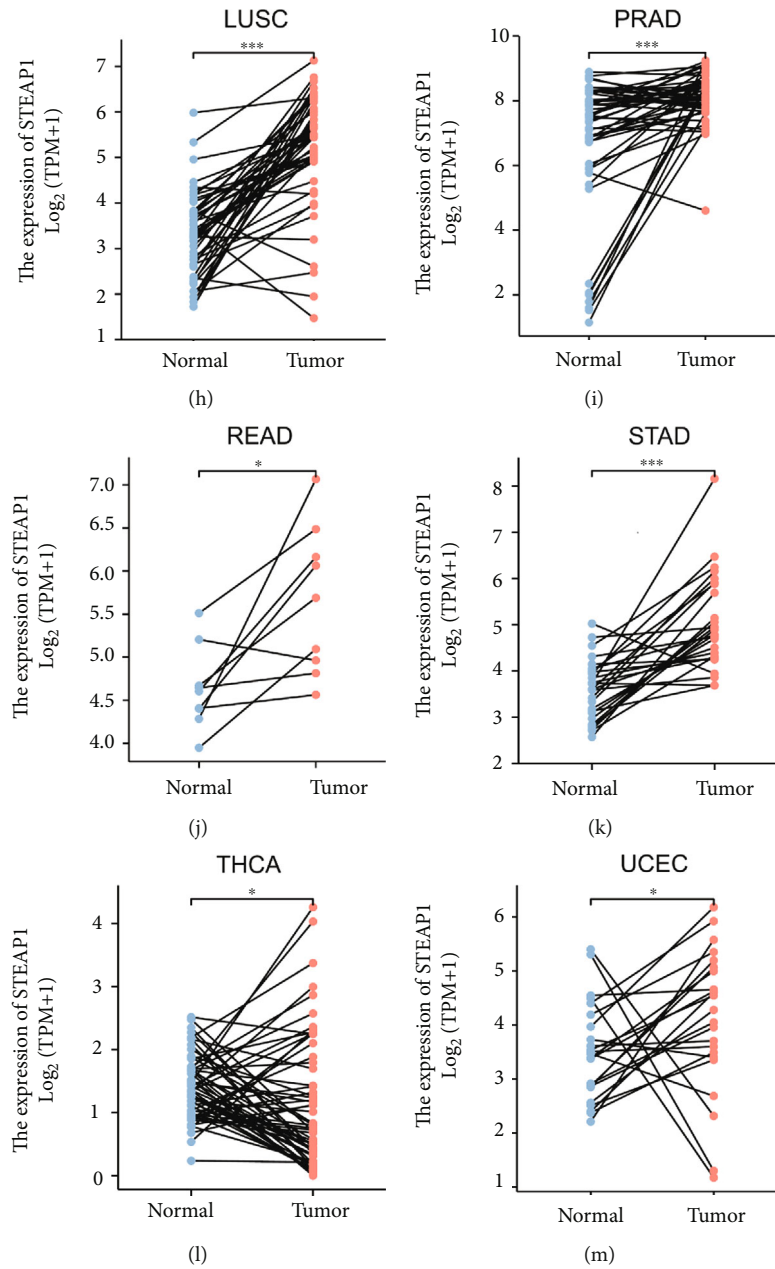


FIGURE 2: (a) The differences of STEAP1 expression level between normal and tumor tissues in 33 cancer types based on TCGA and GTEx cohorts, which were estimated by Wilcoxon rank-sum test (\*\* $p < 0.001$ , \*\* $p < 0.01$ , and \* $p < 0.05$ ; ns: no significance). (b–m) The difference of STEAP1 expression level between normal and tumor tissues in BRCA, ESCA, HNSC, KICH, KIRC, LUAD, LUSC, PRAD, READ, STAD, THCA, and UCEC from TCGA was estimated by paired test.

group by our custom integration with KIRC (Figure 4(j)) and UCEC (Figure 4(m)) had opposite results.

**3.2. Prognostic Analysis.** By conducting univariate Cox proportional hazard regression, Figure 5(a) implied that STEAP1 was a risk factor in ACC ( $p < 0.001$ , hazard ratio (HR) = 1.669, and 95% confidence interval (CI) = 1.266–2.199), CHOL ( $p = 0.030$ , HR = 1.468, and 95%CI = 1.038–2.075), GBM ( $p = 0.011$ , HR = 1.222, and 95%CI = 1.047–1.428), KICH ( $p < 0.001$ , HR = 3.410, and 95%CI = 1.643–7.079), KIRP ( $p = 0.013$ , HR = 1.579, and 95%CI = 1.102–2.261), LAML ( $p = 0.033$ , HR = 3.488, and 95%CI = 1.109

–10.975), LGG ( $p < 0.001$ , HR = 1.798, and 95%CI = 1.422–2.275), LUAD ( $p = 0.014$ , HR = 1.139, and 95%CI = 1.026–1.264), PAAD ( $p = 0.003$ , HR = 1.412, and 95%CI = 1.124–1.773), THCA ( $p = 0.022$ , HR = 1.963, and 95%CI = 1.104–3.490), and THYM ( $p = 0.007$ , HR = 2.868, and 95%CI = 1.342–6.127) for OS while it played an underlying favorable factor in UVM ( $p = 0.004$ , HR = 0.229, and 95%CI = 0.084–0.624).

KM survival analysis for OS revealed that patients with ACC, CHOL, KICH, LAML, LGG, LIHC, LUAD, PAAD, and THYM in the high-expression group at the optimal cut-off experienced poor prognosis whereas folks with BRCA,

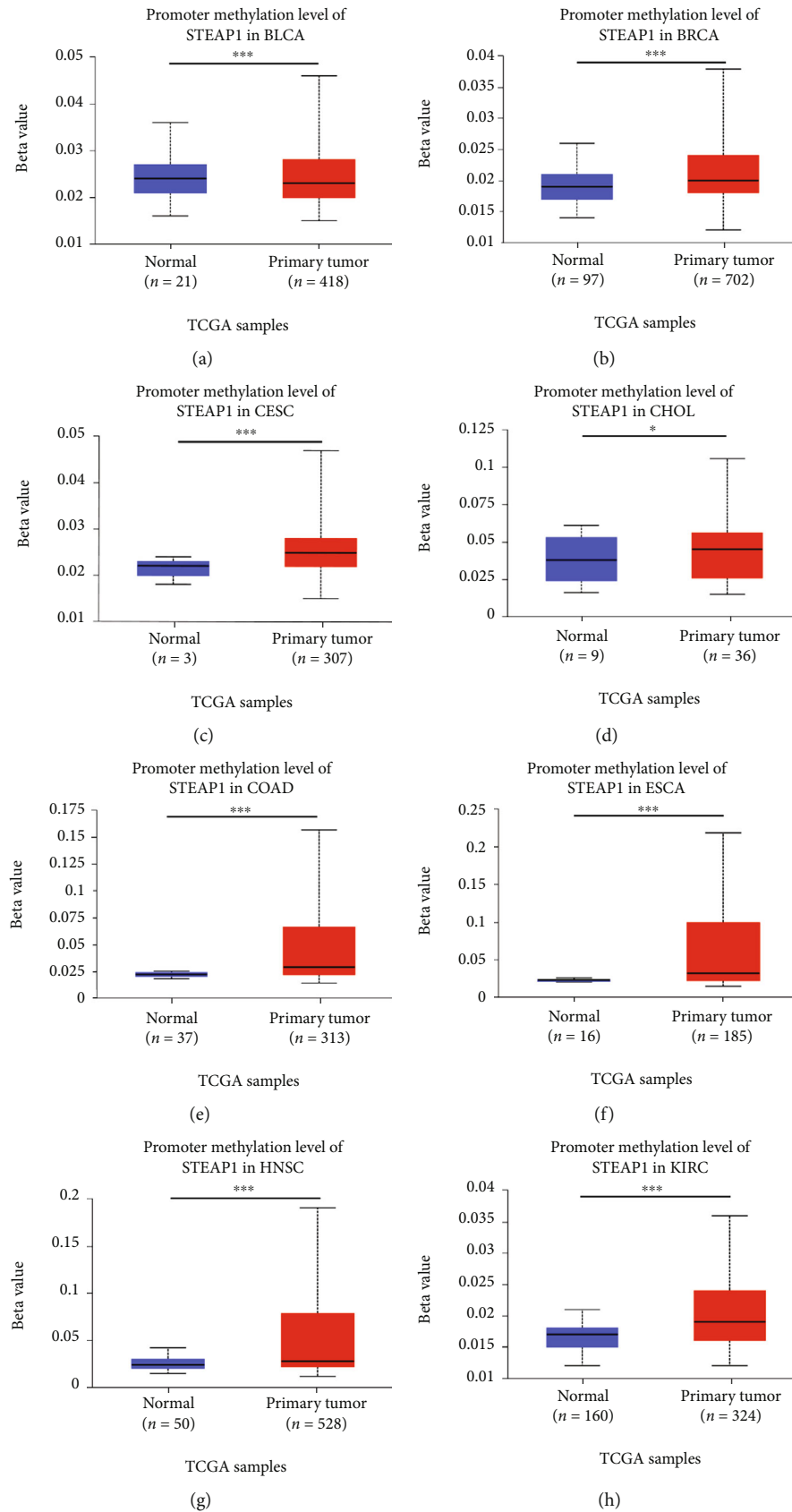


FIGURE 3: Continued.



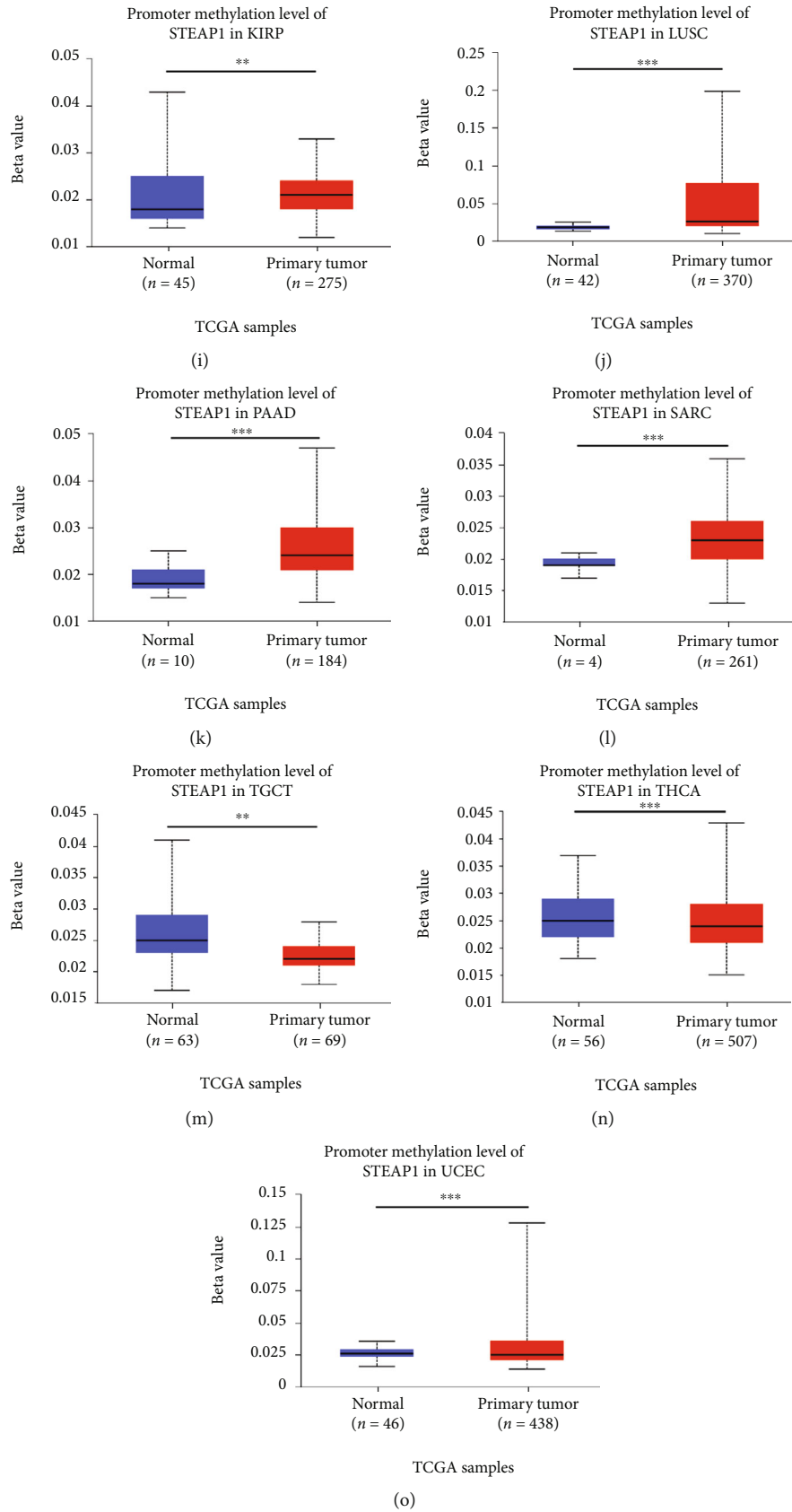


FIGURE 3: Variations of promoter methylation of STEAP1 in several cancers according to the evidence from UALCAN.

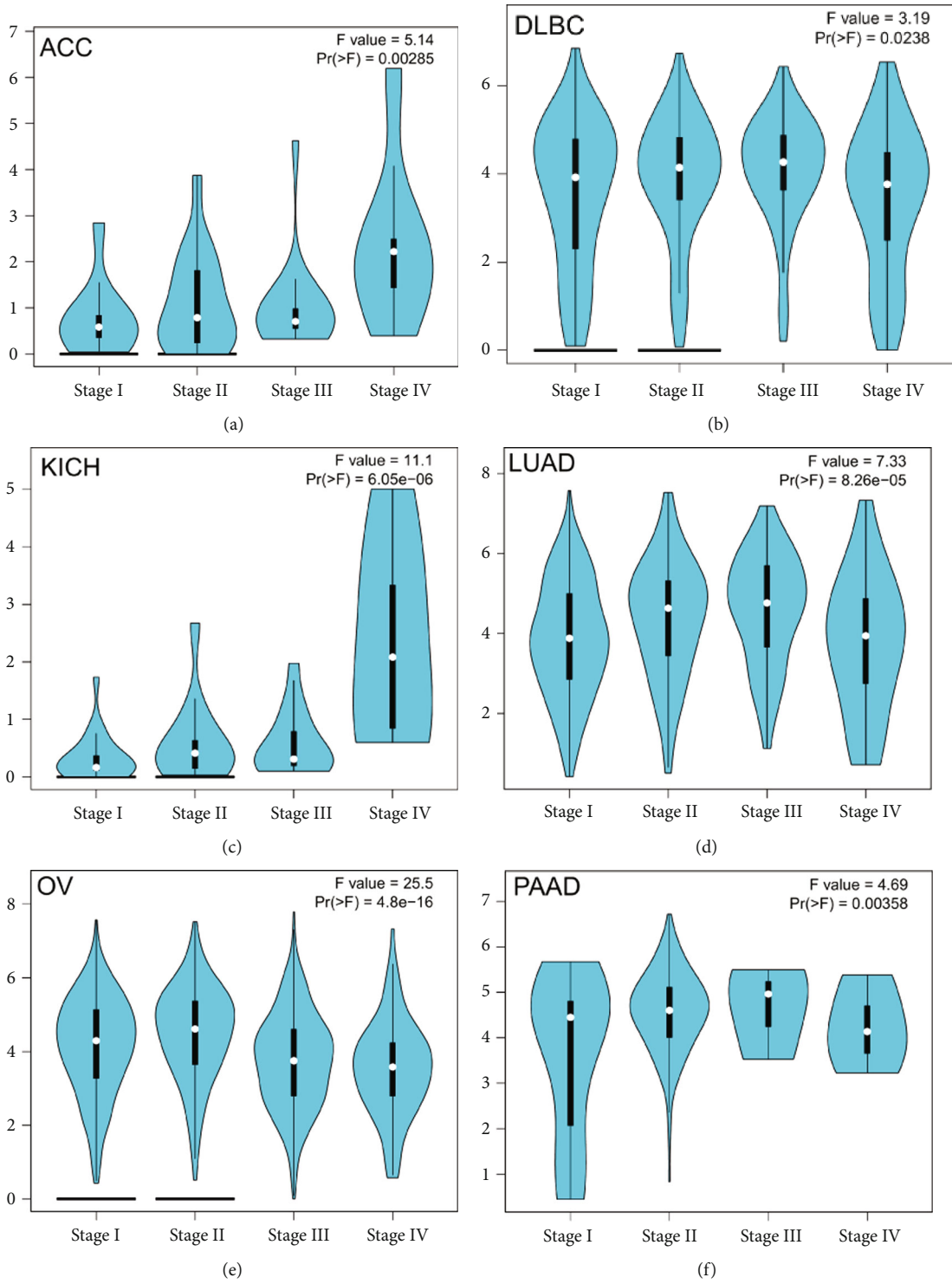


FIGURE 4: Continued.

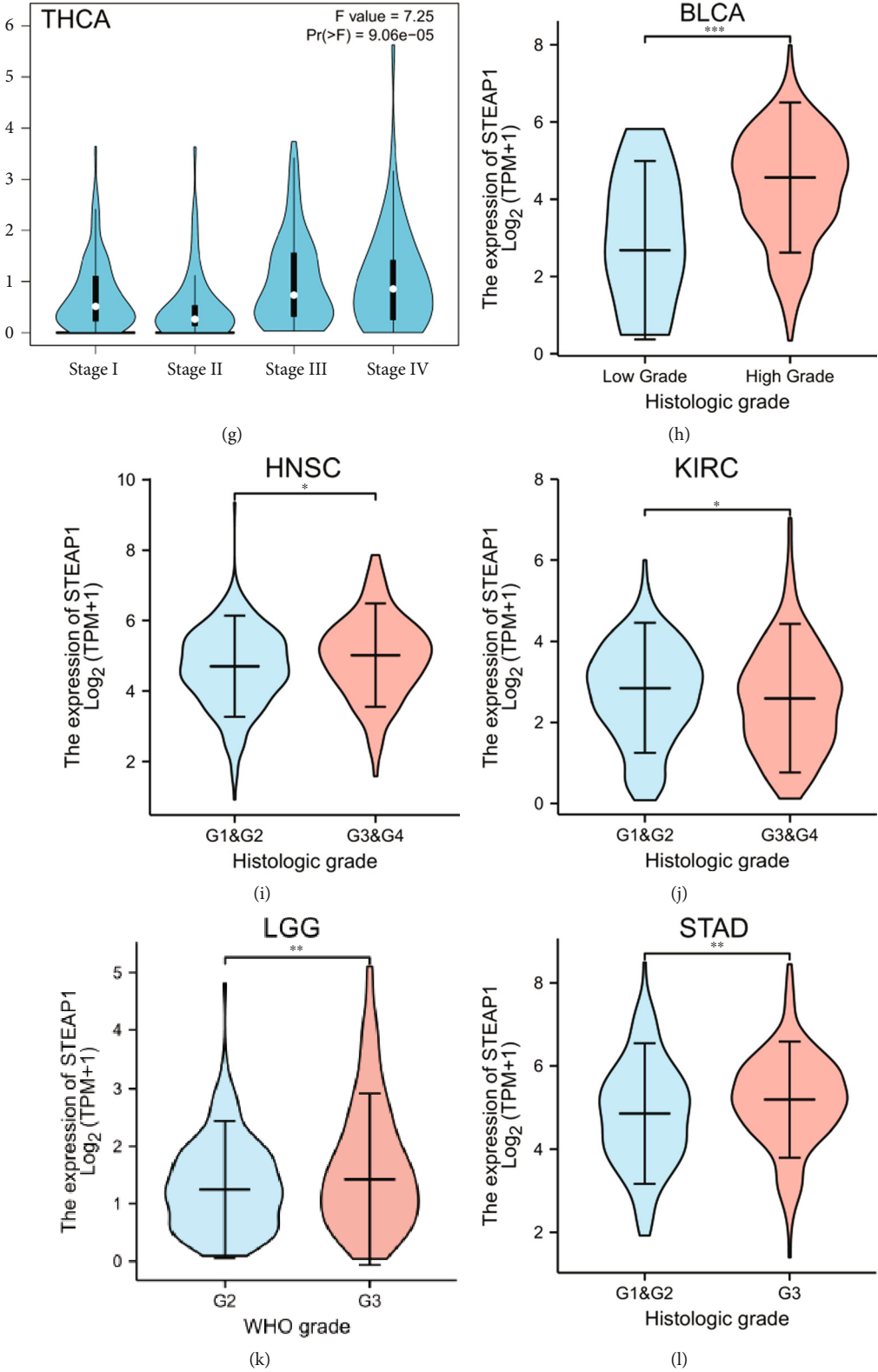


FIGURE 4: Continued.

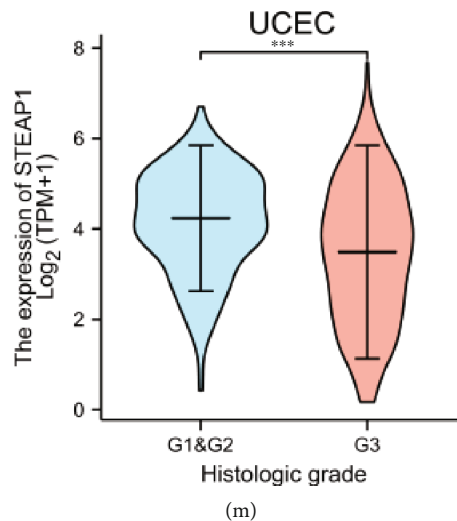


FIGURE 4: (a–g) The difference of STEAP1 expression level between distinct pathological stages in ACC, DLBC, KICH, LUAD, OV, PAAD, and THCA, from GEPIA. (h) The difference of STEAP1 expression level between low and high histological grades in BLCA. (i, j) The difference of STEAP1 expression level between early and advanced grades in HNSC and KIRC. (k) The difference of STEAP1 expression level between WHO G2 and G3 in LGG. (l, m) The difference of STEAP1 expression level between early and advanced grades in STAD and UCEC.

KIRC, LUSC, OV, UCEC, and UVM experienced better survival with high expression of STEAP1 (Figure 5(b)).

The univariate Cox regression for DSS revealed that STEAP1 was a risk factor for ACC, GBM, KICH, KIRP, LGG, LUAD, PAAD, and THCA but a favorable factor for LUSC and UVM (Figure S3a). Survival differences for DSS demonstrated that patients with higher STEAP1 expression in ACC, glioma, KICH, KIRP, LAML, LUAD, and PAAD experienced poor prognosis whereas patients in the high-expression group of STEAP1 with BRCA, ESCA, KIRC, LIHC, UCEC, and UVM had better survival outcomes (Figure S3b). In addition, a univariate Cox regression for PFI indicated that STEAP1 took a risk factor in GBM, KICH, KIRP, LGG, LUAD, and PAAD but a favorable factor in READ and UVM (Figure S4a). KM analysis for PFI demonstrated that patients in the high-expression group stratified by the optimal cutoff with ACC, glioma, KICH, KIRP, LUAD, PAAD, PRAD, and THCA had poor survival while individuals in the same group with BRCA, KIRC, READ, and UVM experienced better prognosis (Figure S4b).

**3.3. Genomic Characteristics.** The mutation frequency and types were analyzed in cBioPortal. As shown in Figure 6(a), the highest frequency of STEAP1 alteration existed in esophageal adenocarcinoma with the amplification accounting for the most. In UCEC patients, mutation accounted for the most among the four alteration types including mutation, structural variant, amplification, and deep deletion. The results of molecular subtypes for different cancer types illustrated in Figure 6(b) implied that STEAP1 expression level exhibited statistically significant differences in BRCA, COAD, GBM, HNSC, KIRP, LGG, LUSC, OV, PCPG, PRAD, STAD, and UCEC.

**3.4. Functional Enrichment Exploration.** The top-100 correlated genes found in Harmonizome (Table S1) were validated in TCGA cohort. It implied that STEAP2 was most positively correlated with STEAP1 in all cancer types as shown in a heatmap (Figure 7(a)). Then, the 100 genes were included in functional enrichment prediction containing GO and KEGG (Table S2). The significant ( $p$ -adjusted < 0.05) signaling-related terms and pathways represented in Figure 7(b) in network style demonstrated that the 100 genes correlated with STEAP1 were enriched in Hippo signaling, integrin-mediated signaling pathway, hepatocyte growth factor receptor signaling pathway, epidermal growth factor receptor signaling pathway, Hippo signaling pathway—multiple species, Hippo signaling pathway, and PI3K-Akt signaling pathway. The outcomes of GSEA analysis are shown in Table S3, and the most significant enriched terms of ACC, BLCA, BRCA, CESC, CHOL, and COAD are shown in Figures 7(c)–7(h).

**3.5. Investigation to TME Related to STEAP1.** According to the evidence from TIMER database (Figure 8(a)), STEAP1 expression level in THCA was positively related to the immune-infiltrating levels of all six cell types where neutrophil and dendritic cell exhibited the maximum correlation coefficients. And the immune-infiltrating of neutrophil correlated with STEAP1 expression level in UVM had the maximum positive coefficient with the value of 0.698. However, STEAP1 expression level in THYM was negatively related to the immune-infiltrating levels of CD4<sup>+</sup> T cell and dendritic cell with the top-2 negative coefficients of -0.489 and -0.426, respectively. It should be also noted that STEAP1 expression in BRCA, COAD, KIRP, and PAAD was positively correlated with the most of immune-infiltrating among the six cell types. To further validate the

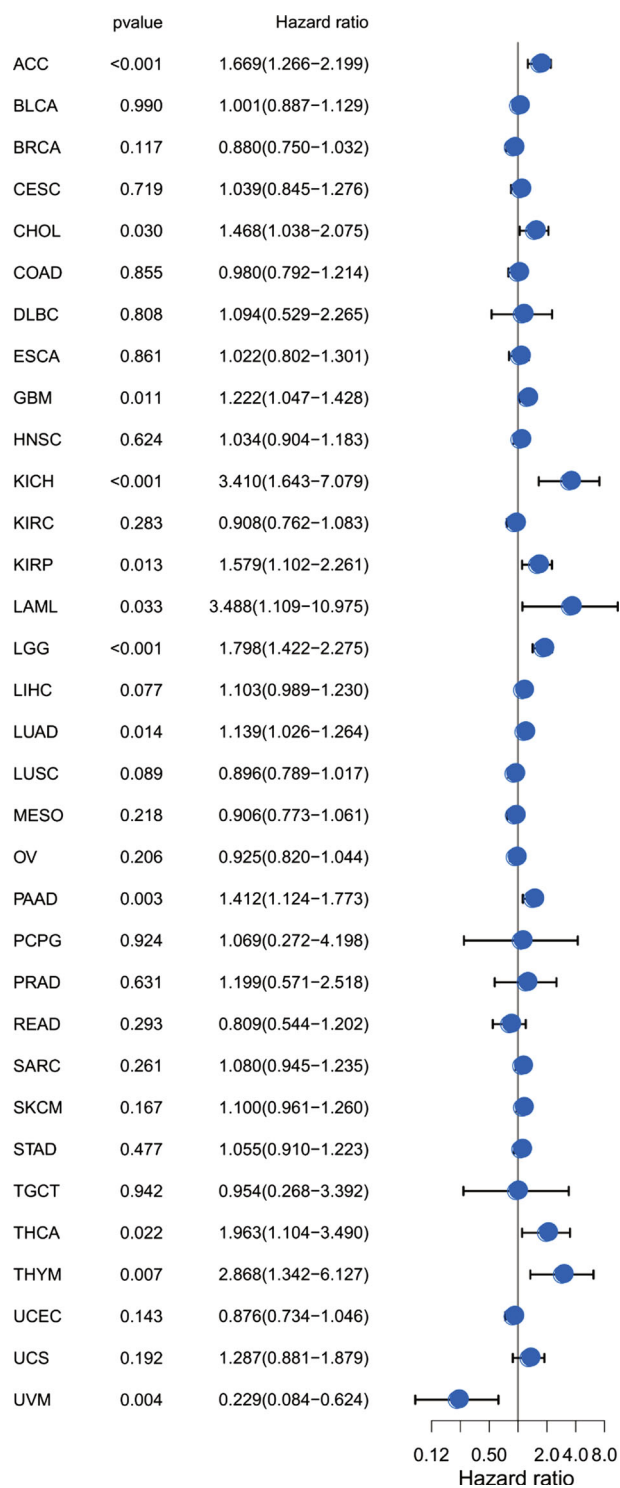
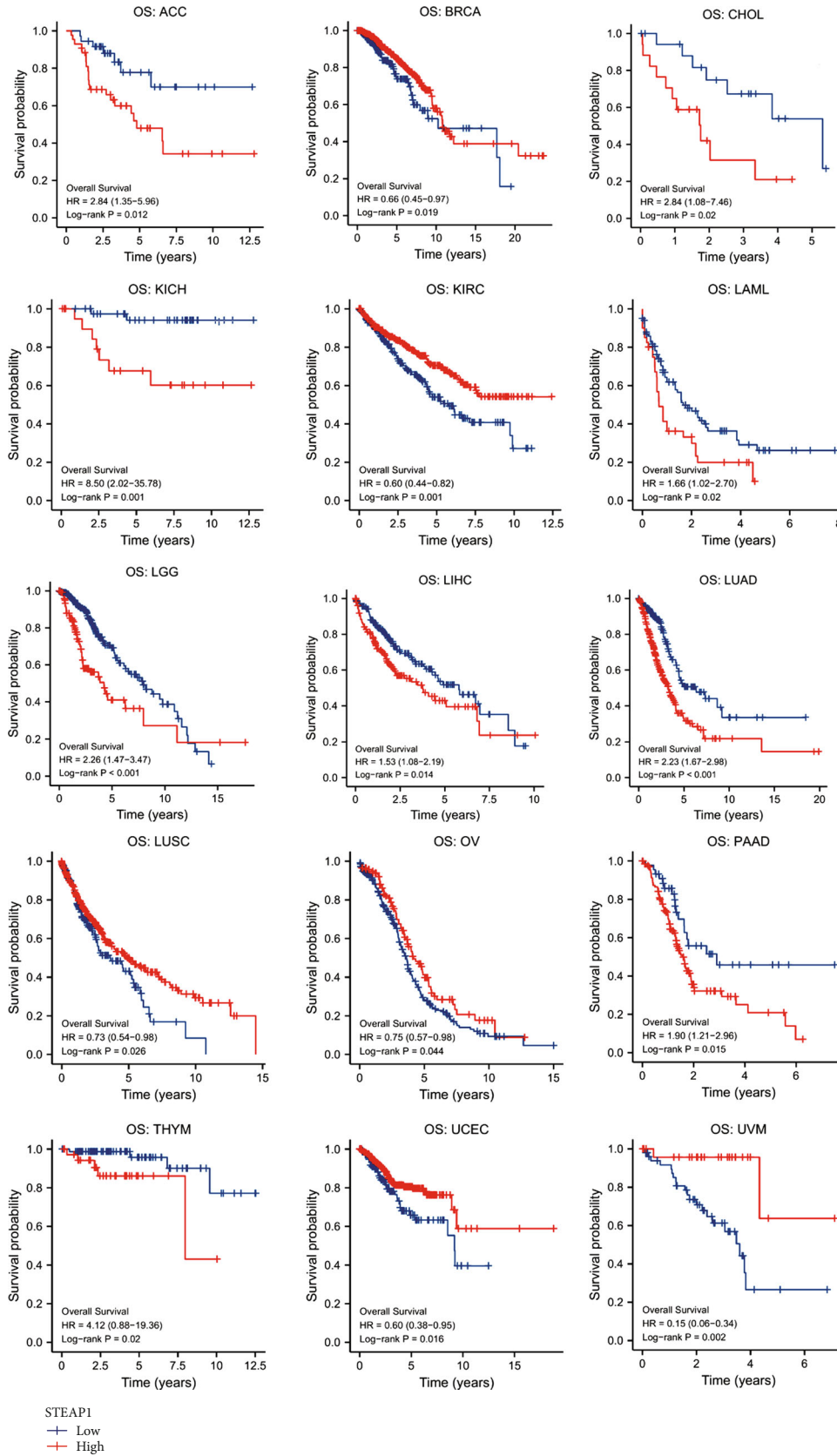


FIGURE 5: Continued.



(b)

FIGURE 5: (a) A univariate Cox proportional hazard regression of OS with STEAP1 expression was illustrated by a forest plot. (b) KM survival analysis of OS between high- and low-expression groups of STEAP1.

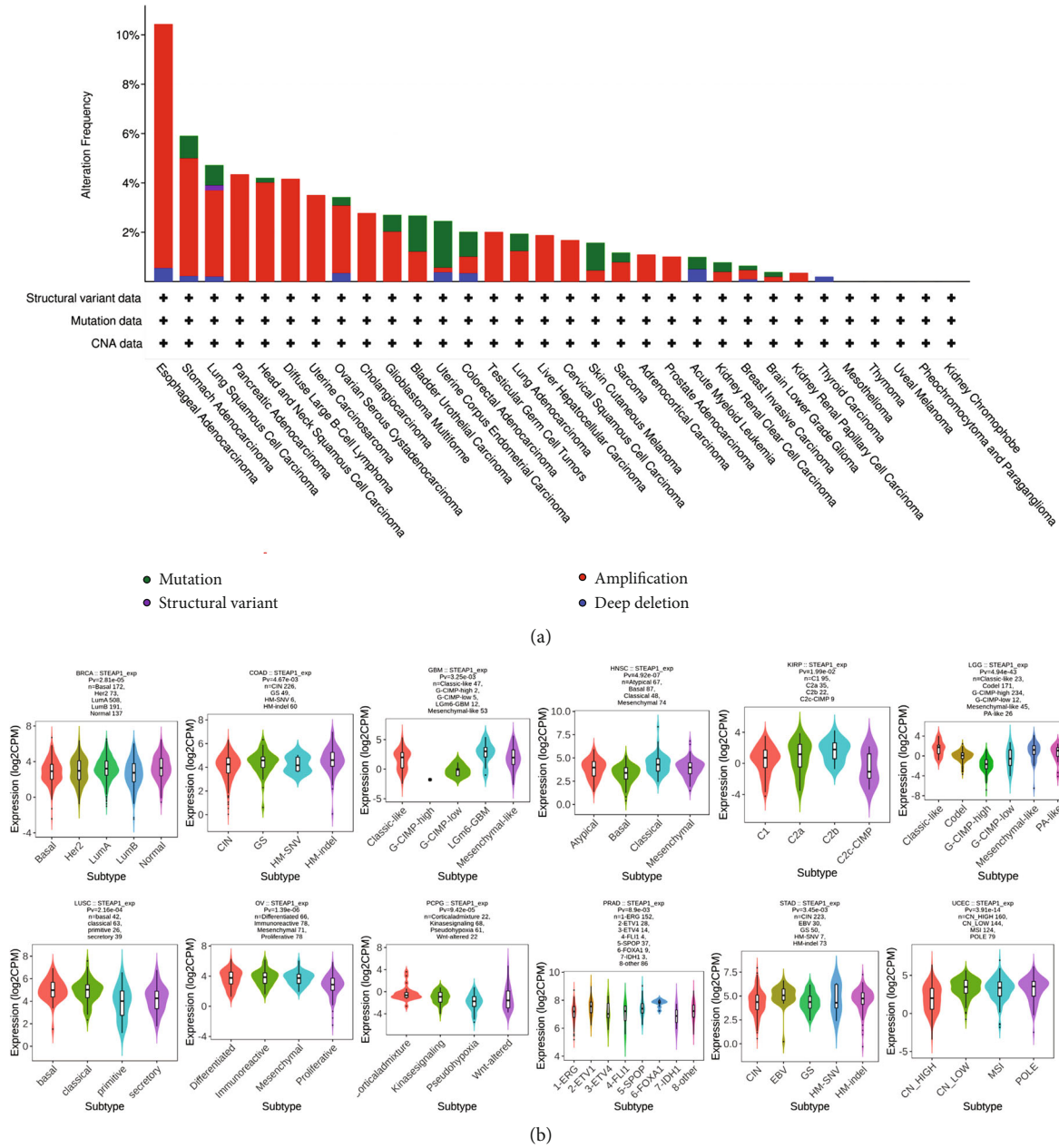
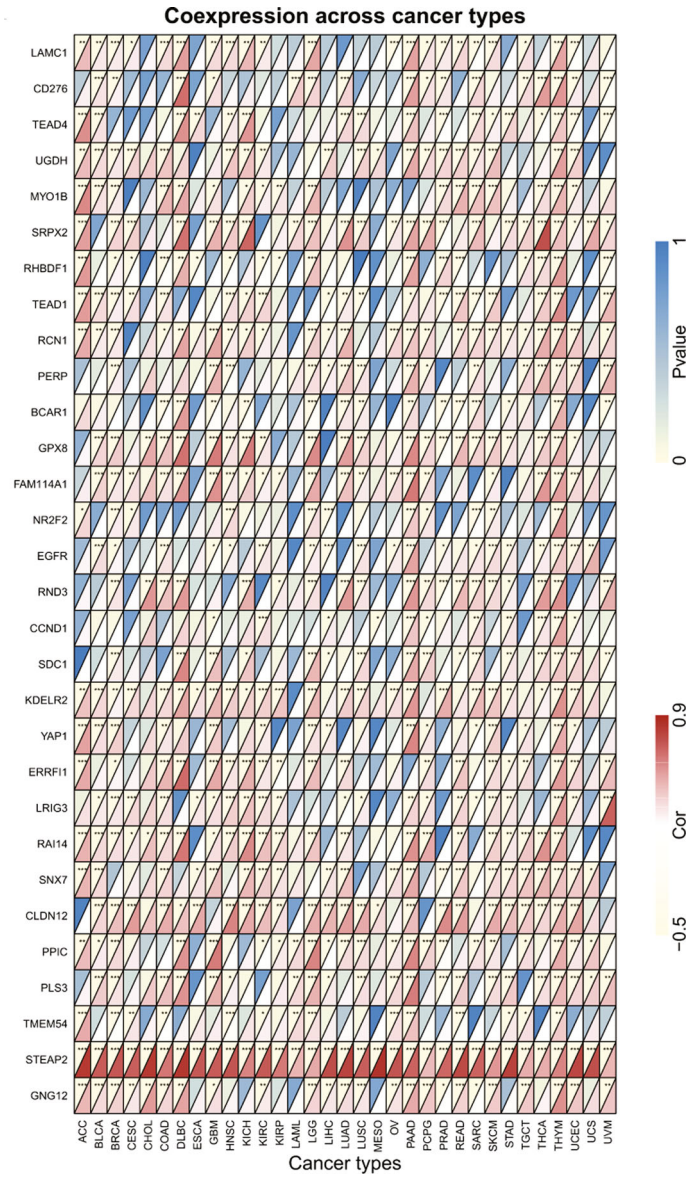


FIGURE 6: (a) The mutation frequency and corresponding mutation types of STEAP1 in different cancers. (b) The differences of STEAP1 expression levels among distinctive molecular subtypes in BRCA, COAD, GBM, HNSC, KIRP, LGG, LUSC, OV, PCPG, PRAD, STAD, and UCEC.

results, TISIDB revealed that STEAP1 expression in THCA was positively related to all cell types for immune-infiltrating including Tcm CD4, Tem CD8, Th1, and Treg, and it was negatively related to infiltrating levels of all cell types in UVM (Figure 8(b)). Moreover, STEAP1 expression had the most significantly positive correlation with molecules in THCA and the most significantly negative correlation with molecules in UVM generally of MHC molecules in human beings including HLA-DOA, HLA-DOB, HLA-DPA1, and HLA-DRA (Figure 8(c)); immune stimulators including CD80, ICOS, ILSRA, and TNFSF18 (Figure 8(d)); immune inhibitors including CTLA4, PDCD1LG2, TIGIT, and VTCN1 (Figure 8(e)); receptors including CCR2, CCR4,

CCR6, and CCR8 (Figure 8(f)); and chemokines including CCL13, CCL17, CCL20, and CCL22 (Figure 8(g)).

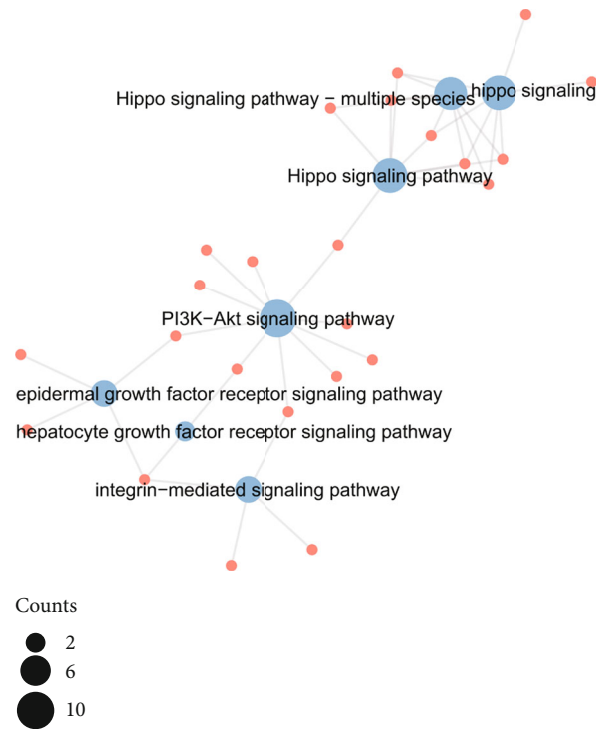
The differences of STEAP1 expression between distinctive immune subtypes including wound healing (C1), IFN- $\gamma$  dominant (C2), inflammatory (C3), lymphocyte depleted (C4), immunologically quiet (C5), and TGF- $\beta$  dominant (C6) were also analyzed. It illustrated that STEAP1 had the lowest expression level in C4 of BRCA, LUAD, and STAD but highest levels in C6 of COAD, in C4 of KIRC, and PRAD. It also exhibited significant differences among immunophenotypes in CHOL, GBM, HNSC, LGG, and UVM. Moreover, LUSC, PAAD, and READ held the lowest STEAP1 expression levels in C3 (Figure S5).



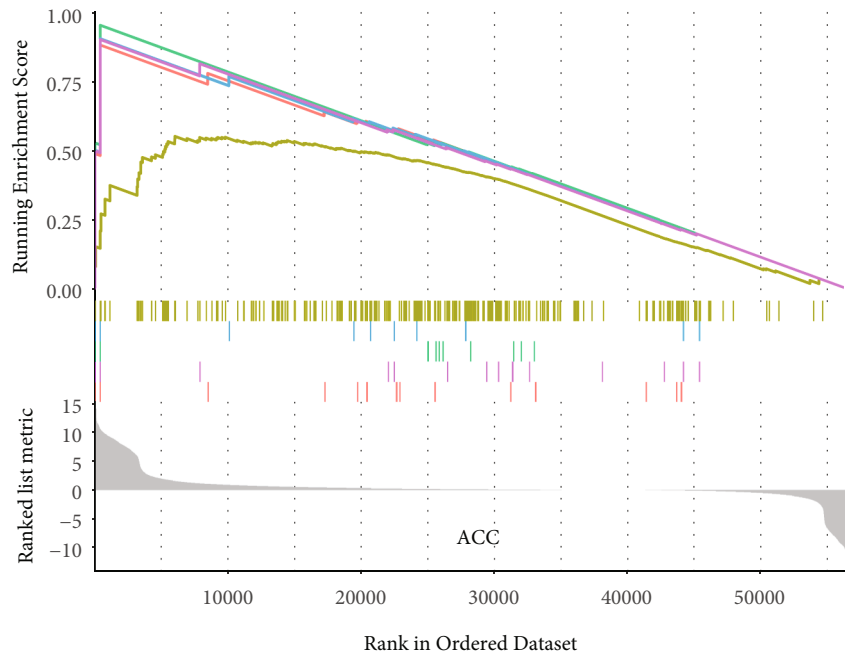
(a)

FIGURE 7: Continued.





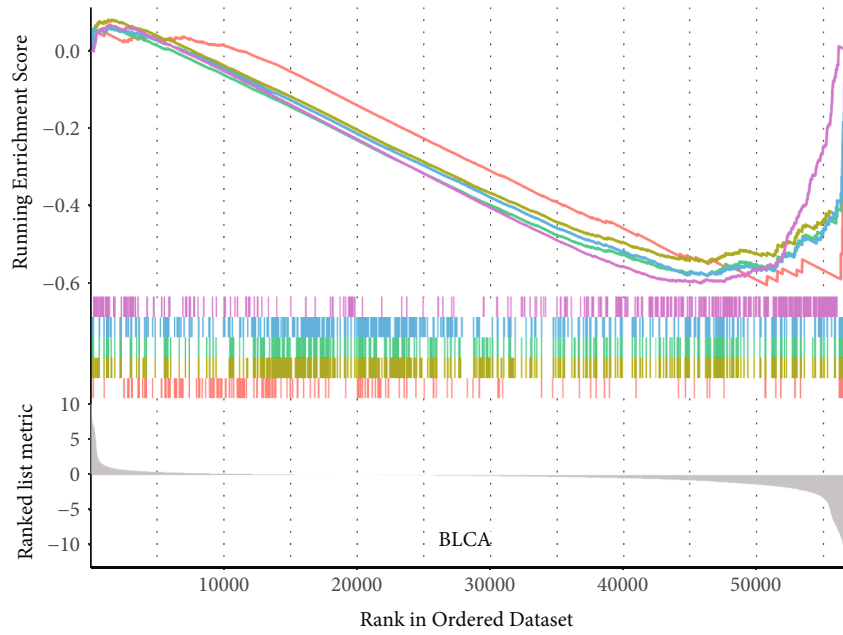
(b)



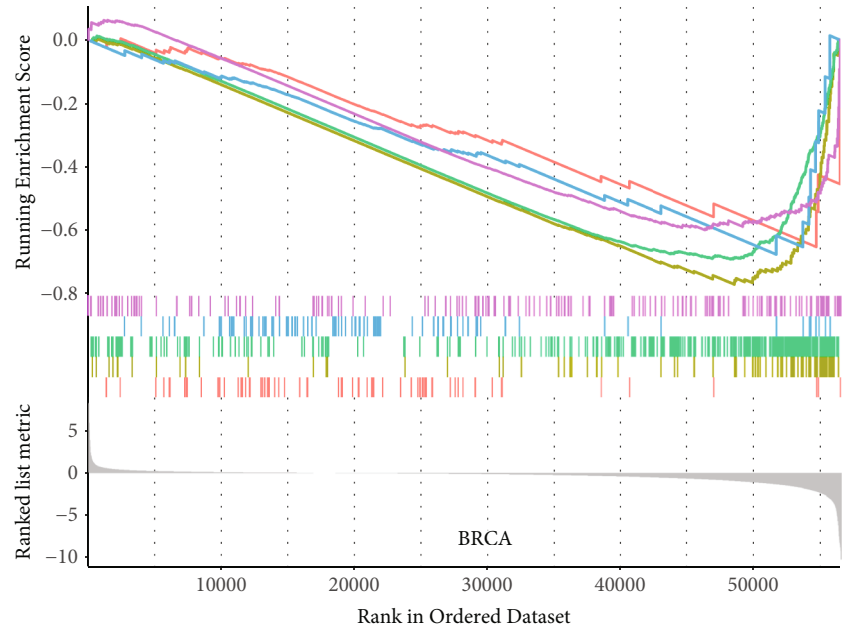
- GO\_MEMBRANE\_RAFT\_ASSEMBLY
- GO\_NEGATIVE\_REGULATION\_OF\_DEFENSE\_RESPONSE
- GO\_NEGATIVE\_REGULATION\_OF\_PROTEIN\_POLYUBIQUITINATION
- GO\_NEGATIVE\_REGULATION\_OF\_SMOOTH\_MUSCLE\_CELL\_APOPTOTIC\_PROCESS
- GO\_VASCULAR\_ASSOCIATED\_SMOOTH\_MUSCLE\_CELL\_APOPTOTIC\_PROCESS

(c)

FIGURE 7: Continued.

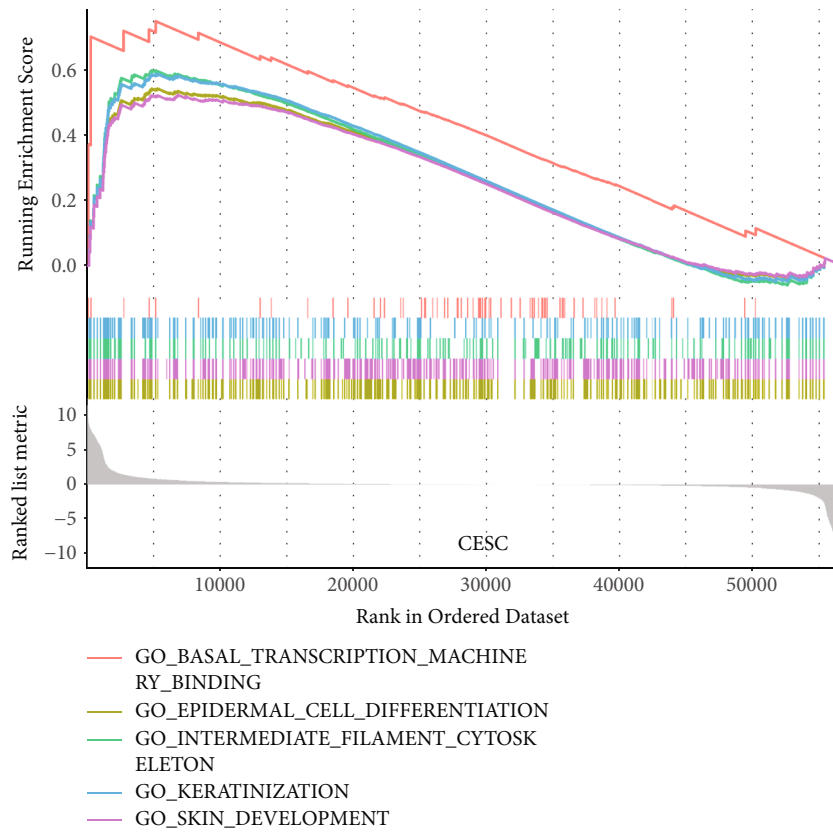


(d)

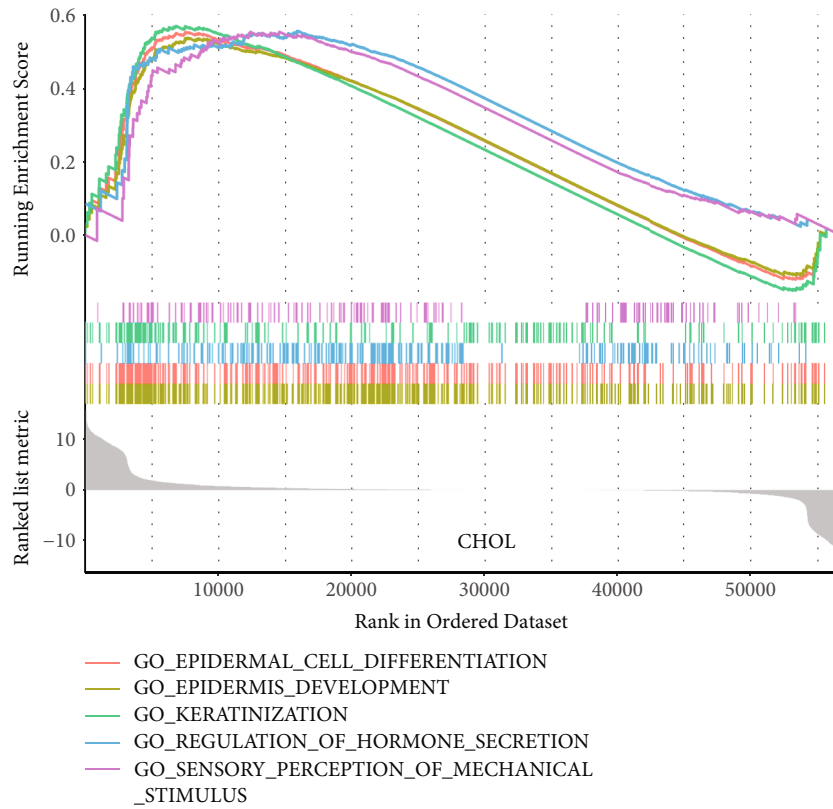


(e)

FIGURE 7: Continued.



(f)



(g)

FIGURE 7: Continued.

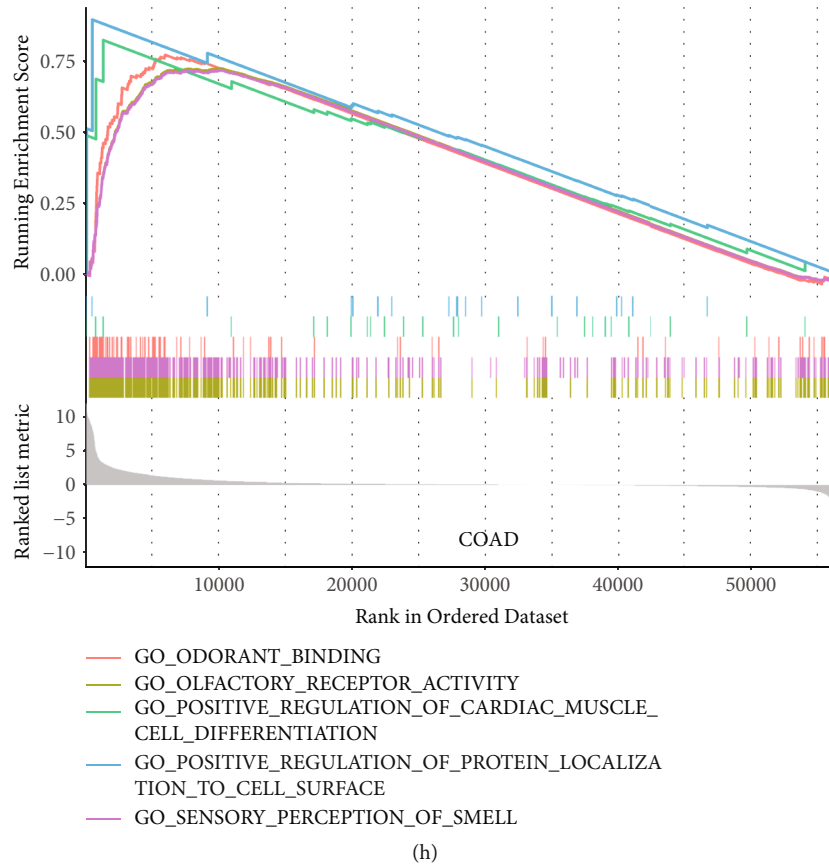


FIGURE 7: (a) Correlations of top-30 correlated genes with STEAP1 obtained from Harmonizome website in different cancer types were shown by a heatmap. (b) The network of significant signaling-related GO terms and KEGG pathways. The blue nodes represented GO terms, and the red nodes represented genes. The size demonstrated the number of enriched genes. (c-h) GSEA enrichment results.

Additional approaches to exploring the relationship of TME and STEAP1 expression, immune scores and stromal scores in different cancer types were computed. Considering the threshold  $p$ -value of 0.001, scatter plots showed that STEAP1 expression was positively correlated with immune scores in BLCA, BRCA, COAD, GBM, LUAD, OV, STAD, THCA whereas negatively correlated with immune scores in SKCM, THYM and UVM (Figure 9). As shown in Figure S6, STEAP1 expression levels were positively correlated with stromal scores in BLCA, BRCA, DLBC, GBM, KIRP, LUAD, OV, THCA, and THYM while negatively in PRAD and UVM.

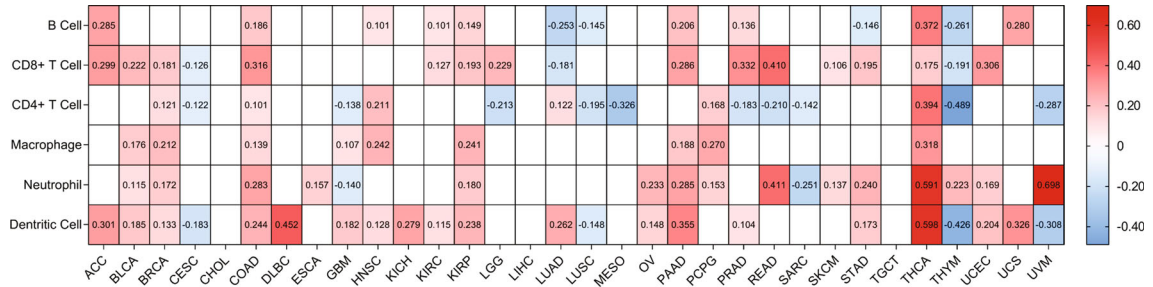
**3.6. Tumor Biomarkers.** The correlations of TMB for 33 cancer types and STEAP1 expression presented in Table S4 implied that expression levels had significantly positive correlations with HNSC, KICH, LGG, LIHC, PAAD, PRAD, THYM, and UCEC but a negative correlation with BRCA. It was apparent from Figure 10(a) that STEAP1 expression level in THYM had the maximum coefficients with  $p$  value < 0.001 followed by KICH. In addition, the correlations of MSI for 33 cancer types and STEAP1 expression were also calculated (Table S5). Figure 10(b) showed by a radar plot that expression levels had significantly positive connections with COAD, KIRC, PRAD, and THCA but a negative connection with CESC.

Furthermore, the correlation of stemness scores based on RNA (RN) as well as DNA methylation and STEAP1 expression level was computed. It showed that STEAP1 expression had the most positive correlation of RNAss in PRAD with the value of 0.464 of DNAss in THYM with the value of 0.472 followed by in LGG with the value of 0.431. Interestingly, DNAss of THYM held the most significantly negative correlation of RNAss with the value of -0.520.

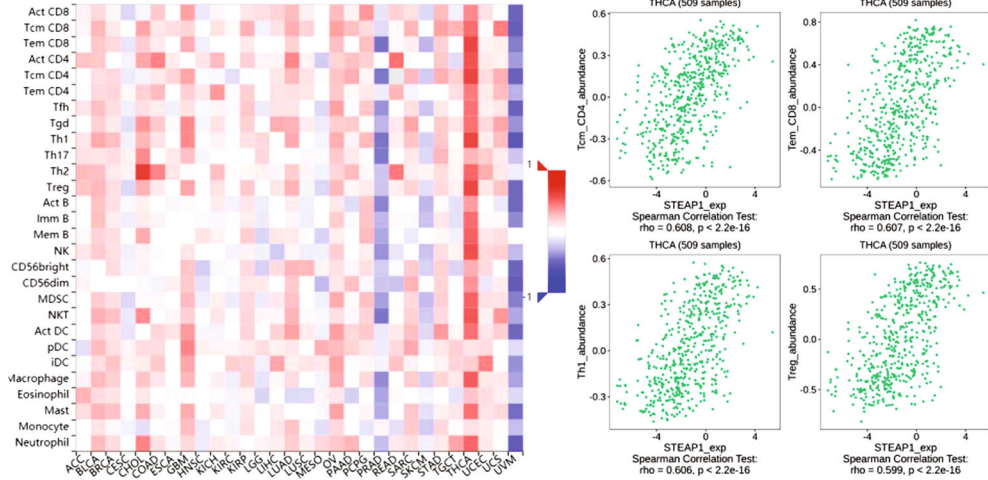
**3.7. Clinical Chemotherapies.** Drug sensitivity measured by  $z$ -score was assessed together with STEAP1 expression levels (Table S6). The most significantly correlated drugs are shown in Figure 11(a), indicated that STEAP1 was associated with increased sensitivity of cells to MEK, MET, ERK, RTK, and RAF inhibitors. The correlations between coexpressed genes with STEAP1 and approved antineoplastic as well as immunotherapies measured by query scores and interaction scores are shown in Figures 11(b) and 11(c), respectively.

## 4. Discussion

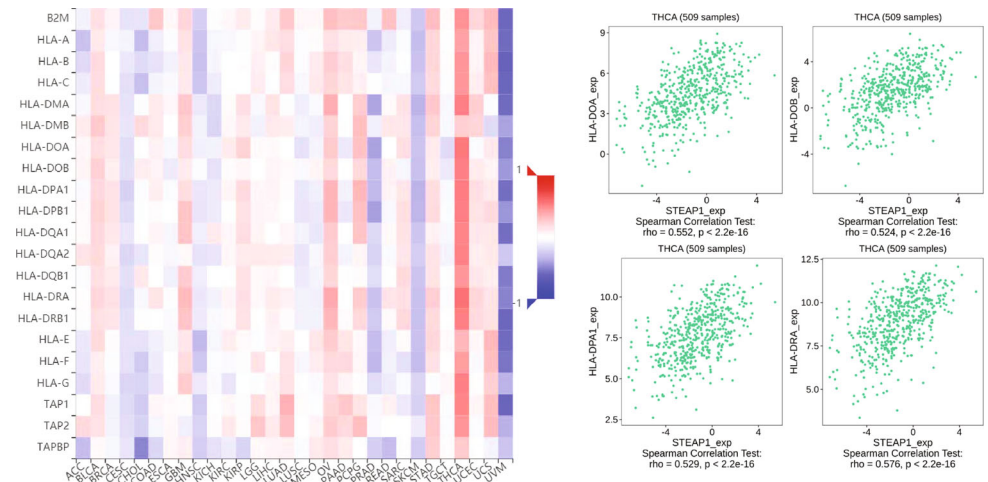
STEAP1 was previously validated as a promising target to discriminate adjacent and tumor samples and a useful tool for antibody therapies in different solid tumors [28, 29].



(a)



(b)



(c)

FIGURE 8: Continued.

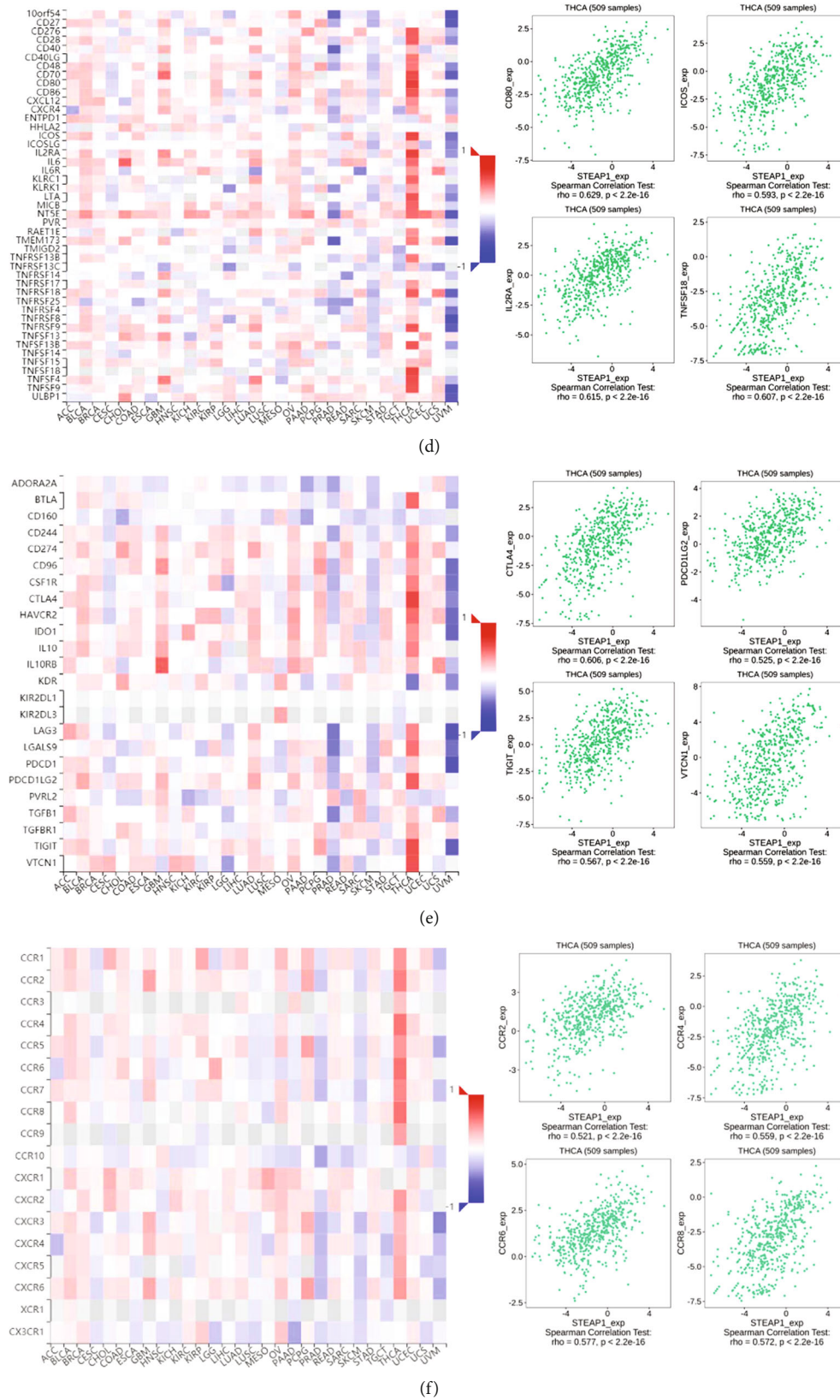


FIGURE 8: Continued.

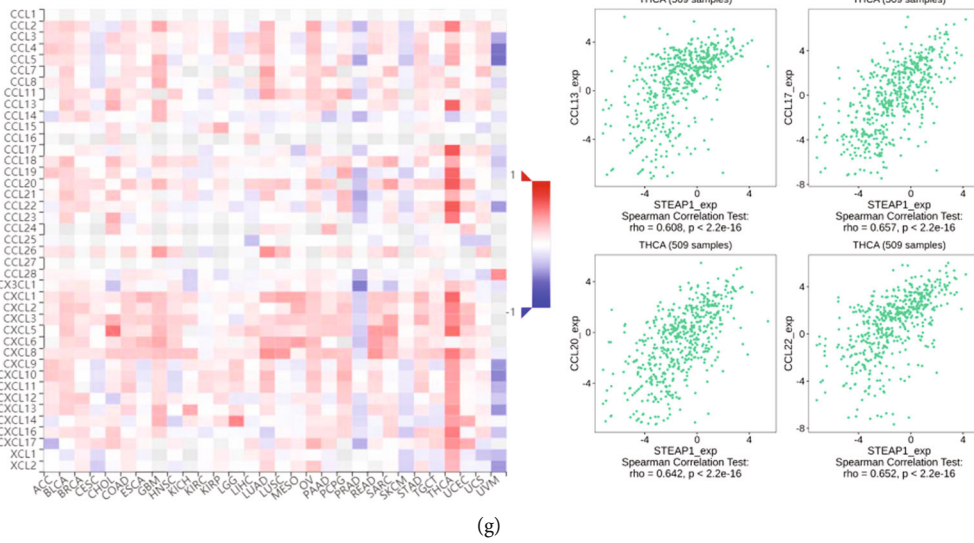


FIGURE 8: (a) The correlations of STEAP1 expression and immune-infiltrating levels of B cell, CD8<sup>+</sup> T cell, CD4<sup>+</sup> T cell, macrophage, neutrophil, and dendritic cell in different cancer types calculated by TIMER. (b-g) The correlations of STEAP1 expression and immune-infiltrating levels of 28 cell types, MHC molecules, immunostimulators, immunoinhibitors, receptors, and chemokines calculated by TISIDB.

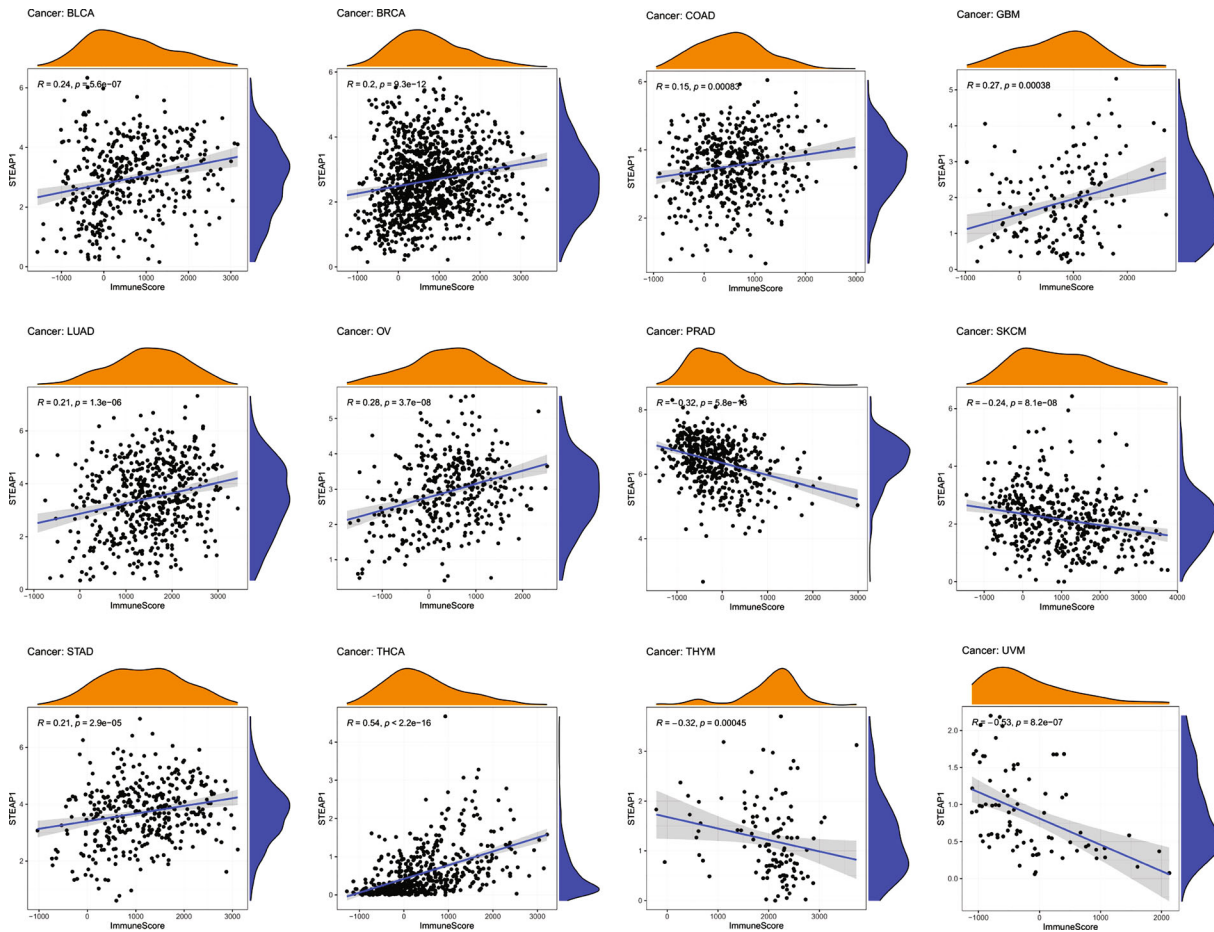


FIGURE 9: Significant correlations of STEAP1 expression and immune score were examined by ESTIMATE algorithm.

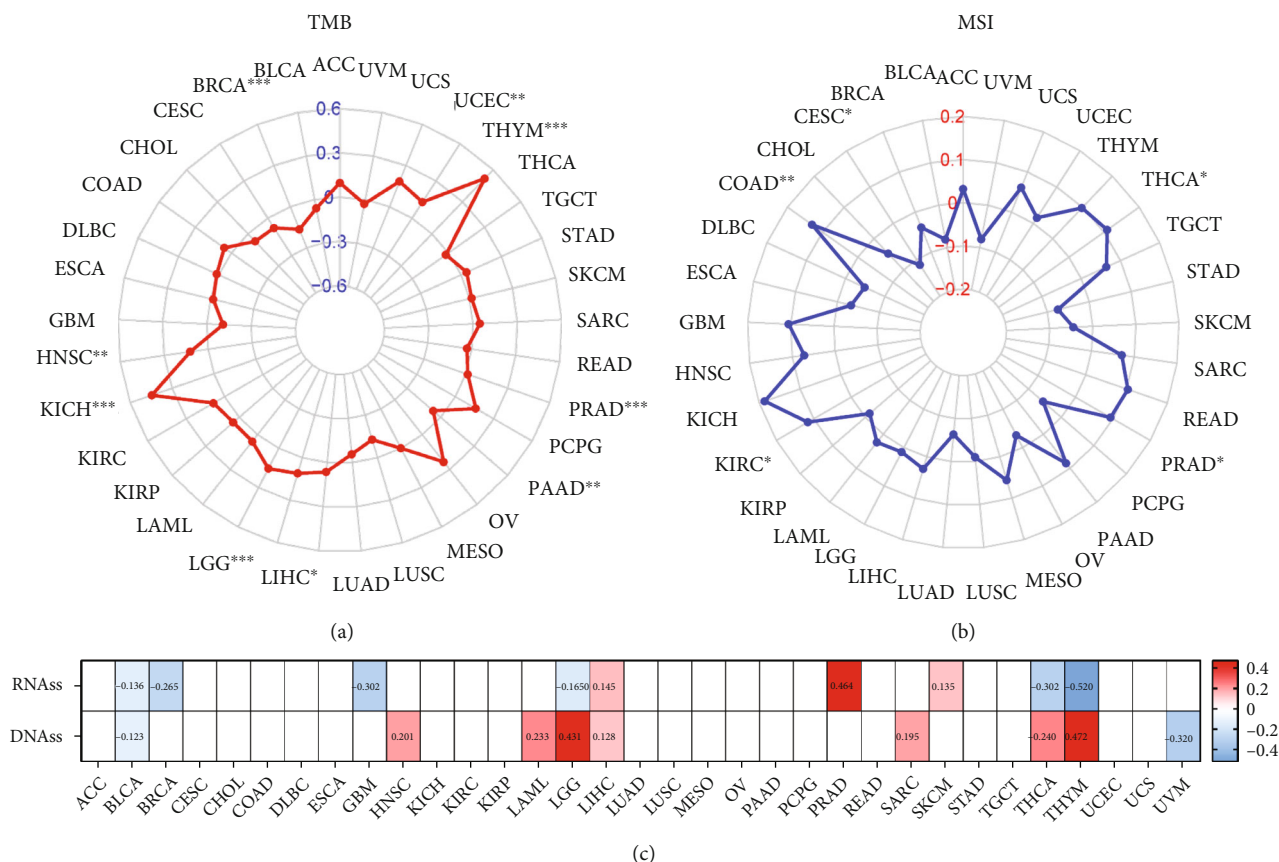


FIGURE 10: (a, b) The relationship between STEAP1 expression and TMB as well as MSI was illustrated by a radar plot. (c) Correlations between STEAP1 expression and stemness score based on RNA-seq and DNA methylation were illustrated by a heatmap.

Nonetheless, there were few systematic studies of STEAP1 in pan-cancer by bioinformatics approaches. The present study was designed to determine the expression pattern, prognostic value, and potential function of STEAP1 in different cancer types systematically.

In the present study, we firstly demonstrated that STEAP1 was overexpressed at mRNA levels in CESC, COAD, DLBC, ESCA, GBM, HNSC, KIRC, LGG, LUAD, LUSC, OV, PAAD, PRAD, READ, SKCM, STAD, TGCT, THYM, UCEC, and UCS cancer tissues compared with corresponding adjacent tissues while STEAP1 was downregulated in ACC, BRCA, KICH, LAML, and THCA, indicating that STEAP1 served as a potential oncogene in most cancers. The finding was consistent with the expression differences in cancers including colon, cervix, gastric, ovary, prostate, pancreas, and testis [9, 30]. STEAP1 expression was upregulated in LUAD cells, and knockdown of STEAP1 suppressed the proliferation and invasion of LUAD epithelial cells [31]. STEAP1 exhibited higher expression levels in advanced stages of ACC, KICH, OV, and THCA. Increased STEAP1 expressions were associated with high grade of BLCA, HNSC, LGG, and STAD while high grade of KIRC and UCEC was associated with lower STEAP1 expression levels, suggested STEAP1 could be considered an underlying biomarker in certain cancers.

Another finding in prostate cancer revealed that knockdown of STEAP1 could inhibit cell growth and induce apoptosis in prostate cancer cells [32]. The further study illustrated STEAP1 can also regulate EMT via JAK2/STAT3 signaling pathway [33]. Therefore, future studies on the function of STEAP1 in cell death, proliferation, and tumor migration with wet-lab approaches need to be explored.

Survival analysis based on KM curves revealed that the upregulated expression of SETAP1 correlated to worse OS survival in ACC, CHOL, KICH, LAML, LGG, LIHC, LUAD, PAAD, and THYM but better OS survival in BRCA, KIRC, LUSC, OV, UCEC, and UVM. Together with DSS and PFI data, STEAP1 played a favorable prognostic role in BRCA and KIRC while a risk factor in ACC, KICH, LUAD, and PAAD. The results of BRCA and LUAD patients were consistent with previous studies via bioinformatics analysis [7, 31]. Furthermore, Liu et al. developed a prognostic risk model for glioblastoma multiforme based on six genes including STEAP1 and STEAP2, indicating that STEAP1 also served as an underlying predicting factor in risk stratification of cancer [34]. Interestingly, a strong positive correlation of STEAP1 and STEAP2 average expression of pan-cancer was identified in our study including glioma and other different tumor tissues. Oppositely, Zhang et al. indicated that STEAP1 was closely related to overall survival in



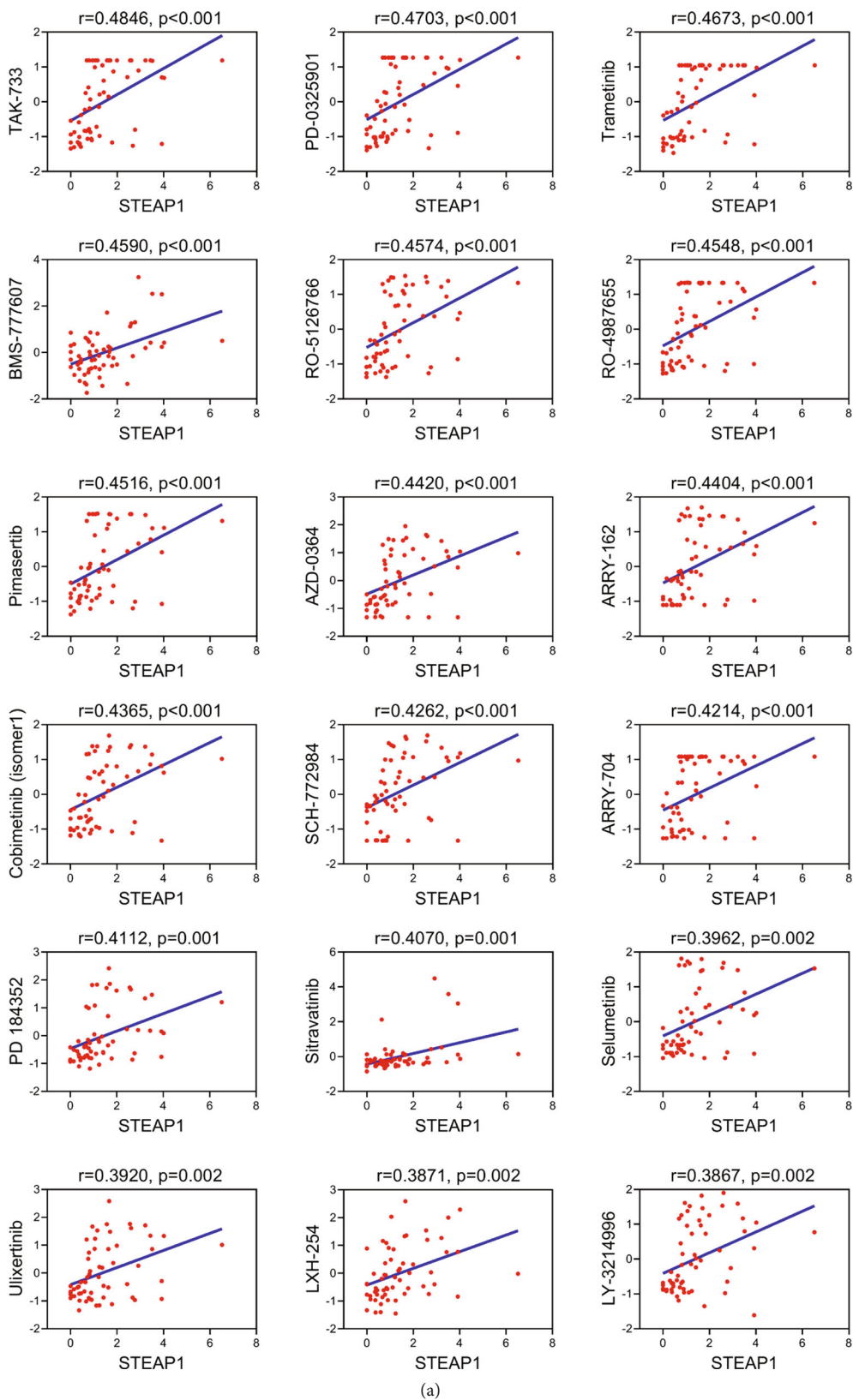


FIGURE 11: Continued.

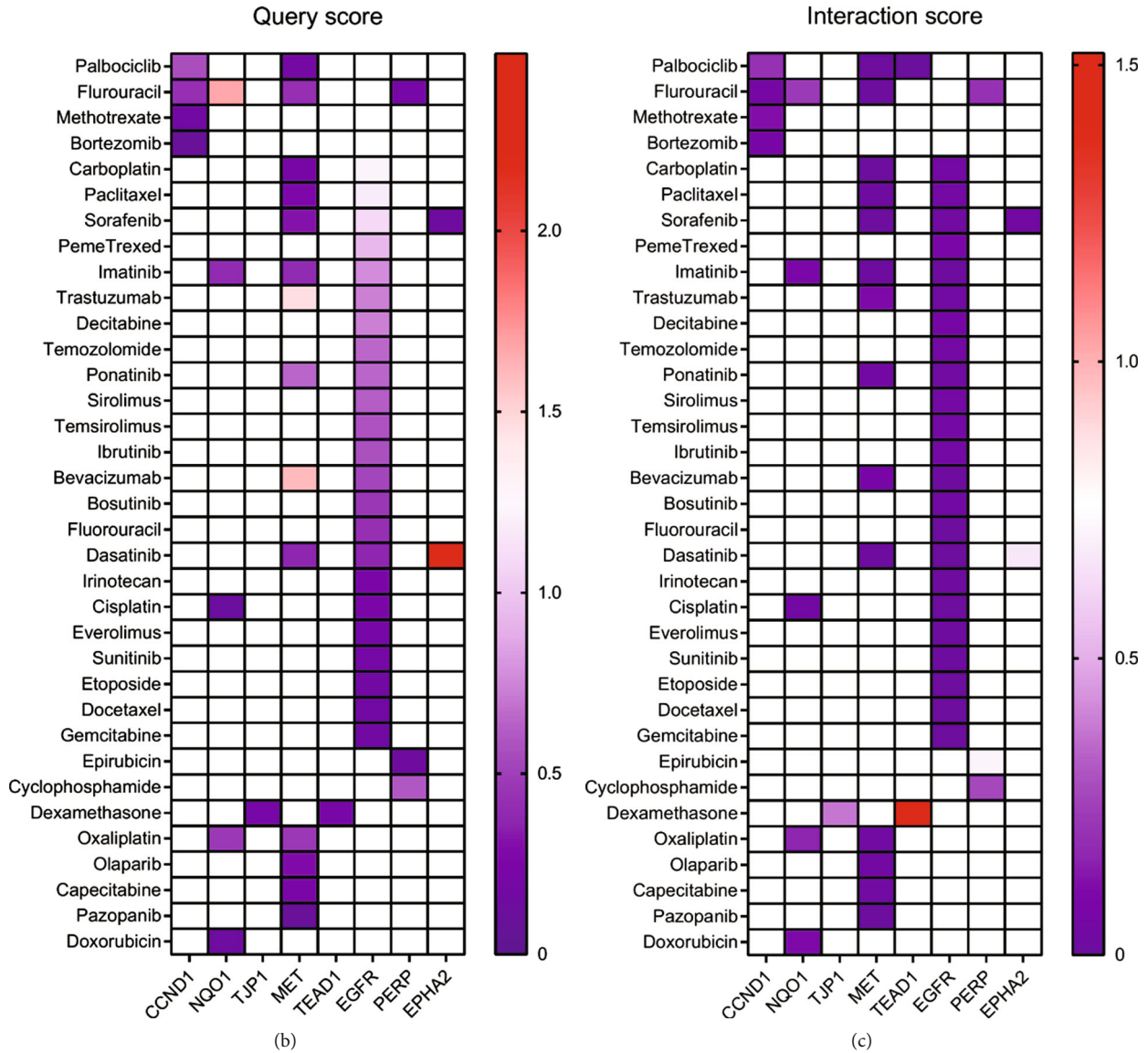


FIGURE 11: (a) The associations of STEAP1 expression and drug sensitivity based on CellMiner dataset were ordered according to  $p$  value from small to large (ERK inhibitor: AZD-0364 and SCH-772984; MEK inhibitor: TAK-733, PD-0325901, trametinib, RO-5162766, RO-4987655, pimasertib, ARRY-162, cobimetinib (isomer1), ARRY-704, PD184352, and selumetinib; MET inhibitor: BMS-777607; and RTK inhibitor: sitravatinib). (b, c) The query score and interaction score for approved antineoplastic and immunotherapies of coexpressed genes with STEAP1.

gastric cancer patients [30], contradicting with TCGA cohort in our study, which is probably caused by racial differences: Zhang et al.'s study included only Chinese people while TCGA cohort mainly contains Caucasian.

DNA methylation is one of the epigenetic mechanisms in transcriptional regulation, and aberrant DNA methylation is a nearly universal finding in cancer [35, 36]. In the present study, promoter methylation levels of STEAP1 were upregulated in BRCA, CHOL, KIRP, and SARC while were downregulated in BLCA and THCA accorded with classical models. Furthermore, high promoter methylation of STEAP1 correlated to high STEAP1 expression levels in tumor samples of CESC, COAD, ESCA, HNSC, KIRC, LUSC, and PAAD and low methylation levels was associated with lower STEAP1 expression in TGCT and UCEC. Spain-

hour et al. illustrated that there was a substantial amount of positive correlation between DNA methylation and gene expression using TCGA cohort, which also revealed the effects of methylation on gene expression are largely tissue independent [37]. In linear correlation, negative relationships were examined between STEAP1 and several cancers such as BRCA, PRAD, SKCM, and UCEC but positive connections in COAD and LUSC. Consistent with a previous study, STEAP1 was downregulated in prostate cancer tissues compared with normal samples and negatively associated with promoter methylation levels integrating both vitro and silico analysis [38].

To further probe into the genomic alternations of STEAP1 in different cancers, data from TCGA were analyzed in cBioPortal. The results suggested that changes in

the STEAP1 gene mainly occur in ESCA, STAD, LUSC, and PAAD. Hence, the correlation of STEAP1 expression and molecular subtypes demonstrated unity with survival analysis in this study. Among the top-100 coexpressed genes with STEAP1, STEAP2 showed the extremely positive correlation with STEAP1 in TCGA cohort. STEAP2 was also reported an overexpressed gene inhibiting apoptosis in several human cancers, especially prostate cancer [9]. Additionally, the 100 genes were involved in functional enrichment analysis. The results implied that genes were significantly enriched in Hippo signaling pathway. Hippo signaling involves in cell proliferation, tissue homeostasis, differentiation, apoptosis, and regeneration. Dysregulation of Hippo signaling, especially the hyperactivation of its downstream effectors YAP/TAZ, can lead to uncontrolled cell proliferation and malignant transformation [39–41]. PI3K-Akt, EGFR, HGFR, and integrin-mediated signaling pathway were also enriched in this study. The PI3K-Akt signaling way played a vital part in tumorigenesis and progression such as brain, breast, and endometrial [42]. A previous study confirmed STEAP2 was downregulated in breast cancer, and its upregulation inhibited tumor proliferation, invasion, and metastasis by suppressing PI3K-Akt signaling pathway *in vitro* and *in vivo* [43]. It could be assumed that STEAP1 may play a similar role in PI3K-Akt signaling pathway. Acting as EMT transcription factors, EGFR and STEAP1 were proved to be highly expressed among pulmonary neuroendocrine carcinomas and downregulated in carcinoid tumors [44], which suggested that STEAP1 may have interaction with EGFR pathway in the process of EMT. However, there are few studies about STEAP1 and HGFR or integrin-mediated signaling pathway. Further research is required to explore their interaction mechanism.

Tumorigenesis is highly associated with TME, which has limited or poorly differentiated vasculature and creating inefficiencies of nutrient and/or oxygen delivery [45]. In the modulation of TME, multiple immune cell types and cancer cell changes contribute to the specificity of the treatment regimen. Therefore, immunometabolism provides an opportunity to identify new targets to improve cancer therapies [46]. Investigation to TME in multiple cancers revealed that STEAP1 was positively correlated with the major of immune infiltration, especially in BRCA, COAD, KIRP, PAAD, and THCA but negatively correlated with tumor-immune infiltration in PRAD, THYM, and UVM. This study identified that STEAP1 had relatively strong positive correlation to immune-infiltrating of CD8<sup>+</sup> T cell in READ while had relatively strong negative correlations to immune-infiltrating of CD4<sup>+</sup> T cell in THYM and UVM. Schirmer et al. found that STEAP1-specific T cell receptors were useful for STEAP1-expressing cancer types in Ewing sarcoma [47]. TISIDB database in THCA samples also showed that STEAP1 had the strongest correlation with MHC molecules, immune stimulators, and immune inhibitors such as CTLA-4, as well as chemokines [48]. In addition, we investigated the expression differences between six immune subtypes, finding that STEAP1 exerted increased expression in C6 which had the worst survival and decreased expression in C3 which had the optimal prognosis in several

cancers such as COAD, LUSC, and STAD, indicating that STEAP1 served as a risk factor in these tumors. By conducting coexpressed strategy, STEAP2 had an obviously strong positive correlation with STEAP1.

TMB is an underlying biomarker in multiple cancers and is measured by the total amount of somatic coding mutations [49, 50]. Previous evidence validated high TMB is sensitive to immunotherapies and contributes to better survival [51, 52]. This study demonstrated STEAP1 expression is positively related to TMB in HNSC, KICH, LGG, LIHC, PAAD, PRAD, THYM, and UCEC. MSI, defined as a phenotype of alterations in microsatellite sequence caused by deficiency in DNA mismatch repair, is associated with increasing cancer predisposition [53, 54]. It has been regarded as a primary biomarker for the treatment with immune checkpoint blockade in the recent years [55]. In the current study, STEAP1 expression was positively correlated with MSI in COAD, KIRC, PRAD, and THCA whereas exhibited negative association in CESC.

CSCs also appear to have resistance to anticancer therapies and subsequent relapse [56]. Stemness indices are conducted by Malta et al. to predict the capability of tumor invasion and risk of recurrence based on DNA methylation and gene expression levels [57]. Here, STEAP1 is related to the stemness scores calculated by RNA and DNA in cancers such as LGG, LIHC, THCA, and THYM, which may participate in tumorigenesis and metastasis. However, further studies regarding the mechanism of STEAP1 mutation and stemness indices are still required.

By retrieving data from NCI-60 cell line, our study illustrated that increased STEAP1 expression level was positively related to increased chemosensitivity for several approved drugs by Food and Drug Administration, such as TAK-733, PD-0325901, trametinib, and BMS-777607. Meanwhile, increased STEAP1 expression was also correlated with increased drug resistance for some agents such as carboplatin, S-63845, arsenic trioxide, and cisplatin. These preliminary findings suggested that STEAP1 acted as an important role in chemosensitivity or resistance in cancer cells and served as a potential target to constrain drug resistance in different cancers.

However, there are some possible limitations of this research. Firstly, the database from TCGA in the study mainly includes Caucasian patients, and the data of other ethnicities has been a relative lack of research in this area. Moreover, further experimental studies in different cancers should be performed in the near future to identify STEAP1 as a key player in several types of cancers.

## 5. Conclusion

In summary, STEAP1 was dysregulated in pan-cancer tissues, and the aberrant expression of STEAP1 was more likely associated with clinicopathological features and predicted prognosis especially in adrenocortical carcinoma, breast cancer, glioma, renal cell carcinoma, lung cancer, prostate cancer, thyroid cancer, and endometrial carcinoma. Additionally, DNA methylation, TME, TMB, MSI, and cancer stemness might contribute to STEAP1 dysregulation in

cancers, and STEAP1 may be a potential therapeutic target for immunotherapy.

### Data Availability

Data used in this study can be downloaded from TCGA (<https://tcga-data.nci.nih.gov/tcga/>), UCSC XENA (<https://xenabrowser.net/datapages/>), CellMiner (<https://discover.nci.nih.gov/cellminer/home.do>), and Harmonizome (<https://maayanlab.cloud/Harmonizome/>).

### Conflicts of Interest

The authors declare no competing interests.

### Authors' Contributions

Chen Zhao and Xiangpan Li designed the study. Kewei Xiong, Zhiqiang Ji, and Fengming Liu collected study data and performed statistical analysis. Chen Zhao, Kewei Xiong, and Zhiqiang Ji wrote the manuscript draft. All authors read and approved the manuscript. Chen Zhao and Kewei Xiong have contributed equally to this work and share first authorship.

### Acknowledgments

This study was supported by “the Fundamental Research Funds for the Central Universities (2042020kf0084).”

### Supplementary Materials

*Supplementary 1.* Table S1: the top-100 correlated genes with STEAP1.

*Supplementary 2.* Table S2: GO and KEGG analysis.

*Supplementary 3.* Table S3: GSEA analysis.

*Supplementary 4.* Table S4: TMB for 33 cancer types and STEAP1 expression.

*Supplementary 5.* Table S5: MSI for 33 cancer types and STEAP1 expression.

*Supplementary 6.* Table S6: associations between drug sensitivity and STEAP1 expression.

*Supplementary 7.* Figure S1: the differences of total protein expression of STEAP1 between normal and tumor samples in BRCA, COAD, LUAD, OV, and UCEC, respectively (a-e).

*Supplementary 8.* Figure S2: correlations of STEAP1 expression and the methylation of its promoter in BRCA, COAD, LUSC, PRAD, SKCM, and UCEC, respectively (a-f). The red dotted lines represented the fitted lines of correlation tests.

*Supplementary 9.* Figure S3: (a) a univariate Cox proportional hazard regression of DSS with STEAP1 expression was illustrated by a forest plot. (b) KM survival analysis of DSS between high- and low-expression groups of STEAP1.

*Supplementary 10.* Figure S4: (a) a univariate Cox proportional hazard regression of PFI with STEAP1 expression

was illustrated by a forest plot. (b) KM survival analysis of PFI between high- and low-expression groups of STEAP1.

*Supplementary 11.* Figure S5: the differences of STEAP1 expression among distinctive immunophenotypes in multiple cancers (C1: wound healing; C2: IFN-gamma dominant; C3: inflammatory; C4: lymphocyte depleted; C5: immunologically quiet; C6: TGF- $\beta$  dominant).

*Supplementary 12.* Figure S6: significant correlations of STEAP1 expression and stromal score were examined by ESTIMATE algorithm.

### References

- [1] J. Luo, N. L. Solimini, and S. J. Elledge, “Principles of cancer therapy: oncogene and non-oncogene addiction,” *Cell*, vol. 136, no. 5, pp. 823–837, 2009.
- [2] F. Bray, J. Ferlay, I. Soerjomataram, R. L. Siegel, L. A. Torre, and A. Jemal, “Global cancer statistics 2018: GLOBOCAN estimates of incidence and mortality worldwide for 36 cancers in 185 countries,” *CA: a Cancer Journal for Clinicians*, vol. 68, no. 6, pp. 394–424, 2018.
- [3] R. J. Gillies, D. Verduzco, and R. A. Gatenby, “Evolutionary dynamics of carcinogenesis and why targeted therapy does not work,” *Nature Reviews. Cancer*, vol. 12, no. 7, pp. 487–493, 2012.
- [4] D. Hanahan and R. A. Weinberg, “Hallmarks of cancer: the next generation,” *Cell*, vol. 144, no. 5, pp. 646–674, 2011.
- [5] B. Kaczkowski, Y. Tanaka, H. Kawaji et al., “Transcriptome analysis of recurrently deregulated genes across multiple cancers identifies new pan-cancer biomarkers,” *Cancer Research*, vol. 76, no. 2, pp. 216–226, 2016.
- [6] R. S. Hubert, I. Vivanco, E. Chen et al., “STEAP: a prostate-specific cell-surface antigen highly expressed in human prostate tumors,” *Proceedings of the National Academy of Sciences of the United States of America*, vol. 96, no. 25, pp. 14523–14528, 1999.
- [7] H. T. Wu, W. J. Chen, Y. Xu, J. X. Shen, W. T. Chen, and J. Liu, “The tumor suppressive roles and prognostic values of STEAP family members in breast cancer,” *BioMed Research International*, vol. 2020, Article ID 9578484, 11 pages, 2020.
- [8] T. G. Grunewald, H. Bach, A. Cossarizza, and I. Matsumoto, “The STEAP protein family: versatile oxidoreductases and targets for cancer immunotherapy with overlapping and distinct cellular functions,” *Biology of the Cell*, vol. 104, no. 11, pp. 641–657, 2012.
- [9] I. M. Gomes, C. J. Maia, and C. R. Santos, “STEAP proteins: from structure to applications in cancer therapy,” *Molecular Cancer Research*, vol. 10, no. 5, pp. 573–587, 2012.
- [10] K. Kim, S. Mitra, G. Wu et al., “Six-transmembrane epithelial antigen of prostate 1 (STEAP1) has a single heme and is capable of reducing metal ion complexes and oxygen,” *Biochemistry*, vol. 55, no. 48, pp. 6673–6684, 2016.
- [11] J. Moreaux, A. Kassambara, D. Hose, and B. Klein, “STEAP1 is overexpressed in cancers: a promising therapeutic target,” *Biochemical and Biophysical Research Communications*, vol. 429, no. 3–4, pp. 148–155, 2012.
- [12] S. M. Rocha, J. Barroca-Ferreira, L. A. Passarinha, S. Socorro, and C. J. Maia, “The Usefulness of STEAP Proteins in Prostate Cancer Clinical Practice,” in *Prostate Cancer*, B. SRJ and K. L. Ng, Eds., Exon Publications, Brisbane (AU), 2021.

- [13] M. J. Goldman, B. Craft, M. Hastie et al., “Visualizing and interpreting cancer genomics data via the Xena platform,” *Nature Biotechnology*, vol. 38, no. 6, pp. 675–678, 2020.
- [14] J. Vivian, A. A. Rao, F. A. Nothhaft et al., “Toil enables reproducible, open source, big biomedical data analyses,” *Nature Biotechnology*, vol. 35, no. 4, pp. 314–316, 2017.
- [15] Z. Tang, C. Li, B. Kang, G. Gao, C. Li, and Z. Zhang, “GEPIA: a web server for cancer and normal gene expression profiling and interactive analyses,” *Nucleic Acids Research*, vol. 45, no. W1, pp. W98–W102, 2017.
- [16] A. D. Rouillard, G. W. Gunderesen, N. F. Fernandez et al., “The Harmonizome: a collection of processed datasets gathered to serve and mine knowledge about genes and proteins,” *Database: The Journal of Biological Databases and Curation*, vol. 2016, 2016.
- [17] G. Yu, L. G. Wang, Y. Han, and Q. Y. He, “clusterProfiler: an R package for comparing biological themes among gene clusters,” *OMICS*, vol. 16, no. 5, pp. 284–287, 2012.
- [18] D. S. Chandrashekar, B. Bashel, S. A. H. Balasubramanya et al., “UALCAN: a portal for facilitating tumor subgroup gene expression and survival analyses,” *Neoplasia*, vol. 19, no. 8, pp. 649–658, 2017.
- [19] W. Ding, G. Feng, Y. Hu, G. Chen, and T. Shi, “Co-occurrence and mutual exclusivity analysis of DNA methylation reveals distinct subtypes in multiple cancers,” *Frontiers in Cell and Development Biology*, vol. 8, p. 20, 2020.
- [20] W. Ding, J. Chen, G. Feng et al., “DNMIVD: DNA methylation interactive visualization database,” *Nucleic Acids Research*, vol. 48, no. D1, pp. D856–D862, 2020.
- [21] W. Ding, G. Chen, and T. Shi, “Integrative analysis identifies potential DNA methylation biomarkers for pan-cancer diagnosis and prognosis,” *Epigenetics*, vol. 14, no. 1, pp. 67–80, 2019.
- [22] T. Li, J. Fan, B. Wang et al., “TIMER: a web server for comprehensive analysis of tumor-infiltrating immune cells,” *Cancer Research*, vol. 77, no. 21, pp. e108–e110, 2017.
- [23] B. Li, E. Severson, J. C. Pignon et al., “Comprehensive analyses of tumor immunity: implications for cancer immunotherapy,” *Genome Biology*, vol. 17, no. 1, p. 174, 2016.
- [24] B. Ru, C. N. Wong, Y. Tong et al., “TISIDB: an integrated repository portal for tumor-immune system interactions,” *Bioinformatics*, vol. 35, no. 20, pp. 4200–4202, 2019.
- [25] U. T. Shankavaram, S. Varma, D. Kane et al., “CellMiner: a relational database and query tool for the NCI-60 cancer cell lines,” *BMC Genomics*, vol. 10, no. 1, p. 277, 2009.
- [26] W. C. Reinhold, M. Sunshine, H. Liu et al., “CellMiner: a web-based suite of genomic and pharmacologic tools to explore transcript and drug patterns in the NCI-60 cell line set,” *Cancer Research*, vol. 72, no. 14, pp. 3499–3511, 2012.
- [27] S. L. Freshour, S. Kiwala, K. C. Cotto et al., “Integration of the Drug-Gene Interaction Database (DGIdb 4.0) with open crowdsourcing efforts,” *Nucleic Acids Research*, vol. 49, no. D1, pp. D1144–D1151, 2021.
- [28] P. M. Challita-Eid, K. Morrison, S. Etessami et al., “Monoclonal antibodies to six-transmembrane epithelial antigen of the prostate-1 inhibit intercellular communication in vitro and growth of human tumor xenografts in vivo,” *Cancer Research*, vol. 67, no. 12, pp. 5798–5805, 2007.
- [29] M. T. Valenti, L. Dalle Carbonare, L. Donatelli et al., “STEAP mRNA detection in serum of patients with solid tumours,” *Cancer Letters*, vol. 273, no. 1, pp. 122–126, 2009.
- [30] Z. Zhang, W. B. Hou, C. Zhang et al., “A research of STEAP1 regulated gastric cancer cell proliferation, migration and invasion in vitro and in vivos,” *Journal of Cellular and Molecular Medicine*, vol. 24, no. 24, pp. 14217–14230, 2020.
- [31] Q. Guo, X. X. Ke, Z. Liu et al., “Evaluation of the prognostic value of STEAP1 in lung adenocarcinoma and insights into its potential molecular pathways via bioinformatic analysis,” *Frontiers in Genetics*, vol. 11, p. 242, 2020.
- [32] I. M. Gomes, S. M. Rocha, C. Gaspar et al., “Knockdown of STEAP1 inhibits cell growth and induces apoptosis in LNCaP prostate cancer cells counteracting the effect of androgens,” *Medical Oncology*, vol. 35, no. 3, p. 40, 2018.
- [33] S. F. Huo, W. L. Shang, M. Yu et al., “STEAP1 facilitates metastasis and epithelial-mesenchymal transition of lung adenocarcinoma via the JAK2/STAT3 signaling pathway,” *Bioscience Reports*, vol. 40, no. 6, 2020.
- [34] Z. Liu, H. Zhang, H. Hu et al., “A novel six-mRNA signature predicts survival of patients with glioblastoma multiforme,” *Frontiers in Genetics*, vol. 12, article 634116, 2021.
- [35] C. A. Demetriou, K. van Veldhoven, C. Relton, S. Stringhini, K. Kyriacou, and P. Vineis, “Biological embedding of early-life exposures and disease risk in humans: a role for DNA methylation,” *European Journal of Clinical Investigation*, vol. 45, no. 3, pp. 303–332, 2015.
- [36] J. Smith, S. Sen, R. J. Weeks, M. R. Eccles, and A. Chatterjee, “Promoter DNA hypermethylation and paradoxical gene activation,” *Trends Cancer*, vol. 6, no. 5, pp. 392–406, 2020.
- [37] J. C. Spainhour, H. S. Lim, S. V. Yi, and P. Qiu, “Correlation patterns between DNA methylation and gene expression in The Cancer Genome Atlas,” *Cancer Informatics*, vol. 18, article 117693511982877, 2019.
- [38] S. M. Rocha, I. Sousa, I. M. Gomes et al., “Promoter demethylation upregulates STEAP1 gene expression in human prostate cancer: in vitro and in silico analysis,” *Life*, vol. 11, no. 11, p. 1251, 2021.
- [39] P. Samji, M. K. Rajendran, V. P. Warriar, A. Ganesh, and K. Devarajan, “Regulation of Hippo signaling pathway in cancer: a microRNA perspective,” *Cellular Signalling*, vol. 78, 2021.
- [40] S. Jiao, C. Li, Q. Hao et al., “VGLL4 targets a TCF4-TEAD4 complex to coregulate Wnt and Hippo signalling in colorectal cancer,” *Nature Communications*, vol. 8, no. 1, article 14058, 2017.
- [41] F. Yin, J. Dong, L. I. Kang, and X. Liu, “Hippo-YAP signaling in digestive system tumors,” *American Journal of Cancer Research*, vol. 11, no. 6, pp. 2495–2507, 2021.
- [42] D. A. Fruman, H. Chiu, B. D. Hopkins, S. Bagrodia, L. C. Cantley, and R. T. Abraham, “The PI3K pathway in human disease,” *Cell*, vol. 170, no. 4, pp. 605–635, 2017.
- [43] Q. Yang, G. Ji, and J. Li, “STEAP2 is down-regulated in breast cancer tissue and suppresses PI3K/AKT signaling and breast cancer cell invasion in vitro and in vivo,” *Cancer Biology & Therapy*, vol. 21, no. 3, pp. 278–291, 2020.
- [44] T. G. Prieto, C. M. Baldavira, J. Machado-Rugolo et al., “Pulmonary neuroendocrine neoplasms overexpressing epithelial-mesenchymal transition mechanical barriers genes lack immune-suppressive response and present an increased risk of metastasis,” *Frontiers in Oncology*, vol. 11, article 645623, 2021.
- [45] C. Roma-Rodrigues, R. Mendes, P. V. Baptista, and A. R. Fernandes, “Targeting tumor microenvironment for cancer

- therapy,” *International Journal of Molecular Sciences*, vol. 20, no. 4, p. 840, 2019.
- [46] J. E. Bader, K. Voss, and J. C. Rathmell, “Targeting metabolism to improve the tumor microenvironment for cancer immunotherapy,” *Molecular Cell*, vol. 78, no. 6, pp. 1019–1033, 2020.
- [47] D. Schirmer, T. G. P. Grünewald, R. Klar et al., “Transgenic antigen-specific, HLA-A\*02: 01-allo-restricted cytotoxic T cells recognize tumor-associated target antigen STEAP1 with high specificity,” *Oncoimmunology*, vol. 5, no. 6, article e1175795, 2016.
- [48] J. D. French, “Immunotherapy for advanced thyroid cancers - rationale, current advances and future strategies,” *Nature Reviews. Endocrinology*, vol. 16, no. 11, pp. 629–641, 2020.
- [49] L. Fancello, S. Gandini, P. G. Pelicci, and L. Mazzarella, “Tumor mutational burden quantification from targeted gene panels: major advancements and challenges,” *Journal for Immunotherapy of Cancer*, vol. 7, no. 1, p. 183, 2019.
- [50] A. M. Goodman, S. Kato, L. Bazhenova et al., “Tumor mutational burden as an independent predictor of response to immunotherapy in diverse cancers,” *Molecular Cancer Therapeutics*, vol. 16, no. 11, pp. 2598–2608, 2017.
- [51] Y. Y. Janjigian, J. Bendell, E. Calvo et al., “CheckMate-032 study: efficacy and safety of nivolumab and nivolumab plus ipilimumab in patients with metastatic esophagogastric cancer,” *Journal of Clinical Oncology*, vol. 36, no. 28, pp. 2836–2844, 2018.
- [52] S. J. Klemptner, D. Fabrizio, S. Bane et al., “Tumor mutational burden as a predictive biomarker for response to immune checkpoint inhibitors: a review of current evidence,” *The Oncologist*, vol. 25, no. 1, pp. e147–e159, 2020.
- [53] T. M. Kim, P. W. Laird, and P. J. Park, “The landscape of microsatellite instability in colorectal and endometrial cancer genomes,” *Cell*, vol. 155, no. 4, pp. 858–868, 2013.
- [54] B. Meier, N. V. Volkova, Y. Hong et al., “Mutational signatures of DNA mismatch repair deficiency in *C. elegans* and human cancers,” *Genome Research*, vol. 28, no. 5, pp. 666–675, 2018.
- [55] E. Picard, C. P. Verschoor, G. W. Ma, and G. Pawelec, “Relationships between immune landscapes, genetic subtypes and responses to immunotherapy in colorectal cancer,” *Frontiers in Immunology*, vol. 11, p. 369, 2020.
- [56] S. Prasad, S. Ramachandran, N. Gupta, I. Kaushik, and S. K. Srivastava, “Cancer cells stemness: a doorstep to targeted therapy,” *Biochimica et Biophysica Acta - Molecular Basis of Disease*, vol. 1866, no. 4, article 165424, 2020.
- [57] T. M. Malta, A. Sokolov, A. J. Gentles et al., “Machine learning identifies stemness features associated with oncogenic dedifferentiation,” *Cell*, vol. 173, no. 2, pp. 338–354.e15, 2018.

## Research Article

# Therapy-resistant and -sensitive lncRNAs, SNHG1 and UBL7-AS1 promote glioblastoma cell proliferation

Mei Cao,<sup>1</sup> Rong Ma,<sup>2</sup> Huaqing Li,<sup>3</sup> Juan Cui,<sup>3</sup> Chi Zhang,<sup>4</sup> and Jian Zhao<sup>5</sup> 

<sup>1</sup>Core Laboratory, School of Medicine, Sichuan Provincial People's Hospital Affiliated to University of Electronic Science and Technology of China, Chengdu 610072, China

<sup>2</sup>Department of Pharmacology, School of Basic Medicine, Tongji Medical College, Huazhong University of Science and Technology, Wuhan 430030, China

<sup>3</sup>Department of Computer Science and Engineering, University of Nebraska-Lincoln, Lincoln, NE 68588, USA

<sup>4</sup>Department of Radiation Oncology, Fred & Pamela Buffet Cancer Center, University of Nebraska Medical Center, Omaha, Nebraska, USA

<sup>5</sup>Key Laboratory of Biological Resource and Ecological Environment of Chinese Education Ministry, College of Life Sciences, Sichuan University, No. 24 South Section 1, Yihuan Road, Chengdu 610064, China

Correspondence should be addressed to Jian Zhao; [zj804@163.com](mailto:zj804@163.com)

Received 17 October 2021; Revised 23 January 2022; Accepted 11 February 2022; Published 11 March 2022

Academic Editor: Qiang Tong

Copyright © 2022 Mei Cao et al. This is an open access article distributed under the Creative Commons Attribution License, which permits unrestricted use, distribution, and reproduction in any medium, provided the original work is properly cited.

The current treatment options for glioblastoma (GBM) can result in median survival of 15-16 months only, suggesting the existence of therapy-resistant factors. Emerging evidence suggests that long non-coding RNAs (lncRNAs) play an essential role in the development of various brain tumors, including GBM. This study aimed to identify therapy-resistant and therapy-sensitive GBM associated lncRNAs and their role in GBM. We conducted a genome-wide transcriptional survey to explore the lncRNA landscape in 195 GBM brain tissues. Cell proliferation was evaluated by CyQuant assay and Ki67 immunostaining. Expression of MAD2L1 and CCNB2 was analyzed by western blotting. We identified 51 lncRNAs aberrantly expressed in GBM specimens compared with either normal brain samples or epilepsy non-tumor brain samples. Among them, 27 lncRNAs were identified as therapy-resistant lncRNAs that remained dysregulated after both radiotherapy and chemoradiotherapy; while 21 lncRNAs were identified as therapy-sensitive lncRNAs whose expressions were reversed by both radiotherapy and chemoradiotherapy. We further investigated the potential functions of the therapy-resistant and therapy-sensitive lncRNAs and demonstrated their relevance to cell proliferation. We also found that the expressions of several lncRNAs, including SNHG1 and UBL7-AS1, were positively correlated with cell-cycle genes' expressions. Finally, we experimentally confirmed the function of a therapy-resistant lncRNA, SNHG1, and a therapy-sensitive lncRNA, UBL7-AS1, in promoting cell proliferation in GBM U138MG cells. Our *in vitro* results demonstrated that knockdown of SNHG1 and UBL7-AS1 showed an additive effect in reducing cell proliferation in U138MG cells.

## 1. Introduction

Glioblastoma (GBM) is the most aggressive type of brain cancer [1]. The current treatment options, such as surgery, radiation, and chemotherapy in combination, can result in median survival of 15-16 months only [2]. There is thus an urgent need to identify novel therapeutic targets for the treatment of GBM. Long non-coding RNAs (lncRNAs) have emerged as critical players in the pathogenesis and develop-

ment of various cancers, including malignant brain tumors such as GBM [3]. Studies have demonstrated that lncRNAs CRNDE [4], H19 [5], NEAT1 [5], LINC00461 [6], and HOTAIR [7] play an essential role in regulating both cell proliferation and migration in GBM. Interestingly, loss-of-function studies have demonstrated that inhibition of lncRNAs MIR22HG [8], SPRY4-IT1 (H. [9]), XIST [10], CCAT2 [11], LUCAT1 [12], and AB073614 (J. [13]) successfully reduced certain GBM features, including proliferation

TABLE 1: Sequences for qPCR Primers and for siRNA Knockdown Oligonucleotides.

(a)

| Gene     | qPCR forward primer 5'-3' | qPCR reverse primer 5'-3' |
|----------|---------------------------|---------------------------|
| GAPDH    | ACCATCTTCCAGGAGCGAGA      | CACCCTGTTGCTGTAGCCAA      |
| SNHG1    | TCTGTGTTCACTCCAGGCTGA     | TGCCTGAGTTTGGGTTCTGG      |
| UBL7-AS1 | ACCTCTGATTGGACTCTTCTCAAG  | GCCTTCAGCTGCTACGATCA      |
| ABL1     | GGGAAATTGTCCAGGCTCAA      | TCACAGCATCAACCAGACTCG     |
| CCNA2    | GGACAAAGCTGGCCTGAATCA     | TGACTGTTGTGCATGCTGTGG     |
| CDK6     | TTCACACCGAGTAGTGCATCG     | TGGAAACTATAGATGCGGGCA     |
| CDKN2D   | ACATGCTGCTGGAGGAGGTT      | CGGTGCTGCCAAACATCAT       |
| GADD45A  | TGGCTCTGCAGATCCACTTCA     | ATTTCGTCACCAGCACGCAGT     |
| WEE1     | GGCTGGATGGATGCATTTATG     | GCCCACGCAGAGAAATATCG      |

(b)

| siRNA target     | Sense oligo (5'-3')   | Antisense oligo (5'-3') |
|------------------|-----------------------|-------------------------|
| Negative control | UAAGGCUAUGAAGAGAUACUU | GUAUCUCUUCUAUAGCCUUAUU  |
| SNHG1 siRNA1     | CAUGUAGGUAGCUCAUUCUU  | UGAAUGAGCUACCUACAUGUU   |
| SNHG1 siRNA2     | CAUAGCUUUAAGAGAUCCUUU | AGGAUCUCUAAAAGCUAUGUU   |
| UBL7-AS1 siRNA1  | GUUGAUCGUAGCAGCUGAAUU | UUCAGCUGCUACGAUCAACUU   |
| UBL7-AS1 siRNA2  | CCUGUAUUCUUCGGACCAUUU | AUGGUCCGAAGAAUACAGUU    |

and migration. Additionally, knockdown of H19 has been shown to sensitize human glioma cells to temozolomide therapy [14]. These findings suggested that lncRNAs could be effective targets for the treatment of GBM.

While the use of GBM cell lines and animal models in some of the studies could limit the clinical significance, there are existing gene expression datasets on human cancer biopsies that could provide vital information on the expression of lncRNAs in GBM patients. Several gene expression profiles on GBM specimens of patients have been generated using Affymetrix Human Genome U133 Plus 2.0 Array, which was designed mainly to detect mRNAs. Reannotation analysis suggests that this Affymetrix microarray can also detect 3053 lncRNAs [15].

The current study was aimed at exploring the lncRNA landscape in GBM patients. We identified 51 lncRNAs aberrantly expressed in GBM specimens compared with either normal brain samples or epilepsy non-tumor brain samples. Among them, the expressions of 27 lncRNAs were resistant to both radiotherapy and chemoradiotherapy; while the expressions of 21 lncRNAs were reversed by both radiotherapy and chemoradiotherapy. We further investigated the potential functions of the therapy-resistant and therapy-sensitive dysregulated lncRNAs and demonstrated their relevance to cell proliferation. We also found that the expressions of several lncRNAs, such as SNHG1 and UBL7-AS1, were positively correlated with the expressions of cell-cycle genes. Finally, we experimentally confirmed the role of therapy-resistant lncRNA SNHG1, and therapy-sensitive lncRNA UBL7-AS1 in promoting cell proliferation in human GBM U138MG cells.

## 2. Materials and methods

**2.1. Microarray data acquisition.** Microarray datasets (GSE50161, GSE4290, and GSE7696) were obtained from the Gene Expression Omnibus (GEO) database of NCBI (<http://www.ncbi.nlm.nih.gov/geo/>) [16, 17]. The statistics and description of the datasets are shown in Supplemental Table 1. All datasets used in this study were generated on the microarray platform GPL570 [HG-U133\_Plus\_2] Affymetrix Human Genome U133 Plus 2.0 Array. The raw data were normalized with the Robust Multichip Average (RMA) method using the R software limma package.

**2.2. Identification of differentially expressed lncRNAs.** The GEO2R (R 3.2.3, Biobase 2.30.0, GEOquery 2.40.0, limma 3.26.8) [17] web tool (<http://www.ncbi.nlm.nih.gov/geo/geo2r/>) was used to identify differentially expressed genes between two given groups of samples in a GEO profile. lncRNAs with  $p \leq 0.05$  and  $|\log \text{fold change}| \geq 1$  were selected for further analysis. Expression of lncRNAs in GBM was further validated in the TCGA database [18].

**2.3. Functional enrichment analysis of lncRNAs based on their correlated mRNAs.** Pathway enrichment analysis on lncRNA-correlating genes was performed using the R2 KEGG Pathway Finder by gene correlation (R2: Genomics Analysis and Visualization Platform (<http://r2.amc.nl>)) using the dataset GSE7696. Genes with a p-value  $< 0.05$ , present calls  $\geq 1$  ( $\text{transform\_log2}$ ) were considered as lncRNA-correlating genes. Pathways with P-value  $\leq 0.01$  (cutoff 0.01) were considered significant over-representation in the dataset and were ranked by the sum of the negative  $\log_{10}$  p-value of each lncRNA for each pathway.



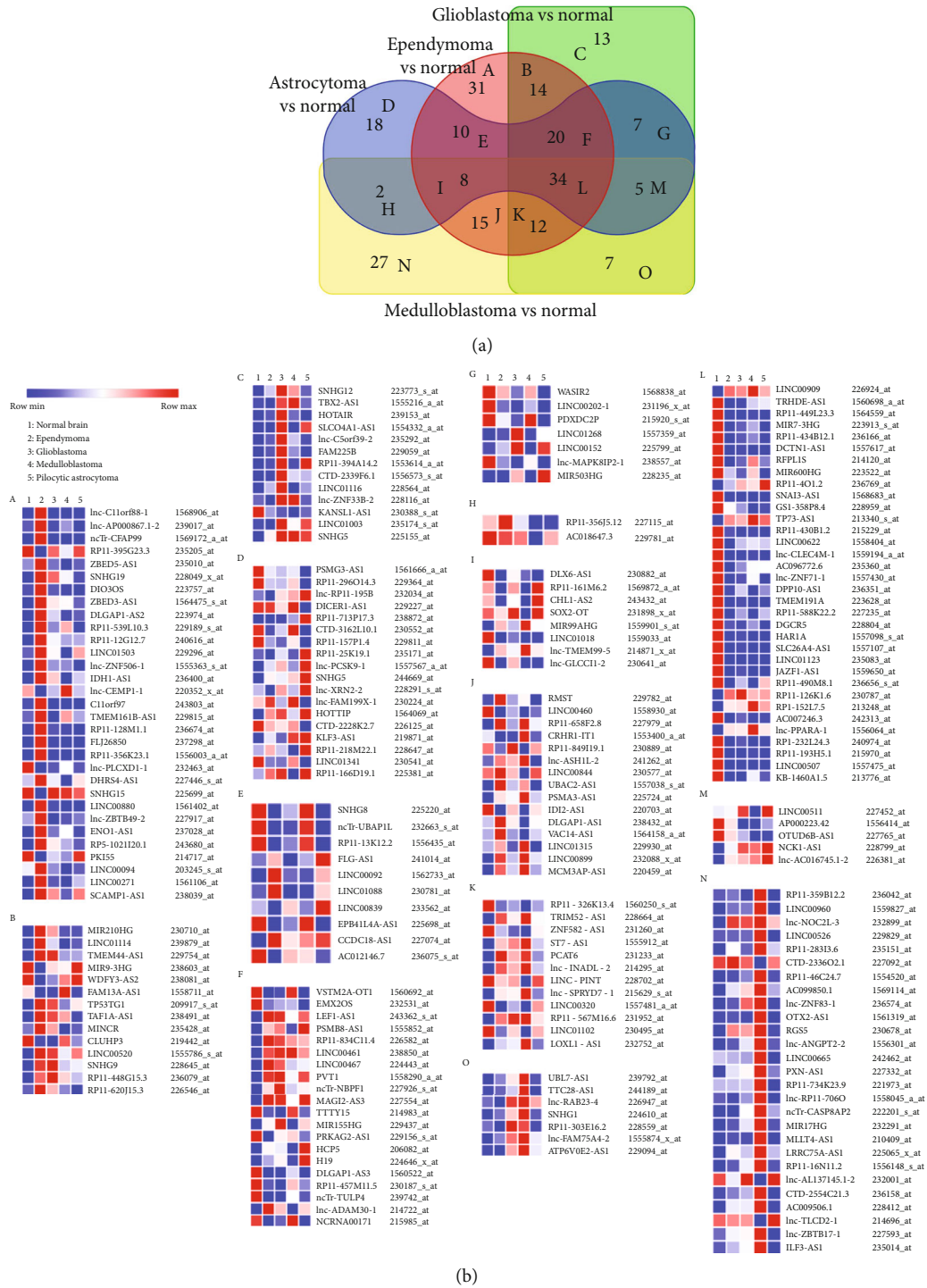


FIGURE 1: Dysregulated lncRNAs in various brain tumors compared with normal brain tissues. (a) Venn diagram showing dysregulated lncRNAs by 1.0-fold or greater ( $p < 0.05$ ) in brain tumors such as ependymoma ( $n = 46$ ), glioblastoma ( $n = 34$ ), medulloblastoma ( $n = 22$ ), and pilocytic astrocytoma ( $n = 15$ ) compared with control brain tissues ( $n = 13$ ) from dataset GSE50161. (b) (A-O) Heatmap illustrating the expression (average log expression value) of the dysregulated lncRNAs between indicated brain tumor and normal brain samples in a. (a and b-A, C, D, N) The expressions of 31, 13, 18, and 27 lncRNAs were exclusively dysregulated in ependymoma, GBM, PA, and medulloblastomas tumors, compared with control samples, respectively. (a and b-B, E, G, H, J, O) The expressions of 14, 10, 7, 2, 15, and 7 lncRNAs were dysregulated in both ependymoma and GBM; ependymoma and PA; GBM and PA; PA and medulloblastomas; ependymoma and medulloblastomas; GBM and medulloblastomas; compared with control samples, respectively. (a and b-F, I, K) The expressions of 20, 8, and 12 lncRNAs were dysregulated in ependymoma, GBM and PA; ependymoma, PA and medulloblastomas; GBM, ependymoma and medulloblastomas, compared with control samples, respectively.

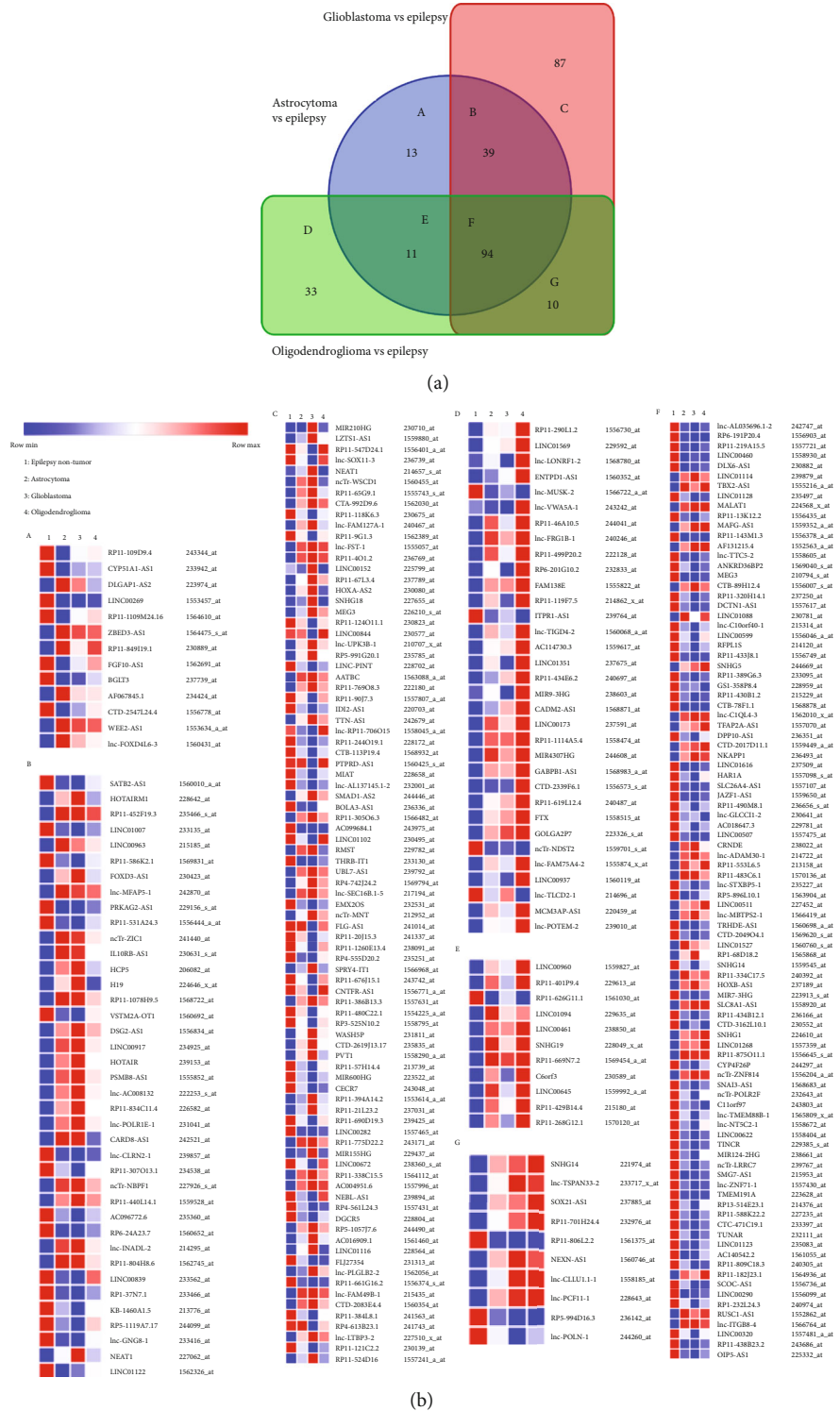


FIGURE 2: Dysregulated lncRNAs in various brain tumors compared with epilepsy non-tumor control brain tissues. (a) Venn diagram showing dysregulated lncRNAs by 1.0-fold or greater ( $p < 0.05$ ) in brain tumors such as astrocytoma ( $n=46$ ), glioblastoma ( $n=81$ ), and oligodendroglioma ( $n=50$ ) compared with control brain tissues from epilepsy patients ( $n=23$ ) from dataset GSE4290. (b) (A-G) Heatmap illustrating the expression (average log expression value) of the dysregulated lncRNAs between indicated brain tumor and epilepsy non-tumor brain samples in a. (a and b-A, C, D) There were 13, 87, and 33 lncRNAs, respectively, differentially expressed in astrocytomas, GBM, and oligodendrogliomas compared with nontumor epilepsy brain samples. (a and b-B, E, G) There were 39, 11, and 10 lncRNAs, respectively, differentially expressed in astrocytomas and GBM; astrocytomas and oligodendrogliomas; GBM and oligodendrogliomas; respectively, compared with non-tumor epilepsy brain samples. (a and b-F) The expressions of 94 lncRNAs were commonly dysregulated in all tumor samples compared with non-tumor epilepsy brain samples simultaneously.

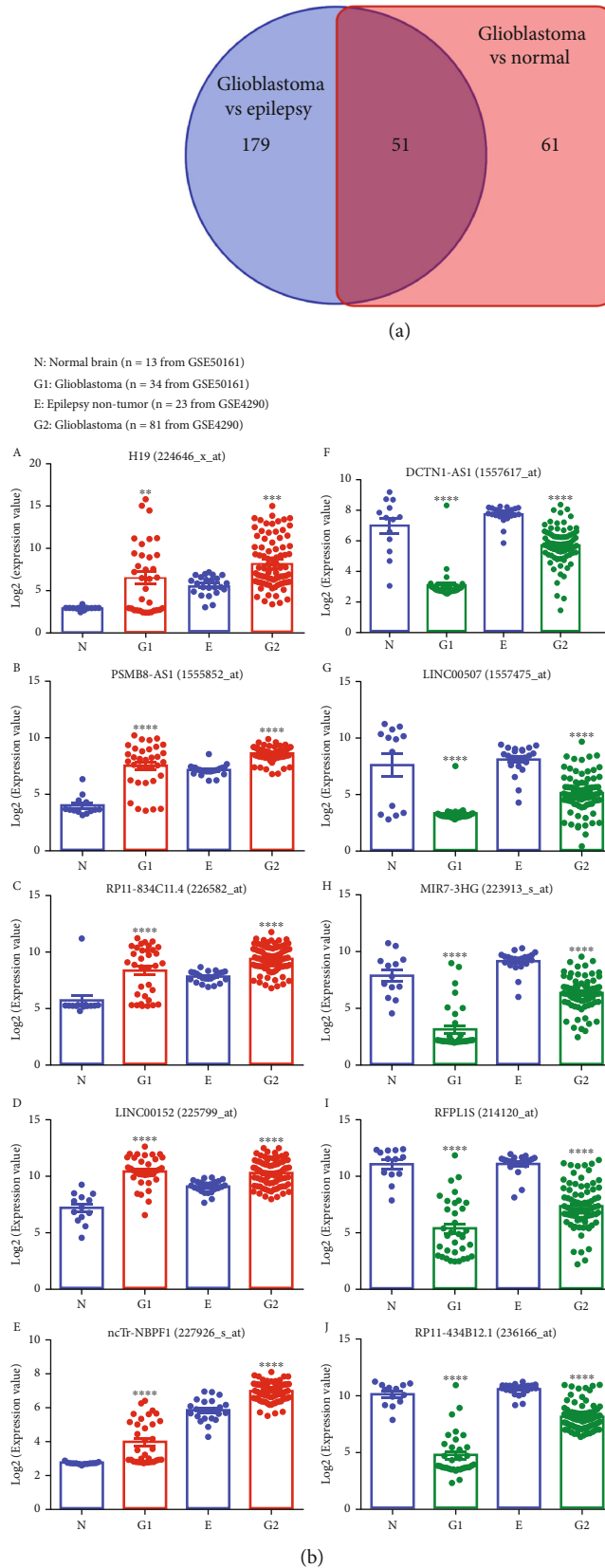
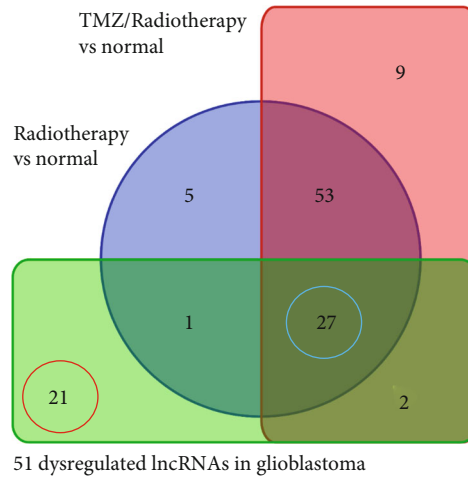


FIGURE 3: Dysregulated lncRNAs in glioblastoma. (a) Venn diagram showing commonly dysregulated lncRNAs by 1.0-fold or greater ( $p < 0.05$ ) in both datasets GSE50161 and GSE4290. (b) (A-J) Boxplots of expression levels of selected up- and down-regulated lncRNAs in glioblastoma compared with normal or epilepsy non-tumor brain tissues. P-values were calculated using on-way ANOVA where: \*\*  $p < 0.01$ , \*\*\*  $p < 0.001$ , \*\*\*\*  $p < 0.0001$ , G1 vs N and G2 vs E.



(a)

27 therapy-resistant lncRNAs

| 1    | 2    | 3    | 4             | 5            | 6    |
|------|------|------|---------------|--------------|------|
| Red  | Blue | Blue | LINC00622     | 1558404_at   | Down |
| Blue | Red  | Red  | LINC00511     | 227452_at    | Up   |
| Red  | Blue | Blue | PRKAG2-AS1    | 229156_s_at  | Down |
| Red  | Blue | Blue | AC096772.6    | 235360_at    | Down |
| Blue | Red  | Red  | TBX2-AS1      | 1555216_a_at | Up   |
| Red  | Blue | Blue | lnc-ZNF71-1   | 1557430_at   | Down |
| Red  | Blue | Blue | DPP10-AS1     | 236351_at    | Down |
| Blue | Red  | Red  | lnc-INADL-2   | 214295_at    | Up   |
| Red  | Blue | Blue | RP11-588K22.2 | 227235_at    | Down |
| Red  | Blue | Blue | EMX2OS        | 232531_at    | Down |
| Red  | Blue | Blue | HAR1A         | 1557098_s_at | Down |
| Red  | Blue | Blue | SLC26A4-AS1   | 1557107_at   | Down |
| Red  | Blue | Blue | MIR7-3HG      | 223913_s_at  | Down |
| Blue | Red  | Red  | RP11-834C11.4 | 226582_at    | Up   |
| Red  | Blue | Blue | RP11-490M8.1  | 236656_s_at  | Down |
| Red  | Blue | Blue | RP11-434B12.1 | 236166_at    | Down |
| Red  | Blue | Blue | DCTN1-AS1     | 1557617_at   | Down |
| Blue | Red  | Red  | SNHG1         | 224610_at    | Up   |
| Blue | Red  | Red  | LINC01268     | 1557359_at   | Up   |
| Red  | Blue | Blue | RFPL1S        | 214120_at    | Down |
| Red  | Blue | Blue | MIR600HG      | 223522_at    | Down |
| Blue | Red  | Red  | LINC00152     | 225799_at    | Up   |
| Red  | Blue | Blue | LINC00507     | 1557475_at   | Down |
| Red  | Blue | Blue | LINC00320     | 1557481_a_at | Down |
| Blue | Red  | Red  | lnc-ADAM30-1  | 214722_at    | Up   |
| Blue | Red  | Red  | ncTr-NBPF1    | 227926_s_at  | Up   |
| Red  | Blue | Blue | GS1-358P8.4   | 228959_at    | Down |

- 1: Non tumor (n = 4, GSE7696)
- 2: Radiotherapy (n = 28, GSE7696)
- 3: TMZ/Radiotherapy (n = 52, GSE7696)
- 4: lncRNA name
- 5: Probe ID
- 6: Regulated in glioblastoma (based on data from GSE50161 and GSE4290)

(b)

FIGURE 4: Continued.

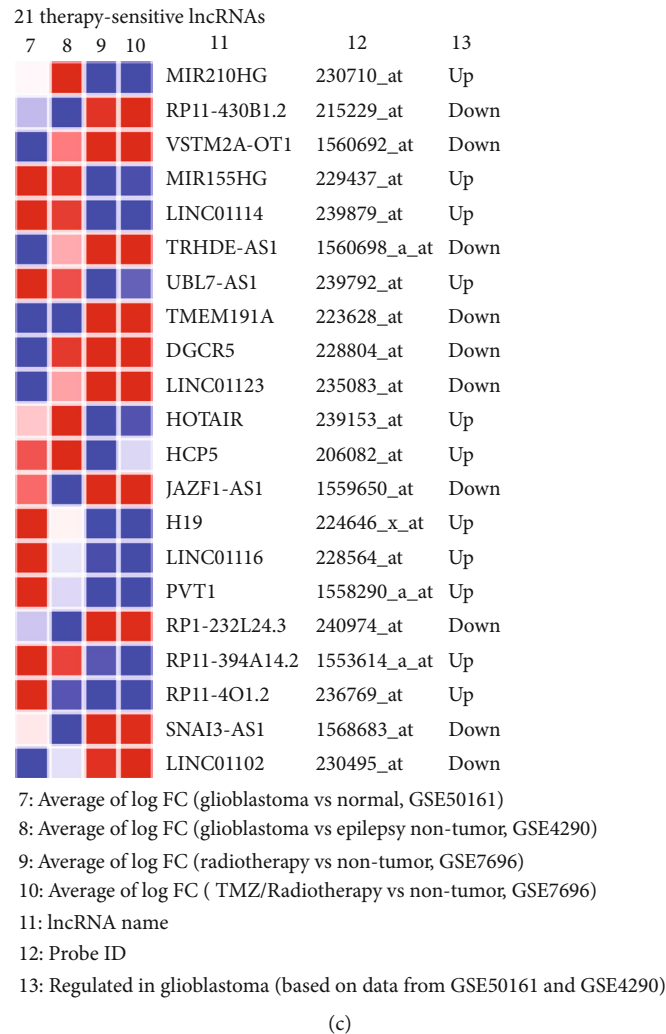


FIGURE 4: Identification of therapy-resistance and sensitive lncRNAs in GBM. (a) Venn diagram illustrating radiotherapy and TMZ/radiotherapy (21) and therapy-resistant lncRNAs (27) according to dataset GSE7696. One lncRNA LINC-PINT remained down-regulated in GBM of patients who received radiotherapy, but its expression was reversed in GBM of patients who received TMZ/radiotherapy compared with non-tumor brain tissues. The expression of two lncRNAs – PSMB8-AS1 and KB-1460A1.5 – was reversed in GBM of patients who received radiotherapy but remained down-regulated in GBM of patients who received TMZ/radiotherapy compared with non-tumor brain tissues. (b) Heatmap showing the expression (average log expression value) of therapy-resistant dysregulated lncRNAs in glioblastoma. (c) Heatmap showing the expression (average log expression value) of therapy-sensitive dysregulated lncRNAs in glioblastoma. (a and b) The expressions of 27 GBM-associated lncRNAs (identified as above) remained either up- or down-regulated in GBM of patients who received with either radiotherapy and TMZ/radiotherapy compared with control samples. (a and c) Both radiotherapy and TMZ/radiotherapy successfully reversed the expression of 21 lncRNAs in GBM.

**2.4. Cell cultures.** Human GBM U138MG (HTB-16™, ATCC) cells were maintained in Dulbecco's Modified Eagle Medium (DMEM) high glucose supplemented with 10% heat-inactivated fetal bovine serum (FBS), glutamine (2 mM), penicillin (100 U/mL), and streptomycin (100 µg/mL). U138MG cells were used within 15 passages. Human primary astrocytes were from ScienCell Research Laboratories (Carlsbad, CA, USA), cultured in astrocyte medium (ScienCell), and used within 12 passages.

**2.5. Small interfering RNA (siRNA) transfection.** The siRNAs used in this study are listed in Table 1. Cells were transfected with 30 nM siRNA using lipofectamine RNAiMAX (Invitro-

gen) in serum-free Opti-MEM according to the manufacturer's instructions.

**2.6. Real-time PCR.** According to the manufacturer's instructions, cDNA was synthesized using a Verso cDNA kit (AB-1453/B; Thermo Fisher Scientific). Real-time PCR was performed using SYBR Green ROX qPCR Master Mix (QIAGEN, 330510) using the primers listed in Table 1. The comparative cycle threshold (Ct) method ( $2^{-\Delta\Delta Ct}$ ) was used to calculate the relative level of gene expression. The Ct values were normalized to GAPDH, which served as an internal control.

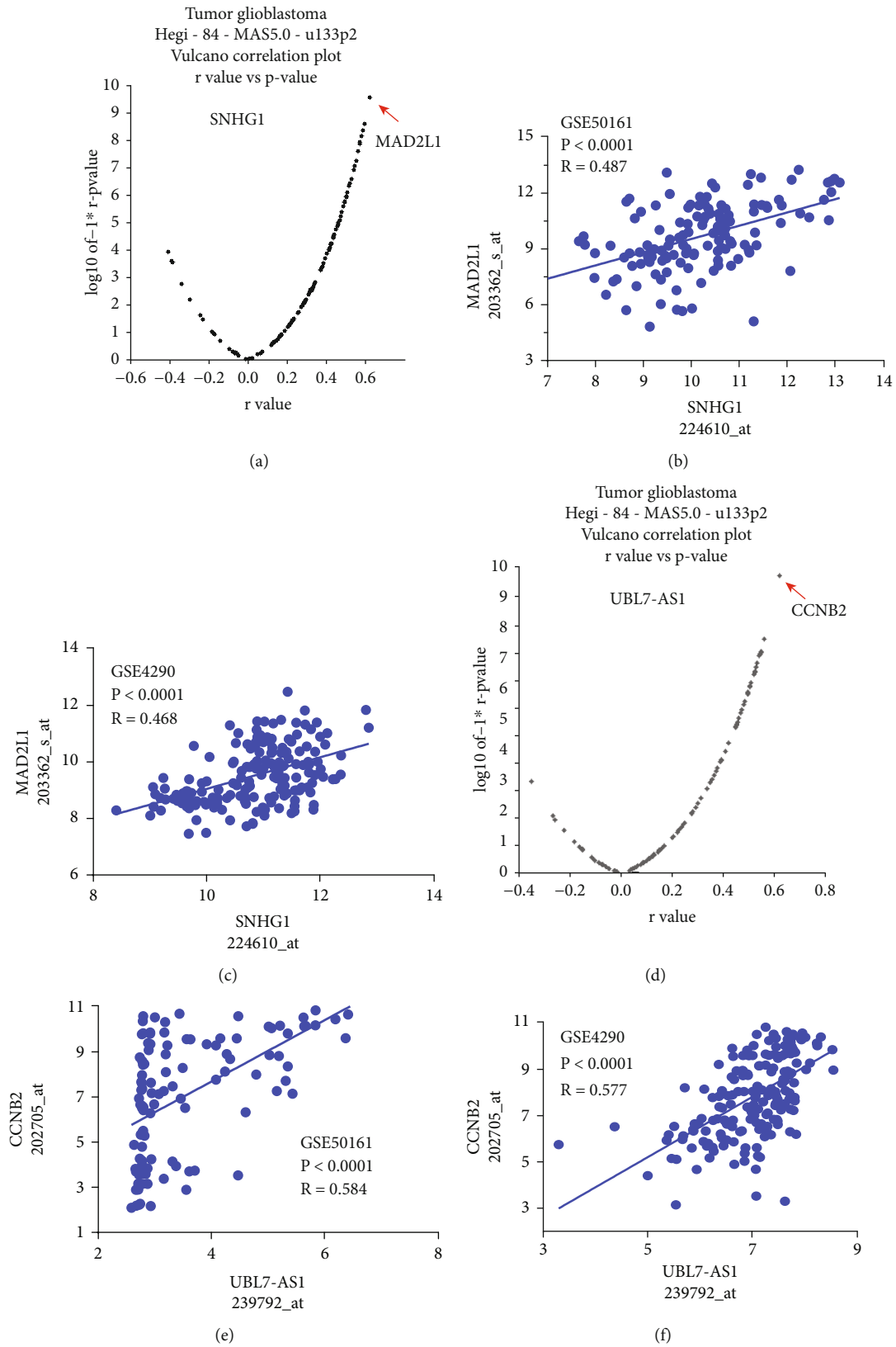


FIGURE 5: Continued.

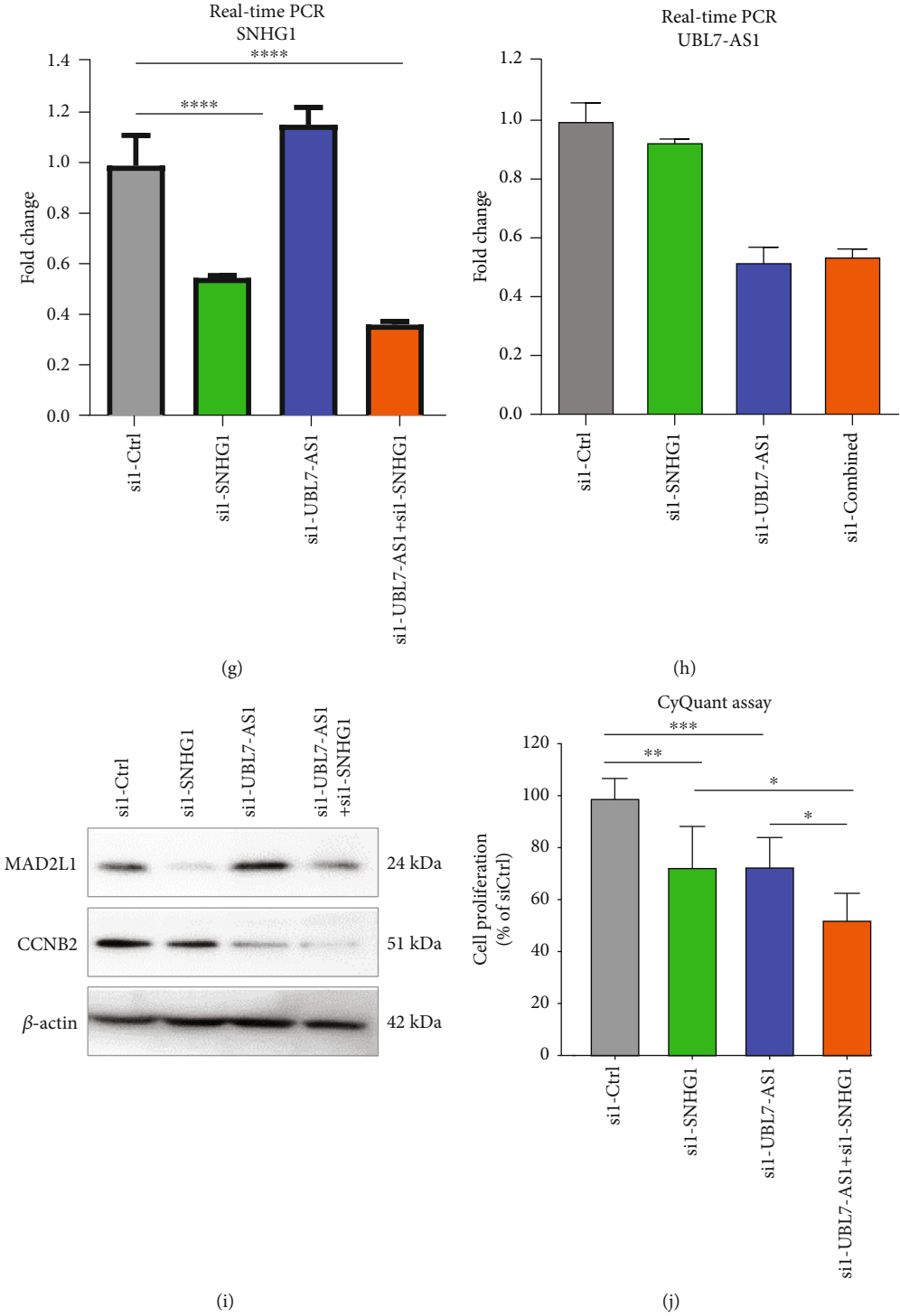
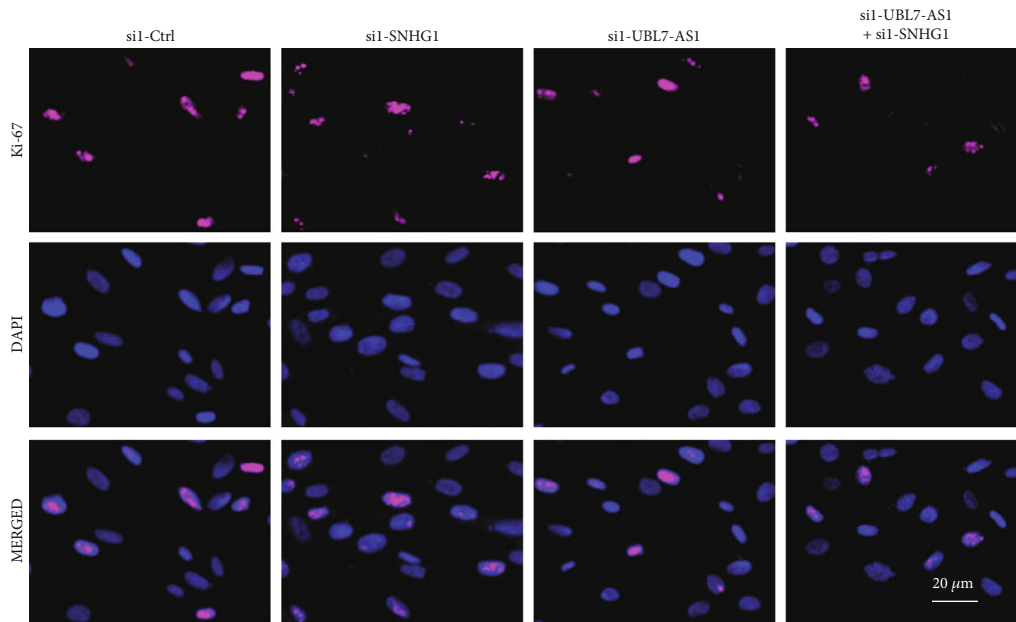
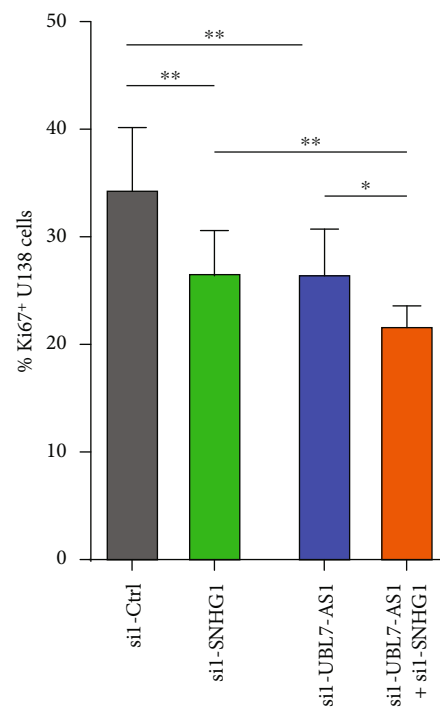


FIGURE 5: Continued.



(k)



(l)

FIGURE 5: Knockdown of SNHG1 and UBL7-AS1 decreases proliferation of U138MG cells. Expression levels of glioblastoma associated lncRNAs correlate with the expression of cell cycle genes. (a) Vulcano correlation plot showing the expression cell-cycle genes positively and negatively correlated with SNHG1 in dataset GSE7696. (b and c) Scatter plots for log expression of lncRNA expression (x-axis) versus log expression of the most positively correlated cell-cycle gene – MAD2L1 in dataset GSE50161 (d) and GSE4290 (e). (d) Vulcano correlation plot showing the expression cell-cycle genes positively and negatively correlated with UBL7-AS1 in dataset GSE7696. (e and f) Scatter plots for log expression of lncRNA expression (x-axis) versus log expression of the most positively correlated cell-cycle gene – CCNB2 in dataset GSE50161 (g) and GSE4290 (h). (g and h) Real-time PCR analysis of the expression of SNHG1 (a) and UBL7-AS1 (b) in U138MG cells transfected with siRNA to SNHG1, UBL7-AS1, or both. (i) Western blotting analysis of the expression of MAD2L1 and CCNB2 in U138MG cells transfected with siRNAs to SNHG1, UBL7-AS1 or both. (j) Cell proliferation analysis in U138MG cells transfected with siRNAs to SNHG1, UBL7-AS1, or both using the CyQUANT assay. (k) Immunostaining for Ki67 in U138MG cells transfected with siRNAs to SNHG1, UBL7-AS1, or both. (l) Quantification of the results in (e). P-values were calculated using one-way ANOVA where: \* $p < 0.05$ , \*\*  $p < 0.01$ , \*\*\*  $p < 0.001$ , \*\*\*\*  $p < 0.0001$ .



**2.7. Western blotting.** Cells were lysed using a mammalian cell lysis kit (Sigma-Aldrich), as described previously [19]. Proteins were separated in an SDS-polyacrylamide gel followed by transfer to a PVDF membrane. The membrane was blocked with 3% nonfat dry milk, 0.05% Tween 20 in Tris-buffered saline (TBS, 150 mM NaCl, 10 mM Tris-HCl, pH 8) (TTBS) for 1 h at room temperature (RT). The membrane was then probed with primary antibody in 5% nonfat milk overnight at 4°C. Primary antibodies specific for MAD2L1 (1:1,000; Proteintech), CCNB2 (1:1,000; Proteintech) and  $\beta$ -actin (1:6,000; Proteintech) were used in this study. Next day, the membrane was washed three times with TTBS for 10 min each and subsequently incubated with secondary antibody – alkaline phosphatase-conjugated to goat anti-mouse/rabbit IgG (1:10,000; Jackson ImmunoResearch Labs) for 1 h at RT. The membrane was washed three times with TTBS for 10 min each and then developed using West Chemiluminescent Substrate (Thermo Fisher Scientific). All experiments were repeated at least three times, and representative blots are presented in the figures.

**2.8. Immunostaining.** Cells cultured on slides or coverslips were fixed with 4% paraformaldehyde for 10 min at room temperature, followed by permeabilization with 0.3% Triton X-100 in PBS. Sections were incubated with a blocking buffer containing 5% BSA in PBS for 1 h at room temperature, followed by addition of rabbit anti-Ki67 (Proteintech) and incubated overnight at 4°C. Primary Abs were labeled with secondary Abs conjugated to the fluorescent probes, and nuclei were labeled with DAPI. Slides were covered with a coverslip with ProLong Gold antifade reagent (Invitrogen) and allowed to dry for 24 h at room temperature. Images were captured with a 20X objective.

**2.9. Cell proliferation assays.** Cells were seeded in the 96-well plate with a density of 5000 cells per well. Cell proliferation assays were performed after transfecting siRNA. Cell proliferation was assessed using the CyQUANT™ Cell Proliferation Assay Kit (Invitrogen) according to the manufacturer's instructions.

**2.10. Statistical analysis and figure generation.** P-values were calculated using either a two-tailed unpaired t-test or one-way analysis of variance (ANOVA) for differential expression as indicated in the figure legends. Boxplots and scatter plots figures were generated using GraphPad Prism version 6.01 for Windows (GraphPad Software). Venn diagrams were generated using the Venny tool at <http://bioinformatics.psb.ugent.be/webtools/Venny/>. Heatmaps were generated using Morpheus, <https://software.broadinstitute.org/morpheus>.

### 3. Results

**3.1. Identification of dysregulated lncRNAs in various human brain tumors compared with normal brain tissues.** To identify dysregulated lncRNAs in human brain tumors, we first examined the dataset GSE50161, which contains brain samples from 46 ependymomas, 34 GBM, 15 pilocytic astrocytoma (PA), and 22 medulloblastomas, and 13 normal

brain samples [20]. The expressions of 31, 13, 18, and 27 lncRNAs were exclusively dysregulated in ependymoma, GBM, PA, and medulloblastomas tumors, compared with control samples, respectively (Figures 1(a) and 1(b)-a, c, d, n). The expressions of 14, 10, 7, 2, 15, and 7 lncRNAs were dysregulated in both ependymoma and GBM; ependymoma and PA; GBM and PA; PA and medulloblastomas; ependymoma and medulloblastomas; GBM and medulloblastomas; compared with control samples, respectively (Figures 1(a) and 1(b)-b, e, g, h, j, o). The expressions of 20, 8, and 12 lncRNAs were dysregulated in ependymoma, GBM and PA; ependymoma, PA and medulloblastomas; GBM, ependymoma and medulloblastomas, compared with control samples, respectively (Figures 1(a) and 1(b)-f, i, k). Moreover, we identified 34 lncRNAs commonly aberrantly expressed in all tumor samples compared with control samples simultaneously (Figures 1(a) and 1(b)-l).

**3.2. Identification of dysregulated lncRNAs in various human brain tumors compared with non-tumor brain tissues from epilepsy patients.** We next sought to examine the expression of lncRNAs in another dataset – GSE4290 – which contains 23 non-tumor control samples from epilepsy patients, 26 astrocytomas (grade 2-3), 81 GBM [21], and 50 oligodendrogliomas. There were 13, 87, and 33 lncRNAs, respectively, differentially expressed in astrocytomas, GBM, and oligodendrogliomas compared with nontumor epilepsy brain samples (Figures 2(a) and 2(b)-a, c, d). There were 39, 11, and 10 lncRNAs, differentially expressed in astrocytomas and GBM; astrocytomas and oligodendrogliomas; GBM and oligodendrogliomas; , respectively, compared with non-tumor epilepsy brain samples (Figures 2(a) and 2(b)-b, e, g). The expressions of 94 lncRNAs were commonly dysregulated in all tumor samples compared with non-tumor epilepsy brain samples simultaneously (Figures 2(a) and 2(b)-f).

**3.3. Dysregulated lncRNAs in GBM.** Having determined the dysregulated lncRNAs in GBM in two unrelated studies, we next sought to find dysregulated lncRNAs in both datasets. As shown in Figure 3(a), there were 51 lncRNAs that aberrantly expressed in GBM compared with either normal control or non-tumor epilepsy controls. Interestingly, among them, 30 and 21 lncRNAs were, respectively, up- and down-regulated in GBM in both datasets (Supplemental Table 2). The representative up- and down-regulated lncRNAs in GBM are shown in Figures 3(a) and 3(b)a-j. We further validated these findings in TCGA databases [18]. The expression of SNHG1 and UBL7-AS1 were up-regulated, while the VSTM2A-OT1 and EMX2OS were down-regulated in GBM cases from public TCGA databases (Supplemental Figures 1).

**3.4. Identification of therapy-resistant and therapy-reversed lncRNAs in GBM.** Owing to the poor outcome of the therapies for GBM, we proposed that GBM-associated lncRNAs that were resistant to therapies could be related to treatment noncompliance. For this, we examined the expression of the 51 GBM-associated lncRNAs in another dataset GSE7696.

This dataset contains 4 non-tumor brain tissue samples, 28 GBM specimens from patients treated with radiotherapy, and 52 GBM specimens of patients treated with adjuvant temozolomide (TMZ) and radiotherapy [22, 23]. Intriguingly, the expressions of 27 GBM-associated lncRNAs (identified as above) remained either up- or down-regulated in GBM of patients who received with either radiotherapy and TMZ/radiotherapy compared with control samples (Figures 4(a) and 4(b)), while both radiotherapy and TMZ/radiotherapy successfully reversed the expression of 21 lncRNAs in GBM (Figures 4(a) and 4(c)). Additionally, one lncRNA LINC-PINT remained down-regulated in GBM of patients who received radiotherapy, but its expression was reversed in GBM of patients who received TMZ/radiotherapy compared with non-tumor brain tissues (Figures 4(a)). The expression of two lncRNAs, PSMB8-AS1 and KB-1460A1.5 was reversed in GBM of patients who received radiotherapy but remained down-regulated in GBM of patients who received TMZ/radiotherapy compared with non-tumor brain tissues (Figures 4(a)).

**3.5. Functional analysis of therapy-resistant and -reversed lncRNAs.** To investigate the potential functions of the therapy-resistant and -reversed lncRNAs in GBM, pathway enrichment analysis on lncRNA-correlating genes was performed using the R2 KEGG Pathway Finder. Data used for the correlation analyses were from the GSE7696 dataset in the R2 platform. The functional pathways were ranked by the sum of each lncRNA's negative log<sub>10</sub> p-value for each pathway. The top 30 pathways correlated with therapy-resistant and -reversed lncRNAs are shown in Supplemental Figures 2A and 2B. Interestingly, the expressions of therapy-resistant and -reversed lncRNAs such as SNHG1, GS1-358P8.4 (Supplemental Figure 2A), UBL7-AS1, and RP11-4O1.2 were significantly correlated with the expression of cell-cycle genes in the dataset, suggesting both therapy-resistant and -reversed lncRNAs could play a role in GBM proliferation.

Notably, the morphine addiction pathway was also ranked in the top 30 enriched pathways among therapy-resistant and -reversed lncRNA-correlating genes (Supplemental Figures 2A and 2B). This result suggests that the use of morphine could dysregulate the expression of lncRNAs, and in turn, affect morphine tolerance and addiction cellular signaling pathways [24, 25]. As shown in Figure 5(a), the expressions of most cell-cycle genes were shown to be positively correlated with the expression of SNHG1, with the strongest correlation between SNHG1 and MAD2L1 - a positive regulator of cell proliferation [26, 27]. The positive correlation between SNHG1 and MAD2L1 was further validated in datasets GSE50161 and GSE4290 (Figures 5(b) and 5(c)). Similarly, we found that the expression of one of the therapy-reversed lncRNAs UBL7-AS1 was positively correlated with most of the cell-cycle genes with the strongest correlation between UBL7-AS1 and CCNB2, another positive regulator of cell proliferation (Figures 5(d)–5(f)). These results thus indicate that therapy-resistant and -reversed lncRNAs could regulate GBM cell proliferation.

**3.6. Both therapy-resistant and -reversed lncRNAs regulate human GBM cell proliferation.** We next sought to examine the functions of SNHG1 and UBL7-AS1 using the gene silencing approach using two siRNAs against each lncRNA (Table 1). For this, human GBM U138MG cells were transfected with SNHG1, UBL7-AS1, or both siRNAs, followed by evaluation of cell proliferation by either CyQuant assay or Ki67 immunostaining. The knockdown efficiency was evaluated by real-time PCR. As shown in Figures 5(g) and 5(h), the expression of lncRNAs, SNHG1 and UBL7-AS1 was significantly down-regulated in cells transfected with corresponding siRNAs compared with cells transfected with scrambled siRNA. Additionally, knockdown of SNHG1 and UBL7-AS1 decreased the expressions of MAD2L1 and CCNB2, respectively, in U138MG cells (Figure 5(h)). As expected, knockdown of SNHG1 and UBL7-AS1 together reduced the expression of MAD2L1 and CCNB2 simultaneously in U138MG cells (Figure 5(h)). Moreover, knockdown of either SNHG1 or UBL7-AS1 significantly decreased cell proliferation in U138MG cells, evidenced by both CyQuant assay and Ki67 immunostaining assays (Figures 5(j)–5(l)). Intriguingly, U138MG cells transfected with SNHG1 and UBL7-AS1 siRNAs exhibited decelerated cell proliferation compared with single siRNA transfected cells (Figures 5(j)–5(l)). These findings were further validated using another set of siRNAs against SNHG1 and UBL7-AS1 (Supplemental Figures 3).

We next sought to examine the role of these two lncRNAs on the expression of cell cycle genes. Interestingly, knockdown of SNHG1, UBL7-AS1 or both decreased the expression of cell-cycle positive regulators including ABL1, CCNA2, CDK6, GADD45A and WEE1 but increased the expression of cell-cycle negative regulator CDKN2D in U138MG cells (Supplemental Figures 4). Furthermore, and as expected, knockdown of SNHG1 and UBL7-AS1 did not show significant effects on proliferation in human primary astrocytes (Supplemental Figures 5). These findings thus suggest that both therapy-resistant and -sensitive lncRNAs control cell proliferation in GBM, which could, in turn, contribute to the pathogenesis and development of GBM.

## 4. Discussion

In the current study, we found that 51 lncRNAs were dysregulated in human GBM tissues. Among them, 27 lncRNAs were shown to be resistant to both radiotherapy and TMZ/radiotherapy, while 21 lncRNAs were sensitive to these therapies. Functional analyses suggest that both therapy-resistant and -sensitive lncRNAs appear to be associated with the cell-cycle pathway. We also found that the expressions of therapy-resistant lncRNA SNHG1 and therapy-sensitive lncRNA UBL7-AS1 were positively correlated with the expressions of cell-cycle genes MAD2L1 and CCNB2, respectively. Using the gene silencing approach, we demonstrated that knockdown of SNHG1 and UBL7-AS1 decreased the expression of MAD2L1 and CCNB2, respectively. Moreover, knockdown of either SNHG1 or UBL7-AS1 reduced the proliferation of human GBM U138MG cells. Additionally, knockdown of SNHG1 and UBL7-AS1

showed an additive effect in reducing cell proliferation in U138MG cells. Previous studies demonstrated that SNHG1 could promote cell proliferation by acting as a sponge of miR-145, miR-143-3p, miR-194, miR-137 and miR-9-5p [28–32]. Interestingly, MAD2L1 is a potential target of these miRNAs, according to Targetscan analysis [33].

Previous studies have demonstrated that numerous lncRNAs are associated with various brain disorders [24, 34, 35], including GBM, such as TP73-AS1 [36], H19 [37], HOTAIR [7], and LINC00152 [38]. In line with these studies, we found that the expression of TP73-AS1 was up-regulated in GBM compared with normal controls, while the expressions of H19, HOTAIR and LINC00152 were significantly up-regulated in GBM compared with either normal controls or epilepsy non-tumor brain samples. Previous studies have also identified a group of lncRNAs resistant to TMZ treatment in various cell lines [39]. Here, we found that 27 lncRNAs were shown to be resistant to both radiotherapy and TMZ/radiotherapy, suggesting that they could contribute to the poor outcome of patients on treatments. Our *in vitro* results further demonstrated that knockdown of therapy-resistant and -sensitive lncRNAs showed an additive reduction of cell proliferation in human GBM cells. These findings suggest that targeting both therapy-resistant and therapy-sensitive lncRNAs could improve therapeutic outcomes in GBM patients. Moreover, understanding the expression patterns of these lncRNAs in individual GBM patients could provide strategies for future personal adjunctive therapeutics for this disease.

## 5. Conclusion

We performed a comprehensive analysis of the lncRNA transcriptome in GBM and identified 27 therapy-resistant and 21 therapy-sensitive lncRNAs associated with various biological functions such as cell proliferation. We also experimentally demonstrated that both therapy-resistant and therapy-sensitive lncRNAs play a role in GBM cell proliferation. Future validation and functional studies on other therapy-resistant and therapy-sensitive lncRNAs, including levels of these lncRNAs in the plasma of GBM patients, would be valuable to extend this study.

## Abbreviations

|                |  |
|----------------|--|
| lncRNA:        | Long non-coding RNA                              |
| GBM:           | Glioblastoma                                     |
| TMZ:           | Temozolomide                                     |
| SNHG1:         | Small nucleolar RNA host gene 1                  |
| UBL7-AS1:      | UBL7 antisense RNA 1                             |
| Real-time PCR: | Real-time quantitative polymerase chain reaction |
| siRNA:         | Small interfering RNA.                           |

## Data Availability

The original data (GSE50161, GSE4290, and GSE7696) published by others are available at the Gene Expression Omnibus (GEO) database of NCBI (<http://www.ncbi.nlm.nih.gov/>

geo/). Anonymized data are available from the corresponding author upon reasonable request.

## Conflicts of Interest

The authors declare no competing financial interests in the work described.

## Authors' Contributions

M.C., R.M., H.L., & J.Z. designed and performed the experiments and collected, analyzed and discussed the data. M.C., R.M., J.C., C.Z., & J.Z. discussed the data and drafted/revised the manuscript. All authors have read and approved the final manuscript.

## Acknowledgments

This work was supported by the Program for New Century Excellent Talents in University [grant numbers NCET-13-0397].

## Supplementary Materials

*Supplementary 1.* Supplementary Figure 1: Expression of SNHG1, UBL7-AS1, VSTM2A-OT1 and EMX2OS in GBM patient samples as determined by analysis of the UALCAN portal.

*Supplementary 2.* Supplementary Figure 2: Expression levels of glioblastoma-associated lncRNAs correlate with the expressions of cell-cycle genes.

*Supplementary 3.* Supplementary Figure 3: Knockdown of SNHG1 and UBL7-AS1 decreases proliferation of U138MG cells.

*Supplementary 4.* Supplementary Figure 4: lncRNAs SNHG1 and UBL7-AS1 cell cycle-related genes in U138MG cells.

*Supplementary 5.* Supplementary Figure 5: Knockdown of SNHG1 and UBL7-AS1 does not affect proliferation of human primary astrocytes.

*Supplementary 6.* Supplementary Table 1: The statistics and description of the datasets used in this study.

*Supplementary 7.* Supplementary Table 2: Fifty-one commonly dysregulated lncRNAs in glioblastoma in both datasets GSE50161 and GSE4290.

## References

- [1] E. C. Holland, "Glioblastoma multiforme: the terminator," *Proceedings of the National Academy of Sciences of the United States of America*, vol. 97, no. 12, pp. 6242–6244, 2000.
- [2] W. L. Bi and R. Beroukhim, "Beating the odds: extreme long-term survival with glioblastoma," *Neuro-Oncology*, vol. 16, no. 9, pp. 1159–1160, 2014.
- [3] Z. Peng, C. Liu, and M. Wu, "New insights into long noncoding RNAs and their roles in glioma," *Molecular Cancer*, vol. 17, no. 1, pp. 1–10, 2018.

- [4] Y. Wang, Y. Wang, J. Li, Y. Zhang, H. Yin, and B. Han, "CRNDE, a long-noncoding RNA, promotes glioma cell growth and invasion through mTOR signaling," *Cancer Letters*, vol. 367, no. 2, pp. 122–128, 2015.
- [5] P. Jiang, P. Wang, X. Sun et al., "Knockdown of long noncoding RNA H19 sensitizes human glioma cells to temozolomide therapy," *Oncotargets and Therapy*, vol. 9, pp. 3501–3509, 2016.
- [6] Y. Yang, M. Ren, C. Song et al., "LINC00461, a long noncoding RNA, is important for the proliferation and migration of glioma cells," *Oncotarget*, vol. 8, no. 48, pp. 84123–84139, 2017.
- [7] C. Pastori, P. Kapranov, C. Penas et al., "The Bromodomain protein BRD4 controls HOTAIR, a long noncoding RNA essential for glioblastoma proliferation," *Proceedings of the National Academy of Sciences of the United States of America*, vol. 112, no. 27, pp. 8326–8331, 2015.
- [8] M. Han, S. Wang, S. Fritah et al., "Interfering with long noncoding RNA MIR22HG processing inhibits glioblastoma progression through suppression of Wnt/ $\beta$ -catenin signalling," *Brain*, vol. 143, no. 2, pp. 512–530, 2020.
- [9] H. Liu, Z. Lv, and E. Guo, "Knockdown of long noncoding RNA SPRY4-IT1 suppresses glioma cell proliferation, metastasis and epithelial-mesenchymal transition," *International Journal of Clinical and Experimental Pathology*, vol. 8, no. 8, pp. 9140–9146, 2015.
- [10] Y. Yao, J. Ma, Y. Xue et al., "Knockdown of long non-coding RNA XIST exerts tumor-suppressive functions in human glioblastoma stem cells by up-regulating miR-152," *Cancer Letters*, vol. 359, no. 1, pp. 75–86, 2015.
- [11] J. Zeng, T. Du, Y. Song et al., "Knockdown of long noncoding RNA CCAT2 inhibits cellular proliferation, invasion, and epithelial-mesenchymal transition in glioma cells," *Oncology Research*, vol. 25, no. 6, pp. 913–921, 2017.
- [12] Y. S. Gao, X. Z. Liu, Y. G. Zhang, X. J. Liu, and L. Z. Li, "Knockdown of long noncoding RNA LUCAT1 inhibits cell viability and invasion by regulating miR-375 in glioma," *Oncology Research*, vol. 26, no. 2, pp. 307–313, 2018.
- [13] J. Li, Y. M. Wang, and Y. L. Song, "Knockdown of long noncoding RNA AB073614 inhibits glioma cell proliferation and migration via affecting epithelial-mesenchymal transition," *European Review for Medical and Pharmacological Sciences*, vol. 20, no. 19, pp. 3997–4002, 2016.
- [14] X. Jiang, Y. Yan, M. Hu et al., "Increased level of H19 long noncoding RNA promotes invasion, angiogenesis, and stemness of glioblastoma cells," *Journal of Neurosurgery*, vol. 2016, no. 1, pp. 129–136, 2016.
- [15] O. Van Grembergen, M. Bizet, E. J. de Bony et al., "Portraying breast cancers with long noncoding RNAs," *Science Advances*, vol. 2, no. 9, article e1600220, 2016.
- [16] T. Barrett and R. Edgar, "Mining microarray data at NCBI's gene expression omnibus (GEO)s," *Methods in Molecular Biology*, vol. 338, pp. 175–190, 2006.
- [17] T. Barrett, S. E. Wilhite, P. Ledoux et al., "NCBI GEO: archive for functional genomics data sets—update," *Nucleic Acids Research*, vol. 41, no. Database issue, pp. D991–D995, 2013.
- [18] D. S. Chandrashekar, B. Bashel, S. A. H. Balasubramanya et al., "UALCAN: a portal for facilitating tumor subgroup gene expression and survival analyses," *Neoplasia*, vol. 19, no. 8, pp. 649–658, 2017.
- [19] G. Hu, F. Niu, K. Liao et al., "HIV-1 tat-induced astrocytic extracellular vesicle miR-7 impairs synaptic architecture," *Journal of Neuroimmune Pharmacology*, vol. 15, no. 3, pp. 538–553, 2020.
- [20] A. M. Griesinger, D. K. Birks, A. M. Donson et al., "Characterization of distinct immunophenotypes across pediatric brain tumor types," *Journal of Immunology*, vol. 191, no. 9, pp. 4880–4888, 2013.
- [21] L. Sun, A. M. Hui, Q. Su et al., "Neuronal and glioma-derived stem cell factor induces angiogenesis within the brain," *Cancer Cell*, vol. 9, no. 4, pp. 287–300, 2006.
- [22] W. L. Lambiv, I. Vassallo, M. Delorenzi et al., "The Wnt inhibitory factor 1 (WIF1) is targeted in glioblastoma and has a tumor suppressing function potentially by induction of senescence," *Neuro-Oncology*, vol. 13, no. 7, pp. 736–747, 2011.
- [23] A. Murat, E. Migliavacca, T. Gorlia et al., "Stem cell-related "self-renewal" signature and high epidermal growth factor receptor expression associated with resistance to concomitant chemoradiotherapy in glioblastoma," *Journal of Clinical Oncology*, vol. 26, no. 18, pp. 3015–3024, 2008.
- [24] G. Hu, K. Liao, F. Niu et al., "Astrocyte EV-induced lincRNA-Cox2 regulates microglial phagocytosis: implications for morphine-mediated neurodegeneration," *Molecular Therapy-Nucleic Acids*, vol. 13, pp. 450–463, 2018.
- [25] R. Ma, N. A. Kutchy, and G. Hu, "Astrocyte-derived extracellular vesicle-mediated activation of primary ciliary signaling contributes to the development of morphine tolerance," *Biological Psychiatry*, vol. 90, no. 8, pp. 575–585, 2021.
- [26] X. Ding, H. Duan, and H. Luo, "Identification of Core gene expression signature and key pathways in colorectal cancer," *Frontiers in Genetics*, vol. 11, p. 45, 2020.
- [27] Y. Li, W. Bai, and J. Zhang, "MiR-200c-5p suppresses proliferation and metastasis of human hepatocellular carcinoma (HCC) via suppressing MAD2L1," *Biomedicine & Pharmacotherapy*, vol. 92, pp. 1038–1044, 2017.
- [28] Y. Fu, Y. Yin, S. Peng et al., "Small nucleolar RNA host gene 1 promotes development and progression of colorectal cancer through negative regulation of miR-137," *Molecular Carcinogenesis*, vol. 58, no. 11, pp. 2104–2117, 2019.
- [29] L. Liu, Y. Shi, J. Shi et al., "The long non-coding RNA SNHG1 promotes glioma progression by competitively binding to miR-194 to regulate PHLDA1 expression," *Cell Death & Disease*, vol. 10, no. 6, pp. 1–14, 2019.
- [30] S. Mi, J. Du, J. Liu et al., "FtMt promotes glioma tumorigenesis and angiogenesis via lncRNA SNHG1/miR-9-5p axis," *Cellular Signalling*, vol. 75, article 109749, 2020.
- [31] T. Tian, R. Qiu, and X. Qiu, "SNHG1 promotes cell proliferation by acting as a sponge of miR-145 in colorectal cancer," *Oncotarget*, vol. 9, no. 2, pp. 2128–2139, 2018.
- [32] W. Xiang, L. Lyu, T. Huang et al., "The long non-coding RNA SNHG1 promotes bladder cancer progression by interacting with miR-143-3p and EZH2," *Journal of Cellular and Molecular Medicine*, vol. 24, no. 20, pp. 11858–11873, 2020.
- [33] S. E. McGeary, K. S. Lin, C. Y. Shi et al., "The biochemical basis of micro RNA targeting efficacy," *Science*, vol. 366, no. 6472, article eaav1741, 2019.
- [34] M. Cao, H. Li, J. Zhao, J. Cui, and G. Hu, "Identification of age- and gender-associated long noncoding RNAs in the human brain with Alzheimer's disease," *Neurobiology of Aging*, vol. 81, pp. 116–126, 2019.

- [35] L. Li, Y. Zhuang, X. Zhao, and X. Li, "Long non-coding RNA in neuronal development and neurological disorders," *Frontiers in Genetics*, vol. 9, p. 744, 2019.
- [36] G. Mazor, L. Levin, D. Picard et al., "The lncRNA TP73-AS1 is linked to aggressiveness in glioblastoma and promotes temozolomide resistance in glioblastoma cancer stem cells," *Cell Death & Disease*, vol. 10, no. 3, pp. 1–14, 2019.
- [37] B. Fazi, S. Garbo, N. Toschi et al., "The lncRNA H19 positively affects the tumorigenic properties of glioblastoma cells and contributes to NKD1 repression through the recruitment of EZH2 on its promoter," *Oncotarget*, vol. 9, no. 21, pp. 15512–15525, 2018.
- [38] J. Cai, J. Zhang, P. Wu et al., "Blocking LINC00152 suppresses glioblastoma malignancy by impairing mesenchymal phenotype through the miR-612/AKT2/NF-kappaB pathway," *Journal of Neuro-Oncology*, vol. 140, no. 2, pp. 225–236, 2018.
- [39] A. Zottel, N. Samec, A. Videtic Paska, and I. Jovcevska, "Coding of glioblastoma progression and therapy resistance through long noncoding RNAs," *Cancers (Basel)*, vol. 12, no. 7, 2020.

## Research Article

# Glycosylation-Related Genes Predict the Prognosis and Immune Fraction of Ovarian Cancer Patients Based on Weighted Gene Coexpression Network Analysis (WGCNA) and Machine Learning

Chen Zhao <sup>1</sup>, Kewei Xiong <sup>2</sup>, Fangrui Zhao,<sup>1</sup> Abdalla Adam <sup>3</sup>, and Xiangpan Li <sup>1</sup>

<sup>1</sup>Department of Oncology, Renmin Hospital of Wuhan University, Wuhan, 430060 Hubei Province, China

<sup>2</sup>School of Mathematics and Statistics, Central China Normal University, Wuhan, 430079 Hubei Province, China

<sup>3</sup>School of Medicine, Wuhan University, Wuhan, 430072 Hubei Province, China

Correspondence should be addressed to Xiangpan Li; [rm001227@whu.edu.cn](mailto:rm001227@whu.edu.cn)

Received 31 October 2021; Revised 10 February 2022; Accepted 21 February 2022; Published 4 March 2022

Academic Editor: Abdur Rauf

Copyright © 2022 Chen Zhao et al. This is an open access article distributed under the Creative Commons Attribution License, which permits unrestricted use, distribution, and reproduction in any medium, provided the original work is properly cited.

**Background.** Ovarian cancer (OC) is a malignancy exhibiting high mortality in female tumors. Glycosylation is a posttranslational modification of proteins but research has failed to demonstrate a systematic link between glycosylation-related signatures and tumor environment of OC. **Purpose.** This study is aimed at developing a novel model with glycosylation-related messenger RNAs (GRmRNAs) to predict the prognosis and immune function in OC patients. **Methods.** The transcriptional profiles and clinical phenotypes of OC patients were collected from the Gene Expression Omnibus and The Cancer Genome Atlas databases. A weighted gene coexpression network analysis and machine learning were performed to find the optimal survival-related GRmRNAs. Least absolute shrinkage and selection operator regression (LASSO) and Cox regression were carried out to calculate the coefficients of each GRmRNA and compute the risk score of each patient as well as develop a prognostic model. A nomogram model was constructed, and several algorithms were used to investigate the relationship between risk subtypes and immune-infiltrating levels. **Results.** A total of four signatures (ALG8, DCTN4, DCTN6, and UBB) were determined to calculate the risk scores, classifying patients into the high- and low-risk groups. High-risk patients exhibited significantly poorer survival outcomes, and the established nomogram model had a promising prediction for OC patients' prognosis. Tumor purity and tumor mutation burden were negatively correlated with risk scores. In addition, risk scores held statistical associations with pathway signatures such as Wnt, Hippo, and reactive oxygen species, and nonsynonymous mutation counts. **Conclusion.** The currently established risk scores based on GRmRNAs can accurately predict the prognosis, the immune microenvironment, and the immunotherapeutic efficacy of OC patients.

## 1. Introduction

Ovarian cancer (OC) is one of the most common gynecological neoplasms with the fourth highest incidence and third highest mortality in the world [1]. Consecutive ovulation, low immunity, hormonal fluctuations, and aberrant reactive oxygen production can contribute to the pathogenesis [2]. In addition, the tumorigenesis of OC is reported to be highly associated with BRCA1 dysfunction [3, 4]. Since ovaries are located in deep pelvic cavities, it is difficult to detect OC in the early stages [5]. Consequently, almost 70% of OC patients have already progressed to advanced stages with

distant metastases present at the time of diagnosis [6, 7]. Despite advances in OC therapies, the 5-year survival rate for OC is still less than 50%, which is significantly lower than the 85% rate for breast cancer [8]. Approximately 70% of OC individuals will develop a recurrence after surgery, and about 75% of high-grade serous ovarian cancer (HGSOC) patients will experience chemoresistance against cisplatin, oxaliplatin, carboplatin, etc. [9, 10]. Identifying novel risk factors that regulate tumorigenesis, migration, and proliferation will contribute to early diagnosis and personalized interventions for OC treatment. Hence, it is imperative to

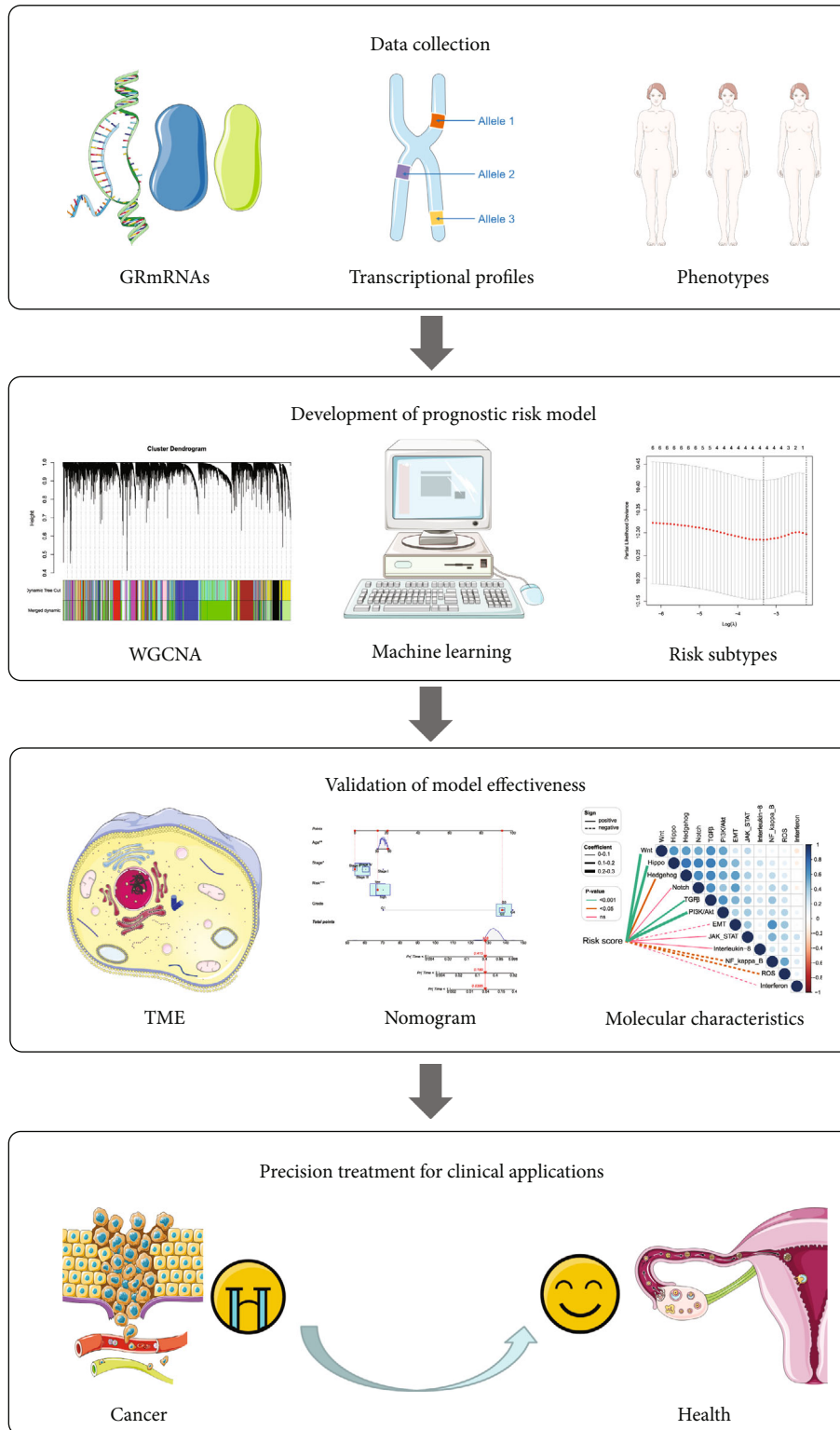


FIGURE 1: The workflow of this study.

explore the biological pathologic mechanisms and develop a reliable prognostic prediction model for OC patients.

Glycosylation is a posttranslational modification of proteins; the main types of which are N-linked and O-linked occurring in the endoplasmic reticulum (ER) and Golgi

complex, respectively; it demonstrates complicated mechanisms due to its variations based on the expression of glycosylating enzymes [11]. The transfer of N-acetyl glucosamine phosphate to the dolichol phosphate can result in N-linked glycosylation, which is mediated by various

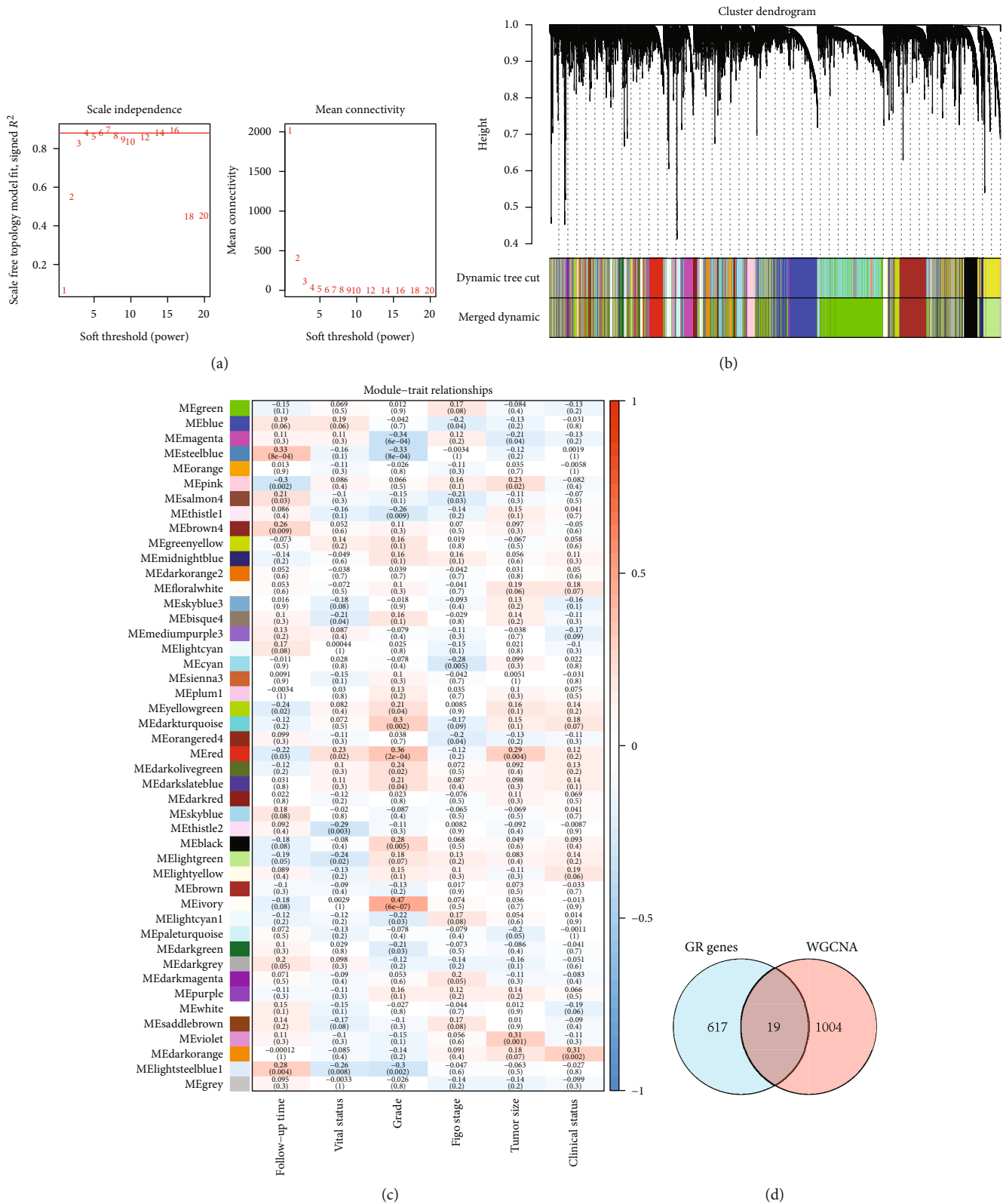


FIGURE 2: Continued.



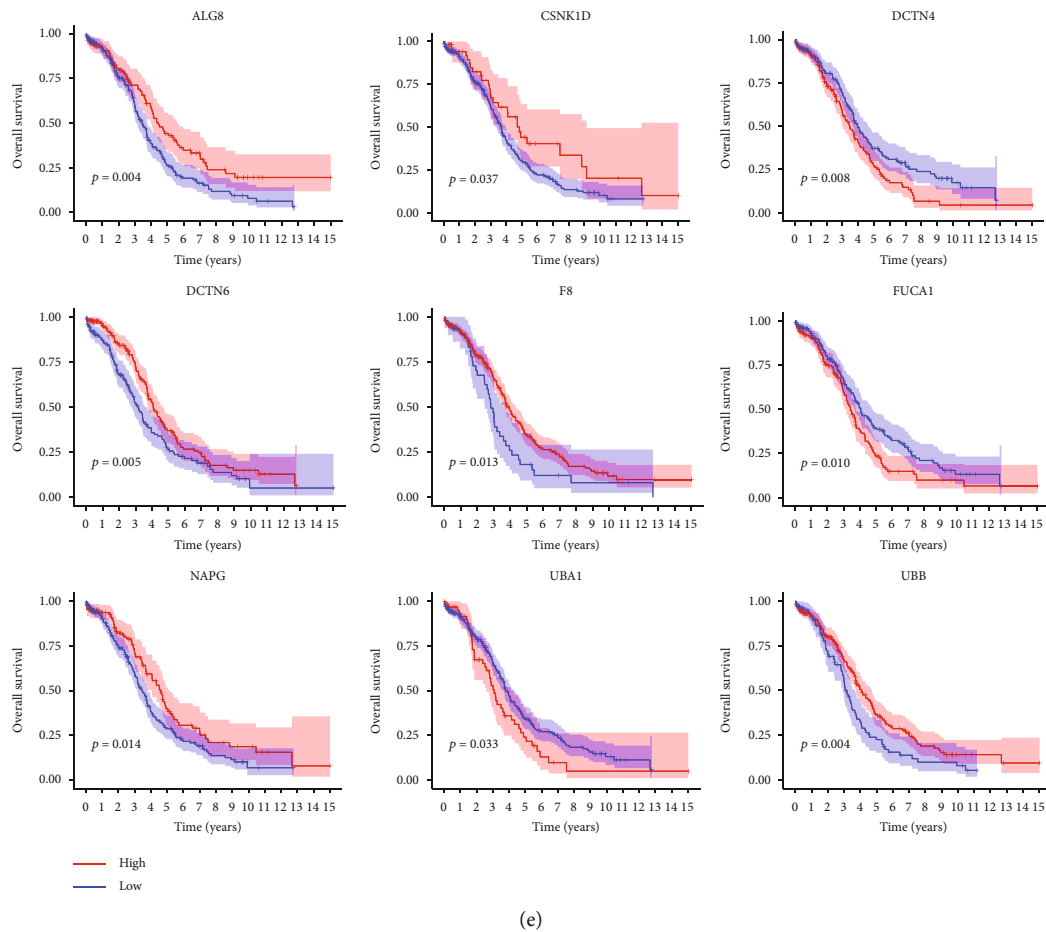


FIGURE 2: Discovery of prognostic GRmRNAs by WGCNA. (a) The distribution and trends of scale free topology model fit and mean connectivity along with soft threshold. (b) The clustering of genes among different modules by the dynamic tree cut and merged dynamic method. The gray modules represent unclassified genes. (c) The average correlations among multiple modules and clinical features. The colors of the cells indicate the strength of the correlation, and the numbers in parentheses represent the  $P$  value of the correlation test. (d) 19 overlapped GRmRNAs from the glycosylation-related gene list and WGCNA were obtained. (e) Significant survival differences between the high- and low-expression groups of GRmRNAs by log-rank test (GRmRNAs: glycosylation-related mRNAs; WGCNA: weighted gene coexpression network analysis).

glycosyltransferases in the ER [12]. O-linked glycosylation is more complex than the N-linked one for the unknown initiation emerging from the consensus sequence [12]. The O-linked modification pattern takes place in the intracellular nuclear and cytoplasmic compartments and does not elongate to create complex structures like other types of glycosylation [13]. It has been reported that glycosylation plays a regulatory role in cell differentiation, neoplastic progression, and immune control of malignant tumors [14, 15]. Aberrant glycosylation has been considered an important indicator of immune modulation induced by tumor and metastasis since it can generate antigens as targets for tumor-specific T cells [16, 17]. Several lines of evidence from clinical practice of OC suggest that glycosylation changes in proteins such as immunoglobulin G,  $\alpha_1$ -acid glycoprotein, and ceruloplasmin. All of this contributes to promoting or obstructing tumorigenesis and invasion [18, 19].

There are also emerging prognostic models for OC with biomarkers associated with post-translational regulatory mechanisms such as alternative splicing and N6-

methyladenosine modification [20, 21]. However, as an important hallmark among over 300 protein posttranscriptional modifications [22], only a few studies regarding glycosylation in OC have been reported. A translational study revealed that the expression levels of 210 glycosyltransferase genes could distinguish six cancer types, including breast, ovarian, glioblastoma, kidney, colon, and lung [23]. Pan et al. identified novel subtypes of HGSOC with glycoproteomics-based signatures for clinical prediction using consensus clustering and verified that the variation in glycan types would coordinate with tumor heterogeneity based on proteomics [24]. Recently, a prognostic model based on glycosylation-related genes for proficient mismatch repair in colorectal cancer has been proposed, from which it can be inferred that glycosylation is capable of serving as a hallmark for prognostic prediction [25]. Nonetheless, the mentioned research has failed to demonstrate a systematic link between glycosylation-related signatures and tumor environment of OC.

TABLE 1: Clinicopathologic information of training set and test set.

| Covariates   | Type      | TCGA ( $n = 375$ ) | Training ( $n = 208$ ) | Test ( $n = 167$ ) | $P$                |
|--------------|-----------|--------------------|------------------------|--------------------|--------------------|
| Vital status | Alive     | 146 (38.93%)       | 80 (38.46%)            | 66 (39.52%)        | 0.834 <sup>a</sup> |
|              | Dead      | 229 (61.07%)       | 128 (61.54%)           | 101 (60.48%)       |                    |
| Age          | ≤60       | 206 (54.93%)       | 105 (50.48%)           | 101 (60.48%)       | 0.053 <sup>a</sup> |
|              | >60       | 169 (45.07%)       | 103 (49.52%)           | 66 (39.52%)        |                    |
| Grade        | G1        | 1 (0.27%)          | 1 (0.48%)              | 0 (0%)             | 0.577 <sup>b</sup> |
|              | G2        | 42 (11.2%)         | 20 (9.62%)             | 22 (13.17%)        |                    |
|              | G3        | 321 (85.6%)        | 181 (87.02%)           | 140 (83.83%)       |                    |
|              | G4        | 1 (0.27%)          | 1 (0.48%)              | 0 (0%)             |                    |
|              | Unknown   | 10 (2.67%)         | 5 (2.4%)               | 5 (2.99%)          |                    |
| Stage        | Stage I   | 1 (0.27%)          | 1 (0.48%)              | 0 (0%)             | 0.451 <sup>b</sup> |
|              | Stage II  | 22 (5.87%)         | 13 (6.25%)             | 9 (5.39%)          |                    |
|              | Stage III | 292 (77.87%)       | 158 (75.96%)           | 134 (80.24%)       |                    |
|              | Stage IV  | 57 (15.2%)         | 33 (15.87%)            | 24 (14.37%)        |                    |
|              | Unknown   | 3 (0.8%)           | 3 (1.44%)              | 0 (0%)             |                    |

<sup>a</sup>Pearson's chi-square test; <sup>b</sup>Fisher's exact test.

TABLE 2: The quantified importance of prognostic glycosylation-related messenger RNAs by machine learning.

|        | LASSO     | Ridge     | XGBoost | Random forest | AdaBoost  |
|--------|-----------|-----------|---------|---------------|-----------|
| ALG8   | 0.255 (3) | 0.276 (3) | 95 (8)  | 0.108 (6)     | 0.088 (5) |
| CSNK1D | 0.025 (8) | 0.065 (8) | 112 (5) | 0.141 (1)     | 0.225 (1) |
| DCTN4  | 0.587 (1) | 0.609 (1) | 120 (3) | 0.113 (5)     | 0.169 (2) |
| DCTN6  | 0.406 (2) | 0.442 (2) | 100 (7) | 0.139 (2)     | 0.161 (3) |
| F8     | 0.108 (6) | 0.124 (6) | 114 (4) | 0.117 (3)     | 0.125 (4) |
| FUCA1  | 0.113 (5) | 0.134 (5) | 88 (9)  | 0.090 (8)     | 0.027 (9) |
| NAPG   | 0.177 (4) | 0.217 (4) | 135 (2) | 0.076 (9)     | 0.086 (6) |
| UBA1   | 0.022 (9) | 0.061 (9) | 148 (1) | 0.101 (7)     | 0.069 (7) |
| UBB    | 0.089 (7) | 0.092 (7) | 106 (6) | 0.115 (4)     | 0.049 (8) |

The number in the parentheses represented the rankings of weight.

With these inadequacies and challenges of OC research, this research is aimed at investigating the clinicopathologic features of glycosylation-related messenger RNAs (GRmRNAs) for the prognostic and tumor microenvironment (TME) prediction of patients with OC. Based on the established risk prognostic model, the associations with risk scores, tumor immune-infiltration, and hallmark signatures were analyzed. Furthermore, we also explore the correlations between risk subtypes and mutation characteristics. These findings were based on transcriptomics to provide a novel insight into the role of glycosylation in ovarian cancer and contribute to precision treatment.

## 2. Materials and Methods

**2.1. Data Acquisition and Processing.** All the datasets included in this study were available online to the public. The transcriptional RNA sequencing (RNA-seq) data of patients with ovarian cancer, including 427 samples, clinicopathologic data, and simple nucleotide variation (SNV) information were retrieved from The Cancer Genome Atlas (TCGA, <https://portal.gdc.cancer.gov/>). The RNA-seq profile in fragments per kilobase million (FPKM) was processed into log<sub>2</sub>-transformed transcripts per million (TPM). Another cohort of gene expression data of 101 aggregated samples and corresponding clinical characteristics were obtained from GSE63885 [26] in the Gene Expression Omnibus (GEO, <https://www.ncbi.nlm.nih.gov/geo/>) database. A total of 636 glycosylation-related (GR) genes (Supplementary Table 1) were downloaded from the Molecular Signatures Database (MSigDB, <http://www.gsea-msigdb.org/gsea/msigdb/>), a web-based assembling of annotated gene sets for biologic function analysis. The levels of tumor immune-infiltration estimated by different methods containing CIBERSORT, CIBERSORT-ASB, QUANTISEQ, MCPOUNTER, XCELL, and EPIC were extracted from the TIMER (<http://timer.cistrome.org>) [27] web server for TME investigations.

**2.2. Identification of Prognostic GRmRNAs.** A weighted gene coexpression network analysis (WGCNA) [28] was performed on GSE63885 based on its expression levels and phenotypes with follow-up time, vital status, tumor grade, FIGO stage, tumor size, and clinical status (Supplementary Table 2) to screen for hub genes. We quantified the goodness of fit by using a scale-free topology model and integrating it with mean connectivity to determine the optimal soft threshold. Multiple modules were detected automatically at first, and then, the topological overlap measure was calculated to estimate the adjacencies and

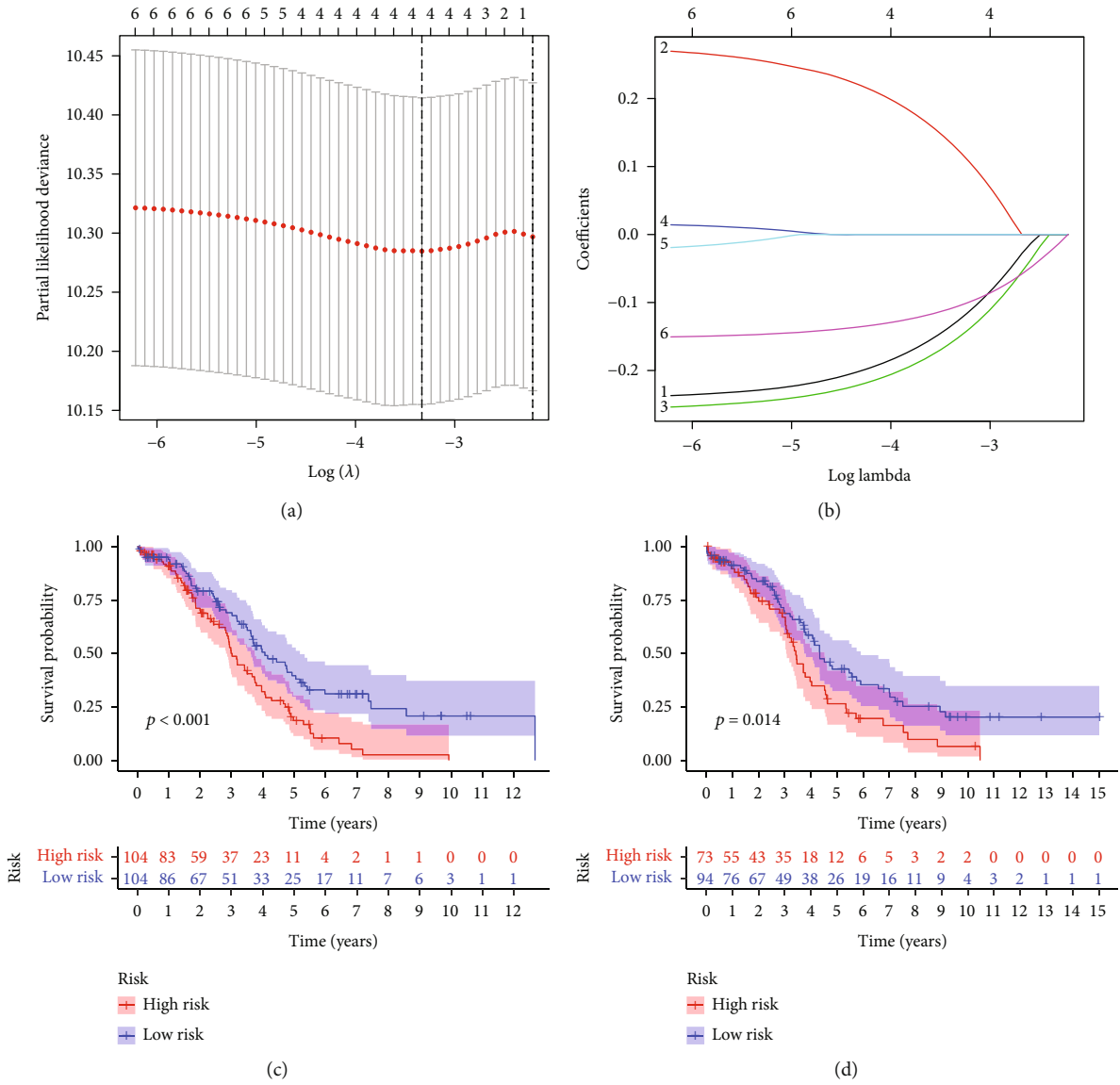


FIGURE 3: Continued.

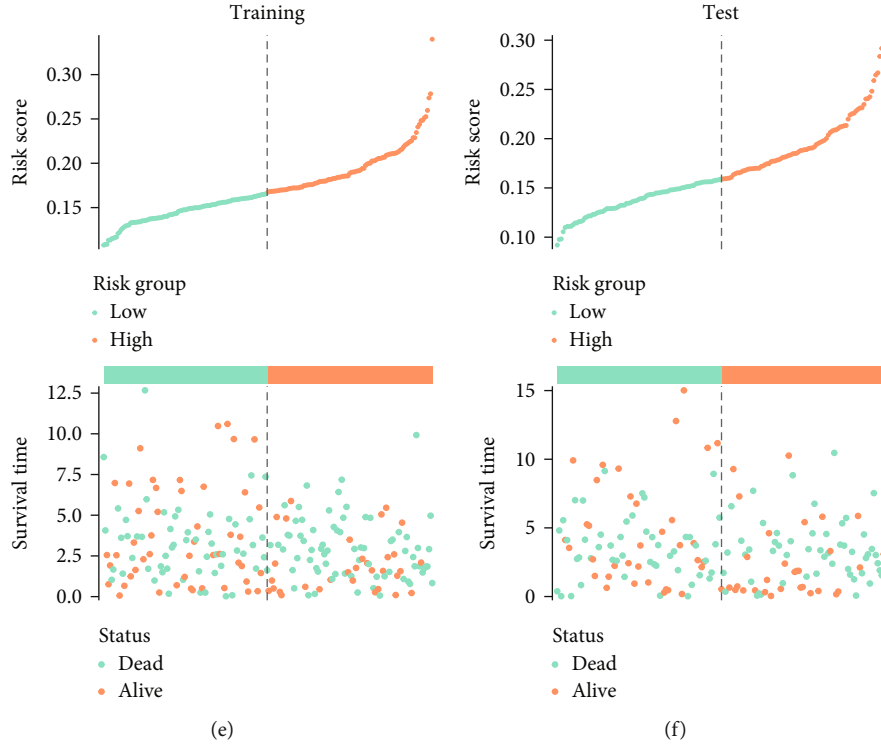


FIGURE 3: Screening for OGRmRNAs. (a) Profiles of LASSO regression regarding partial likelihood deviance, lambda. The lines indicate the 95% confidence interval of the regression, and the dotted line represents the optimal number of variables. (b) The association with regression coefficients and log-transformed lambda. Each line represents a variable. (c, d) Survival differences between the high- and low-risk groups in the training set and test set. The table below the survival curves represents the number of patients alive in each year. (e, f) The risk curves and the distribution of patients in the training set and test set. Samples were ordered according to the risk scores from low to high. The dots in the lower part represent the distribution of cases. (OGRmRNAs: optimal glycosylation mRNAs; LASSO: least absolute shrinkage and selection operator).

similarities among different modules subjected to average hierarchical clustering by the measurement of Euclidean distance. Namely, topologically similar modules were combined into a neocluster. A correlation exploration was performed to assess the correlations between module genes and phenotypes. Modules with relatively strong positive correlations with survival time and vital status were selected. Then, overlapping genes of WGCNA and glycosylation were identified for Kaplan-Meier (KM) analysis. The optimal cutoff of each GRmRNA was determined by the “survminer” package, and patients were divided into the high- and low-expression groups. Only significant signatures by the log-rank test were considered to have prognostic implications and were enrolled in the study. We then used five machine learning methods to estimate the importance of survival associated with GRmRNAs, including two linear models involving least absolute shrinkage and selection operator (LASSO) regression [29] and ridge regression [30], besides a nonlinear model (XGBoost) [31], an ensemble learning method (random forest) [32], and a boosting algorithm (AdaBoost) [33]. GRmRNAs with relatively higher weight were considered to contribute to the prognosis of OC patients.

To further determine the GRmRNAs responsible for the prognosis and establish a prognostic risk model, we ran-

domly classified patients into a training set and a test set at a ratio of 11:9 using the “caret” package [34], and the randomness was verified by a chi-square test. The training set was submitted to LASSO Cox regression to screen for optimal GRmRNAs (OGRmRNAs) at the least of partial likelihood deviance. Based on the regression coefficients and the expression levels of OGRmRNAs, the formula for risk scores could be formed as

$$\text{Risk score}_j = \sum_{i=1}^n \alpha_i k_{ij}, \quad (1)$$

where  $\alpha_i$  represents the regression coefficient of the  $i$ th gene, and  $k_{ij}$  represents the expression of the  $i$ th gene in the  $j$ th sample. Patients were then stratified into the high- and low-risk groups at the median cutoff of risk scores. The differences between the two risk subtypes were estimated by the log-rank test in both the training and test sets.

**2.3. Estimation of Model Effectiveness and Establishment of Combined Diagnosis.** The differences in age, stage, and grade between risk subtypes were estimated by a chi-square test. Principal component analysis (PCA) and  $t$ -distribution stochastic neighbor embedding (tSNE) algorithms were utilized to evaluate the ability of discrimination in the developed

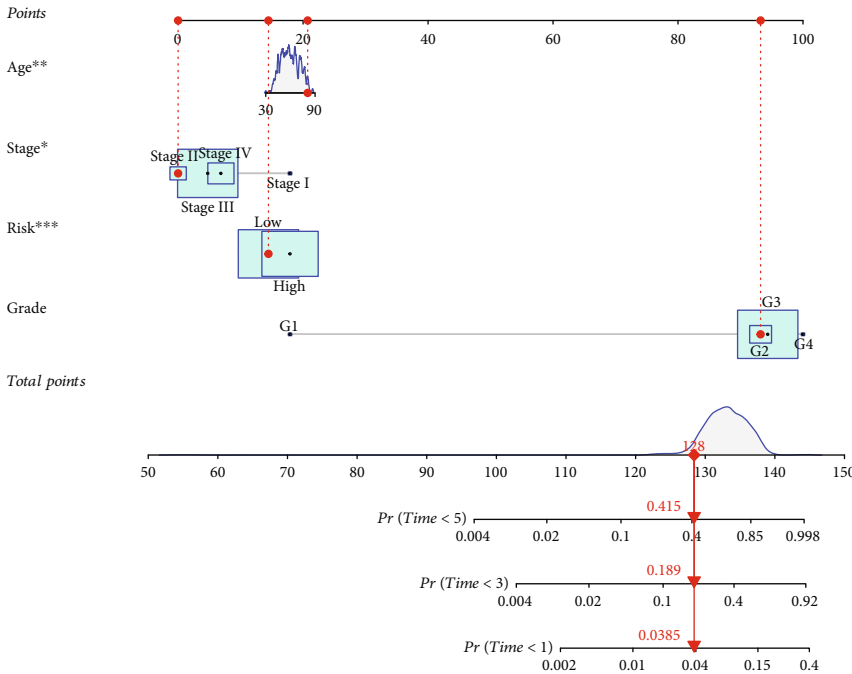
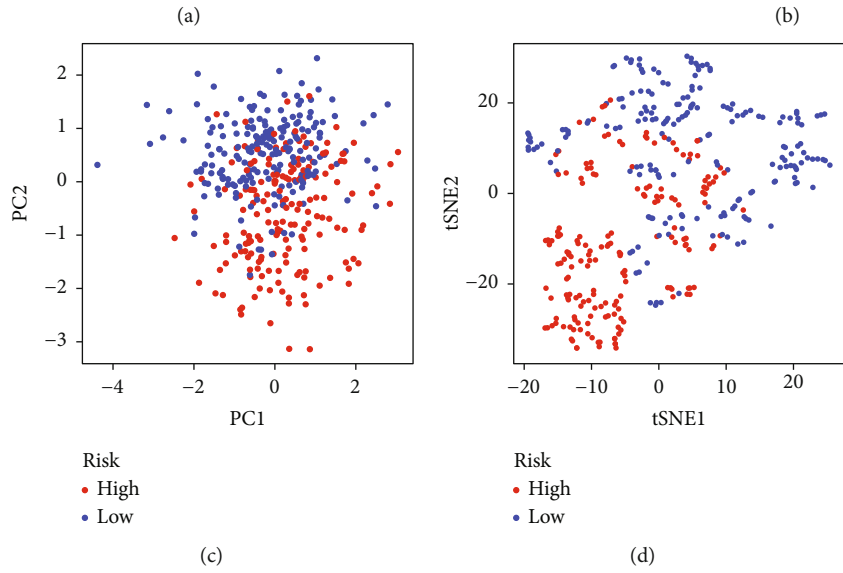
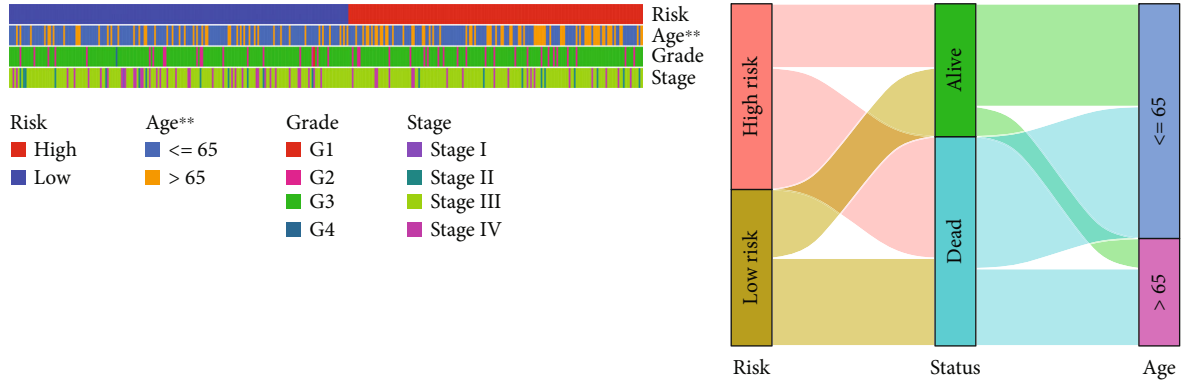


FIGURE 4: Continued.

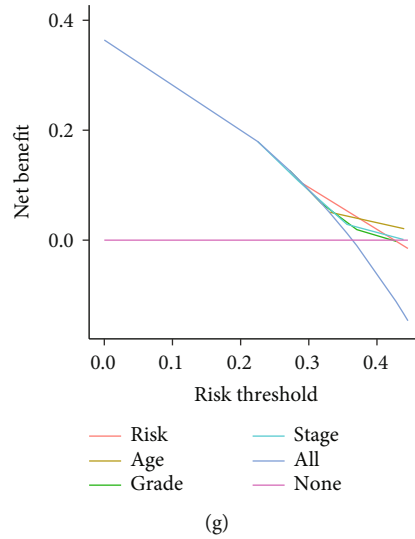


FIGURE 4: Estimation of model effectiveness and a nomogram prediction. (a) Different stratifications of clinical phenotypes in the high- and low-risk groups. (b) Connections among risk subtypes, vital status, and age stratifications. (c, d) Principal component analysis and  $t$ -distribution stochastic neighbor embedding for sample discrimination in the first two dimensions. (e) Nomogram for 1-, 3-, and 5-year overall survival prediction. The red line shows an example of how to predict the prognosis. (f, g) DCA of 1-year and 3-year survival probability. The upper lines indicate more net benefit ( $***P < 0.001$ ,  $**P < 0.01$ , and  $*P < 0.05$ ).

TABLE 3: Independent analysis of all patients.

| Characteristics | Univariate |             |       | Multivariate |             |       |
|-----------------|------------|-------------|-------|--------------|-------------|-------|
|                 | HR         | 95% CI      | $P$   | HR           | 95% CI      | $P$   |
| Age             | 1.024      | 1.010-1.039 | 0.001 | 1.021        | 1.006-1.036 | 0.006 |
| Grade           | 1.186      | 0.784-2.056 | 0.543 | 1.357        | 0.767-2.401 | 0.295 |
| Stage           | 1.078      | 0.761-1.527 | 0.672 | 1.140        | 0.788-1.649 | 0.486 |
| Risk score      | 1.603      | 1.163-2.208 | 0.004 | 1.540        | 1.101-2.154 | 0.012 |

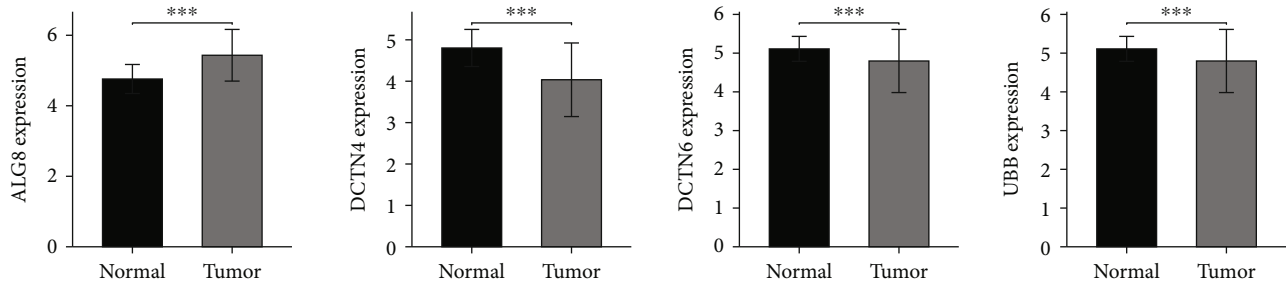
HR: hazard ratio; CI: confidence interval.

model. To determine the independent prognostic value of the model, we conducted a univariate and multivariate Cox proportional hazard regression with age, stage, grade, and risk scores. Furthermore, a nomogram was created to predict the probability of 1-, 3-, and 5-year survival of OC patients. A decision curve analysis (DCA) was performed to ascertain the net benefits of the prognostic risk model in clinical practice.

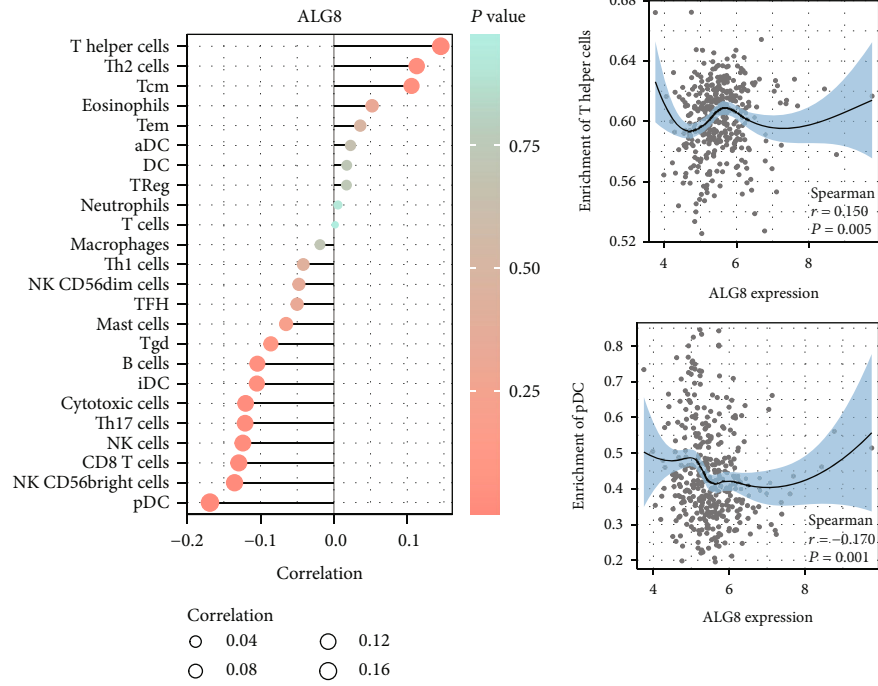
We also estimated the expression differences of OGRmRNAs between normal tissues and tumor tissues in OC with data retrieved from UCSC Xena (<http://xena.ucsc.edu/>) in TPM formation. To reveal the stemness feature, the mRNA expression-based stemness index (mRNAsi) was computed using one-class logistic regression with a machine learning algorithm [35] and compared between the high- and low-expression groups of OGRmRNAs at the median cutoff. Coexpressed genes with OGRmRNAs were determined with a threshold of 0.7, and they were enrolled in Gene Ontology (GO) containing biological processes, cellular components, and molecular functions, and Kyoto Encyclopedia of Genes and Genomes (KEGG) functional enrichment analysis. Single-sample gene set enrichment analysis (ssGSEA) [36] was employed to quantify the correlations between OGRmRNA expression levels and tumor

immune infiltrating. Moreover, GSEA was performed with the gene matrix of “c2.cp.kegg.v7.4.symbols.gmt” to identify the significantly enriched pathways in the high- and low-risk groups, respectively, in the application GSEA (version 4.0.3) downloaded from MSigDB, and we cross-checked the results with the “clusterProfiler” package [37].

**2.4. Investigations on the Correlation of TME and Risk Scores.** TME has important implications for the regulatory mechanisms of immune cells. We mainly investigated the relationships between prognostic risk and the depth of immune-infiltration. The TIMER database was used to explore the correlations between risk scores and immune responses quantified by six methods. The differences in immune function and infiltration of leukocytes between the high- and low-risk groups were estimated by performing the ssGSEA [36] algorithm. In addition, the Pearson correlation coefficients between risk scores and distinct tumor immune infiltrations as well as the proportion of infiltrations in each sample with statistical significance were calculated by the CIBERSORT algorithm (1000 permutations). Moreover, the Wilcoxon rank-sum test was applied to compare the expression differences of typical immune checkpoint molecules between the two risk subtypes. The information

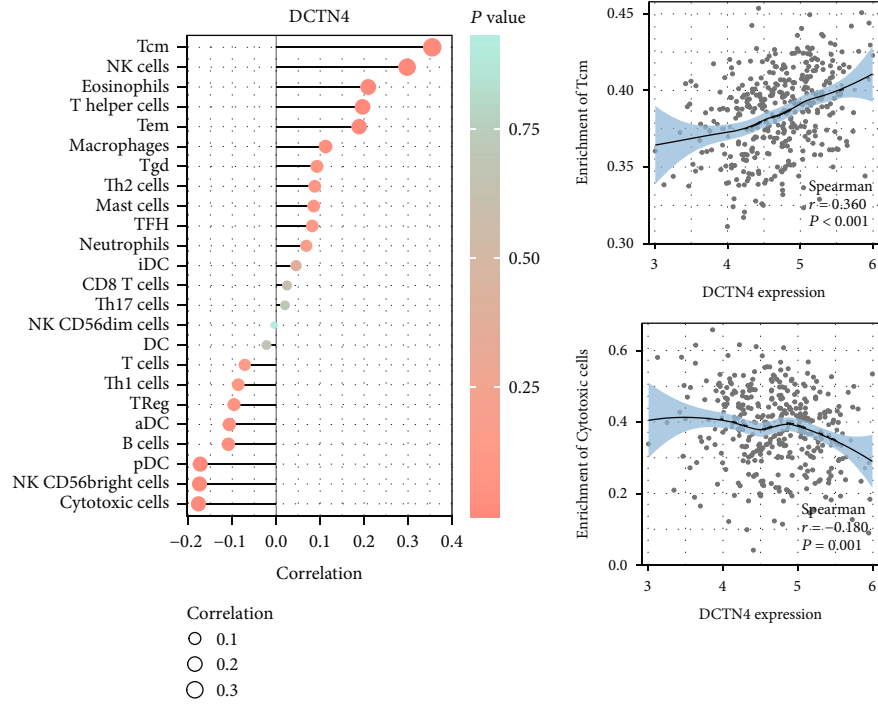


(a)

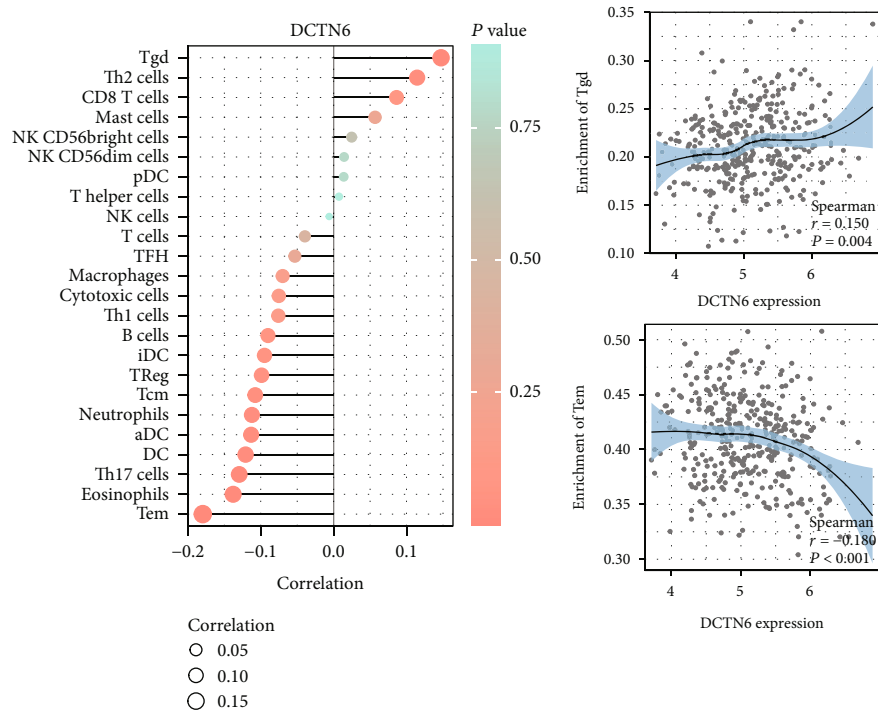


(b)

FIGURE 5: Continued.



(c)



(d)

FIGURE 5: Continued.



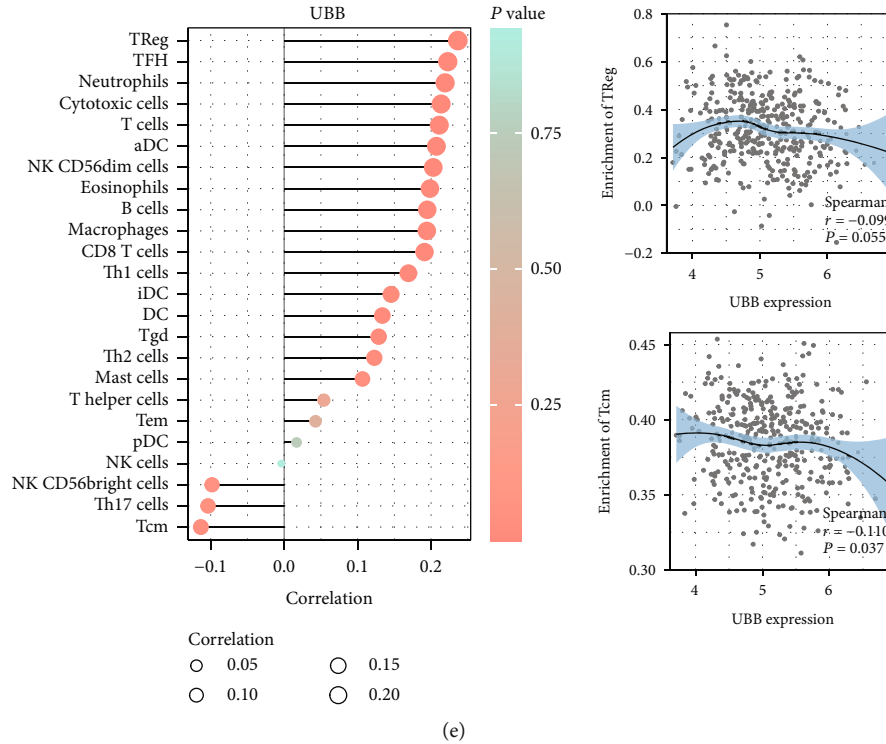


FIGURE 5: Validation of OGRmRNAs. (a) Expression changes of GRmRNAs between normal and tumor tissues. The lines on the bars indicate the values between the median plus and minus the standard error. (b–e) Associations between OGRmRNAs and immune-infiltrating levels. The color represents the significance. The more significant, the more redder. The circle size represents the correlation coefficients (OGRmRNAs: optimal glycosylation mRNAs; \*\*\* $P < 0.001$ ).

on immune subtypes of OC was obtained from Thorsson’s study [38], in which the overlapping immune subtypes included C1 (wound healing), C2 (IFN-gamma dominant), and C4 (lymphocyte depleted). The differences in risk scores among the three subtypes were measured. In addition, to quantify the relationship between tumor purity and risk scores, we employed “estimation of stromal and immune cells in malignant tumors using expression data” (ESTIMATE) algorithm [39] including three types of scores: immune score, stromal score, which represented the nontumor proportion, and their addition consisting of the ESTIMATE score.

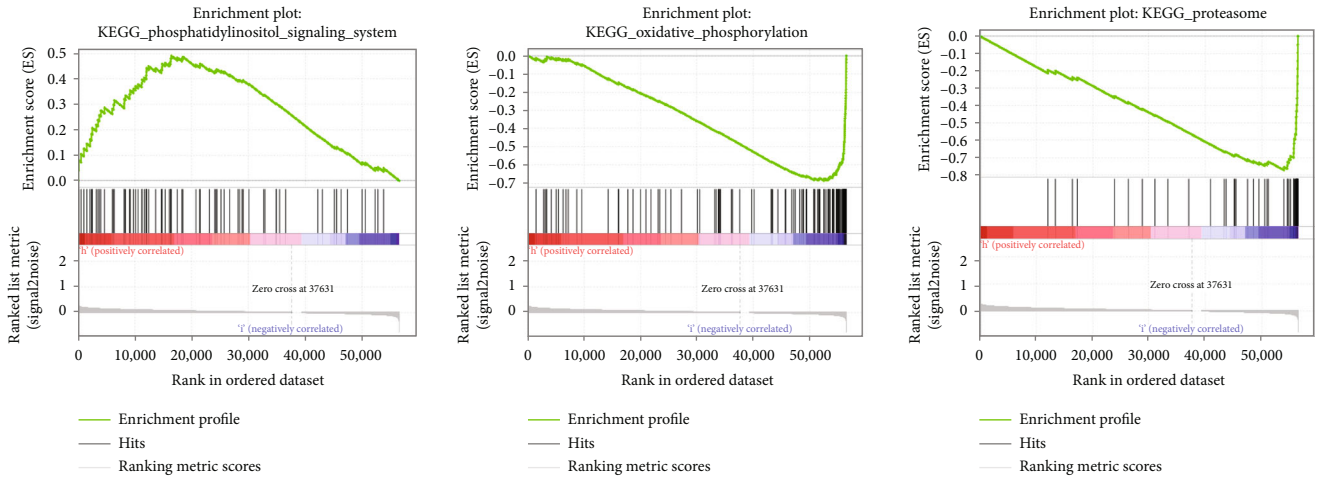
**2.5. Exploration of Risk Subtypes and Molecular Characteristics.** The difference in tumor mutational burden (TMB) between the high- and low-risk groups was analyzed. Furthermore, we collected several important pathway signatures potentially interacting with OC, including Wnt, Hippo, Hedgehog, Notch, TGF- $\beta$ , PI3K/Akt, EMT, JAK\_STAT, interleukin-8, NF- $\kappa$ B, interferon, and ROS (Supplementary Table 3). Gene set variation analysis (GSVA) was adopted to calculate the enrichment score, which was then used to quantify the connection between risk scores and pathways. The landscape of top mutated genes in the two risk groups was shown with their mutation types and frequencies by maftools. Afterward, multiple mutation types were stratified into two novel statuses, including nonsynonymous mutation and synonymous mutation [40].

The changes between the low- and high-risk scores were examined by correlation coefficients and different tests.

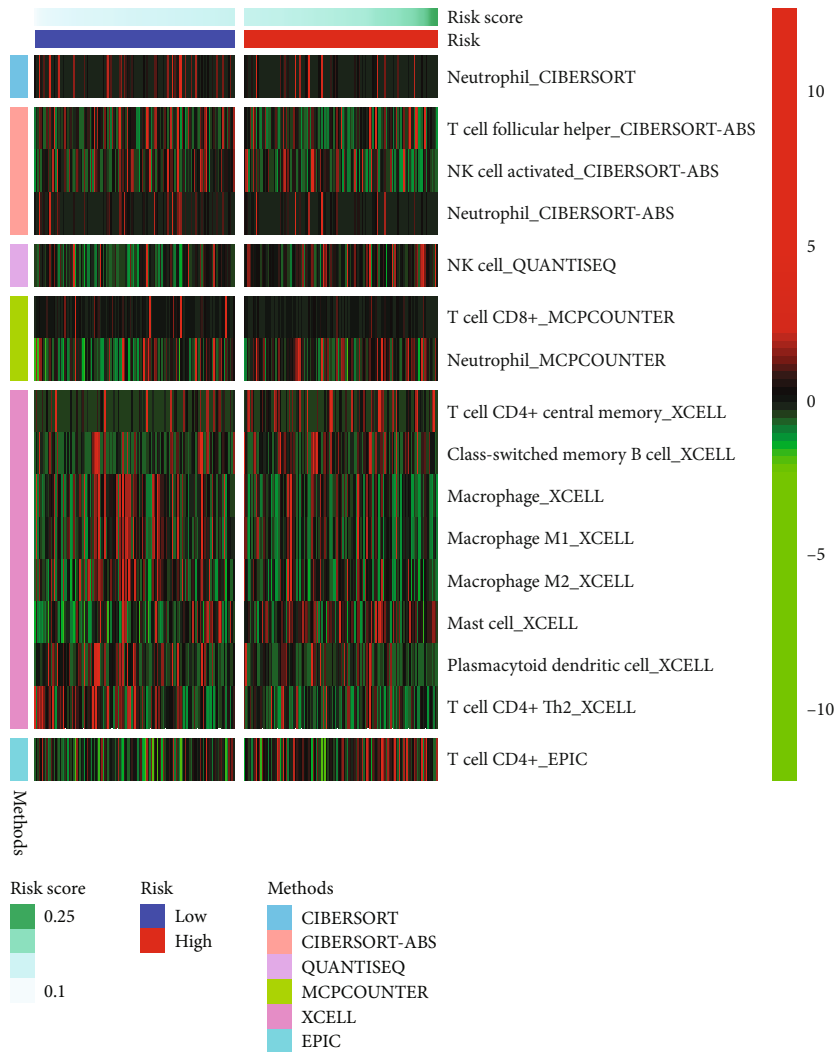
**2.6. Statistical Analysis.** All statistical tests and bioinformatics analysis were conducted by R (versions 3.6.3 and 4.1.1), including the two-sample Wilcoxon rank-sum test and Kruskal-Wallis for continuous data, Pearson chi-square test and Fisher’s exact test for categorical data, log-rank test for KM analysis, and (LASSO) Cox proportional hazard regression to estimate the hazard ratios (HRs) and 95% confidence interval (CI). For correlation explorations, the Pearson correlation coefficients were used. Machine learning predictive models were developed by Python (version 3.8.0) libraries “XGBoost (version 1.2.1)” and “sklearn (version 0.22.1),” technical details of which have been described previously. A two-tailed  $P < 0.05$  for all unadjusted comparisons and an adjusted  $P < 0.05$  for functional enrichment analysis were considered statistically significant.

### 3. Results

**3.1. Identification of Prognostic GRmRNAs.** The workflow of this study is shown in Figure 1. In WGCNA, we determined the soft threshold of 6 by calculating the scale-free model fit and mean connectivity (Figure 2(a)). Different module genes in the dynamic tree cut were reclustered through a topological similarity strategy, where genes were assembled into fewer modules as shown in Figure 2(b). The relationships between modules and clinical phenotypes implied that the

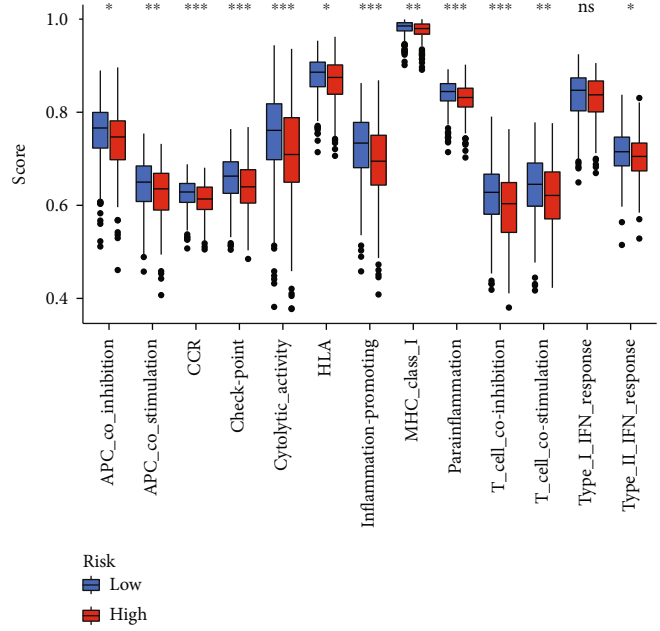
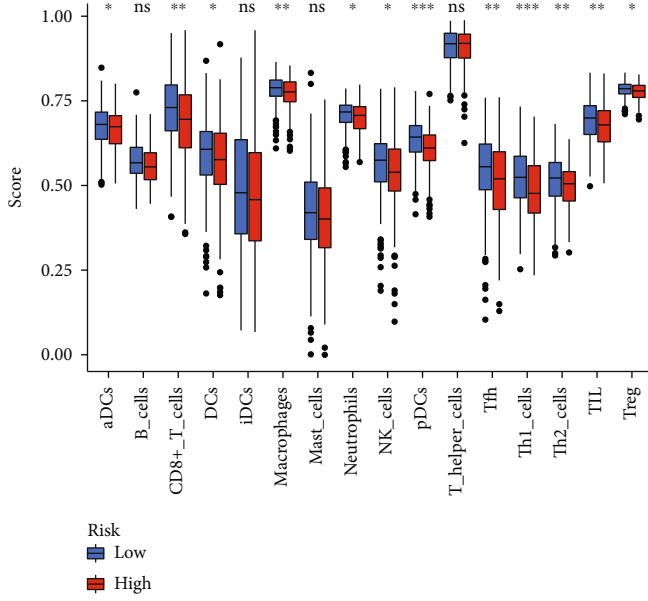


(a)



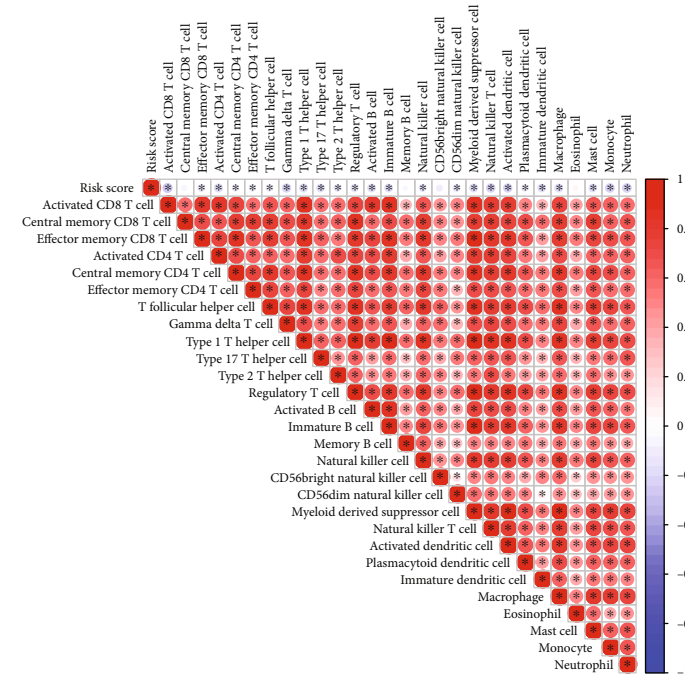
(b)

FIGURE 6: Continued.



(c)

(d)



(e)

FIGURE 6: Continued.

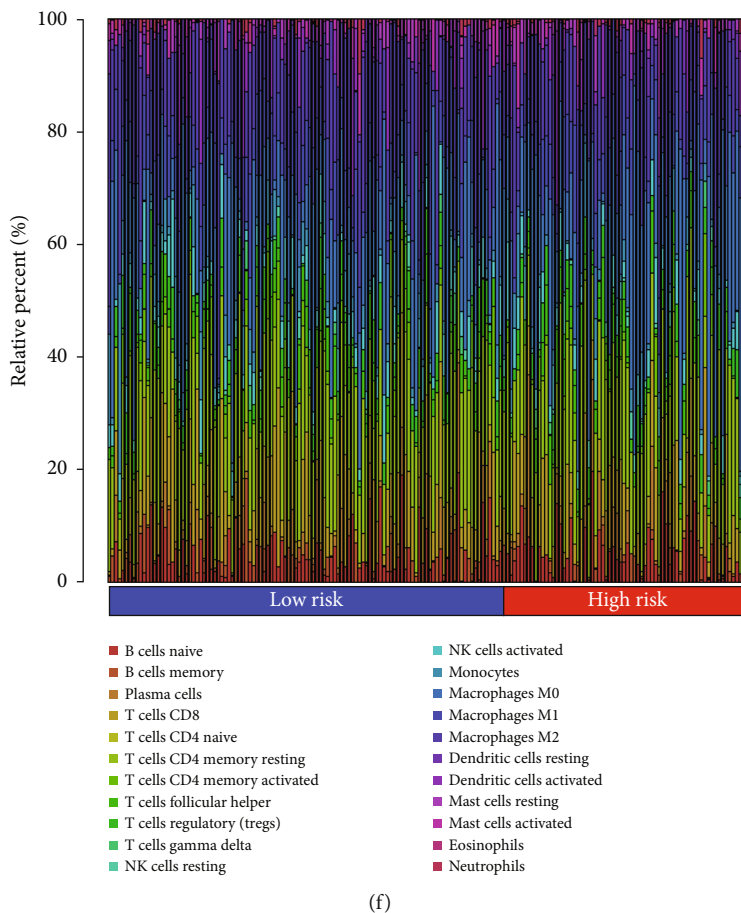


FIGURE 6: Biological functions and TME landscape. (a) Significant enriched pathways in the high- and low-risk groups. The extremum located in the left part indicates a positive association between risk scores and pathway activity, and vice versa. (b) The relationships of risk and tumor immune-infiltrations according to the evidence from the TIMER database. (c, d) The differences of tumor infiltrating of 16 cell types and score of immune pathways between the risk groups by ssGSEA. The lines in the boxes represent the median values. The black dots represent outliers. Asterisks indicate significance. (e) The associations between risk and immune-infiltrations by CIBERSORT algorithm. (f) Proportions of multiple tumor-infiltrating cells (TME: tumor microenvironment; ssGSEA: single-sample gene set enrichment analysis).

modules in steel blue ( $r = 0.33, P < 0.001$ ), brown4 ( $r = 0.26, P = 0.009$ ), and light steel blue1 ( $r = 0.28, P = 0.004$ ) had relatively strong correlations with follow-up time. The red module had a slightly positive correlation with survival status (Figure 2(c)), genes which were used to be analyzed in the following steps. As shown in Figure 2(a), a total of 19 overlapped genes from the glycosylation-related gene list and WGCNA were obtained. By performing KM analysis, 9 prognostic GRmRNAs, including ALG8 ( $P = 0.004$ ), CSNK1D ( $P = 0.037$ ), DCTN4 ( $P = 0.008$ ), DCTN6 ( $P = 0.005$ ), F8 ( $P = 0.013$ ), FUCA1 ( $P = 0.010$ ), NAPG ( $P = 0.014$ ), UBA1 ( $P = 0.033$ ), and UBB ( $P = 0.004$ ) exhibited statistical significance in survival differences at the optimal cutoff (Figure 2(e)).

**3.2. Determination of OGRmRNAs and Validation.** The detected randomness of the split for the training set and test set is shown in Table 1. LASSO regression, ridge regression, XGBoost, random forest, and AdBoost were utilized to sort the importance of weights in the prognosis based on 9

survival-related GRmRNAs. As shown in Table 2, ALG8, DCTN4, DCTN6, F8, NAPG, and UBB held greater weight and they were included to develop the prognostic risk model. A LASSO Cox regression was performed and four OGRmRNAs were selected depending on the optimal value of lambda (Figures 3(a) and 3(b)). Hence, the risk scores could be calculated according to the formula:

$$\text{Risk score} = -0.1277 \times E(\text{ALG8}) + 0.1256 \times E(\text{DCTN4}) - 0.1528 \times E(\text{DCTN6}) + 0.1528 \times E(\text{F8}) \quad (2)$$

where  $E(\bullet)$  represents the expression of OGRmRNAs. Patients were then separated into the high-risk and low-risk groups at the median value of their risk scores (Supplementary Table 4). KM analysis revealed that OC patients experienced significantly different survival outcomes in both the training set ( $P < 0.001$ , Figure 3(c)) and the test set ( $P = 0.014$ , Figure 3(d)). Risk curves also indicated that patients with low risk had better survival outcomes

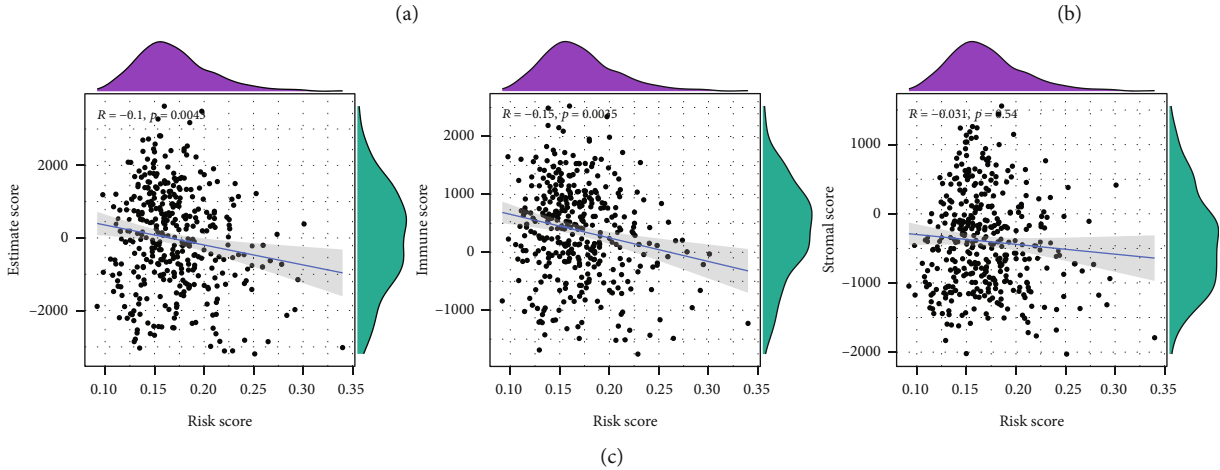
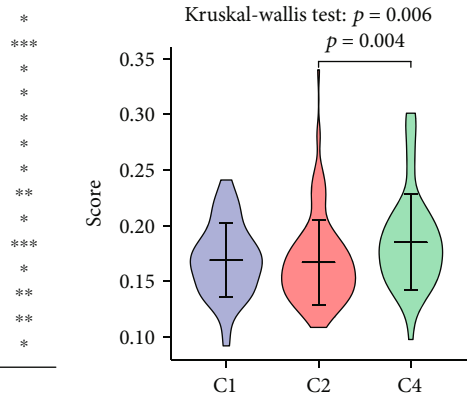
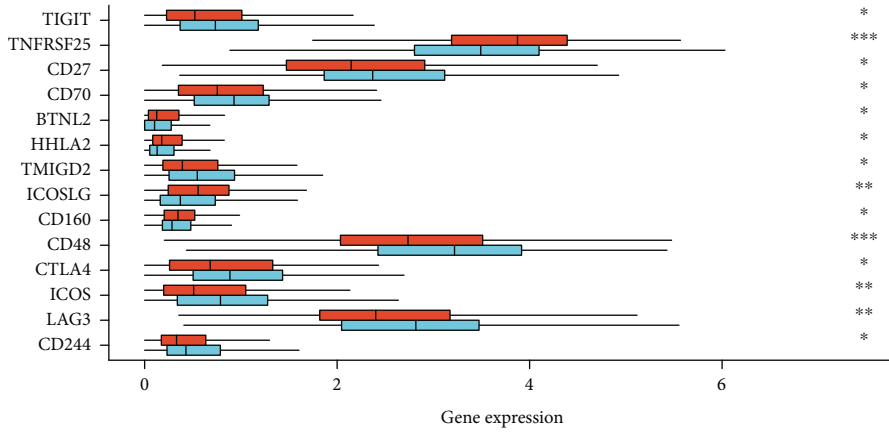


FIGURE 7: Continued.

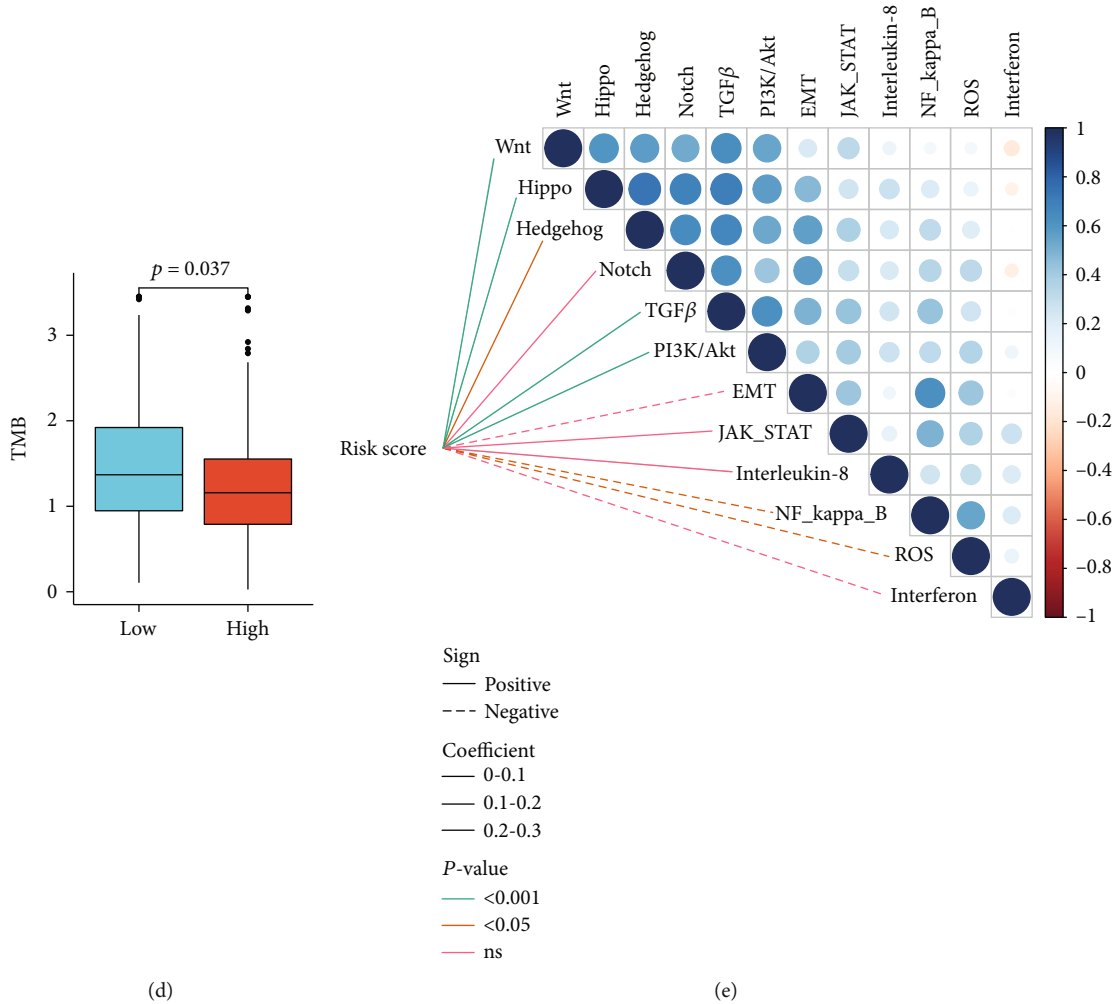


FIGURE 7: Molecular features in risk stratification. (a) The differences of expression levels of immune checkpoints between the high- and low-risk subtypes. The lines inside the boxes represent the median values, and the lines outside the boxes indicate the 95% confidence interval. (b) Relationships between immune subtypes and risk scores. The short horizontal lines represent the median values, and the vertical lines indicate the 95% confidence interval. (c) The correlation between tumor purity and risk scores. The blue lines represent fitted lines, and the gray area represents the 95% confidence interval. The mountain graphs at the top and stuck to the right represent the density of distribution. (d) TMB difference in the high and low groups. The lines inside the boxes represent the median values, and the lines outside the boxes indicate the 95% confidence interval. The black dots show the outliers. (e) Correlations of risk scores and enriched pathways. The circle in the thermogram shows the correlations among the signaling pathways. Blue represents positive correlations, while red indicates negative ones.

(Figures 3(e) and 3(f)). The chi-square test illustrated that old patients had significantly higher risk scores than those under 65 years of age ( $P < 0.01$ , Figure 4(a)). The Sankey diagram showed the degree of connection among risk subtypes, survival status, and age that old patients were more likely to have worse outcomes (Figure 4(b)). PCA and tSNE demonstrated that patients were differentiated well in two dimensions based on the risk scores (Figures 4(c) and 4(d)), which indicates that the model has a promising ability to stratify risk subtypes. By performing Cox regression, we found that age (hazard ratio (HR) = 1.021, 95%confidence interval (CI) = 1.006-1.036,  $P = 0.006$ ) and risk scores (HR = 1.540, 95%CI = 1.101-2.154,  $P = 0.012$ ) could serve as independent prognostic factors (Table 3). A nomogram model was established to predict 1-, 3-, and 5-year survival, where age

( $P < 0.01$ ), stage ( $P < 0.05$ ), and risk ( $P < 0.001$ ) demonstrated significance (Figure 4(e)). The DCA curves analysis nomogram was performed, implying that the combined model of 1-year and 3-year survival probability showed the optimal net benefit compared to a single indicator (Figures 4(f) and 4(g)).

**3.3. Validation of OGRmRNAs.** The Wilcoxon rank-sum test showed that ALG8 ( $P < 0.001$ ) had a higher expression level in tumor tissues compared with normal tissues, while DCTN4 ( $P < 0.001$ ), DCTN6 ( $P < 0.001$ ), and UBB ( $P < 0.001$ ) had lower expression levels in tumor tissues (Figure 5(a)). According to immune-infiltrating results, OGRmRNAs presented significantly positive correlations with immune cells such as helper T cells (Th,  $r = 0.15$ ,  $P = 0.005$ ), central memory T cells (Tcm,  $r = 0.36$ ,  $P < 0.001$ ),

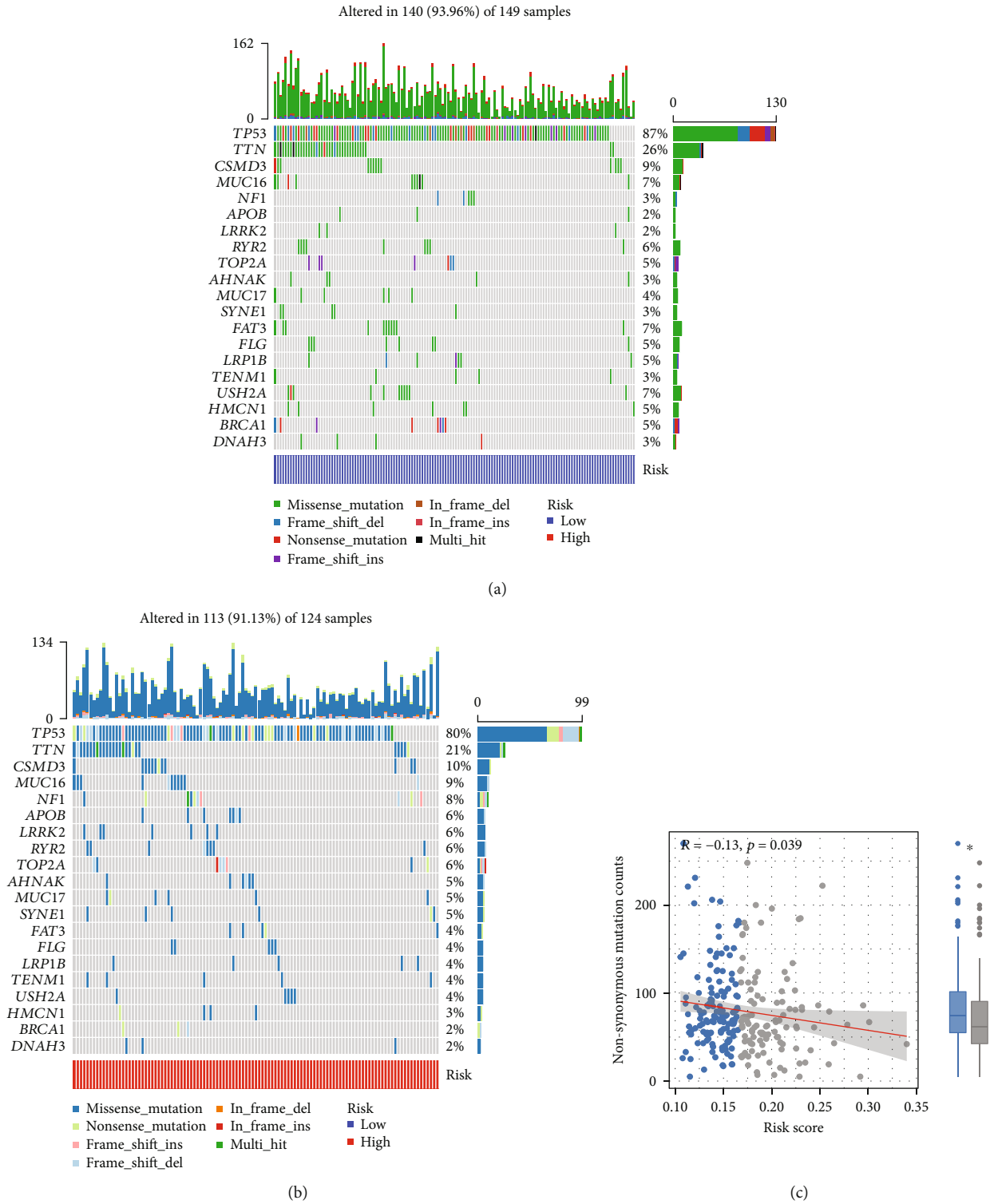


FIGURE 8: Continued.

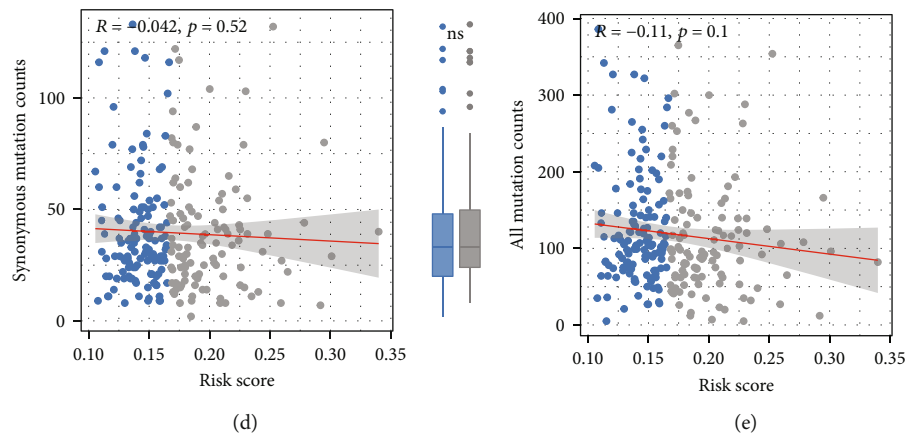


FIGURE 8: Mutation landscape. (a, b) The profiles of the top-25 mutated genes in the high- and low-risk groups. The upper bar shows the total gene mutation amount and corresponding mutation types. The right bar shows the mutation frequency of the top 25 mutated genes. (c–e) Associations of nonsynonymous mutation counts, synonymous mutation counts, all mutation counts, risk scores, and their variations between the low- and high-risk groups. The red lines represent the fitted lines, and the gray area represents the 95% confidence interval. The dots outside the boxes show the outliers ( $*P < 0.05$ ; ns: no significance).

and gamma delta T cells (Tgd,  $r = 0.15$ ,  $P = 0.004$ ) but showed negative connections with plasmacytoid dendritic cells (pDC,  $r = -0.17$ ,  $P = 0.001$ ), cytotoxic cells ( $r = -0.18$ ,  $P = 0.001$ ), effective memory T cells (Tem,  $r = -0.18$ ,  $P < 0.001$ ), and Tcm ( $r = -0.11$ ,  $P = 0.037$ ) shown in Figures 5(b)–5(e). According to the KW test, overexpressed ALG8 exhibited significantly higher mRNA<sub>si</sub>, whereas upregulated DCTN4 presented lower mRNA<sub>si</sub> ( $P < 0.001$ , Supplementary Figure 1A–B). And all the OGRmRNAs exhibited significantly different mRNA<sub>si</sub> scores among the low-expression groups, high-expression groups, and normal tissues ( $P < 0.001$ , Supplementary Figure 1A–D). A total of 225 coexpressed protein coding genes were determined for functional enrichment analysis (Supplementary Table 5). GO terms regarding the metabolic process, catabolic process, nuclear movement (Supplementary Figure 2A), and KEGG pathways of spliceosome and RNA degradation (Supplementary Figure 2B) demonstrated significance.

**3.4. Biological Characteristics and TME Investigation.** To explore the biological functions, GSEA was performed in the high- and low-risk groups, respectively. It demonstrated that high-risk agents were enriched in the “phosphatidylinositol signaling system” while the low-risk genes were significantly enriched in “oxidative phosphorylation” and “proteasome” (Figure 6(a)). The results obtained from the “clusterProfiler” of R foundation are provided in Supplementary Table 6, which indicates that the high-risk group appeared to inhibit pathways such as “ribosome,” “systemic lupus erythematosus,” and “type I diabetes mellitus” but no significant activated terms. The landscape of antitumor immunity was investigated using expression data of OC patients. As shown in Figure 6(b), tumor immune infiltration levels between the high- and low-risk groups were slightly different. It was notable that macrophages, plasmacytoid dendritic cells, and CD4<sup>+</sup> Th2, etc. showed lower infiltration abundance in the high-risk

subtype, whereas mast cells had higher levels in the high-risk subtype. Two distinctive patterns of immune infiltrations could be observed in the high- and low-risk groups by the Wilcoxon rank-sum test. Decreased levels of tumor infiltration of major immune cells (Figure 6(c)) such as CD8<sup>+</sup> T cells ( $P < 0.01$ ), macrophages ( $P < 0.01$ ), Th1 cells ( $P < 0.001$ ), and tumor infiltrating lymphocytes (TILs,  $P < 0.01$ ), also decreased levels of immune pathways (Figure 6(d)) such as cytolytic activity ( $P < 0.001$ ), inflammation-promoting ( $P < 0.001$ ), and coinhibitions of T cells ( $P < 0.001$ ) in the high-risk group were reported. By performing the CIBERSORT algorithm and excluding samples with no statistical significance, we found that risk scores wielded negative correlations with almost all tumor infiltrations (Figure 6(e)). The proportions of immune infiltrations from 22 cell types in the two risk subtypes were shown in a bar plot (Figure 6(f)).

**3.5. Relationships between Molecular Features and Risk.** We compared several immune checkpoint expression levels between the high- and low-risk groups by the Wilcoxon rank-sum test (Supplementary Table 7). It revealed that targets such as TIGIT ( $P < 0.05$ ), TNFRSF25 ( $P < 0.001$ ), CD27 ( $P < 0.05$ ), and CD70 ( $P < 0.05$ ) exhibited significant differences (Figure 7(a)). The KW test demonstrated that patients in the C4 had higher risk scores than those in C1 and C2 ( $P = 0.006$ , Figure 7(b)). Tumor purity was estimated by ESTIMATE scores, which is composed of immune scores and stromal scores. The risk scores were negatively associated with ESTIMATE scores ( $r = -0.1$ ,  $P = 0.043$ ) and immune scores ( $r = -0.15$ ,  $P = 0.004$ ), whereas there was no statistical significance for stromal scores (Figure 7(c)). TMB, a biomarker of immune checkpoint inhibitor therapies, had different levels between the high- and low-risk groups ( $P = 0.037$ , Figure 7(d)). In addition, the high-risk group presented significantly activated pathway signatures including Wnt ( $P < 0.001$ ), Hippo ( $P < 0.001$ ), Hedgehog ( $P < 0.05$ ), TGF- $\beta$  ( $P < 0.001$ ), and



PI3K/Akt ( $P < 0.001$ ) while inhibited signatures include NF- $\kappa$ B ( $P < 0.001$ ) and ROS ( $P < 0.05$ , Figure 7(e)).

**3.6. Mutation Landscape Analysis.** Furthermore, we examined the mutation profiles of risk. As shown in Figures 8(a) and 8(b), TP53, TTN, and CSMD3 had the highest mutation frequency with the most missense mutation, followed by MUC16. Patients in the high-risk group had a lower frequency of TP53 mutations. After classifying different mutation types into nonsynonymous mutation and synonymous mutation, we estimated their associations with risk scores. It was illustrated that risk scores had a slightly negative link with non-synonymous mutation counts ( $r = -0.13$ ,  $P = 0.039$ ; Figure 8(c)), while risk scores exhibited no significant linear correlations with synonymous mutation counts and all mutation counts (Figures 8(d) and 8(e)).

#### 4. Discussion

In this study, a total of four GRmRNAs, including ALG8, DCTN4, DCTN6, and UBB, were selected for the development of the prognostic risk model. The relationship between glycosylation and ALG8 has been studied, particularly in congenital disorders of glycosylation (CDG). The point mutations or small deletions of ALG8 will lead to an unfavorable prognosis [41]. It has been reported that ALG8 could perform as a variate of a prognostic model for gastric cancer [42]. Amplified hotspots on 11q14.1 (NDUFC2, ALG8, and USP35) led to poor prognosis in estrogen receptor-negative breast cancer [43]. Our study found that overexpressed ALG8 was located in OC tissues and was associated with favorable survival outcomes. A similar result for CXCL11 was also illustrated in colorectal cancer [44]. According to previous evidence and this study, we speculate that ALG8 is correlated with a higher proportion of antitumor immune cells, and a lower proportion of protumor immune cells in OC. Nonetheless, further studies should be performed.

A previous study has revealed that DCTN4 was upregulated in colon adenocarcinoma and high expression was associated with prolonged overall survival [45]. DCTN6 has high expression in low-grade glioma but it is associated with unfavorable survival outcomes [46]. Conversely, DCTN4 and DCTN6 were both observed to be downregulated in tumor tissues of OC compared with adjacent tissues in this study. Overexpressed DCTN4 was associated with poor survival, while DCTN6 was correlated with a satisfactory result for overall survival. The relevant results of UBB were similar to DCTN6. However, to determine the role of inhibition or promotion of cancer, analyzing the expression levels is insufficient since more investigations to confirm the biological functions should be undertaken. Subsequently, LASSO Cox regression was used to compute the coefficients of each gene mentioned above and develop a prognostic risk system, which could be considered an independent prognostic factor. High-risk patients had a significantly worse prognosis than those in the low-risk group, and more individuals over 65 years of age were from the high-risk group, which is

consistent with the previous findings [47]. The functional enrichment exploration demonstrated that the high-risk agents were enriched in the “phosphatidylinositol signaling system.” Phosphatidylinositol-associated signaling pathways play a vital role in tumor cell apoptosis, proliferation, invasion, and metabolism [48, 49]. The genes in the low-risk group were mainly enriched in “oxidative phosphorylation” and “proteasome.” The oxidative phosphorylation pathway in tumors and the tumor microenvironment is recognized as a target for novel anticancer therapies. The multimeric complexes of the oxidative phosphorylation pathway are targets for small-molecule inhibitors, which can inhibit metabolism, induce oxidative damage, and lead to cancer cell death. It is indicated that strategies to interfere with oxidative phosphorylation should be considered for the treatment of ovarian tumors [50]. Meanwhile, proteasome activity has been linked to tumor metastasis, and therapy based on inhibiting the proteasome and HDAC6 has been proposed as an underlying strategy for OC treatment [51, 52]. Simultaneously, risk scores were positively correlated with Wnt, Hippo, Hedgehog, TGF- $\beta$ , and PI3K/Akt pathways. In contrast, risk scores demonstrated a negative correlation with NF- $\kappa$ B and reactive oxygen species. These results may contribute to studying the interplay between the signaling pathways and different risk subtypes of OC patients.

Recently, it has been verified that tumor cells avoid being killed by immune cells with the aid of glycosylation in the TME [53]. The explicit interaction of antigens with antibodies is the foundation of the immune response. Glycosylated antigen-specific antibodies are beneficial in cancer therapy by augmenting immunity [54, 55]. To unravel the connection between glycosylation and TME of OC, we used multiple methods to quantify the immune-infiltration levels of leukocytes and the fraction of immune pathways. OC patients of the high-risk group demonstrated increased neutrophils and mast cells, but the majority of cases showed decreased cell types such as activated natural killer (NK) cells, CD8<sup>+</sup> T cells, Th1/2 cells, and macrophages. The results of activated NK cells and macrophages were consistent with previous studies [56, 57] but showed contrary consequences of CD8<sup>+</sup> T cells and Th1/2 cells in OC TME [58]. A possible explanation leading to different predictions might be that the transcriptional data enrolled in this study was in TPM form, whereas the earlier finding used the FPKM expression matrix for ssGSEA explorations. Moreover, decreased tumor-infiltrating lymphocytes (TILs) were presented in the high-risk group. This is also compatible with an earlier observation, which showed that OC patients engaged with more TILs experienced a better prognosis [59]. Thus, the treatment of OC with autologous TILs is currently being applied in several centers as an immunotherapeutic approach.

To further investigate the efficiency of immunotherapy, we conducted an analysis of immune checkpoints and TMB. Low-risk patients had increased levels of immune checkpoints such as TIGIT, CTLA-4, and LAG-3. TIGIT is usually expressed by T cells and NK cells. Data from several sources has identified that the CD155/TIGIT and DNAM-1/TIGIT/CD96 axes play important roles in OC TIGIT-based

immunotherapy and overexpressed TIGIT would be a compelling indicator for promising OC treatment [60, 61]. Results from other studies revealed that high expressions of CTLA-4 and LAG-3 were associated with better survival outcomes after systemic treatment, which broadly supported the work [62]. Furthermore, TMB had a negative correlation with risk scores. Therefore, it could conceivably be assumed that low-risk OC patients might benefit from immune checkpoint blockade therapies.

However, we recognized several limitations in this study. Firstly, the data was not prospective and sufficient because it was obtained from existing public online cohorts. We did not conduct validation experiments to reveal the links between risk scores and immune fraction. The supporting information on transcriptional expression and clinicopathologic characteristics from the real world is still required. Secondly, the intrinsic weakness of merely considering a single hallmark to construct a model was inevitable since various prognostic signatures in OC have been excluded. However, based on the distinct validation to confirm the effectiveness of prognostic prediction for OC, the model was acceptable despite the weakness.

## 5. Conclusion

In summary, this study firstly established a prognostic risk model with four GRmRNAs in OC by integrating machine learning methods and statistical approaches. The prognostic risk system based on GRmRNAs could accurately predict prognosis, the immune microenvironment, and the immunotherapeutic efficacy of OC patients, where high-risk scores showed poor prognosis and low immune-infiltration levels. Glycosylation-related genes may contribute to predicting prognosis and creating personalized immunotherapies, while the regulatory mechanism of the interplay between glycosylation and tumor biology functions is worth studying further. Our model might be a valuable tool for OC risk classification, assisting clinicians to adopt the optimal therapeutic strategies for more personalized treatment in clinical practice.

## Abbreviations

|           |  |
|-----------|--|
| DCA:      | Decision curve analysis  |
| ER:       | Endoplasmic reticulum  |
| ESTIMATE: | Estimation of stromal and immune cells in malignant tumors using expression data |
| FDA:      | Food and Drug Administration   |
| FDR:      | False discovery rate   |
| FPKM:     | Fragments per kilobase million   |
| GEO:      | Gene Expression Omnibus  |
| GO:       | Gene Ontology  |
| GSEA:     | Gene set enrichment analysis   |
| GSVA:     | Gene set variation analysis  |
| ICB:      | Immune checkpoint blockade   |
| KEGG:     | Kyoto Encyclopedia of Genes and Genomes  |
| HGSOC:    | High-grade serous ovarian cancer   |
| KM:       | Kaplan-Meier   |
| KW:       | Kruskal-Wallis   |

|          |  |
|----------|--|
| LASSO:   | Least absolute shrinkage and selection operator      |
| mRNAsi:  | mRNA expression-based stemness index                 |
| MSigDB:  | Molecular Signatures Database                        |
| OC:      | Ovarian cancer                                       |
| OGRmRNA: | Optimal glycosylation-related messenger RNA          |
| PCA:     | Principal component analysis                         |
| RNA-seq: | RNA sequencing                                       |
| ROS:     | Reactive oxygen species                              |
| SNV:     | Simple nucleotide variation                          |
| ssGSEA:  | Single-sample gene set enrichment analysis           |
| TCGA:    | The Cancer Genome Atlas                              |
| TMB:     | Tumor mutational burden                              |
| TME:     | Tumor microenvironment                               |
| TPM:     | Transcripts per million                              |
| tSNE:    | <i>t</i> -distribution stochastic neighbor embedding |
| WGCNA:   | Weighted gene coexpression network analysis.         |

## Data Availability

Data used in this study can be downloaded from TCGA (<https://tcga-data.nci.nih.gov/tcga/>), GEO (<https://www.ncbi.nlm.nih.gov/geo/>), MSigDB (<http://www.gsea-msigdb.org/gsea/msigdb/>), UCSC XENA (<https://xenabrowser.net/datapages/>), and TIMER (<http://timer.cistrome.org>).

## Conflicts of Interest

The authors declare no competing interests.

## Authors' Contributions

Chen Zhao and Xiangpan Li designed the study. Kewei Xiong collected study data and performed statistical analysis and visualization. Chen Zhao, Kewei Xiong, Fangrui Zhao, and Abdalla Adam wrote the manuscript draft. All authors read and approved the manuscript. Chen Zhao, Kewei Xiong, and Fangrui Zhao contributed equally to this work and share first authorship.

## Acknowledgments

We would like to thank Smart (<https://smart.servier.com/>) and Iconfont (<https://www.iconfont.cn/>) for their support in preparing the graphical workflow. This study was supported by the Fundamental Research Funds for the Central Universities (2042020kf0084), grants from the Natural Science Foundation of Hubei Province (2014CFB394, 2019CFB721), Health and Family Planning Commission of Hubei Province (WJ2017M027CN), and Cisco hausen Cancer Research Foundation (Y-HS202101-0079) in China.

## Supplementary Materials

Supplementary Table 1: the 636 glycosylation-related genes. Supplementary Table 2: the phenotypes of 70 OC patients for WGCNA. Supplementary Table 3: pathway signatures and genes. Supplementary Table 4: the expression of

OGRmRNAs and the profiles of risk score in the training and test set. Supplementary Table 5: coexpressed genes with OGRmRNAs in ovarian cancer. Supplementary Table 6: results of GSEA by the “clusterProfiler” package. Supplementary Table 7: the expression of immune checkpoints of OC patients and their corresponding risk subtypes. Supplementary Figure 1: mRNA differences among low expression and high expression of OGRmRNAs and normal tissues. (A) ALG8. (B) DCTN4. (C) DCTN6. (D) UBB. Supplementary Figure 2: functional enrichment analysis with co-expressed genes of OGRmRNAs. (A) Gene Ontology terms. (B) Pathways of KEGG (Kyoto Encyclopedia of Genes and Genomes). (*Supplementary Materials*)


## References

- [1] F. Bray, J. Ferlay, I. Soerjomataram, R. L. Siegel, L. A. Torre, and A. Jemal, “Global cancer statistics 2018: GLOBOCAN estimates of incidence and mortality worldwide for 36 cancers in 185 countries,” *CA: a Cancer Journal for Clinicians*, vol. 68, no. 6, pp. 394–424, 2018.
- [2] A. Khodavandi, F. Alizadeh, and A. F. A. Razis, “Association between dietary intake and risk of ovarian cancer: a systematic review and meta-analysis,” *European Journal of Nutrition*, vol. 60, no. 4, pp. 1707–1736, 2021.
- [3] K. B. Kuchenbaecker, J. L. Hopper, D. R. Barnes et al., “Risks of breast, ovarian, and contralateral breast cancer for BRCA1 and BRCA2 mutation carriers,” *JAMA*, vol. 317, no. 23, pp. 2402–2416, 2017.
- [4] W. Li, X. Gu, C. Liu et al., “A synergetic effect of BARD1 mutations on tumorigenesis,” *Nature Communications*, vol. 12, no. 1, p. 1243, 2021.
- [5] M. Zheng, Y. Hu, R. Gou et al., “Identification three LncRNA prognostic signature of ovarian cancer based on genome-wide copy number variation,” *Biomedicine & Pharmacotherapy*, vol. 124, article 109810, 2020.
- [6] L. Yin, N. Zhang, and Q. Yang, “DNA methylation subtypes for ovarian cancer prognosis,” *FEBS Open Bio*, vol. 11, no. 3, pp. 851–865, 2021.
- [7] Z. Zhang, K. Tu, F. Liu et al., “FoxM1 promotes the migration of ovarian cancer cell through KRT5 and KRT7,” *Gene*, vol. 757, article 144947, 2020.
- [8] Z. Li, L. Huang, L. Wei et al., “KCNH3 predicts poor prognosis and promotes progression in ovarian cancer,” *Oncotargets and Therapy*, vol. Volume 13, pp. 10323–10333, 2020.
- [9] A. Salwa, A. Ferraresi, M. Chinthakindi et al., “*BECN1* and *BRCA1* deficiency sensitizes ovarian cancer to platinum therapy and confers better prognosis,” *Biomedicine*, vol. 9, no. 2, 2021.
- [10] M. Yang, G. Chen, K. Gao, and Y. Wang, “Tumor immunometabolism characterization in ovarian cancer with prognostic and therapeutic implications,” *Frontiers in Oncology*, vol. 11, article 622752, 2021.
- [11] C. Arriagada, P. Silva, and V. A. Torres, “Role of glycosylation in hypoxia-driven cell migration and invasion,” *Cell Adhesion & Migration*, vol. 13, no. 1, pp. 13–22, 2019.
- [12] R. Gupta, F. Leon, S. Rauth, S. K. Batra, and M. P. Ponnusamy, “A systematic review on the implications of O-linked glycan branching and truncating enzymes on cancer progression and metastasis,” *Cell*, vol. 9, no. 2, p. 446, 2020.
- [13] W. Butler and J. Huang, “Glycosylation changes in prostate cancer progression,” *Frontiers in Oncology*, vol. 11, article 809170, 2021.
- [14] D. Josic, T. Martinovic, and K. Pavelic, “Glycosylation and metastases,” *Electrophoresis*, vol. 40, pp. 140–150, 2018.
- [15] K. Ohtsubo and J. D. Marth, “Glycosylation in cellular mechanisms of health and disease,” *Cell*, vol. 126, no. 5, pp. 855–867, 2006.
- [16] J. Munkley and D. J. Elliott, “Hallmarks of glycosylation in cancer,” *Oncotarget*, vol. 7, no. 23, pp. 35478–35489, 2016.
- [17] E. Rodríguez and S. T. T. Schetters, “The tumour glyco-code as a novel immune checkpoint for immunotherapy,” *Nature Reviews. Immunology*, vol. 18, no. 3, pp. 204–211, 2018.
- [18] S. Ren, Z. Zhang, C. Xu et al., “Distribution of IgG galactosylation as a promising biomarker for cancer screening in multiple cancer types,” *Cell Research*, vol. 26, no. 8, pp. 963–966, 2016.
- [19] H. Guo and K. L. Abbott, “Functional impact of tumor-specific *N*-linked glycan changes in breast and ovarian cancers,” *Advances in Cancer Research*, vol. 126, pp. 281–303, 2015.
- [20] R. Su, C. Jin, L. Zhou et al., “Construction of a ceRNA network of hub genes affecting immune infiltration in ovarian cancer identified by WGCNA,” *BMC Cancer*, vol. 21, no. 1, p. 970, 2021.
- [21] J. Zhu, Z. Chen, and L. Yong, “Systematic profiling of alternative splicing signature reveals prognostic predictor for ovarian cancer,” *Gynecologic Oncology*, vol. 148, no. 2, pp. 368–374, 2018.
- [22] M. J. Strumillo, M. Oplova, C. Vieitez et al., “Conserved phosphorylation hotspots in eukaryotic protein domain families,” *Nature Communications*, vol. 10, no. 1, p. 1977, 2019.
- [23] J. Ashkani and K. J. Naidoo, “Glycosyltransferase gene expression profiles classify cancer types and propose prognostic subtypes,” *Scientific Reports*, vol. 6, no. 1, p. 26451, 2016.
- [24] J. Pan, Y. Hu, S. Sun et al., “Glycoproteomics-based signatures for tumor subtyping and clinical outcome prediction of high-grade serous ovarian cancer,” *Nature Communications*, vol. 11, no. 1, p. 6139, 2020.
- [25] Y. Li, D. Li, Y. Chen et al., “Robust glycogene-based prognostic signature for proficient mismatch repair colorectal adenocarcinoma,” *Frontiers in Oncology*, vol. 11, article 727752, 2021.
- [26] K. M. Lisowska, M. Olbryt, V. Dudaladava et al., “Gene expression analysis in ovarian cancer - faults and hints from DNA microarray study,” *Frontiers in Oncology*, vol. 4, p. 6, 2014.
- [27] T. Li, J. Fan, B. Wang et al., “TIMER: a web server for comprehensive analysis of tumor-infiltrating immune cells,” *Cancer Research*, vol. 77, no. 21, pp. e108–e110, 2017.
- [28] P. Langfelder and S. Horvath, “WGCNA: an R package for weighted correlation network analysis,” *BMC Bioinformatics*, vol. 9, no. 1, p. 559, 2008.
- [29] “Regression shrinkage and selection via the lasso,” *Journal of Royal Statistical Society-Series B*, vol. 58, no. 1, pp. 267–288, 1996.
- [30] A. E. Hoerl and R. W. Kennard, “Ridge regression: applications to nonorthogonal problems,” *Technometrics*, vol. 12, no. 1, pp. 69–82, 1970.
- [31] T. Chen and C. Guestrin, “Xgboost: A scalable tree boosting system,” in *In Proceedings of the 22nd acm sigkdd international conference on knowledge discovery and data mining*, California, San Francisco USA, 2016.
- [32] C. Strobl, A. L. Boulesteix, T. Kneib, T. Augustin, and A. Zeileis, “Conditional variable importance for random forests,” *BMC Bioinformatics*, vol. 9, no. 1, p. 307, 2008.

- [33] Y. Zhao, L. Gong, B. Zhou, Y. Huang, and C. Liu, "Detecting tomatoes in greenhouse scenes by combining AdaBoost classifier and colour analysis," *Biosystems Engineering*, vol. 148, pp. 127–137, 2016.
- [34] S. Bao, H. Zhao, J. Yuan et al., "Computational identification of mutator-derived lncRNA signatures of genome instability for improving the clinical outcome of cancers: a case study in breast cancer," *Briefings in Bioinformatics*, vol. 21, no. 5, pp. 1742–1755, 2020.
- [35] T. M. Malta, A. Sokolov, A. J. Gentles et al., "Machine learning identifies stemness features associated with oncogenic dedifferentiation," *Cell*, vol. 173, no. 2, article e315, pp. 338–354, 2018.
- [36] D. A. Barbie, P. Tamayo, J. S. Boehm et al., "Systematic RNA interference reveals that oncogenic *\_KRAS\_*-driven cancers require *TBK1*," *Nature*, vol. 462, no. 7269, pp. 108–112, 2009.
- [37] G. Yu, L. G. Wang, Y. Han, and Q. Y. He, "clusterProfiler: an R package for comparing biological themes among gene clusters," *OMICS*, vol. 16, no. 5, pp. 284–287, 2012.
- [38] V. Thorsson, D. L. Gibbs, S. D. Brown et al., "The immune landscape of cancer," *Immunity*, vol. 48, no. 812–830, article e814, pp. 812–830, 2018.
- [39] K. Yoshihara, M. Shahmoradgoli, E. Martinez et al., "Inferring tumour purity and stromal and immune cell admixture from expression data," *Nature Communications*, vol. 4, no. 1, p. 2612, 2013.
- [40] J. Wu, L. Li, H. Zhang et al., "A risk model developed based on tumor microenvironment predicts overall survival and associates with tumor immunity of patients with lung adenocarcinoma," *Oncogene*, vol. 40, no. 26, pp. 4413–4424, 2021.
- [41] M. Hock, K. Wegleiter, E. Ralser et al., "ALG8-CDG: novel patients and review of the literature," *Orphanet Journal of Rare Diseases*, vol. 10, no. 1, p. 73, 2015.
- [42] W. Zhou, J. Li, X. Lu et al., "Derivation and validation of a prognostic model for cancer dependency genes based on CRISPR-Cas9 in gastric adenocarcinoma," *Frontiers in Oncology*, vol. 11, article 617289, 2021.
- [43] S. F. Chin, A. E. Teschendorff, J. C. Marioni et al., "High-resolution aCGH and expression profiling identifies a novel genomic subtype of ER negative breast cancer," *Genome Biology*, vol. 8, no. 10, p. R215, 2007.
- [44] Y. Cao, N. Jiao, T. Sun et al., "CXCL11 correlates with antitumor immunity and an improved prognosis in colon cancer," *Frontiers in Cell and Development Biology*, vol. 9, article 646252, 2021.
- [45] S. Wang, Q. Wang, X. Zhang et al., "Distinct prognostic value of dynactin subunit 4 (DCTN4) and diagnostic value of DCTN1, DCTN2, and DCTN4 in colon adenocarcinoma," *Cancer Management and Research*, vol. Volume 10, pp. 5807–5824, 2018.
- [46] X. Su, H. Li, S. Chen, and C. Qin, "Study on the prognostic values of dynactin genes in low-grade glioma," *Technology in Cancer Research & Treatment*, vol. 20, p. 153303382110101, 2021.
- [47] H. M. Lu, S. Li, M. H. Black et al., "Association of breast and ovarian cancers with predisposition genes identified by large-scale sequencing," *JAMA Oncology*, vol. 5, no. 1, pp. 51–57, 2019.
- [48] G. N. Schroeder and H. Hilbi, "Molecular pathogenesis of *Shigella* spp.: controlling host cell signaling, invasion, and death by type III secretion," *Clinical Microbiology Reviews*, vol. 21, no. 1, pp. 134–156, 2008.
- [49] C. Sun, R. Mezzadra, and T. N. Schumacher, "Regulation and function of the PD-L1 checkpoint," *Immunity*, vol. 48, no. 3, pp. 434–452, 2018.
- [50] A. P. Nayak, A. Kapur, L. Barroilhet, and M. S. Patankar, "Oxidative phosphorylation: a target for novel therapeutic strategies against ovarian cancer," *Cancers (Basel)*, vol. 10, no. 9, 2018.
- [51] X. Guo, X. Wang, Z. Wang et al., "Site-specific proteasome phosphorylation controls cell proliferation and tumorigenesis," *Nature Cell Biology*, vol. 18, no. 2, pp. 202–212, 2016.
- [52] M. Bazzaro, Z. Lin, A. Santillan et al., "Ubiquitin proteasome system stress underlies synergistic killing of ovarian cancer cells by bortezomib and a novel HDAC6 inhibitor," *Clinical Cancer Research*, vol. 14, no. 22, pp. 7340–7347, 2008.
- [53] C. Reily, T. J. Stewart, M. B. Renfrow, and J. Novak, "Glycosylation in health and disease," *Nature Reviews. Nephrology*, vol. 15, no. 6, pp. 346–366, 2019.
- [54] C. W. Li, S. O. Lim, E. M. Chung et al., "Eradication of triple-negative breast cancer cells by targeting glycosylated PD-L1," *Cancer Cell*, vol. 33, no. 187–201, article e110, pp. 187–201.e10, 2018.
- [55] X. Wu, Z. Yin, C. McKay et al., "Protective epitope discovery and design of MUC1-based vaccine for effective tumor protections in immunotolerant mice," *Journal of the American Chemical Society*, vol. 140, no. 48, pp. 16596–16609, 2018.
- [56] H. Li, M. Li, C. Tang, and L. Xu, "Screening and prognostic value of potential biomarkers for ovarian cancer," *Annals of Translational Medicine*, vol. 9, no. 12, p. 1007, 2021.
- [57] Y. You, Q. Fan, J. Huang, Y. Wu, H. Lin, and Q. Zhang, "Ferroptosis-related gene signature promotes ovarian cancer by influencing immune infiltration and invasion," *Journal of Oncology*, vol. 2021, 2021.
- [58] J. Zheng, J. Guo, B. Cao, Y. Zhou, and J. Tong, "Identification and validation of lncRNAs involved in m6A regulation for patients with ovarian cancer," *Cancer Cell International*, vol. 21, no. 1, p. 363, 2021.
- [59] D. R. Kroeger, K. Milne, and B. H. Nelson, "Tumor-infiltrating plasma cells are associated with tertiary lymphoid structures, cytolytic T-cell responses, and superior prognosis in ovarian cancer," *Clinical Cancer Research*, vol. 22, no. 12, pp. 3005–3015, 2016.
- [60] J. Smazynski, P. T. Hamilton, S. Thornton et al., "The immune suppressive factors CD155 and PD-L1 show contrasting expression patterns and immune correlates in ovarian and other cancers," *Gynecologic Oncology*, vol. 158, no. 1, pp. 167–177, 2020.
- [61] R. J. Maas, J. S. Hoogstad-van Evert, J. M. Van der Meer et al., "TIGIT blockade enhances functionality of peritoneal NK cells with altered expression of DNAM-1/TIGIT/CD96 checkpoint molecules in ovarian cancer," *Oncimmunology*, vol. 9, no. 1, article 1843247, 2020.
- [62] L. Tu, R. Guan, H. Yang et al., "Assessment of the expression of the immune checkpoint molecules PD-1, CTLA4, TIM-3 and LAG-3 across different cancers in relation to treatment response, tumor-infiltrating immune cells and survival," *International Journal of Cancer*, vol. 147, no. 2, pp. 423–439, 2020.

## Research Article

# Quantitative Proteomics Analysis Expands the Roles of Lysine $\beta$ -Hydroxybutyrylation Pathway in Response to Environmental $\beta$ -Hydroxybutyrate

Wanting Hou,<sup>1,2</sup> Guobin Liu,<sup>2,3</sup> Xuelian Ren,<sup>2</sup> Xianming Liu,<sup>4</sup> Lei He,<sup>4</sup> and He Huang<sup>1,2,3,5</sup> 

<sup>1</sup>School of Pharmacy, Nanchang University, Nanchang 330006, China

<sup>2</sup>Shanghai Institute of Materia Medica, Chinese Academy of Sciences, Shanghai 201203, China

<sup>3</sup>School of Chinese Materia Medica, Nanjing University of Chinese Medicine, Nanjing 210023, China

<sup>4</sup>Brucker (Beijing) Scientific Technology Co., Ltd., Beijing 100192, China

<sup>5</sup>University of Chinese Academy of Sciences, Beijing 100049, China

Correspondence should be addressed to He Huang; [hhuang@simm.ac.cn](mailto:hhuang@simm.ac.cn)

Received 28 October 2021; Accepted 27 December 2021; Published 24 February 2022

Academic Editor: Xiangpan Li

Copyright © 2022 Wanting Hou et al. This is an open access article distributed under the Creative Commons Attribution License, which permits unrestricted use, distribution, and reproduction in any medium, provided the original work is properly cited.

Lysine  $\beta$ -hydroxybutyrylation (Kbhb) is a newly identified protein posttranslational modification (PTM) derived from  $\beta$ -hydroxybutyrate (BHB), a product of ketone body metabolism in liver. BHB could serve as an energy source and play a role in the suppression of oxidative stress. The plasma concentration of BHB could increase up to 20 mM during starvation and in pathological conditions. Despite the progress, how the cells derived from extrahepatic tissues respond to elevated environmental BHB remains largely unknown. Given that BHB can significantly drive Kbhb, we characterized the BHB-induced lysine  $\beta$ -hydroxybutyrylome and acetylome by quantitative proteomics. A total of 840 unique Kbhb sites on 429 proteins were identified, with 42 sites on 39 proteins increased by more than 50% in response to BHB. The results showed that the upregulated Kbhb induced by BHB was involved in aminoacyl-tRNA biosynthesis, 2-oxocarboxylic acid metabolism, citrate cycle, glycolysis/gluconeogenesis, and pyruvate metabolism pathways. Moreover, some BHB-induced Kbhb substrates were significantly involved in diseases such as cancer. Taken together, we investigate the dynamics of lysine  $\beta$ -hydroxybutyrylome and acetylome induced by environmental BHB, which reveals the roles of Kbhb in regulating various biological processes and expands the biological functions of BHB.

## 1. Introduction

Protein posttranslational modifications (PTMs) can change the physical and chemical properties of the protein, affecting the spatial conformation, activity, subcellular localization, protein folding, and so on [1]. They play vital roles in various cellular processes, such as gene expression regulation, cell division, protein degradation, signal transduction, and protein interactions [2]. In-depth study of protein PTMs is of great significance in elaborating the mechanism of life activities, discovering drug targets, and laying the foundation for clinical treatment [3]. With the development of high-resolution mass spectrometry (MS) and proteomics techniques, many new types of PTMs have been identified

in recent years, such as lysine 2-hydroxyisobutyrylation, benzoylation, and lactylation [4–8].

A wide array of evidence has demonstrated that endogenous metabolites in mammalian cells are tightly coupled to PTMs [9, 10]. A noteworthy example is  $\beta$ -hydroxybutyrate (BHB), an intermediate product of liver fatty acid oxidation and decomposition [11]. BHB, acetoacetate, and acetone are collectively referred to as ketone bodies, in which BHB accounts for about 80% [12, 13]. BHB can be used as an endogenous biologically active small molecule and has critical protective effects on nerves, cardiovascular, and other tissues and organs [12, 14–18]. Recently, we discovered a new type of PTM, lysine  $\beta$ -hydroxybutyrylation (Kbhb), and revealed that BHB served as a precursor for Kbhb

[19]. Our results showed that starvation, ketogenic diet, and pharmacologically induced diabetes could enhance BHB generation in the liver, in turn mediating cellular signaling functions [20–22]. Notably, when blood sugar levels are low, BHB can be generated in the liver and transported to other energy-consumption tissues as a compensatory energy source [23]. In such conditions, how the cells derived from extrahepatic tissues respond to elevated environmental BHB is still unclear.

To explore the roles of the Kbh pathway induced by elevated BHB levels, we quantitatively analyzed the dynamics of Kbh in response to environmental BHB in mouse embryonic fibroblast (MEF) cells. In total, we identified 840 unique Kbh sites across 429 proteins, and 42 sites from 39 proteins were increased by more than 50% ( $\log_2(\text{treated/untreated}) > 0.585$ ) in response to BHB. Functional enrichment analysis indicated that significant upregulated Kbh sites were involved in aminoacyl-tRNA biosynthesis, 2-oxocarboxylic acid metabolism, citrate cycle, pyruvate metabolism, fructose and mannose metabolism, as well as glycolysis/gluconeogenesis pathways.

We also identified 5587 lysine acetylation (Kac) sites across 2303 proteins. Unlike the Kbh pathway, the dynamic Kac proteins induced by environmental BHB were mainly related to sphingolipid signaling, necroptosis, cellular senescence, and ubiquitin-mediated proteolysis pathways. The diversity of Kbh and Kac pathways indicated their different roles in response to elevated BHB, therefore, mediating diverse downstream cellular processes.

In addition, we found that some dynamic Kbh sites were located on important positions for protein substrate/cofactor binding, implying that elevated BHB may affect the functions of substrate proteins by inducing Kbh on these positions.

Together, this study identified and quantified the dynamics of Kbh and Kac sites in response to environmental BHB, which expanded the roles of Kbh and laid a foundation for further exploring the mechanisms of Kbh pathway under various physiological and pathological conditions.

## 2. Experimental Section

**2.1. Materials.** Pan anti-Kbh (PTM-1204) and anti-Kac antibody (PTM-104) were purchased from PTM Biolabs. Anti-histone H3 antibody (M1306-4) was purchased from Huabio. Anti-beta actin antibody (66009-1) was purchased from Proteintech Group. “Light” ( $^{12}\text{C}_6^{14}\text{N}_2$ -Lys,  $^{12}\text{C}_6^{14}\text{N}_4$ -Arg) (ULM-8766-PK) and “heavy” ( $^{13}\text{C}_6^{15}\text{N}_2$ -Lys,  $^{13}\text{C}_6^{15}\text{N}_4$ -Arg) (CNLM-291-H-PK) amino acids were purchased from Cambridge Isotope Laboratories. Trypsin used for modified sequencing was purchased from Promega (Madison, WI).

**2.2. Stable Isotope Labeling and BHB Treatment of Cells.** MEF cells were cultured in DMEM free of lysine/arginine, 10% dialyzed FBS, and either “light” ( $^{12}\text{C}_6^{14}\text{N}_2$ -Lys,  $^{12}\text{C}_6^{14}\text{N}_4$ -Arg) or “heavy” ( $^{13}\text{C}_6^{15}\text{N}_2$ -Lys,  $^{13}\text{C}_6^{15}\text{N}_4$ -Arg) amino acids (100 mg/L) with 1% penicillin and streptomycin in a 5%  $\text{CO}_2$  atmosphere at 37°C. The cells were cultured for

at least 7 generations to ensure a labeling efficiency of more than 98%. MEF cells were treated with 5 mM BHB for 24 hours in order to perform proteomics.

**2.3. Protein Extraction and Trypsin Digestion.** According to the previously described methods [24], the collected “heavy” and “light” cells were washed three times with precooled phosphate-buffered saline. Then, we added protein lysis buffer (8 M urea, 2 mM EDTA, 3  $\mu\text{M}$  TSA, 50 mM NAM, 5 mM DTT, and 1% Protease inhibitor cocktail III) to resuspend the cells and sonicated them with a sonic dismembrator (JY96-IIN, Jingxin, Shanghai, China) on ice. After centrifugation at 18 000 g for 3 min at 4°C, transfer the proteins to a new tube and determine the concentration by BCA method. Proteins from “heavy” and “light” cells were equally mixed and reduced for 1 h with 10 mM dithiothreitol at 37°C and alkylated with 20 mM iodoacetamide for 45 min in a dark environment at 25°C. Then, block the excess iodoacetamide by 20 mM cysteine. Next, 100 mM  $\text{NH}_4\text{HCO}_3$  was added to the protein samples to make sure the urea concentration was less than 2 M. Then, trypsin was added to the proteins at a 1:50 trypsin-protein mass ratio for digestion overnight to obtain peptide samples.

**2.4. Immunoaffinity Enrichment.** Kbh and Kac peptides were immunoaffinity enriched as previously described [24]. Briefly, the peptides were dissolved in NETN buffer (100 mM NaCl, 1 mM EDTA, 50 mM Tris-HCl, 0.5% NP-40, pH 8.0) and incubated with 20  $\mu\text{L}$  of pan anti-Kbh or pan anti-Kac antibodies conjugated agarose beads on a shaker with gentle shaking at 4°C overnight. In order to remove nonspecific enrichment, we washed the beads with NETN buffer four times and with  $\text{ddH}_2\text{O}$  twice. Finally, using 0.1% trifluoroacetic acid, the eluted peptides were evaporated to dryness in a vacuum and desalted for mass spectrometry identification.

**2.5. Mass Spectrometry.** A nanoElute nanoflow UHPLC was coupled online to a hybrid trapped ion mobility spectrometry-quadrupole time of flight mass spectrometer (timsTOF Pro, Bruker Daltonics, Bremen, Germany). Peptides were separated in 60 min at a flow rate of 300  $\text{nL min}^{-1}$  on a 25 cm  $\times$  75  $\mu\text{m}$  column with a pulled emitter tip, packed with 1.9  $\mu\text{m}$  ReproSil-Pur C18-AQ particles (Dr. Maisch, Germany). Mobile phases A and B were 0.1% formic acid in water and 0.1% formic acid in 80% acetonitrile, respectively. The LC method consisting of a gradient of 2–85% in HPLC mobile phase B (0.1% formic acid in acetonitrile, v/v) and in mobile phase A (0.1% formic acid and 2% acetonitrile in water). The eluted peptides were subjected to capillary source followed by the timsTOF Pro mass spectrometry. The electrospray voltage applied was 1.60 kV. Precursors and fragments were analyzed at the TOF detector, with a MS/MS scan range from 100 to 1700  $m/z$ . The timsTOF Pro was operated in parallel accumulation serial fragmentation (PASEF) mode. Precursors with charge states 0 to 5 were selected for fragmentation, and 10 PASEF-MS/MS scans were acquired per cycle. The dynamic exclusion was set to 30 s.

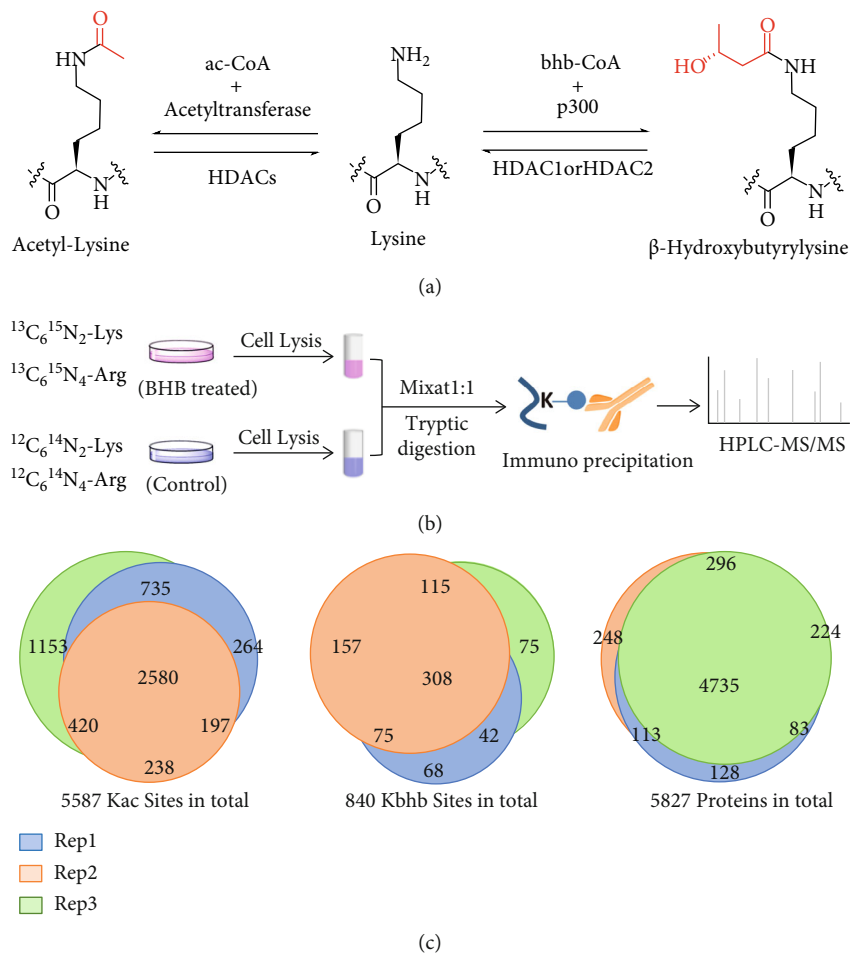


FIGURE 1: Systematic profiling of lysine  $\beta$ -hydroxybutyrylome and acetylome. (a) Illustration of enzymatic reaction for acetyl-lysine and  $\beta$ -hydroxybutyryl-lysine. (b) Schematic representation of experimental workflow for the identification and quantification of Kbhb and Kac in MEF cells. (c) Pie chart shows experimental reproducibility of three biological replicates.

**2.6. Database Search and Data Filter Criteria.** For the acquired raw files, searching was performed based on UniProt Mouse protein database (17027 entries, <http://www.uniprot.org>) using Peaks Studio (Version 10.5, Bioinformatics Solutions Inc). The enzyme was specified as trypsin, the peptide mass tolerance was set at 20 ppm, and the MS/MS mass tolerance was set at 0.05 Da. Oxidation of methionine residues (+15.99 Da), acetylation of proteins N-termini (+42.01 Da),  $\beta$ -hydroxybutyrylation on lysine, and acetylation on lysine were specified as variable modifications. Maximum missed cleavages per peptide were set as 3. Peptide sequences matching the Human UniProt database were obtained at a false discovery rate (FDR)  $\leq 0.01$  for both proteins and peptides. A decoy fusion method was employed by PEAKS for FDR calculation. Quantitative data were generated by the PEAKS Q module using “Precursor Ion Quantification” under the “Quantifications” options, and “SILAC-2plex (R10, K8)” method was selected.

**2.7. Bioinformatics Analysis.** Similar to our previously reported methods [24], use a hypergeometric test in clusterProfiler package in R for KEGG pathway enrichment analysis [25]. The protein-protein interaction network of dynamic

Kbhb proteins was described by STRING database ([v11,http://www.string-db.org/](http://www.string-db.org/)) [26] and visualized in Cytoscape (v.3.8.2) [27].

### 3. Results

**3.1. Systematic Profiling of Kbhb in Response to BHB.** Kbhb is a newly identified PTM driven by a product of lipid metabolism, BHB (Figure 1(a)). To explore the roles of Kbhb pathway in response to environmental BHB, we carried out quantitative Kbhb and Kac proteomics studies in MEF cells treated with BHB (5 mM for 24 hours). To globally identify Kbhb and Kac sites and characterize their diversification stimulated by BHB, we used stable isotope labeling by amino acids in cell culture (SILAC) combined with immunoaffinity enrichment and tandem mass analysis methods. Three biological replicate experiments were performed wherein MEF cells were metabolically labeled with “heavy” amino acids ( $^{13}\text{C}_6$   $^{15}\text{N}_2$ -Lys,  $^{13}\text{C}_6$   $^{15}\text{N}_4$ -Arg) and “light” amino acids ( $^{12}\text{C}_6$   $^{14}\text{N}_2$ -Lys,  $^{12}\text{C}_6$   $^{14}\text{N}_4$ -Arg) which were treated and untreated, respectively (Figure 1(b)). Proteins lysed from “heavy” and “light” cells were equally combined and digested by trypsin. Then, the Kbhb and Kac-containing

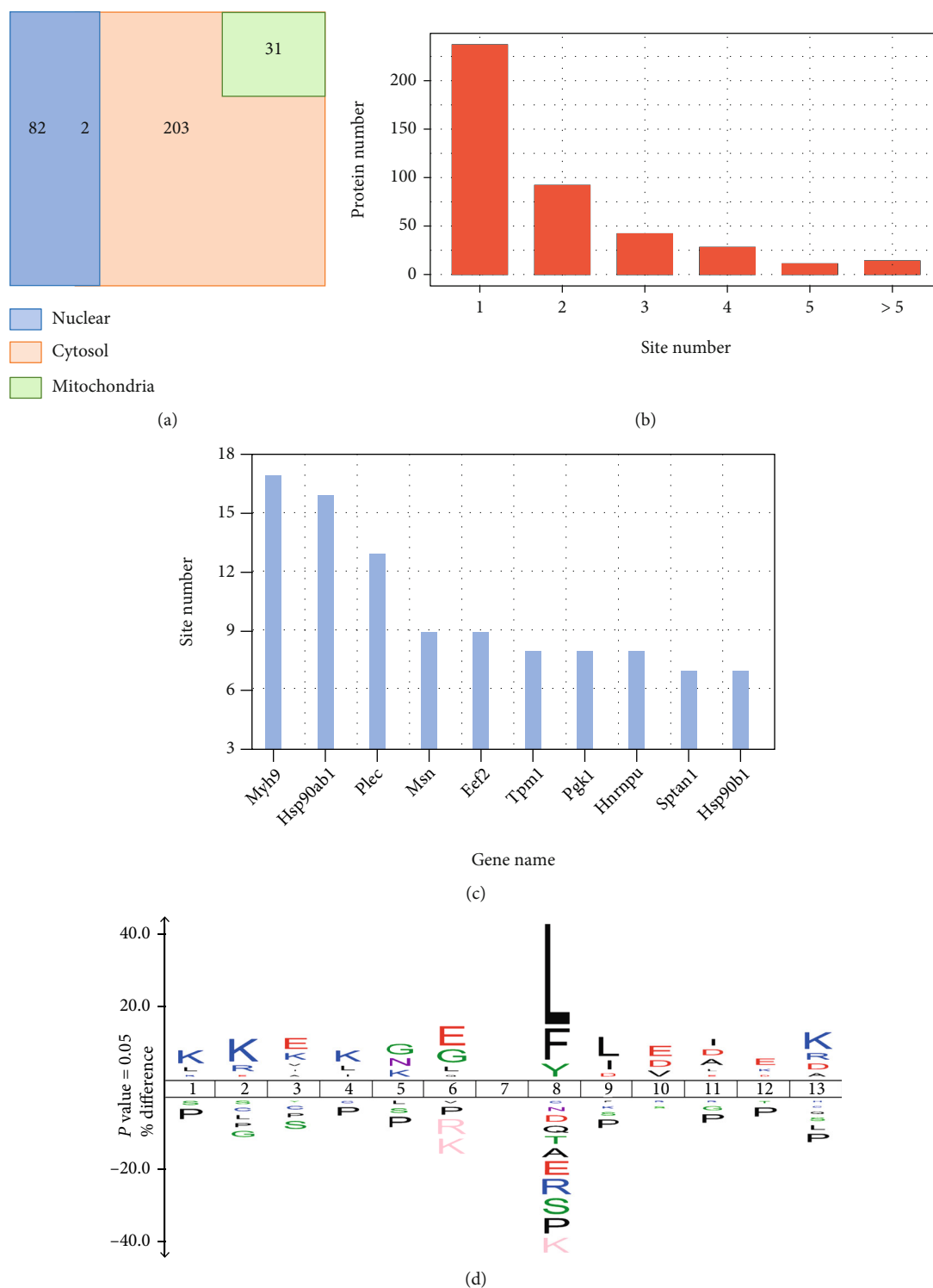
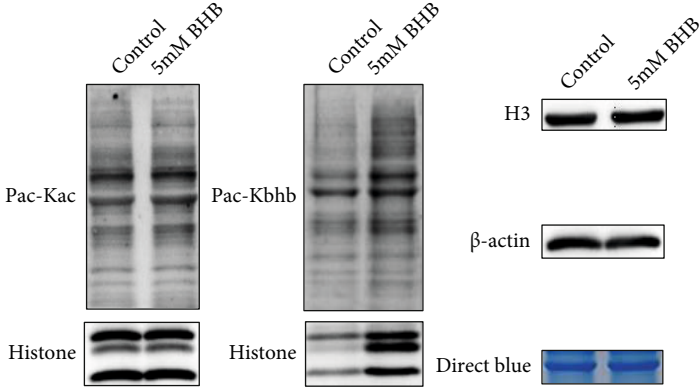


FIGURE 2: Characterization of Kbhb proteome. (a) Venn diagram shows cellular compartment distribution of Kbhb proteins. (b) Distribution of the Kbhb sites number per protein. (c) The bar graph shows the proteins containing more than 6 Kbhb sites. (d) Consensus sequence logo shows a representative sequence for BHB-induced Kbhb sites.

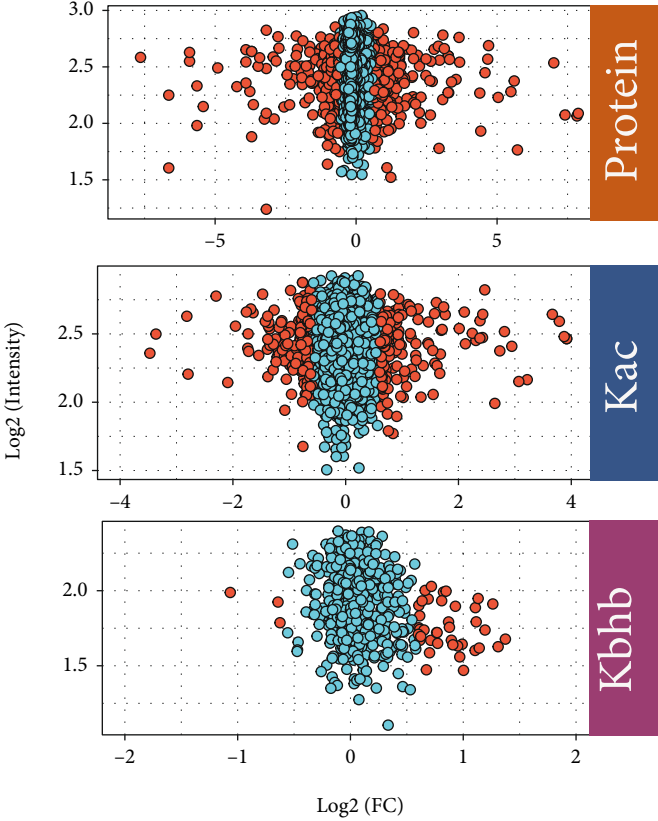
peptides were enriched with immobilized anti-Kbhb and anti-Kac antibodies followed by HPLC-MS/MS analysis on a timsTOF Pro (Bruker) mass spectrometer.

Totally, we identified 840 unique Kbhb sites across 429 proteins and 5587 Kac sites across 2303 proteins. Moreover, 64% Kbhb sites and 70% Kac sites were identified in at least

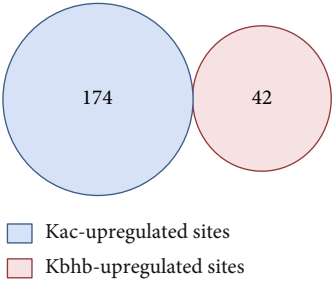




(a)



(b)



(c)

FIGURE 3: Continued.

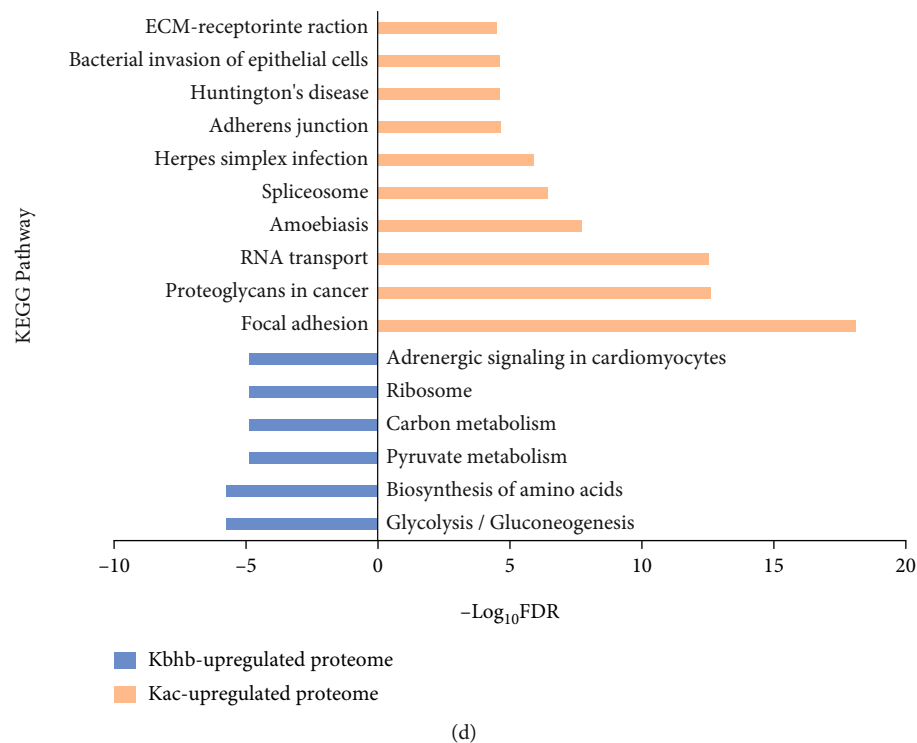


FIGURE 3: Quantitative analysis of BHB-induced Kbhb and Kac proteome. (a) BHB enhances Kbhb of proteins in MEF cells. Histone Kbhb and Kac levels were analyzed in control and BHB treated MEF cells by immuno-blotting with the indicated antibodies. (b) The scatter plot shows quantification of Kbhb and Kac sites. (c) Venn diagram shows no crossover between the upregulated Kbhb and Kac sites. (d) The KEGG pathway of Kbhb and Kac proteome induced by BHB.

2 biological replicates, demonstrating good reproducibility (Figure 1(c) and Table S1, S2, S3).

**3.2. Characterization of Kbhb Proteome.** First, we explored the subcellular distribution of Kbhb substrates in MEF cells by cellular compartment analysis. The results showed that 26% of Kbhb proteins were localized in the nucleus, while 74% were in the cytosol (Figure 2(a)). However, only 10% of Kbhb proteins were annotated in mitochondria. These results differed from our previously reported Kbhb proteome in HEK293 cells, in which 78% of the Kbhb protein were localized in the nucleus [19]. In this study, 74% of Kbhb proteins were localized exclusively or partially in the cytosol, suggesting that Kbhb pathway may play different roles between cells and tissue sources.

The identified Kbhb proteins had various site numbers. For example, 240 (56%) proteins had a single Kbhb site, and 189 (44%) proteins had at least two Kbhb sites (Figure 2(b) and Table S3). Moreover, some proteins were heavily modified by Kbhb. Plectin (Plec), a protein that interlinks intermediate filaments with microtubules and microfilaments and anchors intermediate filaments to desmosomes or hemidesmosomes [28] contains 13 Kbhb sites. Heat shock protein HSP 90-beta (Hsp90ab1) is a molecular chaperone that promotes the maturation, structural maintenance, and proper regulation of specific target proteins involved in cell cycle control and signal transduction [29, 30] and had 16 Kbhb sites. In addition, myosin heavy chain 9 (Myh9) that participates in

cytokinesis, cell shape, secretion, and capping [31, 32] had 17 Kbhb sites (Figure 2(c) and Table S3). Multiple Kbhb sites in these proteins may have significant effects on their cellular functions.

Next, we identified the enriched motifs of BHB-induced Kbhb sites using IceLogo. Flanking sequence analysis suggested that the hydrophobic amino acids Leu and Phe at +1 position were overrepresented, while acidic amino acid Asp or Glu were enriched at +3 and -1 positions (Figure 2(d)). These results were different from our previously reported Kbhb motif in HEK293 cells, in which positive-charged lysine was preferred at most positions (-6, -5, -4, -3, +3, +4, +5, and +6), while underrepresentation of negative-charged amino acids at the -2 position [19]. The difference suggests that environmental BHB may induce Kbhb in specific substrates in the presence of Kbhb transferases.

**3.3. Quantitative Analysis of BHB-Induced Kbhb Proteome.** Western blot analysis confirmed that BHB treatment increased global Kbhb levels obviously in MEF cells, while the global Kac levels were slightly affected (Figure 3(a)). To profile the dynamics of Kbhb and Kac, we quantitatively analyzed the BHB-induced Kbhb and Kac proteomes. Among the identified Kbhb sites, 42 of them from 39 proteins were increased by more than 50% ( $\log_2(\text{treated}/\text{untreated}) > 0.585$ ) in response to BHB treatment in MEF cells (Figure 3(b) and Table S3), while only 6 Kbhb sites from 6 proteins decreased by 33% ( $\log_2(\text{treated}/\text{untreated}) < -0.578$ ). Unlike Kbhb, a similar

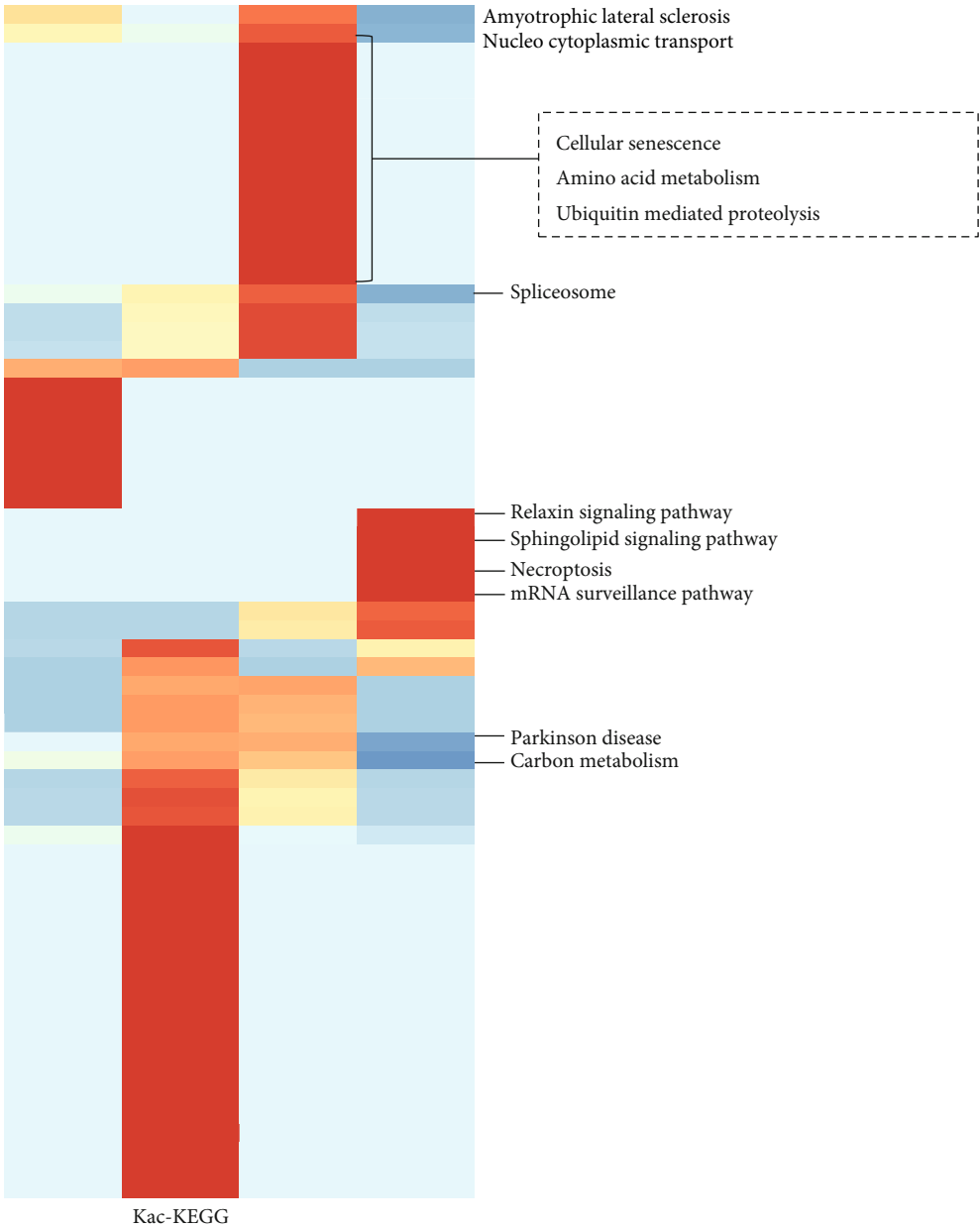
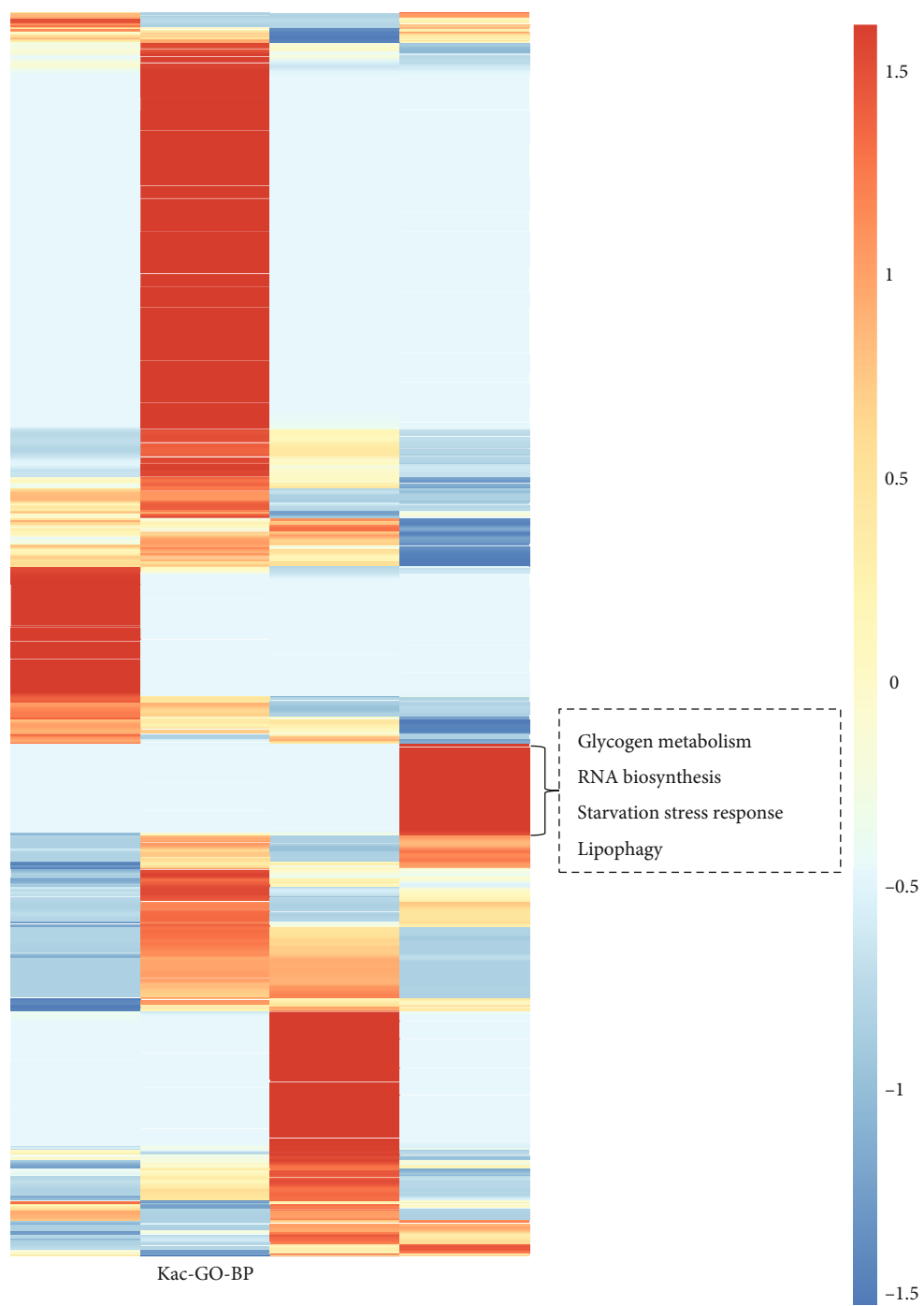
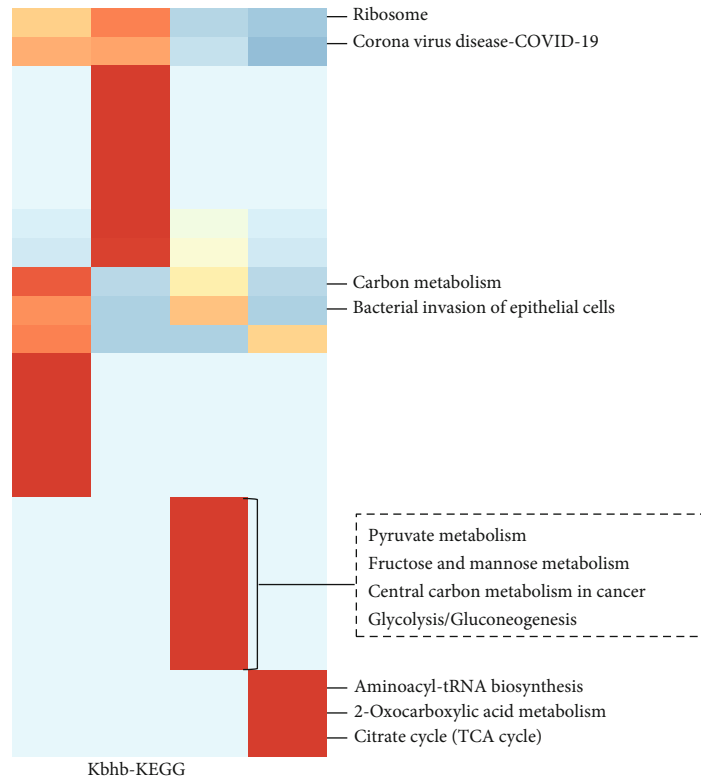


FIGURE 4: Continued.

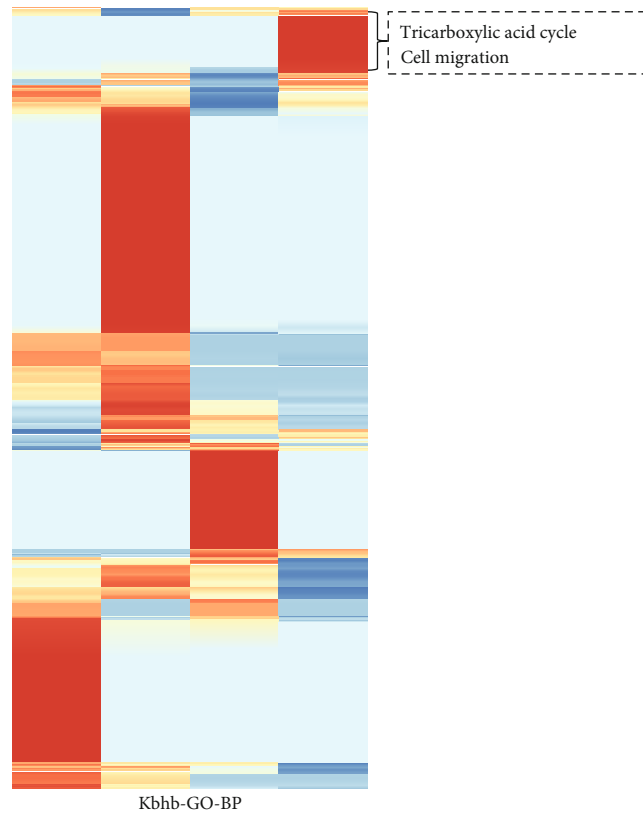


(b)

FIGURE 4: Continued.



(c)



(d)

FIGURE 4: The KEGG and GO biological process analysis. (a) The KEGG pathway of Kac proteome. (b) The GO annotation of Kac proteome. (c) The KEGG pathway of Kbh proteome. (d) The GO annotation of Kbh proteome. All the Kbh and Kac sites were divided into four groups on average according to their dynamics in response to BHB treatment (in ascending order of the treated/control ratio).

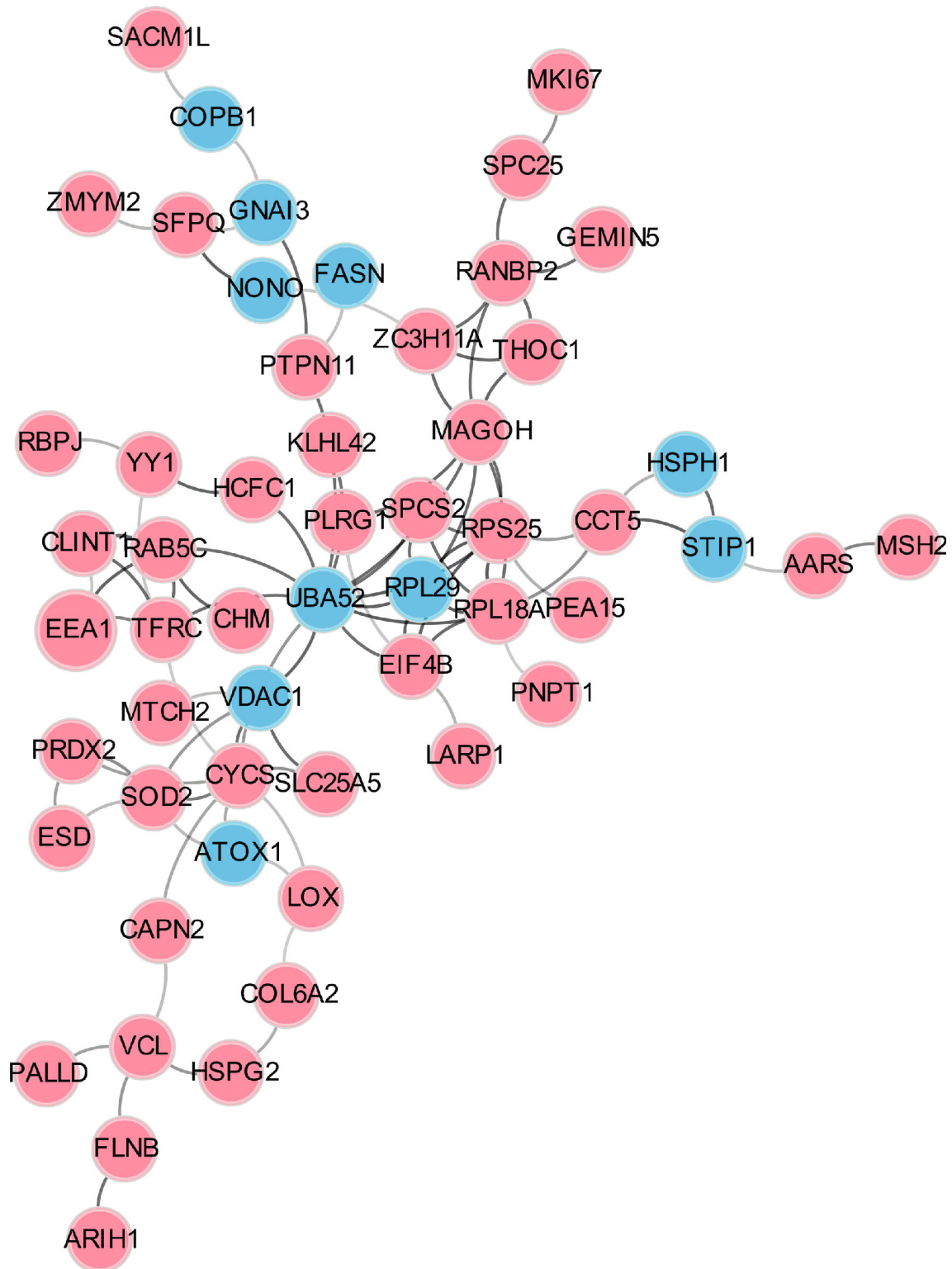


FIGURE 5: Interaction network of Kbh and Kac proteome. The blue and red circle represented the proteins with upregulated Kbh and Kac levels, respectively.

number of Kac sites were increased or decreased after BHB treatment (174 Kac sites increased by more than 50% and 189 Kac sites decreased by 33%, respectively) (Figure 3(c) and Table S2).

Next, we compared the Kbh and Kac sites increased by more than 50% after BHB treatment. Strikingly, none of them is overlapped (Figure 3(c)), suggesting that environmental BHB influenced cellular pathways through Kbh

and Kac differentially. In support of this notion, Kyoto Encyclopedia of Genes and Genomes (KEGG) pathway analysis of the dynamic Kbh and Kac substrates revealed that BHB-induced Kac primarily targeted proteins enriched in focal adhesion, proteoglycans in cancer, and RNA transport, whereas the proteins with BHB-induced Kbh were involved in carbon metabolism, biosynthesis of amino acids, and glycolysis/gluconeogenesis (Figure 3(d)).

**3.4. Biological Functions Potentially Affected by BHB.** To better understand the roles of Kbh and Kac sites induced by environmental BHB, we divided all the Kbh and Kac sites into four groups on average according to their dynamics in response to BHB treatment (in ascending order of the treated/control ratio). Then, KEGG and Gene Ontology (GO) biological process analyses on each group were performed. The adjusted  $p$  values were calculated and normalized by  $z$ -score to compare the four groups (Figure 4). In the KEGG category, pathways related to aminoacyl-tRNA biosynthesis (adjust  $p$  value =  $1.50E-04$ ), 2-oxocarboxylic acid metabolism (adjust  $p$  value =  $1.46E-05$ ), and citrate cycle (TCA cycle) (adjust  $p$  value =  $1.01E-04$ ) were significantly enriched in Kbh substrates with high treated/control ratios, while ribosome (adjust  $p$  value =  $3.87E-05$ ), bacterial invasion of epithelial cells (adjust  $p$  value =  $2.12E-03$ ), and carbon metabolism (adjust  $p$  value =  $1.72E-03$ ) pathways were enriched with low Kbh level upon BHB treatment. Unlike Kbh, necroptosis (adjust  $p$  value =  $1.51E-04$ ), mRNA surveillance pathway (adjust  $p$  value =  $3.41E-03$ ), and sphingolipid signaling (adjust  $p$  value =  $3.40E-02$ ) pathways were largely enriched with increased Kac levels, whereas the proteins with decreased Kac levels in response to BHB treatment were mainly involved in nucleocytoplasmic transport (adjust  $p$  value =  $1.81E-06$ ), spliceosome (adjust  $p$  value =  $1.85E-11$ ), and carbon metabolism (adjust  $p$  value =  $4.08E-04$ ) pathways.

Consistent with above observation, GO biological process analysis showed that BHB treatment produced a more profound impact on the Kbh level among tricarboxylic acid cycle (adjust  $p$  value =  $8.23E-04$ ) and cell programmed cell death (adjust  $p$  value =  $1.18E-02$ ), while the proteins involved in glycogen metabolic process (adjust  $p$  value =  $4.07E-03$ ), RNA biosynthetic process (adjust  $p$  value =  $1.29E-06$ ), and apoptotic process (adjust  $p$  value =  $2.76E-06$ ) were enriched with increased acetylation levels. These patterns further support that the environmental BHB can differentially mediate Kbh and Kac levels in these processes, thereby inducing diverse downstream cellular effects.

**3.5. Interaction Network of BHB-Induced Kbh and Kac Proteomes.** Protein interaction network refers to the interaction between multiple protein molecules to participate in signal transduction, energy metabolism, genetic regulation, and other physiological and biochemical processes [33, 34]. Systematic analysis of the interaction between many proteins in biological systems is crucial for understanding the functional roles of proteins in biological bodies, the regulatory mechanisms of signal transduction and energy metabolism under different physiological states, and the functional rela-

TABLE 1: Kbh sites on key residues involving substrate/cofactor binding, protein interaction, and cancer biomarkers.

| Protein | Site | Feature   |
|---------|------|---|
| Fasn    | 673  | Acyl and malonyl transferases                     |
| Uba52   | 6    | Lung cancer biomarker                             |
| Tsn     | 187  | Leucine-zipper region                             |
| Pdim1   | 254  | Binding with zinc at 258 and 261 sites            |
| Pgam5   | 140  | Phosphatase activity of serine/threonine residues |
| Gstm1   | 136  | Breast cancer biomarker                           |
| Aco2    | 50   | Catalyzes citrate to isocitrate                   |
| Eno1    | 256  | Participates in glycolysis process                |

tionships among proteins [35–37]. Therefore, we next analyzed the interaction networks of the proteins with BHB-induced Kbh and Kac sites based on the Search Tool for the Retrieval of Interacting Genes/Proteins (STRING) database (Figure 5). Interestingly, multiple members of the ribosomal protein family interact tightly, including RPL29, RPL18A, and RPS25. Among them, RPL29 contains upregulated Kac sites, and the other two have upregulated Kbh sites. Ribosomal protein plays an essential role in protein biosynthesis in cells. The results suggested that though the upregulated Kbh and Kac sites did not overlap, fluctuations of these Kbh and Kac sites induced by BHB may synergistically affect the protein synthesis process.

**3.6. Potential Impact of Kbh on Protein Functions.** A growing body of evidence has demonstrated that PTMs on certain residues can regulate protein functions and participate in a range of important biological processes [38–40]. In order to find out the potential influence of Kbh on protein functions better, we mapped the BHB induced Kbh sites with the UniProt database (Table 1). Interestingly, some Kbh sites were located on or close to important residues for protein functions. For example, fatty acid synthase (Fasn) is a key enzyme in the process of fat synthesis. It has acyltransferase and malonyltransferase activities and can catalyze the synthesis of palmitate under certain conditions, such as the presence of NADPH [41, 42]. It is worth noting that Lys673 of Fasn exhibited significantly higher Kbh levels upon BHB treatment. Interestingly, this position was located at the acyl and malonyl transferases region. Crystal structure of Fasn showed that K673 was exposed in the binding pocket of acetyl-CoA, with the nitrogen atom of K673 only 4.2 Å away from acetyl-CoA (Figure 6). Therefore, elevated Kbh level at K673 may potentially influence the transferase activity of Fasn.

Another example is Translin (Tsn), which identifies the ends of single-stranded DNA that break down during chromosomal translocations [43]. This protein has single- and double-stranded endonuclease activity and is primarily involved in immune-related gene fragments. The cyclic heterooctamer consisted of six TSN and two Translin-associated protein X subunits is necessary for DNA/RNA binding [44]. Our data showed that  $\beta$ -hydroxybutyrylation

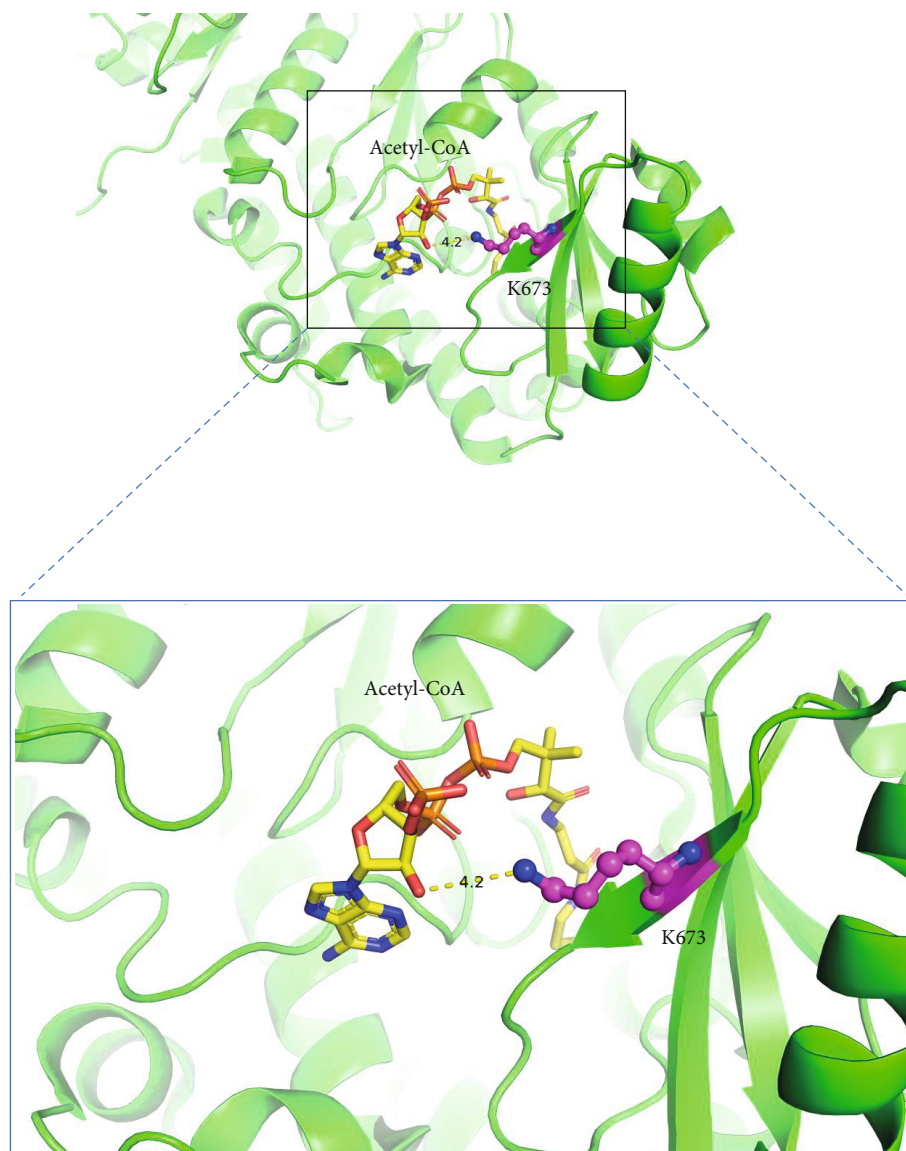


FIGURE 6: Three-dimensional structure of Fasn shows the Kbhb site and the substrate binding pocket.

at residue Lys187 of Tsn was increased by 75% in response to BHB-treatment (Table 1). Notably, Lys187 was located in the leucine zipper region that served as a dimerization module. Kbhb at this position may affect the heterooctamer assemble and regulate its functions.

Apart from the above, Enolase 1 (Eno1) catalyzes the conversion of 2-phosphoglycerate to phosphoenolpyruvate [45, 46]. In addition to glycolysis, it is also involved in the regulation of growth, hypoxia, and allergies [45, 47–49]. It is well known that glycolysis is a common pathway of glucose catabolism in all organisms. Through glycolysis, glucose is degraded to generate ATP, which provides partial energy for life activities and intermediate products or carbon skeleton for other metabolic pathways. The level of Kbhb on key residue Lys256 of Eno1 increased 100% after BHB treatment, which may influence its catalytic function in glycolysis and lead to metabolic stress (Table 1).

#### 4. Discussion

BHB metabolism is one of the key ways to maintain body's physiological homeostasis. In mammals, BHB is produced primarily in the liver by fatty acids and transported to peripheral tissues in response to nutritional deficiencies. In addition to being an energy fuel for tissues other than the liver, BHB plays a pivotal role as a driver of protein PTM. We recently discovered an evolutionarily conserved PTM, Kbhb, on core histones. Levels of Kbhb are very dynamic and are influenced by physiological conditions and nutrition sources (e.g., starvation and absence of dietary carbohydrates). These findings support a model in which BHB functions link the outside environment to cellular functions through Kbhb pathway. In humans, serum concentration of BHB can increase up to 20 mM during starvation and in pathological conditions such as diabetes mellitus (DM) and



alcoholic liver damage. Despite the progress, how the cells derived from extrahepatic tissues respond to elevated environmental BHB remains largely unknown.

Our study identified the Kbh and Kac substrates in MEF cells in response to elevated environmental BHB through quantitative proteomics. We found that 840 unique Kbh sites on 429 proteins, including 42 sites of 39 proteins increased by 1.5 folds ( $\log_2(\text{treated/untreated}) > 0.585$ ) in response to BHB treatment (Table S1, S2, S3). Notably, the results showed that the upregulated Kbh and Kac sites did not overlap after BHB treatment, suggesting that BHB-induced Kbh and Kac regulate different cellular functions. Pathway enrichment analysis also verified these results. For example, aminoacyl-tRNA biosynthesis, 2-oxocarboxylic acid metabolism, and citrate cycle pathways are significantly enriched in the upregulated Kbh substrates, while amino acid metabolism, ubiquitin-mediated proteolysis, and sphingolipid signaling pathways are largely enriched with increased Kac levels. These results suggest that elevated BHB may regulate energy metabolism and protein degradation through Kbh and Kac pathways, respectively, in response to environmental glucose deficiency. Furthermore, we revealed that BHB-induced Kbh may occupy key residues of some proteins with important biological functions, implying that BHB may regulate specific protein functions through the Kbh pathway.

BHB has been reported to be an inhibitor of histone deacetylase (HDACs) [50]. Although the level of Kbh increased significantly after BHB treatment, our results showed that there was no obvious increase in histone Kac level in MEF cells treated with 5 mM of BHB (Figure 3(a)), which is consistent with our previously studies [19]. This is not surprising because it was reported that butyrate, but not  $\beta$ -hydroxybutyrate, promotes histone Kac in multiple cell lines [50].

In summary, our study revealed the dynamic proteomes of Kbh and Kac in response to environmental BHB, which expanded the roles of Kbh pathway and suggested a new understanding of the biological functions of BHB.

## Data Availability

The mass spectrometry proteomics data have been deposited to the ProteomeXchange Consortium via the PRIDE partner repository with the dataset identifier PXD029481.

## Conflicts of Interest

The authors declare that there is no conflict of interest regarding the publication of this paper.

## Authors' Contributions

He Huang conceived the project and is responsible for the supervision. Wanting Hou, Guobin Liu, and Xuelian Ren performed all the experiments and bioinformatical analysis. Xianming Liu and Lei He were involved in the mass spectrometry data analysis. He Huang and Wanting Hou wrote the manuscript. All authors read and approved the final manuscript.

## Acknowledgments

We gratefully acknowledge the National Natural Science Foundation of China (81973164) (He Huang) and the support by Shanghai Municipal Science and Technology Major Project (He Huang).

## Supplementary Materials

Supplementary Materials Table S1/S2/S3 are the complete lists of identified proteins/Kac sites/Kbh sites in MEF cells with or without BHB treated. (*Supplementary Materials*)

## References

- [1] J. Hu, Y. T. Guo, and Y. M. Li, "Research progress in protein post-translational modification," *Chinese Science Bulletin*, vol. 51, no. 6, pp. 633–645, 2006.
- [2] L. D. Vu, K. Gevaert, and I. De Smet, "Protein language: post-translational modifications talking to each other," *Trends in Plant Science*, vol. 23, no. 12, pp. 1068–1080, 2018.
- [3] R. Mnatsakanyan, G. Shema, M. Basik et al., "Detecting post-translational modification signatures as potential biomarkers in clinical mass spectrometry," *Expert Review of Proteomics*, vol. 15, no. 6, pp. 515–535, 2018.
- [4] H. Huang, D. Zhang, Y. Wang et al., "Lysine benzoylation is a histone mark regulated by SIRT2," *Nature Communications*, vol. 9, no. 1, p. 3374, 2018.
- [5] D. Zhang, Z. Y. Tang, H. Huang et al., "Metabolic regulation of gene expression by histone lactylation," *Nature*, vol. 574, no. 7779, 2019.
- [6] H. Huang, S. Lin, B. A. Garcia, and Y. M. Zhao, "Quantitative proteomic analysis of histone modifications," *Chemical Reviews*, vol. 115, no. 6, pp. 2376–2418, 2015.
- [7] L. Chen, S. Liu, and Y. G. Tao, "Regulating tumor suppressor genes: post-translational modifications," *Signal transduction and targeted therapy*, vol. 5, no. 1, 2020.
- [8] H. Huang, B. R. Sabari, B. A. Garcia, C. D. Allis, and Y. M. Zhao, "SnapShot: histone modifications," *Cell*, vol. 159, no. 2, p. 458–+, 2014.
- [9] P. M. Smith, M. R. Howitt, N. Panikov et al., "The microbial metabolites, short-chain fatty acids, regulate colonic Treg cell homeostasis," *Science*, vol. 341, no. 6145, pp. 569–573, 2013.
- [10] B. R. Sabari, D. Zhang, C. D. Allis, and Y. M. Zhao, "Metabolic regulation of gene expression through histone acylations," *Nature Reviews Molecular Cell Biology*, vol. 18, no. 2, pp. 90–101, 2017.
- [11] J. C. Newman and E. Verdin, " $\beta$ -Hydroxybutyrate: a signaling metabolite," *Annual Review of Nutrition*, vol. 37, no. 1, pp. 51–76, 2017.
- [12] J. C. Newman and E. Verdin, " $\beta$ -Hydroxybutyrate: much more than a metabolite," *Diabetes Research and Clinical Practice*, vol. 106, no. 2, pp. 173–181, 2014.
- [13] P. Puchalska and P. A. Crawford, "Multi-dimensional roles of ketone bodies in fuel metabolism, signaling, and therapeutics," *Cell metabolism*, vol. 25, no. 2, pp. 262–284, 2017.
- [14] G. F. Cahill, "Fuel metabolism in starvation," *Annual Review of Nutrition*, vol. 26, no. 1, pp. 1–22, 2006.

- [15] E. O. Balasse and F. Fery, "Ketone body production and disposal: effects of fasting, diabetes, and exercise," *Diabetes/Metabolism Reviews*, vol. 5, no. 3, pp. 247–270, 1989.
- [16] O. E. Owen, A. P. Morgan, H. G. Kemp, J. M. Sullivan, M. G. Herrera, and G. F. Cahill Jr., "Brain metabolism during fasting," *The Journal of Clinical Investigation*, vol. 46, no. 10, pp. 1589–1595, 1967.
- [17] A. M. Sultan, "D-3-hydroxybutyrate metabolism in the perfused rat heart," *Molecular and Cellular Biochemistry*, vol. 79, no. 2, pp. 113–118, 1988.
- [18] R. J. Bing, A. Siegel, I. Ungar, and M. Gilbert, "Metabolism of the human heart," *The American Journal of Medicine*, vol. 16, no. 4, pp. 504–515, 1954.
- [19] H. Huang, D. Zhang, Y. J. Weng et al., "The regulatory enzymes and protein substrates for the lysine  $\beta$ -hydroxybutyrylation pathway," *Science Advances*, vol. 7, no. 9, 2021.
- [20] A. M. Robinson and D. H. Williamson, "Physiological roles of ketone-bodies as substrates and signals in mammalian-tissues," *Physiological Reviews*, vol. 60, no. 1, pp. 143–187, 1980.
- [21] D. H. Williamson, P. Lund, and H. A. Krebs, "The redox state of free nicotinamide-adenine dinucleotide in the cytoplasm and mitochondria of rat liver," *The Biochemical Journal*, vol. 103, no. 2, pp. 514–527, 1967.
- [22] J. C. Newman and E. Verdin, "Ketone bodies as signaling metabolites," *Trends in Endocrinology and Metabolism*, vol. 25, no. 1, pp. 42–52, 2014.
- [23] L. Laffel, "Ketone bodies: a review of physiology, pathophysiology and application of monitoring to diabetes," *Diabetes/Metabolism Research and Reviews*, vol. 15, no. 6, pp. 412–426, 1999.
- [24] H. Huang, D. L. Wang, and Y. M. Zhao, "Quantitative crotonylome analysis expands the roles of p300 in the regulation of lysine crotonylation pathway," *Proteomics*, vol. 18, no. 15, p. e1700230, 2018.
- [25] G. C. Yu, L. G. Wang, Y. Y. Han, and Q. Y. He, "clusterProfiler: an R package for comparing biological themes among gene clusters," *Omics-a Journal of Integrative Biology*, vol. 16, no. 5, pp. 284–287, 2012.
- [26] D. Szklarczyk, A. L. Gable, D. Lyon et al., "STRING v11: protein-protein association networks with increased coverage, supporting functional discovery in genome-wide experimental datasets," *Nucleic Acids Research*, vol. 47, no. D1, pp. D607–D613, 2019.
- [27] P. Shannon, A. Markiel, O. Ozier et al., "Cytoscape: a software environment for integrated models of biomolecular interaction networks," *Genome Research*, vol. 13, no. 11, pp. 2498–2504, 2003.
- [28] K. Natsuga, "Plectin-related skin diseases," *Journal of Dermatological Science*, vol. 77, no. 3, pp. 139–145, 2015.
- [29] A. Chadli, J. D. Graham, M. G. Abel et al., "GCUNC-45 is a novel regulator for the progesterone receptor/hsp90 chaperoning pathway," *Molecular and Cellular Biology*, vol. 26, no. 5, pp. 1722–1730, 2006.
- [30] M. Retzlaff, M. Stahl, H. C. Eberl et al., "Hsp90 is regulated by a switch point in the C-terminal domain," *EMBO Reports*, vol. 10, no. 10, pp. 1147–1153, 2009.
- [31] Z. H. Li and A. R. Bresnick, "The S100A4 metastasis factor regulates cellular motility via a direct interaction with myosin-IIA," *Cancer Research*, vol. 66, no. 10, pp. 5173–5180, 2006.
- [32] V. Betapudi, "Myosin II motor proteins with different functions determine the fate of lamellipodia extension during cell spreading," *PLoS One*, vol. 5, no. 1, p. e8560, 2010.
- [33] A. Athanasios, V. Charalampos, T. Vasileios, and G. M. Ashraf, "Protein-protein interaction (PPI) network: recent advances in drug discovery," *Current Drug Metabolism*, vol. 18, no. 1, pp. 5–10, 2017.
- [34] P. Y. Chen, C. Wang, Y. Zhang et al., "Predicting the molecular mechanism of "Angong Niu Huang pills" in the treatment of COVID-19 based on network pharmacology," *Natural Product Communications*, vol. 16, no. 6, p. 1934578X2110240, 2021.
- [35] S. R. Collins, K. M. Miller, N. L. Maas et al., "Functional dissection of protein complexes involved in yeast chromosome biology using a genetic interaction map," *Nature*, vol. 446, no. 7137, pp. 806–810, 2007.
- [36] D. J. LaCount, M. Vignali, R. Chettier et al., "A protein interaction network of the malaria parasite *Plasmodium falciparum*," *Nature*, vol. 438, no. 7064, pp. 103–107, 2005.
- [37] N. J. Krogan, G. Cagney, H. Y. Yu et al., "Global landscape of protein complexes in the yeast *Saccharomyces cerevisiae*," *Nature*, vol. 440, no. 7084, pp. 637–643, 2006.
- [38] J. Liu, C. Qian, and X. T. Cao, "Post-translational modification control of innate immunity," *Immunity*, vol. 45, no. 1, pp. 15–30, 2016.
- [39] L. C. Czuba, K. M. Hillgren, and P. W. Swaan, "Post-translational modifications of transporters," *Pharmacology & Therapeutics*, vol. 192, pp. 88–99, 2018.
- [40] H. R. Singh and Y. B. Ostwal, "Post-translational modification, phase separation, and robust gene transcription," *Trends in Genetics*, vol. 35, no. 2, pp. 89–92, 2019.
- [41] A. C. Chen, R. N. Re, and M. D. Burkart, "Type II fatty acid and polyketide synthases: deciphering protein-protein and protein-substrate interactions," *Natural Product Reports*, vol. 35, no. 10, pp. 1029–1045, 2018.
- [42] J. Beld, D. J. Lee, and M. D. Burkart, "Fatty acid biosynthesis revisited: structure elucidation and metabolic engineering," *Molecular BioSystems*, vol. 11, no. 1, pp. 38–59, 2015.
- [43] X. C. Ye, N. A. Huang, Y. Liu et al., "Structure of C3PO and mechanism of human RISC activation," *Nature Structural & Molecular Biology*, vol. 18, no. 6, pp. 650–657, 2011.
- [44] J. Wang, E. S. Boja, H. Oubrahim, and P. B. Chock, "Testis brain ribonucleic acid-binding protein/translin possesses both single-stranded and double-stranded ribonuclease activities," *Biochemistry*, vol. 43, no. 42, pp. 13424–13431, 2004.
- [45] H. Huang, S. Tang, M. Ji et al., "p300-mediated lysine 2-hydroxyisobutyrylation regulates glycolysis," *Molecular Cell*, vol. 70, no. 5, pp. 984–984, 2018.
- [46] T. Sugahara, H. Nakajima, S. Shirahata, and H. Murakami, "Purification and characterization of immunoglobulin production stimulating factor-I $\beta$  derived from Namalwa cells," *Cytotechnology*, vol. 10, no. 2, pp. 137–146, 1992.
- [47] R. Ray and D. M. Miller, "Cloning and characterization of a human C-Myc promoter-binding protein," *Molecular and Cellular Biology*, vol. 11, no. 4, pp. 2154–2161, 1991.
- [48] S. Feo, D. Arcuri, E. Piddini, R. Passantino, and A. Giallongo, "ENO1 gene product binds to the c-myc promoter and acts as a transcriptional repressor: relationship with Myc promoter-binding protein 1 (MBP-1)," *FEBS Letters*, vol. 473, no. 1, pp. 47–52, 2000.

- [49] R. Lopez-Alemany, C. Longstaff, S. Hawley et al., "Inhibition of cell surface mediated plasminogen activation by a monoclonal antibody against alpha-enolase," *American Journal of Hematology*, vol. 72, no. 4, pp. 234–242, 2003.
- [50] T. Shimazu, M. D. Hirschey, J. Newman et al., "Suppression of oxidative stress by  $\beta$ -hydroxybutyrate, an endogenous histone deacetylase inhibitor," *Science*, vol. 339, no. 6116, pp. 211–214, 2013.

## Corrigendum

# Corrigendum to “System Analysis of ROS-Related Genes in the Prognosis, Immune Infiltration, and Drug Sensitivity in Hepatocellular Carcinoma”

Jun Hui Xu <sup>1,2,3</sup>, Yong Jun Guan <sup>1</sup>, Zhen Dong Qiu <sup>1</sup>, Xin Zhang <sup>1</sup>, Liu Liu Zi <sup>1</sup>,  
Yu Zhou <sup>1</sup>, Chen Chen <sup>1</sup>, Jia Yu <sup>1</sup>, Yi Chao Zhang <sup>1</sup> and Wei Xing Wang <sup>1</sup>

<sup>1</sup>Department of Hepatobiliary Surgery, Renmin Hospital of Wuhan University, Wuhan, China

<sup>2</sup>Central Laboratory, Renmin Hospital of Wuhan University, Wuhan, China

<sup>3</sup>Hubei Key Laboratory of Digestive System Disease, Wuhan, China

Correspondence should be addressed to Yi Chao Zhang; 409849352@qq.com and Wei Xing Wang; sate.llite@163.com

Received 22 January 2022; Accepted 22 January 2022; Published 21 February 2022

Copyright © 2022 Jun Hui Xu et al. This is an open access article distributed under the Creative Commons Attribution License, which permits unrestricted use, distribution, and reproduction in any medium, provided the original work is properly cited.

In the article titled “System Analysis of ROS-Related Genes in the Prognosis, Immune Infiltration, and Drug Sensitivity in Hepatocellular Carcinoma” [1], the authors identified an error in the abstract that was introduced during the preparation of the manuscript. The last sentence should be corrected as follows:

“Furthermore, we demonstrated that STK25 knockdown could increase the proliferation, migration, and invasion capacity of HCC cells.” should be corrected to “Furthermore, we demonstrated that STK25 knockdown could decrease the proliferation, migration, and invasion capacity of HCC cells.”

## References

- [1] J. H. Xu, Y. J. Guan, Z. D. Qiu et al., “System analysis of ROS-related genes in the prognosis, immune infiltration, and drug sensitivity in hepatocellular carcinoma,” *Oxidative Medicine and Cellular Longevity*, vol. 2021, Article ID 6485871, 30 pages, 2021.

## Research Article

# Quantitative Proteomics Reveals the Role of Lysine 2-Hydroxyisobutyrylation Pathway Mediated by Tip60

Ning Wang,<sup>1</sup> Yue Jiang,<sup>2,3</sup> Ping Peng,<sup>4</sup> Guobin Liu,<sup>3,5</sup> Shankang Qi ,<sup>3</sup> Kun Liu ,<sup>2</sup> Qi Mei ,<sup>4</sup> and Jian Li<sup>6</sup>

<sup>1</sup>Department of Neurosurgery, The First Affiliated Hospital of Xi'an Jiaotong University, Xi'an 710061, China

<sup>2</sup>School of Mechanical Engineering and Automation, Northeastern University, Shenyang 110819, China

<sup>3</sup>Shanghai Institute of Materia Medica, Chinese Academy of Sciences, Shanghai 201203, China

<sup>4</sup>Department of Oncology, Tongji Hospital, Tongji Medical College, Huazhong University of Science and Technology, Wuhan 430030, China

<sup>5</sup>School of Chinese Materia Medica, Nanjing University of Chinese Medicine, Nanjing 210023, China

<sup>6</sup>Institute of Molecular Medicine and Experimental Immunology, University Clinic of Rheinische Friedrich-Wilhelms-University, Germany

Correspondence should be addressed to Shankang Qi; [qishankang@aliyun.com](mailto:qishankang@aliyun.com), Kun Liu; [kliu@mail.neu.edu.cn](mailto:kliu@mail.neu.edu.cn), and Qi Mei; [qimei@tjh.tjmu.edu.cn](mailto:qimei@tjh.tjmu.edu.cn)

Received 27 October 2021; Accepted 12 January 2022; Published 8 February 2022

Academic Editor: Xiangpan Li

Copyright © 2022 Ning Wang et al. This is an open access article distributed under the Creative Commons Attribution License, which permits unrestricted use, distribution, and reproduction in any medium, provided the original work is properly cited.

Lysine 2-hydroxyisobutyrylation (Khib) is a new type of posttranslational modifications (PTMs) extensively reported on eukaryotic cell histones. It is evolutionarily conserved and participates in diverse important biological processes, such as transcription and cell metabolism. Recently, it has been demonstrated that Khib can be regulated by p300 and Tip60. Although the specific Khib substrates mediated by p300 have been revealed, how Tip60 regulates diverse cellular processes through the Khib pathway and the different roles between Tip60 and p300 in regulating Khib remain largely unknown, which prevents us from understanding how this modification executes its biological functions. In this study, we report the first Khib proteome mediated by Tip60. In total, 3502 unique Khib sites from 1050 proteins were identified. Among them, 536 Khib sites from 406 proteins were present only in Tip60 overexpressing cells and 13 Khib sites increased more than 2-fold in response to Tip60 overexpression, indicating that Tip60 significantly affected global Khib. Notably, only 5 of the 549 Tip60-targeted Khib sites overlapped with the 149 known Khib sites targeted by p300, indicating the different Khib substrate preferences of Tip60 and p300. In addition, the Khib substrates regulated by Tip60 are deeply involved in processes such as nucleic acid metabolism and translation, and some are associated with Parkinson's and Prion diseases. In summary, our research reveals the Khib substrates targeted by Tip60, which elucidates the effect of Tip60 in regulating various cellular processes through the Khib pathway, and proposes novel views into the functional mechanism of Tip60.

## 1. Introduction

Protein posttranslational modifications (PTMs) play crucial roles in multiple biological processes such as transcriptional regulation and signal transduction [1–3]. Many studies have demonstrated that aberrant regulation of PTMs is linked to diverse diseases [4–7]. Lysine 2-hydroxyisobutyrylation (Khib) is a new type of PTMs extensively reported on eukaryotic cell histones and is evolutionarily conserved [8].

Cellular levels of 2-hydroxyisobutyrate, the corresponding short-chain fatty acid precursor of Khib, possibly modify environmental implications on biological processes and the epigenome by the Khib pathway [9, 10]. The chemical structure of Khib is distinctive; thus, it exhibits different characteristics from the well-studied lysine methylation (Kme) and acetylation (Kac) markers. This modification adds the enormous hydrophilic 2-hydroxyisobutyryl groups to the electropositive lysine side chains, thus being able to interfere

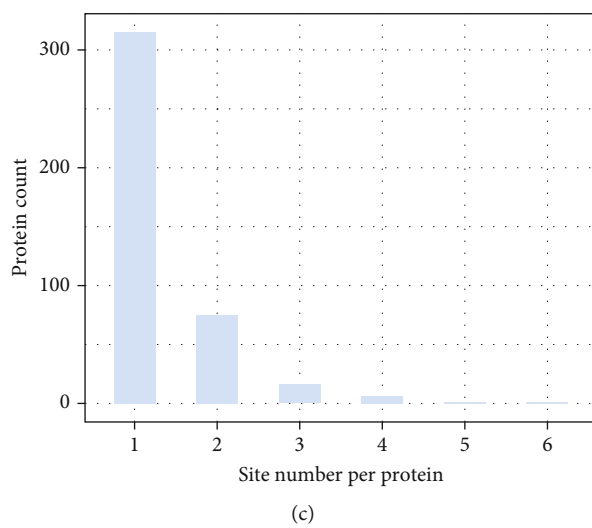
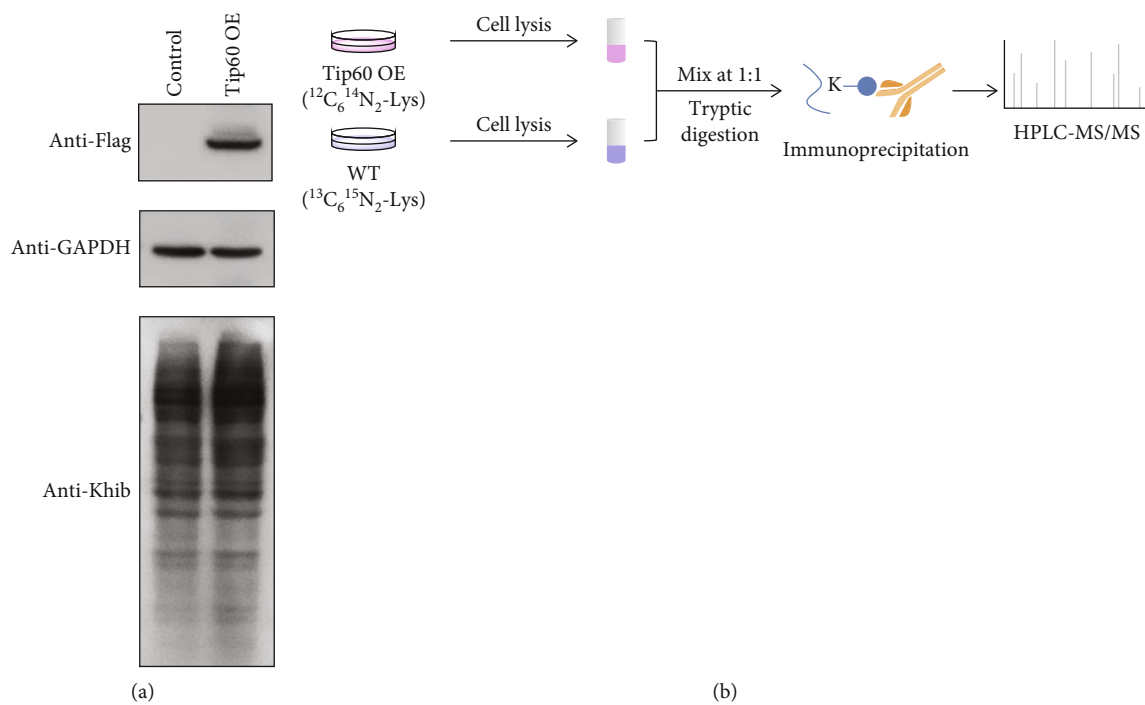


FIGURE 1: Continued.

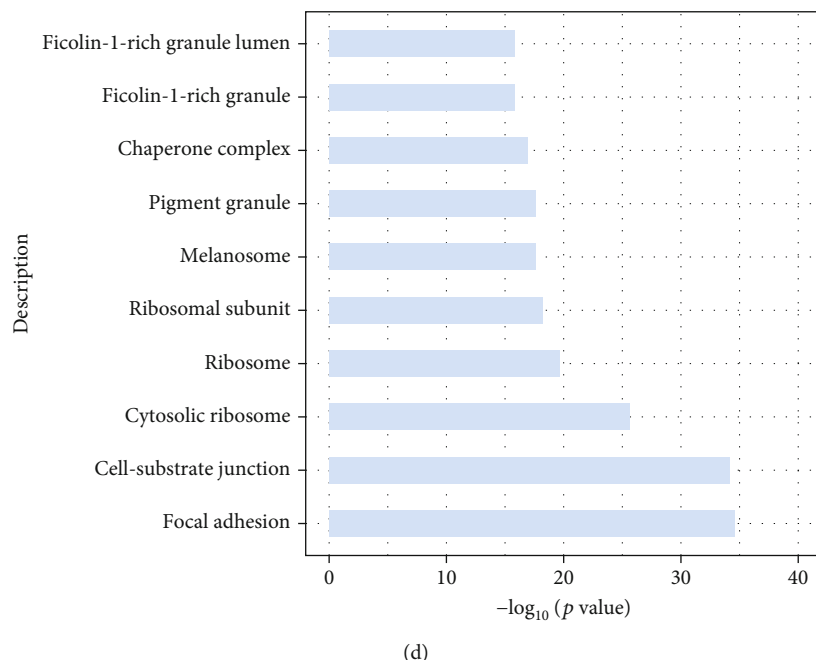


FIGURE 1: Profiling of Khib proteome. (a) Validation of the Khib dynamics in response to Tip60 overexpression. (b) Schematic diagram of the protocol for identifying and quantifying Khib in WT and Tip60 OE cells. (c) Distribution of the amounts of Tip60-targeted Khib sites of each protein. (d) Cellular compartment distribution of Tip60-targeted Khib proteins.

with cofactor binding or bring conformational variations that cause changed turnover and substrate binding. Emerging evidence has shown that Khib has diverse cellular functions, such as transcriptional and metabolic regulation. For example, in colon tumor cells, Khib has been verified to regulate the catalytic activities of glycolytic enzymes [10]. In addition, mutation of H4K8hib (K8A) causes expression level changes in genes associated with carbon transport and carbon metabolism [11].

The levels of lysine acylations in cells are dynamic and modified by the opposite effect of two enzyme families, lysine acetyltransferase (KAT), and lysine deacetylase (KDAC) [12, 13]. For example, H4K8hib is regulated by KDAC Hos3p and Rpd3p in *Saccharomyces cerevisiae*, while HDAC2 and HDAC3 are the main enzymes that erase Khib in mammalian cells [11]. On the other hand, Esa1p in budding yeast and Tip60/p300 in mammalian cells can write Khib to the substrate protein [9]. A quantitative Khib proteomics study revealed that p300 can regulate glycolysis through the Khib on a key glycolytic enzyme ENO1. Interestingly, p300 can selectively catalyze Khib or Kac on distinct protein substrates, thereby mediating different downstream biological processes [10].

Despite the above progress, how Tip60 regulates cellular processes through the Khib pathway and the different roles of Tip60 and p300 in regulating Khib remain largely unknown, which prevents us from understanding how this modification executes its biological functions. Therefore, to reveal the role of the Khib pathway mediated by Tip60, we report a quantitative proteomics study in which candidate Khib substrates regulated by Tip60 were identified.

In our study, the global Khib proteome from wild type (WT) and Tip60 overexpressing (OE) cells was quantified using Stable Isotope Labeling by/with Amino acids in Cell culture (SILAC) and mass spectrometry. In total, we determined 3502 unique Khib sites from 1050 proteins, where 536 Khib sites from 406 proteins were only present in Tip60 overexpressing cells and 13 Khib sites increased more than 2-fold in response to Tip60 overexpression, indicating that Tip60 significantly affected global Khib. Interestingly, only 5 out of the 549 Khib sites regulated by Tip60 overlapped with 149 previously reported p300-regulated Khib sites, suggesting that Tip60 and p300 have a different substrate preference for Khib. Pathway analysis of Tip60-targeted Khib substrates revealed significant roles of Tip60 in mediating nucleic acid metabolism and translation and Parkinson's and Prion diseases, which suggests the potential connection of Tip60 to a variety of biological processes and diseases by the regulation of Khib.

## 2. Methods

**2.1. Materials.** Tip60 was cloned into pcDNA3.0 with a Flag tag. Pan-Khib antibody (PTM Biolabs, China, catalog no. PTM-801, PTM-1204), PARK7 antibody (Cell Signaling Technology, catalog no. 12255), HEK293 cell line (National Collection of Authenticated Cell Cultures, catalog no. GNHu 43), L-Lysine HCl (Lys0) (J&K, catalog no. 611898), and  $^{13}\text{C}_6$   $^{14}\text{N}_2$ -L-Lysine (Lys8) (Silantes, catalog no. 211604102) were purchased and used without further authentication. Trypsin was obtained from Promega (USA). C18 ZipTips were purchased from Millipore Corporation (USA).

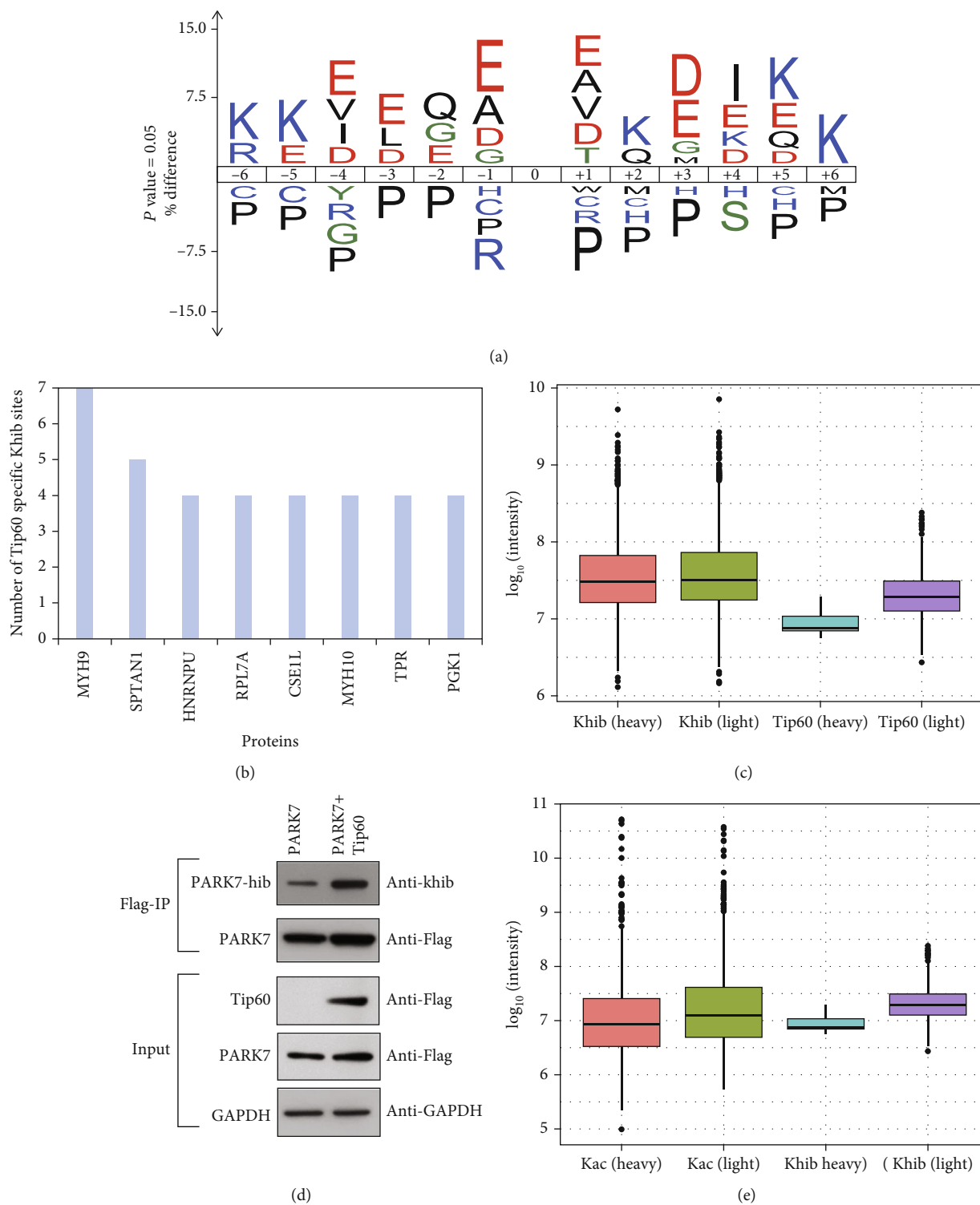


FIGURE 2: Continued.



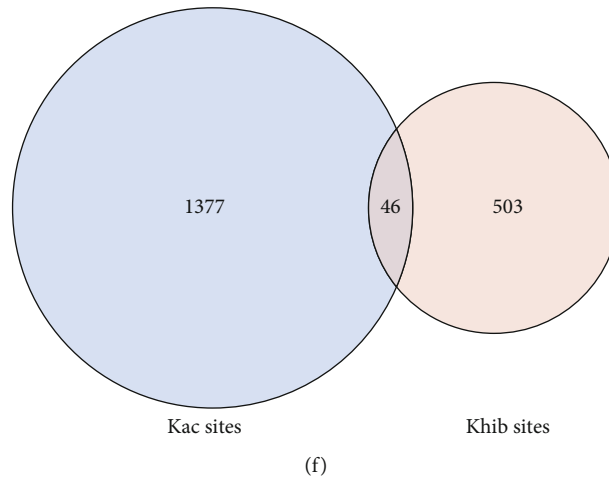


FIGURE 2: Characteristics of the Tip60-targeted Khib proteome. (a) Consensus sequence logo plots illustrate a representative sequence of Tip60-targeted Khib sites. (b) Distribution of amounts of Tip60-targeted Khib sites on various enzymes. (c) Abundance distribution of global and Tip60-targeted Khib peptides. (d) Western blot validation of the Khib dynamics on PARK7 in response to Tip60 OE. (e) Abundance distribution of Tip60-targeted Kac and Khib peptides. (f) Overlaps between Tip60-targeted Kac and Khib sites.

**2.2. Stable Isotope Labeling of Cells and Transfections.** HEK293 cells were cultured in SILAC DMEM containing 10% FBS and isotopically enriched forms of “heavy” ( $^{13}\text{C}_6$   $^{15}\text{N}_2$ -L-Lysine) or “light” ( $^{12}\text{C}_6$   $^{14}\text{N}_2$ -L-Lysine) lysine (100 mg/L). Before being collected, cells were cultured for more than seven generations and analyzed by LC-MS/MS to ensure complete incorporation of the isotopic label (labeling efficiency higher than 98%). Transient overexpression transfection was carried out with Lipofectamine 2000 (Invitrogen) essentially followed by product manuals. HEK293 cells were grown in DMEM (containing 10% FBS, 1% P/S) at 37°C in a 5%  $\text{CO}_2$  incubator.

**2.3. Protein Extraction and Trypsin Digestion.** A total of  $2 \times 10^7$  cells were washed with ice-cold phosphate-buffered saline (PBS) twice. Then, the cells were lysed in buffer (8 M urea, 3  $\mu\text{M}$  Trichostatin A, 2 mM EDTA, 5 mM DTT, 50 mM Nicotinamide, and 1% Protease inhibitor cocktail (Roche, Switzerland)) and sonicated in a ultrasonic processor (JY96-IIN, Jingxin Technology) on ice. The lysate supernatant was collected after centrifugation (16,100  $\times$  g) at 4°C for 15 min, and equal volumes of proteins from Tip60 OE HEK293 and WT cells were mixed.

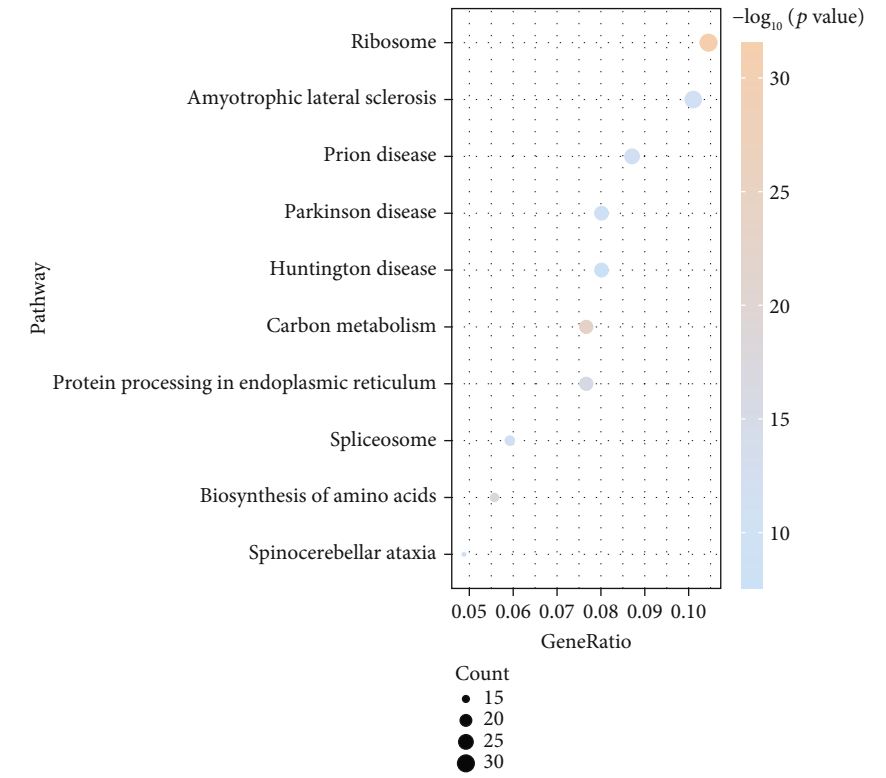
The 2 mg mixed proteins were subjected to reduction by reacting with 10 mM DTT at 37°C for 1 h, followed by alkylation using 20 mM iodoacetamide at 25°C for 45 min in the dark, and the reaction was ended using 20 mM cysteine. The urea concentration was reduced to 2 M using 100 mM  $\text{NH}_4\text{HCO}_3$ . The first digestion was performed by adding trypsin at 1/50 of the weight of the substrate overnight at 37°C. The generated proteolytic peptides were dried in SpeedVac (ThermoFisher Scientific).

**2.4. Immunoaffinity Enrichment.** Khib peptides were immunoaffinity enriched as previously described [9]. Briefly, the peptides obtained from above were resuspended in NTEN buffer (100 mM NaCl, 50 mM Tris-HCl, 1 mM EDTA, and

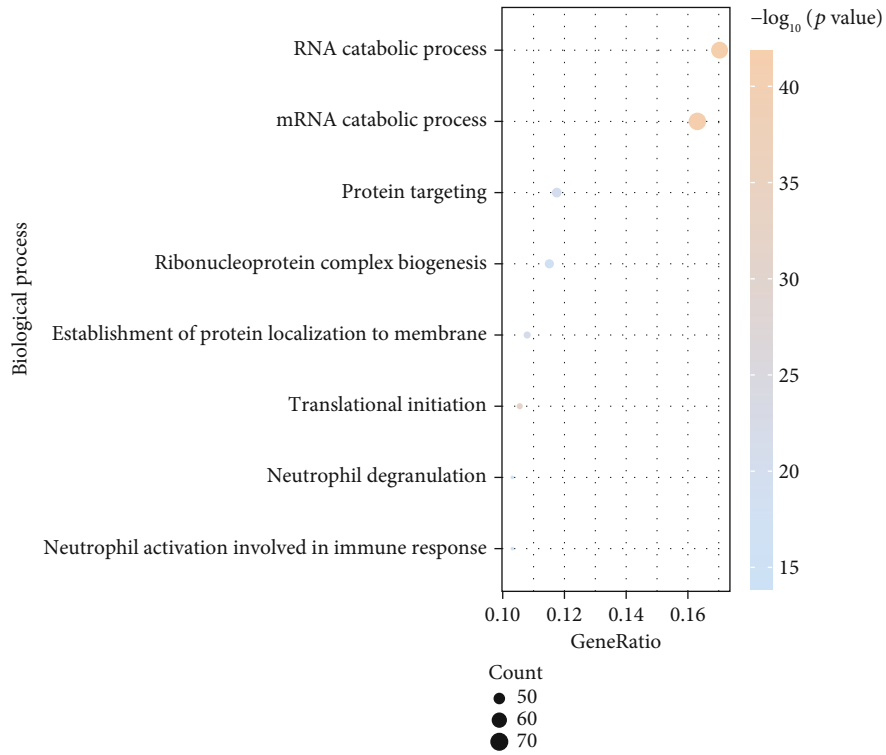
0.5% Nonidet P-40) and incubated with 30  $\mu\text{L}$  of pan anti-Khib beads (PTM Biolabs, China) with tender shaking overnight at 4°C. The beads were washed four times with NTEN buffer and twice with  $\text{ddH}_2\text{O}$ . Peptides bonded on the beads were eluted by 0.1% trifluoroacetic acid, vacuum-dried and desalted using C18 ZipTip (Millipore Corporation, USA).

**2.5. LC-MS/MS Analysis.** The Khib peptides collected above were analyzed on a Q-Exactive mass spectrometer (ThermoFisher Scientific, MA) connected to an EASY-nLC 1000 UHPLC (ThermoFisher Scientific, MA). Peptides in 0.1% formic acid (FA) solution were separated on a reversed-phase HPLC column (75  $\mu\text{m}$  inner diameter with 10 cm length), which was filled with Repronil 100 C18 resin (3  $\mu\text{m}$  particle size). The HPLC mobile phase consisted of a gradient of 2–90% buffer B (0.1% (v/v) FA in 90% acetonitrile) in buffer A (0.1% (v/v) FA in water). The samples were eluted at a velocity of 200 nL/min over 60 min. The mass spectrometer was worked in data-dependent acquisition (DDA) mode that alternated between once full mass scan at 70,000 mass resolution; then, the top 15 most intense precursor ions were implemented with 25 second-dynamic exclusions. MS/MS fragmentation was carried out with the top 15 most intense precursor ions using higher-energy collision dissociation (HCD), with a normalized collision energy (NCE) of 27%, and then analyzed with 17,500 resolution in the Orbitrap. The AGC numbers were 3e6 and 1e5 for MS1 and MS2, respectively. The isolation window was set to 1.5 m/z.

**2.6. Database Search and Data Filter Criteria.** The experimental MS/MS results were searched with the Swiss-Prot human database (20368 entries, <https://www.uniprot.org>) using MaxQuant (v.1.6.15.0) and the integrated Andromeda search engine. Enzyme specificity was set as full cleavage by trypsin, and two missing cleavages were allowed at most. Acetylation on protein N-terminal, oxidation on methionine, and 2-hydroxyisobutyrylation on lysine were set as



(a)



(b)

FIGURE 3: Continued.

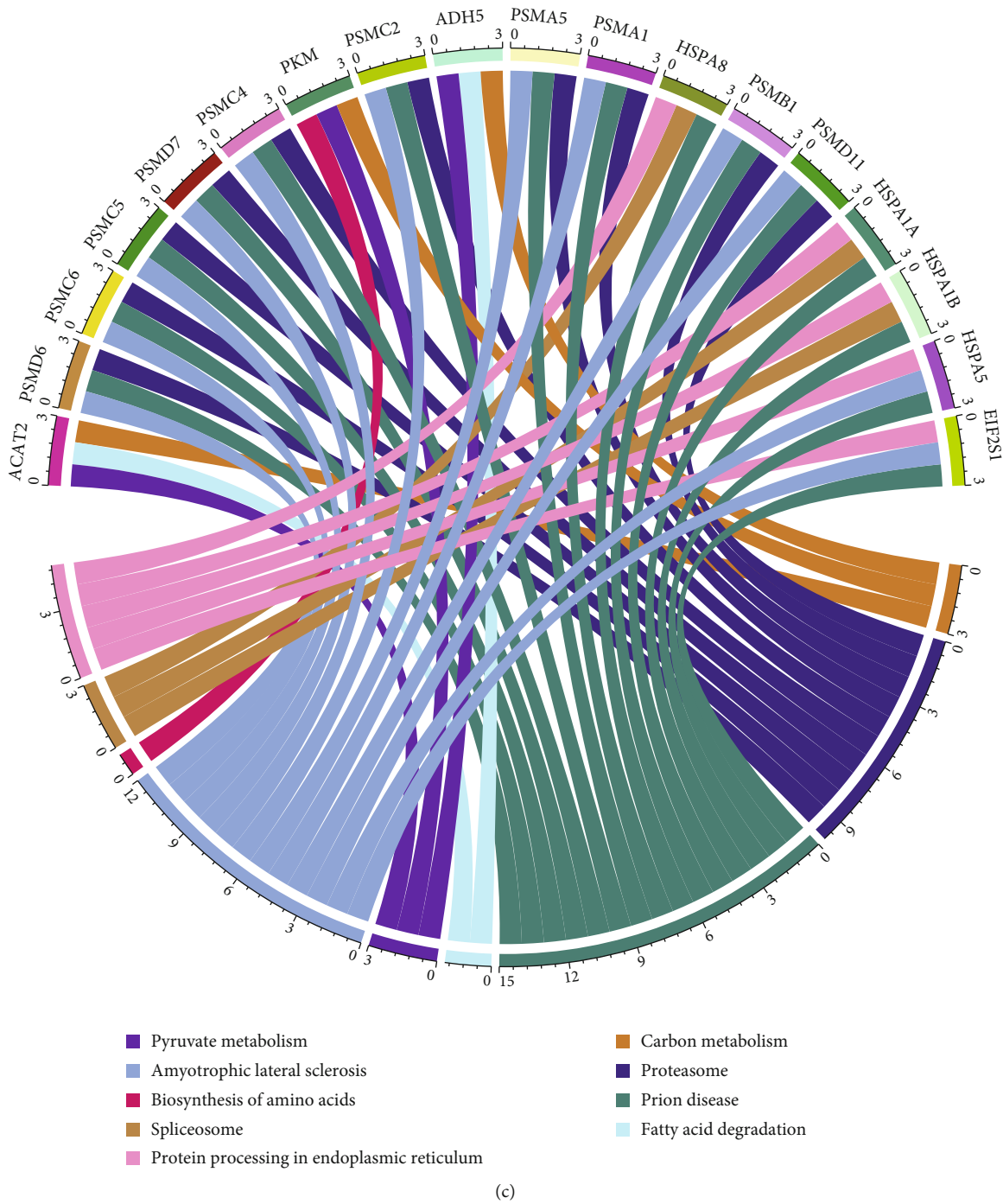


FIGURE 3: Pathway and biological process annotations enriched with the Tip60-targeted Khib proteome. (a) Representative pathway enriched with the Tip60-targeted Khib proteome. (b) GO chord graph shows that Tip60-targeted substrates are involved in multiple pathways. (c) Representative biological process annotations enriched with the Tip60-targeted Khib proteome.

dynamic modifications. Carbamidomethylation on cysteine was set as a fixed modification. The approximated FDR thresholds of modification sites, peptides, and proteins were set to 1%, and the modified peptides with PTM score of more than 40 were chosen for additional bioinformatics analysis. The quality of 100 randomly selected MS/MS spectra of Khib peptides and additional 40 randomly selected

MS/MS spectra of Tip60-mediated Khib peptides were manually checked.

**2.7. Bioinformatics Analysis.** Pathway analysis was carried out with a hypergeometric test in the clusterProfiler package in R [14]. The protein-protein interaction network of Tip60-targeted Khib substrates was established based on the

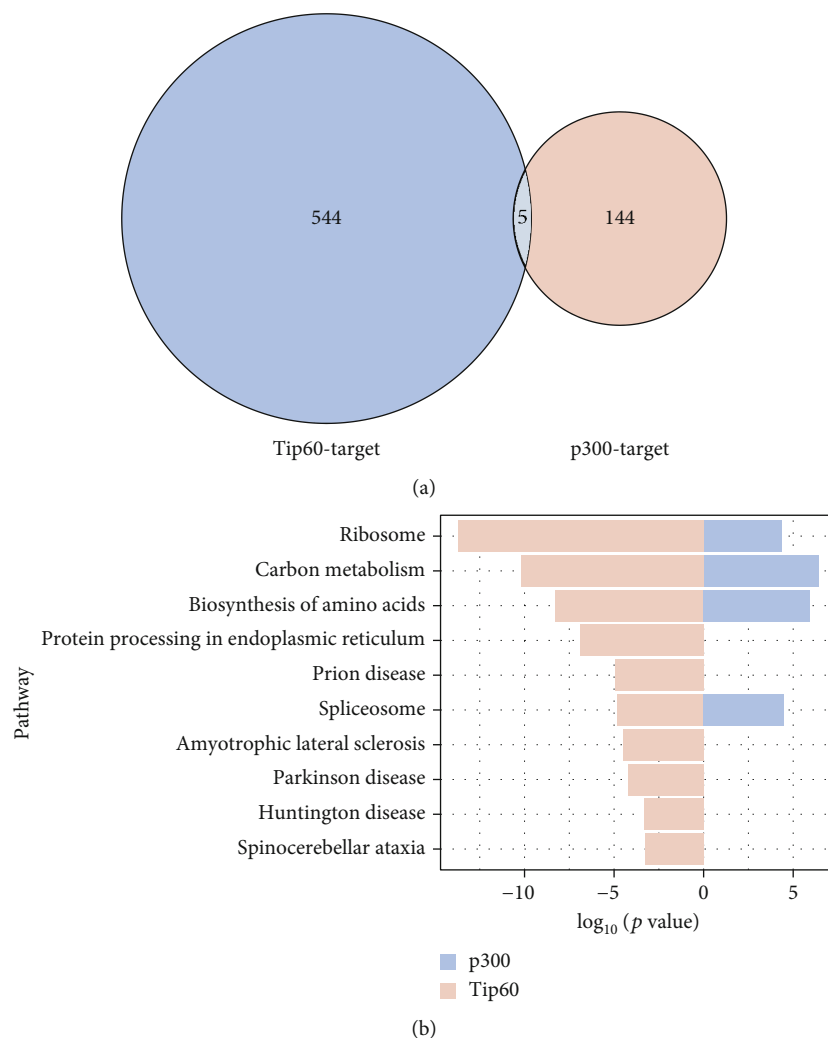


FIGURE 4: Tip60 and P300 regulate different Khib substrates. (a) Overlap between Tip60-targeted Khib and p300-targeted Khib. (b) Bar graphs show representative pathways enriched with p300- and Tip60- targeted Khib proteomes.

STRING database (v11, <http://www.string-db.org/>) [15] and visualized in Cytoscape (v.3.8.2) [16].

### 3. Results

**3.1. Characterization of the Khib Proteome in Response to Tip60 OE.** Given that Tip60 can catalyze Khib reactions, we sought to identify the candidate Khib substrates regulated by Tip60. Indeed, overexpression of Tip60 in HEK293 cells substantially increased Khib levels globally (Figure 1(a)), verifying the significance of Tip60 in regulating Khib modification on a variety of proteins. To determine the dynamics of Khib sites in response to Tip60, we quantified a global Khib proteome between WT and Tip60 OE cells using SILAC and mass spectrometry (Figure 1(b) and Figure S1). Tip60 OE cells and WT HEK293 cells were metabolically labeled with “light” lysine ( $^{12}\text{C}_6^{14}\text{N}_2\text{-Lys}$ ) and “heavy” lysine ( $^{13}\text{C}_6^{15}\text{N}_2\text{-Lys}$ ), respectively (Figure 1(b)). Equal volumes of proteins from “light” and “heavy” cell lysates were mixed and digested with trypsin. Then, the Khib-

containing peptides were captured with anti-Khib antibody and identified by HPLC-MS/MS. The mass data were searched by MaxQuant (v.1.6.15.0) with a total FDR of less than 1%. To enhance the credibility of the identified Khib peptides, we deleted those peptides with scores lower than 40 and localization probability lower than 0.75. In addition, the proteins in the SILAC sample were quantified, and the ratios (WT to OE) of all quantifiable Khib sites were normalized by quantified protein expression level.

In total, we obtained 3502 unique Khib sites from 1050 proteins, where 536 Khib sites were only detected in Tip60 OE cells and the abundance of 13 Khib sites increased more than 2-fold ( $-\log_2(\text{WT/OE}) > 1$ ) in response to Tip60 OE (Table S1). Among these potential Tip60-targeted Khib proteins, 315 (76%) had a single Tip60-targeted Khib site, while the others contained 2-7 Tip60-targeted Khib sites (Figure 1(c) and Table S1).

To describe the subcellular location of Tip60-targeted Khib proteins, we conducted cellular component analysis

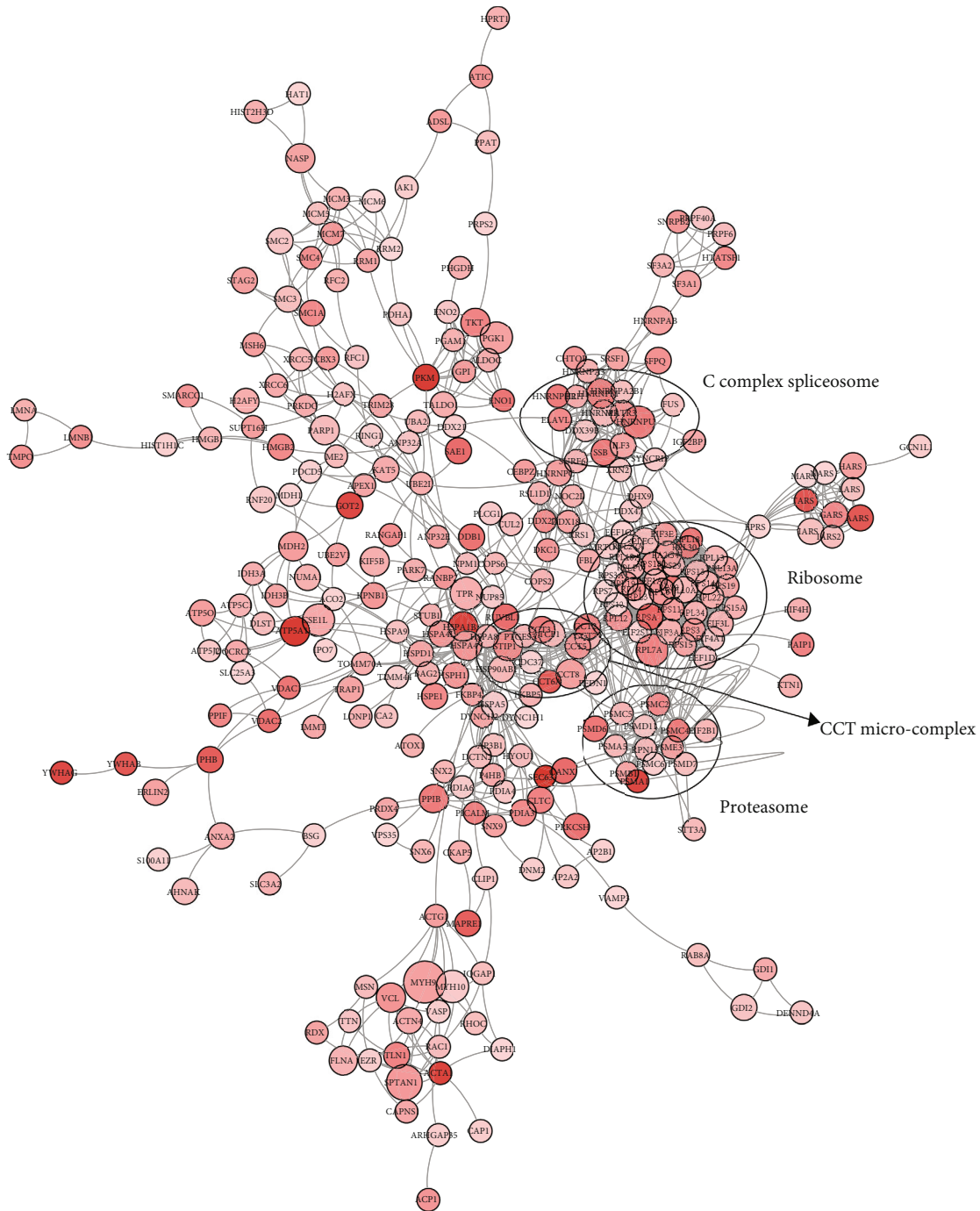


FIGURE 5: Interaction network of Tip60-targeted Khib substrates based on the STRING database (v11). The network is visualized in Cytoscape (v.3.2.1). A larger protein node represents more Khib sites. Darker color represents higher scores.

for Tip60-targeted Khib proteins by Gene Ontology (GO) databases. A significant number of Tip60-targeted Khib proteins were annotated in focal adhesion, cell-substrate junction, and cytosolic ribosome (Figure 1(d)). The diverse distribution of Tip60-targeted Khib proteins suggests that the main functions of the Tip60-mediated Khib pathway may be widely present in different subcellular compartments.

**3.2. Quantitative Analysis of the Tip60-Targeted Khib Proteome.** To explore whether Tip60-targeted Khib peptides have common sequence motifs, we used IceLogo to compare the amino-acid sequences around Khib sites and human background sequences. The results showed that the electro-negative amino acid (glutamic acid) was enriched at many positions, the electropositive amino acid (lysine) was enriched at the -6, -5, +2, +5, and +6 positions, and proline

TABLE 1: Tip60-targeted Khib sites on key residues that participate in cofactor/substrate binding, protein interactions, and cancer biomarkers.

| Gene name | Site | Function                                   |
|-----------|------|--|
| PKM       | 207  | ATP-binding site                           |
| PGK1      | 220  | ATP-binding site                           |
| FDPS      | 123  | Isopentenyl diphosphate binding site       |
| HMGCS1    | 46   | Coenzyme A binding site                    |
| LRPPRC    | 1357 | RNA-binding site                           |
| PLEC      | 3505 | Ovarian cancer biomarker                   |
| ADH5      | 107  | Breast cancer biomarker                    |
| PARK7     | 148  | Lung cancer biomarker                      |
| HSP90AB1  | 69   | Interaction with TP53, BIRC2, NR3C1        |
| LMNA      | 78   | Interaction with MLIP; Spitzoid tumor gene |

was depleted at most positions (Figure 2(a)). The unique flanking sequence features of Tip60-targeted Khib peptides indicate that Tip60 may have a unique substrate preference for Khib. Consistently, although many proteins contain more than 10 Khib sites, only one or a few Khib sites were mediated by Tip60 (Table S1). For example, 20 Khib sites were identified on heterogeneous nuclear ribonucleoprotein U (HNRNPU); however, there were only 4 Tip60-targeted sites (Figure 2(b) and Table S1).

Next, to investigate whether the Tip60-targeted Khib peptides are enriched from high-abundant peptides, we compared the abundance distribution of global Khib peptides with Tip60-targeted Khib peptides. The results show that the abundance of Tip60-targeted Khib peptides is distributed by two orders of magnitude, and that the median abundance of the Tip60-targeted Khib peptides is lower than that of the global Khib peptides, indicating that the screening is not biased toward high-abundance proteins (Figure 2(c) and Table S1).

Among the Tip60-targeted Khib substrates, K148hib on Parkinson disease protein 7 (PARK7) was identified in Tip60 OE cells, while it could not be detected in WT cells, suggesting that the function of PARK7 may be affected at the posttranslational level, potentially by Tip60-targeted Khib. To confirm the mass data, we performed a western blot verification. Flag-tagged PARK7 in combination with either the vector or Tip60 plasmids was cotransfected into 293T cells. After incubation, the immunoprecipitated Flag-tagged PARK7 was analyzed using anti-Flag and anti-Khib antibodies. The results showed that overexpression of Tip60 obviously increased Khib levels on PARK7, while there was almost no change in PARK7 expression (Figure 2(d)), which confirmed our quantitative Khib proteome results.

Because Tip60 is a well-known lysine acetyltransferase, we next compared Tip60-mediated Kac and Khib sites. As expected, Tip60 OE increased the abundance of Kac (Figure 2(e)). Interestingly, only 46 out of the 549 Tip60-mediated Khib sites overlapped with the Tip60-mediated Kac sites (Figure 2(f) and Table S1, Table S2), indicating that Tip60 has different substrate preferences for Khib and

Kac. This result is not surprising because a similar phenomenon was also observed for p300-mediated Khib and Kac sites [10].

**3.3. Cellular Pathway Analysis and Functional Annotation of the Tip60-Targeted Khib Proteome.** To explore the possible cellular pathways and biological functions of Tip60-targeted Khib substrates, we employed Kyoto Encyclopedia of Genes and Genomes (KEGG) and GO databases for enrichment analysis. Our results showed that a total of 30 Tip60-targeted Khib proteins were highly correlated with ribosomal pathways (adjusted  $p = 4.76E - 12$ ), while 16 and 22 Tip60-targeted Khib proteins were deeply involved in the biosynthesis of amino acids (adjusted  $p = 2.98E - 7$ ) and carbon metabolism pathways (adjusted  $p = 7.10E - 9$ ), respectively (Figure 3(a)). Interestingly, some Tip60-targeted Khib proteins are involved in multiple pathways. For example, proteasome subunit alpha type-1 (PSMA1), 26S proteasome regulatory subunit 7 (PSMC2), 26S proteasome non-ATPase regulatory subunit 7 (PSMD7), 26S proteasome regulatory subunit 8 (PSMC5), and the other six proteasome complex members are involved in three pathways, including proteasome (adjusted  $p = 1.53E - 05$ ), Parkinson disease (adjusted  $p = 1.16E - 03$ ), Prion disease (adjusted  $p = 3.74E - 04$ ), and amyotrophic lateral sclerosis (adjusted  $p = 6.80E - 04$ ) (Figure 3(b)).

In addition, protein function annotation revealed that the Tip60-targeted Khib proteins were significantly enriched in the processes related to nucleic acid metabolism and translation, such as RNA catabolic process (adjusted  $p = 4.54E - 39$ ), mRNA catabolic process (adjusted  $p = 4.54E - 39$ ), and translational initiation (adjusted  $p = 5.08E - 29$ ) (Figure 3(c)), suggesting that Tip60 may influence the biosynthesis process of certain proteins by mediating Khib. Additionally, cotranslational protein targeting to membrane (adjusted  $p = 1.17E - 25$ ) and SRP-dependent cotranslational protein targeting to membrane (adjusted  $p = 5.04E - 25$ ) were enriched, implying the potential role of Tip60-mediated Khib in the cotranslational translocation pathway.

**3.4. The Differences in Khib Substrates Regulated by p300 and Tip60.** A previous study identified p300 as a Khib “writer” that can regulate glycolysis through the Khib pathway in response to nutritional cues [10]. Considering the Khib-transferase activity of Tip60, does Tip60-mediated Khib have unique roles? To this end, we next sought to compare the Khib substrates regulated by p300 and Tip60 and investigate the differences in related pathways and biological processes.

Strikingly, only 5 out of the 549 Khib sites regulated by Tip60 coincided with the 149 Khib sites regulated by p300 (Figure 4(a)). Although the Khib levels in different cell lines may be different, the lower coincidence between Tip60- and p300-targeted Khib suggests that Tip60 and p300 have diverse substrate selectivity to Khib and may differentially regulate downstream biological processes through the Khib pathway. In support of this notion, although both Tip60- and p300-targeted Khib substrates are involved in several

pathways such as ribosome (adjusted  $p = 4.76E - 12$ ), biosynthesis of amino acids (adjusted  $p = 2.98E - 07$ ), and carbon metabolism (adjusted  $p = 7.10E - 09$ ), Tip60-mediated Khib substrates are uniquely enriched in protein processing in endoplasmic reticulum (adjusted  $p = 6.10E - 06$ ), Prion disease (adjusted  $p = 3.74E - 04$ ), Parkinson disease (adjusted  $p = 1.16E - 03$ ), and amyotrophic lateral sclerosis (adjusted  $p = 6.80E - 04$ ) (Figure 4(b)).

**3.5. Interaction Network of Tip60-Targeted Khib Substrates.** Numerous proteins act by binding to partners and the deficiency of particular protein-protein interactions (PPIs) results in a variety of diseases [17–19]. PTMs can manage PPIs due to the ability to recruit binding proteins. Therefore, we next visualized the interaction network of Tip60-targeted Khib proteins based on the STRING database [15]. The network indicated that Tip60-targeted Khib proteins are highly connected. Some protein nodes have plural Tip60-targeted Khib sites and represent the subcenters of the protein interaction network mediated by Tip60 (Figure 5). The undulation of these Khib sites mediated by Tip60 may result in great changes in the PPI network and dysfunction of the complex.

Our data reveal several protein complexes that are significantly regulated by Tip60, including Nop56p-associated pre-rRNA complex (adjusted  $p = 1.85E - 42$ ), ribosome (adjusted  $p = 1.95E - 35$ ), CCT microcomplex (adjusted  $p = 6.71E - 13$ ), and C complex spliceosome (adjusted  $p = 8.15E - 10$ ). The Nop56p-associated pre-rRNA complex affects 60S subunit biogenesis in the early-to-mid stages, and the C complex spliceosome plays a vital role in eliminating noncoding introns from nascent pre-mRNAs [20, 21]. Khib on most components of these complexes was only detected in Tip60 OE cells. In addition, the CCT microcomplex is highly involved in protein folding, assembly, and transportation [22, 23], and Khib on all the components of this complex could only be detected in Tip60 OE cells. These results imply the potential roles of Tip60 in protein folding, assembly, and transport processes by regulating Khib.

**3.6. Possible Impact of Tip60 OE on Khib Substrate Functions.** To explore the possible impact of Tip60 OE on the function of Khib substrates, we annotated the Tip60-targeted Khib site based on the UniProt database (<http://www.uniprot.org>). Interestingly, we found that 5 Khib sites are key positions for binding to substrates or cofactors (Table 1). For example, pyruvate kinase (PKM), the rate-limiting enzyme in the glycolysis pathway, catalyzes the transfer of the phosphoryl group from phosphoenolpyruvate (PEP) to ADP and generates ATP [24, 25]. We identified the Tip60-targeted Khib sites at PKM K207 and PGK1 K220, which are the key residues for ATP binding. Hydroxymethylglutaryl-CoA synthase (HMGCS1) catalyzes the condensation of acetyl-CoA and acetoacetyl-CoA to formulate HMG-CoA, and K46 of HMGCS1 is a key residue for coenzyme A binding [26, 27]. Khib on these residues will most likely interrupt substrate/cofactor binding and introduce harmful effects on protein functions.

In addition, some Tip60-targeted Khib sites are located at positions that are important for PPIs. For example, heat shock protein HSP 90- $\beta$  (HSP90AB1) is involved in many important biological processes and contributes to the structural maintenance, ripeness, and proper regulation of particular target proteins [28, 29]. K69 of HSP90AB1 is the key site for interacting with TP53, BIRC2, and NR3C1. Tip60-mediated Khib at this position may affect the interaction of HSP90AB1 with its binding partners.

Moreover, several Tip60-targeted Khib were identified on cancer biomarkers, such as plectin (PLEC, related to ovarian cancer), alcohol dehydrogenase class-3 (ADH5, related to breast cancer), and PARK7 (related to lung cancer), which therefore links Tip60 and the Khib pathway to cancer.

## 4. Discussion

Tip60 and p300 have been identified as Khib “writers,” and p300-catalyzed Khib has been revealed to regulate cellular glucose metabolism [9, 10]. However, Tip60-targeted Khib substrates have not yet been fully studied, hindering our understanding of Khib functions mediated by Tip60. In this study, a quantitative proteomics study was performed and represents the first comprehensive analysis of Khib substrates in response to Tip60 OE. A total of 3502 Khib sites from 1050 proteins were determined in human cells, of which 536 Khib sites from 406 proteins were only detected in Tip60 OE cells, and the abundance of 13 sites in 13 proteins increased more than 2-fold in response to Tip60 OE. These proteins were designated as potential Tip60 substrates. Furthermore, the Tip60-targeted Khib distributes in diverse subcellular compartments, suggesting that the functions of the Tip60-mediated Khib pathway are likely widespread.

We found that some Tip60-targeted Khib substrates are highly correlated with ribosomal pathways, such as mRNA translation and protein cofolding. In addition, Khib sites in all the components of the CCT microcomplex, a complex that is highly involved in protein folding, assembly, and transportation, could only be detected in Tip60 OE cells. This is consistent with the roles of Tip60 in regulating transcription and implies other cellular processes related to Khib.

Emerging evidence has demonstrated that Tip60 and p300 play different roles in diverse cellular processes by differentially regulating PTMs [30]. We also revealed that Tip60- and p300-targeted Khib sites are quite different. Given that the Khib substrates regulated by Tip60 and p300 are associated with different biological functions and enriched in different pathways, this study provides new insights into the different regulatory mechanisms by which Tip60 and p300 exert their functions.

As a widely known acetyltransferase, Tip60 regulates other acylations as well. For example, in a recent study, Tip60 accurately controlled spindle positioning during mitosis by mediating crotonylation at Lys66 on EB1 [31]. Interestingly, the Lys66 site can also be acetylated by Tip60 *in vitro*, which suggests that Tip60 regulates its target

substrates and corresponding biological processes in a complex way.

Moreover, 23 and 25 Tip60-targeted Khib proteins are involved in the Parkinson's disease and Prion disease pathways, respectively, and 43 Tip60-targeted Khib proteins are connected with cancer genes or cancer biomarkers, which therefore link the Tip60-targeted Khib pathway to diseases.

### Data Availability

The mass spectrometry proteomics data have been deposited to the ProteomeXchange Consortium via the PRIDE partner repository with the dataset identifier PXD029297.

### Conflicts of Interest

The authors declare that there is no conflict of interest regarding the publication of this paper.

### Authors' Contributions

Qi Mei, Kun Liu, and Shankang Qi designed the study and are responsible for the supervision. Ning Wang, Yue Jiang, and Shankang Qi performed the experiments, and Guobin Liu performed bioinformatical analysis. Ping Peng and Jian Li were involved in data analysis. Yue Jiang and Ning Wang wrote the manuscript; Qi Mei, Kun Liu, and Shankang Qi revised the manuscript. All authors read and approved the final manuscript. Ning Wang, Yue Jiang, and Ping Peng contributed equally to this work.

### Acknowledgments

This work was financially supported by grants from the Fundamental Research Funds for the Central Universities of the Ministry of Education N2003010 (Kun Liu) and N2103027 (Kun Liu).

### Supplementary Materials

Tables S1 and S2 are the complete lists of identified Khib and Kac sites in WT and Tip60 OE cells. Supplementary Materials Figure S1 is the representative MS2 spectra of the Tip60-targeted Khib peptides. Table S1: complete list of identified Khib sites in WT and Tip60 OE cells. Table S2: complete list of identified Kac sites in WT and Tip60 OE cells. Figure S1: the representative MS2 spectra of the Tip60-targeted Khib peptides, including K147hib of EF1G, K115hib of KPYM, K416hib of SEC63, and K624hib of HS90B. (*Supplementary Materials*)

### References



- [1] H. Huang, S. Lin, B. A. Garcia, and Y. Zhao, "Quantitative proteomic analysis of histone modifications," *Chemical Reviews*, vol. 115, no. 6, pp. 2376–2418, 2015.
- [2] K. B. Koronowski, C. M. Greco, H. Huang et al., "Ketogenesis impact on liver metabolism revealed by proteomics of lysine  $\beta$ -hydroxybutyrylation," *Cell Reports*, vol. 36, no. 5, article 109487, 2021.
- [3] H. Huang, D. Zhang, Y. Weng et al., "The regulatory enzymes and protein substrates for the lysine  $\beta$ -hydroxybutyrylation pathway," *Science Advances*, vol. 7, no. 9, 2021.
- [4] M. A. Dawson and T. Kouzarides, "Cancer epigenetics: from mechanism to therapy," *Cell*, vol. 150, no. 1, pp. 12–27, 2012.
- [5] K. Helin and D. Dhanak, "Chromatin proteins and modifications as drug targets," *Nature*, vol. 502, no. 7472, pp. 480–488, 2013.
- [6] S. B. Baylin and P. A. Jones, "A decade of exploring the cancer epigenome - biological and translational implications," *Nature Reviews Cancer*, vol. 11, no. 10, pp. 726–734, 2011.
- [7] G. H. Eom and H. Kook, "Posttranslational modifications of histone deacetylases: implications for cardiovascular diseases," *Pharmacology & Therapeutics*, vol. 143, no. 2, pp. 168–180, 2014.
- [8] L. Dai, C. Peng, E. Montellier et al., "Lysine 2-hydroxyisobutyrylation is a widely distributed active histone mark," *Nature Chemical Biology*, vol. 10, no. 5, pp. 365–370, 2014.
- [9] H. Huang, Z. Luo, S. Qi et al., "Landscape of the regulatory elements for lysine 2-hydroxyisobutyrylation pathway," *Cell Research*, vol. 28, no. 1, pp. 111–125, 2018.
- [10] H. Huang, S. Tang, M. Ji et al., "p300-mediated lysine 2-hydroxyisobutyrylation regulates glycolysis," *Molecular Cell*, vol. 70, no. 5, p. 984, 2018.
- [11] J. Huang, Z. Luo, W. Ying et al., "2-Hydroxyisobutyrylation on histone H4K8 is regulated by glucose homeostasis in *Saccharomyces cerevisiae*," *Proceedings of the National Academy of Sciences of the United States of America*, vol. 114, no. 33, pp. 8782–8787, 2017.
- [12] Z. Wang, C. Zang, K. Cui et al., "Genome-wide mapping of HATs and HDACs reveals distinct functions in active and inactive genes," *Cell*, vol. 138, no. 5, pp. 1019–1031, 2009.
- [13] R. N. Saha and K. Pahan, "HATs and HDACs in neurodegeneration: a tale of disconcerted acetylation homeostasis," *Cell Death and Differentiation*, vol. 13, no. 4, pp. 539–550, 2006.
- [14] G. Yu, L. G. Wang, Y. Han, and Q. Y. He, "clusterProfiler: an R package for comparing biological themes among gene clusters," *OMICS*, vol. 16, no. 5, pp. 284–287, 2012.
- [15] D. Szklarczyk, A. L. Gable, D. Lyon et al., "STRING v11: protein-protein association networks with increased coverage, supporting functional discovery in genome-wide experimental datasets," *Nucleic Acids Research*, vol. 47, no. D1, pp. D607–D613, 2019.
- [16] P. Shannon, A. Markiel, O. Ozier et al., "Cytoscape: a software environment for integrated models of biomolecular interaction networks," *Genome Research*, vol. 13, no. 11, pp. 2498–2504, 2003.
- [17] M. Vidal, M. E. Cusick, and A. L. Barabasi, "Interactome networks and human disease," *Cell*, vol. 144, no. 6, pp. 986–998, 2011.
- [18] D. E. Scott, A. R. Bayly, C. Abell, and J. Skidmore, "Small molecules, big targets: drug discovery faces the protein-protein interaction challenge," *Nature Review Drug Discovery*, vol. 15, no. 8, pp. 533–550, 2016.
- [19] A. G. Cochran, "Antagonists of protein-protein interactions," *Chemistry & Biology*, vol. 7, no. 4, pp. R85–R94, 2000.
- [20] T. Hayano, M. Yanagida, Y. Yamauchi, T. Shinkawa, T. Isobe, and N. Takahashi, "Proteomic analysis of human Nop56p-associated pre-ribosomal ribonucleoprotein complexes. Possible link between Nop56p and the nucleolar protein treacle



- responsible for Treacher Collins syndrome,” *The Journal of Biological Chemistry*, vol. 278, no. 36, pp. 34309–34319, 2003.
- [21] J. Ilagan, P. Yuh, R. J. Chalkley, A. L. Burlingame, and M. S. Jurica, “The role of exon sequences in C complex spliceosome structure,” *Journal of Molecular Biology*, vol. 394, no. 2, pp. 363–375, 2009.
- [22] C. Dekker, P. C. Stirling, E. A. McCormack et al., “The interaction network of the chaperonin CCT,” *The EMBO Journal*, vol. 27, no. 13, pp. 1827–1839, 2008.
- [23] J. Berger, S. Berger, M. Li et al., “In Vivo Function of the Chaperonin TRiC in  $\alpha$ -Actin Folding during Sarcomere Assembly,” *Cell Reports*, vol. 22, no. 2, pp. 313–322, 2018.
- [24] J. Lee, H. K. Kim, Y. M. Han, and J. Kim, “Pyruvate kinase isozyme type M2 (PKM2) interacts and cooperates with Oct-4 in regulating transcription,” *The International Journal of Biochemistry & Cell Biology*, vol. 40, no. 5, pp. 1043–1054, 2008.
- [25] J. D. Dombrackas, B. D. Santarsiero, and A. D. Mesecar, “Structural basis for tumor pyruvate kinase M2 allosteric regulation and catalysis,” *Biochemistry*, vol. 44, no. 27, pp. 9417–9429, 2005.
- [26] L. L. Rokosz, D. A. Boulton, E. A. Butkiewicz et al., “Human cytoplasmic 3-hydroxy-3-methylglutaryl coenzyme A synthase: expression, purification, and characterization of recombinant wild-type and Cys129 mutant enzymes,” *Archives of Biochemistry and Biophysics*, vol. 312, no. 1, pp. 1–13, 1994.
- [27] C. Vock, F. Doring, and I. Nitz, “Transcriptional regulation of HMG-CoA synthase and HMG-CoA reductase genes by human ACBP,” *Cellular Physiology and Biochemistry*, vol. 22, no. 5–6, pp. 515–524, 2008.
- [28] M. Retzlaff, M. Stahl, H. C. Eberl et al., “Hsp90 is regulated by a switch point in the C-terminal domain,” *EMBO Reports*, vol. 10, no. 10, pp. 1147–1153, 2009.
- [29] S. Verma, S. Goyal, S. Jamal, A. Singh, and A. Grover, “Hsp90: friends, clients and natural foes,” *Biochimie*, vol. 127, pp. 227–240, 2016.
- [30] Y. Lai, Z. He, A. Zhang et al., “Tip60 and p300 function antagonistically in the epigenetic regulation of HPV18 E6/E7 genes in cervical cancer HeLa cells,” *Genes Genomics*, vol. 42, no. 6, pp. 691–698, 2020.
- [31] X. Song, F. Yang, X. Liu et al., “Dynamic crotonylation of EB1 by TIP60 ensures accurate spindle positioning in mitosis,” *Nature Chemical Biology*, vol. 17, no. 12, pp. 1314–1323, 2021.

## Research Article

# Anlotinib Enhances the Antitumor Activity of High-Dose Irradiation Combined with Anti-PD-L1 by Potentiating the Tumor Immune Microenvironment in Murine Lung Cancer

Meng Yuan <sup>1</sup>, Yirui Zhai,<sup>1</sup> Yu Men,<sup>2</sup> Maoyuan Zhao,<sup>1,3</sup> Xin Sun,<sup>1,4</sup> Zeliang Ma,<sup>1</sup> Yongxing Bao,<sup>1</sup> Xu Yang,<sup>1</sup> Shuang Sun,<sup>1</sup> Yunsong Liu,<sup>1</sup> Wanting Zhang,<sup>1</sup> and Zhouguang Hui <sup>2</sup>

<sup>1</sup>Department of Radiation Oncology, National Cancer Center/National Clinical Research Center for Cancer/Cancer Hospital, Chinese Academy of Medical Sciences and Peking Union Medical College, Beijing, China

<sup>2</sup>Department of VIP Medical Services, National Cancer Center/National Clinical Research Center for Cancer/Cancer Hospital, Chinese Academy of Medical Sciences and Peking Union Medical College, Beijing, China

<sup>3</sup>Lung Cancer Center, West China Hospital of Sichuan University, Chengdu, Sichuan, China

<sup>4</sup>Department of Radiation Oncology, The First Affiliated Hospital, Zhejiang University School of Medicine, Hangzhou, Zhejiang, China

Correspondence should be addressed to Zhouguang Hui; [drhuizg@163.com](mailto:drhuizg@163.com)

Received 2 November 2021; Accepted 5 January 2022; Published 1 February 2022

Academic Editor: Xiangpan Li

Copyright © 2022 Meng Yuan et al. This is an open access article distributed under the Creative Commons Attribution License, which permits unrestricted use, distribution, and reproduction in any medium, provided the original work is properly cited.

**Background.** Radioimmunotherapy has become one of the most promising strategies for cancer treatment. Preclinical and clinical studies have demonstrated that antiangiogenic therapy can improve the efficacy of immunotherapy and sensitize radiotherapy through a variety of mechanisms. However, it is undefined whether angiogenesis inhibitors can enhance the effect of radioimmunotherapy. In this study, we aim to explore the role of anlotinib (AL3818) on the combination of radiotherapy and immune checkpoint inhibitors in Lewis lung carcinoma mouse. **Methods.** C57BL/6 mouse subcutaneous tumor model was used to evaluate the ability of different treatment regimens in tumor growth control. Immune response and immunophenotyping including the quantification and activation were determined by flow cytometry, multiplex immunofluorescence, and multiplex immunoassay. **Results.** Triple therapy (radiotherapy combined with anti-PD-L1 and anlotinib) increased tumor-infiltrating lymphocytes and reversed the immunosuppressive effect of radiation on the tumor microenvironment in mouse model. Compared with radioimmunotherapy, the addition of anlotinib also boosted the infiltration of CD8<sup>+</sup> T cells and M1 cells and caused a decrease in the number of MDSCs and M2 cells in mice. The levels of IFN-gamma and IL-18 were the highest in the triple therapy group, while the levels of IL-23, IL-13, IL-1 beta, IL-2, IL-6, IL-10, and Arg-1 were significantly reduced. NF-κB, MAPK, and AKT pathways were downregulated in triple therapy compared with radioimmunotherapy. Thus, the tumor immune microenvironment was significantly improved. As a consequence, triple therapy displayed greater benefit in antitumor efficacy. **Conclusion.** Our findings indicate that anlotinib might be a potential synergistic treatment for radioimmunotherapy to achieve better antitumor efficacy in NSCLC patients by potentiating the tumor immune microenvironment.

## 1. Introduction

Lung cancer remains the most commonly diagnosed cancer and the leading cause of cancer-related death worldwide [1]. Radiotherapy (RT) is an indispensable local treatment method in the treatment of inoperable lung cancer [2].

Despite the success of radiotherapy, it cannot always eradicate the primary tumor, and local recurrence and metastasis are still observed following irradiation, indicating the inadequacy of RT-induced response to maintain antitumor immunity. Immunotherapy, especially the immune checkpoint inhibitor (ICI), has become the most active part in

the research of cancer treatment in the past decade [3–5]. Although immunotherapy can produce even more consistent clinical benefits than chemotherapy or targeted therapy, only about 20% patients would respond to immunotherapy alone [6, 7]. RT, particularly stereotactic body radiation therapy (SBRT) also known as stereotactic ablative radiotherapy (SABR), can promote the antitumor immunity through induction of an immunogenic cell death and in situ vaccination in preclinical studies [8, 9]. Recently, with a robust and growing body of clinical data, RT has been demonstrated to augment the antitumor immune responses elicited by immunotherapy through synergistic effects [10–12]. The combination of RT and ICI has become one of the most promising strategies for cancer treatment.

Even though the brilliant future of RT-ICI combination therapy, radiation, or drug resistance may occur in clinic. How to optimize it has become a hotspot, including how to further improve the response rate and scale up the potential population who can benefit and reduce the incidence rate of adverse events related to combination treatment. Antiangiogenic therapy, represented by a class of vascular endothelial growth factor (VEGF) inhibitors, is an important component of targeted therapy [13]. There is growing evidence that antiangiogenic therapy can improve both radiotherapy and immunotherapy by downregulating the level of angiogenic factors, normalizing blood vessels, alleviating hypoxia, adjusting cell cycle, balancing the tumor microenvironment, and eliminating immunosuppressive factors to some degree [14–16]. However, the evidence of the trinity treatment combining radiotherapy, immunotherapy, and antiangiogenic therapy is rare. In the light of the previously described interactions and synergy, it is becoming increasingly important to explore whether antiangiogenic therapy could enhance the therapeutic effect of radiotherapy combined with immunotherapy, and the trinity strategy could bring about even dramatically tumor shrinking. Therefore, the aim of our study is to comprehensively characterize the role of antiangiogenic therapy on the treatment efficacy of radioimmunotherapy and the tumor microenvironment. Our data suggested a novel possible therapeutic approach for cancer patients, and this treatment paradigm merits evaluation in clinical trials in the future.

## 2. Methods

**2.1. Mice and Cell Lines.** Female C57BL/6 mice (SPF, 6 weeks old) were purchased from HFK Bioscience Co., Ltd. (Beijing, China). All mice were group-housed (5 mice/cage) in the Experimental Animal Center of the Chinese Academy of Medical Sciences and were in specific pathogen-free conditions under a 12 h light-dark schedule. The temperature and humidity of the animal house were maintained at 26°C–28°C and 60 ± 5%, respectively. In vivo study protocols were approved by the Institutional Animal Care and Use Committee (NCC2020A305) at the National Cancer Center/Cancer Hospital, Chinese Academy of Medical Sciences (NCC/CH, CAMS, Beijing, China). Lewis lung carcinoma cells (LLC) were kindly provided by Dr. Li at CAMS Key Lab of Translational Research on Lung Cancer and were cul-

tured in complete DMEM supplemented with 10% FBS, 100 U/ml penicillin, and 100 µg/ml streptomycin at 37°C in a 5% CO<sub>2</sub> atmosphere.

**2.2. Establishment of Subcutaneous Tumor Models.** To establish a mouse model with normal immune system, C57BL/6 mice were subcutaneously implanted with LLC cells ( $6 \times 10^6$ ) in the left inguinal region. Tumor volumes were measured every other day using a caliper and calculated by the following formula:  $\text{volume} = L \times W^2/2$ , where  $L$  was the length and  $W$  the width of the tumor. When tumor volume reached  $50 \pm 20 \text{ mm}^3$ , 10 days after implantation, mice were randomized into six groups of five animals each. The total rates of tumor formation of the subcutaneously implanted tumor cells were 75%. Then, the antitumor treatments began.

**2.3. Antitumor Treatments.** Mice were randomized into the following treatment groups: control, RT (24 Gy/3 f on days 3, 5, and 7), anti-PD-L1 (10 mg/kg, on days 3, 6, 9, and 12, clone 10F.9G2, BioXCell), RT+anlotinib (3 mg/kg, from day 1 to 14, #17321004, Chiatai Tianqing), RT+anti-PD-L1, and RT+anti-PD-L1+anlotinib. Mice received anti-PD-L1 by intraperitoneal injections and anlotinib by intragastric administration. RT (three fractions of 8 Gy) was delivered using a Varian Unique-SN2242 unit at 300 cGy per minute (100 cm source to skin distance). Each mouse was anesthetized with chloral hydrate (30 mg/kg), placed supinely on a fixing device, covered with a 5 mm bolus, and left only the tumor area exposed (Figure 1). Endpoint day was designated as the 15th day after commencement of the initial treatment to harvest tumors. For ethical considerations, mice with a weight loss of 20% or more, tumor diameter larger than 20 mm, or tumor causing severely impaired ambulation were euthanized.

**2.4. Flow Cytometry.** The harvested tumor tissues were digested with 1 mg/ml collagenase IV (Sigma-Aldrich) and 0.01 mg/ml DNAase (Sigma-Aldrich) at 37°C for 60 minutes. Cell suspensions were passed through a 70 µm nylon cell strainer to yield single-cell suspensions. The resulting single-cell suspensions were stained with fluorescent-labeled antibodies, including anti-CD3 (#100329, Biolegend), anti-CD4 (#100405, Biolegend), anti-CD8 (#100733, Biolegend), anti-CD45 (#103113, Biolegend), anti-PD-1 (#135217, Biolegend), anti-PD-L1 (#124311, Biolegend), anti-CD11b (#101245, Biolegend), anti-Gr-1 (#108407, Biolegend), anti-F4/80 (#123107, Biolegend), anti-CD86 (#105029, Biolegend), and anti-CD206 (#141707, Biolegend). The specific anti-mouse CD16/CD32 purified antibody (#70-0161, Tonbo Biosciences) was used to block the FC receptor and thus eliminate nonspecific results caused by binding of fluorescently labeled antibodies to Fc receptors. Isotype controls were used for all antibodies. Gates and quadrants were set based on isotype control staining. Data were acquired using an LSR-II (Becton Dickinson) and were analyzed using FlowJo V.10 software.

**2.5. Immunofluorescence (IF).** Harvested tumors were fixed in 10% neutral-buffered formalin and embedded in paraffin.

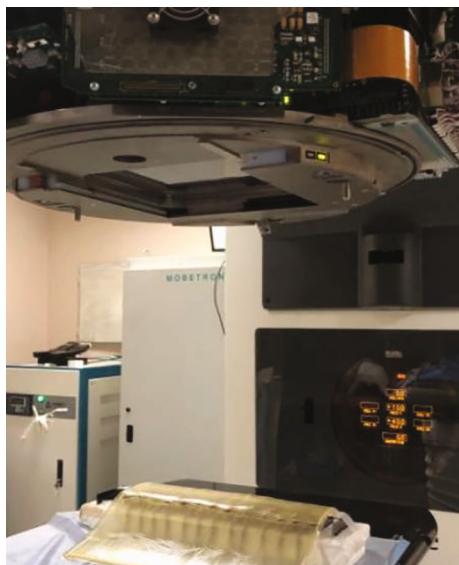


FIGURE 1: Radiation process of the tumor-burdened mice.

The tumor tissue sections ( $4\ \mu\text{m}$ ) were then deparaffinized, rehydrated, and subjected to heat-induced antigen retrieval with Tris-EDTA buffer (pH 8.0). Sections were incubated in 10% normal goat serum at room temperature for 0.5 h. Tumor sections were then stained with primary antibodies (CD4, #GB11064, Servicebio; CD8, #GB11068, Servicebio; CD86, #GB13585, Servicebio and CD206, #GB13438, Servicebio) at  $4^\circ\text{C}$  overnight and corresponding secondary antibody marked with HRP for 50 minutes and then incubated with TSA-FITC (TSA-CY3) solution. Nuclei were stained with DAPI solution. Tumor tissue sections were observed with fluorescence microscopy.

**2.6. Quantification of Cytokines in Tumor Tissues.** Immune cytokine profiles were characterized using the ProcartaPlex Mouse Cytokine Panel (eBioscience). Tumor tissue samples were obtained from mice and run in three times along with serial standards and buffer controls. The median fluorescence intensity of analytes was detected using the Luminex 200. Cytokine concentrations were calculated with Luminex xPONENT V. 4.2 software using a standard curve derived from known reference concentrations supplied by the manufacturer. A five-parameter model was used to calculate final concentrations by interpolation.

**2.7. Protein Extraction and Western Blot.** Total protein was prepared from isolated tumor tissue, and Western blots were performed as previously described [17]. Primary antibodies include anti-MAPK (#4695, CST), anti-p-MAPK (#4370, CST), anti-AKT (#4691, CST), anti-p-AKT (#4060, CST), anti-NF- $\kappa\text{B}$  (#8242, CST), anti-p-NF- $\kappa\text{B}$  (#3033, CST), anti-arginase-1 (Arg-1) (#93668, CST), and anti-GAPDH (#5174, CST). Secondary antibodies include anti-rabbit (#14708, CST) and anti-mouse (#14709, CST).

**2.8. Statistical Analysis.** The data are shown as the means  $\pm$  SEM and were analyzed using two-tailed Student's *T*-test

for comparisons between two groups. One-way analysis of variance was used for the statistical analysis of more than two groups. \*, \*\*, \*\*\*, or \*\*\*\* represents *p* values  $<0.05$ ,  $<0.01$ ,  $<0.001$  or  $<0.0001$ , respectively. Statistical analyses were performed by the GraphPad Prism software 9.0 (GraphPad Software Inc., San Diego, CA, USA).

### 3. Results

**3.1. Anlotinib Enhanced the Therapeutic Effect of Radiotherapy Combined with Immunotherapy, and the Triple Therapy Achieved the Best Antitumor Activity.** Radiotherapy is a fundamental treatment for NSCLC, and radiotherapy combined with immunotherapy has been emerging as the most promising strategy, but there is no conclusion whether adding antiangiogenic therapy to this combination could exhibit even superior antitumor effect. To investigate the efficacy of triple therapy and the impact on the tumor immune microenvironment, we established the LLC mouse model with normal immune system. Considering the tolerance of multiple treatments and the accuracy of measurement, C57BL/6 mice were subcutaneously implanted with LLC cells ( $6 \times 10^6$ ) in the left inguinal region. LLC cells were allowed to grow, allowing the tumors to become established 10 days after implantation (mean starting volume =  $50\ \text{mm}^3$ ). In the experimental groups, mice received one of the following treatments: RT, anti-PD-L1, RT+anlotinib, RT+anti-PD-L1, or RT+anti-PD-L1+anlotinib (Figure 2(a)). Hypofractionated radiotherapy was demonstrated to have brilliant synergetic effect with immunotherapy, and therefore, the irradiation was given as three fractions of 8 Gy and 24 Gy in total. We performed administration of anlotinib 2 days before RT considering of priming with the antiangiogenic therapy to produce a “treatment window” (Figure 2(a)). Anti-PD-L1 injections were given concurrently with and following radiotherapy to make a better synergy (Figure 2(a)). Tumor tissues (five mice each group) were collected on day 15 after the initial treatment. The tumor volumes of 6 groups were shown (Figures 2(b)–2(e)). To better replicate the clinical scenario, we treated LLC-bearing mice with various regimens, observing that compared with radiation alone, radioimmunotherapy and the triple therapy both significantly inhibited tumor growth. Triple therapy exhibited better antitumor efficacy than radioimmunotherapy (mean tumor volume  $\pm$  SEM: RT:  $487.5 \pm 94.39\ \text{mm}^3$  vs. radioimmunotherapy:  $91.01 \pm 32.19\ \text{mm}^3$  vs. triple therapy:  $46.33 \pm 18.32\ \text{mm}^3$ ; Figures 2(b)–2(e)).

What is more, the addition of anlotinib was well tolerated without weight decrease compared with other combination treatments. These data suggested that the triple therapy achieved the best antitumor activity and tolerable in mice.

**3.2. Immunosuppressive Tumor Microenvironment following RT.** RT was reported to alter the tumor immune microenvironment remarkably. We first analyzed the different immune cells, including  $\text{CD4}^+$  T cells ( $\text{CD45}^+$ ,  $\text{CD3}^+$ , and  $\text{CD4}^+$ ),  $\text{CD8}^+$  T cells ( $\text{CD45}^+$ ,  $\text{CD3}^+$ , and  $\text{CD8}^+$ ), myeloid-derived suppressor cells (MDSCs) ( $\text{CD45}^+$ ,  $\text{CD11b}^+$ , and

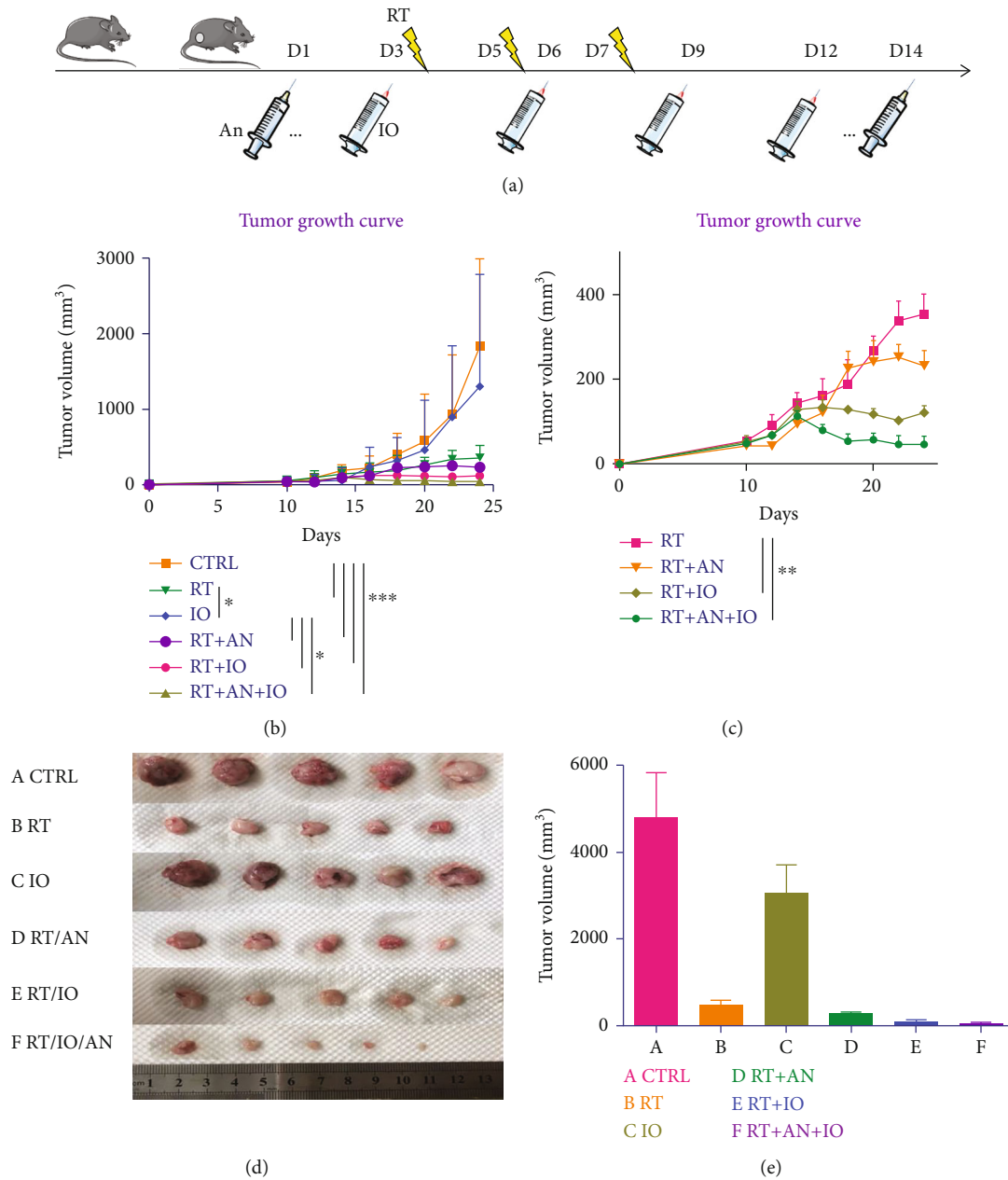
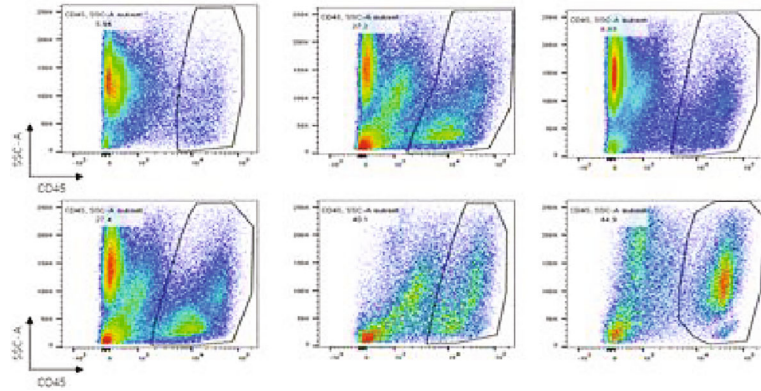
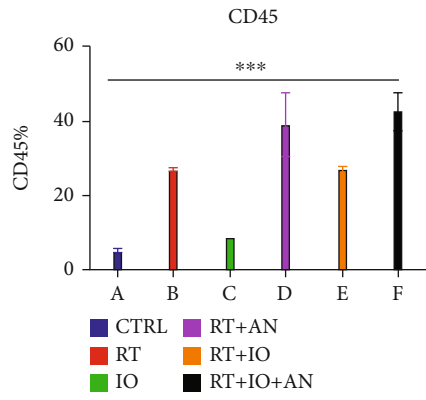


FIGURE 2: Radiotherapy combined with anti-PD-L1 and anlotinib achieved the best antitumor activity. (a) Schematic showing schedules of radiotherapy, anlotinib, and anti-PD-L1. (b–e) Responses of the subcutaneous tumors in different treatment groups. CTRL: control; RT: radiotherapy; IO: immunotherapy; AN: anlotinib.

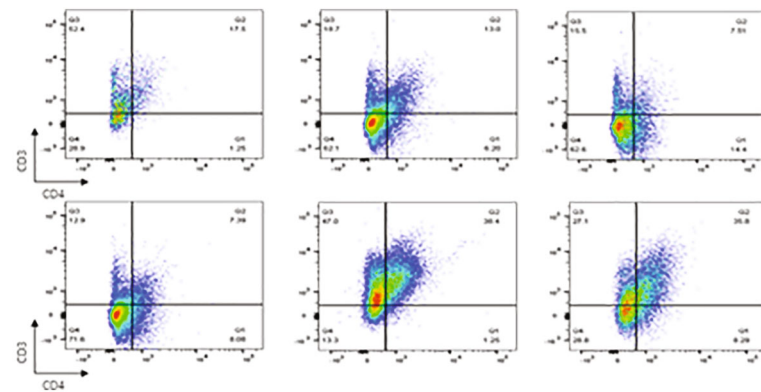
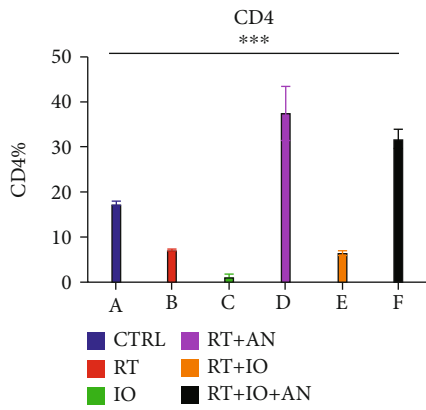
Gr-1<sup>+</sup>), M1 type tumor-associated macrophages (M1 cells) (CD45<sup>+</sup>, CD11b<sup>+</sup>, F4/80<sup>+</sup>, and CD86<sup>+</sup>), and M2 type tumor-associated macrophages (M2 cells) (CD45<sup>+</sup>, CD11b<sup>+</sup>, F4/80<sup>+</sup>, and CD206<sup>+</sup>) in the tumor immune micro-environment of control and RT groups by flow cytometry. Analysis showed that radiation augmented the total immune cell infiltration (CD45<sup>+</sup> cells:  $5.6 \pm 0.2$  vs.  $27.1 \pm 0.4$ ,  $p < 0.0001$ ). In terms of the subsets, we found that CD4<sup>+</sup> T cells, CD8<sup>+</sup> T cells, and M1 cells significantly decreased following RT (CD4<sup>+</sup> T cells:  $17.7 \pm 0.2$  vs.  $7.4 \pm 0.1$ ,  $p < 0.0001$ ; CD8<sup>+</sup> T cells:  $6.0 \pm 0.3$  vs.  $3.6 \pm 0.1$ ,  $p = 0.0012$ ; M1 cells:  $4.0 \pm 0.6$  vs.  $1.71 \pm 0.1$ ,  $p = 0.0258$ ) (Figure 3). On the other hand, the percentage of MDSCs and M2 cells in the tumor tissue

significantly increased after RT (MDSCs:  $15.1 \pm 2.8$  vs.  $26.4 \pm 0.7$ ,  $p = 0.0194$ ; M2 cells:  $28.0 \pm 2.8$  vs.  $45.2 \pm 0.4$ ,  $p = 0.0034$ ) (Figure 3). These data indicate that radiation changed the immune cell distribution in the tumor environment, that is, the infiltration of positive immune cells such as CD8<sup>+</sup> T cells and M1 cells reduced while the suppressor cells such as MDSCs and M2 cells increased. And this can also be demonstrated in the IF (Figure 4).

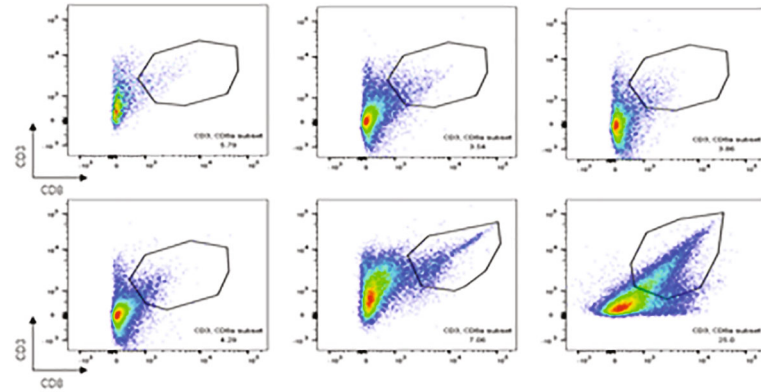
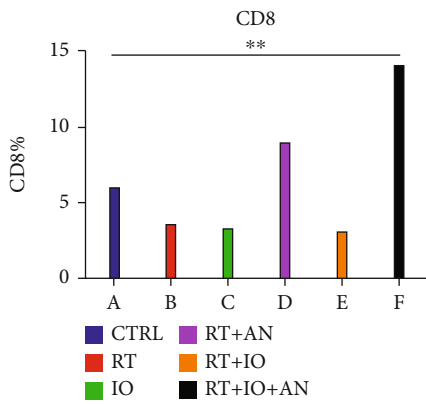
**3.3. Trinity Strategy Could Significantly Potentiate the Tumor Immune Microenvironment Compared with Other Treatment Combinations.** To explore which strategy has the potential to attenuate and reverse the suppressive



(a)



(b)



(c)

FIGURE 3: Continued.

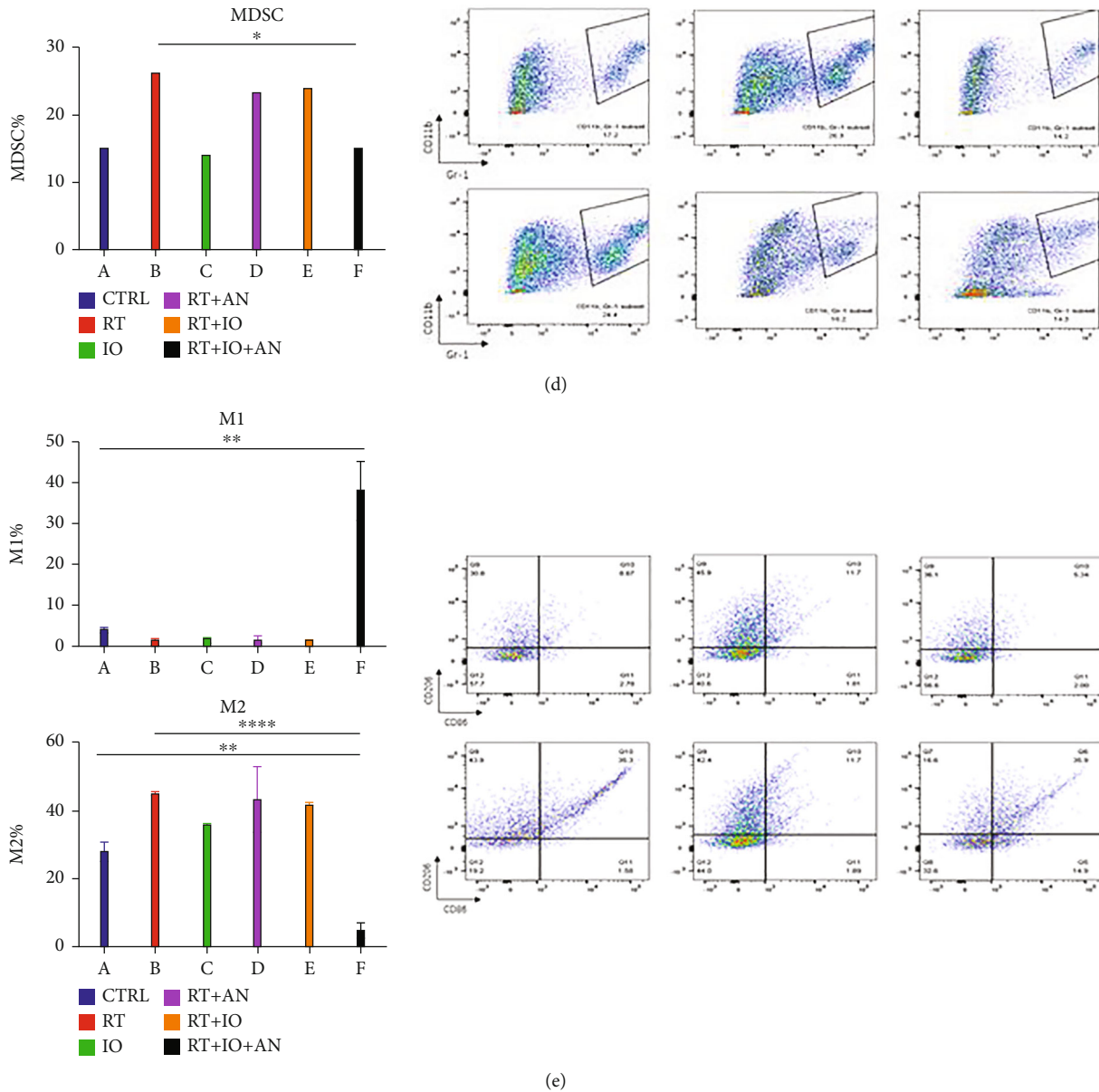


FIGURE 3: Radiotherapy combined with anti-PD-L1 and anlotinib could significantly potentiate the tumor immune microenvironment compared with other treatment combinations. Quantitative data and flow cytometric analysis of CD45<sup>+</sup> T cells (a), CD4<sup>+</sup>T cells (b), CD8<sup>+</sup> T cells (c), MDSCs (d), and M1 cells and M2 cells (e) in tumors. CTRL: control; RT: radiotherapy; IO: immunotherapy; AN: anlotinib.

immune microenvironment, we treated the mice with RT, anti-PD-L1, RT+anlotinib, RT+anti-PD-L1, or RT+anti-PD-L1+anlotinib. The results of flow cytometry illustrated that the trinity strategy brought about the most positive tumor immune microenvironment. All treatments could enhance the total immune cell infiltration comparing with control group. Both RT+anlotinib and RT+anti-PD-L1+anlotinib could significantly increase the CD4<sup>+</sup> T cells comparing with control (CD4<sup>+</sup> T cells: 37.6% ± 5.9% vs. 17.7% ± 0.2%,  $p = 0.01$ ; 31.9% ± 2.1% vs. 17.7% ± 0.2%,  $p = 0.0005$ ), whereas RT, anti-PD-L1, and RT+anti-PD-L1 decreased the CD4<sup>+</sup> T cells in tumor microenvironment. The trinity strategy significantly increased CD8<sup>+</sup> T cell infiltration ( $p = 0.004$ ), with the percentage of 14.1% that was

more than any other treatment. The percentage of M1 cells in the triple therapy was also significantly higher (M1 cells: 38.2% ± 7.2% vs. 4.0% ± 0.6%,  $p = 0.0024$ ) and was the most among all treatment groups. MDSCs significantly decreased in the triple therapy compared with RT (MDSCs: 15.2% ± 6.1% vs. 26.4% ± 1.3%,  $p = 0.0358$ ). The percentage of M2 cells in the triple therapy group was remarkably reduced comparing with RT (M2 cells: 4.9% ± 2.2% vs. 45.2% ± 0.4%,  $p < 0.0001$ ) and was the lowest amongst all treatments (Figure 3). These can also be found in the IF (Figure 4). In brief, triple therapy significantly promoted the filtration of CD45<sup>+</sup>, CD8<sup>+</sup> T cells, and M1 cells and decreased MDSCs and M2 cells. To conclude, the trinity strategy of combining RT, anti-PD-L1, and anlotinib not only has the best

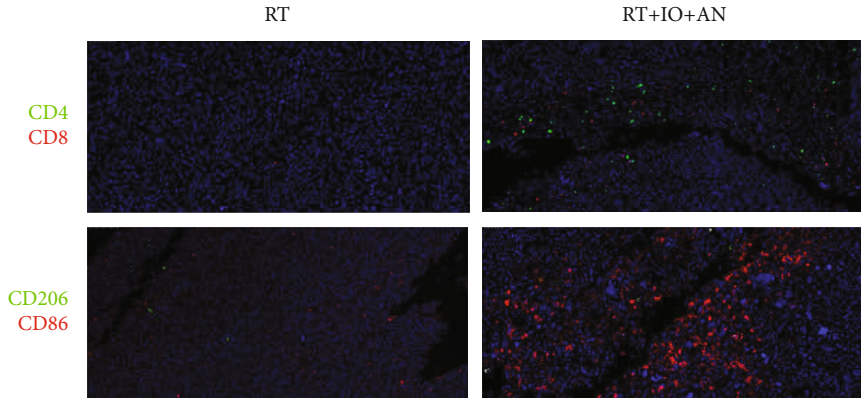


FIGURE 4: Triple therapy (radiotherapy combined with anti-PD-L1 and anlotinib) reversed the immunosuppressive effect of radiation on the tumor microenvironment. CTRL: control; RT: radiotherapy; IO: immunotherapy; AN: anlotinib.

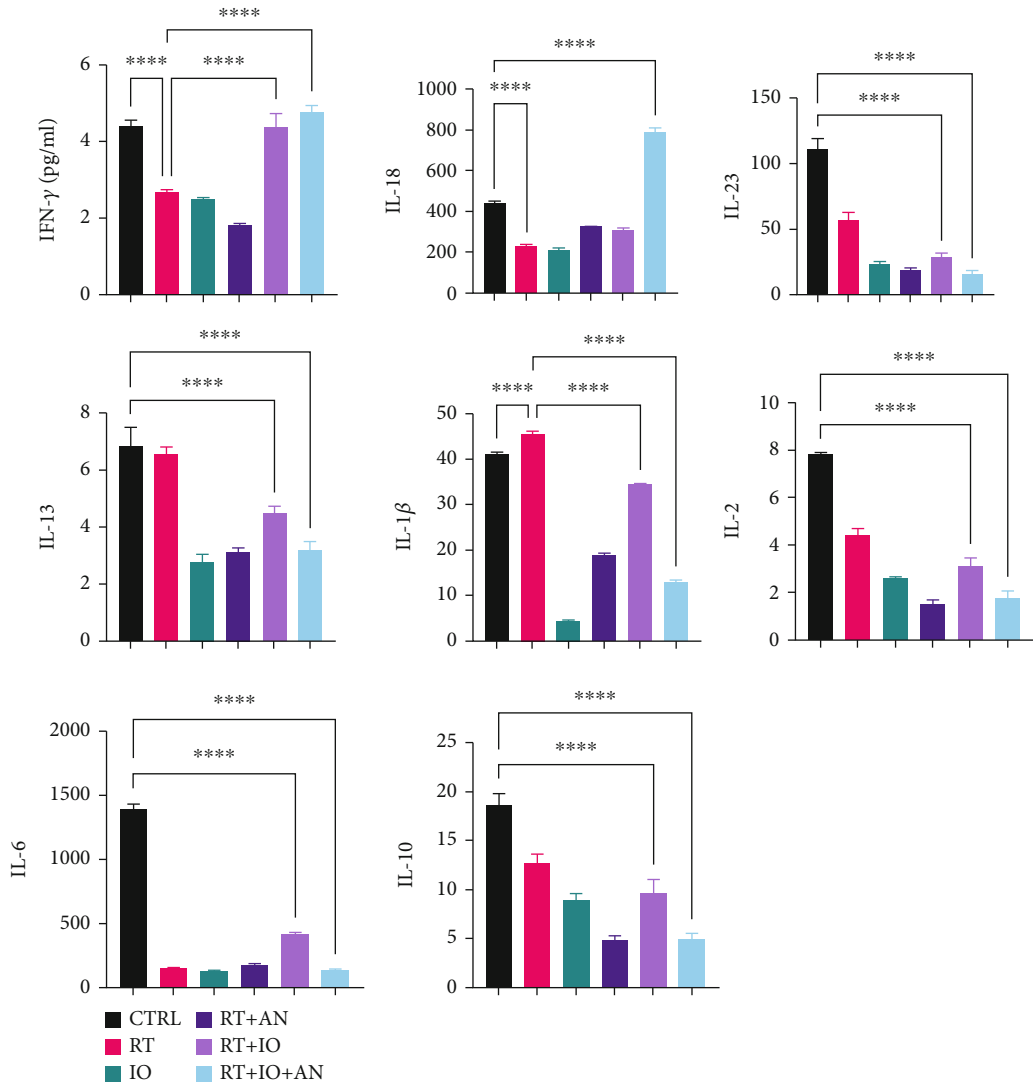


FIGURE 5: Levels of cell cytokines associated with the activity and function of immune cells. CTRL: control; RT: radiotherapy; IO: immunotherapy; AN: anlotinib.



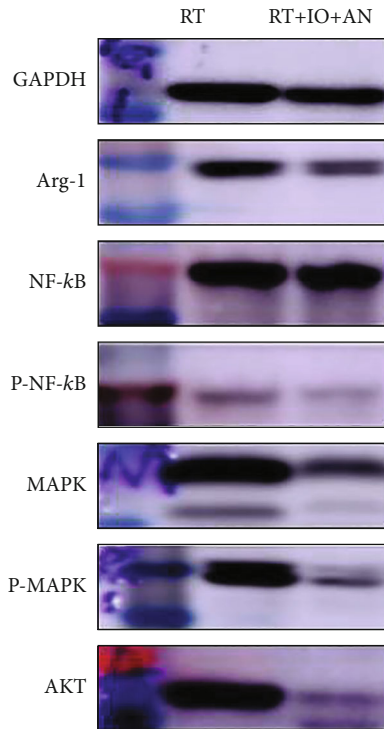


FIGURE 6: Expressions of Arg-1, NF- $\kappa$ B p65, p-NF- $\kappa$ B p65, MAPK, p-MAPK, and AKT in subcutaneous tumors from mice treated with radioimmunotherapy or triple therapy. RT: radiotherapy; IO: immunotherapy; AN: anlotinib.

antitumor activity but also can reverse the suppressive immune microenvironment induced by radiotherapy and significantly potentiate the tumor immune microenvironment compared with all the other treatments.

**3.4. Trinity Strategy Promoted Function of Immune Cells and the Positive Immune Environment in LLC Tumors.** To identify the activity and function of immune cells, we performed quantitative detection of cell cytokines. The levels of IFN- $\gamma$  and IL-18 were the highest in the triple therapy group, while the level of IL-23 was the lowest in the triple therapy group (Figure 5). Besides, IL-13, IL-1  $\beta$ , IL-2, IL-6, and IL-10 were significantly reduced in the triple therapy group (Figure 5). We also conducted the Western blot to examine the level of Arg-1 in the mice tumor tissues. We found that the trinity strategy led to a marked decrease in Arg-1 compared with radioimmunotherapy (Figure 6).

**3.5. Triple Therapy Promoted the Antitumor Effect of Radioimmunotherapy via Downregulation of NF- $\kappa$ B, MAPK, and AKT Pathways.** We also explored the mechanism underlying the synergistic effect of anlotinib and radioimmunotherapy. Previous studies have demonstrated that nuclear factor kappa B (NF- $\kappa$ B) functions in many cellular constituents of the tumor microenvironment and modulates inflammation, tumorigenesis, and metastasis; therefore, we first hypothesized that triple therapy might play a role in blocking NF- $\kappa$ B activation. Analysis of levels of NF- $\kappa$ B p65 and p-NF- $\kappa$ B p65 in LLC subcutaneous tumors from

mice treated with radioimmunotherapy or triple therapy revealed that the triple therapy decreased levels of p-NF- $\kappa$ B, suggesting the addition of anlotinib blocking activation of the NF- $\kappa$ B pathway (Figure 6). Mitogen-activated protein kinase (MAPK) and AKT pathways have also been identified as pivotal regulators of tumor immune microenvironment. We second tested these two signaling pathways. Results of Western blot showed that both of them were decreased in the triple therapy (Figure 6).

#### 4. Discussion

The combination of radiotherapy and immunotherapy has become one of the most promising strategies for cancer treatment. How to optimize it is currently a hotspot, including how to further improve the response rate, scale up the potential population who can benefit and reduce the incidence rate of adverse events related to combination treatment. Antiangiogenic therapy is an important component of targeted therapy, and in combination treatment, it may further prolong survival and improve the quality of life [13]. The present study is aimed at confirming the positive role of antiangiogenic therapy on the combination of radiotherapy and immune checkpoint inhibitors in Lewis lung carcinoma mouse and extending understanding of the potential mechanisms from aspects of tumor immune microenvironment.

Our study demonstrated that anlotinib enhanced the therapeutic effect of radioimmunotherapy, and the triple therapy achieved the best antitumor activity compared with other combination treatments. We found that trinity strategy could significantly potentiate the tumor immune microenvironment compared with other treatment combinations. In addition, triple therapy might promote the antitumor effect of radioimmunotherapy via downregulation of MAPK, AKT, and NF- $\kappa$ B pathways.

The combination of radiotherapy and immunotherapy has been proved in numerous preclinical and clinical studies to have obvious synergistic effects. Immune checkpoint inhibitor (ICI) can enhance the antitumor immunity caused by radiotherapy: due to the immunosuppressive microenvironment already existing in the tumor, radiotherapy alone cannot produce sufficient antitumor immune response. Therefore, the abscopal effect is rare to occur clinically when radiotherapy is implemented alone. CTLA-4 or PD-1/PD-L1 monoclonal antibody can enhance the radiotherapy-induced in situ vaccination [18, 19]. On the other hand, radiotherapy increases the effect of ICI: although CTLA-4 and PD-1/PD-L1 monoclonal antibody can reverse the inhibition of T cells in the immunosuppressive tumor microenvironment to some extent, the activation of T cells still depends on antigen stimulation and participation of activated costimulatory molecule CD28 on the surface of mature APC. Radiotherapy can increase the expression and presentation of tumor antigen and consequently amplify the immune response induced by ICI. Radiotherapy can also improve the immunomodulatory effect by increasing CTL infiltration, enhancing CTL activity, enlarging antigen peptide pool, and triggering the diffusion of tumor antigen determinants [20]. For

unresectable stage III NSCLC, concurrent chemoradiotherapy is the basis of standard treatment. In order to improve the efficacy of chemoradiotherapy, many attempts, including increasing induction chemotherapy, consolidation chemotherapy, and radiotherapy dose, all ended in failure. The Pacific study confirmed that the consolidation of anti-PD-L1 inhibitor durvalumab on the basis of chemoradiotherapy can further improve the overall survival and progression-free survival [12]. Based on this, the treatment regimen was written into the NCCN guidelines as class I recommendation in 2018. Even though immunotherapy combined with radiotherapy displayed a promising antitumor treatment benefit on NSCLC, preclinical or clinical studies to investigate the efficacy of trinity strategy of combining antiangiogenic therapy with radioimmunotherapy are still rare, and the results are immature. Especially in hypofractionated radiotherapy, the reoxygenation utilization rate is lower than that of conventional fractionated radiotherapy. Low fractionated and high-dose radiotherapy lead to an increase in the ratio of hypoxic cells and high expression of VEGF. It can be inferred that the sensitization effect of anlotinib might be more significant in hypofractionated radiotherapy [21].

We innovatively added anlotinib to radioimmunotherapy to investigate whether the trinity strategy can exhibit even superior efficacy. The triple therapy showed the most obvious antitumor effect in all treatments. Then, we detected the tumor immune phenotype of different treatments and found that the trinity strategy led to the most positive immune phenotype in tumor tissue compared with other treatment combinations, which is consistent with the efficacy. The addition of anlotinib to radioimmunotherapy boosted the infiltration of CD8<sup>+</sup> T cells in mice tumor tissues, and the amount of M1 cells also peaked in the triple therapy group, which is significant to the antitumor immune responses. On the other hand, the triple therapy obviously reduced the number of immunosuppressive cells. We found that the infiltration of MDSCs decreased in the triple therapy compared with radiotherapy and other radiotherapy combination treatments. The level of M2 cells in tumor tissues was the lowest in triple therapy.

We next determined the levels of cell cytokines associated with the activity and function of immune cells. The levels of IFN- $\gamma$  was the highest in the triple therapy group, which was secreted primarily by activated lymphocytes such as CD4<sup>+</sup> and CD8<sup>+</sup> T cells [22], gamma delta T cell [23], as well as NK[24] and NK T cells [25]. Numerous antitumor effects of IFN- $\gamma$  have been described, including regulation of antigen presentation, promotion of inflammatory and chemotactic signals, activation and polarization of responding leukocytes, recruiting effector leukocytes, as well as direct antiproliferative and antiangiogenic effects [26]. The level of IL-23 was showed to be the lowest in the triple therapy group, which was mainly secreted by myeloid cells and associated with suppressive immune microenvironment, tumor cell proliferation, and treatment resistant [27]. Besides, IL-13, IL-1 beta, IL-2, IL-6, and IL-10 were significantly reduced in the triple therapy group (Figure 5). Local signals IL-13, IL-6, and IL-10 in the tumor

microenvironment were reported to polarize macrophages into protumoral M2-like cells [28], which was in line with the results of flow cytometry. Tumor-derived IL-1 has been proven to have a role in modulating the composition of TME by recruiting MDSCs, TAM, TAN, Breg cells, and Th17, contributing to the angiogenic switch sustaining the production of angiogenic factors such as VEGF [29]. IL-1 has also been emerging as a cytokine involved in drug resistance [30]. We also conducted the Western blot to examine the level of Arg-1 in mice tumor tissues and found that Arg-1 was substantially decreased in the triple therapy compared with radioimmunotherapy. Elevated levels of Arg-1 expressed by MDSC were reported to mediate the depletion of L-arginine from the TME that leads to a cell cycle arrest in T cells and T cell anergy due to the downregulation of TCR zeta-chain expression [31].

NF- $\kappa$ B, MAPK, and AKT are main signal pathways associated with tumor immune microenvironment. Activating of these pathways was demonstrated to induce an immune-tolerant tumor microenvironment [28, 30, 32]. We found that the expression levels of p-NF- $\kappa$ B, MAPK, p-MAPK, and AKT were reduced in triple therapy compared with radioimmunotherapy, which indicated that the best antitumor effect and the most positive immune microenvironment of trinity strategy might be associated with downregulation of NF- $\kappa$ B, MAPK, and AKT pathways.

There are some limits in our study. First, the influence on survival and tumor recurrence were not observed; second, only one cell line was used in the study; third, whether changing the radiation dose-fractionation will affect the efficacy of triple therapy has not been discussed. Despite these limitations, taken all these benefits of anlotinib combined with radioimmunotherapy together, our data implicated that antiangiogenic therapy could be a promising synergetic treatment for radioimmunotherapy in patients with NSCLC. Although our study was of high clinical significance, the combination of antiangiogenic therapy with radioimmunotherapy merits evaluation on clinical trials.

## 5. Conclusion

In summary, we have demonstrated that the addition of anlotinib to radioimmunotherapy increased the infiltration of CD8<sup>+</sup> T and M1 cells and reduced MDSCs and M2 cells in LLC tumors. Moreover, the combination of anlotinib with radioimmunotherapy led to an increase in the levels of IFN- $\gamma$  and IL-18 and descending in IL-23, IL-13, IL-1 beta, IL-2, IL-6, IL-10, and Arg-1. Thus, anlotinib significantly improved the tumor immune microenvironment combined with radioimmunotherapy. As a consequence, compared with radioimmunotherapy, anlotinib plus radioimmunotherapy displayed better therapeutic efficacy in tumor control in tumor-bearing mice.

Our findings have a high clinical significance. Based on preliminary translational observations, our work raised the possibility that antiangiogenic therapy might be a potential synergistic modality for radioimmunotherapy in NSCLC patients. Remarkably, this study provides a basis for future clinical studies into the treatment of NSCLC.

## Data Availability

The data used to support the findings of this study are available from the corresponding author upon request.

## Conflicts of Interest

The authors declare that they have no known competing financial interests or personal relationships that could have appeared to influence the work reported in this paper.

## Authors' Contributions

Meng Yuan and Yirui Zhai contributed equally to this work.

## Acknowledgments

We deeply thank Prof. Jie Wang, Prof. Hua Bai, Dr. Xue Zhang, Dr. Chao Wang, Dr. Sini Li, Dr. Yan Qu, and Dr. Lihui Liu of CAMS Key Lab of Translational Research on Lung Cancer for generously providing us with the expertise and making this research possible. This work was supported by the CAMS Innovation Fund for Medical Sciences (CIFMS: 2020-I2M-C&T-B-074), CAMS Key Lab of Translational Research on Lung Cancer (2018PT31035), CSCO-Linghang Cancer Research Foundation Project (Y-2019AZMS-0426), and Clinical Application Project of Beijing Municipal Commission of Science and Technology (Z171100001017114).













## References

- [1] R. L. Siegel, K. D. Miller, and A. Jemal, "Cancer statistics, 2020," *CA: a Cancer Journal for Clinicians*, vol. 70, no. 1, pp. 7–30, 2020.
- [2] D. E. Citrin, "Recent developments in radiotherapy," *The New England Journal of Medicine*, vol. 377, no. 11, pp. 1065–1075, 2017.
- [3] A. D. Waldman, J. M. Fritz, and M. J. Lenardo, "A guide to cancer immunotherapy: from T cell basic science to clinical practice," *Nature Reviews. Immunology*, vol. 20, no. 11, pp. 651–668, 2020.
- [4] J. Tang, A. Shalabi, and V. M. Hubbard-Lucey, "Comprehensive analysis of the clinical immuno-oncology landscape," *Annals of Oncology*, vol. 29, no. 1, pp. 84–91, 2018.
- [5] Y. J. Xin, V. M. Hubbard-Lucey, and J. Tang, "Immuno-oncology drug development goes global," *Nature Reviews. Drug Discovery*, vol. 18, no. 12, pp. 899–900, 2019.
- [6] P. Darvin, S. M. Toor, V. Sasidharan Nair, and E. Elkord, "Immune checkpoint inhibitors: recent progress and potential biomarkers," *Experimental & Molecular Medicine*, vol. 50, no. 12, pp. 1–11, 2018.
- [7] J. van den Bulk, E. M. Verdegaal, and N. F. de Miranda, "Cancer immunotherapy: broadening the scope of targetable tumours," *Open Biology*, vol. 8, no. 6, 2018.
- [8] S. Shang, J. Liu, V. Verma et al., "Combined treatment of non-small cell lung cancer using radiotherapy and immunotherapy: challenges and updates," *Cancer Communications*, vol. 41, no. 11, pp. 1086–1099, 2021.
- [9] E. B. Golden and S. C. Formenti, "Is tumor (R) ejection by the immune system the '5th R' of radiobiology?," *Oncoimmunology*, vol. 3, no. 3, article e28133, 2014.
- [10] W. Theelen, H. M. U. Peulen, F. Lalezari et al., "Effect of pembrolizumab after stereotactic body radiotherapy vs pembrolizumab alone on tumor response in patients with advanced non-small cell lung cancer: results of the PEMBRO-RT phase 2 randomized clinical trial," *JAMA Oncology*, vol. 5, no. 9, pp. 1276–1282, 2019.
- [11] C. Faivre-Finn, D. Vicente, T. Kurata et al., "Four-year survival with durvalumab after chemoradiotherapy in stage III NSCLC—an update from the PACIFIC trial," *Journal of Thoracic Oncology*, vol. 16, no. 5, pp. 860–867, 2021.
- [12] S. J. Antonia, A. Villegas, D. Daniel et al., "Overall survival with durvalumab after chemoradiotherapy in stage III NSCLC," *The New England Journal of Medicine*, vol. 379, no. 24, pp. 2342–2350, 2018.
- [13] M. Kamrava, M. B. Bernstein, K. Camphausen, and J. W. Hodge, "Combining radiation, immunotherapy, and antiangiogenesis agents in the management of cancer: the Three Musketeers or just another quixotic combination?," *Molecular BioSystems*, vol. 5, no. 11, pp. 1262–1270, 2009.
- [14] R. P. Dings, M. Loren, H. Heun et al., "Scheduling of radiation with angiogenesis inhibitors anginex and avastin improves therapeutic outcome via vessel normalization," *Clinical Cancer Research*, vol. 13, no. 11, pp. 3395–3402, 2007.
- [15] C. G. Willett, S. V. Kozin, D. G. Duda et al., "Combined vascular endothelial growth factor-targeted therapy and radiotherapy for rectal cancer: theory and clinical practice," *Seminars in Oncology*, vol. 33, pp. S35–S40, 2006.
- [16] M. W. Dewhirst, Y. Cao, and B. Moeller, "Cycling hypoxia and free radicals regulate angiogenesis and radiotherapy response," *Nature Reviews. Cancer*, vol. 8, no. 6, pp. 425–437, 2008.
- [17] J. Gao and D. R. Richardson, "The potential of iron chelators of the pyridoxal isonicotinoyl hydrazone class as effective antiproliferative agents, IV: the mechanisms involved in inhibiting cell cycle progression," *Blood*, vol. 98, no. 3, pp. 842–850, 2001.
- [18] L. Deng, H. Liang, B. Burnette et al., "Irradiation and anti-PD-L1 treatment synergistically promote antitumor immunity in mice," *The Journal of Clinical Investigation*, vol. 124, no. 2, pp. 687–695, 2014.
- [19] C. Twyman-Saint Victor, A. J. Rech, A. Maity et al., "Radiation and dual checkpoint blockade activate non-redundant immune mechanisms in cancer," *Nature*, vol. 520, no. 7547, pp. 373–377, 2015.
- [20] T. Walle, R. Martinez Monge, A. Cerwenka, D. Ajona, I. Melero, and F. Lecanda, "Radiation effects on antitumor immune responses: current perspectives and challenges," *Therapeutic Advances in Medical Oncology*, vol. 10, p. 175883401774257, 2018.
- [21] H. Sheng, Y. Huang, Y. Xiao et al., "ATR inhibitor AZD6738 enhances the antitumor activity of radiotherapy and immune checkpoint inhibitors by potentiating the tumor immune microenvironment in hepatocellular carcinoma," *Journal for Immunotherapy of Cancer*, vol. 8, no. 1, p. e000340, 2020.
- [22] H. Matsushita, A. Hosoi, S. Ueha et al., "Cytotoxic T lymphocytes block tumor growth both by lytic activity and IFN $\gamma$ -dependent cell-cycle arrest," *Cancer Immunology Research*, vol. 3, no. 1, pp. 26–36, 2015.
- [23] Y. Gao, W. Yang, M. Pan et al., "Gamma delta T cells provide an early source of interferon gamma in tumor immunity," *The*

- Journal of Experimental Medicine*, vol. 198, no. 3, pp. 433–442, 2003.
- [24] J. Yu, M. Wei, B. Becknell et al., “Pro- and antiinflammatory cytokine signaling: reciprocal antagonism regulates interferon-gamma production by human natural killer cells,” *Immunity*, vol. 24, no. 5, pp. 575–590, 2006.
- [25] M. C. Leite-de-Moraes, G. Moreau, A. Arnould et al., “IL-4-producing NK T cells are biased towards IFN-gamma production by IL-12. Influence of the microenvironment on the functional capacities of NK T cells,” *European Journal of Immunology*, vol. 28, no. 5, pp. 1507–1515, 1998.
- [26] J. D. Burke and H. A. Young, “IFN- $\gamma$ : a cytokine at the right time, is in the right place,” *Seminars in Immunology*, vol. 43, p. 101280, 2019.
- [27] A. Calcinotto, C. Spataro, E. Zagato et al., “IL-23 secreted by myeloid cells drives castration-resistant prostate cancer,” *Nature*, vol. 559, no. 7714, pp. 363–369, 2018.
- [28] G. J. Szebeni, C. Vizler, K. Kitajka, and L. G. Puskas, “Inflammation and cancer: extra- and intracellular determinants of tumor-associated macrophages as tumor promoters,” *Mediators of Inflammation*, vol. 2017, 9294013 pages, 2017.
- [29] R. Bent, L. Moll, S. Grabbe, and M. Bros, “Interleukin-1 beta—a friend or foe in malignancies?,” *International Journal of Molecular Sciences*, vol. 19, no. 8, p. 2155, 2018.
- [30] V. Gelfo, D. Romaniello, M. Mazzeschi et al., “Roles of IL-1 in cancer: from tumor progression to resistance to targeted therapies,” *International Journal of Molecular Sciences*, vol. 21, no. 17, p. 6009, 2020.
- [31] R. Weber, C. Groth, S. Lasser et al., “IL-6 as a major regulator of MDSC activity and possible target for cancer immunotherapy,” *Cellular Immunology*, vol. 359, p. 104254, 2021.
- [32] G. Giannone, E. Ghisoni, S. Genta et al., “Immuno-metabolism and microenvironment in cancer: key players for immunotherapy,” *International Journal of Molecular Sciences*, vol. 21, no. 12, p. 4414, 2020.

## Research Article

# The ROS/GRK2/HIF-1 $\alpha$ /NLRP3 Pathway Mediates Pyroptosis of Fibroblast-Like Synoviocytes and the Regulation of Monomer Derivatives of Paeoniflorin

Zhongyang Hong <sup>1,2</sup>, Xianzheng Zhang <sup>1</sup>, Tianjing Zhang <sup>1</sup>, Ling Hu <sup>1</sup>, Ruijin Liu <sup>1</sup>, Pan Wang <sup>1</sup>, Han Wang <sup>1</sup>, Qianqian Yu <sup>1</sup>, Dan Mei <sup>1</sup>, Ziyang Xue <sup>1</sup>, Feng Zhang <sup>2</sup>, and Lingling Zhang <sup>1</sup>

<sup>1</sup>Institute of Clinical Pharmacology, Anhui Medical University, Key Laboratory of Anti-Inflammatory and Immune Medicine, Ministry of Education, Anhui Collaborative Innovation Centre of Anti-Inflammatory and Immune Medicine, Center of Rheumatoid Arthritis of Anhui Medical University, Hefei 230032, China

<sup>2</sup>Department of Pharmacy, Affiliated Fuyang Hospital of Anhui Medical University, Fuyang 236000, China

Correspondence should be addressed to Feng Zhang; 1459724796@qq.com and Lingling Zhang; ll-zhang@hotmail.com

Received 28 October 2021; Revised 23 December 2021; Accepted 4 January 2022; Published 29 January 2022

Academic Editor: Bin Duan

Copyright © 2022 Zhongyang Hong et al. This is an open access article distributed under the Creative Commons Attribution License, which permits unrestricted use, distribution, and reproduction in any medium, provided the original work is properly cited.

Hypoxia is an important factor in the development of synovitis in rheumatoid arthritis (RA). The previous study of the research group found that monomeric derivatives of paeoniflorin (MDP) can alleviate joint inflammation in adjuvant-induced arthritis (AA) rats by inhibiting macrophage pyroptosis. This study revealed increased levels of hypoxia-inducible factor- (HIF-) 1 $\alpha$  and N-terminal p30 fragment of GSDMD (GSDMD-N) in fibroblast-like synoviocytes (FLS) of RA patients and AA rats, while MDP significantly inhibited their expression. Subsequently, FLS were exposed to a hypoxic environment or treated with cobalt ion in vitro. Western blot and immunofluorescence analysis showed increased expression of G protein-coupled receptor kinase 2 (GRK2), HIF-1 $\alpha$ , nucleotide-binding oligomerization segment-like receptor family 3 (NLRP3), ASC, caspase-1, cleaved-caspase-1, and GSDMD-N. Electron microscopy revealed FLS pyroptosis after exposure in hypoxia. Next, corresponding shRNAs were transferred into FLS to knock down hypoxia-inducible factor- (HIF-) 1 $\alpha$ , and in turn, NLRP3 and western blot results confirmed the same. The enhanced level of GSDMD was reversed under hypoxia by inhibiting NLRP3 expression. Knockdown and overexpression of GRK2 in FLS revealed GRK2 to be a positive regulator of HIF-1 $\alpha$ . Levels of GRK2 and HIF-1 $\alpha$  were inhibited by eliminating excess reactive oxygen species (ROS). Furthermore, MDP reduced FLS pyroptosis through targeted inhibition of GRK2 phosphorylation. According to these findings, hypoxia induces FLS pyroptosis through the ROS/GRK2/HIF-1 $\alpha$ /NLRP3 pathway, while MDP regulates this pathway to reduce FLS pyroptosis.

## 1. Introduction

Rheumatoid arthritis (RA), a chronic aggressive and debilitating autoimmune disease with an unknown origin, is characterized by systemic inflammation response, the production of abnormal antibodies, and persistent synovitis [1, 2]. Approximately 9.7 million people worldwide are estimated to be suffering from this disease [3]. In recent years, hypoxia

of synovial tissue has been increasingly recognized as an important factor influencing the development of RA [4–6]. Adaptive transcriptional responses to low oxygen tension are mediated mainly through the hypoxia-inducible factors (HIFs), which are tightly regulated by three prolyl hydroxylases and one asparagine hydroxylase [7]. In steady-state conditions, hydroxylases suppress the activity of HIF through the hydroxylation of proline (Pro402 and Pro564)

of HIF-1 $\alpha$ , leading to ubiquitination and proteasomal degradation. A further hydroxylation of Asn803 prevents HIF transcriptional activity [8]. These modifications allow HIF-1 $\alpha$  to bind to Von Hippel-Lindau (VHL) for proteasomal degradation [9]. These processes are blocked by hypoxia, allowing HIF-1 $\alpha$  to accumulate and induce the expression of HIF target genes [10].

Hypoxia induces excessive production of reactive oxygen species (ROS) through mitochondrial damage to increase the synthesis of HIF-1 $\alpha$  [11, 12]. For example, the negative regulatory factor nonselenocysteine-containing phospholipid hydroperoxide glutathione peroxidase (NPGx) of the translational regulator cytoplasmic polyadenylation element-binding protein 2 (CPEB2) is consumed by ROS, leading to elevated HIF-1 $\alpha$  RNA translation. A positive correlation between ROS and G protein-coupled receptor kinase 2 (GRK2) levels was found in sickle erythrocytes [13, 14]. Moreover, the phosphorylation of GRK2 serine 670 (S670) increased the total levels and cytoplasmic shuttling of the mRNA-binding protein human antigen R (HuR) in response to hypoxia, subsequently increasing the synthesis of HIF-1 $\alpha$  in HeLa cells [15].

In a recent study, the expression of nucleotide-binding oligomerization segment-like receptor family 3 (NLRP3) was found to be mediated by HIF-1 $\alpha$  during hypoxic conditions [16]. The integrated regulation of inflammasome activation and pyroptosis promotes the antimicrobial host defense and the clearance of pathogens [17, 18]. However, aberrant activation of NLRP3 inflammasome and pyroptosis may induce pathological autoimmune responses, that are harmful to the host [19–21]. For example, NLRP3 inflammasome is known to recruit and activate caspase-1 through an adaptor molecule ASC, and this activated caspase-1 can then cleave gasdermin D (GSDMD), interleukin (IL)-1 $\beta$ , and IL-18 to mature forms and subsequently trigger pyroptotic cell death [22]. Pyroptosis is redefined as GSDMD-mediated programmed necrosis, accompanied by the secretion of inflammatory cytokines IL-1 $\beta$  and IL-18 [23]. Both IL-1 $\beta$  and IL-18 belong to the IL-1 family and play vital roles in host defense, immune regulation, and inflammatory responses [24].

In RA, HIF-1 $\alpha$  is highly expressed in synovial tissue, which contributes significantly to the expression of inflammatory genes and cell survival in the synovium [25]. Therefore, an effective RA treatment strategy to inhibit HIF-1 $\alpha$  is urgently needed. In this regard, as the major active component of *Paonia lactiflora* Pallas, *Paeoniflorin* (Pae) has been proven to prevent CoCl<sub>2</sub>-induced HIF-1 $\alpha$  accumulation and the expressions of p53 and Bcl-2/adenovirus E1B 19 kDa interacting protein 3 (BNIP3) [26]. A preliminary study by our research group confirmed that Pae could inhibit inflammation in the animal models of autoimmune diseases, such as experimental arthritis, psoriasis in mice, and experimental autoimmune encephalomyelitis [26]. However, the bioavailability of Pae is not ideal due to its high hydrophilicity [27]. To this end, the monomer derivative of Pae (MDP), developed by our group, exhibited superior bioavailability and efficacy than Pae. MDP could reduce macrophage pyroptosis by inhibiting toll-like receptor 4 (TLR4) [28]. It is worth noting that arthritis

is often accompanied by tissue hypoxia [29]. At present, there are only a few studies on the relationship between hypoxia of synovial tissue and pyroptosis, and MDP significantly reversed the pathological changes of synovial tissue in AA rats [28].

Thus, hypoxia in the microenvironment of the joint cavity exacerbates synovial inflammation in multiple ways. Fibroblast-like synoviocytes (FLS) pyroptosis may play a crucial role in the entire pathogenesis of RA. This programmed inflammatory cell death may be regulated by HIF-1 $\alpha$ , and MDP may be an ideal drug to inhibit pyroptosis. In this study, we investigated the molecular mechanism of the correlation between hypoxia and FLS pyroptosis and the role of MDP in vitro. We hypothesize that elevated HIF-1 $\alpha$  in FLS may aggravate synovitis via FLS pyroptosis. The increase in HIF-1 $\alpha$  is partly due to the increase in GRK2 expression caused by oxidative stress. MDP may reduce the expression of HIF-1 $\alpha$  through targeted inhibition of GRK2 and then inhibit FLS pyroptosis to alleviate synovial inflammation.

## 2. Materials and Methods

**2.1. Antibiotics and Reagents.** MDP [C<sub>29</sub>H<sub>32</sub>O<sub>13</sub>S, molecular weight: 620], purity > 98%, was provided by the Chemistry Laboratory of the Institute of Clinical Pharmacology of Anhui Medical University (Hefei, China); LW6 (CAS: 934593-90-5) was obtained from MedChemExpress (USA). N-acetyl-L-cysteine (NAC) was purchased from Beyotime Biotechnology (Shanghai, China). Dulbecco's modified Eagle's medium (DMEM) was obtained from Gibco Co. Ltd. (CA, USA). Fetal calf serum was purchased from Wisent Co. Ltd. (Canada). Streptomycin, penicillin, ROS Assay Kit, and goat anti-rabbit IgG were purchased from Beyotime Biotechnology Co. Ltd. (Shanghai, China). Enzyme-linked immunosorbent assay (ELISA) kits for IL-1 $\beta$  and IL-18 were the products from J&L Biological (Shanghai, China). Antibodies against GRK2, p-GRK2 S670, HIF-1 $\alpha$ , NLRP3, ASC, Caspase-1, GSDMD, and  $\beta$ -actin were purchased from Affinity Bioscience (Taiwan, China). The antibody against VHL was the product from Wanleibio (Shenyang, China).

**2.2. Isolation and Culture of Primary Fibroblast-Like Synoviocytes.** This was performed as described earlier [30]. In brief, the synovial tissues of OA, RA patients, and healthy persons were washed 2-3 times with phosphate-buffered saline (PBS), then minced into 1-2 mm<sup>3</sup> pieces. The tissue fragments were then transferred to the culture flask, placed in an incubator at 37°C and 5% CO<sub>2</sub> for 4 h, then added into 3 mL DMEM supplemented with 20% fetal calf serum and antibiotics (100 U/mL penicillin, 100  $\mu$ g/mL streptomycin) for further culture until confluent (5-7 days) and then dissociated with Trypsin/EDTA into a single-cell suspension. After dissociation, fibroblasts were pelleted by centrifugation at 1,200 rpm for 5 min and cultured in DMEM supplemented with 20% fetal calf serum. FLS were identified based on both cell surface marker and morphological features as described previously [31]. The primary FLS of Sprague-Dawley rats were separated and cultured in the same way.

**2.3. Hypoxia Treatment and Medication of Fibroblast-Like Synoviocytes.** To observe the biological response of cells induced by hypoxia, FLS were exposed to hypoxia (1% O<sub>2</sub> for 2 h or 24 h). Next, FLS were treated with or without MDP (10<sup>-6</sup> mol/L), LW6 (a hypoxia-inducible factor 1 inhibitor; 5 μmol/L), and NAC (100 μmol/L).

**2.4. Scanning Electron Microscopy (SEM) to Observe the Pyroptosis of Fibroblast-Like Synoviocytes.** The cells were fixed with 5% glutaraldehyde, then dehydrated with gradient ethanol and hexamethyldisilazane, and placed in a fume hood overnight. The ion sputtering coating method was used for treatment of the cells. Images of the cells were acquired with an electron microscope (GeminiSEM 300, Carl Zeiss, Germany).

**2.5. The Expression of Nucleotide-Binding Oligomerization Segment-Like Receptor Family 3, Hypoxia-Inducible Factor-1α, and Other Proteins in Fibroblast-Like Synoviocytes Was Detected by Western Blot.** FLS were mixed with RIPA lysate (Beyotime Biotechnology) and ground for 10-15 min. Samples were agitated on ice for 30 min, and the supernatant was collected. The protein levels were quantified using a BCA protein assay kit (Roche, Basel, Switzerland). Then, the protein samples were resolved by sodium dodecyl sulfate-polyacrylamide gel electrophoresis to separate protein bands. Proteins were transferred from the gel onto polyvinylidene fluoride membrane and blocked with 5% nonfat dry milk for 2 h. The membrane was incubated overnight with the primary antibody (1: 500) at 4°C and then with the secondary antibody for 2 h. The bands were visualized by the electrochemiluminescence method, and the overall gray values of protein bands (average gray value area) were quantified. At the same time, β-actin was used as an internal marker to compare the gray value of target protein in different groups.

**2.6. Analysis of N-Terminal p30 Fragment of GSDMD (GSDMD-N) Expression by Immunofluorescence.** FLS were cultured in 35 mm glass-bottom dishes, fixed with 4% paraformaldehyde, permeabilized with 0.1% Triton X-100, and then, blocked with 0.5% bovine serum albumin (BSA). The cells were then incubated with anti-GSDMD-N (1:100) antibody in a 4°C wet chamber. Next, FLS were washed with PBS and then were incubated for 2 h at room temperature with Alexa-Fluor-594-tagged secondary antibodies. The images were detected by fluorescence microscopy (LEICA sp8), and positive images further underwent computerized digital image analysis. The intensity of immunofluorescence was analyzed using Image J.

**2.7. Detection of IL-1β and IL-18 Levels by Enzyme-Linked Immunosorbent Assay.** FLS were treated with or without MDP and then cultured in a 1% oxygen or normoxia environment for 24 h. The cell supernatant was collected for cytokine detection. In brief, IL-1β and IL-18 levels in the culture media were determined using commercially available rat IL-1β and IL-18 ELISA kits according to manufacturer's instructions.

**2.8. Short Hairpin RNAs Were Used to Inhibit HIF-1α and NLRP3 Expressions in FLS.** To study the role of HIF-1α and NLRP3 in the pathway of pyroptosis in FLS, the commercially available short hairpin RNAs for HIF-1α, NLRP3 (Table 1) and empty vector (General Biol, Chuzhou, China) were purchased. Then, FLS were transfected with shRNAs by using Lipofectamine 3000 (Invitrogen, CA, USA) according to manufacturer's instructions.

**2.9. Short Hairpin RNA and Overexpression Plasmid to Alter G Protein-Coupled Receptor Kinase 2 Expression in FLS.** To verify whether GRK2 can promote the expression of HIF-1α, the commercially available GRK2 (Table 1) and empty vector (General Biol, Chuzhou, China) were used. The commercially available GRK2 overexpression plasmid and empty vector were purchased from General Biol (Chuzhou, China). The GRK2 shRNA and overexpression plasmid were transfected to FLS using Lipofectamine 3000 (Invitrogen, CA, USA) according to manufacturer's instructions.

**2.10. Docking of MDP to the G Protein-Coupled Receptor Kinase 2 Structural Model.** Docking simulation of MDP with GRK2 protein (PDB ID: 3KRW, human GRK2 in complex with Gbetgamma subunits and balanol) was carried out using the program Discovery Studio 2.1 (DS 2.1; Accelrys Software Inc.). The active sites and sphere of 10 Å were defined according to the reported important amino acid residues of GRK2 that are generated around the active site pocket of the BSAI model using C-DOCKER, a molecular dynamics (MD) simulated-annealing-based algorithm module from DS 2.1. As previously described [32], the structure of protein and substrate was subjected to energy minimization using chemistry at Harvard macromolecular mechanics force field as implemented in DS 2.1. A full potential final minimization was then conducted to refine the substrate poses. Based on C-DOCKER, energy docked conformation of the substrate was retrieved for postdocking analysis.

**2.11. Imaging Flow Cytometry to Detect the Nuclear Expression of HIF-1α.** The flow cytometry was performed following the earlier published standard protocol [33]. Cells were separated into different tubes and incubated with Cytofix and Cytoperm for simultaneous fixation and permeabilization. Next, cells were stained with a HIF-1α primary antibody according to manufacturer's directions and then sequentially incubated with the corresponding fluorescent secondary antibody and 2-(4-Amidinophenyl)-6-indolecarbamidine (DAPI). The images were detected by imaging flow cytometer (Amnis Imagestream Mark II), and positive images were analyzed by ideas 6.2 analysis.

**2.12. Detection of the mRNA Expression Levels of NLRP3, ASC, and Caspase-1 by Quantitative PCR (qPCR).** Total RNA from the cells was extracted using TRIzol (Biomed, Beijing, China) reagent according to manufacturer's manual. Complementary DNA (cDNA) was synthesized using an oligo (dT) primer and PrimeScript™ RT Reagent Kit (Takara, Shiga, Japan). qPCR was performed to amplify the cDNA using the SYBR Premix Ex Tag Kit (Takara, Shiga, Japan) on an ABI 7500 Sequencing Detection System

TABLE 1: Composition of short hairpin RNAs.

|                   |           |                                   |
|-------------------|-----------|-----------------------------------|
| HIF-1 $\alpha$ 1# | Sense     | 5'-AATCAAAAGCAGTGACGAA-3'         |
|                   | Antisense | 5'-TTCGTCAGTCTTTTGATT-3'          |
| HIF-1 $\alpha$ 2# | Sense     | 5'-CTGATAACGTGAACAAATA-3'         |
|                   | Antisense | 5'-TATTTGTTACGTTATCAG-3'          |
| NLRP3 1#          | Sense     | 5'-CCUGUCUUUGCCGUAGAUUACCGUAAG-3' |
|                   | Antisense | 5'-CUUACGGUAAUCUACGGCAAAGACAGG-3' |
| NLRP3 2#          | Sense     | 5'-GUGGACCUCAAGAAAUUUATT-3'       |
|                   | Antisense | 5'-UAAAUUUCUUGAGGUCCACTT-3'       |
| GRK2 1#           | Sense     | 5'-CCAUGAAGUGUCUGGACAATT-3'       |
|                   | Antisense | 5'-UUGUCCAGACACUUCAUGGTT-3'       |
| GRK2 2#           | Sense     | 5'-GCAGGUACCUCAGAUUCUC-3'         |
|                   | Antisense | 5'-GAGAUCUGGAGGUACCUGC-3'         |

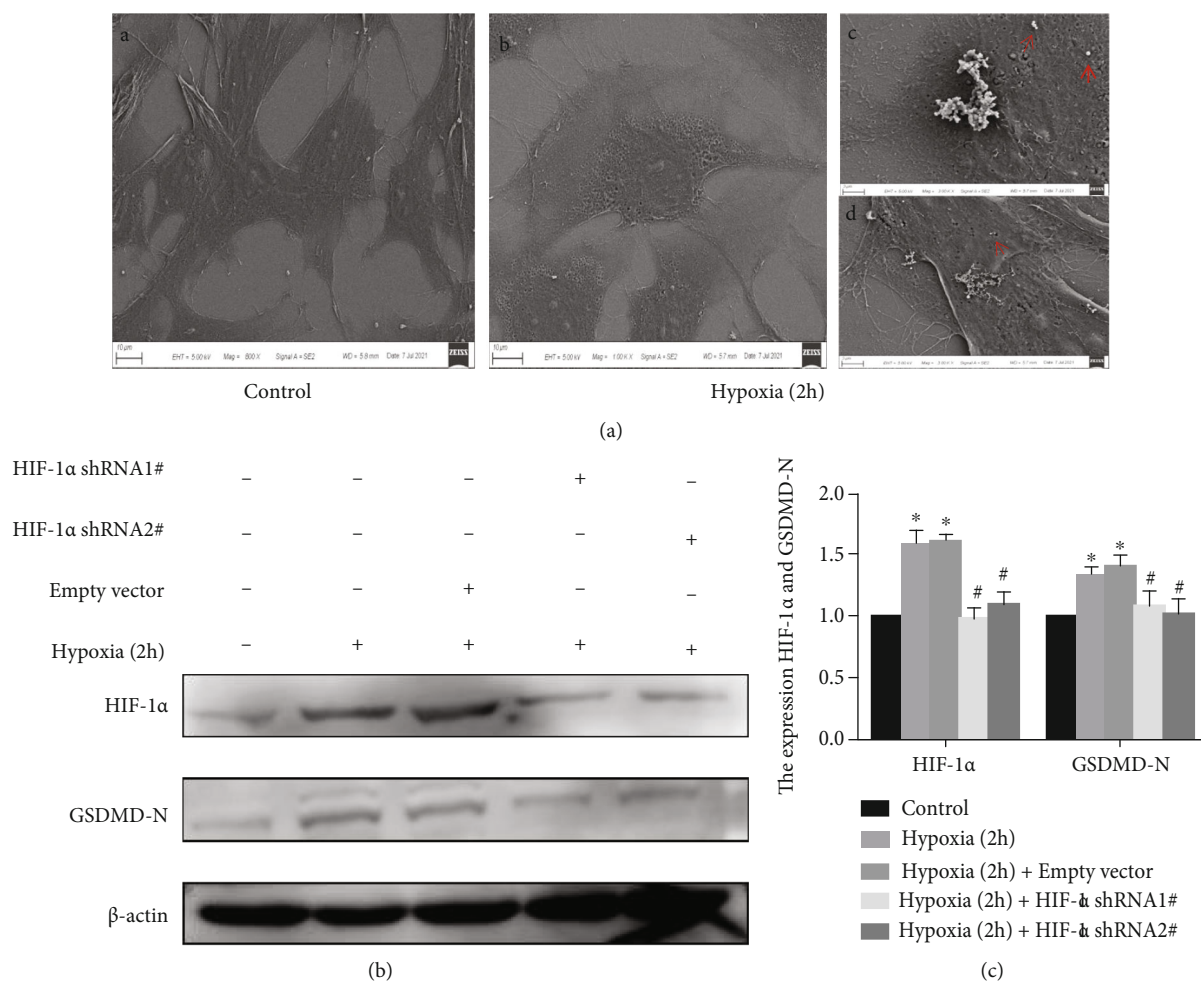
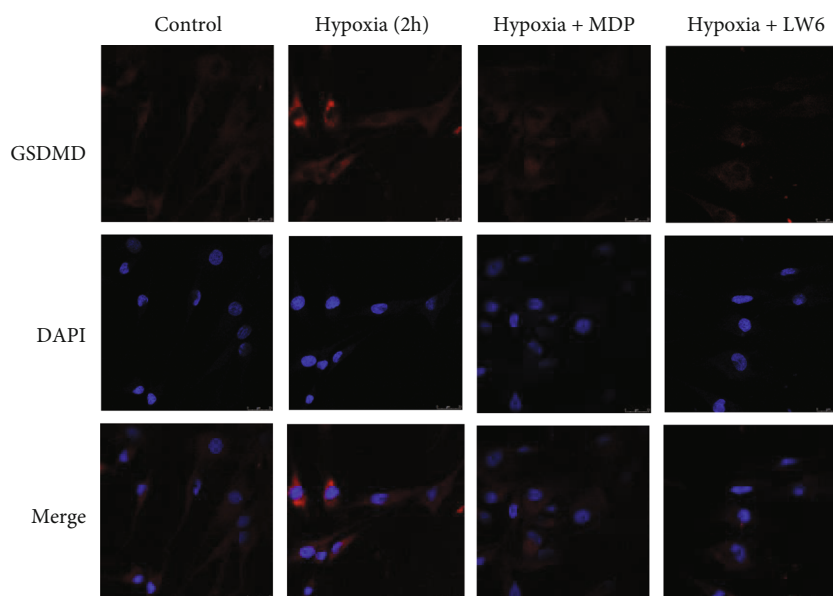
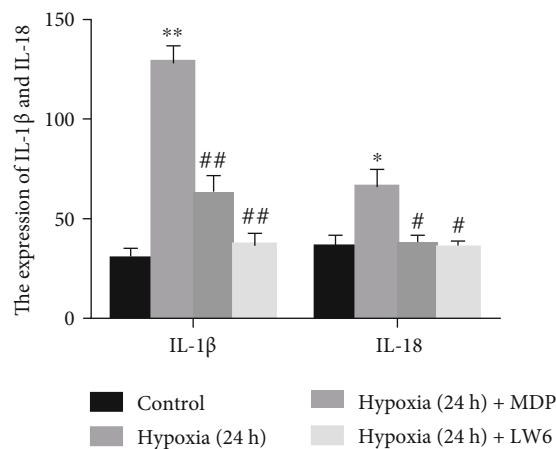


FIGURE 1: Hypoxia-mediated induction of pyroptosis in fibroblast-like synoviocytes (FLS). (a) Representative scanning electron microscope images of FLS pyroptosis. a, b FLS cultured under normoxia and hypoxia, respectively (1000x). c, d FLS cultured under hypoxia for 2 h (3000x). A HIF-1 $\alpha$  short hairpin (shHIF-1 $\alpha$ ) construct was transfected into FLS, and hypoxic condition was imposed for 2 h. (b, c) Immunoblot analysis and quantification of hypoxia-inducible factor (HIF)-1 $\alpha$  and N-terminal domain of human gasdermin D (GSDMD-N). Data are presented as mean  $\pm$  standard deviation.  $n = 3$ . \* $p < 0.05$  compared with the control group and # $p < 0.05$  compared with the empty vector group.





(a)



(b)

FIGURE 2: Monomeric derivatives of paeoniflorin (MDP) reduces hypoxia-induced fibroblast-like synoviocytes (FLS) pyroptosis. (a) Representative images of immunofluorescence of N-terminal domain of human gasdermin D (GSDMD-N) in FLS. (b) Enzyme-linked immunosorbent assay and quantification of interleukin- (IL-) 1 $\beta$  and IL-18 ( $n = 5$ ). Data are expressed as mean + standard deviation. \* $p < 0.05$ , \*\* $p < 0.01$  vs. the control group; # $p < 0.05$ , ## $p < 0.01$  vs. the hypoxia group.

(Applied Biosystems, Foster City, CA, USA). Primers were designed and synthesized by Shanghai General Bio Service Company as per the gene sequences available in the GenBank, together with Oligo v6.6. Sequences for primers were as follows: NLRP3 forward 5'-CTCACCTCACACTCCTGCTG-3', reverse 5'-AGAACCTCACAGAGCGTCAC-3'; Caspase-1 forward 5'-GACCGAGTGGTTCCCTCAAG-3', reverse 5'-GACGTG TACGAGTGGGTGTT-3'. ASC forward 5'-GACAGTACCAGGCAG TTCGT-3', reverse 5'-AGTAGGGCTGTGTTTGCCTC-3'.  $\beta$ -Actin, forward 5'-GGAGATTACTGCCCTGGCTCCTAGC-3', reverse 5'-GGCCGACTCATCGTACTCCTGCT-3'. The mRNA level of individual genes was normalized to  $\beta$ -actin and calculated by the  $2^{-\Delta\Delta Ct}$  data analysis method.

**2.13. Determination of Intracellular Reactive Oxygen Species.** FLS were transferred after different treatments to different EP tubes. Next, cells were stained using the ROS Assay Kit (S0033S) according to the instructions. As previously described [33], the ROS content was estimated with a flow cytometer (FC500, Beckman); the results were analyzed using CytExpert (Beckman), and calculated by mean fluorescence intensity.

**2.14. ROS Relative Quantification.** An equal number of cells were planted in each well of the 96-well plate. The old medium was sucked up, and the cells were washed with PBS once. Under dark conditions, 100  $\mu$ L probe working solution was added to each well, and the cells incubated for 20 min at 37°C. Discarding the probe incubation solution,

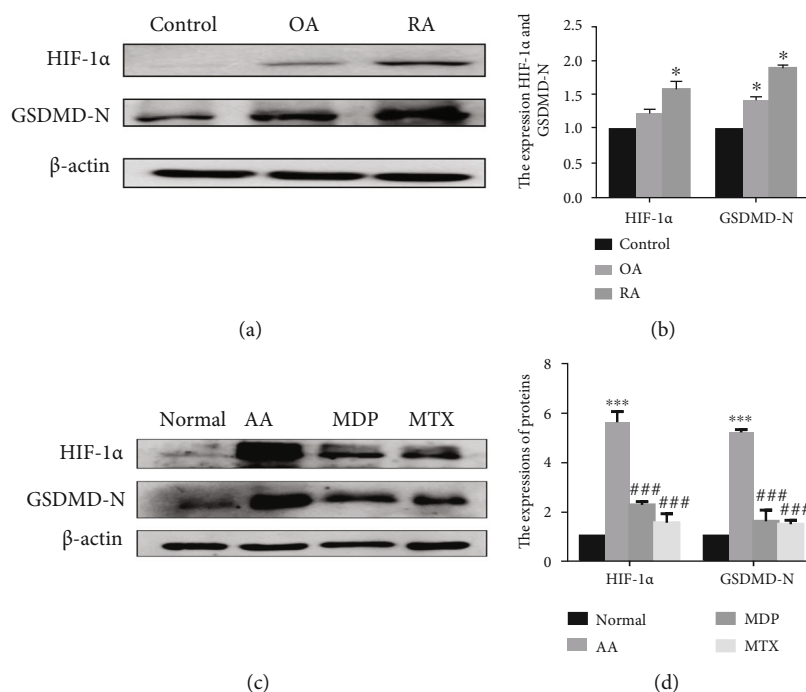


FIGURE 3: The levels of hypoxia-inducible factor (HIF)-1 $\alpha$  and N-terminal domain of human gasdermin D (GSDMD-N) increase in fibroblast-like synoviocytes (FLS) of RA patients and adjuvant-induced arthritis (AA) rats. (a, b) Immunoblot analysis and quantification of HIF-1 $\alpha$  and GSDMD-N in the FLS of RA patients. (c, d) Immunoblot analysis of HIF-1 $\alpha$  and GSDMD-N expression levels in FLS of normal, AA, AA+MDP, and AA+MTX rats. Data are presented as mean  $\pm$  standard deviation.  $n = 3$ . \* $p < 0.05$ , \*\*\* $p < 0.001$  compared with the control group and ### $p < 0.001$  compared with the AA group (MTX: methotrexate; MDP: monomeric derivatives of paeoniflorin).

wash cells gently with PBS once. Then, add 100  $\mu$ L medium to each well. The fluorescence intensity was detected, and the data was saved. Then, the number of cells per well was estimated by CCK-8 method. And the ratio of fluorescence intensity to total cell number is the relative ROS level.

**2.15. Fibroblast-Like Synoviocytes Proliferation Assay.** FLS were counted and seeded in 96-well plates at a density of  $1 \times 10^4$  cells/well and incubated in DMEM at 37°C for 24 h. The cells were then exposed to hypoxia conditions for 24 h and treated with or without MDP for 16 h. After treatment, the cells were washed with PBS and incubated with DAPI dihydrochloride for 5 min. Finally, the number of cells per well was calculated by high-content analysis.

**2.16. Statistical Analysis.** The results were presented as the mean  $\pm$  standard deviation of at least three separate experiments performed in triplicate. SPSS v16.0 software was used to analyze differences among groups by performing a one-way analysis of variance followed by Bonferroni postcomparison test (>two groups) or two-sample  $t$ -test (two groups) with significant differences at  $p < 0.05$ .

### 3. Result

**3.1. Fibroblast-Like Synoviocytes pyroptosis under Hypoxia.** To verify that hypoxia can induce FLS pyroptosis, we compared the morphological differences of FLS cultured under normoxia and hypoxia by electron microscopy. FLS exposed to a hypoxic environment exhibited a large number of mem-

brane pores. Interestingly, under higher magnification, the cell contents overflowing from the membrane pores were also observed (Figure 1(a)). Next, Western blot analysis showed increased expression of GSDMD-N under hypoxia in FLS (Figures 1(b) and 1(c)). Meanwhile, the HIF-1 $\alpha$  shRNA group showed a significant decrease in GSDMD-N compared with the negative control group ( $p < 0.05$ ) (Figures 1(b) and 1(c)).

**3.2. Monomeric Derivatives of Paeoniflorin-Mediated Reduction of the Hypoxia-Induced Pyroptosis of FLS.** Immunofluorescence image analysis showed that the level of GSDMD-N in FLS increased under hypoxia and decreased after MDP treatment (Figure 2(a)). Meanwhile, examination of the FLS supernatant revealed an increase in cytokines levels of IL-1 $\beta$  and IL-18 under hypoxia but decreased significantly after MDP treatment of FLS under hypoxia (Figure 2(b)).

**3.3. Increased Expressions of Hypoxia-Inducible Factor-1 $\alpha$  and Gasdermin D and the Inhibition of Monomeric Derivatives of Paeoniflorin in Fibroblast-Like Synoviocytes in Patients with Rheumatoid Arthritis and Animal Models of Arthritis.** Western blot analysis showed highly expressed HIF-1 $\alpha$  and GSDMD-N in the FLS of RA patients (Figures 3(a) and 3(b)). Higher expressions of HIF-1 $\alpha$  and GSDMD-N were also observed in the FLS of adjuvant arthritis (AA) samples (Figures 3(c) and 3(d)) that were interestingly restored by MDP (Figures 3(e) and 3(f)).

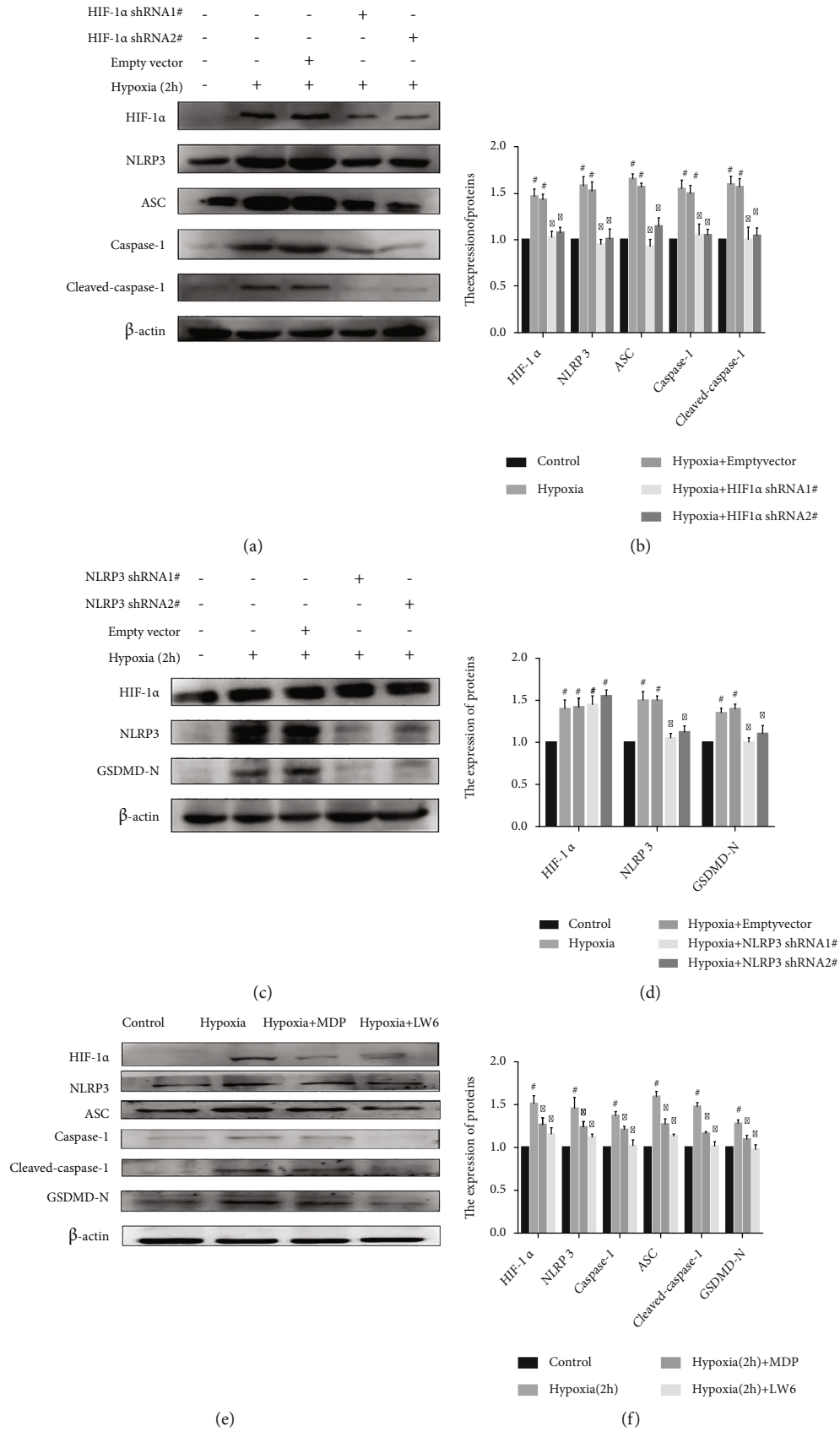


FIGURE 4: Continued.

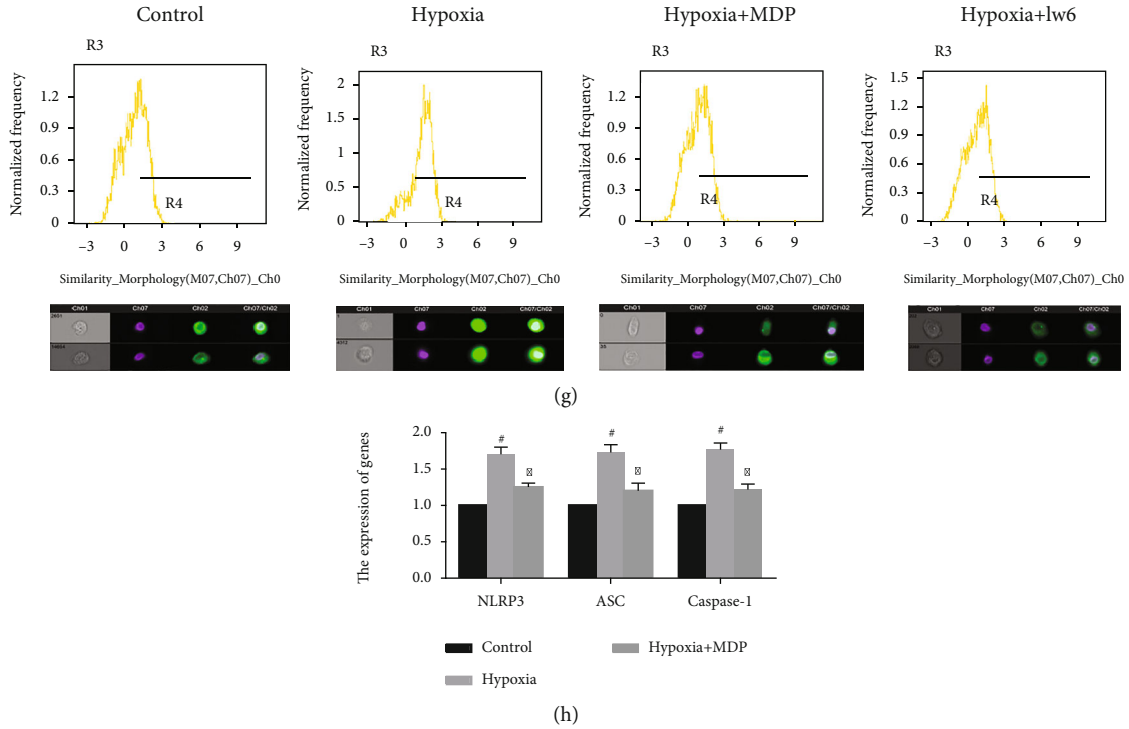


FIGURE 4: Hypoxia induces fibroblast-like synoviocytes (FLS) pyroptosis by upregulating the expression of nucleotide-binding oligomerization segment-like receptor family 3 (NLRP3) inflammasome in FLS and the effect of monomeric derivatives of paeoniflorin (MDP). (a, b) shHIF-1 $\alpha$  was transfected into FLS and exposed to hypoxia for 2 h. The expression of hypoxia-inducible factor (HIF)-1 $\alpha$ , NLRP3, speck-like protein containing CARD (ASC), caspase-1, and cleaved-caspase-1 in FLS was detected by Western blot ( $n = 3$ ). (c, d) NLRP3 short hairpin (shNLRP3) construct was transfected into FLS and exposed to hypoxia for 2 h. The expression of HIF-1 $\alpha$ , NLRP3, and N-terminal domain of human gasdermin D (GSDMD-N) in FLS after exposure to hypoxia for 2 h was detected by Western blot ( $n = 3$ ). (e, f) FLS were treated with or without MDP and exposed to hypoxia for 2 h. The expression of HIF-1 $\alpha$ , NLRP3, ASC, caspase-1, cleaved-caspase-1, and GSDMD-N in FLS was detected by Western blot ( $n = 3$ ). Data are expressed as mean  $\pm$  SD. <sup>#</sup> $p < 0.05$ , <sup>##</sup> $p < 0.01$  vs. the control group; \* $p < 0.05$ , \*\* $p < 0.01$  vs. the hypoxia group. (g) Analysis of expression levels of HIF-1 $\alpha$  in the nucleus. (h) Quantitative PCR analysis and quantification of the mRNA levels of NLRP3, ASC, and caspase-1. Data are expressed as mean SD. <sup>#</sup> $p < 0.05$  vs. the control group; \* $p < 0.05$  vs. the hypoxia group.

**3.4. Induction of FLS pyroptosis by Hypoxia through the Upregulated Expression of NLRP3 Inflammasome and the Role of Monomeric Derivatives of Paeoniflorin.** To explore the mechanism of hypoxia-induced FLS pyroptosis, we tested the levels of NLRP3 inflammasome and cleaved-caspase-1 which were closely related to pyroptosis. Western blot showed a significant increase in the contents of NLRP3 inflammasome and cleaved-caspase-1 in FLS under hypoxia. Further, after HIF-1 $\alpha$  knockdown, the levels of NLRP3 inflammasome and cleaved-caspase-1 also reduced (Figures 4(a) and 4(b)). The expression of GSDMD-N also decreased in the absence of NLRP3 (Figures 4(c) and 4(d)). Treatment with MDP led to a decrease in the levels of NLRP3 inflammasome and cleaved-caspase-1 (Figures 4(e) and 4(f)).

Then, to confirm that the transcription of NLRP3 inflammasome is directly regulated by HIF-1 $\alpha$ , the proportion of HIF-1 $\alpha$  in the nucleus and mRNA expression level of NLRP3 inflammasome were determined. The expression of HIF-1 $\alpha$  in the nucleus increased under hypoxic conditions, as shown by flow cytometry imaging (Figure 4(g)). Meanwhile, the mRNA levels of NLRP3 inflammasome

increased significantly in FLS under hypoxia (Figure 4(h)). However, MDP could suppress this change (Figures 4(g) and 4(h)).

**3.5. Hypoxia Increases HIF-1 $\alpha$  Expression by Upregulating G Protein-Coupled Receptor Kinase 2 Expression in Fibroblast-Like Synoviocytes.** To further clarify the relationship between GRK2 and HIF-1 $\alpha$ , GRK2-knockdown and GRK2-overexpressing cells were examined. Unsurprisingly, HIF-1 $\alpha$  expression decreased in absence of GRK2 (Figures 5(e) and 5(f)) and increased in the presence of excess GRK2 (Figures 5(g) and 5(h)).

**3.6. MDP Reduces HIF-1 $\alpha$  Expression through Targeted Inhibition of G Protein-Coupled Receptor Kinase 2S670 Phosphorylation in Fibroblast-Like Synoviocytes.** The molecular docking assay showed the formation of hydrogen bonds between I197, K319, K220, N322, and G201 in the kinase domain of GRK2 and MDP (Figures 6(a) and 6(b)). Further research showed that MDP inhibited the phosphorylation of GRK2 S670, rather than reducing the expression level of GRK2 (Figures 6(c) and 6(d)).

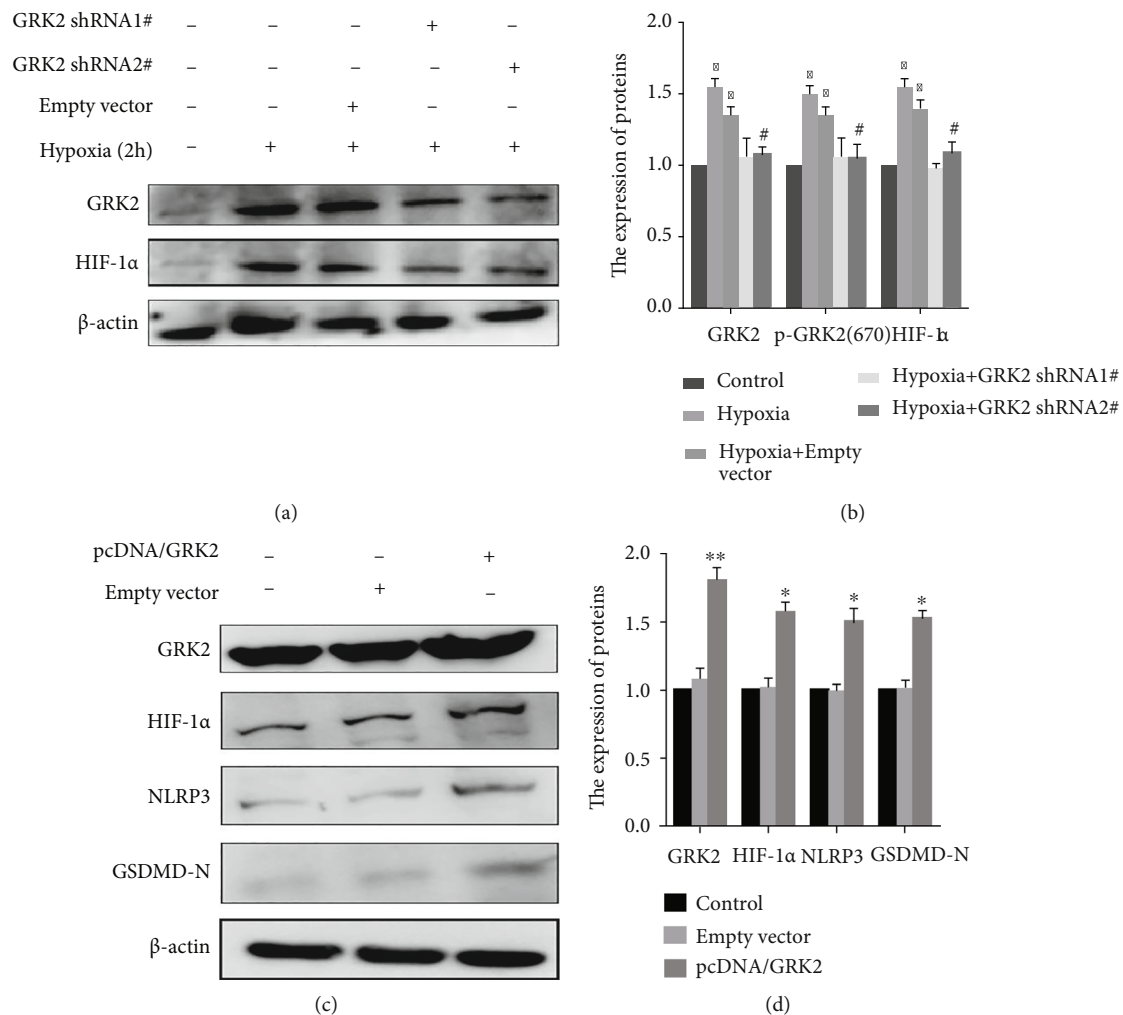


FIGURE 5: G protein-coupled receptor kinase 2 (GRK2) promotes the expression of hypoxia-inducible factor (HIF)-1 $\alpha$ . (a, b) shGRK2 was transfected into fibroblast-like synoviocytes (FLS) and exposed to hypoxia for 2 h. Immunoblot analysis and quantification of GRK2 and HIF-1 $\alpha$ . (c, d) GRK2 overexpression plasmid was transfected into FLS. Immunoblot analysis and quantification of GRK2, HIF-1 $\alpha$ , nucleotide-binding oligomerization segment-like receptor family 3 (NLRP3), and N-terminal domain of human gasdermin D (GSDMD-N). The values are shown as the mean  $\pm$  standard deviation ( $n = 3$ ). \* $p < 0.05$ , \*\* $p < 0.01$  compared with the control group and # $p < 0.05$  compared with the hypoxia group or the NC group.

3.7. *The Increase in G Protein-Coupled Receptor Kinase 2 Level under Hypoxia Is due to the Increase in Reactive Oxygen Species Content in Fibroblast-Like Synoviocytes.* To explore the cause for the increase in GRK2 under hypoxic conditions, the ROS content was assessed. Flow cytometry data and the quantitative results of enzyme reader showed that ROS levels increased significantly after 2 h of hypoxia in FLS (Figures 7(a) and 7(b)). Besides, the levels of GRK2, HIF-1 $\alpha$ , and GSDMD-N reduced significantly in FLS after NAC (a ROS scavenger) treatment (Figures 7(c) and 7(d)). In addition, the high-content analysis showed a decrease in the number of cells after FLS were exposed to a hypoxic environment for 24 h (Figure 7(e)).

#### 4. Discussion

We herein present evidence for hypoxia aggravated synovitis by inducing FLS pyroptosis in RA. Our results showed that

removal of ROS, HIF-1 $\alpha$ , GRK2, or NLRP3 knockdown significantly attenuated hypoxia-induced FLS pyroptosis. Moreover, ROS promoted HIF-1 $\alpha$  synthesis by upregulating GRK2 expression.

The well-known, most obvious characteristic of RA is synovitis [34]. Hypoxia in synovial tissues is one of the important pathological features of synovitis [35]. HIF-1 $\alpha$  is especially prominent in RA pathogenesis because it contributes to almost all aspects of RA-related pathologies, including synovial inflammation, damage of cartilage and bone, and angiogenesis [36]. Therefore, we performed this study demonstrating that the FLS pyroptosis, a proinflammatory mechanism, was triggered by HIF-1 $\alpha$ . Indeed, several studies have shown that HIF-1 $\alpha$  is an important cause of pyroptosis [37]. For example, microglia pyroptosis is thought to be caused by elevated HIF-1 $\alpha$  in stroke [38]. Cell pyroptosis is involved in the occurrence and development of RA, and there may be articular cartilage cell pyroptosis during the

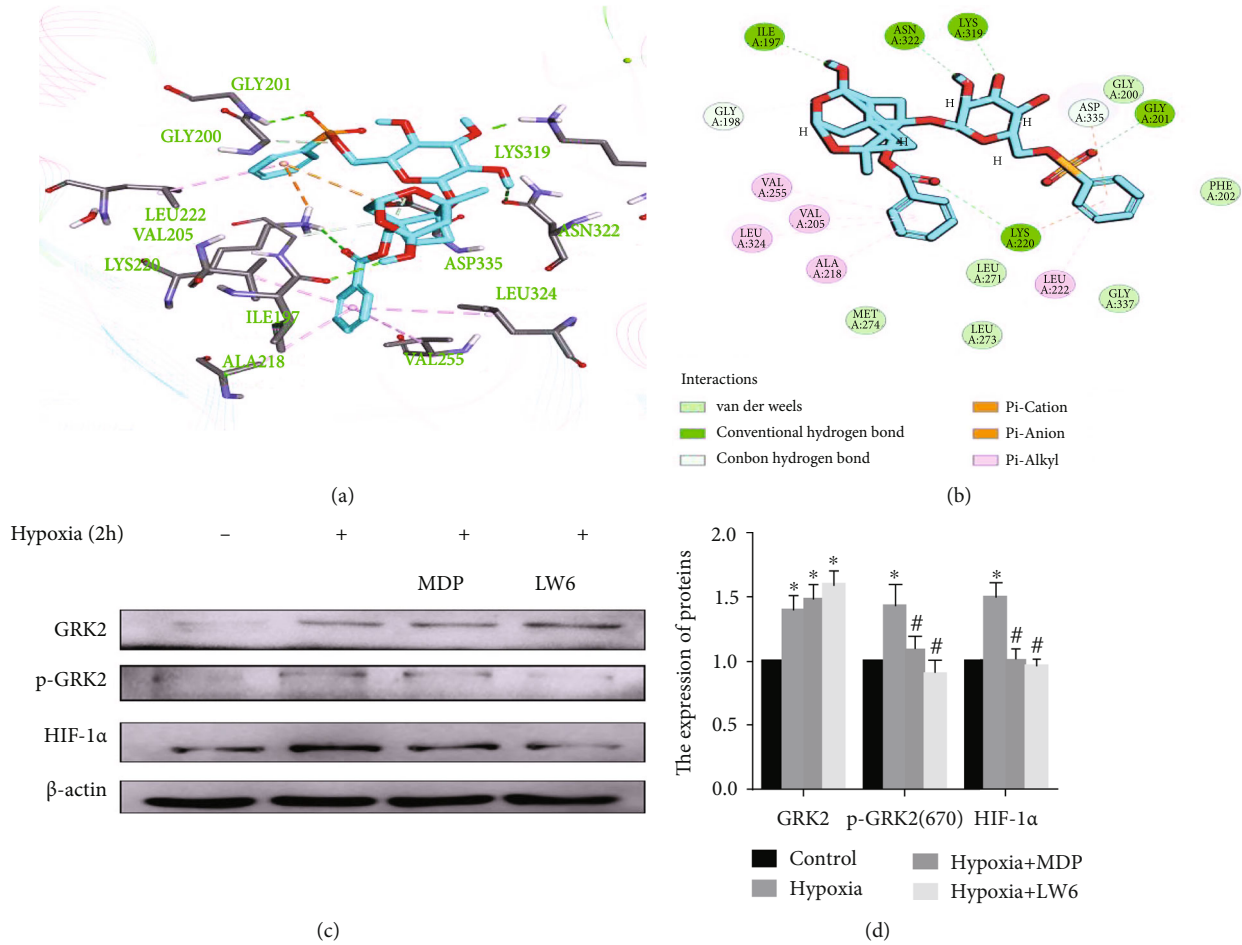


FIGURE 6: Monomeric derivative of paeoniflorin (MDP) inhibits the expression of hypoxia-inducible factor (HIF)-1 $\alpha$  through targeted inhibition of GRK2 S670 phosphorylation. (a) Molecular docking modeling of the compound MDP and G protein-coupled receptor kinase 2 (GRK2), the small molecule, and the critical interaction of 3KRW (human GRK2 in complex with Gbetgamma subunits and balanol) are represented by sticks. (b) A schematic representation of the binding mode of MDP in the GRK2 binding site of 3KRW. (c, d) FLS were treated with or without MDP and exposed to hypoxia for 2 h. Immunoblot analysis and quantification of GRK2, p-GRK2 (S670), and HIF-1 $\alpha$ . The values are shown as the mean  $\pm$  standard error of the mean ( $n = 3$ ). \* $p < 0.05$  compared with the control group and # $p < 0.05$  compared with the hypoxia group.

process [39]. Interestingly, the serum from RA patients was found to induce GSDMD-dependent pyroptosis in monocytes, and this ability was associated with disease activity [40]. Inconsistent with these findings, the current study demonstrated that the synovial hypoxic microenvironment aggravates synovitis by inducing FLS pyroptosis in RA.

Pyroptosis is mainly mediated by the NLRP3 inflammasome [41–43]. NLRP3 gene polymorphism is associated with susceptibility to RA [44]. Kolly and colleagues indicated that endothelial and inflammatory cells in RA synovium express all components needed for inflammasome activation [45, 46]. The treatment of RA patients with MCC950, a targeted inhibitor of NLRP3, resulted in significantly less severe joint inflammation and bone destruction and reduced production of IL-1 $\beta$  [44]. These studies show the vital role of NLRP3 inflammasome in the pathological process of RA. Cosin-Roger and his colleagues discovered one binding site for HIF-1 $\alpha$  at -150 in the NLRP3 pro-

motor through chromatin immunoprecipitation [47]; HIF-1 $\alpha$  regulates inflammatory responses through the NLRP3 inflammasome, thus influencing both apoptotic and pyroptotic cell death after stroke [48]. In this study, we found an essential role of NLRP3 in HIF-1 $\alpha$ -induced FLS pyroptosis and the regulation of the NLRP3 inflammasome mRNA level by HIF-1 $\alpha$ . Accordingly, we propose that the HIF-1 $\alpha$ -induced FLS pyroptosis was achieved by activating the NLRP3 inflammasome in RA.

The finding that MDP inhibits macrophage pyroptosis both in vivo and in vitro seems to give us a strategy to treat RA, although the mechanism is currently not known. One possible mechanism is through the inhibition of GRK2 phosphorylation, given that the phosphorylation of GRK2 S670 positively regulates HIF-1 $\alpha$  [15]. Interestingly, the phosphorylation of GRK2 at S670 is essential for the translocation of GRK2 to the mitochondria of cardiomyocytes post-ischemia reperfusion injury in vitro, and that this localization promotes cell death [49]. From this perspective,

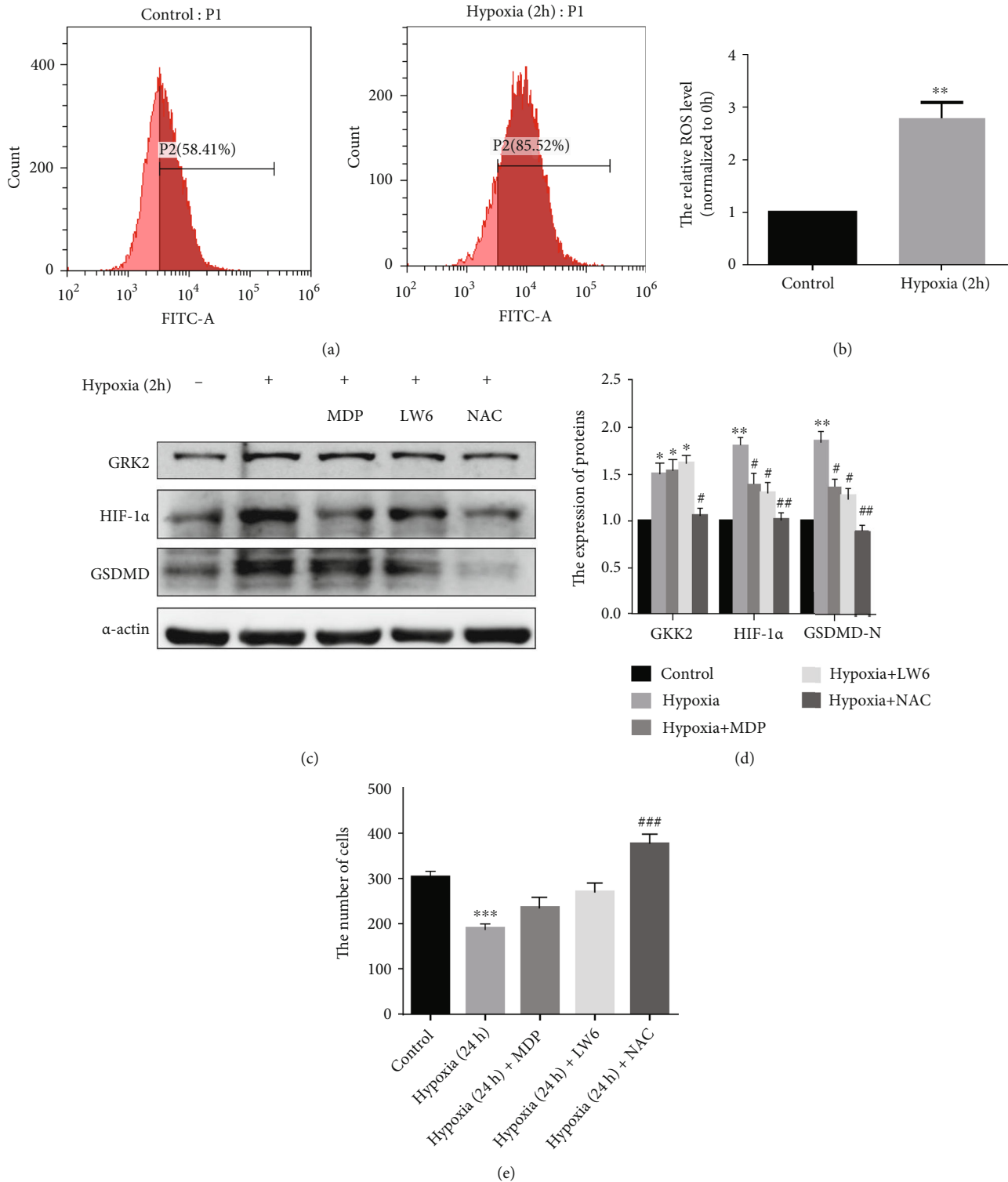


FIGURE 7: Excessive reactive oxygen species (ROS) upregulates the expression level of G protein-coupled receptor kinase 2 (GRK2) under hypoxia in fibroblast-like synoviocytes (FLS). (a, b) The analysis and quantification of ROS in FLS. (c, d) FLS were pretreated with N-acetyl-L-cysteine (NAC) before exposure to hypoxia. Immunoblot analysis and quantification of GRK2, hypoxia-inducible factor (HIF)-1 $\alpha$ , and N-terminal domain of human gasdermin D (GSDMD-N) in FLS. (e) Cell proliferation analysis.

MDP likely exerts a protective effect by inhibiting phosphorylation of GRK2 S670 in FLS. It is also noteworthy that the phosphorylation of GRK2 S670 facilitates mouse double minute 2 (an E3 ubiquitin ligase to the receptor complex)-

mediated GRK2 degradation [50, 51]. Indeed, the expression levels of GRK2 increased slightly in FLS after MDP treatment under hypoxia, which indicates that MDP may only inhibit GRK2 phosphorylation rather than its expression.

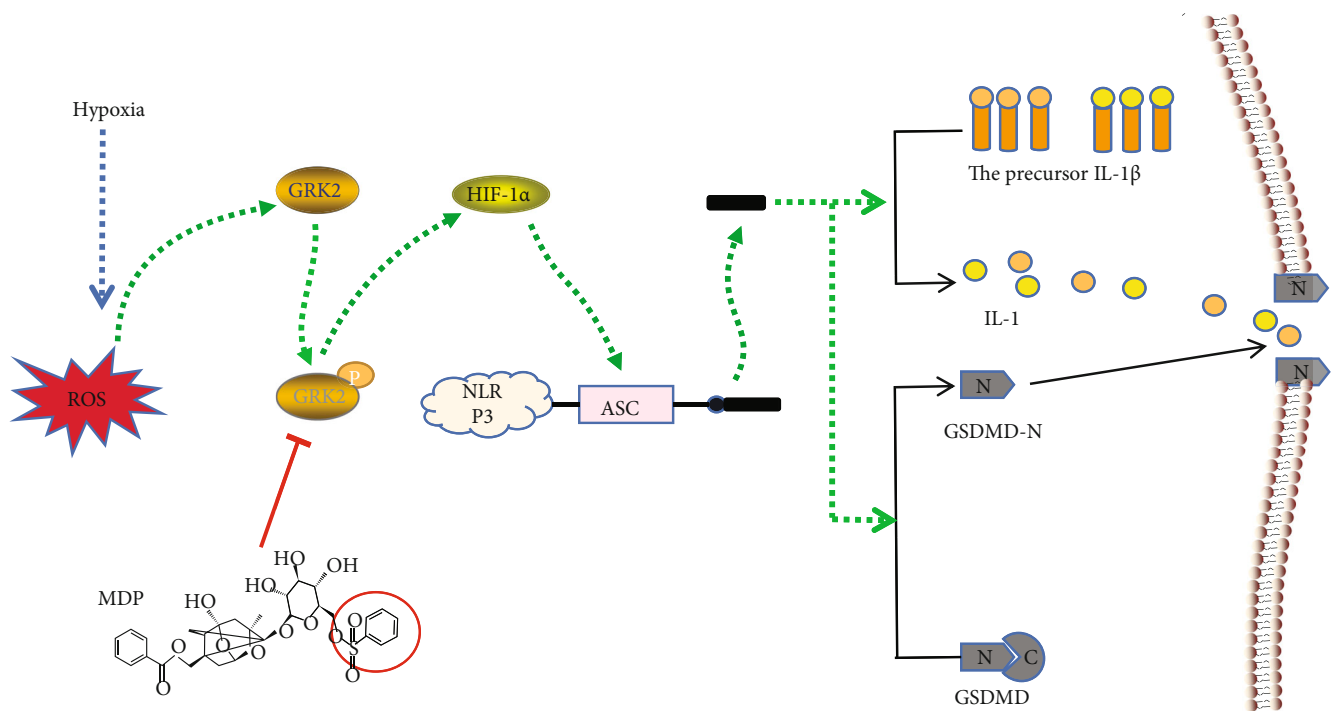


FIGURE 8: Reactive oxygen species/G protein-coupled receptor kinase 2/hypoxia-inducible factor-1 $\alpha$ /nucleotide-binding oligomerization segment-like receptor family 3- (ROS/GRK2/HIF-1 $\alpha$ /NLRP3-) mediated pyroptosis in fibroblast-like synoviocytes (FLS) promotes synovitis under hypoxia and the regulation by monomeric derivatives of paeoniflorin (MDP). The level of ROS in FLS rises sharply under hypoxia. Then, excessive ROS promotes GRK2 expression and increases the levels of phosphorylated GRK2 S670, which then increases HIF-1 $\alpha$  synthesis. This elevated HIF-1 $\alpha$  is transferred to the nucleus to initiate the transcription of the NLRP3 inflammasome. The abnormally high level of NLRP3 inflammasome is activated under hypoxia to form activated cleaved-caspase-1, which, in turn, shears gasdermin D (GSDMD), interleukin- (IL-) 1 $\beta$ , and IL-18 to induce FLS pyroptosis. Monomeric derivative of paeoniflorin (MDP) inhibits the phosphorylation of GRK2 S670 to reduce FLS pyroptosis and relieve synovitis.

However, Chang et al. demonstrated that Pae suppresses the proliferation of FLS and decreases GRK2 expression in FLS *in vitro*, indicating that MDP may have a role in reducing GRK2 expression [52, 53]. The expression of GRK2 was also inhibited by MDP in AA synovial tissue.

To explain this phenomenon, our follow-up experiments revealed that the increase in GRK2 levels under hypoxic conditions was due to the large accumulation of ROS. Increased levels of ROS at the site of inflammation were found to cause cell damage and the progression of inflammatory disease [54, 55]. Under hypoxia, the level of ROS increased significantly in FLS due to a wide spectrum of alterations in mitochondrial structure, dynamics, and genome stability [56]. The accumulation of ROS activates a negative feedback loop in response to oxidative stress [57, 58]. Indeed, the accumulation of the ROS lasts only for a short period under hypoxia, indicating the activation of ROS clearance mechanism in FLS. Recent studies have discovered many ROS clearance mechanisms, such as mitophagy, the activation of superoxide dismutase, and glutathione peroxidase [57, 59]. Interestingly, the highly expressed HIF-1 $\alpha$  can activate mitophagy by increasing BNIP3 transcription [59]. Therefore, *in vitro* inhibition of HIF-1 $\alpha$  expression may cause a transient increase in ROS and GRK2 levels in FLS under hypoxic conditions.

In our experiments, MDP significantly inhibited HIF-1 $\alpha$  expression, which in turn prevented NLRP3 inflammasome activation, resulting in reduced pyroptosis in FLS under hypoxia. Particularly, GSDMD silencing can significantly reduce both gene and protein levels of fibrogenic markers transforming growth factor- $\beta$ , procollagen-lysine 2-oxoglutarate 5-dioxygenase2, collagen type I  $\alpha$ 1 chain, and tissue inhibitor of metalloproteinases 1 [37]. Therefore, MDP may have the ability to relieve synovial fibrosis. Pyroptosis can influence the proliferation, invasion, and metastasis of tumors, which are regulated by some non-coding RNAs and other molecules [60]. FLS of RA have tumor-like growth characteristics, further proving that hypoxia-induced FLS pyroptosis plays a vital role in the course of RA [61]. In summary, MDP, as a natural drug-derived HIF-1 $\alpha$  inhibitor, has great potential for treating RA. MDP may be a multitarget HIF-1 $\alpha$  inhibitor, because in the process of research, surprisingly, we found that MDP could induce VHL production.

In conclusion, the data presented here clearly demonstrated that hypoxia induces FLS pyroptosis by activating the ROS/GRK2/HIF-1 $\alpha$ /NLRP3 pathway and MDP could reduce hypoxia-induced FLS pyroptosis by inhibiting the GRK2/HIF-1 $\alpha$  axis (Figure 8). In this regard, MDP holds great potential to be clinically translated as a therapeutic agent for RA management.



## Data Availability

The data used to support the findings of this study are available from the corresponding author upon request.

## Conflicts of Interest

The authors have declared no conflicts of interest.

## Authors' Contributions

Zhongyang Hong, Xianzheng Zhang, Tianjing Zhang, and Ling Hu, co-first authors, contributed equally to this work.

## Acknowledgments

This work was supported by grants from the National Natural Science Foundation of China and the Open Class of Key Laboratory of Anti-inflammatory and Immunological Drugs of the Ministry of Education (nos. 81803538 and KFJJ-2020-06).

## Supplementary Materials

Extended Data Figure 1: monomeric derivatives of paeoniflorin (MDP) can inhibit fibroblast-like synoviocytes pyroptosis induced by  $\text{Co}^{2+}$ . Extended Data Figure 2: the levels of G protein-coupled receptor kinase 2 (GRK2), hypoxia-induced factor-1 $\alpha$ , and reactive oxygen in fibroblast-like synoviocytes were significantly increased in FLS after 2 h of hypoxia. Extended Data Figure 3: monomeric derivatives of paeoniflorin- (MDP-) mediated inhibition of GRK2 expression and induced Von Hippel-Lindau (VHL) production in fibroblast-like synoviocytes of adjuvant-induced arthritis (AA) rats. (*Supplementary Materials*)

## References

- [1] M. Yang, Y. Liu, B. Mo et al., "Helios but not CD226, TIGIT and Foxp3 is a potential marker for CD4<sup>+</sup> Treg cells in patients with rheumatoid arthritis," *Cellular Physiology and Biochemistry*, vol. 52, no. 5, pp. 1178–1192, 2019.
- [2] B. Moller, F. Kollert, A. Sculean, and P. M. Villiger, "Infectious triggers in periodontitis and the gut in rheumatoid arthritis (RA): a complex story about association and causality," *Frontiers in Immunology*, vol. 11, p. 1108, 2020.
- [3] S. Yu, Y. Lu, M. Zong, Q. Tan, and L. Fan, "Hypoxia-induced miR-191-C/EBP $\beta$  signaling regulates cell proliferation and apoptosis of fibroblast-like synoviocytes from patients with rheumatoid arthritis," *Arthritis Research & Therapy*, vol. 21, no. 1, p. 78, 2019.
- [4] F. Hu, R. Mu, J. Zhu et al., "Hypoxia and hypoxia-inducible factor-1 $\alpha$  provoke toll-like receptor signalling-induced inflammation in rheumatoid arthritis," *Annals of the Rheumatic Diseases*, vol. 73, no. 5, pp. 928–936, 2014.
- [5] J. Kim, H. Y. Kim, S. Y. Song et al., "Synergistic oxygen generation and reactive oxygen species scavenging by manganese ferrite/ceria co-decorated nanoparticles for rheumatoid arthritis treatment," *ACS Nano*, vol. 13, no. 3, pp. 3206–3217, 2019.
- [6] W. Gao, J. McCormick, M. Connolly, E. Balogh, D. J. Veale, and U. Fearon, "Hypoxia and STAT3 signalling interactions regulate pro-inflammatory pathways in rheumatoid arthritis," *Annals of the Rheumatic Diseases*, vol. 74, no. 6, pp. 1275–1283, 2015.
- [7] Q. Ke and M. Costa, "Hypoxia-inducible factor-1 (HIF-1)," *Molecular Pharmacology*, vol. 70, no. 5, pp. 1469–1480, 2006.
- [8] T. Gaber, R. Dziurla, R. Tripmacher, G. R. Burmester, and F. Buttgerit, "Hypoxia inducible factor (HIF) in rheumatology: low O<sub>2</sub>! See what HIF can do!," *Annals of the Rheumatic Diseases*, vol. 64, no. 7, pp. 971–980, 2005.
- [9] K. Lee, J. E. Kang, S. K. Park et al., "LW6, a novel HIF-1 inhibitor, promotes proteasomal degradation of HIF-1 $\alpha$  via upregulation of VHL in a colon cancer cell line," *Biochemical Pharmacology*, vol. 80, no. 7, pp. 982–989, 2010.
- [10] S. Simmen, J. Cosin-Roger, H. Melhem et al., "Iron Prevents Hypoxia-Associated Inflammation Through the Regulation of Nuclear Factor- $\kappa$ B in the Intestinal Epithelium," *Cellular and Molecular Gastroenterology and Hepatology*, vol. 7, no. 2, pp. 339–355, 2019.
- [11] X. Wang, Z. Chen, X. Fan et al., "Inhibition of DNMI1 and mitochondrial fission attenuates inflammatory response in fibroblast-like synoviocytes of rheumatoid arthritis," *Journal of Cellular and Molecular Medicine*, vol. 24, no. 2, pp. 1516–1528, 2020.
- [12] P. Chen, L. Zheng, Y. Wang et al., "Desktop-stereolithography 3D printing of a radially oriented extracellular matrix/mesenchymal stem cell exosome bioink for osteochondral defect regeneration," *Theranostics*, vol. 9, no. 9, pp. 2439–2459, 2019.
- [13] A. MacKinney, E. Woska, I. Spasojevic, I. Batinic-Haberle, and R. Zennadi, "Disrupting the vicious cycle created by NOX activation in sickle erythrocytes exposed to hypoxia/reoxygenation prevents adhesion and vasoocclusion," *Redox Biology*, vol. 25, article 101097, 2019.
- [14] M. Yang, Y. Lin, Y. Wang, and Y. Wang, "High-glucose induces cardiac myocytes apoptosis through Foxo1/GRK2 signaling pathway," *Biochemical and Biophysical Research Communications*, vol. 513, no. 1, pp. 154–158, 2019.
- [15] C. Reglero, V. Lafarga, V. Rivas et al., "GRK2-dependent HuR phosphorylation regulates HIF1 $\alpha$  activation under hypoxia or adrenergic stress," *Cancers (Basel)*, vol. 12, no. 5, p. 1216, 2020.
- [16] N. Gupta, A. Sahu, A. Prabhakar et al., "Activation of NLRP3 inflammasome complex potentiates venous thrombosis in response to hypoxia," *Proceedings of the National Academy of Sciences of the United States of America*, vol. 114, no. 18, pp. 4763–4768, 2017.
- [17] T. Krakauer, "Inflammasomes, autophagy, and cell death: the trinity of innate host defense against intracellular bacteria," *Mediators of Inflammation*, vol. 2019, Article ID 2471215, 10 pages, 2019.
- [18] S. M. Man, R. Karki, and T. D. Kanneganti, "Molecular mechanisms and functions of pyroptosis, inflammatory caspases and inflammasomes in infectious diseases," *Immunological Reviews*, vol. 277, no. 1, pp. 61–75, 2017.
- [19] L. Spel and F. Martinon, "Inflammasomes contributing to inflammation in arthritis," *Immunological Reviews*, vol. 294, no. 1, pp. 48–62, 2020.
- [20] F. Liang, F. Zhang, L. Zhang, and W. Wei, "The advances in pyroptosis initiated by inflammasome in inflammatory and immune diseases," *Inflammation Research*, vol. 69, no. 2, pp. 159–166, 2020.
- [21] F. Lu, Z. Lan, Z. Xin et al., "Emerging insights into molecular mechanisms underlying pyroptosis and functions of

- inflammasomes in diseases,” *Journal of Cellular Physiology*, vol. 235, no. 4, pp. 3207–3221, 2020.
- [22] G. Laghali, K. E. Lawlor, and M. D. Tate, “Die another way: interplay between influenza A Virus, Inflammation and Cell Death, Inflammation and Cell Death,” *Viruses*, vol. 12, no. 4, p. 401, 2020.
- [23] J. Shi, W. Gao, and F. Shao, “Pyroptosis: gasdermin-mediated programmed necrotic cell death,” *Trends in Biochemical Sciences*, vol. 42, no. 4, pp. 245–254, 2017.
- [24] C. A. Dinarello, “Immunological and inflammatory functions of the interleukin-1 family,” *Annual Review of Immunology*, vol. 27, pp. 519–550, 2009.
- [25] B. Muz, M. N. Khan, S. Kiriakidis, and E. M. Paleolog, “Hypoxia. The role of hypoxia and HIF-dependent signalling events in rheumatoid arthritis,” *Arthritis Research & Therapy*, vol. 11, no. 1, p. 201, 2009.
- [26] L. Zhang and W. Wei, “Anti-inflammatory and immunoregulatory effects of paeoniflorin and total glucosides of paeony,” *Pharmacology & Therapeutics*, vol. 207, article 107452, 2020.
- [27] C. Han, Y. Li, Y. Zhang et al., “Targeted inhibition of GRK2 kinase domain by CP-25 to reverse fibroblast-like synoviocytes dysfunction and improve collagen-induced arthritis in rats,” *Acta Pharmaceutica Sinica B*, vol. 11, no. 7, pp. 1835–1852, 2021.
- [28] L. Xu, H. Wang, Q. Q. Yu et al., “The monomer derivative of paeoniflorin inhibits macrophage pyroptosis via regulating TLR4/ NLRP3/ GSDMD signaling pathway in adjuvant arthritis rats,” *International Immunopharmacology*, vol. 101, article 108169, Part A, 2021.
- [29] O. Arjamaa, V. Aaltonen, N. Piippo et al., “Hypoxia and inflammation in the release of VEGF and interleukins from human retinal pigment epithelial cells,” *Graefes Archive for Clinical and Experimental Ophthalmology*, vol. 255, no. 9, pp. 1757–1762, 2017.
- [30] G. Alsaleh, A. François, A. M. Knapp et al., “Synovial fibroblasts promote immunoglobulin class switching by a mechanism involving BAFF,” *European Journal of Immunology*, vol. 41, no. 7, pp. 2113–2122, 2011.
- [31] T. Li, L. Wang, T. Ma et al., “Dynamic calcium release from endoplasmic reticulum mediated by ryanodine receptor 3 is crucial for oligodendroglial differentiation,” *Frontiers in Molecular Neuroscience*, vol. 11, p. 162, 2018.
- [32] X. Q. Wu, C. Huang, Y. M. Jia, B. A. Song, J. Li, and X. H. Liu, “Novel coumarin-dihydropyrazole thio-ethanone derivatives: design, synthesis and anticancer activity,” *European Journal of Medicinal Chemistry*, vol. 74, pp. 717–725, 2014.
- [33] X. Yang, Y. Zhao, X. Jia et al., “CP-25 combined with MTX/ LEF ameliorates the progression of adjuvant-induced arthritis by the inhibition on GRK2 translocation,” *Biomedicine & Pharmacotherapy*, vol. 110, pp. 834–843, 2019.
- [34] G. Yang, C. C. Chang, Y. Yang et al., “Resveratrol alleviates rheumatoid arthritis via reducing ROS and inflammation, inhibiting MAPK signaling pathways, and suppressing angiogenesis,” *Journal of Agricultural and Food Chemistry*, vol. 66, no. 49, pp. 12953–12960, 2018.
- [35] C. M. Quinonez-Flores, S. A. Gonzalez-Chavez, and C. Pacheco-Tena, “Hypoxia and its implications in rheumatoid arthritis,” *Journal of Biomedical Science*, vol. 23, no. 1, p. 62, 2016.
- [36] S. Hua and T. H. Dias, “Hypoxia-inducible factor (HIF) as a target for novel therapies in rheumatoid arthritis,” *Frontiers in Pharmacology*, vol. 7, p. 184, 2016.
- [37] L. Zhang, L. Zhang, Z. Huang et al., “Increased HIF-1 $\alpha$  in Knee Osteoarthritis Aggravate Synovial Fibrosis via Fibroblast-Like Synoviocyte Pyroptosis,” *Oxidative Medicine and Cellular Longevity*, vol. 2019, Article ID 6326517, 11 pages, 2019.
- [38] S. Xu, J. Wang, J. Zhong et al., “CD73 alleviates GSDMD-mediated microglia pyroptosis in spinal cord injury through PI3K/AKT/Foxo1 signaling,” *Clinical and Translational Medicine*, vol. 11, no. 1, article e269, 2021.
- [39] S. Chen, Z. Luo, and X. Chen, “Hsa\_circ\_0044235 regulates the pyroptosis of rheumatoid arthritis via MiR-135b-5p-SIRT1 axis,” *Cell Cycle*, vol. 20, no. 12, pp. 1107–1121, 2021.
- [40] X. Y. Wu, K. T. Li, H. X. Yang et al., “Complement C1q synergizes with PTX3 in promoting NLRP3 inflammasome over-activation and pyroptosis in rheumatoid arthritis,” *Journal of Autoimmunity*, vol. 106, article 102336, 2020.
- [41] N. Li, H. Zhou, H. Wu et al., “STING-IRF3 contributes to lipopolysaccharide-induced cardiac dysfunction, inflammation, apoptosis and pyroptosis by activating NLRP3,” *Redox Biology*, vol. 24, article 101215, 2019.
- [42] Z. Qiu, Y. He, H. Ming, S. Lei, Y. Leng, and Z. Y. Xia, “Lipopolysaccharide (LPS) Aggravates High Glucose- and Hypoxia/Reoxygenation- Induced Injury through Activating ROS-Dependent NLRP3 Inflammasome-Mediated Pyroptosis in H9C2 Cardiomyocytes,” *Journal Diabetes Research*, vol. 2019, article 8151836, 12 pages, 2019.
- [43] S. Wang, Y. H. Yuan, N. H. Chen, and H. B. Wang, “The mechanisms of NLRP3 inflammasome/pyroptosis activation and their role in Parkinson's disease,” *International Immunopharmacology*, vol. 67, pp. 458–464, 2019.
- [44] C. Guo, R. Fu, S. Wang et al., “NLRP3 inflammasome activation contributes to the pathogenesis of rheumatoid arthritis,” *Clinical and Experimental Immunology*, vol. 194, no. 2, pp. 231–243, 2018.
- [45] J. M. Kahlenberg and I. Kang, “Advances in disease mechanisms and translational technologies: clinicopathologic significance of inflammasome activation in autoimmune diseases,” *Arthritis & Rheumatology*, vol. 72, no. 3, pp. 386–395, 2020.
- [46] L. Kolly, N. Busso, G. Palmer, D. Talbot-Ayer, V. Chobaz, and A. So, “Expression and function of the NALP3 inflammasome in rheumatoid synovium,” *Immunology*, vol. 129, no. 2, pp. 178–185, 2010.
- [47] J. Cosin-Roger, S. Simmen, H. Melhem et al., “Hypoxia ameliorates intestinal inflammation through NLRP3/mTOR downregulation and autophagy activation,” *Nature Communications*, vol. 8, no. 1, p. 98, 2017.
- [48] Q. Jiang, X. Geng, J. Warren et al., “Hypoxia Inducible Factor-1 $\alpha$  (HIF-1 $\alpha$ ) Mediates NLRP3 Inflammasome-Dependent-Pyroptotic and Apoptotic Cell Death Following Ischemic Stroke,” *Neuroscience*, vol. 448, pp. 126–139, 2020.
- [49] P. Y. Sato, J. K. Chuprun, L. A. Grisanti et al., “Restricting mitochondrial GRK2 post-ischemia confers cardioprotection by reducing myocyte death and maintaining glucose oxidation,” *Science Signaling*, vol. 11, no. 560, article eaau0144, 2018.
- [50] L. Nogues, A. Salcedo, F. Mayor Jr., and P. Penela, “Multiple scaffolding functions of  $\beta$ -arrestins in the degradation of G protein-coupled receptor kinase 2,” *The Journal of Biological Chemistry*, vol. 286, no. 2, pp. 1165–1173, 2011.
- [51] K. Taguchi, K. Sakata, W. Ohashi, T. Imaizumi, J. Imura, and Y. Hattori, “Tonic inhibition by G protein-coupled receptor kinase 2 of Akt/endothelial nitric-oxide synthase signaling in human vascular endothelial cells under conditions of

- hyperglycemia with high insulin levels,” *The Journal of Pharmacology and Experimental Therapeutics*, vol. 349, no. 2, pp. 199–208, 2014.
- [52] Y. Chang, W. Wei, L. Zhang, and H. M. Xu, “Effects and mechanisms of total glucosides of paeony on synoviocytes activities in rat collagen-induced arthritis,” *Journal of Ethnopharmacology*, vol. 121, no. 1, pp. 43–48, 2009.
- [53] Y. Chang, L. Zhang, C. Wang, X. Y. Jia, and W. Wei, “Paeoniflorin inhibits function of synoviocytes pretreated by rIL-1 $\alpha$  and regulates EP<sub>4</sub> receptor expression,” *Journal of Ethnopharmacology*, vol. 137, no. 3, pp. 1275–1282, 2011.
- [54] A. R. Phull, B. Nasir, I. U. Haq, and S. J. Kim, “Oxidative stress, consequences and ROS mediated cellular signaling in rheumatoid arthritis,” *Chemico-Biological Interactions*, vol. 281, pp. 121–136, 2018.
- [55] M. Mittal, M. R. Siddiqui, K. Tran, S. P. Reddy, and A. B. Malik, “Reactive oxygen species in inflammation and tissue injury,” *Antioxidants & Redox Signaling*, vol. 20, no. 7, pp. 1126–1167, 2014.
- [56] U. Fearon, M. Canavan, M. Biniecka, and D. J. Veale, “Hypoxia, mitochondrial dysfunction and synovial invasiveness in rheumatoid arthritis,” *Nature Reviews Rheumatology*, vol. 12, no. 7, pp. 385–397, 2016.
- [57] C. Giuliani, “The flavonoid quercetin induces AP-1 activation in FRTL-5 thyroid cells,” *Antioxidants (Basel)*, vol. 8, no. 5, 2019.
- [58] R. J. Mailloux, “Protein S-glutathionylation reactions as a global inhibitor of cell metabolism for the desensitization of hydrogen peroxide signals,” *Redox Biology*, vol. 32, article 101472, 2020.
- [59] Z. J. Fu, Z. Y. Wang, L. Xu et al., “HIF-1 $\alpha$ -BNIP3-mediated mitophagy in tubular cells protects against renal ischemia/reperfusion injury,” *Redox Biology*, vol. 36, article 101671, 2020.
- [60] Y. Fang, S. Tian, Y. Pan et al., “Pyroptosis: a new frontier in cancer,” *Biomedicine & Pharmacotherapy*, vol. 121, article 109595, 2020.
- [61] J. Nomura, T. Kobayashi, A. So, and N. Busso, “Febuxostat, a xanthine oxidoreductase inhibitor, decreases NLRP3-dependent inflammation in macrophages by activating the purine salvage pathway and restoring cellular bioenergetics,” *Scientific Reports*, vol. 9, no. 1, p. 17314, 2019.

## Research Article

# HNF4A Regulates the Proliferation and Tumor Formation of Cervical Cancer Cells through the Wnt/ $\beta$ -Catenin Pathway

Hong-Mei Ma <sup>1</sup>, Qian Zhang,<sup>2</sup> Xue-Mei Yang,<sup>3</sup> Yan Hu,<sup>3</sup> Juan Zhang,<sup>4</sup> Lin Chen,<sup>5</sup> Bin Zhao,<sup>6</sup> Wen-ting Yang <sup>1</sup> and Rui Xu <sup>2</sup>

<sup>1</sup>Department of Reproductive Medicine, The First Affiliated Hospital of Xi'an Jiaotong University, Shaanxi, Xi'an 710061, China

<sup>2</sup>Department of Internal Medicine One, Shaanxi Provincial Cancer Hospital, College of Medicine, Xi'an Jiaotong University, Shaanxi, Xi'an 710061, China

<sup>3</sup>Department of Gynecological Oncology, Shaanxi Provincial Cancer Hospital, College of Medicine, Xi'an Jiaotong University, Shaanxi, Xi'an 710061, China

<sup>4</sup>Department of Pathology, Shaanxi Provincial Cancer Hospital, College of Medicine, Xi'an Jiaotong University, Shaanxi, Xi'an 710061, China

<sup>5</sup>Department of Pathology, Shaanxi Provincial People's Hospital, Shaanxi, Xi'an 710061, China

<sup>6</sup>Epidemiology Research Office, Shaanxi Provincial Cancer Hospital, College of Medicine, Xi'an Jiaotong University, Shaanxi, Xi'an 710061, China

Correspondence should be addressed to Wen-ting Yang; 04023031@stu.xjtu.edu.cn and Rui Xu; aduanxu@163.com

Received 29 October 2021; Accepted 22 December 2021; Published 28 January 2022

Academic Editor: Bin Duan

Copyright © 2022 Hong-Mei Ma et al. This is an open access article distributed under the Creative Commons Attribution License, which permits unrestricted use, distribution, and reproduction in any medium, provided the original work is properly cited.

Hepatocyte nuclear factor 4 alpha (HNF4A) is a transcriptional factor which plays an important role in the development of the liver, kidney, and intestines. Nevertheless, its role in cervical cancer and the underlying mechanism remain unknown. In this study, both immunohistochemistry and western blotting revealed that the expression of HNF4A was downregulated in cervical cancer. Xenograft assays suggested that HNF4A could inhibit tumorigenic potential of cervical cancer in vivo. Functional studies illustrated that HNF4A also inhibited the proliferation and viability of cervical cancer cells in vitro. In addition, FACS analysis implied that HNF4A could induce cell cycle arrest from the G0/G1 phase to S phase. Further studies suggested that HNF4A downregulated the activity of the Wnt/ $\beta$ -catenin pathway. Altogether, our data demonstrated that HNF4A inhibited tumor formation and proliferation of cervical cancer cells through suppressing the activity of the Wnt/ $\beta$ -catenin pathway.

## 1. Introduction

Cervical cancer is the fourth most common morbidity and mortality cancer in women worldwide in the latest epidemiological survey on cancers and is the second most common killer cancer in women after breast cancer [1]. It is clear that the incidence of cervical cancer is mainly due to papillomavirus infection [2], while increasing evidence suggests that HPV infection is a necessary but not sufficient factor [3, 4]. Thus, other factors may participate in cervical carcinogenesis. Previous research in our laboratory has shown that a set of stem cell-related genes are involved in the pathogenesis of cervical cancer, such as LGR5 [5], OCT4 [6], NANOG [7], and

SOX2 [8]. Therefore, the alteration of the gene expression state cannot be ignored.

The Wnt/ $\beta$ -catenin signaling pathway plays important roles in various pathophysiological and physiological processes [9–12]. Activation of the Wnt/ $\beta$ -catenin signaling pathway has been reported in various cancers [13–17], including cervical cancer [18, 19]. Activation of the Wnt signaling pathway was considered an important process in the transformation of cervical precancerous lesions into cervical cancer [20, 21].

HNF4A is a member of the ligand-dependent nuclear receptor superfamily [22], which can regulate organism development [23], intestinal development [24], and epithelial-

mesenchymal transformation [25]. HNF4A not only serves as a transcriptional factor but also can bind to the enhancer of specific genes to regulate its expression [26]. On the one side, HNF4A could serve as a cancer promoter by facilitating the proliferation and invasion of cancer cells. HNF4A was upregulated in hepatocellular carcinoma, and its high expression was correlated with poor differentiation of hepatocellular carcinoma cells and vascular invasion [27]. HNF4A was also described as a marker to distinguish metastases of colorectal adenocarcinomas from pulmonary adenocarcinomas *in situ* [28]. HNF4A was upregulated in intestinal cancer and could eradicate aberrant epithelial cell resistance to ROS production during intestinal tumorigenesis [29]. HNF4A could distinguish primary gastric cancer from breast metastasis [30]. On the other side, HNF4A also plays antitumor roles in several types of cancer. Inhibition of HNF4A resulted in cyclin downregulation, cell cycle arrest, and tumor growth inhibition [31]. In colon cancer, HNF4A suppresses the EMT process by upregulating E-cadherin and downregulating vimentin [32]. HNF4A downregulation was correlated with poor prognosis in renal clear cell carcinoma [33]. Upregulation of HNF4A was also reported in esophageal cancer [34]. HNF4A could promote malignant transformation of paediatric neuroblastoma cells through MMP-2 and MMP-14 [35]. To the best of our knowledge, there is no research on the function of HNF4A in cervical cancer.

In the present study, we demonstrated that HNF4A was downregulated in cervical cancers. Ectopic expression of HNF4A inhibited tumor formation and proliferation of cervical cancer cells both *in vivo* and *in vitro*. Further study revealed that HNF4A arrested cell cycle progression by downregulating the activity of the Wnt/ $\beta$ -catenin pathway.

## 2. Materials and Methods

**2.1. Clinical Specimens.** All cancer clinical specimens including 17 normal cervix and 37 cervical cancer tissue samples were obtained from No. 215 Hospital of Shaanxi Nuclear Industry from January 2015 to December 2018 for IHC. All patients did not receive immunotherapy, chemotherapy, or radiotherapy. Eight normal cervixes and 8 cervical cancer fresh tissue samples for western blotting were obtained from the First Affiliated Hospital of Xi'an Jiaotong University.

**2.2. Bioinformatics.** The survival analysis was performed with the Kaplan–Meier plotter ([http://kmplot.com/analysis/index.php?p=service&cancer=pancancer\\_rnaseq](http://kmplot.com/analysis/index.php?p=service&cancer=pancancer_rnaseq)) using the data in TCGA [36]. There are 304 cervical cancer specimens in TCGA database (complex epithelial neoplasms), including 253 squamous cell neoplasms, 31 adenomas and adenocarcinomas, 17 cystic, mucinous, and serous neoplasms, and 3 complex epithelial neoplasms. The expression of HNF4A in the normal cervix and cervical cancers was obtained from the GEO database (GDS3233 (<https://www.ncbi.nlm.nih.gov/sites/GDSbrowser?acc=GDS3233>) and GDS3292 (<https://www.ncbi.nlm.nih.gov/sites/GDSbrowser?acc=GDS3292>)).

**2.3. Western Blotting.** Fresh tissue or adherent cells were firstly washed with PBS 3 times and then lysed with lysis buffer which was added with a certain concentration of cock-

tail (Roche, Basel, Switzerland) for 1 h on ice. The cell lysates were centrifuged and were quantified by using BCA kits (Thermo Scientific, New York, NY, USA). Equal amounts of protein were subjected to SDS-PAGE gel and then transferred to PVDF membranes (Millipore, Billerica, MA, USA). After blocking with 5% nonfat milk for 1 h, primary antibodies diluted with 5% skimmed milk were incubated with the membrane overnight at 4°C. HRP-conjugated anti-mouse IgG and anti-rabbit IgG (Thermo Scientific, New York, NY, USA) were used to detect the signal of the primary antibodies. The immunoblot bands were visualized with an enhanced chemiluminescence reagent (Millipore, Billerica, MA, USA) on the Tanon system (Tanon, Shanghai, China). The primary antibodies used were as follows: anti-HNF4A (1:2000, EPR16885, Abcam, Cambridge, MA, USA), anti- $\beta$ -catenin (1:500, sc-7963, Santa Cruz), anti-c-Myc (1:1000, 10828-1-AP, Wuhan, China), anti-cyclin D1 (1:1000, sc-8396, Santa Cruz), and anti-GAPDH (1:1000, 10494-1-AP, Wuhan, China).

**2.4. Immunohistochemistry and Immunocytochemistry.** Paraffin-embedded sections were conventionally dewaxed to water. Then, the antigens of paraffin sections were retrieved by using 10 mM citrate buffer (pH 6.0) for 5 min. Adherent cells on slides were fixed with formalin and permeabilized with 0.1% Triton X-100. The paraffin sections or slides were incubated with specific primary antibodies overnight. HRP-conjugated anti-mouse IgG was used to detect the signal of primary antibodies. The expression of specific protein was visualized using the DAB kits (ZSGB-Bio, Beijing, China). The nucleus of cells was visualized with hematoxylin. PBS was used as a negative control. The immunoreactivity score (IRS) was calculated as previously described [18]. The primary antibodies used were as follows: anti-HNF4A (1:50, sc-374229, Abcam, Cambridge, MA, USA), anti-Ki67 (1:100, sc-23900, Santa Cruz), anti-cyclin D1 (1:100, sc-8396, Santa Cruz), and anti-c-Myc (1:100, sc-40, Santa Cruz).

**2.5. Vector Construction and Cell Transfection.** The CDS of HNF4A was cloned by PCR and subsequently inserted into pIRES2-AcGFP (Clontech, Mountain View, CA) to construct pIRES2-AcGFP-HNF4A plasmids. The pIRES2-AcGFP plasmids were used as control vectors. The primers used were shown as follows: HNF4A-CDS-F: CCGGAA TTCATGCGACTCTCCAAAA, and HNF4A-CDS-R: CGCGGATCCCTAGATAACTTCCTGCTT.

The Lipofectamine 2000 (Invitrogen, Carlsbad, CA, USA) was used as a transfection reagent according to the manufacturer's instructions. The G418 reagent (MCE, New Jersey, CA, USA) was used as selection pressure for stable transfection cell lines.

**2.6. Cell Culture, Cell Counting Assays, and MTT Assays.** The cell culture methods were the same as previously described [37]. For cell counting assays,  $2 \times 10^4$  cells were seeded into 35 mm dishes, and the cell numbers of each dish were counted after 1, 3, 5, and 7 days. The growth curves were depicted by using Prism software. For MTT assays, cells were seeded into 96-well plates  $10^3$  per well, and the absorbance of each well was performed using 3-(4,5-dimethylthiazole-yl)-2,5-diphenyl

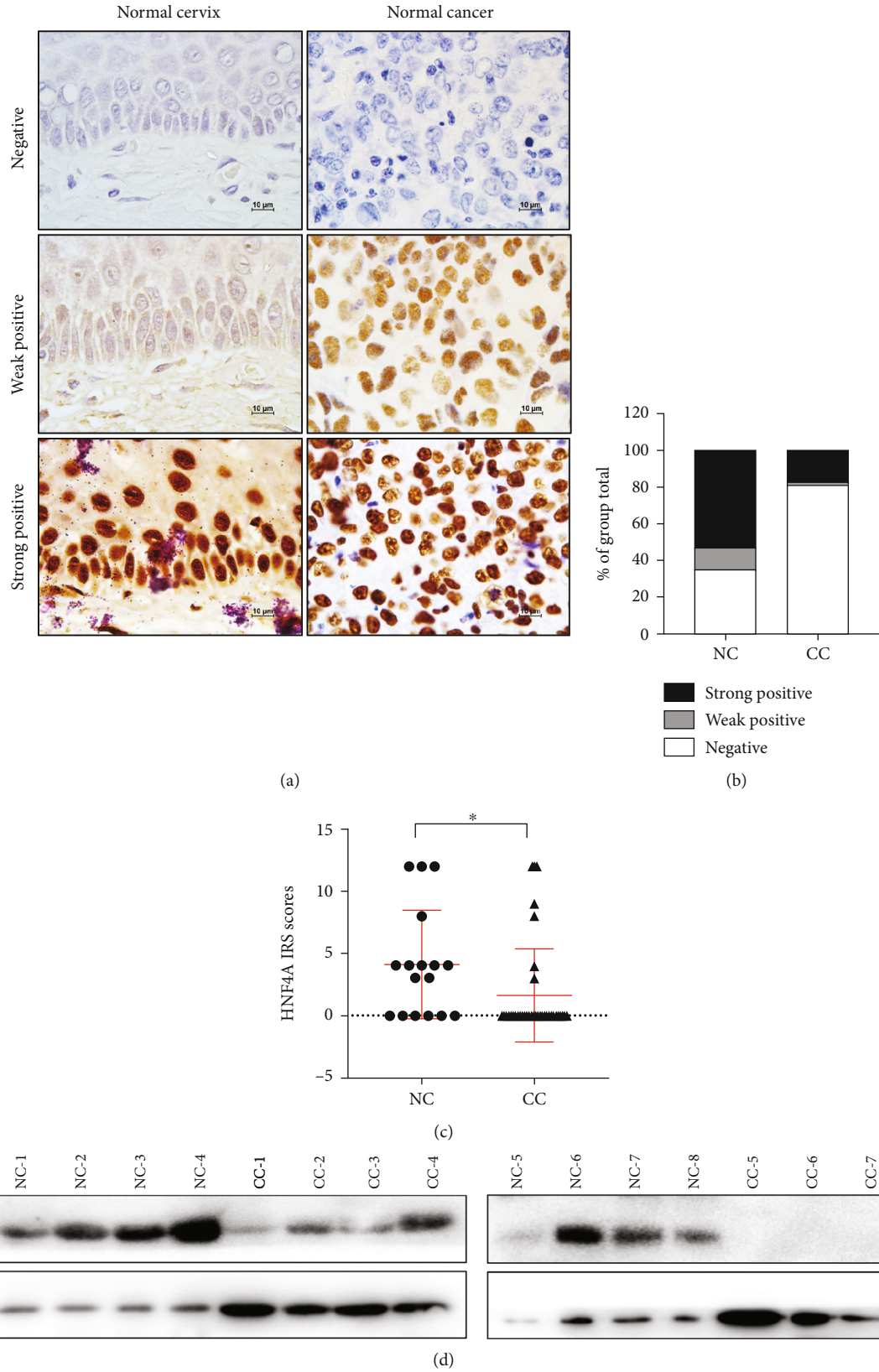


FIGURE 1: Continued.

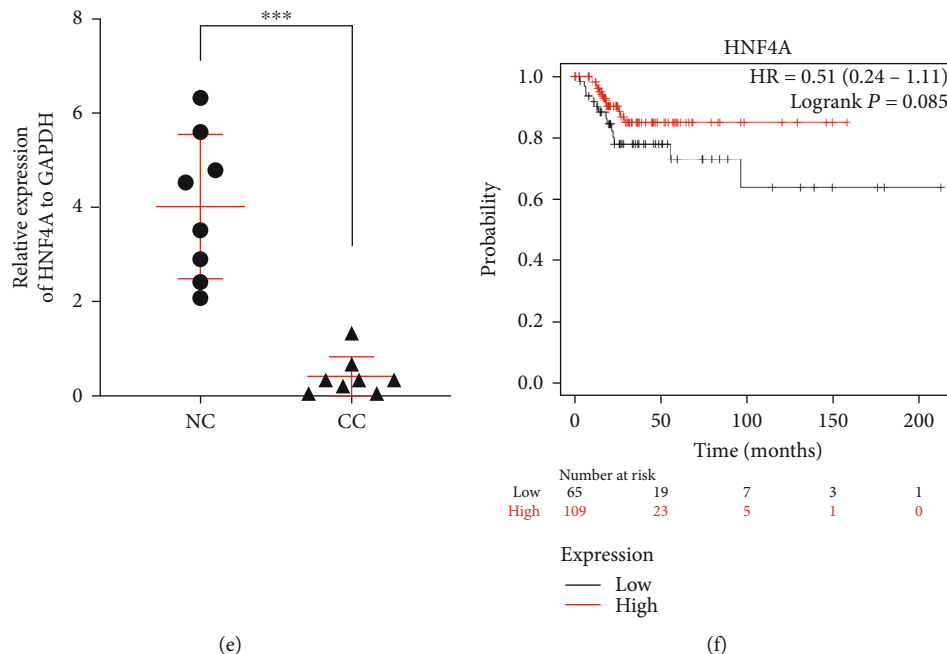


FIGURE 1: The expression of HNF4A is downregulated in cervical cancer. (a) Immunohistochemical staining of HNF4A in clinical samples, including the normal cervix (NC,  $n = 17$ ) and cervical carcinomas (CC,  $n = 37$ ) (original magnification, 1000x). (b) The immunohistochemical staining intensity was classified into negative, weak positive, and strong positive, and the percentage of each group was shown. (c) The scatter plots showed the IHC scores obtained for the staining of HNF4A in different cervix lesion samples (points represent the IHC score per specimen, and Student's  $t$ -test is performed). (d) HNF4A expression was detected by western blot in 8 normal cervix samples and 8 cervical carcinoma samples. GAPDH was used as a loading control. (e) The quantitative illustration of the levels of HNF4A protein using densitometry to measure the density of the corresponding bands in (d). Student's  $t$ -test was carried out. (f) The relationship between relapse-free survival (RFS) probability of CESC patients ( $n = 304$ ) and the expression level of HNF4A in their tumors was shown by the Kaplan–Meier estimator in TCGA database. \* $p < 0.05$ , \*\*\* $p < 0.001$ .

tetrazolium bromide (MTT, Sigma-Aldrich) at a wavelength of 490 nm. The viability curves were also depicted by using Prism software.

**2.7. Tumor Xenograft Assay.** A total of  $5 \times 10^5$  HNF4A-modeified cells and their control cells were injected on both sides of the back of nude mice subcutaneously. The volumes of tumors were measured every 3 days. The nude mice were purchased from Charles River (Beijing, China). The nude mice were all 5 weeks old. There were 6 mice in each group. The procedure of this experiment was approved by the Animal Ethics Committee of Xi'an Jiaotong University.

**2.8. Cell Cycle Analysis.**  $3 \times 10^5$  HNF4A-modeified cells and their control cells were seeded into 35 mm dishes. After 24 h, the cells were harvested and washed with PBS for 3 times. The cells were fixed with precooled 75% ethanol overnight. Before fluorescence-activated cell sorting (FACS), the cells were pretreated with PI (propidium iodide, 1 mg/ml, Sigma-Aldrich, St. Louis, MO, USA) and RNaseA (1 mg/ml, Sigma-Aldrich, St. Louis, MO, USA). The flow cytometer used was FACSCalibur (BD Biosciences, San Jose, CA, USA). The data were analyzed by using FlowJo.

**2.9. Real-Time (RT) Quantitative PCR.** The adherent cells were harvested with the RNAiso reagent (Takara, Osaka, Japan). The extraction of RNA was performed according to

TABLE 1: HNF4A expression levels in different tissue specimens.

| Specimens | Total | HNF4A staining    |                   | $p$                 |
|-----------|-------|-------------------|-------------------|---------------------|
|           |       | Negative, no. (%) | Positive, no. (%) |                     |
| Normal    | 17    | 6 (35.3)          | 11 (64.7)         |                     |
| Carcinoma | 37    | 30 (81.1)         | 7 (18.9)          | <0.001 <sup>a</sup> |

HNF4A: hepatocyte nuclear factor 4 alpha. The Pearson 2-tailed chi-square test was used to determine the statistical significance of the level of expression of HNF4A in different tissue specimens.

the manufacturer's manual. The cDNA was reverse transcribed from RNA using the PrimeScript RT reagent Kit (Takara, Osaka, Japan). The cDNA was used as templates, and the SYBR Premix ExTaq II (Takara, Osaka, Japan) was used for real-time quantitative PCR. The procedure of PCR was finished by using the TianLong TL988 System (Tian-Long, Xi'an, China). The results were analyzed using the MED-TL-4CH software. The primers used were shown as follows: CTNNB1-F: TCTGAGGACAAGCCACAAGAT TACA; CTNNB1-R: TGGGCACCAATATCAAGTCCAA; CCND1-F: AACAGATCATCCGCAAACAC; CCND1-R: GTTGGGGCTCCTCAGGTTC; MYC-F: CCTGGTGCTCC ATGAGGAGA; MYC-R: TCCAGCAGAAGGTGATCCA GAC; GAPDH-F: GCACCGTCAAGGCTGAGAAC; and GAPDH-R: TGGTGAAGACGCCAGTGA.

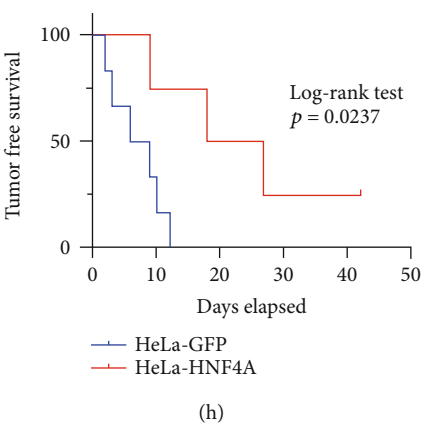
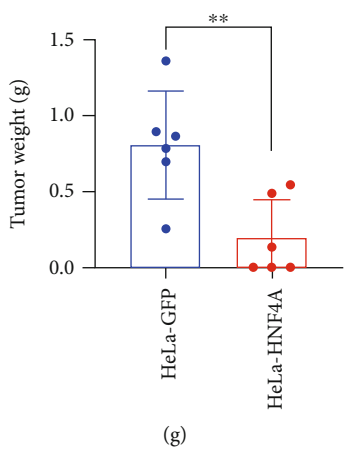
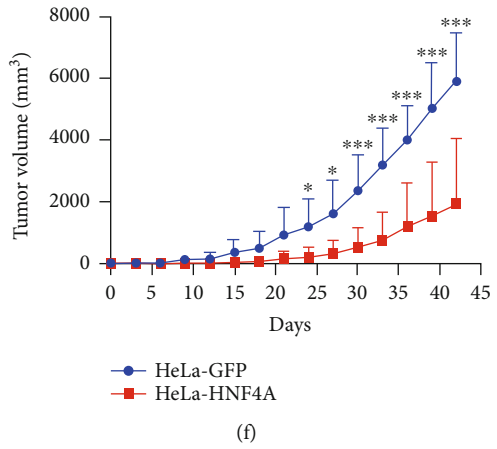
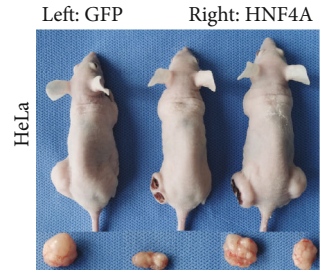
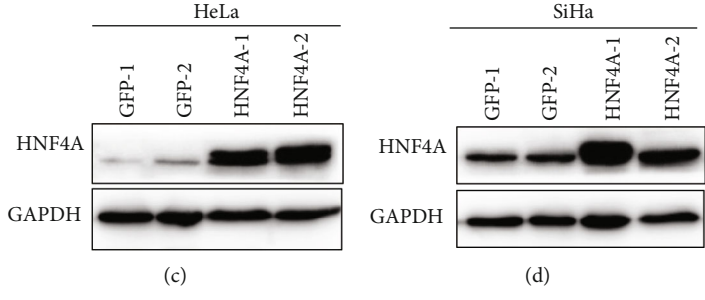
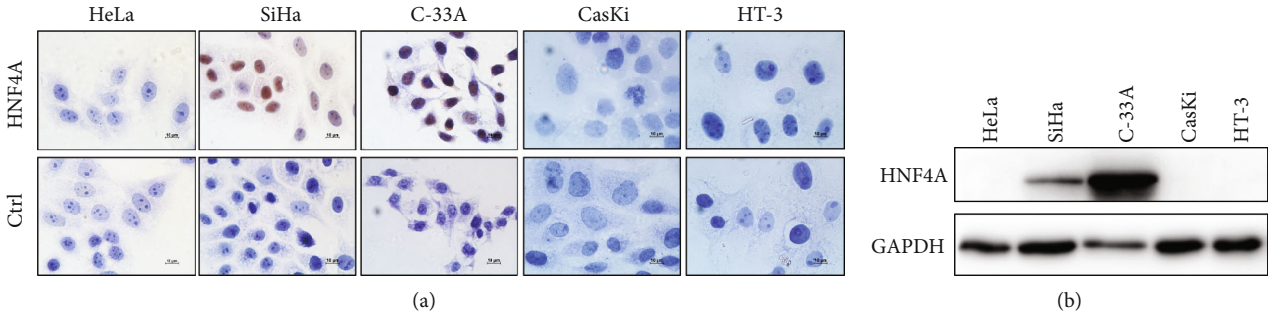


FIGURE 2: Continued.



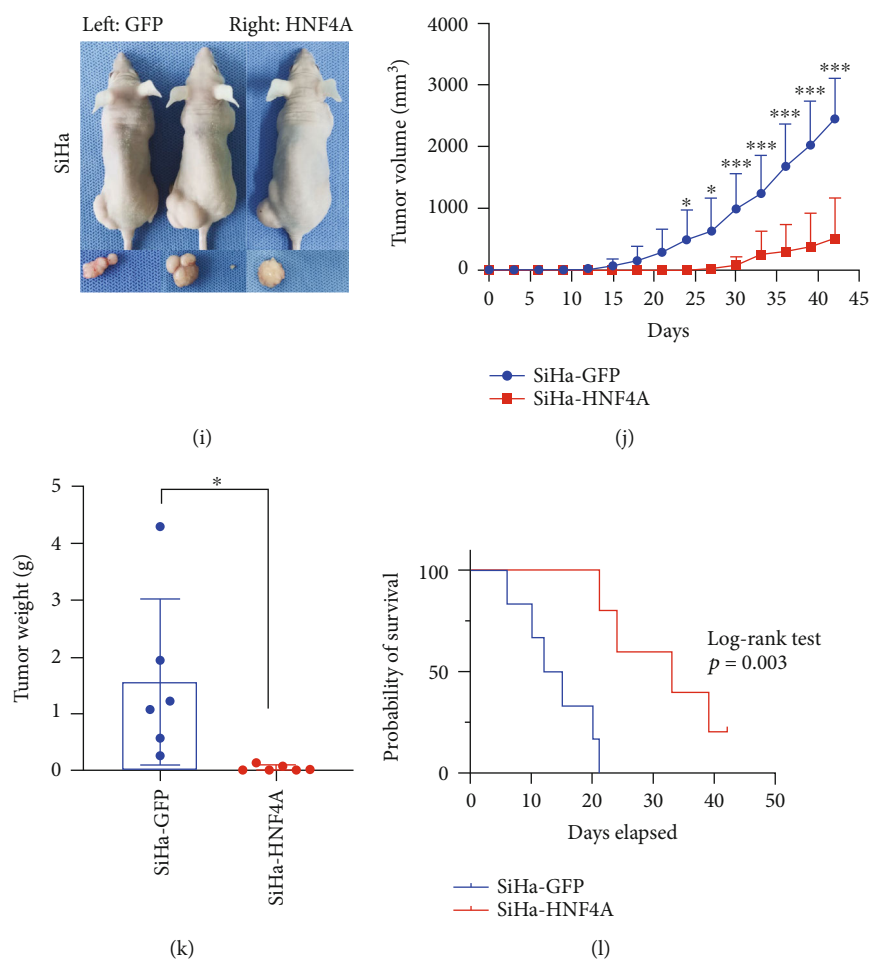


FIGURE 2: HNF4A inhibits tumor formation and tumor growth of cervical cancer cells *in vivo*. The expression of HNF4A in human cervical cancer cell lines was detected using immunocytochemistry (a) and western blotting (b). Stably transfected HNF4A-modified cervical cancer cells were identified by western blotting (c, d). (e) Xenograft tumor formation of HeLa-GFP and HeLa-HNF4A cells. The tumor growth curve (f), tumor weight (g), and tumor-free survival (h) of HeLa-GFP and HeLa-HNF4A cells, respectively. (i) Xenograft tumor formation of SiHa-GFP and SiHa-HNF4A cells. The tumor growth curve (j), tumor weight (k), and tumor-free survival (l) of SiHa-GFP and SiHa-HNF4A cells, respectively. \* $p < 0.05$ , \*\* $p < 0.01$ , and \*\*\* $p < 0.001$ .

**2.10. Statistical Analysis.** The statistical analysis was carried out using SPSS 19.0 software (SPSS Inc., Chicago, IL). The data in this article was all shown as means  $\pm$  standard deviation of the mean (SD). Gene expression in tumor tissues and cells was compared by the unpaired *t*-test, and paired samples were compared by the paired *t*-test. In all tests,  $p < 0.05$  is regarded as statistically significant.

### 3. Results and Discussion

**3.1. HNF4A Is Downregulated in Cervical Cancer.** To explore the function of HNF4A in cervical carcinoma, we conducted immunohistochemistry in the normal cervix (NC) and cervical carcinoma (CC). The results showed that the HNF4A protein was mainly expressed in the nucleus (Figure 1(a)). The positive rate of HNF4A protein in the normal cervix was much higher than that in cervical carcinoma (Table 1 and Figure 1(b),  $p < 0.001$ ). Statistical significance was observed between the two groups ( $p < 0.05$ ). Furthermore, the IHC

scores of HNF4A staining were  $4.12 \pm 4.37$  in NC and  $1.62 \pm 3.74$  in CC (Figure 1(c)). We also performed western blotting in eight NC specimens and eight CC specimens (Figure 1(d)). The results showed that the average relative expression of HNF4A in NC was enormously higher than that in CC (Figure 1(e),  $4.01 \pm 1.535$  vs.  $0.4169 \pm 0.1492$ ,  $p < 0.001$ ). To further understand the expression pattern of HNF4A in cervical cancers, the expression of HNF4A was searched in the GEO database. The relative expression of HNF4A mRNA in GSD3222 was  $5.732 \pm 3.304$  in NC and  $4.07 \pm 2.03$  in CC (Figure S1a,  $p < 0.05$ ). Similarly, the relative expression of HNF4A mRNA in GSD3222 was  $9.052 \pm 0.4381$  in NC and  $8.817 \pm 0.5171$  in CC (Figure S1b,  $p < 0.05$ ). Moreover, the survival analysis in TCGA database ( $n = 304$ ) showed that the patients who had higher expression of HNF4A had a higher relapse-free survival (RFS) probability (Figure 1(f)). Collectively, these data demonstrated that HNF4A was downregulated in cervical cancers and the high expression of HNF4A in cervical cancer may suggest a better prognosis.

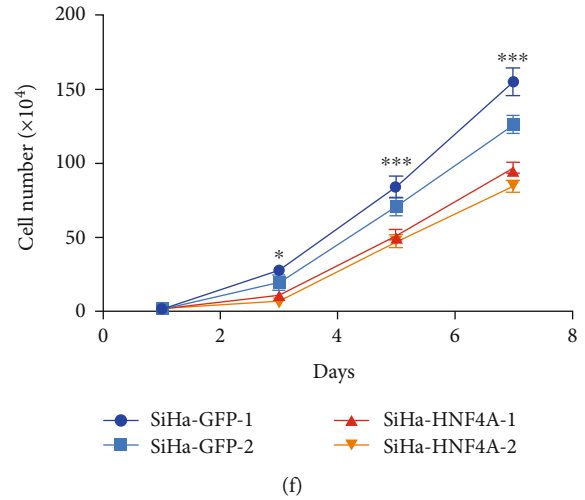
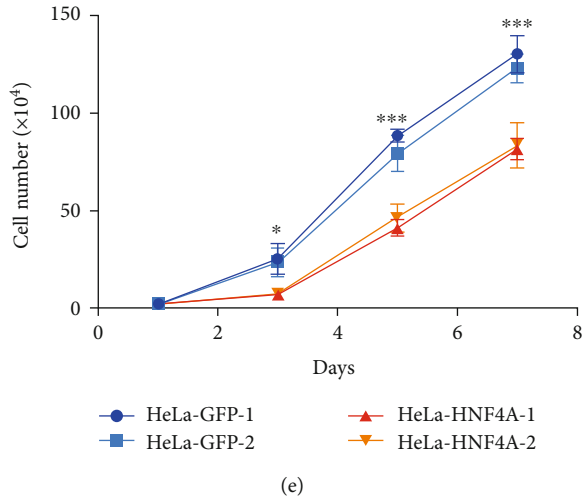
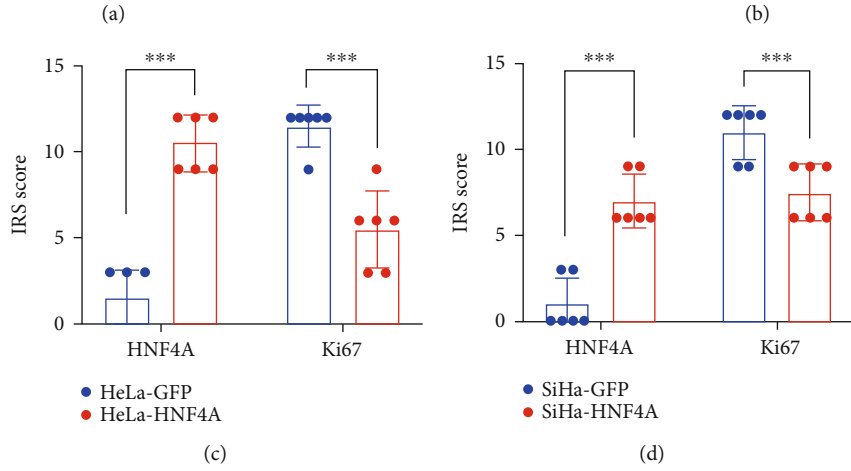
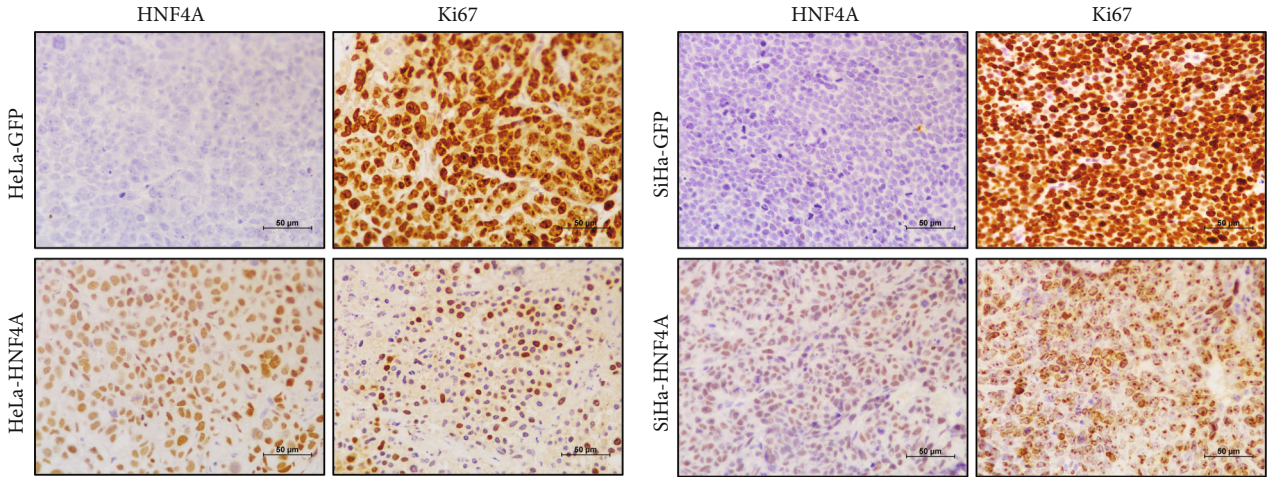


FIGURE 3: Continued.

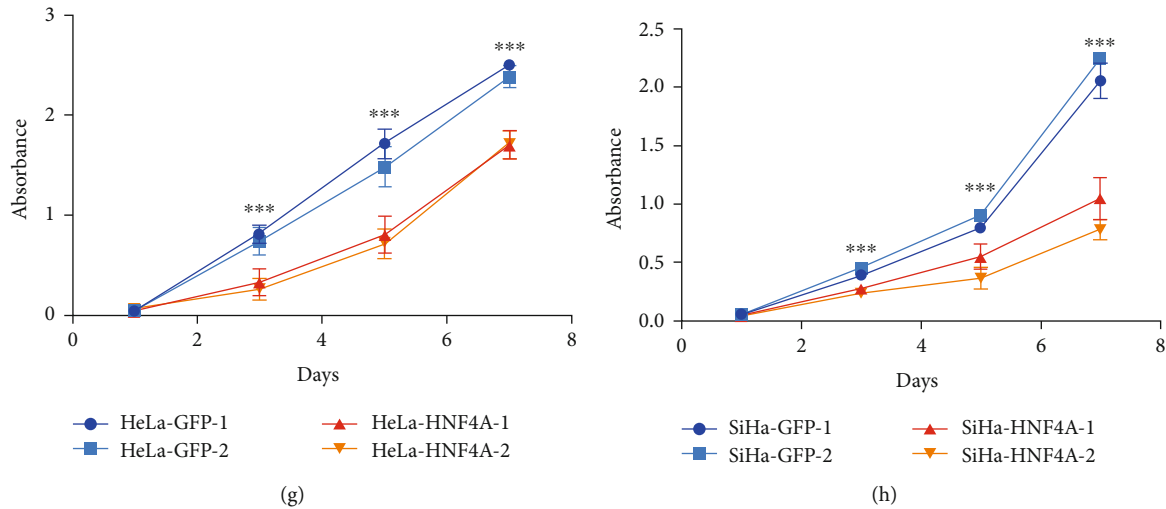


FIGURE 3: HNF4A inhibits tumor formation and tumor growth of cervical cancer cells by inhibiting cell proliferation. (a, b) Immunohistochemical staining of HNF4A and Ki67 in xenograft tumor tissues derived from HeLa-GFP cells, HeLa-HNF4A cells, and SiHa-GFP and SiHa-HNF4A cells, respectively. (c, d) Immunoreactivity scores of HNF4A and Ki67 in xenograft tumor tissues derived from HeLa-GFP cells, HeLa-HNF4A cells, SiHa-GFP, and SiHa-HNF4A cells. Data were statistically analyzed by Student's *t*-test, and values are shown as mean  $\pm$  SD. The proliferation was detected using growth curves in HeLa-GFP and HeLa-HNF4A cells (e) and SiHa-GFP and SiHa-HNF4A cells (f). The viability was detected by the MTT assay in HeLa-GFP and HeLa-HNF4A cells (g) and SiHa-GFP and SiHa-HNF4A cells (h). \* $p < 0.05$ , \*\*\* $p < 0.001$ .

**3.2. HNF4A Inhibits Tumor Formation and Tumor Growth of Cervical Cancer Cells In Vivo.** The expression of HNF4A in cervical cancer cells was detected by immunocytochemistry and western blotting (Figures 2(a) and 2(b)). The results showed that HNF4A was expressed in C-33A and SiHa cells but almost not expressed in HeLa, CaSki, and HT-3 cells. Thus, we established stable overexpression of HNF4A in HeLa and SiHa cell lines. The overexpression efficiencies were verified by western blotting (Figures 2(c) and 2(d)).

To illustrate the function of HNF4A *in vivo*, xenograft experiments were carried out in nude mice. HNF4A-modified cells (HeLa-HNF4A, SiHa-HNF4A) and their control cells (HeLa-GFP, SiHa-GFP) were injected into the backs of the nude mice subcutaneously (Figures 2(e) and 2(i)). The results showed that the tumors developed from HeLa-HNF4A cells grew slower (Figure 2(f),  $p < 0.001$ ) and were lighter than those developed from HeLa-GFP cells (Figure 2(g),  $0.1946 \pm 0.2991$  vs.  $0.8092 \pm 0.3564$ ,  $p < 0.01$ ). Furthermore, the survival analysis of the tumor-free period in HeLa-HNF4A cells was significantly longer than that in HeLa-GFP cells (Figure 2(h),  $p < 0.05$ ). Similar results were obtained in SiHa-HNF4A and SiHa-GFP cells (Figure 2(j),  $p < 0.001$ ; Figure 2(k),  $0.0373 \pm 0.0523$  vs.  $1.559 \pm 1.460$ ,  $p < 0.05$ ; Figure 2(i),  $p < 0.01$ ). In conclusion, these results suggested that HNF4A suppressed tumor formation and tumor growth of cervical cancer cells *in vivo*.

**3.3. HNF4A Inhibits Tumor Formation and Tumor Growth of Cervical Cancer Cells by Inhibiting Cell Proliferation.** To explore whether HNF4A inhibits tumor formation and tumor growth of cervical cancer cells by inhibiting cell proliferation, the expression of Ki67, which is an important cell proliferation marker, was evaluated in xenografts by IHC (Figures 3(a) and 3(b)). The results suggested that Ki67

staining was weaker in xenografts derived from HeLa-HNF4A cells than in those derived from HeLa-GFP cells (Figure 3(c), HNF4A:  $10.5 \pm 1.643$  vs.  $1.5 \pm 1.643$ ,  $p < 0.001$ ; Ki67:  $5.5 \pm 2.258$  vs.  $11.5 \pm 1.225$ ,  $p < 0.001$ ). Similar results were obtained in xenografts derived from SiHa-HNF4A and SiHa-GFP cells (Figure 3(d), HNF4A:  $7.1 \pm 1.549$  vs.  $1.1 \pm 1.549$ ,  $p < 0.001$ ; Ki67:  $7.5 \pm 1.634$  vs.  $11.1 \pm 1.549$ ,  $p < 0.001$ ). These results demonstrated that HNF4A inhibits tumor formation and tumor growth of cervical cancer cells by inhibiting cell proliferation.

To further demonstrate the inhibitory function of HNF4A on cell proliferation, the cell growth curve and MTT assays were conducted. It was apparent that after HNF4A overexpression, the cell proliferation ability was severely inhibited (Figure 3(e),  $p < 0.001$ ; Figure 3(f),  $p < 0.001$ ). At the same time, the MTT assays revealed that overexpression of HNF4A significantly suppressed the cell viability of cervical cancer (Figure 3(g),  $p < 0.001$ ; Figure 3(h),  $p < 0.001$ ). These data suggested that HNF4A could inhibit the proliferation and viability of cervical cancer cells *in vitro*. Taken together, these data demonstrated that HNF4A inhibited tumor formation and tumor growth through suppressing proliferation and viability of cervical cancer cells.

**3.4. HNF4A Inhibits Cell Proliferation through Inducing Cell Cycle Arrest from the G0/G1 Phase to S Phase.** Cell proliferation is closely related to the cell cycle. The cell cycle is precisely regulated by a set of cell cycle-related proteins, which consist of cyclins, cyclin-dependent kinases (CDKs), and cyclin kinase inhibitors (CKIs), and can be detected by fluorescence-activated cell sorting (FACS). Thus, we performed FACS for cell cycle analysis on HNF4A-modified cells and their control cells. Compared with HeLa-GFP cells, the proportion of HeLa-HNF4A cells in the G0/G1 phase

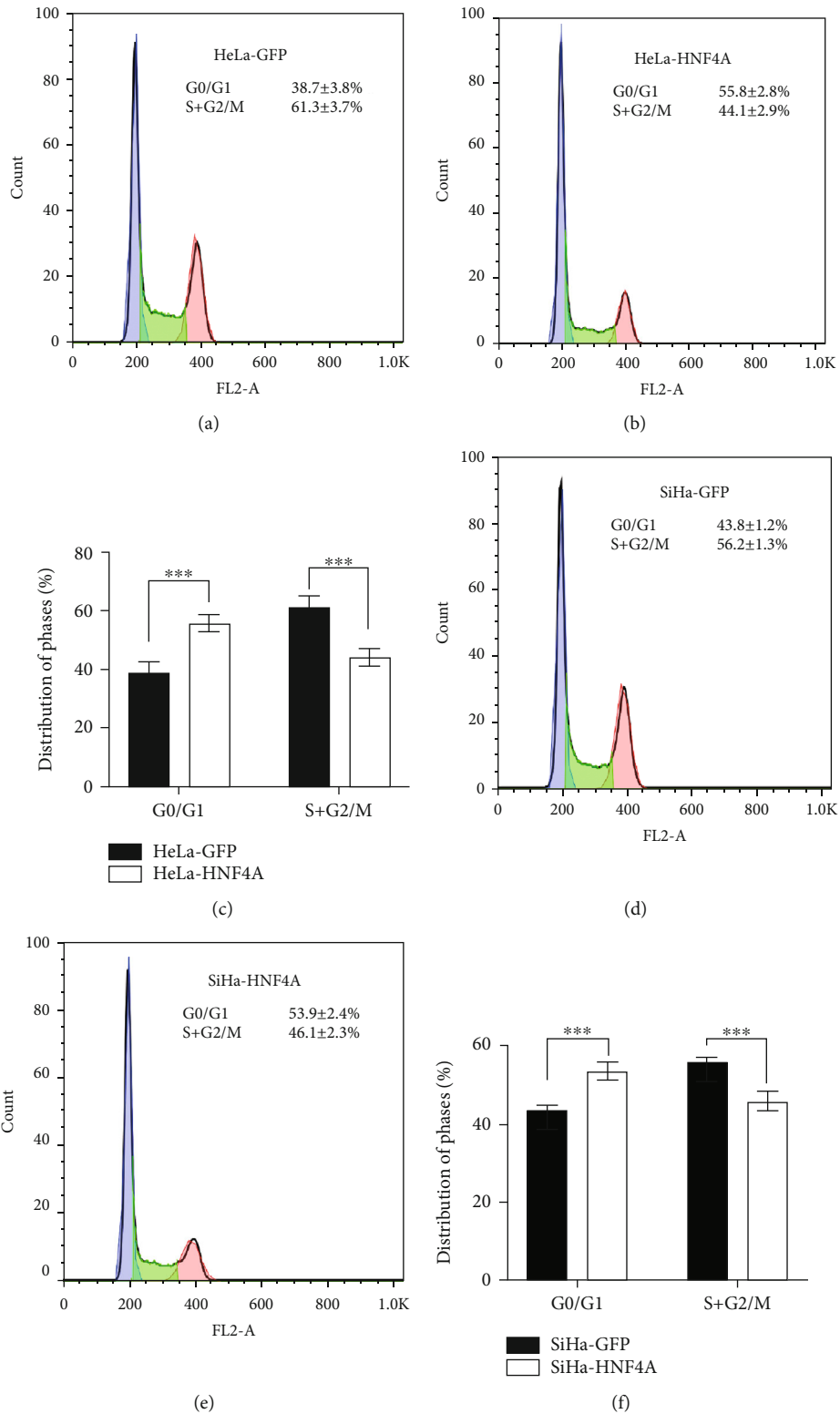
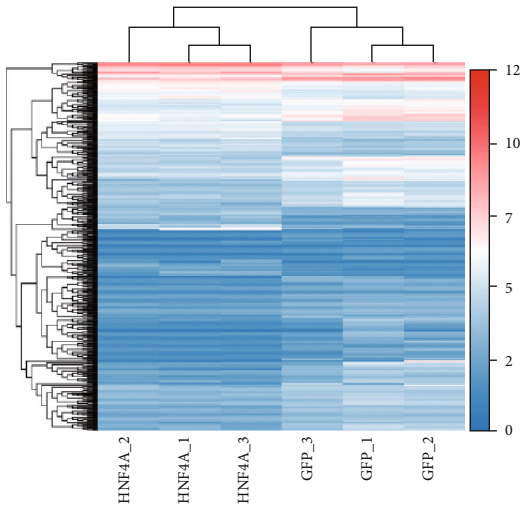
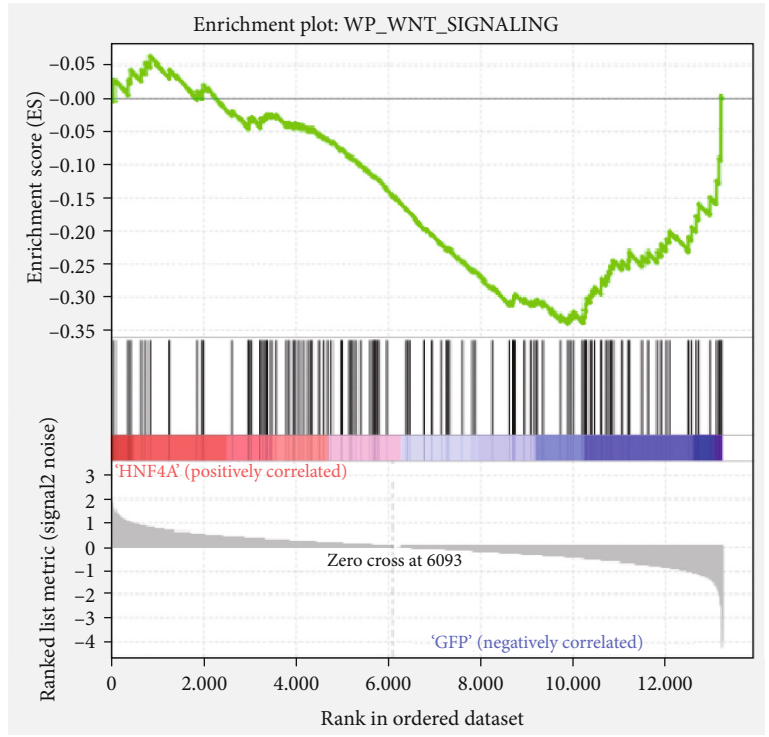


FIGURE 4: HNF4A inhibited cell proliferation through inducing cell cycle arrest from the G0/G1 phase to S phase. In the flow cytometry figures, the y-axis shows the count of effective cells and the x-axis shows the DNA content. Each colored area represents the cells of different phases of the cell cycle: blue area refers to the cells in the G0/G1 phase, green area refers to the cells in the S phase, and pink area refers to the cells in the G2/M phase. The cell cycles of HeLa-GFP (a) and HeLa-HNF4A (b) cells were analyzed using flow cytometry, and a quantitative analysis of the cell cycle is shown (c). The cell cycles of SiHa-GFP (d) and SiHa-HNF4A (e) cells and the quantitative analysis (f) are shown. The data were shown as the mean  $\pm$  SD of three independent experiments. Data were statistically analyzed by Student's *t*-test, and values are shown as mean  $\pm$  SD. \*\*\**p* < 0.001.



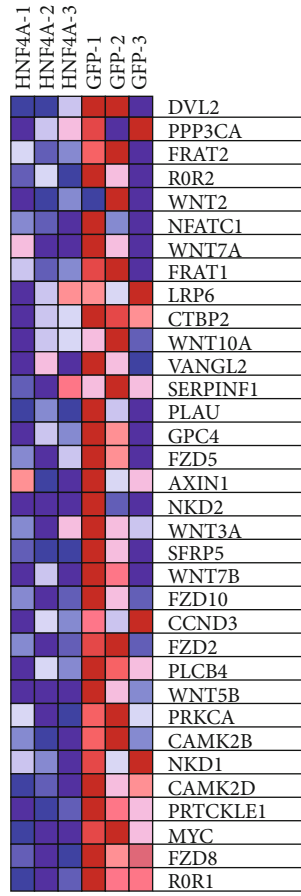
(a)



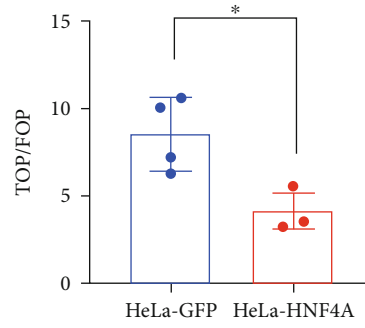
— Enrichment profile  
— Hits  
— Ranking metric scores

(b)

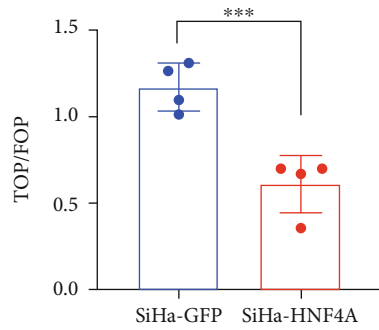
FIGURE 5: Continued.



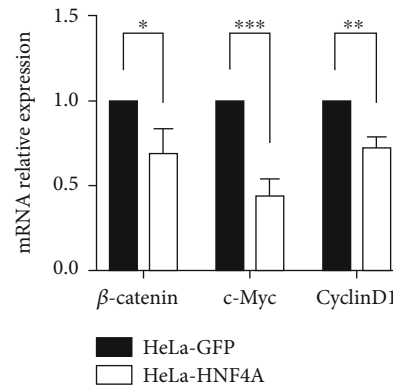
(c)



(d)



(e)



(f)

FIGURE 5: Continued.

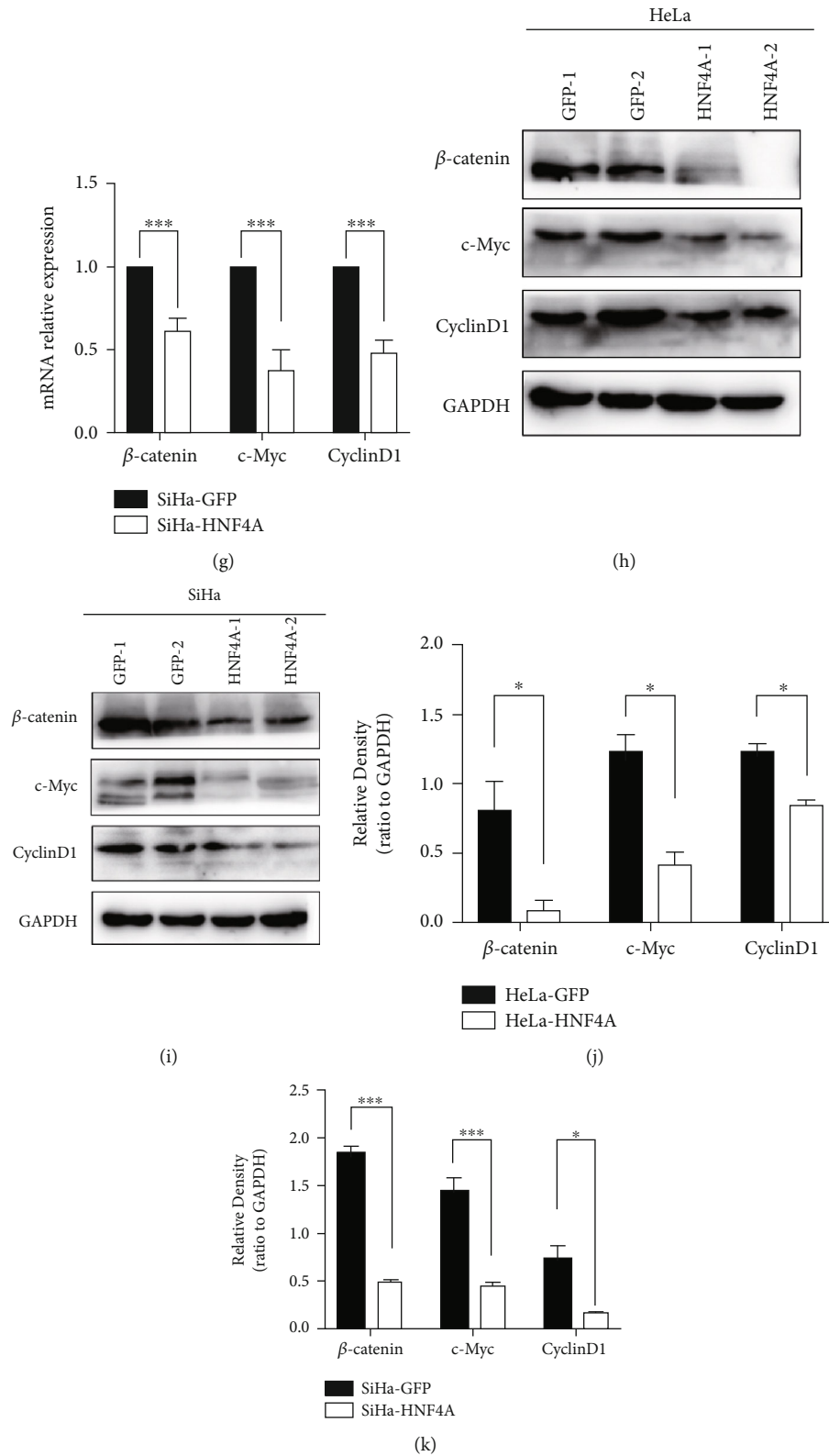


FIGURE 5: HNF4A downregulated the activity of the Wnt/ $\beta$ -catenin pathway. (a) Heatmap of the data from RNA-seq. (b) The result of gene set enrichment analysis. (c) The significantly changed genes in GSEA. (d, e) TOP/FOP-Flash reporter assays were carried out in HNF4A-modified cervical cancer cells. (f, g) Real-time PCR analysis is shown for the mRNA levels of the Wnt/ $\beta$ -catenin pathway key genes in HNF4A-modified cervical cancer cells. (h, i) The expression of Wnt/ $\beta$ -catenin pathway key proteins in HNF4A-modified cervical cancer cells was determined by western blotting. (j, k) The quantitative analysis of the western blotting in (h) and (i). Data represent mean  $\pm$  SD of triplicate experiments, and statistical analysis was done by Student's *t*-test. \* $p < 0.05$ , \*\* $p < 0.01$ , and \*\*\* $p < 0.001$ .

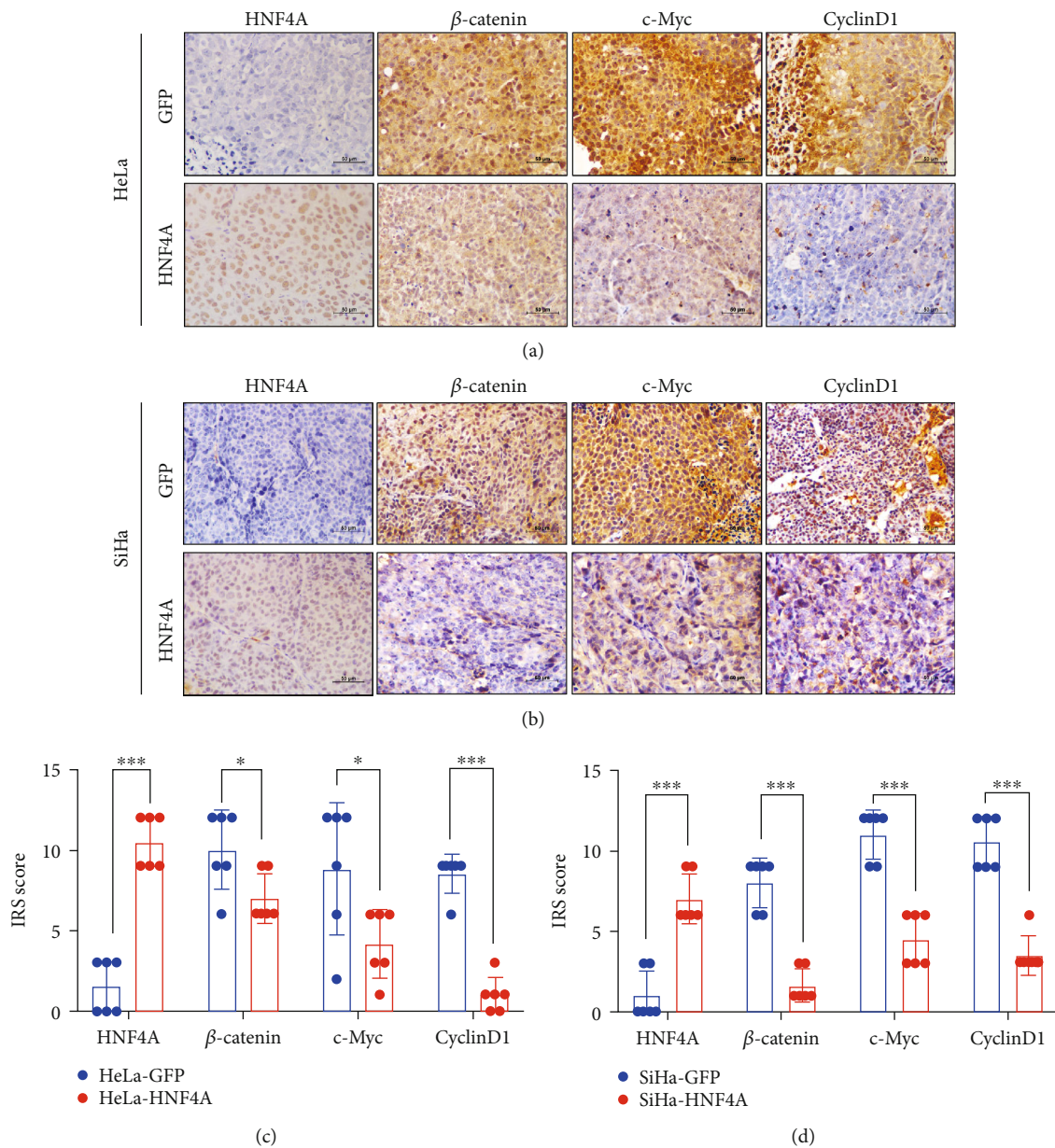


FIGURE 6: HNF4A suppressed the Wnt/ $\beta$ -catenin pathway in a mouse xenograft. (a) Expression of HNF4A,  $\beta$ -catenin, c-Myc, and cyclin D1 in tumor xenografts derived from HeLa-GFP cells and HeLa-HNF4A cells. (b) Immunoreactivity scores of HNF4A,  $\beta$ -catenin, c-Myc, and cyclin D1 in xenograft tissues derived from HeLa-GFP cells and HeLa-HNF4A cells. (c) Expression of HNF4A,  $\beta$ -catenin, c-Myc, and cyclin D1 in xenografts derived from SiHa-GFP and SiHa-HNF4A cells. (d) Immunoreactivity scores of HNF4A,  $\beta$ -catenin, c-Myc, and cyclin D1 in xenograft tissues derived from SiHa-GFP cells and SiHa-HNF4A cells. Representative images were shown. Scale bar: 10  $\mu$ m. Data represent mean  $\pm$  SD of triplicate experiments, and statistical analysis was done by Student's *t*-test. \**p* < 0.05, \*\*\**p* < 0.001.

( $38.7 \pm 3.8\%$  vs.  $55.8 \pm 2.8\%$ ,  $p < 0.001$ ) cells sharply increased, while the proportion of HeLa-HNF4A cells in S and G2/M phases ( $61.3 \pm 3.7\%$  vs.  $44.1 \pm 2.9\%$ ) abruptly increased (Figures 4(a)–4(c)). The same results were observed in SiHa-HNF4A and SiHa-GFP cells (Figures 4(d)–4(f), G0/G1:  $43.8 \pm 1.2\%$  vs.  $53.9 \pm 2.4\%$ ,  $p < 0.001$ ; S and G2/M:  $56.2 \pm 1.3\%$  vs.  $46.1 \pm 2.3\%$ ,  $p < 0.001$ ). Collectively, these data illustrated that HNF4A inhibited cell proliferation via arresting cell cycle progression.

**3.5. HNF4A Arrests Cell Cycle Progression via Downregulating the Activity of the Wnt/ $\beta$ -Catenin Pathway.** To further explore the particular mechanism by which HNF4A regulated the cell cycle, we perform RNA-seq in three SiHa-HNF4A and three SiHa-GFP cells (Figure 5(a)). The RNA-seq results showed that 189 genes were significantly upregulated and 459 genes significantly were downregulated. Next, the gene set enrichment analysis (GSEA) was performed using the data obtained from RNA-seq. The results of GSEA strongly indicated that the



Wnt/ $\beta$ -catenin pathway was downregulated in HNF4A-overexpressing cells (Figure 5(b) and Supplementary Table 1). The genes that changed significantly are shown in Figure 5(c) (listed in Supplementary Table 2). We conducted the TOP/FOP-Flash luciferase reporter assay, which is always used to measure the activity of the Wnt/ $\beta$ -catenin pathway, in HNF4A-overexpressing cells and their control cells. Compared with their control cells, the TOP-Flash luciferase was strongly decreased in HNF4A-overexpressing cells (Figures 5(d) and 5(e)). These data suggested that HNF4A could inhibit the activity of the Wnt/ $\beta$ -catenin pathway.

$\beta$ -Catenin is the core molecule of the pathway. At the same time, c-Myc and cyclin D1, which are downstream of the Wnt/ $\beta$ -catenin pathway, were involved in cell cycle regulation. To further explore the mechanism underlying, the expression levels of these proteins were measured. At the transcriptional level, the mRNA levels of CTNNB1, MYC, and CCND1 were significantly decreased in HeLa-HNF4A and SiHa-HNF4A cells compared with HeLa-GFP and SiHa-GFP cells (Figures 5(f) and 5(g)). Furthermore, at the protein level, a strong decrease in  $\beta$ -catenin, c-Myc, and cyclin D1 was observed in HeLa-HNF4A and SiHa-HNF4A cells (Figures 5(h) and 5(i)). The quantitative analysis of western blotting is shown in Figures 5(j) and 5(k). In conclusion, these data illustrated that the activity of the Wnt/ $\beta$ -catenin pathway was downregulated by HNF4A in cervical cancer cells.

**3.6. HNF4A Suppressed the Wnt/ $\beta$ -Catenin Pathway in Mouse Xenografts.** To further detect the relationship between HNF4A and Wnt/ $\beta$ -catenin pathway, immunohistochemistry was conducted in xenografts derived from HNF4A-modified cells and their control cells with specific antibodies (Figures 6(a) and 6(b)). Compared with xenografts derived from HeLa-GFP cells, the IRS scores of  $\beta$ -catenin, c-Myc, and cyclin D1 were strongly decreased in xenografts derived from HeLa-HNF4A cells (Figure 6(c), HNF4A:  $10.5 \pm 1.643$  vs.  $1.5 \pm 1.643$ ,  $p < 0.001$ ;  $\beta$ -catenin:  $7.0 \pm 1.549$  vs.  $10.0 \pm 2.449$ ,  $p < 0.05$ ; c-Myc:  $4.167 \pm 2.137$  vs.  $8.833 \pm 4.119$ ,  $p < 0.05$ ; and cyclin D1:  $1.0 \pm 1.095$  vs.  $8.5 \pm 1.225$ ,  $p < 0.001$ ). Similar results were obtained in xenografts derived from SiHa-GFP and SiHa-HNF4A cells (Figure 6(d), HNF4A:  $7.0 \pm 1.549$  vs.  $1.0 \pm 1.549$ ,  $p < 0.001$ ;  $\beta$ -catenin:  $1.667 \pm 1.033$  vs.  $8.0 \pm 1.549$ ,  $p < 0.001$ ; c-Myc:  $4.50 \pm 1.643$  vs.  $11.0 \pm 1.549$ ,  $p < 0.001$ ; and cyclin D1:  $3.5 \pm 1.225$  vs.  $10.5 \pm 1.643$ ,  $p < 0.001$ ).

Taken together, our results demonstrated that HNF4A inhibited the proliferation and tumor formation of cervical cancer cells through downregulating the activity of the Wnt/ $\beta$ -catenin pathway.

#### 4. Discussion

HNF4A belongs to the HNF family which plays important roles in regulating the expression of cell-specific genes in many tissues, especially in the liver [38]. HNF4A is not only the main regulator of liver organogenesis but also the tumor suppressor in the liver [39]. The exogenous expression of HNF4A and FOXA3 in hepatoma cells initiated the endoge-

nous expression of a large number of hepatocyte nuclear factors and promoted the transformation of hepatoma cells into hepatocyte-like cells [40]. HNF4A and FOXA2 are important targets which control embryonic hepatoblast differentiation into hepatocytes through the Hippo signaling pathway [26]. Mutations in the HNF4A protein can cause juvenile-onset diabetes mellitus (MODY) [41] and haemophilia [42]. In genome-wide association studies, HNF4A was also described as a susceptibility gene for ulcerative colitis [43]. At the same time, HNF4A is the core factor in the pathogenesis of nonalcoholic fatty liver disease (NAFLD) [44]. Researches about HNF4A in cancer mostly focused on liver cancer, and HNF4A mainly functions as a tumor suppressor in liver cancer [45]. To the best of our knowledge, there is no report on the function of HNF4A in cervical cancer.

In the present study, IHC and western blotting were used to detect the expression level of HNF4A in cervical cancer. The results both revealed that the expression levels of HNF4A protein were low in cervical cancer tissue (Figure 1). Unfortunately, we did not collect enough cervical cancer specimens to measure the mRNA levels of HNF4A. Thus, we turn our attention to the cancer database. The analysis in the GEO database suggested that the mRNA levels of HNF4A were also low in cervical cancer tissue (Figure S1). To further explore the relationship between HNF4A and cervical cancer, the Kaplan-Meier estimator survival analysis in TCGA database revealed that the patients who have higher expression of HNF4A would obtain higher relapse-free survival (RFS) probability. This is the first report that describes the expression of HNF4A in cervical cancer.

Next, HNF4A-modified cell lines were constructed to study the function of HNF4A. Xenograft assays suggested that HNF4A inhibited tumor formation and tumor growth in vivo (Figure 2). Further, MTT and cell counting assays suggested that HNF4A inhibited the proliferation and viability of cervical cancer cells in vitro (Figure 3). Cell proliferation is closely related to the cell cycle which is precisely regulated by a set of cell cycle-related proteins [46]. Previous studies revealed that HNF4A regulated the cell cycle through various approaches. Takashima et al. reported that upregulation of HNF4A combined with two liver-specific transcriptional factors strongly inhibited hepatocellular carcinoma cell proliferation and promoted stem-like cell differentiation into hepatocytes [47]. Li et al. found that HNF4A could downregulate the expression of E2F and thus inhibit the cell cycle process through lncRNAs and miRNAs [48]. Walesky et al. reported that downregulation of HNF4A resulted in the abnormal activation of c-Myc which is an important regulator of the cell cycle [49]. It was also reported that HNF4A suppressed the expression of cyclin D1 in hepatocytes [50]. Cell cycle analysis showed that HNF4A could induce cell cycle arrest from the G0/G1 phase to S phase (Figure 4). Collectively, these data demonstrated that HNF4A could inhibit tumor formation and the proliferation of cervical cancer cells through inducing cell cycle arrest from the G0/G1 phase to S phase. These findings consist in the results of previous studies in hepatocellular carcinoma and strongly imply that HNF4A may induce the cycle arrest through cell cycle-related proteins.

It is well known that the Wnt/ $\beta$ -catenin pathway participates in a variety of tumorigenesis processes. Yang et al. found that there was a feedback loop between HNF4A and the Wnt/ $\beta$ -catenin pathway during the EMT process in hepatocellular carcinoma [51]. Colletti et al. reported that HNF4A could interact with LEF1, which is a downstream of the Wnt/ $\beta$ -catenin pathway, in hepatocellular carcinoma [52]. Another study revealed that the deletion of HNF4A in the liver induced cyclin D1 expression and hepatocyte cell cycle progression [50]. To our knowledge, there is no report about the relationship between HNF4A and the Wnt/ $\beta$ -catenin pathway in cervical cancer.

To further detect the mechanism how HNF4A regulated the cell cycle, RNA-seq analysis was performed. The results suggested that the Wnt/ $\beta$ -catenin pathway may be involved in this process. TOP/FOP-Flash assays suggested that the Wnt/ $\beta$ -catenin pathway was suppressed in HNF4A-overexpressing cells. Subsequent real-time PCR and western blotting showed that the molecules of the Wnt/ $\beta$ -catenin pathway were all downregulated at both mRNA and protein levels (Figure 5). The IHC in a mouse tumor xenograft further verified that HNF4A could inhibit the activity of the Wnt/ $\beta$ -catenin pathway (Figure 6).

## 5. Conclusions

Altogether, our findings firstly described that HNF4A was downregulated in cervical cancer specimens and HNF4A inhibited tumor formation and proliferation of cervical cancer cells through suppressing the activity of the Wnt/ $\beta$ -catenin pathway.

## Data Availability

No data were used to support this study.

## Conflicts of Interest

The authors declare that they have no conflicts of interest.

## Authors' Contributions

Hong-Mei Ma, Qian Zhang, and Xue-Mei Yang contributed equally to this work.

## Acknowledgments

This work was supported by a grant to Dr. Rui Xu from the National Natural Science Foundation (No. 81602307) and the Xi'an Science and Technology Bureau (No. 2019115213yx007SF040(6)). This work was also supported by a grant to Dr. Qian Zhang from the National Natural Science Foundation of Shaanxi Province (grant no. 2021JM-583).

## Supplementary Materials

*Supplementary 1.* Figure S1: the mRNA of HNF4A is downregulated in cervical cancer.

*Supplementary 2.* Table S1: the GSEA result summary in the WP\_WNT\_SIGNALING GeneSet.

*Supplementary 3.* Table S2: detailed rank-ordered gene list for all features in the WP\_WNT\_SIGNALING dataset.

## References



- [1] F. Bray, J. Ferlay, I. Soerjomataram, R. L. Siegel, L. A. Torre, and A. Jemal, "Global cancer statistics 2018: GLOBOCAN estimates of incidence and mortality worldwide for 36 cancers in 185 countries," *CA: a Cancer Journal for Clinicians*, vol. 68, no. 6, pp. 394–424, 2018.
- [2] E. M. Burd and C. L. Dean, "Human papillomavirus," *Microbiology Spectrum*, vol. 4, no. 4, p. 4, 2016.
- [3] K. K. Mighty and L. A. Laimins, "The role of human papillomaviruses in oncogenesis," *Recent results in cancer research Fortschritte der Krebsforschung Progres dans les recherches sur le cancer*, vol. 193, pp. 135–148, 2014.
- [4] N. Egawa, K. Egawa, H. Griffin, and J. Doorbar, "Human papillomaviruses; epithelial tropisms, and the development of neoplasia," *Viruses*, vol. 7, no. 7, pp. 3863–3890, 2015.
- [5] H. Z. Cao, X. F. Liu, W. T. Yang, Q. Chen, and P. S. Zheng, "LGR5 promotes cancer stem cell traits and chemoresistance in cervical cancer," *Cell Death & Disease*, vol. 8, no. 9, article e3039, 2017.
- [6] Y. D. Wang, N. Cai, X. L. Wu, H. Z. Cao, L. L. Xie, and P. S. Zheng, "OCT4 promotes tumorigenesis and inhibits apoptosis of cervical cancer cells by miR-125b/BAK1 pathway," *Cell Death & Disease*, vol. 4, no. 8, article e760, 2013.
- [7] T. T. Gu, S. Y. Liu, and P. S. Zheng, "Cytoplasmic NANOG-positive stromal cells promote human cervical cancer progression," *The American Journal of Pathology*, vol. 181, no. 2, pp. 652–661, 2012.
- [8] X. F. Liu, W. T. Yang, R. Xu, J. T. Liu, and P. S. Zheng, "Cervical cancer cells with positive Sox2 expression exhibit the properties of cancer stem cells," *PLoS One*, vol. 9, no. 1, article e87092, 2014.
- [9] T. Zhan, N. Rindtorff, and M. Boutros, "Wnt signaling in cancer," *Oncogene*, vol. 36, no. 11, pp. 1461–1473, 2017.
- [10] R. Nusse and H. Clevers, "Wnt/ $\beta$ -Catenin Signaling, Disease, and Emerging Therapeutic Modalities," *Cell*, vol. 169, no. 6, pp. 985–999, 2017.
- [11] H. Clevers and R. Nusse, "Wnt/ $\beta$ -catenin signaling and disease," *Cell*, vol. 149, no. 6, pp. 1192–1205, 2012.
- [12] A. De, "Wnt/Ca<sup>2+</sup> signaling pathway: a brief overview," *Acta Biochimica et Biophysica Sinica*, vol. 43, no. 10, pp. 745–756, 2011.
- [13] V. Murillo-Garzón and R. Kypta, "WNT signalling in prostate cancer," *Nature Reviews Urology*, vol. 14, no. 11, pp. 683–696, 2017.
- [14] J. Yu, D. Liu, X. Sun, K. Yang, J. Yao, and C. Cheng, et al., "CDX2 inhibits the proliferation and tumor formation of colon cancer cells by suppressing Wnt/ $\beta$ -catenin signaling via transactivation of GSK-3 $\beta$  and Axin2 expression," *Cell Death & Disease*, vol. 10, no. 1, p. 26, 2019.
- [15] X. Xu, M. Zhang, F. Xu, and S. Jiang, "Wnt signaling in breast cancer: biological mechanisms, challenges and opportunities," *Molecular Cancer*, vol. 19, no. 1, p. 165, 2020.

- [16] S. He and S. Tang, "WNT/ $\beta$ -catenin signaling in the development of liver cancers," *Biomedicine & Pharmacotherapy = Biomedicine & Pharmacotherapie*, vol. 132, article 110851, 2020.
- [17] M. Ram Makena, H. Gatla, D. Verlekar, S. Sukhvasi, K. M. Pandey, and C. K. Pramanik, "Wnt/ $\beta$ -catenin signaling: the culprit in pancreatic carcinogenesis and therapeutic resistance," *International Journal of Molecular Sciences*, vol. 20, no. 17, p. 4242, 2019.
- [18] H. M. Ma, N. Cui, and P. S. Zheng, "HOXA5 inhibits the proliferation and neoplasia of cervical cancer cells via downregulating the activity of the Wnt/ $\beta$ -catenin pathway and transactivating TP53," *Cell Death & Disease*, vol. 11, no. 6, p. 420, 2020.
- [19] A. Bahrami, M. Hasanazadeh, S. ShahidSales, Z. Yousefi, S. Kadkhodayan, and M. Farazestanian, et al. et al., "Clinical significance and prognosis value of Wnt signaling pathway in cervical cancer," *Journal of Cellular Biochemistry*, vol. 118, no. 10, pp. 3028–3033, 2017.
- [20] A. Uren, S. Fallen, H. Yuan, A. Usubütün, T. Küçükali, and R. Schlegel, et al. et al., "Activation of the canonical Wnt pathway during genital keratinocyte transformation: a model for cervical cancer progression," *Cancer Research*, vol. 65, no. 14, pp. 6199–6206, 2005.
- [21] M. Yang, M. Wang, X. Li, Y. Xie, X. Xia, and J. Tian, et al. et al., "Wnt signaling in cervical cancer?," *Journal of Cancer*, vol. 9, no. 7, pp. 1277–1286, 2018.
- [22] A. DeLaForest, F. Di Furio, R. Jing et al., "HNF4A regulates the formation of hepatic progenitor cells from human iPSC-derived endoderm by facilitating efficient recruitment of RNA Pol II," *Genes*, vol. 10, no. 1, 2019.
- [23] V. Dubois, B. Staels, P. Lefebvre, M. P. Verzi, and J. Eeckhoutte, "Control of cell identity by the nuclear receptor HNF4 in organ pathophysiology," *Cell*, vol. 9, no. 10, 2020.
- [24] L. T. Ang, A. K. Y. Tan, M. I. Autio, S. H. Goh, S. H. Choo, and K. L. Lee, et al. et al., "A roadmap for human liver differentiation from pluripotent stem cells," *Cell Reports*, vol. 22, no. 8, pp. 2190–2205, 2018.
- [25] K. Rajamäki, A. Taira, R. Katainen, N. Välimäki, A. Kuosmanen, and R. M. Plaketti, et al. et al., "Genetic and epigenetic characteristics of inflammatory bowel disease-associated colorectal cancer," *Gastroenterology*, vol. 161, no. 2, pp. 592–607, 2021.
- [26] O. Alder, R. Cullum, S. Lee, A. C. Kan, W. Wei, and Y. Yi, et al. et al., "Hippo signaling influences HNF4A and FOXA2 enhancer switching during hepatocyte differentiation," *Cell Reports*, vol. 9, no. 1, pp. 261–271, 2014.
- [27] S. H. Cai, S. X. Lu, L. L. Liu, C. Z. Zhang, and J. P. Yun, "Increased expression of hepatocyte nuclear factor 4 alpha transcribed by promoter 2 indicates a poor prognosis in hepatocellular carcinoma," *Therapeutic Advances in Gastroenterology*, vol. 10, no. 10, pp. 761–771, 2017.
- [28] M. Kriegsmann, A. Harms, R. Longuespée, T. Muley, H. Winter, and K. Kriegsmann, et al. et al., "Role of conventional immunomarkers, HNF4- $\alpha$  and SATB2, in the differential diagnosis of pulmonary and colorectal adenocarcinomas," *Histopathology*, vol. 72, no. 6, pp. 997–1006, 2018.
- [29] M. Darsigny, J. P. Babeu, E. G. Seidman, F. P. Gendron, E. Levy, and J. Carrier, et al. et al., "Hepatocyte nuclear factor-4alpha promotes gut neoplasia in mice and protects against the production of reactive oxygen species," *Cancer Research*, vol. 70, no. 22, pp. 9423–9433, 2010.
- [30] P. C. . F. C. Jucá, S. Corrêa, G. M. Vignal et al., "HNF4A expression as a potential diagnostic tool to discriminate primary gastric cancer from breast cancer metastasis in a Brazilian cohort," *Diagnostic Pathology*, vol. 12, no. 1, p. 43, 2017.
- [31] H. R. Chang, S. Nam, M. C. Kook et al., "HNF4 $\alpha$  is a therapeutic target that links AMPK to WNT signalling in early-stage gastric cancer," *Gut*, vol. 65, no. 1, pp. 19–32, 2016.
- [32] H. S. Yao, J. Wang, X. P. Zhang et al., "Hepatocyte nuclear factor 4 $\alpha$  suppresses the aggravation of colon carcinoma," *Molecular Carcinogenesis*, vol. 55, no. 5, pp. 458–472, 2016.
- [33] Y. Gao, Y. Yan, J. Guo, Q. Zhang, D. Bi, and F. Wang, et al. et al., "HNF-4 $\alpha$  downregulation promotes tumor migration and invasion by regulating E-cadherin in renal cell carcinoma," *Oncology Reports*, vol. 42, no. 3, pp. 1066–1074, 2019.
- [34] J. Sun, X. Li, W. Wang, W. Li, S. Gao, and J. Yan, "Mir-483-5p promotes the malignant transformation of immortalized human esophageal epithelial cells by targeting HNF4A," *International Journal of Clinical and Experimental Pathology*, vol. 10, no. 9, pp. 9391–9399, 2017.
- [35] Z. Li and H. Chen, "miR-34a inhibits proliferation, migration and invasion of paediatric neuroblastoma cells via targeting HNF4 $\alpha$ ," *Artificial cells, nanomedicine, and biotechnology*, vol. 47, no. 1, pp. 3072–3078, 2019.
- [36] Á. Nagy, G. Munkácsy, and B. Györffy, "Pancancer survival analysis of cancer hallmark genes," *Scientific Reports*, vol. 11, no. 1, p. 6047, 2021.
- [37] L. Li, W. T. Yang, P. S. Zheng, and X. F. Liu, "SOX17 restrains proliferation and tumor formation by down-regulating activity of the Wnt/ $\beta$ -catenin signaling pathway via trans-suppressing  $\beta$ -catenin in cervical cancer," *Cell Death & Disease*, vol. 9, no. 7, p. 741, 2018.
- [38] H. Taniguchi, A. Fujimoto, H. Kono, M. Furuta, M. Fujita, and H. Nakagawa, "Loss-of-function mutations in Zn-finger DNA-binding domain of HNF4A cause aberrant transcriptional regulation in liver cancer," *Oncotarget*, vol. 9, no. 40, pp. 26144–26156, 2018.
- [39] G. Song, M. Pacher, A. Balakrishnan, Q. Yuan, H. C. Tsay, and D. Yang, et al. et al., "Direct reprogramming of hepatic myofibroblasts into hepatocytes in vivo attenuates liver fibrosis," *Cell Stem Cell*, vol. 18, no. 6, pp. 797–808, 2016.
- [40] Z. Cheng, Z. He, Y. Cai, C. Zhang, G. Fu, and H. Li, et al. et al., "Conversion of hepatoma cells to hepatocyte-like cells by defined hepatocyte nuclear factors," *Cell Research*, vol. 29, no. 2, pp. 124–135, 2019.
- [41] T. R. Özdemir, Ö. Kirbiyık, B. N. Dündar et al., "Targeted next generation sequencing in patients with maturity-onset diabetes of the young (MODY)," *Journal of Pediatric Endocrinology & Metabolism*, vol. 31, no. 12, pp. 1295–1304, 2018.
- [42] M. Borhany, H. Boijout, J. L. Pellequer, T. Shamsi, G. Moulis, and P. Aguilar-Martinez, et al. et al., "Genotype and phenotype relationships in 10 Pakistani unrelated patients with inherited factor VII deficiency," *Haemophilia : the official journal of the World Federation of Hemophilia*, vol. 19, no. 6, pp. 893–897, 2013.
- [43] J. P. Babeu and F. Boudreau, "Hepatocyte nuclear factor 4-alpha involvement in liver and intestinal inflammatory networks," *World Journal of Gastroenterology*, vol. 20, no. 1, pp. 22–30, 2014.
- [44] C. Baciú, E. Pasini, M. Angeli, K. Schwenger, J. Afrin, and A. Humar, et al. et al., "Systematic integrative analysis of gene expression identifies HNF4A as the central gene in pathogenesis

- of non-alcoholic steatohepatitis,” *PLoS One*, vol. 12, no. 12, article e0189223, 2017.
- [45] Q. Xu, Y. Li, X. Gao, K. Kang, J. G. Williams, and L. Tong, et al. et al., “HNF4 $\alpha$  regulates sulfur amino acid metabolism and confers sensitivity to methionine restriction in liver cancer,” *Nature Communications*, vol. 11, no. 1, p. 3978, 2020.
- [46] K. A. Schafer, “The cell cycle: a review,” *Veterinary Pathology*, vol. 35, no. 6, pp. 461–478, 1998.
- [47] Y. Takashima, K. Horisawa, M. Udono, Y. Ohkawa, and A. Suzuki, “Prolonged inhibition of hepatocellular carcinoma cell proliferation by combinatorial expression of defined transcription factors,” *Cancer Science*, vol. 109, no. 11, pp. 3543–3553, 2018.
- [48] S. Y. Li, Y. Zhu, R. N. Li et al., “LncRNA Lnc-APUE is repressed by HNF4 $\alpha$  and promotes G1/S phase transition and tumor growth by regulating miR-20b/E2F1 axis,” *Advanced Science*, vol. 8, no. 7, article 2003094, 2021.
- [49] C. Walesky, G. Edwards, P. Borude, S. Gunewardena, M. O’Neil, and B. Yoo, et al. et al., “Hepatocyte nuclear factor 4 alpha deletion promotes diethylnitrosamine-induced hepatocellular carcinoma in rodents,” *Hepatology*, vol. 57, no. 6, pp. 2480–2490, 2013.
- [50] H. Wu, T. Reizel, Y. J. Wang et al., “A negative reciprocal regulatory axis between cyclin D1 and HNF4 $\alpha$  modulates cell cycle progression and metabolism in the liver,” *Proceedings of the National Academy of Sciences of the United States of America*, vol. 117, no. 29, pp. 17177–17186, 2020.
- [51] M. Yang, S. N. Li, K. M. Anjum, L. X. Gui, S. S. Zhu, and J. Liu, et al. et al., “A double-negative feedback loop between Wnt- $\beta$ -catenin signaling and HNF4 $\alpha$  regulates epithelial-mesenchymal transition in hepatocellular carcinoma,” *Journal of Cell Science*, vol. 126, Part 24, pp. 5692–5703, 2013.
- [52] M. Colletti, C. Cicchini, A. Conigliaro, L. Santangelo, T. Alonzi, and E. Pasquini, et al. et al., “Convergence of Wnt signaling on the HNF4 $\alpha$ -driven transcription in controlling liver zonation,” *Gastroenterology*, vol. 137, no. 2, pp. 660–672, 2009.

## Research Article

# Liensinine Inhibits Osteosarcoma Growth by ROS-Mediated Suppression of the JAK2/STAT3 Signaling Pathway

Fei Jia <sup>1,2,3</sup>, Yu Liu,<sup>1,2,3</sup> Xinyu Dou,<sup>1,2,3</sup> Chuanchao Du,<sup>1,2,3</sup> Tianli Mao,<sup>1,2,3</sup>  
and Xiaoguang Liu <sup>1,2,3</sup>

<sup>1</sup>Department of Orthopedics, Peking University Third Hospital, North Garden Street No. 49, Haidian District, Beijing 100191, China

<sup>2</sup>Beijing Key Laboratory of Spinal Diseases, Haidian District, Beijing 100191, China

<sup>3</sup>Engineering Research Center of Bone and Joint Precision Medicine, Haidian District, Beijing 100191, China

Correspondence should be addressed to Xiaoguang Liu; puth13@pku.edu.cn

Received 10 August 2021; Revised 25 November 2021; Accepted 13 December 2021; Published 25 January 2022

Academic Editor: Peichao Chen

Copyright © 2022 Fei Jia et al. This is an open access article distributed under the Creative Commons Attribution License, which permits unrestricted use, distribution, and reproduction in any medium, provided the original work is properly cited.

Osteosarcoma (OS) is the most common malignancy of bone. Liensinine exerts antitumor effects on cancers of the colon, breast, and gallbladder. However, its antitumor activity in OS remains unclear. This study is aimed at investigating the efficacy of liensinine against OS and the underlying mechanism of action. Cell proliferation, apoptosis, and cycle arrest in OS were detected using the Cell Counting Kit-8 (CCK-8), colony formation, and flow cytometry assays, respectively. The production of reactive oxygen species (ROS), glutathione (GSH) and glutathione disulfide (GSSG) concentrations, and mitochondrial membrane potential (MMP) of OS cells were measured by flow cytometry, colorimetry, and JC-1 staining. The expressions of factors related to apoptosis, cell cycle, and activation of the JAK2/STAT3 pathway were determined by Western blotting. To examine the potential role of ROS, an antioxidant (N-acetyl cysteine, NAC) was used in combination with liensinine. *In vivo*, we generated a xenograft mouse model to assess its antitumor efficacy. Tissue level expressions of factors related to apoptosis and activation of the JAK2/STAT3 pathway were assessed by immunohistochemistry or Western blotting. Liensinine inhibited the proliferation and induced G0/G1 phase arrest and apoptosis of OS cells in a dose-dependent manner. Additionally, liensinine promoted intracellular ROS production, enhanced the GSSG/GSH ratio, and induced MMP loss and ROS-mediated suppression of the JAK2/STAT3 pathway. NAC significantly attenuated the liensinine-induced antitumor activities and activated the JAK2/STAT3 pathway. *In vivo*, liensinine effectively inhibited the OS growth and promoted apoptosis; however, it had no negative effect on the internal organs. In conclusion, liensinine-induced ROS production could suppress the activation of the JAK2/STAT3 pathway and inhibit the OS growth both *in vivo* and *in vitro*. Our findings provided a new rationale for subsequent academic and clinical research on OS treatment.

## 1. Introduction

Osteosarcoma (OS) is a malignant tumor originating from mesenchymal tissues, accounts for 20% of the primary malignant bone acanthomas; it is the most common primary malignant bone tumor in adolescents [1]. OS is characterized by high malignancy, rapid growth, early metastasis, and poor prognosis. It is the leading cause of cancer-related death among children and adolescents [2, 3]. At present, surgery combined with multiagent chemotherapy is the standard treatment regime for OS [2, 4]. However, long-term chemotherapy causes many irreversible systemic side

effects, including cardiotoxicity, secondary malignancies, neurotoxicity, and infertility. In addition, physical disability caused by surgical procedures has a great impact on the mental health and quality of life of the patients [2, 5]. Therefore, the development of novel anti-OS drugs is important for effectively inhibiting tumor progression and prolonging the survival duration of patients.

Liensinine, a natural isoquinoline alkaloid, is isolated from the seed embryo of *Nelumbo nucifera* Gaertn [6]. Multiple biological effects of liensinine are reported in recent pharmacological studies, including antihypertension and antiarrhythmias, as well as anticancer properties [6–8]. For

example, liensinine can induce apoptosis and growth cessation of gallbladder cancer [9]. It can also induce apoptosis of colorectal cancer by stimulating mitochondrial dysfunction and sensitize breast cancer cells towards chemotherapy through DNMI1-mediated mitochondrial fission [6, 10]. However, unlike the aforementioned cancer types, OS is distinct in both origin and biological behavior. The role of liensinine in OS remains unknown and warrants investigation.

Reactive oxygen species (ROS) are the by-products of oxidative stress, which include peroxides, superoxides, hydroxyl radicals, and singlet oxygen [11]. Accumulating evidence demonstrates that several anticancer drugs, such as Glucocalyxin A, metformin, cisplatin, isoalantolactone, and docetaxel, can induce apoptosis and proliferation cessation of cancer cells by intracellular ROS generation [11–13]. According to previous studies, the inhibitory effect of liensinine on gastric cancer cells is achieved by inducing ROS production [14]. In addition, other similar dibenzyl tetrahydroisoquinoline alkaloids, such as cepharanthine or tetrandrine, can also induce ROS-mediated apoptosis of tumor cells [15, 16]. Typically, tumor cells can withstand oxidative stress by maintaining the balance between oxidation and antioxidation levels; however, antineoplastic drugs can fatally break the redox balance not just by increasing oxidant accumulation but also by interfering with the antioxidant production [11]. The role of liensinine in the oxidation/antioxidation system of OS cells is unknown.

In this study, we aimed to investigate the antitumor effect of liensinine on OS and further explore its underlying mechanism of action, so as to elucidate the regulation of ROS on the JAK2/STAT3 pathway.

## 2. Materials and Methods

**2.1. Cell Culture.** The source and culture conditions of human normal osteoblasts, hFOB 1.19, and human OS cell lines SaOS-2, MG-63, 143B, and U-2OS were the same as described in our previous study [17].

**2.2. Drug Treatment.** Liensinine (HY-N0484) with 99.89% purity was obtained from MedChemExpress (Princeton, New Jersey, USA). N-Acetyl cysteine (NAC, ST1546), an antioxidant and a ROS inhibitor, was purchased from Beyotime (Shanghai, China). For liensinine treatment, the cells were cultured in the medium containing 0  $\mu$ M, 5  $\mu$ M, 10  $\mu$ M, 20  $\mu$ M, 40  $\mu$ M, or 80  $\mu$ M liensinine for 24 h; following which, they were observed under an inverted microscope (Leica, Wetzlar, Germany). For cotreatment with liensinine and NAC, the cells were treated with 80  $\mu$ M liensinine for 24 h following a 2 h pretreatment with 5 mM NAC.

**2.3. Cell Viability Assay.** The Cell Counting Kit-8 (CCK-8) (C0038, Beyotime) was used to detect the inhibitory effect at different concentrations of liensinine (0  $\mu$ M, 5  $\mu$ M, 10  $\mu$ M, 20  $\mu$ M, 40  $\mu$ M, or 80  $\mu$ M) as described previously [18].

**2.4. Colony Formation Assay.** 1000 cells per well were plated onto 6-well plates (each well contained 2 mL medium supplemented with 10% FBS). After adherence for 24 h, the cells

were treated with 0  $\mu$ M, 40  $\mu$ M, and 80  $\mu$ M liensinine for 24 h; following which, the medium was replaced with the complete medium. The cells were cultured for 14 days; subsequently, they were fixed with 4% ice-cold paraformaldehyde, stained with 0.1% crystal violet, and washed thrice with PBS (P1010, Solarbio, Beijing, China). Images of cell colonies were captured by a camera (Alpha 7R IV, SONY, Tokyo, Japan), and the cell colony numbers were analyzed using the Image J software.

**2.5. Flow Cytometric Analysis of Apoptosis.** The apoptosis was evaluated by flow cytometry (FCM) using an Annexin V-FITC/PI Apoptosis Detection Kit (C1062L, Beyotime). After SaOS-2 and 143B cells were treated with liensinine or cotreated with NAC and liensinine in 6-well plates for 24 h, approx.  $1 \times 10^6$  cells/well were harvested and detected as described previously [19].

**2.6. Flow Cytometric Analysis of Cell Cycle Distribution.** The cell cycle distribution of cells was evaluated by FCM using a Cell Cycle Detection Kit (C1052, Beyotime). After SaOS-2 and 143B cells were treated with liensinine for 24 h, approx.  $1 \times 10^6$  cells/well were harvested and washed twice with PBS. The resuspended cells were then fixed with prechilled 70% ethanol (E111994, Aladdin, Shanghai, China) for 2 h at 4°C. Following this, the collected cells were incubated with 500  $\mu$ L PI/RNase A staining fluid for 30 min at 37°C in dark. The cell cycle distribution was detected and analyzed on a CytoFLEX flow cytometer (Beckman Coulter, Brea, CA, USA) with 488 nm excited wavelength.

**2.7. Flow Cytometric Analysis of ROS.** The ROS production in the cells was evaluated by FCM using a DCFH-DA probe-based ROS Detection Kit (S0033, Beyotime). DCFH-DA was diluted with FBS-free medium to a final concentration of 10  $\mu$ M. After SaOS-2, 143B, and hFOB 1.19 cells were treated with liensinine or cotreated with NAC and liensinine for 24 h, the cells ( $1 \times 10^6$ ) were harvested and washed twice with PBS. The cells were then incubated with 500  $\mu$ L of 10  $\mu$ M DCFH-DA for 20 min in a 37°C incubator and washed thrice with FBS-free medium. Finally, the ROS in the cells was detected and analyzed on a CytoFLEX flow cytometer with 488 nm excited wavelength.

**2.8. Colorimetric Analysis of Glutathione (GSH) and Glutathione Disulfide (GSSG).** The level of GSH and GSSG in the cells was evaluated by colorimetry using a GSH and GSSG Detection Kit (S0053, Beyotime). After SaOS-2 and 143B cells were treated with liensinine or NAC, the cells were collected and washed with PBS. 30  $\mu$ L of protein removal reagent M solution was added. The samples were then subjected to two rapid freeze-thaws using liquid nitrogen and water at 37°C. After the samples were placed at 4°C for 5 min, they were centrifuged for 10 min at  $10,000 \times g$ , and the supernatant was collected for the determination of total glutathione. In addition, part of the above supernatant was pipetted and added with the GSH clearance auxiliary solution as well as the GSH clearance working solution at the ratios of 100  $\mu$ L : 20  $\mu$ L and 100  $\mu$ L : 4  $\mu$ L. The solutions were mixed by vortex and reacted for 60 min at room

temperature to obtain samples for GSSG determination. In a 96-well plate, 10  $\mu$ L of the supernatant was mixed with 150  $\mu$ L of the prepared total glutathione detection working solution and incubated at room temperature for 5 min, followed by the addition of 50  $\mu$ L of 0.5 mg/mL NADPH. After 25 minutes of reaction, the absorbance of each well was measured by a microplate reader at 412 nm wavelength. GSSG was determined in the same way. The GSH and GSSG levels were further calculated according to the kit manufacturer's protocol and the formula:  $GSH = \text{total glutathione} - GSSG \times 2$ .

**2.9. JC-1 Staining.** The mitochondrial membrane potential (MMP) of the cells was evaluated by a JC-1 Kit (C2006, Beyotime). After SaOS-2 and 143B cells were treated with liensinine or NAC in the 6-well plates for 24 h, the medium was discarded and 1 mL JC-1 working solution was added to the wells, and cells were incubated for 20 min at 37°C. The cells were then washed twice with 1 $\times$  JC-1 staining buffer. After adding 1 mL PBS per well, the fluorescence signal of the cells was observed under an inverted fluorescence microscope (DMI8, Leica) at  $\times 200$  magnification. Polymers were excited by green light, monomers were excited by blue light, and merged images were collected.

**2.10. In Vivo Assay.** The animal study design was approved by the ethics committee of Peking University Third Hospital (No. IRB00006761-2016048) and complied with the ARRIVE guidelines. All experiments with animals were performed in the Department of Laboratory Animal Science, Peking University Health Science Center. Eighteen 4-week-old BALB/c nude female mice weighing  $18 \pm 2$  g were purchased from Beijing WeiTongLiHua Laboratory Animal Technology Co., Ltd. The mice were kept in a specific pathogen free (SPF) environment and provided an ad libitum diet. After feeding for five days, the mice adapted to the environment; next, 143B cells at a density of  $2 \times 10^6/100 \mu\text{L}$  were subcutaneously injected into the right axilla of each mouse. When the tumor volume reached  $100 \text{ mm}^3$ , the mice were randomly divided into three groups: (1) sham treatment ( $n = 6$ ), (2) liensinine-L treatment ( $n = 6$ ), and (3) liensinine-H treatment ( $n = 6$ ). The mice in the three groups were orally administered with 200  $\mu\text{L}$  PBS, 15 mg/kg liensinine solution, or 30 mg/kg liensinine solution, respectively, once every two days for 14 days. The tumor sizes and body weights were measured every two days with the volume calculation formula:  $L \times W^2/2$  ( $L$ , the long diameter of the tumor and  $W$ , the short diameter of the tumor). On the last day, the mice were sacrificed. Subcutaneous tumors from each mouse were excised and weighed; one portion was immediately frozen for Western blot analysis, while another was preserved in 4% paraformaldehyde for histopathological analysis. In addition, the heart, liver, spleen, lung, and kidney from each mouse were removed, photographed, and collected for later use.

**2.11. Immunohistochemistry and H&E Staining.** Tumor tissues were fixed using neutral formalin fixative for 24 h. Next, the tissues were dehydrated with graded ethanol, incubated

with xylene (1330-20-7, Aladdin), and embedded into paraffin (P100936, Aladdin). The paraffin blocks were cut into 4  $\mu\text{m}$  sections, deparaffinized, rehydrated, and repaired using sodium citrate antigen retrieval solution (BB-2351-1, BestBio, Beijing, China). After the tissues were incubated with proliferating cell nuclear antigen (PCNA) antibody (1:1000, ab92552, Abcam, Cambridge, UK) and cleaved caspase 3 antibody (1:100, ab2302, Abcam) overnight at 4°C, they were washed with PBS and incubated with goat anti-rabbit IgG-HRP-conjugated secondary antibody (CW0103S, CWBIO, Taizhou, China) and diaminobenzidine (36201ES03, YEASEN, Shanghai, China). After sealing the tissues with neutral gum (BB-23474-1, BestBio), cell positive for PCNA and cleaved caspase 3 were observed under an inverted microscope. Tumor and five visceral tissues (heart, liver, spleen, lung, and kidney) were fixed, dehydrated, embedded, sectioned, and stained with hematoxylin-eosin solution (G1120, Solarbio), and the efficacy and safety of liensinine treatment were assessed.

**2.12. Western Blotting.** The protein in the SaOS-2, 143B, and hFOB 1.19 cells as well as in the tumor tissue was isolated by the NP-40 Lysis Buffer (N8032, Solarbio) containing PMSF (BB-3341-1, BestBio) and protease inhibitor mixture (P6730, Solarbio). Then, the protein concentration was quantified using a BCA kit (PC0020, Solarbio). 20  $\mu\text{g}$  of protein was electrophoresed inside the SDS-PAGE gel (P1200, Solarbio) and further transferred onto the PVDF membrane (YA1701, Solarbio) which further blocked with Western blot blocking buffer (BB-3512-1, BestBio) at room temperature for 2 h. Then, the membrane was, respectively, soaked overnight under the primary antibodies at 4°C: Bcl-2 (1:1000, ab32124, Abcam), Bax (1:2000, ab32503, Abcam), cleaved caspase 3 (1:2000, ab2302, Abcam), cleaved PARP1 (1:2000, ab32064, Abcam), Cyclin D1 (1:1000, ab16663, Abcam), p-STAT3 (1:3000, ab76315, Abcam), STAT3 (1:5000, ab119352, Abcam), p-JAK2 (1:4000, ab32101, Abcam), JAK2 (1:5000, ab108596, Abcam), and  $\beta$ -actin (1:1000, ab8226, Abcam). On the second day, the membrane was incubated with goat anti-rabbit IgG-HRP-conjugated secondary antibody (1:10000, ab205718, Abcam) or goat anti-mouse IgG-HRP-conjugated secondary antibody (1:10000, ab205719, Abcam) for 2 h at room temperature. The proteins were visualized by enhanced chemiluminescence (ECL) (BB-3501-2, BestBio) according to the manufacturer's protocol.

**2.13. Routine Blood Tests and Liver/Renal Function Tests.** After treatment, mice were anesthetized by intraperitoneal injection of 3% pentobarbital sodium, and eyeballs were removed for blood collection. 20  $\mu\text{L}$  whole blood was added into the EP tube containing 1 mL anticoagulant (1.5 mg/ml EDTA dipotassium salt dihydrate, Macklin, Shanghai, China) for routine blood test at the Animal Experimental Center, Peking University Health Science Center. At the same time, the blood in other EP tubes was placed at room temperature for 2 h, and then, the supernatant was taken and centrifuged at room temperature (3000 rpm, 10 min).

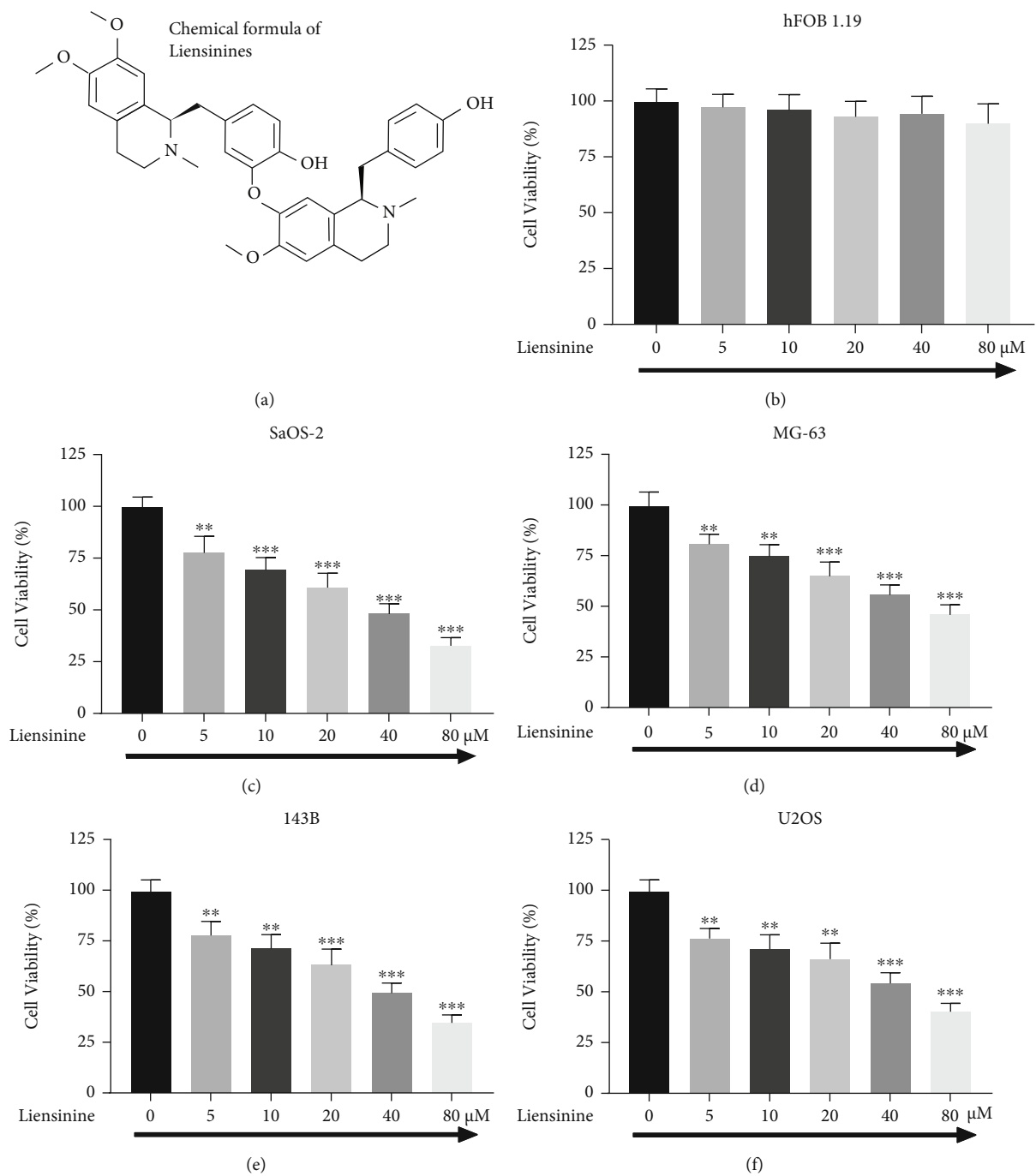


FIGURE 1: Continued.



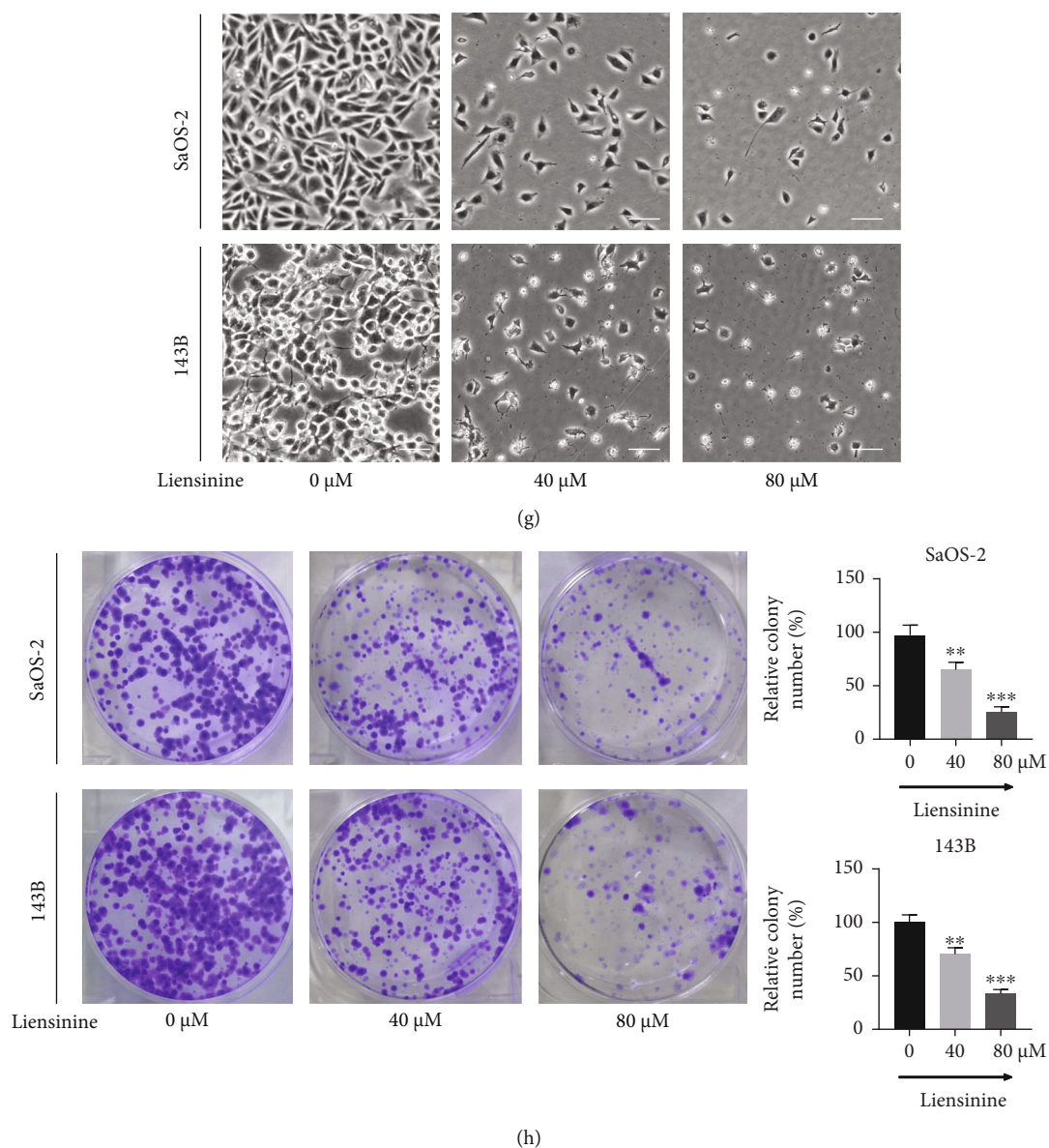


FIGURE 1: Liensinine inhibited the viability and proliferation of osteosarcoma cells. (a) The chemical structure of liensinine. (b) The viability of human normal osteoblasts (hFOB 1.19) after being treated with liensinine for 24 h was detected by CCK-8 assay. (c–f) The viability of human osteosarcoma cells (SaOS-2, MG-63, 143B, and U2OS) after being treated with liensinine for 24 h was detected by CCK-8 assay. (g) Changes in cell morphology of SaOS-2 and 143B cells were observed after liensinine treatment for 24 h; bar scale = 50  $\mu\text{m}$ . (h) The proliferation of SaOS-2 and 143B cells after being treated with liensinine was detected by colony formation assay.  $n = 3$  in each group. The columns and errors bars represent means and SD. \* $P < 0.05$ , \*\* $P < 0.01$ , and \*\*\* $P < 0.001$  vs. 0  $\mu\text{M}$ .

About 200  $\mu\text{L}$  serum was collected for liver and renal function detection in the above institution.

**2.14. Statistical Analysis.** Statistical significances for independent data were assessed using an unpaired Student's  $t$ -test. For multiple comparisons, one-way ANOVA was used to analyze the data with post hoc Bonferroni correction. The data were analyzed using the IBM SPSS Statistics 22.0 software (IBM, Armonk, NY, USA), and the results were depicted as mean  $\pm$  standard deviation (SD). Differences were considered significant at  $P < 0.05$ .

### 3. Results

**3.1. Liensinine Inhibits the Proliferation of OS Cells but Not of the Human Normal Osteoblasts.** Liensinine (Figure 1(a)) was used to treat human normal osteoblasts (hFOB 1.19) and human OS cells (SaOS-2, MG-63, 143B, and U2OS). Cell viability was evaluated by the CCK-8 assay, which showed that liensinine at 5  $\mu\text{M}$ , 10  $\mu\text{M}$ , 20  $\mu\text{M}$ , 40  $\mu\text{M}$ , and 80  $\mu\text{M}$  did not inhibit the viability of hFOB 1.19 cells (Figure 1(b)); however, it significantly reduced the viability of SaOS-2 (Figure 1(c)), MG-63 (Figure 1(d)), 143B (Figure 1(e)), and U2OS (Figure 1(f)) cells. The viability of

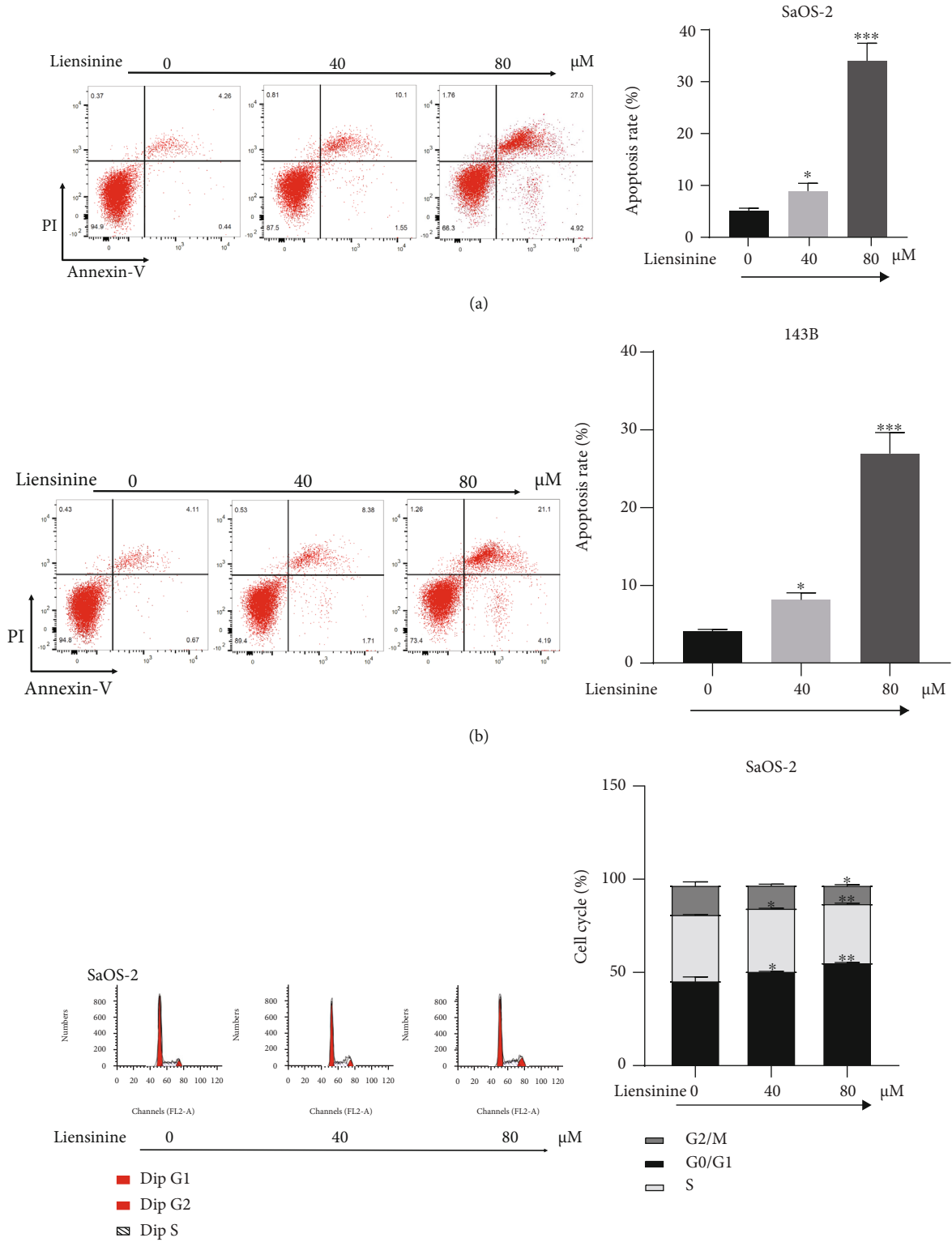


FIGURE 2: Continued.

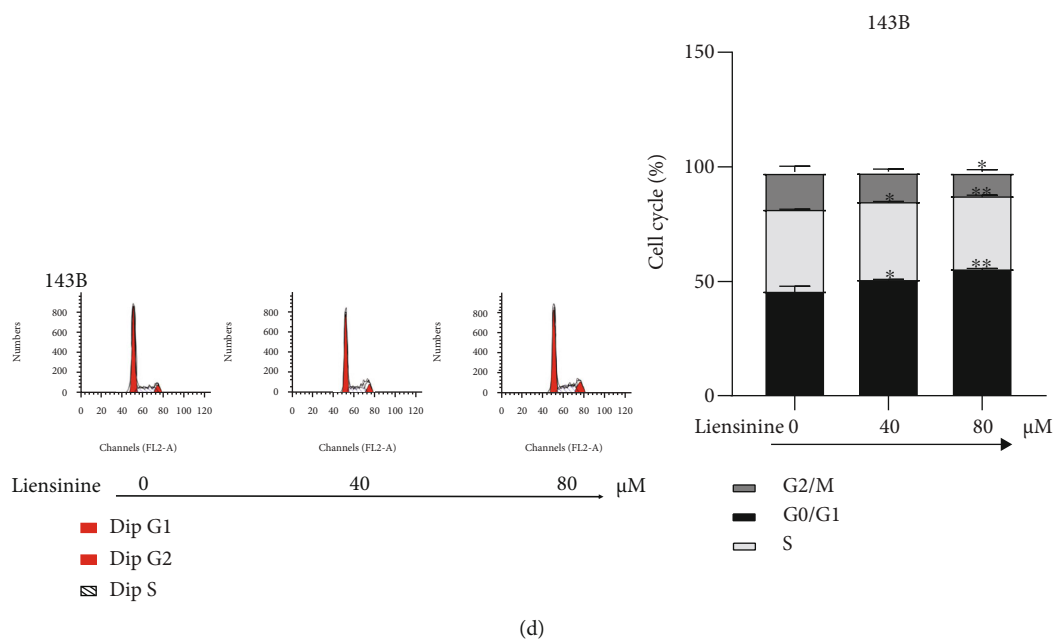


FIGURE 2: Liensinine induced the cell cycle arrest and apoptosis of osteosarcoma cells. (a, b) The apoptosis rates of SaOS-2 and 143B cells after being treated with liensinine were detected by FCM. (c, d) The cell cycle distribution of SaOS-2 and 143B cells after being treated with liensinine was detected by FCM.  $n = 3$  in each group. \* $P < 0.05$ , \*\* $P < 0.01$ , \*\*\* $P < 0.001$  vs.  $0 \mu\text{M}$ .

these cells reduced significantly after treatment with  $5 \mu\text{M}$  liensinine for 24 h ( $P < 0.01$ ). The SaOS-2 and 143B cell lines showed the most significant effect of inhibition and were used for subsequent assays. After treated with  $80 \mu\text{M}$  liensinine for 24 h, their viability decreased to about a third of the control. Based on this result, we selected  $40 \mu\text{M}$  and  $80 \mu\text{M}$  liensinine to treat the cells in the following experiments. After exposure to  $40 \mu\text{M}$  and  $80 \mu\text{M}$  liensinine, morphological changes such as cell shrinkage, deformation, and cytoplasmic vesicles of SaOS-2 and 143B cells were observed by an optical microscope (Figure 1(g)). The results of the colony formation assay also indicated that liensinine inhibited cell proliferation and cloning efficiencies of SaOS-2 and 143B cells (Figure 1(h)). The number of colonies formed in both liensinine-treated groups was lower than that in the control group, and the inhibitory effect was clearly concentration-dependent. The cloning efficiencies of SaOS-2 at  $40 \mu\text{M}$  and  $80 \mu\text{M}$  compared with the control were 58.9% and 23.7% vs. 100.0% ( $40 \mu\text{M}$  or  $80 \mu\text{M}$  vs. control:  $P = 0.004$  or  $P < 0.0001$ ), respectively. Correspondingly, the cloning efficiencies of 143B at  $40 \mu\text{M}$  and  $80 \mu\text{M}$  compared with the control were 67.4% and 30.3% vs. 100.0% ( $40 \mu\text{M}$  or  $80 \mu\text{M}$  vs. control:  $P = 0.005$  or  $P < 0.001$ ), respectively.

**3.2. Liensinine Induces Apoptosis of OS Cells.** After treatment with  $40 \mu\text{M}$  and  $80 \mu\text{M}$  of liensinine, FCM showed that the total number of apoptotic cells in both the SaOS-2 and 143B cell lines increased significantly (Figures 2(a) and 2(b)). The apoptosis rates of SaOS-2 cells under 0, 40, and  $80 \mu\text{M}$  liensinine treatment were 4.8%, 9.6%, and 32.2%, respectively ( $40$  or  $80$  vs.  $0 \mu\text{M}$ :  $P = 0.034$  or  $P < 0.001$ ). Similarly, the apoptosis rates of 143B cells were 4.3%, 8.7%, and 27.4%, respectively ( $40$  or  $80$  vs.  $0 \mu\text{M}$ :  $P = 0.028$  or  $P < 0.001$ ).

**3.3. Liensinine Induces Cycle Arrest in OS Cells.** In both OS cell lines, liensinine increased the proportion of cells in G0/G1 phase and reduced the proportion of cells in S phase in a dose-dependent manner. The G0/G1 phase proportion of SaOS-2 cells under 0, 40, and  $80 \mu\text{M}$  liensinine treatment was 46.2%, 51.4%, and 55.9%, respectively ( $40$  or  $80$  vs.  $0 \mu\text{M}$ :  $P = 0.031$  or  $P = 0.004$ ). Similarly, the G0/G1 phase proportion of 143B cells was 45.8%, 49.5%, and 54.1%, respectively ( $40$  or  $80$  vs.  $0 \mu\text{M}$ :  $P = 0.012$  or  $P = 0.001$ ). Furthermore, liensinine at  $80 \mu\text{M}$  concentration significantly reduced the proportion of G2/M cells in SaOS-2 cells as compared to the corresponding control group (11.0% vs. 16.9%,  $P = 0.018$ ) (Figures 2(c) and 2(d)). These results indicated that liensinine caused G0/G1 phase arrest, thereby inhibiting OS proliferation.

**3.4. Liensinine Induces ROS Production and Causes Imbalance of GSSG/GSH.** To evaluate if oxidative stress underlies the inhibitory effect of liensinine on OS cells, the ROS productions in SaOS-2 and 143B cells after liensinine treatment were examined by FCM analysis. Liensinine treatment substantially upregulated ROS production in both cell lines as compared to the control group (Figures 3(a) and 3(b)). The fold change of ROS production of SaOS-2 cells under 0, 40, and  $80 \mu\text{M}$  liensinine treatment was 1.0, 4.6 and 5.1, respectively ( $40$  or  $80$  vs.  $0 \mu\text{M}$ :  $P < 0.001$  or  $P < 0.001$ ). Similarly, the fold change of ROS production of 143B cells was 1.0, 3.9, and 4.5, respectively ( $40$  or  $80$  vs.  $0 \mu\text{M}$ :  $P < 0.001$  or  $P < 0.001$ ). In comparison, we evaluated the effect of the same concentration of liensinine on the intracellular ROS levels of hFOB 1.19 cells. The results showed that liensinine did not significantly affect the intracellular ROS levels of human normal osteoblasts

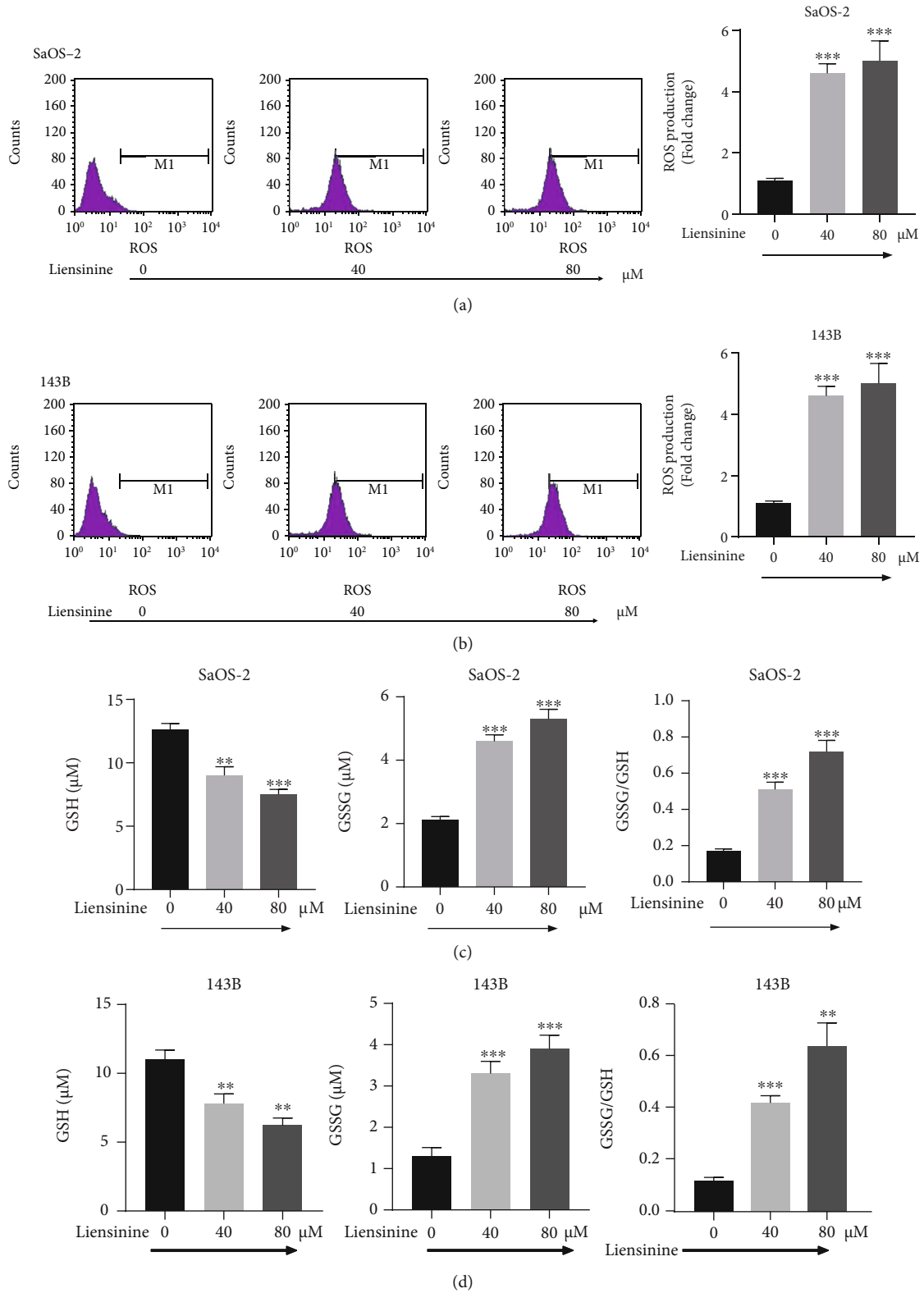


FIGURE 3: Continued.

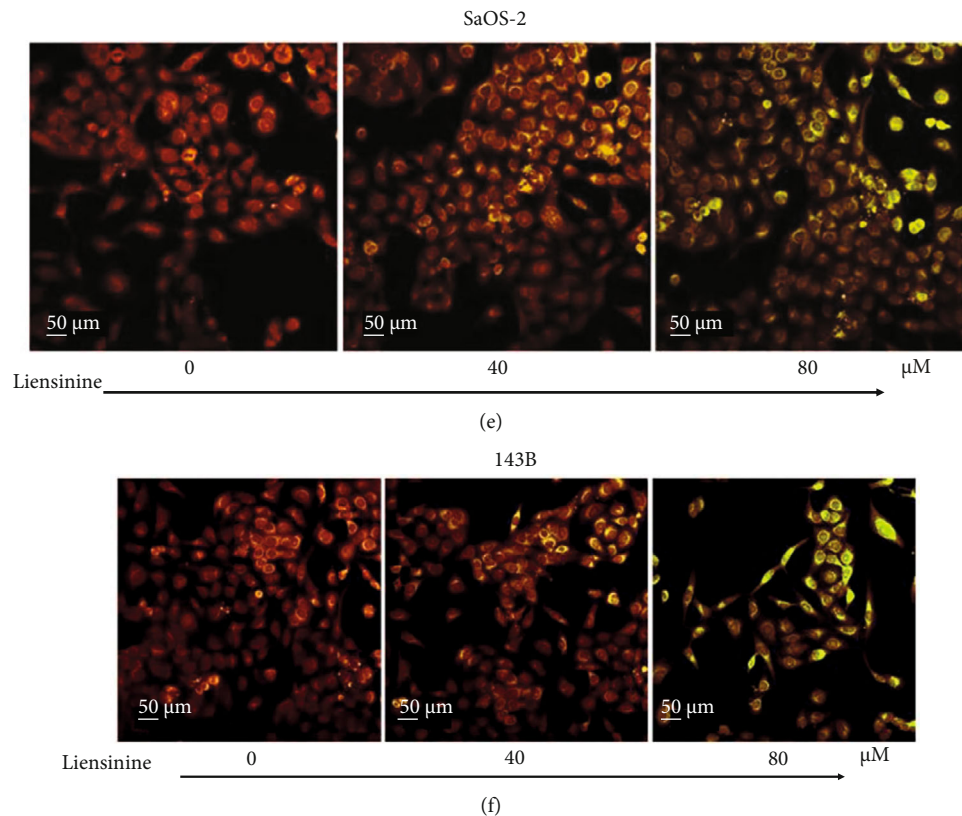


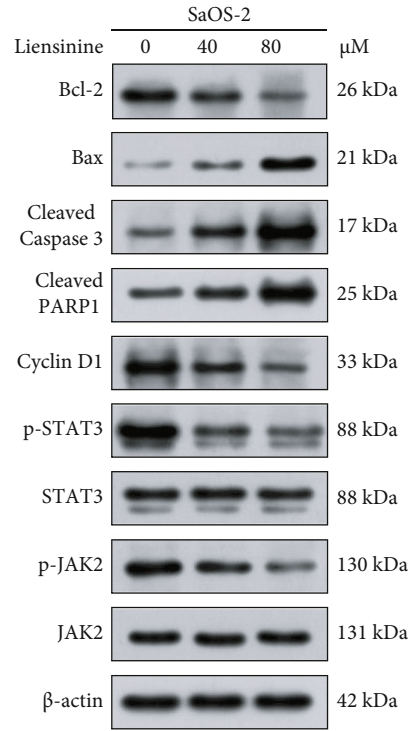
FIGURE 3: Liensinine-induced ROS production, GSSG/GSH imbalance, and MMP loss in osteosarcoma cells. (a, b) The ROS production in SaOS-2 and 143B cells after being treated with liensinine was detected by FCM. (c, d) The concentrations of GSH and GSSG, as well as the GSSG/GSH rate in SaOS-2 and 143B cells after being treated with liensinine, were detected by colorimetry. (e, f) The MMP of SaOS-2 and 143B cells after being treated with liensinine was detected by JC-1 staining.  $n = 3$  in each group.  $**P < 0.01$  and  $***P < 0.001$  vs.  $0 \mu\text{M}$ .

(Figures S1(a)). In addition, we evaluated the changes in cellular GSH and GSSG levels in OS cell lines by colorimetric analysis. As compared to the control group, liensinine treatment significantly attenuated the GSH concentration (0, 40, and  $80 \mu\text{M}$  liensinine treatment of SaOS-2 cells: 12.6, 9.0, and  $7.5 \mu\text{M}$ , respectively, and 0, 40, and  $80 \mu\text{M}$  liensinine treatment of 143B cells: 11.1, 7.8, and  $6.2 \mu\text{M}$ , respectively); however, the GSSG concentration in both cell lines was elevated (0, 40, and  $80 \mu\text{M}$  liensinine treatment of SaOS-2 cells: 2.1, 4.6, and  $5.3 \mu\text{M}$ , respectively, and 0, 40, and  $80 \mu\text{M}$  liensinine treatment of 143B cells: 1.3, 3.3, and  $3.9 \mu\text{M}$ , respectively), thereby leading to a significantly increased GSSG/GSH ratio (0, 40, and  $80 \mu\text{M}$  liensinine treatment of SaOS-2 cells: 0.17, 0.51, and 0.71, respectively, and 0, 40, and  $80 \mu\text{M}$  liensinine treatment of 143B cells: 0.12, 0.42, and 0.64, respectively) (Figures 3(c) and 3(d)). These results indicated that liensinine could enhance ROS production and cause an imbalance of GSH/GSSG antioxidant system in OS cells.

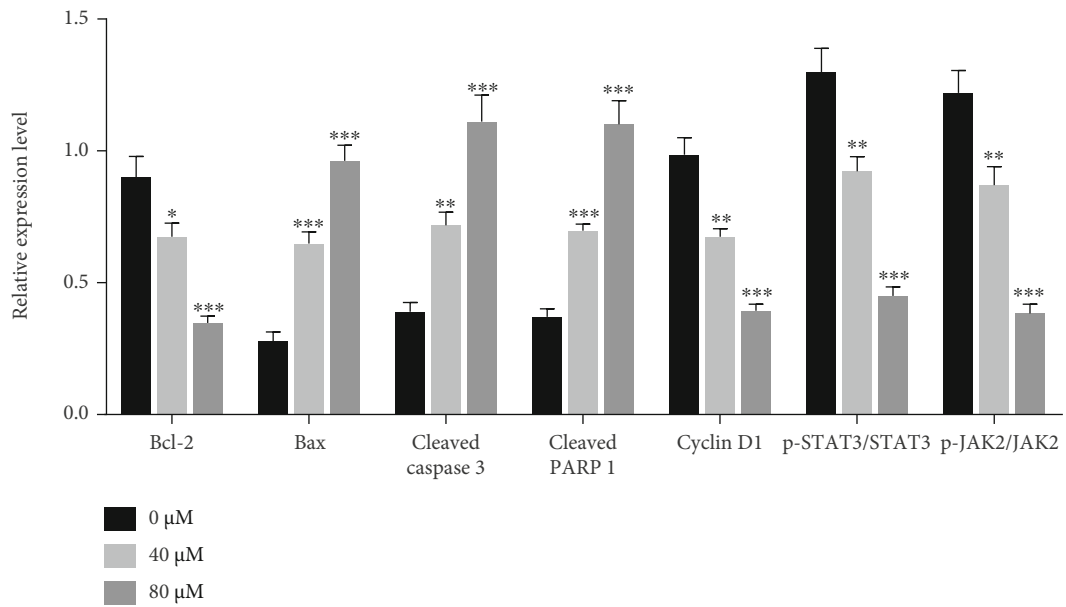
**3.5. Liensinine Induces MMP Loss.** MMP was determined using JC-1 staining and was indicative of the extent of mitochondrial oxidative damage in OS cells. As shown in Figures 3(e) and 3(f), after exposure to  $40 \mu\text{M}$  and  $80 \mu\text{M}$  liensinine, the merged fluorescence color of SaOS-2 and

143B cells transformed from red to green in a dose-dependent manner under fluorescence microscope. It was proved that JC-1 existed in the cytoplasm as monomer, indicating that liensinine could induce substantial MMP decrease or loss in OS cells.

**3.6. Liensinine Regulates the Expressions of Apoptosis and Cycle Arrest-Related Factors and Activates the JAK2/STAT3 Pathway.** To study the potential mechanism of liensinine affecting apoptosis and cell cycle progression, the expressions of factors related to apoptosis (Bcl-2, Bax, cleaved caspase 3, and cleaved PARP1) and cell cycle regulation (Cyclin D1) in OS cells were analyzed by Western blotting. Treatment with 40 and  $80 \mu\text{M}$  liensinine significantly upregulated the expressions of Bax, cleaved caspase 3, and cleaved PARP1, while downregulated those of Bcl-2 and Cyclin D1 (Figures 4(a)–4(d)), which were consistent with above findings for enhancing apoptosis and G0/G1 phase arrest. Many natural compounds affect tumor progression by suppressing activation of pathways involved in cell growth and proliferation, such as the JAK2/STAT3 pathway [20, 21]. We assessed the effect of liensinine on the expressions of proteins involved in the JAK2/STAT3 pathway by Western blotting. As shown in Figures 4(a)–4(d), treatment with 40 and  $80 \mu\text{M}$  liensinine significantly inhibited the expressions of



(a)



(b)

FIGURE 4: Continued.

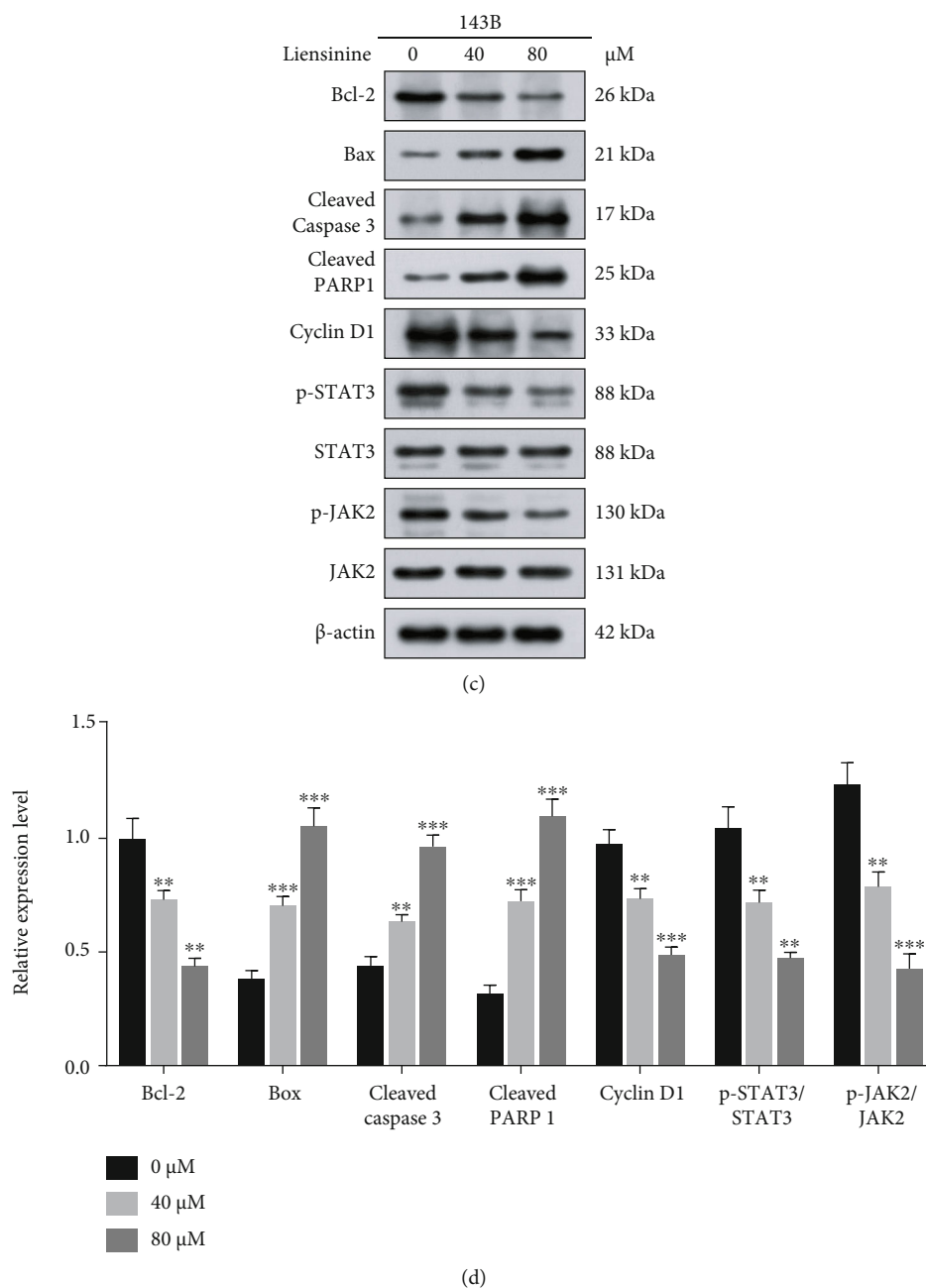


FIGURE 4: Liensinine regulated the expressions of factors related to apoptosis, cycle arrest, and JAK2/STAT3 pathway activation in osteosarcoma cells. (a, b) The expressions of factors related to apoptosis (Bcl-2, Bax, cleaved caspase 3, and cleaved PARP1), cycle arrest (Cyclin D1), and JAK2/STAT3 pathway activation (p-STAT3, STAT3, p-JAK2, and JAK2) in SaOS-2 cells after being treated with liensinine were detected by Western blotting. (c, d) The expressions of factors related to apoptosis, cycle arrest, and JAK2/STAT3 pathway activation in 143B cells after being treated with liensinine were detected by Western blotting.  $n = 3$  in each group. \* $P < 0.05$ , \*\* $P < 0.01$ , and \*\*\* $P < 0.001$  vs. 0  $\mu\text{M}$ .

p-STAT3 and p-JAK2, thereby reducing the ratio of p-STAT3/STAT3 and p-JAK2/JAK2. These results were negatively correlated with Bax expression and positively correlated with that of Bcl-2. Therefore, we reasonably speculated that liensinine-induced oxidative stress suppressed the activation of the JAK2/STAT3 pathway and further inhibited biological activity of OS cells. As the control, we also evaluated the effect of the same concentration of

liensinine on apoptosis (cleaved caspase 3 and cleaved PARP1) and JAK2/STAT3 pathway activation (p-STAT3, STAT3, p-JAK2, and JAK2) of hFOB 1.19 cells. The results showed that the expressions of the above proteins remained unchanged upon liensinine treatment, which implied that, liensinine did not induce excessive apoptosis and activation of the JAK2/STAT3 pathway in human normal osteoblasts (Figures S1(b) and S1(c)).

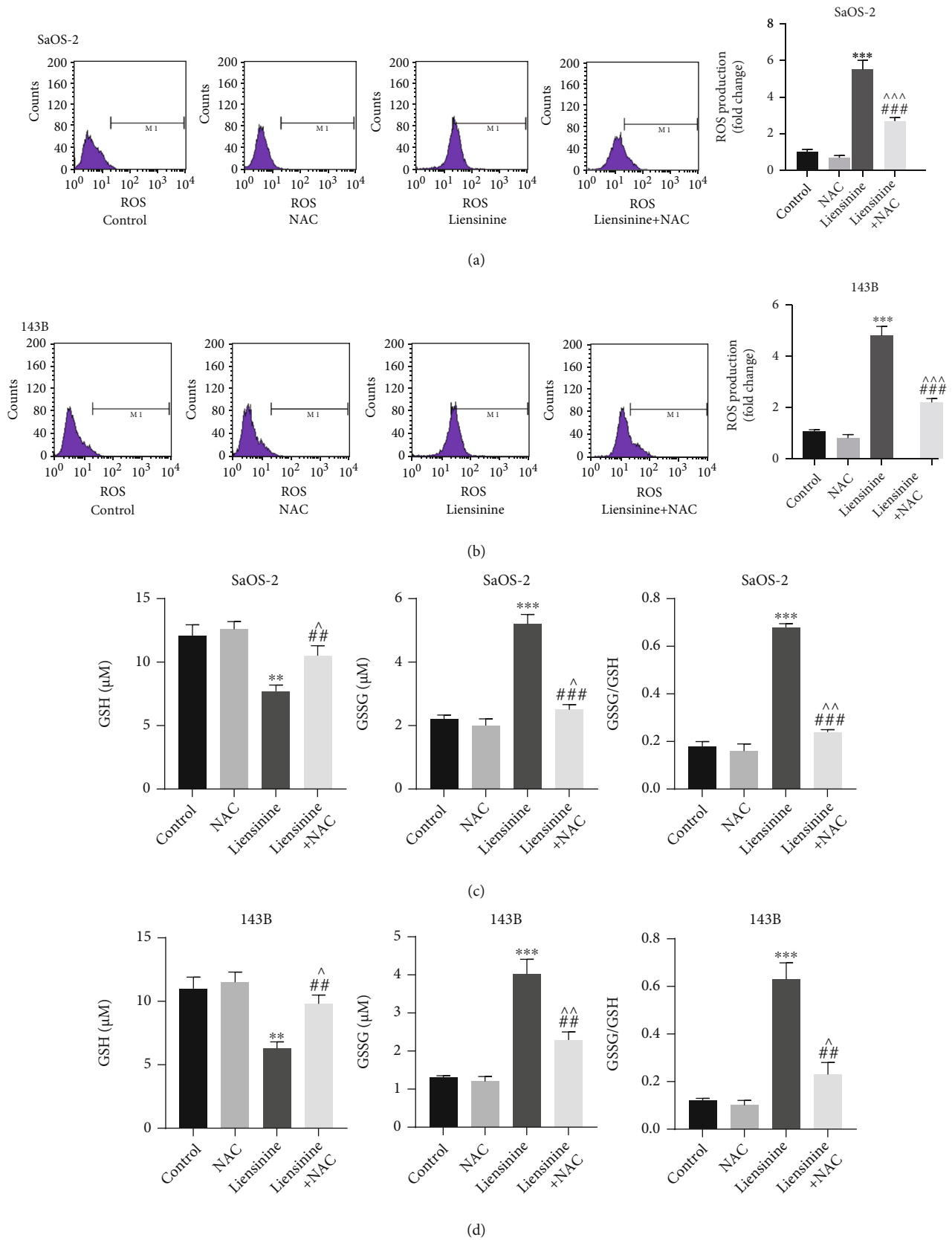


FIGURE 5: Continued.



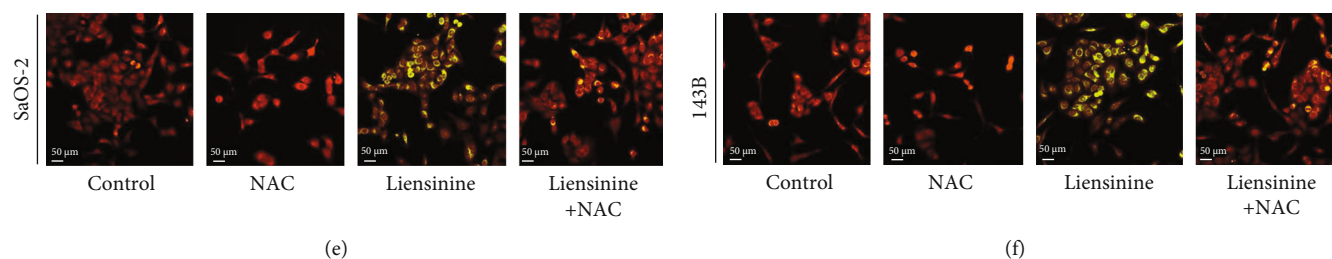


FIGURE 5: NAC reversed the effects of liensinine on ROS production, GSSG/GSH imbalance, and MMP loss in osteosarcoma cells. (a, b) The ROS production in SaOS-2 and 143B cells after being treated with NAC and liensinine was detected by FCM. (c, d) The concentrations of GSH and GSSG, as well as the GSSG/GSH rate in SaOS-2 and 143B cells after being treated with NAC and liensinine, were detected by colorimetry. (e, f) The MMP of SaOS-2 and 143B cells after being treated with NAC and liensinine was detected by JC-1 staining.  $n = 3$  in each group.  $**P < 0.01$  and  $***P < 0.001$  vs. control;  $^{\wedge}P < 0.05$ ,  $^{\wedge\wedge}P < 0.01$ , and  $^{\wedge\wedge\wedge}P < 0.001$  vs. NAC;  $##P < 0.01$  and  $###P < 0.001$  vs. liensinine.

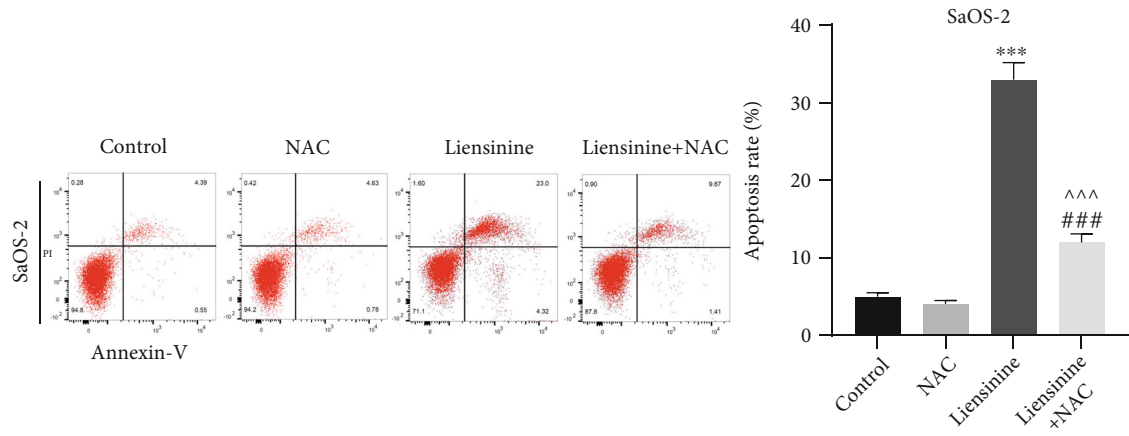
**3.7. ROS Scavenger Reverses the Effects of Liensinine on ROS Production, GSSG/GSH Imbalance, MMP Loss, Cell Apoptosis, and JAK2/STAT3 Pathway Activation.** To further validate the inhibiting effect of liensinine treatment mediated by oxidative stress on OS, the two cell lines were treated with a combination of an antioxidant (NAC) and liensinine. NAC reversed intracellular ROS productions in SaOS-2 and 143B cells induced by 40 and 80  $\mu\text{M}$  liensinine (liensinine vs. liensinine+NAC treatment of SaOS-2 cells: 5.5 vs. 2.7,  $P < 0.001$  and liensinine vs. liensinine+NAC treatment of 143B cells: 4.8 vs. 2.2,  $P < 0.001$ ) (Figures 5(a) and 5(b)); NAC also reversed the decrease of GSH (liensinine vs. liensinine+NAC treatment of SaOS-2 cells: 7.7 vs. 10.5  $\mu\text{M}$ ,  $P = 0.007$  and liensinine vs. liensinine+NAC treatment of 143B cells: 6.3 vs. 9.8,  $P = 0.002$ ) and the increase of GSSG (liensinine vs. liensinine+NAC treatment of SaOS-2 cells: 5.2 vs. 2.5,  $P < 0.001$  and liensinine vs. liensinine+NAC treatment of 143B cells: 4.0 vs. 2.3,  $P = 0.003$ ) in both cell lines (Figures 5(c) and 5(d)). NAC remarkably alleviated the loss of MMP induced by liensinine treatment, corresponding to the change of merged fluorescence color from green to red (Figures 5(e) and 5(f)). In addition, FCM showed that NAC significantly inhibited the apoptosis of OS cells induced by liensinine treatment (Figures 6(a) and 6(b)). The apoptosis rates of SaOS-2 cells under liensinine and liensinine+NAC treatment were 33.8% and 12.4% (liensinine vs. liensinine+NAC:  $P < 0.001$ ); the apoptosis rates of 143B cells under liensinine and liensinine+NAC treatment were 27.3% and 10.1% (liensinine vs. liensinine+NAC:  $P < 0.001$ ). On protein expression, NAC reversed the liensinine-induced upregulation of the expressions of cleaved caspase 3 and cleaved PARP1 (Figures 6(c)–6(f)), consistent with the decline in the apoptosis rates in OS cells; NAC also reversed the liensinine-induced downregulation of p-STAT3 and p-JAK2 and significantly increased the ratio of p-STAT3/STAT3 and p-JAK2/JAK2 (Figures 6(c)–6(f)). Taken together, these results indicated that the antitumor effect and the activation of JAK2/STAT3 pathway upon liensinine treatment were mediated by excessive oxidative stress.

**3.8. Liensinine Inhibits OS Growth In Vivo.** To evaluate the effect of liensinine on OS growth *in vivo*, we established subcutaneous-xenograft models using 143B cells. The mice were treated with liensinine at doses of 15 mg/kg and

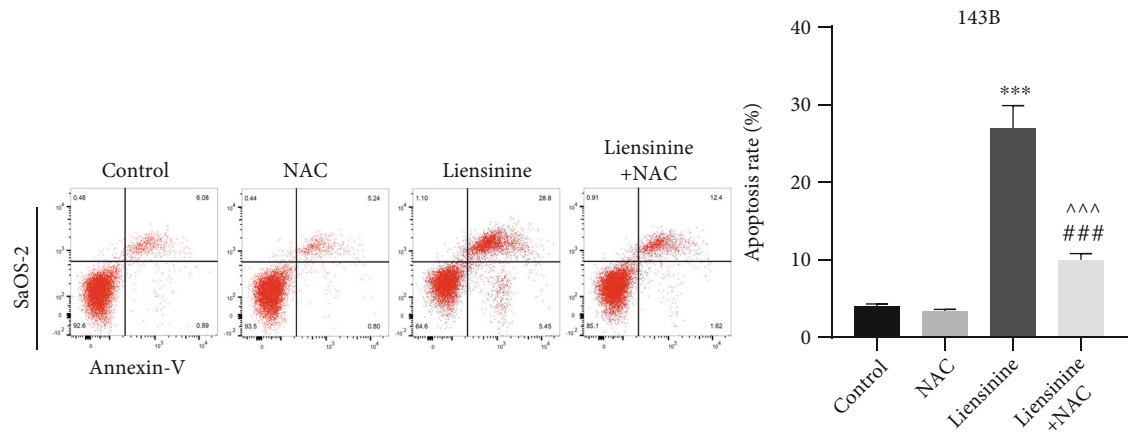
30 mg/kg for two weeks. The photos of excised tumors from each group are shown in Figure 7(a). Changes in tumor volume during the two-week treatment are shown in Figure 7(b); the final tumor weights are shown in Figure 7(c). Liensinine treatment could significantly slow down the growth of tumor volume and weight in a dose-dependent manner. The body weight changes of mice during two weeks were similar among the groups, as shown in Figure 7(d), suggesting that liensinine exerted no systemic toxicity in mice. PCNA immunohistochemical staining was used to evaluate the proliferation status of tumor cells. After liensinine treatment, the proportion of PCNA positive cells decreased substantially, while the number of cleaved caspase 3 positive cells increased in tumor tissues. H&E staining results clearly demonstrated serious tumor cell damage by liensinine, characterized by the reduction of cells with hyperchromatic nuclei and the proliferation of fibrous tissues (Figure 7(e)). In addition, H&E staining results of the heart, liver, spleen, lung, and kidney excised from the mice showed that liensinine had no negative effect on internal organs as compared to the control group (Figure 7(f)). Through Western blot analysis of tumor tissues, we found that liensinine treatment significantly downregulated the expressions of p-STAT3 and p-JAK2, thereby causing a significant reduction in the ratio of p-STAT3/STAT3 and p-JAK2/JAK2 (Figures 7(f) and 7(g)). These results were consistent with the suppression of JAK2/STAT3 pathway by liensinine *in vitro*. In addition, no significant change was found in the routine blood test as well as the liver and renal function blood test (Figures 7(i) and 7(j); Figure S1(d)–S1(g)). Thus, the administration of liensinine was biocompatible in mice.

## 4. Discussion

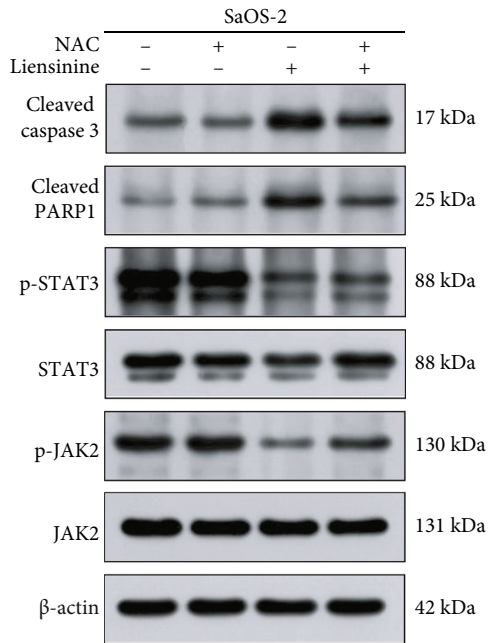
Traditional Chinese medicine (TCM) has been widely used to treat various diseases for thousands of years. Among them, liensinine, a natural isoquinoline alkaloid, can be isolated from a Chinese medicinal herb (*Nelumbo nucifera* Gaertn) and possesses several medicinal benefits [6–8]. Increasing evidence shows that liensinine may be a potential antitumor agent, and its efficacy against human colorectal, gallbladder, and breast cancers has been validated by



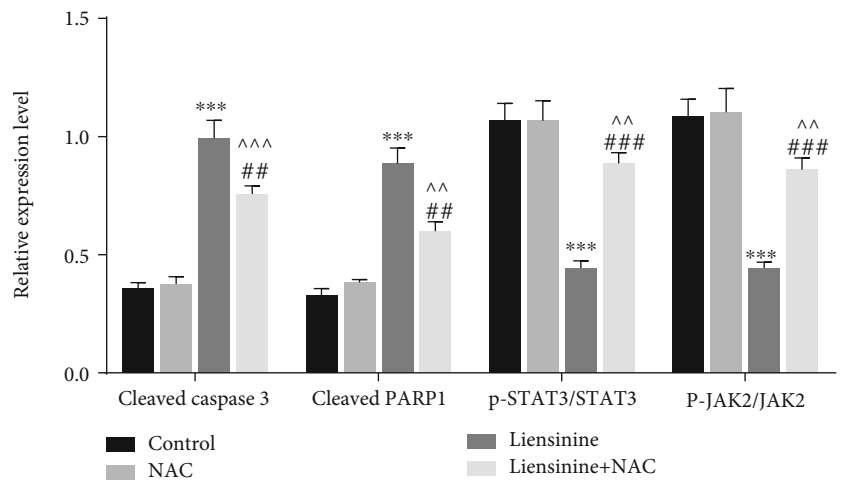
(a)



(b)



(c)



(d)

FIGURE 6: Continued.

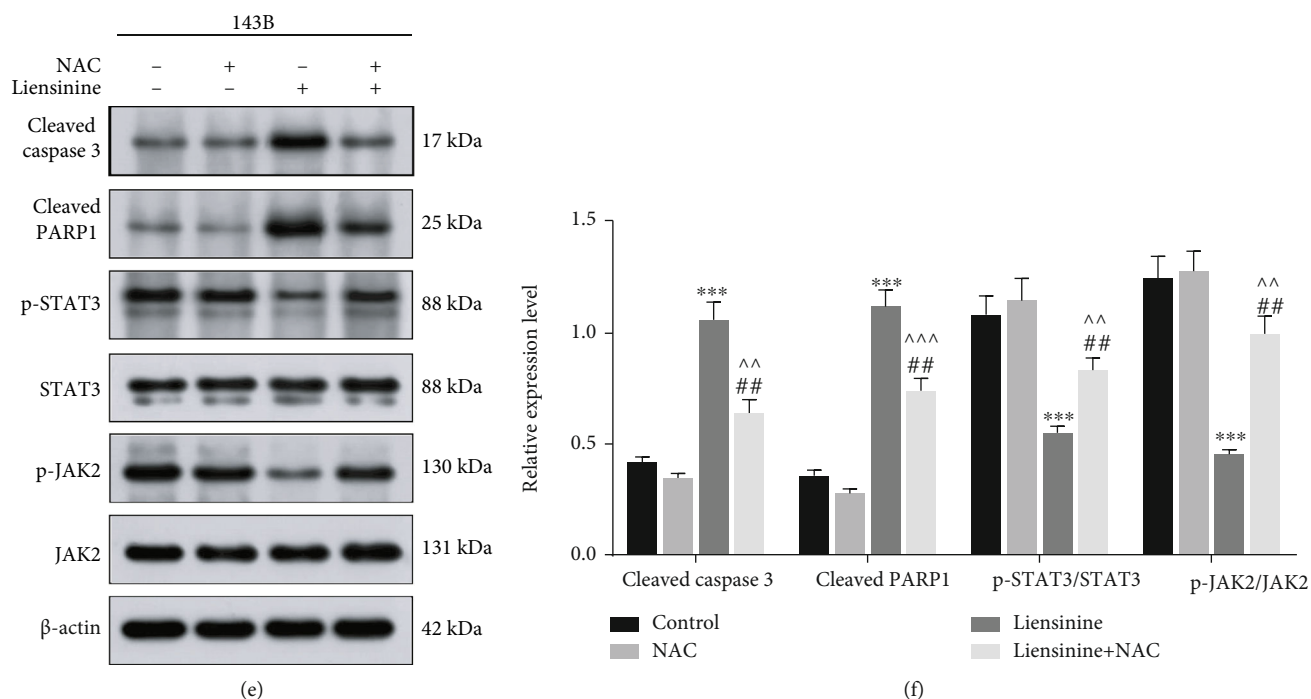


FIGURE 6: NAC reversed the effect of liensinine on apoptosis and the expressions of factors related to JAK2/STAT3 pathway activation in osteosarcoma cells. (a, b) The apoptosis rates of SaOS-2 and 143B cells after being treated with NAC and liensinine were detected by FCM. (c, d) The expressions of factors related to apoptosis (cleaved caspase 3 and cleaved PARP1) and JAK2/STAT3 pathway activation (p-STAT3, STAT3, p-JAK2, and JAK2) in SaOS-2 cells after being treated with liensinine were detected by Western blotting. (e, f) The expressions of factors related to apoptosis and JAK2/STAT3 pathway activation in 143B cells after being treated with liensinine were detected by Western blotting.  $n = 3$  in each group. \*\*\* $P < 0.001$  vs. control; ^^ $P < 0.01$  and ^^ $P < 0.001$  vs. NAC; ## $P < 0.01$  and ### $P < 0.001$  vs. liensinine.

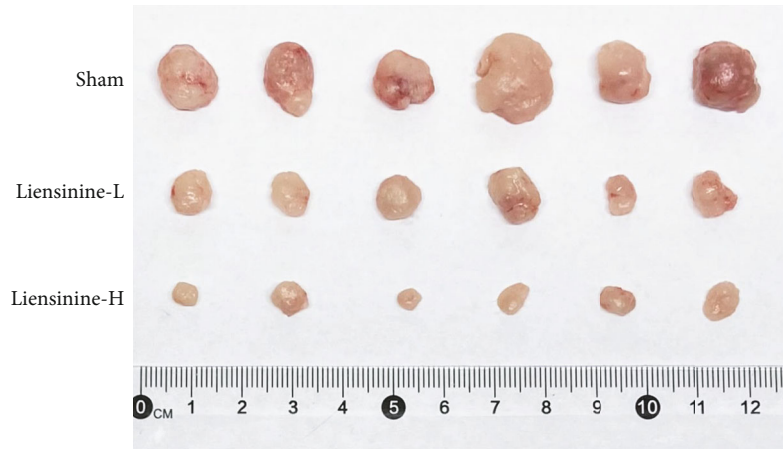
previous studies [6, 9, 10]. As a malignant tumor originating from mesenchymal tissue, OS has faster progression, earlier hematogenous metastasis, and fewer targeted drugs available than the aforementioned cancer types. Thus, it requires more radical resection as it causes more misery to the patients [22]. Therefore, it is important to develop efficient and safe pharmacotherapy for OS. To date, the effect of liensinine in OS has not been reported, both *in vitro* and *in vivo*.

In this study, liensinine was found to significantly reduce the viabilities and cloning efficiencies of multiple OS cell lines in a dose-dependent manner; it exerted no negative effect on human normal osteoblasts, even at a relatively higher dose. Tumor cells usually have higher metabolic activities and ROS levels as compared to the normal cells and are more vulnerable to liensinine-induced ROS insults [17, 23]. The mechanism underlying liensinine-mediated elevation in oxidative stress in tumor cells requires further study. In addition, tumor cells show higher cellular uptake of natural compounds but have lower intracellular glutathione levels than normal cells, which may be related to the selective cytotoxic effect of liensinine on OS cells [24, 25]. The results of flow cytometry analysis indicated that liensinine could substantially block G0/G1 progression into S phase and promote apoptosis in OS cells, consistent with the previous studies that reported the apoptosis-induction effect of liensinine on other cancer cell types [9, 10, 14]. We also confirmed the antitumor activity of liensinine in xenografted-tumor mice, which further validated our

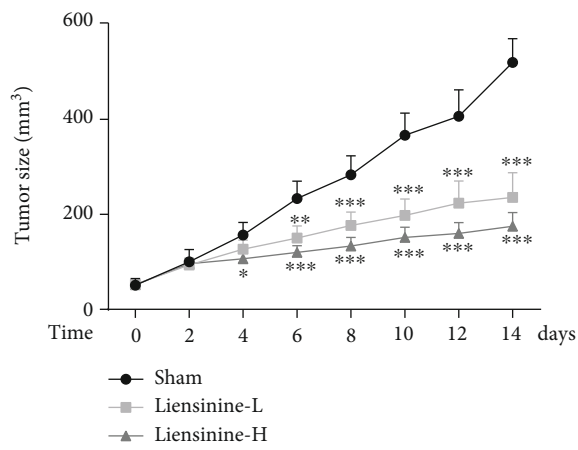
*in vitro* findings as indicated by the subcutaneous tumor sizes and immunohistochemical results post 2-week treatment. Moreover, according to the H&E staining of the visceral slices, routine blood test, and liver and renal function test, we concluded that the appropriate dosage of liensinine was safe and reliable for *in vivo* application.

To validate the above findings at the molecular level, we performed Western blot analysis. The imbalance in the expressions of Bax and Bcl-2 is involved in mitochondrial apoptosis, inducing the expression of cleaved caspase 3 and promoting tumor apoptosis [26]. Once caspase 3 is cleaved and activated, cascading effects ensue, and the apoptosis process is irreversible. Therefore, caspase 3 is considered to be a key factor in triggering apoptosis [27]. PARP is a nuclear protein that is activated by DNA damage and participates in DNA repair. However, it is also a substrate of the caspases, which can lose enzymatic activity and accelerate apoptosis after cleavage [28, 29]. Cyclin D1 is a regulatory subunit of cyclin-dependent kinases (CDKs) that promotes G0/G1 progression [30]. Hence, changes in expressions of Bcl-2, Bax, cleaved caspase 3, cleaved PARP, and Cyclin D1 reflect the apoptosis and cell cycle status. After liensinine treatment, Bax, cleaved caspase 3, and cleaved PARP were found to be upregulated, while those of Bcl-2 and Cyclin D1 were downregulated in OS cells, which indicated that liensinine may be a potential agent for inhibiting OS progression.

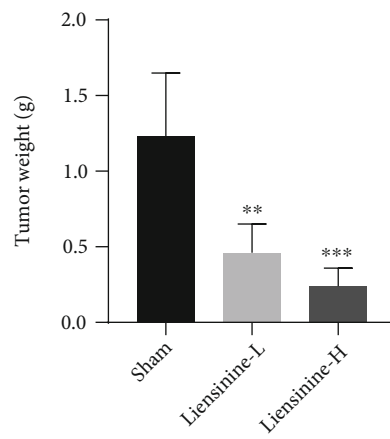
The key roles of ROS in biological processes include cell signaling, biosynthetic processes, and host defense [31]. A



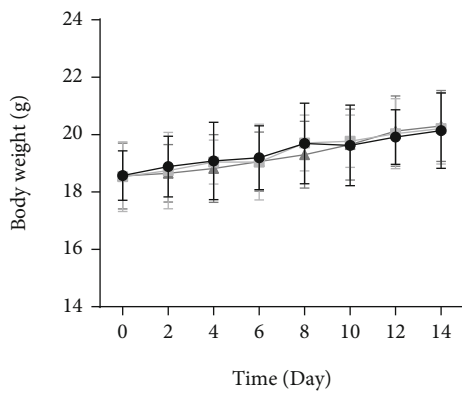
(a)



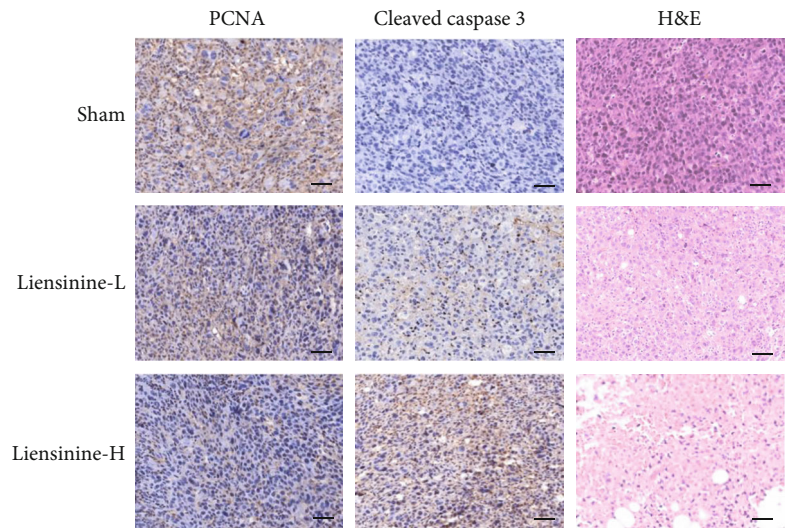
(b)



(c)



(d)



(e)

FIGURE 7: Continued.

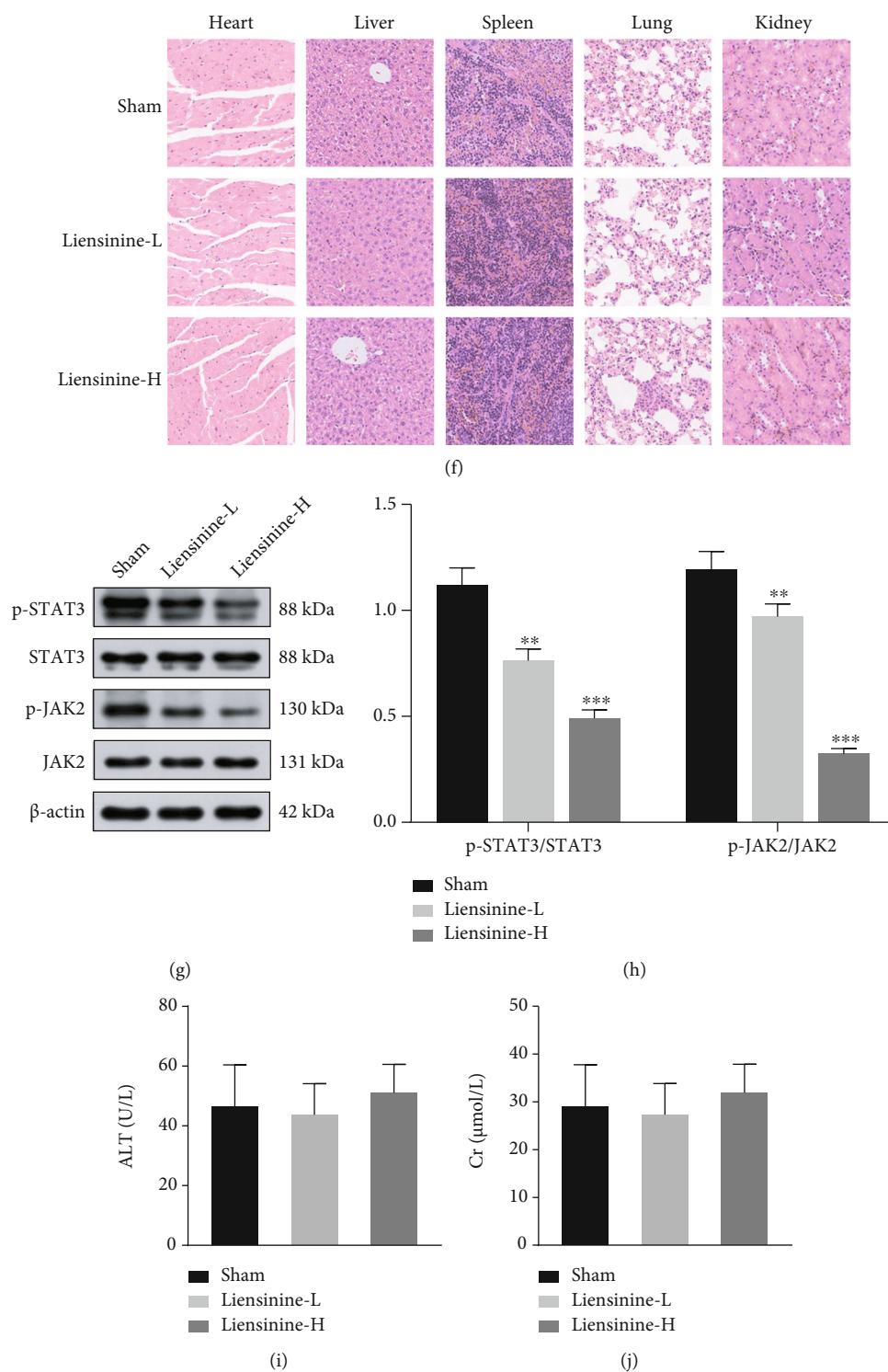


FIGURE 7: Liensinine inhibited growth and induced apoptosis of subcutaneous xenografts *in vivo*. (a) The final subcutaneous xenografts were photographed. (b) The tumor volumes were recorded for 14 days. (c) The final subcutaneous tumors were weighed. (d) The body weights of mice were weighed. (e) The expressions of PCNA and cleaved caspase 3 in tumor tissues were analyzed by immunohistochemical staining, and the tumor structure destruction was demonstrated by H&E staining; bar scale = 100  $\mu$ m. (f) The effect of liensinine on general organ structures was analyzed by H&E staining of heart, liver, spleen, lung, and kidney; bar scale = 100  $\mu$ m. (g) The expressions of p-STAT3, STAT3, p-JAK, and JAK in tumor tissues were detected by Western blotting. (h) The ratios of p-STAT3/STAT3 and p-JAK/JAK were calculated based on the strip gray values of Western blotting. (i, j) Liver and renal function of mice post 2-week indicated treatment were tested. Representative items: ALT: alanine aminotransferase; Cr: creatinine.  $n = 6$  in each group of (b–d, i, j).  $n = 3$  in each group of (g). \* $P < 0.05$ , \*\* $P < 0.01$ , and \*\*\* $P < 0.001$  vs. sham.

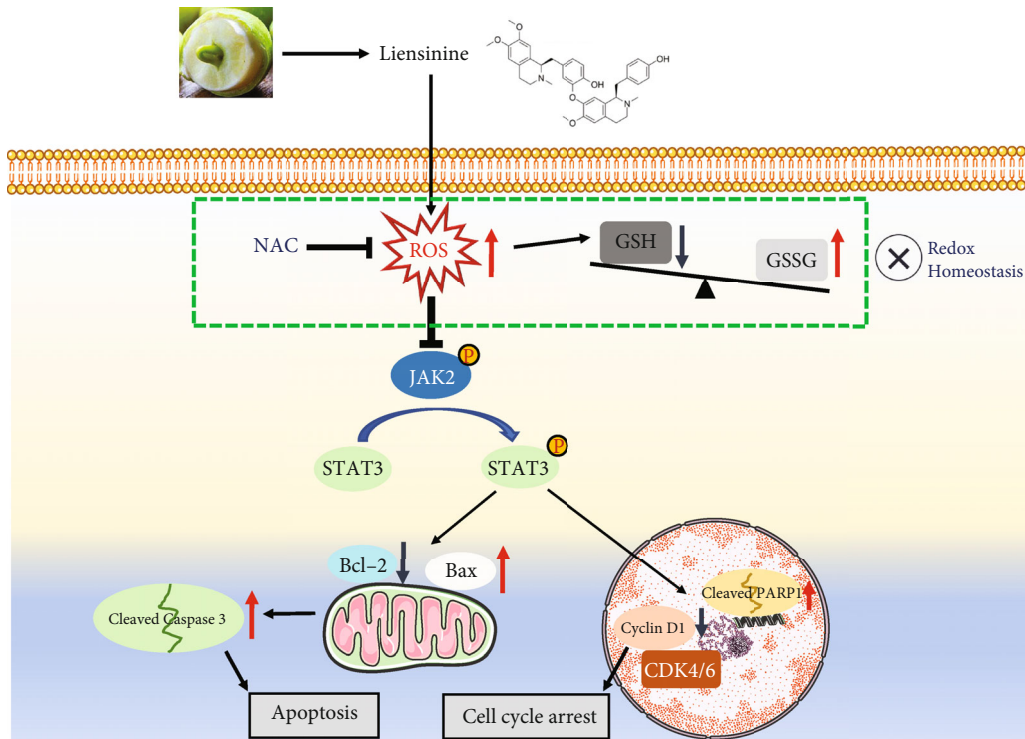


FIGURE 8: Proposed model for the role of liensinine-induced ROS accumulation in the osteosarcoma treatment. Increased ROS generation can lead to oxidant and antioxidant imbalance and suppress the activation of JAK2/STAT3 pathway, promoting OS cell cycle arrest and apoptosis.

mild elevation of ROS levels and ROS scavenging rate within tumor cells, termed as “mild oxidative” stress, is their normal physiological state and is associated with the activation of oncogenic pathways [32, 33]. However, sustained accumulation of ROS, especially free radicals, will cause damage to DNA, lipids, and proteins, eventually leading to adverse cellular outcomes [11–13]. Many drugs exert potent cytotoxic effects through this mechanism, for example, Glaucoalyxin A inhibits OS progression by inducing excessive oxidative stress [11]. GSH is a potent antioxidant that eliminates intracellular ROS through a redox reaction, by itself being oxidized to GSSG [34]. The imbalance of GSSG/GSH system reflects a notable deficiency in ROS scavenging capacity [11, 35]. To explore whether liensinine can promote ROS production, the levels of ROS, GSSG, and GSH in OS cells were evaluated. The ROS and GSSG levels were found to be upregulated while that of GSH was downregulated after treatment, suggesting that liensinine could induce excessive oxidative stress in OS cells. With the decrease of MMP, ROS increase and are released from mitochondria into the cytoplasm, further resulting in excessive oxidative stress, which subsequently triggers more release of ROS from the neighboring mitochondria, ultimately leading to cell death [36]. A decline in MMP is therefore a hallmark event in the early stage of apoptosis [37]. We found significant MMP loss in liensinine-treated tumor cells by JC-1 staining, confirming the occurrence of oxidative stress damage. Moreover, pretreatment with NAC, an antioxidant or ROS scavenger, could significantly reduce ROS production and apoptosis of OS cells stimulated by liensinine, which indi-

cated that the liensinine-induced oxidative stress injury was directly responsible for the inhibition of OS survival.

Previous studies have demonstrated that the biological activities of tumor cells are regulated by multiple signaling pathways including the JAK2/STAT3 cascade [20, 21, 38, 39]. Activation of the JAK2/STAT3 pathway can promote cell survival and proliferation, inhibit apoptosis, and is implicated in the occurrence and development of various cancers [40, 41]. Its antiapoptotic effect may be realized by reducing the Bax/Bcl-2 apoptotic switch ratio and inhibiting the activation of key proapoptotic enzymes in cells [42, 43]. In this study, we first reported that liensinine could suppress the activation of the JAK2/STAT3 pathway in tumor cells. Furthermore, excessive intracellular ROS can induce cell cycle arrest and apoptosis [32, 44]. Therefore, we reasonably speculated that the liensinine-induced intracellular ROS accumulation may suppress the activation of the JAK2/STAT3 pathway, thereby inhibiting the proliferation and promoting the apoptosis of OS cells. The mediating role of ROS was confirmed when NAC was found to significantly reverse the liensinine-induced JAK2/STAT3 pathway blockade. Together, the results suggested that liensinine could exert antitumor effect by affecting JAK2/STAT3 pathway activation through excessive oxidative stress (Figure 8). The finding that the JAK2/STAT3 pathway could be blocked by excessive ROS was consistent with the tumor-related reports [11, 13, 45], but contrary to the conclusions of some inflammation-related studies [46, 47]. This may be due to differential roles and mechanisms of ROS in tumor cells and macrophages, which requires further exploration.

In conclusion, the present study showed that the liensinine-induced ROS production could suppress the activation of the JAK2/STAT3 pathway and inhibited the OS growth both *in vivo* and *in vitro*. Our findings provided a new rationale for subsequent academic and clinical research on OS treatment.

## Abbreviations

|          |                                    |
|----------|------------------------------------|
| OS:      | Osteosarcoma                       |
| CCK-8:   | Cell Counting Kit-8                |
| ROS:     | Reactive oxygen species            |
| GSH:     | Glutathione                        |
| GSSG:    | Glutathione disulfide              |
| MMP:     | Mitochondrial membrane potential   |
| NAC:     | N-Acetyl cysteine                  |
| FCM:     | Flow cytometry                     |
| SPF:     | Specific pathogen free             |
| PCNA:    | Proliferating cell nuclear antigen |
| p-JAK2:  | Phosphorylated JAK2                |
| p-STAT3: | Phosphorylated STAT3               |
| SD:      | Standard deviation                 |
| TCM:     | Traditional Chinese medicine       |
| CDKs:    | Cyclin-dependent kinases           |
| WBC:     | White blood cells                  |
| RBC:     | Red blood cells                    |
| ALT:     | Alanine aminotransferase           |
| AST:     | Aspartate aminotransferase         |
| Cr:      | Creatinine                         |
| BUN:     | Blood urea nitrogen.               |

## Data Availability

The data collected for the study are available from the corresponding author upon request.

## Conflicts of Interest

The authors have no competing interests to declare.

## Authors' Contributions

FJ, YL, XD, and XL participated in the study design, data analysis, and manuscript drafting. FJ, YL, CD, and TM participated in the experimental operation. Fei Jia is the first author. All authors read and approved the final manuscript, and all authors consent to its publication.

## Acknowledgments

We are grateful for the technical support provided by the Peking University Third Hospital Central Laboratory. The study was supported by grants from the National Natural Science Foundation of China (No. 81972103) and the Capital's Funds for Health Improvement and Research (No. 2020-2-4091).

## Supplementary Materials

Figure S1: effect of liensinine on ROS production and JAK2/STAT3 pathway activation in hFOB 1.19 cells and hematological evaluation of its biocompatibility. (*Supplementary Materials*)

## References

- [1] M. Gambarotti, A. P. Dei Tos, D. Vanel et al., "Osteoblastoma-like osteosarcoma: high-grade or low-grade osteosarcoma?," *Histopathology*, vol. 74, no. 3, pp. 494–503, 2019.
- [2] L. Kager, G. Tamamyan, and S. Bielack, "Novel insights and therapeutic interventions for pediatric osteosarcoma," *Future Oncology*, vol. 13, no. 4, pp. 357–368, 2017.
- [3] N. Ebrahimi, S. Aslani, F. Babaie et al., "MicroRNAs Implications in the Onset, Diagnosis, and Prognosis of Osteosarcoma," *Current Molecular Medicine*, vol. 21, no. 7, pp. 573–588, 2021.
- [4] R. Qiu, D. Sun, Y. Bai, J. Li, and L. Wang, "Application of tumor-targeting peptide-decorated polypeptide nanoparticles with doxorubicin to treat osteosarcoma," *Drug Delivery*, vol. 27, no. 1, pp. 1704–1717, 2020.
- [5] S. Wang, B. Lin, W. Liu et al., "Acacetin induces apoptosis in human osteosarcoma cells by modulation of ROS/JNK activation," *Drug Design, Development and Therapy*, vol. Volume 14, pp. 5077–5085, 2020.
- [6] J. Zhou, G. Li, Y. Zheng et al., "A novel autophagy/mitophagy inhibitor liensinine sensitizes breast cancer cells to chemotherapy through DNML-mediated mitochondrial fission," *Autophagy*, vol. 11, no. 8, pp. 1259–1279, 2015.
- [7] R. Taneja and G. D. Gupta, "Development and characterization pulsatile microspheres of nifedipine for hypertension," *Recent Patents on Drug Delivery & Formulation*, vol. 11, no. 1, pp. 67–76, 2017.
- [8] F. Cao, T. Wang, W. Ding, Z. Li, S. Shi, and X. Wang, "Effects of diacetyl-liensinine on electrophysiology in rabbit ventricular myocytes," *BMC Pharmacology and Toxicology*, vol. 18, no. 1, p. 33, 2017.
- [9] Y. Shen, R. Bian, Y. Li et al., "Liensinine induces gallbladder cancer apoptosis and G2/M arrest by inhibiting ZFX-induced PI3K/AKT pathway," *Acta Biochimica et Biophysica Sinica*, vol. 51, no. 6, pp. 607–614, 2019.
- [10] Y. Wang, Y. J. Li, X. H. Huang et al., "Liensinine perchlorate inhibits colorectal cancer tumorigenesis by inducing mitochondrial dysfunction and apoptosis," *Food & Function*, vol. 9, no. 11, pp. 5536–5546, 2018.
- [11] M. Mao, T. Zhang, Z. Wang et al., "Glucocalyxin A-induced oxidative stress inhibits the activation of STAT3 signaling pathway and suppresses osteosarcoma progression in vitro and in vivo," *Biochimica et Biophysica Acta - Molecular Basis of Disease*, vol. 1865, no. 6, pp. 1214–1225, 2019.
- [12] B. Li, P. Zhou, K. Xu et al., "Metformin induces cell cycle arrest, apoptosis and autophagy through ROS/JNK signaling pathway in human osteosarcoma," *International Journal of Biological Sciences*, vol. 16, no. 1, pp. 74–84, 2020.
- [13] W. Chen, P. Li, Y. Liu et al., "Isoalantolactone induces apoptosis through ROS-mediated ER stress and inhibition of STAT3 in prostate cancer cells," *Journal of Experimental & Clinical Cancer Research*, vol. 37, no. 1, p. 309, 2018.

- [14] J. H. Yang, K. Yu, X. K. Si et al., "Liensinine inhibited gastric cancer cell growth through ROS generation and the PI3K/AKT pathway," *Journal of Cancer*, vol. 10, no. 25, pp. 6431–6438, 2019.
- [15] P. Hua, M. Sun, G. Zhang et al., "Cepharanthine induces apoptosis through reactive oxygen species and mitochondrial dysfunction in human non-small-cell lung cancer cells," *Biochemical and Biophysical Research Communications*, vol. 460, no. 2, pp. 136–142, 2015.
- [16] N. Bhagya, K. R. Chandrashekar, A. Prabhu, and P. D. Rekha, "Tetrandrine isolated from *Cyclea peltata* induces cytotoxicity and apoptosis through ROS and caspase pathways in breast and pancreatic cancer cells," *Vitro Cellular & Developmental Biology-Animal*, vol. 55, no. 5, pp. 331–340, 2019.
- [17] G. He, Y. Ma, Y. Zhu et al., "Cross talk between autophagy and apoptosis contributes to ZnO nanoparticle-induced human osteosarcoma cell death," *Advanced Healthcare Materials*, vol. 7, no. 17, article e1800332, 2018.
- [18] Y. Ma, B. Zhu, X. Liu et al., "Inhibition of oleandrin on the proliferation and invasion of osteosarcoma cells in vitro by suppressing Wnt/ $\beta$ -catenin signaling pathway," *Journal of Experimental & Clinical Cancer Research*, vol. 34, p. 115, 2015.
- [19] C. du, M. Zhou, F. Jia et al., "D-arginine-loaded metal-organic frameworks nanoparticles sensitize osteosarcoma to radiotherapy," *Biomaterials*, vol. 269, article 120642, 2021.
- [20] J. Huynh, N. Etemadi, F. Hollande, M. Ernst, and M. Buchert, "The JAK/STAT3 axis: a comprehensive drug target for solid malignancies," *Seminars in Cancer Biology*, vol. 45, pp. 13–22, 2017.
- [21] S. Sun, X. Zhang, M. Xu et al., "Berberine downregulates CDC6 and inhibits proliferation via targeting JAK-STAT3 signaling in keratinocytes," *Cell Death & Disease*, vol. 10, no. 4, p. 274, 2019.
- [22] D. D. Moore and H. H. Luu, "Osteosarcoma," *Cancer Treatment and Research*, vol. 162, pp. 65–92, 2014.
- [23] X. Zhang, X. Wang, T. Wu et al., "Isoliensinine induces apoptosis in triple-negative human breast cancer cells through ROS generation and p38 MAPK/JNK activation," *Scientific Reports*, vol. 5, no. 1, article 12579, 2015.
- [24] A. Kunwar, A. Barik, B. Mishra, K. Rathinasamy, R. Pandey, and K. I. Priyadarsini, "Quantitative cellular uptake, localization and cytotoxicity of curcumin in normal and tumor cells," *Biochimica et Biophysica Acta*, vol. 1780, no. 4, pp. 673–679, 2008.
- [25] C. Syng-Ai, A. L. Kumari, and A. Khar, "Effect of curcumin on normal and tumor cells: role of glutathione and bcl-2," *Molecular Cancer Therapeutics*, vol. 3, no. 9, pp. 1101–1108, 2004.
- [26] B. D'Orsi, J. Mateyka, and J. H. M. Prehn, "Control of mitochondrial physiology and cell death by the Bcl-2 family proteins Bax and Bok," *Neurochemistry International*, vol. 109, pp. 162–170, 2017.
- [27] G. S. Choudhary, S. Al-Harbi, and A. Almasan, "Caspase-3 activation is a critical determinant of genotoxic stress-induced apoptosis," *Methods in Molecular Biology*, vol. 1219, pp. 1–9, 2015.
- [28] J. Mateo, C. J. Lord, V. Serra et al., "A decade of clinical development of PARP inhibitors in perspective," *Annals of Oncology*, vol. 30, no. 9, pp. 1437–1447, 2019.
- [29] E. Sachdev, R. Tabatabai, V. Roy, B. J. Rimel, and M. M. Mita, "PARP inhibition in cancer: an update on clinical development," *Targeted Oncology*, vol. 14, no. 6, pp. 657–679, 2019.
- [30] V. Baldin, J. Lukas, M. J. Marcote, M. Pagano, and G. Draetta, "Cyclin D1 is a nuclear protein required for cell cycle progression in G1," *Genes & Development*, vol. 7, no. 5, pp. 812–821, 1993.
- [31] J. Zhang, X. Wang, V. Vikash et al., "ROS and ROS-mediated cellular signaling," *Oxidative Medicine and Cellular Longevity*, vol. 2016, Article ID 4350965, 2016.
- [32] A. Ghoneum, A. Y. Abdulfattah, B. O. Warren, J. Shu, and N. Said, "Redox homeostasis and metabolism in cancer: a complex mechanism and potential targeted therapeutics," *International Journal of Molecular Sciences*, vol. 21, no. 9, p. 3100, 2020.
- [33] L. Sullivan and N. S. Chandel, "Mitochondrial reactive oxygen species and cancer," *Cancer & Metabolism*, vol. 2, no. 1, p. 17, 2014.
- [34] J. Oestreicher and B. Morgan, "Glutathione: subcellular distribution and membrane transport," *Biochemistry and Cell Biology*, vol. 97, no. 3, pp. 270–289, 2019.
- [35] S. Sentellas, O. Morales-Ibanez, M. Zanuy, and J. J. Albertí, "GSSG/GSH ratios in cryopreserved rat and human hepatocytes as a biomarker for drug induced oxidative stress," *Toxicology In Vitro*, vol. 28, no. 5, pp. 1006–1015, 2014.
- [36] S. Parvez, M. J. C. Long, J. R. Poganik, and Y. Aye, "Redox Signaling by reactive electrophiles and oxidants," *Chemical Reviews*, vol. 118, no. 18, pp. 8798–8888, 2018.
- [37] N. Wang, H. Liu, G. Liu et al., "Yeast  $\beta$ -D-glucan exerts anti-tumour activity in liver cancer through impairing autophagy and lysosomal function, promoting reactive oxygen species production and apoptosis," *Redox Biology*, vol. 32, article 101495, 2020.
- [38] M. W. Chen and X. J. Wu, "SLC25A22 promotes proliferation and metastasis of osteosarcoma cells via the PTEN signaling pathway," *Technology in Cancer Research & Treatment*, vol. 17, article 1533033818811143, 2018.
- [39] C. Gong, J. Ai, Y. Fan et al., "NCAPG promotes the proliferation of hepatocellular carcinoma through PI3K/AKT signaling," *Oncotargets and Therapy*, vol. Volume 12, pp. 8537–8552, 2019.
- [40] X. Zhang, H. Feng, J. Du et al., "Aspirin promotes apoptosis and inhibits proliferation by blocking G0/G1 into S phase in rheumatoid arthritis fibroblast-like synoviocytes via downregulation of JAK/STAT3 and NF- $\kappa$ B signaling pathway," *International Journal of Molecular Medicine*, vol. 42, no. 6, pp. 3135–3148, 2018.
- [41] X. Zhao, Z. Cheng, and J. Wang, "Long noncoding RNA FEZF1-AS1 promotes proliferation and inhibits apoptosis in ovarian cancer by activation of JAK-STAT3 pathway," *Medical Science Monitor*, vol. 24, pp. 8088–8095, 2018.
- [42] Y. J. Gu, W. Y. Sun, S. Zhang, X. R. Li, and W. Wei, "Targeted blockade of JAK/STAT3 signaling inhibits proliferation, migration and collagen production as well as inducing the apoptosis of hepatic stellate cells," *International Journal of Molecular Medicine*, vol. 38, no. 3, pp. 903–911, 2016.
- [43] X. B. Zhao, Y. Qin, Y. L. Niu, and J. Yang, "Matrine inhibits hypoxia/reoxygenation-induced apoptosis of cardiac microvascular endothelial cells in rats via the JAK2/STAT3 signaling pathway," *Biomedicine & Pharmacotherapy*, vol. 106, pp. 117–124, 2018.
- [44] S. Ghavami, M. Eshragi, S. R. Ande et al., "S100A8/A9 induces autophagy and apoptosis via ROS-mediated cross-talk between mitochondria and lysosomes that involves BNIP3," *Cell Research*, vol. 20, no. 3, pp. 314–331, 2010.



- [45] H. S. Choi, S. L. Kim, J. H. Kim, Y. C. Ko, and D. S. Lee, "Plant volatile, phenylacetaldehyde targets breast cancer stem cell by induction of ROS and regulation of Stat3 signal," *Antioxidants*, vol. 9, no. 11, p. 1119, 2020.
- [46] S. Chakrabarti and S. S. Visweswariah, "Intramacrophage ROS primes the innate immune system via JAK/STAT and toll activation," *Cell Reports*, vol. 33, no. 6, article 108368, 2020.
- [47] J. Ma, X. Zhen, X. Huang, and X. Jiang, "Folic acid supplementation repressed hypoxia-induced inflammatory response via ROS and JAK2/STAT3 pathway in human promyelomonocytic cells," *Nutrition Research*, vol. 53, pp. 40–50, 2018.

## Research Article

# The Effects of RBP4 and Vitamin D on the Proliferation and Migration of Vascular Smooth Muscle Cells via the JAK2/STAT3 Signaling Pathway

Wan Zhou <sup>1</sup>, Wei Wang,<sup>1</sup> Xiao-Jing Yuan,<sup>2</sup> Chun-Chun Xiao,<sup>1</sup> Yan Xing,<sup>1</sup> Shan-Dong Ye <sup>1</sup> and Qiang Liu <sup>3</sup>

<sup>1</sup>Laboratory for Diabetes, Department of Endocrinology, The First Affiliated Hospital of USTC, Division of Life Sciences and Medicine, University of Science and Technology of China, Hefei, 230001 Anhui Province, China

<sup>2</sup>The First Affiliated Hospital of USTC, Division of Life Sciences and Medicine, University of Science and Technology of China, Hefei 230001, China

<sup>3</sup>Institute on Aging and Brain Disorders, The First Affiliated Hospital of USTC, Division of Life Sciences and Medicine, Hefei National Laboratory for Physical Sciences at the Microscale, University of Science and Technology of China, Hefei 230026, China

Correspondence should be addressed to Shan-Dong Ye; [yeshandong123@163.com](mailto:yeshandong123@163.com) and Qiang Liu; [liuq2012@ustc.edu.cn](mailto:liuq2012@ustc.edu.cn)

Received 14 October 2021; Revised 2 December 2021; Accepted 17 December 2021; Published 17 January 2022

Academic Editor: Qiang Tong

Copyright © 2022 Wan Zhou et al. This is an open access article distributed under the Creative Commons Attribution License, which permits unrestricted use, distribution, and reproduction in any medium, provided the original work is properly cited.

Abnormal proliferation and migration of vascular smooth muscle cells (VSMCs) are one of the main causes of the development of diabetic atherosclerotic process. The aim of our study was to assess the role of RBP4 in the proliferation and migration of VSMCs and the inhibitory effect of vitamin D on the mechanisms. In an in vivo experiment, rats were randomly classified into 6 groups: the control group, diabetic rats, diabetic atherosclerotic rats (diabetic rats intraperitoneally injected with RBP4), diabetic atherosclerotic rats treated with  $0.075 \mu\text{g kg}^{-1} \text{d}^{-1}$  vitamin D,  $0.15 \mu\text{g kg}^{-1} \text{d}^{-1}$  vitamin D and  $0.3 \mu\text{g kg}^{-1} \text{d}^{-1}$  vitamin D. We found that the levels of JAK2, STAT3, cyclinD1, and Bcl-2 were increased in diabetic atherosclerotic rats, and these increases were improved after vitamin D supplementation. Furthermore, to investigate the underlying molecular mechanisms, cells were cultured with glucose in the presence of RBP4 and the absence of RBP4, respectively, and vitamin D of different concentrations and different intervention times was simultaneously adopted. The proliferation and migration of VSMCs was enhanced and the levels of JAK2, STAT3, cyclinD1, and Bcl-2 were increased in the cells transfected with RBP4 overexpression plasmid. Moreover, vitamin D supplementation was detected to lower the expressions of JAK2, STAT3, cyclinD1, and Bcl-2 and inhibit the abnormal proliferation of VSMCs caused by the RBP4/JAK2/STAT3 signaling pathway. RBP4 can promote the proliferation and migration of VSMCs and contributes to the development of diabetic macroangiopathy via regulating the JAK2/STAT3 signaling pathway. This mechanism of RBP4 can be inhibited by vitamin D supplementation.

## 1. Introduction

Diabetic macroangiopathy, a specific form of atherosclerosis secondary to diabetes, causes cerebro-cardiovascular diseases, which are correlated with high mortality and morbidity in diabetic patients. Previous studies have shown that subclinical inflammation and insulin resistance play significant roles in the development of atherosclerosis and diabetes mellitus (DM) [1, 2]. In addition, the role of adipocytokines

in the pathological physiology of diabetic macroangiopathy has attracted considerable attention of the scientific community in recent years. It is known that obesity-activated adipocytes release adipocytokines such as leptin and adiponectin, which can induce energy balance, metabolic regulation, and immunoregulation. Retinol binding protein 4 (RBP4), an adipokine derived from adipocyte and hepatocyte, is responsible for transporting retinol to systemic tissues [3]. Elevated circulating RBP4 levels were found to contribute to systemic

insulin resistance and type 2 diabetes mellitus (T2DM) by inhibiting phosphatidylinositol 3 kinase (PI3K) activity in the skeletal muscles and promoting phosphoenolpyruvate carboxylase (PEPCK) expression in the liver of mouse models, which was first reported by Yang in 2005 [4]. Furthermore, the injection of recombinant RBP4 has been discovered to lead to insulin resistance, whereas genetic deletion of RBP4 enhanced insulin sensitivity [4]. Recent reports have revealed that circulating RBP4 concentrations were high in patients with documented carotid atherosclerosis and were paralleled with the degree of carotid stenosis [5, 6]. In addition, elevated serum levels of RBP4 were associated with the prognosis and severity of acute ischemic stroke. Thus, RBP4 might potentially be used as a diagnostic biomarker of ischemic stroke [7]. RBP4 levels are closely correlated to hypertension in diabetic patients and may be engaged in regulating left ventricular diastolic function in individuals with essential hypertension [8]. In contrast, Mansouri et al. showed that serum levels of RBP4 were not the potential predictors of carotid intima-media thickness (CIMT) in T2DM patients [9]. Moreover, elevated concentrations of RBP4 did not relate to an increased risk of ischemic stroke, which was reported by Rist et al. [10]. Several studies even suggested that increased levels of RBP4 might potentially serve a cardiovascular protective role [11, 12]. Therefore, the precise role of RBP4 was yet unclear, and the association between RBP4 and diabetic macroangiopathy remains controversial.

The imbalance of the proliferation and migration of vascular smooth muscle cells (VSMCs) is a vital mechanism potentially causing the pathological of cardiovascular diseases [13]. The Janus kinase/signal transducers and activators of transcription (JAK/STAT) pathway is an evolutionary signaling cascade that regulates cell proliferation, differentiation, apoptosis, and survival. Signal transducer and activator of transcription 3 (STAT3) is a potential cytoplasmic transcriptional factor that is triggered by phosphorylation. Once phosphorylated by Janus-activated kinases 2 (JAK2), the activated STAT3 dimerizes and translocates to the nucleus, which binds to specific enhancer sequences and ultimately results in gene transcription [14]. Various studies have shown that the activation of JAK2/STAT3 signaling pathway promotes the proliferation of VSMCs and involves in the progression of atherosclerosis by modulating apoptotic regulatory proteins such as B cell lymphoma-2 (Bcl-2) and cyclinD1 [15, 16]. However, the regulatory role of JAK2/STAT3 signaling pathway in the proliferation of the VSMCs has not been previously elucidated under diabetic conditions.

As a steroid hormone, vitamin D is not only a key component in mineral homeostasis and bone metabolism but also plays an essential role in immune modulation and glycometabolism [17]. It is hydroxylated to 25-hydroxyvitamin D (25(OH)D), the stable metabolite for assessing the individual status of vitamin D, first in the liver. Then, 25(OH)D is further converted into 1,25-dihydroxyvitamin D (1,25(OH)<sub>2</sub>D) by renal 1- $\alpha$ -hydroxylase. Since the overall prevalence of vitamin D deficiency exceeds 50% worldwide, further investigations of the role of vitamin D in metabolic syndromes and other diseases are warranted

[18]. Multiple studies have suggested that lower 25(OH)D levels are correlated with higher risks of cardiovascular diseases [19, 20]. However, it is noteworthy to mention that epidemiological studies focusing on the impact of vitamin D supplementation on diabetic macroangiopathy have produced inconsistent results. For example, a randomized double-blind study indicated that blood glucose levels could be improved in patients with diabetes and coronary heart diseases by prolonging sun exposure and increasing vitamin D supplementation [21]. On the other hand, some randomized controlled trials (RCTs) concluded that vitamin D was ineffective in improving cardiovascular diseases [22]. Thus, in this study, we hoped to gain insight into the possible role of vitamin D in the development of diabetic macroangiopathy.

Our previous findings have indicated that elevated RBP4 levels are involved in the pathogenesis of diabetic atherosclerotic rats via the JAK2/STAT3 signaling pathway and vitamin D can negatively regulate RBP4 [23]. Based on these findings, we speculated that RBP4 could potentially contribute to the development of diabetic atherosclerosis by regulating the proliferation and migration of VSMCs, and vitamin D supplementation has cardioprotective benefits. This study is aimed at determining (1) the role of the JAK2/STAT3 signaling pathway on proliferation and migration of VSMCs in the pathogenesis of diabetic atherosclerosis, (2) the potential cellular mechanism of RBP4 involved in the development of diabetic macroangiopathy, and (3) the impact of vitamin D on the regulation of RBP4 and the proliferation and migration of VSMCs.

## 2. Methods

**2.1. Animals.** The present study was sanctioned by the Ethics Committee of Anhui Provincial Hospital, Medical Institution Animal Care and Research Advisory Committee. According to the Animal Research: Reporting In Vivo Experiments (ARRIVE) Guidelines, the animals were kept under specific pathogen-free (SPF) conditions. A total of 130 male Wistar rats (7-week-old, 190–210 g) were acquired from the Experimental Animal Center of Anhui Medical University (certificate no. SCXK 2017-001) and were randomly classified into the control group fed with normal pellet diet (NC group,  $n = 20$ ) and the diabetic group fed with a high-fat and high-sugar diet ( $n = 110$ ), which was composed of 0.2% propylthiouracil, 10% lard, 3% cholesterol, 0.5% sodium cholate, 5% sugar, and 81.3% chow diet [24]. The rats in the diabetic group were further divided into diabetes without macrovascular disease group (DM group,  $n = 20$ ) and the ones with macrovascular disease group ( $n = 90$ ). After 1 week of acclimatisation, all the rats in the diabetic group were intraperitoneally injected with streptozotocin (STZ) at 30 mg/kg for 5 days, whereas the rats in the NC group were intraperitoneally injected with citric acid-sodium citrate buffer. Additionally, rats in diabetes with macrovascular disease group were intraperitoneally injected with recombinant RBP4 (ab109146, abcam, UK) at 3  $\mu$ g/g every 12 h for 3 weeks. Glucose tolerance tests were carried out in rats which were fasted for 12 h to confirm T2DM.

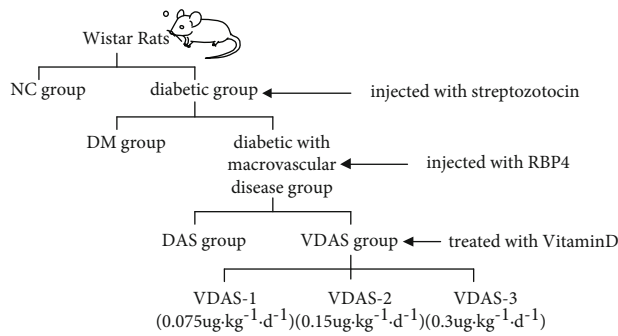
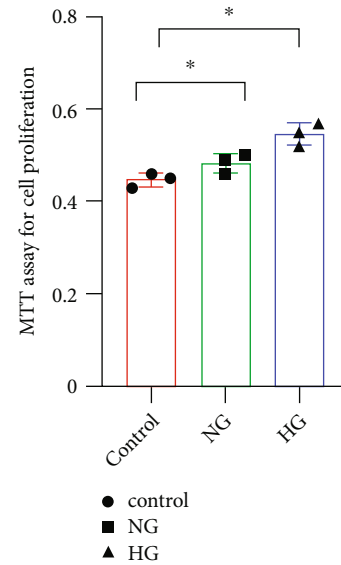


FIGURE 1: Animal grouping.

As a result, 107 rats in the diabetic group were considered T2DM rats with fasting plasma glucose (FPG) over 11.1 mmol/l [25], and 3 rats were died. After 8 weeks of feeding, the rats in the diabetes with macrovascular disease group were randomly divided into 2 subgroups, namely, the diabetic atherosclerosis group treated with vitamin D (VDAS,  $n = 62$ ) and the untreated diabetic atherosclerosis group (DAS,  $n = 25$ ). Rats in the VDAS group were treated with varying levels of vitamin D ( $0.075 \mu\text{g kg}^{-1} \text{d}^{-1}$  (VDAS-1,  $n = 21$ ),  $0.15 \mu\text{g kg}^{-1} \text{d}^{-1}$  (VDAS-2,  $n = 20$ ), and  $0.3 \mu\text{g kg}^{-1} \text{d}^{-1}$  (VDAS-3,  $n = 21$ ) dissolved in peanut oil for 8 weeks, respectively. The remaining rats received an equal volume of distilled water daily (Figure 1).

**2.2. Biochemical Analysis In Vivo.** Once the treatment ended, rats were fasted overnight and anesthetized by intraperitoneal injection with sodium pentobarbital (30 mg/kg). Blood was collected from the tail vein of rats. Total cholesterol (TC), low-density lipoprotein-cholesterol (LDL-c), triglyceride (TG), high-density lipoprotein-cholesterol (HDL-c) levels were quantified using an automatic biochemical analyzer (Hitachi 7600-020, Santa Clara, CA, USA). Serum levels of RBP4 and (25(OH)D) were detected by enzyme-linked immunosorbent assay (ELISA) kits (BIOHJSW, USA). Hemoglobin A1c (HbA1C) was measured by high-pressure liquid chromatography (BIO-RAB-D10, USA). Fasting insulin (FINS) were tested by the insulin radioimmunoassay kit (Atom Hi-Tech, China). The insulin sensitivity index (ISI) was calculated according to the formula  $\text{ISI} = \text{Ln}1/(\text{FPG} \times \text{FINS})$  and the homeostasis model assessment of insulin resistance (HOMA-IR) was estimated by the formula  $\text{HOMA-IR} = \text{FINS} \times \text{FPG}/22.5$ . The thoracic aortas from the aortic arch were separated and extracted for hematoxylin and eosin (HE) staining, immunofluorescence tests, real-time quantitative reverse transcription polymerase chain reaction (qRT-PCR) analysis, and western blot. After HE staining, 16 slices were selected randomly from each group, and the media thickness (MT) and the lumen diameter (LD) of the tube wall were detected by Image-Pro Plus 6.0 software. Ultimately, the results were averaged together.

**2.3. Cell Culture and Biochemical Analysis In Vitro.** The rat aortic smooth muscle cells were acquired from the American Type Culture Collection (Manassas, VA, USA). The cells

FIGURE 2: The proliferation of VSMCs by MTT. The ability of cells proliferation were analyzed by MTT (\* $P < 0.05$ , for HG and NG group compared to the control group).

were cultured under standard conditions in DMEM (supplemented with 100 U/ml penicillin, 100  $\mu\text{g/ml}$  streptomycin, 10% fetal bovine serum, and 3.7 g/l  $\text{NaHCO}_3$ ) without glucose (control), DMEM with normal glucose (NG, 5.5 mM), and DMEM with high glucose (HG, 30 mM), respectively, to choose an appropriate condition by exploring the ability of VSMC proliferation. The proliferation ability of the cells was elevated under 30 mM glucose conditions which we choose for further experiments (Figure 2). VSMCs were then divided into 8 groups (Figure 3): (1) Group NC: the cells kept in high-glucose medium were treated as a control group. (2) Group RCMV-RBP4: the cells were transfected with RBP4 overexpression plasmid (RCMV-RBP4) using Lipofectamine 2000 (Invitrogen, Thermo Fisher Scientific, USA) according to standard procedures and the cells treated with empty plasmid were considered as a control group (RCMV-control). The efficiency of the RBP4 gene overexpression was evaluated by western blot. (3) Group siRNA-RBP4: the cells were treated with small interfering RNA (siRNA) targeting RBP4 (Santa Cruz Biotechnology, Dallas, TX, USA) (siRNA-RBP4). Control siRNA was purchased from Bioneer and used as a negative control (siRNA-control). The interference sequence of RBP4 was evaluated by western blot. (4) Group VD-1: after the cells were transfected with RCMV-RBP4 for 48 h, they were treated with  $1,25(\text{OH})_2\text{D}$  (25 nM) for 24 h. (5) Group VD-2: After transfected with RCMV-RBP4, the cells were treated with  $1,25(\text{OH})_2\text{D}$  (25 nM) for 48 h. (6) Group VD-3: after transfection with RCMV-RBP4, the cells were treated with  $1,25(\text{OH})_2\text{D}$  (50 nM) for 24 h. (7) Group VD-4: after transfection with RCMV-RBP4, the cells were treated with  $1,25(\text{OH})_2\text{D}$  (50 nM) for 48 h. (8): Group AG490: after transfected with RCMV-RBP4, the cells were treated with AG490 (inhibitor of JAK2,  $5 \times 105 \text{ m}$ ) for 1 h. Cell cycle and apoptosis were assessed with flow cytometric analysis,

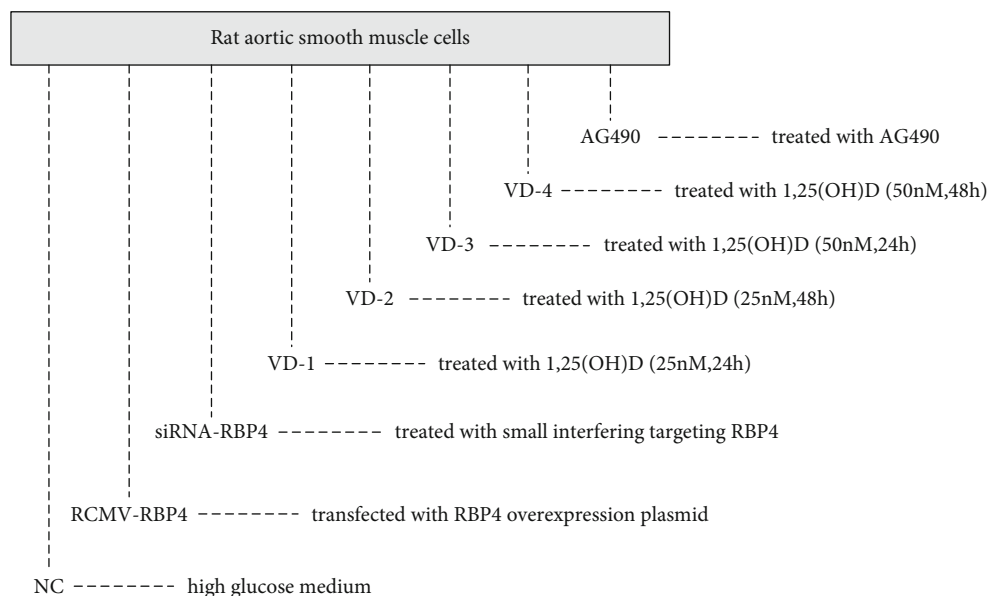


FIGURE 3: Cell culture in each group.

TABLE 1: Primer sequences of target genes and internal reference genes.

| Gene           | Amplicon size (bp) | Forward primer (5' → 3') | Reverse primer (5' → 3') |
|----------------|--------------------|--------------------------|--------------------------|
| STAT3          | 115                | GCAATACCATTGACCTGCCG     | AACGTGAGCGACTCAAACCTG    |
| RBP4           | 131                | GCGAGGAAACGATGACCACT     | TGGGGTCACGAGAAAACACA     |
| JAK2           | 179                | ACAAGCAGGACGGGAAGTTC     | AATTGGGCCCGTGACAGTTGC    |
| Bcl2           | 102                | GAGTACCTGAACCGGCATCT     | GAAATCAAACAGAGGTCGCA     |
| $\beta$ -Actin | 150                | CCCATCTATGAGGGTTACGC     | TTTAATGTCACGCACGATTTTC   |
| cyclinD1       | 138                | TCAAGTGTGACCCGGACTG      | GACCAGCTTCTTCTCCACTT     |

STAT3: signal transducer and activator of transcription 3; RBP4: retinol binding protein 4; JAK2: Janus kinase 2; Bcl-2: B cell lymphoma-2.

Transwell assay, scratch test, and MTT assay. The levels of JAK2, STAT3, cyclinD1, and Bcl-2 were analyzed using western blot, qRT-PCR, and immunofluorescence assays.

**2.4. Western Blot.** Protein from tissues and cells was lysed by ice-cold RIPA lysis buffer, and the protein level was measured by the BCA Protein Assay Kit. After centrifugation at 12000 g at 4°C for 5 min, the same quantity of protein was extracted with 10% sodium dodecyl sulfate-polyacrylamide gel electrophoresis (SDS-PAGE) gels and then transferred to polyvinylidene fluoride (PVDF) membranes. Then, the membranes were blocked in 5% skim milk. Afterwards, incubation was carried out with primary antibodies (1:1000, anti-RBP4 (Bioss, China); anti-Bcl-2 (Bioss, China) 1:300; anti-JAK2 (Bioss, China); 1:5000; anti-STAT3 (Bioss, China); 1:10000; anti-p-JAK2 (abcam, USA); 1:1000; anti-p-STAT3 (abcam, USA); 1:300, anti-Cyclin D1 (Bioss, China); 1:1000) at 4°C overnight. After washing with TBST for four times, the membranes were then cultured with secondary antibody horseradish peroxidase-conjugated goat anti-rabbit IgG (1:10000, Zs-BIO, China) for 1 h. Finally, the protein were visualized with an enhanced chemiluminescence (ECL) detection kit (Thermo, USA), and band intensity was quantified by densitometry with ImageJ software version 1.40 (National Institutes of Health, Bethesda, USA).

**2.5. Real-Time Quantitative RT-PCR.** Total RNA was extracted from tissues and cells by TRIzol reagent (Invitrogen, USA) and reverse-transcribed into cDNA by the PrimeScript™ RT reagent Kit (Takara, Tokyo, Japan). Real-time quantitative RT-PCR amplification was run on the LightCycler 96 Real-Time PCR System (Thermo, USA) in which the Novostart SYBR qPCR SuperMix Plus (Novoprotein, China) was used as the readout. Results were analyzed using the  $2^{-\Delta\Delta}$  cycle threshold (CT) approach to evaluate relative gene expression. The primer sequences are exhibited in Table 1.

**2.6. ELISA Assay.** The levels of serum RBP4 and 25(OH)D were assessed using ELISA Kit (MSKBIO, China) following the instructions given by the manufacturer. The absorbance value (optical density) was detected at 450 nm under a microplate reader (Thermo Fisher Scientific).

**2.7. Immunofluorescence.** Formaldehyde-fixed aortic tissue was incubated in PBS overnight at 4°C. Then, it was embedded in an OCT compound (Tissue-Tek) and serially sectioned on a cryostat. Serial 8  $\mu$ M sections were stained with HE staining and immunofluorescence. For immunofluorescence, paraffin-embedded sections were deparaffinised with xylene and rehydrated through graded ethanol and then

TABLE 2: Biochemical parameters of rats in different groups.

|            | NC (n = 20)    | DM (n = 20)                 | DAS (n = 25)                  | VDAS-1 (n = 21)                 | VDAS-2 (n = 20)                   | VDAS-3 (n = 21)                     | F       | P      |
|------------|----------------|-----------------------------|-------------------------------|---------------------------------|-----------------------------------|-------------------------------------|---------|--------|
| Weight (g) | 421.30 ± 33.58 | 553.81 ± 38.06 <sup>a</sup> | 582.35 ± 37.19 <sup>a,b</sup> | 554.26 ± 37.92 <sup>a,c</sup>   | 524.86 ± 33.76 <sup>a,b,c,d</sup> | 518.72 ± 43.68 <sup>a,b,c,d</sup>   | 46.973  | ≤0.001 |
| MT (μm)    | 73.15 ± 8.70   | 92.16 ± 7.05 <sup>a</sup>   | 116.30 ± 9.62 <sup>a,b</sup>  | 111.68 ± 11.03 <sup>a,b</sup>   | 108.19 ± 9.59 <sup>a,b,c</sup>    | 100.20 ± 9.93 <sup>a,b,c,d,e</sup>  | 59.350  | ≤0.001 |
| LD (mm)    | 1.80 ± 0.17    | 1.76 ± 0.14                 | 2.09 ± 0.18 <sup>a,b</sup>    | 2.09 ± 0.20 <sup>a,b</sup>      | 1.92 ± 0.21 <sup>a,b,c,d</sup>    | 1.63 ± 0.16 <sup>a,b,c,d,e</sup>    | 24.540  | ≤0.001 |
| LDL-c      | 0.35 ± 0.03    | 0.51 ± 0.05 <sup>a</sup>    | 0.57 ± 0.06 <sup>a,b</sup>    | 0.54 ± 0.03 <sup>a,b</sup>      | 0.55 ± 0.05 <sup>a,b</sup>        | 0.48 ± 0.05 <sup>a,b,c,d,e</sup>    | 66.648  | ≤0.001 |
| TG         | 0.65 ± 0.04    | 1.35 ± 0.13 <sup>a</sup>    | 1.82 ± 0.19 <sup>a,b</sup>    | 1.58 ± 0.15 <sup>a,b,c</sup>    | 1.79 ± 0.16 <sup>a,b,d</sup>      | 1.52 ± 0.15 <sup>a,b,c,e</sup>      | 177.841 | ≤0.001 |
| TC         | 2.02 ± 0.17    | 2.24 ± 0.19 <sup>a</sup>    | 2.95 ± 0.19 <sup>a,b</sup>    | 2.37 ± 0.18 <sup>a,b,c</sup>    | 2.44 ± 0.18 <sup>a,b,c</sup>      | 2.21 ± 0.21 <sup>a,c,d,e</sup>      | 66.424  | ≤0.001 |
| HDL-c      | 1.06 ± 0.10    | 1.02 ± 0.06 <sup>a</sup>    | 0.72 ± 0.05 <sup>a,b</sup>    | 0.79 ± 0.07 <sup>a,b,c</sup>    | 0.76 ± 0.06 <sup>a,b</sup>        | 0.94 ± 0.08 <sup>a,b,c,d,e</sup>    | 83.240  | ≤0.001 |
| HbA1C      | 5.06 ± 0.36    | 9.94 ± 1.04 <sup>a</sup>    | 10.80 ± 1.23 <sup>a,b</sup>   | 11.27 ± 0.72 <sup>a,b</sup>     | 9.99 ± 0.97 <sup>a,c,d</sup>      | 9.66 ± 0.85 <sup>a,c,d</sup>        | 121.350 | ≤0.001 |
| FPG        | 5.44 ± 0.55    | 13.39 ± 1.32 <sup>a</sup>   | 13.80 ± 1.51 <sup>a</sup>     | 14.22 ± 1.12 <sup>a</sup>       | 12.49 ± 1.20 <sup>a,b,c,d</sup>   | 12.60 ± 0.97 <sup>a,b,c,d</sup>     | 160.800 | ≤0.001 |
| FINS       | 9.73 ± 1.15    | 14.41 ± 1.39 <sup>a</sup>   | 19.43 ± 1.81 <sup>a,b</sup>   | 19.24 ± 1.77 <sup>a,b</sup>     | 18.85 ± 1.75 <sup>a,b</sup>       | 15.70 ± 1.53 <sup>a,b,c,d,e</sup>   | 117.934 | ≤0.001 |
| RBP4       | 15.39 ± 1.24   | 21.24 ± 1.23 <sup>a</sup>   | 31.33 ± 3.15 <sup>a,b</sup>   | 28.92 ± 2.97 <sup>a,b,c</sup>   | 27.98 ± 3.12 <sup>a,b,c</sup>     | 21.57 ± 1.96 <sup>a,c,d,e</sup>     | 127.386 | ≤0.001 |
| HOMA-IR    | 2.35 ± 0.32    | 8.56 ± 1.05 <sup>a</sup>    | 11.92 ± 1.72 <sup>a,b</sup>   | 12.15 ± 1.36 <sup>a,b</sup>     | 10.44 ± 1.16 <sup>a,b,c,d</sup>   | 8.78 ± 1.05 <sup>a,c,d,e</sup>      | 182.703 | ≤0.001 |
| 25(OH)D    | 156.77 ± 11.46 | 124.80 ± 8.56 <sup>a</sup>  | 95.10 ± 8.48 <sup>a,b</sup>   | 448.61 ± 52.19 <sup>a,b,c</sup> | 544.00 ± 50.22 <sup>a,b,c,d</sup> | 721.61 ± 89.11 <sup>a,b,c,d,e</sup> | 656.205 | ≤0.001 |
| ISI        | -3.96 ± 0.15   | -5.25 ± 0.13 <sup>a</sup>   | -5.58 ± 0.15 <sup>a,b</sup>   | -5.60 ± 0.11 <sup>a,b</sup>     | -5.45 ± 0.12 <sup>a,b,c,d</sup>   | -5.28 ± 0.12 <sup>a,c,d,e</sup>     | 475.785 | ≤0.001 |

<sup>a</sup>P < 0.05 vs. the NC group, <sup>b</sup>P < 0.05 vs. the DM group, <sup>c</sup>P < 0.05 vs. the VDAS-1 group, and <sup>d</sup>P < 0.05 vs. the VDAS-2 group. NC: control group; DM: diabetes without macrovascular disease group; DAS: diabetic atherosclerosis group; VDAS-1: Diabetic atherosclerosis group treated with vitamin D 0.075 μg kg<sup>-1</sup> d<sup>-1</sup>; VDAS-2: diabetic atherosclerosis group treated with vitamin D 0.15 μg kg<sup>-1</sup> d<sup>-1</sup>; VDAS-3: diabetic atherosclerosis group treated with vitamin D 0.3 μg kg<sup>-1</sup> d<sup>-1</sup>; MT: the media thickness of the artery; LD: lumen diameter; LDL-c: low-density lipoprotein cholesterol; TG: triglycerides; TC: total cholesterol; HDL-c: high-density lipoprotein cholesterol; HbA1C: hemoglobin A1c; FPG: fasting plasma glucose; FINS: fasting insulin; RBP4: retinol binding protein 4; HOMA-IR: homeostasis model assessment of insulin resistance; ISI: insulin sensitivity index.

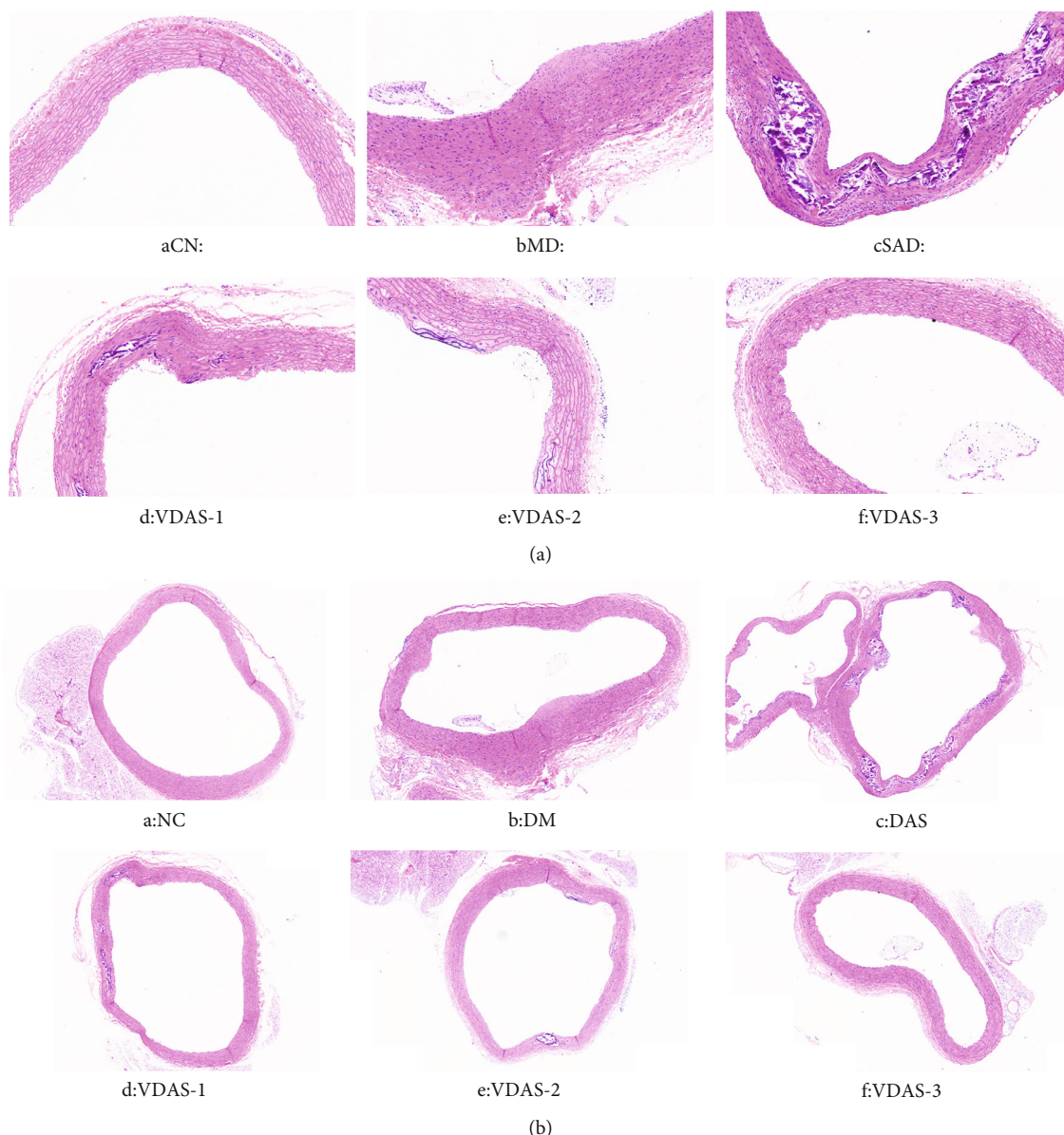


FIGURE 4: Representative HE staining of thoracic aortas. (a) 10x; scale bar, 200  $\mu\text{m}$ . (b) 20x; scale bar, 50  $\mu\text{m}$ . (A) There were no obvious changes in the structure of aortas in the group NC. (B) The intima became thicker and the VSMCs arranged disorderly in group DM. (C) A large number of VSMCs migrated and proliferated and distinct plaques with abundant lipids and calcification formed in the aortas of the rats in group DAS. (D, E) There were small formations of plaques and calcification on the walls of aortas in the groups VDAS-1 and VDAS-2. (F) The intima was smooth and VSMCs arranged neatly in the group VDAS-3.

incubated in 10 mmol/l citrate buffer for antigen retrieval. Primary antibodies (1:200, anti-JAK2 (abcam, USA); 1:100, anti-STAT3 (Bioworld, China); 1:200) were used and then incubation of samples were treated with anti-rat Alexa Fluor 488 secondary antibody (abcam, USA) for 30 min at 37°C. Afterwards, the samples were incubated with DAPI solution for 5 min in the dark; they were washed 3 times with PBS and examined under a fluorescence microscope. Then, cells were plated on autoclaved glass coverslips placed in sterile 6-well plates, fixed in 4% paraformaldehyde, permeabilised in 0.1% Triton, and prevented with 10% goat serum. Subsequently, cells were treated with primary antibodies (1:200, anti-JAK2 (abcam, USA); 1:100, anti-

STAT3 (Bioworld, China)) for 1 h at 37°C. After rinsing with PBS 3 times, the fluorescent secondary antibodies were added and the cells were stained as detailed above.

**2.8. Transwell Migration Assay.** A hundred microliters of cell suspension containing  $5 \times 10^4$  cells of serum-free DMEM were planted into the top chamber of each Transwell insert, whereas the bottom chamber was filled with 500  $\mu\text{l}$  media containing 10% FBS. The top chamber cells were attached 4% paraformaldehyde and stained with a 10-fold-diluted Giemsa solution at room temperature after incubation at 37°C for 48 hours. Later, five randomly visual fields were selected randomly, and the migrated cells were calculated

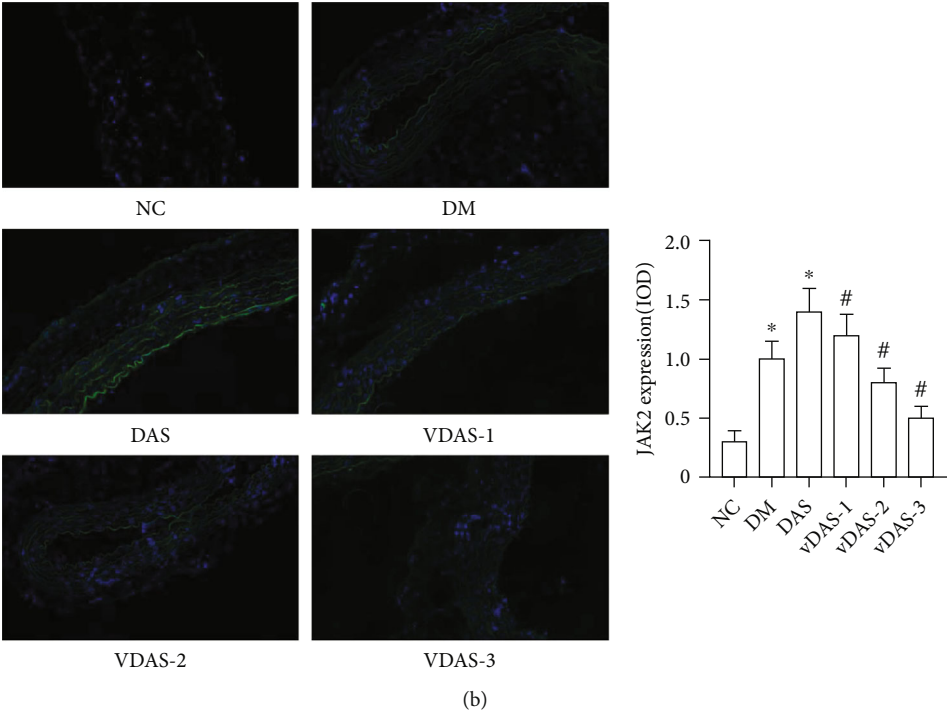
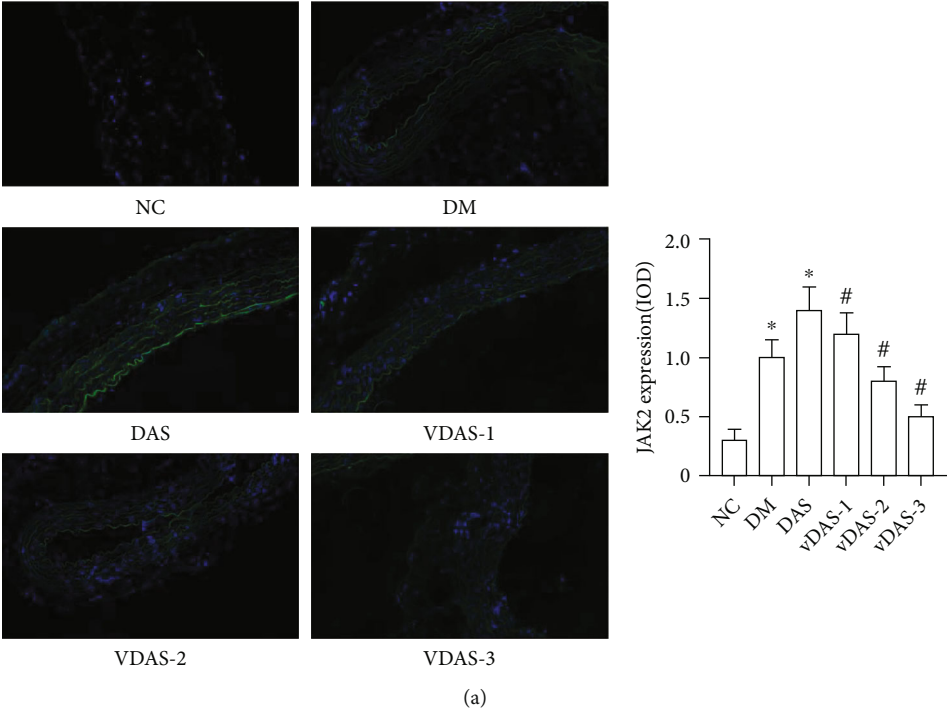


FIGURE 5: Continued.



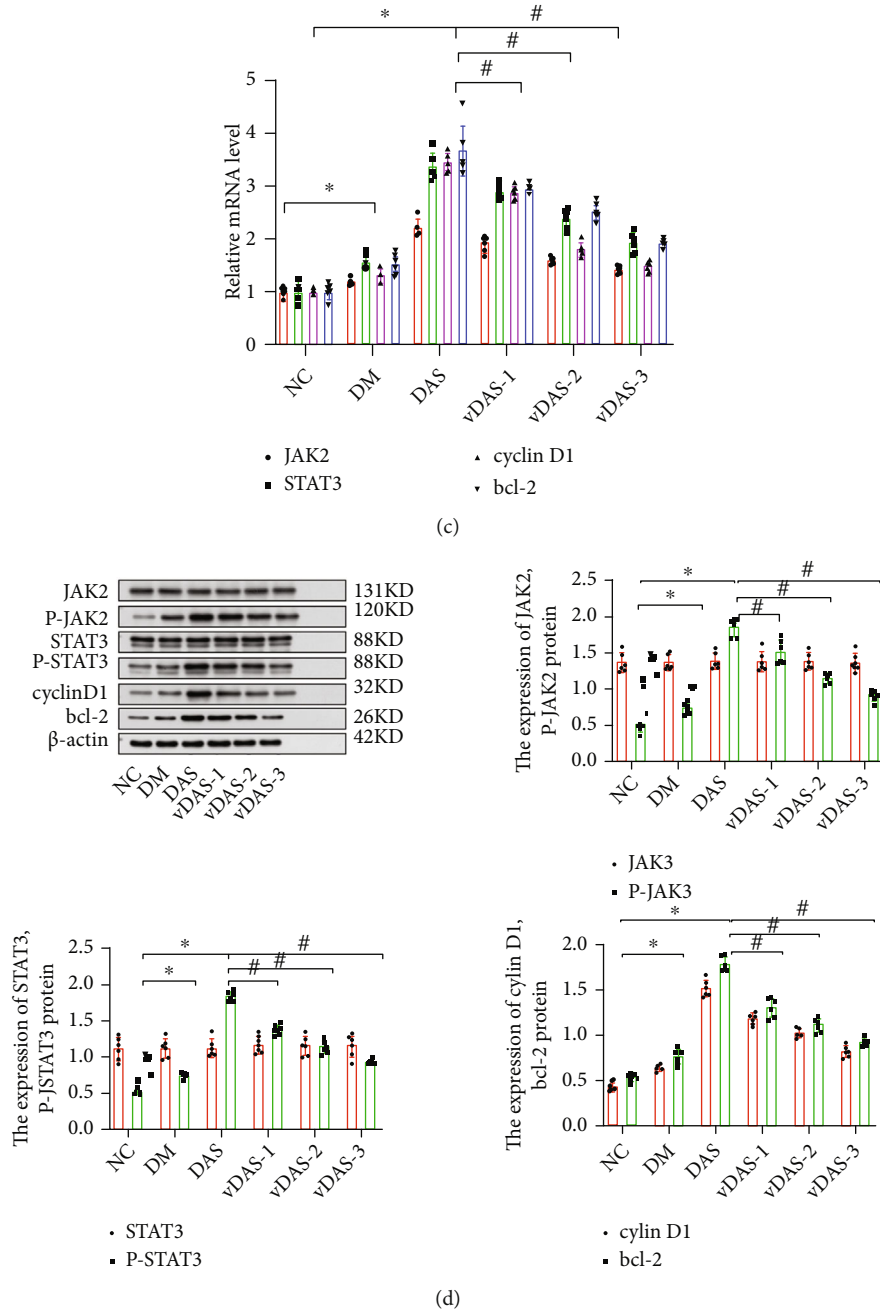


FIGURE 5: The expressions of JAK2, STAT3, cyclinD1 and Bcl-2 were increased in diabetic rats intraperitoneally injected with RBP4, which can be improved after vitamin D supplementation. (a) Immunofluorescence was performed to detect JAK2 (green) in aortic tissue, and blue indicates DAPI-stained nuclei (scale bar, 25  $\mu$ m). The corresponding OD values are presented (\* $P$  < 0.05 for group DM and group DAS compared to group NC, # $P$  < 0.05 for groups VDAS compared to group DAS). (b) Immunofluorescence was performed to detect STAT3 (green) in aortic tissue, and blue indicates DAPI-stained nuclei (scale bar, 25  $\mu$ m). The corresponding OD values are presented (\* $P$  < 0.05 for group DM and group DAS compared to group NC, # $P$  < 0.05 for groups VDAS compared to group DAS). (c) The expressions of JAK2, STAT3, cyclinD1, and Bcl-2 were analyzed by qRT-PCR (\* $P$  < 0.05 for group DM and group DAS compared to group NC, # $P$  < 0.05 for groups VDAS compared to group DAS). (d) The expressions of JAK2, STAT3, cyclinD1, and Bcl-2 were analyzed by western blot (\* $P$  < 0.05 for group DM and group DAS compared to group NC, # $P$  < 0.05 for groups VDAS compared to group DAS).

and photographed with a microscope (Olympus, Tokyo, Japan). The relative migration rate was calculated as the fold change of the number of migrated VSMCs when compared with the control group.

2.9. *MTT Assay.* Cell proliferation assay was performed using MTT assay. The VSMCs were harvested into flat-bottomed 96-well plates at a density of  $5 \times 10^4$ /ml. After that, the culture medium was removed and substituted with

serum-free DMEM. The cells were then rinsed twice with PBS, followed by incubation along with 10  $\mu$ l of MTT (Sigma, USA) at 37°C for 4 h in the dark. Consequently, to dissolve MTT crystals, 150 ml of DMSO (Sigma, USA) was added. The absorbance was calculated using an enzyme-labelled instrument (Thermo Fisher Scientific) at 490 nm.

**2.10. Scratch Assay.** VSMCs were cultured until >90% confluent in 6 well dishes and then were incubated for 0 h, 6 h, 24 h, and 48 h to form a cell monolayer in the presence of different culture media. At the incubation times of 0 h, 6 h, 24 h, and 48 h incubations, the scratch across cell monolayer was made with a sterile 10  $\mu$ l pipette tip by drawing a line through cells perpendicular to the line above. Finally, the wound gap was photographed to measure the scratch width and calculate the relative ratio of width reduction.

**2.11. Flow Cytometric Analysis.** VSMCs in the logarithmic growth phase were collected with EDTA-free trypsin and rinsed two times with 2 ml ice-cold 70% ethanol overnight. After centrifugation, the cells were resuspended in 500  $\mu$ l PBS containing 10  $\mu$ g/ml RNase and 50  $\mu$ g/ml propidium iodide (PI) for 30 minutes at 4°C in the dark. After the cells were rinsed twice with PBS, the cell cycle was detected by NAVIOS cytometer and was analyzed using Kaluza software (Beckman Coulter, USA).

**2.12. Statistical Analysis.** All statistical analyses were carried out using SPSS 23.0 statistical software (IBM, Armonk, USA). Data are expressed as mean  $\pm$  or median. Student's *t*-test was employed for the comparison of two groups, and one-way analysis of variance (ANOVA) was carried out for the comparison of multiple groups. In addition, Pearson's correlation coefficient was performed to evaluate the relationship between RBP4 and other markers.

### 3. Results

**3.1. Biochemical Characters of Rats in Each Group.** As shown in Table 2, the weights of rats in groups DM and DAS increased at the end of the 16th week compared to those in group NC. The body weights were significantly reduced by the vitamin D supplementation in the VDAS group. The rats in group DAS showed higher levels of LD and MT than the ones in groups NC and DM. Furthermore, vitamin D could decrease the thickness of the carotid artery in a dose-dependent manner. Compared with the NC group and DM groups, LDL-c, TG, TC, HbA1C, HOMA-IR, and RBP4 in DAS group were pronouncedly increased while the levels of 25(OH)D, HDL-c and ISI were decreased ( $P < 0.05$ ). Furthermore, intervention with vitamin D significantly decreased the levels of LDL-c, TG, TC, HOMA-IR, HbA1C, and RBP4 and promoted the levels of 25(OH)D, HDL-c, and ISI in the VDAS group ( $P < 0.05$ ). Thus, vitamin D could significantly reverse the expressions of RBP4 and biochemical parameters in a concentration-dependent manner.

**3.2. HE Staining of Thoracic Aortas.** As illustrated in Figures 4(a, A–F) and 4(b, A–F), there were no obvious changes in the structure of aortas in the group NC; the

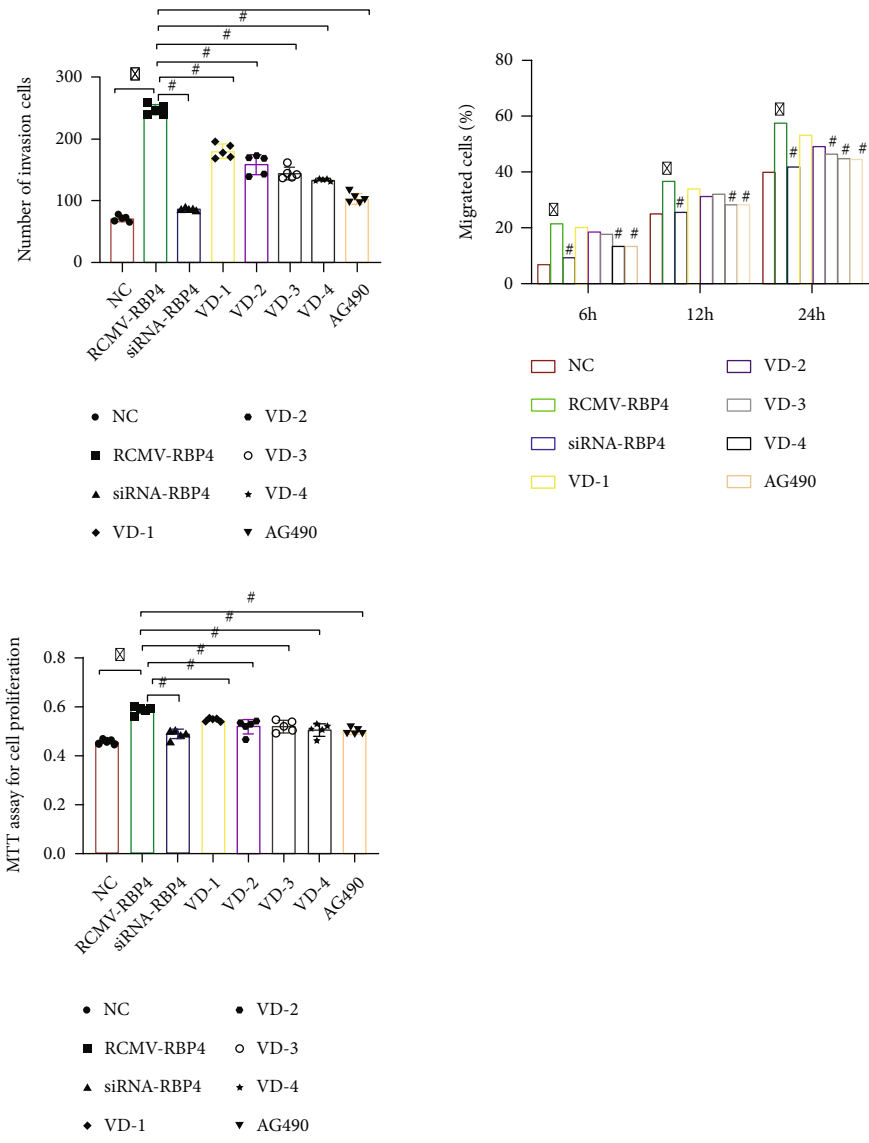
TABLE 3: Correlation among RBP4, 25(OH)D, and the other indicators in T2DM groups ( $n = 107$ ).

|          | RBP4     |              | 25(OH)D  |              |
|----------|----------|--------------|----------|--------------|
|          | <i>r</i> | <i>P</i>     | <i>r</i> | <i>P</i>     |
| LDL-c    | 0.401    | $\leq 0.001$ | -0.294   | 0.002        |
| TG       | 0.456    | $\leq 0.001$ | -0.051   | 0.604        |
| TC       | 0.616    | $\leq 0.001$ | -0.480   | $\leq 0.001$ |
| HDL-c    | -0.733   | $\leq 0.001$ | 0.435    | $\leq 0.001$ |
| HbA1C    | 0.162    | 0.078        | -0.201   | 0.037        |
| FPG      | 0.177    | 0.069        | -0.273   | 0.004        |
| FINS     | 0.655    | $\leq 0.001$ | -0.063   | 0.522        |
| RBP4     | —        | —            | -0.274   | 0.004        |
| HOMA-IR  | 0.606    | $\leq 0.001$ | -0.200   | 0.039        |
| 25(OH)D  | -0.274   | 0.004        | —        | —            |
| ISI      | -0.626   | $\leq 0.001$ | 0.345    | $\leq 0.001$ |
| Weight   | 0.241    | 0.013        | -0.471   | $\leq 0.001$ |
| MT       | 0.587    | $\leq 0.001$ | -0.052   | 0.592        |
| LD       | 0.592    | $\leq 0.001$ | -0.348   | $\leq 0.001$ |
| JAK2     | 0.753    | $\leq 0.001$ | -0.374   | $\leq 0.001$ |
| STAT3    | 0.758    | $\leq 0.001$ | -0.238   | 0.014        |
| cyclinD1 | 0.699    | $\leq 0.001$ | -0.365   | $\leq 0.001$ |
| Bcl-2    | 0.744    | $\leq 0.001$ | -0.220   | 0.023        |

LDL-c: low-density lipoprotein cholesterol; TG: triglycerides; TC: total cholesterol; HDL-c: high-density lipoprotein cholesterol; HbA1C: hemoglobin A1c; FPG: fasting plasma glucose; FINS: fasting insulin; RBP4: retinol binding protein 4; HOMA-IR: homeostasis model assessment of insulin resistance; ISI: insulin sensitivity index; MT: the media thickness of the artery; LD: lumen diameter; JAK2: Janus kinase 2; STAT3: signal transducer and activator of transcription 3; Bcl-2: B cell lymphoma-2.

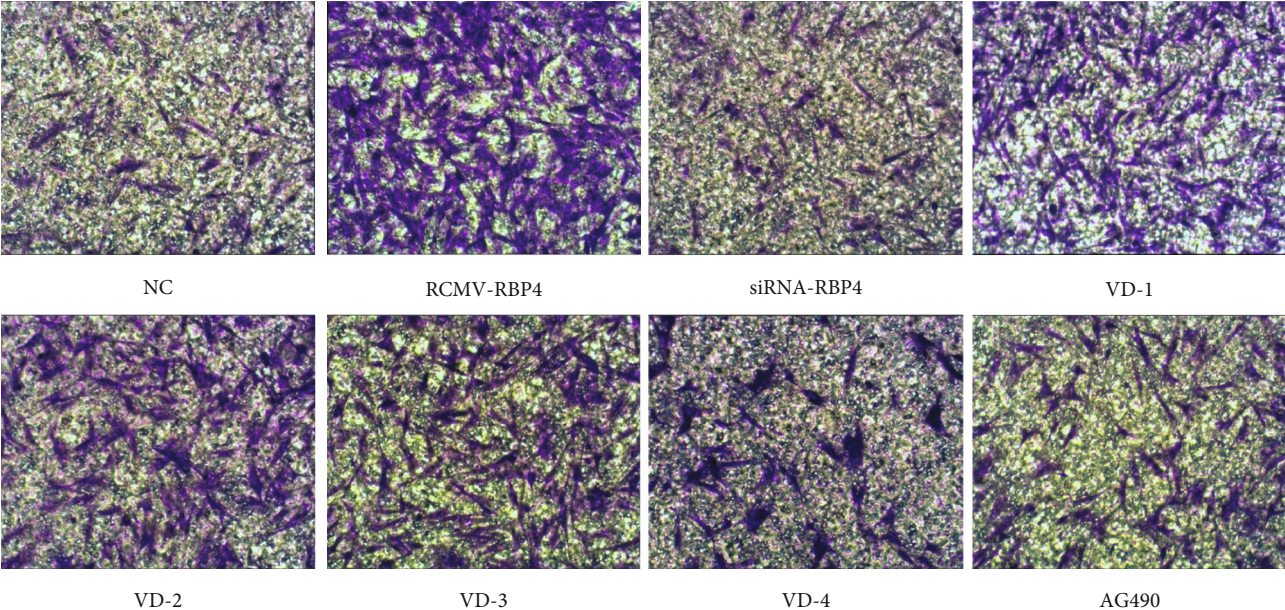
intima became thicker and the VSMCs arranged disorderly in group DM; a large amount of VSMCs migrated and proliferated in group DAS and simultaneously distinct plaques with abundant lipids and calcification formed in the aortas of the rats; there were small formations of plaques and calcification on the walls of aortas in the groups VDAS-1 and VDAS-2; the intima of the aorta was smooth and VSMCs arranged neatly in the group VDAS-3. These findings indicated that vitamin D could potentially have a protective effect during the progression of atherosclerosis.

**3.3. The Expressions of JAK2, STAT3, cylinD1, and Bcl-2 Were Increased in Diabetic Rats Intraperitoneally Injected with RBP4, Which Can Be Improved after Vitamin D Supplementation.** To determine the potential role of RBP4 and vitamin D in the progression of diabetic atherosclerosis, we assessed the expressions of JAK2, STAT3, cylinD1, and Bcl-2 in aortic tissues using different experimental methods. According to the results of immunofluorescence analyses, we found the expressions of JAK2 and STAT3 were markedly increased in the neointima of aortas of rats intraperitoneally injected with RBP4. On the other hand, the expressions were decreased in the neointima of aortas of vitamin D-treated rats (Figures 5(a) and 5(b)). This finding was further confirmed by western blot and qRT-PCR. Quantitative RT-



(a)

FIGURE 6: Continued.



NC

RCMV-RBP4

siRNA-RBP4

VD-1

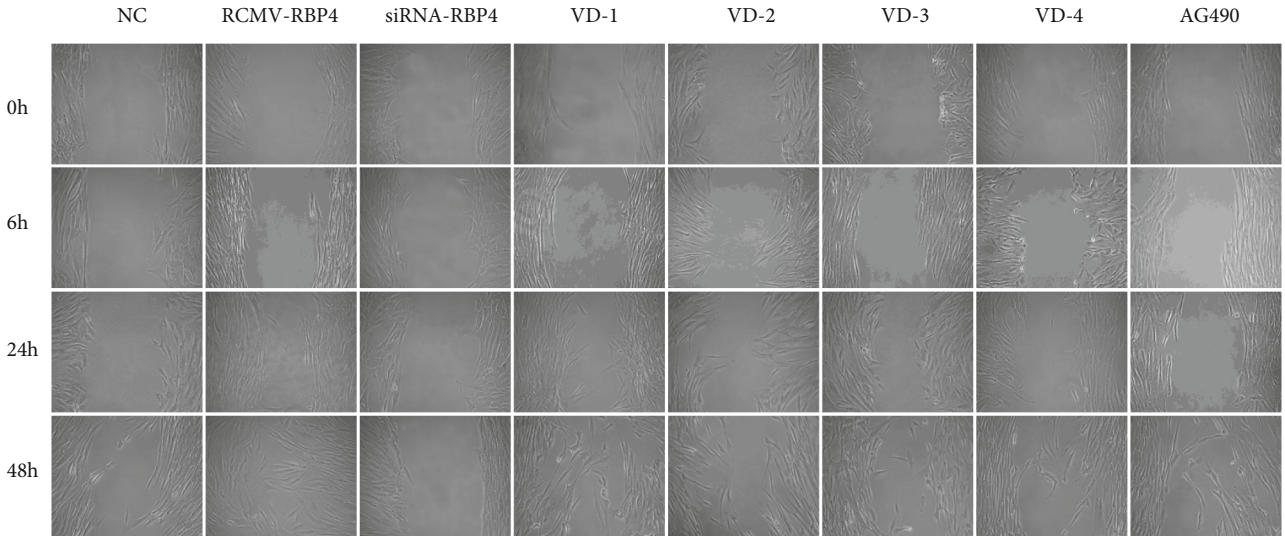
VD-2

VD-3

VD-4

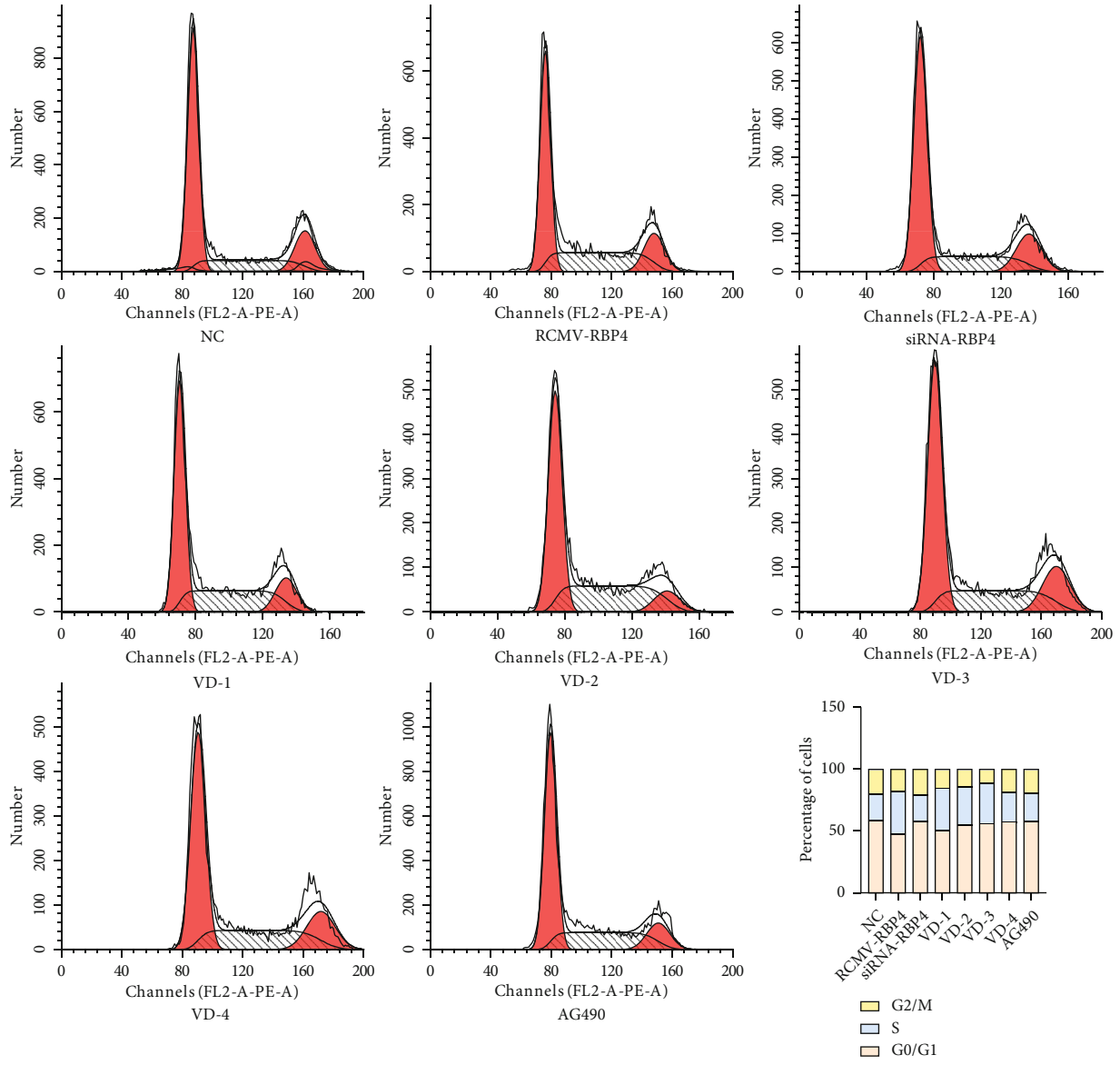
AG490

(b)



(c)

FIGURE 6: Continued.



(d)

FIGURE 6: Continued.

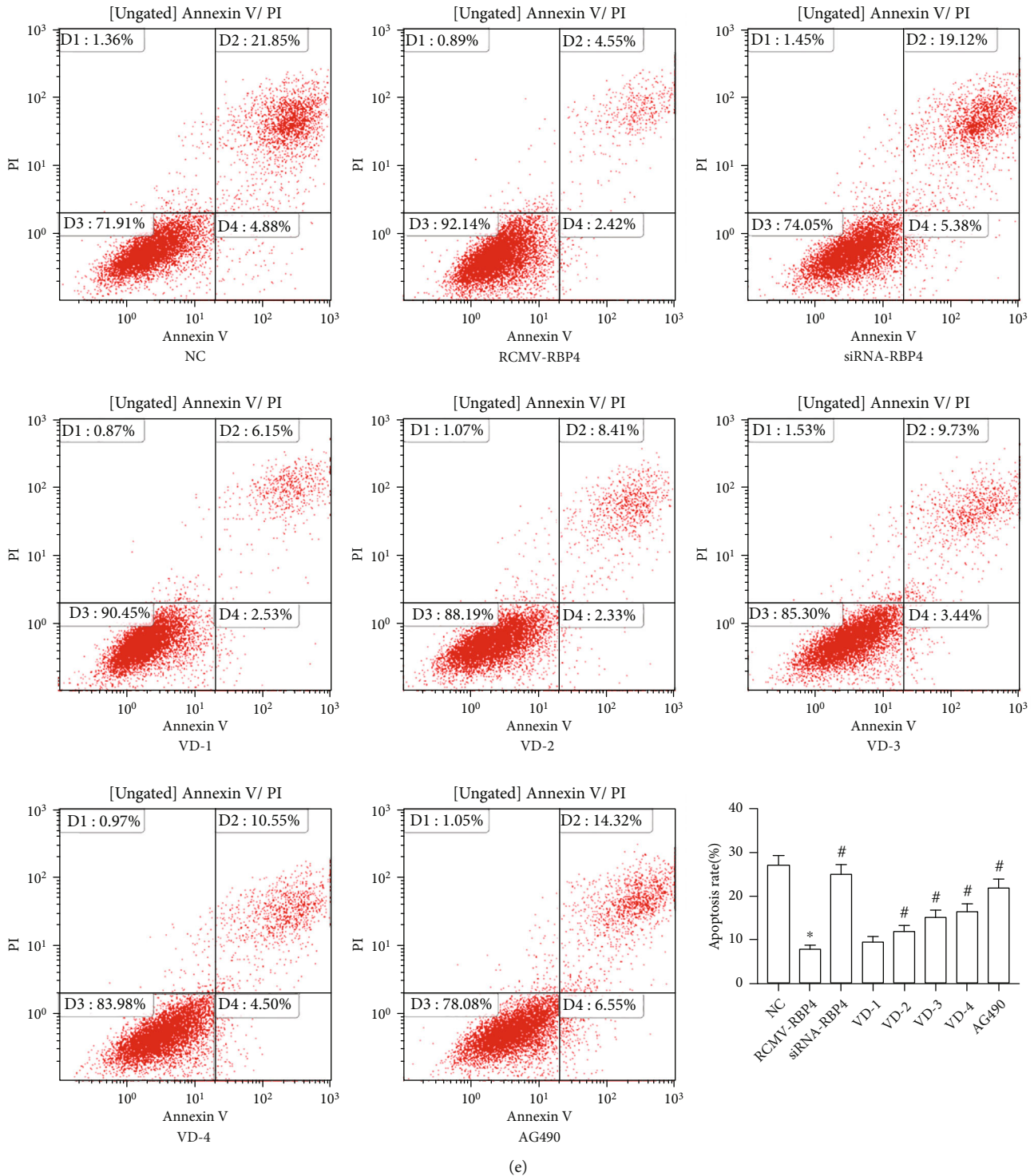
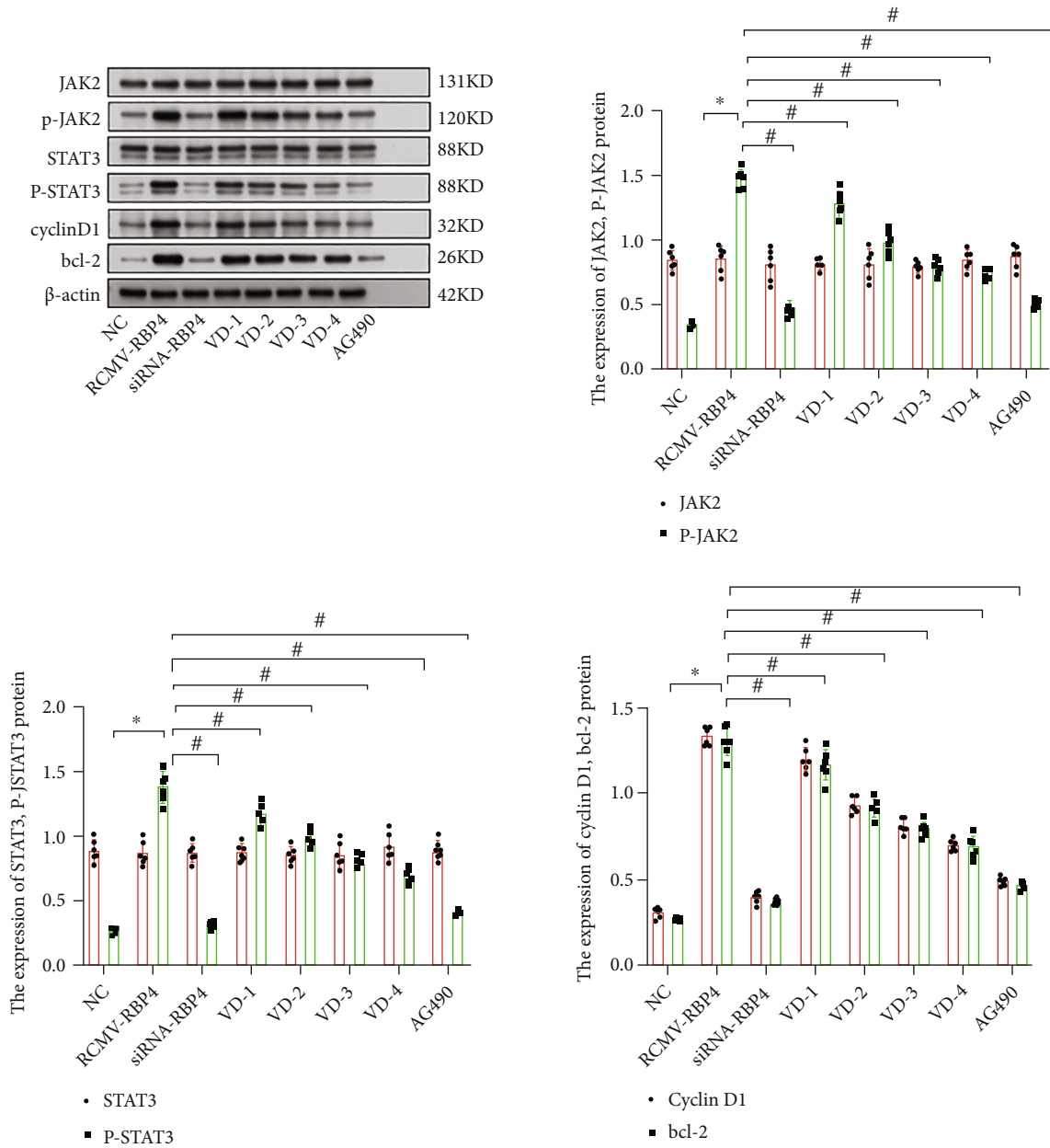


FIGURE 6: RBP4 can promote VSMCs proliferation and migration under high glucose condition, which can be inhibited by vitamin D. (a) The proliferation ability of VSMCs was measured by MTT, scratch wound-healing, and Transwell migration assay (\* $P < 0.05$  for the RCMV-RBP4 group compared to the NC group, # $P < 0.05$  for siRNA-RBP4-, AG490-, and vitamin D-treated groups compared to RCMV-RBP4). (b) VSMC migration ability was measured by Transwell assays. (c) VSMC migration ability was measured by scratch wound assays. (d) Flow cytometry was applied to detect the cell cycle of VSMCs. (e) Flow cytometry was applied to detect the apoptosis rate of VSMCs (\* $P < 0.05$  for the RCMV-RBP4 group compared to the NC group, # $P < 0.05$  for siRNA-RBP4-, AG490-, and vitamin D-treated groups compared to RCMV-RBP4).



(a)

FIGURE 7: Continued.

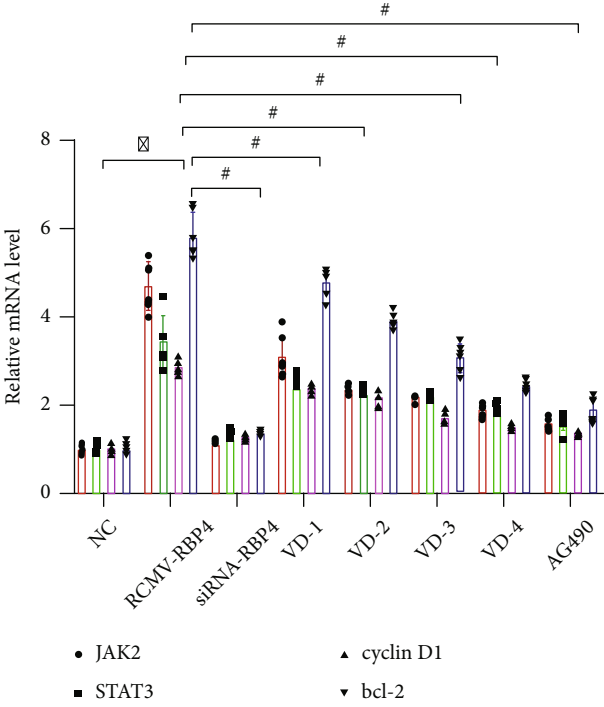
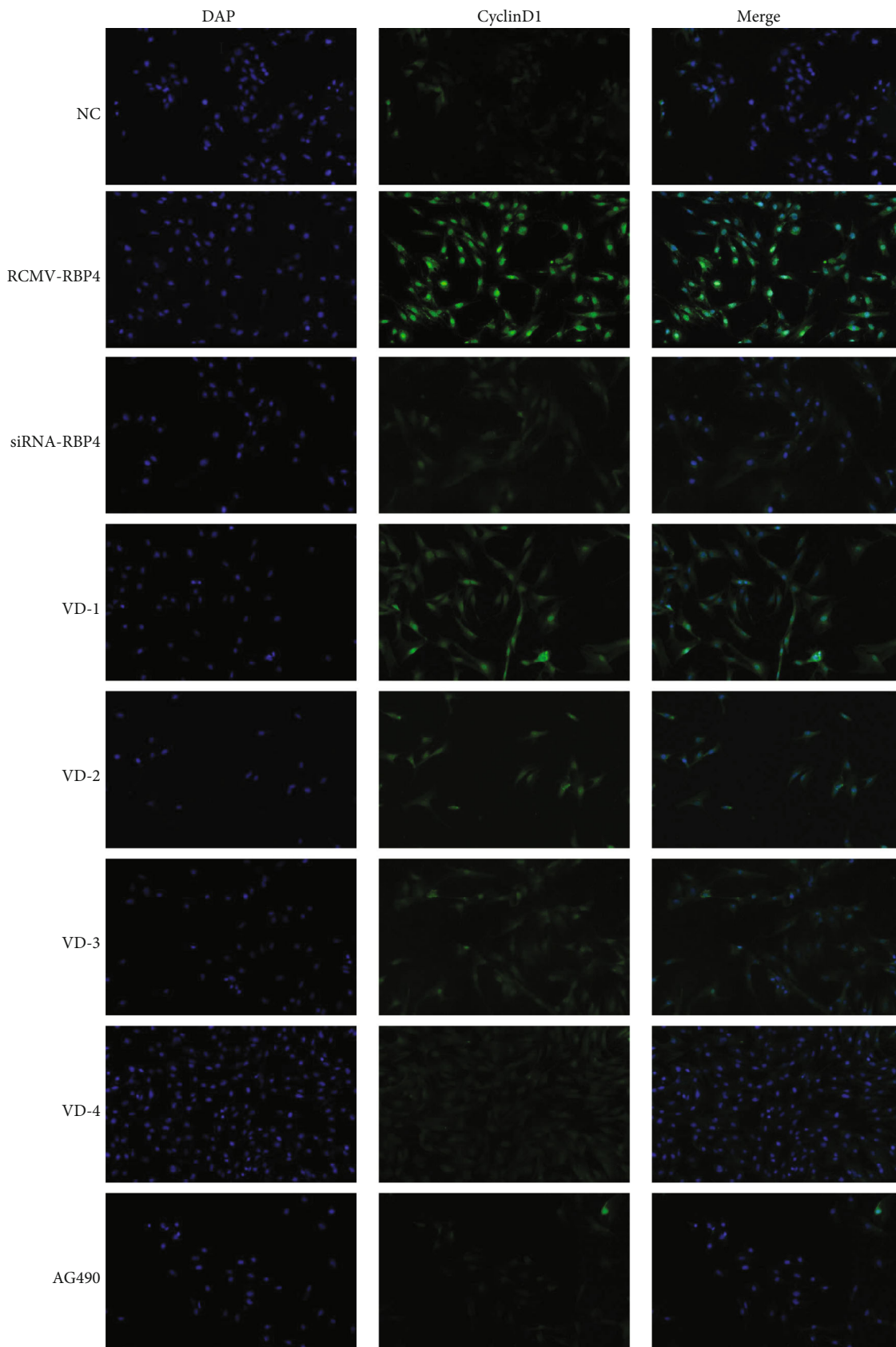


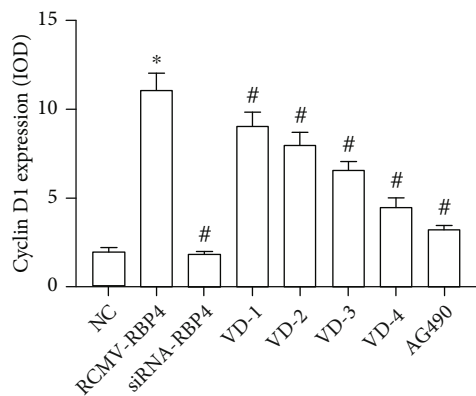
FIGURE 7: Continued.





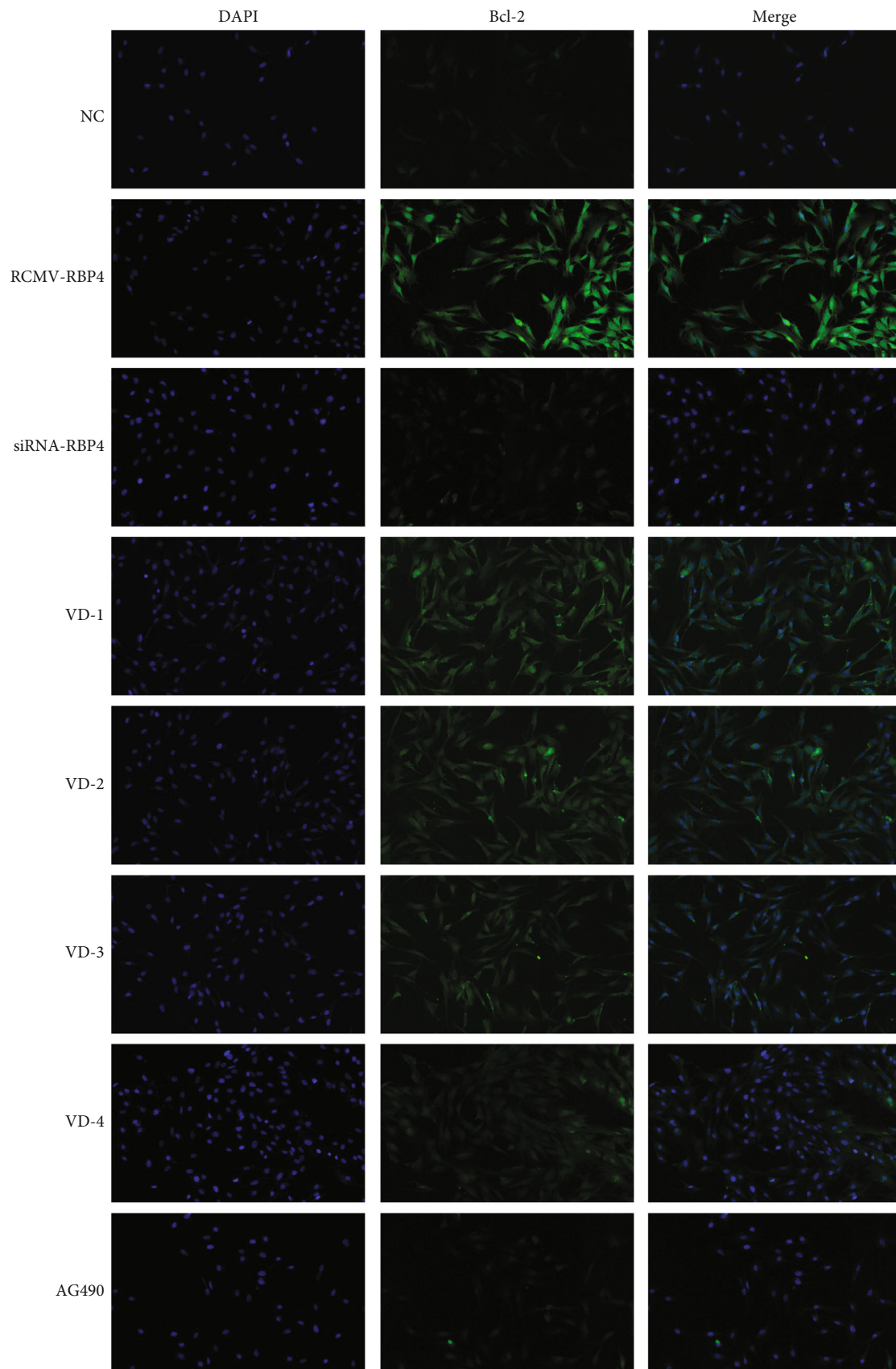
(c)

FIGURE 7: Continued.



(d)

FIGURE 7: Continued.



(e)

FIGURE 7: Continued.

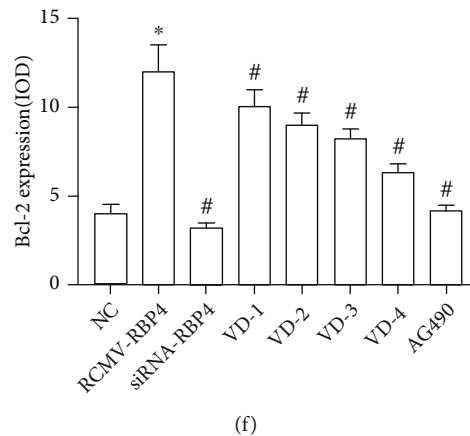


FIGURE 7: RBP4 can promote VSMCs proliferation and migration under high glucose condition, which can be inhibited by vitamin D. (a) The expressions of JAK2, STAT3, cyclinD1, and Bcl-2 were analyzed by western blot (\* $P < 0.05$  for the RCMV-RBP4 group compared to the NC group, # $P < 0.05$  for siRNA-RBP4-, AG490-, and vitamin D-treated groups compared to RCMV-RBP4). (b) The expressions of JAK2, STAT3, cyclinD1, and Bcl-2 were analyzed by qRT-PCR (\* $P < 0.05$  for the RCMV-RBP4 group compared to the NC group, # $P < 0.05$  for siRNA-RBP4-, AG490-, and vitamin D-treated groups compared to RCMV-RBP4). (c) Immunofluorescence was performed to detect cyclinD1 (green) in the nucleus, and blue indicates DAPI-stained nuclei (scale bar, 25  $\mu\text{m}$ ). (d) The corresponding OD values of cyclinD1 are presented (\* $P < 0.05$  for the RCMV-RBP4 group compared to the NC group, # $P < 0.05$  for siRNA-RBP4-, AG490-, and vitamin D-treated groups compared to RCMV-RBP4). (e) Immunofluorescence was performed to detect Bcl-2 (green) in the cytoplasm, and blue indicates DAPI-stained nuclei (scale bar, 25  $\mu\text{m}$ ). (f) The corresponding OD values of Bcl-2 are presented (\* $P < 0.05$ , for the RCMV-RBP4 group compared to the NC group, # $P < 0.05$  for siRNA-RBP4-, AG490-, and vitamin D-treated groups compared to RCMV-RBP4).

PCR showed that the expressions of JAK2 mRNA in aortic tissues were  $1.0 \pm 0.08$ ,  $1.23 \pm 0.12$ ,  $3.09 \pm 0.15$ ,  $2.65 \pm 0.13$ ,  $1.75 \pm 0.13$ , and  $1.55 \pm 0.11$  in groups NC, DM, DAS, VDAS-1, VDAS-2, and VDAS-3, respectively. Interestingly, the expression of STAT3 mRNA in aortic tissues was higher in the DAS group than those in the NC group and DM group. When compared with group DAS, the mRNA expressions of STAT3 in groups VDAS-1, VDAS-2, and VDAS-3 were significantly lower, and this difference of STAT3 expression was more significant in group VDAS-3. In addition, the mRNA expressions of cyclinD1 and Bcl-2 in the DAS group were significantly increased compared to the NC group and the DM group. After the 8-week treatment with vitamin D, the expressions of cyclinD1 and Bcl-2 decreased in a dose-dependent manner in group VDAS as compared with those in group DAS (Figure 5(c)). Consistently with mRNA levels, western blot (Figure 5(d)) revealed that the protein expressions of p-JAK2, p-STAT3, cyclinD1, and Bcl-2 in group DAS were also aberrantly elevated in contrast to control subjects, group DM, and group VDAS. However, no significant difference was observed in JAK2 and STAT3 expressions among the groups. Furthermore, vitamin D exhibited dose-dependent effects in decreasing the protein expressions of p-JAK2, p-STAT3, cyclinD1, and Bcl-2. These findings reveal that the expressions of JAK2, STAT3, cyclinD1, and Bcl-2 were increased significantly after the diabetic rats were intraperitoneally injected with RBP4, and vitamin D can decrease the expressions in a dose-dependent manner. Pearson's correlation analysis was employed to further validate the relationship between RBP4 and the development of diabetic atherosclerosis. The results indicated that serum RBP4 was positively associated with the LDL-c, TG, HbA1C, TC, FINS, Bcl-2, p-JAK2,

cyclinD1, p-STAT3, and HOMA-IR but negatively correlated with 25(OH)D and HDL-c (Table 3).

**3.4. RBP4 Promotes VSMC Proliferation and Migration under High Glucose Condition, Which Can Be Inhibited by Vitamin D.** To elucidate the molecular mechanism of RBP4 and vitamin D in regulating VSMC proliferation, we evaluated the ability of proliferation and migration of VSMCs under high glucose condition. An MTT proliferation assay demonstrated that RBP4 treatment significantly enhanced the proliferation of VSMCs compared to the remaining groups (Figure 6(a)). The Transwell migration assay showed that the number of invaded cells exposed to RCMV-RBP4 was significantly higher than those of cells exposed to siRNA-RBP4. It also revealed that vitamin D could attenuate the proliferation of VSMCs in a time- and dose-dependent manner (Figures 6(a) and 6(b)). Since AG490 is a known inhibitor of JAK2, group AG490 was set up as a reference to clarify the mechanisms by which RBP4 triggers VSMC proliferation. As shown in Figure 6(a), the number of invaded cells exposed to siRNA-RBP4 and AG490 simultaneously was lower than the one of VSMCs exposed to RCMV-RBP4, which reveals that RBP4 promotes VSMC proliferation partly associated with the JAK2 pathway. The scratch wound-healing assay showed that gaps were nearly closed in RBP4-overexpressing VSMCs, whereas gaps remained large in control wells and wells exposed to siRNA-RBP4, AG490, and 1,25(OH)<sub>2</sub>D (50 nM, 48 h). Furthermore, gaps were visible in wells exposed to 1,25(OH)<sub>2</sub>D (25 nM, 24 h) (25 nM, 48 h) (50 nM, 24 h), respectively (Figures 6(a) and 6(c)). In flow cytometric analysis, RBP4 overexpression was found to stimulate an increase in cells in the S phase, which implied that RBP4 could potentially induce migration

in VSMCs. Furthermore, supplementation with vitamin D resulted in an increased percentage of cells in the G0/G1 phase in a dose-dependent manner (Figure 6(d)). The results of flow cytometric analysis further revealed that VSMCs transfected with overexpressed RBP4 had a significantly lower apoptosis rate compared to cells treated with 50 nM  $1,25(\text{OH})_2\text{D}$  (Figure 6(e)). These findings suggest that vitamin D reduced the abnormal proliferation and migration of VSMCs caused by RBP4 under high glucose condition.

**3.5. RBP4 Upgrades the Expressions of JAK2, STAT3, cyclinD1, and Bcl-2, Which Can be Inhibited by Vitamin D Intervention.** To evaluate the signaling pathway associated with RBP4 and vitamin D, several critical molecules were examined in the present study. Western blot showed that the phosphorylation levels of JAK2 and STAT3 were increased dramatically in VSMCs incubated with RCMV-RBP4 compared with those in VSMCs treated with siRNA-RBP4 (Figure 7(a)). Furthermore, a similar elevation of JAK2 and STAT3 mRNA levels were also observed in the VSMCs (Figure 7(b)). cyclinD1 and Bcl-2 mRNA levels as well as the protein expressions were increased significantly in group RCMV-RBP4 compared with group NC and group siRNA-RBP4. Moreover, vitamin D was reported to lower the expressions of JAK2, STAT3, Bcl-2, and cyclinD1 in a dose-dependent manner in both western blot and qRT-PCR analysis (Figures 7(a) and 7(b)). Cell immunofluorescence assays indicated that fluorescence intensities of JAK2, STAT3, cyclinD1, and Bcl-2 were brighter in RBP4-overexpressing cells compared to cells treated with siRNA-RBP4 or vitamin D (Figures 7(c)–7(f)).

#### 4. Discussion

Diabetic macroangiopathy is identified as a major cause of death in diabetic patients and significantly reduces their quality of life. One of the major contributors to diabetic macroangiopathy is the alterations in vascular homeostasis due to the dysfunction of vascular smooth muscle cell [26]. JAK2 is a nonreceptor tyrosine kinase which phosphorylates and activates STAT3, leading to its dimerization and translocation to the nucleus where STAT3 binds to downstream targets such as cyclinD1 and promotes the proliferation of VSMCs. Thus, the JAK2/STAT3 signaling pathway seems to be one of the critical pathways regulating VSMC proliferation and resulting in the development of metabolic diseases [27, 28]. In this study, the expressions of JAK2, STAT3, cyclinD1, and Bcl-2 in the serum as well as in aortic tissue were significantly elevated in diabetic atherosclerotic rats. To further validate the effect of the JAK2 pathway on the migration and proliferation of VSMCs, AG490, a JAK2-specific inhibitor, was used in the present study. The results indicated that the proliferation abilities of VSMCs were limited compared to control cells, which was in accordance with previous viewpoints.

RBP4, the specific vitamin A carrier in the circulation, is secreted primarily from the liver and adipose tissues. As a newly identified adipokine, RBP4 was suggested to be associated with the pathogenesis of insulin resistance and T2DM.

Transgenic overexpression of human RBP4 in rat was found to induce insulin resistance [4]. Conversely, heterozygous and homozygous RBP4 knockout rats exhibited improved insulin sensitivity [29]. Several studies have suggested a potential association between elevated RBP4 levels and the development of diabetes complicated with cardiovascular diseases [30, 31]. However, the literatures have not reached a consensus on this issue [32]. In our study, atherosclerosis of the aorta was observed in HE staining after injection of recombinant RBP4 in diabetic rats, which suggests that RBP4 may be involved in the occurrence of diabetic macroangiopathy. The role of RBP4 in the diabetic atherosclerotic process is connected to an increased level of proinflammatory cell surface adhesion molecules, an unfavourable proatherogenic plasma lipoprotein profile, and insulin resistance [33–35]. Both our previous studies and the present study revealed that RBP4 is associated with IR, inflammation, and glucolipid metabolism, which is in agreement with the results of most previous research [36, 37]. However, it should be pointed out that only a few studies have been conducted on the potential role of RBP4 in the proliferation and migration of VSMCs. Previous research revealed that RBP4 could potentially promote the proliferation of VSMCs [38]. However, they failed to explore and illustrate the concrete mechanisms of RBP4 involved in the proliferation of VSMCs. Adipocytes generate endocrine hormones which engage the JAK/STAT signaling pathway in target tissues [39], implying that JAK2/STAT3 is an adipocyte-derived signaling pathway. Trovati et al. reported that leptin can affect VSMC proliferation and vascular endothelial cell function through the JAK/STAT pathway [40]. In addition to leptin, other JAK inducing factors including IL-6 and prolactin are also produced by adipocytes [41]. Li et al. [42] found that RBP4 can significantly promote the hyperinsulinism-induced proliferation of VSMCs via JAK2/STAT3. Randolph and Ross showed that the treatment of RBP4 for cultured adipocytes triggers the activation of JAK2 and STAT, phosphorylation of stimulated by retinoic acid gene 6 (STRA6), and the subsequent upregulation of suppressor of cytokine signaling 3 (SOCS3), leading to the inhibition of insulin responses [43]. Similarly, the injection of recombinant RBP4 in mice led to the phosphorylation of JAK2 and STAT and upregulation of SOCS3 expression in adipose and muscle tissues [44]. Our previous study had confirmed that RBP4 is associated with the JAK2/STAT3 signaling pathway [23], which may contribute to the development of diabetic macroangiopathy. In the present study, the levels of p-JAK2, p-STAT3, cyclinD1, and Bcl-2 increased after the rats were intraperitoneally injected with recombinant RBP4. Moreover, they were all positively associated with RBP4, indicating that RBP4 participates in the formation of atherosclerosis by the JAK2/STAT3 signaling pathway. To explore if the RBP4/JAK2/STAT3 pathway could initiate the transformation of VSMCs, cells were incubated with glucose conditions in the presence or absence of RBP4. At the cellular level, we found that RBP4 overexpression significantly increased the proliferation and migration of VSMCs and enhanced the expressions of JAK2, STAT3, cyclinD1, and Bcl-2. However, RBP4 knockdown induced the opposite

effects, which indicates that elevated RBP4 may contribute to the pathogenesis of diabetic atherosclerosis by the JAK2/STAT3 pathway. Thus, the RBP4/JAK2/STAT3 cascade appears to be a promising novel therapeutic target for diabetic macroangiopathy.

Vitamin D insufficiency may contribute to the pathogenesis of diabetic macroangiopathy by numerous potential pathophysiologic mechanisms. The impacts of vitamin D deficiency are known to cause endothelial dysfunction, dyslipidemia, inflammation, and insulin resistance [45]. Vitamin D supplementation can potentially modulate the oxidative-inflammatory reaction, balance arterial remodeling, and increase insulin sensitivity [46]. In our previous clinical trials, after 12 weeks of vitamin D therapy, the incidence rate of lower extremity arterial disease in the T2DM group and the level of RBP4 both decreased significantly [36]. In the present study, vitamin D supplementation alleviated the progression of aortic diseases in diabetic rats with macroangiopathy and attenuated the ability of cell proliferation and migration in the cellular experiment, suggesting that vitamin D supplementation plays a cardioprotective role. Previous researches have shown that vitamin D can influence the production and function of certain adipokines such as leptin and adiponectin [47, 48]. Nevertheless, only a few studies have explored the relationship between vitamin D and RBP4. In our study, the levels of RBP4 were reduced in diabetic atherosclerotic rats after vitamin D supplementation. Additionally, in line with the findings of our previous studies, RBP4 was negatively correlated with 25(OH)D. Vitamin A receptor and 1,25(OH)<sub>2</sub>D receptor belong to the steroid and thyroid hormone receptor family, and their functions often interfere with each other [49]. Kong et al. found that 1,25(OH)<sub>2</sub>D can inhibit the production of transcription factors and the accumulation of lipid during adipocyte differentiation [50]. Metheniti et al. [51] showed that the expression of 25(OH)D was decreased in ultraobese young females and was negatively correlated with RBP4. We therefore speculated that vitamin D might play a pivotal role in the progression of diabetic atherosclerosis partly by influencing the expression of RBP4. Zhang et al. [52] suggested that 1,25(OH)<sub>2</sub>D suppresses the inflammatory responses by inhibiting Th1 cell differentiation and cytokine generation via the JAK/STAT pathway. In this study, we were able to gain insight into the possible mechanisms of the vitamin D and JAK2 pathway. As expected, we found that JAK2 and STAT3 levels of rats in the diabetic atherosclerosis group were negatively correlated with 25(OH)D concentrations and significantly decreased after vitamin D intervention. Similarly, vitamin D lowered the expressions of JAK2, STAT3, cyclinD1, and Bcl-2 in a dose-dependent manner in vitro experiment, indicating that vitamin D supplementation exerts potent inhibitory effects on the proliferation and migration of VSMCs via the RBP4/JAK2/STAT3 pathway.

## 5. Conclusion

Our results cast a new light on how RBP4 induces proliferation and migration of VSMCs via the JAK2/STAT3 signaling

pathway and promotes the pathogenesis of diabetic atherosclerosis. We also found that vitamin D supplementation can downgrade RBP4 expression and have a protective role in the development of diabetic macroangiopathy, which is partially associated with suppressing proliferation of VSMCs via the JAK2/STAT3 signaling pathway. Finding new and effective therapeutic targets by thoroughly exploring the regulation and mechanisms of diabetic macrovascular disease is crucial for achieving optimal clinical outcomes. Hence, our present findings provide novel insights into the potential role of RBP4 and vitamin D in the development of diabetic macroangiopathy.

## Data Availability

The datasets used and/or analyzed during the current study are available from the corresponding author on reasonable request.

## Conflicts of Interest

No potential conflicts of interest relevant to this article were reported.

## Authors' Contributions

Wan Zhou designed the research, carried out the experiment, analyzed the data, and wrote the manuscript. Yan Xing, Chunchun Xiao, and Xiaojing Yuan collected data and carried out the experiment. Wei Wang reviewed the manuscript. Shandong Ye and Qiang Liu reviewed and edited the manuscript. Shandong Ye and Qiang Liu are the guarantors of this work. All authors provided final approval of the version to be submitted.

## Acknowledgments

This work was supported by the Project of National Natural Science Foundation of China (Grant No. 81800713 to Wan Zhou and Grant No. 81971264 to Wei Wang), the project of Natural Science Foundation of Anhui Province (Grant No. 1808085QH292 to Wan Zhou), and the Fundamental Research Funds for the Central Universities (Grant No. WK9110000041 to Wan Zhou).

## Supplementary Materials

Figure S1: RBP4 can promote the proliferation and migration of VSMCs via regulating the JAK2/STAT3 signaling pathway. This mechanism of RBP4 can be inhibited by vitamin D supplementation. (*Supplementary Materials*)

## References

- [1] A. Sciacqua, E. Ventura, G. Tripepi et al., "Ferritin modifies the relationship between inflammation and arterial stiffness in hypertensive patients with different glucose tolerance," *Cardiovascular Diabetology*, vol. 19, no. 1, p. 123, 2020.
- [2] E. Muzurović, Z. Stanković, Z. Kovačević, B. Š. Škrijelj, and D. P. Mikhailidis, "Inflammatory markers associated with

- diabetes mellitus – old and new players,” *Current Pharmaceutical Design*, vol. 27, no. 27, pp. 3020–3035, 2021.
- [3] M. A. González-López, J. G. Ocejo-Viñals, C. Mata et al., “Association of retinol binding protein4 (RBP4) and ghrelin plasma levels with insulin resistance and disease severity in non-diabetic patients with hidradenitis suppurativa,” *Experimental Dermatology*, vol. 29, no. 9, pp. 828–832, 2020.
  - [4] Q. Yang, T. E. Graham, N. Mody et al., “Serum retinol binding protein 4 contributes to insulin resistance in obesity and type 2 diabetes,” *Nature*, vol. 436, no. 7049, pp. 356–362, 2005.
  - [5] G. Aust, M. Uptaite-Patapoviene, M. Scholz, O. Richter, S. Rohm, and M. Blüher, “Circulating Nampt and RBP4 levels in patients with carotid stenosis undergoing carotid endarterectomy (CEA),” *Clinica Chimica Acta*, vol. 412, no. 13-14, pp. 1195–1200, 2011.
  - [6] N. P. E. Kadoglou, V. Lambadiari, A. Gastounioli et al., “The relationship of novel adipokines, RBP4 and omentin-1, with carotid atherosclerosis severity and vulnerability,” *Atherosclerosis*, vol. 235, no. 2, pp. 606–612, 2014.
  - [7] V. Llombart, T. García-Berrocoso, A. Bustamante et al., “Plas-matic retinol-binding protein 4 and glial fibrillary acidic protein as biomarkers to differentiate ischemic stroke and intracerebral hemorrhage,” *Journal of Neurochemistry*, vol. 136, no. 2, pp. 416–424, 2016.
  - [8] M. Wang, Y. Han, Q. Li et al., “Higher serum retinol binding protein 4 may be a predictor of weak metabolic control in Chinese patients with type 2 diabetes mellitus,” *Journal of International Medical Research*, vol. 40, no. 4, pp. 1317–1324, 2012.
  - [9] M. Mansouri, R. Heshmat, O. Tabatabaei-Malazy et al., “The association of carotid intima media thickness with retinol binding protein-4 and total and high molecular weight adiponectin in type 2 diabetic patients,” *Journal of Diabetes & Metabolic Disorders*, vol. 11, no. 1, p. 2, 2012.
  - [10] P. M. Rist, M. C. Jiménez, S. S. Tworoger et al., “Plasma retinol-binding protein 4 levels and the risk of ischemic stroke among women,” *Journal of Stroke and Cerebrovascular Diseases*, vol. 27, no. 1, pp. 68–75, 2018.
  - [11] L. A. Calò, G. Maiolino, E. Pagnin, U. Vertolli, and P. A. Davis, “Increased RBP4 in a human model of activated anti-atherosclerotic and antiremodelling defences,” *European Journal of Clinical Investigation*, vol. 44, no. 6, pp. 567–572, 2014.
  - [12] K. Takebayashi, R. Sohma, Y. Aso, and T. Inukai, “Effects of retinol binding protein-4 on vascular endothelial cells,” *Biochemical and Biophysical Research Communications*, vol. 408, no. 1, pp. 58–64, 2011.
  - [13] G. L. Basatemur, H. F. Jørgensen, M. C. H. Clarke, M. R. Bennett, and Z. Mallat, “Vascular smooth muscle cells in atherosclerosis,” *Nature Reviews Cardiology*, vol. 16, no. 12, pp. 727–744, 2019.
  - [14] Q. B. Lu, H. Wang, Z. H. Tang et al., “Nesfatin-1 functions as a switch for phenotype transformation and proliferation of VSMCs in hypertensive vascular remodeling,” *Biochimica et Biophysica Acta (BBA) - Molecular Basis of Disease*, vol. 1864, no. 6, pp. 2154–2168, 2018.
  - [15] G. Niu, K. L. Wright, M. Huang et al., “Constitutive Stat3 activity up-regulates VEGF expression and tumor angiogenesis,” *Oncogene*, vol. 21, no. 13, pp. 2000–2008, 2002.
  - [16] N. Jing and D. J. Tweardy, “Targeting Stat3 in cancer therapy,” *Anti-Cancer Drugs*, vol. 16, no. 6, pp. 601–607, 2005.
  - [17] S. Chesdachai and V. Tangpricha, “Treatment of vitamin D deficiency in cystic fibrosis,” *The Journal of Steroid Biochemistry and Molecular Biology*, vol. 164, pp. 36–39, 2016.
  - [18] A. Prentice, “Vitamin D deficiency: a global perspective,” *Nutrition Reviews*, vol. 66, pp. S153–S164, 2008.
  - [19] R. A. Małgorzata, M. Anna, and P. Beata, “Cardiovascular risk factors in obese children and adolescents,” *Advances in Clinical Science*, vol. 2016, no. 878, pp. 39–47, 2016.
  - [20] Y. Wang and H. Zhang, “Serum 25-hydroxyvitamin D3 levels are associated with carotid intima-media thickness and carotid atherosclerotic plaque in type 2 diabetic patients,” *Journal of Diabetes Research*, vol. 2017, Article ID 3510275, 6 pages, 2017.
  - [21] F. Raygan, V. Ostadmohammadi, F. Bahmani, and Z. Asemi, “The effects of vitamin D and probiotic co-supplementation on mental health parameters and metabolic status in type 2 diabetic patients with coronary heart disease: a randomized, double-blind, placebo-controlled trial,” *Progress in Neuro-Psychopharmacology and Biological Psychiatry*, vol. 84, no. Part A, pp. 50–55, 2018.
  - [22] P. Veloudi, C. L. Blizzard, C. H. Ding et al., “Effect of vitamin D supplementation on aortic stiffness and arterial hemodynamics in people with osteoarthritis and vitamin D deficiency,” *Journal of the American College of Cardiology*, vol. 66, no. 23, pp. 2679–2681, 2015.
  - [23] W. Zhou, S. D. Ye, and W. Wang, “Elevated retinol binding protein 4 levels are associated with atherosclerosis in diabetic rats via JAK2/STAT3 signaling pathway,” *World Journal of Diabetes*, vol. 12, no. 4, pp. 466–479, 2021.
  - [24] N. Lian, J. Tong, W. Li, J. Wu, and Y. Li, “Ginkgetin ameliorates experimental atherosclerosis in rats,” *Biomedicine & Pharmacotherapy*, vol. 102, pp. 510–516, 2018.
  - [25] Y. Ti, G. Xie, Z. Wang et al., “TRB3 gene silencing alleviates diabetic cardiomyopathy in a type 2 diabetic rat model,” *Diabetes*, vol. 60, no. 11, pp. 2963–2974, 2011.
  - [26] N. Katakami, “Mechanism of development of atherosclerosis and cardiovascular disease in diabetes mellitus,” *Journal of Atherosclerosis and Thrombosis*, vol. 25, no. 1, pp. 27–39, 2018.
  - [27] H. Song, Y. Cui, L. Zhang et al., “Ruxolitinib attenuates intimal hyperplasia via inhibiting JAK2/STAT3 signaling pathway activation induced by PDGF-BB in vascular smooth muscle cells,” *Microvascular Research*, vol. 132, p. 104060, 2020.
  - [28] J. Zhao, M. Zhang, W. Li, X. Su, L. Zhu, and C. Hang, “Suppression of JAK2/STAT3 signaling reduces end-to-end arterial anastomosis induced cell proliferation in common carotid arteries of rats,” *PLoS One*, vol. 8, no. 3, article e58730, 2013.
  - [29] H. H. Earl, “Digestion and Intestinal Absorption of Dietary Carotenoids and Vitamin A,” *Physiology of the Gastrointestinal Tract*, vol. 2, pp. 1663–1680, 2012.
  - [30] P. Li, Y. Lu, G. Song et al., “Association of RBP4 levels with increased arterial stiffness in adolescents with family history of type 2 diabetes,” *International Angiology*, vol. 35, no. 6, pp. 546–551, 2016.
  - [31] M. A. M. Domingos, M. Queiroz, P. A. Lotufo, I. J. Benseñor, and S. M. . O. Titan, “Serum RBP4 and CKD: association with insulin resistance and lipids,” *Journal of Diabetes and its Complications*, vol. 31, no. 7, pp. 1132–1138, 2017.
  - [32] G. Liu, M. Ding, S. E. Chiuvé et al., “Plasma levels of fatty acid-binding protein 4, retinol-binding protein 4, high-molecular-weight adiponectin, and cardiovascular mortality among

- men with type 2 diabetes,” *Arteriosclerosis, Thrombosis, and Vascular Biology*, vol. 36, no. 11, pp. 2259–2267, 2016.
- [33] J. J. Fuster, N. Ouchi, N. Gokce, and K. Walsh, “Obesity-induced changes in adipose tissue microenvironment and their impact on cardiovascular disease,” *Circulation Research*, vol. 118, no. 11, pp. 1786–1807, 2016.
- [34] T. F. Zabetian, M. J. Mahmoudi, N. Rezaei, and M. Mahmoudi, “Retinol binding protein 4 in relation to diet, inflammation, immunity, and cardiovascular diseases,” *Advances in Nutrition*, vol. 6, no. 6, pp. 748–762, 2015.
- [35] H. Wessel, A. Saeed, J. Heegsma, M. A. Connelly, K. N. Faber, and R. P. F. Dullaart, “Plasma levels of retinol binding protein 4 relate to large VLDL and small LDL particles in subjects with and without type 2 diabetes,” *Journal of Clinical Medicine*, vol. 8, no. 11, p. 1792, 2019.
- [36] W. Zhou and S. D. Ye, “Relationship between serum 25-hydroxyvitamin D and lower extremity arterial disease in type 2 diabetes mellitus patients and the analysis of the intervention of vitamin D,” *Journal of Diabetes Research*, vol. 2015, Article ID 815949, 6 pages, 2015.
- [37] W. Zhou, S. Ye, and J. Li, “Expression of retinol binding protein 4 and nuclear factor- $\kappa$ B in diabetic rats with atherosclerosis and the intervention effect of pioglitazone,” *Experimental and Therapeutic Medicine*, vol. 12, no. 2, pp. 1000–1006, 2016.
- [38] D. Gao, G. Hao, Z. Meng et al., “Rosiglitazone suppresses angiotensin II-induced production of KLF5 and cell proliferation in rat vascular smooth muscle cells,” *PLoS One*, vol. 10, no. 4, article e0123724, 2015.
- [39] A. J. Richard and J. M. Stephens, “Emerging roles of JAK-STAT signaling pathways in adipocytes,” *Trends in Endocrinology and Metabolism*, vol. 22, no. 8, pp. 325–332, 2011.
- [40] M. Trovati, G. Doronzo, C. Barale, C. Vaccheris, I. Russo, and F. Cavalot, “Leptin and vascular smooth muscle cells,” *Current Pharmaceutical Design*, vol. 20, no. 4, pp. 625–634, 2014.
- [41] P. A. Martínez-Neri, G. López-Rincón, R. Mancilla-Jiménez et al., “Prolactin modulates cytokine production induced by culture filtrate proteins of *M. bovis* through different signaling mechanisms in THP1 cells,” *Cytokine*, vol. 71, no. 1, pp. 38–44, 2015.
- [42] F. Li, K. Xia, M. S. A. Sheikh, J. Cheng, C. Li, and T. Yang, “Involvement of RBP4 in hyperinsulinism-induced vascular smooth muscle cell proliferation,” *Endocrine*, vol. 48, no. 2, pp. 472–482, 2015.
- [43] R. K. Randolph and A. C. Ross, “Vitamin A status regulates hepatic lecithin: retinol acyltransferase activity in rats,” *Journal of Biological Chemistry*, vol. 266, no. 25, pp. 16453–16457, 1991.
- [44] R. Kawaguchi, M. Zhong, M. Kassai, T. M. Stepanian, and H. Sun, “Differential and isomer-specific modulation of vitamin a transport and the catalytic activities of the RBP receptor by Retinoids,” *The Journal of Membrane Biology*, vol. 246, no. 8, pp. 647–660, 2013.
- [45] O. I. Bratchikov, S. O. Artishchev, I. A. Tyuzikov, Kursk State Medical University of Minzdrav of Russia, Kursk, Russia, and Clinic of Professor Kalinchenko, Moscow, Russia, “Vitamin D deficiency, metabolic syndrome, and prostate adenoma: current epidemiological trends and pathophysiological mechanisms of interaction,” *Urologiia (Moscow, Russia: 2018)*, vol. 4\_2018, no. 4, pp. 179–185, 2018.
- [46] I. Mozos, D. Jianu, C. Gug, and D. Stoian, “Links between high-sensitivity C-reactive protein and pulse wave analysis in middle-aged patients with hypertension and high normal blood pressure,” *Disease Markers*, vol. 2019, Article ID 2568069, 9 pages, 2019.
- [47] M. A. Abbas, “Physiological functions of vitamin D in adipose tissue,” *The Journal of Steroid Biochemistry and Molecular Biology*, vol. 165, no. Part B, pp. 369–381, 2017.
- [48] A. Mousa, N. Naderpoor, K. Wilson et al., “Vitamin D supplementation increases adipokine concentrations in overweight or obese adults,” *European Journal of Nutrition*, vol. 59, no. 1, pp. 195–204, 2020.
- [49] E. Daneshzad, A. Farsad-Naeimi, J. Heshmati, K. Mirzaei, Z. Maghbooli, and S. A. Keshavarz, “The association between dietary antioxidants and adipokines level among obese women,” *Diabetes and Metabolic Syndrome: Clinical Research and Reviews*, vol. 13, no. 2, pp. 1369–1373, 2019.
- [50] J. Kong, Y. Chen, G. Zhu, Q. Zhao, and Y. C. Li, “1, 25-Dihydroxyvitamin D3 upregulates leptin expression in mouse adipose tissue,” *Journal of Endocrinology*, vol. 216, no. 2, pp. 265–271, 2013.
- [51] D. Metheniti, S. Sakka, M. Dracopoulou et al., “Decreased circulating 25-(OH) vitamin D concentrations in obese female children and adolescents: positive associations with retinol binding protein-4 and neutrophil gelatinase-associated Lipocalin,” *Hormones*, vol. 12, no. 3, pp. 397–404, 2013.
- [52] Z. Zhang, F. Chen, J. Li et al., “1,25(OH)<sub>2</sub>D<sub>3</sub> suppresses proinflammatory responses by inhibiting Th1 cell differentiation and cytokine production through the JAK/STAT pathway,” *American Journal of Translational Research*, vol. 10, no. 8, pp. 2737–2746, 2018.



## Research Article

# The Hypoxia-Related Gene COL5A1 Is a Prognostic and Immunological Biomarker for Multiple Human Tumors

Hua Zhu <sup>1,2</sup>, Xinyao Hu <sup>3</sup>, Shi Feng <sup>2</sup>, Zhihong Jian <sup>2</sup>, Ximing Xu <sup>3</sup>, Lijuan Gu <sup>4,5</sup>,  
and Xiaoxing Xiong <sup>1,2</sup>

<sup>1</sup>Department of Neurosurgery, The Affiliated Huzhou Hospital, Zhejiang University School of Medicine (Huzhou Central Hospital), Huzhou, China

<sup>2</sup>Department of Neurosurgery, Renmin Hospital of Wuhan University, Wuhan, China

<sup>3</sup>Cancer Center, Renmin Hospital of Wuhan University, Wuhan, China

<sup>4</sup>Central Laboratory, Renmin Hospital of Wuhan University, Wuhan, China

<sup>5</sup>Department of Anesthesiology, Renmin Hospital of Wuhan University, Wuhan, China

Correspondence should be addressed to Lijuan Gu; [gulijuan@whu.edu.cn](mailto:gulijuan@whu.edu.cn) and Xiaoxing Xiong; [xiaoxingxiong@whu.edu.cn](mailto:xiaoxingxiong@whu.edu.cn)

Received 21 July 2021; Revised 15 October 2021; Accepted 14 December 2021; Published 17 January 2022

Academic Editor: Bin Duan

Copyright © 2022 Hua Zhu et al. This is an open access article distributed under the Creative Commons Attribution License, which permits unrestricted use, distribution, and reproduction in any medium, provided the original work is properly cited.

**Background.** Collagen type V alpha 1 chain (COL5A1) is a hypoxia-related gene (a collagen family protein) and participates in the formation of the extracellular matrix. Although some evidence supports a significant role for COL5A1 in the progression of several cancers, a pan-cancer analysis of COL5A1 is not currently available. Herein, we aimed to assess the prognostic value of COL5A1 in 33 human cancers and to investigate its underlying immunological function. **Methods.** Through multiple bioinformatics methods, we analyzed the data from Oncomine, TCGA, CCLE, HPA, DNMIIVD, and cBioPortal database to explore the potential underlying carcinogenic effect of COL5A1, including the relevance of COL5A1 to the outcome, DNA methylation, tumor microenvironment, immune cells infiltration, and drug sensitivity in 33 human cancers. The effects of COL5A1 on glioma cell proliferation, migration, and invasion were verified in cellular experiments. **Results.** Our findings indicated that COL5A1 was expressed at high levels in 13 cancers and was negatively related to the prognosis of 11 cancers. Additionally, COL5A1 was coexpressed with genes encoding the major histocompatibility complex, immune activators, immune suppressors, chemokines, chemokine receptors, mismatch repair genes, and immune checkpoints. We also identified different roles for COL5A1 in the immunocyte infiltration in different cancers. The correlation between COL5A1 and drug sensitivity was found in several cancers. COL5A1 potentially influenced the tumor progression through immune-related pathways, negative regulation of immune system processes, chemokine signaling pathways, JAK-STAT pathways, T cell receptor pathways, lymphocyte migration, and antigen processing and presentation, among other processes. **Conclusions.** Based on our study, COL5A1 may be employed as a prognostic marker in different malignancies because of its impact on tumorigenesis and immune cell infiltration and have implications for cancer immune checkpoint inhibitors and chemotherapy.

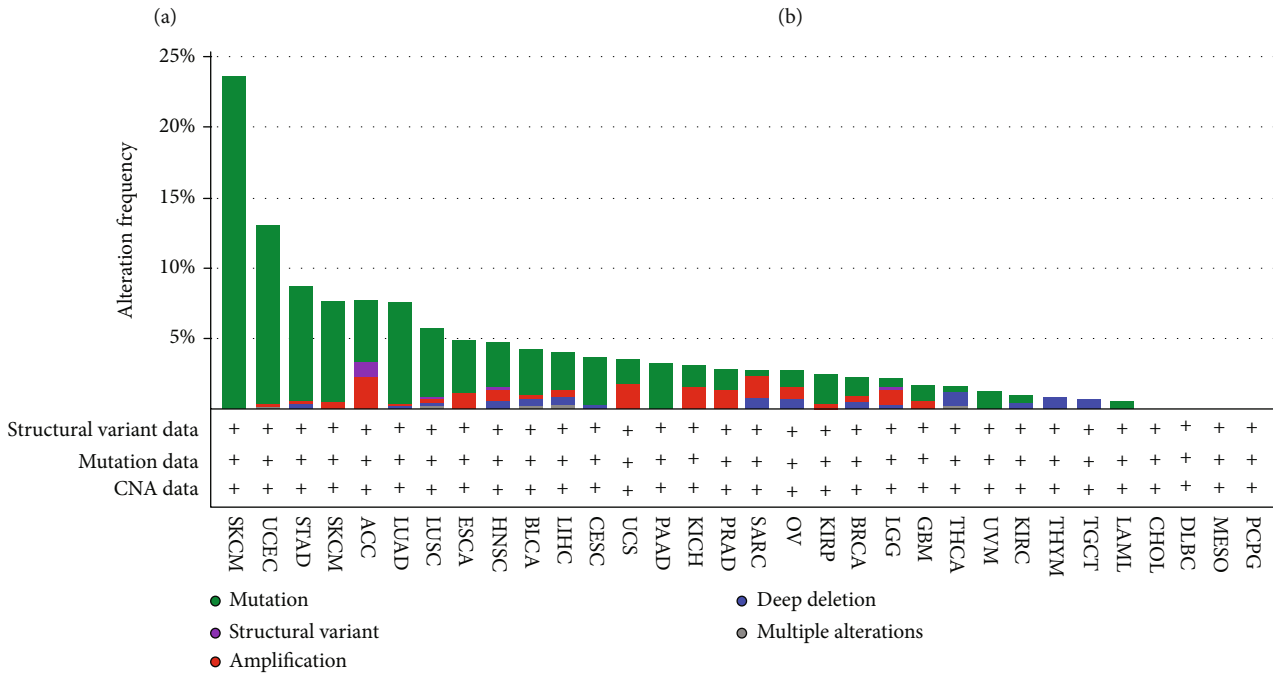
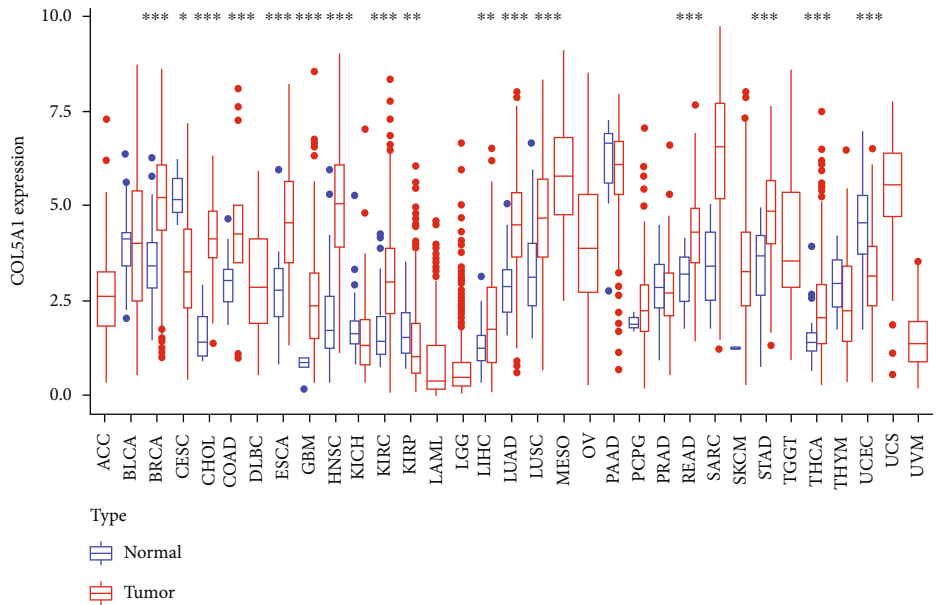
## 1. Introduction

Malignant tumor is a leading cause of death and a main cause of poor quality of life of patients in many countries worldwide, but no absolute cure is currently available for malignant tumors [1], such as central nervous tumors with neurorestorative treatment [2, 3]. Immunotherapy for tumors has recently emerged as a new approach to oncology treatment, specifically immune checkpoint blockade (ICB) therapy [4]. The emer-

gence and refinement of gene expression databases have enabled explorations of new immunotherapeutic targets through pan-cancer analysis of the expression of particular gene and assessments of its relevance to patients' prognoses and potential mechanisms [5, 6].

Collagen type V alpha 1 chain (COL5A1), a collagen family protein (the most abundant matrix protein polymer in vertebrates), participates in the formation of extracellular matrix [7]. Additionally, COL5A1 was also reported to be a

| Analysis type by cancer     | Cancer vs. normal |    |
|-----------------------------|-------------------|----|
| Bladder cancer              |                   | 2  |
| Brain and CNS cancer        | 14                |    |
| Breast cancer               |                   |    |
| Cervical cancer             |                   |    |
| Colorectal cancer           | 7                 | 1  |
| Esophageal cancer           | 6                 |    |
| Gastric cancer              | 6                 |    |
| Head and neck cancer        | 4                 |    |
| Kidney cancer               | 1                 | 1  |
| Leukemia                    | 6                 | 2  |
| Liver cancer                | 3                 |    |
| Lung cancer                 | 5                 |    |
| Lymphoma                    | 4                 |    |
| Melanoma                    |                   | 2  |
| Myeloma                     |                   |    |
| Other cancer                | 7                 |    |
| Ovarian cancer              | 2                 |    |
| Pancreatic cancer           | 3                 |    |
| Prostate cancer             |                   | 1  |
| Sarcoma                     | 9                 | 1  |
| Significant unique analyses | 80                | 11 |
| Total unique analyses       | 313               |    |



(c)  
FIGURE 1: Continued.

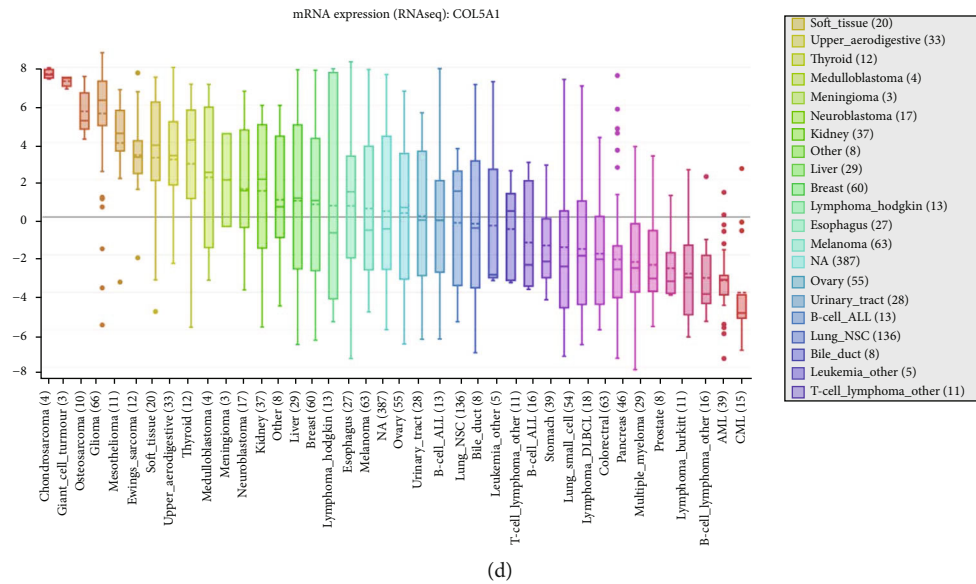


FIGURE 1: Differential COL5A1 expression in normal and tumor tissues. (a) COL5A1 mRNA expression was elevated in most tumors than normal tissues. (b) Different levels of COL5A1 expression in various human tumors and normal tissues. (c) The alteration frequency of COL5A1 in different cancers. (d) Expression of the COL5A1 mRNA in various cell lines. \* $p < 0.05$ , \*\* $p < 0.01$ , and \*\*\* $p < 0.001$ .

hypoxia-related gene [8]. Hypoxia is known to trigger the production of reactive oxygen species [9], which play an important role in cancer biology. Collagen deposition is often regarded as a pathological characteristic in tumor microenvironment [10]. In addition, chemotherapy resistance is associated with increased tissue stiffness mediated by specific collagen cross-linking. Collagen V is one of the components of fibril-forming collagen and has a critical role in extracellular matrix organization by forming copolymers with collagen I or II to regulate the length and abundance of heterotypic collagenous protofibrils [11].  $\alpha1(V)$ ,  $\alpha2(V)$ , and  $\alpha3(V)$  polypeptide chains, encoded by COL5A1, COL5A2, and COL5A3, respectively, comprise the protein of collagen V [12]. As previously reported, COL5A1 is associated with head and neck squamous cell carcinoma (HNSC), oral squamous cell carcinoma [13], breast cancer [14], and gastric cancer [15]. Furthermore, COL5A1 has recently been reported to be a key gene correlated with macrophage infiltration and M2 polarization and is related to the proportion of infiltrating immunocyte in ovarian cancer (OV), indicating that COL5A1 may be an immunotherapeutic target in OV [16]. However, the role of COL5A1 in other human cancers is still unidentified. The prognostic predictive value of COL5A1 across cancers has not been adequately studied. Therefore, more work is urgently needed to investigate the role of COL5A1 in human tumors.

Tumor-infiltrating immune cells (TIIC) are important components of the tumor microenvironment (TME) and monitor tumor cells during their life cycle, and cancer only develops when immune cells cannot destroy precancerous cells [17]. The infiltration levels of TIIC in TME also impact on the prognoses of cancers. For example, high levels of B, CD4+, and dendritic cells infiltration are associated with a better outcome in thymomas, which may be partially regulated by ASF1B [6]. Lower grade glioma (LGG) patients with

high TUBA1C expression may have a better response to ICB [18]. More and more versatile immunotherapeutic targets for human tumors need to be discovered. Herein, we mainly used numerous silico analyses to discover the role of COL5A1 in the prognosis, TIIC infiltration, and drug sensitivity in 33 human cancers.

## 2. Methods

**2.1. Data Collection and Different Expression Analysis.** Oncomine (<https://www.oncomine.org/>), an online cancer microarray database [19], was employed to analyze the COL5A1 expression in 33 human tumors as we used to do [20]. We downloaded mRNA expression data and clinical information from the UCSC Xena website (<https://xena.ucsc.edu/>). Next, we extracted and integrated COL5A1 expression data in TCGA (<https://tcga.xenahubs.net>) through the Perl software to perform pan-cancer analysis. The “Wilcoxon test” was employed to evaluate the differences in COL5A1 mRNA expression levels in 33 cancer types. Then, mRNA sequencing data from different cancer cell lines were assessed using CCLE (<https://portals.broadinstitute.org/ccle>). The R package “ggpubr” was employed for the box diagram. Mutation in COL5A1 in 33 cancers was investigated through cBioPortal (<https://www.cbioportal.org>).

**2.2. Immunohistochemical (IHC) Staining.** Images of immunohistochemical staining for the COL5A1 protein were used for expression analyses, and the differences in the COL5A1 protein level were assessed in normal and eight tumor tissues, including bladder urothelial carcinoma (BLCA), colon adenocarcinoma (COAD), glioblastoma multiforme (GBM), liver hepatocellular carcinoma (LIHC), ovarian cancer (OV), prostate adenocarcinoma (PRAD), stomach

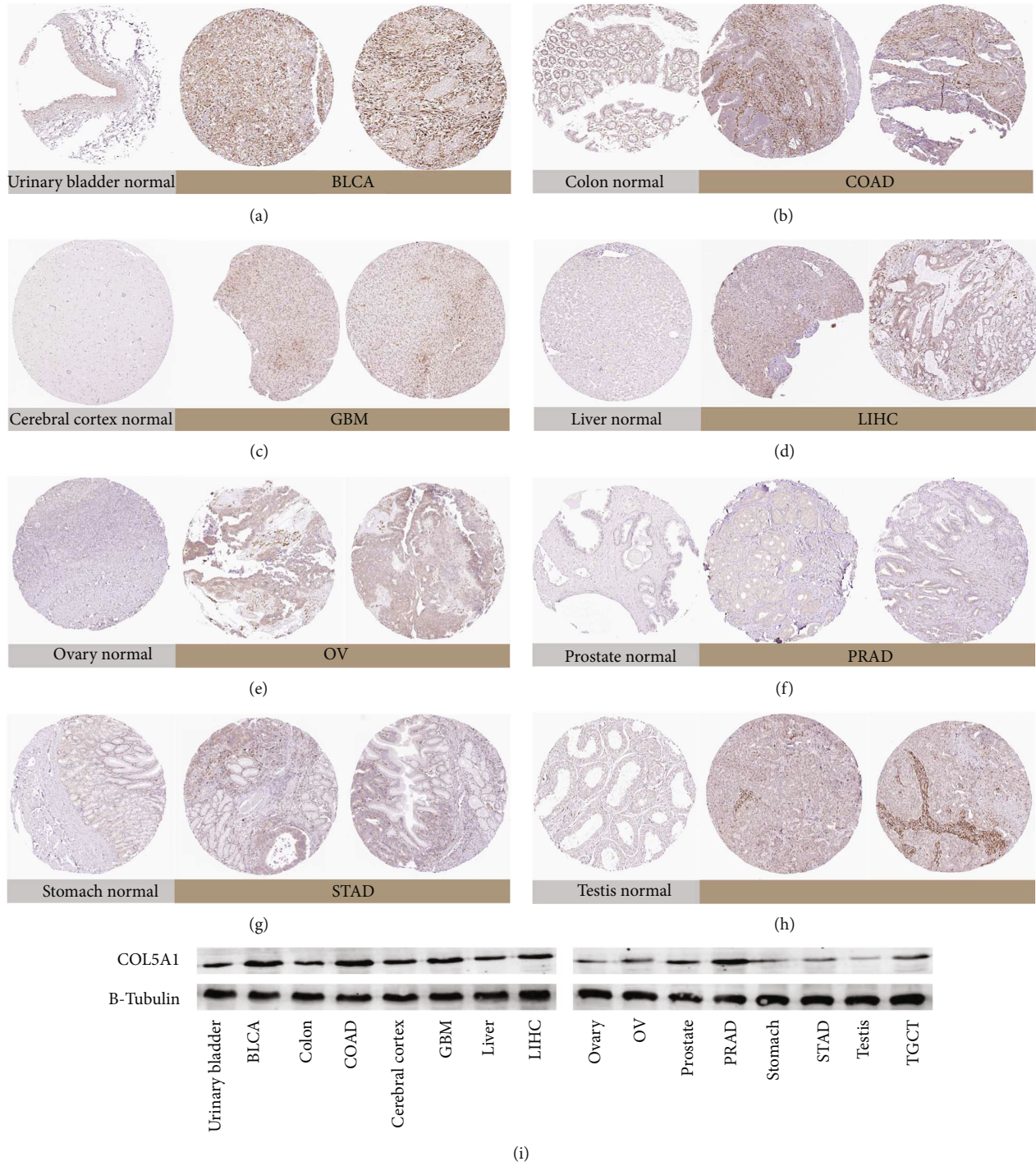


FIGURE 2: Continued.

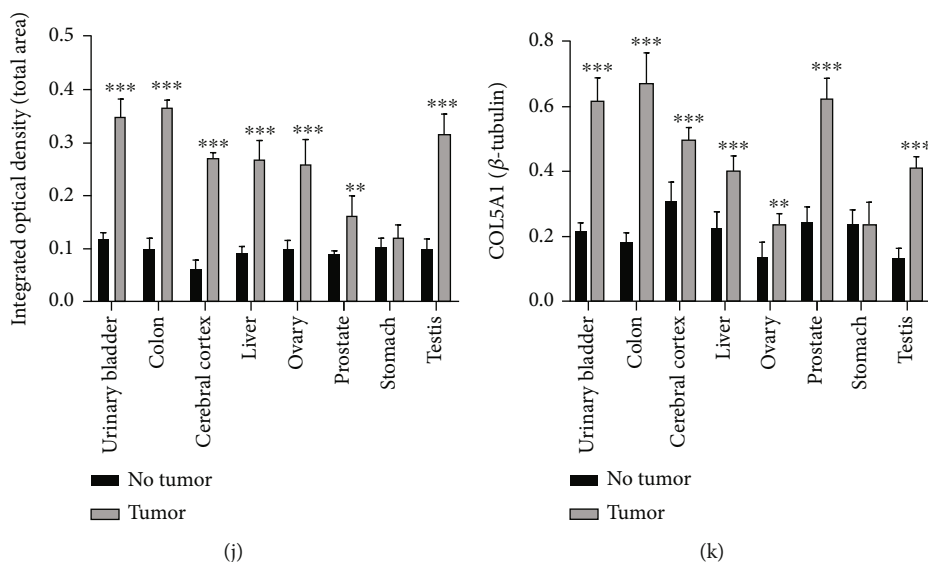


FIGURE 2: Representative photographs of immunohistochemical staining and western blots of different normal tissues (left panels) and tumor tissues (right panels). The level of the COL5A1 protein was increased in bladder urothelial carcinoma (BLCA), colon adenocarcinoma (COAD), glioblastoma multiforme (GBM), liver hepatocellular carcinoma (LIHC), ovarian cancer (OV), prostate adenocarcinoma (PRAD), and testicular germ cell tumors (TGCTs). (a) Urinary bladder. (b) Colon. (c) Cerebral cortex. (d) Liver. (e) Ovary. (f) Prostate. (g) Stomach. (i) Testis. (j) Quantitative analysis of immunohistochemical staining from the HPA database.  $n = 3$  samples per normal group,  $n = 5$  samples per tumor group. (i, k) Western blot results showing the expression of COL5A1,  $n = 5$ , \*\* $p < 0.01$  and \*\*\* $p < 0.001$ .

adenocarcinoma (STAD), and testicular germ cell tumors (TGCTs) from the HPA (<http://www.proteinatlas.org/>). Three normal tissue and five tumor tissue samples were randomly chosen for quantitative analysis.

**2.3. Western Blot Analysis.** U251 cells, tumor, and paraneoplastic tissues were collected (representative clinicopathological data are presented in Figure S1), homogenized, and then lysed on ice in cold RIPA buffer. Next, the samples were separated on gels and then transferred onto polyvinylidene difluoride membranes. Membranes were blocked by blocking buffer for 1 hour and then incubated with anti-COL5A1 (Sigma-Aldrich; Merck KGaA) and anti-β-tubulin (Cell Signaling Technology, Boston, USA) primary antibodies at 4°C overnight. Membranes were then incubated with secondary antibody (diluted 1:10000; Li-Cor Bioscience, USA) for 1 hour. Membranes were assessed with the Odyssey software (LI-COR, Lincoln, NE, USA).

**2.4. Identification of the Correlation between COL5A1 Expression and the Clinicopathological Characteristics or Survival of Patients with Various Cancers.** Survival information for each sample in TCGA was used to elucidate the relationship between COL5A1 expression and prognosis of patients with different cancers. Overall survival (OS), disease-specific survival (DSS), disease-free interval (DFI), and progression-free interval (PFI) were analyzed. The Kaplan–Meier (KM) survival curves and log-rank test were employed to analyze the survival of patients ( $p < 0.05$ ) through R packages “survminer” and “survival.” Subsequently, “survival” and “forestplot” R packages were applied for the Cox analysis to verify the correlation of COL5A1

expression with survival. High or low expressions are defined by median. R packages “ggpubr” and “limma” were employed for the clinicopathological correlation analysis. The DNMIVD dataset (<http://www.unimd.org/dnmivd/>) was applied to assess the DNA methylation levels of COL5A1 and the association between COL5A1 methylation and prognosis.

**2.5. Correlation Analysis of COL5A1 with Tumor Mutation Burden (TMB) or Microsatellite Instability (MSI).** The correlation of COL5A1 with TMB or MSI was analyzed as previously described [6, 20]. We also applied cBioPortal to investigate the correlation between COL5A1 mutations and prognosis.

**2.6. Exploration of Association between COL5A1 and TME or Infiltration of TIIC.** We employed the ESTIMATE algorithm and the R packages “estimate” and “limma” to evaluate immune and stromal scores [21] as we used to [6, 20, 22]. For more reliable immune score evaluation, we then employed the “immuneconv” R package that integrated the six algorithms, including TIMER, xCell, MCP-counter, CIBERSORT, EPIC, and quanTIseq. We next analyzed the correlation of COL5A1 expression with the TME or TIIC infiltration by R packages “ggplot2,” “ggpubr,” and “ggExtra.”

**2.7. Pathway Enrichment Analysis and Coexpression of COL5A1 with Immune-Related, Mismatch Repair (MMR) Genes, and Immune Checkpoint-Related Genes in Tumors.** Gene Ontology (GO) and Kyoto Encyclopedia of Genes and Genomes (KEGG) and the coexpression of COL5A1 with immune checkpoint genes and immune-

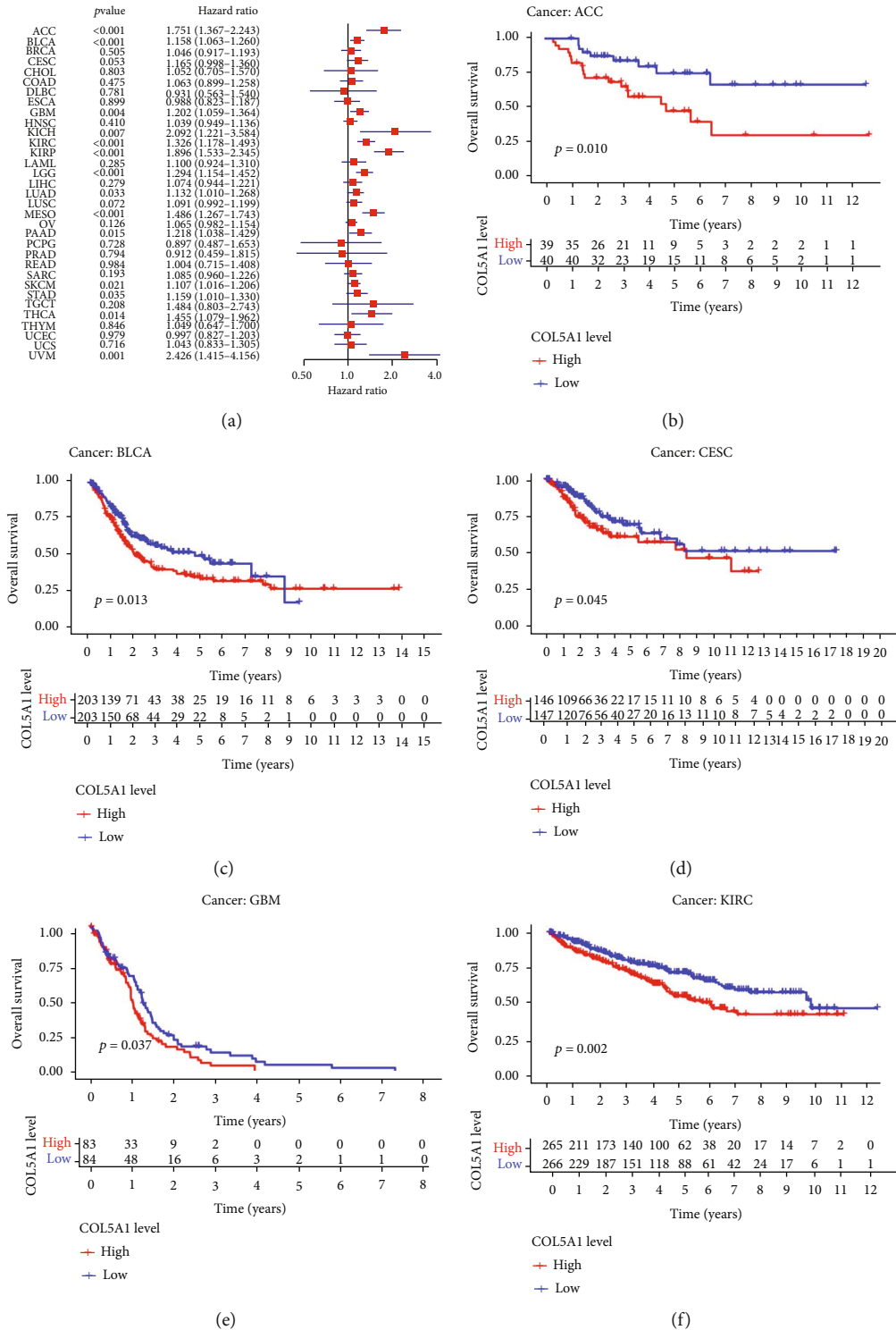


FIGURE 3: Continued.

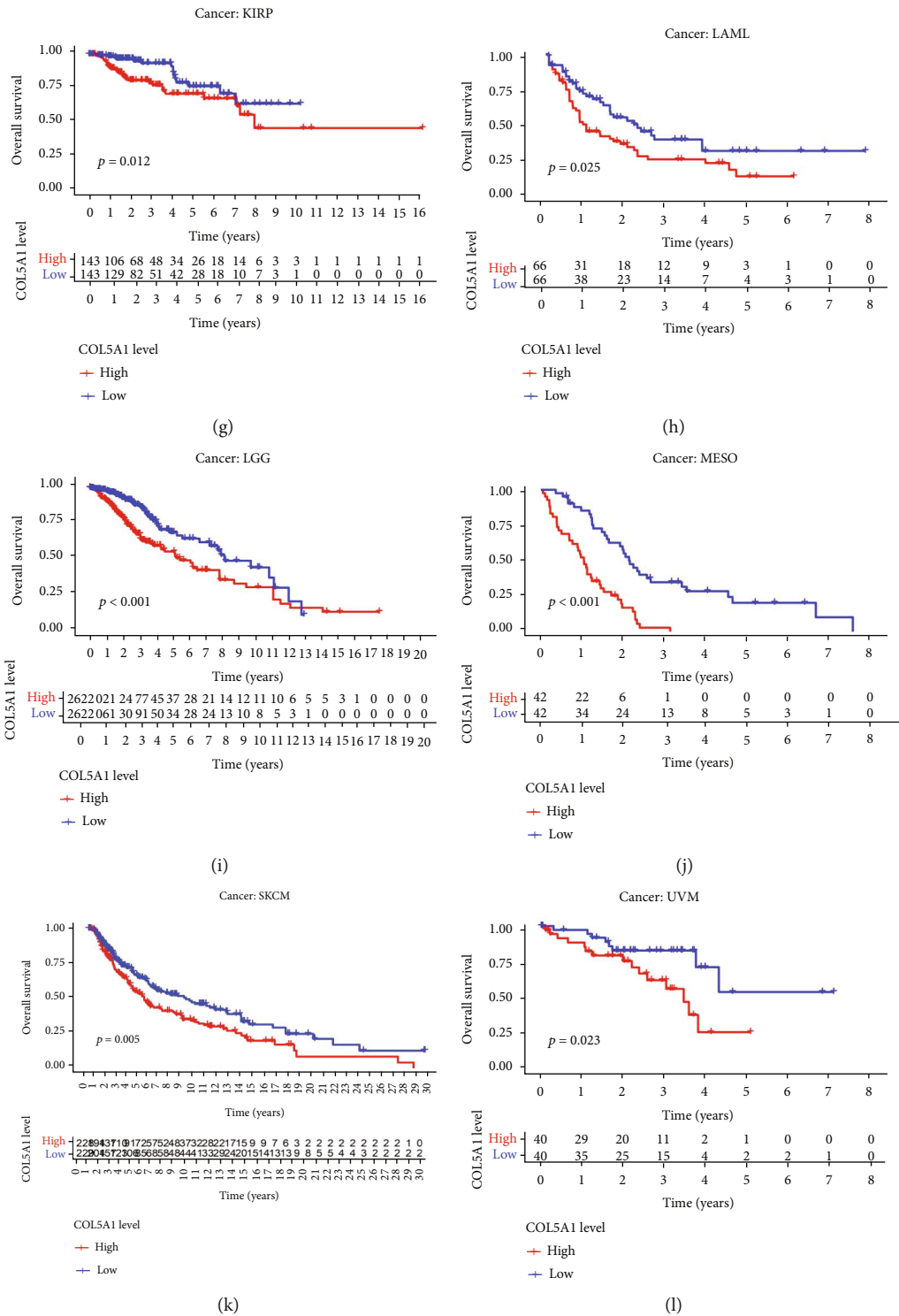
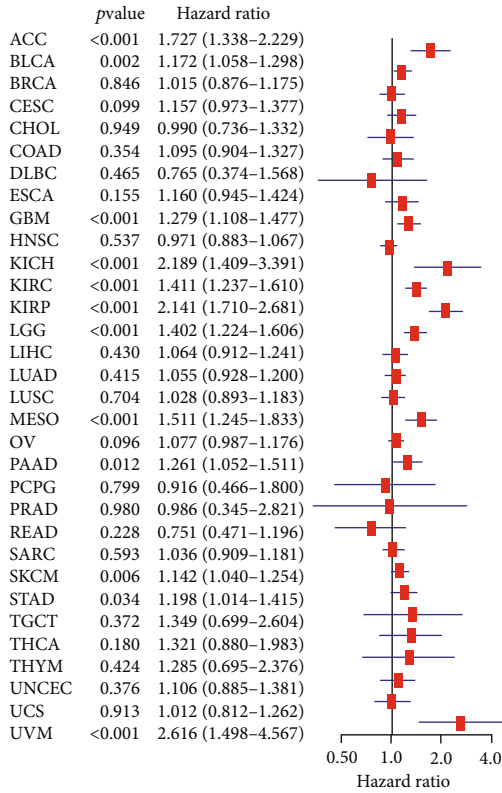


FIGURE 3: Correlations of COL5A1 with OS. (a) Forest plots and KM analyses (b–l) of the correlations of COL5A1 with OS in various human cancers.

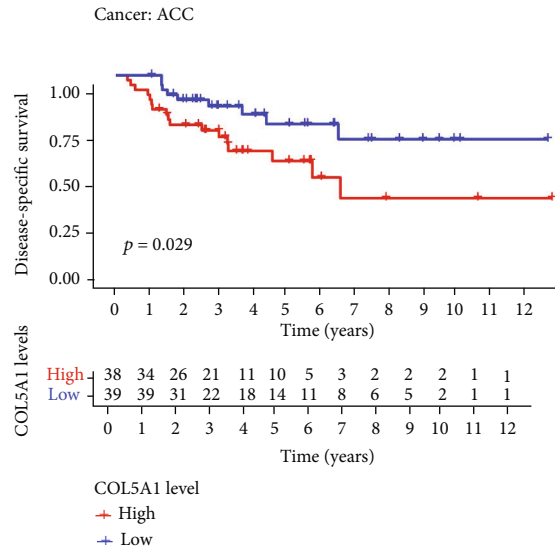
related genes were conducted as we described previously [6, 20].

2.8. Predicting the Correlation of COL5A1 with Drug Sensitivity. We predicted the chemotherapeutic response for samples of cancers which had a correlation of COL5A1

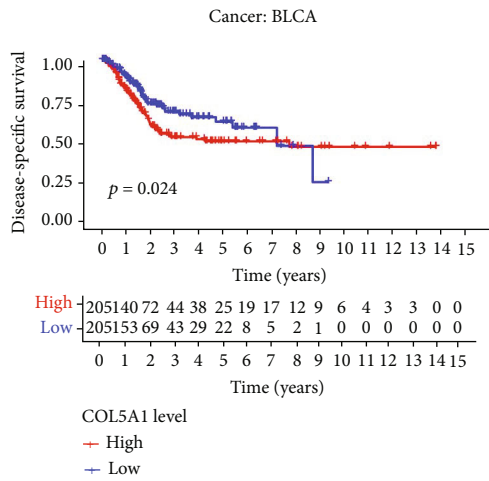
with OS based on the Genomics of Drug Sensitivity in Cancer (GDSC) (<https://www.cancerrxgene.org/>). The prediction was implemented by the R package “pRRophetic.” All parameters were set by the default values with removal of the batch effect of “combat” and tissue type of “allSolidTumours,” and we generalized duplicate gene expression to mean value [23].



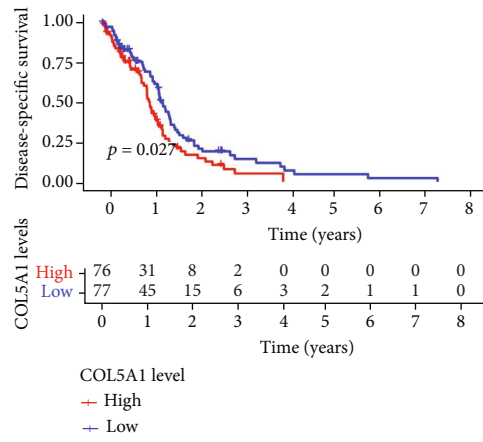
(a)



(b)



(c)



(d)

FIGURE 4: Continued.



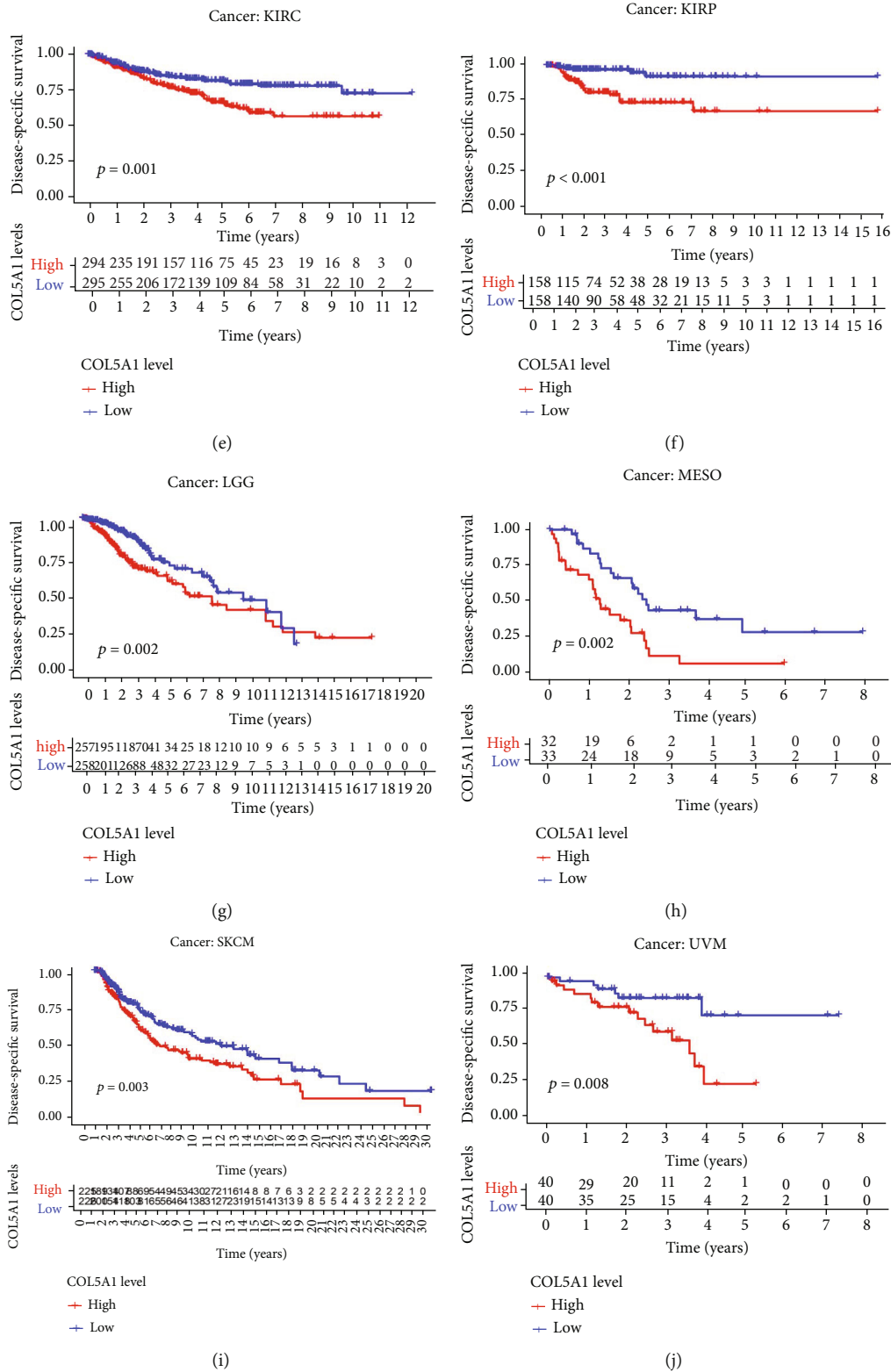
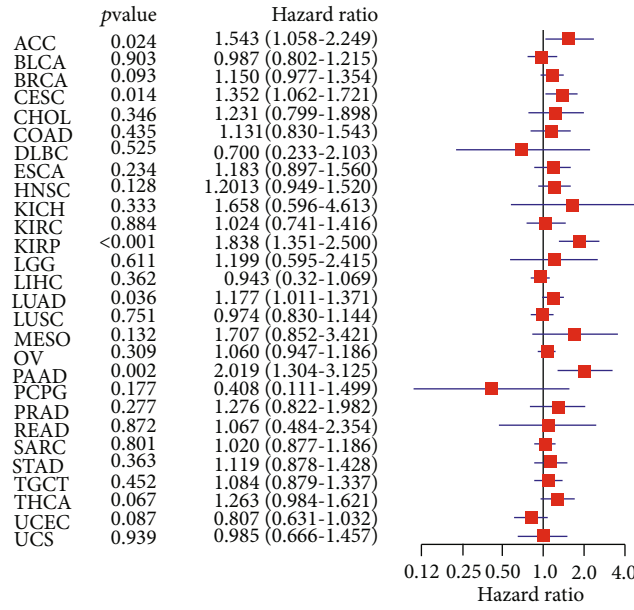
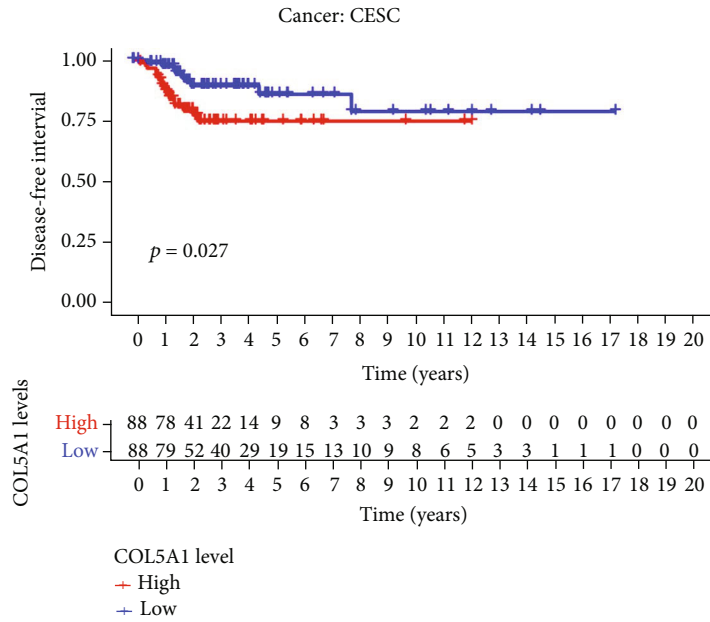


FIGURE 4: Correlations between COL5A1 and DSS. (a) Forest plots and KM analyses (b–j) of the relationships between COL5A1 and DSS.

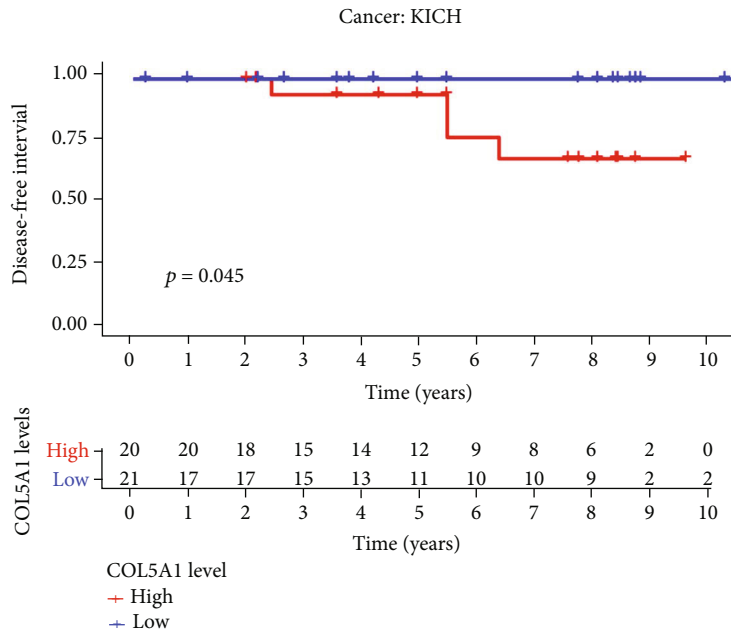


(a)

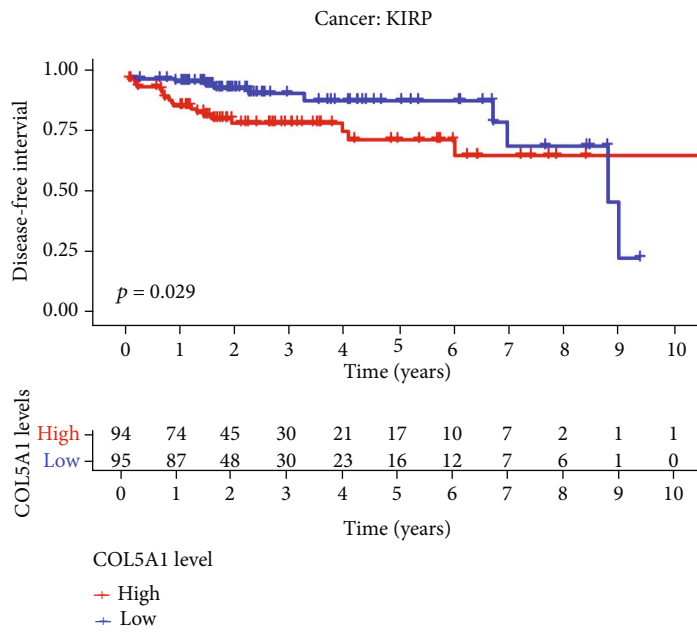


(b)

FIGURE 5: Continued.



(c)



(d)

FIGURE 5: Continued.

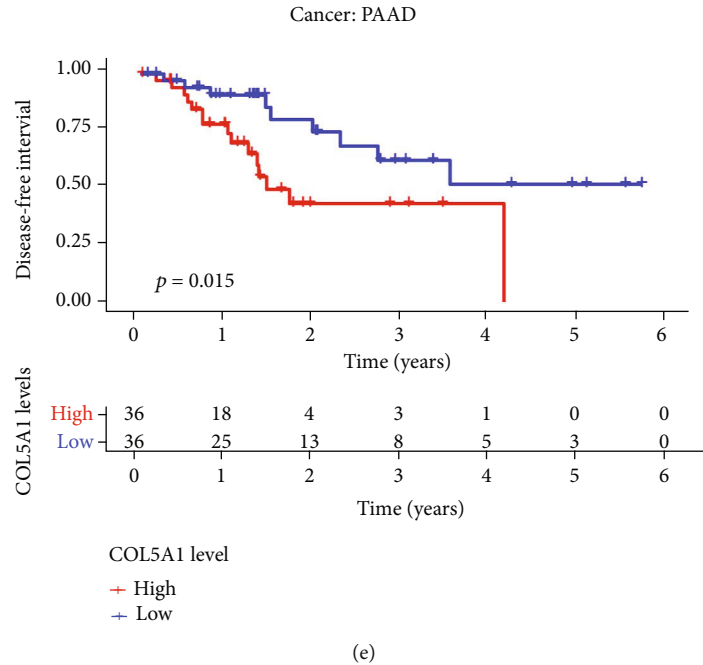


FIGURE 5: Correlations between COL5A1 and DFI. (a) Forest plots and KM analyses (b–e) of the relationships between COL5A1 and DFI.

2.9. *qRT-PCR, Wound Healing, and Transwell Migration to Confirm the Role of COL5A1 in U251 Cells.* U251 cell line was obtained from Genoscreen (Shanghai, China). Cells were cultured in DMEM with 10% FBS and 100 U/mL penicillin-streptomycin in an incubator at 37°C with 5% CO<sub>2</sub>. The sequence of siRNA to knock down COL5A1 was 5'-AAGGAGAGGGGUGAGACCUAUA-3', and the sequence for control siRNA was 5'-CAGAGGGAGUGGGAGCCAAUAUUA-3' [24]. Lipofectamine 3000 was employed for cell transfection with siRNA-COL5A1 or siRNA-control. 48 hours after the transfection process, transfected cells were collected, and then the transfection efficiency was verified by western blotting and qRT-PCR assays. Then, the cells were plated in six-well plates until fused to 80%. The cells were scratched using a pipette tip and washed, then incubated at 37°C and 5% CO<sub>2</sub>. The viability of U251 cells was assessed by CCK-8 assay. After 24h, the picture of the wound was taken under a microscope.

qRT-PCR was carried out as a previous study [25]. The primer sequences were as follows: COL5A1, F: GCCCGGATGTCGCTTACAG, R: AAATGCAGACGCAGGGTACAG; GAPDH, F: GCACCGTCAAGGCTGAGAAC, R: TGGTGAAGACGCCAGTGGGA. The mRNA expression was quantified by normalizing it with the internal reference GAPDH expression.

Cell invasion assay was performed as we previously performed [26]. The cells were photographed at 200X magnification, and the number cells crossing membrane was counted in five random fields by ImageJ (version 1.61, NIH, Bethesda, MD, USA).

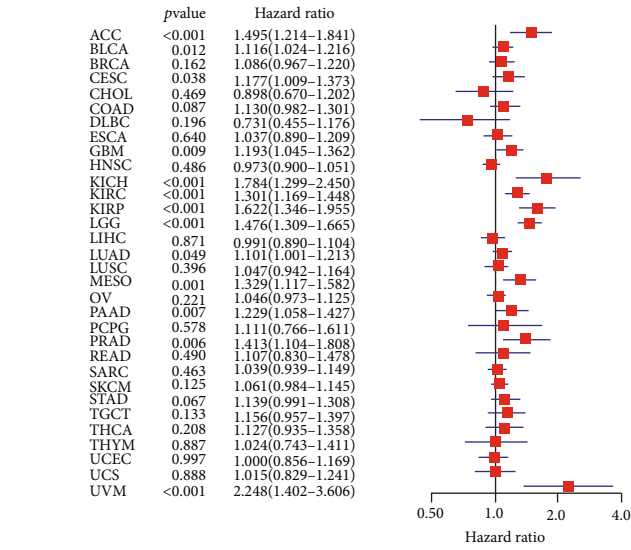
2.10. *Statistical Analysis.* All gene expression data were normalized by log<sub>2</sub> transformation. Experimental data were

presented as mean ± SD, and Student's *t*-test was employed for two-group comparison. KM analysis, Cox proportional hazards model, and log-rank test were performed for all survival analyses. Correlation between two variables was evaluated by Pearson's or Spearman's test. Statistical analyses were carried out using GraphPad Prism 8.0 (GraphPad Software Inc.) and R software (version 4.0.2).  $p < 0.05$  was defined as a significant difference.

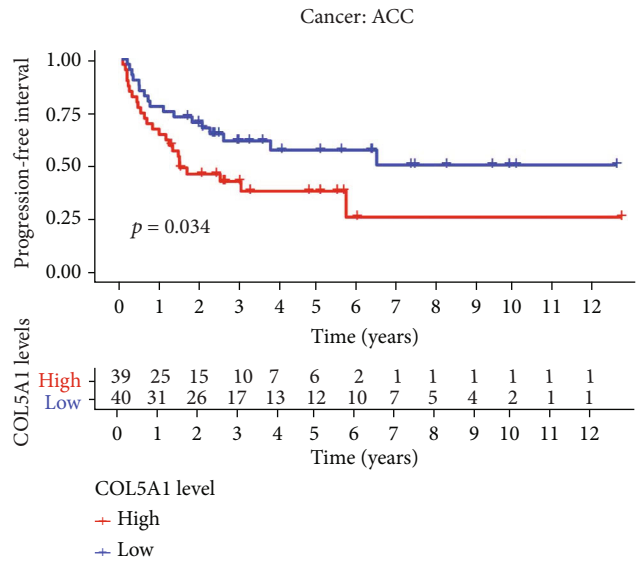
### 3. Results

3.1. *Differential Expression of COL5A1 in Normal and Tumor Tissues.* Firstly, OncoPrint was used to assess the COL5A1 expression in normal and tumor tissues. We found that COL5A1 was highly expressed in most human cancers, including the brain and central nervous system (CNS), breast, colorectal, esophageal, gastric, head and neck, kidney, leukemia, liver, lung, lymphoma, ovarian, pancreatic, sarcoma, and other cancers. It was interesting to note that lower expression of COL5A1 was also detected in bladder, colorectal, kidney, leukemia, melanoma, ovarian, sarcoma, and prostate cancer datasets (Figure 1(a)). Different data collection methods may be partially responsible for these contradictory results.

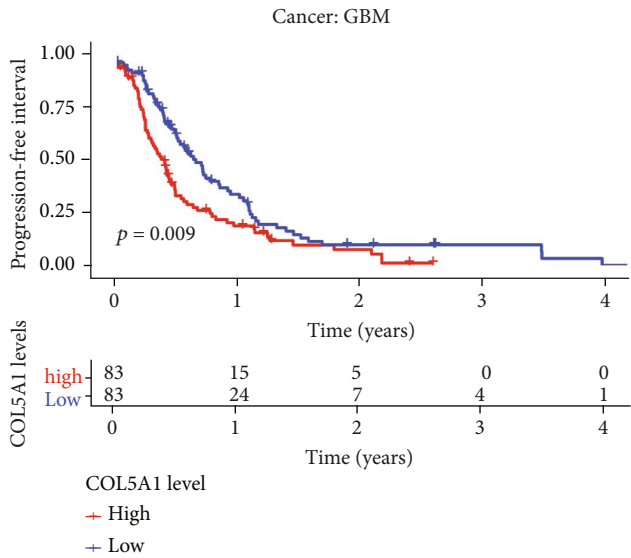
We analyzed the RNA sequencing data from TCGA through using the R software to further evaluate the expression of COL5A1 in different cancers. The results illustrated that COL5A1 was upregulated in 13 cancers, including breast invasive carcinoma (BRCA), cholangiocarcinoma (CHOL), COAD, esophageal carcinoma (ESCA), GBM, HNSC, kidney renal clear cell carcinoma (KIRC), LIHC, lung squamous cell carcinoma (LUSC), lung adenocarcinoma (LUAD), rectal adenocarcinoma (READ), STAD, and thyroid carcinoma (THCA). Meanwhile, lower COL5A1



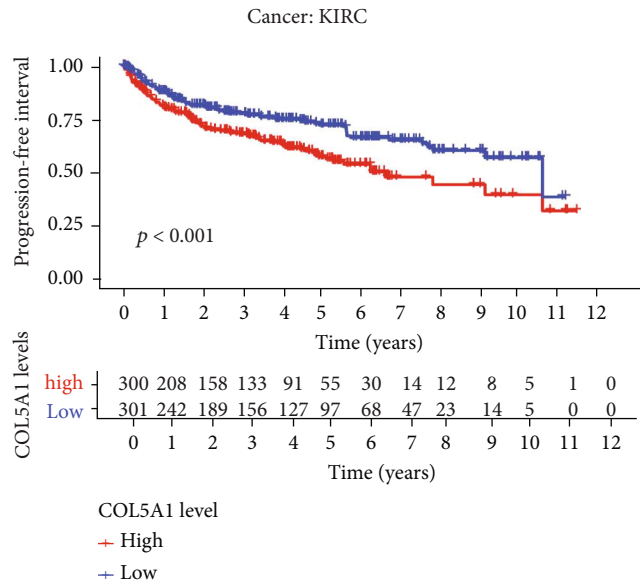
(a)



(b)

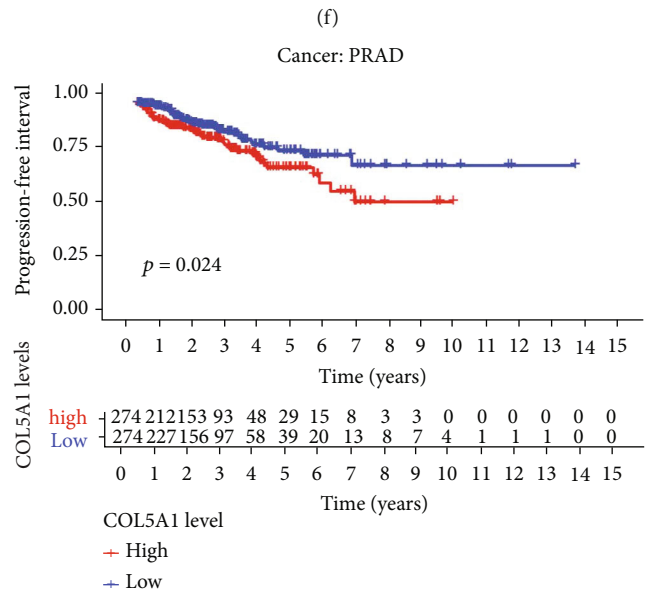
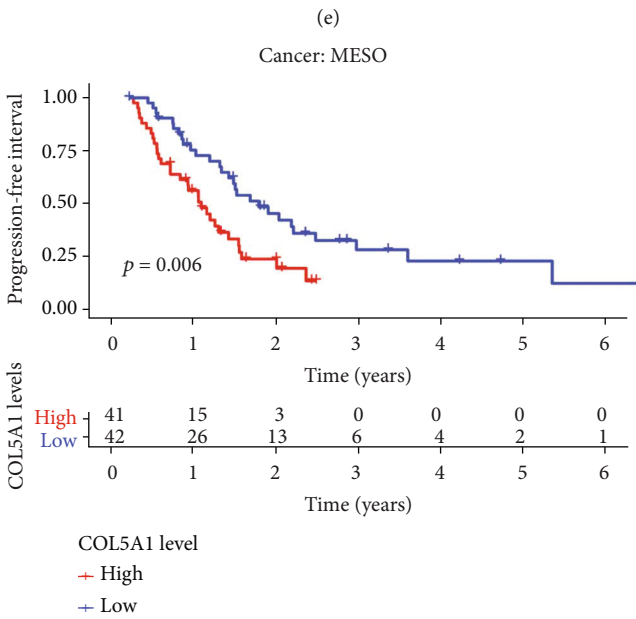
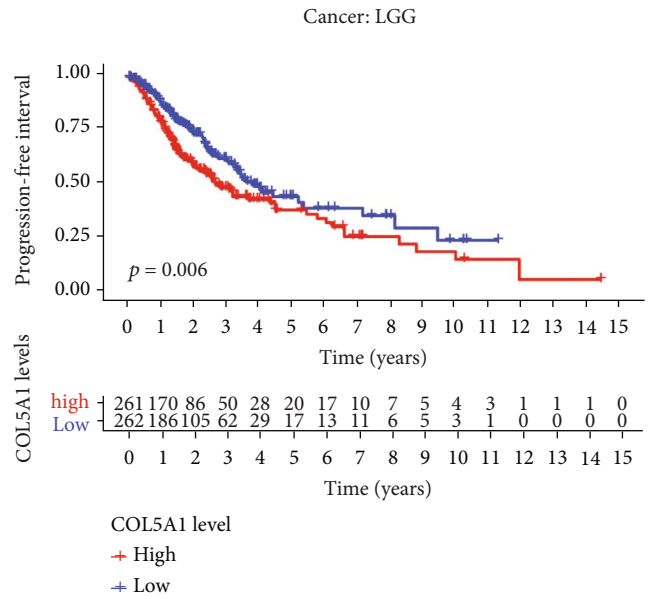
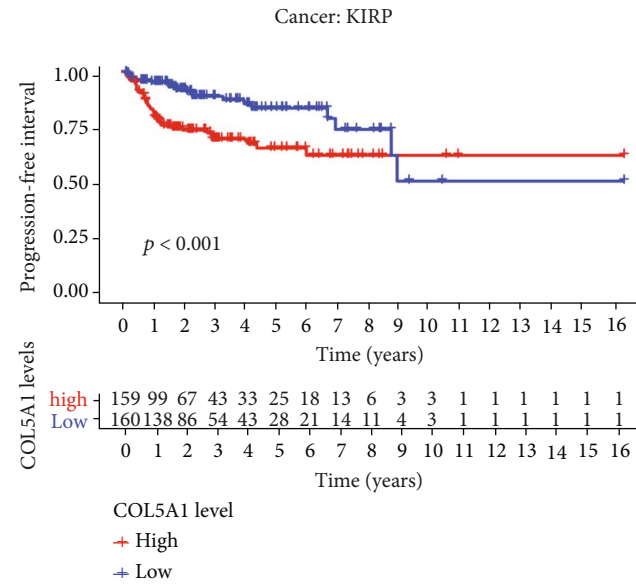


(c)



(d)

FIGURE 6: Continued.



(g)

(h)

FIGURE 6: Continued.

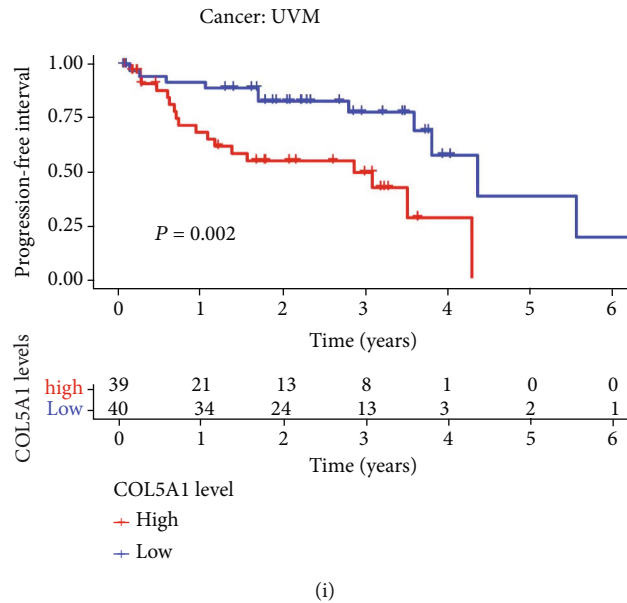


FIGURE 6: Correlation between COL5A1 and PFI. (a) Forest plots and KM analyses (b–i) of the relationships of COL5A1 with PFI.

expression was detected in 3 cancers compared to normal tissues, including cervical squamous cell carcinoma (CESC), uterine corpus endometrial carcinoma (UCEC), and kidney renal papillary cell carcinoma (KIRP). No significant difference was observed in some cancers with a few normal samples (e.g., only one normal tissue sample from patients with skin cutaneous melanoma (SKCM)); this may be because of the small sample size (Figure 1(b)). Then, we evaluated the changes in COL5A1 based on the cBioPortal database. COL5A1 expression was altered in 531 of 10,953 patients (~5%) included in TCGA. The highest alteration ratio was related to mutation, followed by amplifications and deep deletions. SKCM presented the highest alteration frequency among all cancers. Meanwhile, we assessed the mRNA sequence of COL5A1 in 33 cancers in the CCLE database. The five cancer cell lines with the highest mRNA expression of COL5A1 were chondrosarcoma, giant cell tumor, osteosarcoma, glioma, and mesothelioma (Figure 1(d)).

Subsequently, the IHC photographs in HPA dataset were analyzed to investigate the expression of the COL5A1 protein. The results from HPA and TCGA were consistent with each other. COL5A1 IHC staining was weak in the normal ovary, cerebral cortex, liver, prostate, and testis, while GBM, LIHC, PRAD, and TGCTs showed low COL5A1 IHC staining and OV exhibited moderate COL5A1 IHC staining. COL5A1 IHC staining was weak in the normal urinary bladder, colon, and stomach, while BLCA and COAD displayed strong COL5A1 IHC staining and STAD presented weak COL5A1 IHC staining (Figures 2(a)–2(h) and 2(j)). We further collected tissues for western blots, and the results verified the IHC staining from the HPA database (Figures 2(i) and 2(k)).

**3.2. Prognostic Value of COL5A1 in Various Cancers.** Survival analyses, including OS, DSS, DFI, and PFI, were carried out for patients with 33 cancers to investigate the correlation

between COL5A1 expression and prognosis. The Cox analysis illustrated that COL5A1 expression was closely correlated with the OS of patients with adrenocortical carcinoma (ACC), GBM, kidney chromophobe (KICH), KIRC, KIRP, LGG, LUAD, mesothelioma (MESO), pancreatic adenocarcinoma (PAAD), SKCM, STAD, THCA, and uveal melanoma (UVM) (Figure 3(a)). Furthermore, COL5A1 was a high-risk gene in these cancers, particularly UVM (hazard ratio = 2.426). In addition, KM plotter survival curves demonstrated that among the patients with ACC (Figure 3(b),  $p = 0.01$ ), BLCA (Figure 3(c),  $p = 0.013$ ), CESC (Figure 3(d),  $p = 0.045$ ), GBM (Figure 3(e),  $p = 0.037$ ), KIRC (Figure 3(f),  $p = 0.002$ ), KIRP (Figure 3(g),  $p = 0.012$ ), acute myeloid leukemia (LAML) (Figure 3(h),  $p = 0.025$ ), LGG (Figure 3(i),  $p < 0.001$ ), MESO (Figure 3(j),  $p < 0.001$ ), SKCM (Figure 3(k),  $p = 0.005$ ), and UVM (Figure 3(l),  $p = 0.023$ ), those with high COL5A1 expression experienced a shorter survival.

Moreover, in the patients with ACC, BLCA, GBM, KICH, KIRC, KIRP, LGG, MESO, PAAD, SKCM, STAD, and UVM, DSS survival analyses verified a correlation between high COL5A1 expression and poor prognosis (Figure 4(a)). KM analyses also revealed a correlation between high COL5A1 expression levels and adverse outcome of patients with ACC (Figure 4(b),  $p = 0.029$ ), BLCA (Figure 4(c),  $p = 0.024$ ), GBM (Figure 4(d),  $p = 0.027$ ), KIRC (Figure 4(e),  $p < 0.001$ ), KIRP (Figure 4(f),  $p < 0.001$ ), LGG (Figure 4(g),  $p = 0.002$ ), MESO (Figure 4(h),  $p = 0.002$ ), SKCM (Figure 4(i),  $p = 0.003$ ), and UVM (Figure 4(b),  $p = 0.008$ ). Correlations of high COL5A1 expression with a poor DFI were revealed in patients with ACC, CESC, KIRP, LUA, and PAAD (Figure 5(a)). Additionally, the KM analysis revealed significant correlations between COL5A1 with DFI in CESC (Figure 5(b),  $p = 0.027$ ), KICH (Figure 5(c),  $p = 0.045$ ), KIRP (Figure 5(d),  $p = 0.029$ ), and PAAD (Figure 5(e),  $p = 0.015$ ). In addition, forest plots

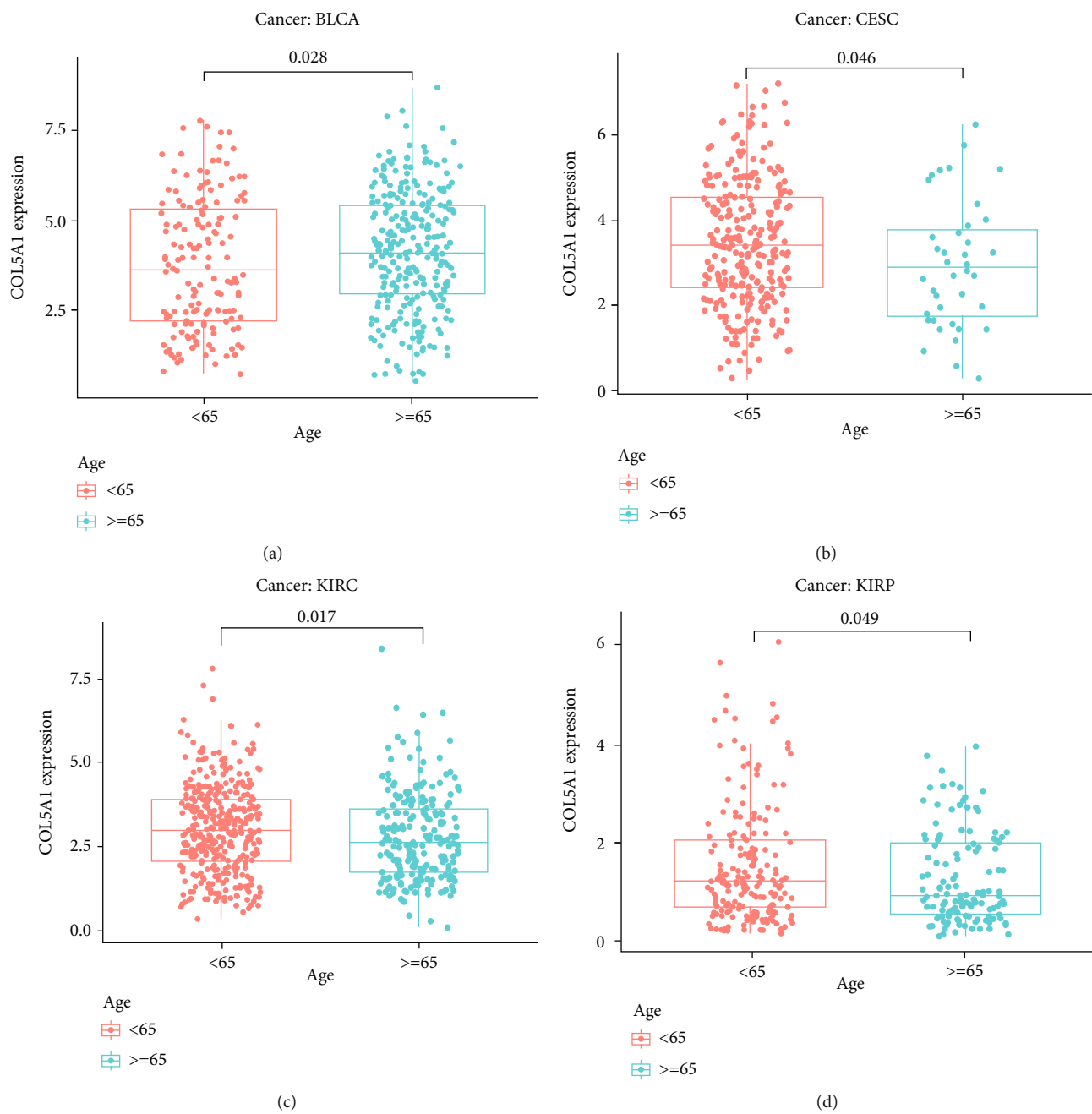


FIGURE 7: Continued.



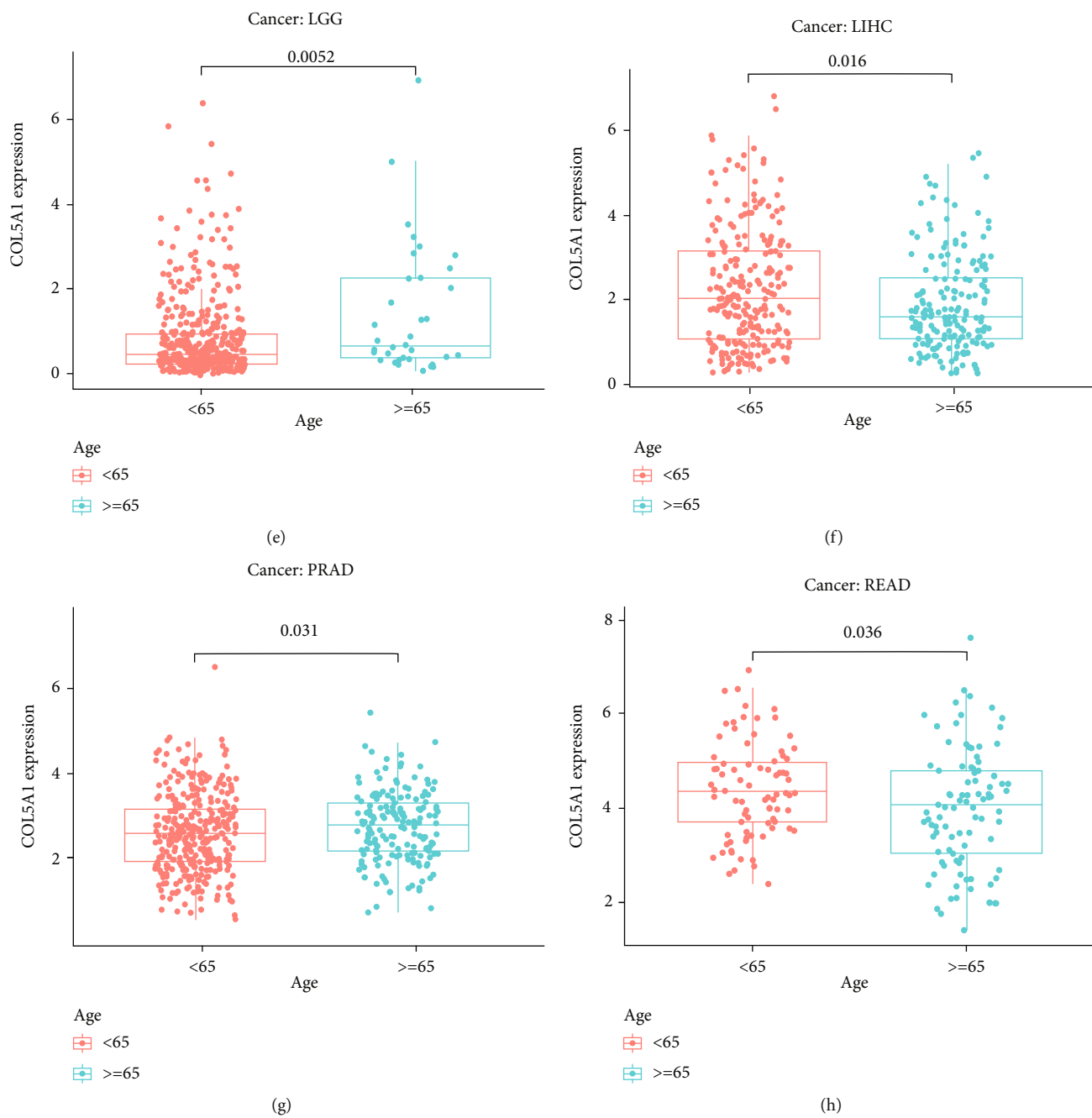


FIGURE 7: Continued.

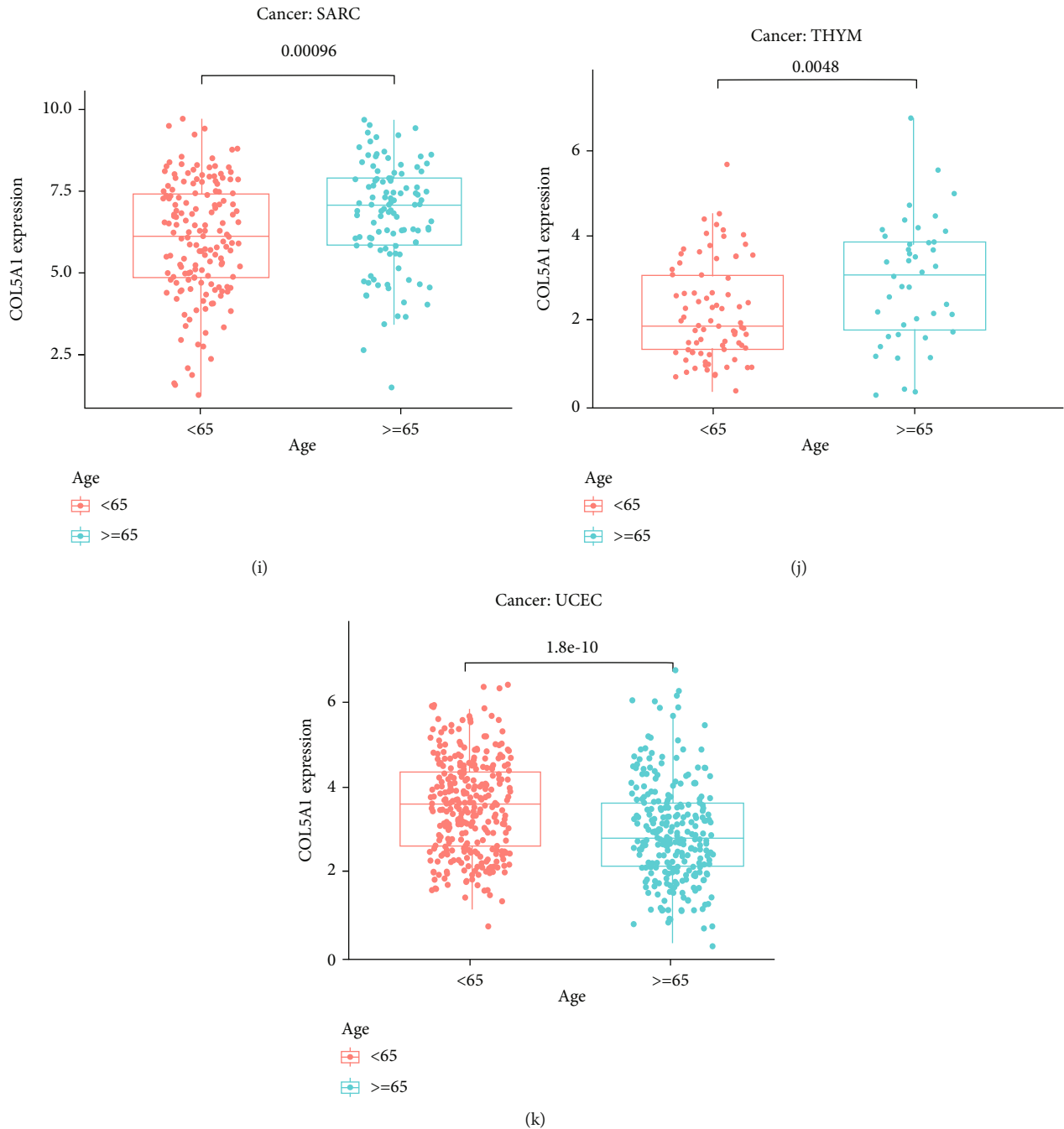


FIGURE 7: Relationships between COL5A1 and age in patients with (a) BLCA, (b) CESC, (c) KIRC, (d) KIRP, (e) LGG, (f) LIHC, (g) PRAD, (h) READ, (i) SARC, (j) THYM, and (k) UCEC.

demonstrated the relationship between high COL5A1 expression and a poor PFI in patients with ACC, BLCA, CESC, GBM, KICH, KIRC, KIRP, LGG, LUAD, MESO, PAAD, PRAD, and UVM (Figure 6). KM analyses illustrated that patients with ACC (Figure 6(b),  $p = 0.034$ ), GBM (Figure 6(c),  $p = 0.009$ ), KIRC (Figure 6(d),  $p < 0.001$ ), KIRP (Figure 6(e),  $p < 0.001$ ), LGG (Figure 6(f),  $p = 0.006$ ), MESO (Figure 6(g),  $p = 0.006$ ), PRAD (Figure 6(h),  $p = 0.024$ ), and UVM (Figure 6(i),  $p = 0.002$ ) who exhibited low expression of COL5A1 had longer survival time.

**3.3. Correlations between COL5A1 Expression and Clinicopathology in Human Tumors.** Subsequently, we investigated the differences in COL5A1 expression levels in patients with different tumors stratified based on age and revealed that patients aged  $\geq 65$  years with CESC (Figure 7(b),  $p = 0.046$ ), KIRC (Figure 7(c),  $p = 0.017$ ), KIRP (Figure 7(d),  $p = 0.049$ ), LIHC (Figure 7(f),  $p = 0.016$ ), READ (Figure 7(h),  $p = 0.036$ ), and UCEC (Figure 7(k),  $p < 0.001$ ) had lower expression of COL5A1, while patients aged  $\geq 65$  with BLCA (Figure 7(a),  $p = 0.028$ ), LGG

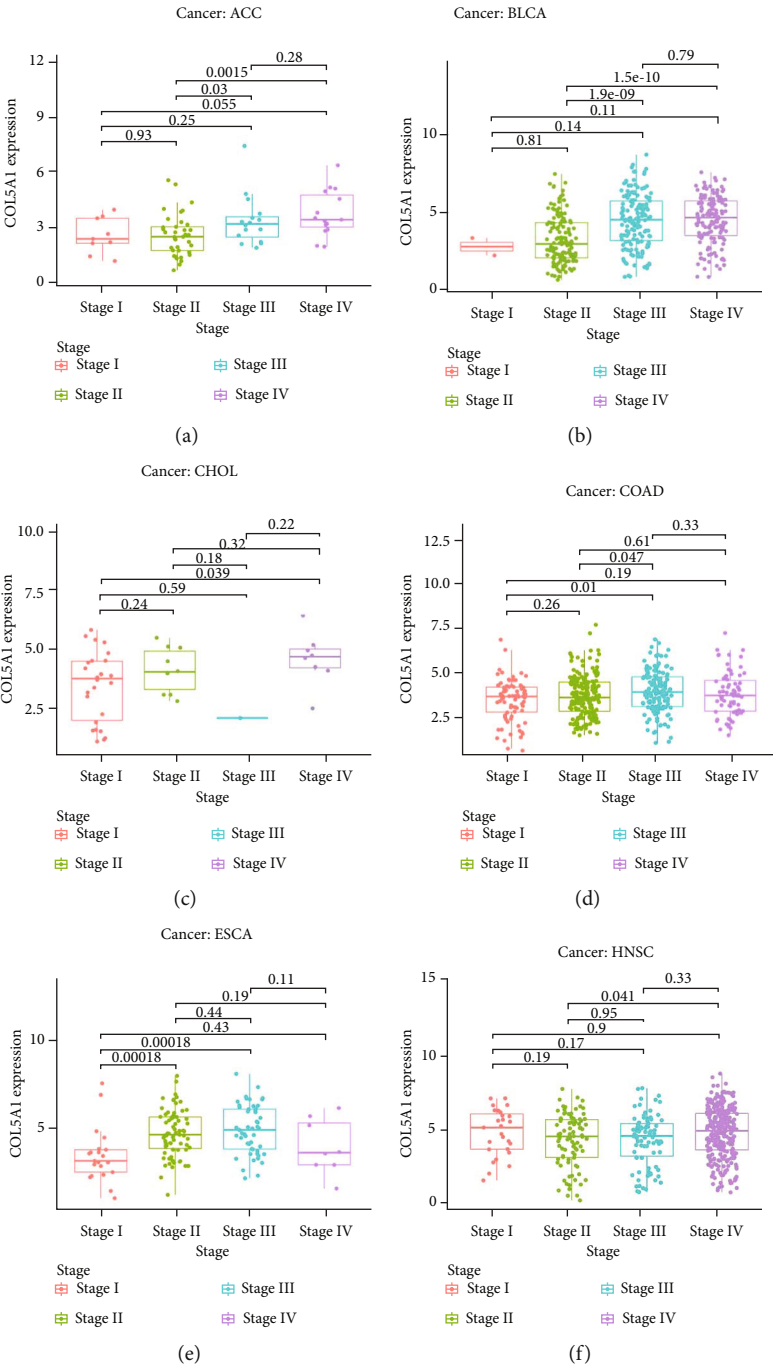


FIGURE 8: Continued.

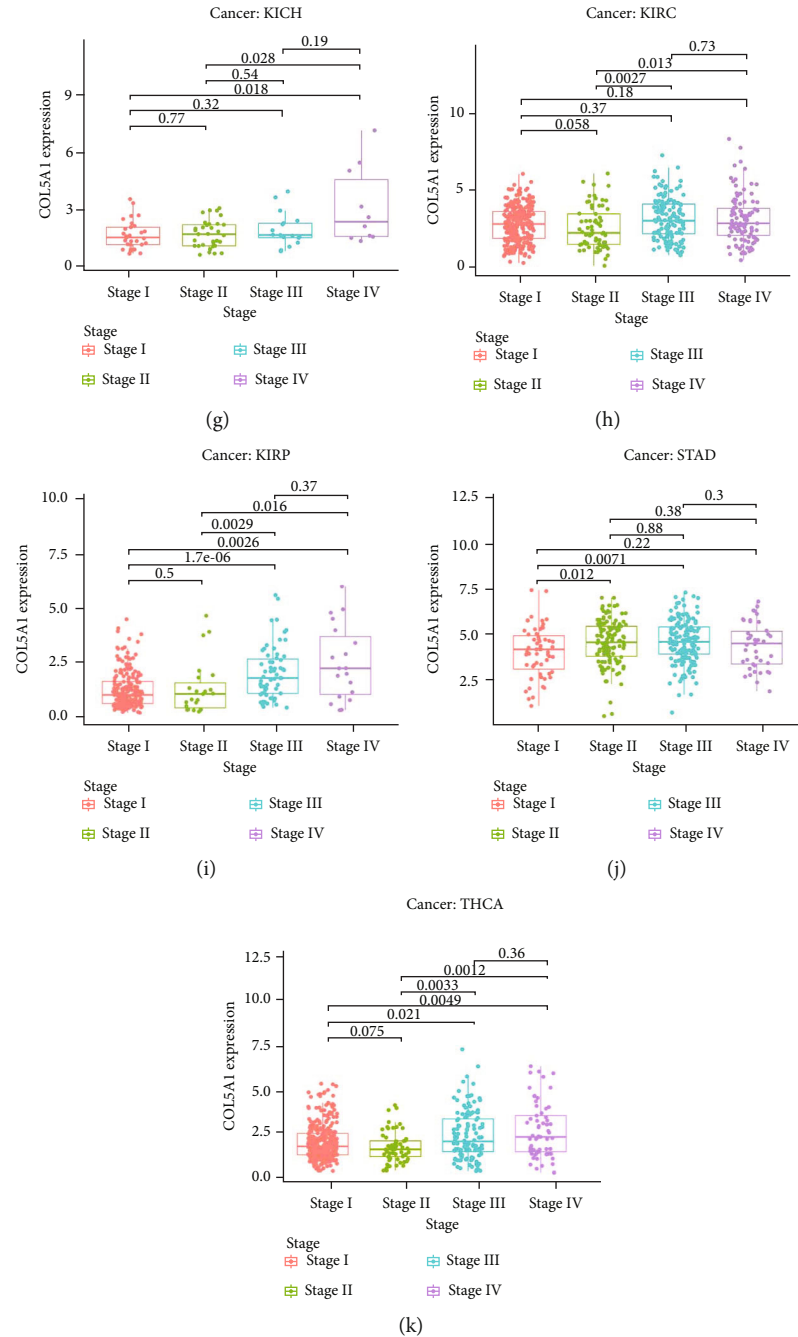


FIGURE 8: Associations between COL5A1 expression and the tumor stage in (a) ACC, (b) BLCA, (c) CHOL, (d) COAD, (e) ESCA, (f) HNSC, (g) KICH, (h) KIRC, (i) KIRP, and (j) STAD and THCA.

(Figure 7(e),  $p = 0.0052$ ), PRAD (Figure 7(g),  $p = 0.031$ ), SARC (Figure 7(i),  $p < 0.001$ ), and THYM (Figure 7(j),  $p = 0.048$ ) displayed higher expression of COL5A1 than patients aged  $< 65$  years. However, no obvious correlation was observed between age and COL5A1 expression in other cancers (Figure S2).

We analyzed the correlation between COL5A1 and tumor stage and found that COL5A1 expression was significantly correlated to the tumor stage in 13 human tumors, including ACC, BLCA, CHOL, COAD, ESCA, HNSC, THCA, KICH, KIRC, KIRP, STAD, PAAD, and UVM

(Figure 8; Figure S3). Notably, in patients with CHOL (Figure 8(c),  $p = 0.039$ ), KICH (Figure 8(g),  $p = 0.018$ ), KIRP (Figure 8(i),  $p = 0.0026$ ), and THCA (Figure 8(k),  $p = 0.0049$ ), COL5A1 expression was significantly increased in stage IV tumors than stage I tumors. In addition, COL5A1 was also expressed at higher levels in stage III tumors than in stage I tumors in COAD (Figure 8(d),  $p = 0.01$ ), ESCA (Figure 8(e),  $p < 0.001$ ), KIRC (Figure 8(h),  $p = 0.036$ ), KIRP (Figure 8(i),  $p < 0.001$ ), STAD (Figure 8(j),  $p = 0.0071$ ), and THCA (Figure 8(k),  $p = 0.021$ ). COL5A1 was overexpressed in stage IV tumors than in stage II

TABLE 1: Correlation between COL5A1 expression and TMB and MSI. \* $p < 0.05$ , \*\* $p < 0.01$ , and \*\*\* $p < 0.001$ .

| TMB         |             |                    | MSI         |             |                 |
|-------------|-------------|--------------------|-------------|-------------|-----------------|
| Cancer type | Cor         | $p$ value          | Cancer type | Cor         | $p$ value       |
| ACC         | 0.43733147  | ***/ $5.58e-05$    | COAD        | 0.14783620  | **/ $0.002193$  |
| BRCA        | -0.07340527 | */ $0.02196037$    | HNSC        | -0.15164437 | ***/ $0.000703$ |
| CESC        | -0.12802692 | */ $0.03042103$    | KIRC        | -0.14245300 | **/ $0.00903$   |
| HNSC        | -0.21248963 | ***/ $0.00000198$  | SKCM        | -0.13520964 | **/ $0.003382$  |
| KIRP        | -0.25583301 | ***/ $0.00001571$  | STAD        | -0.10750443 | */ $0.0377$     |
| LAML        | 0.34680128  | **/ $0.00536082$   | TGCT        | 0.17807180  | */ $0.029247$   |
| LGG         | 0.25972873  | ***/ $3.62e-09$    |             |             |                 |
| LIHC        | -0.31014868 | ***/ $1.91692e-09$ |             |             |                 |
| LUSC        | -0.13299831 | **/ $0.00324439$   |             |             |                 |
| SKCM        | -0.11416702 | */ $0.01376592$    |             |             |                 |
| STAD        | -0.12401527 | */ $0.01730668$    |             |             |                 |
| THYM        | 0.51906320  | ***/ $2.03e-09$    |             |             |                 |
| UCEC        | -0.13110071 | **/ $0.00261476$   |             |             |                 |

tumors in patients with ACC (Figure 8(a),  $p = 0.0015$ ), BLCA (Figure 8(b),  $p < 0.001$ ), HNSC (Figure 8(f),  $p = 0.041$ ), KICH (Figure 8(g),  $p = 0.028$ ), KIRC (Figure 8(h),  $p = 0.013$ ), KIRP (Figure 8(i),  $p = 0.016$ ), and THCA (Figure 8(k),  $p = 0.0012$ ). Therefore, we hypothesized that high COL5A1 expression may lead to shorter survival time in these patients with advanced cancer. Although the differences were remarkable between stages I and IV, stages I and III, and stages II and IV, the differences between stages in other cancers were comparatively small (Figure 8, Figure S3), and a statistically significant difference was not observed in other human tumors (Figure S3).

**3.4. Associations of COL5A1 Expression with TMB, MSI, Mismatch Repair Genes, and the Mutation-Related Prognosis in Various Human Tumors.** We investigated the associations between COL5A1 expression and the TMB and MSI, both of which are involved in the sensitivity to ICB. Therefore, an investigation of the relationships between the TMB and COL5A1 across cancers is necessary. COL5A1 expression was related to the TMB in 13 cancer types. In particular, COL5A1 expression positively linked to the TMB in 4 tumors, including ACC, LAML, LGG, and THYM, while it negatively related to the TMB in BRCA, CESC, HNSC, KIRP, LIHC, LUSC, SKCM, STAD, and UCEC (Table 1; Figure 9(a)). Furthermore, COL5A1 expression was positively related to MSI in COAD and TGCTs but negatively associated with MSI in HNSC, KIRC, SKCM, and STAD (Table 1; Figure 9(b)). Then, we assessed the correlation of COL5A1 expression with MMR genes, including MLH1, MSH2, MSH6, PMS2, and EPCAM. Figure 9(c) illustrates the correlations between COL5A1 expression and the expression of individual MMR genes. COL5A1 expression correlated with the expression of MMR genes in most tumors, except for UCEC and UVM. In addition, we used cBioPortal to investigate the correlation between COL5A1 mutations and prognosis. Patients with UCEC in the unaltered COL5A1 group experienced a shorter OS

(Figure 9(d)), DSS (Figure 9(e)), and PFI (Figure 9(f)) than those in the altered group. However, patients with ESCA presenting altered COL5A1 expression experienced a shorter OS (Figure 9(g)) and PFI (Figure 9(h)).

**3.5. Correlations of COL5A1 Methylation with Prognosis.** We further investigated the DNA methylation levels of COL5A1 in 33 cancer types. The DNA methylation of COL5A1 was increased in BLCA ( $p = 7.57e-05$ ), BRCA ( $p = 2.60e-10$ ), CHOL ( $p = 0.014$ ), COAD ( $p = 3.92e-53$ ), ESCA ( $p = 0.046$ ), KIRC ( $p = 1.03e-16$ ), KIRP ( $p = 9.10e-03$ ), LIHC ( $p = 3.63e-05$ ), LUAD ( $p = 3.33e-10$ ), LUSC ( $p = 1.07e-05$ ), PAAD ( $p = 9.36e-06$ ), PRAD ( $p = 1.17e-05$ ), and READ ( $p = 2.24e-07$ ) compared with normal tissues (Figure 10(a)). The DNA methylation of COL5A1 in other cancers was not significantly different from that in normal tissues. Additionally, the correlation between COL5A1 methylation and the prognosis was evaluated. Patients with HNSC presenting low COL5A1 methylation levels experienced a shorter OS than those with high COL5A1 methylation levels ( $p = 0.015$ ) (Figure 10(b)). Nevertheless, in patients with KIRP ( $p = 1.62e-03$ ) and PAAD ( $p = 0.041$ ), high COL5A1 methylation levels were related to a shorter OS (Figure 10(b)). High COL5A1 methylation levels were correlated to a better PFI in BLCA patients ( $p = 0.013$ ) but linked to a poor PFI in KIRC patients ( $p = 0.031$ ), KIRP ( $p = 0.026$ ), and THCA ( $p = 4.13e-03$ ) (Figure 10(c)).

**3.6. Correlations of COL5A1 Expression with TME across Cancers.** It has been demonstrated that TME has an influential action in tumorigenesis [27], multidrug resistance, and metastasis of cancer cells [28]. Therefore, an investigation of the associations of COL5A1 expression with the TME is necessary. The ESTIMATE algorithm was employed to assess the correlations of COL5A1 expression with stromal and immune scores. The results elucidated that COL5A1 expression positively related to immune scores in 19 cancers

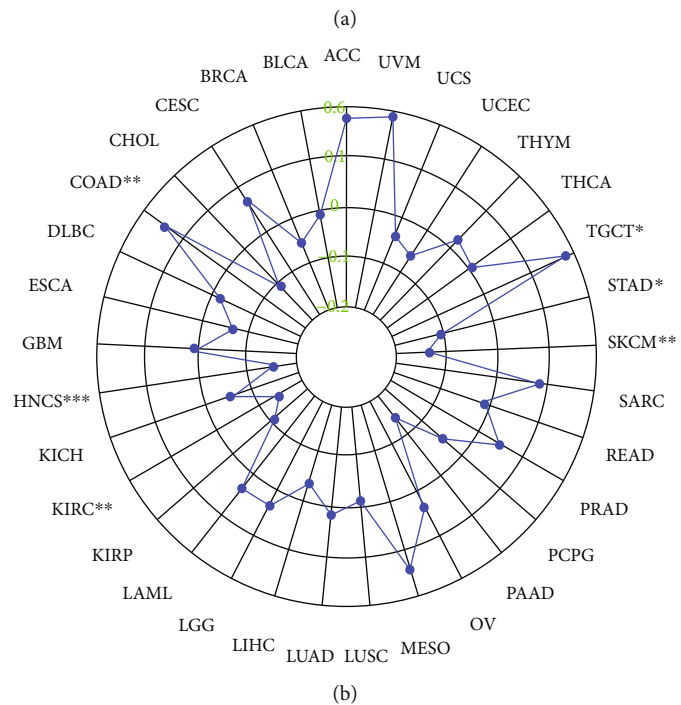
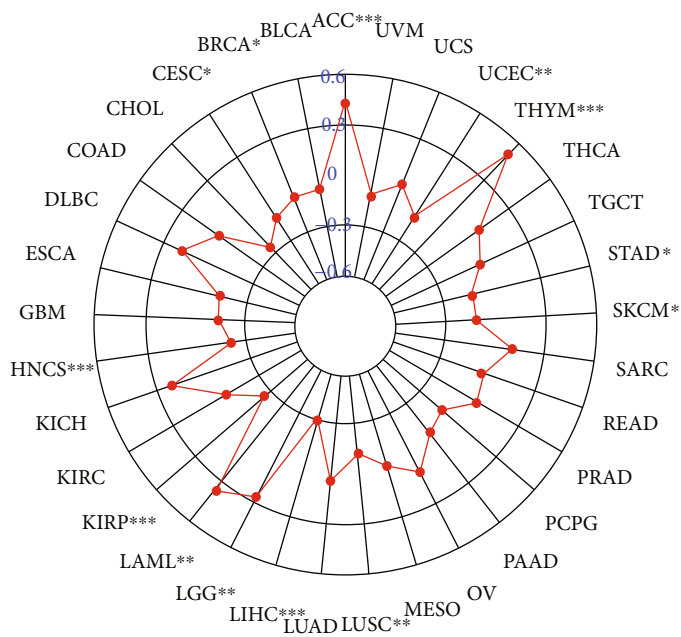


FIGURE 9: Continued.

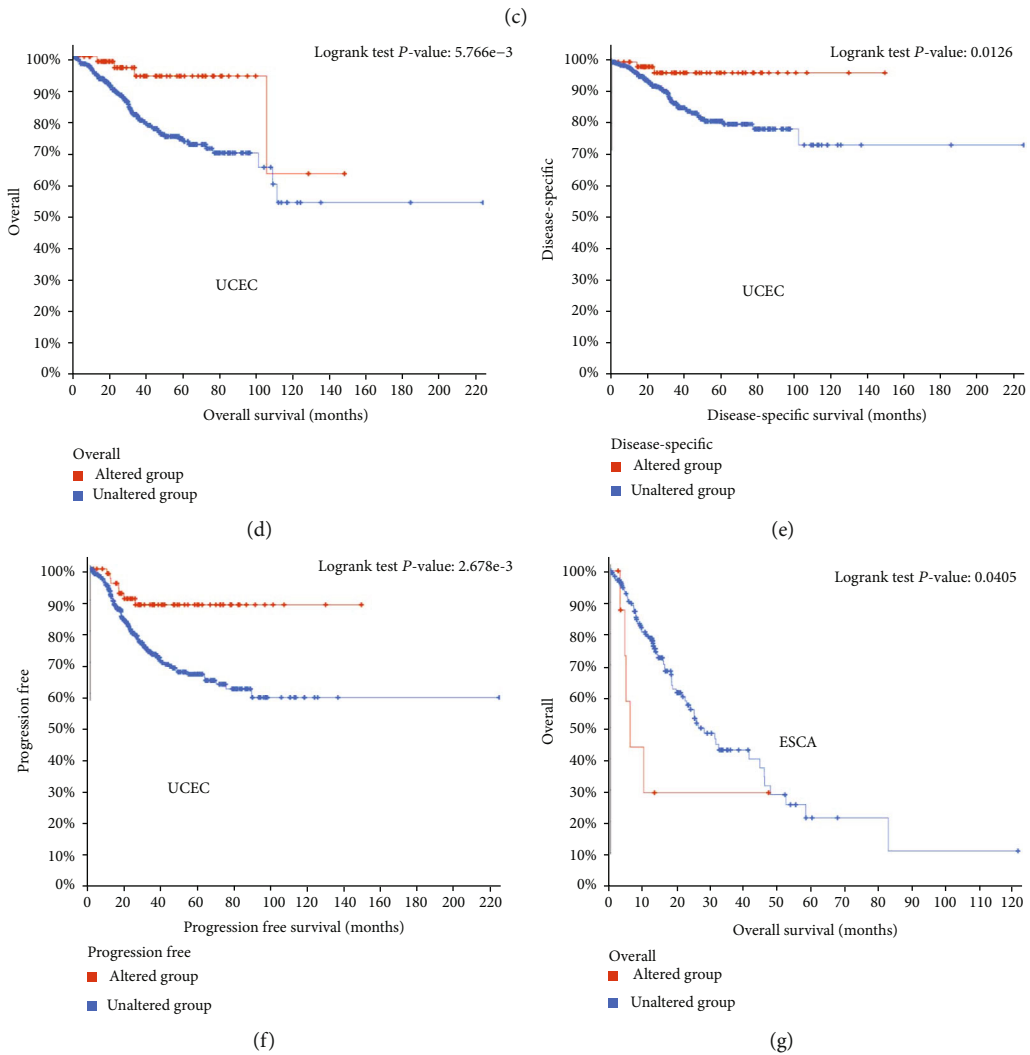
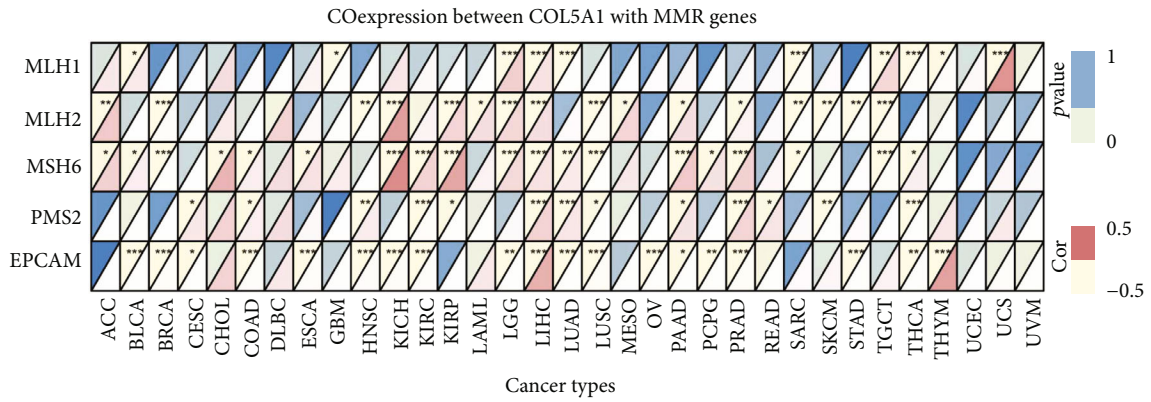


FIGURE 9: Continued.

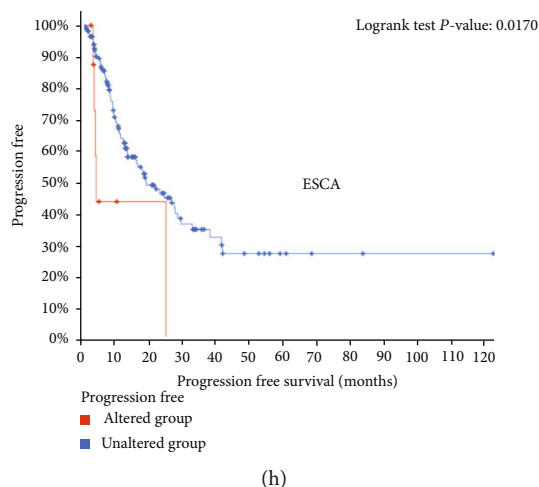


FIGURE 9: Correlations of COL5A1 expression with the TMB, MSI, MMR genes, and mutation-related prognosis in various human cancers. (a) Radar plot showing the relationship between COL5A1 expression and MSI in human cancers. (b) Radar plot showing the relationship between COL5A1 expression and TMB across human cancers. (c) Coexpression of COL5A1 with MMR genes. Correlations of COL5A1 gene mutations with (d) OS, (e) DSS, and (f) PFI of patients with UCEC. Correlations of COL5A1 gene mutations with (g) OS and (h) PFI of patients with ESCA.

but negatively associated with immune scores in TGCTs (Figure 11(a); Figure S4). Additionally, COL5A1 expression was positively linked to stromal scores in 30 human cancers (Figure 11(a); Figure S4). The five cancers with the highest correlation coefficients between the TME and COL5A1 expression are shown in Figure 11; data for other tumors are presented in Figure S4.

**3.7. Association of COL5A1 Expression with the TIIC Infiltration in Human Tumors.** The relationship of COL5A1 expression with the infiltration levels of 22 immunocyte subtypes was investigated. The levels of TIIC infiltration were correlated significantly with COL5A1 expression in most human tumors (Table S1). Six cancer types, including PRAD ( $n = 15$ ), BRCA ( $n = 13$ ), THCA ( $n = 12$ ), BLCA ( $n = 11$ ), KIRC ( $n = 11$ ), GBM ( $n = 10$ ), and KIRP ( $n = 10$ ), showed the highest correlation between COL5A1 expression and levels of infiltrating TIIC, and the results are presented in Table 2. COL5A1 expression correlated positively with the infiltration of naive B cells in PRAD, THCA, BLCA, KIRC, and KIRP and negatively with the infiltration of memory B cells in PRAD, BRCA, BLCA, KIRC, and KIRP. Additionally, COL5A1 expression was positively correlated with the infiltration of monocytes in PRAD, BRCA, THCA, and BLCA but had a negative association with KIRC.

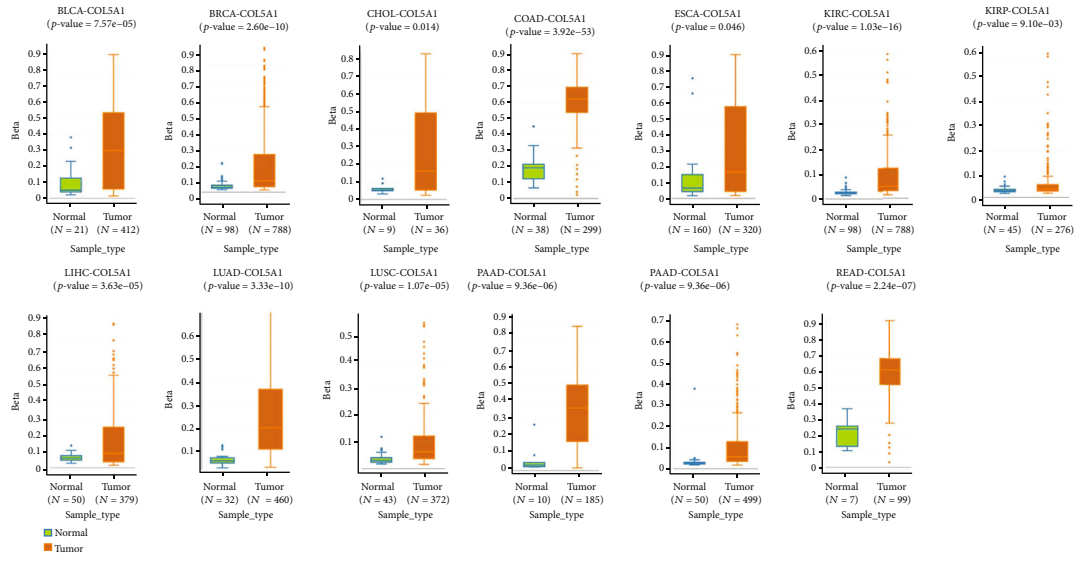
Furthermore, different correlations were observed between COL5A1 expression and different subtypes of infiltrating macrophages and T cells. For example, the expression levels of COL5A1 were negatively linked to the infiltration of CD8 T cells in PRAD, BRCA, THCA, and BLCA but showed a positive relationship with the infiltrating degrees of activated memory CD4 T cells in THCA, KIRC, GBM, and KIRP (Table 2). In addition, COL5A1 expression was positively correlated with the infiltration of M0 macrophages in BRCA, BLCA, KIRC, and GBM but

negatively linked to the infiltration of M2 macrophages in THCA, GBM, and KIRP. The infiltrated immune cells with the highest correlation between COL5A1 expressions in 31 cancer types are presented in Figure 12; data for other cancers are shown in Table S1. In addition, we subsequently used five algorithms, including TIMER, xCell, MCP-counter, EPIC, and quantIseq, to confirm the correlation of COL5A1 expression with TIIC. As shown in Figures 13(a)–13(e), COL5A1 expression was correlated with TIIC in almost all cancer types.

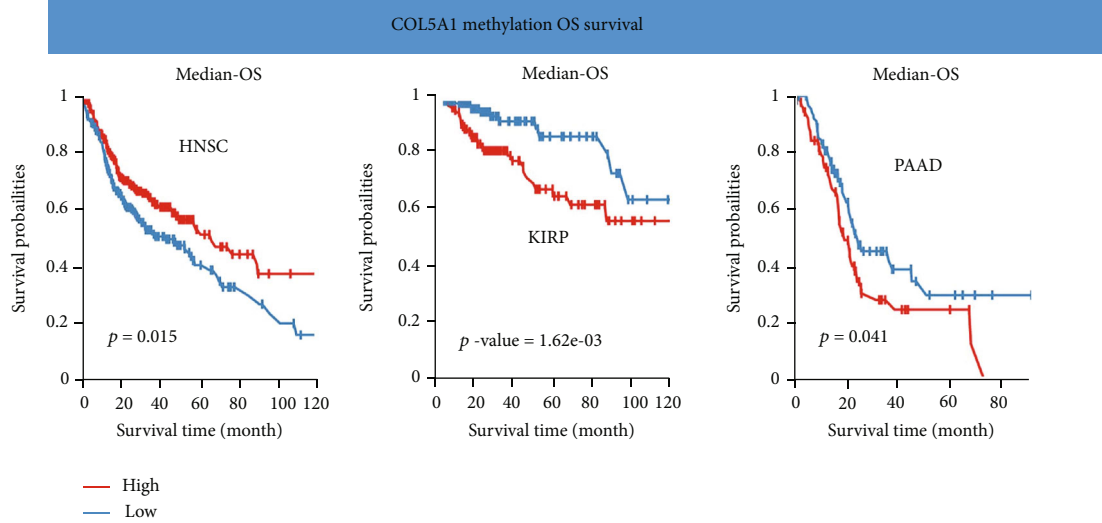
**3.8. Coexpression of COL5A1 with Immune-Related Genes and Pathway Enrichment Analyses in Human Tumors.** Gene coexpression analyses were carried out to assess the correlations of COL5A1 expression with immune-associated genes in human tumors. The genes encoding MHC, immune activators, immune suppressors, chemokines, and chemokine receptors were investigated. The heat map demonstrated that most immune-related genes were coexpressed with COL5A1, and major immune activation, chemokine, and chemokine receptor genes exhibited a positive correlation with COL5A1 expression in major cancers (Figure 14).

Afterward, we carried out GO functional annotations and KEGG pathways related to COL5A1 in human tumors. As shown in Figure 15 and Figure S5, the data illustrated that COL5A1 regulated some immune-related functions in 18 cancer types (Figure 15, Figure S5). In GBM, COL5A1 expression positively regulated the acute inflammatory response, B cell receptor signaling pathway, chemokine signaling pathway, cytokine cytokine-receptor interaction, JAK-STAT pathway, and NOD-like receptor pathway, which are all immune-related signaling pathways. GO functional annotations revealed that COL5A1 positively regulated the immune response regulating cell surface receptor signaling in KIRC and LGG, and KEGG pathway analyses also showed that COL5A1 positively regulated

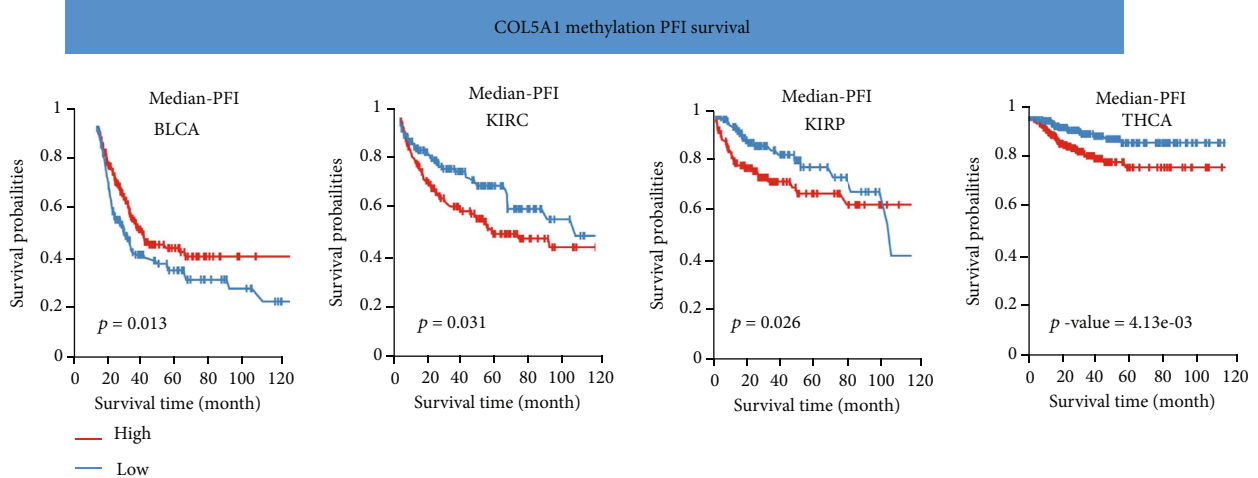




(a)



(b)



(c)

FIGURE 10: Correlations of COL5A1 with DNA methylation. (a) Differential COL5A1 methylation levels in tumor and normal tissues. Correlations between COL5A1 methylation and (b) OS and (c) PFI survival.

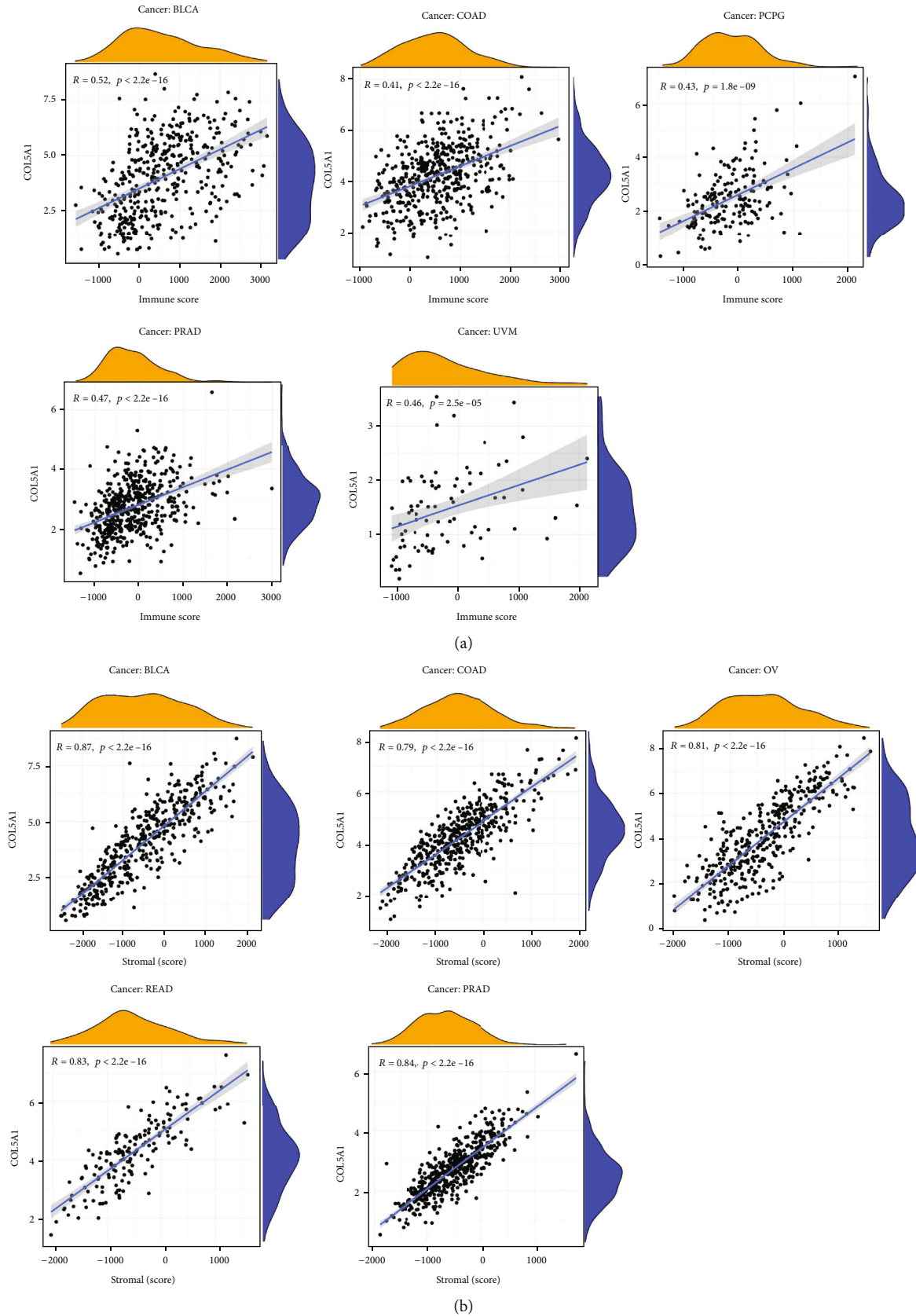


FIGURE 11: Five cancers with the highest correlation coefficients between COL5A1 expression and the TME. (a) Correlation between COL5A1 expression and stromal scores in BLCA, COAD, PCPG, PRAD, and UVM. (b) Correlation of COL5A1 expression with immune scores in BLCA, COAD, OV, READ, and PRAD.

TABLE 2: Relationship between COL5A1 expression and immune cell infiltration in different cancers. \* $p < 0.05$ , \*\* $p < 0.01$ , and \*\*\* $p < 0.001$ .

| Cancer type                  | PRAD<br>$p$ value/Cor | BRCA<br>$p$ value/Cor | THCA<br>$p$ value/Cor | BLCA<br>$p$ value/Cor | KIRC<br>$p$ value/Cor | GBM<br>$p$ value/Cor | KIRP<br>$p$ value/Cor |
|------------------------------|-----------------------|-----------------------|-----------------------|-----------------------|-----------------------|----------------------|-----------------------|
| B cells naive                | ***/0.24              |                       | */0.10                | */0.14                | ***/0.23              |                      | ***/0.46              |
| B cells memory               | **/-0.17              | **/-0.09              |                       | ***/-0.23             | **/-0.14              |                      | ***/-0.31             |
| Plasma cells                 | ***/-0.22             |                       |                       |                       |                       |                      | ***/0.27              |
| T cells CD8                  | ***/-0.28             | ***/-0.19             | ***/-0.23             | **/-0.17              |                       |                      |                       |
| T cells CD4 naive            |                       |                       |                       |                       |                       |                      |                       |
| T cells CD4 memory resting   | ***/0.32              | ***/0.26              |                       | **/0.16               |                       |                      |                       |
| T cells CD4 memory activated | */-0.10               | ***/-0.19             | */0.10                |                       | ***/0.16              | ***/0.29             | ***/0.28              |
| T cells follicular helper    | ***/-0.23             | ***/-0.20             | */0.10                | ***/-0.28             | ***/-0.21             | ***/-0.28            | **/0.19               |
| T cells regulatory (Tregs)   | ***/0.18              | */0.07                | ***/0.18              |                       | **/-0.09              |                      | */0.15                |
| T cells gamma delta          |                       | **/-0.09              |                       |                       | **/-0.13              |                      |                       |
| NK cells resting             |                       |                       | **/-0.16              |                       |                       | ***/0.27             |                       |
| NK cells activated           | */-0.10               |                       |                       |                       | ***/-0.18             | **/-0.21             |                       |
| Monocytes                    | **/0.16               | */0.07                | ***/0.18              | */0.13                | **/-0.13              |                      |                       |
| Macrophages M0               | ***/-0.21             | */0.07                | ***/-0.18             | ***/0.22              | ***/0.23              | ***/0.38             |                       |
| Macrophages M1               | */-0.11               | ***/-0.13             | */0.11                |                       |                       | */-0.19              | ***/0.35              |
| Macrophages M2               | **/0.14               |                       | ***/-0.25             | ***/0.27              | */0.09                | */-0.19              | ***/-0.32             |
| Dendritic cells resting      | ***/0.23              | ***/0.11              | ***/0.40              |                       |                       |                      | ***/0.24              |
| Dendritic cells activated    | ***/0.23              |                       | ***/0.18              | ***/-0.23             | ***/-0.23             |                      |                       |
| Mast cells resting           |                       | ***/0.23              |                       | **/0.14               |                       | **/-0.20             | */-0.13               |
| Mast cells activated         |                       |                       |                       |                       |                       | */0.15               |                       |
| Eosinophils                  |                       |                       |                       |                       |                       |                      |                       |
| Neutrophils                  |                       | **/0.09               |                       | **/0.17               |                       | ***/0.27             |                       |

cytokine cytokine-receptor interactions and the MAPK pathway. In addition, COL5A1 positively regulated cytokine production, negative regulation of immune system process, cytokine cytokine-receptor interaction, JAK-STAT pathway, T cell receptor pathway in LGG; positively regulated lymphocyte migration, NOD-like receptor pathway, and the WNT pathway in SKCM; positively regulated antigen processing and presentation, chemokine pathway, JAK-STAT pathway, and cytokine cytokine-receptor interaction in THCA; positively regulated cell growth, chemokine pathway, MAPK pathway, and cytokine cytokine-receptor interaction in UVM; positively regulated adaptive immune response based on somatic recombination of immune receptors built from immunoglobulin superfamily domains in KIRP and PRAD; positively regulated antigen receptor mediated pathway in KIRP; and positively regulated B cell activation in PRAD. Furthermore, the chemokine pathway and cytokine cytokine-receptor interaction were positively regulated in READ, while antigen processing and presentation and the RIG I-like receptor pathway were negatively regulated by COL5A1 in MESO. Data for other cancers are shown in Figure S5.

**3.9. Correlation of COL5A1 with Immune Checkpoint-Related Genes and Drug Sensitivity.** Immunotherapy or targeted therapy is now more and more used for a variety of tumor patients, particularly ICB therapy for patients with unsatisfactory radiotherapy and chemotherapy [20]. There-

fore, it is necessary to preliminarily reveal the value of COL5A1 in predicting drug sensitivity and immunotherapy sensitivity of tumor cells through biological methods. Hence, we investigated the correlation of COL5A1 and immune checkpoints, including PDCD1, LAG3, CD274, SIGLEC15, CTLA4, TIGIT, HAVCR2, and PDCD1LG2, which were associated with response to ICB [29, 30]. The relationship between COL5A1 and immune checkpoints may be a predictor for ICB. In the cancers which had a correlation of COL5A1 with OS, including SKCM, ACC, GBM, BLCA, CESC, KIRC, LAML, KIRP, LGG, MESO, and UVM (Figure 3), the expression of COL5A1 had a correlation with immune checkpoints, especially in LGG and KIRP (Figure 16(a)). We further assessed the relationship between COL5A1 and the IC50 of chemotherapeutic drug usually used in these cancer types. We found that in BLCA, COL5A1 expression had a negative correlation between the IC50 of cisplatin, while having a positive relationship with the IC50 of gemcitabine (Figures 16(b) and 16(c)). In KIRC, the IC50 of pazopanib and sunitinib was negatively related to the expression of COL5A1 (Figures 16(d) and 16(e)). Additionally, COL5A1 expression was also negative correlated with the IC50 of sorafenib and sunitinib in KIRP (Figures 16(f) and 16(g)). In LAML, the IC50 of doxorubicin and etoposide had a positive correlation with COL5A1 expression (Figures 16(h) and 16(i)). However, the expression of COL5A1 negatively related to the IC50 of cisplatin and paclitaxel in MESO (Figures 16(j) and 16(k)). These results may have implications for cancer ICB and

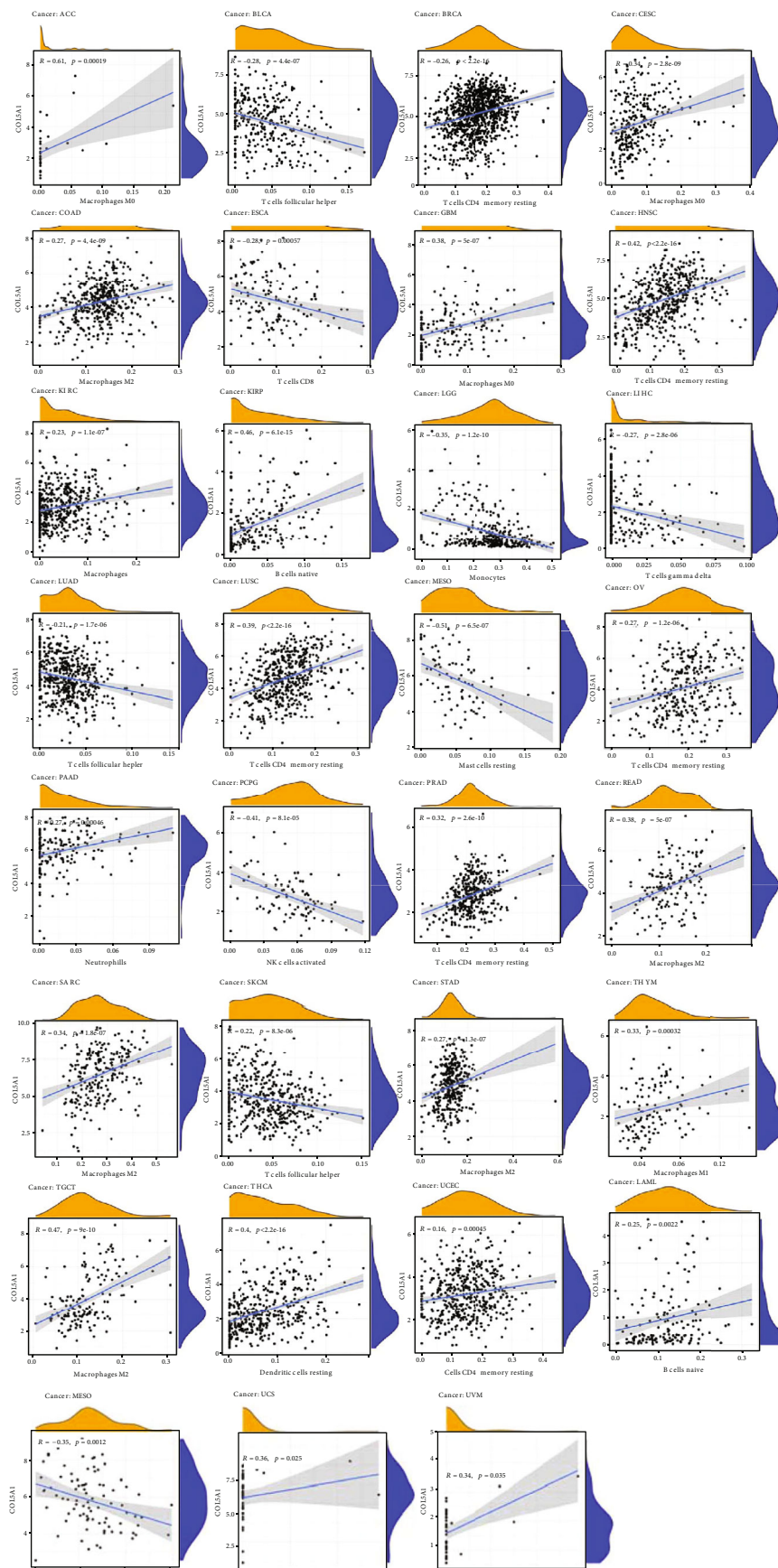


FIGURE 12: Association of COL5A1 with the degree of infiltration of different TIICs in different human tumors.

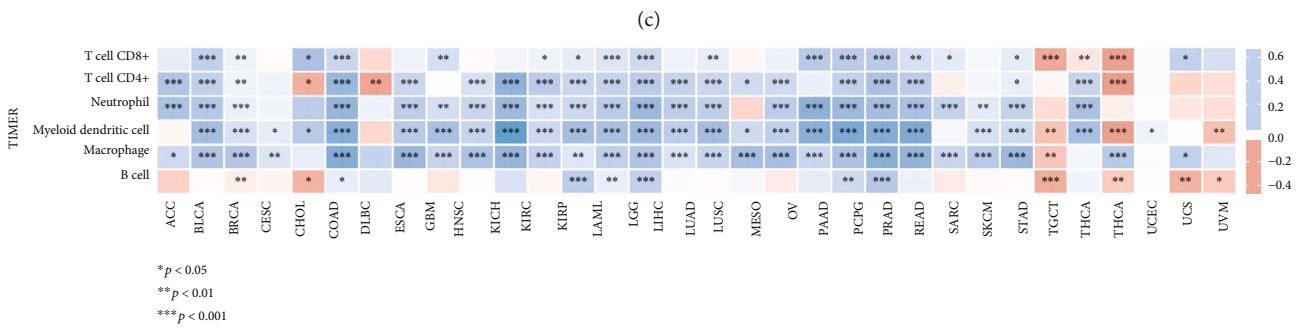
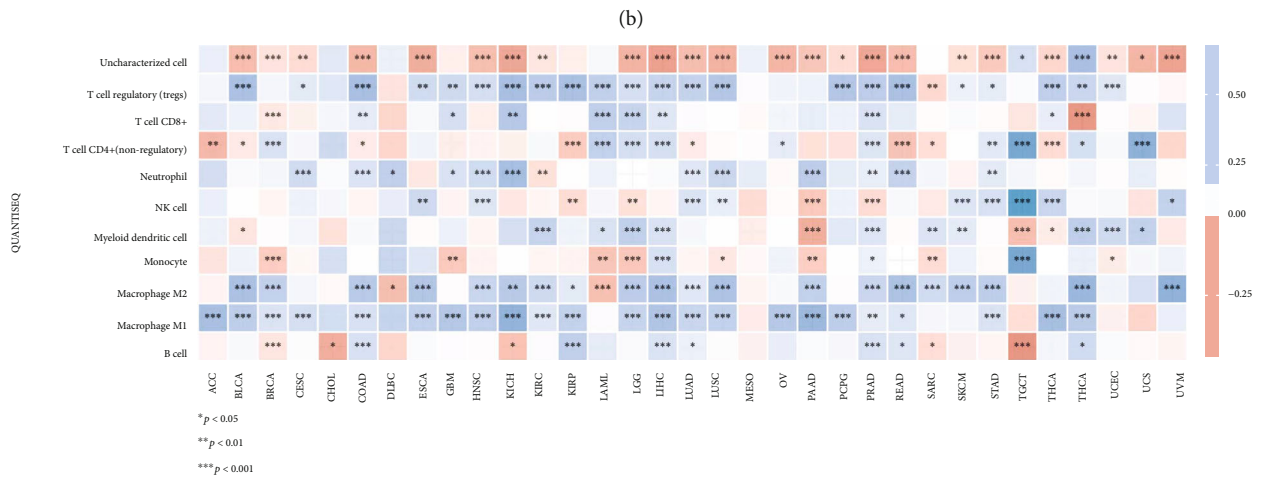
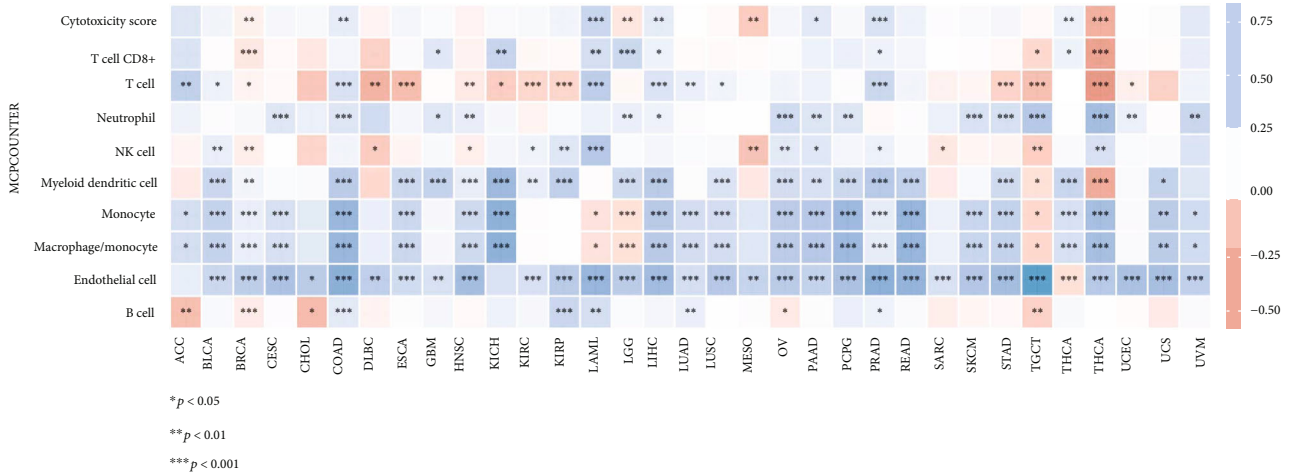
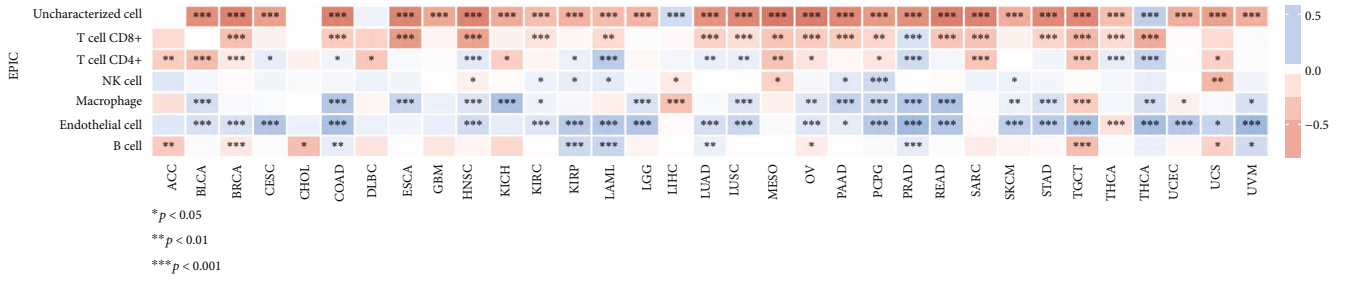
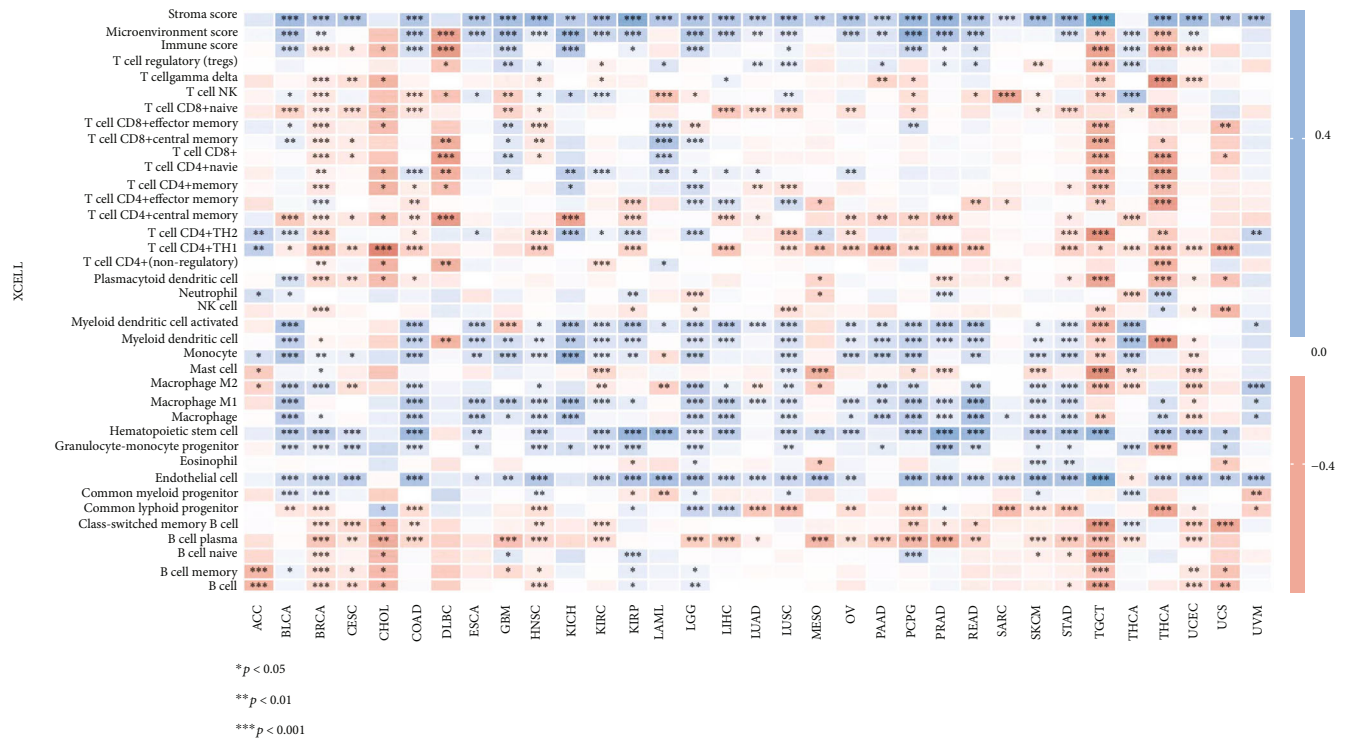


FIGURE 13: Continued.



(e)

FIGURE 13: Heat map showing the correlations of COL5A1 expression with TIIC based on EPIC (a), MCP-counter (b), quanTIseq (c), TIMER (d), and xCell (e) algorithm.

chemotherapy, for example, BLCA patients with high COL5A1 expression may have a more sensitive response to cisplatin treatment, which may provide accurate treatment protocols for chemotherapy.

**3.10. Primary Validation of the Role of COL5A1 in Glioma Cells.** We found that COL5A1 was related to the prognosis of GBM and LGG patients (Figures 3(e) and 3(i)). The human glioblastoma cell line U251 was used to confirm whether COL5A1 knockdown could impact the growth of glioma cells. The results elucidated that COL5A1 knockdown decreased the proliferation of U251 cells (Figures 17(a)–17(c)). Wound healing was remarkably inhibited by COL5A1 knockdown in U251 cells (Figures 17(d) and 17(e)). The Transwell assay demonstrated that the migration and invasion of U251 cells were significantly inhibited by COL5A1 knockdown (Figures 17(f) and 17(g)).

#### 4. Discussion

As shown in the present study, COL5A1 was expressed at high levels in 13 human tumors, and IHC and western blot results confirmed this trend at the protein level. Furthermore, our findings for BRCA, ESCA, HNSC, LUAD, and STAD were similar to the results reported in previous studies [12, 31–35]. We found for the first time that COL5A1 was overexpressed in CHOL, READ, COAD, GBM, KIRC, LUSC, LIHC, and THCA. Interestingly, COL5A1 was expressed at low levels in CESC, KIRP, and UCEC compared

to normal tissues. Additionally, we detected high COL5A1 expression in MESO and UCS, but insufficient expression data were available for normal tissues in TCGA. We also found that COL5A1 genetic variants existed in multiple cancer types. Additionally, DNA methylation of COL5A1 was increased in several cancers and affected the survival of patients.

KM survival analyses indicated that high COL5A1 expression was linked to a poor prognosis for patients with ACC and BLCA. Moreover, patients with BLCA presenting COL5A1 alterations showed lower disease-free survival rates [36]. Similarly, high COL5A1 expression was reported to be related to tumorigenesis, TIIC, and paclitaxel resistance in OV [16]. Chemotherapy resistance may be associated with increased tissue stiffness mediated by specific collagen cross-linking. In addition, COL5A1 was dramatically elevated in metastatic KIRC tumors compared to primary tumors [37]. In this work, high COL5A1 expression was linked to poor prognosis in patients with ACC, BLCA, GBM, KIRC, KIRP, LGG, MESO, SKCM, and UVM. Additionally, the role of COL5A1 in glioma cells was verified in vitro experiments.

Additionally, COL5A1 expression was related to age in patients with some tumors. COL5A1 was expressed at lower levels in older patients with CESC, KIRC, KIRP, LIHC, READ, and UCEC but at higher levels in older patients with BLCA, LGG, PRAD, SARC, and THYM. These results may be instructive in the selection of immunotherapy regimens for patients of different ages. Our study also revealed that COL5A1 expression was related to tumor stage in most

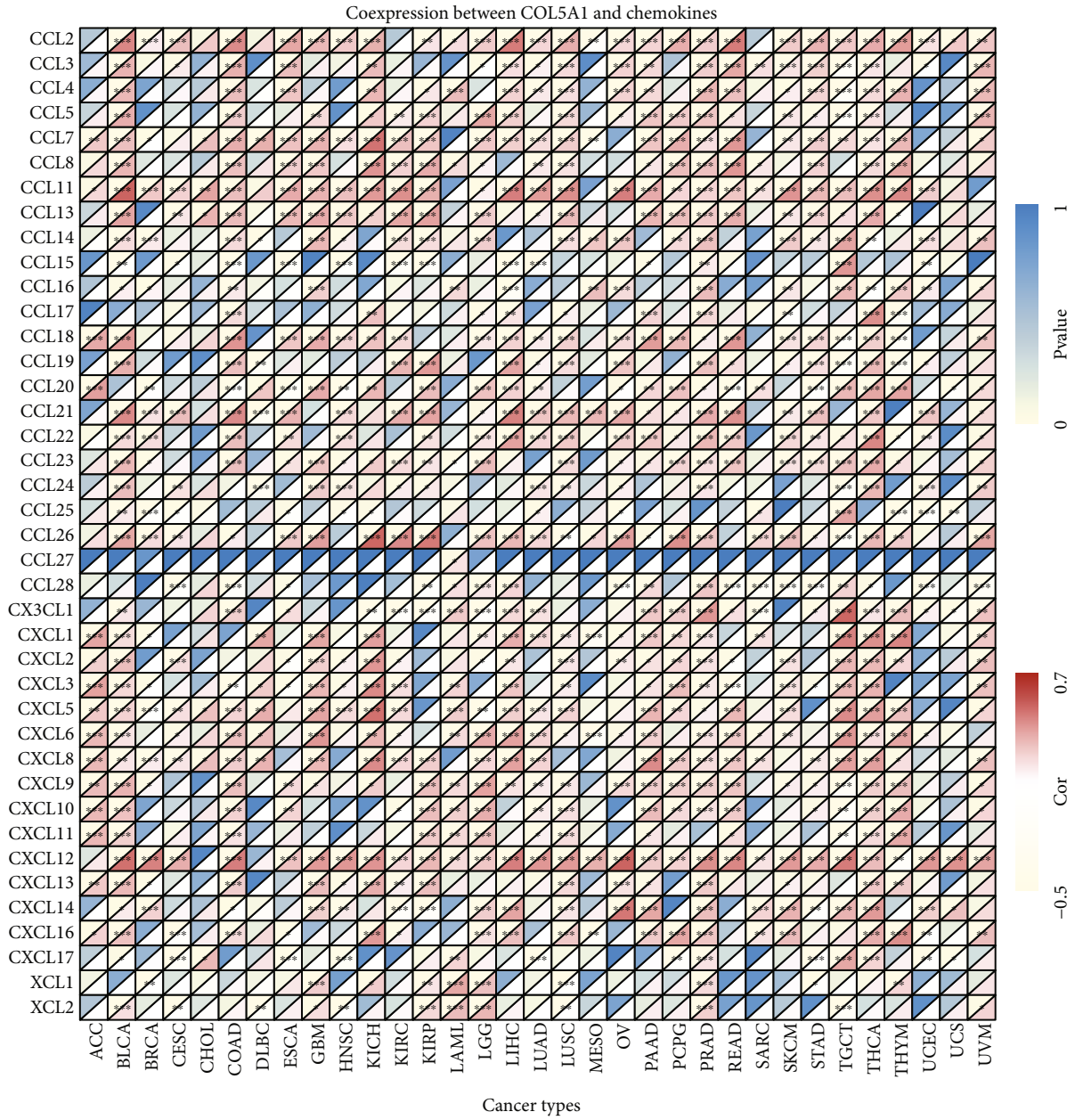


FIGURE 14: Continued.

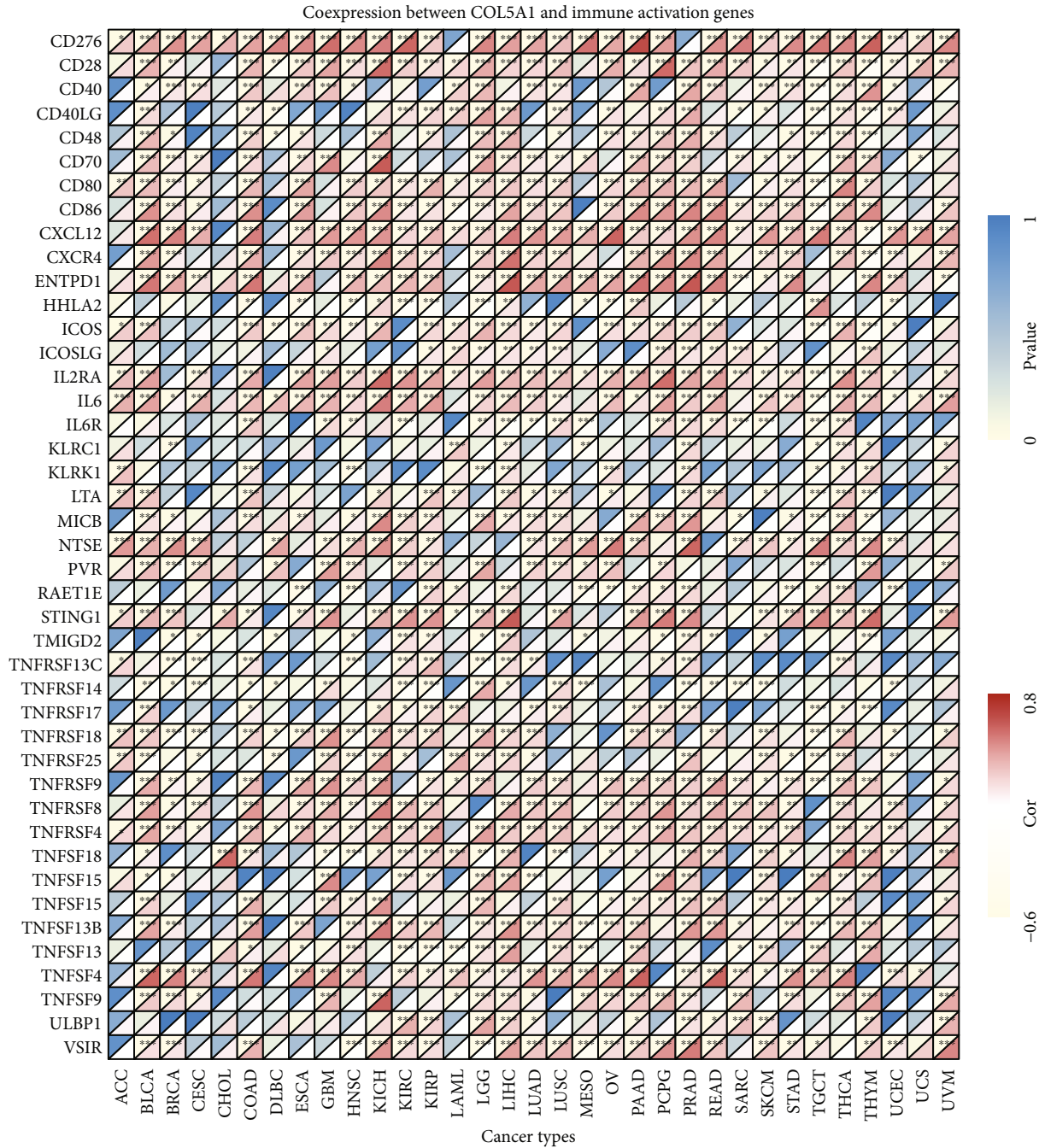
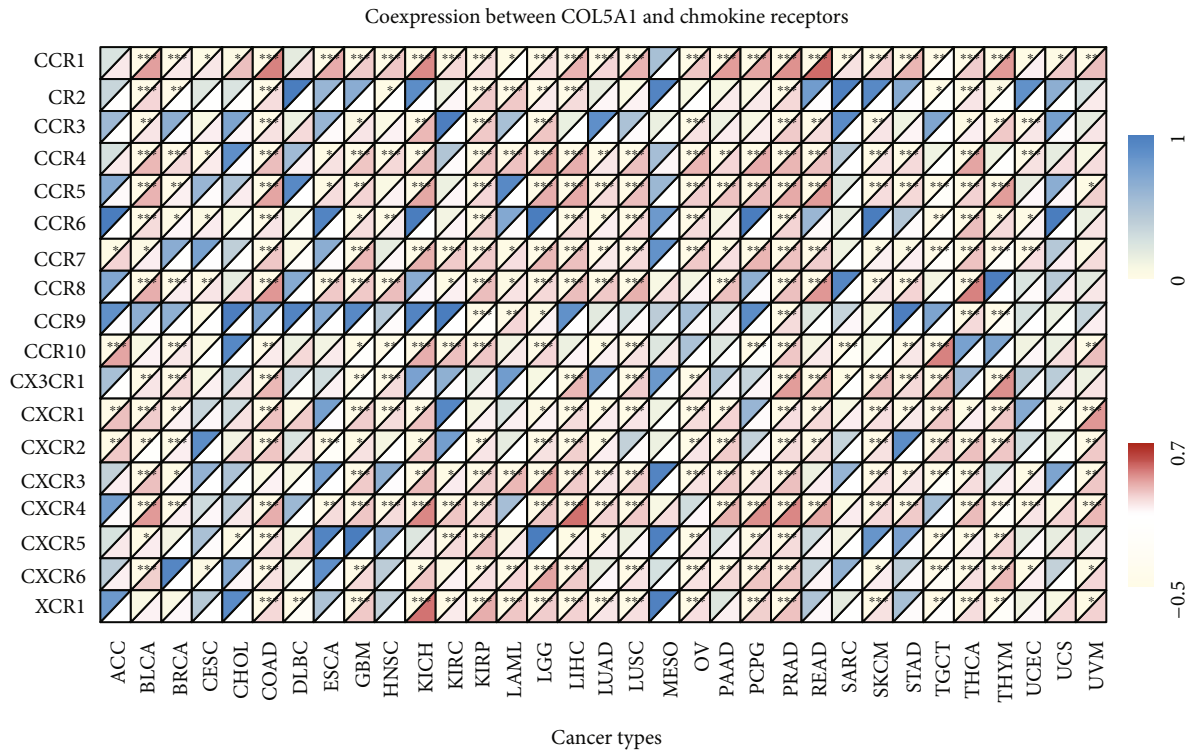
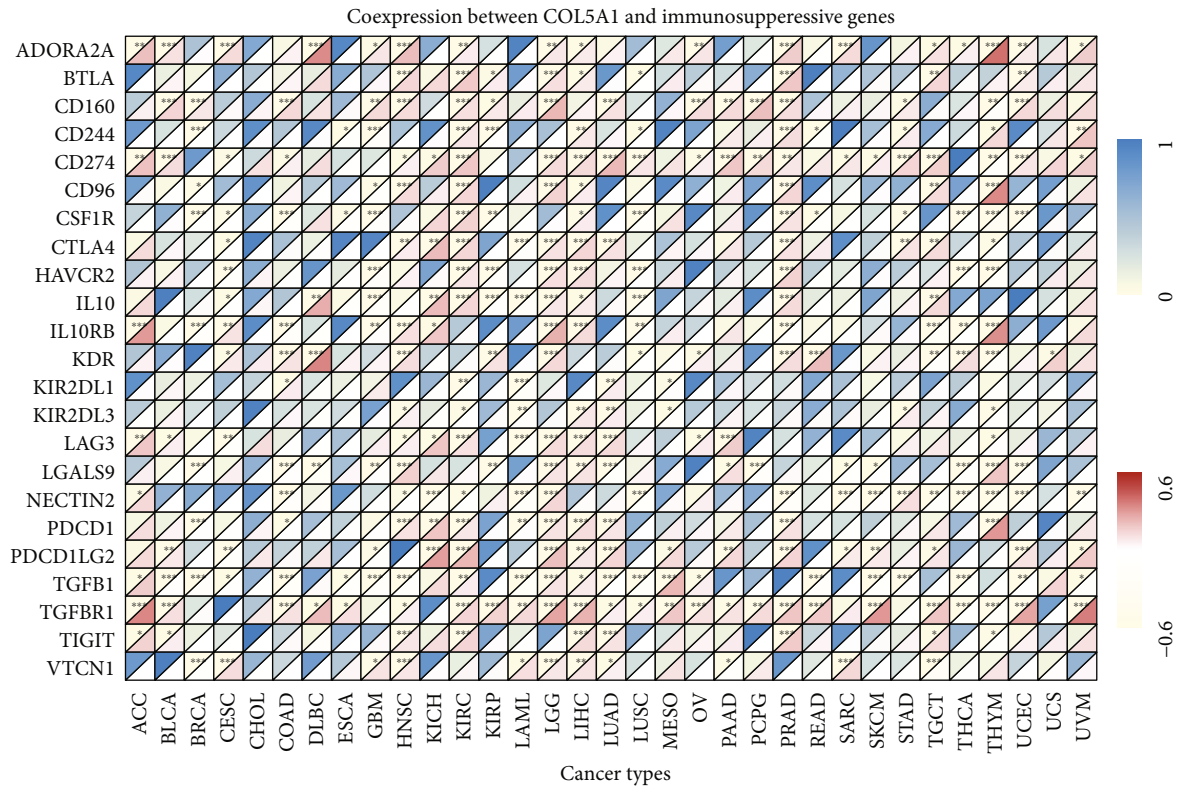


FIGURE 14: Continued.





(c)



(d)

FIGURE 14: Continued.

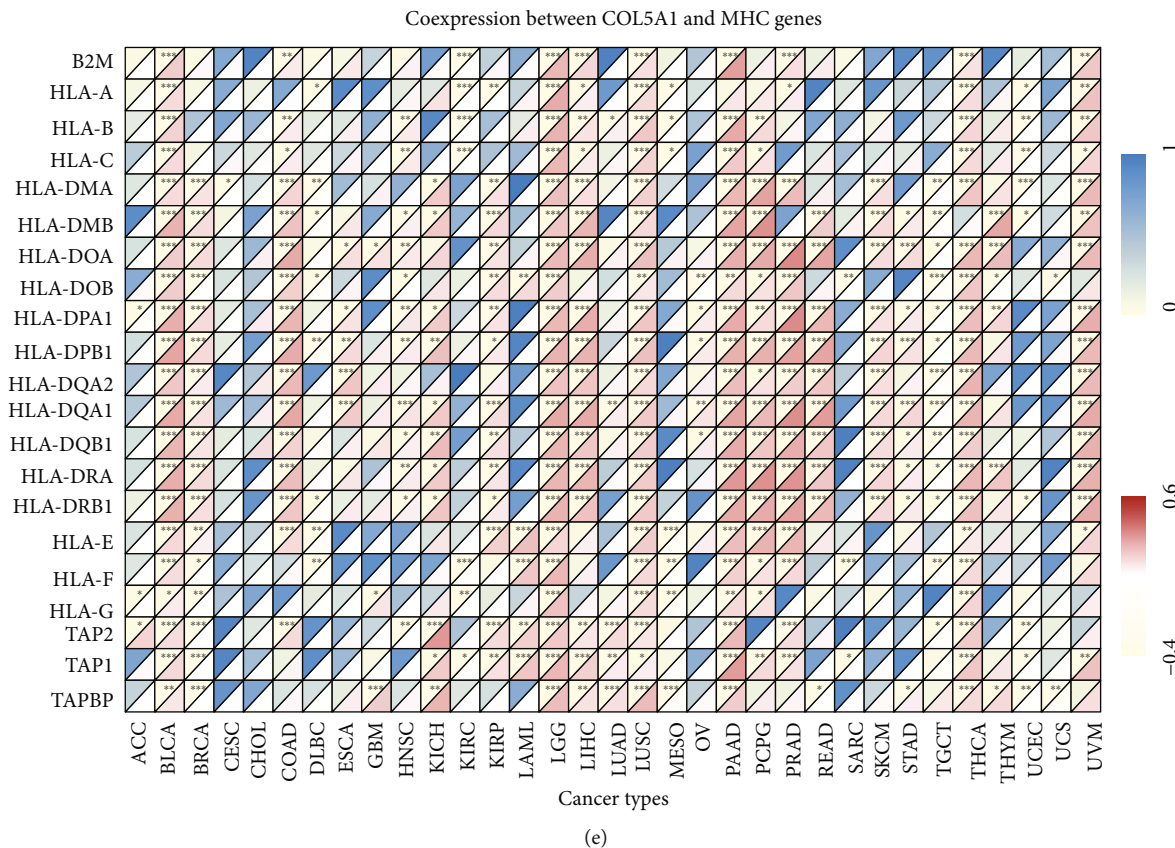


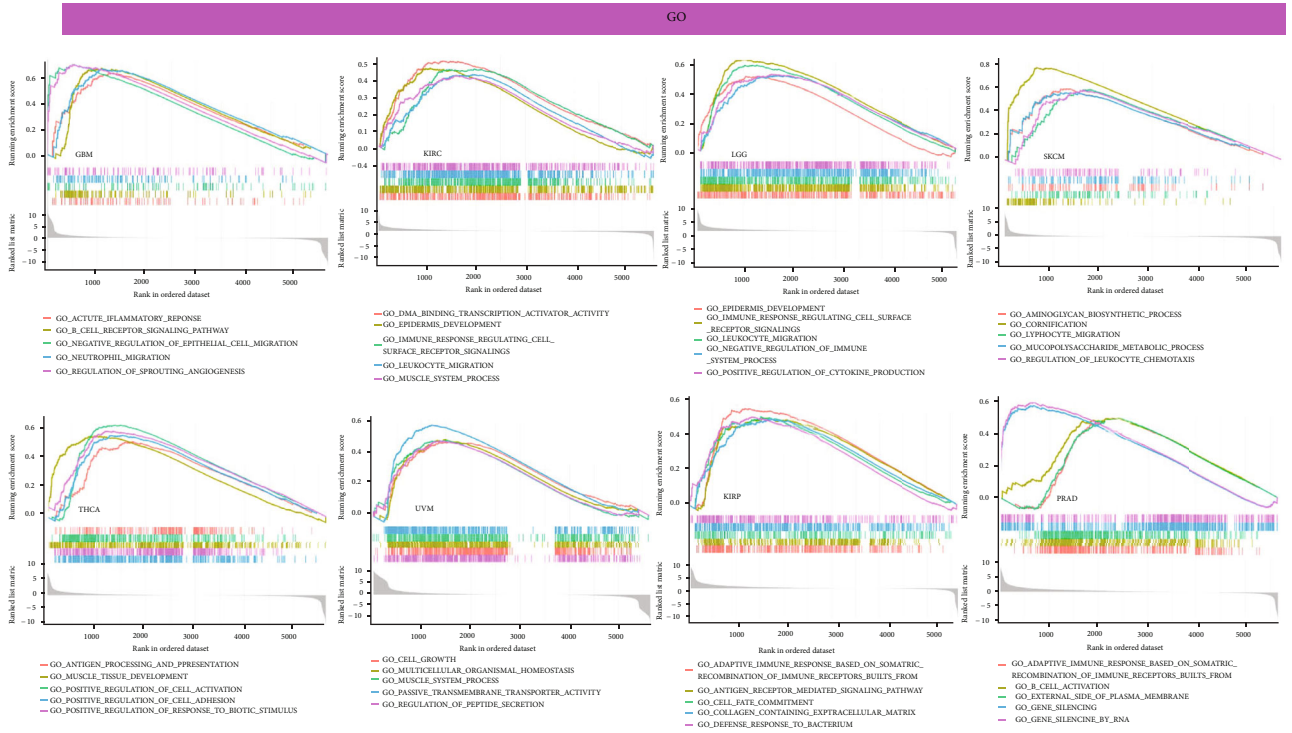
FIGURE 14: Coexpression of COL5A1 with immune-associated genes. \* $p < 0.05$ , \*\* $p < 0.01$ , and \*\*\* $p < 0.001$ .

cancers and was particularly different between stages I and IV, stages II and IV, and stages I and III. For example, in patients with CHOL, KICH, KIRP, and THCA, COL5A1 was overexpressed in stage IV tumors than in stage I tumors. A previous study revealed that COL5A1 may serve as a biomarker of the early stage of systemic sclerosis based on its autoimmune function [38]. These results suggest that COL5A1 can be served as a biomarker to determine the prognosis of a variety of cancers.

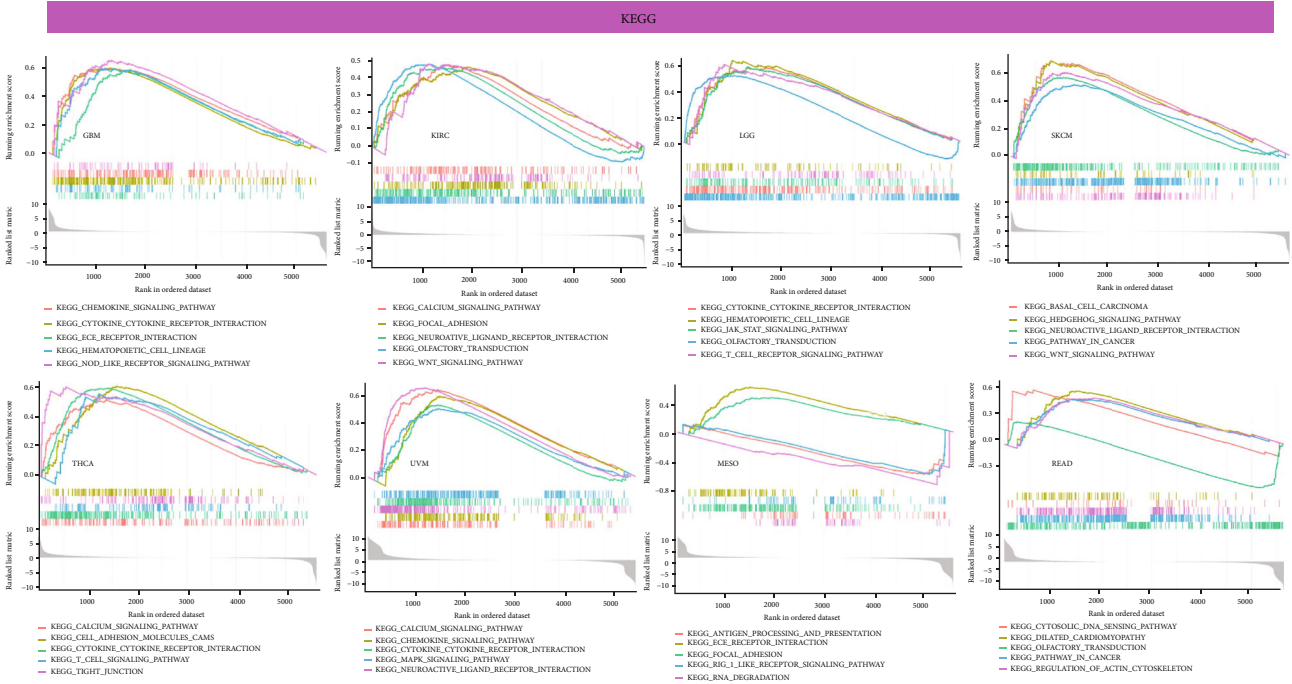
TMB has a role in providing guidance for the precise treatment of immunotherapy [39]. TMB is a biomarker linked to ICB efficacy, and higher TMB is linked to better response to ICB and prolonged OS [40]. MSI is also a biomarker linked to the ICB response [41, 42], and high-frequency MSI in COAD is a predictor for prognosis [43]. The present study illustrated that COL5A1 expression was related to the TMB in 13 tumors and MSI in 6 tumors. Thus, the expression level of COL5A1 may impact the TMB and MSI, thus affecting the patient's response to ICB. These results have a novel guiding value for immunotherapy in patients with different cancers. We assumed that among tumors showing a positive correlation between COL5A1 expression and TMB, patients with tumors presenting high COL5A1 expression and high TMB and MSI may experience a better sensitivity to ICB. We further investigated the correlation of COL5A1 with the immune checkpoints which were strongly associated with response to ICB. These results also

indicated that the expression of COL5A1 may also be a predictor for the response of ICB. Additionally, the correlation of COL5A1 with the sensitivity of chemotherapeutic drugs may have implications for chemotherapy, for example, BLCA patients with high COL5A1 expression may have a more sensitive response of cisplatin treatment (Figure 16(b)).

TME can serve as predictors to assess tumor cell responses to immunotherapy [44]. In our study, COL5A1 played a critical role in the cancer immunity. This study demonstrated that COL5A1 expression was significantly and positively related to the immune component of the TME in 19 tumors and positively linked to the stromal component of the TME in 30 tumors. COL5A1 was reported as a potential target necessary for ICB in HNSC [33]. Additionally, COL5A1 expression correlated with several tumor-infiltrating cells in OV [16]. In addition, COL5A1 was reported to be negatively related to tumor purity but positively linked to immune cell infiltration, and the COL5A1-mediated cell proliferation of STAD may be mediated by effects on the TME [35]. Our study further illuminates that COL5A1 has broader oncological applicability in other tumors, and COL5A1 expression was linked to the biological progression of various TIICs. Additionally, COL5A1 is coexpressed with genes that encode MHC, immune activators, immune suppressors, chemokines, chemokine receptors, and proteins involved in the MMR. These results suggest that COL5A1 expression is related to TIIC infiltration in



(a)



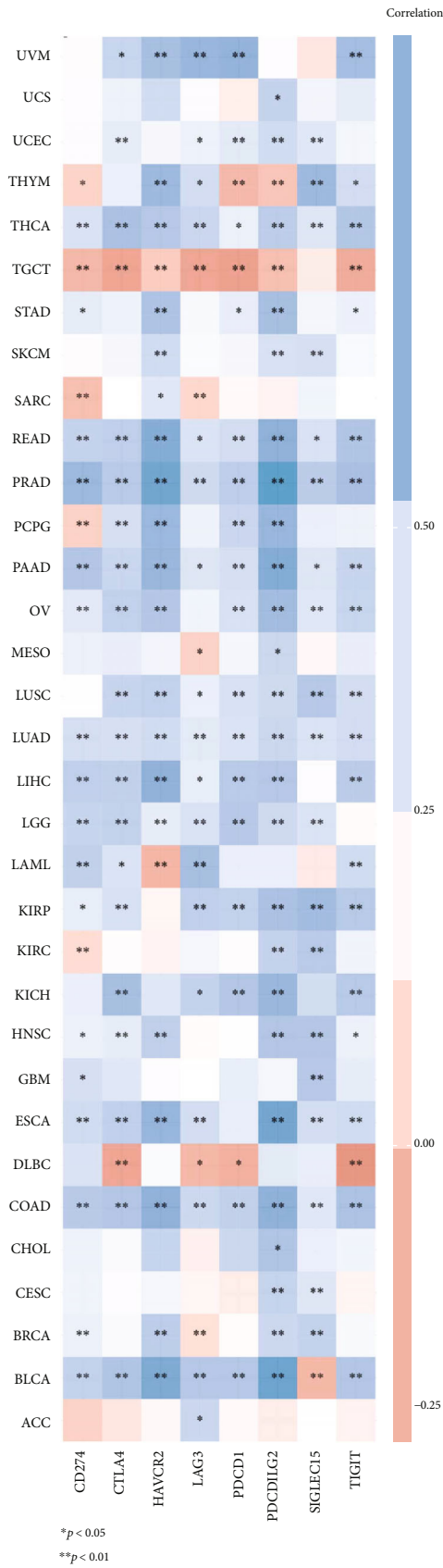
(b)

FIGURE 15: Pathway analyses of COL5A1 in different cancers. (a) GO functional annotations of COL5A1 and (b) KEGG pathway analyses of COL5A1 in various cancers.

the tumor, affects the prognosis, and provides a novel target for improving the efficacy of immunotherapy for patients with various human tumors.

Presently, very few works have assessed the immunological action of COL5A1 in cancers, and COL5A1 is commonly presumed to be a collagen family protein (the most

abundant matrix protein polymer in vertebrates) that is involved in the formation of ECM [7]. It is regarded as a key gene participating in endurance running performance [45]. COL5A1 also has a critical role in tumor development and was reported to promote the proliferation and metastasis of BRCA [46] and LUAD [47]. Notably, high COL5A1



(a)

FIGURE 16: Continued.

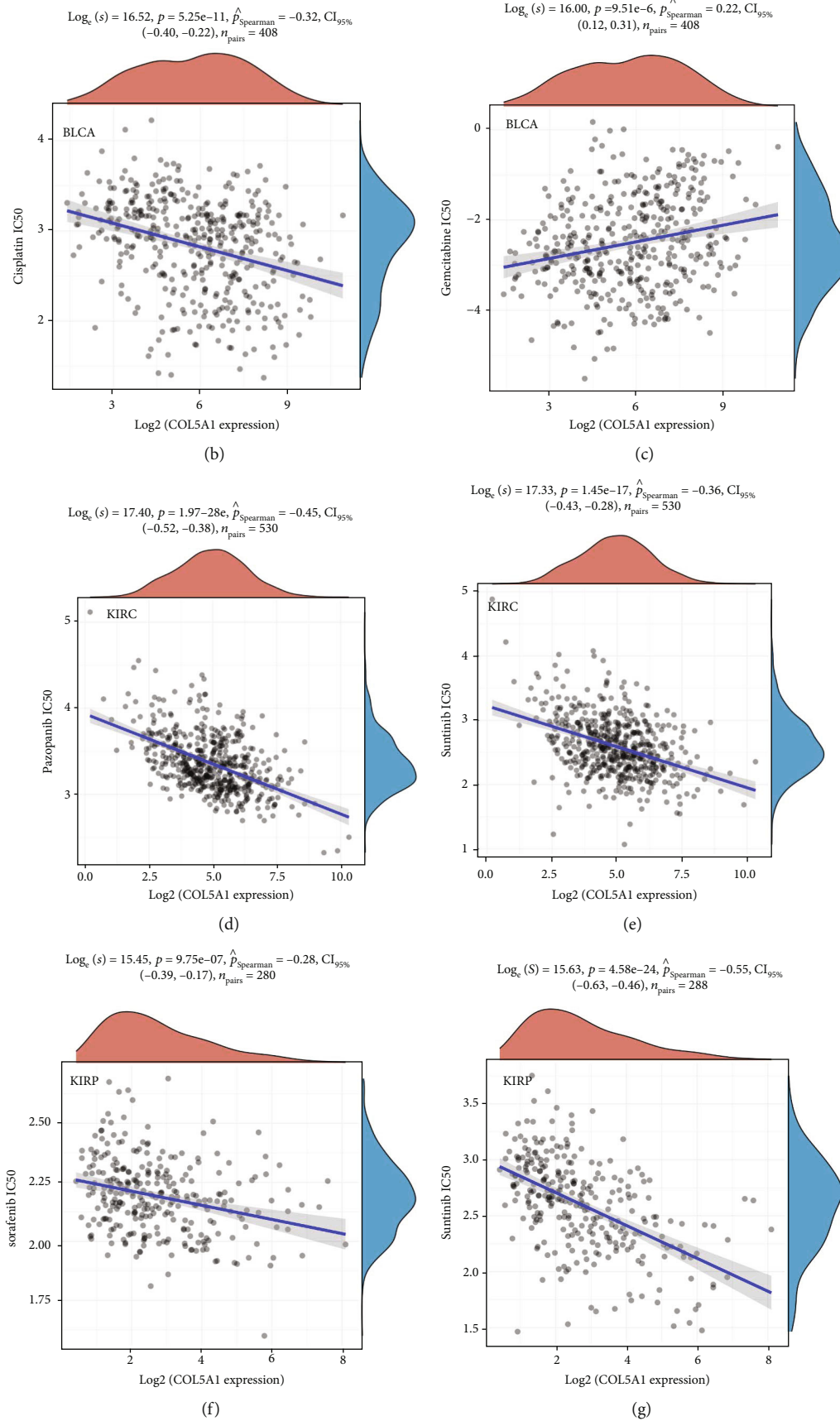


FIGURE 16: Continued.

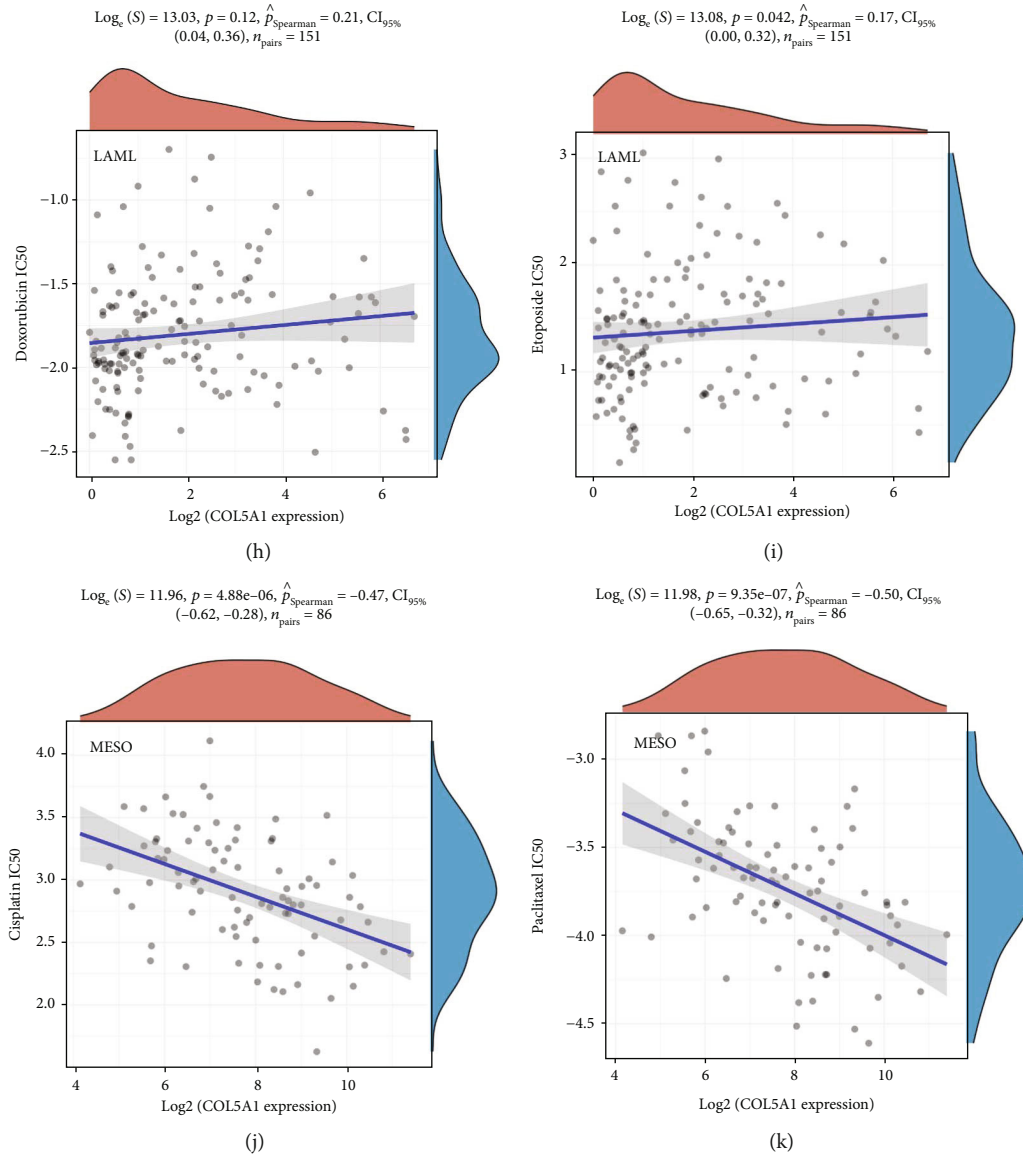


FIGURE 16: Correlation of COL5A1 with immune checkpoint-related genes and drug sensitivity. (a) Heatmap showing the correlation between the COL5A1 and immune checkpoint-related genes. (b–k) Correlation between the COL5A1 and the IC50 of chemotherapeutic drug in various tumors. \* $p < 0.05$ , \*\* $p < 0.01$ .

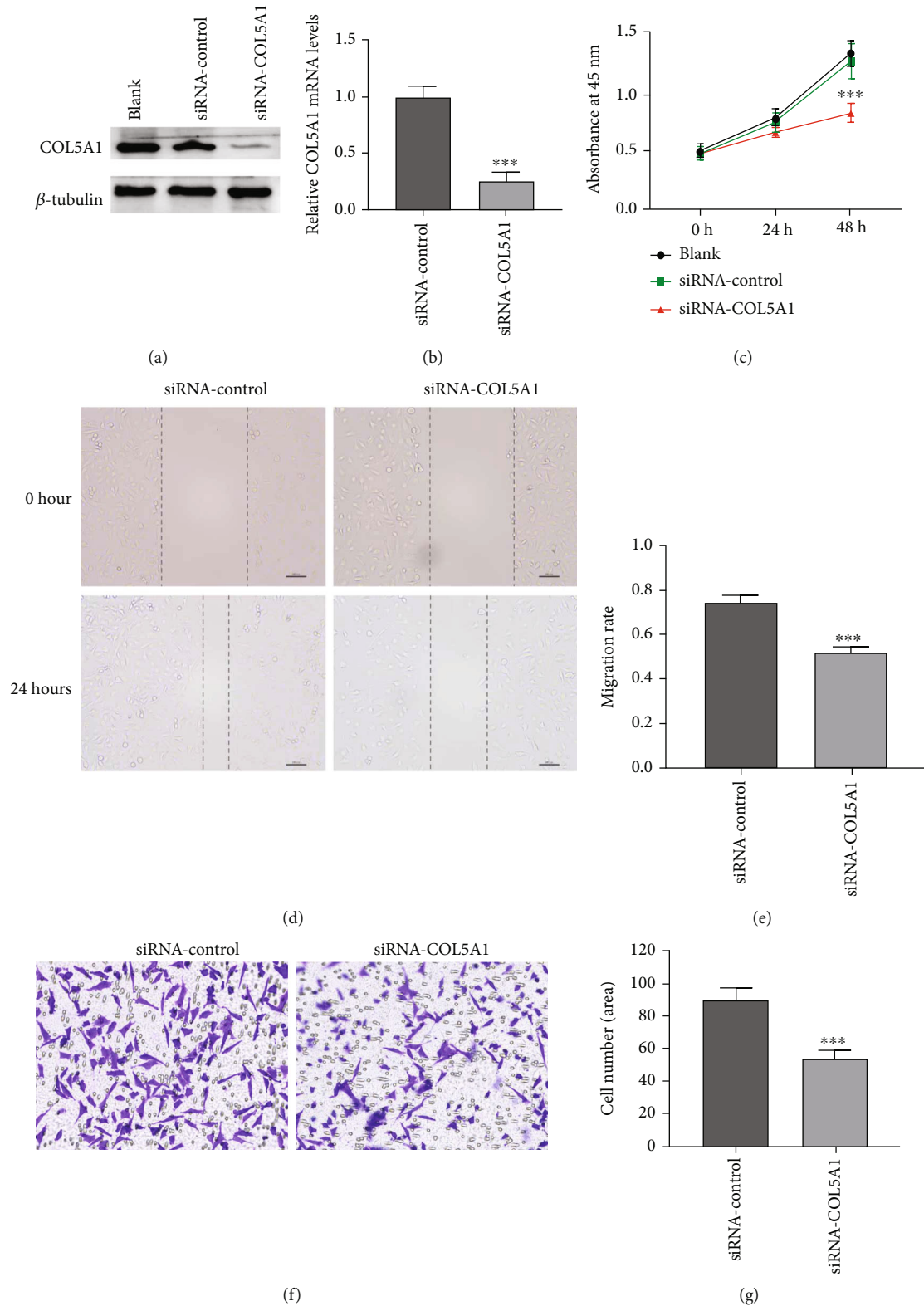


FIGURE 17: Role of COL5A1 in U251 cell proliferation, migration, and invasion. Efficiency of COL5A1 knockdown in U251 cells analyzed by (a) western blotting and (b) qRT-PCR. (d) Representative photographs of wound healing assay, bar = 100  $\mu$ m. (e) siRNA-COL5A1 suppressed U251 cells migration. (f, g) Transwell assay of cell migration and invasion. Amplification,  $\times 200$ . \*\*\* $p < 0.001$ .

expression is related to CD8 T cell, CD4 T cell, dendritic, macrophage, and neutrophil infiltration in STAD [35]. In addition, COL5A1 is regarded as a novel biomarker that

determines sensitivity to ICB therapies in melanoma [48]. In various cancers, our enrichment analysis revealed that COL5A1 potentially influences the etiology or pathogenesis

of cancer through immune-related pathways, chemokine pathways, negative regulation of immune system processes, JAK-STAT pathways, T cell receptor pathways, lymphocyte migration, NOD-like receptor pathways, antigen processing and presentation, MAPK pathways, and adaptive immune responses based on the somatic recombination of immune receptors built from immunoglobulin superfamily domains.

## 5. Conclusions

This first pan-cancer analysis of COL5A1 showed high COL5A1 expression in most tumors compared with normal tissues and revealed a correlation between COL5A1 expression and the prognosis. Based on these findings, COL5A1 may represent an independent prognostic factor for several tumors and that high COL5A1 expression levels in most tumors are linked to poor prognosis. In addition, COL5A1 expression is related to the TMB, MSI, and TIIC infiltration in some human tumors. COL5A1 may serve as a predictor for chemotherapy and immune-based ICB.

## Data Availability

The datasets generated and/or analyzed during the current study are available from the corresponding authors upon reasonable request in compliance with ethical standards.

## Ethical Approval

This study was approved by the Ethics Committee of Renmin Hospital of Wuhan University.

## Conflicts of Interest

The authors declare that they have no conflicts of interest.

## Authors' Contributions

Xiaoxing Xiong and Lijuan Gu designed the experiments. All the authors contributed to performing the experiments. Shi Feng, Zhihong Jian, and Ximing Xu analyzed the data. Hua Zhu and Xinyao Hu wrote the article. All authors read and approved the final manuscript. Hua Zhu and Xinyao Hu contributed equally to this work and share first authorship.

## Acknowledgments

This work was supported by grants from the National Natural Science Foundation of China (No. 81870939 to Xiaoxing Xiong, No. 81771283 and 82071339 to Lijuan Gu) and the Natural Science Foundation of Hubei Province, China (No. 2019CFB498 to Lijuan Gu). We thank the Central Laboratory of Renmin Hospital of Wuhan University and “Linhuang Shengxin Zhi Jia” for providing technical support. We thank all the public datasets that we have used in this study, including TCGA, HPA, GDSC, Oncomine, CCLE, TIMER, and DNMIIVD.

## Supplementary Materials

Table S1: the infiltration of TIIC correlated with COL5A1 expression in various cancer types. Figure S1: representative clinicopathological photographs of the tumor and paracancerous tissues. Figure S2: correlation between age and COL5A1 expression in patients with various cancer types. Figure S3: association between COL5A1 expression and the tumor stage. Figure S4: correlation between COL5A1 expression and stromal or immune scores. Figure S5: GO and KEGG pathway analyses of COL5A1 in various tumors. (*Supplementary Materials*)

## References

- [1] F. Bray, J. Ferlay, I. Soerjomataram, R. L. Siegel, L. A. Torre, and A. Jemal, “Global cancer statistics 2018: GLOBOCAN estimates of incidence and mortality worldwide for 36 cancers in 185 countries,” *CA: a Cancer Journal for Clinicians*, vol. 68, no. 6, pp. 394–424, 2018.
- [2] X. Y. Wang, N. Sun, X. Q. Meng, M. Chen, C. L. Jiang, and J. Q. Cai, “Review of clinical nerve repair strategies for neurorestoration of central nervous system tumor damage,” *Journal of Neurorestoration*, vol. 8, no. 3, pp. 172–181, 2020.
- [3] Z. Deng, H. Yu, N. Wang et al., “Impact of preoperative Karnofsky Performance Scale (KPS) and American Society of Anesthesiologists (ASA) scores on perioperative complications in patients with recurrent glioma undergoing repeated operation,” *Journal of Neurorestoration*, vol. 7, no. 3, pp. 143–152, 2019.
- [4] D. M. Pardoll, “The blockade of immune checkpoints in cancer immunotherapy,” *Nature Reviews. Cancer*, vol. 12, no. 4, pp. 252–264, 2012.
- [5] A. Blum, P. Wang, and J. C. Zenklusen, “SnapShot: TCGA-analyzed tumors,” *Cell*, vol. 173, no. 2, p. 530, 2018.
- [6] X. Hu, H. Zhu, X. Zhang, X. He, and X. Xu, “Comprehensive analysis of pan-cancer reveals potential of ASF1B as a prognostic and immunological biomarker,” *Cancer Medicine*, vol. 10, no. 19, pp. 6897–6916, 2021.
- [7] F. An, Z. Zhang, M. Xia, and L. Xing, “Subpath analysis of each subtype of head and neck cancer based on the regulatory relationship between miRNAs and biological pathways,” *Oncology Reports*, vol. 34, no. 4, pp. 1745–1754, 2015.
- [8] M. Jiang, L. Ren, Y. Chen, H. Wang, H. Wu, S. Cheng et al., “Identification of a hypoxia-related signature for predicting prognosis and the immune microenvironment in bladder cancer,” *Frontiers in Molecular Biosciences*, vol. 8, article 613359, 2021.
- [9] X. L. Tang, Z. Wang, Y. Y. Zhu et al., “Hypoxia-activated ROS burst liposomes boosted by local mild hyperthermia for photo/chemodynamic therapy,” *Journal of Controlled Release*, vol. 328, pp. 100–111, 2020.
- [10] A. C. Martins Cavaco, S. Dâmaso, S. Casimiro, and L. Costa, “Collagen biology making inroads into prognosis and treatment of cancer progression and metastasis,” *Cancer Metastasis Reviews*, vol. 39, no. 3, pp. 603–623, 2020.
- [11] R. J. Wenstrup, J. B. Florer, E. W. Brunskill, S. M. Bell, I. Chervoneva, and D. E. Birk, “Type V Collagen Controls the Initiation of Collagen Fibril Assembly,” *The Journal of Biological Chemistry*, vol. 279, no. 51, pp. 53331–53337, 2004.



- [12] M. Wu, Q. Sun, C. H. Mo et al., "Prospective molecular mechanism of COL5A1 in breast cancer based on a microarray, RNA sequencing and immunohistochemistry," *Oncology Reports*, vol. 42, no. 1, pp. 151–175, 2019.
- [13] J. M. Garcia, S. A. Stillings, J. L. Leclerc et al., "Role of interleukin-10 in acute brain injuries," *Frontiers in Neurology*, vol. 8, p. 244, 2017.
- [14] F. Chai, Y. Liang, F. Zhang, M. Wang, L. Zhong, and J. Jiang, "Systematically identify key genes in inflammatory and non-inflammatory breast cancer," *Gene*, vol. 575, no. 2, pp. 600–614, 2016.
- [15] X. Zhao, H. Cai, X. Wang, and L. Ma, "Discovery of signature genes in gastric cancer associated with prognosis," *Neoplasia*, vol. 63, no. 2, pp. 239–245, 2016.
- [16] J. Zhang, J. Zhang, F. Wang et al., "Overexpressed COL5A1 is correlated with tumor progression, paclitaxel resistance, and tumor-infiltrating immune cells in ovarian cancer," *Journal of Cellular Physiology*, vol. 236, no. 10, pp. 6907–6919, 2021.
- [17] M. Carlsten and M. Järås, "Natural killer cells in myeloid malignancies: immune surveillance, NK cell dysfunction, and pharmacological opportunities to bolster the endogenous NK cells," *Frontiers in Immunology*, vol. 10, p. 2357, 2019.
- [18] H. Zhu, X. Hu, L. Gu et al., "TUBA1C is a prognostic marker in low-grade glioma and correlates with immune cell infiltration in the tumor microenvironment," *Frontiers in Genetics*, vol. 12, article 759953, 2021.
- [19] D. R. Rhodes, J. Yu, K. Shanker et al., "ONCOMINE: A Cancer Microarray Database and Integrated Data-Mining Platform," *Neoplasia*, vol. 6, no. 1, pp. 1–6, 2004.
- [20] H. Zhu, X. Hu, Y. Ye et al., "Pan-cancer analysis of PIMREG as a biomarker for the prognostic and immunological role," *Frontiers in Genetics*, vol. 12, article 687778, 2021.
- [21] I. Diboun, L. Wernisch, C. A. Orengo, and M. Koltzenburg, "Microarray analysis after RNA amplification can detect pronounced differences in gene expression using limma," *BMC Genomics*, vol. 7, no. 1, p. 252, 2006.
- [22] A. M. Newman, C. L. Liu, M. R. Green et al., "Robust enumeration of cell subsets from tissue expression profiles," *Nature Methods*, vol. 12, no. 5, pp. 453–457, 2015.
- [23] X. Lu, L. Jiang, L. Zhang et al., "Immune signature-based subtypes of cervical squamous cell carcinoma tightly associated with human papillomavirus type 16 expression, molecular features, and clinical outcome," *Neoplasia*, vol. 21, no. 6, pp. 591–601, 2019.
- [24] G. Feng, H. M. Ma, H. B. Huang et al., "Overexpression of COL5A1 promotes tumor progression and metastasis and correlates with poor survival of patients with clear cell renal cell carcinoma," *Cancer Management and Research*, vol. - Volume 11, pp. 1263–1274, 2019.
- [25] X. D. Guo, J. Ji, T. F. Xue et al., "FTY720 exerts anti-glioma effects by regulating the glioma microenvironment through increased CXCR4 internalization by glioma-associated microglia," *Frontiers in Immunology*, vol. 11, p. 178, 2020.
- [26] B. Pu, X. Zhang, T. Yan et al., "MICAL2 promotes proliferation and migration of glioblastoma cells through TGF- $\beta$ /p-Smad2/EMT-like signaling Pathway," *Oncology*, vol. 11, no. 4454, 2021.
- [27] M. Fane and A. T. Weeraratna, "How the ageing microenvironment influences tumour progression," *Nature Reviews. Cancer*, vol. 20, no. 2, pp. 89–106, 2020.
- [28] S. Gasser, L. H. K. Lim, and F. S. G. Cheung, "The role of the tumour microenvironment in immunotherapy," *Endocrine-Related Cancer*, vol. 24, no. 12, pp. T283–t295, 2017.
- [29] C. A. Nebhan and D. B. Johnson, "Predictive biomarkers of response to immune checkpoint inhibitors in melanoma," *Expert Review of Anticancer Therapy*, vol. 20, no. 2, pp. 137–145, 2020.
- [30] S. Marwitz, S. Scheufele, S. Perner, M. Reck, O. Ammerpohl, and T. Goldmann, "Epigenetic modifications of the immune-checkpoint genes CTLA4 and PDCD1 in non-small cell lung cancer results in increased expression," *Epigenetics*, vol. 9, no. 1, p. 51, 2017.
- [31] W. Ren, Y. Zhang, L. Zhang, Q. Lin, J. Zhang, and G. Xu, "Overexpression of collagen type V  $\alpha$ 1 chain in human breast invasive ductal carcinoma is mediated by TGF- $\beta$ 1," *International Journal of Oncology*, vol. 52, no. 5, pp. 1694–1704, 2018.
- [32] F. F. Chen, S. R. Zhang, H. Peng, Y. Z. Chen, and X. B. Cui, "Integrative genomics analysis of hub genes and their relationship with prognosis and signaling pathways in esophageal squamous cell carcinoma," *Molecular Medicine Reports*, vol. 20, no. 4, pp. 3649–3660, 2019.
- [33] Y. Chen, Z. Y. Li, G. Q. Zhou, and Y. Sun, "An immune-related gene prognostic index for head and neck squamous cell carcinoma," *Clinical Cancer Research*, vol. 27, no. 1, pp. 330–341, 2021.
- [34] M. Wu, L. Xu, Y. Wang et al., "S100A8/A9 induces microglia activation and promotes the apoptosis of oligodendrocyte precursor cells by activating the NF- $\kappa$ B signaling pathway," *Brain Research Bulletin*, vol. 143, pp. 234–245, 2018.
- [35] Z. Wei, L. Chen, L. Meng, W. Han, L. Huang, and A. Xu, "LncRNA HOTAIR promotes the growth and metastasis of gastric cancer by sponging miR-1277-5p and upregulating COL5A1," *Gastric Cancer*, vol. 23, no. 6, pp. 1018–1032, 2020.
- [36] C. Guo, T. Shao, D. Wei et al., "Bioinformatic identification of potential hub genes in muscle-invasive bladder urothelial carcinoma," *Cell Transplantation*, vol. 29, article 963689720965178, 2020.
- [37] S. Gao, L. Yan, H. Zhang, X. Fan, X. Jiao, and F. Shao, "Identification of a metastasis-associated gene signature of clear cell renal cell carcinoma," *Frontiers in Genetics*, vol. 11, article 603455, 2021.
- [38] A. P. P. Velosa, L. Brito, Z. A. de Jesus Queiroz et al., "Identification of autoimmunity to peptides of collagen V  $\alpha$ 1 chain as newly biomarkers of early stage of systemic sclerosis," *Frontiers in Immunology*, vol. 11, article 604602, 2021.
- [39] J. D. Fumet, C. Truntzer, M. Yarchoan, and F. Ghiringhelli, "Tumour mutational burden as a biomarker for immunotherapy: current data and emerging concepts," *European Journal of Cancer*, vol. 131, pp. 40–50, 2020.
- [40] R. M. Samstein, C. H. Lee, A. N. Shoushtari et al., "Tumor mutational load predicts survival after immunotherapy across multiple cancer types," *Nature Genetics*, vol. 51, no. 2, pp. 202–206, 2019.
- [41] D. W. Lee, S. W. Han, J. M. Bae et al., "Tumor mutation burden and prognosis in patients with colorectal cancer treated with adjuvant fluoropyrimidine and oxaliplatin," *Clinical Cancer Research*, vol. 25, no. 20, pp. 6141–6147, 2019.
- [42] C. R. Boland and A. Goel, "Microsatellite instability in colorectal cancer," *Gastroenterology*, vol. 138, no. 6, pp. 2073–2087.e3, 2010.

- [43] R. Gryfe, H. Kim, E. T. Hsieh et al., "Tumor microsatellite instability and clinical outcome in young patients with colorectal cancer," *The New England Journal of Medicine*, vol. 342, no. 2, pp. 69–77, 2000.
- [44] T. Wu and Y. Dai, "Tumor microenvironment and therapeutic response," *Cancer Letters*, vol. 387, pp. 61–68, 2017.
- [45] M. Posthumus, M. P. Schwellnus, and M. Collins, "The COL5A1 Gene," *Medicine and Science in Sports and Exercise*, vol. 43, no. 4, pp. 584–589, 2011.
- [46] B. Zhao, X. Song, and H. Guan, "CircACAP2 promotes breast cancer proliferation and metastasis by targeting miR-29a/b-3p-COL5A1 axis," *Life Sciences*, vol. 244, article 117179, 2020.
- [47] W. Liu, H. Wei, Z. Gao et al., "\_COL5A1\_ may contribute the metastasis of lung adenocarcinoma," *Gene*, vol. 665, pp. 57–66, 2018.
- [48] H. Chen, M. Yang, Q. Wang, F. Song, X. Li, and K. Chen, "The new identified biomarkers determine sensitivity to immune check-point blockade therapies in melanoma," *Oncoimmunology*, vol. 8, no. 8, p. 1608132, 2019.

## Research Article

# lncRNA SNHG15 Induced by SOX12 Promotes the Tumorigenic Properties and Chemoresistance in Cervical Cancer via the miR-4735-3p/HIF1 $\alpha$ Pathway

Jiang Yang, Mei Yang, Huabing Lv, Min Zhou, Xiaogang Mao, Xiaomin Qin, Ying Xu, Lin Li , and Hui Xing 

Department of Obstetrics and Gynecology, Xiangyang Central Hospital, Affiliated Hospital of Hubei University of Arts and Science, Xiangyang, Hubei, China

Correspondence should be addressed to Lin Li; ll119@tom.com and Hui Xing; huixinghx123@163.com

Received 31 July 2021; Revised 2 November 2021; Accepted 8 November 2021; Published 12 January 2022

Academic Editor: Peichao CHEN

Copyright © 2022 Jiang Yang et al. This is an open access article distributed under the Creative Commons Attribution License, which permits unrestricted use, distribution, and reproduction in any medium, provided the original work is properly cited.

Cervical cancer (CC) is one of the most common malignancies in females, with high prevalence and mortality globally. Despite advances in diagnosis and therapeutic strategies developed in recent years, CC is still a major health burden worldwide. The molecular mechanisms underlying the development of CC need to be understood. In this study, we aimed to demonstrate the role of lncRNA SNHG15 in CC progression. Using qRT-PCR, we determined that lncRNA SNHG15 is highly expressed in CC tumor tissues and cells. lncRNA SNHG15 knockdown also reduces the tumorigenic properties of CC *in vitro*, as determined using the MTT, EdU, flow cytometry, and transwell assays. Using bioinformatics analysis, RNA pull-down, ChIP, and luciferase reporter assays, we verified the molecular mechanisms of lncRNA SNHG15 in CC progression and found that lncRNA SNHG15 expression in CC cells is transcriptionally regulated by SOX12; moreover, lncRNA SNHG15 promotes CC progression via the miR-4735-3p/HIF1 $\alpha$  axis. This study can provide a potential target for CC diagnosis or therapeutic strategies in the future.

## 1. Introduction

Cervical cancer (CC) ranks next to breast cancer as the most common malignancy and is the third leading cause of cancer-related deaths in females globally [1]. The health burden associated with CC is more severe in developing countries [2], particularly in low-income countries, than in developed countries [2]. Multiple risk factors contribute to the initiation and progression of CC, such as viral infection, genetic influences, and human papillomavirus (HR-HPV) genotype infection [3, 4]. Despite improvement in clinical intervention strategies, such as the global application of standard vaccination, surgical resection innovation, and periodic cancer screening in recent decades, the outcomes of patients with CC remain poor. Therefore, the molecular mechanisms underlying CC development need to be understood, and novel therapeutic targets for the prevention and treatment of CC have to be urgently developed.

Long noncoding RNAs (lncRNAs) are newly discovered no-coding RNAs longer 200 nt [5]. Emerging evidence has elucidated the crucial role of lncRNAs in various diseases, including cancers. lncRNA NBR2 suppresses tumorigenesis in hepatocellular cancer via modulating autophagy level [6]. lncRNA GATA3-AS1 regulates triple-negative breast cancer by facilitating tumorigenesis and immune escape phenomena [7]. lncRNA HOTAIR facilitates exosome secretion in hepatocellular cancer by regulating RAB35 and SNAP23 [8]. lncRNA ASB16-AS1 plays an oncogenic role in renal cell carcinoma progression by acting as a ceRNA for miR-185-5p/miR-214-3p [9]. The lncRNA small nucleolar RNA host gene 15 (lncRNA SNHG15) is located on chromosome 7p13 and was first elucidated in a study of cellular stress responses [10, 11]. The function of lncRNA SNHG15 in various cancers has also been investigated, including breast cancer, colorectal cancer, gastric cancer, hepatocellular cancer, and lung cancer [12–16]. Meanwhile, whether

lncRNA SNHG15 participates in CC progression remains unclear.

In this study, we aimed to demonstrate the role of lncRNA SNHG15 in CC progression. We found that lncRNA SNHG15 was abundantly expressed in CC tumors and cells. lncRNA SNHG15 knockdown significantly attenuated tumorigenesis in CC *in vitro* and *in vivo*, as determined using the MTT, EdU, flow cytometry, and transwell assays, in addition to animal experiments. Further, our study revealed that lncRNA SNHG15 influenced the chemoresistance of CC cells to cisplatin. We then investigated the molecular mechanisms of lncRNA SNHG15 in CC cells by conducting bioinformatics analysis, RNA pull-down, ChIP, and luciferase reporter assay. It was found that lncRNA SNHG15 expression in CC cells was transcriptionally regulated by SRY-Box Transcription Factor 12 (SOX12). Further, we found that lncRNA SNHG15 upregulated HIF1a expression to regulate tumorigenesis in CC by sponging miR-4735-3p. Thus, our study elucidated the effect of SOX12/lncRNA SNHG15/miR-4735-3p/HIF1a axis on the biological features of CC.

## 2. Materials and Methods

**2.1. Clinical Samples.** A total of twenty-eight pairs of CC tumor tissues and comparative normal tissues were collected from Xiangyang Central Hospital within the period 2019/06 to 2020/06. All CC tissues were immediately stored in  $-80^{\circ}\text{C}$  liquid nitrogen until the experiment was conducted. Informed consent was obtained from each patient. All CC tissues were confirmed by two pathologists, independently. This study was performed following the principles of the Declaration of Helsinki and was approved by the ethical committee of Xiangyang Central Hospital.

**2.2. Cell Culture and Transfection.** All cervical cancer cell lines (SiHa, HeLa, Caski, C-33A, and MS751) and normal cell line HEK293T were commercially obtained from the Committee on Type Culture Collection of the Chinese Academy of Sciences (Shanghai, China). Cells were cultured using Dulbecco's Modified Eagle's Medium (DMEM; Invitrogen, USA) supplied with 10% fetal bovine serum (FBS) at  $37^{\circ}\text{C}$  in a humidified 5%  $\text{CO}_2$  environment.

All siRNAs targeting lncRNA SNHG15 were synthesized and obtained from Sigma-Aldrich (USA). Moreover, miRNA mimics, inhibitors, and normal controls were procured from GenePharma (Shanghai, China). The pcDNA3.1 (+) vector (GenePharma, Shanghai) was applied to generate overexpression vectors. The siRNA sequences are as follows: si-NC: F: 5'-CAGUCGCGUUUGCGACUGGC-3' and R: 5'-GCCAGUCGCAAACGCGACUG-3', si-SNHG15#1: F: 5'-CCUUGAGUCUCAUGUCAA-3' and R: 5'-UUGAAC AUGAGACUCAAGG-3', si-SNHG15#2: F: 5'-GAGCUU ACUGUCACAGCAA-3' and R: 5'-UUGCUGUGACA GUAAGCUC-3'. A Lipofectamine 3000 (Invitrogen) was applied to conduct transfections.

**2.3. RNA Extraction and qRT-PCR.** All RNAs were collected from tissues and cells by using the TRIzol Reagent (Thermo

Fisher Scientific) in accordance with the manufacturer protocols. Reverse-transcription was performed using the SuperScript™ III First-Strand Synthesis System (Thermo Fisher Scientific). The expression level of the indicated gene was measured using the SYBR Green Real-Time PCR Master Mixes (Thermo Fisher Scientific) on the ABI Prism 700 thermal cycler (Applied Biosystems, Foster City, CA). U6 and GAPDH were used as internal controls. The relative gene expression was calculated using the  $2^{-\Delta\Delta\text{Ct}}$  method. The primers applied in this study are as follows: lncRNA SNHG15: F: GCTGAGGTGACGGTCTCAA and R: GCCTCCAGTTTCATGGACA, miR-4735-3p: F: 5'-GGTAGCTGAGAACATTACAG-3' and R: 5'-CTATTC TGGAACATCAAGCC-3', HIF1a: F: 5'-TGTGAACCCAT TCCTCATCCA-3' and R: 5'-GGTCATAACCCATCA ACTCA-3', SOX12: F: 5'-CGCGATGGTGCAGCAGCG-3' and R: 5'-GCCACTGGTCCATGATCTTC-3', U6: F: TCCGATCGTGAAGCGTTC and R: GTGCAGGGTCC GAGGT, GAPDH: F: CGGAGTCAACGGATTTGGTGC TAT and R: AGCCTTCTCCATGGTGGTGAAGAC.

**2.4. Western Blot.** All proteins were isolated from tissues and cells by using the RIPA Buffer (Solarbio, R0020). Protein samples were maintained by SDS-PAGE using 8%-12% gels (Beyotime, P0012A). Subsequently, protein samples were then electronically transferred onto a polyvinylidene difluoride membrane (0.45  $\mu\text{m}$ ) (Millipore, IPVH00010) and then blocked using 5% skimmed milk. Next, primary antibodies were subsequently used to incubate with membranes at  $4^{\circ}\text{C}$  for 12 hours, followed by incubation with secondary antibodies at room temperature for 2 hours. Results were visualized using the UVP ChemiDoc-It Imaging System (UVP, CA, USA). The antibodies used in this study were as follows: HIF1a (1:1000; ab237544; Abcam) and GAPDH (1:1000; # 5174S; CST).

**2.5. Cell Proliferation Detection.** 3-(4,5-Dimethylthiazol-2-yl)-2,5-diphenyltetrazolium bromide (MTT) assay. Cells were cultured in a 96 well-plate for proliferation detection. The culture medium was added sequentially with 10  $\mu\text{L}$  MTT (Invitrogen) for 24, 48, and 72 h. Formazan was dissolved using DMSO (Sigma, USA). After 4 h, the absorbance of each well was measured on a plate reader at 570 nm. The experiment was conducted in triplicate.

**5-Ethynyl-2'-deoxyuridine (EdU) experiment.** The experimental cells were first cultured in a 96-well plate after transfection. The EdU kit (KeyGEN BioTECH) was used to stain cells in the well in accordance with instructions provided by the manufacturer. The results (EdU-positive cells) were recorded by a fluorescence microscopy.

**2.6. Cell Apoptosis Detection.** The apoptosis rate of infected CC cells was detected by flow cytometry analysis. The infected CC cells were stained using an Annexin V-fluorescein isothiocyanate (FITC)/propidium iodide (PI) kit (BD Biosciences, USA), and the results were calculated with a flow cytometer using the CellQuest software version 0.9.3.1 (BD Biosciences, USA).

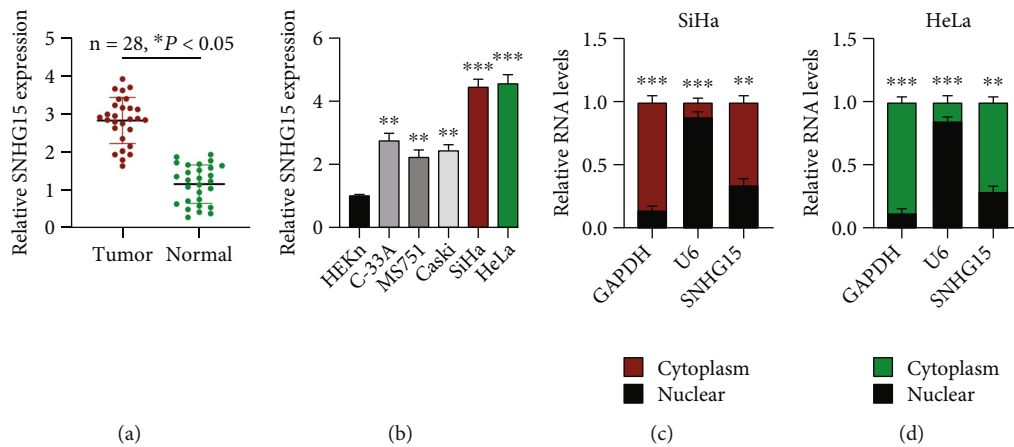


FIGURE 1: Expression characteristics of lncRNA SNHG15 in cervical cancer (CC). (a) lncRNA SNHG15 expression in CC tumor samples ( $n = 28$ ) and adjacent normal samples ( $n = 28$ ), measured by qRT-PCR. (b) lncRNA SNHG15 expression in CC cell lines, assessed by qRT-PCR. (c, d) lncRNA SNHG15 expression distribution in (c) SiHa and (d) HeLa cells, assessed using the cellular distribution assay. Data are presented as mean  $\pm$  SD; \* $p < 0.5$ , \*\* $p < 0.01$ , and \*\*\* $p < 0.001$ .

**2.7. Cell Migration Detection.** The migratory ability of infected CC cells was detected using the transwell assay. In summary, the infected CC cells were seeded in the upper chambers (Costar, USA) supplied with the serum-free RPMI-1640 medium, and the lower chambers without cells were supplied with full medium. After incubation for one day, the migrated cells were fixed with 4% paraformaldehyde and then stained with crystal violet. The results were recorded by a microscopy.

**2.8. Murine Xenograft Assay.** SiHa and HeLa cells stably transfected with si-SHNG15#1, si-SHNG15#2, or si-NC were injected into mice aged 4 weeks at a density of  $1 \times 10^6$  cells. The dimensions of the tumors were determined, and their weights were recorded after injection for 28 d. The animal procedures conducted in this study complied with the guidelines set by the ethical committee of Xiangyang Central Hospital.

**2.9. RNA Pull-down Assay.** SiHa and HeLa cells were infected using 50 nM biotinylated probes, which were synthesized and procured from GenePharma (Shanghai, China). After 2 d, the M-280 streptavidin magnetic beads (Sigma-Aldrich, USA) were used to incubate with the cell lysate at 4°C for 3 h. The beads were then washed, and the bound RNAs were isolated using the TRIzol Reagent. The results were analyzed by qRT-PCR. The experiment was performed 3 times.

**2.10. Luciferase Assays.** Cells were first cultured in a 24-well plate ( $1 \times 10^4$  cells per well) for 2 d. They were then transfected with the indicated vectors using a Lipofectamine 3000 kit (Invitrogen) in accordance with the manufacturer protocols. After 2 d, the luciferase activities were measured using the Dual-Luciferase Reporter Assay System (Promega). The experiment was performed 3 times.

**2.11. Chromatin Immunoprecipitation (ChIP) Assay.** Infected CC cells were stained with 1% formaldehyde and lysed at room temperature for 10 min. The genome was frag-

mented to ~500 bp upon sonication. Antibodies were used to incubate the cell lysate for 12 hours. The lysate was subsequently incubated with Protein A Agarose/Salmon Sperm DNA (50% Slurry) beads for 6 hours. The results were analyzed by qRT-PCR assay.

**2.12. Statistical Analysis.** The GraphPad Prism software (GraphPad, USA) was used to calculate all data in this study. Statistical analysis was performed using two-tailed Student's  $t$ -test.  $p < 0.05$  indicated a significant difference. Data in this study are presented using the mean  $\pm$  square deviation (SD).

### 3. Results

**3.1. Expression Characteristics of lncRNA SNHG15 in Cervical Cancer.** To identify the possible function of lncRNA SNHG15 in CC progression, we first investigated the expression profile of lncRNA SNHG15 in CC. Twenty-eight pairs of CC tumor tissues and its comparative normal tissues were examined. lncRNA SNHG15 was noticeably upregulated in CC tumor tissues relative to that in normal tissues (Figure 1(a)). We further found that lncRNA SNHG15 was abundantly expressed in CC cell lines (Figure 1(b)) and mainly located in the cell cytoplasm (Figures 1(c) and 1(d)). On the basis of these combined findings, we hypothesized that lncRNA SNHG15 is involved in CC progression.

**3.2. lncRNA SNHG15 Knockdown Attenuates CC Tumorigenesis and Chemoresistance In Vitro.** Given the abundant expression of lncRNA SNHG15 in CC tumor tissues and cells, we generated knockdown cell models of lncRNA SNHG15 to explore its cellular function (Figure 2(a)). We first examined the proliferation level of lncRNA SNHG15 knockdown cells by using the MTT assay (Figures 2(b) and 2(c)) and the EdU assay (Figures 2(d) and 2(e)) in SiHa and HeLa cells and found that lncRNA SNHG15 downregulation markedly suppressed CC cell proliferation. lncRNA SNHG15 downregulation significantly promoted the cell apoptosis rate (Figures 2(f) and 2(g)), as

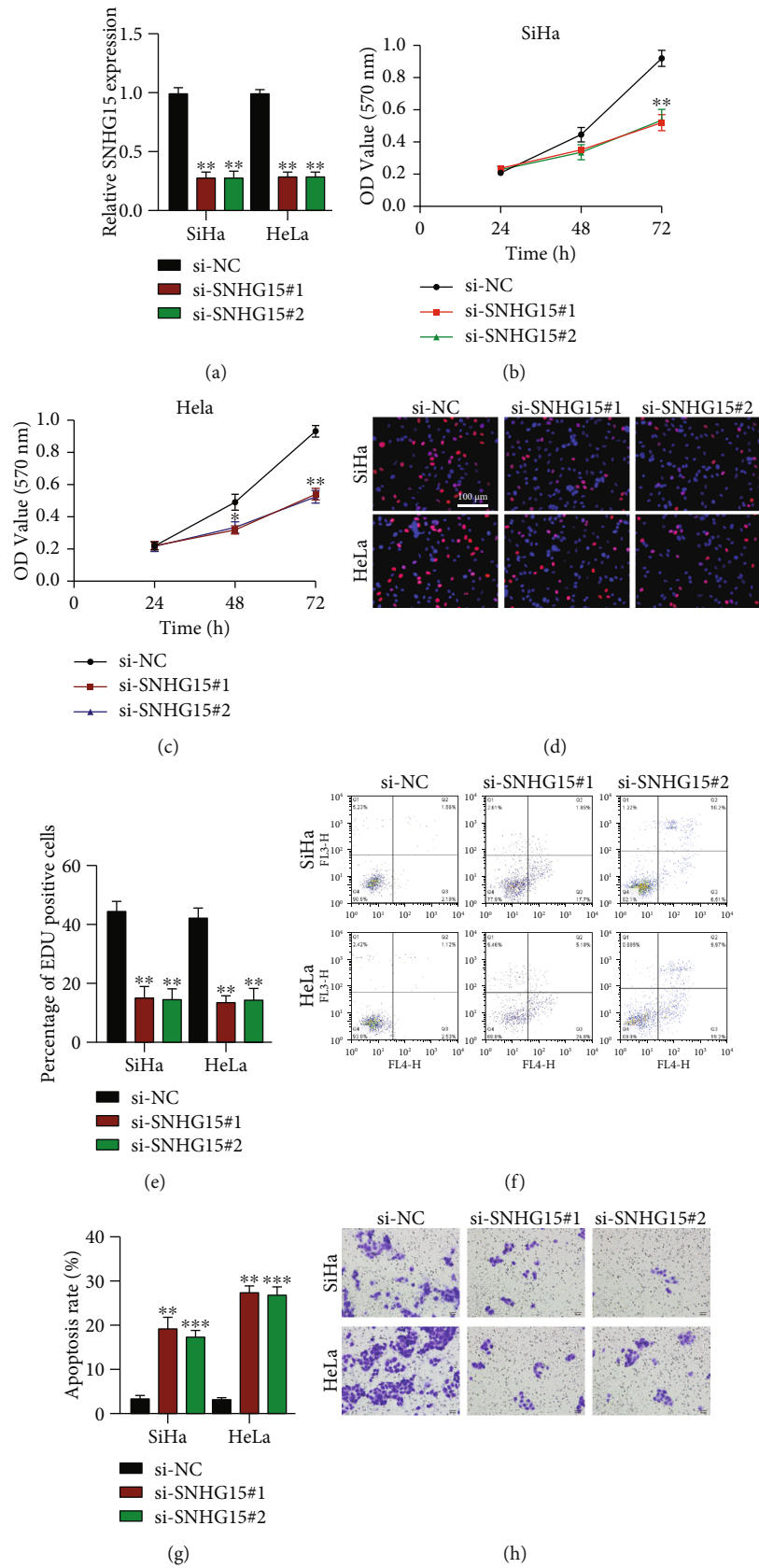


FIGURE 2: Continued.

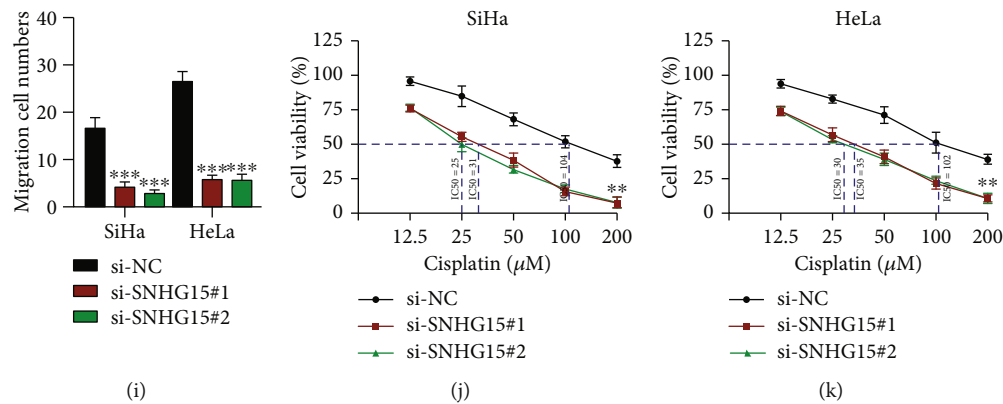


FIGURE 2: lncRNA SNHG15 knockdown attenuates cervical cancer (CC) tumorigenesis and chemoresistance *in vitro*. (a) lncRNA SNHG15 expression in CC cells after knockdown with two siRNAs, measured by qRT-PCR. (b, c) Cell proliferation in (b) SiHa and (c) HeLa cells, detected using the MTT assay. (d, e) Cell viabilities in (d) SiHa and HeLa cells, evaluated using the EdU assay; (e) analysis of results. (f) Cell apoptosis measured by flow cytometry assay and (g) calculation of the results. (h) Cell migration, assessed using the transwell migration experiment; (i) statistical analysis. (j) SiHa and (k) HeLa cells were treated with cisplatin at varying concentrations; chemoresistance of CC cells was evaluated using the MTT assay. Data are presented as mean  $\pm$  SD; \*\* $p$  < 0.01 and \*\*\* $p$  < 0.001.

determined by flow cytometer assay. Moreover, lncRNA SNHG15 downregulation distinctly inhibited the CC cell migration, as determined using the transwell assay (Figures 2(h) and 2(i)). Notably, we examined whether lncRNA SNHG15 influences the resistance of CC cells to cisplatin, and lncRNA SNHG15 knockdown reduced the inhibitory concentration 50% (IC<sub>50</sub>) of SiHa and HeLa cells (Figures 2(j) and 2(k), respectively), respectively, indicating that lncRNA SNHG15 downregulation reduced the chemoresistance of CC cells to cisplatin. The results demonstrated that lncRNA SNHG15 knockdown inhibited cell proliferation, migration, and chemoresistance to cisplatin, as well as promoted cell apoptosis. Gain-of-function assays were also performed to confirm the functional role of lncRNA SNHG15 in CC progression (Supplementary Materials Figure S1); lncRNA SNHG15 overexpression promoted cell proliferation, migration, and chemoresistance to cisplatin but repressed cell apoptosis.

**3.3. lncRNA SNHG15 Expression in CC Is Transcriptionally Regulated by SOX12.** We investigated the upstream regulator of lncRNA SNHG15 in CC cells. Bioinformatics analysis was conducted, and 6 potential transcriptional regulators were predicted. We found that lncRNA SNHG15 expression was markedly decreased in CC cells under SRY-Box Transcription Factor 12 (SOX12) knockdown (Figures 3(a) and 3(b)) and increased in CC cells upon SOX12 overexpression (Figure 3(c)). The binding motif in SOX12 and the binding sites of the lncRNA SNHG15 promoter were acquired from the JASPAR database (Figures 3(e) and 3(e)). Chromatin immunoprecipitation (ChIP) assay results showed that the lncRNA SNHG15 promoter was pulled down by the SOX12 antibody in the SiHa and HeLa cells (Figure 3(f)). The interaction between SOX12 and the lncRNA SNHG15 promoter was verified by the luciferase reporter assay conducted on the SiHa and HeLa cells (Figures 3(g) and 3(h)). Combined, these findings indicated that SOX12 modulated lncRNA SNHG15 transcription in CC cells.

**3.4. lncRNA SNHG15 Sponges miR-4735-3p.** The downstream target of lncRNA SNHG15 in CC cells was explored. The prediction from the starBase dataset showed 8 putative miRNA targets. Data from the biotinylated RNA pull-down assay revealed that 4 miRNA targets could potentially interact with lncRNA SNHG15 in CC cells (Figures 4(a) and 4(b)). Among the potential interactions, those between lncRNA SNHG15 and miR-188-5p [17, 18], miR-346 [19], and miR-18b-5p [20] have been previously verified. In the current study, we investigated the relation between lncRNA SNHG15 and miR-4735-3p in CC cells. Results from the RNA pull-down assay indicated that lncRNA SNHG15 could be pulled down by miR-4735-3p probes in SiHa and HeLa cells (Figure 4(c)). Binding sites between lncRNA SNHG15 and miR-4735-3p were revealed (Figure 4(d)), and the transfection efficiency of the miR-4735-3p mimic was assessed (Figure 4(e)). Results from the luciferase reporter assay suggested that lncRNA SNHG15 directly targeted miR-4735-3p in CC cells (Figures 4(f) and 4(g)). Moreover, miR-4735-3p expression in CC cells was upregulated under lncRNA SNHG15 knockdown (Figure 4(h)) and upregulated in CC tumors relative to that in normal samples (Figure 4(i)). These data revealed the miR-4735-3p as a downstream target for lncRNA SNHG15 in CC.

**3.5. miR-4735-3p Modulates Tumorigenesis and Chemoresistance in Cervical Cancer.** We revealed miR-4735-3p as a target for lncRNA SNHG15 in CC cells; however, the function of miR-4735-3p remained unverified. Thus, we conducted a gain- or loss-of-function experiment on miR-4735-3p in CC cells. Cell models were generated as indicated (Figure 5(a)). CC cell proliferation was markedly suppressed by the miR-4735-3p mimic but promoted by the miR-4735-3p inhibitor, as determined using the MTT assay (Figures 5(b)–5(e)) and the EdU assay (Figures 5(f) and 5(g), Supplementary Materials Figures S2A–S2B). Flow cytometry results showed that the CC cell apoptosis rate was promoted by the miR-4735-3p mimic and inhibited by

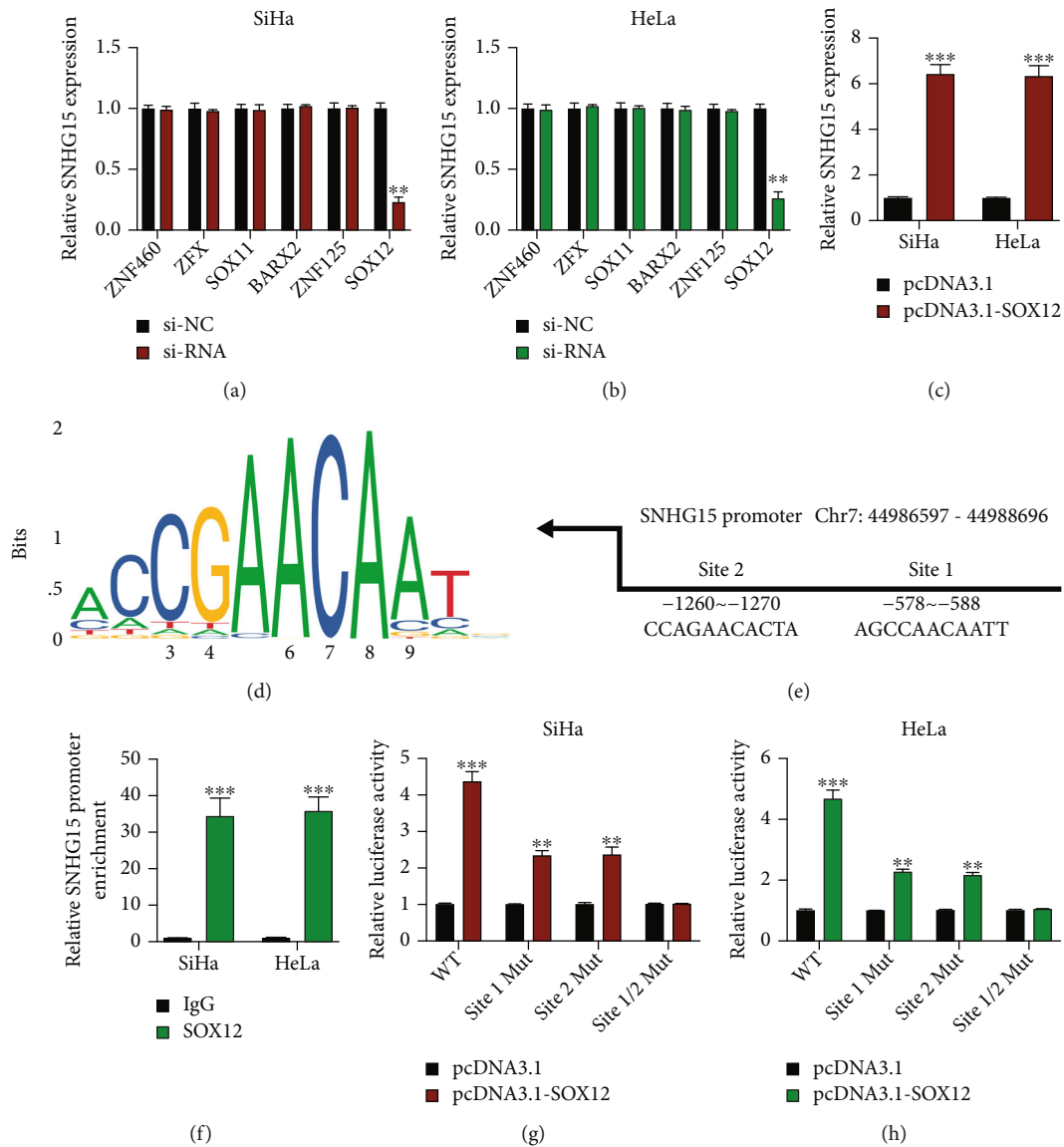


FIGURE 3: lncRNA SNHG15 expression in cervical cancer is transcriptionally regulated by SOX12. The upstream regulator of lncRNA SNHG15, predicted using the JASPAR (<http://jaspar.genereg.net/>) database. (a, b) SiHa and HeLa cells stably transfected with siRNAs; lncRNA SNHG15 expression, measured by qRT-PCR. (c) SiHa and HeLa cells transfected with pcDNA3.1-SOX12 and its normal control; lncRNA SNHG15 expression was assessed by qRT-PCR. (d) Binding motif of SOX12 predicted by JASPAR. (e) Putative binding sites for the lncRNA SNHG15 promoter, determined using JASPAR. (f) Binding possibility between SOX12 and the lncRNA SNHG15 promoter, assessed by ChIP assay. (g, h) Interaction between SOX12 and the lncRNA SNHG15 promoter in (g) SiHa and (h) HeLa cells, verified using the luciferase reporter gene assay. Data are presented as mean  $\pm$  SD; \*\* $p$  < 0.01; \*\*\* $p$  < 0.001.

the miR-4735-3p inhibitor (Figures 5(h) and 5(i)). Transwell migration assay results suggested that CC cell migration was suppressed by the miR-4735 mimic but aggravated by the miR-4735-3p inhibitor (Figures 5(j) and 5(k), Supplementary Materials Figure S2C–S2D). For the same occurrence, the chemoresistance of CC cells to cisplatin was reduced by the miR-4735-3p mimic but aggravated by the miR-4735-3p inhibitor (Figures 5(l)–5(o)). Our results suggested that miR-4735-3p acted as a tumor suppressor in CC progression.

**3.6. miR-4735-3p Targets to HIF1a.** A total of 13 mRNA targets of miR-4735-3p were found by bioinformatics analysis

(Figure 6(a)). We then found that HIF1a expression was decreased in miR-4735-3p overexpressed CC cells (Figures 6(b) and 6(c)) and increased in miR-4735-3p knockdown CC cells (Figure 6(d)), indicating that miR-4735-3p could be a potential target to HIF1a. The binding sites between miR-4735-3p and HIF1a were then obtained as indicated (Figure 6(e)). Data from the RNA pull-down assay showed that HIF1a was noticeably enriched in biotinylated miR-4735-3p probes in CC cells (Figures 6(f) and 6(g)). Meanwhile, luciferase reporter gene assay results confirmed that miR-4735-3p directly sponged to HIF1a in CC cells (Figures 6(h) and 6(i)). The interaction between miR-4735-3p and HIF1a was verified. HIF1a expression in CC



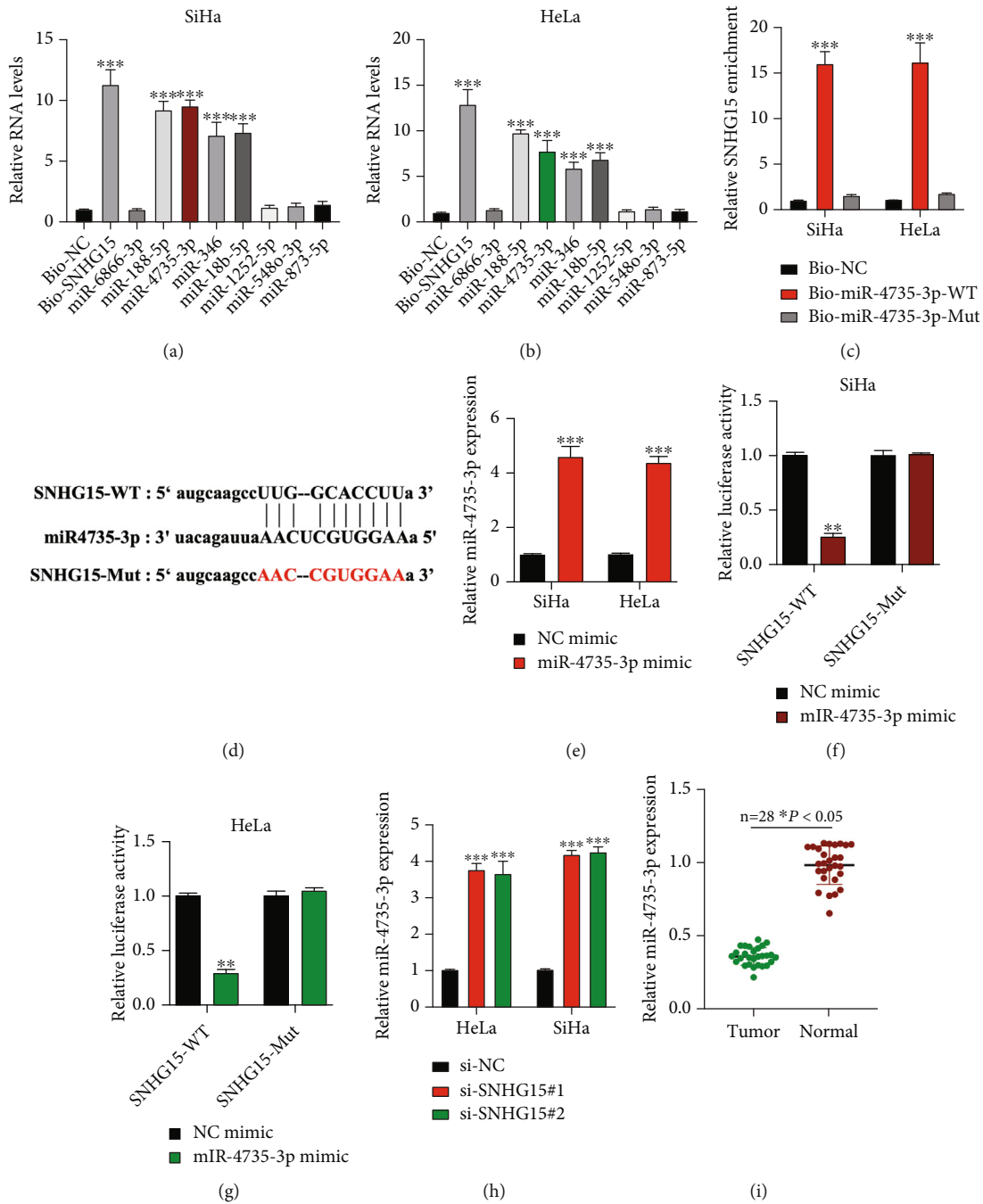


FIGURE 4: lncRNA SNHG15 sponges miR-4735-3p. Putative downstream targets for lncRNA SNHG15, predicted using the starBase (<http://starbase.sysu.edu.cn/>) dataset (CLIP Data: strict stringency ( $\geq 5$ )). (a, b) Potential miRNA targets for lncRNA SNHG15 in SiHa and HeLa cells, evaluated by biotinylated RNA pull-down; expression levels of putative miRNA targets in biotinylated probe bounds were measured by qRT-PCR. (c) Expression levels of lncRNA SNHG15 in Bio-miR-4735-3p-WT or Bio-miR-4735-3p-Mut bounds, measured by qRT-PCR. (d) Binding sites between lncRNA SNHG15 and miR-4735-3p, obtained using the starBase dataset. (e) Transfection efficiency of the miR-4735-3p mimic, evaluated by qRT-PCR. (f, g) Association between lncRNA SNHG15 and miR-4735-3p, assessed using the luciferase reporter gene assay in (f) SiHa and (g) HeLa. (h) miR-4735-3p expression in lncRNA SNHG15 knockdown cervical cancer (CC) cells, assessed by qRT-PCR. (i) miR-4735-3p expression in CC tumor samples ( $n = 28$ ) and adjacent normal samples ( $n = 28$ ), measured by qRT-PCR. Data are presented as mean  $\pm$  SD; \* $p < 0.05$ ; \*\* $p < 0.01$ ; \*\*\* $p < 0.001$ .

tissues was measured; HIF1a expression in CC tumors was markedly higher than that in comparative normal tissues (Figures 6(j) and 6(k)).

3.7. lncRNA SNHG15 Regulates the Tumorigenesis and Chemoresistance of Cervical Cancer via the miR-4735-3p/HIF1a Pathway. To further verify the molecular and cellular

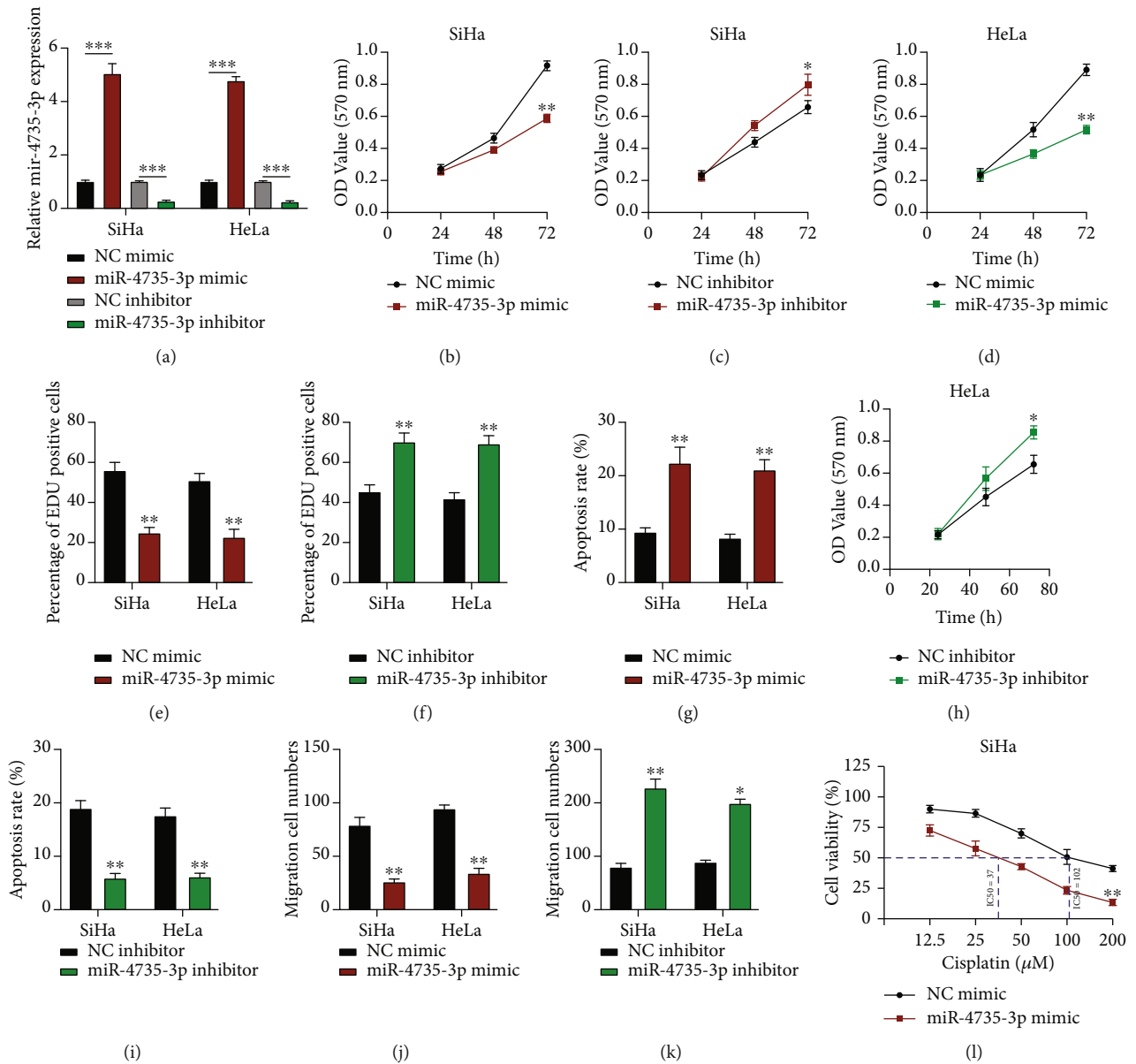


FIGURE 5: Continued.

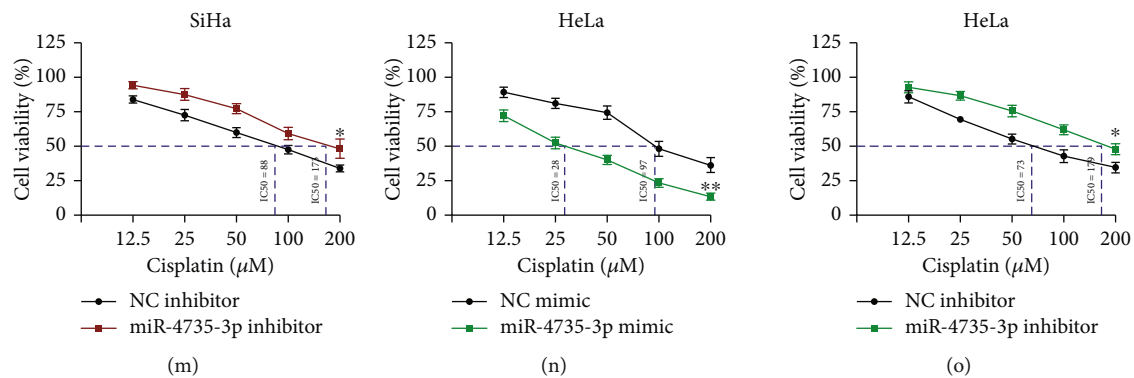


FIGURE 5: miR-4735-3p modulates tumorigenesis and chemoresistance in cervical cancer. (a) The gain- or loss-of-function of miR-4735-3p cell models was generated as indicated. (b–d) Cell proliferation of SiHa and HeLa cells upon miR-4735-3p dysregulation, detected using the MTT assay. (f, g) Cell proliferation levels of SiHa and HeLa cells upon miR-4735-3p (f) overexpression or (g) downregulation, evaluated using the EdU assay. (h, i) Cell apoptosis of SiHa and HeLa cells upon miR-4735-3p (h) overexpression or (i) downregulation, measured by flow cytometry. (j, k) Cell migration levels of SiHa and HeLa cells upon miR-4735-3p (j) overexpression or (k) downregulation, assessed using the transwell migration assay. (l–o) Chemoresistance of SiHa and HeLa cells upon miR-4735-3p dysregulation, detected using the MTT assay. Data are presented as mean  $\pm$  SD, \* $p < 0.5$ ; \*\* $p < 0.01$ ; \*\*\* $p < 0.001$ .

functions of lncRNA SNHG15 in CC progression, we generated cell models by transfecting si-NC, si-SNHG15#1, and si-SNHG15#1+pcDNA3.1-HIF1a into SiHa and HeLa cells, and lncRNA SNHG15 or HIF1a expression was detected (Figures 7(a) and 7(b)). HIF1a reversed the inhibitory effect of lncRNA SNHG15 knockdown on cell proliferation as detected using the MTT assay and the EdU assay (Figures 7(c)–7(e), Supplementary Materials Figure S3A). The cell apoptosis rate increased subsequent to lncRNA SNHG15 knockdown attenuated by HIF1a in CC cells (Figure 7(f)). Moreover, lncRNA SNHG15 knockdown suppressed cell migration level, and those occurrences were rescued by HIF1a in CC cells (Figure 7(g), Supplementary Materials Figure S3B). With regard to the chemoresistance of CC cells to cisplatin, lncRNA SNHG15 knockdown inhibited the IC50 value of SiHa and HeLa cells, but this occurrence was reversed by HIF1a (Figures 7(h) and 7(i)). Our results showed that lncRNA SNHG15 modulated HIF1a expression to regulate CC progression.

**3.8. lncRNA SNHG15 Knockdown Suppresses CC Tumor Growth In Vivo.** The aforementioned experiments demonstrated the function of lncRNA SNHG15 *in vitro*. We generated mouse models to examine the role of lncRNA SNHG15 *in vivo*. lncRNA SNHG15 knockdown cells ( $10^6$  per murine) were subcutaneously injected into the mice, and after 4 weeks, tumors were collected. The representative image of xenograft tumors is presented in Figure 8(a). The tumor volume and the end weight were significantly inhibited by lncRNA SNHG15 knockdown (Figures 8(b) and 8(c)). Further, the expression levels of SNHG15, miR-4735-3p, and HIF1a in lncRNA SNHG15 knockdown tumor tissues were measured (Figures 8(d)–8(g)), and  $t$  and the trends were consistent with our *in vitro* experiments. The results obtained suggest that lncRNA SNHG15 regulated tumor growth in murine models via the miR-4735-3p/HIF1a axis.

## 4. Discussion

The role of the lncRNA/miRNA/mRNA network in various biological progression has been elucidated in recent decades. As a major cause of cancer initiation and progression, multiple gene mutations have drawn wide scientific interests, and considerable effort has been exerted to elucidate the molecular mechanisms that contribute to tumorigenesis via the lncRNA/miRNA/mRNA network, such as bladder cancer, hepatocellular carcinoma, osteosarcoma, gastric cancer, oral cancer, and CC [21–26]. lncRNA-CTS regulates CC progression via the miR-505/ZEB2 axis [27], lncRNA TP73-AS1 modulates CC development via the miR-329-3p/ARF1 axis [28], lncRNA CAR10 promotes CC progression via the miR-125b-5p/PDPK1 pathway [29], and lncRNA DANCR aggravates CC development via the miR-335-5p/ROCK1 axis [30]. Despite the accumulating reports on the lncRNA/miRNA/mRNA network globally, the main mechanism underlying gene dysregulation in cancer development has yet to be clarified.

In this study, we clarified elucidated that lncRNA SNHG15 was highly expressed in CC tissues and cells. Downregulated lncRNA SNHG15 attenuated tumorigenic properties *in vitro* and CC tumor growth *in vivo*. lncRNA SNHG15 dysregulation also influenced the chemoresistance of CC cells to cisplatin. Cisplatin belongs to the alkylating antineoplastic agent and is used in the clinical management of several malignancies, including CC [31–36]. With the wide clinical application of cisplatin, its side effects are been revealed, such as nausea, vomiting, kidney damage, hearing loss, and cell chemoresistance [37]. Understanding the molecular mechanisms underlying chemoresistance, among its side effects, is crucial to improving the therapy efficiency of cisplatin. The results of this study indicate that lncRNA SNHG15 downregulation inhibited the IC50 value of CC cells upon cisplatin treatment.

Further, for the upstream regulator of lncRNA SNHG15, we found that lncRNA SNHG15 expression in CC cells was

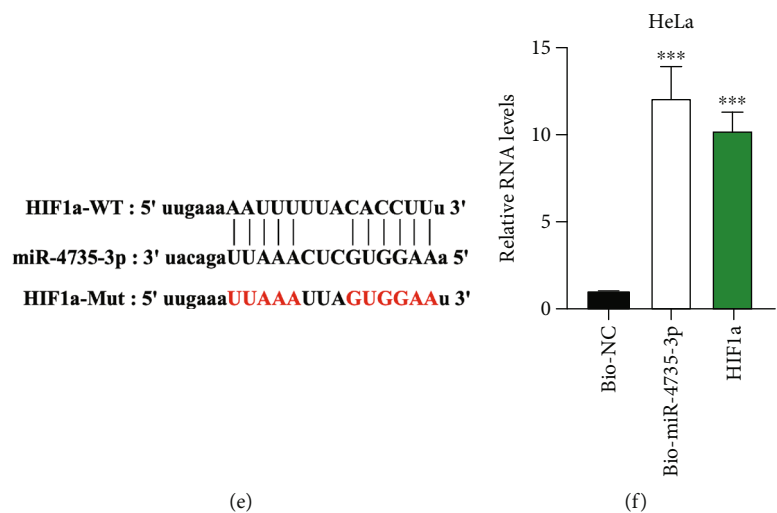
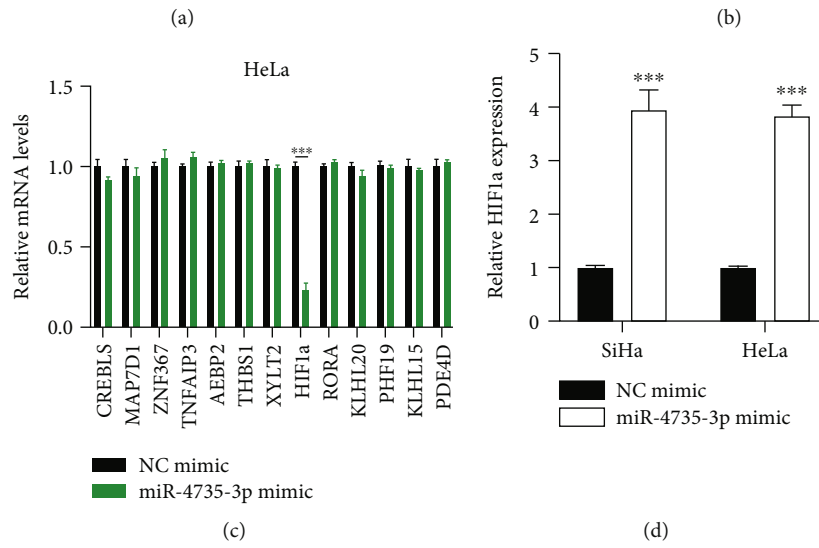
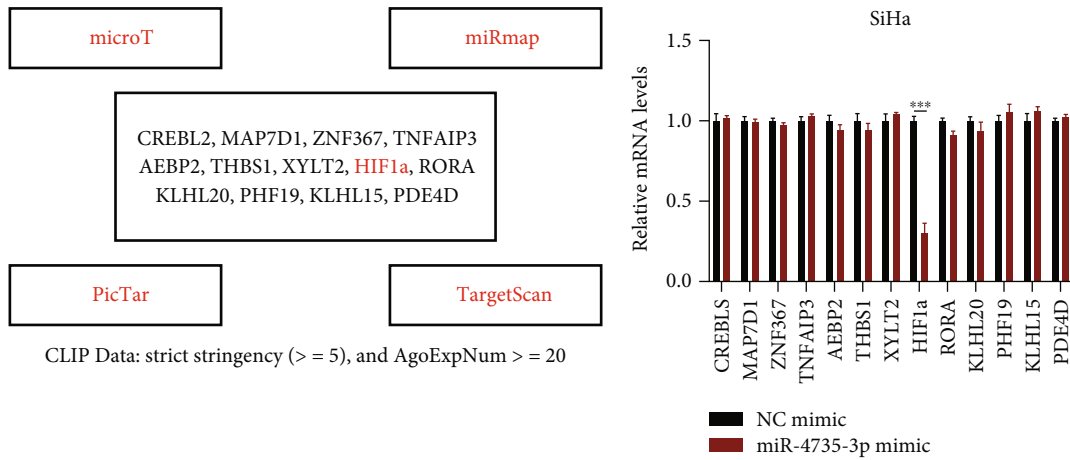


FIGURE 6: Continued.

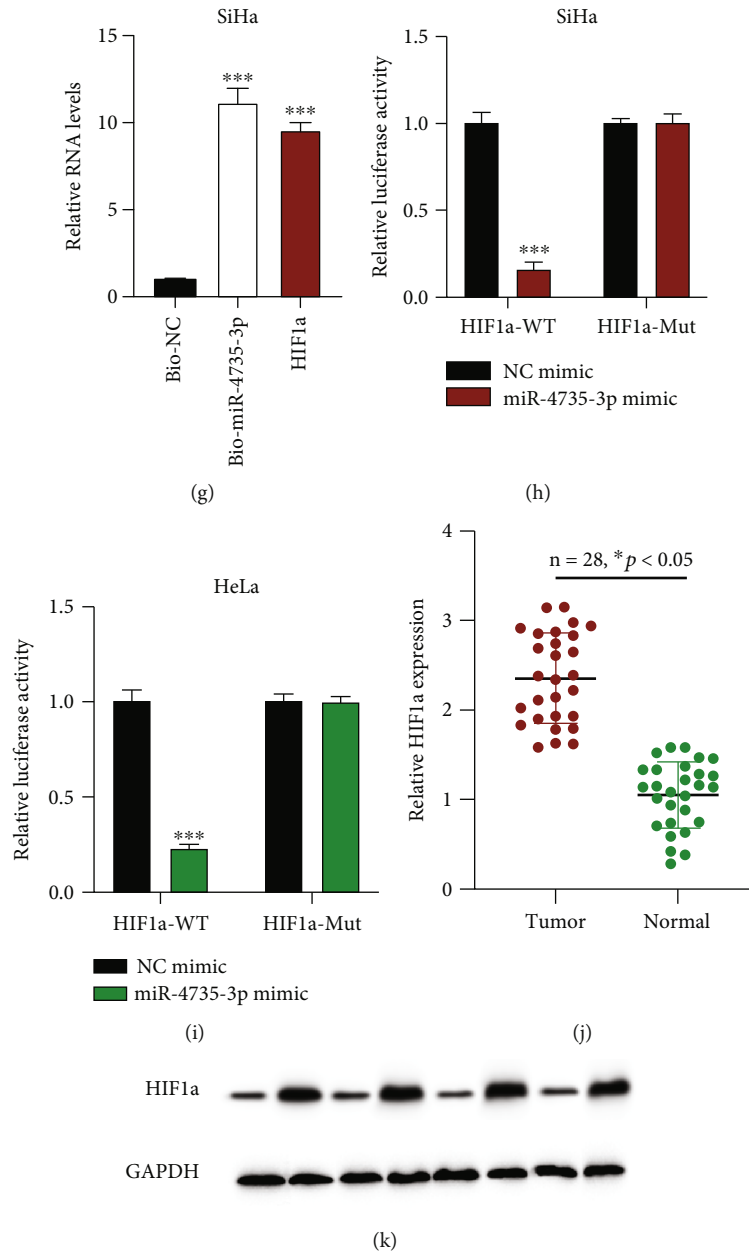


FIGURE 6: miR-4735-3p targets to HIF1a. (a) Putative downstream targets for miR-4735-3p, predicted by microT (<http://www.microrna.gr/microT>), miRmap (<http://mirnamap.mbc.nctu.edu.tw/>), PicTar (<http://www.pictar.org/>), and TargetScan (<http://www.targetscan.org/>) with CLIP Data: strict stringency ( $\geq 5$ ) and AgoExpNum  $\geq 20$ . (b, c) Putative mRNA targets in (b) SiHa and (c) HeLa cells upon miR-4735-3p overexpression were measured by qRT-PCR. (d) HIF1a expression in cervical cancer (CC) cells upon miR-4735-3p downregulation, measured by qRT-PCR. (e) Binding sites between HIF1a and miR-4735-3p. (f, g) Association between miR-4735-3p and HIF1a in (f) SiHa and (g) HeLa cells, evaluated by ChIP assay; analysis of results was by qRT-PCR. (h, i) Interaction between HIF1a and miR-4735-3p, assessed using the luciferase reporter gene assay in (h) SiHa and (i) HeLa. (j) HIF1a expression in CC tumor samples ( $n = 28$ ) and adjacent normal samples ( $n = 28$ ), measured by qRT-PCR. (k) HIF1a expression in 4 randomly chosen pairs of CC tissues, detected by Western blot. Data are presented as mean  $\pm$  SD; \* $p < 0.05$ ; \*\*\* $p < 0.001$ .

transcriptionally regulated by SOX12. For the downstream factors of lncRNA SNHG15, our results demonstrated that lncRNA SNHG15 promoted HIF1a expression via sponging of miR-4735-3p in CC cells. Our biological experiments revealed that lncRNA SNHG15 promotes the tumorigenic properties and chemoresistance of CC cells via the miR-4735-3p/HIF1a axis. Meanwhile, this study has several limitations. First, more human samples are

required to confirm the clinical significance of lncRNA SNHG15 in CC tumors. Second, a larger scale of samples than the one used in this study is needed to examine the correlation of expression between lncRNA SNHG15, miR-4735-3p, and HIF1a in CC tumors. Finally, the specific molecular relation between HIF1a and CC cellular progression requires an in-depth investigation, such as determining the involved pathway.

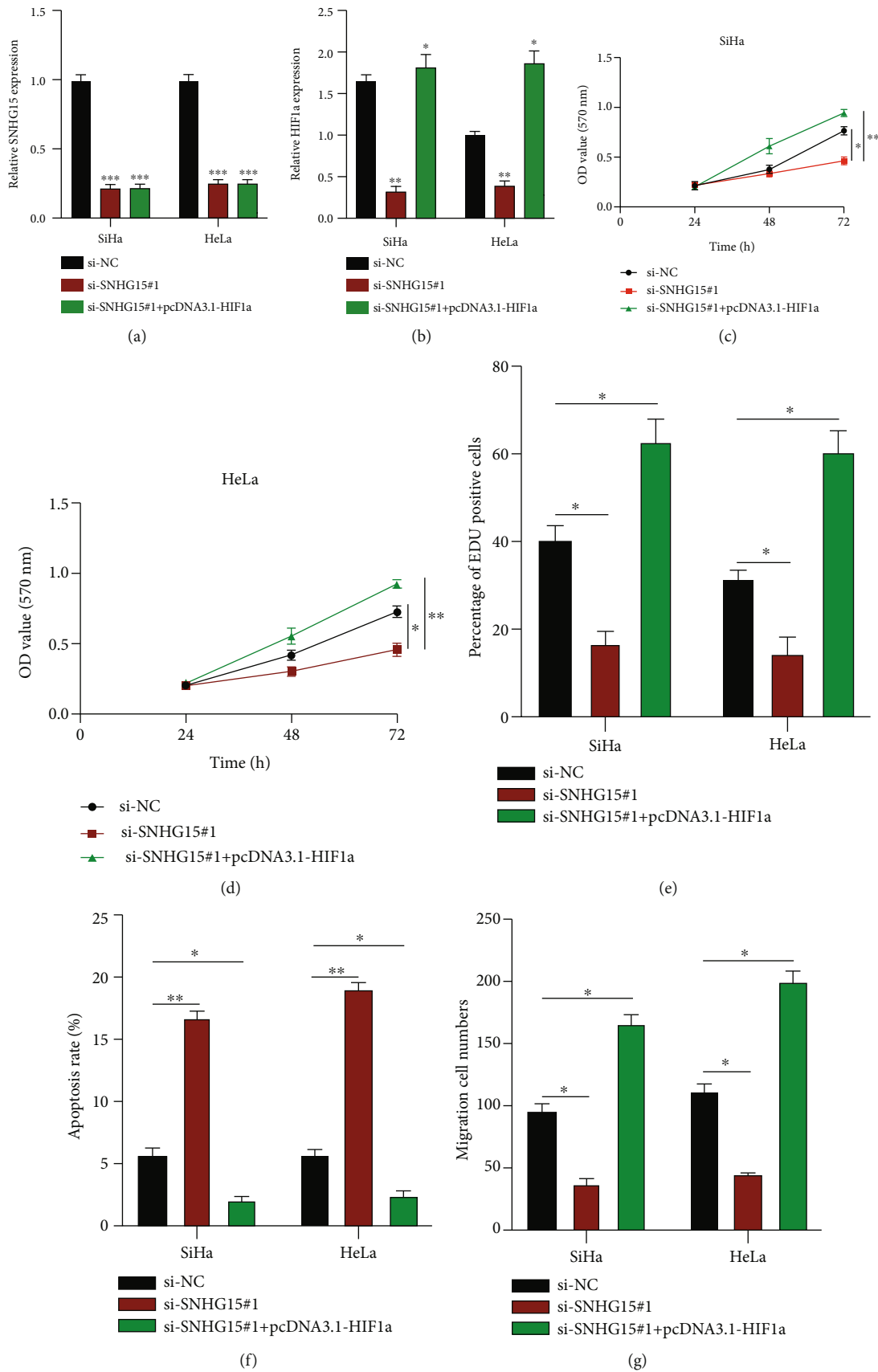


FIGURE 7: Continued.

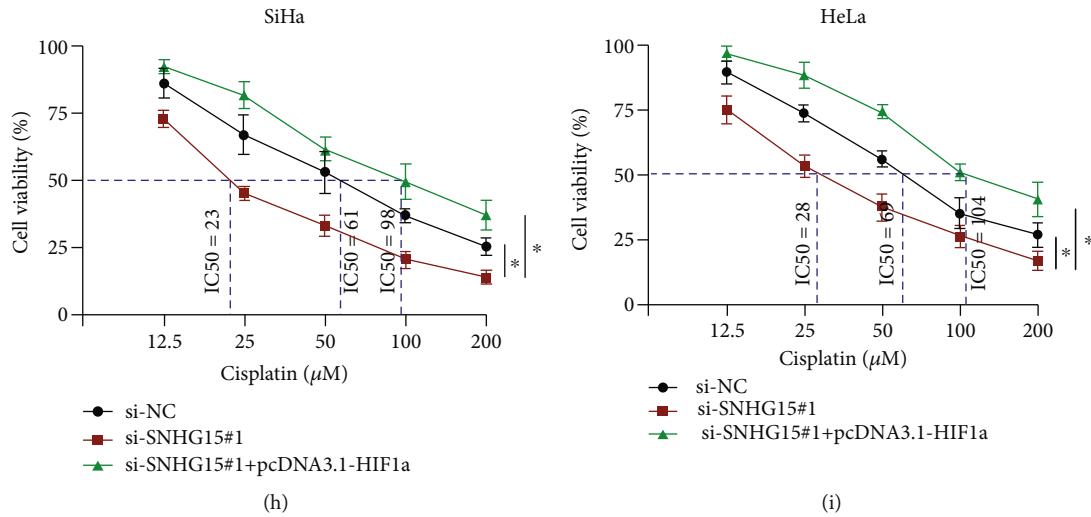


FIGURE 7: lncRNA SNHG15 regulates the tumorigenesis and chemoresistance of cervical cancer (CC) via the miR-4735-3p/HIF1a pathway. (a, b) Gain- or loss-of-function cell models were generated as indicated; assessment of transfection efficiencies. (c–e) Cell proliferation detected using the (c, d) MTT assay and the (e) EdU assay, respectively. (f) Cell apoptosis rate evaluated by flow cytometry. (g) Cell migration level assessed using the transwell migration assay. (h, i) SiHa and HeLa cells were treated with cisplatin at varying concentrations; the chemoresistance of CC cells was determined using the MTT assay. Data are presented as mean  $\pm$  SD; \* $p$  < 0.5; \*\* $p$  < 0.01; \*\*\* $p$  < 0.001.

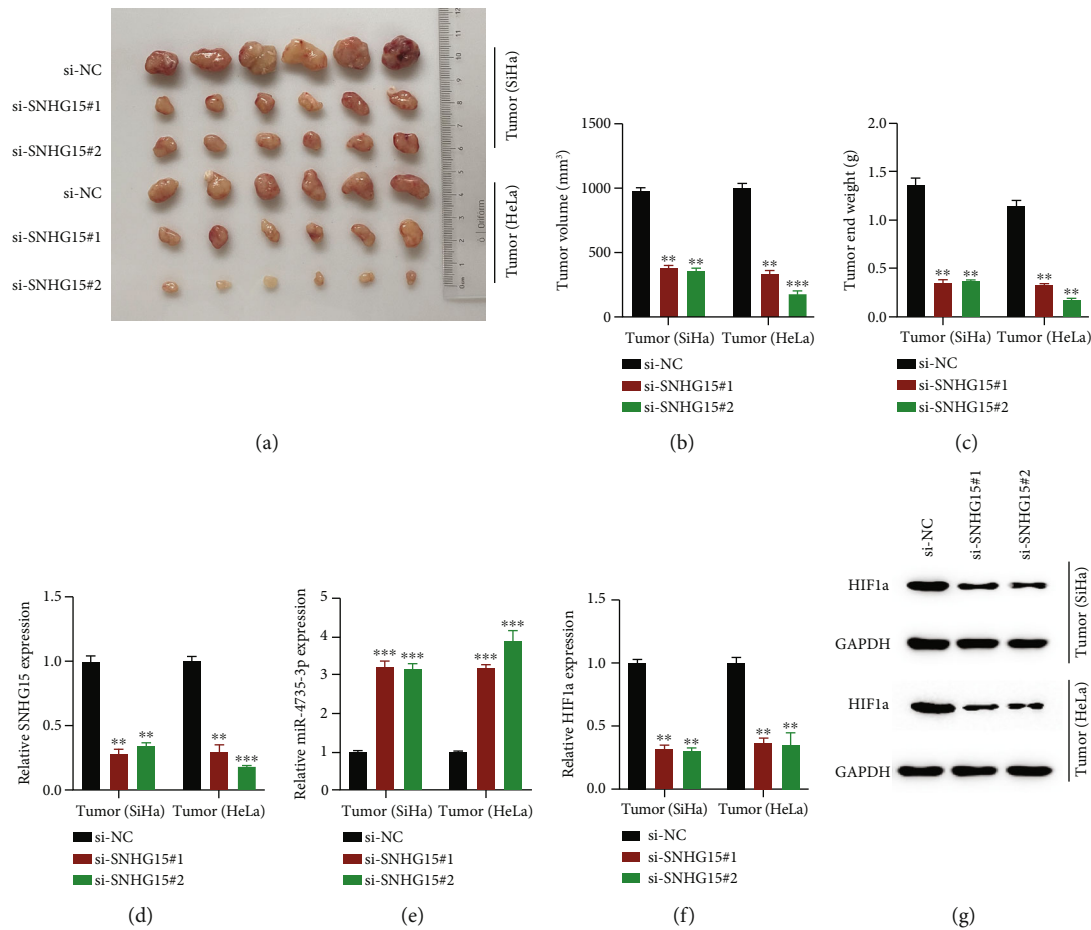


FIGURE 8: lncRNA SNHG15 knockdown suppresses tumor growth in cervical cancer *in vivo*. SiHa and HeLa cells stably transfected with si-NC, si-SNHG15#1, and si-SNHG15#2 were subcutaneously injected into the murine models ( $10^6$  cells/tumor;  $n = 6$ ). (a) Representative image of xenograft tumors. (b) Tumor volume was recorded and calculated. (c) Tumor end weight was recorded. (d) lncRNA SNHG15 expression in tumors, measured by qRT-PCR. (e) miR-4735-3p expression determined by qRT-PCR. (f, g) HIF1a expression in resected tumor tissues, measured by qRT-PCR and Western blot analysis. Data are presented as mean  $\pm$  SD; \*\* $p$  < 0.01; \*\*\* $p$  < 0.001.

## 5. Conclusion

In summary, our study elucidates the expression and biological function of lncRNA SNHG15 in CC. This study also indicates that SOX12 could transcriptionally regulate lncRNA SNHG15 expression in CC cells. lncRNA SNHG15 promotes CC progression by regulating the miR-4735-3p/HIF1 $\alpha$  axis, which could be a potential target for the diagnosis of CC or clinical intervention for the disease in the future.

## Data Availability

The research data used to support the findings of this study are included within the article.

## Ethical Approval

The studies involving human participants were reviewed and approved by the Medical Research Ethics Committee of Xiangyang Central Hospital.

## Consent

Written informed consent for participation was not required for this study in accordance with the national legislation and the institutional requirements.

## Conflicts of Interest

The authors declare that the research was conducted in the absence of any commercial or financial relationships that could be construed as a potential conflict of interest.

## Authors' Contributions

HX and LL contributed to the study concept, design, administrative, and study supervision. JY, MY, and HL contributed to the acquisition of data, analysis, and interpretation of data. HX, XQ, YX, and LL contributed to the drafting of the manuscript and critical revision of the manuscript for important intellectual content. MZ, XM, and XQ contributed to the statistical analysis and technical and material support. All authors have read and approved the manuscript. Jiang Yang, Mei Yang, and Huabing Lv are considered as co-first authors.

## Acknowledgments

This work was supported by the National Natural Science Foundation of China (81972449), the Hubei Provincial Natural Science Foundation of China (2019CFA016), Hubei Province's Outstanding Medical Academic Leader Program, the Research Foundation of Health Commission of Hubei Province, China (WJ2019M069), and the Scientific Research Ability Cultivation Fund of Hubei University of Arts and Science (2021kpgj06).

## Supplementary Materials

Figure S1: lncRNA SNHG15 overexpression aggravates CC tumorigenesis and chemoresistance in vitro. (A) lncRNA SNHG15 level was measured by qRT-PCR in CC cells. (B, C) Cell proliferation was detected by MTT assay in SiHa (B) and HeLa cells (C). (D, E): EdU assay was applied to evaluate cell viabilities in SiHa and HeLa cells (D), and results were analyzed as indicated (E). (F, G) Cell apoptosis rate was measured by flow cytometer assay (F), and results were calculated as indicated (G). (H, I) Transwell migration experiment was performed to assess cell migration level (H), and statistical analysis was presented (I). (J, K) SiHa (J) and HeLa (K) cells were treated with cisplatin at various concentrations as indicated, and MTT assay was applied to evaluate the chemoresistance of CC cells. Data were presented as mean  $\pm$  SD; \*\* $p < 0.01$  and \*\*\* $p < 0.001$ . Figure S2: (A, B) EdU assay was applied to evaluate cell proliferation of SiHa and HeLa cells upon miR-4735-3p overexpression (A) or downregulation (B). (C, D) Transwell migration assay was conducted to assess cell migration level of SiHa and HeLa cells upon miR-4735-3p overexpression (C) or downregulation (D). Figure S3: (A) Cell proliferation was detected by EdU assay as indicated. (B) Cell migration level was assessed by transwell migration assay. (*Supplementary Materials*)

## References

- [1] C. de Martel, M. Plummer, J. Vignat, and S. Franceschi, "Worldwide burden of cancer attributable to HPV by site, country and HPV type," *International Journal of Cancer*, vol. 141, no. 4, pp. 664–670, 2017.
- [2] N. C. Nkfusai, S. N. Cumber, T. Williams et al., "Cervical cancer in the Bamenda regional hospital, north west region of Cameroon: a retrospective study," *The Pan African Medical Journal*, vol. 32, p. 90, 2019.
- [3] W. Hsu, L. Liu, X. Chen, Y. Zhang, and W. Zhu, "lncRNA CASC11 promotes the cervical cancer progression by activating Wnt/beta-catenin signaling pathway," *Biological Research*, vol. 52, no. 1, p. 33, 2019.
- [4] S. Park, J. Kim, K. Eom et al., "microRNA-944 overexpression is a biomarker for poor prognosis of advanced cervical cancer," *BMC Cancer*, vol. 19, no. 1, p. 419, 2019.
- [5] C. P. Ponting, P. L. Oliver, and W. Reik, "Evolution and functions of long noncoding RNAs," *Cell*, vol. 136, no. 4, pp. 629–641, 2009.
- [6] J. Q. Sheng, M. R. Wang, D. Fang et al., "lncRNA NBR2 inhibits tumorigenesis by regulating autophagy in hepatocellular carcinoma," *Biomedicine & Pharmacotherapy*, vol. 133, article 111023, 2021.
- [7] M. Zhang, N. Wang, P. Song et al., "lncRNA GATA3-AS1 facilitates tumour progression and immune escape in triple-negative breast cancer through destabilization of GATA3 but stabilization of PD-L1," *Cell Proliferation*, vol. 53, no. 9, article e12855, 2020.
- [8] L. Yang, X. Peng, Y. Li et al., "Long non-coding RNA HOTAIR promotes exosome secretion by regulating RAB35 and SNAP23 in hepatocellular carcinoma," *Molecular Cancer*, vol. 18, no. 1, p. 78, 2019.
- [9] M. Li, B. Yin, M. Chen et al., "Downregulation of the lncRNA ASB16-AS1 decreases LARP1 expression and promotes clear



- cell renal cell carcinoma progression via miR-185-5p/miR-214-3p,” *Frontiers in Oncology*, vol. 10, article 617105, 2021.
- [10] H. Tani and M. Torimura, “Identification of short-lived long non-coding RNAs as surrogate indicators for chemical stress response,” *Biochemical and Biophysical Research Communications*, vol. 439, no. 4, pp. 547–551, 2013.
- [11] H. Tani, S. Okuda, K. Nakamura, M. Aoki, and T. Umemura, “Short-lived long non-coding RNAs as surrogate indicators for chemical exposure and LINC00152 and MALAT1 modulate their neighboring genes,” *PLoS One*, vol. 12, no. 7, article e0181628, 2017.
- [12] Q. Kong and M. Qiu, “Long noncoding RNA SNHG15 promotes human breast cancer proliferation, migration and invasion by sponging miR-211-3p,” *Biochemical and Biophysical Research Communications*, vol. 495, no. 2, pp. 1594–1600, 2018.
- [13] H. Jiang, T. Li, Y. Qu et al., “Long non-coding RNA SNHG15 interacts with and stabilizes transcription factor Slug and promotes colon cancer progression,” *Cancer Letters*, vol. 425, pp. 78–87, 2018.
- [14] S. X. Chen, J. F. Yin, B. C. Lin et al., “Upregulated expression of long noncoding RNA SNHG15 promotes cell proliferation and invasion through regulates MMP2/MMP9 in patients with GC,” *Tumour Biology*, vol. 37, no. 5, pp. 6801–6812, 2016.
- [15] J. H. Zhang, H. W. Wei, and H. G. Yang, “Long noncoding RNA SNHG15, a potential prognostic biomarker for hepatocellular carcinoma,” *European Review for Medical and Pharmacological Sciences*, vol. 20, no. 9, pp. 1720–1724, 2016.
- [16] B. Jin, H. Jin, H. B. Wu, J. J. Xu, and B. Li, “Long non-coding RNA SNHG15 promotes CDK14 expression via miR-486 to accelerate non-small cell lung cancer cells progression and metastasis,” *Journal of Cellular Physiology*, vol. 233, no. 9, pp. 7164–7172, 2018.
- [17] D. Chen, Z. Zhang, X. Lu, and X. Yang, “Long non-coding RNA SNHG15 regulates cardiomyocyte apoptosis after hypoxia/reperfusion injury via modulating miR-188-5p/PTEN axis,” *Archives of Physiology and Biochemistry*, pp. 1–8, 2020.
- [18] T. Wang, D. Liang, and H. Yang, “SNHG15 facilitated malignant behaviors of oral squamous cell carcinoma through targeting miR-188-5p/DAAM1,” *Journal of Oral Pathology & Medicine*, vol. 50, no. 7, pp. 681–691, 2021.
- [19] B. Xiong, Y. Wang, Y. Liu, C. Wu, and J. Chen, “The circulating LncRNA SNHG15/miR-346 axis may be a potential biomarker of cardiomyocyte apoptosis during myocardial ischemia/reperfusion injury,” *International Journal of Cardiology*, vol. 334, p. 30, 2021.
- [20] W. Chen, L. Huang, J. Liang, Y. Ye, S. Yu, and Y. Zhang, “Long noncoding RNA small nucleolar RNA host gene 15 deteriorates liver cancer via microRNA-18b-5p/LIM-only 4 axis,” *IUBMB Life*, vol. 73, no. 2, pp. 349–361, 2021.
- [21] M. Huang, Y. Long, Y. Jin et al., “Comprehensive analysis of the lncRNA-miRNA-mRNA regulatory network for bladder cancer,” *Translational Andrology and Urology*, vol. 10, no. 3, pp. 1286–1301, 2021.
- [22] L. Zhang, H. Tao, J. Li, E. Zhang, H. Liang, and B. Zhang, “Comprehensive analysis of the competing endogenous circRNA-lncRNA-miRNA-mRNA network and identification of a novel potential biomarker for hepatocellular carcinoma,” *Aging (Albany NY)*, vol. 13, no. 12, article 203056, pp. 15990–16008, 2021.
- [23] J. Y. Wang, Y. Yang, Y. Ma et al., “Potential regulatory role of lncRNA-miRNA-mRNA axis in osteosarcoma,” *Biomedicine & Pharmacotherapy*, vol. 121, article 109627, 2020.
- [24] J. Wang, Y. Ding, Y. Wu, and X. Wang, “Identification of the complex regulatory relationships related to gastric cancer from lncRNA-miRNA-mRNA network,” *Journal of Cellular Biochemistry*, vol. 121, no. 1, pp. 876–887, 2020.
- [25] J. Yin, X. Zeng, Z. Ai, M. Yu, Y. Wu, and S. Li, “Construction and analysis of a lncRNA-miRNA-mRNA network based on competitive endogenous RNA reveal functional lncRNAs in oral cancer,” *BMC Medical Genomics*, vol. 13, no. 1, p. 84, 2020.
- [26] J. Wang and C. Zhang, “Identification and validation of potential mRNA- microRNA- long-noncoding RNA (mRNA-miRNA-lncRNA) prognostic signature for cervical cancer,” *Bioengineered*, vol. 12, no. 1, pp. 898–913, 2021.
- [27] S. Feng, W. Liu, X. Bai et al., “LncRNA-CTS promotes metastasis and epithelial-to-mesenchymal transition through regulating miR-505/ZEB2 axis in cervical cancer,” *Cancer Letters*, vol. 465, pp. 105–117, 2019.
- [28] J. Xu and J. Zhang, “LncRNA TP73-AS1 is a novel regulator in cervical cancer via miR-329-3p/ARF1 axis,” *Journal of Cellular Biochemistry*, vol. 121, no. 1, pp. 344–352, 2020.
- [29] T. Hu, Q. Zhang, and L. Gao, “LncRNA CAR10 upregulates PDPK1 to promote cervical cancer development by sponging miR-125b-5p,” *BioMed Research International*, vol. 2020, Article ID 4351671, 16 pages, 2020.
- [30] H. Liang, C. Zhang, H. Guan, J. Liu, and Y. Cui, “LncRNA DANCR promotes cervical cancer progression by upregulating ROCK1 via sponging miR-335-5p,” *Journal of Cellular Physiology*, vol. 234, no. 5, pp. 7266–7278, 2019.
- [31] S. Dasari and P. Bernard Tchounwou, “Cisplatin in cancer therapy: molecular mechanisms of action,” *European Journal of Pharmacology*, vol. 740, pp. 364–378, 2014.
- [32] J. P. Pignon, H. Tribodet, G. V. Scagliotti et al., “Lung adjuvant cisplatin evaluation: a pooled analysis by the LACE Collaborative Group,” *Journal of Clinical Oncology*, vol. 26, no. 21, pp. 3552–3559, 2008.
- [33] X. C. Hu, J. Zhang, B. H. Xu et al., “Cisplatin plus gemcitabine versus paclitaxel plus gemcitabine as first-line therapy for metastatic triple-negative breast cancer (CBCSG006): a randomised, open-label, multicentre, phase 3 trial,” *The Lancet Oncology*, vol. 16, no. 4, pp. 436–446, 2015.
- [34] R. Agarwal and S. B. Kaye, “Ovarian cancer: strategies for overcoming resistance to chemotherapy,” *Nature Reviews. Cancer*, vol. 3, no. 7, pp. 502–516, 2003.
- [35] J. S. Cooper, T. F. Pajak, A. A. Forastiere et al., “Postoperative concurrent radiotherapy and chemotherapy for high-risk squamous-cell carcinoma of the head and neck,” *The New England Journal of Medicine*, vol. 350, no. 19, pp. 1937–1944, 2004.
- [36] H. Zhu, H. Zhu, H. Luo, W. Zhang, Z. Shen, and X. Hu, “Molecular mechanisms of cisplatin resistance in cervical cancer,” *Drug Design, Development and Therapy*, vol. 10, pp. 1885–1895, 2016.
- [37] M. R. Trendowski, O. el Charif, P. C. Dinh Jr., L. B. Travis, and M. E. Dolan, “Genetic and modifiable risk factors contributing to cisplatin-induced toxicities,” *Clinical Cancer Research*, vol. 25, no. 4, pp. 1147–1155, 2019.

## Research Article

# Signature Construction and Molecular Subtype Identification Based on Pyroptosis-Related Genes for Better Prediction of Prognosis in Hepatocellular Carcinoma

Ji Chen <sup>1</sup>, Qiqi Tao,<sup>1</sup> Zhichao Lang,<sup>1</sup> Yuxiang Gao,<sup>1</sup> Yan Jin,<sup>1</sup> Xiaoqi Li,<sup>1</sup> Yajing Wang,<sup>1</sup> Yuxiao Zhang,<sup>1</sup> Suhui Yu,<sup>2</sup> Boyu Lv <sup>3</sup>, Zhengping Yu <sup>2</sup> and Changyong Lin <sup>4</sup>

<sup>1</sup>Key Laboratory of Diagnosis and Treatment of Severe Hepato-Pancreatic Diseases of Zhejiang Province, The First Affiliated Hospital of Wenzhou Medical University, Wenzhou 325000, China

<sup>2</sup>Department of Hepatobiliary Surgery, The First Affiliated Hospital of Wenzhou Medical University, Wenzhou 325000, China

<sup>3</sup>Department of Pathology, The First Affiliated Hospital of Wenzhou Medical University, Wenzhou 325000, China

<sup>4</sup>Department of General Surgery, Wenzhou Hospital of Traditional Chinese Medicine Affiliated to Zhejiang Chinese Medical University, Wenzhou 325000, China

Correspondence should be addressed to Boyu Lv; 13780109835@163.com, Zhengping Yu; yzpwk@126.com, and Changyong Lin; linchangyong111@126.com

Received 29 September 2021; Revised 11 November 2021; Accepted 1 December 2021; Published 11 January 2022

Academic Editor: Bin Duan

Copyright © 2022 Ji Chen et al. This is an open access article distributed under the Creative Commons Attribution License, which permits unrestricted use, distribution, and reproduction in any medium, provided the original work is properly cited.

Hepatocellular carcinoma (HCC) is one of the most common malignancies worldwide. However, there is a lack of adequate means of treatment prognostication for HCC. Pyroptosis is a newly discovered way of programmed cell death. However, the prognostic role of pyroptosis in HCC has not been thoroughly investigated. Here, we generated a novel prognostic signature to evaluate the prognostic value of pyroptosis-related genes (PRGs) using the data from The Cancer Genome Atlas (TCGA) database. The accuracy of the signature was validated using survival analysis through the International Cancer Genome Consortium cohort ( $n = 231$ ) and the First Affiliated Hospital of Wenzhou Medical University cohort ( $n = 180$ ). Compared with other clinical factors, the risk score of the signature was found to be associated with better patient outcomes. The enrichment analysis identified multiple pathways related with pyroptosis in HCC. Furthermore, drug sensitivity testing identified six potential chemotherapeutic agents to provide possible treatment avenues. Interestingly, patients with low risk were confirmed to be associated with lower tumor mutation burden (TMB). However, patients at high risk were found to have a higher count of immune cells. Consensus clustering was performed to identify two main molecular subtypes (named clusters A and B) based on the signature. It was found that compared with cluster B, better survival outcomes and lower TMB were observed in cluster A. In conclusion, signature construction and molecular subtype identification of PRGs could be used to predict the prognosis of HCC, which may provide a specific reference for the development of novel biomarkers for HCC treatment.

## 1. Introduction

The etiology and molecular mechanism of hepatocellular carcinoma (HCC), a significant subtype of liver cancer, remain largely unknown [1]. HCC ranks fourth among the most lethal cancers and lacks appropriate treatment [2]. In the United States, the 5-year survival rate for patients with HCC is approximately 18% [3]. In addition, HCC is a highly heterogeneous disease, which has been documented at inter-

patient, intertumoral, and intertumoral level [4–6]. Previous studies have indicated that hepatocyte death chronically promotes HCC, but the related molecular mechanism is not well defined [7]. Thus, both the poor prognostic conditions and the unknown molecular mechanisms indicate the urgent need to improve the prognosis of HCC.

Pyroptosis, a type of programmed cell death, manifests as the continuous swelling of cells until the cell membrane ruptures, resulting in the release of intracellular contents,

TABLE 1: The clinical characteristics of TCGA cohort, ICGC cohort and FAHWMU cohort.

| Variables        | TCGA cohort (N = 365) | ICGC cohort (N = 231) | FAHWMU cohort (N = 180) |
|------------------|-----------------------|-----------------------|-------------------------|
| Survival status  |                       |                       |                         |
| OS days (median) | 556                   | 780                   | 803                     |
| Age (median)     | 61                    | 69                    | 64                      |
| Gender           |                       |                       |                         |
| Female           | 119                   | 61                    | 114                     |
| Male             | 246                   | 170                   | 66                      |
| TNM stage        |                       |                       |                         |
| Stage I          | 170                   | 36                    | 62                      |
| Stage II         | 84                    | 105                   | 50                      |
| Stage III        | 83                    | 71                    | 59                      |
| Stage IV         | 4                     | 19                    | 9                       |
| Unknown          | 24                    | 0                     | 0                       |
| Grade            |                       |                       |                         |
| G1               | 55                    | NA                    | 24                      |
| G2               | 175                   | NA                    | 76                      |
| G3               | 118                   | NA                    | 64                      |
| G4               | 12                    | NA                    | 13                      |
| Unknown          | 5                     | NA                    | 3                       |

followed by the activation of a strong inflammatory response [8]. As programmed necrosis mediated by gasdermin, pyroptosis is different from other cell death modalities, such as apoptosis and necrosis in the morphological features, occurrence, and regulatory mechanism [9]. Pyroptosis has been reported to take a part in tumor genesis, invasion, and metastasis [10]. Some studies have been found that pyroptosis is widely involved in the occurrence and development of various types of diseases [11, 12] and could inhibit the onset of associated diseases to improve the overall survival (OS) of patients [13]. Pyroptosis has also been confirmed to have strong associations with multiple known biomarkers [14, 15]. A recent study demonstrated the critical regulatory role of pyroptosis in the tumor microenvironment (TME), which provides new therapeutic insights for cancer treatment [16]. Therefore, an in-depth study of pyroptosis may help understand its role in the occurrence and development of cancers including HCC and provide new ideas for the clinical prevention and treatment [17, 18].

The tumor mutation burden (TMB) is the total number of substitution and insertion/deletion mutations that occur/megabase in the exon coding regions of the genes evaluated in one tumor sample. TMB, as a biomarker for high-frequency mutations and neoantigens, plays an important role in the immunotherapy in various cancers [19, 20]. Elevated TMB in tumor cells have more neoantigens, resulting in an increase in antitumor T cells in the TME. Interestingly, patients with high TMB have a higher probability in the response to tumor immunotherapy [21]. Dysregulated TMB has also been reported to be involved in the prognosis of cancers [22]. Different cancer species vary in the expression of TMB [23]. In HCC, the higher of TMB means the worse in the OS of patients [24]. However, whether TMB could serve as a biomarker in HCC is still unclear.

Herein, we constructed a novel prognostic gene signature to explore the prognostic value of pyroptosis-related genes (PRGs) and the relationships with tumor mutation and immunotherapy. Our data suggested that risk score was identified as an independent prognostic factor. Notably, the prognostic prediction of our risk signature was also confirmed by the International Cancer Genome Consortium (ICGC) cohort ( $n = 231$ ) and the First Affiliated Hospital of Wenzhou Medical University (FAHWMU) cohort ( $n = 180$ ). Finally, the effects of risk scores and molecular subtypes on TMB and immune filtration were explored to further evaluate the value of the signature in molecular therapy.

## 2. Materials and Methods

**2.1. Data Preparation.** The RNA sequencing data and relevant clinical characteristics of 371 HCC patients were downloaded from TCGA database (<https://portal.gdc.cancer.gov/>). We matched the RNA sequencing data and clinical features according to each patient's ID number and excluded six follow-up tumor samples. Thus, TCGA cohort with 365 HCC patients was finally enrolled as the training cohort. The other 231 patients with HCC, along with their RNA-seq data and clinical features, were obtained from the ICGC database (<https://dcc.icgc.org/projects/LIRI-JP/>). HCC patients obtained from the ICGC database were derived from a subset of Japanese population with HBV or HCV infection [25]. Thus, the ICGC cohort was used as the testing cohort. The data of TCGA cohort and ICGC cohort were downloaded from public databases; thus, our study followed the public data access policies; there was no ethical relationship involved. The FAHWMU cohort ( $n = 180$ ) was obtained from the First Affiliated Hospital of Wenzhou Medical University (Wenzhou, China). HCC samples in

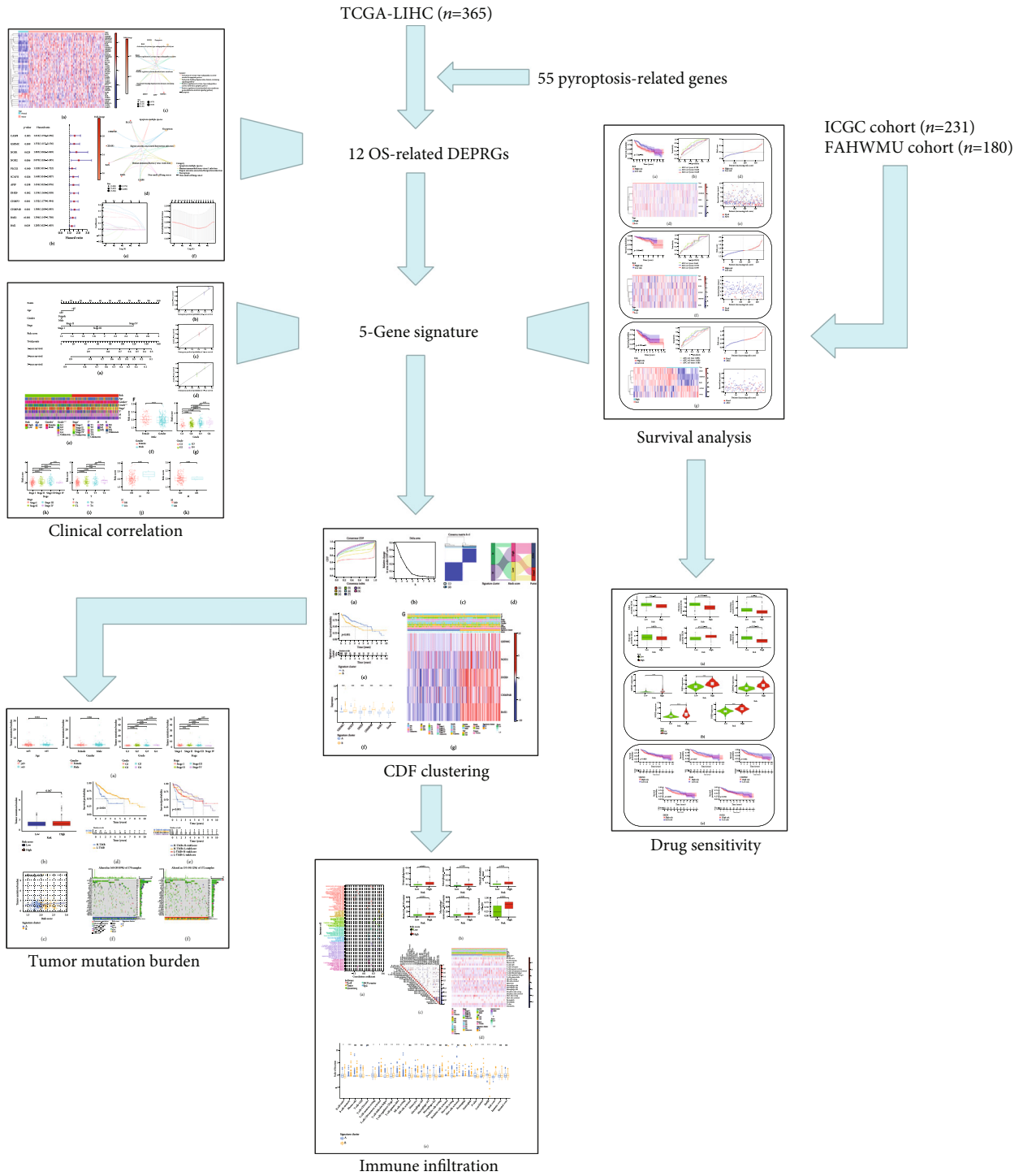


FIGURE 1: The flow chart of this study.

the FAHWMU cohort were collected from 2010 to 2020, and OS time was used as the main indicator of the survival time. The collection of this cohort was reviewed and approved by the human research ethics committee of the First Affiliated Hospital of Wenzhou Medical University. The patients/participants provided their written informed consent to participate in this study. All the clin-

ical characters of these patients with HCC are shown in Table 1. Meanwhile, 55 pyroptosis-related genes (PRGs) used in this study were extracted from the MsigDB database (<http://www.gsea-msigdb.org/gsea/msigdb/>) and prior reviews (Table S1) [26–28]. In addition, the data of TMB and immune infiltration of HCC patients in TCGA cohort were also obtained from TCGA database.

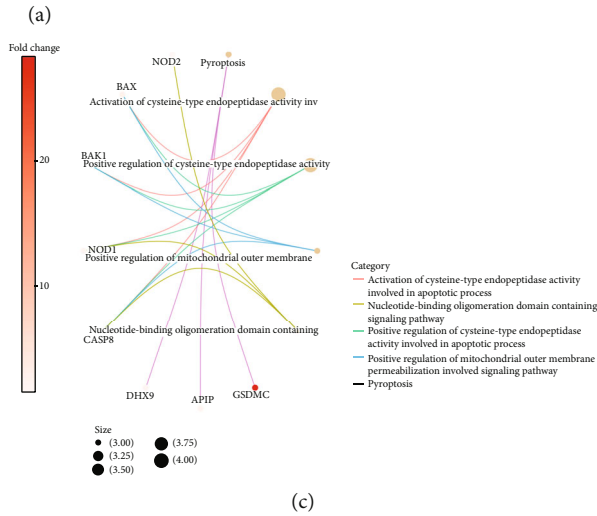
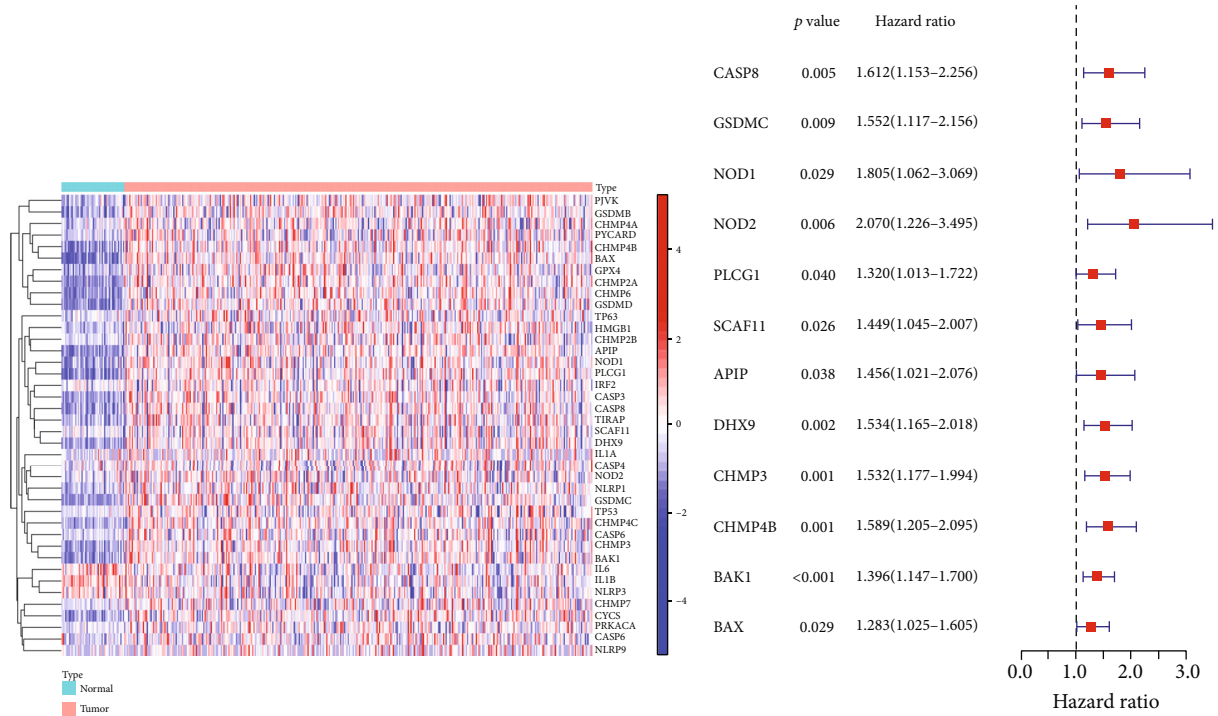


FIGURE 2: Continued.

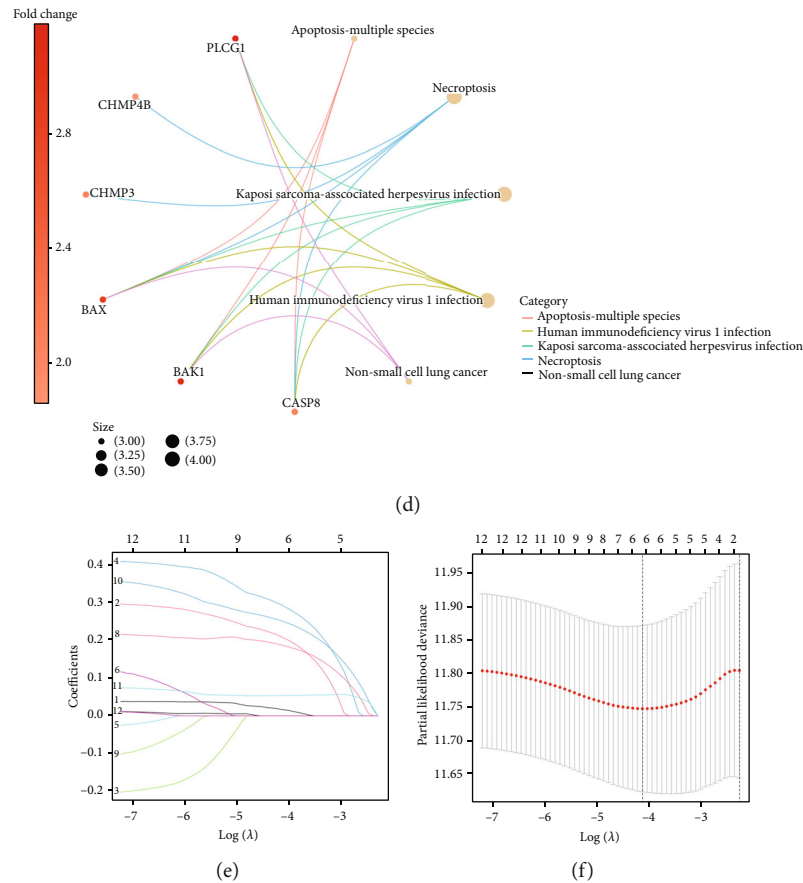


FIGURE 2: Identification of five optimal prognosis-related DEPRGs. (a) The heat map illustrated the differential expression of 40 PRGs between tumor samples and adjacent normal samples. (b) The Forest plot displayed the univariate Cox regression analyses regarding overall survival, and only DEPRGs with  $P < 0.05$  and HR  $> 1$  were regarded as prognosis-related DEPRGs. (c) CIRC plot for GO function enrichment of 12 prognosis-related DEPRGs. (d) CIRC plot for KEGG pathway enrichment of 12 prognosis-related DEPRGs. (e, f) LASSO regression analyses for screening five optimal PRGs.

**2.2. Identification of Prognosis-Related DEPRGs.** The Wilcoxon rank sum test was used for the differential analysis to identify differentially expressed pyroptosis-related genes (DEPRGs) between HCC samples and adjacent nontumorous samples ( $P < 0.05$ ). Then, univariate Cox regression analysis was used to further identify prognosis-related DEPRGs. The expression of each gene ( $i$ ) was adjusted to  $\log_2(i + 1)$  to increase the accuracy of the Cox regression results. In the univariate Cox regression analysis, FDR  $< 0.05$  was set as the cut-off value. The Gene Ontology (GO) and Kyoto Encyclopedia of Genes and Genomes (KEGG) enrichment analyses were performed using the “http://org.Hs.eg.db” and “enrichplot” package.

**2.3. Generation and Validation of the Signature.** The LASSO Cox regression analysis was applied to identify hub DEPRGs to minimize the risk of overfitting among the signature [29, 30]. The independent variable in the regression was the normalized expression matrix of candidate prognostic DEPRGs, and the response variables were OS and the status of patients in TCGA cohort. Penalty parameter ( $\lambda$ ) for the gene signature was determined by tenfold cross-validation following the minimum criteria (i.e., the value of  $\lambda$  corresponding to

the lowest partial likelihood deviance). Thus, a total of five optimal genes were screened, and their relevant coefficients were calculated. Next, we used the following formula to calculate the risk score for each patient:

$$\text{risk score} = \text{expression for each gene} * \text{coefficient for each gene.} \quad (1)$$

Based on the median risk score, all HCC patients were separated into high- and low-risk groups. The different OS between high- and low-risk groups was analyzed via the log rank test. The sensitivity and specificity of the signature were evaluated by time-dependent receiver operating characteristic (ROC) analysis.

The hazard proportional model was constructed by employing multivariate Cox regression analysis to determine the independent prognostic factors. A novel nomogram, including the risk score and other three clinical factors (age, gender, and TNM stage), was constructed to explore the proportional hazards assumption of the multivariate Cox model. Next, the calibration curves of the 1<sup>st</sup>, 2<sup>nd</sup>, and 3<sup>rd</sup> years were generated to verify the accuracy of the

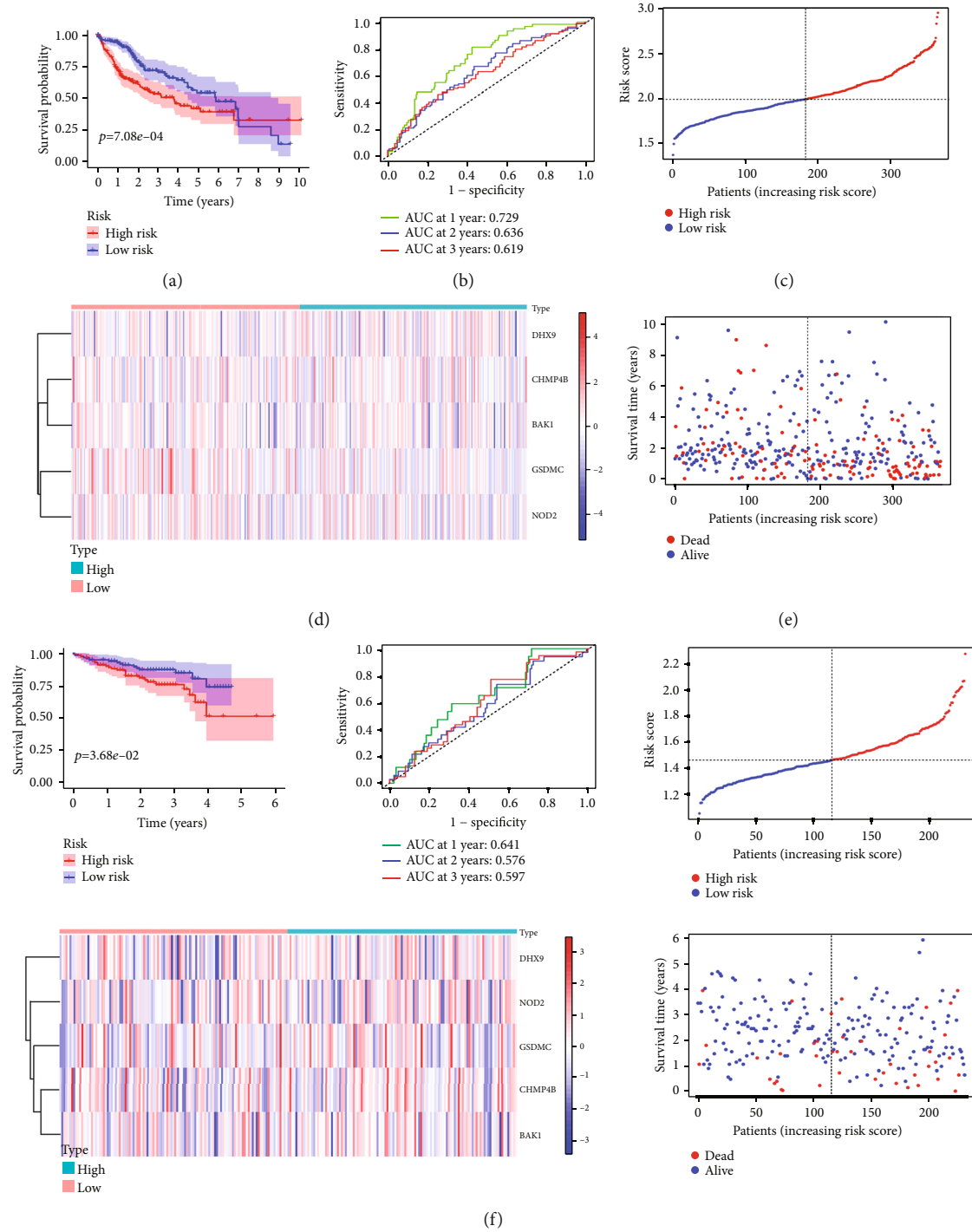


FIGURE 3: Continued.

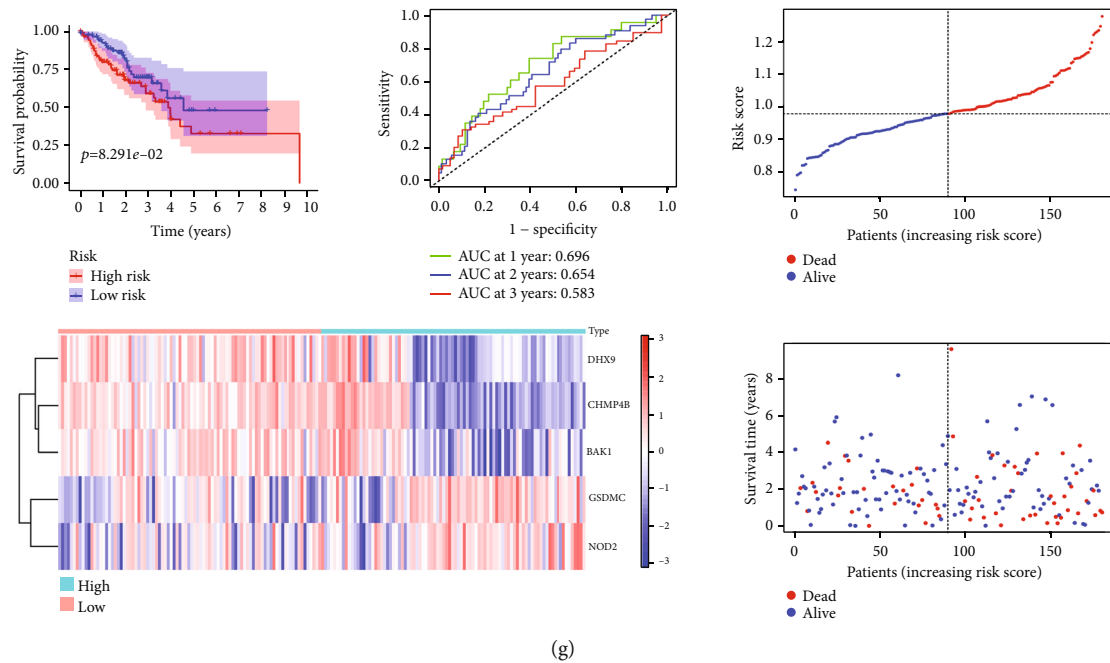


FIGURE 3: Generation and validation of the signature. (a) K-M survival curve displays the OS of patients between different risk groups in TCGA cohort. (b) Time-dependent ROC curves of the patients in TCGA cohort. (c) Heat map illustrated the expression patterns of five PRGs in TCGA cohort. (d) Distribution of the risk score in TCGA cohort. (e) Survival status scatter plots of patients in TCGA cohort. (f) Survival analysis with respect to the ICGC cohort ( $n = 231$ ). (g) Survival analysis of the FAHWMU cohort ( $n = 180$ ).

nomogram. The correlation between risk scores and individual clinical characteristics was analyzed via Wilcoxon rank sum test.

**2.4. Function Enrichment Analyses and Drug Sensitivity Test.** All DEGs were screened between the high-risk and low-risk groups using the following filter ( $|\log 2FC| \geq 1$ ,  $FDR < 0.05$ ). The GO and KEGG enrichment analyses were performed based on the “clusterProfiler” R package. Estimated by the Gene Set Variation Analysis algorithm, the infiltrating score of 16 immune cells and the activity of 13 immune-related pathways were calculated. The half-maximal inhibitory concentration ( $IC_{50}$ ) was estimated by R package “pRRophetic” to evaluate the drug sensitivity [31]. The Connectivity Map (CMap) database (<https://portals.broadinstitute.org/cmap/>) was used to predict potential chemotherapeutic drugs.

**2.5. Consensus Clustering Analyses.** In the consensus clustering, the cumulative distribution function (CDF) and consistent matrix were used to evaluate the optimal number of subtypes [32]. Thus, two robust subtypes (clusters A and B) were obtained according to the transcription matrix of the five genes in the signature. The Kaplan-Meier survival curves were performed to analyze the OS of subtypes. The correlations between the subtypes, OS status, and risk score were explored using the “ggalluvial” R package.

**2.6. Tumor Mutation Burden Correlation.** The TMB score of each HCC patient in TCGA cohort was evaluated using the somatic mutation analysis. We constructed correlation scatter and boxplots based on the Pearson correlation analysis to

search the effect of risk score on TMB. Waterfall plots regarding high- and low-risk groups were generated by R package “maftools.”

**2.7. Immune Infiltration Analysis.** The immune infiltration analysis was performed to calculate the correlation coefficient and construct bubble chart. The ESTIMATE algorithm was applied to derive the corresponding immune score, stromal score, and ESTIMATE score [33]. Next, the proportions of 22 immune cell types of HCC patients were calculated via the CIBERSORT algorithm.

**2.8. Quantitative Real-Time PCR (qRT-PCR).** The total RNA from the liver tissues of the FAHWMU cohort was extracted using TRIzol reagent. The mRNA was then reverse transcribed into cDNA using ribo SCRIPTTM reverse transcription kit. The expression level of mRNA was calibrated with glyceraldehyde-3-phosphate dehydrogenase (GAPDH). The designed primers are shown in Table S2. SYBR Green master mix was added, and real-time PCR was carried out using a 7500 rapid quantitative PCR system (Applied Biosystems, USA). The CT value of each well was recorded, and the relative quantification of the amplified products was performed using the  $2^{-\Delta Ct}$  method.

**2.9. Statistical Analysis.** Here, the R version 3.6.1 (<http://www.R-project.org>) and its appropriate packages were used to perform all statistical analyses.  $P < 0.05$  was considered as the standard of significantly statistical difference. The FDR method was used for multiple testing. Pearson test



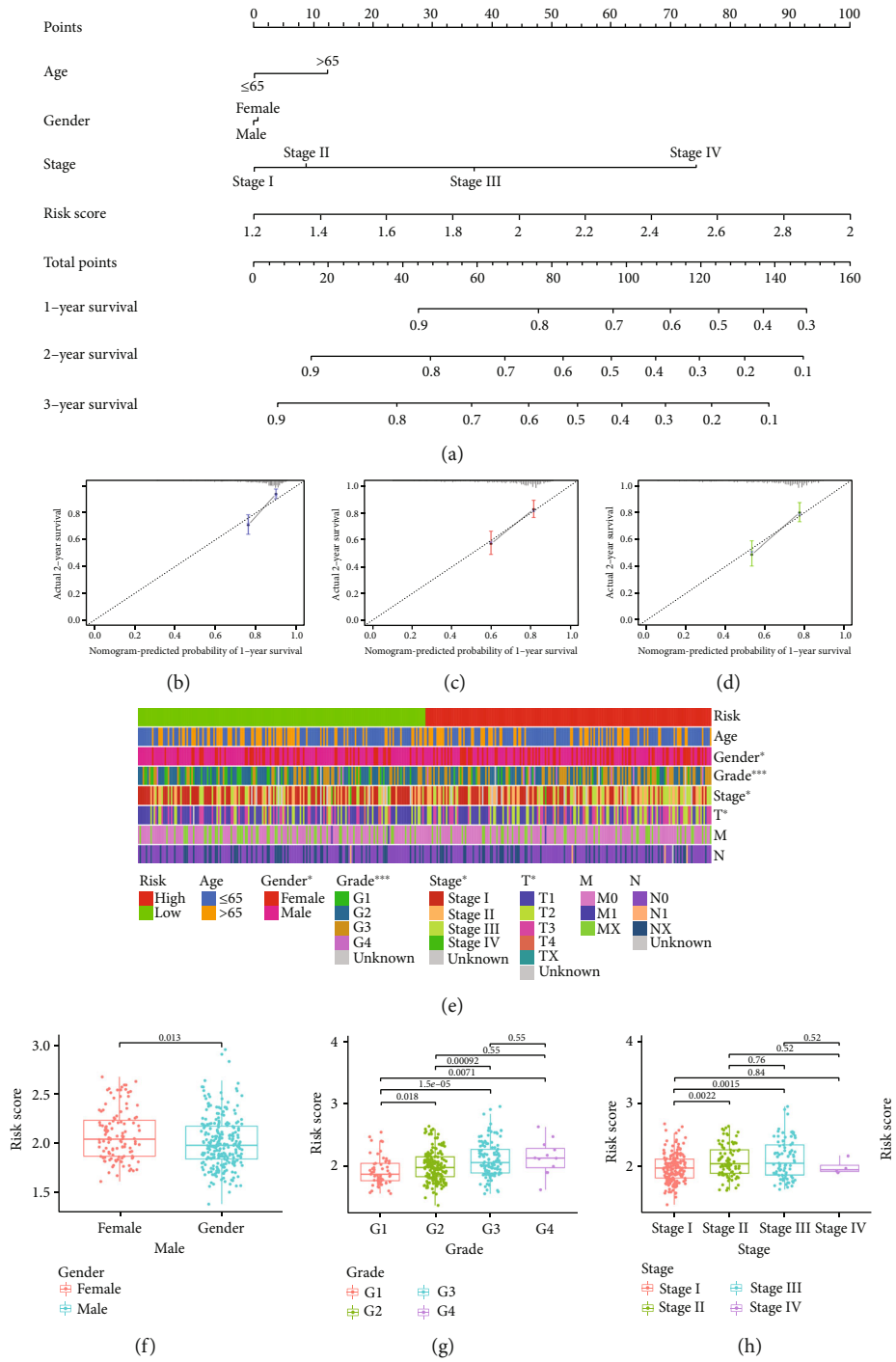


FIGURE 4: Continued.

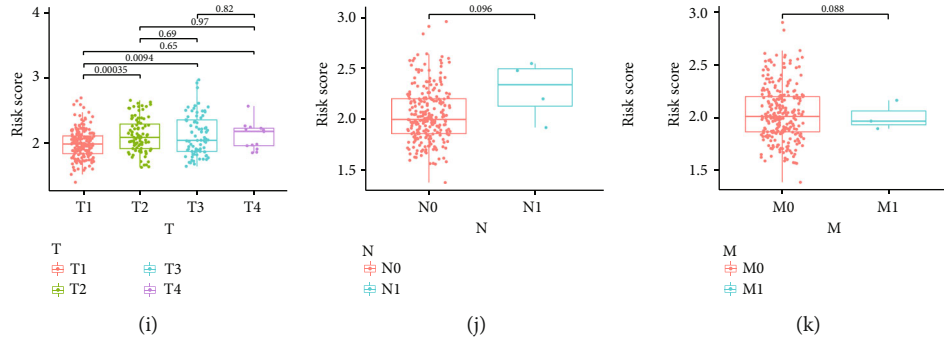


FIGURE 4: Selection of the independent prognostic factors. (a) The nomogram of the risk score and clinical parameters (age, gender, and TNM stage) in TCGA cohort. (b–d) The calibration curves displayed the accuracy of the nomogram in the 1<sup>st</sup>, 2<sup>nd</sup>, and 3<sup>rd</sup> years. (e) Complex heat map illustrated the correlation between risk and clinical characteristics (\* $P < 0.05$ , \*\* $P < 0.01$ , and \*\*\* $P < 0.001$ ). (f–k) Boxplots demonstrated the differences in risk scores across clinical features (F: gender; G: grade; H: TNM stage; I: T stage; J: N stage; K: M stage).

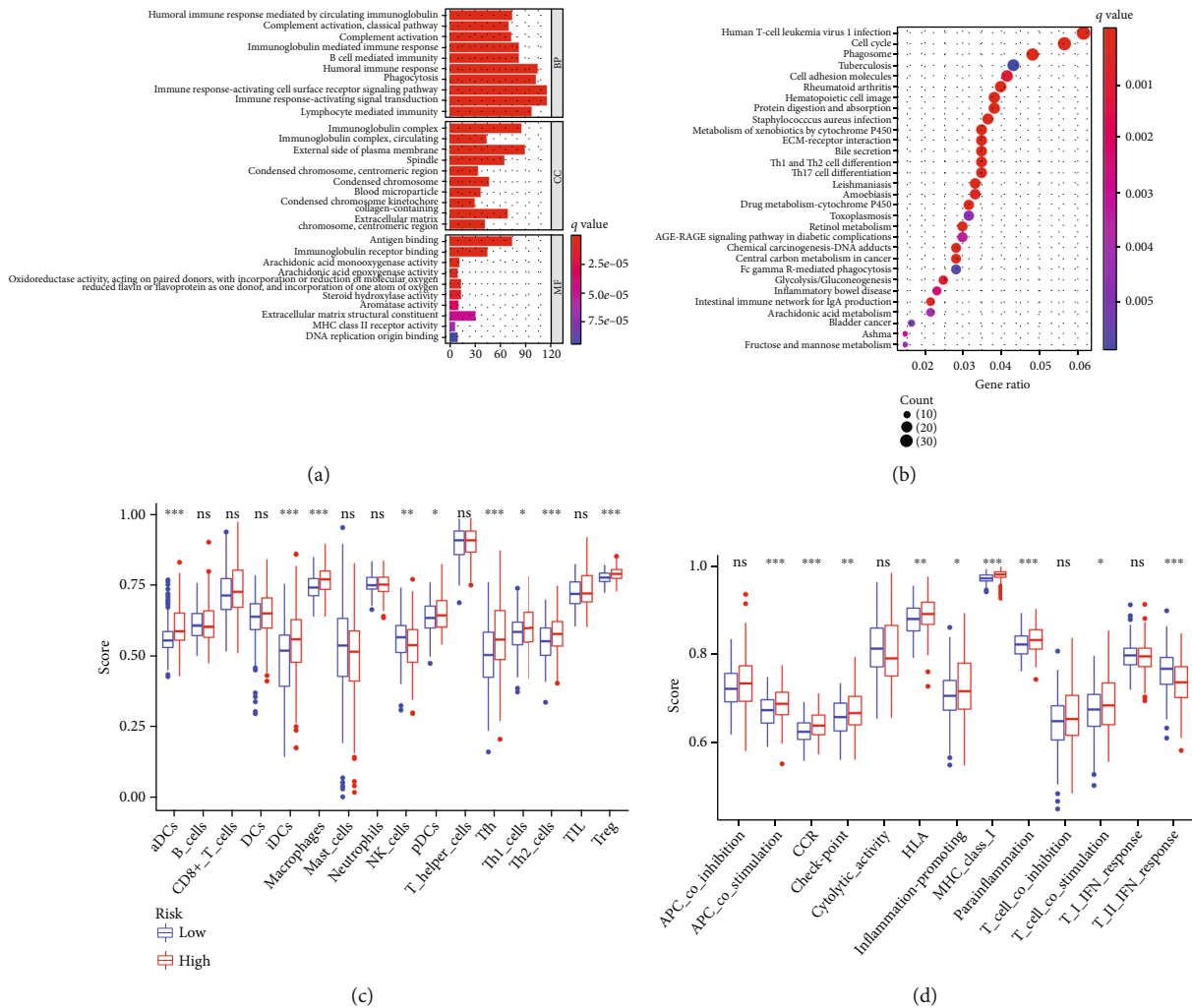
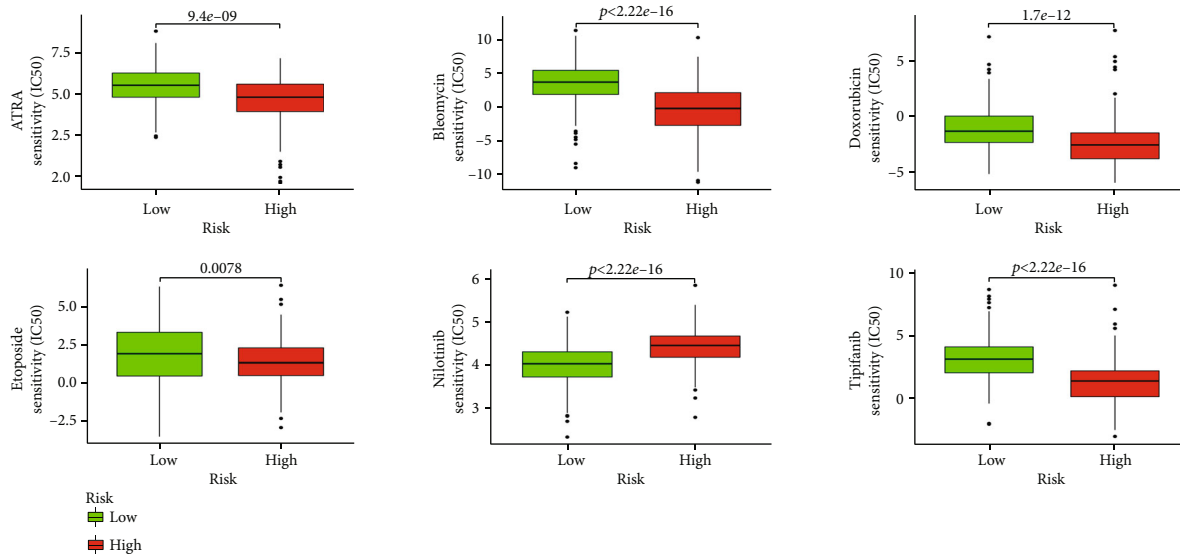
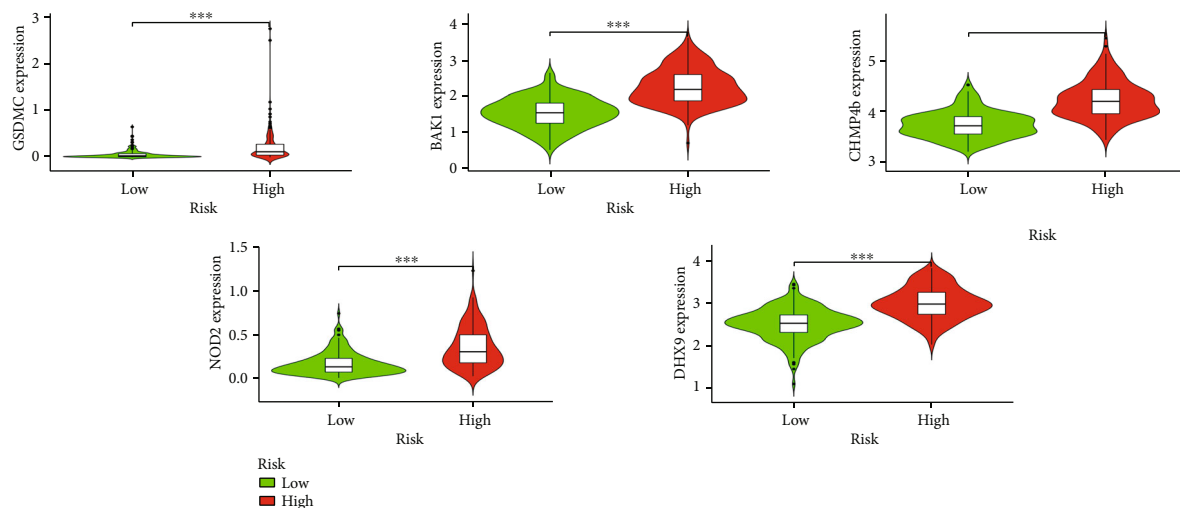


FIGURE 5: The enrichment analyses of the signature. (a) GO function enrichment of the signature (abscissa: number of DEGs,  $P < 0.05$ ,  $Q < 0.05$ ). (b) KEGG pathway enrichment of the signature (abscissa: number of DEGs,  $P < 0.05$ ,  $Q < 0.05$ ). (c) Comparison of the enrichment scores of 16 immune cells between different risk groups. (d) Comparison of the enrichment scores of 13 immune-related functions between different risk groups.

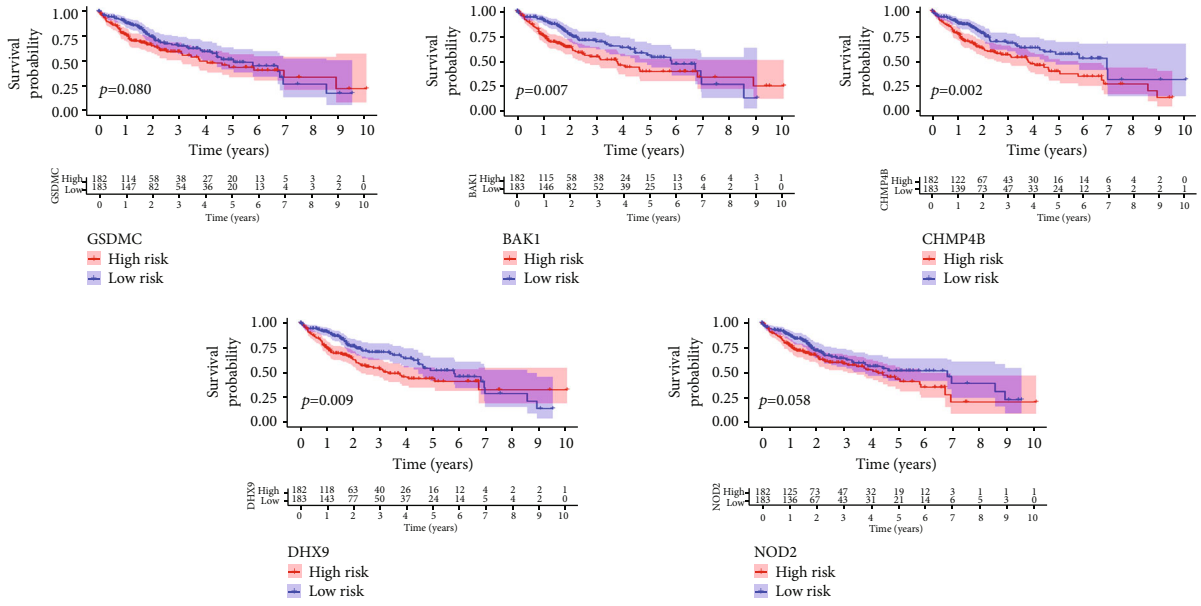


(a)



(b)

FIGURE 6: Continued.



(c)

FIGURE 6: Drug sensitivity of the signature. (a) Boxplots displayed the estimated IC<sub>50</sub> of different potential drug sensitivity (ATRA, Bleomycin, Doxorubicin, Etoposide, Nilotinib, and Tipifarnib) between low- and high-risk groups (all  $P < 0.05$ ). (b) Violin plots presented significant differences in the expression of individual genes across the signature in high- and low-risk groups ( $***P < 0.001$ ). (c) K-M survival curves illustrated that the lower expression of individual genes across signature had better OS ( $P < 0.1$ ).

was used to compare the categorical variables. The overall workflow of this study is shown in Figure 1.

### 3. Results

**3.1. Twelve Prognosis-Related DEPRGs Were Identified between Adjacent Nontumorous Samples and HCC Samples.** The expressions of 55 PRGs were compared between 50 adjacent nontumorous and 365 HCC samples, and 40 DEGs were identified ( $P < 0.05$ ). Among these, the expressions of 3 genes (IL6, IL1B, and NLRP3) were found to be downregulated in the tumor group while others were upregulated compared to the adjacent nontumorous group. The expression of these DEGs was shown in the heat maps (Figure 2(a)). The univariate Cox regression analyses further identified 12 DEPRGs regarding OS. The DEPRGs with  $P < 0.05$  and hazard ratio (HR)  $> 1.000$  were regarded as prognosis-related DEPRGs (Figure 2(b)). In addition, the GO enrichment analyses revealed that prognosis-related DEPRGs were mainly enriched in the pathways, including activation of cysteine-type endopeptidase activity involved in the apoptotic processes (Figure 2(c),  $P < 0.05$  and  $Q < 0.05$ ). The KEGG pathway enrichment plots demonstrated enrichment in Kaposi sarcoma-associated herpesvirus infection, necroptosis, and human immunodeficiency virus 1 infection (Figure 2(d),  $P < 0.05$  and  $Q < 0.05$ ). The overfitting of genes during the signature generation was prevented by LASSO regression analysis and finally identified the optimal five genes (GSDMC, DHX9, CHMP4B, BAK1, and NOD2) (Figures 2(e) and 2(f)).

**3.2. Prognostic Value of the Signature Was Validated in TCGA Cohort and the Extra Validation Cohort.** In TCGA cohort, using five optimal genes and the relevant coefficients, the risk score was calculated using the following formula:

$$\begin{aligned} \text{risk score} = & (0.132 * \text{GSDMC exp.}) + (0.217 * \text{NOD2 exp.}) \\ & + (0.149 * \text{DHX9 exp.}) + (0.201 * \text{CHMP4B exp.}) \\ & + (0.055 * \text{BAK1 exp.}) \end{aligned} \quad (2)$$

According to the median score calculated by the risk score formula, 365 patients were separated into low- and high-risk groups (Figures 3(c) and 3(d)). With an increase in the risk score, there was a gradual decrease in the survival time as well as an increase in the number of patients in death status (Figure 3(e)). Compared to the high-risk group, the low-risk group showed a better OS probability (Figure 3(a),  $P < 0.05$ ). We found that the area under the ROC curve (AUC) reached 0.729 for 1<sup>st</sup> year, and the AUC value for 2<sup>nd</sup> and 3<sup>rd</sup> years was both  $> 0.600$  (Figure 3(b)). HCC patients in the ICGC cohort and the FAHWMU cohort were also divided into high-risk group and low-risk group. The results of the survival analysis were similar to TCGA cohort (Figures 3(f) and 3(g)). Taken together, our results suggest the potential prognostic value of our signature in the prognosis of HCC patients.

**3.3. Risk Score Was Identified as an Independent Prognostic Factor.** In the univariate Cox analysis, the risk score and clinical factors (age, gender, and TNM stage) were significantly

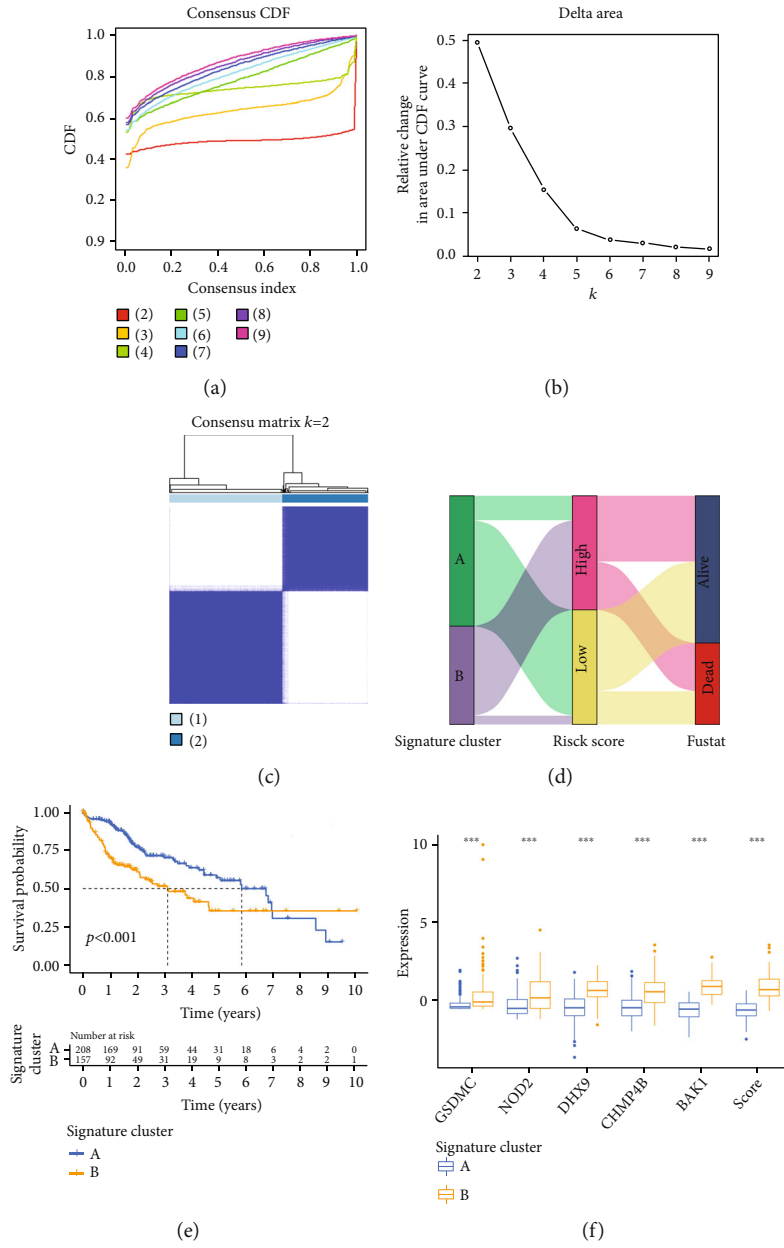


FIGURE 7: Continued.

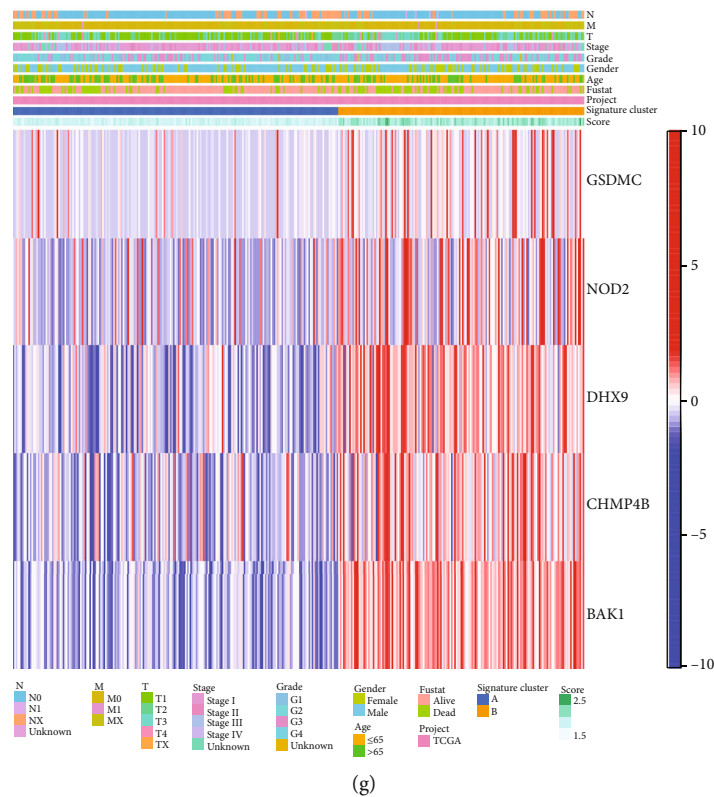
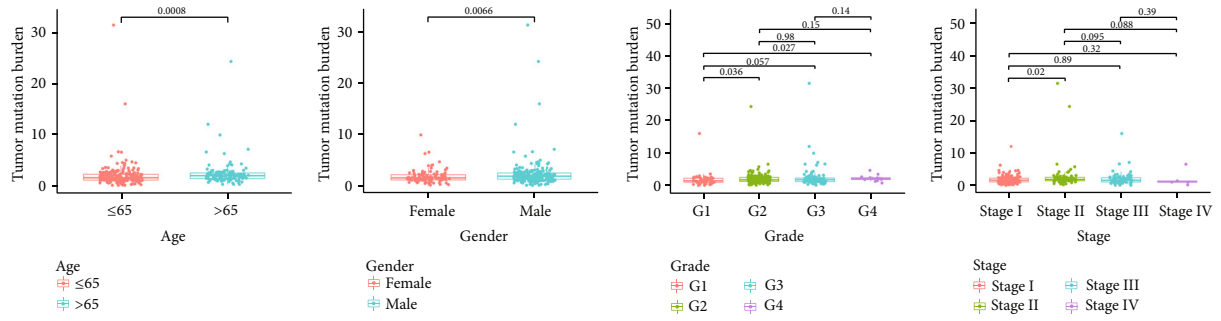


FIGURE 7: Clustering analyses of the signature. (a, b) Cumulative distribution function based on the signature indicated that the optimal number of subtypes was 2. (c) Concordance matrix of subtypes. (d) ggalluvial of two clusters displayed the correlation between clusters, risk, and survival status. (e) K-M survival curve of the two clusters. (f) Expression of individual genes across signature and risk score between cluster A and cluster B. (g) Complex heat map illustrated the expression patterns between cluster A and cluster B.

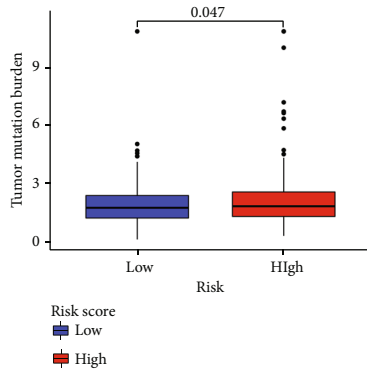
correlated with OS (Fig. S1A). Importantly, the risk score was confirmed as an independent predictor for OS in the multivariate Cox model (Fig. S1B). The OS-related nomogram was constructed to test the proportional hazards assumption in the multivariate Cox model (Figure 4(a)). Compared with other clinical factors, risk score had a better effect on the OS in the nomogram. With the integration of the risk score and clinical features (age, gender, and TNM stage), the 1<sup>st</sup>, 2<sup>nd</sup>, and 3<sup>rd</sup> years of OS of patients with HCC could be predicted accurately. The subsequent calibration curves further verified the accuracy of the nomogram (Figures 4(b)–4(d)). The correlations between the risk and clinical characteristics (age, gender, tumor grade, TNM stage, T stage, N stage, and M stage) were shown in the complex heat map (Figure 4(e)). With increasing risk, the correlation between tumor grade and risk score was most significant ( $P < 0.001$ ). The boxplot further confirmed that there was a significant upward trend of risk score with tumor grade from G1 to G4 (Figure 4(j), G1-G4:  $P = 0.0071$ ). Additionally, with stage T from T1 to T3, the risk score was also significantly increased (Figure 4(i), T1-T3:  $P = 0.0094$ ). The results of TNM stage were consistent with the results of stage I to stage III (Figure 4(h), stages I-III,  $P = 0.0015$ ). Compared to the female patients with HCC, a lower risk score was found in male patients with HCC (Figure 4(f)).

**3.4. Functional and the Immunological Activity Analyses.** GO function enrichment and KEGG pathway enrichment were performed based on the risk score. In the results of GO enrichment, we found that the DEGs were mainly associated with immune response-activating cell surface receptor signaling pathway and immune response-activating signal transduction (Figure 5(a)), suggesting the involvement of immune infiltration in pyroptosis. KEGG pathway enrichment indicated that DEGs were mainly enriched in human T cell leukemia virus 1 infection, cell cycle, and phagosome (Figure 5(b)). ssGSEA was used to further analyze the scores of immune cells and immune-related pathways between the low- and high-risk groups. The scores of most immune cells (aDCs, DCs, iDCs, Tfh, Th2 cells, and Treg) were significantly increased with the increasing of risk (Figure 5(c),  $P < 0.001$ ). In addition, the activity of 8 immune pathways in the high-risk group was higher than that in the low-risk group, except for the APC coinhibition, Cytolytic activity, T cell coinhibition, and type I IFN response (Figure 5(d)). Notably, type II IFN response was significantly lower in the high-risk group.

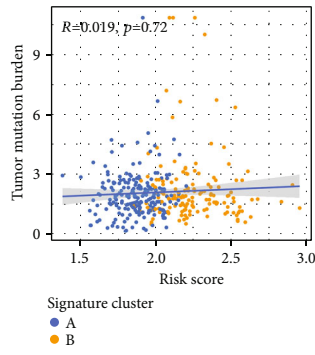
**3.5. Drug Sensitivity Test Screened Six Potential Chemotherapy Drugs.** The boxplots showed the results of drug sensitivity test (Figure 6(a)). By estimating  $IC_{50}$  between



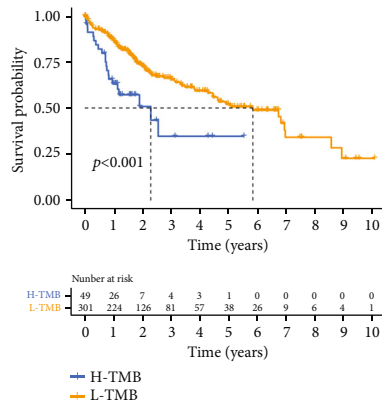
(a)



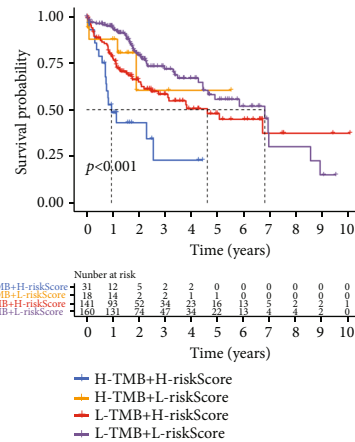
(b)



(c)



(d)



(e)

FIGURE 8: Continued.

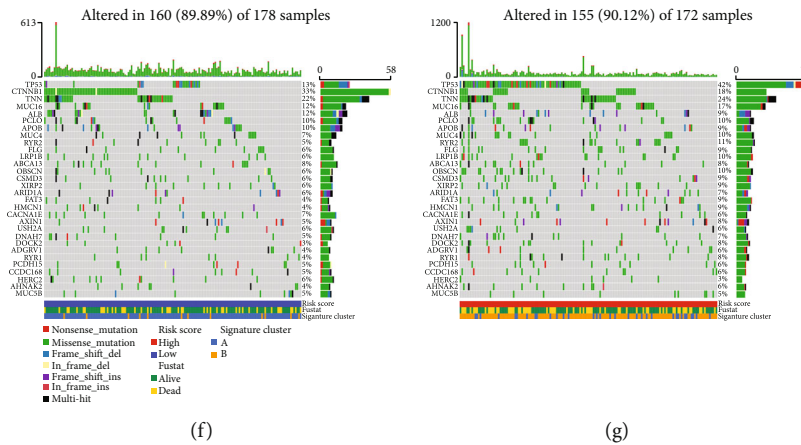


FIGURE 8: Tumor mutation burden analyses. (a) Boxplots showed the differences in TMB value among different clinical characteristics (age:  $P = 0.0008$ , gender:  $P = 0.0066$ , and G1-G4:  $P = 0.027$ ). (b) Boxplot illustrated that the TMB value was significantly higher in the high-risk group ( $P = 0.047$ ). (c) Scatter plot of correlations between the TMB value and the risk score. (d) K-M survival curve of the high-TMB group and the low-TMB group. (e) K-M survival curve of the comprehensive analyses between TMB and risk score. (f) Comparison of mutation frequencies in the low-risk group. (g) Comparison of mutation frequencies in the high-risk group.

the low-risk and high-risk groups, 6 potential chemotherapy drugs were identified. The patients with HCC in the high-risk subtype showed obvious sensitivity to chemotherapy drugs, like ATRA, Bleomycin, Doxorubicin, Etoposide, Nilotinib, and Tipifarnib (all  $P < 0.05$ ). Moreover, violin plots showed that individual genes in the signature were enhanced in the high-risk group (Figure 6(b)). Additionally, the K-M survival curves of individual genes in the signature showed a better OS in the low-expression group (Figure 6(c)).

**3.6. Two Main Subtypes Were Divided Based on the Consensus Clustering Analysis.** According to the  $k$  value selected by the highest cophenetic correlation coefficient, we divided all patients with HCC into two main subtypes (clusters A and B) (Figures 7(a)–7(c)). Compared to cluster A, patients in cluster B had higher risk scores and worse OS (Figures 7(d) and 7(e)). Moreover, all the expressions of individual genes were found to be higher in cluster B (Figure 7(f),  $P < 0.001$ ). Combined with other clinical characteristics (age, gender, grade, TNM stage, T stage, N stage, and M stage) and risk score, the complex cluster-based heat map was constructed (Figure 7(g)).

**3.7. The Potential Correlation between Signature and Tumor Mutation.** The association between clinical features and TMB is shown in Figure 8(a). We found that patients with male and  $>65$  y had a higher TMB value. TMB values were obviously increased with tumor grade from G1 to G4 and TNM stage from stages I to II. With an increase in risk score, TMB values were additionally increased (Figure 8(b),  $P = 0.047$ ). Unfortunately, the correlation between TMB value and risk score was not significant (Figure 8(c),  $R = 0.019$ ,  $P = 0.72$ ). Our results showed that the higher level of TMB was observed in cluster A. Interestingly, K-M survival curves showed that the combination of higher TMB value and higher risk score was associated with worse OS (Figures 8(d) and 8(e),  $P < 0.001$ ). Additionally, waterfall plots revealed that the

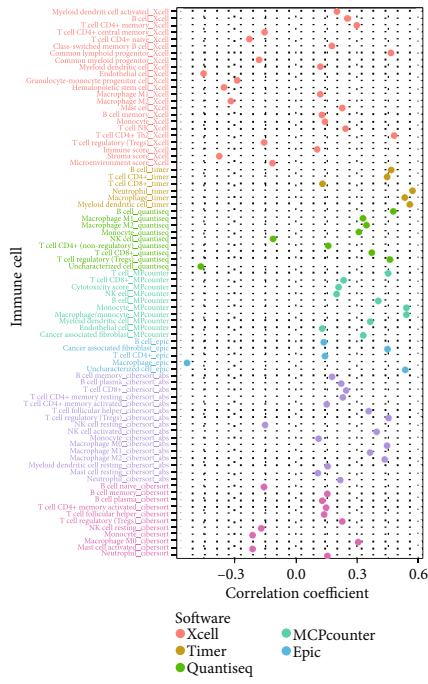
mutation profiles of patients with HCC was lower in the low-risk group (Figures 8(f) and 8(g)).

**3.8. Significant Correlation between Immune Infiltration and Signature.** Next, positive correlations were found between immune infiltration and risk score (Figure 9(a)). Boxplots showed that the contents of 6 immune cells were significantly higher in all the high-risk groups (Figure 9(b), all  $P < 0.001$ ). Based on the ESTIMATE and CIBERSOFT algorithms, the proportions of 22 immune cell types in patients with HCC, the relevant ESTIMATE scores were calculated (Figure 9(c)). We found that the coefficients of immune cells including T cells and macrophages were significant. The complex heat map revealed the expression patterns of clinical features and the proportions of 22 immune cell types (Figure 9(d)). The boxplot showed the differences in scale of fraction of different immune cells in two clusters (Figure 9(e)).

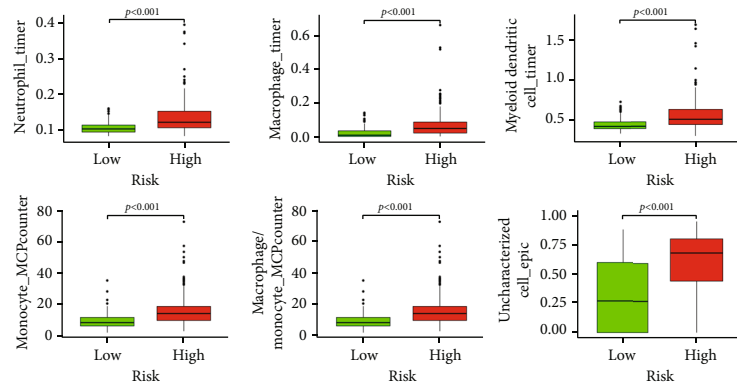
## 4. Discussion

Recent studies have identified pyroptosis as a new form of programmed cell death, which plays an essential role in tumor development and treatment mechanisms [8]. Pyroptosis has been found to play a crucial role in various cancers, such as non-small-cell lung cancer and head and neck cancer [34, 35]. Currently, the pyroptosis-related prognostic signature has been constructed in ovarian cancer and gastric cancer, with an excellent prognostic potential [36, 37]. Thus, targeting PRGs may be a promising therapeutic strategy for HCC. However, comprehensive analysis of PRGs for prognosis prediction and targeted therapy in the patients with HCC still remains unclear. In the present study, we aimed to construct a novel prognostic risk signature and identify potential molecular subtypes to better predict the prognosis in HCC. The signature, which was validated by the ICGC cohort and the FAHWMU cohort,

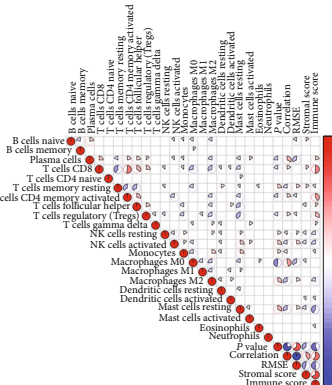




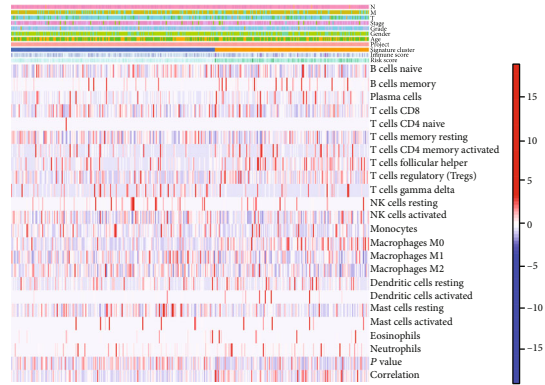
(a)



(b)



(c)



(d)

FIGURE 9: Continued.

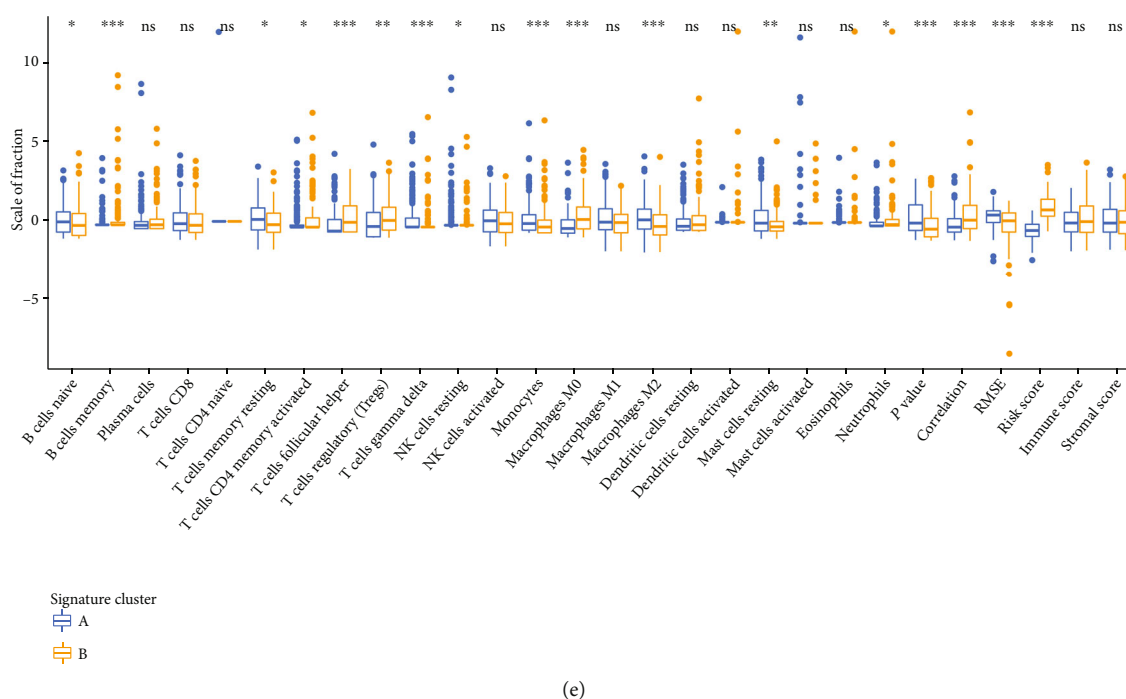


FIGURE 9: Immune correlation analyses and immune differential analyses of three clusters in the HCC patients. (a) Correlation coefficients between different immune cells and risk score. (b) Boxplots showed the content of immune cells with high correlation coefficients is significantly higher in the high-risk group. (c) The correlation plot of immune cells in TCGA cohort. (d) Complex heat map displayed the association between the expression levels of immune cells and clinical features in the HCC patients. (e) The differential analyses between immune cells and the scale of fraction for cluster A and cluster B.

contributed to accurate prediction of the OS in patients with HCC. In addition, the high-risk patients identified by this signature were confirmed to be associated with higher TMB, drug sensitivity, and tumor immune cell content. Molecular subtypes (clusters A and B) were identified based on the signature. Further studies revealed that compared with cluster B, better survival outcomes and lower TMB were observed in cluster A. All these results suggest that this signature could serve as a new biomarker to improve the prognosis of HCC.

DHX9, CHMP4B, BAK1, NOD2, and GSDMC were the PRGs included in the prognostic signature. Wang et al. found that DHX9 could interact with CDK6 to promote the growth of HCC [38]. Elevated expression of CHMP4B has been found to play a key role in accelerating cell proliferation and resistance to doxorubicin in HCC [39]. In addition, elevated expression of BAK1 could exacerbate pyroptosis and further aggravate the invasion of HCC [40]. Hepatic NOD2, a well-characterized intracellular PRR of the NOD-like receptor (NLR) family, has been shown to promote hepatocarcinogenesis [41]. In addition, GSDMC, metabolized by  $\alpha$ -ketoglutarate and mediated through caspase-8, results in pyroptosis [42]. Overall, increasing studies have confirmed the roles of these genes (DHX9, CHMP4B, BAK1, NOD2, and GSDMC) in HCC.

Previously, Hage et al. found that pyroptosis in macrophages mediates natural killer cell cytotoxicity against HCC [43]. In the present study, the effect of this signature

on immune infiltration was also explored. Moreover, there was a positive correlation between macrophages under the TIMER database and risk score. The relative content of macrophages under the TIMER database was elevated in the high-risk group. It is known that drug therapy is crucial for the treatment of HCC [44, 45]. Previous studies have identified Doxorubicin as an effective drug to inhibit HCC via the regulation of apoptosis [46]. Herein, Doxorubicin was also confirmed as a potential drug against HCC, with higher drug sensitivity in the high-risk group. TMB, as a novel biomarker, has been intensively studied in precision medicine for HCC [47, 48]. Xu et al. found that TMB is positively correlated with clinical features in HCC [49]. Liu et al. found that LRP1B mutations are associated with higher TMB and poor prognosis in patients with HCC [50]. We also analyzed the correlation between TMB and the signature. Clearly, there was an obviously lower TMB value in the low-risk group, suggesting a potential correlation between TMB value and the signature.

There are several advantages in this study. First, the prognostic signature could accurately predict the OS for patients with HCC. In addition, the signature is significantly correlated with immune infiltration and TMB, suggesting its biomarker potential in HCC. The prognosis prediction of the signature is further confirmed by the FAHWMU cohort, suggesting its good prognostic prediction ability. More clinical samples are needed to validate the reliability of HCC prognostic value of this signature.

In conclusion, a novel prognostic PRG-signature is constructed for better prediction of prognosis in HCC, which may provide new insights into the treatment of HCC. In addition, this signature is closely associated with TMB and immune infiltration.

## Abbreviations

|          |  |
|----------|--|
| HCC:     | Hepatocellular carcinoma                                     |
| TCGA:    | The Cancer Genome Atlas                                      |
| ICGC:    | International Cancer Genome Consortium                       |
| PRGs:    | Pyroptosis-related genes                                     |
| LASSO:   | Least absolute shrinkage and selection operator              |
| DEPRGs:  | Differentially expressed pyroptosis-related genes            |
| PDEPRGs: | Prognostic differentially expressed pyroptosis-related genes |
| FDR:     | False-discovery rate   |
| OS:      | Overall survival   |
| AUC:     | Area under the curve   |
| ROC:     | Receiver operating characteristic                            |
| ssGSEA:  | Single-sample gene set enrichment analysis                   |
| K-M:     | Kaplan-Meier   |
| GO:      | Gene Ontology  |
| KEGG:    | Kyoto Encyclopedia of Genes and Genomes                      |
| CDF:     | Cumulative distribution function                             |
| TME:     | Tumor microenvironment                                       |
| FAHWMU:  | The First Affiliated Hospital of Wenzhou Medical University. |

## Data Availability

The data and materials can be obtained by contacting the corresponding author.

## Conflicts of Interest

The authors declare that they have no conflicts of interest.

## Authors' Contributions

Ji Chen and Changyong Lin designed the study; Zhengping Yu, Boyu Lv, and Suhui Yu obtained and assembled data; Qiqi Tao and Zhichao Lang wrote the manuscript; Yuxiang Gao and Yan Jin sorted out all the figures and tables; Xiaoqi Li and Yajing Wang revised the manuscript; Yuxiao Zhang performed the literature search. The manuscript was edited by all authors, who have approved the final version for submission. Ji Chen, Qiqi Tao, Zhichao Lang, and Yuxiang Gao contributed equally to this work.

## Acknowledgments

The project was supported by the National College Students Innovation and Entrepreneurship Training Program (No. 202110343028).

## Supplementary Materials

Figure S1: univariate Cox analysis and multivariate Cox analysis containing risk score and clinical factors. Table S1: 55 pyroptosis-related genes used in this study. Table S2: list of primer sequences. (*Supplementary Materials*)

## References

- [1] J. Yang, P. Hainaut, G. Gores, A. Amadou, A. Plymoth, and L. Roberts, "A global view of hepatocellular carcinoma: trends, risk, prevention and management," *Nature Reviews. Gastroenterology & Hepatology*, vol. 16, no. 10, pp. 589–604, 2019.
- [2] J. Llovet, R. Kelley, A. Villanueva et al., "Hepatocellular carcinoma," *Nature Reviews Disease Primers*, vol. 7, no. 1, 2021.
- [3] A. Jemal, E. Ward, C. Johnson et al., "Annual Report to the Nation on the Status of Cancer, 1975–2014, Featuring Survival," *JNCI: Journal of the National Cancer Institute*, vol. 109, no. 9, 2017.
- [4] Y. Hoshida, S. Nijman, M. Kobayashi et al., "Integrative transcriptome analysis reveals common molecular subclasses of human hepatocellular carcinoma," *Cancer Research*, vol. 69, no. 18, pp. 7385–7392, 2009.
- [5] J. Nault and A. Villanueva, "Intratumor molecular and phenotypic diversity in hepatocellular carcinoma," *Clinical Cancer Research*, vol. 21, no. 8, pp. 1786–1788, 2015.
- [6] S. Torrecilla, D. Sia, A. Harrington et al., "Trunk mutational events present minimal intra- and inter-tumoral heterogeneity in hepatocellular carcinoma," *Journal of Hepatology*, vol. 67, no. 6, pp. 1222–1231, 2017.
- [7] Y. Boege, M. Malehmir, M. E. Healy et al., "A dual role of caspase-8 in triggering and sensing proliferation-associated DNA damage, a key determinant of liver cancer development," *Cancer Cell*, vol. 32, no. 3, pp. 342–359.e10, 2017.
- [8] S. Kovacs and E. A. Miao, "Gasdermins: effectors of pyroptosis," *Trends in Cell Biology*, vol. 27, no. 9, pp. 673–684, 2017.
- [9] P. Broz, P. Pelegrin, and F. Shao, "The gasdermins, a protein family executing cell death and inflammation," *Nature Reviews. Immunology*, vol. 20, no. 3, pp. 143–157, 2020.
- [10] R. Kolb, G.-H. Liu, A. M. Janowski, F. S. Sutterwala, and W. Zhang, "Inflammasomes in cancer: a double-edged sword," *Protein & Cell*, vol. 5, no. 1, pp. 12–20, 2014.
- [11] X. Huang, Z. Feng, Y. Jiang et al., "Nlrp3Vsig4 mediates transcriptional inhibition of  $\alpha$  and  $\beta$  in macrophages," *Science Advances*, vol. 5, no. 1, article eaau7426, 2019.
- [12] M. Mamik and C. Power, "Inflammasomes in neurological diseases: emerging pathogenic and therapeutic concepts," *Brain: A Journal Of Neurology*, vol. 140, no. 9, pp. 2273–2285, 2017.
- [13] F. Zhang, B. Zhou, Z. Yan et al., "6-Gingerol attenuates macrophages pyroptosis via the inhibition of MAPK signaling pathways and predicts a good prognosis in sepsis," *Cytokine*, vol. 125, article 154854, 2020.
- [14] Y. Ma, J. Pitt, Q. Li, and H. Yang, "The renaissance of anti-neoplastic immunity from tumor cell demise," *Immunological Reviews*, vol. 280, no. 1, pp. 194–206, 2017.
- [15] I. Gerhauser, L. Li, D. Li et al., "Dynamic changes and molecular analysis of cell death in the spinal cord of SJL mice infected with the BeAn strain of Theiler's murine encephalomyelitis virus," *Apoptosis: An International Journal On Programmed Cell Death*, vol. 23, no. 2, pp. 170–186, 2018.

- [16] Y. Liu, W. Zhen, Y. Wang, S. Song, and H. Zhang, "NaSO nanoparticles trigger antitumor immunotherapy through reactive oxygen species storm and surge of tumor osmolarity," *Journal of the American Chemical Society*, vol. 142, no. 52, pp. 21751–21757, 2020.
- [17] W. Tonnus, A. Belavgeni, F. Beuschlein et al., "The role of regulated necrosis in endocrine diseases," *Nature reviews. Endocrinology*, vol. 17, no. 8, pp. 497–510, 2021.
- [18] E. Koren and Y. Fuchs, "Modes of regulated cell death in cancer," *Cancer Discovery*, vol. 11, no. 2, pp. 245–265, 2021.
- [19] J. Chen, N. Esteghamat, E. Kim et al., "PD-1 blockade in a liver transplant recipient with microsatellite unstable metastatic colorectal cancer and hepatic impairment," *Journal of the National Comprehensive Cancer Network*, vol. 17, no. 9, pp. 1026–1030, 2019.
- [20] D. T. le, J. Durham, K. Smith et al., "Mismatch repair deficiency predicts response of solid tumors to PD-1 blockade," *Science*, vol. 357, no. 6349, pp. 409–413, 2017.
- [21] J. Hainesworth, "Researchers Strive to Refine TMB," *Cancer Discovery*, vol. 11, no. 6, p. 1314, 2021.
- [22] W. Gu, N. Wang, W. Gu et al., "Molecular gene mutation profiles, TMB and the impact of prognosis in Caucasians and east Asian patients with lung adenocarcinoma," *Translational Lung Cancer Research*, vol. 9, no. 3, pp. 629–638, 2020.
- [23] R. Samstein, C. Lee, A. Shoushtari et al., "Tumor mutational load predicts survival after immunotherapy across multiple cancer types," *Nature Genetics*, vol. 51, no. 2, pp. 202–206, 2019.
- [24] R. Shrestha, P. Prithviraj, M. Anaka et al., "Monitoring immune checkpoint regulators as predictive biomarkers in hepatocellular carcinoma," *Frontiers in Oncology*, vol. 8, p. 269, 2018.
- [25] A. Fujimoto, M. Furuta, Y. Totoki et al., "Whole-genome mutational landscape and characterization of noncoding and structural mutations in liver cancer," *Nature Genetics*, vol. 48, no. 5, pp. 500–509, 2016.
- [26] R. Karki and T. D. Kanneganti, "Diverging inflammasome signals in tumorigenesis and potential targeting," *Nature Reviews. Cancer*, vol. 19, no. 4, pp. 197–214, 2019.
- [27] X. Xia, X. Wang, Z. Cheng et al., "The role of pyroptosis in cancer: pro-cancer or pro-"host"?", *Cell Death & Disease*, vol. 10, no. 9, p. 650, 2019.
- [28] B. Wang and Q. Yin, "AIM2 inflammasome activation and regulation: a structural perspective," *Journal of Structural Biology*, vol. 200, no. 3, pp. 279–282, 2017.
- [29] N. Simon, J. Friedman, T. Hastie, and R. Tibshirani, "Regularization paths for Cox's proportional hazards model via coordinate descent," *Journal of Statistical Software*, vol. 39, no. 5, pp. 1–13, 2011.
- [30] R. Tibshirani, "The lasso method for variable selection in the Cox model," *Statistics in Medicine*, vol. 16, no. 4, pp. 385–395, 1997.
- [31] P. Geeleher, N. Cox, and R. Huang, "pRRophetic: an R package for prediction of clinical chemotherapeutic response from tumor gene expression levels," *PLoS One*, vol. 9, no. 9, article e107468, 2014.
- [32] R. Gaujoux and C. Seoighe, "A flexible R package for nonnegative matrix factorization," *BMC Bioinformatics*, vol. 11, no. 1, 2010.
- [33] K. Yoshihara, M. Shahmoradgoli, E. Martínez et al., "Inferring tumour purity and stromal and immune cell admixture from expression data," *Nature Communications*, vol. 4, no. 1, p. 2612, 2013.
- [34] R. Yuan, W. Zhao, Q. Wang et al., "Cucurbitacin B inhibits non-small cell lung cancer in vivo and in vitro by triggering TLR4/NLRP3/GSDMD-dependent pyroptosis," *Pharmacological Research*, vol. 170, p. 105748, 2021.
- [35] J. Cai, M. Yi, Y. Tan et al., "Natural product triptolide induces GSDME-mediated pyroptosis in head and neck cancer through suppressing mitochondrial hexokinase-IotaIota," *Journal of Experimental & Clinical Cancer Research*, vol. 40, no. 1, p. 190, 2021.
- [36] W. Shao, Z. Yang, Y. Fu et al., "The pyroptosis-related signature predicts prognosis and indicates immune microenvironment infiltration in gastric cancer," *Frontiers In Cell And Developmental Biology*, vol. 9, article 676485, 2021.
- [37] Y. Ye, Q. Dai, and H. Qi, "A novel defined pyroptosis-related gene signature for predicting the prognosis of ovarian cancer," *Cell Death Discovery*, vol. 7, no. 1, p. 71, 2021.
- [38] Y. Wang, J. Liu, J. Yang et al., "Lnc-UCID promotes G1/S transition and hepatoma growth by preventing DHX9-mediated CDK6 down-regulation," *Hepatology*, vol. 70, no. 1, pp. 259–275, 2019.
- [39] B. Hu, D. Jiang, Y. Chen et al., "High CHMP4B expression is associated with accelerated cell proliferation and resistance to doxorubicin in hepatocellular carcinoma," *Tumour Biology : The Journal Of The International Society For Oncodevelopmental Biology And Medicine*, vol. 36, no. 4, pp. 2569–2581, 2015.
- [40] H. Hikita, T. Kodama, S. Shimizu et al., "Bak deficiency inhibits liver carcinogenesis: a causal link between apoptosis and carcinogenesis," *Journal Of Hepatology*, vol. 57, no. 1, pp. 92–100, 2012.
- [41] Y. Zhou, L. Hu, W. Tang et al., "Hepatic NOD2 promotes hepatocarcinogenesis via a RIP2-mediated proinflammatory response and a novel nuclear autophagy-mediated DNA damage mechanism," *Journal Of Hematology & Oncology*, vol. 14, no. 1, p. 9, 2021.
- [42] J. Zhang, B. Zhou, R. Sun et al., "The metabolite  $\alpha$ -KG induces GSDMC-dependent pyroptosis through death receptor 6-activated caspase-8," *Cell Research*, vol. 31, no. 9, pp. 980–997, 2021.
- [43] C. Hage, S. Hoves, L. Strauss et al., "Sorafenib induces pyroptosis in macrophages and triggers natural killer cell-mediated cytotoxicity against hepatocellular carcinoma," *Hepatology*, vol. 70, no. 4, pp. 1280–1297, 2019.
- [44] M. Arechederra, S. K. Bazai, A. Abdouni et al., "ADAMTSL5 is an epigenetically activated gene underlying tumorigenesis and drug resistance in hepatocellular carcinoma," *Journal of Hepatology*, vol. 74, no. 4, pp. 893–906, 2021.
- [45] Y. Hsu, T. Yip, H. Ho et al., "Development of a scoring system to predict hepatocellular carcinoma in Asians on antivirals for chronic hepatitis B," *Journal Of Hepatology*, vol. 69, no. 2, pp. 278–285, 2018.
- [46] Y. Liu, L. Liu, Y. Zhou et al., "CKLF1 enhances inflammation-mediated carcinogenesis and prevents doxorubicin-induced apoptosis via IL6/STAT3 signaling in HCC," *Clinical Cancer Research : An Official Journal Of The American Association For Cancer Research*, vol. 25, no. 13, pp. 4141–4154, 2019.

- [47] A. Mauriello, R. Zeuli, B. Cavalluzzo et al., “High somatic mutation and neoantigen burden do not correlate with decreased progression-free survival in HCC patients not undergoing immunotherapy,” *Cancers*, vol. 11, no. 12, p. 1824, 2019.
- [48] H. Peng, Y. Zhang, Z. Zhou et al., “Integrated analysis of ELMO1, serves as a link between tumour mutation burden and epithelial-mesenchymal transition in hepatocellular carcinoma,” *eBioMedicine*, vol. 46, pp. 105–118, 2019.
- [49] Q. Xu, H. Xu, R. Deng et al., “Multi-omics analysis reveals prognostic value of tumor mutation burden in hepatocellular carcinoma,” *Cancer Cell International*, vol. 21, no. 1, p. 342, 2021.
- [50] F. Liu, W. Hou, J. Liang, L. Zhu, and C. Luo, “LRP1B mutation: a novel independent prognostic factor and a predictive tumor mutation burden in hepatocellular carcinoma,” *Journal of Cancer*, vol. 12, no. 13, pp. 4039–4048, 2021.

## Research Article

# Downregulation of CYP39A1 Serves as a Novel Biomarker in Hepatocellular Carcinoma with Worse Clinical Outcome

Dan Li,<sup>1</sup> Tao Yu,<sup>2</sup> Junjie Hu,<sup>3</sup> Jie Wu,<sup>1</sup> Shi Feng,<sup>4</sup> Qingxue Xu,<sup>4</sup> Hua Zhu,<sup>4</sup> Xu Zhang,<sup>4</sup> Yonggang Zhang,<sup>4</sup> BenHong Zhou,<sup>1</sup> Lijuan Gu ,<sup>4</sup> and Zhi Zeng <sup>5</sup>

<sup>1</sup>Department of Pharmacy, Renmin Hospital of Wuhan University, Wuhan, China

<sup>2</sup>Department of Oncology, Integrated Traditional Chinese and Western Medicine, The Central Hospital of Wuhan, Tongji Medical College, Huazhong University of Science and Technology, Wuhan, China

<sup>3</sup>College of Pharmacy, Hubei University of Chinese Medicine, Wuhan, China

<sup>4</sup>Central Laboratory, Renmin Hospital of Wuhan University, Wuhan, China

<sup>5</sup>Department of Pathology, Renmin Hospital of Wuhan University, Wuhan, China

Correspondence should be addressed to Lijuan Gu; [gulijuan@whu.edu.cn](mailto:gulijuan@whu.edu.cn) and Zhi Zeng; [zhizeng@whu.edu.cn](mailto:zhizeng@whu.edu.cn)

Received 21 July 2021; Revised 19 November 2021; Accepted 3 December 2021; Published 31 December 2021

Academic Editor: Guoku Hu

Copyright © 2021 Dan Li et al. This is an open access article distributed under the Creative Commons Attribution License, which permits unrestricted use, distribution, and reproduction in any medium, provided the original work is properly cited.

**Background.** CYP39A1 is a poorly characterized metabolic enzyme that has been investigated in a few tumors. However, the role of CYP39A1 in hepatocellular carcinoma (HCC) has not yet been clarified. In this study, the expression and clinical significance of CYP39A1 in HCC were explored. **Methods.** CYP39A1 protein expression was detected in Akt/c-Met-induced HCC mice and 14 paired fresh HCC samples as well as another 159 HCC and matched noncancerous tissues. Meanwhile, the mRNA expression was analyzed by GEO and TCGA analysis and validated in 14 paired fresh HCC tissues. Furthermore, the relationships between CYP39A1 expression and clinicopathologic features as well as prognosis were analyzed. HCC cell growth changes were analyzed by cell viability assays after CYP39A1 overexpression and then validated after CYP39A1 knockout by DepMap database analysis. **Results.** CYP39A1 protein expression was lower expressed in HCC mouse models, and its mRNA and protein expression were also downregulated in HCC compared with noncancerous liver tissues. Higher CYP39A1 expression was associated with well differentiation. Moreover, survival analysis indicated that lower CYP39A1 expression was associated with poorer overall survival. In addition, HepG2 and SMMC-7721 cell viability were inhibited after CYP39A1 overexpression. Genome-wide CRISPR/Cas9 proliferation screening indicated that knockout of CYP39A1 could promote HCC cell growth. Likewise, p-NF- $\kappa$ B and Nrf2 were suppressed after CYP39A1 overexpression. It is worth mentioning that total bile acid, total bilirubin, and direct bilirubin were significantly increased in the patients with low CYP39A1 expression. **Conclusions.** Downregulation of CYP39A1 is associated with HCC carcinogenesis, tumor differentiation, and poor overall survival, suggesting that CYP39A1 may serve as a tumor suppressor gene and novel biomarker for HCC patients.

## 1. Introduction

Hepatocellular carcinoma (HCC) is one of the most common malignancies with increasing burden globally. Until recently, systemic therapies for HCC have been limited, and the prognosis for advanced HCC is generally poor [1]. It remains essential to identify new biomarkers for early diagnosis and prognostic evaluation in HCC.

Cytochrome P450 (CYP450) is a monooxygenase, which mainly exists in human liver and intestines. It can catalyze

the metabolism of a variety of endogenous and exogenous substances, including approximately 90% of drugs in the clinic. Recently, the roles of CYP450 family members in tumor diagnosis and treatment have been gradually investigated in an increasing number of studies. For instance, CYP1A2 expression levels can serve as a biomarker of HCC recurrence caused by hepatitis C [2], and CYP3A5 can act as a tumor suppressor gene by regulating the mTORC2/Akt signaling pathway in HCC [3]. Furthermore, CYP2W1 can be used as an independent prognostic

biomarker in liver cancer [4], and CYP17A1 can be used as a molecular marker in the diagnosis of liver cancer [5].

CYP39A1, as a novel member of the cytochrome P450 superfamily, is known as an oxysterol 7  $\alpha$ -hydroxylase that participates in the metabolism of 24 hydroxycholesterol (24OHC) [6–8]. It is located on human chromosome 6 and contains 14 coding exons. CYP39A1 is mainly expressed in the liver, and its mRNA was also discovered in nonpigmented epithelial cells in the eye and brain [9]. A recent whole-exome sequencing case-control study indicated that rare CYP39A1 variants were associated with exfoliation syndrome involving the anterior chamber of the eye [10]. Furthermore, the CYP39A1 single nucleotide polymorphism was associated with adverse reactions to chemotherapeutic drugs [11, 12]. In addition to its function in metabolism and inflammation reported in previous studies [13–15], the role of CYP39A1 in carcinoma has been gradually investigated. Currently, CYP39A1 is expressed at lower levels in malignant melanoma [16] and cholangiocarcinoma [17]. However, there have been no definitive data showing a correlation between CYP39A1 expression and the clinicopathological features of HCC. The exact role of CYP39A1 in the development and progression of HCC remains unclear.

Therefore, CYP39A1 mRNA and protein expression were analyzed by bioinformatic methods and validated in HCC and noncancerous tissue samples as well as HCC mouse models. Then, the correlations between CYP39A1 expression and clinicopathological factors, overall survival, and serum biochemical indices were investigated. Moreover, the function of CYP39A1 in HCC cell lines was further analyzed.

## 2. Materials and Methods

**2.1. Tissue Sample and Data Collection.** A total of 159 patients with HCC (123 men and 36 women; age range, 26–73 years) were included in the present study. All patients did not receive radiotherapy or chemotherapy before surgery. Demographic and clinical pathological data were collected including age, sex, tumor size, tumor differentiation, distant metastasis, nodal metastasis, and TNM stage. Additionally, serum biochemical indices were obtained from the inspection report of medical records. A total of 159 formalin-fixed, paraffin-embedded HCC tissues, and matched adjacent noncancerous liver tissue samples were selected. An additional 14 pairs of fresh samples of HCC and noncancerous liver tissues were gathered, snap-frozen immediately in liquid nitrogen, and stored at  $-80^{\circ}\text{C}$  following surgery for real-time PCR and Western blot analysis. The research was approved by the Ethics Committee of Renmin Hospital of Wuhan University which conformed to the provisions of the Declaration of Helsinki.

Furthermore, 159 patients were followed up for survival analysis; however, 81 patients were lost to follow-up. The overall survival duration was from the date of operation to the date of death or the last known survival date. Moreover, 81 cases from the GEO database were also utilized for survival analysis as a complementary validation.

**2.2. Immunohistochemistry (IHC).** IHC staining procedures were performed according to a standard protocol that was described in detail in our previous study [18]. In brief, the sections were deparaffinized with xylene and rehydrated with ethanol, then washed with deionized water and stirred. The sections were then treated with 3%  $\text{H}_2\text{O}_2$  and then antigen retrieval by citric acid buffer (pH 6.0). After sealing at room temperature for 20 min with 5% bovine serum albumin, the slices are incubated overnight at  $4^{\circ}\text{C}$  with primary antibody (1:400 dilution for human liver tissues and 1:100 dilution for mice liver tissues, Abcam, USA). Then, sections were incubated with horseradish peroxidase-labeled polymer with secondary antibody (UltraSensitive™ SP (Mouse/Rabbit) IHC Kit-9710; Maixin Bio, Fujian, China) at room temperature for 15 min each. Then, the reaction products were stained with 3,3'-diaminobenzidine (DAB) and lightly counterstained with hematoxylin. The sections with PBS instead of primary antibody served as negative control.

**2.3. Evaluation of IHC Staining.** CYP39A1 expression levels were evaluated according to the average score of two independent pathologists' evaluations. If the difference of score was  $\geq 2$ , the final score was determined by a third pathologist. CYP39A1 was mainly located in the cytoplasm and presented in a different staining intensity, hence, CYP39A1 expression in tumor cells was classified according to a four-tier grading system (scores: 0 = absent, 1 = weak, 2 = moderate, and 3 = strong staining), as described in a previous study [19]. Generally, a score less than or equal to 1 was considered as negative, and a score more than 1 was considered as positive.

**2.4. Quantitative Real-Time Polymerase Chain Reaction (qRT-PCR).** Total RNA was extracted from fresh HCC and matched noncancerous liver tissue samples using TRIzol reagent (Invitrogen, USA) according to the manufacturer's instructions, and qRT-PCR analysis was carried out with Power SYBR Green (Takara, Japan). The primer sequences used were as follows:  $\beta$ -actin forward: AGCGCGCATCC CCCAAAGTT;  $\beta$ -actin reverse: GGGCACGAAGGCTCAT CATT; CYP39A1 forward: ACAATGGACCTGAACAAC; and CYP39A1 reverse: AAGACACTCTGGCAACTG.

**2.5. Western Blotting.** The homogenized matched liver samples were extracted by RIPA and then quantified by BCA kit (Thermo, USA). Briefly, the supernatant of the lysate was used for Western blot analysis. The protein was separated by electrophoresis in a 10% SDS-PAGE and then transferred onto a PVDF membrane, and the membranes were blocked with 5% skim milk powder, then it was incubated with CYP39A1 (1:1000 dilution, ab129334, Abcam), Anti-Nrf2 (NF-E2 related factor 2, 1:1000 dilution, ab92946, Abcam), Keap 1 (1:1000 dilution, 7705, Cell Signaling Technology), or Phospho-NF- $\kappa$ B p65 (1:1000 dilution, 3033, Cell Signaling Technology) at  $4^{\circ}\text{C}$  overnight. After incubation with the horseradish peroxidase (HRP) conjugated IgG antibody (1:5000 dilution, Sigma Chemical Co., St Louis, MO) at room temperature for 1 h, the chemiluminescence

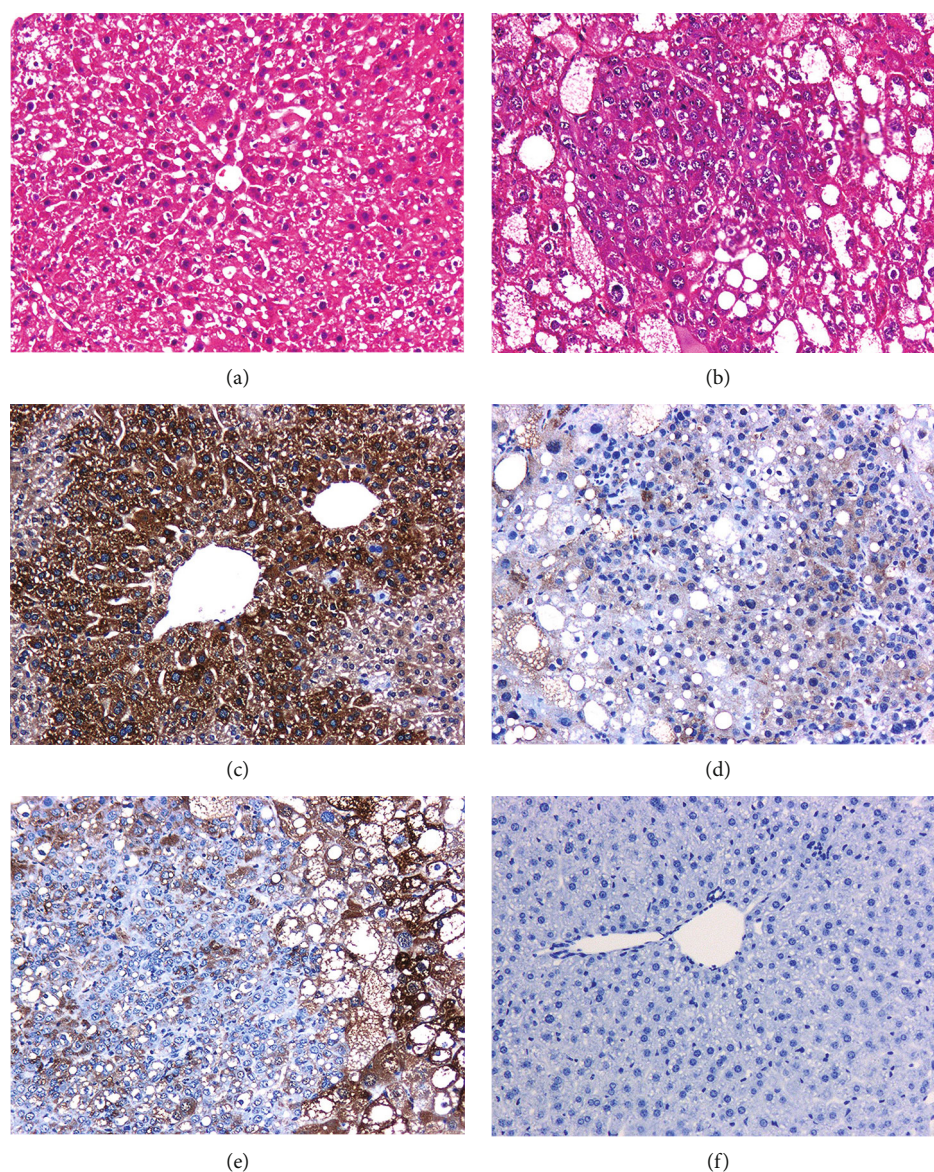


FIGURE 1: H&E and IHC staining of CYP39A1 proteins in representative tissue of HCC mice. (a) Wild-type mice, H&E staining; (b) HCC mice, H&E staining; (c) wild-type mice, IHC staining of CYP39A1; (d) HCC mice, IHC staining of CYP39A1; (e) the junction of hepatocellular carcinoma and paracancerous liver tissue in the same field of HCC mice, IHC staining of CYP39A1; (f) negative control; original magnification,  $\times 100$ .

phototope-HRP kit (Pierce, Rockford, IL) was employed, and the band intensity was visualized by Quantity One software (BioRad, Hercules, CA). The CYP39A1 protein level was normalized to that of Vinculin (1:10000 dilution, ab129002, Abcam) in 14 fresh liver tissues or beta tubulin (1:1000 dilution, 2148S, Cell Signaling Technology) in the *in vitro* transfection study or HCC mouse models. These antibodies can be used both in human and mouse.

**2.6. Hydrodynamic Transfection to Construct a Rapid HCC Model.** Hydrodynamic transfection was performed in FVB/N mice ( $n=6$ ) from Charles River (Beijing, China) as described in our previous study [20] to construct a rapid HCC model. In brief, the three plasmids pT3-EF1 $\alpha$ -HA-

myr-AKT, pT3-EF1 $\alpha$ -V5-c-Met, and pCMV-SB with the corresponding quality of 20  $\mu\text{g}$ , 20  $\mu\text{g}$ , and 1.6  $\mu\text{g}$  were diluted in a 2 mL saline (0.9% NaCl) solution and promptly injected into the lateral tail vein of the FVB/N mice within 7 s. Approximately 6 weeks later, the HCC model was successfully constructed. The mice were divided into four groups. Wild type groups and the other three AKT/c-Met induced HCC modeling groups. Low-dose (122 mg/kg/day) and high-dose (244 mg/kg/day) of osthole or vehicle were intraperitoneally injected once daily for 3 weeks after 3 weeks of hydrodynamic injection. At 6 weeks posthydrodynamic injection, the livers were taken after pentobarbital anesthesia. The animal study was reviewed and approved by the Animal Ethics Committees of the Hubei University



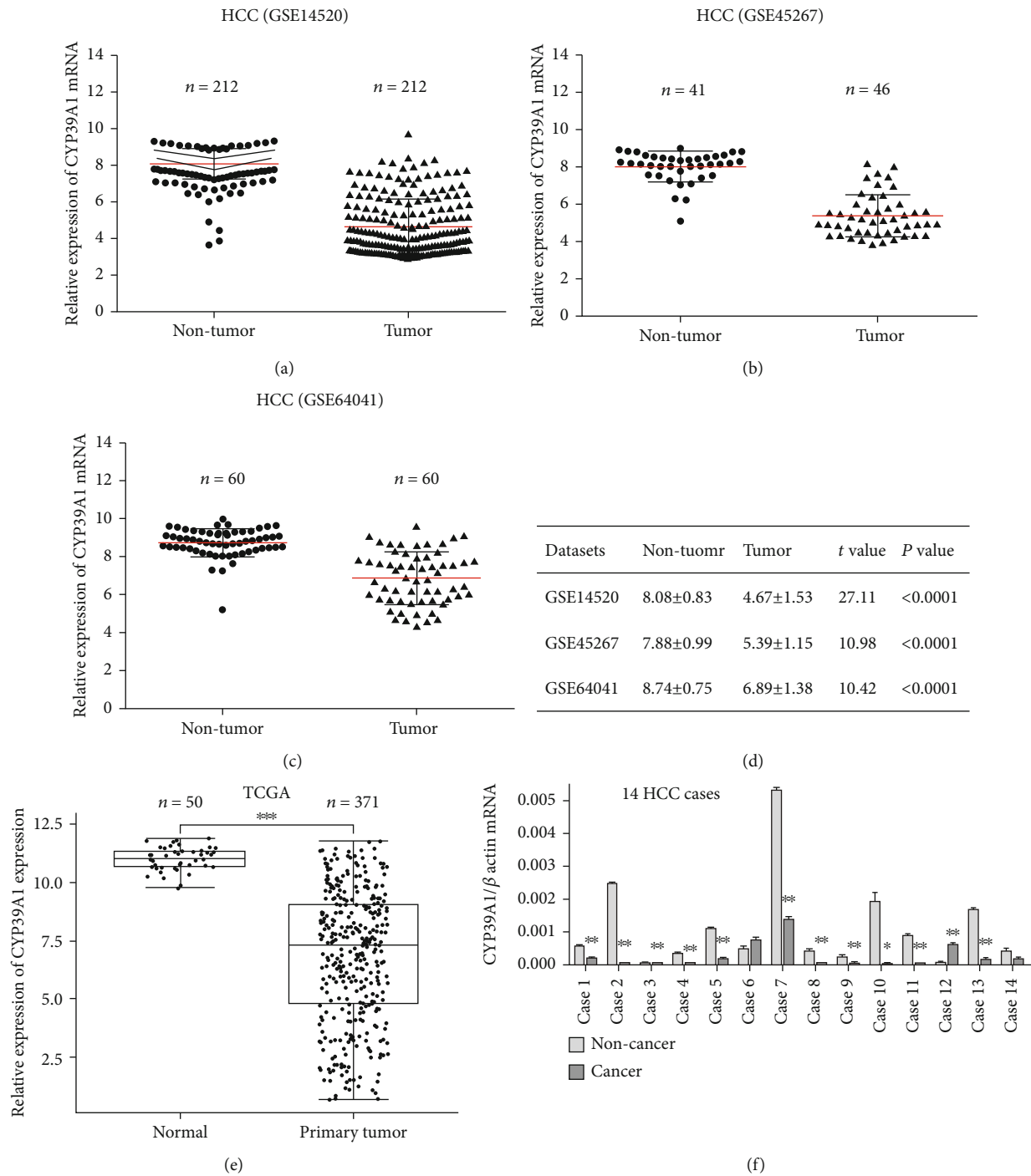


FIGURE 2: Differential mRNA expression of CYP39A1 between HCC and noncancerous liver tissues. (a) The GSE14520 dataset with two cohorts showed that CYP39A1 mRNA expression was decreased in HCC tissues compared with adjacent noncancerous liver tissues ( $P < 0.001$ , paired  $t$ -test). (b) The GSE45267 dataset showed that CYP39A1 mRNA expression was decreased in HCC tissues compared with unpaired noncancerous liver tissues ( $P < 0.001$ , unpaired  $t$ -test). (c) Sixty paired HCC biopsies from an unselected patient population with all tumor stages from GSE64041 indicated that CYP39A1 mRNA was lower in HCC tissues than in adjacent noncancerous liver tissues ( $P < 0.001$ , paired  $t$ -test). (d) Relative expression value of CYP39A1 in HCC and noncancerous liver tissues in the three GSE datasets. (e) CYP39A1 mRNA expression was downregulated in HCC tissues in the TCGA dataset analysis. (f) CYP39A1 mRNA expression in 14 fresh-frozen liver tissues. (C: cancer tissue; N: noncancerous tissue).

of Chinese Medicine. CYP39A1 expression in the wild-type and model groups was detected by IHC, and the corresponding protein was determined by Western Blotting.

**2.7. Lentiviral Plasmid Construction and Cell Proliferation Assay.** To construct pLV-EGFP-flag-CYP39A1, a 1451 bp CYP39A1 gene fragment was successfully amplified and

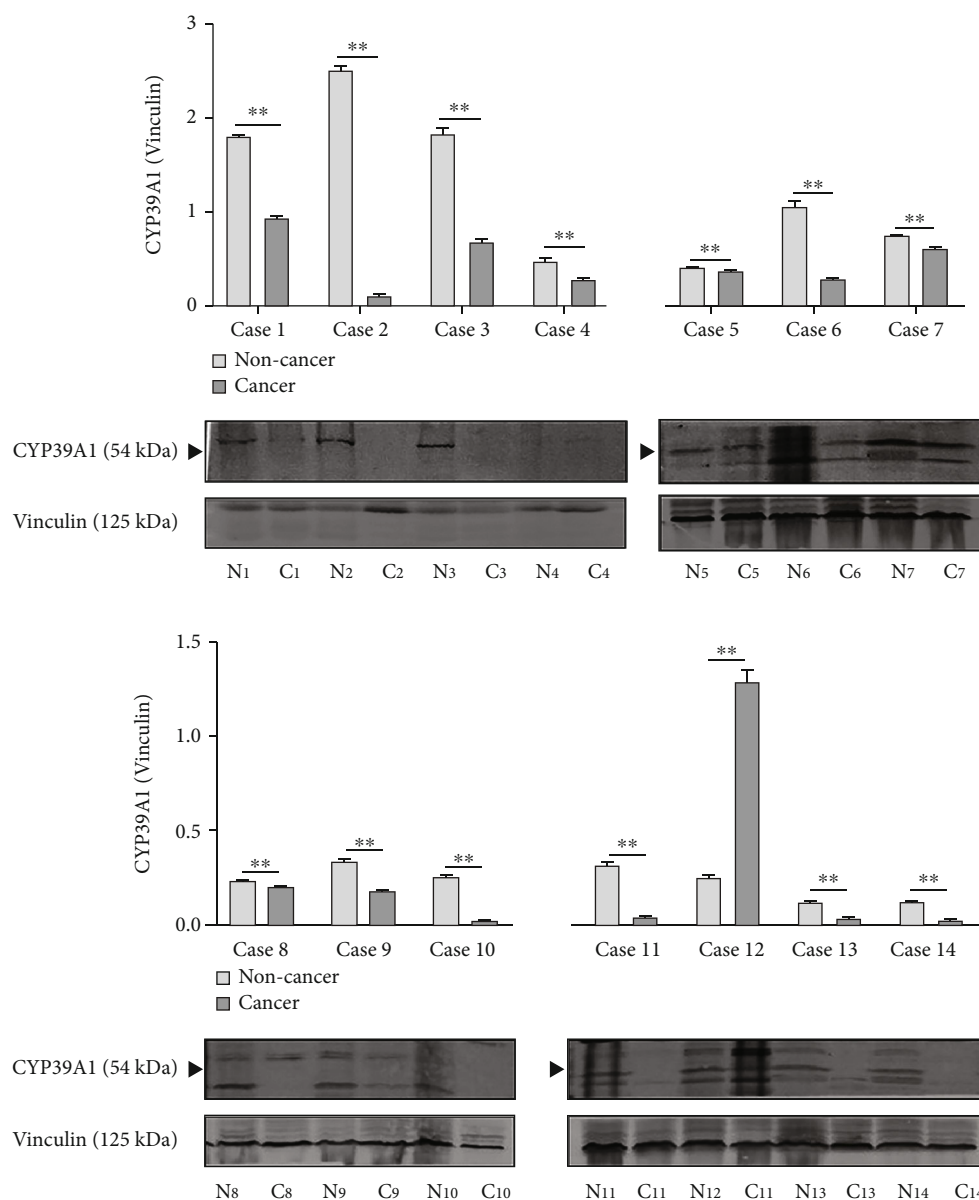


FIGURE 3: CYP39A1 protein expression was relatively lower in fresh-frozen HCC tissues than in adjacent noncancerous liver tissues. (C: cancer tissue; N: noncancerous tissue.)

inserted into the GV492 plasmid with the restriction enzyme BamHI-AgeI (New England Biolabs, USA). Then, it was packaged into recombinant lentiviral particles after enzymatic digestion and DNA sequencing. HepG2 and SMMC-7721 cells in the exponential growth phase were infected with empty vector (EV) and CYP39A1 overexpression (OE) virus. To achieve an optimal infection state,  $4 \times 10^6$  lentivirus was added to  $4 \times 10^5$  cells per well in a six-well plate according to the MOI of HepG2 and SMMC-7721 cells.

For the cell viability assay, HepG2 and SMMC-7721 cells were infected with EV or OE for 24, 48, 72, 96, and 120 h, and then 2000 cells per well were plated into 96-well plates. After CCK-8 treatment for 4 hours, the variation in the absorption rate at 450 nm with time in the EV and OE groups was compared. The relative CYP39A1 mRNA and protein expression levels were detected.

**2.8. Analysis of Publicly Available Data.** Human HCC datasets of patients with HCC and corresponding clinical data, as well as their CYP39A1 mRNA expression data, were retrieved from the publicly available GEO database (<http://www.ncbi.nlm.nih.gov/gds>) and The Cancer Genome Atlas (TCGA) datasets (<https://cancergenome.nih.gov/>). Three independent datasets, GSE14520, GSE45267, and GSE64041, were used to calculate the relative expression level of CYP39A1 mRNA between noncancer livers and HCC. Then, the correlation between CYP39A1 mRNA expression and clinicopathologic features from the TCGA database (<https://xenabrowser.net/>) was utilized for further validation. Moreover, survival analysis was validated by analyzing the data from GSE54236.

In order to analyze the Genome-wide CRISPR/Cas9 Proliferation Screening Data in HCC Cell Lines, Gene knockout

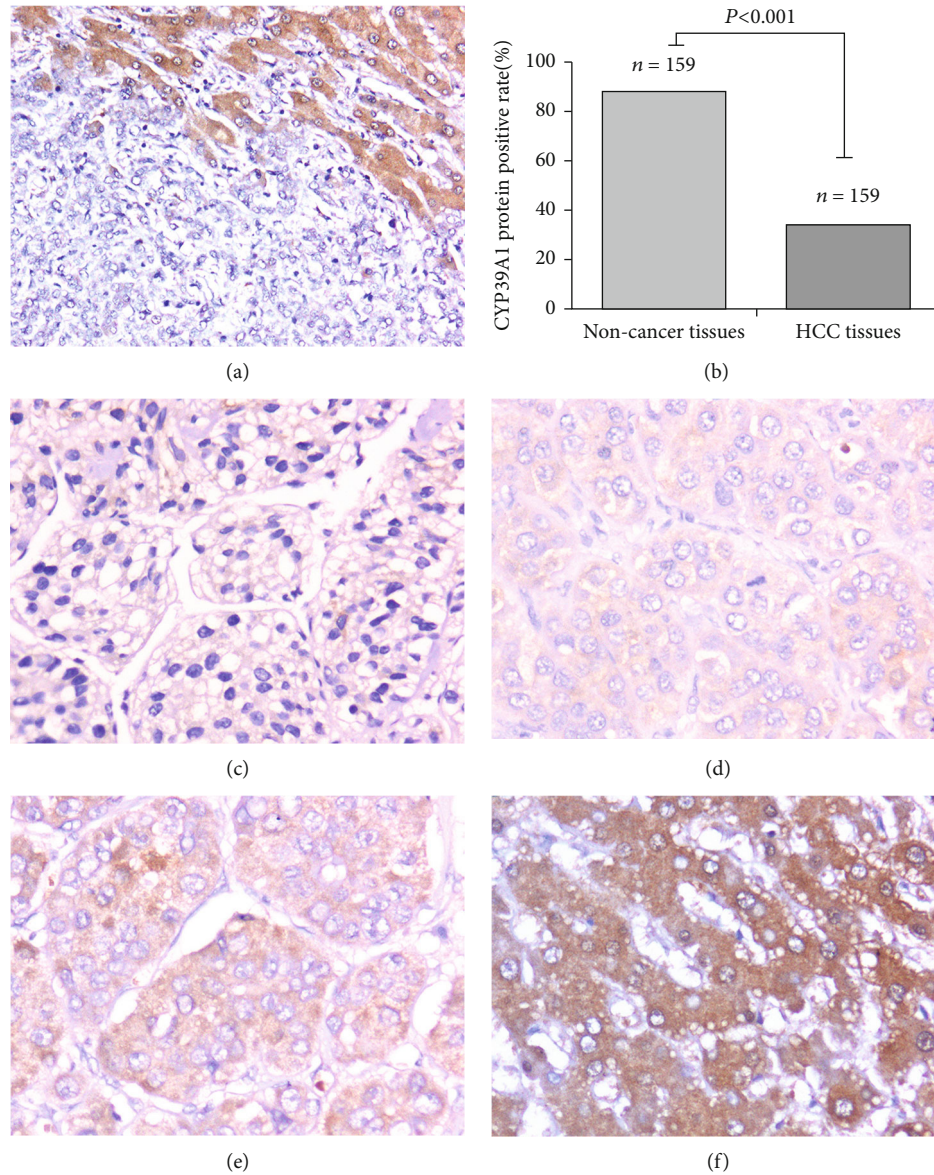


FIGURE 4: CYP39A1 protein expression in HCC and noncancerous liver tissues and its immunohistochemical staining in representative tissue specimens. (a) Immunohistochemical staining of CYP39A1 proteins in representative liver tissue specimens. Left bottom corner represents cancer tissues and top right corner represents noncancer tissues. DAB staining (brown); nuclear counterstaining (hematoxylin); original magnification,  $\times 100$ ; (b) CYP39A1 protein positive rate in adjacent noncancerous liver tissues and HCC tissues ( $P < 0.001$ , cancer vs. noncancerous tissues). Statistical analysis was performed by the chi-squared test; (c)–(e) Expression of CYP39A1 in representative tumor cells of HCC ((c) score = 0, (d) score = 1, and (e) score = 2); (f) Expression of CYP39A1 in representative normal hepatocytes ((f) score = 3). DAB staining (brown); nuclear counterstaining (hematoxylin); original magnification,  $\times 200$ . Among them, (c) and (d) were defined as negative expression of CYP39A1, and (e) and (f) were defined as positive expression of CYP39A1.

data for 808 cell lines of 29 primary diseases from CRISPR were obtained from the DepMap database (<https://depmap.org/portal/>), and then 22 HCC cell lines (HLF, JHH4, SNU398, HUH7, JHH2, HUH6, SNU387, SKHEP1, JHH6, HEPG2, JHH7, LI7, SNU182, SNU886, SNU761, SNU449, PLCPRF5, SNU423, SNU475, JHH1, HUH1, and JHH5) were employed to extract CYP39A1 knockout data. As described in a previous study [21], the CERES dependency score was used to represent the changes in cell growth after genes of interest were knocked out. A score of 0 indicates that a gene is not essential for cell growth; correspondingly,

a score of -1 is comparable to the median of all pan-essential genes [22]. The lower the score, the more likely the gene is an oncogene. The higher the score, the more likely the gene is a tumor suppressor gene.

**2.9. Statistical Analysis.** Statistical tests were carried out by SPSS 20.0. Student's *t*-test was used to analyze the difference between 2 groups. One-way analysis of variance was employed to compare the data more than 2 groups. The chi-square test was used to analyze the relationship between CYP39A1 expression and the clinicopathological factors of

TABLE 1: Correlation between CYP39A1 expression in tumor cells and clinicopathologic features of HCC.

| Clinicopathological features | All cases | CYP39A1 in HCC tissues (%) |            | P value <sup>a</sup> |
|------------------------------|-----------|----------------------------|------------|----------------------|
|                              |           | Negative                   | Positive   |                      |
| Gender                       |           |                            |            |                      |
| Male                         | 123       | 78 (63.41)                 | 45 (36.59) | 0.197                |
| Female                       | 36        | 27 (75.00)                 | 9 (25.00)  |                      |
| Age at diagnosis (years)     |           |                            |            |                      |
| <51                          | 72        | 51 (70.83)                 | 21 (29.17) | 0.245                |
| ≥51                          | 87        | 54 (62.07)                 | 33 (37.93) |                      |
| Size (diameter, cm)          |           |                            |            |                      |
| <5.5                         | 90        | 57 (63.33)                 | 33 (36.67) | 0.411                |
| ≥5.5                         | 69        | 48 (69.57)                 | 21 (30.43) |                      |
| Differentiation              |           |                            |            |                      |
| Well                         | 51        | 24 (47.06)                 | 27 (52.94) | 0.001                |
| Moderately and poorly        | 108       | 81 (75)                    | 27 (25)    |                      |
| Nodal metastasis             |           |                            |            |                      |
| N0                           | 135       | 90 (66.67)                 | 45 (33.33) | 0.691                |
| N1                           | 24        | 15 (62.50)                 | 9 (37.50)  |                      |
| Distant metastasis           |           |                            |            |                      |
| M0                           | 114       | 75 (65.79)                 | 39 (34.21) | 0.689                |
| M1                           | 48        | 30 (62.50)                 | 18 (37.50) |                      |
| TNM stage                    |           |                            |            |                      |
| I-II                         | 78        | 54 (69.23)                 | 24 (30.77) | 0.729                |
| III-IV                       | 81        | 54 (66.67)                 | 27 (33.33) |                      |

<sup>a</sup>Chi-square test.

HCC. For survival analysis, the Kaplan-Meier method was employed to draw the survival curves and the difference was compared by log-rank test. *P* values less than or equal to 0.05 were considered to be statistically significant.

### 3. Results

#### 3.1. Expression of CYP39A1 Protein in HCC Mouse Model.

The results of H&E staining and histological analysis confirmed that the HCC mouse model was successfully established. Representative tissue specimens showed that the hepatic lobule structure was clear and that the hepatic cell cord was well-organized in the WT mice. In the Akt/c-Met-induced HCC mouse model, the tumor cells showed hepatocytic differentiation by morphology. Meanwhile, HCC cells were arranged in solid or nest-like growth patterns, showing loss of normal hepatic architecture, such as reduction or loss of the normal reticulin framework. Cytological atypia was very obvious, such as an increased nucleus-to-cytoplasm ratio (Figures 1(a) and 1(b)). Next, CYP39A1 protein expression in Akt/c-Met-induced HCC mouse model was assessed by performing IHC. The results indicated that the immunoreaction for CYP39A1 protein was more intense in the normal liver tissues of WT mice than in the cancer tissues of Akt/c-Met-induced HCC mice (Figures 1(c)–1(f)).

#### 3.2. CYP39A1 mRNA Expression Was Downregulated in Human HCC.

The distinction of CYP39A1 mRNA expres-

sion between noncancerous liver and HCC tissues was analyzed from three independent microarray datasets, namely, GSE14520, GSE45267, and GSE64041. Overall, the three GSE datasets indicated that CYP39A1 mRNA expression was downregulated in HCC compared with normal or adjacent noncancerous liver tissues ( $P < 0.0001$ , Figures 2(a)–2(d)). Moreover, CYP39A1 mRNA expression was lower in HCC tissues in the TCGA dataset analysis ( $P < 0.001$ , Figure 2(e)). To further verify the results of bioinformatics analysis, 14 fresh tissue samples were collected and detected by real-time PCR. Similarly, it was also found that CYP39A1 mRNA expression in the cancer tissues (7.14%, 1/14) was lower than that in matched adjacent noncancerous tissues (78.57%, 11/14) ( $P < 0.01$ , paired *t*-test, Figure 2(f)).

#### 3.3. Expression and Location of CYP39A1 Protein in HCC Tissues and Adjacent Noncancerous Liver Tissues.

Next, the above mentioned 14 paired HCC and noncancerous liver tissues were employed to compare the protein expression difference by Western blotting analysis. Study results indicated that CYP39A1 protein expression was also lower expressed in HCC tissues (7.14%, 1/14) than that in matched noncancerous liver tissues (85.71%, 12/14) in these paired liver samples ( $P < 0.01$ , paired *t*-test, Figure 3).

To investigate the protein expression and location of CYP39A1 in noncancerous liver and HCC tissues, the CYP39A1 protein expression was detected further in a larger size of 159 HCC tissues and its adjacent noncancerous liver tissues by IHC staining. Our results indicated that CYP39A1

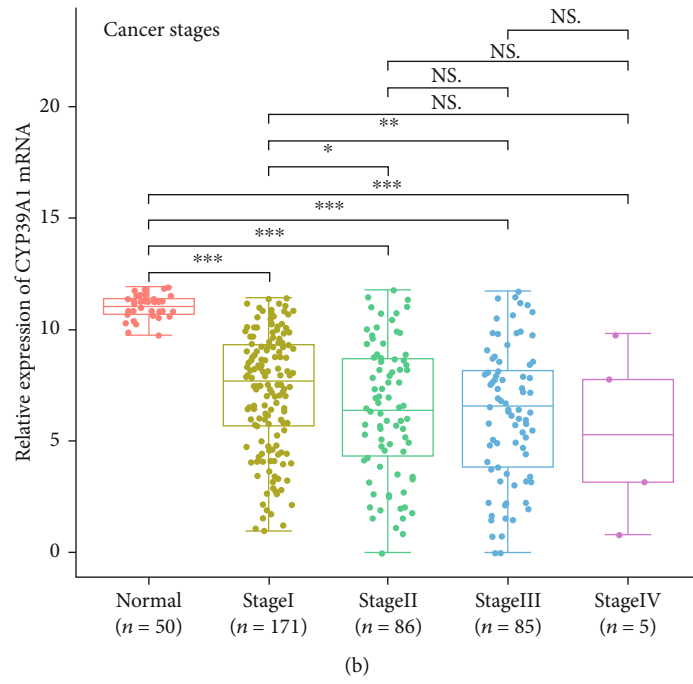
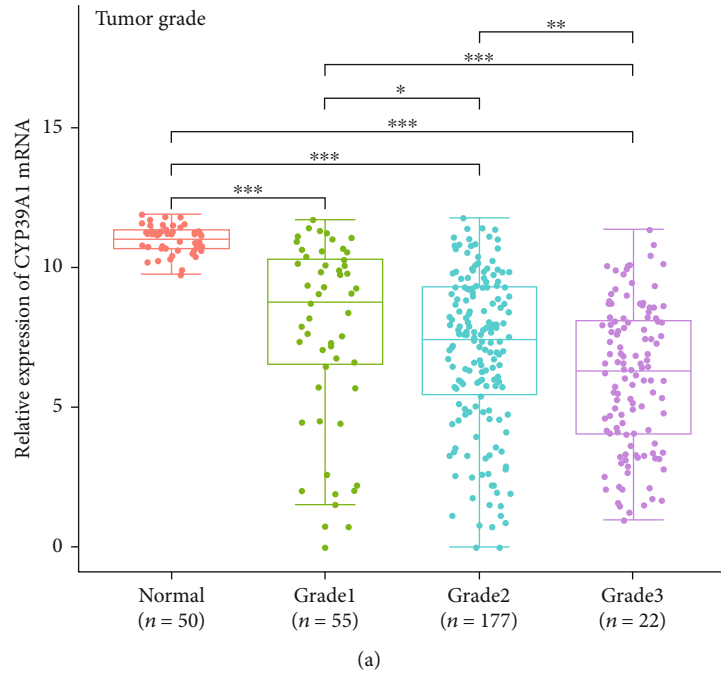


FIGURE 5: Continued.

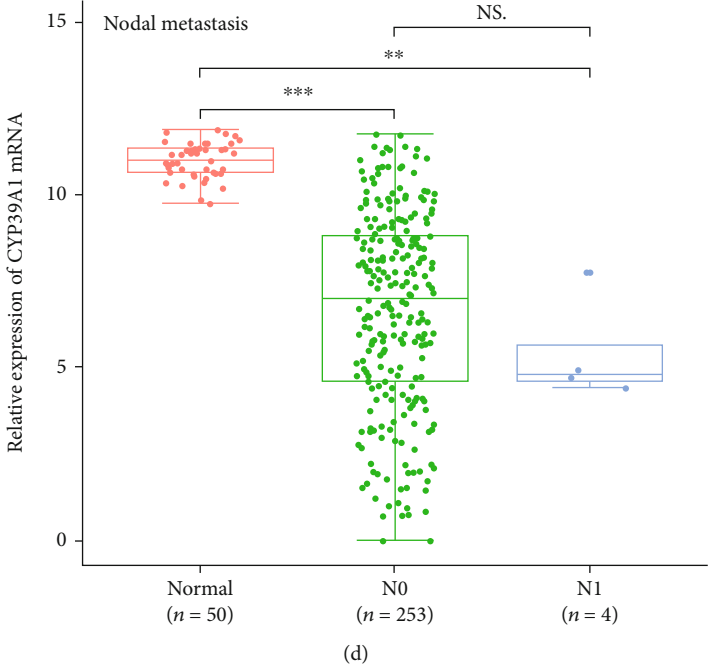
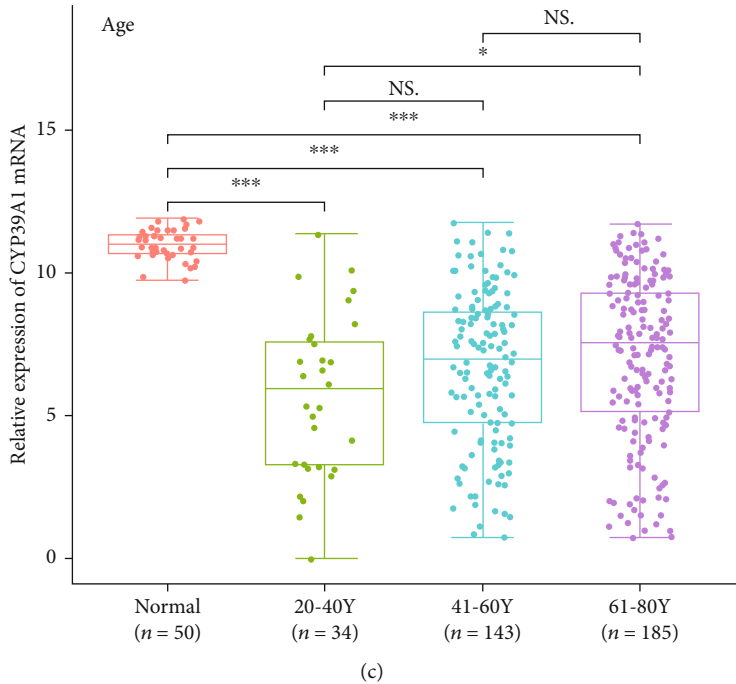


FIGURE 5: Continued.

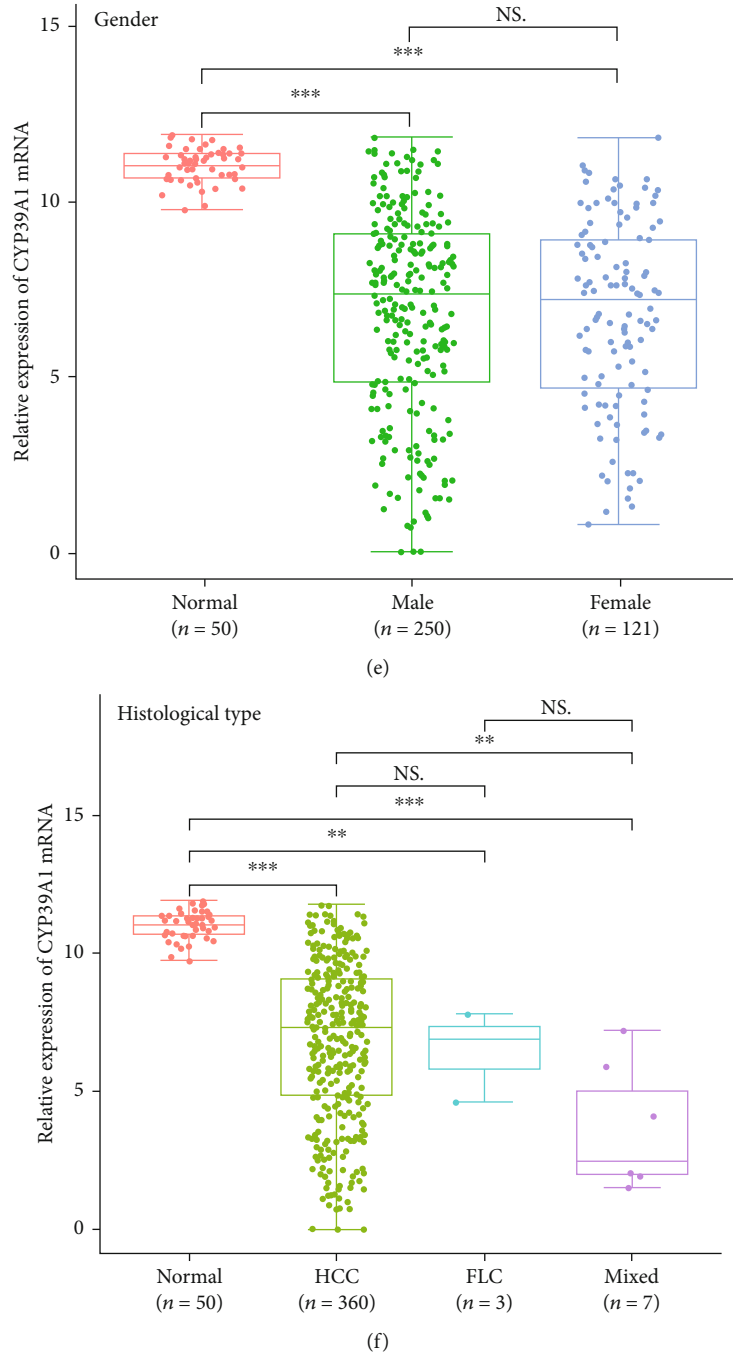


FIGURE 5: Correlation between CYP39A1 mRNA expression and clinicopathologic features of HCC in the TCGA database. (a) Tumor grade; (b) cancer stage; (c) patient age; (d) nodal metastasis; (e) gender; (f) histological type. (HCC: hepatocellular carcinoma; FLC: fibrolamellar carcinoma; mixed: hepatocholangio carcinoma).

was mainly expressed in the cytoplasm of hepatocellular carcinoma cells or hepatocytes rather than in stromal cells. The immunoreaction for CYP39A1 protein was more intense in the normal cells than that in the HCC cells (Figure 4(a)). Similarly, it was also found that the positive expression rate of CYP39A1 was higher in normal liver tissues (88.05%) than that in HCC tissues (33.96%) ( $P < 0.001$ , Figure 4(b)). The scores of CYP39A1 protein expression ranging from 0, 1, and 2 in representative HCC tissue specimens were presented in Figures 4(c)–4(e). Moreover, a typical representa-

tive IHC image of noncancerous liver tissue (score = 3) was shown in Figure 4(f). Generally, a score less than or equal to 1 was considered as negative, and a score more than 1 was considered as positive.

**3.4. Relationship between CYP39A1 Protein Expression and Clinicopathologic Features of HCC.** The relationship between CYP39A1 protein expression detected by IHC and the clinicopathologic features of 159 HCC patients was further analyzed. The statistical results were shown in Table 1. The

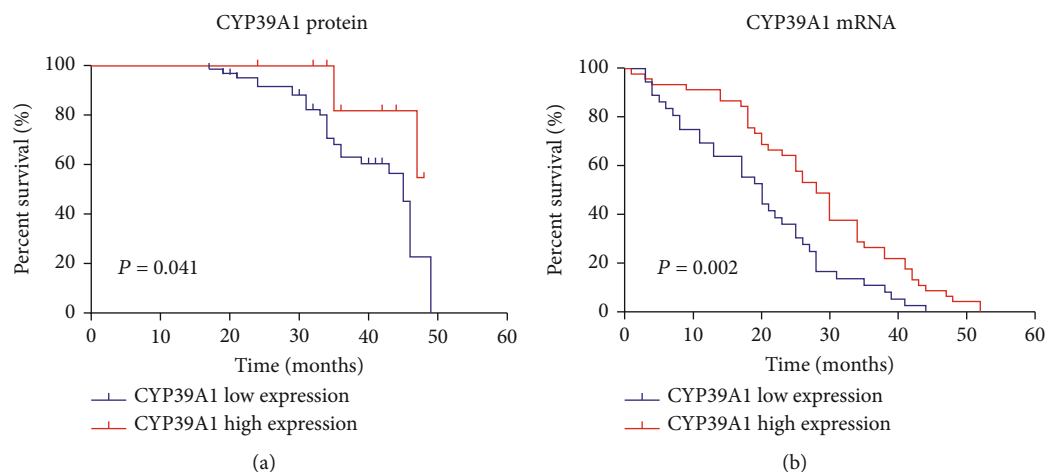


FIGURE 6: Relationship of CYP39A1 expression and patient prognosis. (a) Relationship of CYP39A1 protein expression and overall survival ( $P = 0.041$ ) (log-rank test). IHC score = 0 or 1 was considered CYP39A1 protein negative expression,  $n = 61$ , and IHC score = 2 or 3 was considered CYP39A1 protein positive expression,  $n = 17$ ; (b) GSE54236 showed the relationship of CYP39A1 mRNA expression and overall survival ( $P = 0.002$ ). Low expression group,  $n = 36$ ; high expression group,  $n = 45$ .

results indicated that CYP39A1 expression was positively correlated with tumor cell differentiation. High levels of CYP39A1 were associated with well-differentiated HCC tissues ( $P = 0.001$ ). However, CYP39A1 expression was not correlated with sex, age, tumor size, nodal metastasis, distant metastasis, or TNM stage ( $P > 0.05$ ; Table 1). Furthermore, bioinformatic analysis also indicated that CYP39A1 mRNA expression was correlated with tumor grade (cell differentiation). There was a significant difference among grade 1, grade 2, and grade 3 ( $P < 0.05$ ; Figure 5(a)), whereas CYP39A1 mRNA expression was not correlated with cancer stage, age, nodal metastasis, gender, or histological type of HCC ( $P > 0.05$ ; Figures 5(b)–5(f)).

**3.5. Correlation between CYP39A1 Expression and HCC Patients' Overall Survival.** In order to further investigate the correlation between CYP39A1 expression and the prognosis of HCC patients, the overall survival information for 78 patients in our study was obtained by a postoperative follow-up. Kaplan-Meier analysis and the log-rank test showed that the expression of CYP39A1 protein was also associated with HCC overall survival ( $P = 0.041$ , Figure 6(a)). Furthermore, in order to verify the role of CYP39A1 in the prognosis of HCC patients, GSE54236, with 81 patients' survival information, was utilized to compare CYP39A1 mRNA expression and patients' overall survival. Our results indicated that CYP39A1 mRNA expression was positively correlated with HCC patients' survival ( $P = 0.002$ , Figure 6(b)). Therefore, our findings indicated that lower expression of CYP39A1 might serve as a prognostic marker in HCC patients with worse clinical outcomes.

**3.6. CYP39A1 Inhibited the Proliferation of HCC Cells In Vitro.** The results from our clinical samples indicated that CYP39A1 was lower expressed in HCC and correlated with the differentiation and prognosis of HCC. Then, cell viability was detected in HepG2 and SMMC-7721 cells infected with the CYP39A1 empty vector (EV) or overexpressing (OE)

lentiviral plasmid. CYP39A1 mRNA was overexpressed in the OE group compared with the EV group ( $P < 0.01$ , Figure 7(a)). Meanwhile, the proliferation of HepG2 and SMMC-7721 cells was inhibited after CYP39A1 overexpression ( $P < 0.05$ , Figure 7(b)). To further understand the function of CYP39A1 in more HCC cell lines, the DepMap database was employed to analyze cell growth after the genes of interest were knocked out. The CERES dependency scores of 22 HCC cell lines for CYP39A1 in the genome-wide CRISPR/Cas9 screening database were extracted. The score was more than 0 in most of the HCC cell lines (20/22) (Figure 7(c)). As it described in the materials and methods section, the higher the score, the more likely the gene is a tumor suppressor gene. Therefore, it can be inferred that CYP39A1 might serve as a tumor suppressor gene in HCC. In order to clarify the possible mechanism of CYP39A1 in HCC, the protein of HepG2 and SMMC-7721 cells infected with the CYP39A1 EV or OE lentiviral plasmid was collected and determined. Similarly, CYP39A1 protein expression was also significantly higher in the OE group while p-NF- $\kappa$ B and Nrf2 protein were decreased after CYP39A1 protein was overexpressed (Figures 7(d) and 7(e)). Furthermore, we found that CYP39A1 was decreased in the tumor cells of Akt/c-Met-induced HCC mouse model ( $P < 0.001$ ), however, it was increased in the oral administration of osthole group, especially in the high dose of osthole group. Likewise, the p-NF- $\kappa$ B and Nrf2 were activated in the AKT/c-Met induced HCC models; however, with the increasing of CYP39A1 protein expression by treating with osthole, p-NF- $\kappa$ B and Nrf2 protein levels were decreased in a dose-dependent manner. Moreover, Keap 1 protein was upregulated with the increased expression of CYP39A1 after treating with osthole (Figures 7(f)). Thereby, these all results suggested that CYP39A1 might be involved in the regulation of HCC growth through p-NF- $\kappa$ B and Keap 1-Nrf2 pathway.

**3.7. Correlation between CYP39A1 and Serum Biochemical Indices in HCC.** To investigate whether the change in



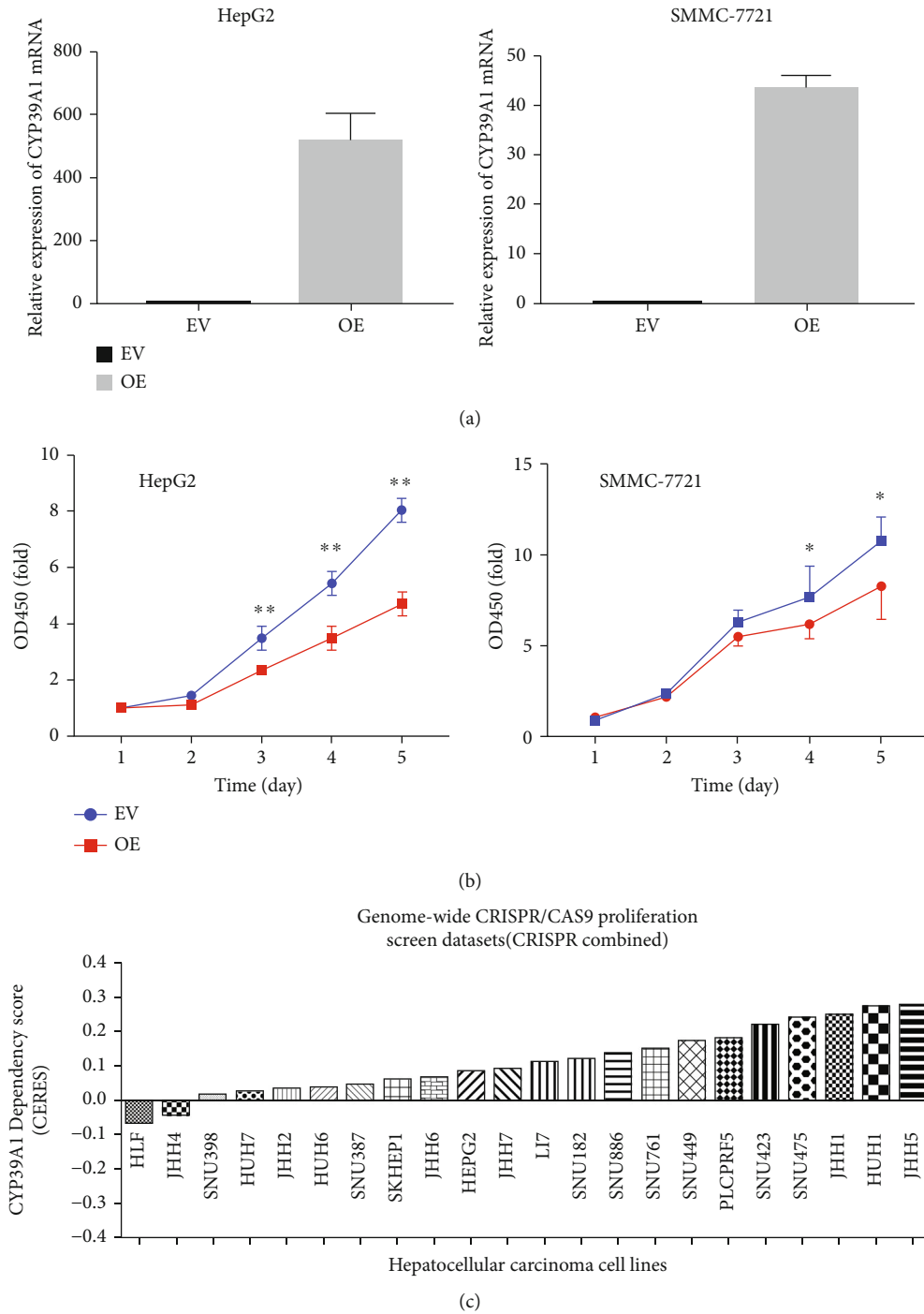


FIGURE 7: Continued.

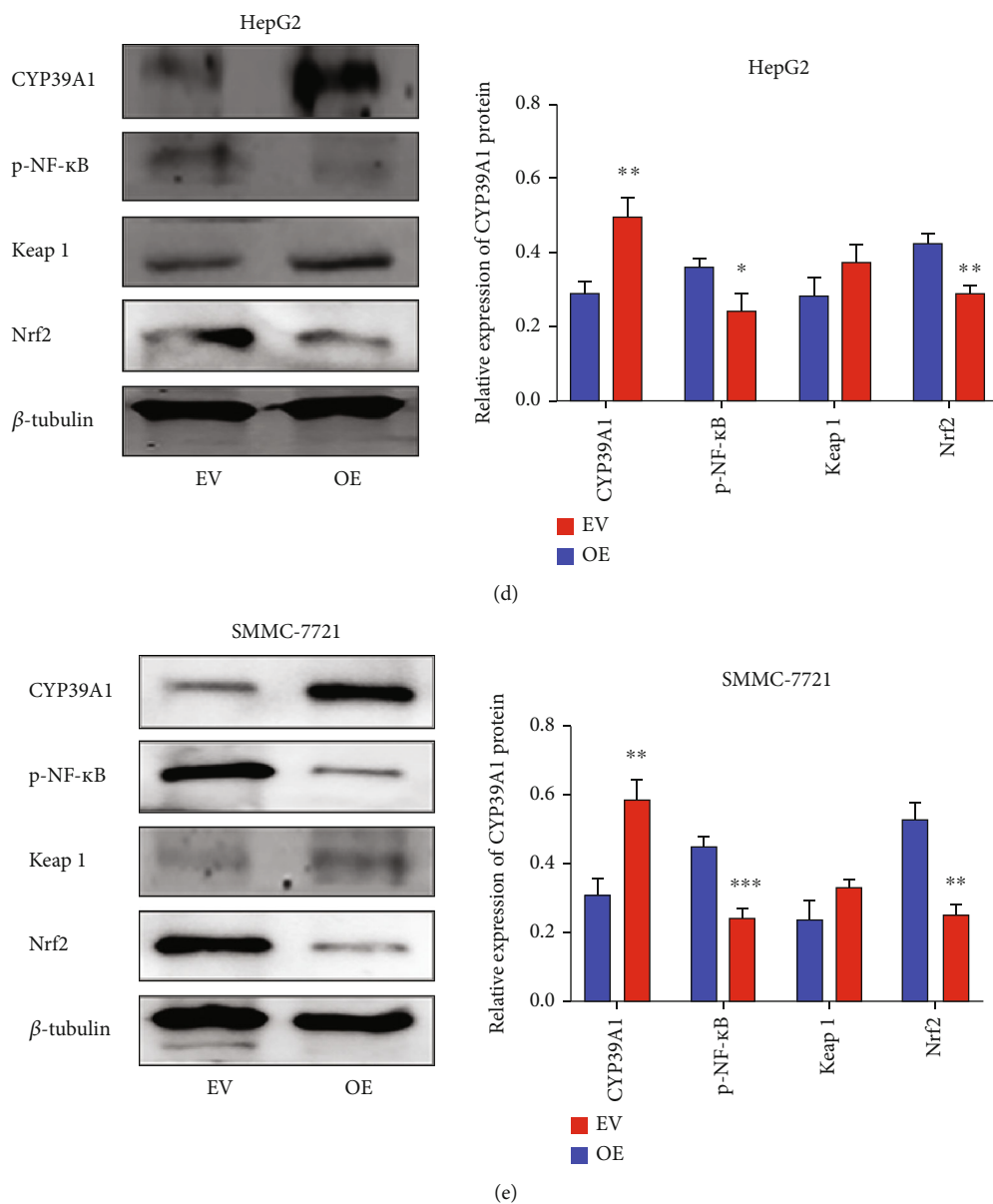
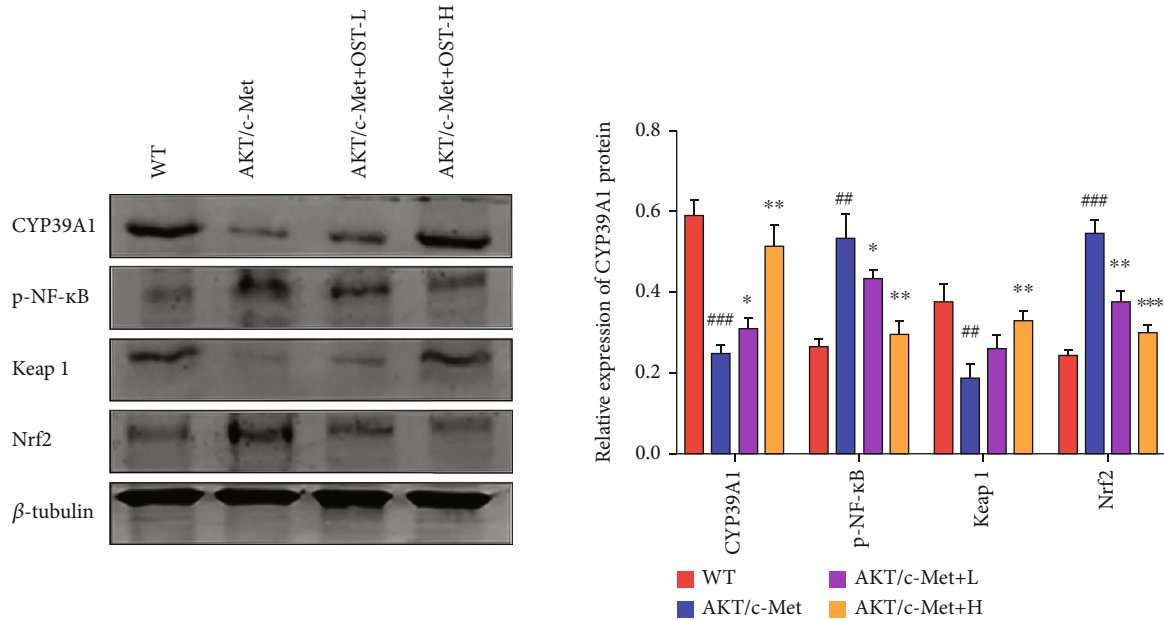


FIGURE 7: Continued.



(f)

FIGURE 7: The relationship between CYP39A1 and the cell growth of HCC. (a) Relative CYP39A1 mRNA expression in the EV and OE groups after infection with CYP39A1 lentiviral plasmid in HepG2 and SMMC-7721 cells; (b) cell viability was inhibited after CYP39A1 was overexpressed in HepG2 and SMMC-7721 cells; (c) CERES dependency score of CYP39A1 in 22 HCC cell lines in the CRISPR combined database; (d) and (e) the relative protein expression of CYP39A1, p-NF-κB, Keap1, and Nrf2 after infection with CYP39A1 lentiviral plasmid in HepG2 and SMMC-7721 cells; histograms indicated the relative expression levels of CYP39A1, p-NF-κB, Keap1, and Nrf2. Data were expressed as the mean  $\pm$  S.D.;  $n = 3$ . \* $P < 0.05$ , \*\* $P < 0.01$ , \*\*\* $P < 0.001$  versus the EV group; (f) the protein expression of CYP39A1, p-NF-κB, Keap1, and Nrf2 in AKT/c-Met-induced HCC mouse models were determined by Western blot analysis; histograms indicated the relative expression levels of CYP39A1, p-NF-κB, Keap1, and Nrf2. Data were expressed as the mean  $\pm$  S.D.;  $n = 3$ . \* $P < 0.05$ , \*\* $P < 0.01$ , \*\*\* $P < 0.001$  versus the WT group; \* $P < 0.05$ , \*\* $P < 0.01$ , \*\*\* $P < 0.001$  versus the AKT/c-Met group.

CYP39A1 will affect liver function and other serum biochemical indices, the serum biochemical indices of HCC patients, including alanine aminotransferase (ALT), aspartate aminotransferase (AST), total bile acid (TBA), total bilirubin (TBIL), direct bilirubin (DBIL), and total cholesterol (TCh), were detected. The relationships between CYP39A1 expression and serum biochemical indices were shown in Table 2. Interestingly, TBA, TBIL, and DBIL were significantly lower in the high CYP39A1 expression group than that in the low CYP39A1 expression group. Conversely, PA, UA, Cr, etc. were significantly higher in the high CYP39A1 expression group than that in the low CYP39A1 expression group.

#### 4. Discussion

HCC, a multifactorial disease characterized by multistep-multistage hepatocarcinogenesis, is the third leading cause of cancer-related mortality [23]. The incidence and mortality of HCC are still increasing rapidly. Hence, it is urgent to develop specific strategies and effective treatments for HCC patients. It has been reported that gene dysregulation could induce the occurrence and development of numerous types of carcinomas [24], including HCC [24]. In this study, our findings indicated that CYP39A1 protein and mRNA levels were lower in HCC than in noncancerous liver tissues, suggesting that decreased CYP39A1 expression might be

associated with HCC carcinogenesis. Similarly, this finding was consistent with a previous report that CYP3A4 was identified as a tumor suppressor gene related to a poor prognosis in HCC [25, 26].

Furthermore, for CYP2C subfamily members, CYP2C8, CYP2C9, and CYP2C19 were reported to be potential serum biomarkers for the early diagnosis of HCC, and high expression levels of them were associated with a reduced risk of death [27]. Also, downregulation of CYP2A6 and CYP2C8 in HCC tissues was linked to poor overall survival and recurrence-free survival [28]. These study results were consistent with our research results that CYP39A1 was downregulated in HCC. However, these studies have some limitations. First, most of the studies were only performed by bioinformatic analysis, which needs larger population studies for further validation. Second, CYP expression in most of these studies was limited to the mRNA level, which may not necessarily reflect the activities of CYPs. Third, further well-designed studies concentrating on functional and phenotypic validation are needed to clarify whether these genes can serve as novel markers of HCC. Recently, newly identified CYP family members, such as CYP4F2, CYP4F12, CYP4V2 [29], and CYP2W1 [30], have also shown correlations with prognosis in HCC.

At present, mouse was the commonly used animal model of HCC to evaluate the pathogenesis of HCC, with the advantages of small size and very close genomic

TABLE 2: Difference of serum biochemical indices between CYP39A1 low expression and CYP39A1 high expression in HCC patients.

| Serum biochemical indices                             | CYP39A1 low expression<br>Mean $\pm$ sd | CYP39A1 high expression<br>Mean $\pm$ sd | P value <sup>a</sup> |
|---|---|--|----------------------|
| Alanine aminotransferase (ALT)                        | 55.75 $\pm$ 74.15                       | 66.21 $\pm$ 51.60                        | 0.38                 |
| Aspartic transaminase (AST)                           | 51.44 $\pm$ 57.93                       | 52.32 $\pm$ 43.71                        | 0.93                 |
| ALT/AST (ratio)                                       | 1.06 $\pm$ 0.46                         | 1.28 $\pm$ 0.53                          | 0.01                 |
| Alkaline phosphatase (ALP)                            | 121.61 $\pm$ 101.48                     | 149.39 $\pm$ 243.51                      | 0.33                 |
| $\gamma$ -Glutamyltransferase (GGT)                   | 112.10 $\pm$ 156.95                     | 83.84 $\pm$ 64.29                        | 0.23                 |
| Total bile acid (TBA)                                 | 9.43 $\pm$ 7.03                         | 6.46 $\pm$ 5.61                          | 0.02                 |
| Prealbumin (PA)                                       | 69.51 $\pm$ 92.25                       | 138.36 $\pm$ 115.40                      | <0.001               |
| Total protein (TP)                                    | 65.13 $\pm$ 7.98                        | 63.97 $\pm$ 8.39                         | 0.42                 |
| Albumin (ALB)   | 38.28 $\pm$ 5.71                        | 36.53 $\pm$ 6.09                         | 0.09                 |
| Globulin (GLB)  | 26.85 $\pm$ 4.23                        | 27.44 $\pm$ 4.81                         | 0.45                 |
| Ratio of albumin to globulin (A/G)                    | 1.45 $\pm$ 0.28                         | 11.57 $\pm$ 40.04                        | 0.01                 |
| Total bilirubin (TBIL)                                | 25.86 $\pm$ 32.48                       | 12.72 $\pm$ 5.16                         | 0.01                 |
| Direct bilirubin (DBIL)                               | 14.82 $\pm$ 28.96                       | 4.89 $\pm$ 1.72                          | 0.02                 |
| Leucine aminopeptidase (LAP)                          | 68.92 $\pm$ 38.34                       | 77.19 $\pm$ 37.51                        | 0.25                 |
| Glutamate dehydrogenase (GLDH)                        | 7.23 $\pm$ 6.69                         | 8.37 $\pm$ 9.68                          | 0.44                 |
| Fibronectin (Fn)                                      | 199.18 $\pm$ 40.63                      | 183.90 $\pm$ 31.82                       | 0.04                 |
| Urea (urea)   | 5.69 $\pm$ 1.38                         | 5.37 $\pm$ 2.07                          | 0.28                 |
| Creatinine (Cr)                                       | 67.37 $\pm$ 16.49                       | 78.96 $\pm$ 36.44                        | 0.01                 |
| Urea nitrogen/creatinine (U/Cr)                       | 0.12 $\pm$ 0.16                         | 0.07 $\pm$ 0.02                          | 0.06                 |
| $\beta$ 2-microglobulin ( $\beta$ 2-m)                | 2.18 $\pm$ 0.68                         | 2.52 $\pm$ 1.39                          | 0.06                 |
| Total carbon dioxide (TCO2)                           | 26.39 $\pm$ 2.97                        | 26.39 $\pm$ 2.97                         | 0.19                 |
| Uric acid (UA)  | 294.55 $\pm$ 92.49                      | 343.93 $\pm$ 121.40                      | 0.01                 |
| Total cholesterol (TCh)                               | 3.95 $\pm$ 0.93                         | 4.32 $\pm$ 1.38                          | 0.10                 |
| Triacylglycerol (TG)                                  | 1.13 $\pm$ 0.63                         | 1.07 $\pm$ 0.40                          | 0.62                 |
| High-density lipoprotein cholesterol (HDL-Ch)         | 1.07 $\pm$ 0.33                         | 1.09 $\pm$ 0.28                          | 0.79                 |
| Low-density lipoprotein cholesterol (LDL-Ch)          | 2.41 $\pm$ 0.71                         | 2.67 $\pm$ 1.13                          | 0.16                 |
| Total/high density lipoprotein cholesterol (T/HDL-Ch) | 4.28 $\pm$ 3.22                         | 3.98 $\pm$ 0.77                          | 0.61                 |
| Lipoprotein alpha (LP( $\alpha$ ))                    | 154.70 $\pm$ 156.60                     | 144.93 $\pm$ 150.92                      | 0.78                 |

<sup>a</sup>Student's *t*-test.

sequence to human [31]. The commonly used HCC model was carcinogen-induced mice, tumor transplanted mice, and transgenic mice. However, there are some shortcomings of these models, such as long modeling cycle, high cost of use or inhomogenous performance among individuals, and these models could not meet the requirement of research on the interaction of multiple genes and multiple signaling pathways in the occurrence of liver cancer. The Akt/c-Met-induced HCC mice were launched by Chenxin's Lab that refers to Sleeping Beauty (SB) transposon-mediated high-pressure caudal vein hydrodynamic plasmid transfection [32], which has become one of the effective methods for the establishment of mouse liver cancer models because of the short modeling cycle, uniform tumor formation, and simple operation [32]. In this study, the Akt/c-met-induced HCC mice were successfully established as in our previous research [20] and used to evaluate the CYP39A1 differential

expression in HCC occurrence which was consistent with the results in human HCC tissues. In addition, in order to study the possible mechanism of CYP39A1 in HCC, the related protein with HCC was detected. It was reported that NF- $\kappa$ B and Nrf2 was activated in HCC [33–36], which was also found in our HCC model group with the downregulation of CYP39A1. However, CYP39A1 expression was increased after treating with osthole, while p-NF- $\kappa$ B and Nrf2 protein expression were decreased. And that it was consistent with previous study that osthole significantly decreased the nuclear factor, Nrf2 protein levels in cervical cancer [37]. Furthermore, Keap 1 protein, an adaptor for the degradation of Nrf2, was lower expressed in HCC mouse models; however, Keap 1 was upregulated with the increase expression of CYP39A1 which was consistent with previous study that it was a negative regulator of Nrf2 protein [38]. Likewise, p-NF- $\kappa$ B and Nrf2 were downregulated after

CYP39A1 protein overexpression *in vitro*. Thereby, these all indicated that CYP39A1 might participate in the occurrence and development of the HCC through the NF- $\kappa$ B and Keap1-Nrf2 pathway.

Cholesterol is the starting point for the biosynthesis of steroid hormones, vitamin D, and bile acids, which are primarily metabolized into 24(s)-hydroxycholesterol by CYP46A1 in the brain and 7 $\alpha$ -hydroxylated by CYP39A1 in the liver, and it is also engaged in the bile acid synthesis pathway. CYP450 plays crucial roles in these intertwined mechanisms of cholesterol homeostasis, such as CYP7A1, 27A1, 46A1, CYP8B1, and CYP39A1, which are cholesterol oxidation products whose expression may be dysregulated in inflammation-related diseases, including cancer [17, 39]. Some of these proteins have been investigated in HCC or cholangiocarcinoma (CCA). For instance, cholesterol elimination-associated genes, such as CYP7A1, 27A1, and CYP8B1, have been investigated in CCA, indicating that only CYP8B1 was associated with CCA overall survival [40]. Another study indicated that hub genes, such as CYP2C8, CYP2C9, and CYP8B1, might be useful as predictive biomarkers for HCC prognosis [41].

To date, CYP39A1, as a novel gene, has been investigated in several other tumors. Currently, it was reported that 24-hydroxycholesterol is involved in the development of pancreatic neuroendocrine tumors [42]. A CYP39A1 single nucleotide polymorphism (rs7761731) was associated with paclitaxel-induced severe neutropenia in patients undergoing chemotherapy for ovarian and endometrial cancer [11]. Furthermore, the promoter of the CYP39A1 gene was hypermethylated in ovarian cancer, resulting in its transcriptional disorder, which caused metabolic disorders of cholesterol and quinoline acid and contributed to the occurrence of ovarian cancer [43]. Moreover, CYP39A1 was expressed at lower levels in malignant melanoma [16] and cholangiocarcinoma [17]. These findings indicated that CYP39A1 was downregulated in several tumors, which was consistent with our study results conducted in HCC.

In the present study, it is worth mentioning that the CYP39A1 mRNA expression difference was not only validated by data from different GSE datasets but also analyzed using data from the TCGA database. Moreover, 14 additional fresh matched liver cases were selected and analyzed by qPCR analysis and Western blotting to validate the expression difference of CYP39A1 mRNA and protein expression. Furthermore, 159 matched noncancerous liver and HCC tissues as well as Akt/c-met-induced HCC mouse models were subjected to IHC analysis to determine the protein expression difference. To analyze the correlation between CYP39A1 expression and clinicopathologic features or HCC survival, protein expression was analyzed by IHC and mRNA expression as analyzed by TCGA database analysis. All the results commonly suggested that CYP39A1 might serve as a prognostic biomarker in HCC occurrence and progression. A similar study also showed that CYP39A1 might be a promising protective-prognostic factor and that altered expression of CYP39A1 might play a useful role in cholangiocarcinoma progression [17].

In addition, to elucidate the role of CYP39A1 in HCC, cell viability and bioinformatic analysis were performed. It is beneficial to take advantage of the DepMap database, which contains genome-wide CRISPR/Cas9 proliferation screening database that can help identify which genes are essential for cell survival and growth. This bioinformatic database provided a simple and effective way for defining and predicting genes that are essential for cell viability [22]. In our previous study, these methods were employed to confirm that RNASET2 was neither a tumor suppressor gene nor an oncogene in gastric carcinoma [21]. Similarly, in this study, by using complete gene knockout techniques, most of the CYP39A1 CERES dependency score of HCC cell lines was >0 with higher score. Therefore, combining the results from cell viability data *in vitro*, CYP39A1 might serve as a tumor suppressor gene in HCC.

Interestingly, in this study, TBA, TBIL, and DBIL were significantly higher in the CYP39A1 low expression group than that in the CYP39A1 high expression group. Recent studies also indicated that CYP39A1 was lower expressed in patients with liver dysfunction. It was reported that CYP39A1 was significantly downregulated in the blood plasma of severe COVID-19 patients with liver dysfunction [44]. Another study revealed that higher hepatic mRNA levels of hepatic CYP39A1 were linked to higher serum cholesterol but protect against steatosis, steatohepatitis, and liver fibrosis in a subset of patients [45]. Furthermore, CYP39A1 could be served as liver toxicity gene markers [46]. Moreover, it was found that CYP39A1 mRNA was increased in models of hepatoprotection mice from cholestasis induced by lithocholic acid (LCA), which toward the formation of less toxic bile acids therefore leading less liver injury [47]. These all recent investigations suggested that CYP39A1 expression levels were associated with the liver function, which was consistent with our observation in the HCC patients. This may suggest the HCC patients with lower expression of CYP39A1 should be prevented from diseases related to the disorder of bile acid metabolism in the clinical treatment. The regulation mechanism between CYP39A1 levels and disorder of bile acid metabolism in HCC needs further investigation.

## 5. Conclusion

In summary, low expression of CYP39A1 was associated with carcinogenesis, tumor differentiation and progression, and poor overall survival of patients with HCC. CYP39A1 might play a role as a tumor suppressor gene and could serve as a potential novel biomarker for HCC.

## Abbreviations

|               |   |
|---------------|---|
| HCC:          | Hepatocellular carcinoma  |
| CYP450:       | Cytochrome P450   |
| 24OHC:        | 24 hydroxycholesterol   |
| IHC:          | Immunohistochemistry  |
| DepMap:       | The cancer dependency map                                       |
| CRISPR/Cas 9: | Clustered regularly interspaced short palindromic repeats/Cas 9 |

GEO: Gene Expression Omnibus  
 TCGA: The Cancer Genome Atlas  
 qRT-PCR: Quantitative real-time polymerase chain reaction  
 p-NF- $\kappa$ B: Phosphorylated nuclear factor kappa-B p65  
 Keap1: Kelch-like ECH-associated protein 1  
 Nrf2: NF-E2-related factor 2.

## Data Availability

The datasets used and analyzed during the current study are available from the corresponding authors on reasonable request.

## Conflicts of Interest

The authors declare no potential conflicts of interest for this article.

## Authors' Contributions

DL, LG, and ZZ conceived and designed the study. TY, JH, JW, SF, QX, XZ, YZ, and DL performed the research. DL and TY wrote the manuscript. LG, ZZ, TY, and BZ performed the bioinformatic analysis and analyzed the data. HZ, DL, and ZZ revised the manuscript. All authors contributed to manuscript revision, read, and approved the submitted version. Dan Li and Tao Yu contributed equally to this work.

## Acknowledgments

This study was supported by the National Natural Science Foundation of China (Grant no. 81803789 to DL, no. 81704023 to TY, and no. 81602535 to ZZ), Wu Jieping Medical Foundation (Grant no. 320.6750), and the guidance funding of Renmin Hospital of Wuhan University (Grant no. RMYD2018M79).

## References

- [1] A. Noonan and T. M. Pawlik, "Hepatocellular carcinoma: an update on investigational drugs in phase I and II clinical trials," *Expert Opinion on Investigational Drugs*, vol. 28, no. 11, pp. 941–949, 2019.
- [2] A. Sciarra, B. Pintea, J. H. Nahm et al., "CYP1A2 is a predictor of HCC recurrence in HCV-related chronic liver disease: a retrospective multicentric validation study," *Digestive and Liver Disease*, vol. 49, no. 4, pp. 434–439, 2017.
- [3] F. Jiang, L. Chen, Y. C. Yang et al., "CYP3A5 functions as a tumor suppressor in hepatocellular carcinoma by regulating mTORC2/Akt signaling," *Cancer Research*, vol. 75, no. 7, pp. 1470–1481, 2015.
- [4] Y. Pan and E. C. Ong, "Cytochrome P450 2W1 (CYP2W1) - ready for use as the biomarker and drug target for cancer?," *Xenobiotica*, vol. 47, no. 10, pp. 923–932, 2017.
- [5] F. Wang, J. Huang, Z. Zhu et al., "Transcriptome analysis of WHV/c-myc transgenic mice implicates cytochrome P450 enzyme 17A1 as a promising biomarker for hepatocellular carcinoma," *Cancer Prevention Research (Philadelphia, Pa.)*, vol. 9, no. 9, pp. 739–749, 2016.
- [6] R. Lathe, "Steroid and sterol 7-hydroxylation: ancient pathways," *Steroids*, vol. 67, no. 12, pp. 967–977, 2002.
- [7] I. P. Grabovec, S. V. Smolskaya, A. V. Baranovsky et al., "Ligand-binding properties and catalytic activity of the purified human 24-hydroxycholesterol 7 $\alpha$ -hydroxylase, CYP39A1," *The Journal of Steroid Biochemistry and Molecular Biology*, vol. 193, article 105416, 2019.
- [8] J. Li-Hawkins, E. G. Lund, A. D. Bronson, and D. W. Russell, "Expression cloning of an oxysterol 7 $\alpha$ -hydroxylase selective for 24-hydroxycholesterol," *Journal of Biological Chemistry*, vol. 275, no. 22, pp. 16543–16549, 2000.
- [9] H. Ikeda, M. Ueda, M. Ikeda, H. Kobayashi, and Y. Honda, "Oxysterol 7 $\alpha$ -hydroxylase (CYP39A1) in the ciliary nonpigmented epithelium of bovine eye," *Laboratory Investigation*, vol. 83, no. 3, pp. 349–355, 2003.
- [10] Z. Li, Z. Wang, M. C. Lee et al., "Association of Rare CYP39A1 Variants with exfoliation syndrome involving the anterior chamber of the eye," *JAMA*, vol. 325, no. 8, pp. 753–764, 2021.
- [11] T. Uchiyama, H. Kanno, K. Ishitani et al., "An SNP in CYP39A1 is associated with severe neutropenia induced by docetaxel," *Cancer Chemotherapy and Pharmacology*, vol. 69, no. 6, pp. 1617–1624, 2012.
- [12] T. Melchardt, C. Hufnagl, T. Magnes et al., "CYP39A1 polymorphism is associated with toxicity during intensive induction chemotherapy in patients with advanced head and neck cancer," *BMC Cancer*, vol. 15, no. 1, p. 725, 2015.
- [13] S. Aslibekyan, E. E. Brown, R. J. Reynolds et al., "Genetic variants associated with methotrexate efficacy and toxicity in early rheumatoid arthritis: results from the treatment of early aggressive rheumatoid arthritis trial," *Pharmacogenomics Journal*, vol. 14, no. 1, pp. 48–53, 2014.
- [14] M. Oscarson, U. M. Zanger, O. F. Rifki, K. Klein, M. Eichelbaum, and U. A. Meyer, "Transcriptional profiling of genes induced in the livers of patients treated with carbamazepine," *Clinical Pharmacology & Therapeutics*, vol. 80, no. 5, pp. 440–456, 2006.
- [15] B. M. Ten, T. van Bavel, J. J. Swen et al., "Effect of genetic variants GSTA1 and CYP39A1 and age on busulfan clearance in pediatric patients undergoing hematopoietic stem cell transplantation," *Pharmacogenomics*, vol. 14, no. 14, pp. 1683–1690, 2013.
- [16] V. N. Sumantran, P. Mishra, R. Bera, and N. Sudhakar, "Microarray analysis of differentially-expressed genes encoding CYP450 and phase II drug metabolizing enzymes in psoriasis and melanoma," *Pharmaceutics*, vol. 8, no. 1, p. 4, 2016.
- [17] C. Khenjanta, R. Thanan, A. Jusakul et al., "Association of CYP39A1, RUNX2 and oxidized alpha-1 antitrypsin expression in relation to cholangiocarcinoma progression," *Asian Pacific Journal of Cancer Prevention*, vol. 15, no. 23, pp. 10187–10192, 2014.
- [18] X. C. Peng, Z. Zeng, Y. N. Huang, Y. C. Deng, and G. H. Fu, "Clinical significance of TM4SF1 as a tumor suppressor gene in gastric cancer," *Cancer Medicine*, vol. 7, no. 6, pp. 2592–2600, 2018.
- [19] Z. Zeng, D. Li, T. Yu et al., "Association and clinical implication of the USP10 and MSH2 proteins in non-small cell lung cancer," *Oncology Letters*, vol. 17, no. 1, pp. 1128–1138, 2019.
- [20] J. Hu, L. Che, L. Li et al., "Co-activation of AKT and c-Met triggers rapid hepatocellular carcinoma development via the mTORC1/FASN pathway in mice," *Scientific Reports*, vol. 6, no. 1, article 20484, 2016.

- [21] Z. Zeng, X. Zhang, D. Li et al., “Expression, location, clinical implication, and bioinformatics analysis of RNASET2 in gastric adenocarcinoma,” *Frontiers in Oncology*, vol. 10, p. 836, 2020.
- [22] T. Hart, K. R. Brown, F. Sircoulomb, R. Rottapel, and J. Moffat, “Measuring error rates in genomic perturbation screens: gold standards for human functional genomics,” *Molecular Systems Biology*, vol. 10, no. 7, p. 733, 2014.
- [23] J. Ferlay, I. Soerjomataram, R. Dikshit et al., “Cancer incidence and mortality worldwide: sources, methods and major patterns in GLOBOCAN 2012,” *International Journal of Cancer*, vol. 136, no. 5, pp. E359–E386, 2015.
- [24] N. Rodriguez-Salas, G. Dominguez, R. Barderas et al., “Clinical relevance of colorectal cancer molecular subtypes,” *Critical Reviews in Oncology/Hematology*, vol. 109, pp. 9–19, 2017.
- [25] R. Ashida, Y. Okamura, K. Ohshima et al., “CYP<sub>3A4</sub> gene is a novel biomarker for predicting a poor prognosis in hepatocellular carcinoma,” *Cancer Genomics Proteomics*, vol. 14, no. 6, pp. 445–453, 2017.
- [26] X. Ma, L. Zhou, and S. Zheng, “Transcriptome analysis revealed key prognostic genes and microRNAs in hepatocellular carcinoma,” *PeerJ*, vol. 8, article e8930, 2020.
- [27] X. Wang, T. Yu, X. Liao et al., “The prognostic value of CYP2C subfamily genes in hepatocellular carcinoma,” *Cancer Medicine*, vol. 7, no. 4, pp. 966–980, 2018.
- [28] X. Ren, Y. Ji, X. Jiang, and X. Qi, “Downregulation of CYP2A6 and CYP2C8 in tumor tissues is linked to worse overall survival and recurrence-free survival from hepatocellular carcinoma,” *BioMed Research International*, vol. 2018, Article ID 5859415, 9 pages, 2018.
- [29] H. S. Eun, S. Y. Cho, B. S. Lee, I. O. Seong, and K. H. Kim, “Profiling cytochrome P450 family 4 gene expression in human hepatocellular carcinoma,” *Molecular Medicine Reports*, vol. 18, no. 6, pp. 4865–4876, 2018.
- [30] K. Zhang, J. Jiang, R. He et al., “Prognostic value of CYP2W1 expression in patients with human hepatocellular carcinoma,” *Tumor Biology*, vol. 35, no. 8, pp. 7669–7673, 2014.
- [31] K. K. Frese and D. A. Tuveson, “Maximizing mouse cancer models,” *Nature Reviews Cancer*, vol. 7, no. 9, pp. 645–658, 2007.
- [32] X. Chen and D. F. Calvisi, “Hydrodynamic transfection for generation of novel mouse models for liver cancer research,” *American Journal of Pathology*, vol. 184, no. 4, pp. 912–923, 2014.
- [33] J. Li, Q. Wang, Y. Yang et al., “GSTZ1 deficiency promotes hepatocellular carcinoma proliferation via activation of the KEAP1/NRF2 pathway,” *Journal of Experimental & Clinical Cancer Research*, vol. 38, no. 1, p. 438, 2019.
- [34] S. Mattu, P. Zavattari, M. A. Kowalik et al., “Nrf2 mutation/activation is dispensable for the development of chemically induced mouse HCC,” *Cellular and Molecular Gastroenterology and Hepatology*, vol. 13, no. 1, pp. 113–127, 2022.
- [35] K. Lee, S. Kim, Y. Lee et al., “The clinicopathological and prognostic significance of Nrf2 and Keap1 expression in hepatocellular carcinoma,” *Cancers*, vol. 12, no. 8, p. 2128, 2020.
- [36] F. Meng, S. Zhang, R. Song et al., “NCAPG2 overexpression promotes hepatocellular carcinoma proliferation and metastasis through activating the STAT3 and NF- $\kappa$ B/miR-188-3p pathways,” *eBioMedicine*, vol. 44, pp. 237–249, 2019.
- [37] J. Su, F. Zhang, X. Li, and Z. Liu, “Osthole promotes the suppressive effects of cisplatin on NRF2 expression to prevent drug-resistant cervical cancer progression,” *Biochemical and Biophysical Research Communications*, vol. 514, no. 2, pp. 510–517, 2019.
- [38] Y. Liu, S. Tao, L. Liao et al., “TRIM25 promotes the cell survival and growth of hepatocellular carcinoma through targeting Keap1-Nrf2 pathway,” *Nature Communications*, vol. 11, no. 1, p. 348, 2020.
- [39] G. Lorbek, M. Lewinska, and D. Rozman, “Cytochrome P450s in the synthesis of cholesterol and bile acids—from mouse models to human diseases,” *FEBS Journal*, vol. 279, no. 9, pp. 1516–1533, 2012.
- [40] C. Yoo, J. Kang, D. Kim et al., “Multiplexed gene expression profiling identifies the FGFR4 pathway as a novel biomarker in intrahepatic cholangiocarcinoma,” *Oncotarget*, vol. 8, no. 24, pp. 38592–38601, 2017.
- [41] X. Wang, X. Liao, C. Yang et al., “Identification of prognostic biomarkers for patients with hepatocellular carcinoma after hepatectomy,” *Oncology Reports*, vol. 41, no. 3, pp. 1586–1602, 2019.
- [42] M. Soncini, G. Corna, M. Moresco et al., “24-Hydroxycholesterol participates in pancreatic neuroendocrine tumor development,” *Proceedings of the National Academy of Sciences of the United States of America*, vol. 113, no. 41, pp. E6219–E6227, 2016.
- [43] Y. W. Huang, R. A. Jansen, E. Fabbri et al., “Identification of candidate epigenetic biomarkers for ovarian cancer detection,” *Oncology Reports*, vol. 22, no. 4, pp. 853–861, 2009.
- [44] S. M. Hammoudeh, A. M. Hammoudeh, P. M. Bhamidimarri et al., “Insight into molecular mechanisms underlying hepatic dysfunction in severe COVID-19 patients using systems biology,” *World Journal of Gastroenterology*, vol. 27, no. 21, pp. 2850–2870, 2021.
- [45] S. Grimaudo, P. Dongiovanni, J. Pihlajamäki et al., “NR1H4rs35724 G>C variant modulates liver damage in non-alcoholic fatty liver disease,” *Liver International*, vol. 41, no. 11, pp. 2712–2719, 2021.
- [46] B. P. Smith, L. S. Auvil, M. Welge et al., “Identification of early liver toxicity gene biomarkers using comparative supervised machine learning,” *Scientific Reports*, vol. 10, no. 1, p. 19128, 2020.
- [47] L. D. Beilke, L. M. Aleksunes, R. D. Holland et al., “Constitutive androstane receptor-mediated changes in bile acid composition contributes to hepatoprotection from lithocholic acid-induced liver injury in mice,” *Drug Metabolism and Disposition*, vol. 37, no. 5, pp. 1035–1045, 2009.

## Research Article

# Ionizing Radiation Upregulates Glutamine Metabolism and Induces Cell Death via Accumulation of Reactive Oxygen Species

Pengfei Yang,<sup>1,2</sup> Xiangxia Luo,<sup>3</sup> Jin Li,<sup>1,4</sup> Tianyi Zhang,<sup>1,2</sup> Xiaoling Gao<sup>5</sup>, Junrui Hua,<sup>1,2</sup> Yonghong Li,<sup>5</sup> Nan Ding,<sup>1,2</sup> Jinpeng He,<sup>1,2</sup> Yanan Zhang,<sup>1,2</sup> Wenjun Wei,<sup>1,2</sup> Jufang Wang<sup>1,2</sup> and Heng Zhou<sup>1,2</sup>

<sup>1</sup>Key Laboratory of Space Radiobiology of Gansu Province & Key Laboratory of Heavy Ion Radiation Biology and Medicine, Institute of Modern Physics, Chinese Academy of Sciences, Lanzhou 730000, China

<sup>2</sup>University of Chinese Academy of Sciences, Beijing 100049, China

<sup>3</sup>Gansu Provincial Hospital of TCM, Lanzhou 730050, China

<sup>4</sup>School of Nuclear Science and Technology, Lanzhou University, Lanzhou 730000, China

<sup>5</sup>NHC Key Laboratory of Diagnosis and Therapy of Gastrointestinal Tumor, Gansu Provincial Hospital, Lanzhou 730000, China

Correspondence should be addressed to Jufang Wang; [jufangwang@impcas.ac.cn](mailto:jufangwang@impcas.ac.cn) and Heng Zhou; [hengzhou@impcas.ac.cn](mailto:hengzhou@impcas.ac.cn)

Received 23 July 2021; Revised 22 November 2021; Accepted 30 November 2021; Published 30 December 2021

Academic Editor: Guoku Hu

Copyright © 2021 Pengfei Yang et al. This is an open access article distributed under the Creative Commons Attribution License, which permits unrestricted use, distribution, and reproduction in any medium, provided the original work is properly cited.

Glutamine metabolism provides energy to tumor cells and also produces reactive oxygen species (ROS). Excessive accumulation of ROS can damage mitochondria and eventually lead to cell death. xCT (SLC7A11) is responsible for the synthesis of glutathione in order to neutralize ROS. In addition, mitophagy can remove damaged mitochondria to keep the cell alive. Ionizing radiation kills tumor cells by causing the accumulation of ROS, which subsequently induces nuclear DNA damage. With this in mind, we explored the mechanism of intracellular ROS accumulation induced by ionizing radiation and hypothesized new methods to enhance the effect of radiotherapy. We used MCF-7 breast cancer cells and HCT116 colorectal cancer cells in our study. The above-mentioned cells were irradiated with different doses of X-rays or carbon ions. Clone formation assays were used to detect cell proliferation, enzyme-linked immunosorbent assay (ELISA) detected ATP, and glutathione (GSH) production, while the expression of proteins was detected by Western blot and quantitative real-time PCR analysis. The production of ROS was detected by flow cytometry, and immunofluorescence was used to track mitophagy-related processes. Finally, BALB/C tumor-bearing nude mice were irradiated with X-rays in order to further explore the protein expression found in tumors with the use of immunohistochemistry. Ionizing radiation increased the protein expressions of ASCT2, GLS, and GLUD in order to upregulate the glutamine metabolic flux in tumor cells. This caused an increase in ATP secretion. Meanwhile, ionizing radiation inhibited the expression of the xCT (SLC7A11) protein and reduced the generation of glutathione, leading to excessive accumulation of intracellular ROS. The mitophagy inhibitor, or knockdown Parkin gene, is able to enhance the ionizing radiation-induced ROS production and increase nucleus DNA damage. This combined treatment can significantly improve the killing effect of radiation on tumor cells. We concluded that ionizing radiation could upregulate the glutamine metabolic flux and enhance ROS accumulation in mitochondria. Ionizing radiation also decreased the SLC7A11 expression, resulting in reduced GSH generation. Therefore, inhibition of mitophagy can increase ionizing radiation-induced cell death.

## 1. Introduction

The Warburg effect states that tumor cells consume large amounts of glucose for energy via the glycolytic pathway [1]; however, recent studies have shown that tumor cells rely

heavily on glutamine metabolism to maintain cell survival rather than on glucose metabolism [2]. Glutamine is involved in cellular activities such as the preparation of nucleotides, the construction of DNA and RNA, and NADPH synthesis [3, 4]. Glutamine metabolism is considered to be the central



metabolic pathway in tumor cells; this pathway contributes to oncogenic transformation [5] and promotes tumor growth [6]. Glutamine is transported to cells mainly via the alanine, serine, and cysteine-preferring transporter 2 (ASCT2) avenues [7]. It is then broken down into glutamic acid by glutaminase (GLS), which is then catalyzed by either glutamate dehydrogenase (GLUD) or aminotransferase to generate  $\alpha$ -ketoglutaric acid, the molecule that can participate in oxidative phosphorylation or the tricarboxylic acid (TCA) cycle [8]. This increased glutamine consumption can enhance the ROS accumulation and reduce the antioxidant activity of tumor cells [9]. The glutamine metabolite also plays an important role in the promotion of cellular antioxidant defense. Glutamic acid can be used for biosynthesis of glutathione (GSH) [10]. xCT (SLC7A11) is a critical subunit of the amino acid antiporter system xc(-), which is involved in the synthesis of GSH [11]. xCT can transfer intracellular glutamic acid out of a cell and cysteine into the cell. This is a crucial mechanism by which tumor cells inhibit oxidative stress [12]. Inhibition of xCT resulted in reduced glutathione synthesis and an inability to respond to excessive accumulation of cellular peroxides, which ultimately led to cell death [13, 14]. In addition, studies have shown that tumor cells cannot survive if they run out of glutamine, a phenomenon called “glutamine addiction” [15, 16]. Under glutamine deprivation conditions, if additional metabolites related to TCA flux, such as succinic acid, fumaric acid, or malic acid, are added, they induce significant accumulation of lipid ROS in tumor cells [17, 18]. This indicated that although excessive glutamine intake can generate a large amount of energy through the TCA cycle, it also produces excessive ROS, which accelerates the process of intracellular lipid peroxidation and ultimately leads to cell death.

Mitochondria act as the energy factories of the cell. They produce energy to support cell survival. Oxidative phosphorylation and the TCA cycle are two of the processes that take place inside the mitochondria to provide energy. In the mitochondria, the oxidative phosphorylation process is accompanied by ROS production, so these organelles are especially vulnerable to oxidative damage. In this way, timely removal of damaged mitochondria is essential to cell survival [19]. Mitophagy is the targeted phagocytosis of damaged mitochondria via the lysosomal degradation pathway, which is the primary quality control mechanism for mitochondria [20, 21]. Depolarized mitochondria are enclosed by autophagosomes, and they combine with lysosomes to form autolysosomes. Eventually, the damaged mitochondria are degraded in the autolysosome [22]. Several studies have shown that Parkin plays a crucial role in mitophagy [23]. When mitochondria are damaged, PINK1 accumulates on the surfaces of the mitochondria and phosphorylates Parkin. In this way, Parkin is transported to the depolarized mitochondrial outer membrane, where it then recruits the P62 protein in order to promote the binding of the damaged mitochondria to the autophagosomes [24]. In tumor cells, mitophagy promotes both cell survival and therapeutic resistance [25]. In tumor stem cells, mitophagy degrades damaged mitochondria and reduces intracellular ROS accumulation, which help to maintain cell differentiation. Mitophagy also plays an antiapoptotic

role in liver tumor cells [26, 27]. In this way, blocking mitophagy can reduce the therapeutic resistance of tumor cells and promote cell death.

Radiotherapy is a commonly used tumor treatment method that can induce a variety of cell death modes, such as apoptosis, necrosis, and ferroptosis. Ionizing radiation leads to DNA damage and causes the increase in intracellular ROS accumulation [28]. ROS then attack proteins, fatty acids, nucleotides, and other molecules, which initiates the peroxidation reaction and leads to cell death [29]. Ionizing radiation can also induce mitophagy, which helps maintain the dynamic balance of oxidative phosphorylation in the mitochondria. This is one reason that tumor cells become resistant to radiotherapy. Studies have shown that the mitophagy inhibitor temozolomide-perillyl alcohol conjugate (TMZ-POH) induces lysosome dysfunction in nonsmall cell lung cancer (NSCLC) cells and then destroys mitophagic function and improves tumor radiosensitivity, resulting in a reduced cell survival rate [30]. Based on this investigation, we hypothesized that ionizing radiation could induce excessive glutamine intake and thus cause ROS overproduction and increase lipid peroxidation levels to induce cell death. We also examined the effects of the inhibition of mitophagy and whether this process could promote ionizing radiation-induced cell death. The results of this study may provide a reference for further research into improving the effectiveness of radiotherapy.

## 2. Materials and Methods

**2.1. Radiotherapy.** The X-ray was generated by an X-Rad 225 generator (Precision, North Branford, CT, US) with an energy of 225 KV/13.3 mA. Carbon ion ( $^{12}\text{C}^{6+}$ ) beam radiation was performed at the treatment terminal of the Institute of Modern Physics with an energy of 80 MeV/u, peak LET: 50 KeV/ $\mu\text{m}$ , SOBP. The cells or breast tumor-bearing nude mice were placed on a platform after the mice were anesthetized (pentobarbital sodium (30 mg/kg), intraperitoneal). The bodies of the mice were protected with a lead plate, and only the tumor site was exposed to radiation.

**2.2. The Cell Lines.** Breast cancer cells (MCF-7) and colorectal cancer cells (HCT116) were purchased from the Chinese Academy of Sciences Cell Bank. Cells were cultured in Dulbecco's Modified Eagle Medium (DMEM) containing 10% fetal bovine serum (FBS) and 100 U/mL penicillin and 100  $\mu\text{g}/\text{mL}$  streptomycin. The culture was maintained at 37°C and 5%  $\text{CO}_2$  in a constant temperature incubator with saturated humidity.

**2.3. Experiments on Mice Models.** Six-week-old female BALB/C nude mice were purchased from Xi'an Keao Biological Technology Co. Ltd. and maintained in the animal facility at the Institute of Modern Physics under specific pathogen-free conditions in a temperature-controlled environment with 12 h of light and 12 h of dark cycles. Mice received food and water ad libitum. All of the animal experiments were approved by the Ethical Committee of the Institute of Modern Physics and followed the EU

Directive 2010/63/EU guidelines. MCF-7 tumors were established in BALB/C nude mice hosts by subcutaneously inoculating 1,000,000 cells. When the tumors became palpable at about 50 mm<sup>3</sup>, they were locally irradiated with 2 Gy X-ray.

**2.4. Western Blot.** The cells were collected by RIPA lysate, containing a protease inhibitor and a phosphatase inhibitor, and then crushed with ultrasonic. Then, samples were mixed with 5× loading buffer. The protein was placed in a 98°C metal bath and heated for 10 min in order to denature the protein. For analysis, we used constant pressure electrophoresis. The voltage was set at 80 V for protein concentration and at 120 V for separation. The membrane was transferred at 120 V and 0.2 A, although the specific transfer time depended on the molecular weight. Samples were then incubated with 5% BSA at room temperature for 2 h. The primary antibody was incubated overnight at 4°C. The next day, after washing five times with PBST, an HRP-labeled secondary antibody was incubated at room temperature for 90 min. Images were obtained by electrochemiluminescence immunoassay and analyzed with Image J software [31]. All antibody information is presented in Supplementary Table 1.

**2.5. Real-Time Quantitative PCR.** We used the Trizol method to extract RNA, and cDNA was obtained by conducting reverse transcription of 3 µg of RNA according to the GeneCoprovia (Rockville, MD, US) reverse transcription kit manual (Cat: AORT-0020). The cDNA was diluted three times, and the SYBR Green system was used for real-time quantitative detection. The final volume was 20 µL, with a total of 40 cycles. Settings were as follows: predenaturation at 95°C for 10 min, denaturation at 95°C for 10 s, annealing at 60°C for 20 s, and extension at 72°C for 15 s, and the heating rate from 72°C to 95°C was 0.5°C/6 s. All data were collected by the software of the Bio-Rad CFX96 PCR system. The collected Ct values were calibrated with GAPDH as an internal reference. The target gene expression was analyzed using the 2<sup>-ΔCT</sup> method [31]. Primers and sequences are listed in Supplementary Table 2.

**2.6. Flow Cytometry.** The cells were digested with trypsin and collected in a medium containing 5% serum. Single-cell suspensions were prepared by gentle teasing through disposable 70 µm sieves into cold PBS. Then, cells were spun at 800 rpm for 10 min. The supernatant was discarded, and 1 × 10<sup>6</sup> cells were resuspended in the cell staining buffer (#420201, Biolegend) containing dihydrorhodamine 123 (DHR123). Cells were then incubated in the dark at room temperature for 10 min. ROS expression was detected using a Merck Millipore FlowSight flow cytometer.

**2.7. ELISA Assay.** MCF-7/HCT-116 cells were cultured in a dish, and the supernatant medium was collected after irradiation for 48 h. Following the instructions provided in the Luminescent ATP Detection Assay Kit (Abcam, AB113849), ATP was measured at a spectrophotometer wavelength of 450 nm. Following the instructions provided in the Micro Reduced Glutathione Assay Kit (Solarbio, BC1175), GSH was measured at a spectrophotometer wavelength of 412 nm.

**2.8. Immunofluorescence.** For live image collection, cells were incubated in the medium mixed with Mito-Tracker Green (100 nM) and Lyso-Tracker Red (60 nM) in the dark for a total of 10 min. Then, Hoechst 33342 (1 µM) was added, and cells were further incubated at room temperature for 10 min. Images were obtained using a fluorescence microscope.

For fixed image collection, 4% paraformaldehyde was used to fix cells for about 10 min. Then, the supernatant was discarded, and cells were incubated with cold methanol for 20 min. Finally, the cells were prepared by cleaning with 75% glacial ethanol. After rehydration, 0.5% Triton X-100 was used to permeate the cell membrane for about 5 min. The samples were then placed in goat serum diluted with PBS (1:20) and blocked for 2 h. This was followed by the addition of primary antibody at a dilution ratio of 1:500 and incubation for an additional 2 h. After rinsing with PBST five times, the corresponding fluorescent secondary antibody at a dilution ratio of 1:1000 was incubated in the dark for 1.5 h. Then, 10 µl of DAPI was added, and the images were captured by a fluorescence microscope [31].

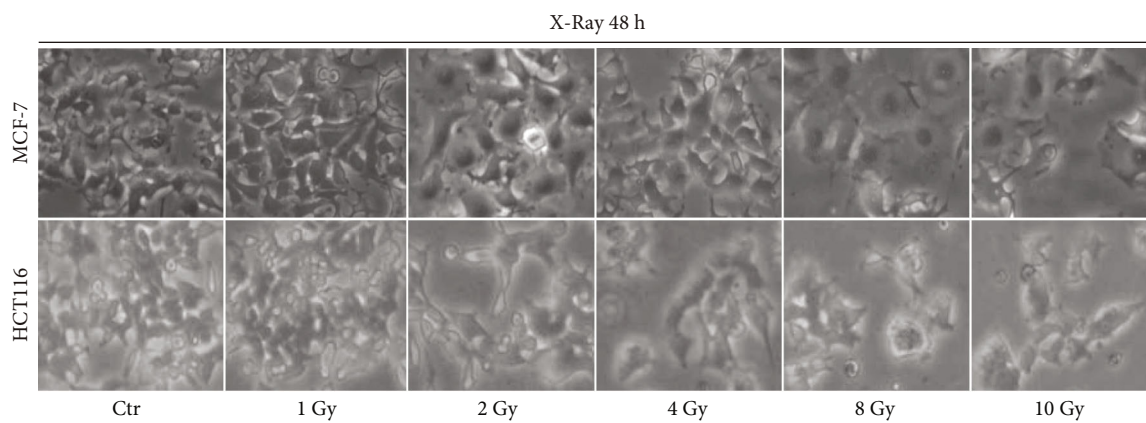
**2.9. Immunohistochemical.** The tumor was embedded in paraffin and cut into 3 µm slices. After dewaxing and hydration, the slices were put in 0.01-M sodium citrate buffer solution at pH 6.0 and heated at 95°C for 10 min. Then, 0.5% Triton X-100 was used to permeate the cell membrane, and 3% H<sub>2</sub>O<sub>2</sub> was added to remove endogenous peroxides. After blocking, the primary antibody against Ki67 (1:500) and MDA (1:500) was incubated overnight with conditions maintained at 4°C. On the second day, after PBST washing, biotin was labeled with secondary antibodies. The antibody was incubated at room temperature for 30 min. Then, DAB staining and hematoxylin redyeing were performed.

**2.10. Data Statistics and Analysis.** Origin 9.0 was used to analyze the results, and the data were represented as  $x \pm SE$ . Student's *t*-test, one-way ANOVA with post hoc Dunnett-test, one-way repeated ANOVA test, and Kaplan-Meier analysis with Log-Rank-test tested significant differences, and \**p* < 0.05, \*\**p* < 0.01, and \*\*\**p* < 0.001 were considered to be statistically significant. Each experiment was performed at least three times independently.

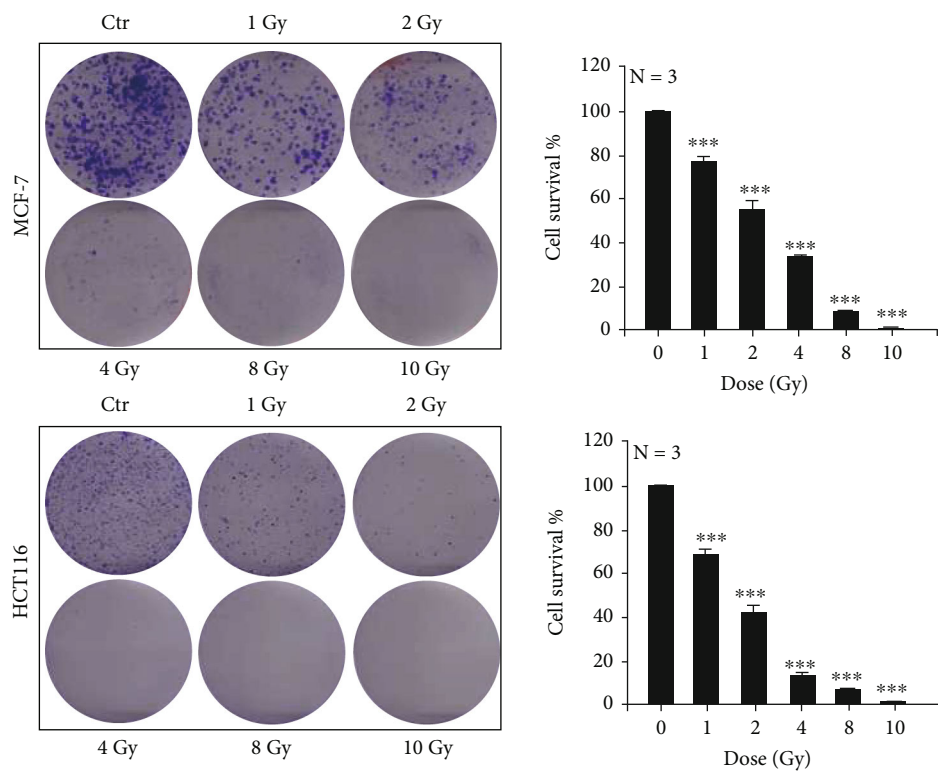
### 3. Results and Discussion

#### 3.1. Results

**3.1.1. Ionizing Radiation Inhibits Cell Proliferation.** Breast cancer cells (MCF-7) and colorectal cancer cells (HCT116) were irradiated with different doses of X-rays. We found that the cellular morphology became swollen and flat at 48 h after irradiation, and the number of cells decreased (Figure 1(a)). The clone formation was measured at 15 days after irradiation. The number of clones reduced after irradiation in a dose-dependent manner, and the dots formed by clones appeared smaller (Figure 1(b)). In addition, we also irradiated tumor cells with X-rays and a carbon ion beam. Results showed that ionizing radiation significantly reduced the expression of the malignant proliferative protein C-myc



(a)



(b)

FIGURE 1: Continued.

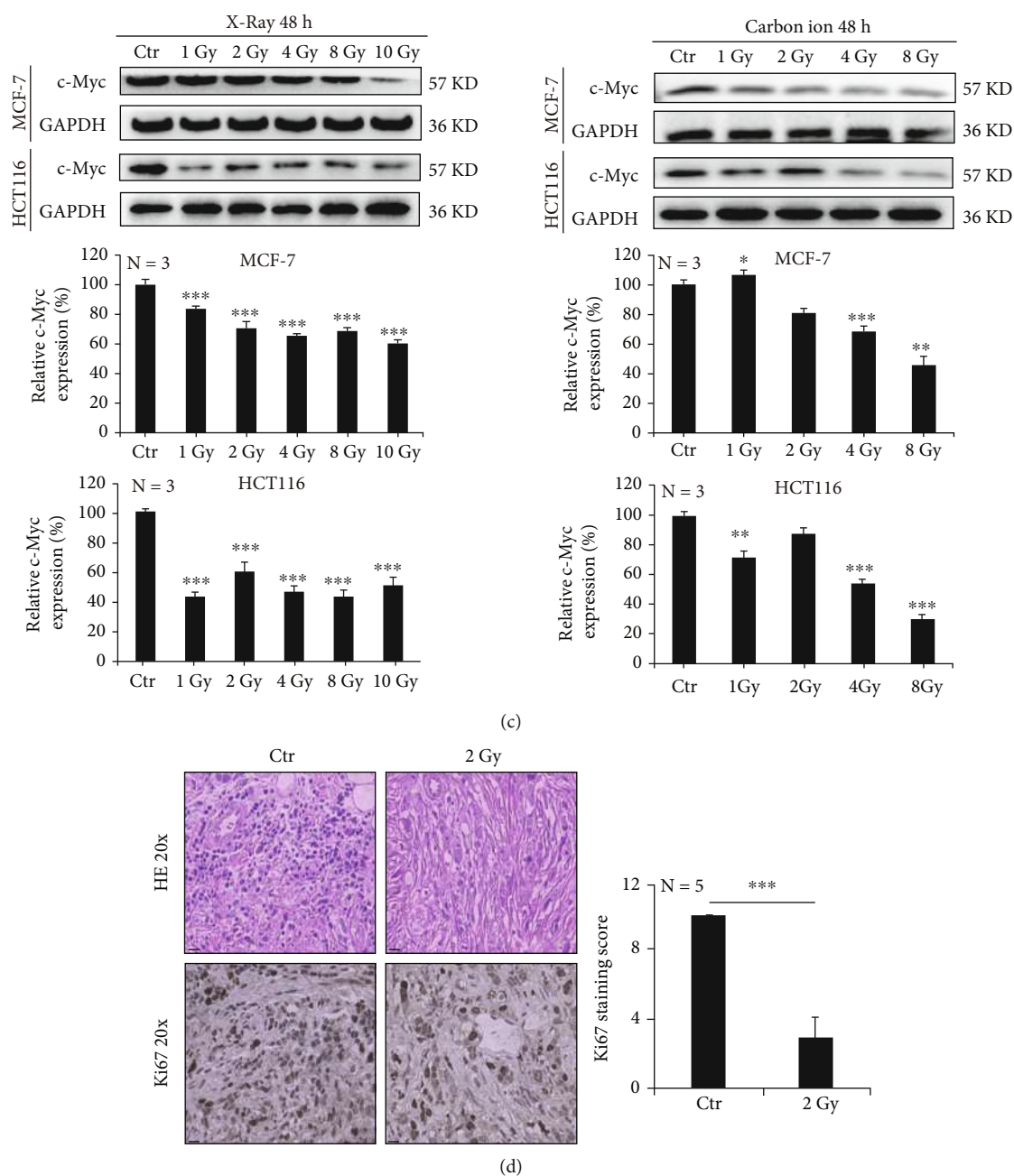
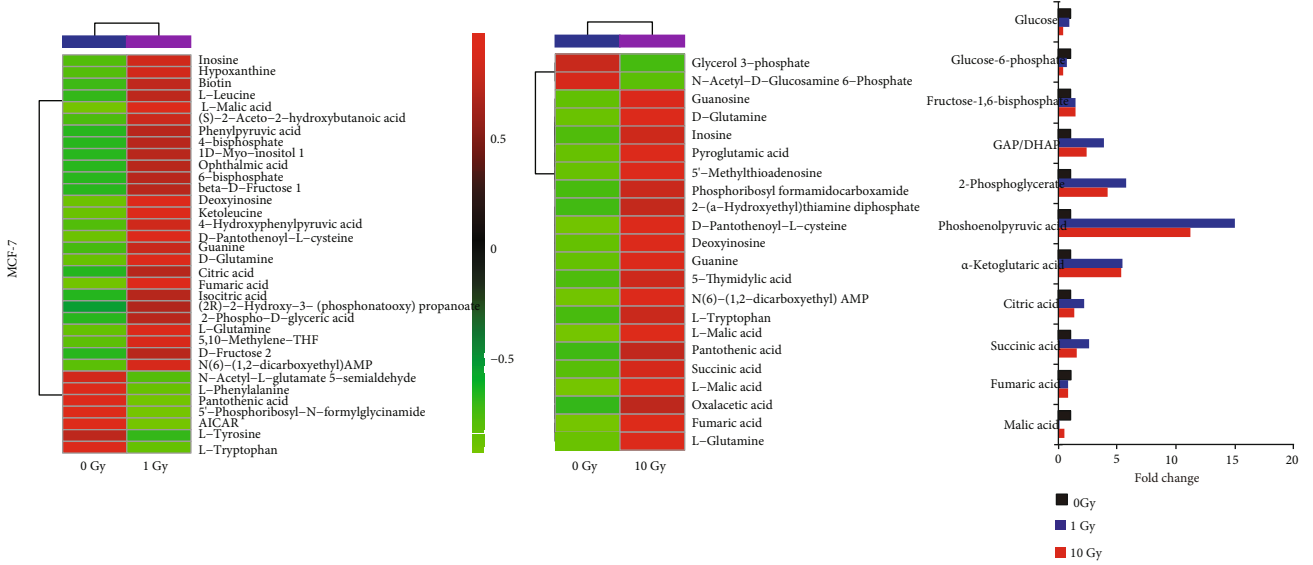


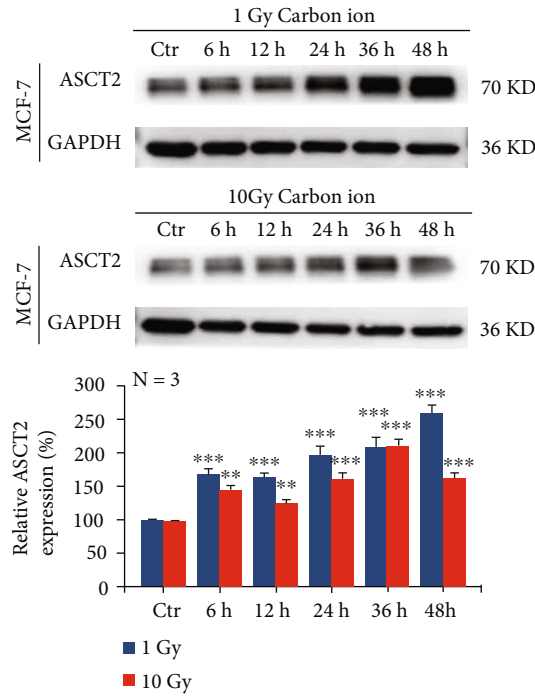
**FIGURE 1: Ionizing radiation inhibits cell proliferation.** MCF-7 and HCT-116 cells were irradiated with X-rays at different doses. At 48 h after irradiation, the morphology of cells became swollen (a). Clonal formation was inhibited by radiation in a dose-dependent manner (b). The expression of c-Myc protein was decreased after irradiation with different doses of X-rays and carbon ions (c). 2 Gy X-ray irradiation reduced the malignancy index of the MCF-7 tumor cells (d). Mean  $\pm$  SD of triplicate assessments, one-way ANOVA with post hoc Dunnett test, \* $p < 0.05$ , \*\* $p < 0.01$ , and \*\*\* $p < 0.001$  (b, c). Student's unpaired *t*-test, \*\*\* $p < 0.001$  (d).

(Figure 1(c)). In the *in vivo* experiment, 2 Gy X-rays were used to irradiate the tumor site of MCF-7 tumor-bearing nude mice. After 10 days of irradiation, the tumor was harvested and paraffin-embedded. We found that many cells in the tumor tissue died after hematoxylin-eosin staining, and Ki67 staining showed that the malignant proliferation of tumor cells was significantly decreased (Figure 1(d)). These results indicate that ionizing radiation can dramatically inhibit cell's malignant proliferation.

**3.1.2. Ionizing Radiation Upregulates Glutamine Metabolism in Tumour Cells.** In order to explore the reasons for the inhibition of cell proliferation, we explored whether ionizing radiation inhibited the energy supply of tumor cells from the perspective of glutamine metabolism. We irradiated MCF-7 cells with 1 Gy and 10 Gy carbon ion beams and found that the glucose metabolic flux was decreased, while the trichloroacetic acid (TCA) flux was increased considerably (Figure 2(a)). Meanwhile, Western blot analysis also

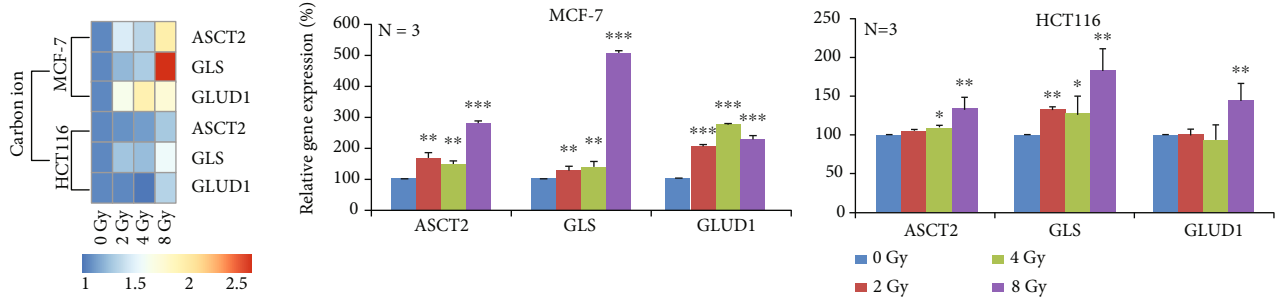


(a)

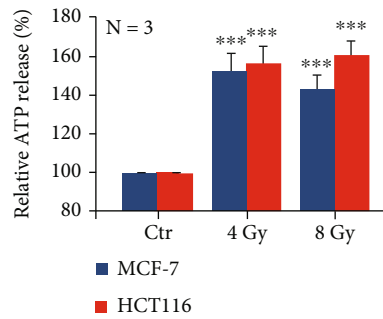


(b)

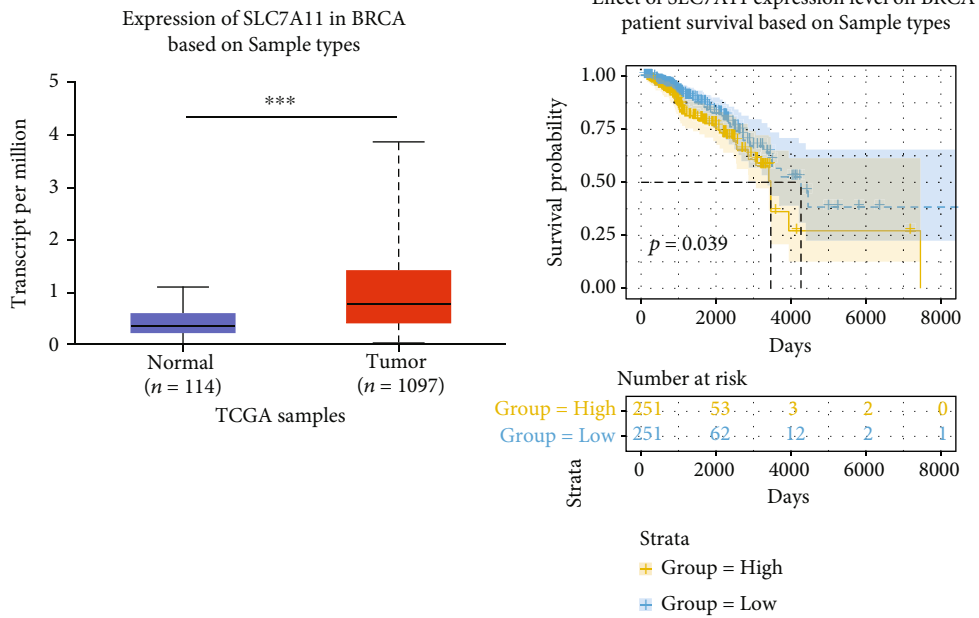
FIGURE 2: Continued.



(c)



(d)



(e)

FIGURE 2: Continued.

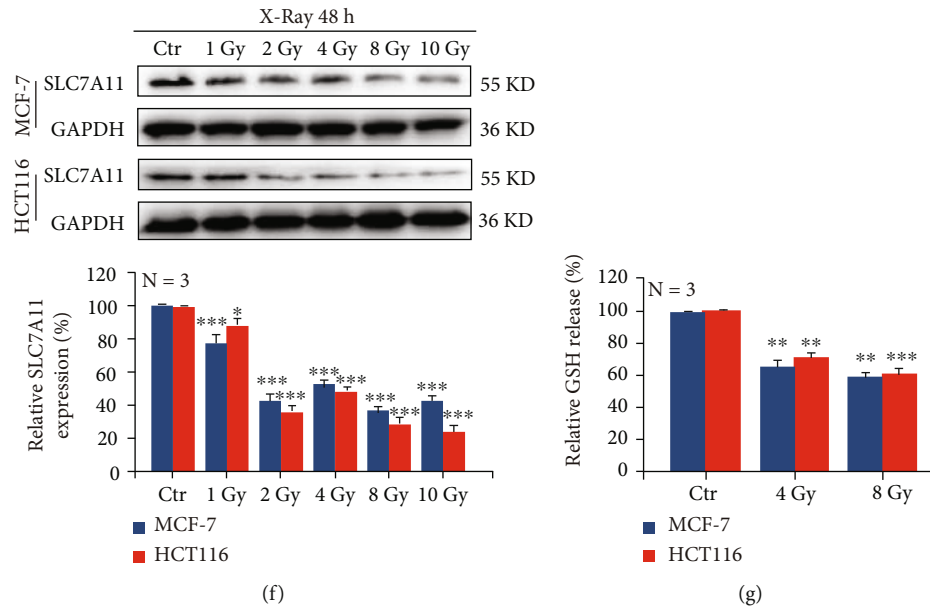


FIGURE 2: Ionizing radiation upregulates glutamine metabolism in tumor cells. MCF-7 cells were irradiated with 1 Gy and 10 Gy carbon ions. After 2 days, we performed an untargeted metabolome analysis and found that (a) the protein expression of ASCT2 increased in a time-dependent manner under carbon ion irradiation (b). Carbon ions could upregulate the mRNA expressions of ASCT2, GLS, and GLUD in MCF-7 cells, by real-time quantitative PCR detection (c). X-rays induced the increase of extracellular ATP secretion in MCF-7 cells, by ELISA detection (d). SLC7A11 gene was analyzed based on sample types in the TCGA database (e). The protein expression of SLC7A11 decreased in a dose-dependent manner under X-ray irradiation (f). ELISA detection revealed that X-ray irradiation reduced the GSH production in MCF-7 cells (g). Mean  $\pm$  SD of triplicate assessments, one-way repeated ANOVA test,  $^{**}p < 0.01$ , and  $^{***}p < 0.001$  (b). One-way ANOVA with post hoc Dunnett test,  $^{*}p < 0.05$ ,  $^{**}p < 0.01$ , and  $^{***}p < 0.001$  (c, d). Kaplan-Meier analysis with log-rank test,  $^{*}p < 0.05$ ,  $^{**}p < 0.01$ , and  $^{***}p < 0.001$  (e). One-way ANOVA with post hoc Dunnett test,  $^{*}p < 0.05$ ,  $^{**}p < 0.01$ , and  $^{***}p < 0.001$  (f, g).

confirmed that the carbon ion beam could upregulate the protein expression of ASCT2 (Figure 2(b)). In addition, we irradiated MCF-7 and HCT116 cells with 2 Gy, 4 Gy, and 8 Gy carbon ion beams and found that the mRNA expression of ASCT2, GLS, and GLUD increased 48 h after exposure (Figure 2(c)). We also found that ATP production increased at 48 h after 4 Gy and 8 Gy X-ray irradiation in MCF-7 and HCT116 cells by ELISA kit detection (Figure 2(d)).

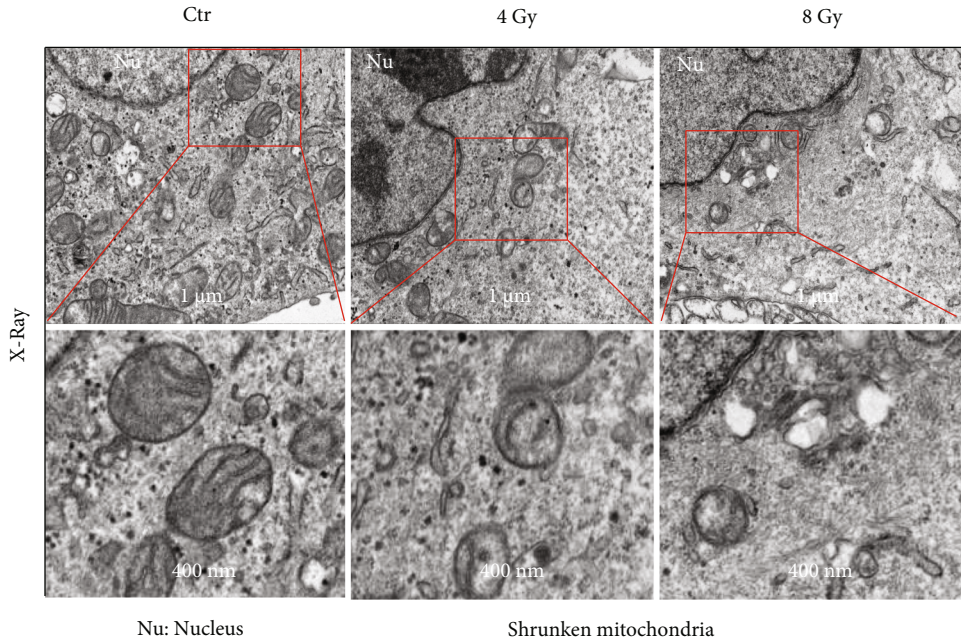
Furthermore, we analyzed the TCGA database and found that cancer patients with high SLC7A11 gene expression had a lower survival rate, which supports the idea that high SLC7A11 expression is usually an indicator of poor patient prognosis (Figure 2(e)). The protein expression of SLC7A11 decreased at 48 h after irradiation with different doses of X-rays in both MCF-7 and HCT116 cells (Figure 2(f)). In addition, we detected a significant decrease in GSH secretion in MCF-7 and HCT116 cells at 48 h after X-ray irradiation (Figure 2(g)). These results indicated that ionizing radiation did not inhibit the energy supply of tumor cells but upregulated the metabolic flux of glutamine instead.

**3.1.3. Ionizing Radiation Enhances Oxidative Stress in Tumor Cells.** According to the above results, ionizing radiation could induce tumor cells to produce more ATP, but cell proliferation was still inhibited. Therefore, we focused on the energy factory mitochondria to explore the mechanism. We irradiated MCF-7 and HCT116 cells with 4 Gy and

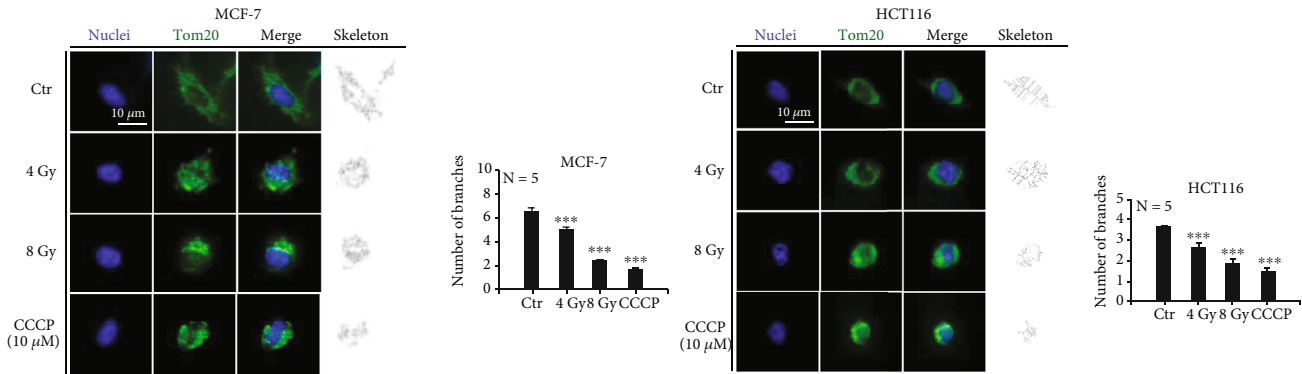
8 Gy X-rays. After 48 h, the mitochondria swelled, became deformed, and cristae broke in MCF-7 cells (Figure 3(a)). Subsequently, we used Tomm20 antibody to label mitochondria, and immunofluorescence results showed that both branched and unbranched cristae were smaller in MCF-7 and HCT116 cells after X-ray irradiation (Figure 3(b)).

In addition, some cells were labeled dihydrorhodamine 123 (DHR123). We found via flow cytometry that ROS has accumulated in an irradiation dose-dependent manner in the mitochondria (Figure 3(c)). In animal experiments, 2 Gy X-rays irradiated the MCF-7 tumor site, and we found by immunohistochemical analysis that the lipid peroxidation (MDA) was significantly increased (Figure 3(d)). In order to verify the relationship between the increased glutamine metabolic flux and the accumulation of ROS in mitochondria, which was induced by ionizing radiation, we irradiated MCF-7 and HCT116 cells, in combination with the glutaminase inhibitor epigallocatechin gallate (EGCG). We found that the combination treatment significantly decreased ROS accumulation (Figure 3(e)), and  $\gamma$ H2Ax staining and Western blot detection revealed that the nuclear DNA damage was also alleviated (Figures 3(f) and 3(g)). These results indicated that ionizing radiation induced intracellular ROS overaccumulation and enhanced cellular oxidative stress.

**3.1.4. Ionizing Radiation Induces Mitophagy in Tumor Cells.** Ionizing radiation caused excess ATP production in tumor



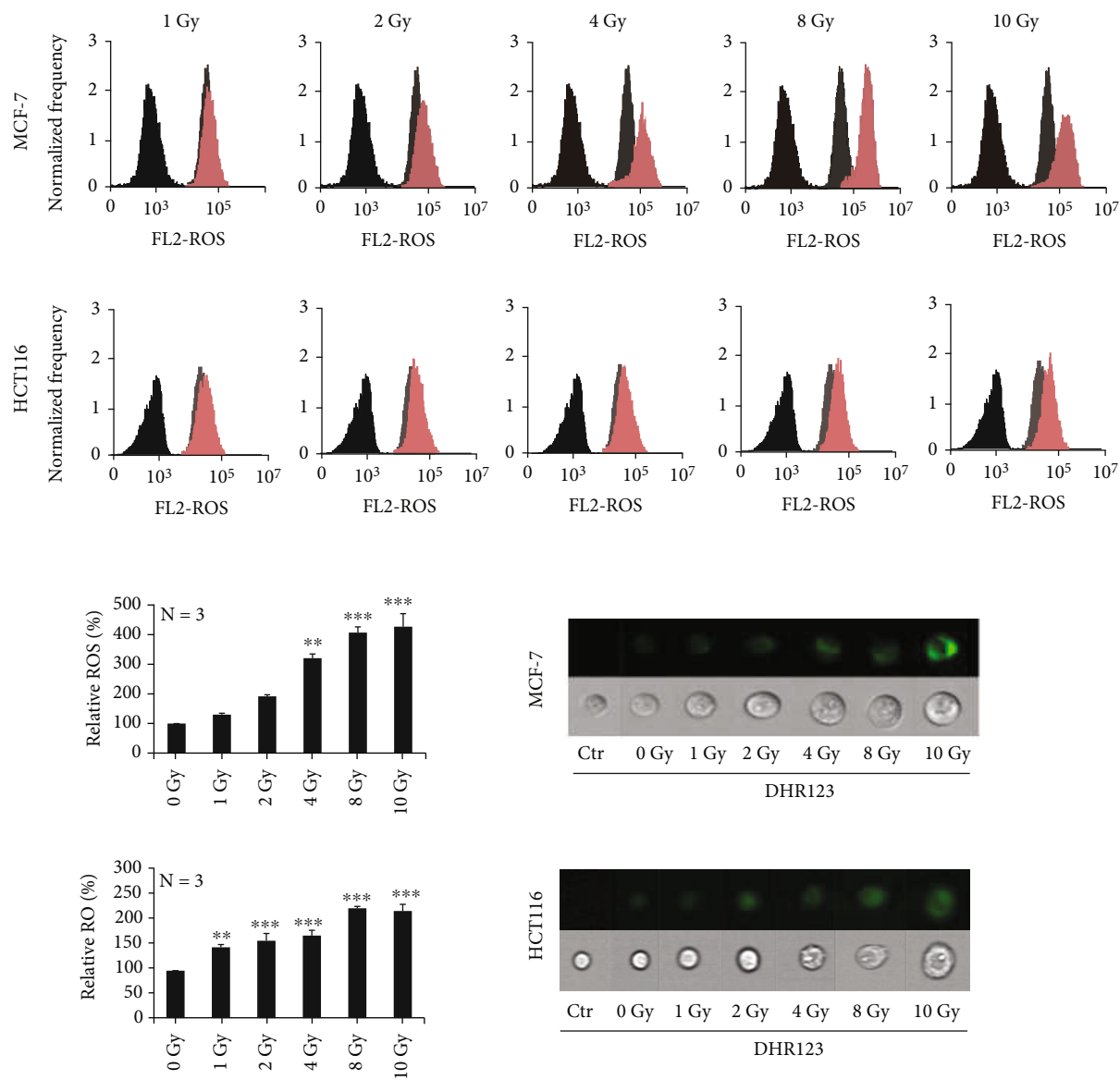
(a)



(b)

FIGURE 3: Continued.





(c)

FIGURE 3: Continued.

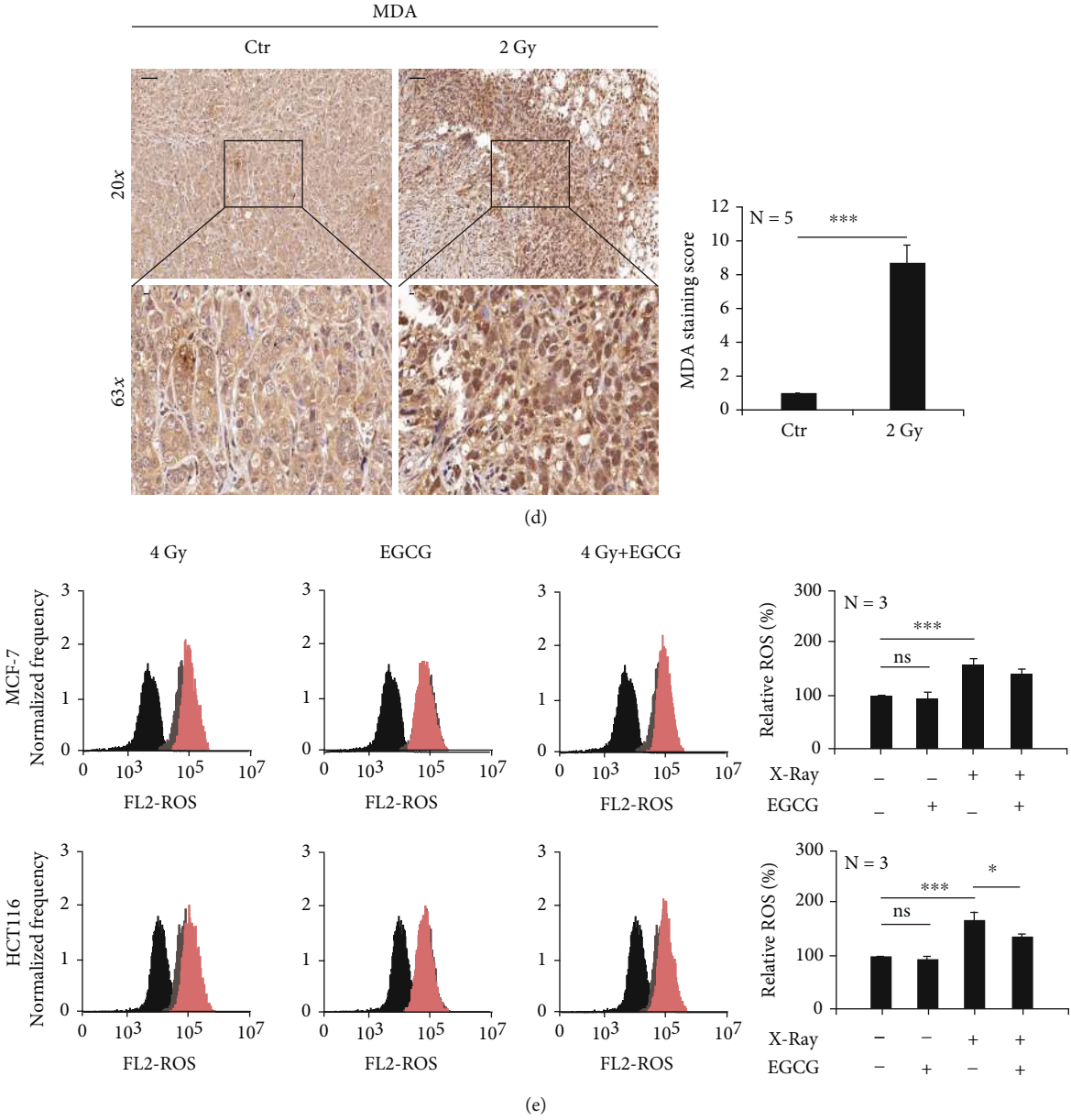
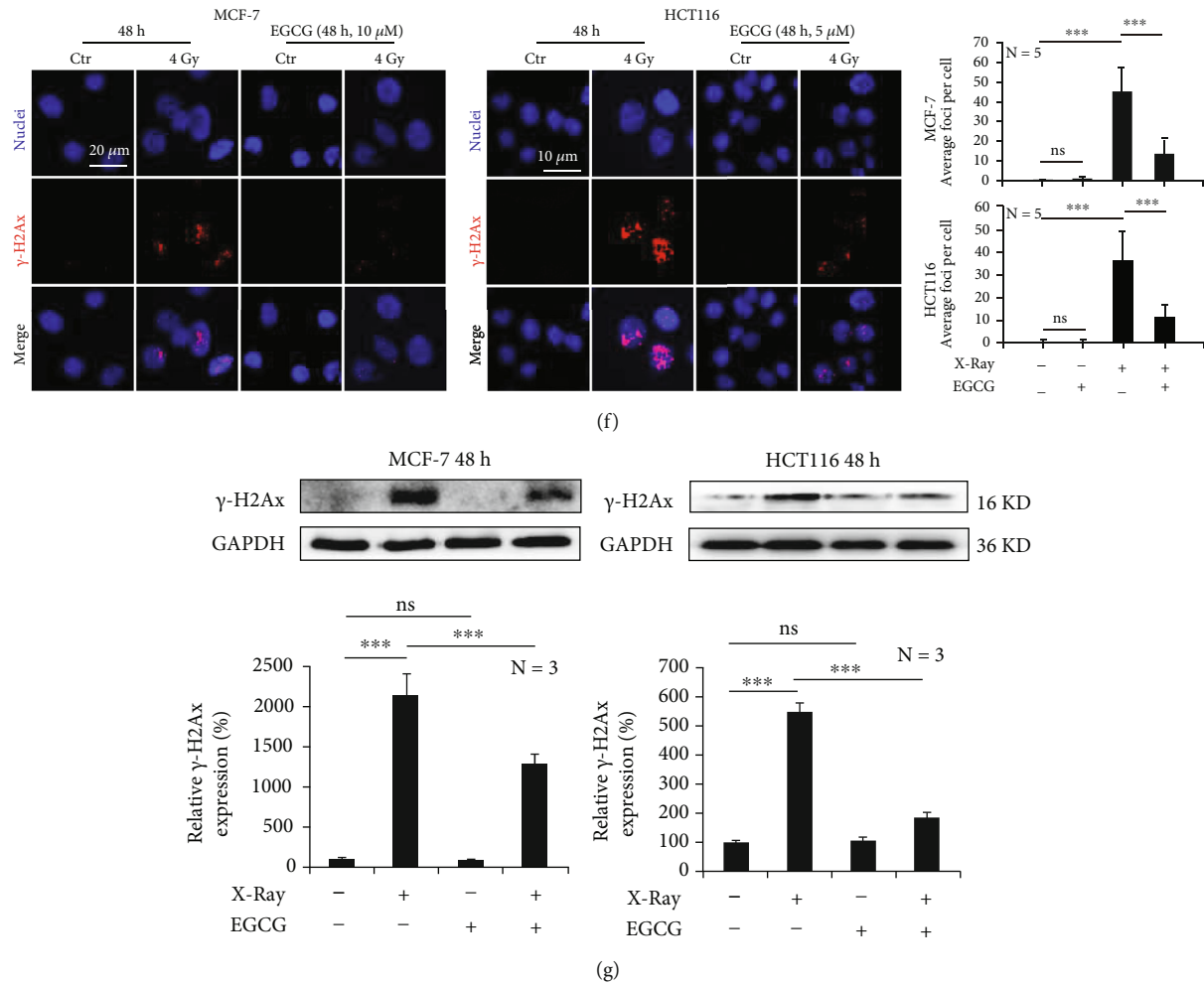


FIGURE 3: Continued.



**FIGURE 3: Ionizing radiation enhances oxidative stress in tumor cells.** MCF-7 and HCT-116 cells were irradiated with X-rays at different doses. The morphology of the mitochondria of MCF-7 cells was observed by transmission electron microscopy (a). Immunofluorescence staining showed that X-rays caused mitochondrial shrinkage (b). DHR123 staining showed that X-rays induced ROS accumulation in mitochondria in a dose-dependent manner (c). 2 Gy X-ray irradiation increased the peroxidation index of the MCF-7 tumor cells (d). Inhibition of glutamine metabolic flux reduces the accumulation of ROS (e) and reduces DNA damage (f, g) induced by ionizing radiation. Mean  $\pm$  SD of triplicate assessments, one-way ANOVA with post hoc Dunnett test,  $**p < 0.01$ , and  $***p < 0.001$  (b, c). Student's unpaired *t*-test,  $***p < 0.001$  (d). One-way ANOVA with post hoc Dunnett test,  $*p < 0.05$ ,  $**p < 0.01$ , and  $***p < 0.001$  (e-g).

cells, which resulted in ROS-induced oxidative stress in the mitochondria. Knowing this, we wanted to explore how mitochondria respond to oxidative stress. MCF-7 and HCT116 cells were irradiated with 1 Gy, 2 Gy, 4 Gy, 8 Gy, and 10 Gy of X-rays. After 48 h, acridine orange staining via flow cytometry detection revealed that the acidity of cells was significantly increased (Figure 4(a)). Results indicated that the expression of LC3B and Beclin 1 proteins was increased, while the expression of p62 was decreased (Figure 4(b)).

Furthermore, MCF-7 cells were irradiated with 4 Gy and 8 Gy X-rays. After 48 h, mitochondria and lysosomes were labeled using Mito-Tracker Green and Lyso-Tracker Red, respectively. We found that ionizing radiation induced a significant increase in mitochondrial and lysosome colocalization (Figure 4(c)). Subsequently, the expression of Parkin and LAMP2, a lysosomal marker protein, was also significantly increased in an irradiation dose-dependent manner

(Figure 4(d)). Although X-rays were found to increase the protein expression of cytochrome c in MCF-7 cells (Figure 4(e)), only mild apoptosis was detected by flow cytometry (Figure 4(f)). According to the above results, mitochondria activated mitophagy in order to resist the oxidative stress caused by ionizing radiation.

**3.1.5. Inhibition of Mitophagy Promotes Ionizing Radiation-Induced Cell Death.** Radiotherapy typically induces ROS accumulation in tumor cells, which causes DNA strand damage and leads to cell death. Therefore, we wanted to investigate whether cell death can be improved by preventing ROS clearing with the use of a mitophagy inhibitor.

MCF-7 and HCT116 cells were irradiated with X-rays and combined with Mdivi-1 treatment, which functioned as the mitophagy inhibitor. We found that branched and unbranched cristae in the mitochondria became smaller; however, immunofluorescence detection revealed that

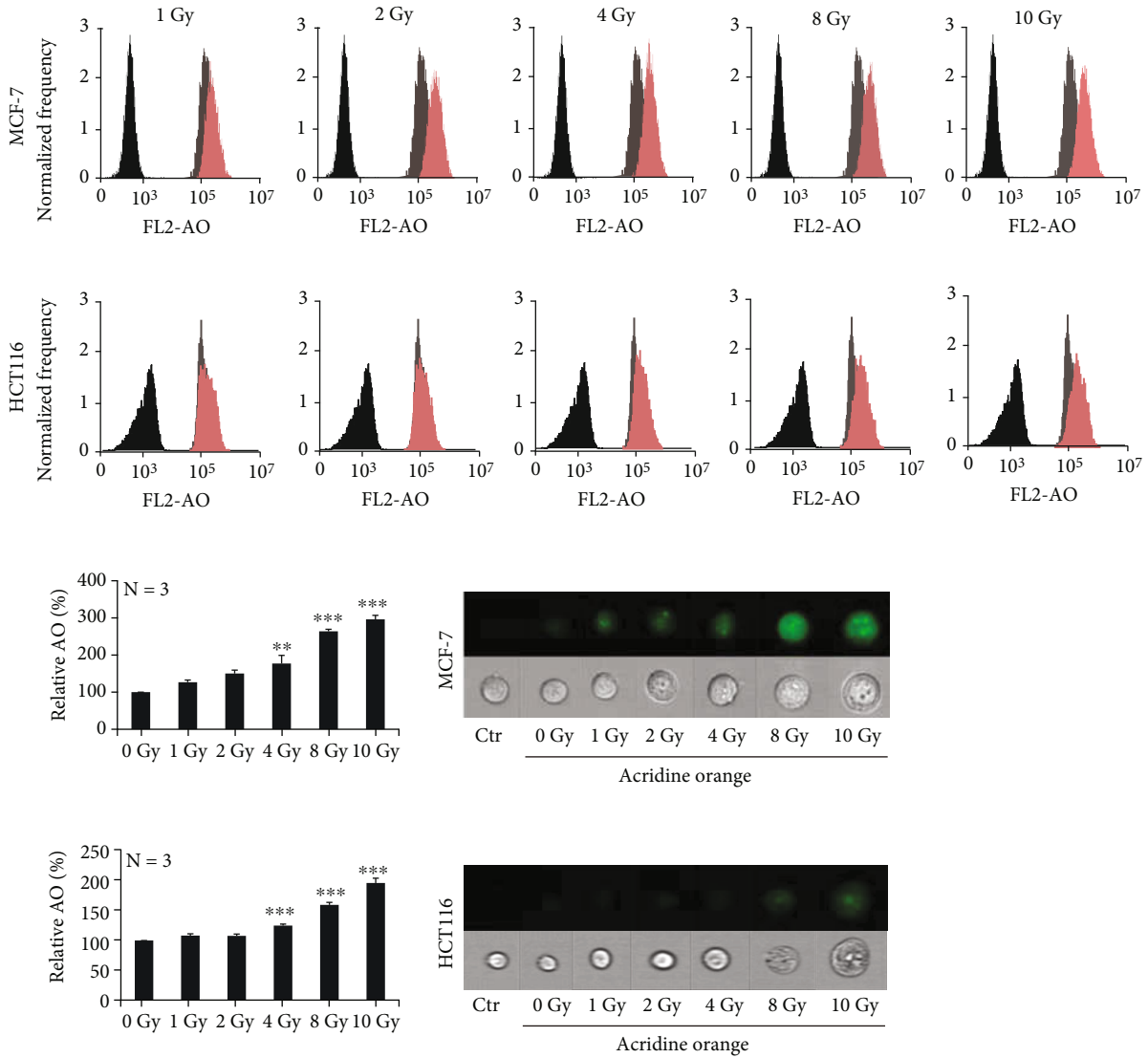
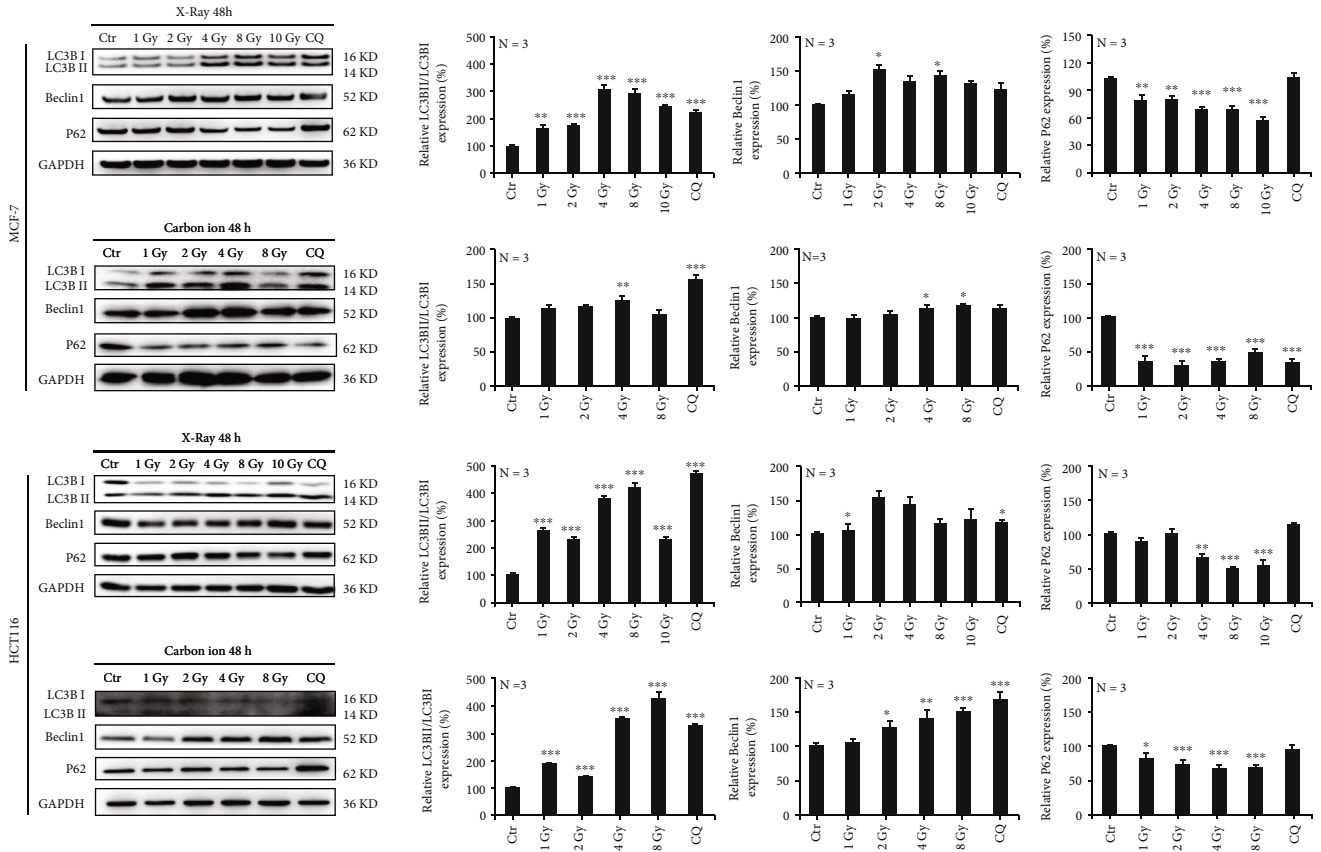
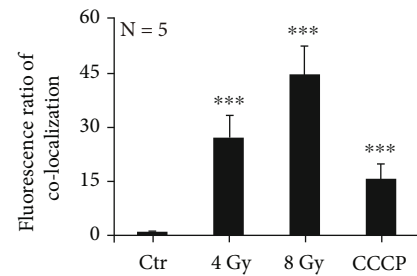
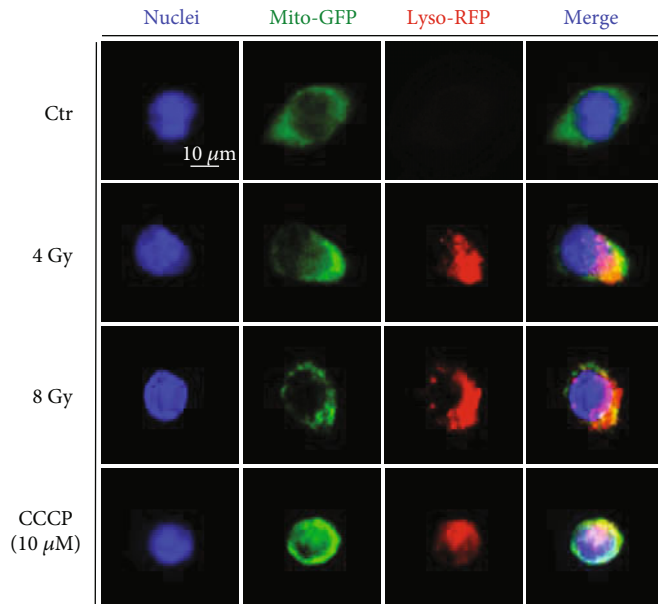


FIGURE 4: Continued.

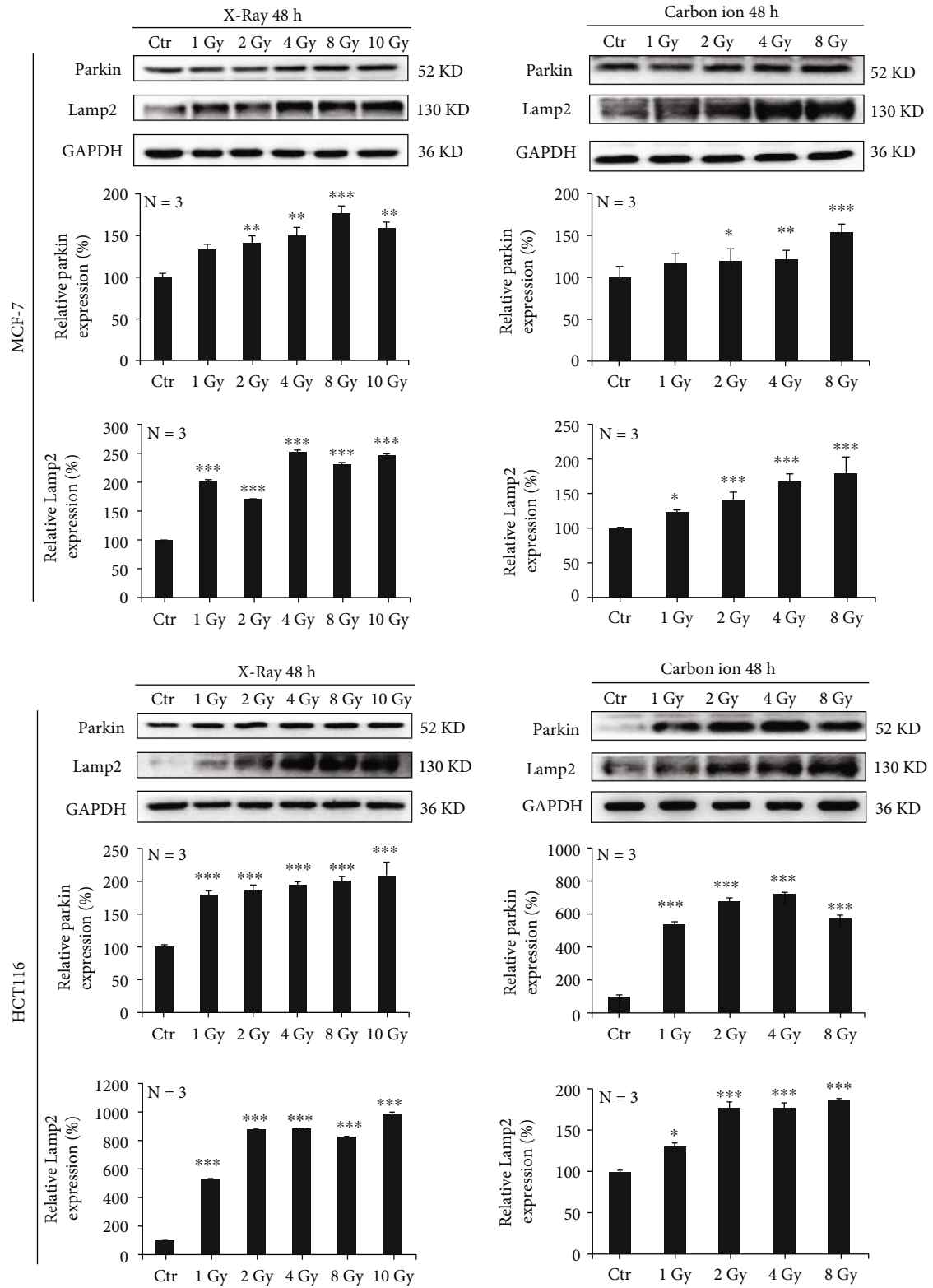


(b)



(c)

FIGURE 4: Continued.



(d)

FIGURE 4: Continued.

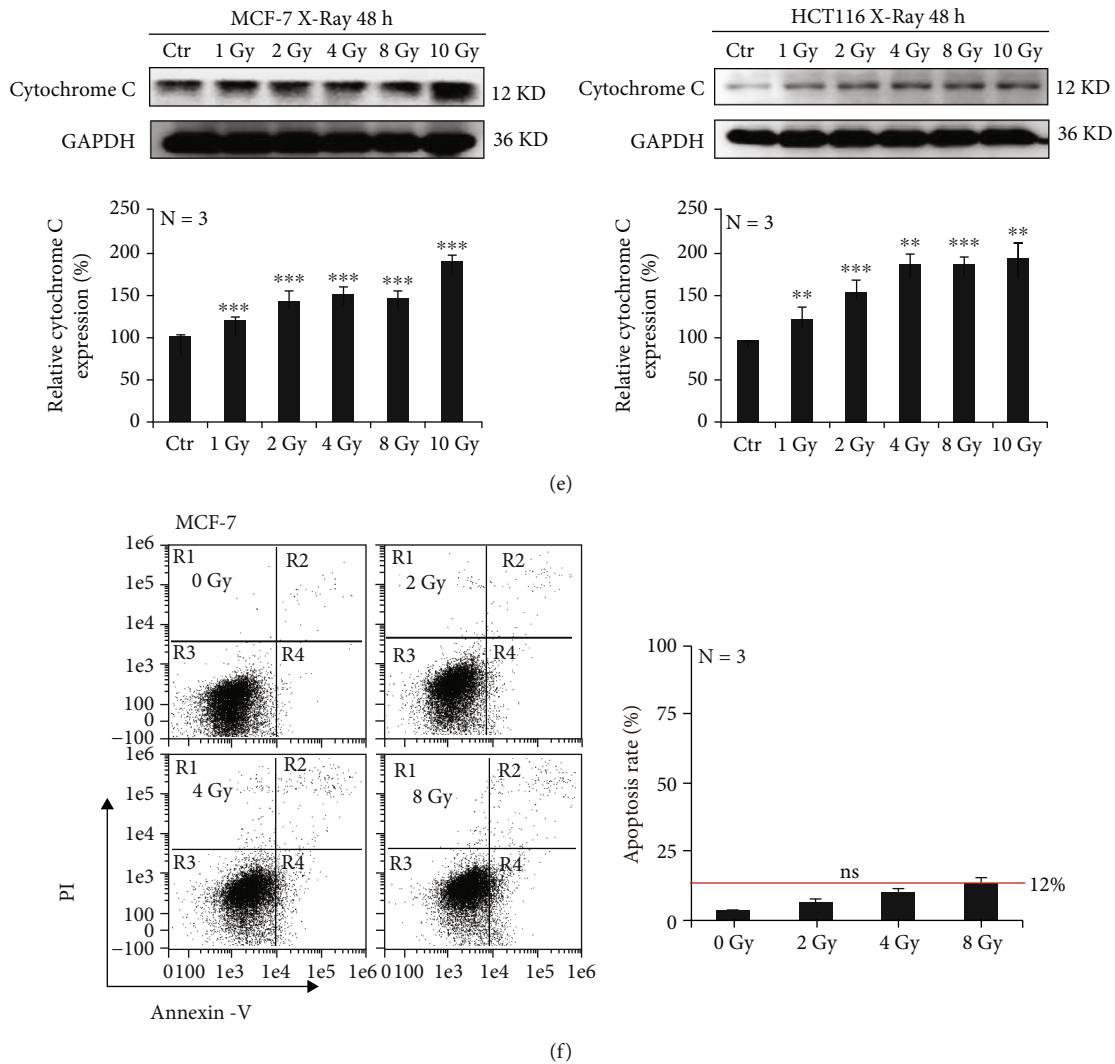


FIGURE 4: Ionizing radiation induces mitophagy in tumor cells. MCF-7 and HCT-116 cells were irradiated with X-rays at different doses. The acidity of cells was detected by flow cytometry with acridine orange staining (a). The expression of autophagy-associated proteins LC3B and Beclin 1 was increased, while that of p62 was decreased (b). X-rays increased the mitochondrial and lysosome colocalization (c). The expression of mitophagy-associated proteins Parkin and LAMP2 was increased in a dose-dependent manner (d). MCF-7 cells were irradiated with X-rays at different doses, and this induced the increased expression of cytochrome C (e) and very mild apoptosis at 24 h after irradiation (f). Mean  $\pm$  SD of triplicate assessments, one-way ANOVA with post hoc Dunnett test, \* $p < 0.05$ , \*\* $p < 0.01$ , and \*\*\* $p < 0.001$  (a–f).

Parkin expression was significantly reduced in MCF-7 cells (Figure 5(a)). We also found that Mdivi-1 significantly downregulated the protein expressions of Parkin, LAMP2, and LC3 induced by ionizing radiation in MCF-7 and HCT116 cells (Figure 5(b)). In addition, Mdivi-1 further downregulated mitochondrial membrane potential (Figure 5(c)) and caused increased ROS accumulation after ionizing radiation in both MCF-7 and HCT-116 cells (Figure 5(d)). Ultimately, the combination treatment led to more nuclear DNA damage (Figures 5(e) and 5(f)). When the Parkin gene was knocked down in MCF-7 and HCT116 cells (Figure 5(g)), X-rays were able to significantly induce ROS production (Figure 5(h)). The use of Mdivi-1 and the knockdown of the Parkin gene significantly increased X-ray-induced cell death (Figures 5(i) and 5(j)) and reduced clone formation (Figure 5(k)). Based on

these results, it can be concluded that the inhibition of mitophagy can increase the accumulation of ROS and induce an increased level of cell death.

#### 4. Discussion

Ionizing radiation downregulated the glucose metabolic flux of cells, which in turn upregulated the glutamine metabolic flux in order to provide sufficient energy to maintain survival. Our study showed that high glutamine metabolic flux induces the production of a large amount of  $\alpha$ -ketoglutaric acid, which greatly increases the productivity of the TCA cycle and leads to the accumulation of a large amount of ROS. The expression of SLC7A11 in MCF-7 and HCT116 cells decreased after ionizing radiation, leading to reduced

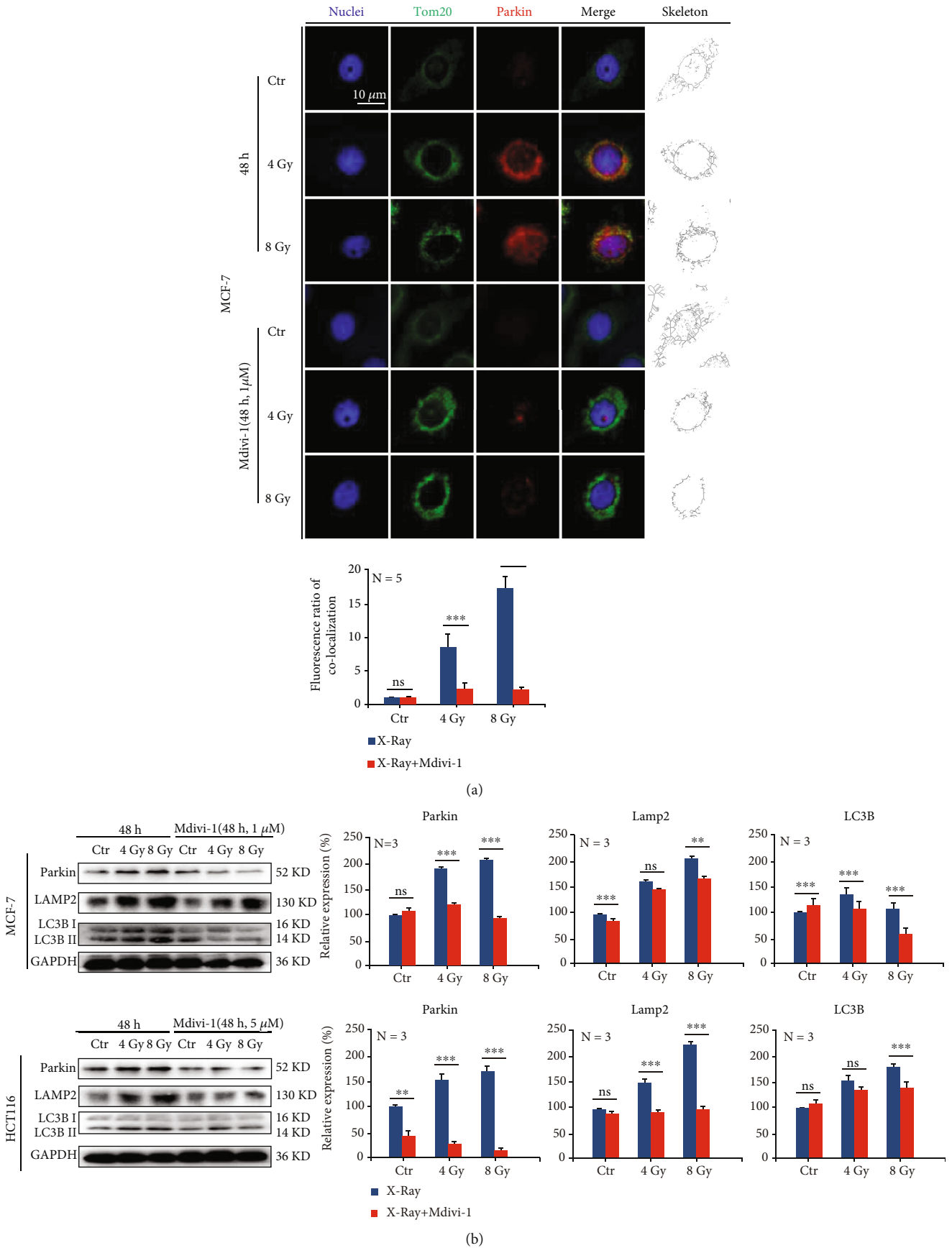


FIGURE 5: Continued.



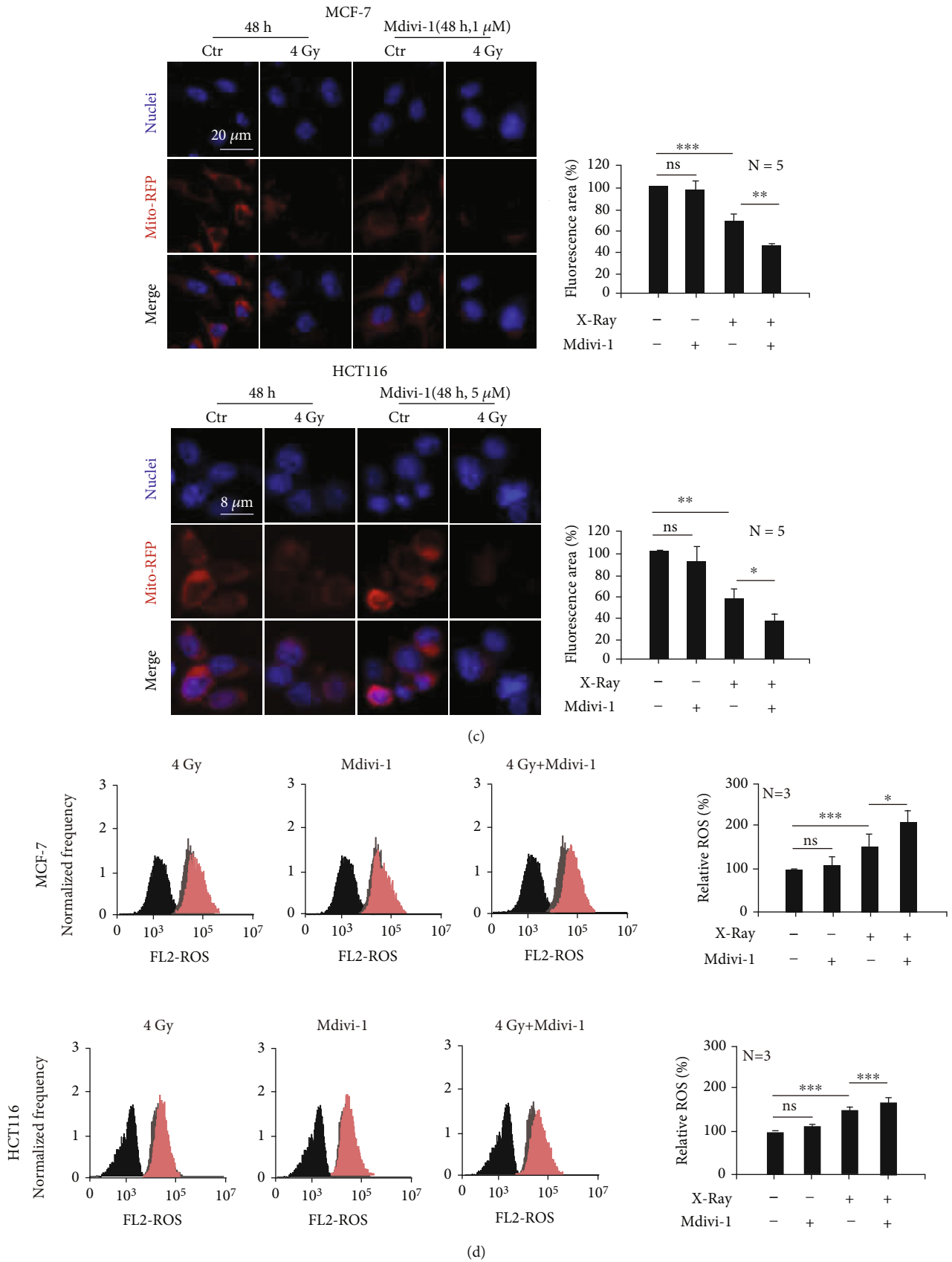


FIGURE 5: Continued.

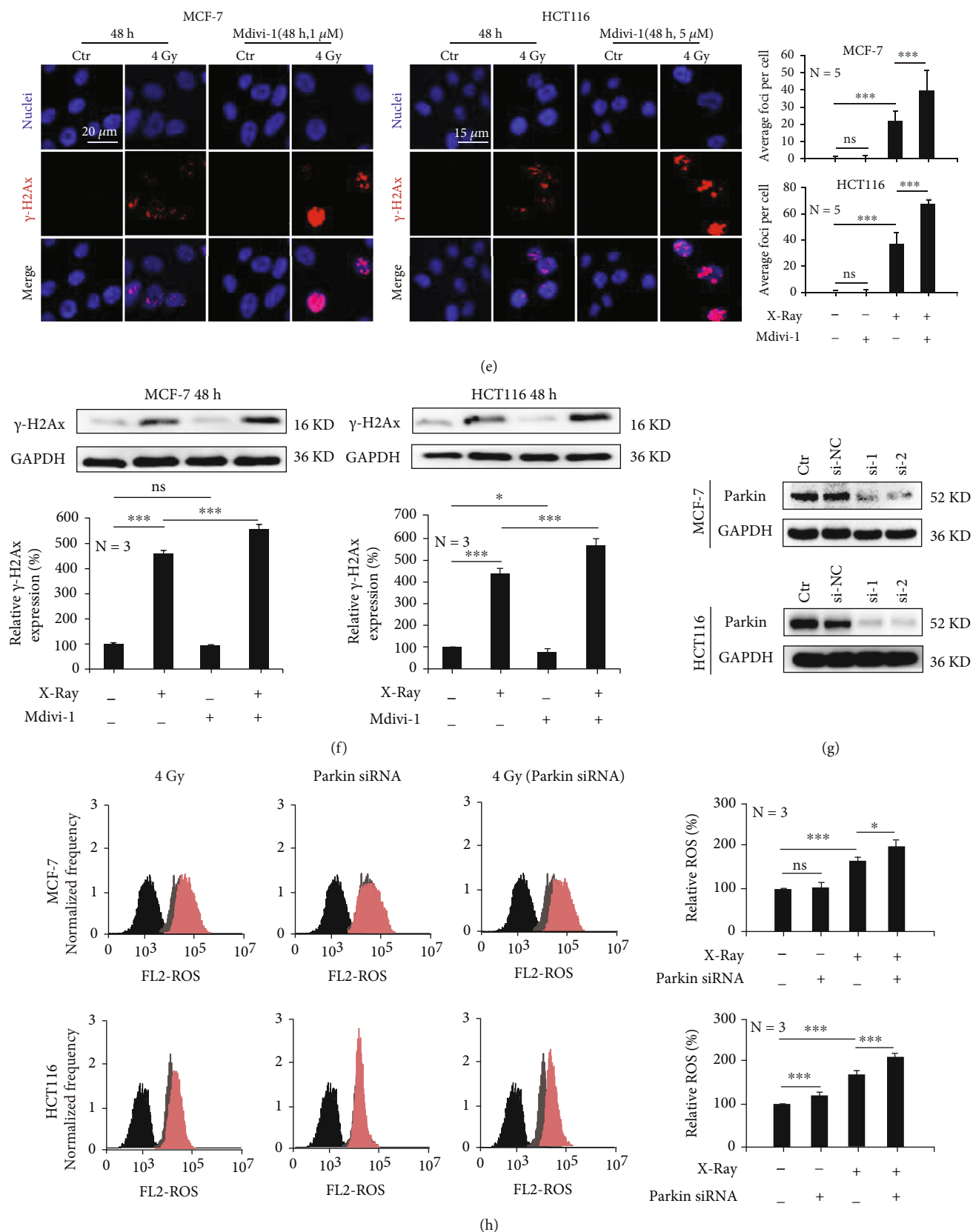


FIGURE 5: Continued.

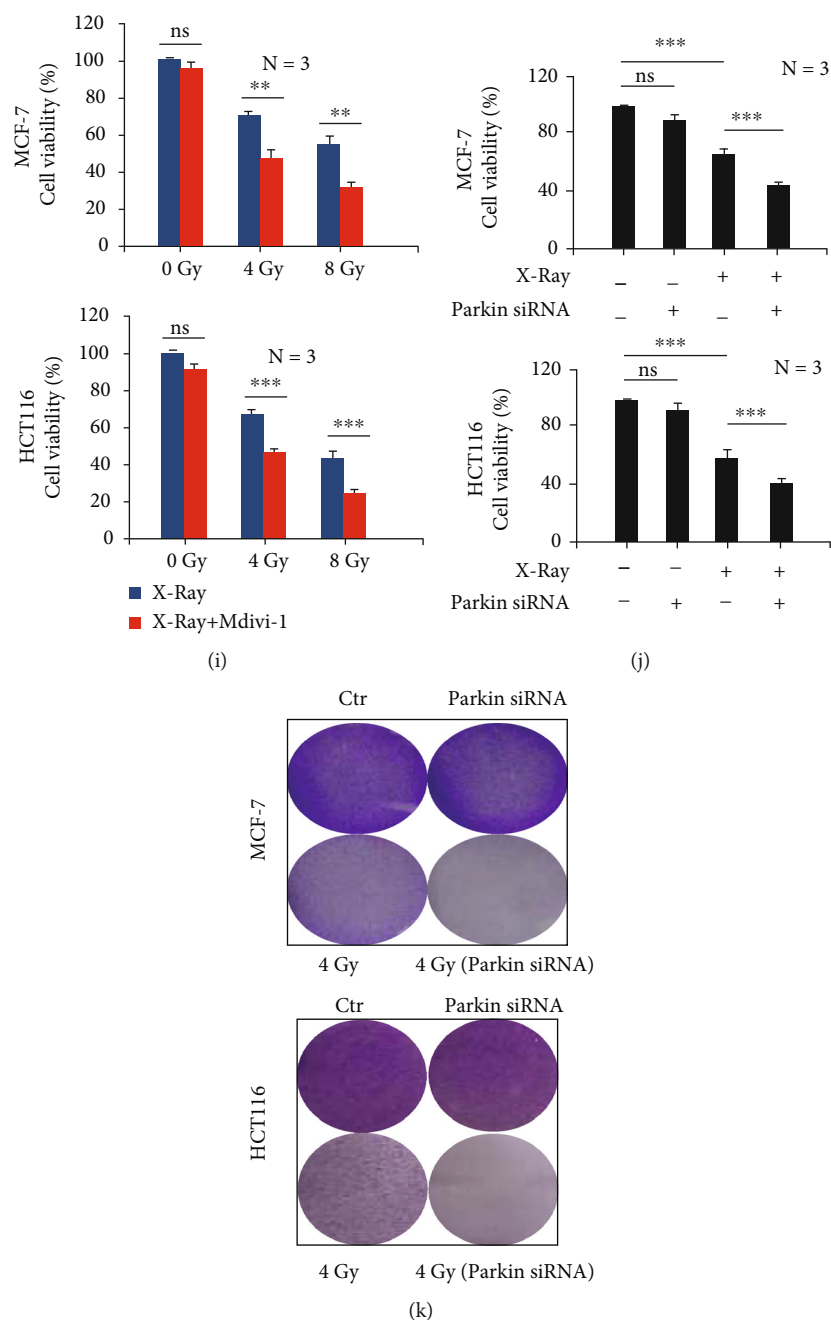


FIGURE 5: Inhibition of mitophagy promotes ionizing radiation-induced cell death. MCF-7 and HCT-116 cells were irradiated with 4 Gy and/or 8 Gy X-rays. Mdivi-1 decreased X-ray-induced expression of mitophagy-related proteins (a, b) and the mitochondrial membrane potential (c). Mdivi-1 led to increased ROS accumulation (d) and increased DNA damage (e, f). Silencing the Parkin gene (g) led to increased ROS accumulation induced by X-rays (h). Mdivi-1 or silencing the Parkin gene enhanced cell death induced by X-rays (i, j) and reduced clone formation (k). Mean  $\pm$  SD of triplicate assessments, one-way ANOVA with post hoc Dunnett test, \* $p < 0.05$ , \*\* $p < 0.01$ , and \*\*\* $p < 0.001$  (a–k).

glutathione synthesis and the inability to consume the ROS that had been produced by the TCA cycle. This resulted in oxidative stress injury to cells and ultimately led to cell death.

It has been previously reported that a high glutamine metabolic flux can inhibit the apoptosis of tumor cells [32]. In our study, it was also confirmed that the rate of apoptosis in MCF-7 cells was only about 10% after 4 Gy X-ray irradiation;

however, the expression of cytochrome c was elevated. We believe that the release of cytochrome c may be associated with decreased mitochondrial membrane potential because this also induced mitophagy and then cleared the damaged mitochondria. Cytochrome c may help maintain cell survival instead of apoptosis. Studies have shown that the upregulation of the c-Myc gene can increase the metabolic flux of glutamine in tumor cells [33]. In our study,

ionizing radiation downregulated the expression of c-Myc and upregulated the metabolic flux of glutamine. This indicates that the high flux of glutamine metabolism induced by ionizing radiation does not depend on the regulation of the c-Myc gene.

The wide application of stereotactic body radiotherapy improves the accuracy and safety of clinical radiotherapy and dramatically reduces the damage to normal tissues [34]. Although high doses of ionizing radiation induce cell death, cells can also change their fate through other mechanisms, such as mitophagy [35]. ROS production induced by ionizing radiation can cause autophagy as a stress response, and excessive accumulation of ROS can cause mitophagy. Our study confirmed that ionizing radiation could significantly induce increases in Parkin expression. Mitophagy not only saves a cell by clearing out damaged mitochondria but also reduces the effectiveness of radiotherapy for cancer patients. Blocking mitophagy may help inhibit the self-rescue mechanism of tumor cells. We further irradiated MCF-7 and HCT116 cells and combined these cells with the mitophagy inhibitor Mdivi-1. Results showed that cell death increased significantly. We further demonstrated that inhibition of mitophagy by knockdown of the Parkin gene could markedly reduce ionizing radiation-induced cell death. We therefore believe that targeting Parkin can help regulate cell death, so it could be a new radio sensitization target in tumor radiotherapy.

## 5. Conclusions

In conclusion, ionizing radiation could upregulate the glutamine metabolic flux and enhance ROS accumulation in mitochondria. Ionizing radiation was also found to decrease SLC7A11 expression, which resulted in reduced GSH generation. In this way, inhibition of mitophagy can increase ionizing radiation-induced cell death.

## Data Availability

All data generated and analyzed during this study are included in this article. Each experiment was performed at least three times independently.

## Conflicts of Interest

None of the authors have any conflicts to disclose.

## Authors' Contributions

Pengfei Yang and Xiangxia Luo contributed equally to this work.

## Acknowledgments

We would like to thank the staff of the Biological Centre of Modern Physics, CAS for their contributions to this work. This work was supported by the National Nature Science Foundation of China (no. 11905264, Heng Zhou), the Nonprofit Central Research Institute Found of Chinese Academy of Medical Sciences (no. 2019PT320005, Xiaoling

Gao), the Science and Technology Research Project of Gansu Province (nos. 17JR5RA307 and 145RTSA012, Jufang Wang), the National Nature Science Foundation of China (no. 81960888, Xiangxia Luo).

## Supplementary Materials

*Supplementary 1.* Supplementary Table 1: list of antibodies and chemicals.

*Supplementary 2.* Supplementary Table 2: list of primers.

*Supplementary 3.* R language analysis code.

*Supplementary 4.* SLC7A11-BRCA-patient database.

## References

- [1] O. Warburg, "On the origin of cancer cells," *Science*, vol. 123, no. 3191, pp. 309–314, 1956.
- [2] B. I. Reinfeld, M. Z. Madden, M. M. Wolf et al., "Cell-programmed nutrient partitioning in the tumour microenvironment," *Nature*, vol. 593, no. 7858, pp. 282–288, 2021.
- [3] W. Durante, "The emerging role of l-glutamine in cardiovascular health and disease," *Nutrients*, vol. 11, no. 9, p. 2092, 2019.
- [4] W. Dai, L. Xu, X. Yu et al., "\_OGDHL\_ silencing promotes hepatocellular carcinoma by reprogramming glutamine metabolism," *Journal of Hepatology*, vol. 72, no. 5, pp. 909–923, 2020.
- [5] A. J. Bott, S. Maimouni, and W. X. Zong, "The pleiotropic effects of glutamine metabolism in cancer," *Cancers (Basel)*, vol. 11, no. 6, p. 770, 2019.
- [6] P. Lee, D. Malik, N. Perkons et al., "Targeting glutamine metabolism slows soft tissue sarcoma growth," *Nature Communications*, vol. 11, no. 1, p. 498, 2020.
- [7] E. Teixeira, C. Silva, and F. Martel, "The role of the glutamine transporter ASCT2 in antineoplastic therapy," *Cancer Chemotherapy and Pharmacology*, vol. 87, no. 4, pp. 447–464, 2021.
- [8] T. Li and A. Le, "Glutamine metabolism in cancer," *Advances in Experimental Medicine and Biology*, vol. 1063, pp. 13–32, 2018.
- [9] D. G. Ogando, M. Choi, R. Shyam, S. Li, and J. A. Bonanno, "Ammonia sensitive SLC4A11 mitochondrial uncoupling reduces glutamine induced oxidative stress," *Redox Biology*, vol. 26, article ???, 2019.
- [10] A. K. Bachhawat and S. Yadav, "The glutathione cycle: glutathione metabolism beyond the  $\gamma$ -glutamyl cycle," *IUBMB Life*, vol. 70, no. 7, pp. 585–592, 2018.
- [11] L. Wang, Y. Liu, T. du et al., "ATF3 promotes erastin-induced ferroptosis by suppressing system Xc<sup>-</sup>," *Cell Death and Differentiation*, vol. 27, no. 2, pp. 662–675, 2020.
- [12] P. Koppula, L. Zhuang, and B. Gan, "Cystine transporter SLC7A11/xCT in cancer: ferroptosis, nutrient dependency, and cancer therapy," *Protein & Cell*, vol. 12, no. 8, pp. 599–620, 2021.
- [13] G. Lei, Y. Zhang, P. Koppula et al., "The role of ferroptosis in ionizing radiation-induced cell death and tumor suppression," *Cell Research*, vol. 30, no. 2, pp. 146–162, 2020.
- [14] C. S. Shin, P. Mishra, J. D. Watrous et al., "The glutamate/cystine xCT antiporter antagonizes glutamine metabolism and

- reduces nutrient flexibility,” *Nature Communications*, vol. 8, no. 1, p. 15074, 2017.
- [15] H. Jin, S. Wang, E. A. Zaal et al., “A powerful drug combination strategy targeting glutamine addiction for the treatment of human liver cancer,” *eLife*, vol. 9, 2020.
- [16] S. Qie, A. Yoshida, S. Parnham et al., “Targeting glutamine-addiction and overcoming CDK4/6 inhibitor resistance in human esophageal squamous cell carcinoma,” *Nature Communications*, vol. 10, no. 1, p. 1296, 2019.
- [17] M. Gao, J. Yi, J. Zhu et al., “Role of mitochondria in ferroptosis,” *Molecular Cell*, vol. 73, no. 2, pp. 354–363.e3, 2019.
- [18] M. Gao, P. Monian, N. Quadri, R. Ramasamy, and X. Jiang, “Glutaminolysis and transferrin regulate ferroptosis,” *Molecular Cell*, vol. 59, no. 2, pp. 298–308, 2015.
- [19] V. Eisner, M. Picard, and G. Hajnoczky, “Mitochondrial dynamics in adaptive and maladaptive cellular stress responses,” *Nature Cell Biology*, vol. 20, no. 7, pp. 755–765, 2018.
- [20] M. Onishi, K. Yamano, M. Sato, N. Matsuda, and K. Okamoto, “Molecular mechanisms and physiological functions of mitophagy,” *The EMBO Journal*, vol. 40, no. 3, article e104705, 2021.
- [21] N. M. Held and R. H. Houtkooper, “Mitochondrial quality control pathways as determinants of metabolic health,” *BioEssays*, vol. 37, no. 8, pp. 867–876, 2015.
- [22] G. Ashrafi and T. L. Schwarz, “The pathways of mitophagy for quality control and clearance of mitochondria,” *Cell Death and Differentiation*, vol. 20, no. 1, pp. 31–42, 2013.
- [23] J. P. Bernardini, M. Lazarou, and G. Dewson, “Parkin and mitophagy in cancer,” *Oncogene*, vol. 36, no. 10, pp. 1315–1327, 2017.
- [24] P. M. J. Quinn, P. I. Moreira, A. F. Ambrosio, and C. H. Alves, “PINK1/PARKIN signalling in neurodegeneration and neuroinflammation,” *Acta Neuropathologica Communications*, vol. 8, no. 1, p. 189, 2020.
- [25] H. Wu, T. Wang, Y. Liu et al., “Mitophagy promotes sorafenib resistance through hypoxia-inducible ATAD3A dependent axis,” *Journal of Experimental & Clinical Cancer Research*, vol. 39, no. 1, p. 274, 2020.
- [26] K. Liu, J. Lee, J. Y. Kim et al., “Mitophagy controls the activities of tumor suppressor p53 to regulate hepatic cancer stem cells,” *Molecular Cell*, vol. 68, no. 2, pp. 281–292.e5, 2017.
- [27] J. Lee, K. Liu, B. Stiles, and J. J. Ou, “Mitophagy and hepatic cancer stem cells,” *Autophagy*, vol. 14, no. 4, pp. 715–716, 2018.
- [28] K. Kawamura, F. Qi, and J. Kobayashi, “Potential relationship between the biological effects of low-dose irradiation and mitochondrial ROS production,” *Journal of Radiation Research*, vol. 59, suppl\_2, pp. ii91–ii97, 2018.
- [29] L. J. Su, J. H. Zhang, H. Gomez et al., “Reactive oxygen species-induced lipid peroxidation in apoptosis, autophagy, and ferroptosis,” *Oxidative Medicine and Cellular Longevity*, vol. 2019, 13 pages, 2019.
- [30] M. Chang, X. Song, X. Geng et al., “Temozolomide-perillyl alcohol conjugate impairs mitophagy flux by inducing lysosomal dysfunction in non-small cell lung cancer cells and sensitizes them to irradiation,” *Journal of Experimental & Clinical Cancer Research*, vol. 37, no. 1, p. 250, 2018.
- [31] P. Yang, X. Feng, J. Li et al., “Ionizing radiation downregulates estradiol synthesis via endoplasmic reticulum stress and inhibits the proliferation of estrogen receptor-positive breast cancer cells,” *Cell Death & Disease*, vol. 12, no. 11, p. 1029, 2021.
- [32] A. R. Kallweit, C. H. Baird, D. K. Stutzman, and P. E. Wischmeyer, “Glutamine prevents apoptosis in intestinal epithelial cells and induces differential protective pathways in heat and oxidant injury models,” *JPEN Journal of Parenteral and Enteral Nutrition*, vol. 36, no. 5, pp. 551–555, 2012.
- [33] N. Venkateswaran, M. C. Lafita-Navarro, Y. H. Hao et al., “MYC promotes tryptophan uptake and metabolism by the kynurenine pathway in colon cancer,” *Genes & Development*, vol. 33, no. 17–18, pp. 1236–1251, 2019.
- [34] A. Bezjak, R. Paulus, L. E. Gaspar et al., “Safety and efficacy of a five-fraction stereotactic body radiotherapy schedule for centrally located non-small-cell lung cancer: NRG oncology/RTOG 0813 trial,” *Journal of Clinical Oncology*, vol. 37, no. 15, pp. 1316–1325, 2019.
- [35] M. Chaurasia, A. N. Bhatt, A. Das, B. S. Dwarakanath, and K. Sharma, “Radiation-induced autophagy: mechanisms and consequences,” *Free Radical Research*, vol. 50, no. 3, pp. 273–290, 2016.

## Research Article

# The Synergistic Reducing Drug Resistance Effect of Cisplatin and Ursolic Acid on Osteosarcoma through a Multistep Mechanism Involving Ferritinophagy

Zhen Tang,<sup>1</sup> Hui Dong,<sup>1</sup> Tian Li ,<sup>2</sup> Ning Wang,<sup>1</sup> Xinghui Wei,<sup>1</sup> Hao Wu,<sup>1</sup> Yichao Liu,<sup>1</sup> Wei Wang ,<sup>3</sup> Zheng Guo ,<sup>4</sup> and Xin Xiao <sup>1</sup>

<sup>1</sup>Department of Orthopedics, Xijing Hospital, Fourth Military Medical University, Xi'an, China

<sup>2</sup>School of Basic Medicine, Fourth Military Medical University, Xi'an, China

<sup>3</sup>Department of Immunology, State Key Laboratory of Cancer Biology, Fourth Military Medical University, Xi'an, China

<sup>4</sup>Department of Orthopaedics, Tangdu Hospital, Fourth Military Medical University, Xi'an, China

Correspondence should be addressed to Wei Wang; [wwang115@fmmu.edu.cn](mailto:wwang115@fmmu.edu.cn), Zheng Guo; [guozheng@fmmu.edu.cn](mailto:guozheng@fmmu.edu.cn), and Xin Xiao; [xiao\\_xxyfsxx@sina.com](mailto:xiao_xxyfsxx@sina.com)

Received 6 October 2021; Revised 3 November 2021; Accepted 29 November 2021; Published 21 December 2021

Academic Editor: Xiangpan Li

Copyright © 2021 Zhen Tang et al. This is an open access article distributed under the Creative Commons Attribution License, which permits unrestricted use, distribution, and reproduction in any medium, provided the original work is properly cited.

Increasing evidence suggests that traditional Chinese medicine strategies are obviously beneficial for cancer treatment, but scientific research on the underlying molecular mechanisms is lacking. We report that ursolic acid, a bioactive ingredient isolated from *Radix Actinidiae chinensis*, has strong antitumour effects on osteosarcoma cells. Functional studies showed that ursolic acid inhibited tumour cell proliferation and promoted the apoptosis of a variety of osteosarcoma cells. Ursolic acid had a synergistic cytotoxic effect with cisplatin on osteosarcoma cells. In a mouse osteosarcoma xenograft model, low-dose cisplatin combined with ursolic acid significantly reduced tumour growth. Notably, ursolic acid reversed weight loss in mice treated with cisplatin. Mechanistic studies showed that ursolic acid degraded ferritin by activating autophagy and induced intracellular overload of ferrous ions, leading to ferroptosis. In addition, ursolic acid enhanced the DNA-damaging effect of cisplatin on osteosarcoma cells. Taken together, these findings suggest that ursolic acid is a nontoxic adjuvant that may enhance the effectiveness of chemotherapy in osteosarcoma.

## 1. Introduction

Osteosarcoma (OS) is a type of sarcoma that originates from osteoblast mesenchymal cells and is most commonly seen in children and adolescents aged 15-19 years [1]. Current treatment strategies, including chemotherapy combined with aggressive surgical resection, have significantly improved the survival of patients with OS [2]. However, the recurrence rate is still 30-40%, and the 10-year survival rate is 20-30% due to pulmonary metastasis [3]. Chemotherapy, such as cisplatin (Cis), is the most effective treatment for cancer and OS [4-6]. However, these chemotherapeutic agents are limited by the acquisition of resistance and serious side effects at high doses. Therefore, there is an urgent need to investigate alternative anticancer approaches, such as the use of food

and herbal supplements in combination with current chemotherapy to improve the therapeutic effectiveness of existing drugs. The development of effective, nontoxic therapeutic strategies, i.e., the application of natural active substances with proven anticancer effects, may be a more promising approach for the prevention and treatment of OS.

Evidence-based studies on traditional Chinese medicine (TCM) strategies for cancer treatment have shown that TCM compounds target tumour cells and treat the whole body. Bioactive TCM compounds exert antitumour effects through multilevel targeting and affecting signalling pathways [7]. Therefore, TCM compounds can be used as adjunctive treatments for cancer. Ursolic acid (UA) is a natural pentacyclic triterpenoid carboxylic acid found in *Radix Actinidiae chinensis*. Studies have shown that UA has a wide

range of biological activities, including antiviral, antibacterial, hepatoprotective, and anti-inflammatory effects [8]. In addition, it is involved in the prevention of and protection against cancer. Its antitumour effect is due to its ability to prevent tumour occurrence, inhibit proliferation, and induce apoptosis. Previous studies have shown that UA can inhibit the proliferation and induce apoptosis of prostate, lung, pancreatic, and other tumour cells [9]. In addition, UA has been reported to inhibit tumour progression, induce tumour cell differentiation, and inhibit angiogenic activity [10]. UA has also been found to exert chemoprophylaxis effects in different animal models by inhibiting tumour invasion. However, the antitumour effects of UA, its effectiveness as an adjuvant chemotherapy in OS cells, and its underlying molecular mechanism remain unclear.

In this study, the effects of UA components from *Radix Actinidiae chinensis* on OS cells were comprehensively studied. We used two OS cell lines and a mouse tumour xenograft model to demonstrate that UA is nontoxic and has strong antitumour activity and a marked effect against chemotherapy resistance in OS cells in vitro and in vivo when combined with Cis. These findings suggest that UA may serve as an adjuvant to enhance the therapeutic effectiveness of current chemotherapy-based regimens.

## 2. Materials and Methods

**2.1. Cell Culture and Reagents.** The human OS cell lines HOS and 143B were purchased from the Cell Bank of the Chinese Academy of Medical Science (Shanghai, China). HOS and 143B cells were grown in Eagle's minimum essential medium (Gibco, Los Angeles, CA) containing 10% foetal bovine serum (Gibco), 100 U/mL penicillin, and 100 µg/mL streptomycin at 37°C and 5% CO<sub>2</sub>. Cis, UA, desferrioxamine (DFO), and 3-methyladenine (3-MA) were purchased from Sigma-Aldrich (St. Louis, Missouri, USA).

**2.2. Cell Viability Assay.** Adhering to the previous protocol [11], cells were seeded in a 96-well plate at a density of  $1 \times 10^4$  cells per well in 100 µL medium overnight. After the cells were treated with reagents and incubated for 24 h, 10 µL Cell Counting Kit-8 (CCK-8) reagent was added according to the manufacturer's instructions. The absorbance was measured at 450 nm with a microplate reader.

**2.3. Clonogenic Assay.** HOS and 143B cells in the logarithmic growth phase were seeded into a 10 cm dish at a density of 200 cells per millilitre. After treatment with Cis (20 µmol/L), UA (35 µmol/L), or Cis (20 µmol/L)+UA (35 µmol/L) for 2 weeks, cell clones were fixed with 4% paraformaldehyde for 15 min. The cell clones were stained with crystal violet solution at room temperature for 15 min before they were photographed.

**2.4. Cell Apoptosis Analysis.** To study the synergistic effect of Cis and UA on apoptosis, HOS and 143B cells were incubated with Cis (20 µmol/L) or UA (35 µmol/L) for 24 h and then harvested and stained using an Annexin V-PE Apoptosis Detection Kit (BD, Shanghai, China). The number of

apoptotic cells was quantified by flow cytometry. All experiments were performed in triplicate.

**2.5. Live/Dead Staining Assay.** HOS and 143B cells were seeded in 24-well plates ( $2.5 \times 10^4$ /well) and cultured overnight. Cis (20 µmol/L), UA (35 µmol/L), or Cis (20 µmol/L)+UA (35 µmol/L) was added to the wells for 24 h. Then, a calcein-AM/PI staining kit (Beyotime, Shanghai, China) was used to detect dead and live cells. PI was used to stain dead cells, and calcein-AM was used to stain live cells.

**2.6. 5-Ethynyl-2'-deoxyuridine Assay (EdU) Incorporation Assay.** HOS cells were seeded in 24-well plates and cultured overnight in complete medium. Cis (20 µmol/L), UA (35 µmol/L), or Cis (20 µmol/L)+UA (35 µmol/L) was added to the wells. Twenty-four hours after treatment, cell proliferation was measured with the EdU Cell Proliferation Assay Kit (Beyotime, Shanghai, China) according to the manufacturer's instructions. The cell nuclei were stained with 1 µg/mL DAPI (Solarbio, Beijing, China) for 5 min. The proportion of EdU-incorporated cells was determined by fluorescence microscopy.

**2.7. Cell Cycle Analysis.** HOS cells were seeded in 6-well plates and treated with Cis (20 µmol/L), UA (35 µmol/L), or Cis (20 µmol/L)+UA (35 µmol/L) for approximately 24 h. Then, the cells were collected and fixed in ice-cold 70% ethanol at 4°C overnight. A Cell Cycle Staining Kit (MultiSciences, Hangzhou, China) was used to analyse the cell cycle phases according to the manufacturer's protocol. After being washed three times with cold PBS, the cells were immersed in RNase A for 30 min at room temperature and then incubated with propidium iodide (PI) in the dark. The samples were analysed by flow cytometry.

**2.8. Determination of Reactive Oxygen Species (ROS) Generation.** HOS cells ( $5 \times 10^5$ ) plated in six-well plates were incubated with Cis (20 µmol/L), UA (35 µmol/L), or Cis (20 µmol/L)+UA (35 µmol/L) for approximately 24 h, and then, the medium was replaced with 1 mL fresh medium containing 5 µM BODIPY 581/591 C11 (Glpbio, Guangzhou, China) for 30 min at 37°C. The cells were then washed twice and analysed under a fluorescence microscope.

Cellular ROS levels and superoxide levels were measured using 2',7'-dichlorofluorescein diacetate (DCF-DA). According to the manufacturer's protocol, HOS and 143B cells were washed with PBS and stained with DCF-DA (4 µM) in the dark at 37°C for 30 min. Flow cytometry was used to determine ROS production.

**2.9. Detection of Malondialdehyde (MDA) and 4-Hydroxynonenal (4-HNE).** The Lipid Peroxidation (MDA) Assay Kit (MAK085, Sigma-Aldrich, USA) and Lipid Peroxidation (4-HNE) Assay Kit (ab238538, Abcam, USA) were used to measure the concentration of MDA and 4-HNE in cell lysates according to the manufacturer's instructions. For MDA detection, the samples were mixed with thiobarbituric acid and incubated at 100°C for 1 h. The MDA concentration was determined at 532 nm absorbance. For 4-HNE detection, the samples were added into the 4-HNE

conjugate-coated plate and incubated for 10 min. Then, the conjugated 4-HNE was incubated with anti-4-HNE antibody and secondary antibody-HRP. Finally, substrate solution was added, and the absorbance at 450 nm was measured. Herein, the amount of MDA or 4-HNE was calculated in  $1 \times 10^6$  cells after treatment.

**2.10. Measurement of Intracellular  $Fe^{2+}$  Content.** FerroOrange (Mkbio, Shanghai, China) was used to measure intracellular and mitochondrial  $Fe^{2+}$  levels according to the manufacturer's protocol. HOS cells were treated with Cis, UA, UA/Cis, UA/Cis/DFO, or UA/Cis/3-MA and stained with  $1 \mu\text{M}$  FerroOrange for 30 min at  $37^\circ\text{C}$ . Images were acquired using a fluorescence microscope.

**2.11. Autophagic Flux Analysis.** mCherry-GFP-labelled LC3 was used to analyse autophagic flux in cells according to the manufacturer's instructions. HOS cells were transfected with mCherry-GFP-LC3 adenovirus for 6 h and then incubated with Cis ( $20 \mu\text{mol/L}$ ), UA ( $35 \mu\text{mol/L}$ ), or Cis ( $20 \mu\text{mol/L}$ )+UA ( $35 \mu\text{mol/L}$ ) for 24 h. mCherry-GFP-LC3 expression was tracked and imaged by fluorescence microscopy.

**2.12. Western Blotting.** OS cells were lysed with RIPA buffer and centrifuged at 12000 rpm for 15 min to collect the supernatant. The protein samples were separated by 10% SDS-PAGE and transferred to PVDF membranes (Millipore, Billerica, MA, USA). The PVDF membranes were blocked with 5% skim milk for 1.5 h and then incubated overnight with primary antibody at  $4^\circ\text{C}$ . After being washed with TBST 3 times (15 min each), the membranes were incubated with an HRP-conjugated secondary antibody at room temperature for 1 h. The protein bands were visualized with an Amersham Imager 600. Primary antibodies against Beclin-1 (ab207612, Abcam), LC3 (ab192890, Abcam), P62 (ab109012, Abcam),  $\gamma$ -H2AX (ab81299, Abcam), GPX4 (DF6701, Affinity), TFR (AF5343, Affinity), and NCOA4 (DF4255, Affinity) were diluted 1:1000; an antibody against GAPDH (#5174, CST, USA) was diluted 1:2000.

**2.13. Transmission Electron Microscopy.** Cells cultured in a 6-well plate were treated with drugs for 24 h and fixed with 2.5% glutaraldehyde in PBS. After being washed in 0.1 M PBS, the cells were treated with 0.1% Millipore-filtered cacodylate-buffered tannic acid and postfixed with 1% osmium tetroxide at  $4^\circ\text{C}$  for 30 min. Then, the cells were incubated in a graded series of acetone solutions for 10 min each. After dehydration and embedding for 2 h at  $60^\circ\text{C}$ , the cells were embedded, and the embedded tissues were sliced at a thickness of 50–70 nm for follow-up observation using a transmission electron microscope.

**2.14. Immunofluorescence.** OS cells were seeded in 24-well plates at a density of  $5 \times 10^4$  cells per well and treated with the indicated drugs for 24 h. Then, the cells were fixed in 4% paraformaldehyde for 20 min and incubated with a primary antibody against LC3 (ab192890, Abcam),  $\gamma$ -H2AX (ab81299, Abcam), and TFR (AF5343, Affinity) at  $4^\circ\text{C}$  overnight. The cells were washed with PBS three times for 3 min

each and then incubated with secondary antibodies for 1 h at room temperature. DAPI was used to stain the nuclei for 1 min. The samples were sealed and observed under a fluorescence microscope.

**2.15. Xenograft Model of Human OS.** All animal experiments were carried out following the guidelines of the Ethics Committee of the Fourth Military Medical University (IACUC No. 2020-1004) and were performed according to institutional guidelines for the care and use of laboratory animals. The guidelines were complied with the *Guide for the Care and Use of Laboratory Animals* NIH publication No. 86-23, revised 2011. NU/NU mice (the Fourth Military Medical University, Shaanxi, China) were injected with 143B cells ( $100 \mu\text{L}$ ,  $5 \times 10^7$  cells/mL, i.h.). Seven days after the injection, the mice were divided into 6 different groups ( $n = 3$ ) and intraperitoneally injected with different drugs twice a week. Then, on day 28, the mice were sacrificed, and the tumours in the different groups were weighed. Body weight and tumour size were measured every 3 days from day 7 to day 28. The tumour tissue was fixed with 4% paraformaldehyde, embedded in paraffin, and cut into  $4 \mu\text{m}$  thick sections for haematoxylin-eosin (H&E) and immunofluorescence staining.

**2.16. Statistical Analysis.** Statistical analyses were performed with GraphPad Prism 8.2 (GraphPad Software, Inc., La Jolla, CA, USA). The data are presented as the mean  $\pm$  SD of 3 independent experiments. Statistical significance between the groups was analysed with one-way analysis of variance (ANOVA).  $p < 0.05$  was considered statistically significant.

### 3. Results

**3.1. Synergistic Antitumour Effect of UA and Cis on OS Cells In Vitro.** To determine the optimal concentration of UA for treating OS cells, we used the CCK-8 assay to determine the effects of different concentrations of UA on the proliferation of HOS and 143B cells. The results showed that  $35 \mu\text{M}$  UA combined with  $20 \mu\text{M}$  Cis had the most obvious effect on the proliferation of OS cells (Figure 1(a)). Then, the CCK-8 assay was used to evaluate the effects of Cis and UA and their combination on the proliferation of HOS and 143B cells. Cis or UA treatment significantly decreased cell viability, and this decrease was more significant in the combined UA and Cis treatment group (Figure 1(b)). The results of the clonogenic assay also showed that OS cell viability was the lowest in the UA+Cis group, followed by the monotherapy group (Figure 1(c)). Flow cytometry was used to analyse the apoptosis of HOS and 143B cells after various drug treatments. The results showed that the apoptosis rate of OS cells was the highest in the UA+Cis group and was higher in the UA+Cis group than that in the Cis or UA alone group but that the apoptosis rate in all three groups was significantly higher than that in the control group (Figure 1(d)). We performed calcein-AM/PI staining to further clarify the synergistic effect of UA and Cis on HOS and 143B cells. The experiment demonstrated that the combination of UA and



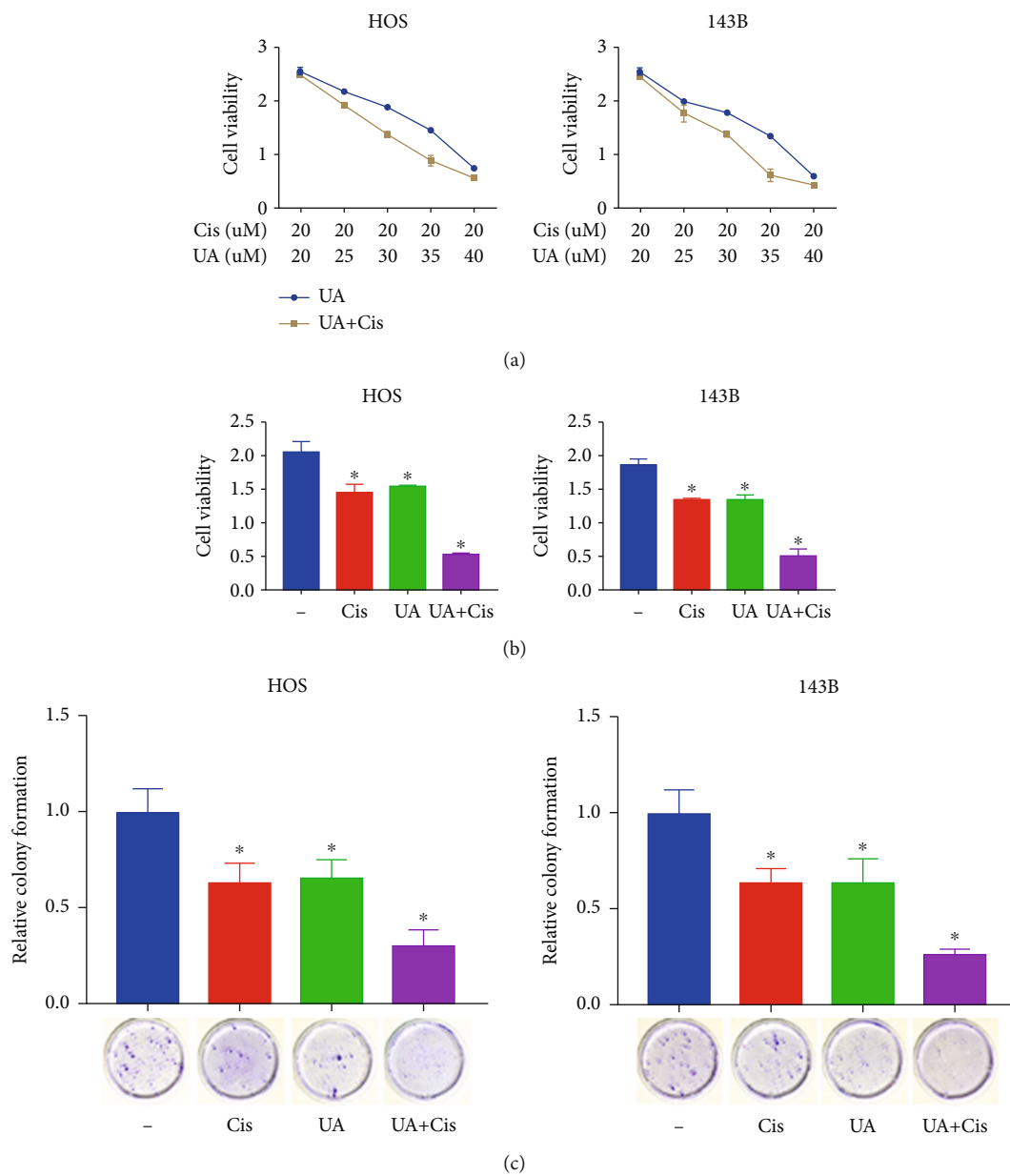


FIGURE 1: Continued.

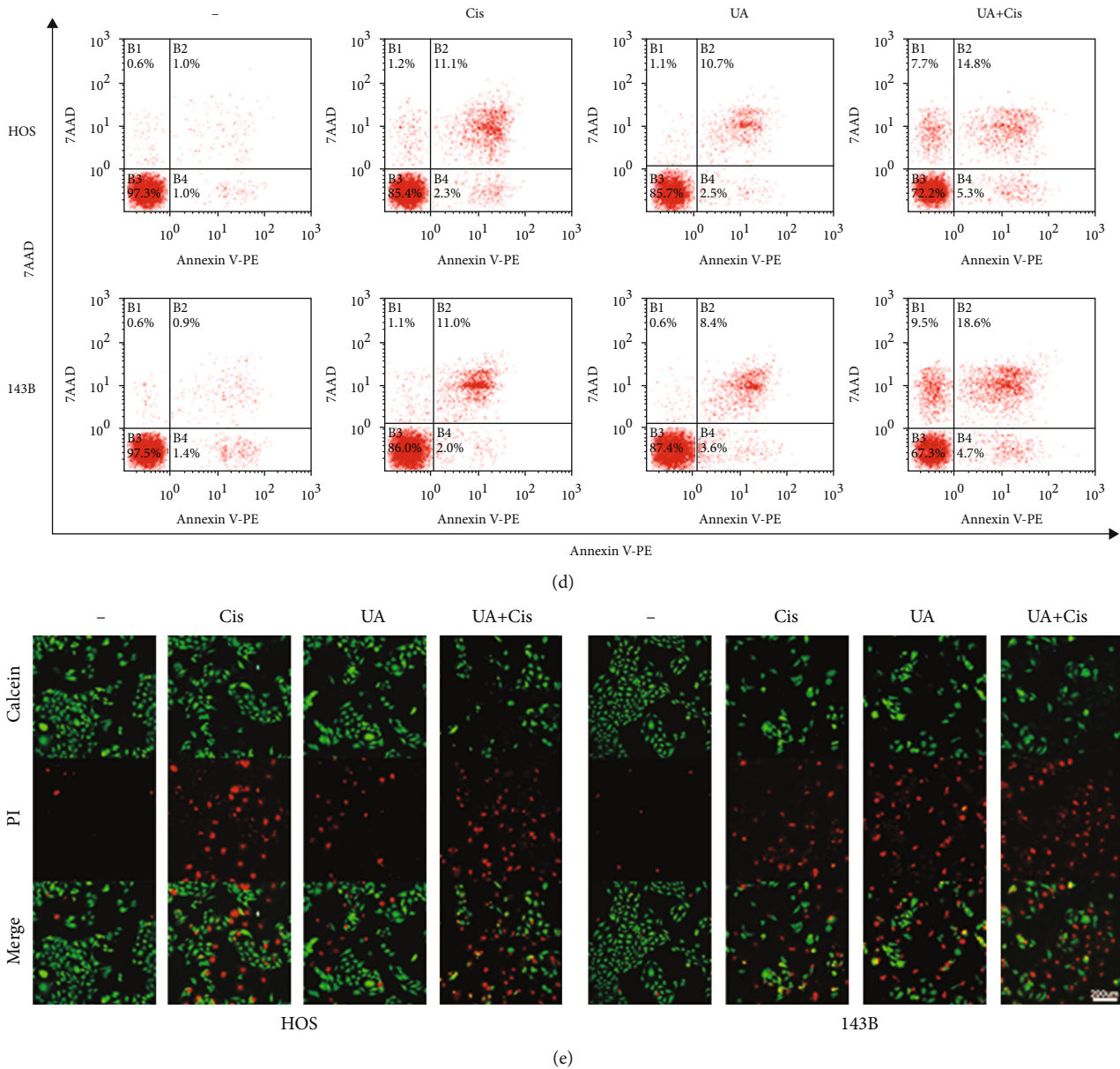


FIGURE 1: Synergistic antitumour effect of UA and Cis on OS cells in vitro. HOS and 143B cells were treated with different concentrations of UA and Cis for 24 h, and cell viability was assessed by the CCK-8 assay (a) ( $n = 3$ ). The CCK-8 assay was used to evaluate cell viability under UA and/or Cis treatment (b) ( $n = 3$ ). The colony formation ability of HOS and 143B cells was assessed after monotherapy or treatment with the combination of UA and Cis for 14 days (c) ( $n = 3$ ). HOS and 143B cells were treated with UA and/or Cis for 24 h, and the apoptosis rate was measured by flow cytometry (d) ( $n = 3$ ). HOS and 143B cells were pretreated with UA and/or Cis for 24 h and subjected to calcein-AM/PI staining (e) ( $n = 3$ , scale bar: 200  $\mu\text{m}$ ; calcein-AM: live cells; PI: dead cells). The data are presented as the mean  $\pm$  SD. \* $p < 0.05$  vs. the control group.

Cis synergistically increased the number of dead cells and decreased the number of viable cells (Figure 1(e)).

**3.2. The Combination of UA and Cis Inhibits Proliferation and Induces DNA Damage in OS Cells.** Subsequently, we explored whether the combination of UA and Cis can inhibit the proliferation of OS cells. As expected, both UA and Cis treatment modestly reduced the percentage of EdU<sup>+</sup> cells, and UA+Cis treatment significantly reduced the percentage of EdU<sup>+</sup> cells, suggesting that UA combined with Cis signif-

icantly blocked the growth of OS cells (Figures 2(a) and 2(b)). To further investigate the mechanism underlying the inhibitory effect of the drugs on OS cell growth, flow cytometry was used to analyse cell cycle distribution. As shown in Figures 2(c) and 2(d), the cell cycle distribution of HOS cells changed significantly under UA and Cis treatment, as the proportion of cells in G2 phase was significantly increased and that of cells in G1 phase was significantly decreased. Previous studies have reported that the main anticancer mechanism of Cis involves the formation of intrachain

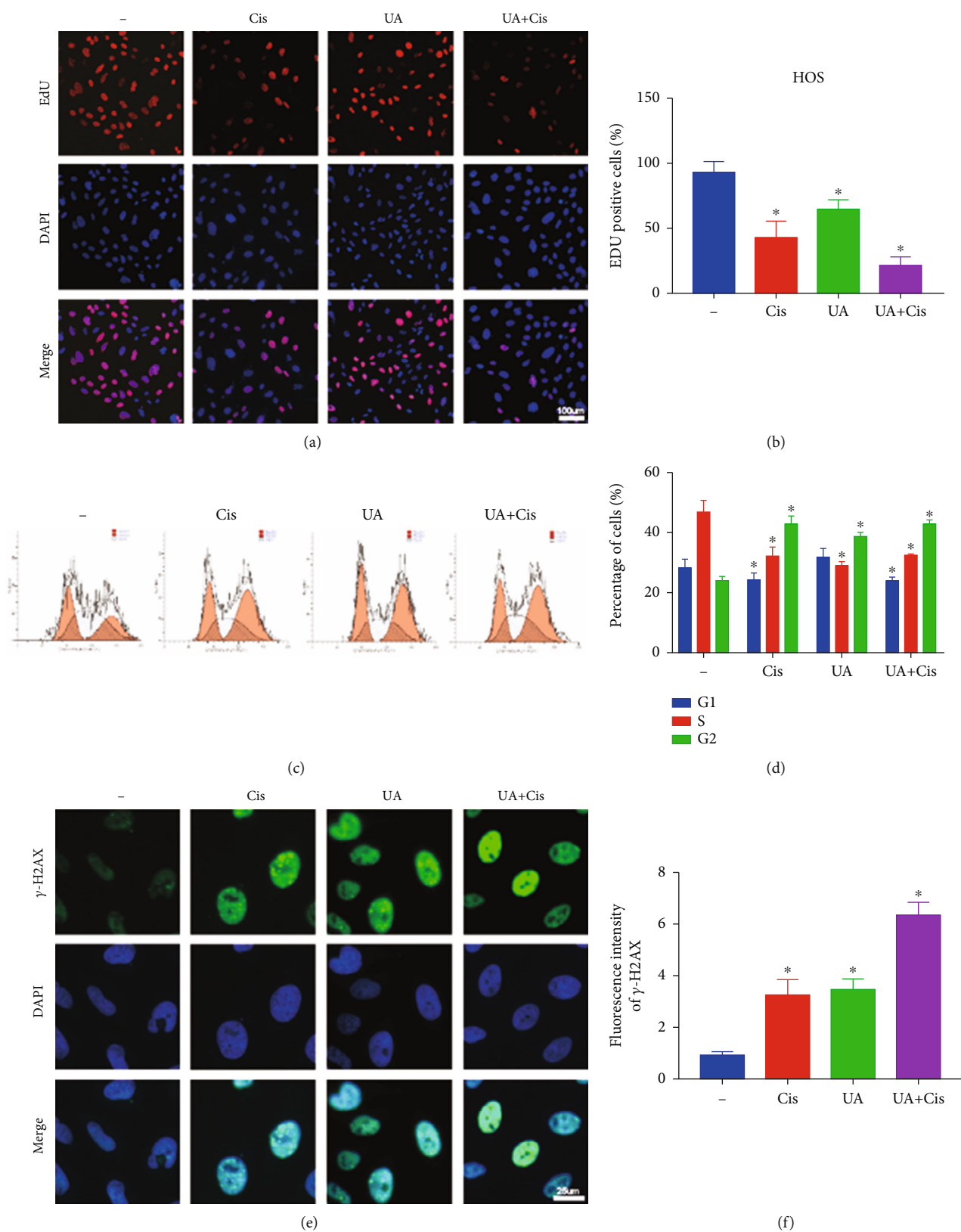


FIGURE 2: Combination treatment with UA and Cis inhibited OS cell proliferation by increasing DNA damage in OS cells. The proliferation of OS cells was assessed by the EdU incorporation assay after monotherapy or treatment with the combination of UA and Cis for 24 h (a, b) ( $n = 3$ , scale bar: 100  $\mu\text{m}$ ). OS cells were treated with the combination of UA and Cis or either drug alone for 24 h, and cell cycle distribution was analysed by flow cytometry (c, d) ( $n = 3$ ). OS cells were treated with the combination of UA and Cis or either drug alone for 24 h and stained with a  $\gamma$ -H2AX antibody (e, f) ( $n = 3$ , scale bar: 25  $\mu\text{m}$ ). The data are presented as the mean  $\pm$  SD. \* $p < 0.05$  vs. the control group.

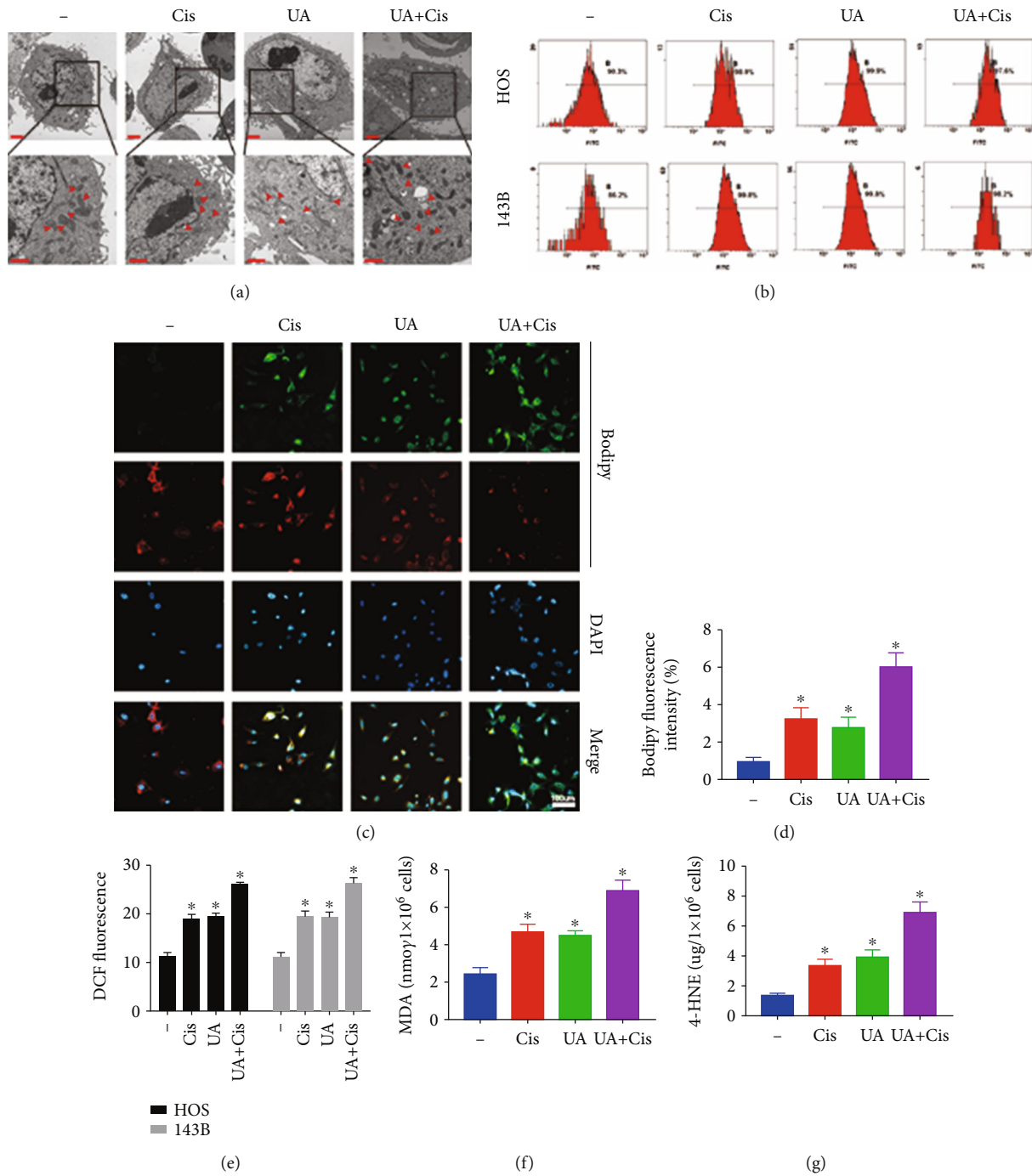


FIGURE 3: The combination of UA and Cis synergistically triggered an evident increase in cellular ROS production and lipid peroxide generation and morphological changes in mitochondria. The subcellular structural changes in HOS cells treated with the combination of UA and Cis or either drug alone for 24 h were analysed by TEM. The red arrows indicated mitochondria (a) ( $n = 3$ , scale bar: 2  $\mu\text{m}$ , scale bar: 1  $\mu\text{m}$ ). Cellular ROS levels were measured by flow cytometry (b, e) ( $n = 3$ ). Representative immunofluorescence images of BODIPY were obtained after UA and/or Cis treatment (c, d) ( $n = 3$ , scale bar: 100  $\mu\text{m}$ ). MDA and 4-HNE levels in HOS cells treated with UA and/or Cis for 24 h (f, g) ( $n = 3$ ). The data are presented as the mean  $\pm$  SD. \* $p < 0.05$  vs. the control group.

crosslinking adducts through the interaction of Cis with DNA, leading to an increase in DNA damage and cell cycle arrest [12]. Immunofluorescence was performed to assess the expression of  $\gamma$ -H2AX, a marker of early DNA damage.

The results showed that UA increased DNA damage in HOS cells, while the combination therapy further significantly increased the DNA damage, as indicated by a significant increase in the fluorescence intensity of  $\gamma$ -H2AX

(Figures 2(e) and 2(f)). Therefore, our experimental results suggest that UA and Cis exert a synergistic effect to inhibit OS cell proliferation and induce DNA damage.

**3.3. Combined Treatment with UA and Cis Synergistically Increases Ferroptosis of OS Cells.** We tested whether UA combined with Cis amplifies mitochondrial dysfunction in OS cells. We focused first on mitochondrial morphology, which is upstream of mitochondrial dysfunction. Electron microscopy analysis showed that compared to monotherapy, UA+Cis treatment induced more severe changes in mitochondrial morphology, such as loss of the mitochondrial crest and an increase in the mitochondrial membrane density (Figure 3(a)). After UA+Cis administration, the mitochondria became disordered and smaller, and the network around the perinuclear region collapsed (Figure 3(a)). The formation of lipid peroxides and the accumulation of free iron are two main characteristics of ferroptosis. Therefore, oxidative stress damage was quantified by measuring (i) total ROS production in the cells with DCF-DA (Figures 3(b) and 3(e)), (ii) lipid ROS levels with BODIPY C11 (Figures 3(c) and 3(d)), and (iii) the content of secondary products of lipid peroxidation (as determined by immunofluorescence staining for MDA and 4-HNE) (Figures 3(f) and 3(g)). These results showed that ROS production and lipid peroxidation production were significantly increased by the combination treatment.

**3.4. The Combined Use of UA and Cis Results in Iron Homeostasis Disruption in OS Cells.** To examine whether ferroptosis is caused by an increase in free iron pools, we examined the effects of UA and Cis on iron metabolism in OS cells. We first used a selective fluorescent ferrous ion probe to monitor intracellular free iron levels. Fluorescence staining showed that UA combined with Cis resulted in significant accumulation of unstable iron, as shown by an increase in the fluorescence intensity of  $\text{Fe}^{2+}$  (Figures 4(a) and 4(d)). Next, the expression of transferrin receptor (TFR) was assessed by immunofluorescence staining (Figures 4(b) and 4(e)). Consistent with the above results, the accumulation of TFR and reduced expression of nuclear receptor coactivator 4 (NCOA4), which mediates autophagy-mediated degradation of ferritin, led to the accumulation of a large amount of nonchelated iron under UA and Cis treatment. We further investigated the expression of key proteins associated with iron homeostasis in OS cells. The results showed that the expression of proteins related to iron metabolism, such as TFR and NCOA4, was regulated by UA and that the iron starvation effect of OS cells was further enhanced under the combined action of Cis and UA. In addition, UA and Cis synergistically induced the degradation of GPX4 and NCOA4, autophagy cargo receptors that bind ferritin to degrade and release free iron (Figure 4(c)). Overall, our results suggest that the combination therapy caused significant accumulation of intracellular free iron, leading to ferroptosis.

**3.5. The Combination of UA and Cis Induces Autophagy in OS Cells.** As shown by the immunofluorescence results pre-

sented in Figure 5(a), after treatment with UA+Cis, the recruitment of LC3 to the autophagic membrane was significantly increased. Similarly, previous studies have reported that the main anticancer mechanism of Cis involves the formation of intrachain crosslinking adducts through the interaction of Cis with DNA (Figure 5(b)). Ultrastructural analysis of autophagosomes using TEM also showed that the number of intracellular autophagosomes was significantly increased after treatment with UA+Cis (Figure 5(c)). The expression levels of autophagy-related proteins were analysed by western blotting. LC3 and Beclin-1 expression was significantly increased in the UA+Cis group compared to the control group and the monotherapy group, whereas P62 expression showed a downward trend (Figure 5(d)). These results suggested that autophagy played an important role in the treatment of OS cells.

**3.6. Pharmacologic Elimination of Free Iron and Inhibition of Autophagy Attenuate Ferroptosis Induced by UA and Cis.** Due to the significant increase in intracellular free iron levels and the significant activation of autophagy, we proposed that the synergistic toxic effect of UA and Cis on OS cells may be caused by the accumulation of free iron due to excessive autophagy. We tested the above hypothesis using the iron-chelating agent DFO and the autophagy inhibitor 3-MA. The evidence showed that DFO and 3-MA reduced UA+Cis-induced apoptosis (Figures 6(a) and 6(b)) and that DFO and 3-MA partially reversed the UA+Cis-induced decrease in cell viability (Figure 6(c)). In addition, UA +Cis-induced mitochondrial morphological changes and autophagy were partially reversed by DFO and 3-MA (Figure 6(d)). Furthermore, DFO and 3-MA were found to reduce lipid peroxidation and MDA and 4-HNE contents in OS cells (Figures 6(e)–6(g) and 6(k)). Notably, we demonstrated that DFO and 3-MA effectively alleviated the intracellular overload of free iron (Figures 6(h) and 6(l)). DFO and 3-MA also reduced the increased expression of TFR induced by UA+Cis treatment (Figures 6(i) and 6(m)). The western blot results showed that the expression levels of TFR, NCOA4,  $\gamma$ -H2AX, and LC3 were decreased while GPX4 and P62 expression was increased after treatment with the iron-chelating agent DFO and the autophagy inhibitor 3-MA (Figure 6(j)). These data suggested that the enhancement of autophagy induced by UA+Cis treatment led to the accumulation of free iron and that free iron overload acted upstream of mitochondrial dysfunction, ultimately leading to the production of lipid peroxides that cause ferroptosis. Taken together, these data indicated that pharmacological chelation of free iron and inhibition of autophagy effectively alleviated UA+Cis-mediated ferroptosis and mitochondrial dysfunction.

**3.7. UA and Cis Treatment Increases Autophagy and Thus Induces Ferroptosis in Mouse Xenograft Models.** We established a subcutaneous tumour model to study the therapeutic potential of the combination of UA and Cis in vivo, and tumour growth was observed periodically (Figure 7(a)). We found that compared with control treatment and monotherapy, UA+Cis treatment significantly slowed tumour growth

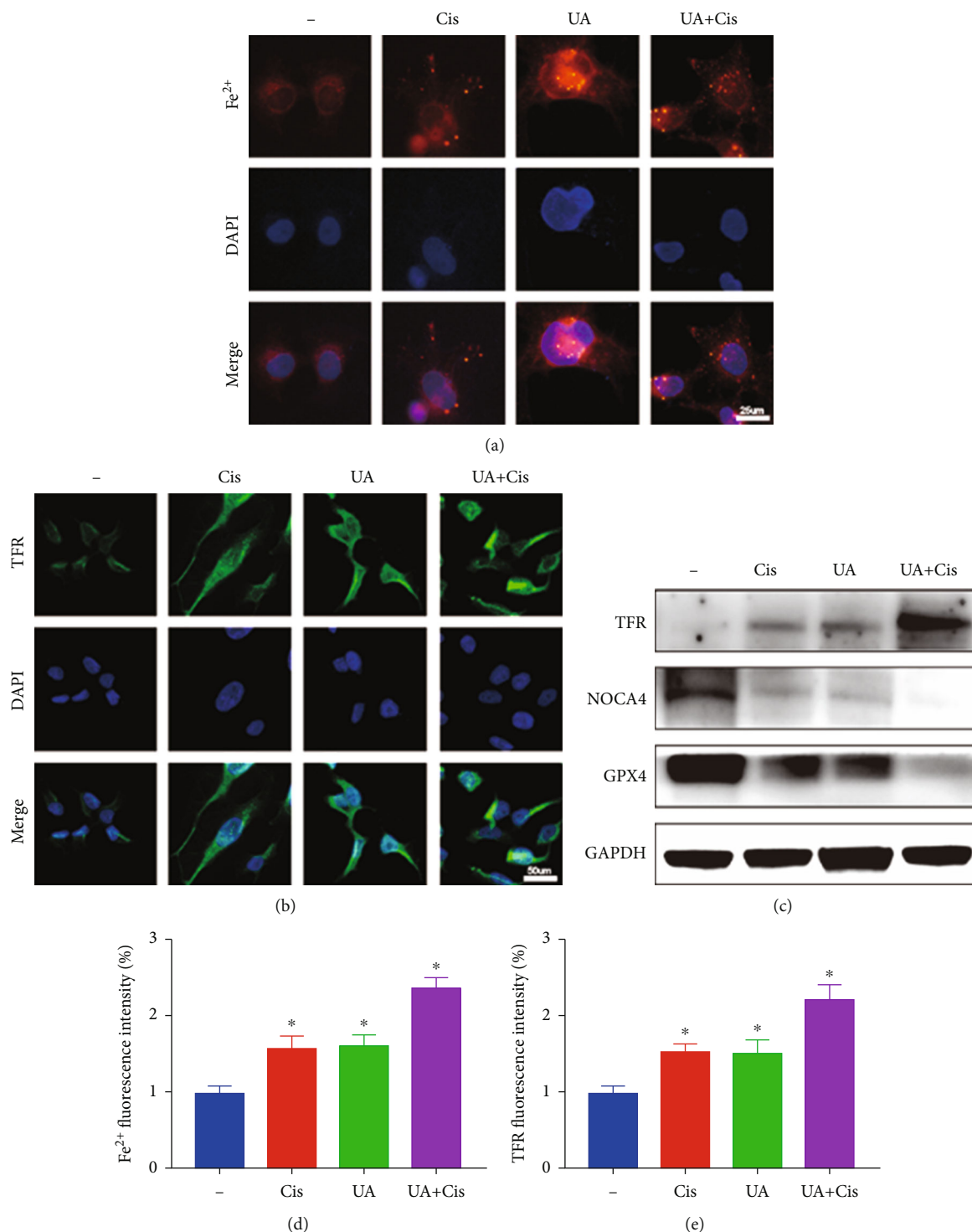


FIGURE 4: Iron accumulation in OS cells treated with the combination treatment of UA and Cis. Intracellular Fe<sup>2+</sup> levels were measured after treatment with UA and/or Cis as indicated (a, d) (*n* = 3, scale bar: 25 μm). The expression quantity of TFR was assessed by immunofluorescence staining of HOS cells after the indicated treatment (b, e) (*n* = 3, scale bar: 50 μm). The expression of iron metabolism-related proteins in UA- and/or Cis-treated HOS cells was determined by western blotting (c) (*n* = 3). The data are presented as the mean ± SD. \**p* < 0.05 vs. the control group.

(Figure 7(b)); the tumour volume and weight were significantly decreased in the UA+Cis treatment group compared with the control group and the monotherapy group

(Figures 7(c) and 7(e)). As shown in Figure 7(d), the Cis-treated mice showed significant weight loss, while the weight of the UA-treated mice was almost unchanged, indicating no

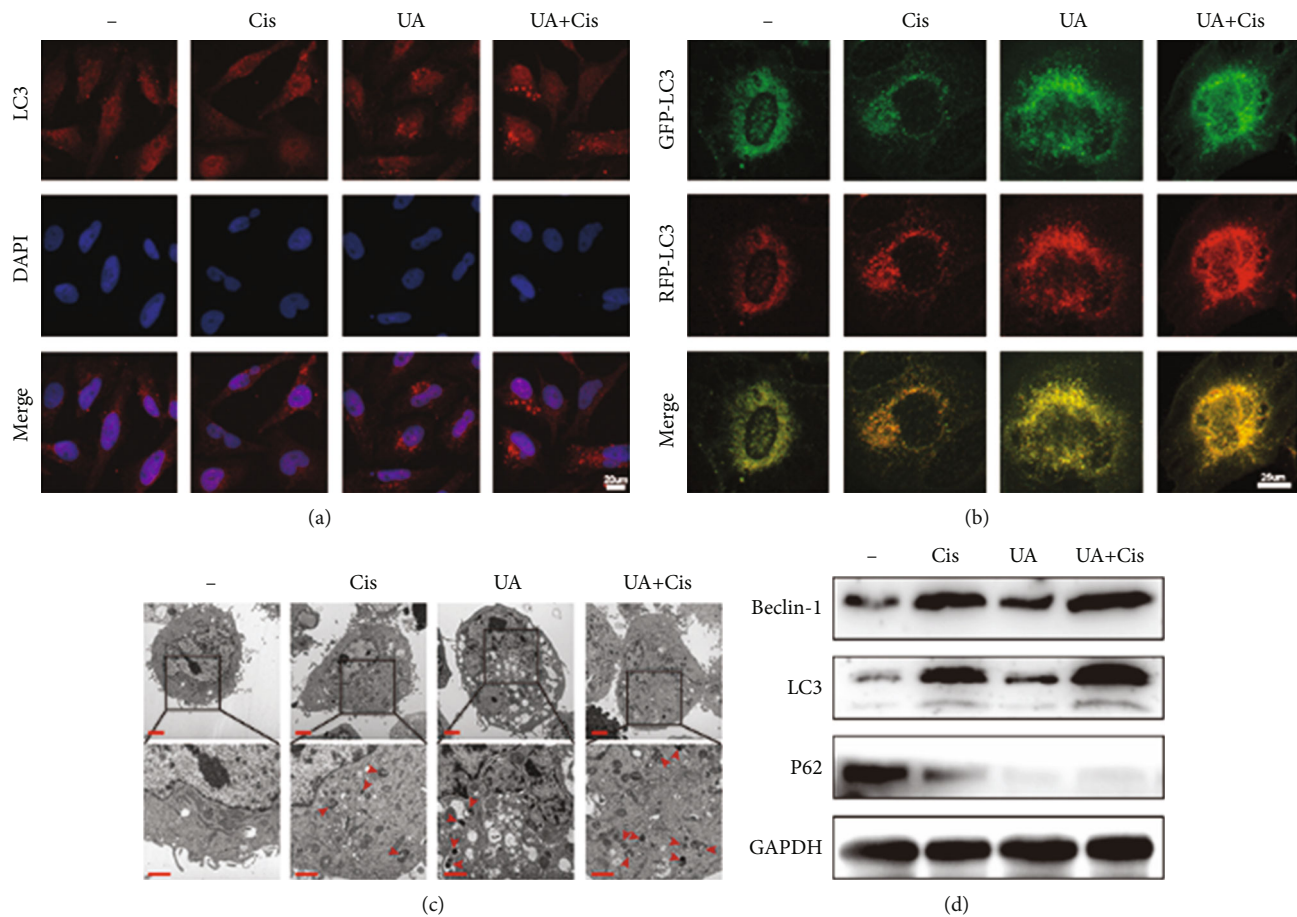


FIGURE 5: The combination of UA and Cis induced ferroptosis dependent on ferritinophagy. After treatment with UA and/or Cis for 24 h, LC3 puncta formation was analysed by immunofluorescence (a) ( $n = 3$ , scale bar: 20  $\mu\text{m}$ ). Autophagic flux in 143B cells transiently expressing GFP-RFP-LC3 was monitored by fluorescence microscopy (b) ( $n = 3$ , scale bar: 25  $\mu\text{m}$ ). Intracellular autophagosomes were observed by TEM (c) ( $n = 3$ , scale bar: 2  $\mu\text{m}$ , scale bar: 1  $\mu\text{m}$ ). 143B cells were subjected to western blotting to measure the expression of LC3, P62, and Beclin-1 (d) ( $n = 3$ ). The data are presented as the mean  $\pm$  SD. \* $p < 0.05$  vs. the control group.

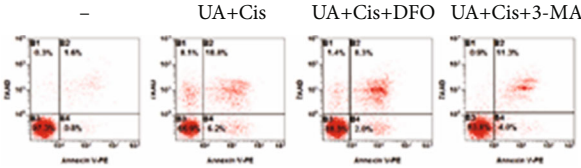
significant toxicity. It is worth noting that the combination of Cis and UA not only inhibited tumour growth but also reduced the toxicity and side effects of Cis to a certain extent, making it safer for clinical use. The immunofluorescence results showed that UA synergized with Cis to increase the necrotic area; increase the expression of TFR,  $\gamma$ -H2AX, and LC3; and decrease TUNEL, Ki67, GPX4, NCOA4, and P62 staining (Figure 7(f)). However, DFO and 3-MA significantly reversed these changes by inhibiting ferroptosis and autophagy. The results also confirmed that the combination of UA and Cis exerted a cytotoxic effect on OS cells by promoting autophagy, leading to ferroptosis due to intracellular overload of iron ions.

#### 4. Discussion

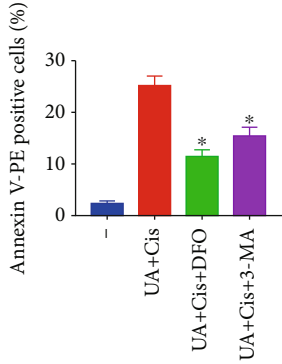
Traditional treatments for OS mainly include a combination of surgery, chemotherapy, and radiation, as well as advanced alternative therapies such as targeted therapy and immunotherapy [13]. However, these therapies have limited efficacy, and their use is limited by their side effects and ultimately

the development of multidrug resistance (MDR). Therefore, it is imperative to optimize cancer treatment strategies. For complex diseases such as cancer, TCM compounds can affect multiple targets rather than a single target, with a few exceptions [14]. UA, a natural pentacyclic triterpenoid found in plants, plays an anticancer role by targeting multiple signalling pathways and is becoming a promising compound for cancer prevention and treatment [15]. Notably, we demonstrated that UA synergizes with Cis to activate autophagy, leading to degradation of ferritin and resulting in the catastrophic accumulation of free iron and lipid peroxidation and thus ferroptosis, which has an inhibitory effect on OS.

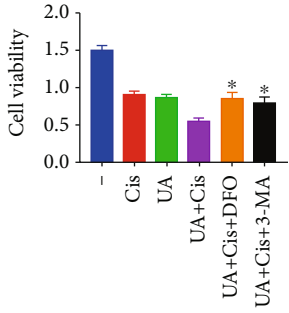
It has been reported that UA can inhibit tumour cell growth, promote tumour cell apoptosis, and inhibit the invasion and metastasis of tumour cells to exert an antitumour effect [9, 16]. However, the regulatory effect of UA on OS has rarely been studied. Studies have shown that UA and Cis exert synergistic antitumour effects by inducing apoptosis of tumour cells, including ovarian cancer, bladder cancer, and lung adenocarcinoma cells [17–19].



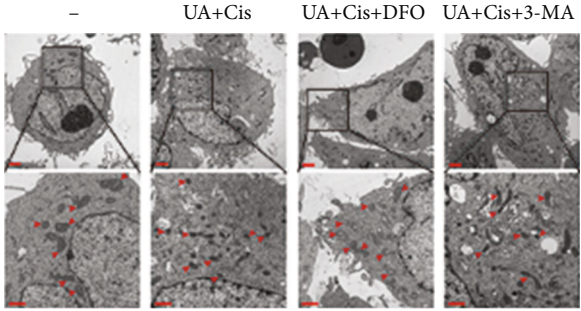
(a)



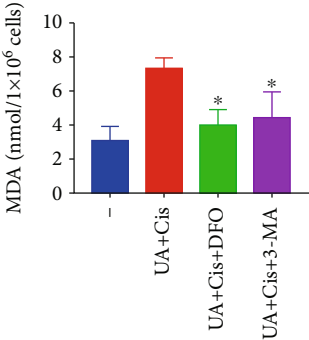
(b)



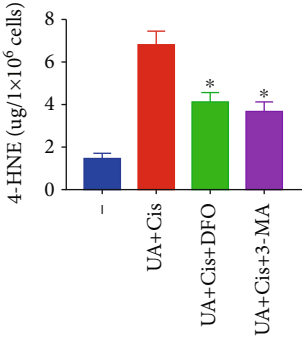
(c)



(d)



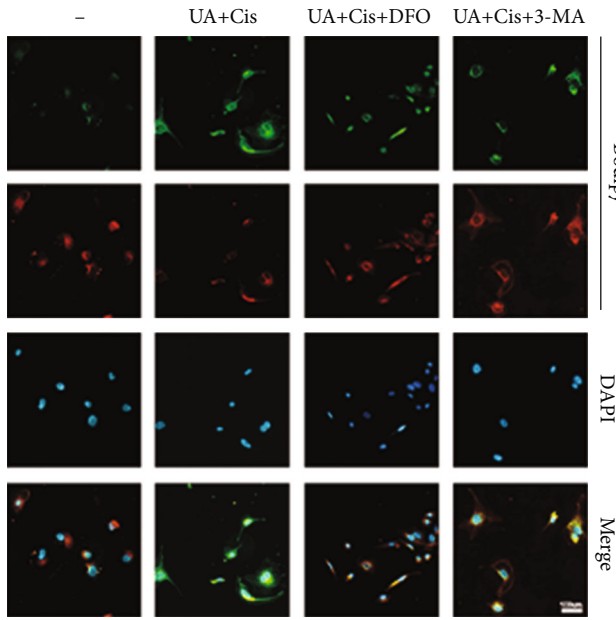
(e)



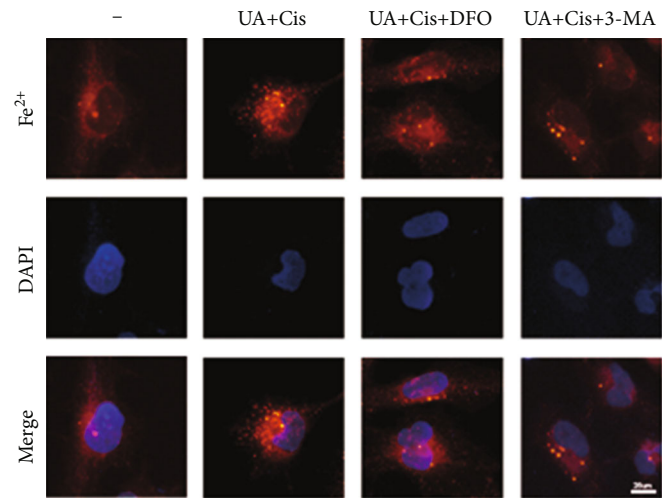
(f)

FIGURE 6: Continued.

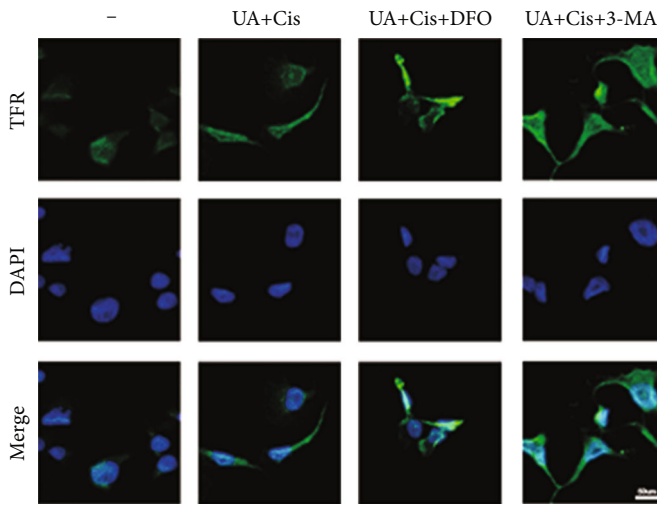




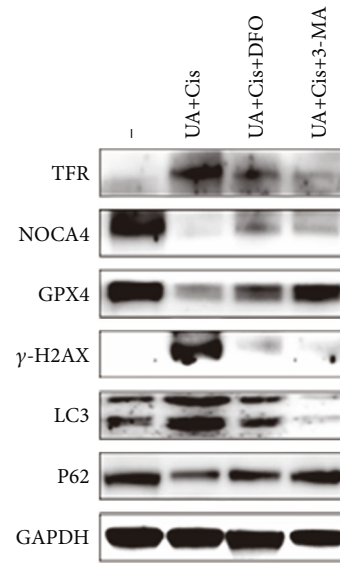
(g)



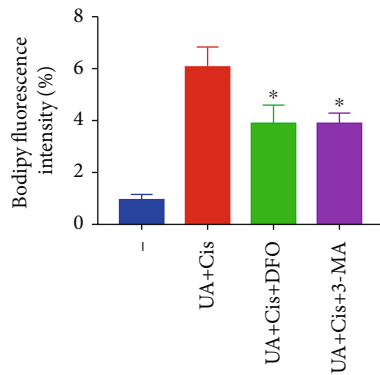
(h)



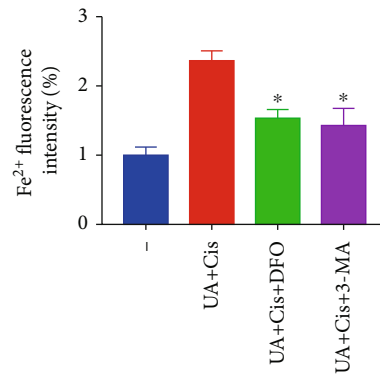
(i)



(j)



(k)



(l)

FIGURE 6: Continued.

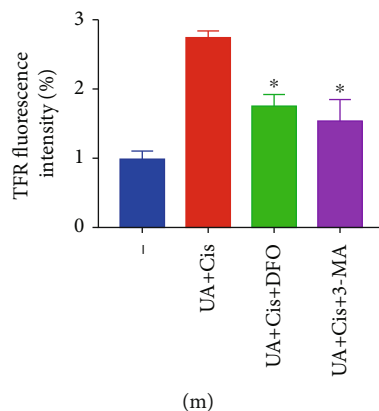


FIGURE 6: Depletion of free iron reservoirs by DFO and inhibition of autophagy by 3-MA attenuated UA/Cis-induced ferroptosis. The apoptosis rate of HOS cells treated with UA/Cis, UA/Cis/DFO, or UA/Cis/3-MA was measured by flow cytometry (a, b) ( $n = 3$ ). The viability of HOS cells treated with Cis, UA, UA/Cis, UA/Cis/DFO, or UA/Cis/3-MA was assessed by the CCK-8 assay (c) ( $n = 3$ ). Mitochondrial morphology changes and autophagy in HOS cells were observed by TEM (d) ( $n = 3$ , scale bar:  $2 \mu\text{m}$ , scale bar:  $1 \mu\text{m}$ ). MDA and 4-HNE levels in HOS cells treated with UA/Cis, UA/Cis/DFO, or UA/Cis/3-MA (e, f) ( $n = 3$ ). Representative immunofluorescence images of BODIPY were obtained after UA/Cis, UA/Cis/DFO, or UA/Cis/3-MA treatment (g, k) ( $n = 3$ , scale bar:  $100 \mu\text{m}$ ). Intracellular  $\text{Fe}^{2+}$  levels were measured after treatment with UA/Cis, UA/Cis/DFO, or UA/Cis/3-MA (h, l) ( $n = 3$ , scale bar:  $25 \mu\text{m}$ ). Measurement of TFR level by immunofluorescence staining of HOS cells after treatment with UA/Cis, UA/Cis/DFO, or UA/Cis/3-MA (i, m) ( $n = 3$ , scale bar:  $50 \mu\text{m}$ ). The expression of iron metabolism-related proteins in UA/Cis-, UA/Cis/DFO-, or UA/Cis/3-MA-treated HOS cells was determined by western blotting (j) ( $n = 3$ ). The data are presented as the mean  $\pm$  SD. \* $p < 0.05$  vs. the UA/Cis group.

In addition, the combination of UA and Cis can significantly disrupt mitochondrial homeostasis and inhibit OS cell proliferation. Further experiments have shown that iron-chelating agents and autophagy inhibitors can block cell death. Importantly, the accumulation of lipid peroxides before OS cell death was detected by staining for MDA and 4-HNE or fluorescent staining with BODIPY C11, and the accumulation of lipid peroxides could be reversed by pharmacological chelation of free iron. The same phenomenon was observed in a tumour xenograft model. In summary, we found that UA can effectively optimize the anti-OS activity of Cis and reduce the toxicity and side effects of Cis, which involve multiple mechanisms. UA not only increases DNA damage but also causes lipid peroxidation in OS cells, ultimately leading to ferroptosis. These results indicate that the application of UA combined with Cis is a promising strategy to decrease iron levels in OS.

Iron plays an important role in mammalian cells. Iron is necessary for cell replication, metabolism, and growth, as it allows important iron-containing enzymes in the blood to function [20]. Unstable iron pool overload is a biochemical hazard. Ferrous iron contributes electrons when it reacts with hydrogen peroxide, producing hydroxyl radicals, which are ROS [21, 22]. This process, known as the Fenton reaction, not only destroys lipids and proteins but also leads to oxidative damage to DNA, including modification of DNA bases and breakage of DNA strands [23]. Therefore, iron is both essential and potentially toxic. Ferritin, which includes ferritin light peptide 1 (FTL1) and ferritin heavy peptide 1 (FTH1), is the main intracellular iron-storage protein complex. Ferroptosis can be inhibited by increasing iron storage in inert pools through upregulation of cytoplasmic ferritin

expression [24]. Autophagy is an evolutionarily conserved degradation mechanism that maintains homeostasis. Induction of autophagy promotes cell survival in response to environmental stresses such as nutritional starvation and energy expenditure in many cases. However, excessive and impaired autophagy may lead to cell death [25]. Recent studies have shown that increased autophagy can degrade ferritin and increase iron levels, leading to the Fenton reaction and oxidative damage [24]. Increasing evidence suggests that induction of ferroptosis is a promising therapeutic strategy for inhibiting cancer cell resistance resulting from drug-induced apoptosis [26]. Mechanistically, the combination of UA and Cis activates autophagy to degrade the iron storage protein ferritin through a process mediated by the cargo receptor NCOA4. This NCOA4-mediated autophagic degradation of ferritin, also known as ferritinophagy, promotes the accumulation of ROS by maintaining high intracellular iron levels, thus leading to ferroptosis of OS cells. In this paper, we present convincing evidence that ferroptosis is a form of autophagic cell death that causes OS cell death after UA and Cis combination therapy. It was noted that treatment with UA and Cis exacerbated DNA damage in OS cells and arrested OS cells in G2 phase of the cell cycle. These results suggest that the treatment of OS cells with the combination of UA and Cis can alleviate drug resistance by enhancing DNA damage and ferroptosis in a multistep and multimechanism manner.

Thus, our study provides evidence that UA may be a promising adjuvant for improving the effectiveness of Cis-based chemotherapy in patients with OS. We also reveal the underlying mechanisms to further elucidate the effect of targeting ferroptosis for OS therapy.

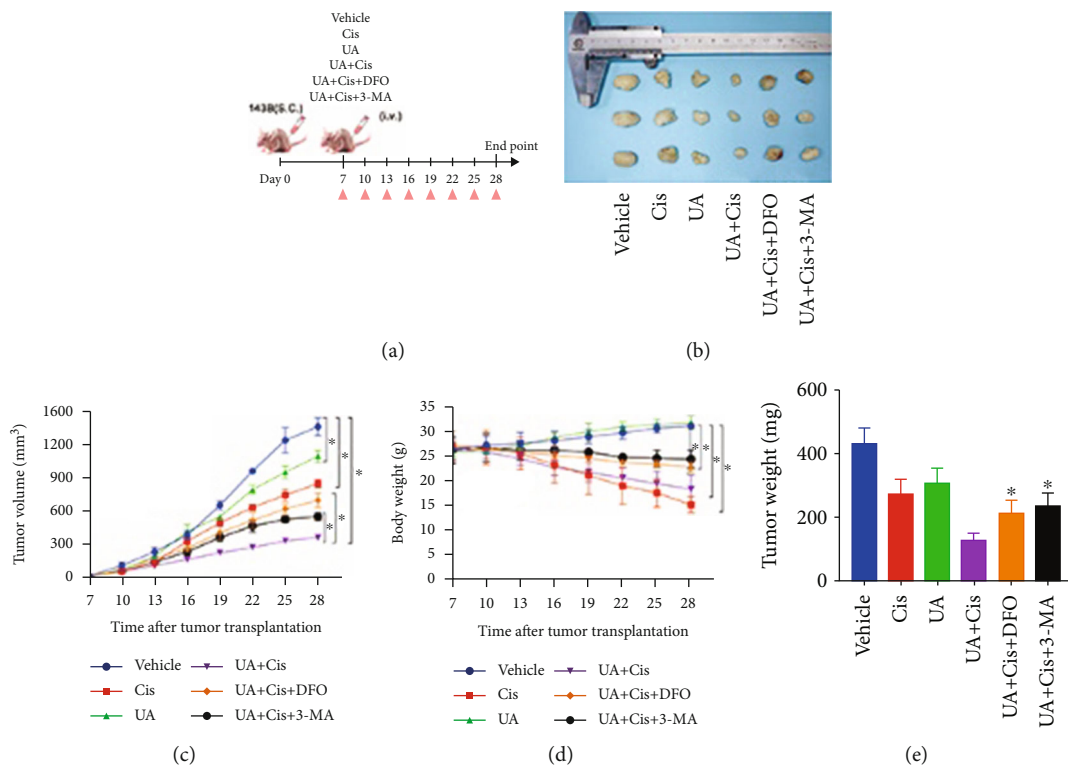
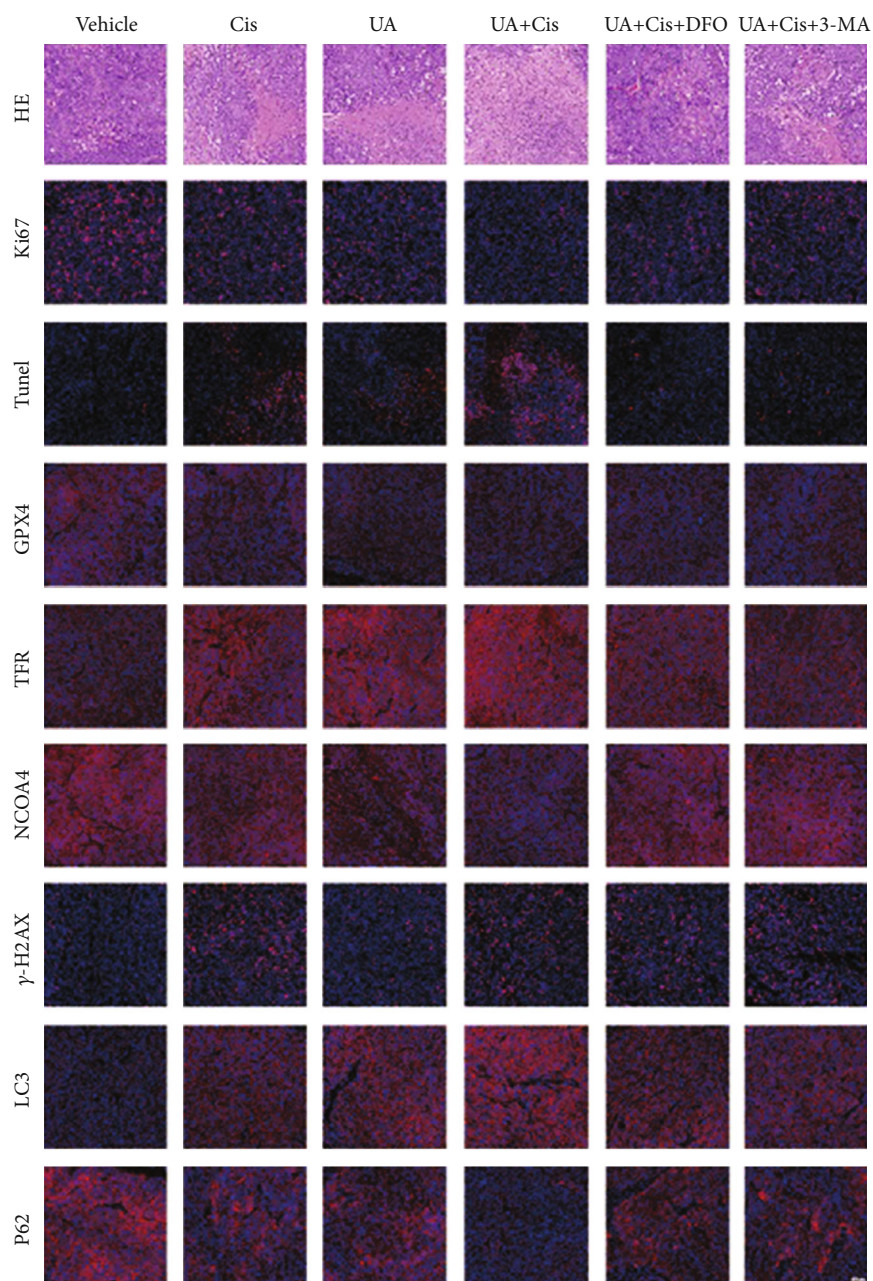


FIGURE 7: Continued.



(f)

FIGURE 7: The combination of UA and Cis inhibited the growth of xenografts in vivo. Time flow chart of in vivo mouse xenograft models (a). Macroscopic view of xenograft tumours at the endpoint of the experiment (b) ( $n = 3$ ). The average tumour volume and weight and body weight of the different groups (c–e) ( $n = 3$ ). H&E staining and immunofluorescence staining of autophagy-, ferroptosis-, and iron metabolism-related proteins in xenograft tissue sections (f) ( $n = 3$ , scale bar:  $50 \mu\text{m}$ ). The data are presented as the mean  $\pm$  SD. \* $p < 0.05$  vs. the control group.

## 5. Conclusion

This study provides strong evidence that UA can strongly enhance the DNA damage induced by Cis. Moreover, UA and Cis can synergistically exert regulatory effects at multiple levels by affecting multiple targets simultaneously, making OS cells susceptible to ferroptosis. Notably, the properties of UA enhance its anticancer activity and its effect against chemotherapy resistance in OS, which may be a promising thera-

peutic strategy. This supports its use as an adjuvant to synergistically improve the efficacy of current chemotherapy regimens for OS.

## Abbreviations

OS: Osteosarcoma  
 Cis: Cisplatin  
 TCM: Traditional Chinese medicine

|         |                                     |
|---------|-------------------------------------|
| UA:     | Ursolic acid                        |
| DFO:    | Desferrioxamine                     |
| 3-MA:   | 3-Methyladenine                     |
| CCK-8:  | Cell Counting Kit-8                 |
| EdU:    | 5-Ethynyl-2'-deoxyuridine assay     |
| PI:     | Propidium iodide                    |
| ROS:    | Reactive oxygen species             |
| MDA:    | Malondialdehyde                     |
| 4-HNE:  | 4-Hydroxynonenal                    |
| H&E:    | Haematoxylin-eosin                  |
| MDR:    | Multidrug resistance                |
| FTL1:   | Ferritin light peptide 1            |
| FTH1:   | Ferritin heavy peptide 1            |
| DCF-DA: | 2',7'-Dichlorofluorescein diacetate |
| TFR1:   | Transferrin receptor 1              |
| NCOA4:  | Nuclear receptor coactivator 4.     |

### Data Availability

The raw data supporting the conclusions of this article will be made available by the authors, without undue reservation, to any qualified researcher.

### Ethical Approval

All animal work was carried out following the guidelines of the Ethics Committee of the Fourth Military Medical University and was performed according to the institutional guidelines for the care and use of laboratory animals.

### Conflicts of Interest

The authors declare that the research was conducted in the absence of any commercial or financial relationships that could be construed as a potential conflict of interest.

### Authors' Contributions

Zhen Tang, Hui Dong, Tian Li, Zheng Guo, and Xin Xiao are responsible for the concept and design. Zhen Tang, Hui Dong, Tian Li, Ning Wang, Wei Wang, and Xin Xiao acquired the data. Zhen Tang, Zheng Guo, and Xinghui Wei analysed the data and drafted the manuscript. Zhen Tang, Hao Wu, Ning Wang, and Yichao Liu acquired, analysed, and interpreted the data and performed the statistical analysis. The authors read and approved the final manuscript. Zhen Tang, Hui Dong, Tian Li, and Ning Wang contributed equally to this study.

### Acknowledgments

We thank all researchers involved in this study for their constructive comments. This work was supported by grants from the Key R&D program of Shaanxi Province (2020SF-075), the National Natural Science Foundation of China (No. 81902897), and the Independent Program of the State Key Laboratory of Cancer Biology, China (CBSKL2019ZZ21).

### References

- [1] F. Li, L. Miao, T. Xue et al., "Inhibiting PAD2 enhances the anti-tumor effect of docetaxel in tamoxifen-resistant breast cancer cells," *Journal of Experimental & Clinical Cancer Research*, vol. 38, no. 1, p. 414.
- [2] K. Huang, Y. Chen, R. Zhang et al., "Honokiol induces apoptosis and autophagy via the ROS/ERK1/2 signaling pathway in human osteosarcoma cells in vitro and in vivo," *Cell Death & Disease*, vol. 9, no. 2, p. 157.
- [3] J. H. Yen, S. T. Huang, H. S. Huang et al., "HGK-sestrin 2 signaling-mediated autophagy contributes to antitumor efficacy of Tanshinone IIA in human osteosarcoma cells," *Cell Death & Disease*, vol. 9, no. 10, p. 1003.
- [4] F. Arnesano and G. Natile, "Interference between copper transport systems and platinum drugs," in *Seminars in Cancer Biology*, Nature Publishing Group, New York, NY, 2018.
- [5] V. Shaw, S. Srivastava, and S. K. Srivastava, "Repurposing antipsychotics of the diphenylbutylpiperidine class for cancer therapy," *Seminars in Cancer Biology*, vol. 68, pp. 75–83.
- [6] A. Ghoneum, S. Almousa, B. Warren et al., "Exploring the clinical value of tumor microenvironment in platinum-resistant ovarian cancer," *Seminars in Cancer Biology*, 2021.
- [7] D. W. Chan, M. M. Yung, Y. S. Chan et al., "MAP30 protein from *Momordica charantia* is therapeutic and has synergic activity with cisplatin against ovarian cancer *in vivo* by altering metabolism and inducing ferroptosis," *Pharmacological Research*, vol. 161, p. 105157, 2020.
- [8] J. Chen, H. Fu, Z. Wang et al., "A new synthetic ursolic acid derivative IUA with anti-tumor efficacy against osteosarcoma cells via inhibition of JNK signaling pathway," *Cellular Physiology and Biochemistry*, vol. 34, no. 3, pp. 724–733, 2014.
- [9] Y. Pei, Y. Zhang, K. Zheng et al., "Ursolic acid suppresses the biological function of osteosarcoma cells," *Oncology Letters*, vol. 18, no. 3, pp. 2628–2638.
- [10] R. X. Zhang, Y. Li, D. D. Tian et al., "Ursolic acid inhibits proliferation and induces apoptosis by inactivating Wnt/ $\beta$ -catenin signaling in human osteosarcoma cells," *International Journal of Oncology*, vol. 49, no. 5, pp. 1973–1982.
- [11] T. Li, Y. Yin, N. Mu et al., "Metformin-enhanced cardiac AMP-activated protein kinase/atrogin-1 pathways inhibit charged multivesicular body protein 2B accumulation in ischemia-reperfusion injury," *Frontiers in Cell and Development Biology*, vol. 8, p. 621509.
- [12] S. Rottenberg, C. Disler, and P. Perego, "The rediscovery of platinum-based cancer therapy," *Nature Reviews. Cancer*, vol. 21, no. 1, pp. 37–50.
- [13] Q. Ding, W. Zhang, C. Cheng et al., "Dioscin inhibits the growth of human osteosarcoma by inducing G2/M-phase arrest, apoptosis, and GSDME-dependent cell death in vitro and in vivo," *Journal of Cellular Physiology*, vol. 235, no. 3, pp. 2911–2924.
- [14] C. L. Yao, J. Q. Zhang, J. Y. Li, W. L. Wei, S. F. Wu, and D. A. Guo, "Traditional Chinese medicine (TCM) as a source of new anticancer drugs," *Natural Product Reports*, 2020.
- [15] N. S. Yarla, A. Bishayee, G. Sethi et al., "Targeting arachidonic acid pathway by natural products for cancer prevention and therapy," *Seminars in Cancer Biology*, vol. 40–41, pp. 48–81.
- [16] S. Sommerwerk, L. Heller, J. Kuhfs, and R. Csuk, "Urea derivatives of ursolic, oleanolic and maslinic acid induce apoptosis

- and are selective cytotoxic for several human tumor cell lines,” *European Journal of Medicinal Chemistry*, vol. 119, pp. 1–16.
- [17] K. W. Lin, A. M. Huang, C. C. Lin et al., “Anti-cancer effects of ursane triterpenoid as a single agent and in combination with cisplatin in bladder cancer,” *European Journal of Pharmacology*, vol. 740, pp. 742–751.
- [18] Y. Wang, Z. Luo, D. Zhou et al., “Nano-assembly of ursolic acid with platinum prodrug overcomes multiple deactivation pathways in platinum-resistant ovarian cancer,” *Biomaterials Science*, vol. 9, no. 11, pp. 4110–4119.
- [19] Y. Li, D. Xing, Q. Chen, and W. R. Chen, “Enhancement of chemotherapeutic agent-induced apoptosis by inhibition of NF-kappaB using ursolic acid,” *International Journal of Cancer*, vol. 127, no. 2, pp. 462–473.
- [20] S. V. Torti and F. M. Torti, “Iron and cancer: more ore to be mined,” *Nature Reviews. Cancer*, vol. 13, no. 5, pp. 342–355.
- [21] K. Salnikow, *Role of iron in cancer*, *Semin Cancer Biol*, 2013.
- [22] E. B. Garon and P. Brodrick, “Targeted therapy approaches for MET abnormalities in non-small cell lung cancer,” *Drugs*, vol. 81, no. 5, pp. 547–554.
- [23] J. Bordini, F. Morisi, A. R. Elia et al., “Iron induces cell death and strengthens the efficacy of antiandrogen therapy in prostate cancer models,” *Clinical Cancer Research*, vol. 26, no. 23, pp. 6387–6398.
- [24] M. Tang, Z. Chen, D. Wu, and L. Chen, “Ferritinophagy/ferroptosis: iron-related newcomers in human diseases,” *Journal of Cellular Physiology*, vol. 233, no. 12, pp. 9179–9190.
- [25] W. Hou, Y. Xie, X. Song et al., “Autophagy promotes ferroptosis by degradation of ferritin,” *Autophagy*, vol. 12, no. 8, pp. 1425–1428.
- [26] G. Greco, E. Catanzaro, and C. Fimognari, “Natural products as inducers of non-canonical cell death: a weapon against cancer,” *Cancers (Basel)*, vol. 13, no. 2, p. 304.

## Research Article

# LINC00467, Driven by Copy Number Amplification and DNA Demethylation, Is Associated with Oxidative Lipid Metabolism and Immune Infiltration in Breast Cancer

Hao Bo,<sup>1,2,3</sup> Wancong Zhang<sup>4,5</sup>, Xiaoping Zhong<sup>4,5</sup>, Jiasheng Chen<sup>4,5</sup>, Yang Liu<sup>6</sup>,  
Kit-Leong Cheong<sup>6</sup>, Pengju Fan<sup>1</sup> and Shijie Tang<sup>4,5</sup>

<sup>1</sup>Department of Plastic and Esthetic Surgery, Xiangya Hospital of Central South University, Changsha, Hunan 410008, China

<sup>2</sup>Key Laboratory of Reproductive and Stem Cell Engineering, National Health and Family Planning Commission, Institute of Reproductive and Stem Cell Engineering, Basic Medicine College, Central South University, Changsha, Hunan 410078, China

<sup>3</sup>Clinical Research Center for Reproduction and Genetics in Hunan Province, Reproductive and Genetic Hospital of CITIC-Xiangya, Changsha, Hunan 410078, China

<sup>4</sup>Department of Plastic Surgery and Burn Center, Second Affiliated Hospital, Shantou University Medical College, Shantou, Guangdong 515000, China

<sup>5</sup>Plastic Surgery Institute of Shantou University Medical College, Guangdong 515000, China

<sup>6</sup>Guangdong Provincial Key Laboratory of Marine Biotechnology, Department of Biology, College of Science, Shantou University, Shantou, Guangdong 515063, China

Correspondence should be addressed to Pengju Fan; fanpj2005@126.com and Shijie Tang; sjtang3@stu.edu.cn

Received 27 July 2021; Revised 30 October 2021; Accepted 10 November 2021; Published 15 December 2021

Academic Editor: Guoku Hu

Copyright © 2021 Hao Bo et al. This is an open access article distributed under the Creative Commons Attribution License, which permits unrestricted use, distribution, and reproduction in any medium, provided the original work is properly cited.

Breast cancer (BRCA) is a malignant tumor with a high incidence and poor prognosis in females. However, its pathogenesis remains unclear. In this study, based on bioinformatic analysis, we found that LINC00467 was highly expressed in BRCA and was associated with tumor metastasis and poor prognosis. The genomic and epigenetic analysis showed that LINC00467 may also be regulated by copy number amplification (CNA), chromatin openness, and DNA methylation. In vitro experiments showed that it could promote the proliferation, migration, and invasion of BRCA cells. Competitive endogenous RNA (ceRNA) regulatory network analysis and weighted gene coexpression network analysis (WGCNA) suggested that LINC00467 may play a role in signaling pathways of peroxisomal lipid metabolism, immunity, and others through microRNAs (miRNAs) targeting transforming growth factor beta 2 (TGFB2). In addition, copy number amplification and high expression of LINC00467 were associated with the low infiltration of CD8+ and CD4+ T cells. In conclusion, we found that LINC00467, driven by copy number amplification and DNA demethylation, may be a potential biomarker for the diagnosis and prognosis of BRCA and a tumor promoter acting as a potential therapeutic target for BRCA as well.

## 1. Introduction

Breast cancer (BRCA) is one of the most common malignancies affecting women worldwide, and approximately more than 1.3 million women will develop BRCA during their lifetime each year. BRCA also has a high mortality rate and continues to be the most common cause of death among female cancer patients in the world, causing 458,000 deaths every year [1], and its incidence continues to grow globally [2].

BRCA can be mainly divided into subtypes of luminal A, luminal B, normal breast-like, HER-2, and basal-like. The causes of BRCA are complicated, among which obesity and smoking are the most common risk factors [3, 4]. BRCA treatments include surgery, chemotherapy, hormone therapy, radiotherapy, and immunotherapy; however, due to the intratumor heterogeneity in breast cancer, its pathogenesis has remained unclear. Furthermore, the predictive biomarker(s) for recurrence and metastasis of BRCA are still

unavailable. Distal metastasis of the lung, liver, bone, and brain [5–7] from BRCA have been identified as the most common and troublesome consequences; therefore, it is of great significance to find new therapeutic targets and molecular biomarkers for BRCA.

LncRNA is a type of noncoding RNA (ncRNA) molecule with a length of more than 200 nucleotides. It can regulate the gene expression at the epigenetic, transcriptional, translational, and posttranslational levels. Studies have shown that lncRNA is dysexpressed and involved in the pathological process of a variety of cancers, including BRCA. LINC00152 acts as a tumor promoter in BRCA and other carcinomas [8], and lincROR has also been found to promote the invasion, migration, and drug resistance of BRCA through various signaling pathways such as EMT and MAPK/ERK [9–12]. In addition, LINC00673 can promote the proliferation of BRCA cells through the signaling pathway of miR-515-5p/MARK4/Hippo [13]. The above evidence suggests that lncRNA plays a crucial role in BRCA, but its mechanism remains unclear. Furthermore, few biomarkers of lncRNA related to BRCA are available in clinical practice.

In this study, through data mining of the public databases, including Gene Expression Omnibus (GEO), the Cancer Genome Atlas (TCGA), Molecular Taxonomy of Breast Cancer International Consortium (METABRIC), and Cancer Cell Line Encyclopedia (CCLE), we found that the LINC00467 expression rose significantly in BRCA and could be used as the potential diagnostic and prognostic biomarker for it. Furthermore, we confirmed LINC00467 as a tumor promoter *in vitro* and predicted the mechanism of LINC00467 dysexpression as well as its regulation of downstream signaling pathways based on bioinformatics analysis, providing a new insight for the development of biomarkers and therapeutic targets for BRCA.

## 2. Material and Methods

**2.1. Meta-Analysis Based on the Databases of GEO and TCGA.** Firstly, GSE7904 [14], GSE45827 [15], GSE65194 [16, 17], GSE22820 [18, 19], and GSE38959 were selected from the GEO database. Then, difference analysis was performed using GEO2R, with cut-off values of  $\log_2|FC| > 1$  and adjusted  $p$  value  $< 0.05$  for the screening of differential genes (Supplementary Table 1–5). Based on the Ensemble and RefSeq database annotation, the top 10 lncRNAs with significant differential expression were extracted, and heat maps were constructed through meta-analysis via the RobustRankAggreg of *R* package [20]. The TCGA-BRCA cohort in the Gene Expression Profiling Interactive Analysis (GEPIA) [21] database (<http://gepia.cancer-pku.cn/index.html>) was used to verify the 10 lncRNAs (5 upregulated and 5 downregulated, Supplementary Table 6). GSE57297 [22, 23], a dataset containing 25 BRCA samples and 7 nontumor samples, was downloaded from the GEO database, among which the data of 4 probes of LINC00467 were extracted (A\_23\_P1014, A\_19\_P00318494, A\_33\_P3223097, and A\_19\_P00318495), helping to further verify the differential expression of LINC00467 in BRCA.

Similarly, GSE1299 [24] was downloaded from the GEO database, and the expression levels of LINC00467 in breast cancer cell lines were displayed. The expression levels of LINC00467 in BRCA cell lines (CCLE data) were downloaded from the University of California Santa Cruz (UCSC) Xena [25] database (<https://xena.ucsc.edu/>).

**2.2. Association Analysis between LINC00467 and BRCA.** The ROC curves of the LINC00467 expression in TCGA-BRCA cohort obtained from the UCSC Xena database were calculated. GSE9893 [26] was downloaded from the GEO database to analyze the association between LINC00467 and BRCA metastasis. The LINC00467 expression in circulating tumor cells (CTCs), including GSE41245 [27] and GSE55807 [28], was downloaded from the ctcRbase [29] database (<http://www.origin-gene.cn/database/ctcRbase/index>). Kaplan–Meier survival curves of LINC00467 based on different datasets were present with Kaplan–Meier Plotter [30] (<http://kmplot.com/analysis/index>).

**2.3. Data Mining of Single-Cell Sequencing (SCS).** GSE113197 [31, 32], a dataset of single-cell transcriptome sequencing of human breast, was downloaded from the Human Cell Landscape [33] database (<http://bis.zju.edu.cn/HCL/>). SCS and its relevant enrichment analysis of BRCA CTCs were all performed by the CancerSEA [34] database (<http://biocc.hrbmu.edu.cn/CancerSEA/home.jsp>) according to the default parameters.

**2.4. Analysis of Copy Number Variation (CNV) of LINC00467.** The information data of patients, the expression data, and CNV data of LINC00467 in the TCGA-BRCA cohort and METABRIC cohort were downloaded from the cbiportal [35, 36] database (<https://www.cbiportal.org/>), as well as the expression data and CNV data of LINC00467 in the BRCA cell lines (CCLE data). Bar charts, pie charts, and box plots were displayed with ggplot2 [37] of the *R* package, while survival curves were calculated by survminer of the *R* package.

**2.5. Epigenetic Mechanisms of LINC00467.** Expression data of LINC00467, chromatin openness data, and methylation data of the promoter region in the TCGA-BRCA cohort were downloaded from the UCSC Xena database. H3K27ac, H3K4me3, and sensitivity data of DNA enzyme related to LINC00467 in the BRCA cell line MCF7 were downloaded and calculated with the UCSC Genome Browser [38] database (<https://genome.ucsc.edu/index.html>).

**2.6. Cell Culture, siRNA Transfection, and 5-Aza-Deoxycytidine Treatment.** The BRCA cell lines of MCF-7 and MDA-MB-231 were donated by the Cancer Research Institute of Central South University. Classically, Dulbecco's Modified Eagle's Medium (DMEM, GIBCO, NY - Grand Island, USA) containing 10% fetal bovine serum (FBS, GIBCO, NY - Grand Island, USA) and 1% penicillin-streptomycin is used as the culture medium in an incubator (5% CO<sub>2</sub>, 37°C). According to the protocol of Lipofectamine3000 (Lipo3K, Life Technologies, CA-Carlsbad, USA), short interfering ribonucleic acid (siRNA, RIBOBIO,



Guangzhou, China) of LINC00467 and its negative controls (NC, RIBOBIO, Guangzhou, China) were transfected with a final siRNA concentration of 50 nM in a 6-well plate. Cells were collected 48 hours after transfection for subsequent experiments. When the cell density reached 70%, we treated the cells with 10  $\mu$ M concentration of 5-aza-deoxycytidine in a 6-well plate and collected the cell pellet after 48 hours.

**2.7. RNA Isolation and Quantitative Real-Time PCR (qRT-PCR).** Cells were collected 48 hours after siRNA transfection and then washed with PBS. RNA was isolated by the TRIzol-based method (Life Technologies, CA-Carlsbad, USA). RNA integrity was verified by agar gel electrophoresis, while RNA concentration was detected using a nanopore spectrophotometer. Subsequently, the corresponding cDNA was synthesized using one microgram of qualified RNA per well as the template through a reverse transcription system kit. Then, qRT-PCR was performed using cDNA as the template through the Roche Transcriptor First Strand cDNA Synthesis Kit (Roche, Basel, Switzerland). Primer sequences were as follows: LINC00467 forward: 5'-TCGTCTTCAGGAAGCCAGAC-3' and reverse: 5'-TGGAAATCAAAGGGTCAGC-3'.  $\beta$ -Actin (ACTB) forward: 5'-CTGAGGATGCGAGGTTCTGCTTG-3', reverse: 5'-GTCACCGGAGTCCATCACGAT-3' (Sangon Biotech, Shanghai, China).  $\beta$ -Actin was used as the reference gene.

**2.8. Cell Migration and Invasion by Transwell Assay.** The ability to migrate and invade the capacities of cells was determined by transwell assay. For cell migration, 10,000 cells were inoculated above the 8  $\mu$ M chamber (Corning Inc., NY-Corning, USA) with a medium containing 200 microliters of 1% FBS and below the chamber with a medium containing 15% FBS of 800 microliters for 24 hours. For cell invasion, different from cell migration, the number of inoculated cells was increased up to 20,000, 1:5 diluted matrix glue was added above the chamber, and cells were incubated for 36 hours under the same medium with cell migration. Finally, five fields were randomly selected to take photos, and the number of cells passing through the chamber was counted.

**2.9. WGCNA and Pathway Enrichment Analysis.** Compared with traditional coexpression analysis, WGCNA is more suitable for constructing gene coexpression network in large samples and can construct more stable coexpression network [39]. So, it has great advantages in finding phenotype-related gene modules. In this study, gene expression data of the TCGA-BRCA cohort were downloaded from the UCSC Xena database, and the genes with the top 75% of the median absolute deviation were selected for subsequent WGCNA analysis. The WGCNA of the R package was used to construct the network with a power of 3. All the genes in the module where LINC00467 was located were extracted. Pathway enrichment analysis was carried out using Metascape software (<http://metascape.org/gp/index.html#/main/step1>) in accordance with the default parameters [40].

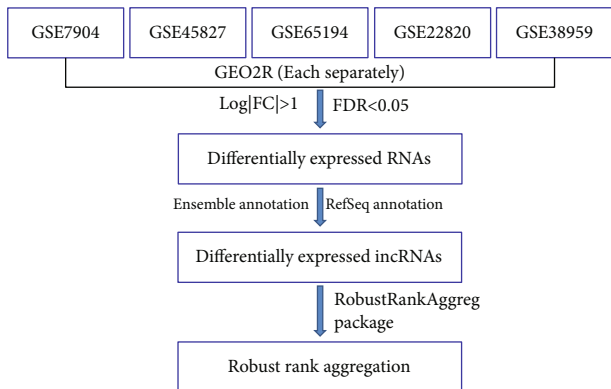
**2.10. Analysis of Competitive Endogenous RNA (ceRNA) Network Driven by the CNV of LINC00467.** Data analysis of ceRNA regulation network, enrichment, and ceRNA prognosis of LINC00467 was all performed by LnCeVar (<http://www.bio-bigdata.net/LnCeVar/index.jsp>) based on the TCGA-BRCA cohort according to the default parameters [41]. The expression correlation data of LINC00467 and TGFB2 (METABRIC cohort) were downloaded from the cBioportal database. Symbiosis of the copy number of both LINC00467 and TGFB2 was analyzed by cBioportal.

**2.11. Analysis of Immune Cell Infiltration.** Analysis of immune cell infiltration associated with different types of CNV of LINC00467 was performed by the TIMER2.0 [42] database (<http://timer.cistrome.org/>), while analysis of immune cell infiltration associated with the expression levels of LINC00467 was performed by the ImmLnc [43] database (<http://bio-bigdata.hrbmu.edu.cn/ImmLnc/index.jsp>). BRCA is a very common type of tumor. These two tools, TIMER2.0 and ImmLnc, are also developed for analysis of immune cell infiltration in common tumor types including BRCA. Thus, both were performed based on TCGA-BRCA cohort according to the default parameters.

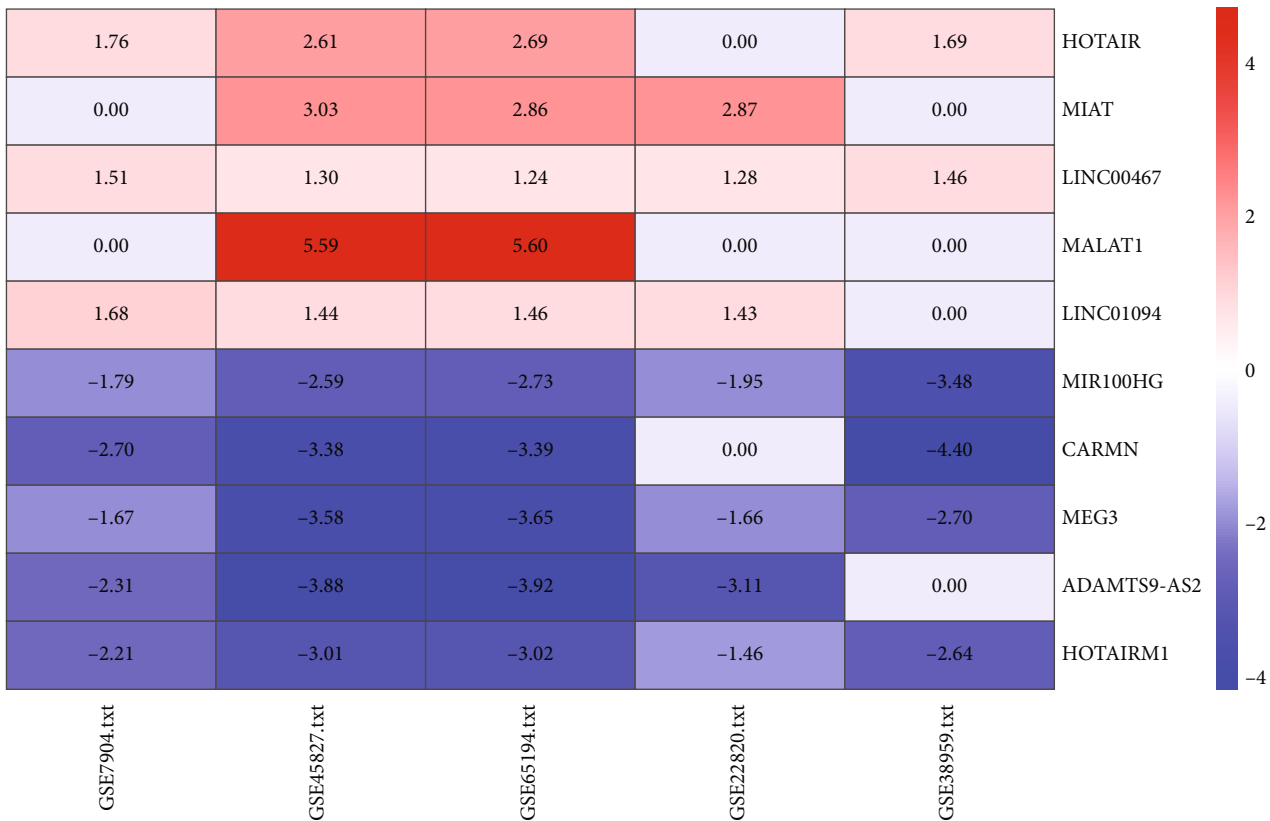
**2.12. Statistical Analysis.** The Student *t*-test was used for comparison between two groups, and ANOVA was used for comparison among groups. The descriptive data were expressed as mean  $\pm$  standard error (SE). Statistical analysis and graphs were performed by GraphPad Prism, R statistical software, or bioinformatics online tool (<http://www.bioinformatics.com.cn/>). *p* value <0.05 was considered significantly different for *t*-test and ANOVA. Adjusted *p* value <0.05 was considered significantly different for multiple tests.

### 3. Results

**3.1. The Significant Upregulation of the LINC00467 Expression in BRCA.** Meta-analysis based on GEO was conducted to find the 10 lncRNAs with the most significant difference and the most stable expression in 5 groups of gene chips (Figure 1(a)). We selected five upregulated and five downregulated lncRNAs, including LINC00467 and MALAT1 (Figure 1(b)), as candidates for further study. Expression data in BRCA from the GEPIA database showed that all of the lncRNAs were significantly different expressed except for MAIT; however, the trend of the differential expression of MALAT1 was not consistent with the gene chips of GEO (Supplementary Figure. 1A, 1B). Based on the gene chips of the GEO and GEPIA databases, we recognized LINC00467 as the molecule whose expression was upregulated most significantly and selected it for further study. Furthermore, we also verified the differential expression of LINC00467 in another GEO chip GSE57297 (the results of four probes of LINC00467 were consistent, as shown in Figure 1(c)). Compared with nontumor samples, the LINC00467 expression was also significantly upregulated in BRCA cell lines of HCC1954 and MDA-MB-436 (Figure 1(d)). We also found that the expression of



(a)



(b)

FIGURE 1: Continued.

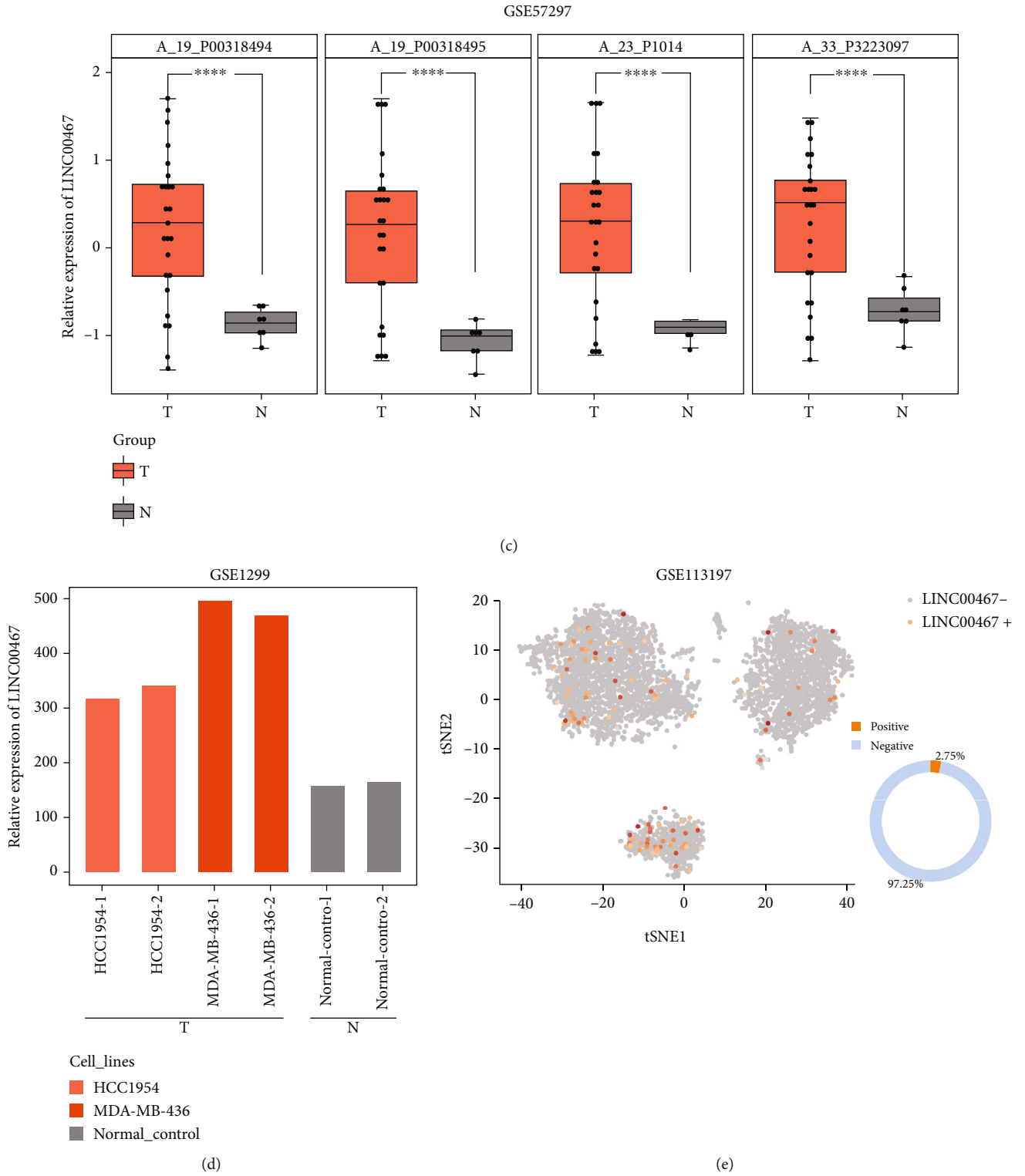


FIGURE 1: Continued.

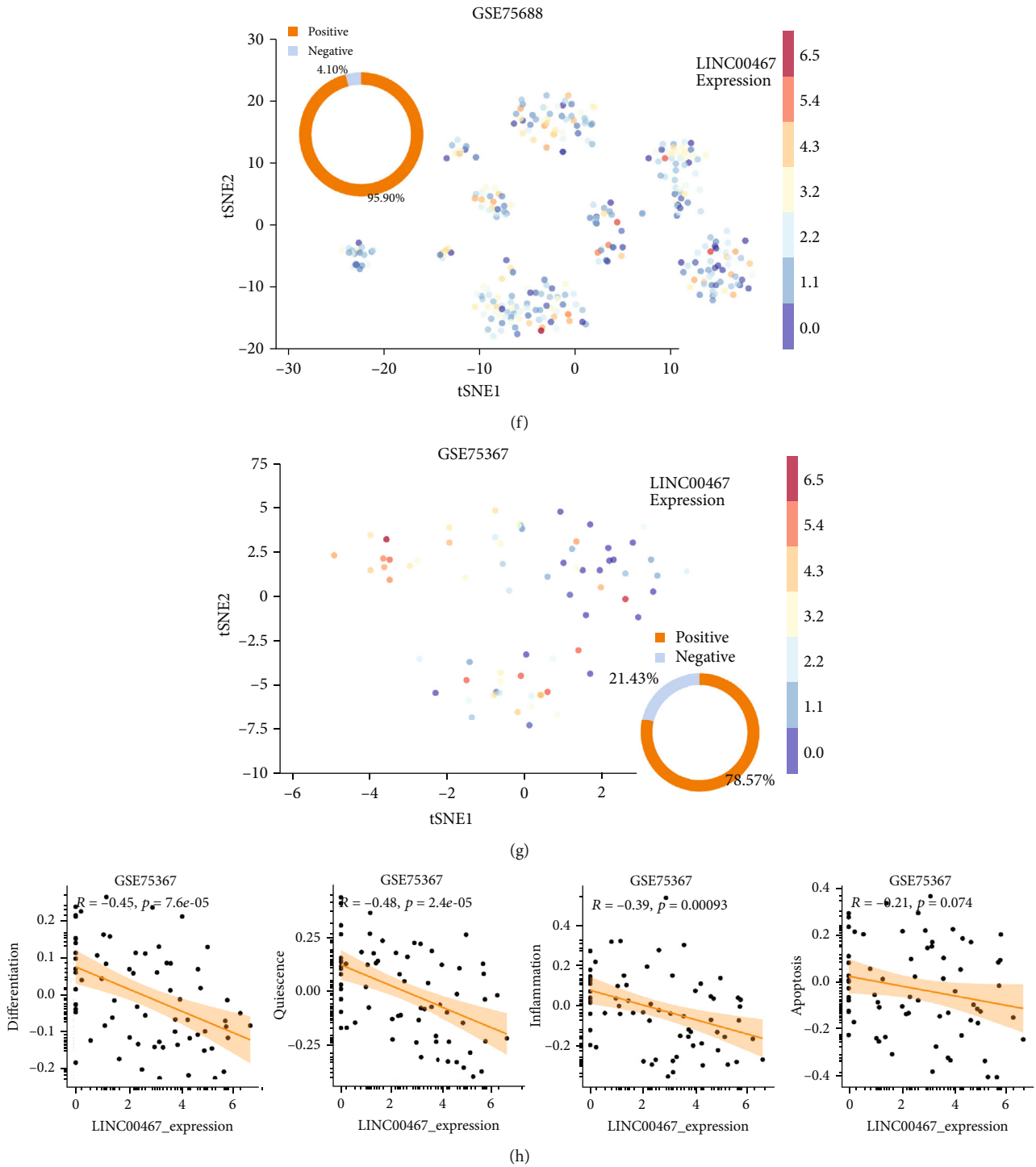


FIGURE 1: Upregulation of the LINC00467 expression in BRCA based on the integration of gene chips and RNA sequencing. (a) Flow chart: after the five gene chips of GEO were, respectively, analyzed with GEO2R, differentially expressed lncRNAs were screened out based on annotations of the Ensembl and RefSeq database, and then the RRA of the R package was used to screen the significantly different molecules in multiple datasets. (b) The top 10 differentially expressed lncRNAs based on RRA analysis (five upregulated and five downregulated) were calculated in the heat maps. (c) Another dataset of GEO was used to verify the differential expression of LINC00467 (samples of tissues). (d) Gene chips of GEO were used to verify differential expression of LINC00467 (samples of cell lines). (e) LINC00467 expression in breast cells (extreme low positive rate). (f) LINC00467 expression in BRCA (extreme high positive rate). (g) LINC00467 expression in BRCA CTCs. (h) Correlation between LINC00467 and phenotypes of BRCA CTCs based on the analysis of GSE75367. \*\*\*\* $p < 0.0001$ .

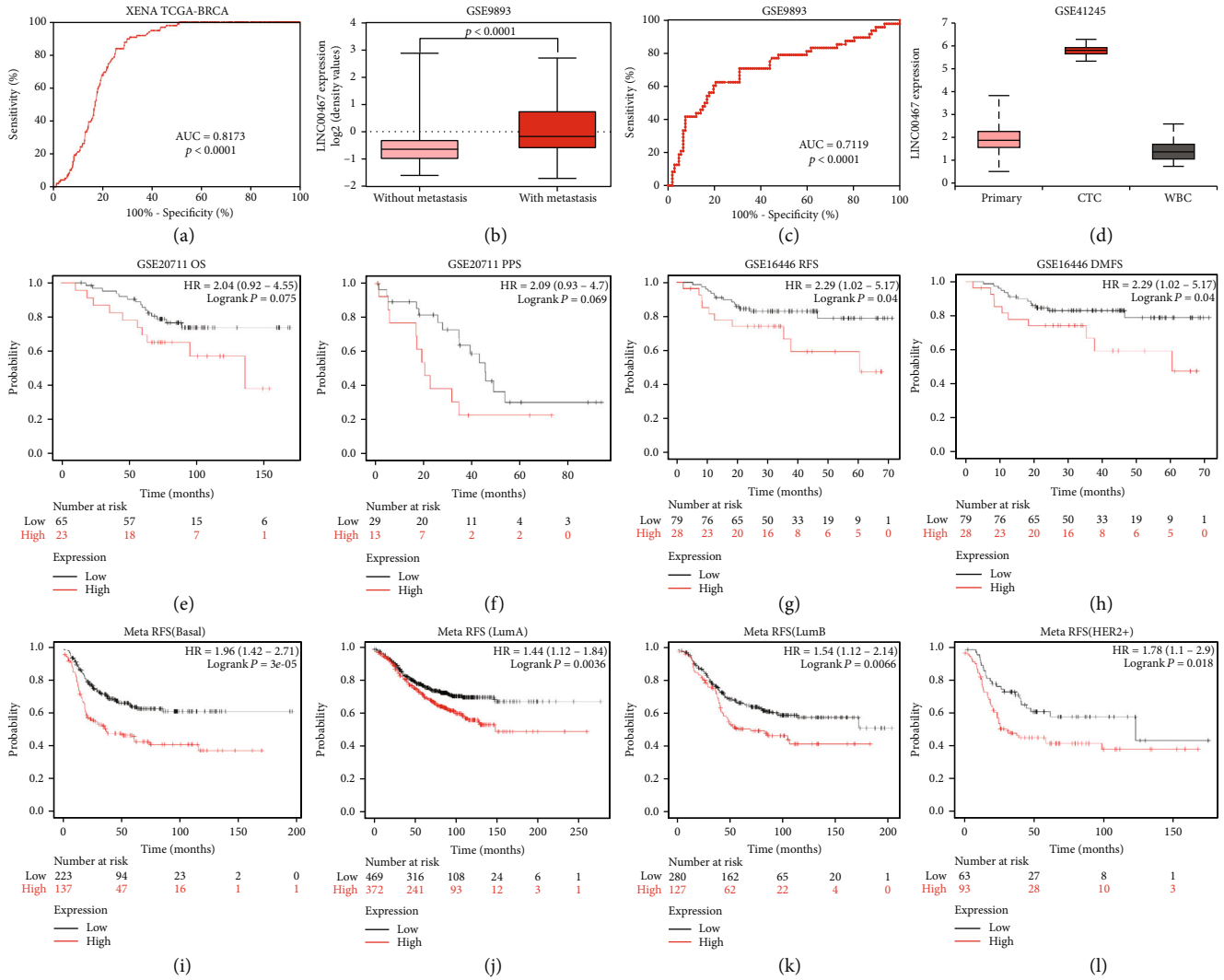


FIGURE 2: Diagnostic and prognostic values of LINC00467 in BRCA. (a) The diagnostic value of LINC00467 for BRCA based on TCGA BRCA cohort in the XENA database. (b) High expression of LINC00467 in metastatic BRCA based on GSE9893. (c) LINC00467 expression could distinguish metastatic and nonmetastatic tumor tissues. (d) LINC00467 expression was significantly higher in CTCs than in BRCA in situ. (e)–(h) The correlation between LINC00467 expression and OS/PPS/RFS/DMFS in different BRCA datasets. (i)–(l) The correlation between LINC00467 expression in different types of samples and RFS in multiple datasets.

LINC00467 in normal breast epithelial cell lines was lower than that of breast cancer cell lines based on CCLE data (Supplementary Figure 1C). These results suggested that LINC00467 may be a good biomarker for BRCA.

Single-cell sequencing (SCS) data showed that there were multiple cell types in both breast and BRCA. In order to explore the cell types where LINC00467 was expressed, we analyzed the data of SCS of breast tissues in the Human Cell Landscape database and that of BRCA tissues in the CancerSEA database, respectively, showing that the positive rate of LINC00467 in normal breast cells was very low, only 2.75% (Figure 1(e)), while the positive rate of LINC00467 in BRCA cells was high, reaching up to 95.9% (Figure 1(f)). What is more, the positive rate of LINC00467 in circulating tumor cells (CTCs) of BRCA was 78.57% (Figure 1(g)), suggesting that LINC00467 may be related to the occurrence and metastasis of BRCA. In addition, we also analyzed the relationship between LINC00467 and tumor-related signaling pathway

using CancerSEA, finding that the LINC00467 expression was significantly negatively correlated with the differentiation, rest, inflammation, and apoptosis of BRCA CTCs (Figure 1(h)), suggesting that LINC00467 may also play a role in promoting the survival of CTCs.

**3.2. Biomarker Value of LINC00467 in BRCA.** In order to explore the clinical value of LINC00467, we analyzed the diagnostic specificity and sensitivity of LINC00467 for BRCA based on the UCSC Xena database, finding that the LINC00467 expression could distinguish tumor and non-tumor tissues very well (Figure 2(a)). Besides, data analysis of GEO found that LINC00467 was significantly more highly expressed in metastatic BRCA tissues (Figure 2(b)), with good diagnostic specificity and sensitivity (Figure 2(c)). In addition, we also found that LINC00467 was significantly overexpressed in CTCs of BRCA (Figure 2(d), Supplementary Figure 2). These results suggested that LINC00467

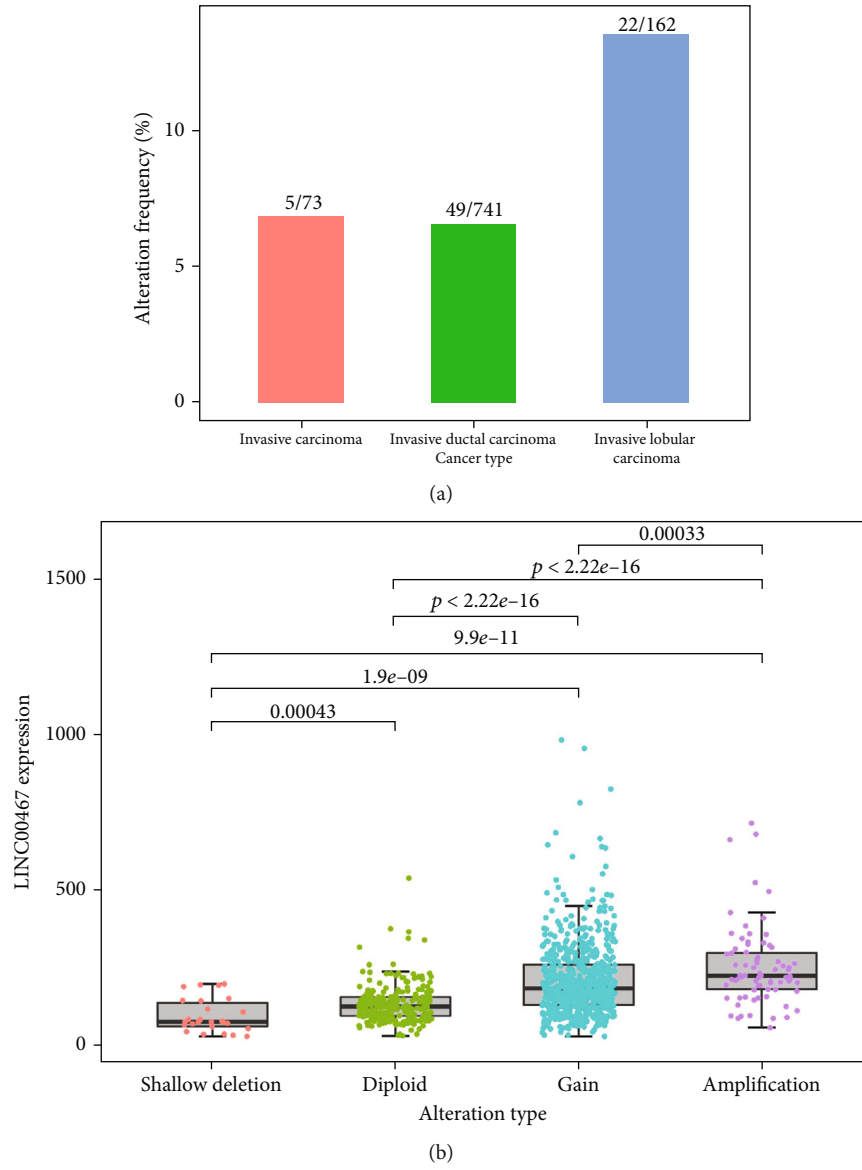


FIGURE 3: Continued.

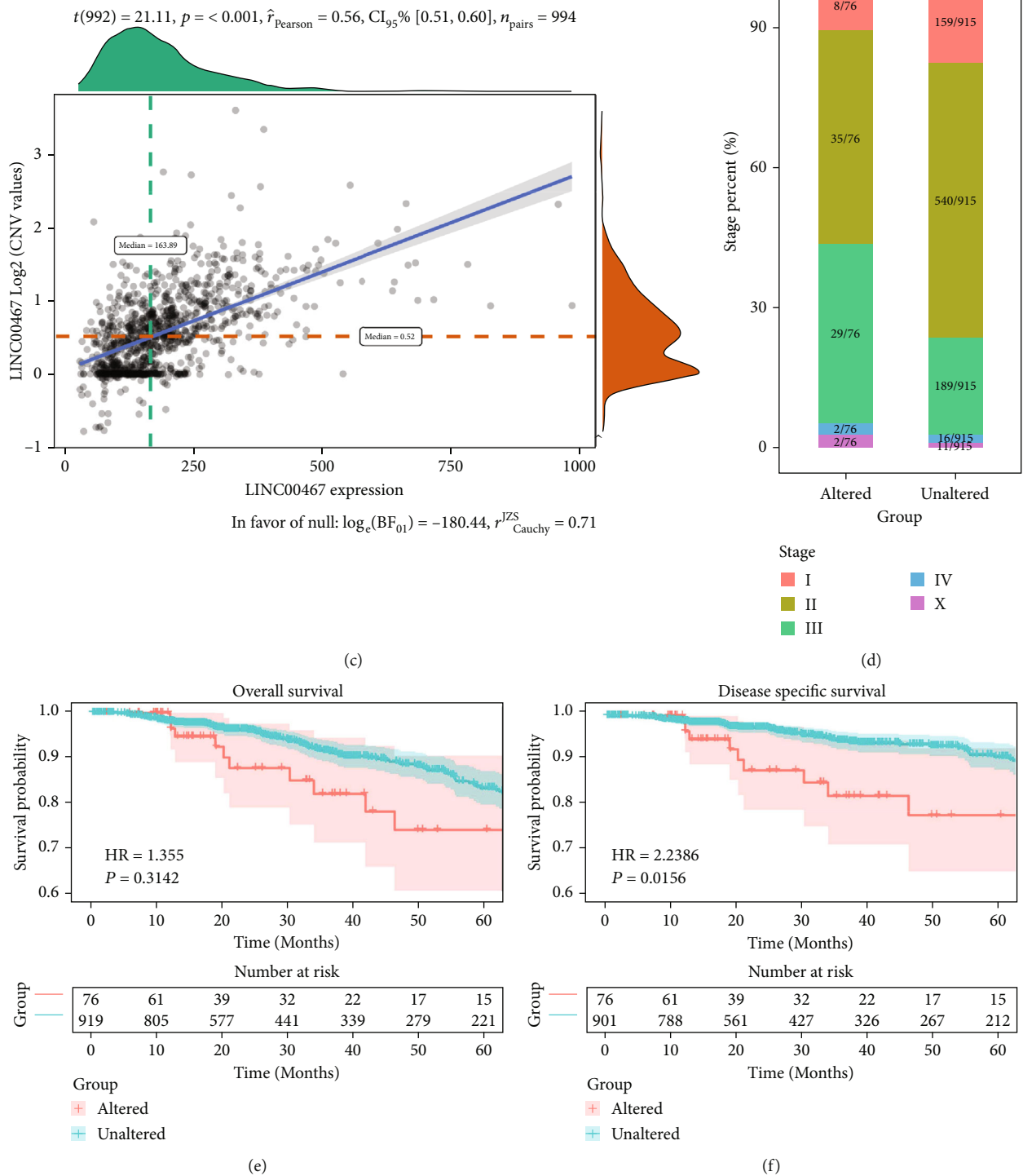


FIGURE 3: Continued.

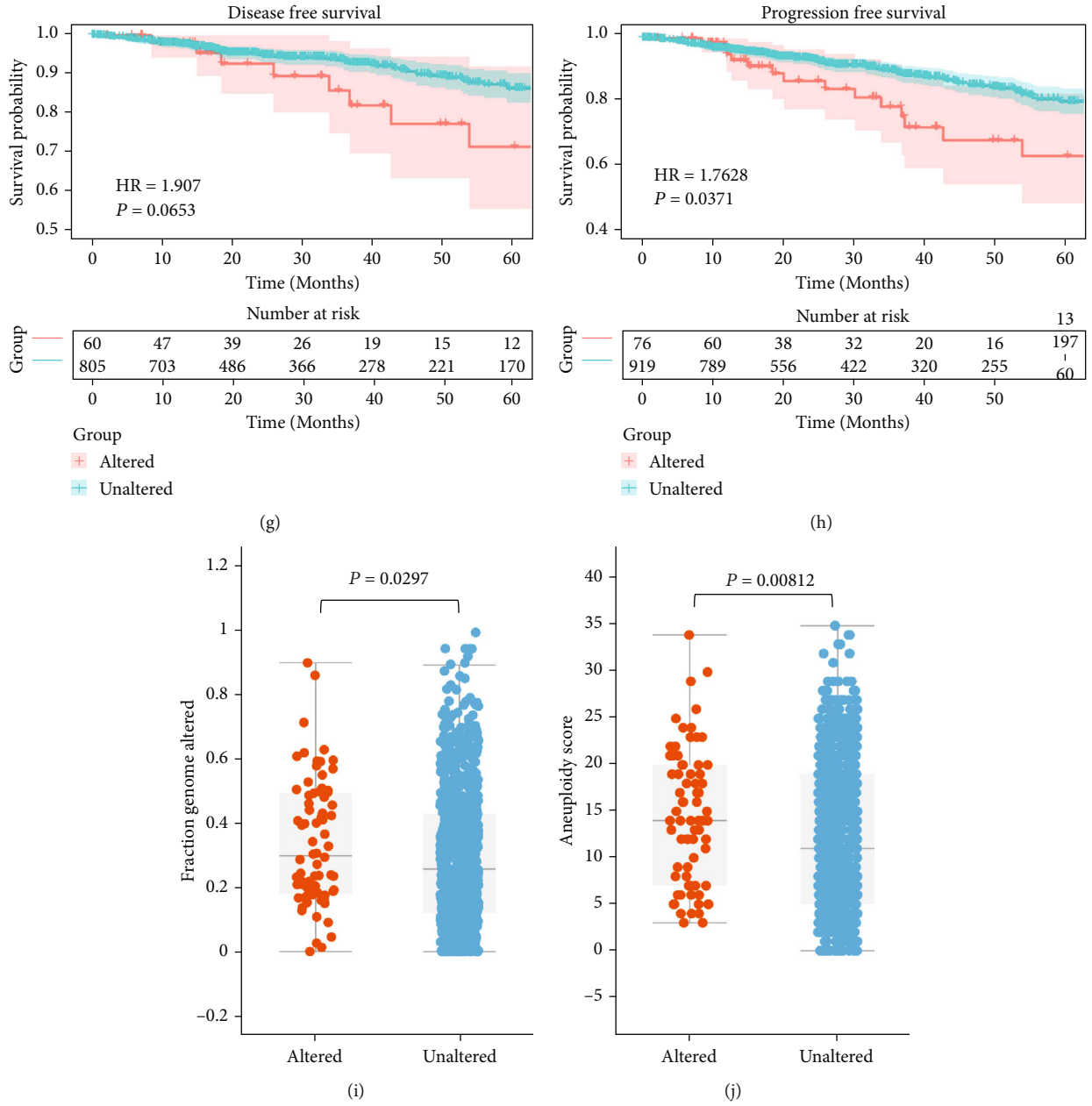


FIGURE 3: Continued.



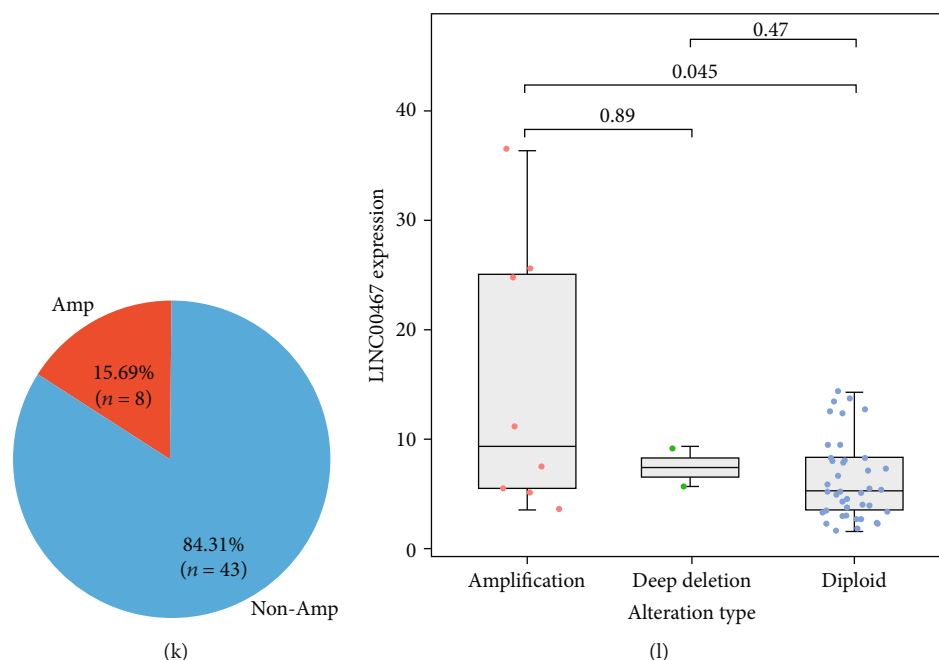


FIGURE 3: Analysis of LINC00467 CNV in BRCA. (a) LINC00467 has different frequencies of copy number amplification in different types of BRCA. (b) Relationship between LINC00467 expression and types of CNV. (c) The positive correlation between LINC00467 expression and its copy number level. (d) The positive correlation between copy number amplification of LINC00467 and stages of diseases. (e)–(h) Patients with LINC00467 amplified had a worse prognosis. (i) Patients with LINC00467 amplified showed more genomic changes. (j) Patients with LINC00467 amplified had higher aneuploidy scores. (k) LINC00467 showed a higher frequency of amplification in BRCA cell lines. (l) LINC00467 was more highly expressed in the amplified cell lines.

may be an excellent biomarker for the diagnosis and metastasis of BRCA.

Furthermore, we analyzed the association between LINC00467 and BRCA prognosis with Kaplan–Meier Plotter. Based on the analysis of the independent dataset, we found that LINC00467 was correlated with four prognostic parameters of BRCA (OS: overall survival/PPS: postprogression survival/RFS: relapse-free survival/DMFS: distant metastasis-free survival). The higher the expression of LINC00467, the lower the four parameters of BRCA would be (Figures 2(e)–2(h)). In addition, a meta-analysis of multiple groups of RFS data in Kaplan–Meier Plotter revealed that LINC00467 had a prognostic value for RFS among different pathological types of BRCA (Basal/LumA/LumB/Her2+) (Figures 2(i)–2(l)).

**3.3. Genomic Copy Number Amplification of LINC00467 in BRCA.** Studies have proven that a lot of lncRNAs had dose effects and were regulated by the genomic CNV [44, 45]. Therefore, we analyzed BRCA data in the Pan-Cancer Atlas based on TCGA and found that LINC00467 had a certain frequency of amplification in different types of BRCA, with the highest frequency in invasive lobular carcinoma, up to approximately 15% (Figure 3(a)). Furtherly, we analyzed the LINC00467 expression in different types of genomic variation, finding it was significantly higher in the increased or amplified genome than that in the deleted or normal diploid samples (Figure 3(b)), and significantly positively correlated with its CNV value (Figure 3(c)). In addition, we analyzed the correlation between the CNV of LINC00467 and the

clinicopathological characteristics of BRCA, finding that patients with CNV of LINC00467 were more likely to be at advanced Stage IV and Stage X of the tumor (Figure 3(d)). CNV of LINC00467 was also associated with the prognosis of the patients with BRCA, including OS, disease-specific survival (DSS), disease-free survival (DFS), progression-free survival (PFS), and patients with copy number amplification of LINC00467 that had a worse prognosis (Figures 3(e)–3(h)). In addition, we found that patients with copy number amplification of LINC00467 had greater genomic fragment changes and aneuploidy scores (Figures 3(i) and 3(j)), suggesting that LINC00467 may be associated with genomic instability of BRCA. Similarly, in the BRCA cell lines (based on CCLE data), LINC00467 also showed a high frequency of amplification, reaching up to 15.69% (Figure 3(k)), and was significantly more highly expressed in the samples with copy number amplification (Figure 3(l)). To verify the above results, we also analyzed the CNV of LINC00467 in another dataset of breast cancer (TCGA Firehose Legacy) finding that LINC00467 had a high frequency of copy number amplification in BRCA (Supplementary Figure. 3A), and the patients with dose-dependent effect and copy number amplification had a worse prognosis (Supplementary Figure. 3B–3D). Patients with copy number amplification of LINC00467 also had a higher proportion of advanced stages and more changes of genome fragments (Supplementary Figure. 3E–3G). These results fully indicated that genome amplification of LINC00467 may be one of the causes of upregulation of LINC00467 expression, LINC00467 may be one of the driver genes of BRCA, and its copy number

amplification may be a molecular biomarker of metastasis and recurrence for BRCA patients as well.

**3.4. Epigenetic Regulation of LINC00467.** Studies have shown that the expression of lncRNA is regulated by epigenetic factors such as DNA methylation and histone modification [46, 47]. Therefore, we analyzed the relationship between LINC00467 and its epigenetic modifications based on the TCGA BRCA cohort, finding that samples with high expression of LINC00467 also had high chromatin openness in the promoter (Figure 4(a)), and there was a close correlation between the LINC00467 expression and its chromatin openness (Figure 4(b)). Besides, patients with the high expression of LINC00467 had a lower 5-year overall survival rate (Figure 4(c)). These results suggest that epigenetic regulation may indeed be associated with a high expression of LINC00467. Further, we measured the average methylation level of the promoter of LINC00467, finding it was lower in tumor samples (Figure 4(d)) and significantly negatively correlated with the LINC00467 expression (Figures 4(e) and 4(f)). After MCF-7 cells treated with the DNA methyltransferase inhibitor 5-aza-deoxycytidine, we detected the expression of LINC00467 and found that the expression of LINC00467 was significantly upregulated (Figure 4(g)). In addition, we also found significant enrichment of H3K27ac/H3K4me3 (activated epigenetic modification) and peaks in the sensitivity of DNA enzyme near the LINC00467 promoter (Figure 4(h)). These results suggest that epigenetic modifications, including methylation and histone modifications, may lead to high expression of LINC00467.

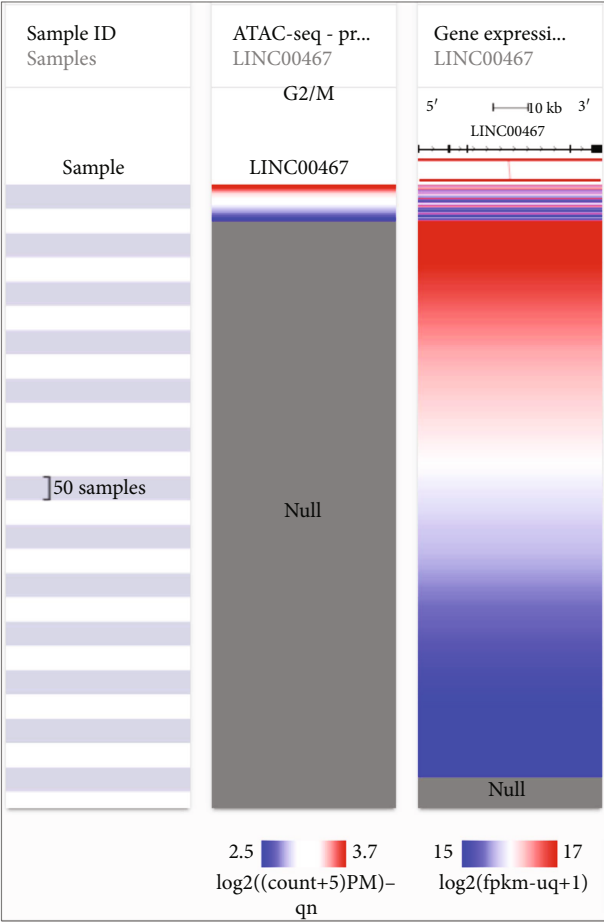
**3.5. Proliferation, Migration, and Invasion of BRCA Cells Inhibited by Silencing LINC00467.** In order to investigate the biological functions of LINC00467 in BRCA, we conducted the tests of cell migration and invasion using transwell assay after LINC00467 was silenced in BRCA cell lines (Figure 5(a)), and finding the proliferation ability of BRCA cells was significantly reduced after LINC00467 was silenced (Figure 5(b)). Similarly, we found that the number of migrating cells in LINC00467 siRNAs was significantly fewer than that in its NC group (Figure 5(c)), and their invasion ability was also significantly reduced (Figure 5(d)). These results confirmed that LINC00467 could promote the migration and invasion of BRCA cells.

**3.6. Screening of the Downstream Signals Regulated by LINC00467.** In order to explore the downstream signals regulated by LINC00467, we downloaded the data of the TCGA BRCA cohort and performed WGCNA. First, we filtered with the values of power and recognized 3 was the most appropriate power value (Supplementary Figure. 4A). Then, based on gene coexpression analysis, a total of 25 coexpression modules were obtained after merging their cluster trees (Figure 6(a)), with LINC00467 in the red module. Based on coexpressed molecules often coparticipate in some biological processes or pathways, we carried out tissue-specific and cell-specific enrichment analysis. We subsequently showed that this red module's genes were mainly concentrated in

breast cells and BRCA cells MCF-7 (Supplementary Figure. 4B), which was consistent with the high positive rate of LINC00467 in BRCA cells previously found in the SCS. Enrichment analysis revealed that these specific genes were mainly regulated by TFs such as FOXA1/TP53/TWIST1, which were highly related to the occurrence or progression of tumors (Supplementary Figure. 4C). The biological functions of these genes were mainly served for the phenotypes related to the development, proliferation, and growth of cells (Figure 6(b)). Finally, KEGG enrichment analysis showed that these molecules were mainly concentrated in signaling pathways related to tumorigenesis, lipid peroxide metabolism, or immunity, such as peroxisomal lipid metabolism, metabolism of lipids, antigen presentation, P53, and NOTCH (Figure 6(c)).

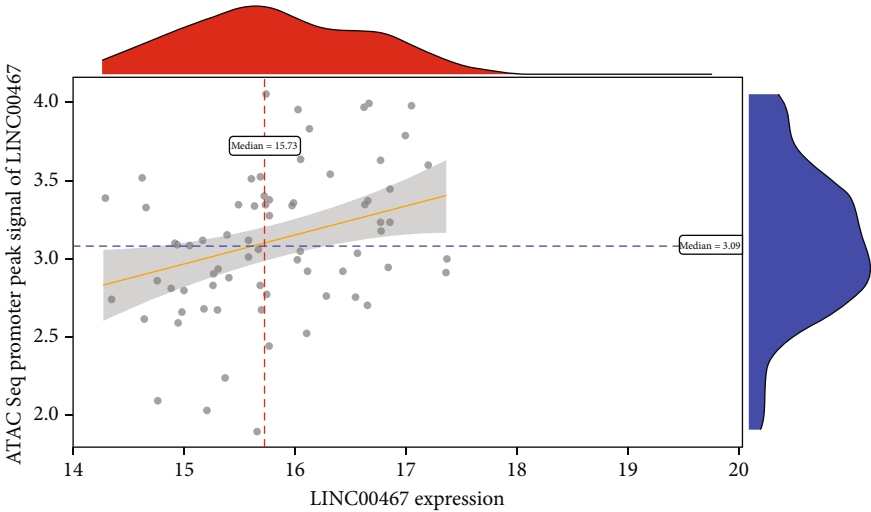
Previous studies have shown that LINC00467 may be involved in the regulation of gene expression through competing endogenous RNA (ceRNA) [48, 49]. Therefore, we speculated that LINC00467 may also play a role in BRCA through ceRNA. Based on the TCGA BRCA cohort, we analyzed ceRNA regulatory network mediated by LINC00467 using LnCeVar online tool and found that LINC00467 could regulate the gene expression through multiple miRNAs (Figure 6(d)), and a more multilevel regulatory network was further formed (Figure 6(e)), exerting a profound and lasting influence. Subsequently, enrichment analysis showed that the LINC00467-mediated ceRNA regulatory network functions were mainly concentrated in the malignant biological phenotypes of growth, apoptosis escape, migration/invasion, immune escape, and genomic instability, which were closely related to the tumors (Figure 6(f)). Among these ceRNAs, there was an important molecule, TGFB2, existing in the TGF- $\beta$  signaling pathway. And the expression correlation between LINC00467 and TGFB2 was also been further validated in the METABRIC data (Supplementary Figure. 4D). BRCA patients with the high TGFB2 expression showed a significantly lower overall survival rate (Figure 6(g)). Additionally, it is interesting that both TGFB2 and LINC00467 were located on the short arm of chromosome 1 (Figure 6(h)), and they were co-amplified in BRCA samples (Figure 6(i)).

**3.7. Immune Regulation of BRCA by LINC00467.** Studies have shown that many lncRNAs were involved in immune regulation of the tumors [50, 51]. However, whether LINC00467 was involved in tumor immunity of BRCA has remained unknown. Therefore, we analyzed the correlation between LINC00467 and the immune cells within the tumor microenvironment (TME) based on the TCGA BRCA cohort. Grouping according to the CNV types of LINC00467, we found that infiltrations of CD8+ T cells, CD8+ effector memory T cells, and CD8+ central memory T cells were all significantly reduced in the highly amplified LINC00467 group (Figure 7(a)). Meanwhile, infiltrations of CD4+ T cells, CD4+ effector memory T cells, and CD4+ central memory T cells were also significantly reduced (Figure 7(b)). These results suggested that the genomic variation of LINC00467 may be related to the infiltration of immune cells. Our previous analysis found that LINC00467



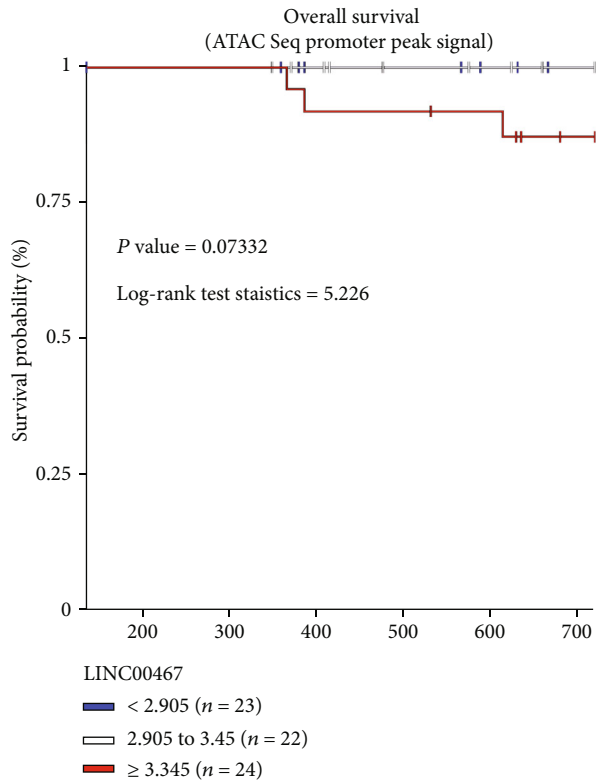
(a)

$t(70) = 2.72, p = 0.008, \hat{r}_{\text{Pearson}} = 0.31, CI_{95\%} [0.08, 0.50], n_{\text{pairs}} = 72$

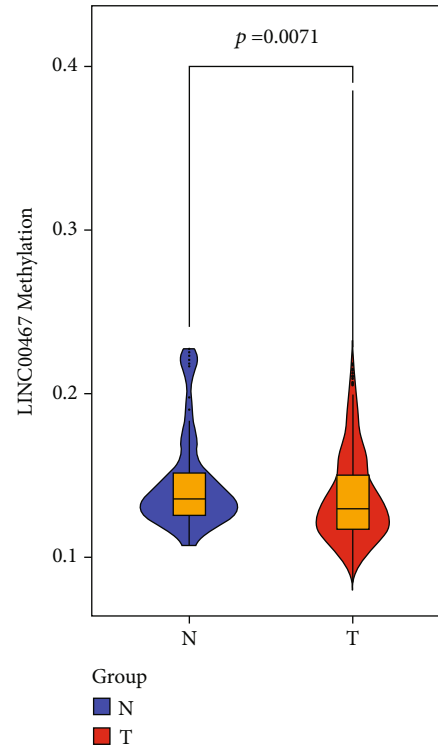


(b)

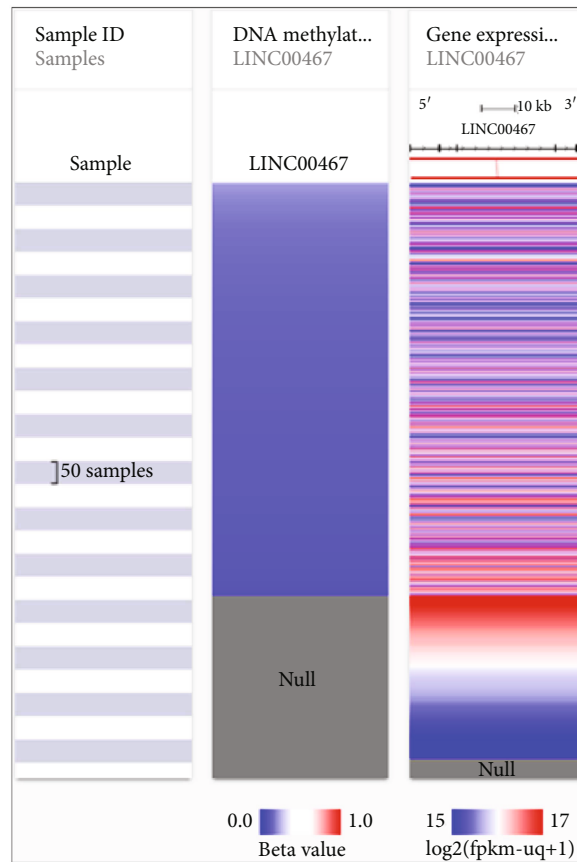
FIGURE 4: Continued.



(c)



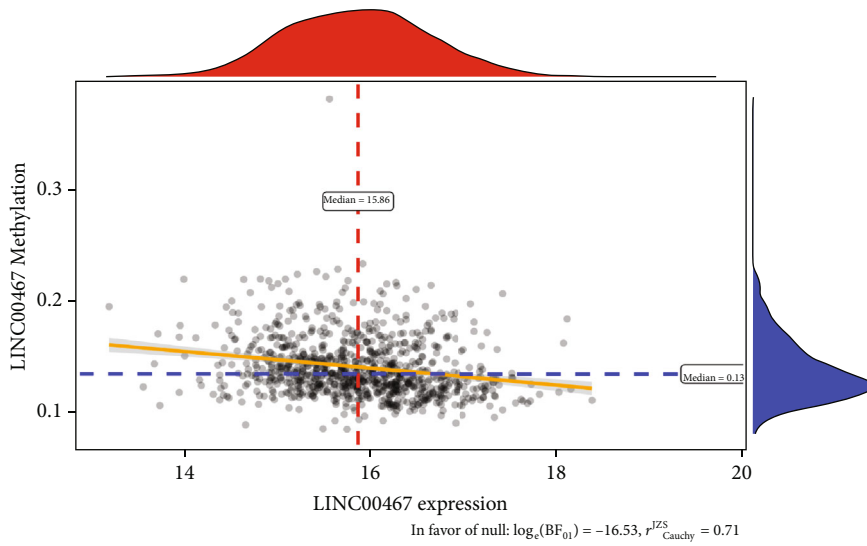
(d)



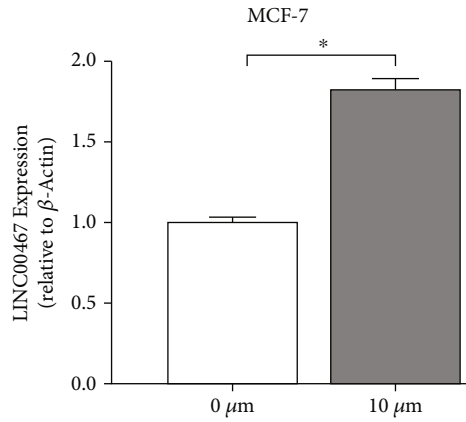
(e)

FIGURE 4: Continued.

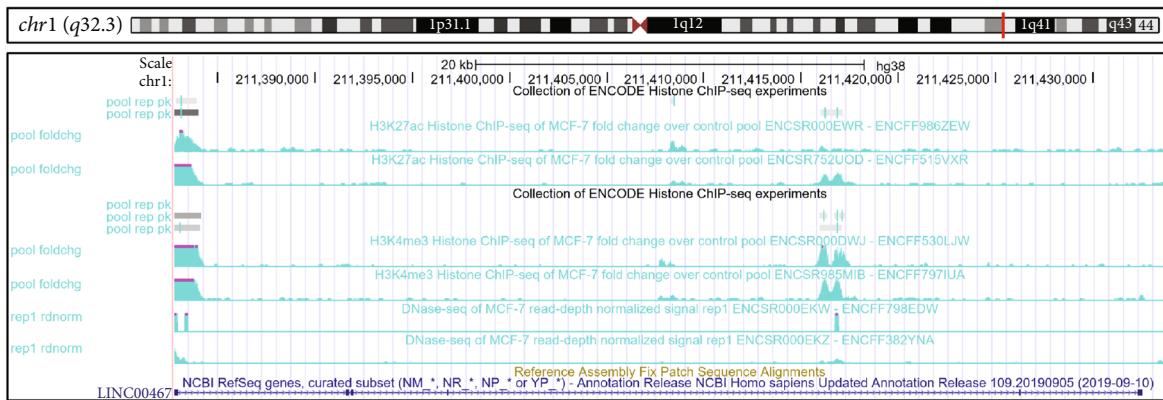
$$t(864) = -6.32, p < 0.001, \hat{r}_{\text{pearson}} = -0.21, \text{CI}_{95\%} [-0.27, -0.15], n_{\text{pairs}} = 866$$



(f)



(g)



(h)

FIGURE 4: Epigenetics and transcriptional regulatory mechanisms of LINC00467. (a) Heat map of the correlation between chromatin openness and LINC00467 expression based on the BRCA ATAC-Seq data and the expression data of the UCSC Xena database. (b) Correlation analysis of chromatin openness and expression level in LINC00467 promoter. (c) Association of chromatin openness of LINC00467 and the prognosis. (d) The significant differences of the methylation in LINC00467 promoter of BRCA. (e) Heat map of correlation between the methylation in LINC00467 promoter and LINC00467 expression. (f) The significant correlation between the methylation in the promoter and the expression of LINC00467. (g) The expression of LINC00467 in 5-aza-deoxycytidine treated cells was detected by qRT-PCR. (h) Active histone modifications of H3K27ac and H3K4me3 and sensitivities of DNA enzyme near the LINC00467 promoter in BRCA cells based on UCSC. \* $p < 0.05$ .

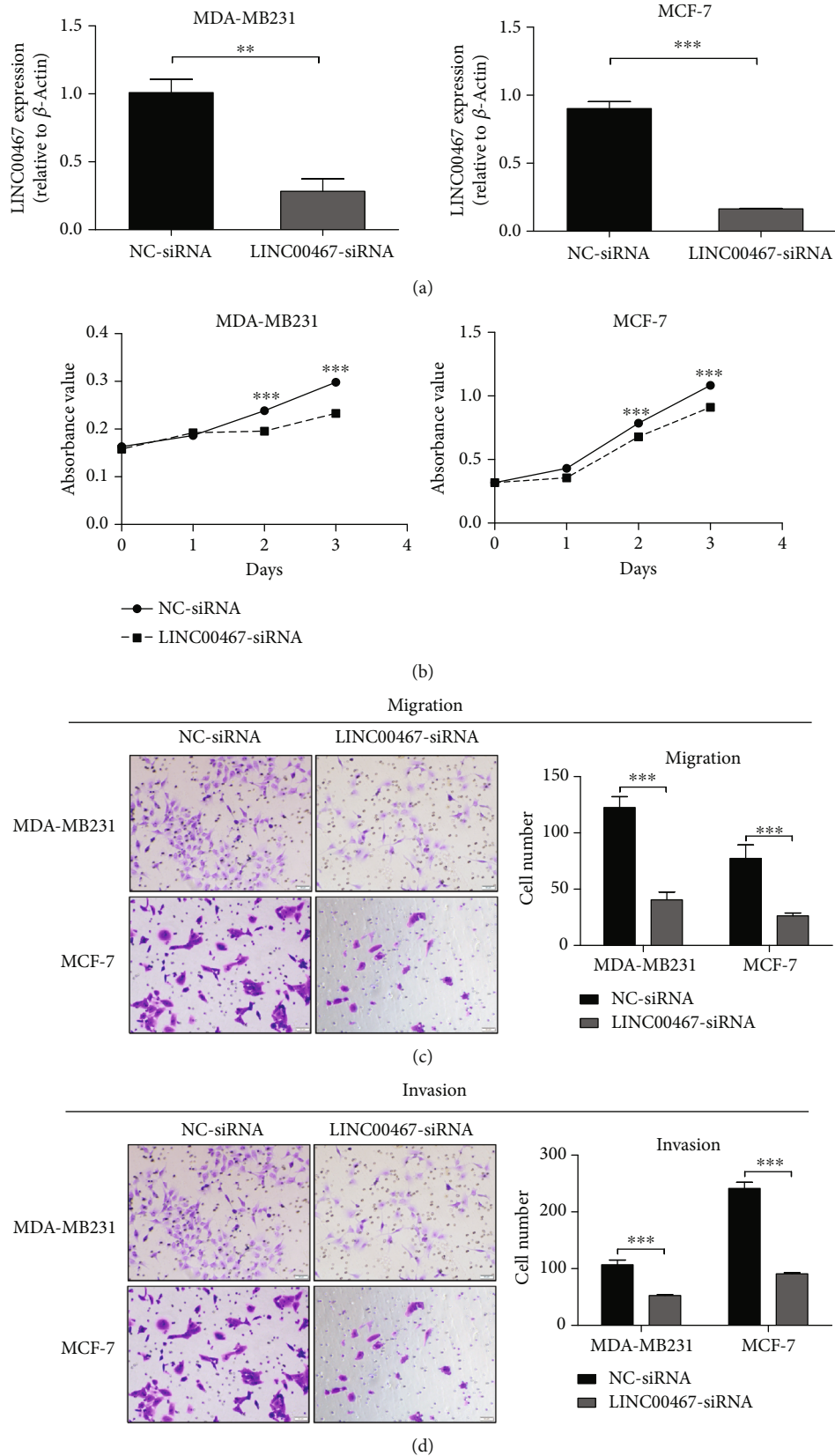


FIGURE 5: Silencing LINC00467 inhibits the malignant phenotypes of BRCA. (a) qRT-PCR was used to detect the silencing effect of LINC00467. (b) Changes in cell proliferation were detected by MTT assay after LINC00467 silenced. (c) Changes in cell migration were detected by transwell assay after LINC00467 silenced. (d) Changes in cell invasion were detected by transwell assay after LINC00467 silenced. \*\* $p < 0.01$ , \*\*\* $p < 0.001$ .

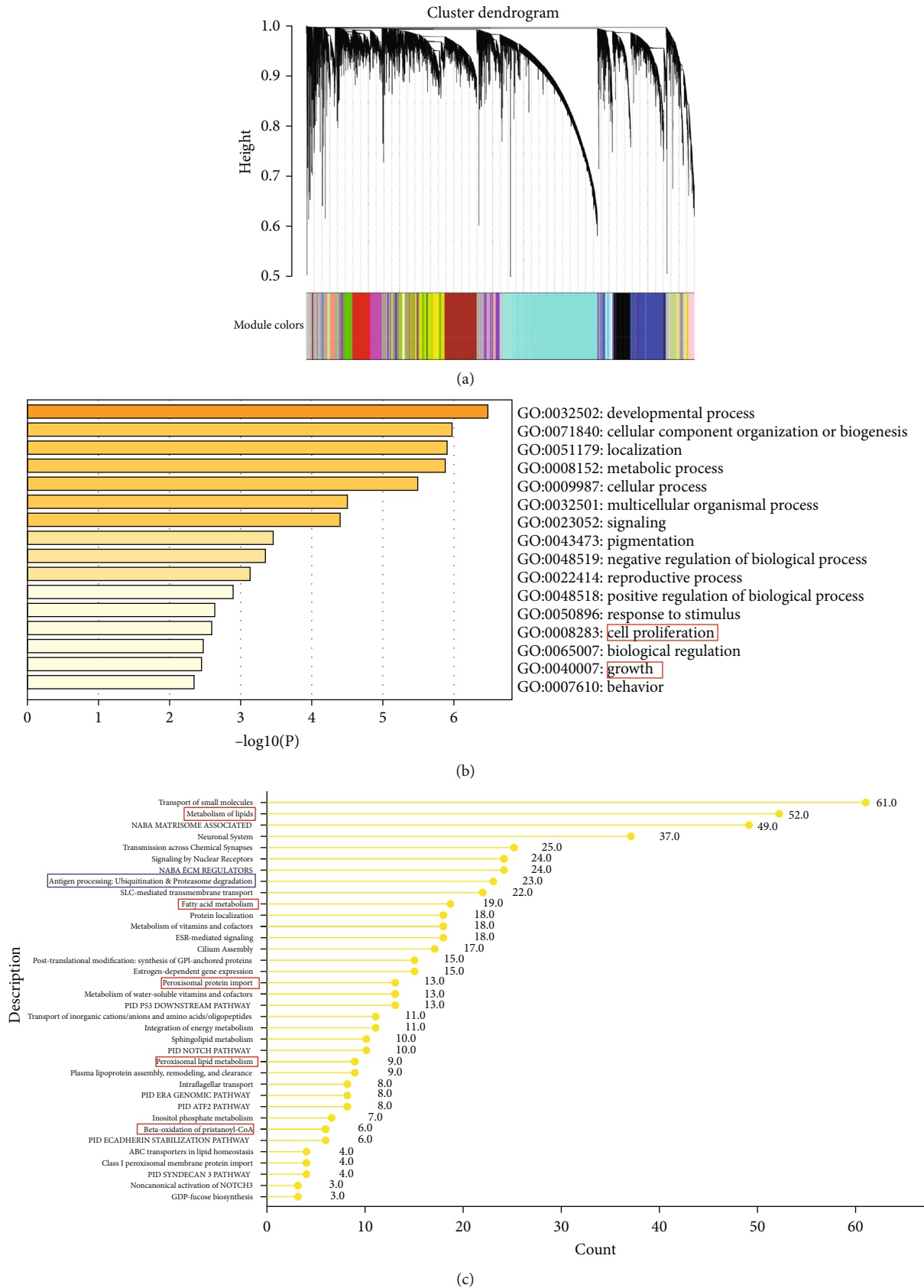
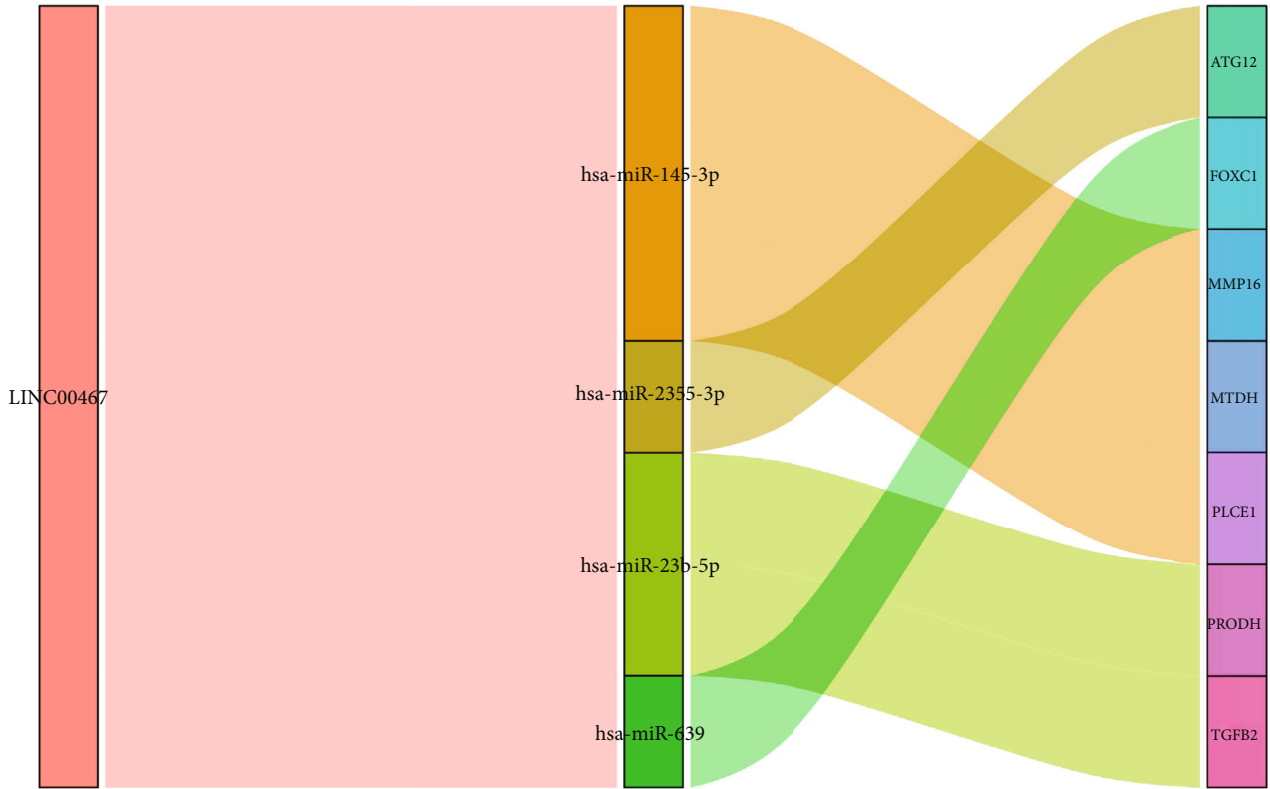
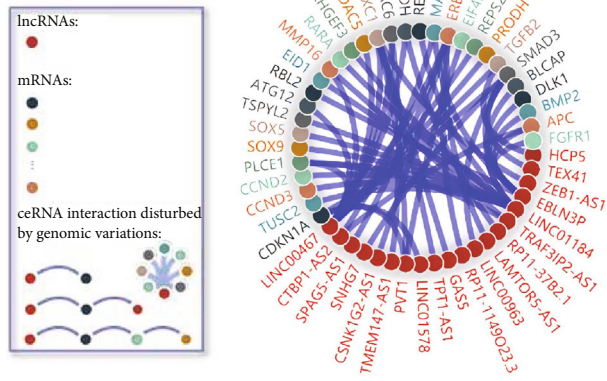


FIGURE 6: Continued.



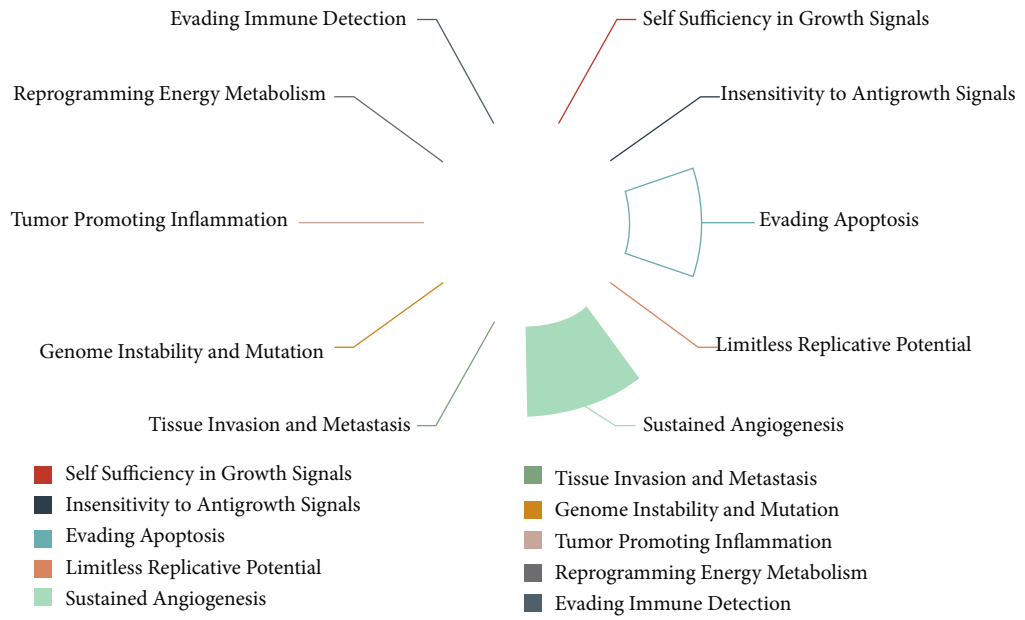
(d)



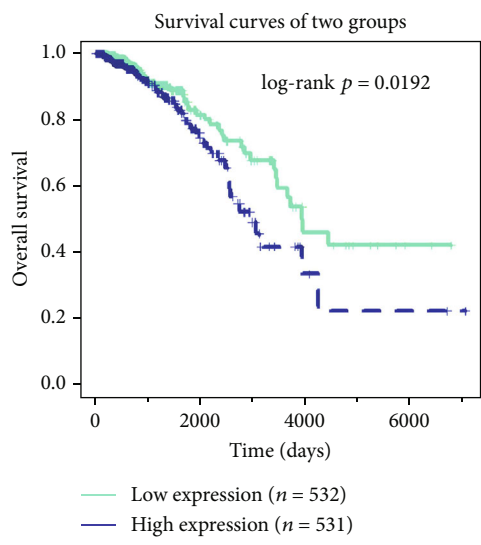
(e)

FIGURE 6: Continued.

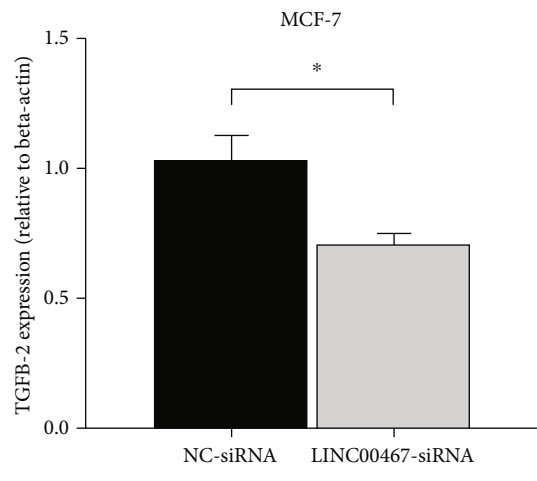




(f)



(g)



(h)

FIGURE 6: Continued.

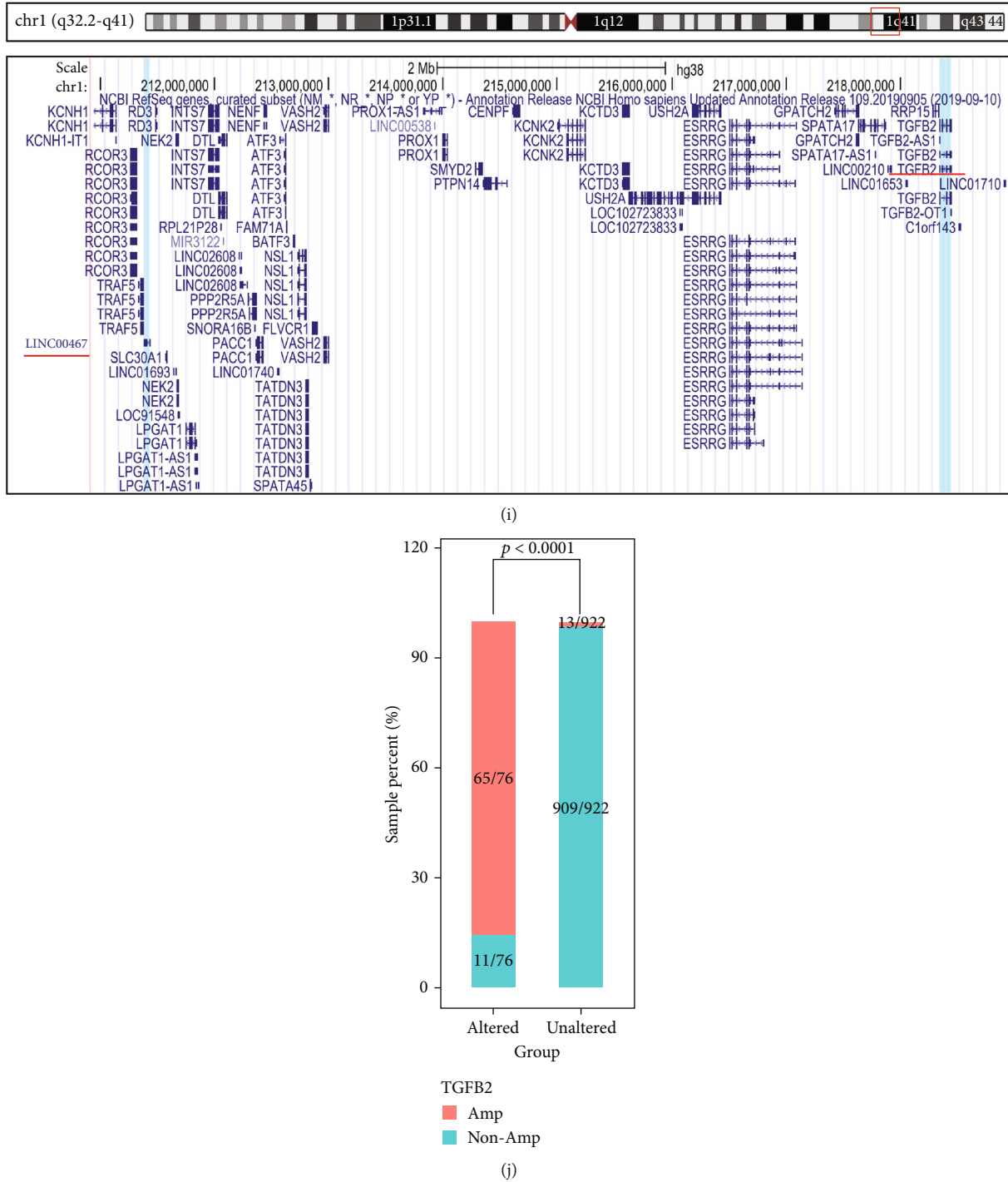


FIGURE 6: Biological processes, signaling pathways, and ceRNA regulatory network associated with LINC00467. (a) Hierarchical clustering and module clustering based on gene expression. (b, c) GO and KEGG Enrichment analysis of the genes at the module where LINC00467 is located. (d) CeRNA regulatory network of LINC00467 in BRCA using LnCeVar and the Sankey diagrams presenting the correlated primary network. (e) The secondary network of ceRNA mediated by LINC00467. (f) enrichment analysis of immunity, apoptosis escape, and other signaling pathways in ceRNA network. (g) Patients with high expressions of both LINC00467 and TGFB2 had a lower overall survival rate. (h) The location of LINC00467 and TGFB2 on chromosomes, based on UCSC. (i) Frequent co-amplification of LINC00467 and TGFB2 based on TCGA BRCA cohort. \* $p < 0.05$ .

was a dose-dependent gene. Further analysis found that LINC00467 was significantly negatively correlated with the immune scores and stromal scores of BRCA samples (Figure 7(c)). At the same time, we also found that

LINC00467 was significantly negatively correlated with infiltrations of various immune cells, such as CD8+ T cells, CD4 + T cells, and macrophages (Figure 7(d)) and significantly negatively correlated with the TCR signaling pathway

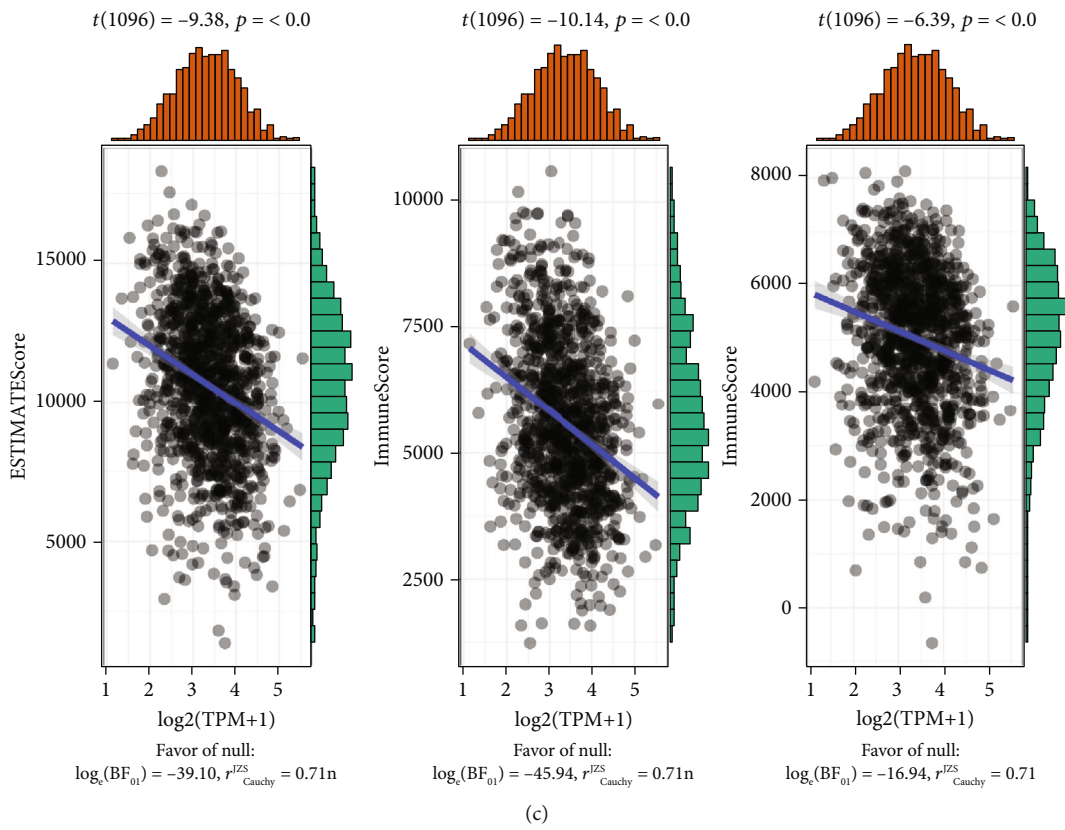
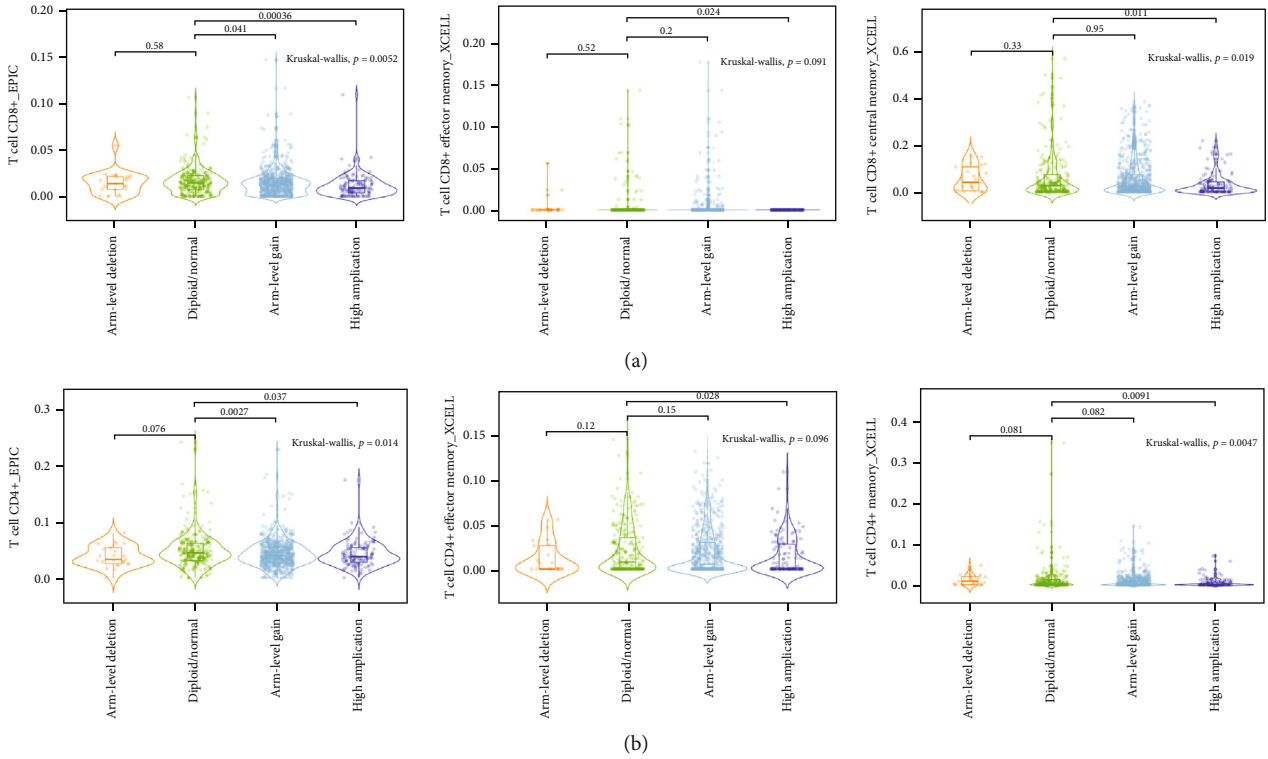


FIGURE 7: Continued.

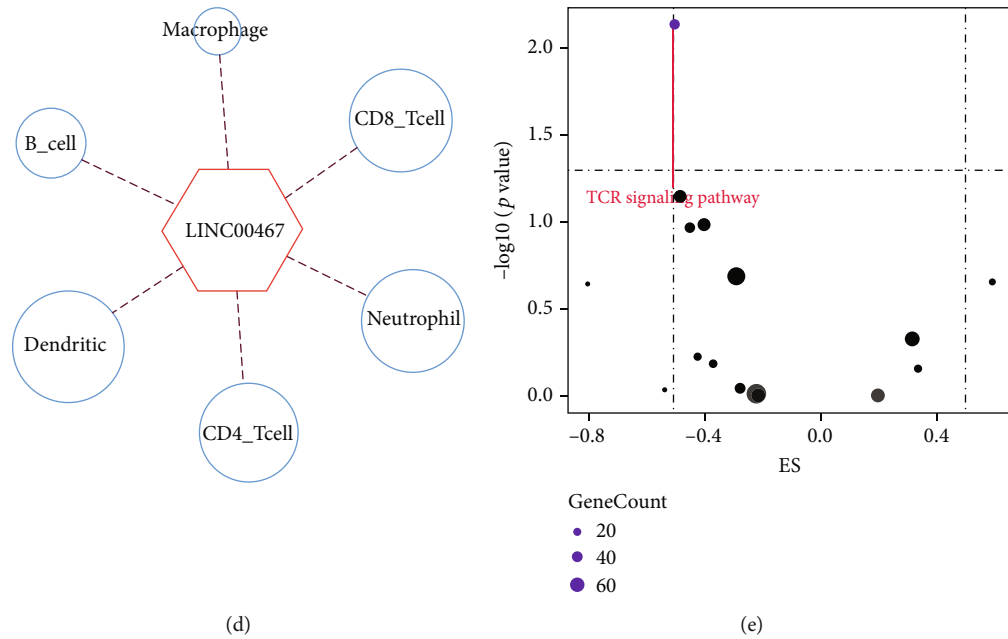


FIGURE 7: Genome amplification and expression levels of LINC00467 were associated with T cell infiltration. (a) CD8+ T cells showed lower infiltration in samples with LINC00467 amplified based on the TIMER2.0 database. (b) CD4+ T cells showed lower infiltration in samples with LINC00467 amplified based on the TIMER2.0 database. (c) The LINC00467 expression was significantly negatively correlated with ESTIMATE Score/Immune Score/Stromal Score based on the TIMER2.0 database. (d) The LINC00467 expression in the TCGA BRCA cohort was negatively correlated with a variety of immune cells based on the ImmLnc database. (e) GSEA enrichment analysis based on the ImmLnc database showed that the LINC00467 expression in TCGA BRCA cohort had the highest negative correlation with the TCR signal pathway.

(Figure 7(e)). Based on these results, we speculated that LINC00467 might be a negative regulator of anti-tumor immunity, which promoted tumor progression by inhibiting the infiltration of immune cells.

#### 4. Discussion

Global Cancer Statistics 2018 show that the incidence of breast cancer was 46.3%, and the mortality rate was 13.0%, remaining the top cause of death among female cancer patients [52]. Patients of breast cancer mainly die of metastasis of BRCA. However, we still lack effective biomarkers to predict the metastasis [53]. In our study, by integrating BRCA data from multiple databases, we found for the first time that LINC00467 was significantly more highly expressed in BRCA. Further analysis showed that LINC00467 was mainly expressed in BRCA cells and its CTCs, but not in normal tissues. The expression level of LINC00467 can effectively distinguish whether the tumor has metastasized or not. In addition, LINC00467 was significantly more highly expressed in CTCs of BRCA, and the survival rate of patients with high expression of LINC00467 was significantly lower than that of patients with low expression of LINC00467. These results indicated for the first time that LINC00467 was a promising biomarker predicting BRCA. One of our published studies and other studies also found LINC00467 to be the biomarker for the metastasis and recurrence of lung cancer [47], colorectal cancer [54], and glioma [55]. In conclusion, LINC00467 could be a

molecular biomarker of the metastasis and recurrence of multiple tumors, needing to be further studied.

Studies have shown that the genome of breast cancer tissue was highly unstable and had many types of variation. Data from multiple cohorts showed high-frequency amplification in 1q32 [56–58], suggesting that this region may be the location of tumor driver genes. Coincidentally, LINC00467 was also located in this region. Analysis of BRCA data from the cBioPortal database found that there were different levels of LINC00467 amplification in breast cancer, presenting a dose-dependent effect with the LINC00467 expression. These results proved that the LINC00467 expression was driven by its CNV, and patients with copy number amplification of LINC00467 had a poor prognosis, which fully indicated that LINC00467 may be a driver gene of breast cancer. An indepth study of the carcinogenic mechanism of LINC00467 would provide new ideas and targets for the treatment of BRCA.

Epigenetic regulation was involved in the development and progression of a variety of tumors, as well as the expression of a variety of RNAs, including lncRNA. Corces et al. constructed the open chromatin atlas of various tumors and described their uniqueness using ATAC-Seq, revealing the heterogeneity of the gene expression between different cancers to some extent [59]. We downloaded the BRCA data from the UCSC Xena database and found that the LINC00467 expression was significantly positively correlated with the level of chromatin openness in the promoter, suggesting that LINC00467 may be regulated by epigenetic modifications, among which DNA methylation was the most

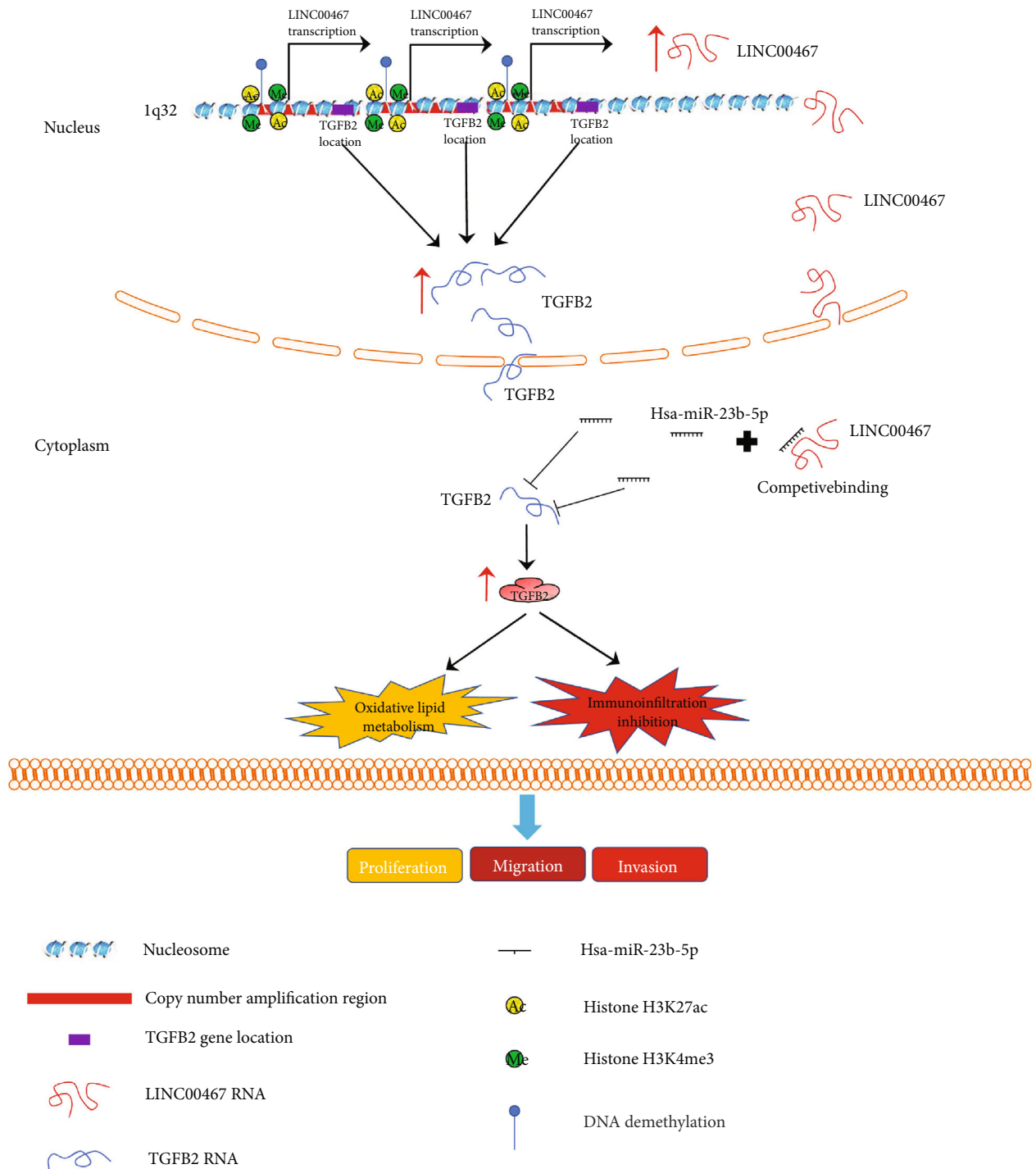


FIGURE 8: The potential mechanism of LINC00467 regulation in BRCA cells.

common and apparent one. A number of studies have confirmed that DNA methylation played an important role in the expression of lncRNA [46, 60]. We found that the expression of LINC00467 was significantly negatively correlated with the average methylation level of the promoter, indicating that DNA methylation of LINC00467 may also be one of the mechanisms for its up-regulation, which was the second new discovery of our team, considering that the LINC00467 expression could be regulated by histone modi-

fication as the first discovery in our previous study, fully demonstrating the complexity of regulation of the LINC00467 expression. Consistent with the previous results, we also found the presence of active histone modifications in LINC00467 promoters in this study, such as H3K27ac/H3K4me3. In conclusion, we found for the first time that LINC00467 may be a molecule regulated by multiple factors, which provided a new perspective for the study of the regulation mechanism of lncRNA expression.

Similar to the findings in lung cancer, glioma, liver cancer, and other cancers, our experiment showed that LINC00467 could also significantly promote the migration, invasion, and proliferation of BRCA *in vitro*. In addition, LINC00467 has been shown to promote chemotherapy resistance in colon and liver cancer, suggesting that the function of LINC00467 may be slightly different in different cancers, but in general, it acts in a similar manner as a tumor promotion gene, suggesting that LINC00467 may be a therapeutic target for multiple tumors.

The results of WGCNA showed that LINC00467 may affect the biological processes, such as cell proliferation and growth of BRCA, and could also participate in signal pathways related to cell proliferation and cell cycle transformation, such as TP53 and Notch, which was similar to the result of the research about LINC00467 regulating TP53 to promote glioma progression [61]. In addition, we also found that LINC00467 may also be involved in the regulation of lipid peroxide metabolism and epithelial-mesenchymal transition and its relevant signaling pathways. This suggests that LINC00467 may affect the metabolic reprogramming of BRCA cells, thereby improving the antioxidant capacity of cells and promoting cell proliferation. CeRNA hypothesis was one of the common molecular mechanisms of lncRNAs, through which a number of lncRNAs located in the cytoplasm could adsorb miRNAs, so as to regulate the gene expression [62, 63]. Zheng et al. found that LINC00467/miR-18a-5p/NEDD9 could promote the malignant growth and migration of HCC [64]. In head and neck squamous cell carcinoma, some researchers have also found that LINC00467 could promote EMT and malignant progression of tumors through ceRNA hypothesis [65], indicating that LINC00467 may be able to combine with different miRNAs, and ceRNA hypothesis may be one of the important functional mechanisms for LINC00467. Similarly, based on LncCeVar database, we first identified the LINC00467-miR-23b-5p-TGFB2 axis as a link of LINC00467 to the occurrence of BRCA. For the patients with high expression of this axis, they had a poor prognosis, and interestingly, LINC00467 was co-amplified with TGFB2, suggesting that the amplification of both LINC00467 and TGFB2 in this axis and their stable expression may be one of the important reasons for BRCA metastasis and recurrence. The treatment targeting this axis may be effective for the metastasis and recurrence of breast cancer. At the same time, our findings also provide new evidence for the regulation mechanism of ceRNA by LINC00467, which organically links genome-level changes with epigenetic regulation.

Tumor immunotherapy has become a common treatment for refractory and recurrent BRCA, but the responses to immunotherapy vary greatly among different patients. Multiple studies have shown that lncRNA could participate in the regulation of immune cells of TME by regulating the survival of T cells and the process of antigen presentation [50, 51]. Our results showed that both copy number level and expression level of LINC00467 were significantly negatively correlated with the infiltration of CD4+ and CD8+ T cells. Furthermore, LINC00467 was significantly negatively correlated with the TCR signaling pathway. These results

suggested that LINC00467 was likely to inhibit antitumor immunity by inhibiting the immune infiltration of T cells and the TCR signaling pathway. The amplification and high expression of LINC00467 may also be biomarkers of both the infiltration of T cells and the response of immunotherapy.

## 5. Conclusions

In conclusion, based on bioinformatic analysis, a molecular biomarker, LINC00467, was screened out with the values of diagnosis, metastasis, and recurrence for BRCA. In addition, it was also found that LINC00467 may be a tumor driver gene in BRCA and may be involved in the regulation of tumor immunity and lipid peroxide metabolism through ceRNA hypothesis (Figure 8). Treatment targeting LINC00467 and its downstream signaling pathways may be a new direction for the research and development of drugs for BRCA.

## Data Availability

Some of the data and figures (Figures 1(e)-1(h), Figure 2, Figures 3(i)-3(k), Figures 4(a), 4(c), 4(e), and 4(h), Figures 6(b), 6(c), 6(e)-(6g), and 6(i), Figures 7(a)-7(d), supplementary figure 1, supplementary figure 2, supplementary figure 3F/G, supplementary figure 4B/C) used to support the findings of this study are generated and downloaded from online tools. We have provided the Web links of these online tools in the material methods section of the main text. All related scripts and supported data are available for download at <https://github.com/Bohao1990/4586319>.

## Conflicts of Interest

The authors declare that there are no conflicts of interests.

## Authors' Contributions

Hao Bo and Wancong Zhang contributed equally to this work. They are the co-first authors of the article.

## Acknowledgments

We thank Qiaohua Li (Kunming University of Science and Technology) and Tingwei Chen (Kunming University of Science and Technology) for the excellent technical assistance. The work was supported by the Natural Science Foundation of Hunan Province (No. 2019JJ80039), the Changsha Municipal Natural Science Foundation (kq2014033), the Guangdong Higher Education Teaching Reform Project (No. 246), the Grant for Key Disciplinary Project of Clinical Medicine under the Guangdong High-level University Development Program (002-18120314, 002-18120311), and the 2020 Li Ka Shing Foundation Cross-Disciplinary Research Grant (2020LKSFG18B, 2020LKSFG02E).

## Supplementary Materials

Supplementary Figure 1: Validation of differentially expressed lncRNAs in GEPIA BRCA dataset. (a, b)

Differential expression was verified with GEPIA, with LINC00467 showing the most significant difference. (c) Expression of LINC00467 in BRCA cell line and normal mammary epithelial cell line of CCLE database. N: normal; T: tumor. Supplementary Figure 2: Expression of LINC00467 in CTCs of BRCA. LINC00467 expression in CTCs and BRCA in situ based on GSE41245. Supplementary Figure 3: TCGA Firehose Legacy dataset verifies the finding that LINC00467 had a high frequency of copy number amplification in BRCA. (a) LINC00467 has different frequencies of copy number amplification in different types of BRCA in Firehose Legacy dataset. (b) Relationship between LINC00467 expression and types of CNV. (c) The positive correlation between LINC00467 expression and its copy number level. (d) Patients with LINC00467 amplified had a worse overall survival. (e) The positive correlation between copy number amplification of LINC00467 and grades of BRCA. (f) Patients with LINC00467 amplified showed bigger lymph node examined number. (g) Patients with LINC00467 amplified showed more genomic changes. Supplementary Figure 4: WGCNA, enrichment, and correlation analysis. (a) Screening of the best soft thresholding with WGCNA. (b) Cell-specific and tissue-specific enrichment analysis of the genes at the red module where LINC00467 is located. (c) TF prediction of genes within the regulatory module. (d) Correlation analysis of LINC00467 and TGFB2 expression. Supplementary Table 1: Differentially expressed genes of GSE7904 dataset. Supplementary Table 2: Differentially expressed genes of GSE22820 dataset. Supplementary Table 3: Differentially expressed genes of GSE38959 dataset. Supplementary Table 4: Differentially expressed genes of GSE45827 dataset. Supplementary Table 5: Differentially expressed genes of GSE65194 dataset. Supplementary Table 6: Differentially expressed genes of TCGA BRCA dataset. (*Supplementary Materials*)

## References

- [1] J. Ferlay, H. R. Shin, F. Bray, D. Forman, C. Mathers, and D. M. Parkin, "Estimates of worldwide burden of cancer in 2008: GLOBOCAN 2008," *International Journal of Cancer*, vol. 127, no. 12, pp. 2893–2917, 2010.
- [2] A. Jemal, R. Siegel, J. Xu, and E. Ward, "Cancer statistics, 2010," *CA: a Cancer Journal for Clinicians*, vol. 60, no. 5, pp. 277–300, 2010.
- [3] A. J. White, H. B. Nichols, P. T. Bradshaw, and D. P. Sandler, "Overall and central adiposity and breast cancer risk in the sister study," *Cancer*, vol. 121, no. 20, pp. 3700–3708, 2015.
- [4] K. C. Johnson, A. B. Miller, N. E. Collishaw et al., "Active smoking and secondhand smoke increase breast cancer risk: the report of the Canadian expert panel on tobacco smoke and breast cancer risk (2009)," *Tobacco Control*, vol. 20, no. 1, article e2, 2011.
- [5] S. Valastyan and R. A. Weinberg, "Tumor metastasis: molecular insights and evolving paradigms," *Cell*, vol. 147, no. 2, pp. 275–292, 2011.
- [6] B. L. Eckhardt, P. A. Francis, B. S. Parker, and R. L. Anderson, "Strategies for the discovery and development of therapies for metastatic breast cancer," *Nature Reviews. Drug Discovery*, vol. 11, no. 6, pp. 479–497, 2012.
- [7] H. Cao, Z. Zhang, S. Zhao et al., "Hydrophobic interaction mediating self-assembled nanoparticles of succinobucol suppress lung metastasis of breast cancer by inhibition of VCAM-1 expression," *Journal of Controlled Release*, vol. 205, pp. 162–171, 2015.
- [8] S. Xu, L. Wan, H. Yin et al., "Long noncoding RNA Linc00152 functions as a tumor propellant in pan-cancer," *Cellular Physiology and Biochemistry*, vol. 44, pp. 2476–2490, 2017.
- [9] P. Hou, Y. Zhao, Z. Li et al., "LincRNA-ROR induces epithelial-to-mesenchymal transition and contributes to breast cancer tumorigenesis and metastasis," *Cell Death & Disease*, vol. 5, no. 6, article e1287, 2014.
- [10] H. X. Zhan, Y. Wang, C. Li et al., "LincRNA-ROR promotes invasion, metastasis and tumor growth in pancreatic cancer through activating ZEB1 pathway," *Cancer Letters*, vol. 374, no. 2, pp. 261–271, 2016.
- [11] Y. M. Chen, Y. Liu, H. Y. Wei, K. Z. Lv, and P. Fu, "Linc-ROR induces epithelial-mesenchymal transition and contributes to drug resistance and invasion of breast cancer cells," *Tumour Biology*, vol. 37, no. 8, pp. 10861–10870, 2016.
- [12] W. X. Peng, J. G. Huang, L. Yang, A. H. Gong, and Y. Y. Mo, "Linc-RoR promotes MAPK/ERK signaling and confers estrogen-independent growth of breast cancer," *Molecular Cancer*, vol. 16, no. 1, p. 161, 2017.
- [13] K. Qiao, S. Ning, L. Wan et al., "LINC00673 is activated by YY1 and promotes the proliferation of breast cancer cells via the miR-515-5p/MARK4/hippo signaling pathway," *Journal of Experimental & Clinical Cancer Research*, vol. 38, no. 1, p. 418, 2019.
- [14] A. L. Richardson, Z. C. Wang, A. De Nicolo et al., "X chromosomal abnormalities in basal-like human breast cancer," *Cancer Cell*, vol. 9, no. 2, pp. 121–132, 2006.
- [15] T. Gruosso, V. Mieulet, M. Cardon et al., "Chronic oxidative stress promotes H2AX protein degradation and enhances chemosensitivity in breast cancer patients," *EMBO Molecular Medicine*, vol. 8, no. 5, pp. 527–549, 2016.
- [16] V. Maire, F. Némati, M. Richardson et al., "Polo-like kinase 1: a potential therapeutic option in combination with conventional chemotherapy for the management of patients with triple-negative breast cancer," *Cancer Research*, vol. 73, no. 2, pp. 813–823, 2013.
- [17] S. Maubant, B. Tesson, V. Maire et al., "Transcriptome analysis of Wnt3a-treated triple-negative breast cancer cells," *PLoS One*, vol. 10, no. 4, article e0122333, 2015.
- [18] R. Z. Liu, K. Graham, D. D. Glubrecht, D. R. Germain, J. R. Mackey, and R. Godbout, "Association of FABP5 expression with poor survival in triple-negative breast cancer: implication for retinoic acid therapy," *The American Journal of Pathology*, vol. 178, no. 3, pp. 997–1008, 2011.
- [19] M. Wuest, M. Kuchar, S. K. Sharma et al., "Targeting lysyl oxidase for molecular imaging in breast cancer," *Breast Cancer Research*, vol. 17, no. 1, p. 107, 2015.
- [20] R. Kolde, S. Laur, P. Adler, and J. Vilo, "Robust rank aggregation for gene list integration and meta-analysis," *Bioinformatics*, vol. 28, no. 4, pp. 573–580, 2012.
- [21] Z. Tang, C. Li, B. Kang, G. Gao, C. Li, and Z. Zhang, "GEPIA: a web server for cancer and normal gene expression profiling and interactive analyses," *Nucleic Acids Research*, vol. 45, no. W1, pp. W98–W102, 2017.
- [22] J. Fu, W. Allen, A. Xia, Z. Ma, and X. Qi, "Identification of biomarkers in breast cancer by gene expression profiling

- using human tissues,” *Genomics Data*, vol. 2, pp. 299–301, 2014.
- [23] J. Fu, R. Khaybullin, Y. Zhang, A. Xia, and X. Qi, “Gene expression profiling leads to discovery of correlation of matrix metalloproteinase 11 and heparanase 2 in breast cancer progression,” *BMC Cancer*, vol. 15, no. 1, p. 473, 2015.
- [24] B. H. Mecham, G. T. Klus, J. Strovel et al., “Sequence-matched probes produce increased cross-platform consistency and more reproducible biological results in microarray-based gene expression measurements,” *Nucleic Acids Research*, vol. 32, no. 9, article e74, 2004.
- [25] M. J. Goldman, B. Craft, M. Hastie et al., “Visualizing and interpreting cancer genomics data via the Xena platform,” *Nature Biotechnology*, vol. 38, no. 6, pp. 675–678, 2020.
- [26] M. Chanrion, V. Negre, H. Fontaine et al., “A gene expression signature that can predict the recurrence of tamoxifen-treated primary breast cancer,” *Clinical Cancer Research*, vol. 14, no. 6, pp. 1744–1752, 2008.
- [27] M. Yu, A. Bardia, B. S. Wittner et al., “Circulating breast tumor cells exhibit dynamic changes in epithelial and mesenchymal composition,” *Science*, vol. 339, no. 6119, pp. 580–584, 2013.
- [28] M. Yu, A. Bardia, N. Aceto et al., “Ex vivo culture of circulating breast tumor cells for individualized testing of drug susceptibility,” *Science*, vol. 345, no. 6193, pp. 216–220, 2014.
- [29] L. Zhao, X. Wu, T. Li, and J. Luo, “ctcRbase: the gene expression database of circulating tumor cells and microemboli,” *Database: The Journal of Biological Databases and Curation*, vol. 2020, article baaa020, 2020.
- [30] B. Gyorffy, “Survival analysis across the entire transcriptome identifies biomarkers with the highest prognostic power in breast cancer,” *Computational and Structural Biotechnology Journal*, vol. 19, pp. 4101–4109, 2021.
- [31] Q. H. Nguyen, N. Pervolarakis, K. Blake et al., “Profiling human breast epithelial cells using single cell RNA sequencing identifies cell diversity,” *Nature Communications*, vol. 9, no. 1, p. 1, 2018.
- [32] W. Chen, S. J. Morabito, K. Kessenbrock, T. Enver, K. B. Meyer, and A. E. Teschendorff, “Single-cell landscape in mammary epithelium reveals bipotent-like cells associated with breast cancer risk and outcome,” *Communications Biology*, vol. 2, no. 1, p. 306, 2019.
- [33] X. Han, Z. Zhou, L. Fei et al., “Construction of a human cell landscape at single-cell level,” *Nature*, vol. 581, no. 7808, pp. 303–309, 2020.
- [34] H. Yuan, M. Yan, G. Zhang et al., “CancerSEA: a cancer single-cell state atlas,” *Nucleic Acids Research*, vol. 47, no. D1, pp. D900–D908, 2019.
- [35] J. Gao, B. A. Aksoy, U. Dogrusoz et al., “Integrative analysis of complex cancer genomics and clinical profiles using the cBioPortal,” *Science Signaling*, vol. 6, no. 269, p. p11, 2013.
- [36] E. Cerami, J. Gao, U. Dogrusoz et al., “The cBio cancer genomics portal: an open platform for exploring multidimensional cancer genomics Data: Figure 1,” *Cancer Discovery*, vol. 2, no. 5, pp. 401–404, 2012.
- [37] K. Ito and D. Murphy, “Application of *ofggplot2* to Pharmacometric graphics,” *CPT: Pharmacometrics & Systems Pharmacology*, vol. 2, no. 10, article e79, 2013.
- [38] W. J. Kent, C. W. Sugnet, T. S. Furey et al., “The human genome browser at UCSC,” *Genome Research*, vol. 12, no. 6, pp. 996–1006, 2002.
- [39] P. Langfelder and S. Horvath, “WGCNA: an R package for weighted correlation network analysis,” *BMC Bioinformatics*, vol. 9, no. 1, p. 559, 2008.
- [40] Y. Zhou, B. Zhou, L. Pache et al., “Metascape provides a biologist-oriented resource for the analysis of systems-level datasets,” *Nature Communications*, vol. 10, no. 1, p. ???, 2019.
- [41] P. Wang, X. Li, Y. Gao et al., “LnCeVar: a comprehensive database of genomic variations that disturb ceRNA network regulation,” *Nucleic Acids Research*, vol. 48, pp. D111–D117, 2019.
- [42] T. Li, J. Fu, Z. Zeng et al., “TIMER2.0 for analysis of tumor-infiltrating immune cells,” *Nucleic Acids Research*, vol. 48, no. W1, pp. W509–W514, 2020.
- [43] Y. Li, T. Jiang, W. Zhou et al., “Pan-cancer characterization of immune-related lncRNAs identifies potential oncogenic biomarkers,” *Nature Communications*, vol. 11, no. 1, p. 1000, 2020.
- [44] H. Liu, X. Gu, G. Wang et al., “Copy number variations primed lncRNAs deregulation contribute to poor prognosis in colorectal cancer,” *Aging (Albany NY)*, vol. 11, no. 16, pp. 6089–6108, 2019.
- [45] Y. Zhang, G. Liao, J. Bai et al., “Identifying cancer driver lncRNAs bridged by functional effectors through integrating multi-omics data in human cancers,” *Molecular Therapy - Nucleic Acids*, vol. 17, pp. 362–373, 2019.
- [46] F. Hadji, M. C. Boulanger, S. P. Guay et al., “Altered DNA methylation of Long noncoding RNAH19in calcific aortic valve disease promotes mineralization by Silencing-NOTCH1,” *Circulation*, vol. 134, no. 23, pp. 1848–1862, 2016.
- [47] Y. Zhu, J. Li, H. Bo et al., “LINC00467 is up-regulated by TDG-mediated acetylation in non-small cell lung cancer and promotes tumor progression,” *Oncogene*, vol. 39, no. 38, pp. 6071–6084, 2020.
- [48] K. Cai, T. Li, L. Guo et al., “Long non-coding RNA LINC00467 regulates hepatocellular carcinoma progression by modulating miR-9-5p/PPARA expression,” *Open Biology*, vol. 9, no. 9, article 190074, 2019.
- [49] H. Bo, Z. Liu, F. Zhu et al., “Long noncoding RNAs expression profile and long noncoding RNA-mediated competing endogenous RNA network in nonobstructive azoospermia patients,” *Epigenomics*, vol. 12, no. 8, pp. 673–684, 2020.
- [50] D. Huang, J. Chen, L. Yang et al., “NKILA lncRNA promotes tumor immune evasion by sensitizing T cells to activation-induced cell death,” *Nature Immunology*, vol. 19, no. 10, pp. 1112–1125, 2018.
- [51] Q. Hu, Y. Ye, L. C. Chan et al., “Oncogenic lncRNA downregulates cancer cell antigen presentation and intrinsic tumor suppression,” *Nature Immunology*, vol. 20, no. 7, pp. 835–851, 2019.
- [52] F. Bray, J. Ferlay, I. Soerjomataram, R. L. Siegel, L. A. Torre, and A. Jemal, “Global cancer statistics 2018: GLOBOCAN estimates of incidence and mortality worldwide for 36 cancers in 185 countries,” *CA: a Cancer Journal for Clinicians*, vol. 68, no. 6, pp. 394–424, 2018.
- [53] H. Yousefi, M. Maheronnaghsh, F. Molaei et al., “Long non-coding RNAs and exosomal lncRNAs: classification, and mechanisms in breast cancer metastasis and drug resistance,” *Oncogene*, vol. 39, no. 5, pp. 953–974, 2020.
- [54] X. He, S. Li, B. Yu et al., “Up-regulation of LINC00467 promotes the tumorigenesis in colorectal cancer,” *Journal of Cancer*, vol. 10, no. 25, pp. 6405–6413, 2019.



- [55] X. H. Jiang and Y. Y. Liu, "LINC00467 promotes proliferation and invasion in glioma via interacting with miRNA-485-5p," *European Review for Medical and Pharmacological Sciences*, vol. 24, pp. 766–772, 2020.
- [56] T. Ried, K. E. Just, H. Holtgreve-Grez et al., "Comparative genomic hybridization of formalin-fixed, paraffin-embedded breast tumors reveals different patterns of chromosomal gains and losses in fibroadenomas and diploid and aneuploid carcinomas," *Cancer Research*, vol. 55, pp. 5415–5423, 1995.
- [57] L. W. Loo, D. I. Grove, E. M. Williams et al., "Array comparative genomic hybridization analysis of genomic alterations in breast cancer subtypes," *Cancer Research*, vol. 64, no. 23, pp. 8541–8549, 2004.
- [58] F. Forozan, E. H. Mahlamäki, O. Monni et al., "Comparative genomic hybridization analysis of 38 breast cancer cell lines: a basis for interpreting complementary DNA microarray data," *Cancer Research*, vol. 60, pp. 4519–4525, 2000.
- [59] M. R. Corces, J. M. Granja, S. Shams et al., "The chromatin accessibility landscape of primary human cancers," *Science*, vol. 362, no. 6413, 2018.
- [60] W. Wu, T. D. Bhagat, X. Yang et al., "Hypomethylation of Noncoding DNA Regions and Overexpression of the Long Noncoding RNA, *AFAP1-AS1*, in Barrett's Esophagus and Esophageal Adenocarcinoma," *Gastroenterology*, vol. 144, no. 5, pp. 956–966.e4, 2013.
- [61] B. Atmadibrata, P. Y. Liu, N. Sokolowski et al., "The novel long noncoding RNA linc00467 promotes cell survival but is down-regulated by N-Myc," *PLoS One*, vol. 9, no. 2, article e88112, 2014.
- [62] Y. Lian, F. Xiong, L. Yang et al., "Long noncoding RNA AFAP1-AS1 acts as a competing endogenous RNA of miR-423-5p to facilitate nasopharyngeal carcinoma metastasis through regulating the rho/Rac pathway," *Journal of Experimental & Clinical Cancer Research*, vol. 37, no. 1, p. 253, 2018.
- [63] C. Ou, Z. Sun, X. He et al., "Targeting YAP1/LINC00152/FSCN1 signaling axis prevents the progression of colorectal cancer," *Advanced Science*, vol. 7, no. 3, p. 1901380, 2020.
- [64] Y. Zheng, P. Nie, and S. Xu, "Long noncoding RNA linc00467 plays an oncogenic role in hepatocellular carcinoma by regulating the miR-18a-5p/NEDD9 axis," *Journal of Cellular Biochemistry*, vol. 121, no. 5-6, pp. 3135–3144, 2020.
- [65] Y. Chen and Y. Ding, "LINC00467 enhances head and neck squamous cell carcinoma progression and the epithelial-mesenchymal transition process via miR-299-5p/ubiquitin specific protease-48 axis," *The Journal of Gene Medicine*, vol. 22, no. 7, article e3184, 2020.

## Research Article

# Moderate Static Magnet Fields Suppress Ovarian Cancer Metastasis via ROS-Mediated Oxidative Stress

Chao Song <sup>1,2</sup>, Biao Yu <sup>1,2</sup>, Junjun Wang <sup>1</sup>, Xinmiao Ji <sup>1</sup>, Lei Zhang <sup>1</sup>,  
Xiaofei Tian <sup>3</sup>, Xin Yu <sup>1,2</sup>, Chuanlin Feng <sup>3</sup>, Xinyu Wang <sup>3</sup> and Xin Zhang <sup>1,2,3,4</sup>

<sup>1</sup>High Magnetic Field Laboratory, Hefei Institutes of Physical Science, Chinese Academy of Sciences, Hefei, Anhui 230031, China

<sup>2</sup>Science Island Branch of Graduate School, University of Science and Technology of China, Hefei, Anhui 230036, China

<sup>3</sup>Institutes of Physical Science and Information Technology, Anhui University, Hefei, Anhui 230601, China

<sup>4</sup>International Magnetobiology Frontier Research Center, Science Island, Hefei, Anhui 230036, China

Correspondence should be addressed to Xin Zhang; [xinzhang@hmfl.ac.cn](mailto:xinzhang@hmfl.ac.cn)

Received 12 September 2021; Accepted 8 November 2021; Published 7 December 2021

Academic Editor: Xiangpan Li

Copyright © 2021 Chao Song et al. This is an open access article distributed under the Creative Commons Attribution License, which permits unrestricted use, distribution, and reproduction in any medium, provided the original work is properly cited.

Metastasis is the leading cause of cancer patient death, which is closely correlated with reactive oxygen species (ROS) levels. It is well known that the effects of ROS on tumors are diverse, depending on ROS concentration and cell type. We found that ovarian cancer cells have significantly lower levels of ROS than normal ovarian cells. Moreover, increased ROS levels in ovarian cancer cells can substantially inhibit their migration and invasion ability. Furthermore, the results show that moderate static magnetic field (SMF) can inhibit ovarian cancer cell migration, invasion, and stemness in a ROS-dependent manner. RNA sequencing results confirm that SMFs increased the oxidative stress level and reduced the stemness of ovarian cancer cells. Consistently, the expressions of stemness-related genes were significantly decreased, including hyaluronan receptor (CD44), SRY-box transcription factor 2 (Sox2), and cell myc proto-oncogene protein (C-myc). Furthermore, moderate SMFs provided by a superconducting magnet and permanent magnet have good biosafety and can both inhibit ovarian cancer metastasis in mice. Therefore, our study demonstrates the effects of SMFs on oxidative stress and metastasis in the ovarian cancer cells, which reveals the potential of applying SMF as a physical method in cancer therapy in the future.

## 1. Introduction

Ovarian cancer (OC) is a common gynecologic malignancy and accounts for 5% of female cancer deaths [1]. In 2018, a report showed that there were approximately 22,240 new cases of ovarian cancer diagnosed and 14,070 ovarian cancer deaths in the USA [2]. Due to a lack of specific initial symptoms and limited methods for early diagnosis, most OC patients are diagnosed at advanced stages [3], at which the 5-year survival rate is only ~30% [4]. At advanced OC stages, the leading cause of patient death is metastasis, a complex process regulated by multiple factors. In particular, the presence of cancer stem cells (CSCs) is an essential factor for cancer recurrence, metastasis, and chemotherapy resistance [5–7].

ROS contain a large number of reactive oxygen molecules and oxygen-free radicals, including hydrogen peroxide ( $H_2O_2$ ), hydroxyl radical ( $OH\cdot$ ), superoxide anion ( $O_2^{\cdot-}$ ), and hydroxyethyl radical (HER). Although they are essential messengers for multiple signal transduction processes, excessive amount of ROS can cause cellular oxidative stress and cytotoxicity. Moreover, ROS can also inhibit tumor metastasis and reduce cancer stemness. For example, Lu et al. found that high ROS levels induced by *malic enzyme 2* knockdown could suppress tumor growth, lung metastasis, and peritoneal dissemination in gastric cancer *in vivo* [8]. In addition, elevated ROS levels were intimately related to cell growth and migration reduction in nasopharyngeal carcinoma [9] and non-small-cell lung cancer [10]. Furthermore, Favre et al. confirmed that increased ROS levels could reduce

cancer stemness and played an essential role in the transition of quiescent mesenchymal-like states into proliferative epithelial-like states in breast CSCs [11]. Therefore, ROS have been explored as antitumor targets in multiple cancer types [12–14].

Magnetic field (MF) is able to affect ROS levels both *in vitro* and *in vivo* [15]. For example, Van Huizen et al. found that weak SMFs could alter stem cell proliferation and differentiation through regulating ROS levels and the downstream heat shock protein 70 [16]. Recently, two papers both show that SMF or SMF combined with electric field could regulate the redox process and ROS levels, which are essential for their role in alleviating mouse type 2 diabetes [17, 18]. However, the effect of SMF on cancer metastasis is unclear and whether SMF could regulate ROS levels to interfere with cancer metastasis is still unknown.

Here, we investigated the effects of ~0.5 T moderate SMFs, which have been shown to be able to inhibit tumor growth and regulate ROS levels in previous studies [19]. We examined their effects on ovarian cancer cell migration and invasion *in vitro*, as well as ovarian cancer metastasis *in vivo*. We also performed mechanistic studies and found that SMF-induced ovarian cancer metastasis is through elevated ROS levels and oxidative stress, which reduced ovarian cancer cell migration, invasion, and cancer stemness.

## 2. Materials and Methods

**2.1. Magnetic Field Exposure.** In this study, SMFs of ~0.5 T with gradient were provided by superconducting magnet or permanent magnets. A superconducting magnet (Western Superconducting, Xi'an, China) with proper temperature, gas, and humidity control [20] was operated at 9.4 T at the maximum intensity at the center. Our samples were placed in the upper part of the superconducting magnet, where the magnetic field is approximately 0.5 T. Besides, N38 neodymium permanent magnets (NdFeB) were also used to provide SMFs of ~0.5 T (Sans, Nanjing, China). The magnets were placed in a regular cell incubator to treat cells. For mouse exposure, we made a magnetic plate with 12 neodymium magnet cubes (length  $\times$  width  $\times$  height = 250 mm  $\times$  160 mm  $\times$  45 mm). The maximum intensity on the surface of the magnet is also ~0.5 T. To measure the distributions of the magnetic fields at different positions, a magnet analyzer (FE-2100RD, Forever Elegance, China) was used to scan the SMF distribution above the magnets. The sham groups were set up for all experiments. For the superconducting magnet, cells were placed into an identical cellular incubation device without inserting in the magnet. For permanent magnets, the sham groups were set up using unmagnetized neodymium cubes/plates.

**2.2. Cell Culture.** The normal human ovarian cells (IOSE386) and ovarian cancer cells (SKOV3 and HO8910) were obtained from Cell Resource Center of the Shanghai Institutes for Biological Sciences (Shanghai, China). All cells were cultured in RPMI-1640 medium (Corning, USA) containing 10% fetal bovine serum (FBS) (Clark, Germany) and 1% penicillin-streptomycin solution (Hyclone, USA). The cells

were maintained in a humidified incubator (Thermo, USA) at 37°C with 5% CO<sub>2</sub>. Same batch of cells was used for the sham and SMF groups. The cell passage numbers were lower than 20 for all experiments.

**2.3. Analyses of Gene Expression and Transcriptomes.** SKOV3 cells were exposed to ~0.5 T SMFs in the superconducting magnet or the sham for 24 hours before their total RNAs were extracted with the RNAeasy™ Animal Long RNA Isolation Kit with Spin Column (R0027, Beyotime). NovoScript Plus All-in-One 1st Strand cDNA Synthesis SuperMix (E047-01A, Novoprotein) was used for RNA reverse transcription, and Novostart SYBR qPCR Supermix Plus (E096-01A, Novoprotein) was used to amplify target gene using specific primers. The thermal cycling conditions comprised an initial denaturation step at 95°C for 30 s, 40 cycles at 95°C for 5 s, and 61°C for 30 s. All the steps were performed according to the manufacturer's instructions. Primers were designed and synthesized by Sangon Biotech Co., Ltd. (Shanghai, China). The detailed primer sequences are shown in Table S1. The expression levels were calculated according to the  $2^{-\Delta\Delta Ct}$  method [21], where  $\Delta Ct$  is the difference in threshold cycles for the target gene and reference (ACTB), and  $\Delta\Delta Ct$  is the difference between the  $\Delta Ct$ s of the SMF group and sham control. Thus, the expression levels were reported as fold changes relative to the calibrator. The value was used to plot the expression of related genes with the formula  $2^{-\Delta\Delta Ct}$ .

SKOV3 cells were exposed to ~0.5 T SMFs in the superconducting magnet or the sham for 24 hours before being collected and frozen at -80°C with RNAiso Plus (Takara, Japan). Total RNA was extracted, and a genome-wide transcriptomics analysis was conducted by LC-Bio Technology Co., Ltd (Hangzhou, China). After the final transcriptome was generated, StringTie and Ballgown (<http://www.bioconductor.org/packages/release/bioc/html/ballgown.html>) were used to estimate the expression levels of all transcripts by calculating FPKM (FPKM = [total\_exon\_fragments/mapped\_reads (millions)  $\times$  exon\_length (kB)]), (command line: ~stringtie-e-B-p 4-G merged.gtf-o samples.gtf samples.bam). The differentially expressed mRNAs were selected with fold change > 1.5 or fold change < 0.65 and *P* value < 0.05 by R package edgeR (<https://bioconductor.org/packages/release/bioc/html/edgeR.html>) or DESeq2 (<http://www.bioconductor.org/packages/release/bioc/html/DESeq2.html>). Gene Ontology (GO) and gene set enrichment analysis (GSEA) of the genes with differential expression were performed with LC-Bio Technology Co., Ltd. (<https://www.omicstudio.cn/tool>). All gene sets from the MSigDB database gene set were used for the GSEA of the differential genes (<http://www.gsea-msigdb.org/gsea/msigdb/index.jsp>).

**2.4. Wound Healing and Transwell Assays.** Cell migration was evaluated by the wound healing assay. Cultured cells were seeded in 35 mm culture dishes and grown to full confluence in a complete medium. The cell monolayer was scratched and exposed to ~0.5 T SMFs or 20  $\mu$ M H<sub>2</sub>O<sub>2</sub> for

24 or 48 hours. The areas of wound healing were imaged by microscope and quantified by the ImageJ software.

Transwell migration assays were also used to detect the cell migration ability.  $5.0 \times 10^4$  cells were placed in the upper chamber of 24-well plates with  $8.0 \mu\text{m}$  pore size chamber inserts (Corning, USA) and cultured in serum-free medium with  $10 \mu\text{M}$  NAC or PBS, and  $500 \mu\text{L}$  medium with 10% FBS was added to the lower chamber, which was exposed to  $\sim 0.5$  T SMFs for 48 hours. At last, cells on the lower surface were fixed with 4% paraformaldehyde, stained with 0.1% crystal violet, and counted under an inverted microscope.

The ability of cell invasion was analyzed by Transwell invasion assay using 24-well plates with  $8.0 \mu\text{m}$  pore size chamber (Corning, USA). The upper surface of the filter was coated with  $80 \mu\text{L}$  of Matrigel (BD Biosciences, San Jose, CA) diluted 1 : 10 in a serum-free medium. The other procedures are the same as the Transwell migration experiment.

**2.5. Sphere Formation Array.** 1000 cells were mixed with the stem cell medium containing serum-free DMEM/F12 medium supplemented with 20% B27 (Gibco, USA), 20 ng/mL epidermal growth factor (EGF), and 10 ng/mL basic fibroblast growth factor (bFGF) and seeded in 35 mm ultra-low attachment dishes (Corning, USA). The dishes with seeded cells were exposed to 0.5 T SMF for 12 days to assess their ability of sphere formation.

**2.6. Intracellular ROS Test.** SKOV3 and HO8910 cells ( $1.0 \times 10^5$  cells/mL) were seeded in 35 mm culture dishes and supplied with complete medium. After attachment, the cells were exposed to SMFs for 12 or 24 hours. ROS detection kit (Sigma, USA) containing 2',7'-dichlorodihydrofluorescein diacetate (DCFH-DA) was used to detect cellular ROS. Cultured cells were incubated with  $10 \mu\text{M}$  DCFH-DA at  $37^\circ\text{C}$  for 30 minutes before their ROS levels were evaluated using flow cytometry.

**2.7. Cell Number.** SKOV3 and HO8910 cells ( $5.0 \times 10^4$  cells/mL) were seeded in 35 mm culture dishes and supplied with a complete medium. After attachment, the dishes were placed in 0.5 T SMF for 24 hours, and the cell numbers were counted by flow cytometry. Additionally, cultured cells were seeded in a 96-well plate and supplied with a complete medium with  $20 \mu\text{M}$   $\text{H}_2\text{O}_2$  for 24, 48, 72, or 96 hours. Cell counting kit-8 (Beyotime, China) was used to assess cell viability.

**2.8. Animal Experiment.** Six-week-old female BALB/c nude mice were obtained from Nanjing Biomedical Research Institute of Nanjing University (Nanjing, China). In this study, all mice were injected with  $1.0 \times 10^5$  SKOV3 cells intraperitoneally and randomly divided into two groups (sham vs. SMF). The sham group was treated with "fake" magnetic condition, which was used as a control group for magnetic field experiments. In the pilot study, mice were exposed to  $\sim 0.5$  T SMF in the superconducting magnet (10 hours/day, 7 days/week, 6 weeks) to evaluate the *in vivo* effects of moderate SMF on OC. The food consumption and body weight were recorded during the whole experiment.

Serum was collected in a 1.5 mL centrifuge tube and analyzed by an automated biochemical analyzer (HITACHI 7020, Japan). The heart, liver, spleen, lung, kidney, and intestine were collected for imaging by the small animal live imaging system (IVIS Spectrum, PerkinElmer) and further H&E staining and immunohistochemistry analysis. The physiological conditions of mice were monitored by the small animal vital sign monitor (STARR Life Sciences, USA). The signal sensor was placed on the neck of the mice and monitored for 6 minutes. The breath rate, pulse distention, heart rate, and arterial  $\text{O}_2$  were calculated using MouseOx Plus software (STARR Life Sciences, USA). Another set of mice were exposed to the permanent magnet plate for 24 hours/day, 7 days/week, for 6 weeks. Subsequently, all mice were executed to collect tumors in the abdominal cavity. Tumor weight and metastasis nodule numbers were recorded, and tumors were stored at  $-80^\circ\text{C}$  for further assay. All animal experiments were conducted according to the NIH *Guide for the Care and Use of Laboratory Animals* and carried out strictly in accordance with the related protocols of Anhui Medical University (Hefei, China).

**2.9. H&E Staining and Immunohistochemistry.** All nude mice were dissected to collect organs, including the heart, liver, spleen, lung, and kidney. Then, organs were fixed and processed with formalin to obtain  $5 \mu\text{m}$  thick sections and stained with H&E. Five random areas were examined in each section.

The tumors treated by a permanent magnetic plate were fixed and processed with formalin to obtain  $5 \mu\text{m}$  thick sections. Tissue immunohistochemistry was performed using the antibodies for C-myc (GB13076, Servicebio), Sox2 (GB11249, Servicebio), and CD44 (GB113500, Servicebio). All steps were performed according to the manufacturer's instructions.

**2.10. Statistical Analysis.** All statistical analysis was performed using GraphPad Prism version 8. Data from the experiments were showed as the means  $\pm$  SEM. The *P* values were calculated using the one-way or two-way analysis of variance (ANOVA) with Bonferroni correction for comparison between three groups or two-tailed unpaired *t*-test for comparison between two groups. *P* < 0.05 was considered statistically significant.

### 3. Results

**3.1. High Levels of Cellular ROS Inhibit Ovarian Cancer Cell Migration and Invasion.** It is well known that cancer and noncancer cells usually have different levels of ROS. We compared the cellular ROS levels of three ovarian cell lines, including the IOSE386 noncancer cells and HO8910 and SKOV3 cancer cells. Since cell density could also affect cellular ROS levels, we seeded these cells at the same density onto the cell culture plates. Our results show that the ROS levels in IOSE386 noncancer cells are much higher than those in HO8910 and SKOV3 cancer cells (Figure 1(a)). Since excessive ROS are known to cause cell death, which is the key mechanism for some treatment modalities such as radiation

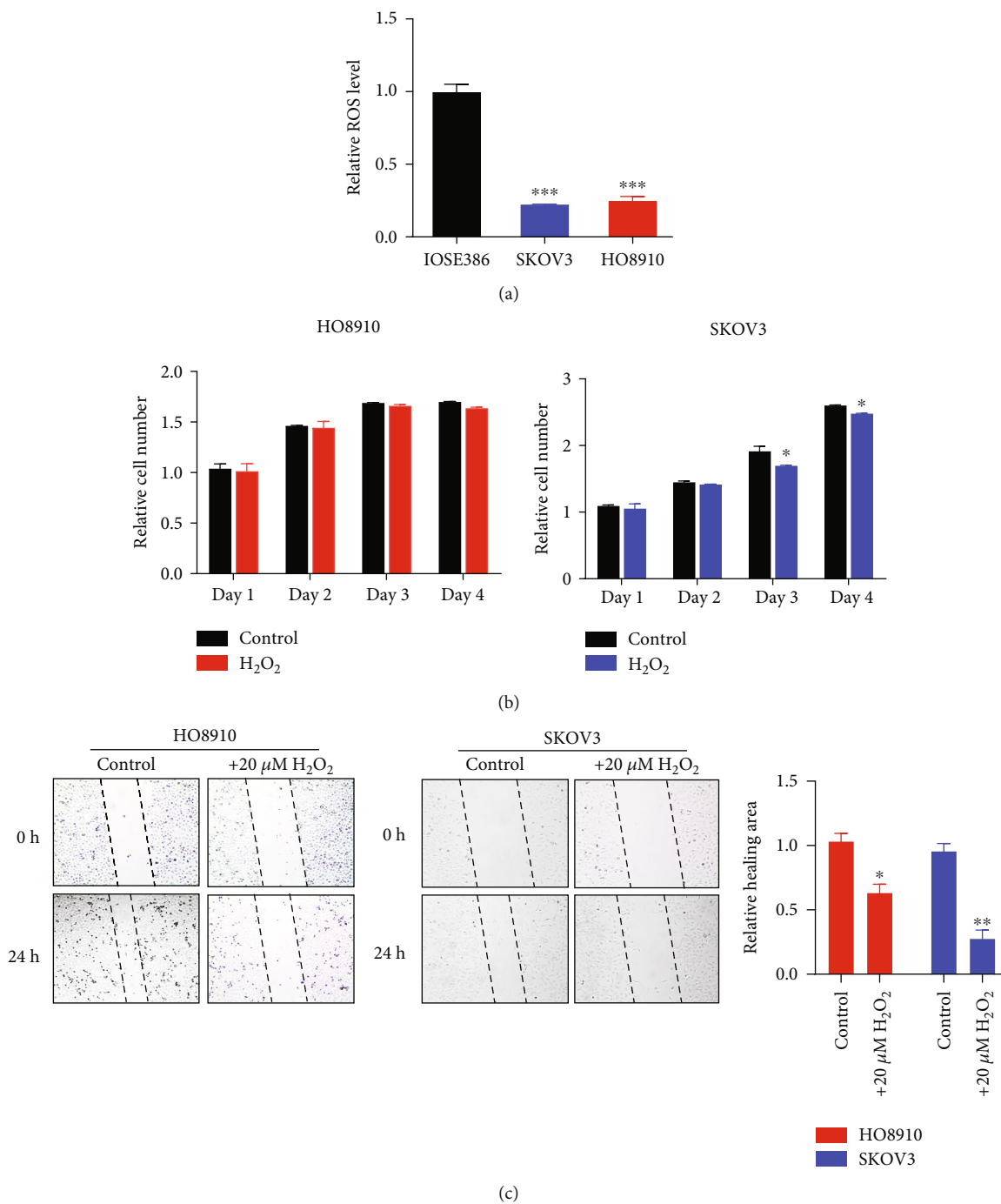


FIGURE 1: Continued.

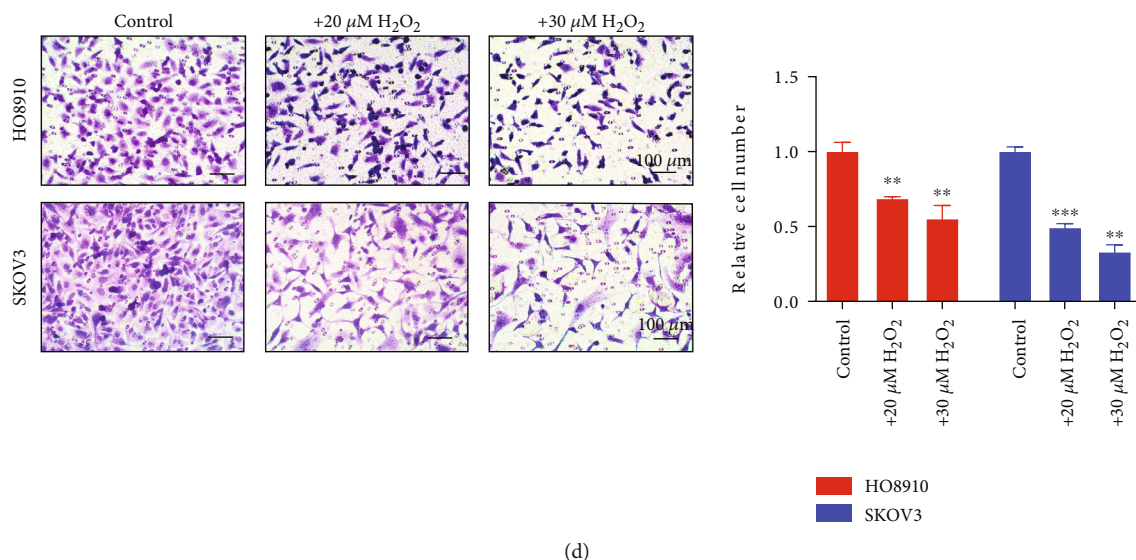


FIGURE 1: High levels of cellular ROS inhibit ovarian cancer cell migration and invasion. (a) ROS levels of three cell lines (IOSE386, HO8910, and SKOV3) were measured using  $10 \mu\text{M}$  DCFH-DA and flow cytometry. Comparisons were made between the experimental group and the sham control group by Student's *t*-test. (b) The relative cell number of HO8910 and SKOV3 cells treated with or without  $20 \mu\text{M}$   $\text{H}_2\text{O}_2$ . Comparisons were made between the experimental groups and the control groups by two-way analysis of variance (ANOVA) with Bonferroni correction. (c) Wound healing assays of HO8910 and SKOV3 cells treated with or without  $20 \mu\text{M}$   $\text{H}_2\text{O}_2$ . Quantification of the relative healing area is shown on the right. Comparisons were made between the experimental group and the sham control group by Student's *t*-test. (d) Transwell migration assays of HO8910 and SKOV3 cells treated with or without  $20 \mu\text{M}$   $\text{H}_2\text{O}_2$ . Quantification of the relative migrated cells is shown on the right and one-way analysis of variance (ANOVA) with Bonferroni correction for comparison between three groups. \* $P < 0.05$ , \*\* $P < 0.01$ , and \*\*\* $P < 0.001$ .

therapy, we treated HO8910 and SKOV3 cancer cells with  $20 \mu\text{M}$   $\text{H}_2\text{O}_2$  for different time points to examine the role of ROS in ovarian cancer cell viability. Our results show that  $\text{H}_2\text{O}_2$  decreased SKOV3 cells in a time-dependent manner but not HO8910 cells (Figure 1(b)). However, it is obvious that the SKOV3 and HO8910 cell migration in the wound healing assays was evidently reduced by  $\text{H}_2\text{O}_2$  (Figure 1(c)). Moreover, the invasive abilities of SKOV3 and HO8910 cells were also inhibited by  $\text{H}_2\text{O}_2$  in a dose-dependent manner (Figure 1(d)). Therefore, the increased  $\text{H}_2\text{O}_2$ -induced ROS levels can reduce ovarian cancer cell migration and invasion *in vitro*.

**3.2. Moderate SMFs Increase Ovarian Cancer Cell ROS Levels and Inhibit Cell Migration.** To examine the effects of moderate-intensity SMF on ovarian cancer cells, we exposed HO8910 and SKOV3 ovarian cancer cells to a moderate-intensity SMF provided by a permanent magnet (Figure 2(a)). The surface of SMF distribution is uneven and ranges from 0.1 T to 0.5 T where the cells were positioned (Figure 2(b)). Our results show that this moderate-intensity SMF could increase cellular ROS levels in HO8910 and SKOV3 cells (Figure 2(c)). After 24 hours of SMF treatment, the cellular ROS levels of HO8910 cells were increased by 23.55% ( $P < 0.05$ ) and SKOV3 cells were increased by 32.88% ( $P < 0.01$ ) (Figure 2(c)). Moreover, wound healing assays show that the migrations of both HO8910 and SKOV3 cells were inhibited by SMFs, but not the IOSE386 noncancerous cells (Figure 2(d)). Similarly, Transwell invasion assays show that the invasions of these two ovarian cancer

cell lines were both significantly suppressed by the SMF (54.67% and 53.74% reduction,  $P < 0.01$  and  $P < 0.005$ , respectively), but not the IOSE386 noncancerous cells, which had a low invasion activity (Figure 2(e)). We also examined the effect of this moderate SMF on cell proliferation by examining the cell numbers, which showed no obvious changes after SMF treatment (Figure 2(f)). Taken together, our results show that these moderate SMFs of 0.1 to 0.5 T could increase cellular ROS levels and inhibit ovarian cancer cell migration and invasion *in vitro*.

**3.3. Moderate SMFs Reduce Ovarian Cancer Stemness.** ROS could affect the epithelial-mesenchymal transition (EMT), which promotes the transition of mesenchymal CSCs into epithelial CSCs and then bulk cells [11] (Figure 3(a)). To investigate whether SMFs can reduce cancer stemness, SKOV3 cells were exposed to moderate SMF for 24 hours. Then, the total RNA was extracted and examined by real-time PCR to detect the expression of cancer stem genes (Figure 3(b)). We found that the stemness-related genes were significantly downregulated by SMF treatment, including Sox2, Nanog, C-myc, CD44, and CD133 (Figure 3(b)). For example, the mRNA expression of Nanog, a CSC biomarker, was decreased by 62.48% after SMF exposure ( $P < 0.01$ ) (Figure 3(b)). The mRNA expression of CD44, another CSC marker, was also decreased by 60.94% after SMF exposure ( $P < 0.01$ ) (Figure 3(b)). Moreover, we also observed that the cell morphology of SKOV3 cells changed from mesenchymal-like states to epithelial-like states after SMF exposure (Figure 3(c)). Furthermore, we exposed the

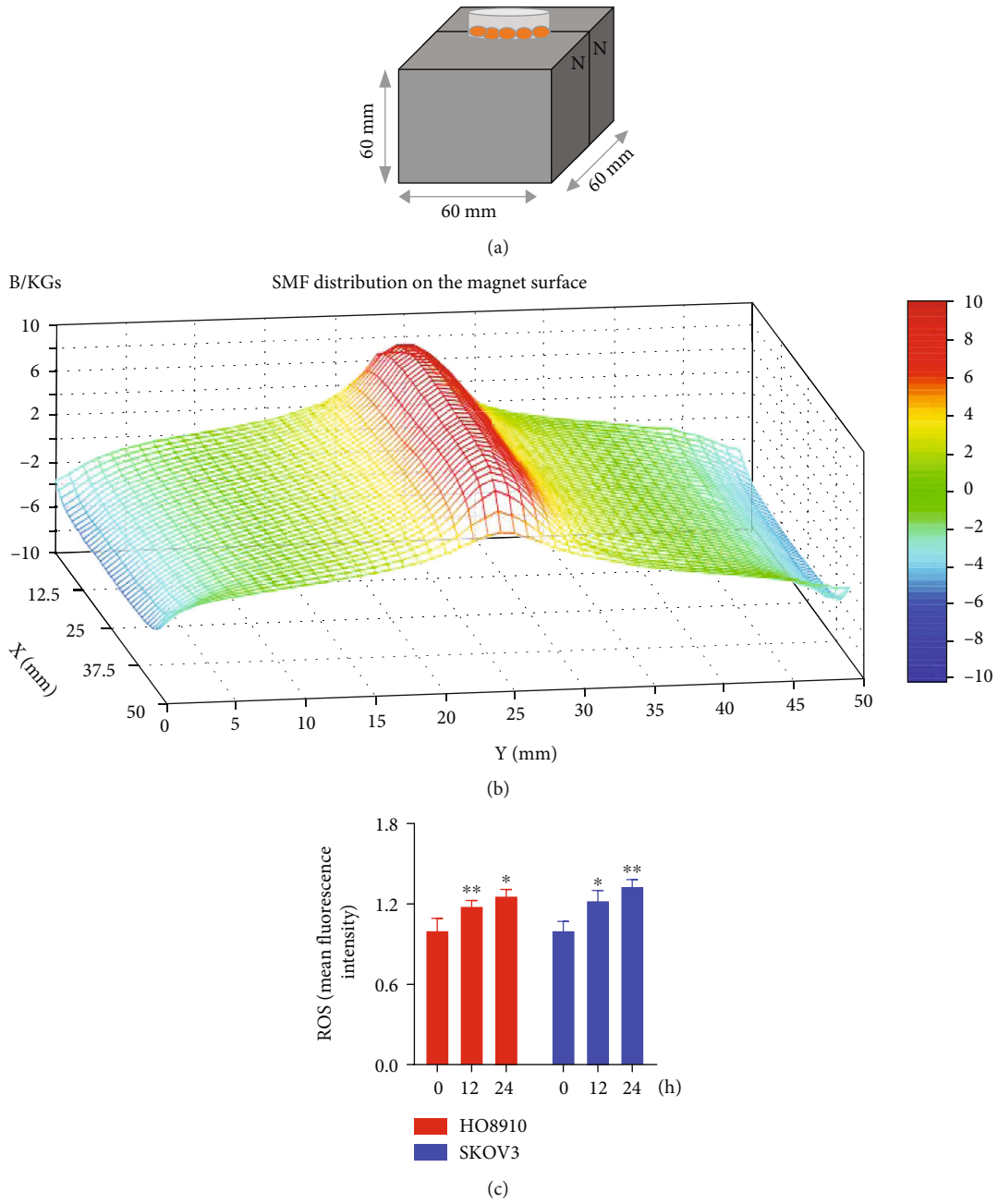


FIGURE 2: Continued.

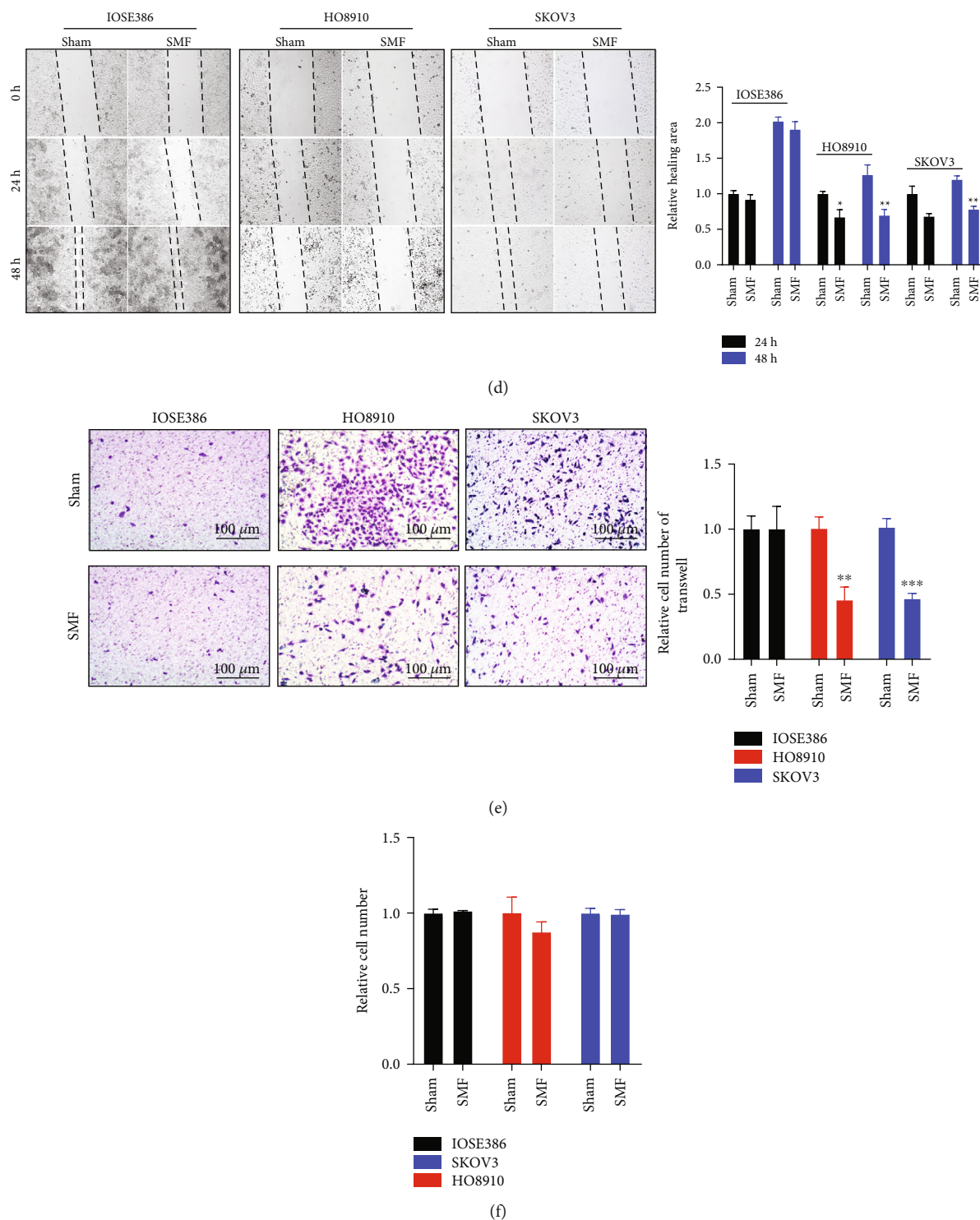
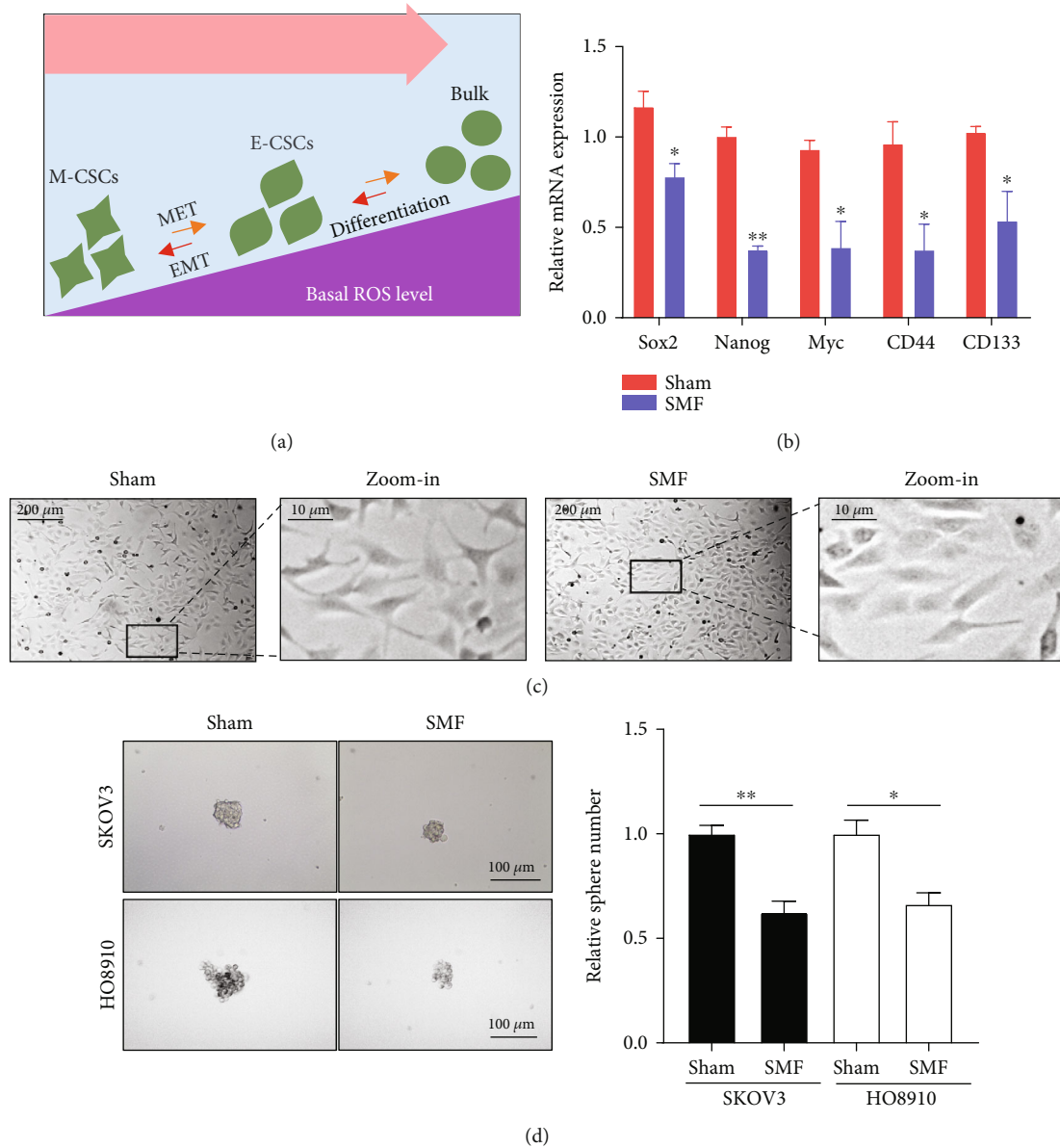


FIGURE 2: Moderate SMFs increase ovarian cancer cell ROS levels and inhibit cell migration. (a) Illustration of cells exposed to a moderate SMF provided by a permanent magnet. (b) Magnetic field distribution on the magnet surface was measured by a magnet analyzer. The SMF range in the cell culture dish area is 0.1 T~0.5 T. (c) ROS levels of HO8910 and SKOV3 cells exposed to the moderate SMF at different time points and one-way analysis of variance (ANOVA) with Bonferroni correction for comparison between three groups. (d) Wound healing assays of IOSE386, HO8910, and SKOV3 cells exposed to moderate SMF. Quantification of the relative healing area is shown on the right. Comparisons were made between two groups by Student's *t*-test. (e) Transwell invasion assays of HO8910 and SKOV3 cells treated with or without 20  $\mu$ M H<sub>2</sub>O<sub>2</sub>. Quantification of the invasive cells is shown on the right. Comparisons were made between two groups by Student's *t*-test. (f) Relative cell numbers of IOSE386, HO8910, and SKOV3 cells exposed to moderate SMF for 24 hours. Comparisons were made between the experimental group and the sham control group by Student's *t*-test. \**P* < 0.05, \*\**P* < 0.01, and \*\*\**P* < 0.001.





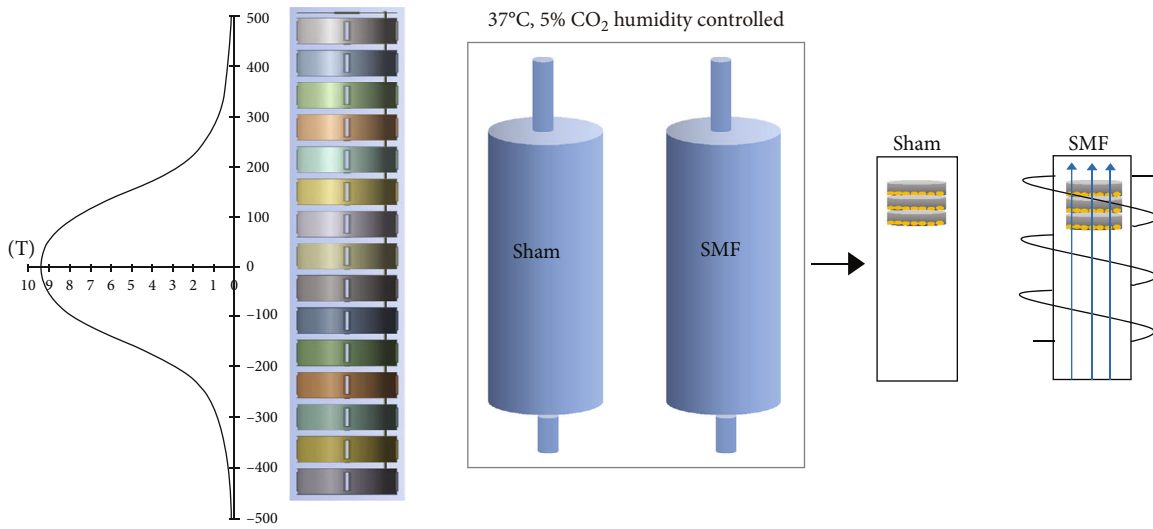
**FIGURE 3: Moderate SMFs reduce ovarian cancer stemness.** (a) Illustration of the effects of ROS level on CSCs. (b) The relative mRNA expressions of stemness genes were measured by qPCR, including Sox2, Nanog, C-myc, CD44, and CD133. (c) Representative bright-field images of SKOV3 cells exposed to sham or moderate SMF for 24 h. (d) The sphere number and size were measured in SKOV3 and HO8910 cells treated with SMF for 12 days. All comparisons were made between the experimental group and the sham control group by Student's *t*-test. \* $P < 0.05$  and \*\* $P < 0.01$ .

HO8910 and SKOV3 cells to SMF for 12 days and detected their sphere-forming ability. The number and size of OC cell spheres were obviously decreased by SMF (Figure 3(d)). These data suggested that ovarian cancer stemness was significantly reduced by this moderate SMF treatment.

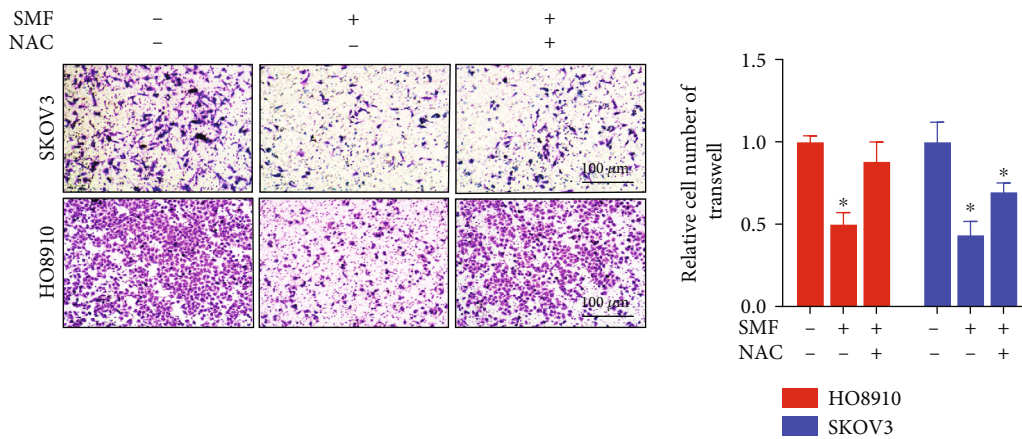
**3.4. Moderate SMFs Inhibit Ovarian Cancer Invasion in a ROS-Dependent Manner.** To further examine the effects of moderate SMFs on ovarian cancer cells, we used a superconducting magnet that has a cell culture compatible system (Figure 4(a)) [20]. We placed the cells at the upper part of the magnet where the intensity of SMF is  $\sim 0.5$  T. Similar to the permanent magnet, this 0.5 T SMF also significantly

decreased HO8910 and SKOV3 ovarian cancer cell invasion (Figure 4(b)) and migration (Figure 4(c)) in Transwell assays. To further examine the effects of increased ROS on ovarian cancer metastasis when exposed to moderate SMFs, we used N-acetyl-L-cysteine (NAC), a frequently used reagent to eliminate cellular ROS. Interestingly, the reduction effects of 0.5 T SMF in cell invasion and migration were abolished by NAC (Figures 4(b) and 4(c)), which confirms that SMF reduces ovarian cancer cell invasion and migration via ROS elevation.

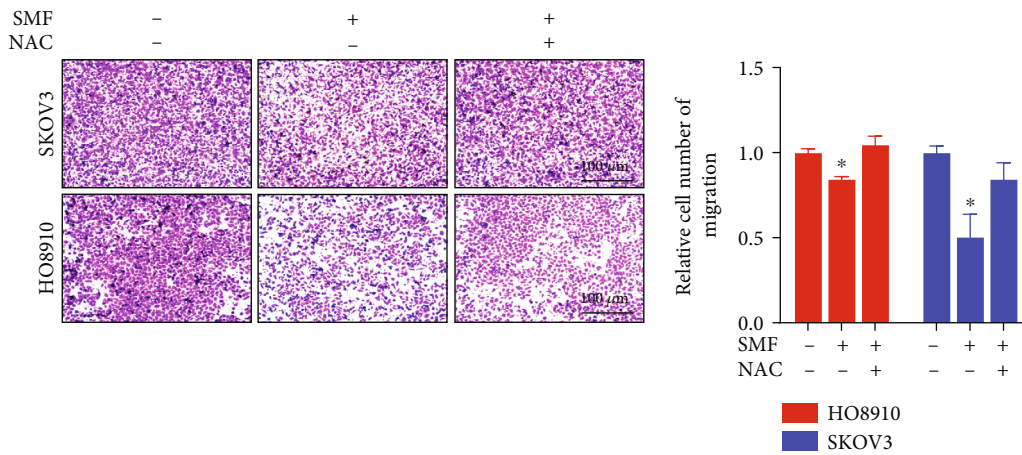
**3.5. RNA-Seq Reveals That Moderate SMFs Regulate Redox Process and Reduce Ovarian Cancer Stemness.** To assess the



(a)



(b)



(c)

FIGURE 4: Moderate SMFs inhibit ovarian cancer invasion in a ROS-dependent manner. (a) The SMF intensity distribution inside a superconducting magnet. Cells were placed in the upper part of the superconducting magnet, where the SMF is about 0.5 T. (b) Transwell invasion assays and (c) migration assays of SKOV3 and HO8910 ovarian cancer cells in the absence or presence of SMF and/or NAC. Quantifications of the relative cell numbers on the bottom plates are shown on the right. All comparisons were made between the experimental group and the sham control group by Student's *t*-test. \**P* < 0.05.

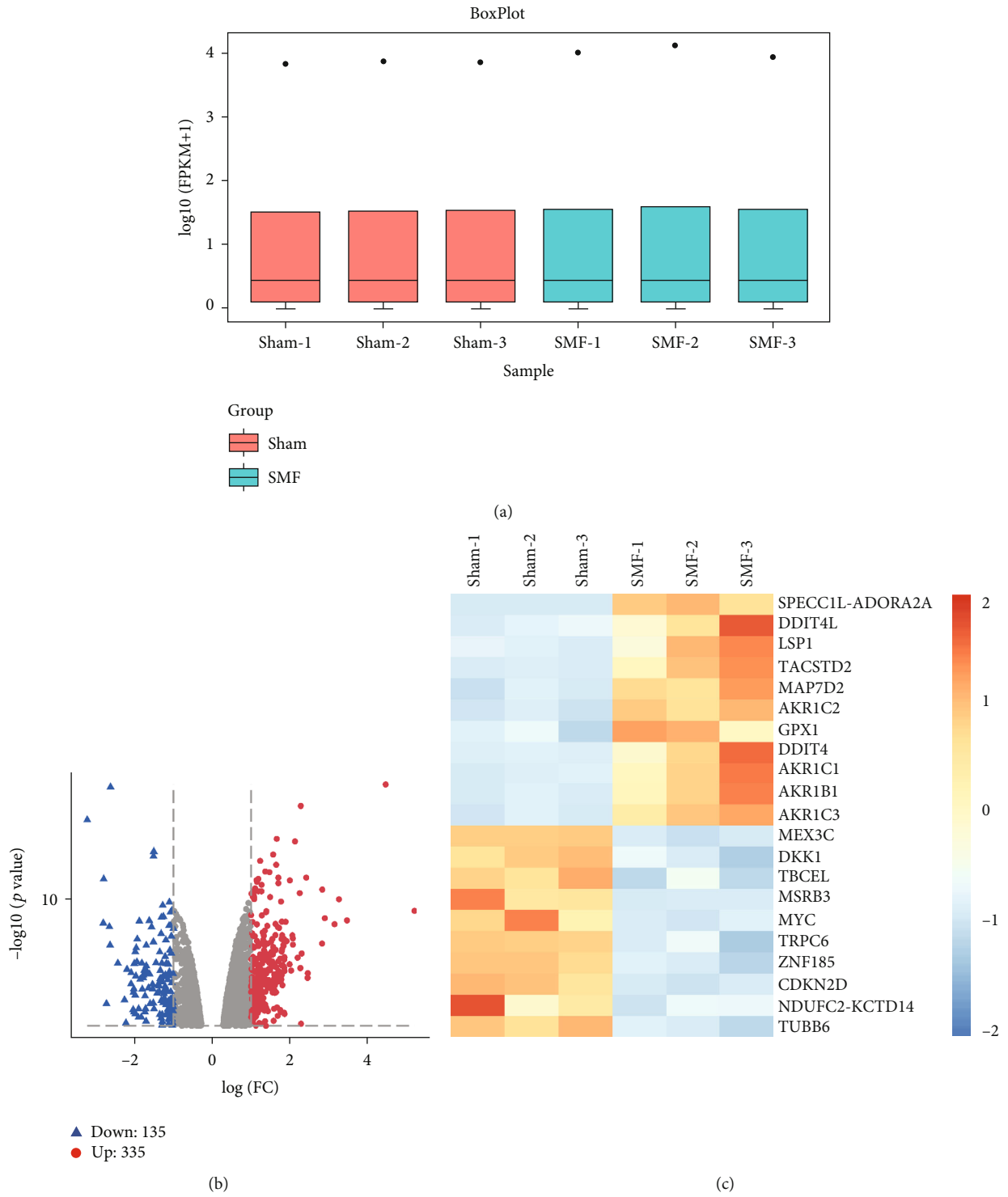


FIGURE 5: Continued.

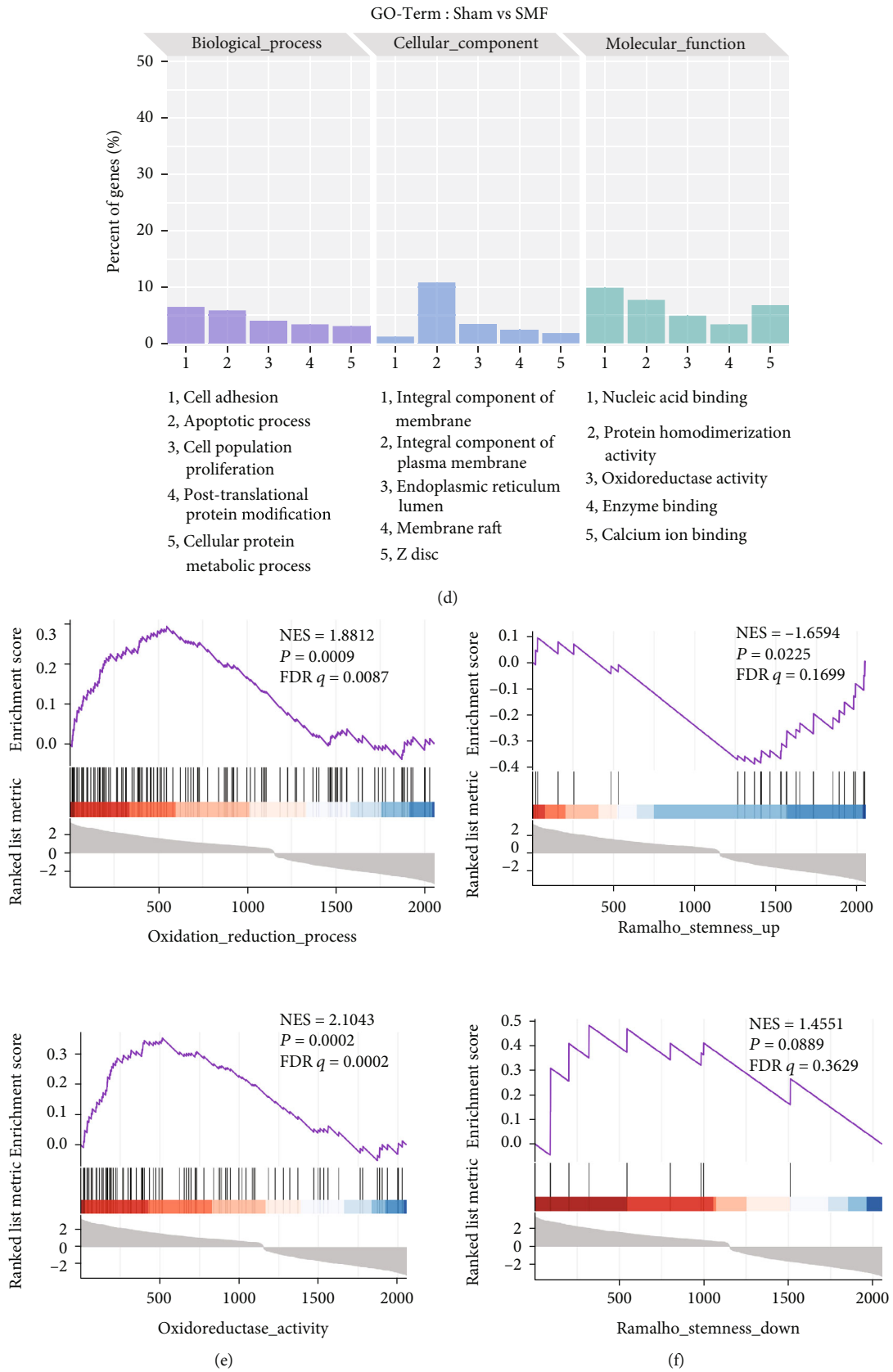


FIGURE 5: Continued.

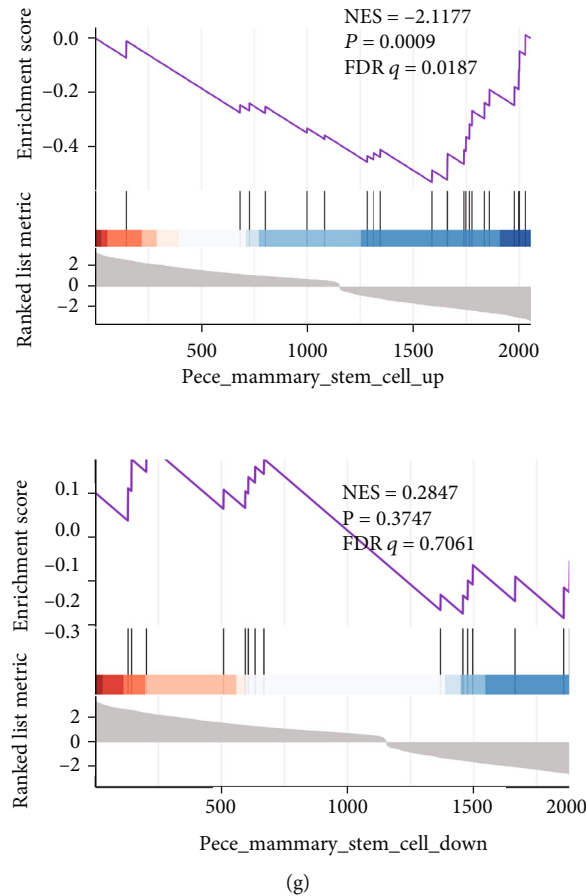


FIGURE 5: RNA-seq reveals that moderate SMFs regulate the redox process and reduce ovarian cancer stemness. (a) Box plot analysis was used to assess the biological duplication between sample groups. Volcano map (b), heat map of top 20 genes (c), and GO term (d) of the differential expression genes by RNA seq. (e–g) The GSEA was used to assess the relation of the differential genes and gene sets from the MSigDB database gene set, including OXIDATION\_REDUCTION\_PROCESS, OXIDOREDUCTASE ACTIVITY, PECE\_MAMMARY\_STEM\_CELL\_UP, PECE\_MAMMARY\_STEM\_CELL\_DOWN, RAMALHO\_STEMNESS\_UP, and RAMALHO\_STEMNESS\_DOWN.

effects of SMF on the ovarian cancer transcriptomes, we placed the SKOV3 ovarian cancer cells in the upper part of the superconducting magnet, where the SMF is approximately 0.5 T, or in the sham device. Six dishes of cells were treated for 24 hours before their total RNA was extracted for RNA sequencing analysis. The box plot analysis showed a good biological duplication among the samples (Figure 5(a)). Then, we analyzed and selected 467 genes with significant differential expressions, including 332 upregulated and 135 downregulated genes (Figure 5(b)). Moreover, the gene heat map indicated that the nuclear factor E2-related factor 2- (NRF2-) mediated antioxidant genes were activated significantly. For example, glutathione peroxidase 1 (GPX1) and aldo-keto reductase family 1 members (AKR1B1, AKR1C1, AKR1C2, and AKR1C3) are all in the top 20 of the most upregulated expressions (Figure 5(c)). GO term suggested that the differentially expressed genes are closely associated with oxidoreductase activity, protein homodimerization activity, cell adhesion, apoptotic process, cell population proliferation and cell membrane, etc. (Figure 5(d)). Furthermore, we found that the genes were enriched in the OXIDATION\_REDUCTION\_PRO-

CESS (NES = 1.8812,  $P = 0.0009$ ) and OXIDOREDUCTASE ACTIVITY (NES = 2.1043,  $P = 0.0002$ ) (Figure 5(e)) from GSEA, indicating that moderate SMF participates in the redox process regulation.

Interestingly, the GSEA results also indicated that the differential genes were enriched in the OUELLET\_OVARIAN\_CANCER\_INVASIVE\_VS\_LMP\_UP (NES = -2.14,  $P = 0.0013$ ), but not the OUELLET\_OVARIAN\_CANCER\_INVASIVE\_VS\_LMP\_DOWN (NES = 0.87,  $P = 0.6665$ ) (Supplementary Figure 1), indicating that SMFs could be closely related to the ovarian cancer metastasis. Since CSCs have unique abilities, including high metastasis and chemotherapy drug resistance, the reduction of cancer stemness will be an effective antitumor strategy. To examine the effects of moderate SMFs on CSCs in ovarian cancer, we analyzed the correlation between the differential genes and cancer stemness by the GSEA. It is interesting that the genes were enriched in the PECE\_MAMMARY\_STEM\_CELL\_UP (NES = -2.1177,  $P = 0.0009$ ) and RAMALHO\_STEMNESS\_UP (NES = -1.6594,  $P = 0.0225$ ). Consistent with the results at cellular level, the GSEA also showed that SMF-induced gene expressions

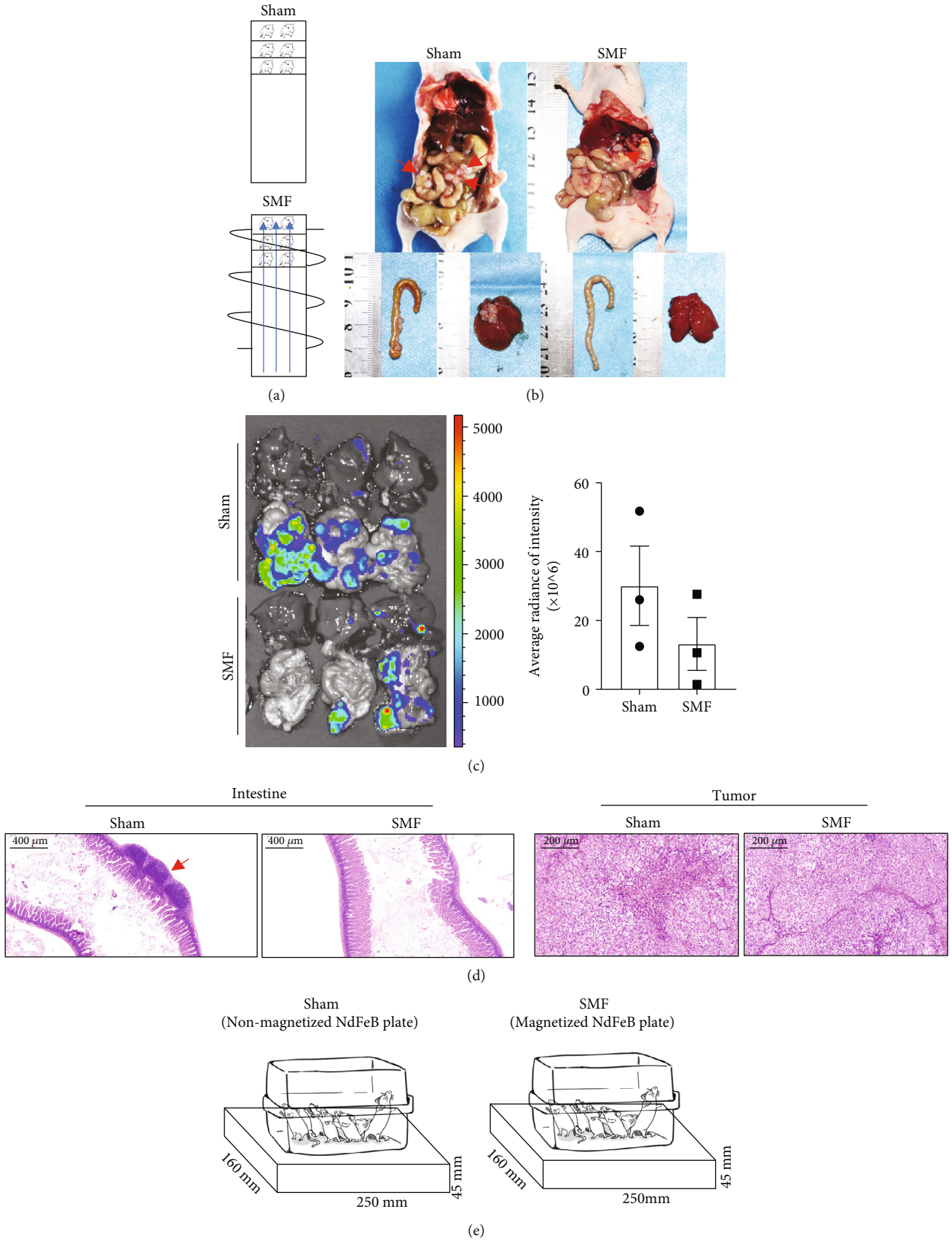


FIGURE 6: Continued.

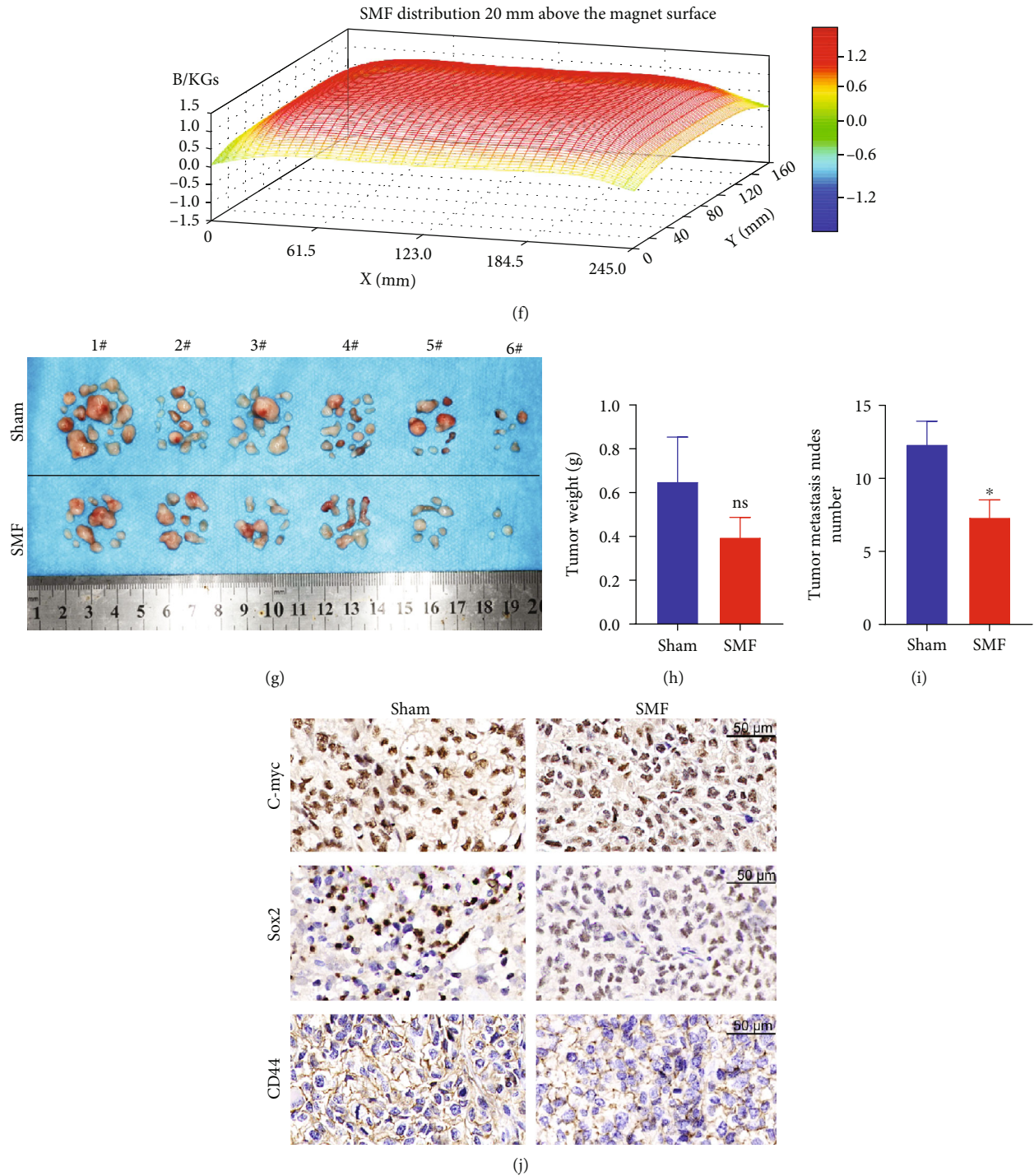


FIGURE 6: Moderate SMFs inhibit ovarian cancer metastasis in mice. Mice bearing ovarian cancer were exposed to moderate SMFs using a superconducting magnet (a–d) or a permanent magnet plate (e–j). (a) Mice bearing ovarian cancer were exposed to the sham or SMF conditions using a superconducting magnet. The mice were exposed for 10 hours/day and 7 days/week for 6 weeks. (b) Mice were examined for metastasis at the end of the experiment. (c) Heart, liver, spleen, lung, kidney, and intestine in mice were imaged by IVIS spectrum. (d) Representative HE staining images of the tumor and intestinal tissues sections. (e) The mice bearing OC were exposed to an unmagnetized sham NdFeB or a magnetized NdFeB plate for continuous 6 weeks. (f) The magnetic field distribution was scanned by a magnet analyzer at 20 mm above the magnetic surface. (g–i) All tumor nodules from the abdominal cavity of mice were collected at the end of the experiment to be imaged (g), weighted (h), and counted (i). (j) The immunohistochemistry of tumor tissue sections was used to detect the expressions of C-myc, Sox2, and CD44. All comparisons were made between the experimental group and the sham control group by Student's *t*-test. \* $P < 0.05$ ; ns: not significant.

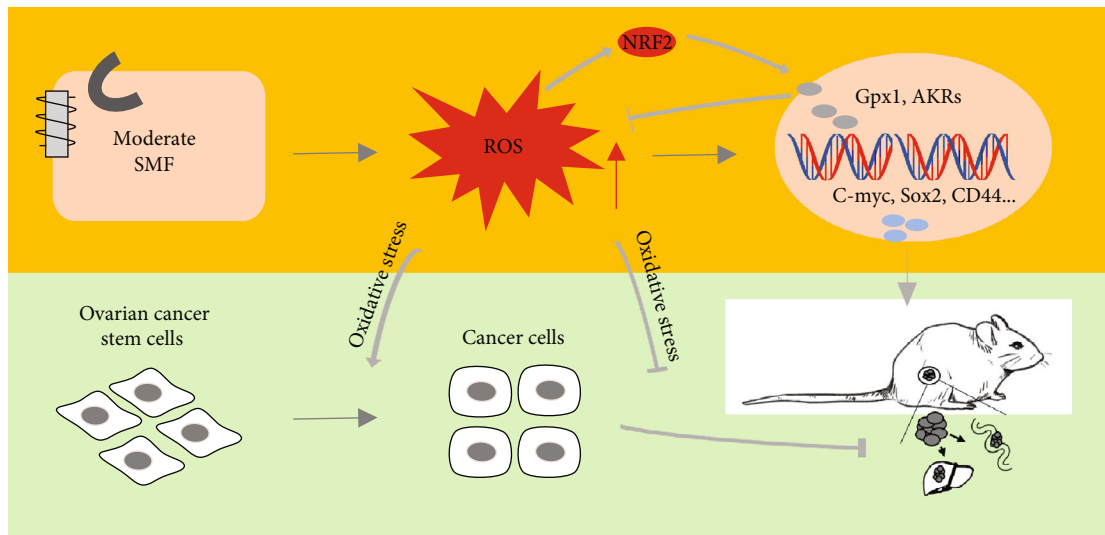


FIGURE 7: The mechanical diagram of SMF suppressing ovarian cancer metastasis. SMFs suppress the OC metastasis *in vivo* and *in vitro* through regulating ROS level and oxidative stress, which inhibits the transition of normal cancer cells to CSCs.

were negatively related to the upregulated genes of stem cells, which suggested moderate SMFs could reduce cancer stemness in ovarian cancer (Figures 5(f) and 5(g)).

**3.6. Moderate SMFs Inhibit Ovarian Cancer Metastasis in Mice.** To evaluate the effect of SMF on ovarian cancer metastasis *in vivo*, we injected  $1.0 \times 10^5$  SKOV3 cells into the abdominal cavity of 24 nude mice and exposed them to moderate-intensity SMFs by a superconducting magnet (Figures 6(a)–6(d)) or by a NdFeB permanent magnet plate (Figures 6(e)–6(j)). Both SMFs are upward direction and within the range of 0.1 ~ 0.5 T.

For the superconducting magnet group (Figures 6(a)–6(d)), the mice were randomly divided into two groups and exposed to the sham condition or SMF for 10 hours/day, 7 days/week for 6 weeks (total of 420 hours). We recorded food and water consumption as well as mouse body weight every week and found no significant changes after SMF exposure (Supplementary Figures 2(a)–2(c)). We also monitored their vital signs at the last pre- and post-exposure. It seems that SMF can increase arterial  $O_2$  while keeping the breath rate stable, and no other significant differences were found (Supplementary Figure 2(d)). In the 6<sup>th</sup> week, all mice were executed to collect serum and organs. No significant differences were observed in the blood chemistry analysis, including triglyceride (TG), lactate dehydrogenase (LDH), total protein (TP), alanine aminotransferase (ALT), aspartate aminotransferase (AST), creatine kinase (CK), uric acid (UA), and creatinine (CREA) (Supplementary Figure 2(e)). We also performed H&E staining for the heart, liver, spleen, lung, and kidney. Similarly, no obvious changes were found in comparison with the sham groups (Supplementary Figure 2(f)). These results demonstrate the biosafety of moderate SMF exposure for 420 hours on ovarian metastatic cancer-bearing mice. For the metastatic cancer nodules, a number of tumor nodules were found in the abdominal cavity of sham group mice, especially in the intestine and liver

tissues (Figure 6(b)). In contrast, moderate SMFs significantly reduced the tumor growth and metastasis in mice (Figure 6(c)). Moreover, the histological analysis confirmed to the reduction of metastasis nodules in the intestine (Figure 6(d)).

For the permanent magnet group (Figures 6(e)–6(j)), mice were randomly divided into two groups and exposed to the unmagnetized sham control plate or magnetized SMF plate for 24 hours/day, 7 days/week for 6 weeks (total of 1008 hours) (Figure 6(e)). The magnetic field distribution of the magnetized plate was scanned by a magnetic analyzer at 2 mm above the magnet plate, where the mouse bodies were located (Figure 6(f)). We collected total tumor nodules in mice (Figure 6(g)) and found that although moderate SMFs did not obviously affect the weight of these tumor metastasis nodules, the tumor nodule number was significantly reduced (Figures 6(h) and 6(i)). To examine the effect of SMF on cancer stemness in mice, we used immunohistochemistry staining to detect the expressions of C-myc, Sox2, and CD44. Consistent with the *in vitro* cell assay results, the expressions of stemness genes were obviously downregulated by SMF treatment, confirming that SMF could reduce cancer stemness and metastasis in mice.

## 4. Discussion and Conclusion

Our results show that the moderate SMFs we used here could increase the ROS levels of ovarian cancer cells to regulate the expression of antioxidant and stemness genes, which inhibits CSC transition into bulk cells (Figure 7). Consequently, the ovarian cancer metastasis in mice is significantly inhibited by these moderate SMFs.

**4.1. ROS Levels and Cancer Metastasis.** We compared the ROS levels in IOSE386 normal ovarian epithelial cells and SKOV3 and HO8910 ovarian cancer cells and found that the ROS levels in ovarian cancer cells are much lower than those of normal ovarian cells. Low ROS have been indicated



to be critical for the self-renewal of stem cells [22, 23]. Diehn et al. showed that normal mammary epithelial stem cells have lower ROS levels than their mature progeny cells. Moreover, subsets of CSCs in some breast tumors contained lower ROS levels than the nontumorigenic cells [24]. In the meantime, increased ROS promoted the transition of CSCs into the normal cancer cells and inhibited tumor metastasis in breast cancer and ovarian cancer [11, 25]. Clearly, altering ROS levels could affect the states of CSCs. Our results show that moderate SMFs can increase ROS levels in ovarian cancer cells and reduce their stemness, which inhibits cancer metastasis.

However, it is well known that ROS are involved in cell growth, differentiation, progression, and death; the effects of altering ROS levels in cancer cells are complicated. ROS-mediated oxidative stress can cause cell death, which is the cytotoxicity mechanism caused by many treatment modalities, including radiotherapy and some chemotherapy drugs. Cancer and noncancer cells often have different levels of ROS, but the relationship between ROS levels and cancer cells is complicated. In many cases, the cancer cells have higher ROS levels than noncancer cells. However, we found that for ovarian cells, the ovarian cancer cells have ~10 times lower ROS levels than normal ovarian cells. The increased ROS levels by either  $H_2O_2$  or moderate SMF treatment can reduce their stemness and metastasis.

**4.2. The Differential Effects of SMFs on ROS Levels.** Magnetic field can control the movement and transfer of electrons, so as to manipulate the unpaired electrons in free radicals, which provides a theoretical basis for cellular ROS regulation by SMF [26, 27]. It has been shown that SMFs can affect cellular ROS levels, but the results are variable in different studies [15]. Many studies show that SMFs can increase cellular ROS levels. For example, Nicola et al. found that 6 mT SMF for 2 hours triggered the increase of ROS in human monocyte tumor cells U937 [28]. Also, Calabrò et al. and Vergallo et al. confirmed that the cellular ROS,  $H_2O_2$ , and  $\cdot O_2^-$  could be elevated by 6 mT~232 mT SMFs in human neuroblastoma SH-SY5Y cells [29, 30]. In addition, 1.2 T high-gradient magnetic field treatment for 24 hours significantly increased cellular ROS in human monocytic leukemia cells THP-1 [31]. It is similar that ROS levels are increased by 8.5 T SMFs in human-hamster hybrid A(L) cells, mitochondria-deficient rho(0) A(L) cells, and double-strand break repair-deficient cells XRS-5, as well as mouse embryonic stem (ES) cells and derived cells [32]. Meanwhile, our previous study showed that the ROS levels were obviously increased by 9.4 T SMF, causing cell cycle arrest in human lung cancer cells A549 [20]. However, multiple studies demonstrate SMFs could reduce cellular ROS levels. For example, Van Huizen et al. found that weak SMFs (<1 mT) altered stem cell proliferation and differentiation through decreasing ROS levels [16]. Moreover, Carter et al. showed that 3 mT SMF in the combination with a static electric field could treat type 2 diabetes (T2D) through regulating the redox process and reducing cellular ROS [17]. Additionally, the reductions of ROS levels were found in human peripheral blood neutrophils [33] and bronchial epithelial cells

[34] when exposed to 60 mT and 389 mT SMFs, respectively. In our previous study, exposure to SMFs of 0.1 T~0.5 T could reduce ROS levels and improve gut microbes, which improved T2D mice [18].

Various factors could result in these differential effects of SMF on cellular ROS levels, including SMF intensity, gradient, exposure time, tissue type, or cell type. For instance, human breast cancer cell lines (MCF-7 and MDA-MB-231) were exposed to 1 T SMF for one day, and the results showed a reduction of ROS levels, while the exposure to 10 mT SMF for one day increased ROS levels in MCF-7 [35, 36]. Moreover, Csillag et al. placed human lung cancer cells (A549) in 389 mT SMF for 30 minutes and observed an obvious decrease in ROS levels [34]. On the contrary, our previous study showed that 9.4 T SMF could significantly increase A549 cellular ROS levels [20]. It is obvious that SMFs with different parameters could generate various effects on cancer cells. It seems that lower intensities and gradient SMFs often tend to decrease cellular ROS levels, while higher intensities and gradient SMFs tend to increase cellular ROS levels, but it is not always the case. SMF exposure time, cell type, the potential heat effect of some electromagnetic devices, and specific types of ROS ( $H_2O_2$ ,  $OH\cdot$ , or  $O_2\cdot^-$ , etc.) are also important factors that contribute to the differential effects of SMF on cellular ROS levels, which unquestionably still needs further systematic investigations.

**4.3. SMF and Cancer.** SMF is a safe physical method, even for strong SMFs that are ~10 times higher than the moderate SMFs we used in this study [37–40]. Here, we have also shown that exposure of ovarian cancer-bearing mice to 0.1 T~0.5 T moderate SMFs for 420 hours does not have any safety issues. Moreover, it has been demonstrated by multiple studies that SMFs have some tumor growth inhibition effects [20, 41, 42]. The mechanism involves microtubule assemble disturbance, epidermal growth factor receptor (EGFR) membrane protein orientation and activation, DNA synthesis inhibition, etc. [43–45].

In the current study, although the ovarian cancer cell growth was not obviously affected, we found that moderate SMF could increase ROS levels and oxidative stress in ovarian cancer cells to suppress their stemness, which inhibits cancer metastasis. The effects of MFs on cancer metastasis have always been a hot spot of people's attention. In 2002, Tofani et al. found that 5.5 mT-modulated MF (static with a superimposition of extremely low-frequency fields at 50 Hz) significantly inhibited tumor growth and metastasis in breast cancer MDA-MB-435 [46]. In 2007, Sommer et al. exposed AKR/J mice bearing lymphoma to an electromagnetic field and showed an obvious reduction in tumor metastasis [47]. Moreover, a report in 2009 showed that 42 mT SMF with a MF (150~300 nT, 1~16.5 Hz) obviously suppressed metastasis in Ehrlich ascites cancer [48]. In addition, Nie et al. found that a rotating magnetic field of ~0.4 T and 7.5 Hz could inhibit metastasis in melanoma B16-F10 cells in 2013 [49]. However, the study of alone SMF affecting cancer metastasis is insufficient. There was only one study reported that a hypomagnetic field could reduce the migration and invasion of human neuroblastoma SH-SY5Y [50].

In summary, our work reveals that moderate SMFs could suppress ovarian cancer metastasis *in vivo* and *in vitro*. Cellular studies show that SMF inhibits cell migration and invasion and reduces cancer stemness in ovarian cancer cells. Animal studies show that moderate SMFs could suppress ovarian cancer metastasis *in vivo*. Mechanistically, we show that SMF increases cellular ROS levels and oxidative stress, which promotes the transition of CSCs into normal cancer cells. Therefore, our study demonstrates the potential to develop SMF as a physical tool for cancer therapy in the future.

## Data Availability

The data used to support the findings of this study are included within the article.

## Conflicts of Interest

The authors declare that they have no conflicts of interest.

## Acknowledgments

This work was supported by the National Natural Science Foundation of China (31900506 and 52007185), the CASH-IPS Director's Fund (BJPY2021A06, YZJJ2020QN26, YZJJZX202014), and the Heye Health Technology Foundation (HYJJ20190801). A portion of this work was supported by the High Magnetic Field Laboratory of Anhui Province. We would like to thank Shu-tong Maggie Wang for cartoon illustration.

## Supplementary Materials

Supplementary Figure 1: the GSEA of the differential genes. Supplementary Figure 2: biosafety evaluation of mice exposed to the superconducting magnet. Table S1: sequence-based reagents for analyses of gene expression. (*Supplementary Materials*)

## References

- [1] R. L. Siegel, K. D. Miller, and A. Jemal, "Cancer statistics, 2020," *CA: a Cancer Journal for Clinicians*, vol. 70, no. 1, pp. 7–30, 2020.
- [2] R. L. Siegel, K. D. Miller, and A. Jemal, "Cancer statistics, 2018," *CA: a Cancer Journal for Clinicians*, vol. 68, no. 1, pp. 7–30, 2018.
- [3] U. H. Weidle, F. Birzele, G. Kollmorgen, and R. Rueger, "Mechanisms and targets involved in dissemination of ovarian cancer," *Cancer Genomics Proteomics*, vol. 13, no. 6, pp. 407–424, 2016.
- [4] A. J. Cortez, P. Tudrej, K. A. Kujawa, and K. M. Lisowska, "Advances in ovarian cancer therapy," *Cancer Chemotherapy and Pharmacology*, vol. 81, no. 1, pp. 17–38, 2018.
- [5] T. Reya, S. J. Morrison, M. F. Clarke, and I. L. Weissman, "Stem cells, cancer, and cancer stem cells," *Nature*, vol. 414, no. 6859, pp. 105–111, 2001.
- [6] A. Singh and J. Settleman, "EMT, cancer stem cells and drug resistance: an emerging axis of evil in the war on cancer," *Oncogene*, vol. 29, no. 34, pp. 4741–4751, 2010.
- [7] F. Li, B. Tiede, J. Massagué, and Y. Kang, "Beyond tumorigenesis: cancer stem cells in metastasis," *Cell Research*, vol. 17, no. 1, pp. 3–14, 2007.
- [8] Y. X. Lu, H. Q. Ju, Z. X. Liu et al., "ME1 regulates NADPH homeostasis to promote gastric cancer growth and metastasis," *Cancer Research*, vol. 78, no. 8, pp. 1972–1985, 2018.
- [9] F. J. Zheng, H. B. Ye, M. S. Wu, Y. F. Lian, C. N. Qian, and Y. X. Zeng, "Repressing malic enzyme 1 redirects glucose metabolism, unbalances the redox state, and attenuates migratory and invasive abilities in nasopharyngeal carcinoma cell lines," *Chinese Journal of Cancer*, vol. 31, no. 11, pp. 519–531, 2012.
- [10] X. Wu, Y. Zhu, H. Yan et al., "Isothiocyanates induce oxidative stress and suppress the metastasis potential of human non-small cell lung cancer cells," *BMC Cancer*, vol. 10, no. 1, p. 269, 2010.
- [11] M. Luo, L. Shang, M. D. Brooks et al., "Targeting breast cancer stem cell state equilibrium through modulation of redox signaling," *Cell Metabolism*, vol. 28, no. 1, pp. 69–86.e6, 2018.
- [12] T. Xin, F. Zhang, Q. Jiang et al., "Extraction, purification and antitumor activity of a water-soluble polysaccharide from the roots of *Polygala tenuifolia*," *Carbohydrate Polymers*, vol. 90, no. 2, pp. 1127–1131, 2012.
- [13] J. A. Vassie, J. M. Whitelock, and M. S. Lord, "Endocytosis of cerium oxide nanoparticles and modulation of reactive oxygen species in human ovarian and colon cancer cells," *Acta Biomaterialia*, vol. 50, pp. 127–141, 2017.
- [14] M. Kleih, K. Böppe, M. Dong et al., "Direct impact of cisplatin on mitochondria induces ROS production that dictates cell fate of ovarian cancer cells," *Cell Death & Disease*, vol. 10, no. 11, p. 851, 2019.
- [15] H. Wang and X. Zhang, "Magnetic fields and reactive oxygen species," *International Journal of Molecular Sciences*, vol. 18, no. 10, p. 2175, 2017.
- [16] A. V. van Huizen, M. J. Morton, L. J. Kinsey et al., "Weak magnetic fields alter stem cell-mediated growth," *Science Advances*, vol. 5, no. 1, article eaau7201, 2019.
- [17] C. S. Carter, S. C. Huang, C. C. Searby et al., "Exposure to static magnetic and electric fields treats type 2 diabetes," *Cell Metabolism*, vol. 32, no. 4, pp. 561–574.e7, 2020.
- [18] B. Yu, J. J. Liu, J. Cheng et al., "A static magnetic field improves iron metabolism and prevents high-fat-diet/streptozocin-induced diabetes," *The Innovation*, vol. 2, no. 1, p. 100077, 2021.
- [19] X. F. Tian, D. M. Wang, M. Zha et al., "Magnetic field direction differentially impacts the growth of different cell types," *Electromagnetic Biology and Medicine*, vol. 37, no. 2, pp. 114–125, 2018.
- [20] X. Yang, C. Song, L. Zhang et al., "An upward 9.4 T static magnetic field inhibits DNA synthesis and increases ROS-P53 to suppress lung cancer growth," *Translational Oncology*, vol. 14, no. 7, p. 101103, 2021.
- [21] K. J. Livak and T. D. Schmittgen, "Analysis of relative gene expression data using real-time quantitative PCR and the  $2^{-\Delta\Delta C_T}$  method," *Methods*, vol. 25, no. 4, pp. 402–408, 2001.
- [22] K. Ito, A. Hirao, F. Arai et al., "Regulation of oxidative stress by ATM is required for self-renewal of haematopoietic stem cells," *Nature*, vol. 431, no. 7011, pp. 997–1002, 2004.

- [23] Z. Tothova, R. Kollipara, B. J. Huntly et al., "FoxOs are critical mediators of hematopoietic stem cell resistance to physiologic oxidative stress," *Cell*, vol. 128, no. 2, pp. 325–339, 2007.
- [24] M. Diehn, R. W. Cho, N. A. Lobo et al., "Association of reactive oxygen species levels and radioresistance in cancer stem cells," *Nature*, vol. 458, no. 7239, pp. 780–783, 2009.
- [25] A. K. Srivastava, A. Banerjee, T. Cui et al., "Inhibition of miR-328-3p impairs cancer stem cell function and prevents metastasis in ovarian cancer," *Cancer Research*, vol. 79, no. 9, pp. 2314–2326, 2019.
- [26] N. Ikeya and J. R. Woodward, "Cellular autofluorescence is magnetic field sensitive," *Proceedings of the National Academy of Sciences of the United States of America*, vol. 118, no. 3, article e2018043118, 2021.
- [27] C. R. Timmel, P. J. Hore, K. A. Mclauchlan, and B. Brocklehurst, "The effects of weak static magnetic fields on the yields of radical recombination reactions," *Abstracts of Papers of the American Chemical Society*, vol. 217, pp. U287–U287, 1999.
- [28] M. D. Nicola, S. Cordisco, C. Cerella et al., "Magnetic fields protect from apoptosis via redox alteration," *Annals of the New York Academy of Sciences*, vol. 1090, pp. 59–68, 2010.
- [29] C. Vergallo, M. Ahmadi, H. Mobasheri, and L. Dini, "Impact of inhomogeneous static magnetic field (31.7–232.0 mT) exposure on human neuroblastoma SH-SY5Y cells during cisplatin administration," *PLoS One*, vol. 9, no. 11, article e113530, 2014.
- [30] E. Calabrò, S. Condello, M. Currò et al., "Effects of low intensity static magnetic field on FTIR spectra and ROS production in SH-SY5Y neuronal-like cells," *Bioelectromagnetics*, vol. 34, no. 8, pp. 618–629, 2013.
- [31] V. Zablotskii, T. Syrovets, Z. W. Schmidt, A. Dejneka, and T. Simmet, "Modulation of monocytic leukemia cell function and survival by high gradient magnetic fields and mathematical modeling studies," *Biomaterials*, vol. 35, no. 10, pp. 3164–3171, 2014.
- [32] G. Zhao, S. Chen, L. Wang et al., "Cellular ATP content was decreased by a homogeneous 8.5 T static magnetic field exposure: role of reactive oxygen species," *Bioelectromagnetics*, vol. 32, no. 2, pp. 94–101, 2011.
- [33] B. Poniedziałek, P. Rzymiski, J. Karczewski, F. Jaroszyk, and K. Wiktorowicz, "Reactive oxygen species (ROS) production in human peripheral blood neutrophils exposed in vitro to static magnetic field," *Electromagnetic Biology and Medicine*, vol. 32, no. 4, pp. 560–568, 2013.
- [34] A. Csillag, B. V. Kumar, K. Szabó et al., "Exposure to inhomogeneous static magnetic field beneficially affects allergic inflammation in a murine model," *Journal of the Royal Society Interface*, vol. 11, no. 95, p. 20140097, 2014.
- [35] H. Wang and X. Zhang, "ROS reduction does not decrease the anticancer efficacy of X-ray in two breast cancer cell lines," *Oxidative Medicine and Cellular Longevity*, vol. 2019, Article ID 3782074, 12 pages, 2019.
- [36] B. H. Verdom, P. Abdolmaleki, and M. Behmanesh, "The static magnetic field remotely boosts the efficiency of doxorubicin through modulating ROS behaviors," *Scientific Reports*, vol. 8, no. 1, p. 990, 2018.
- [37] S. Wang, J. Luo, H. Lv et al., "Safety of exposure to high static magnetic fields (2 T–12 T): a study on mice," *European Radiology*, vol. 29, no. 11, pp. 6029–6037, 2019.
- [38] X. Tian, D. Wang, S. Feng et al., "Effects of 3.5–23.0 T static magnetic fields on mice: a safety study," *NeuroImage*, vol. 199, pp. 273–280, 2019.
- [39] X. Tian, Y. Lv, Y. Fan et al., "Safety evaluation of mice exposed to 7.0–33.0 T high-static magnetic fields," *Journal of Magnetic Resonance Imaging*, vol. 53, no. 6, pp. 1872–1884, 2021.
- [40] X. Tian, Z. Wang, L. Zhang et al., "Effects of 3.7 T–24.5 T high magnetic fields on tumor-bearing mice," *Chinese Physics B*, vol. 27, no. 11, article 118703, 2018.
- [41] R. R. Raylman, A. C. Clavo, R. L. Wahl et al., "Exposure to strong static magnetic field slows the growth of human cancer cells in vitro," *Bioelectromagnetics*, vol. 17, no. 5, pp. 358–363, 1996.
- [42] X. Zhang, K. Yarema, and A. Xu, *Biological Effects of Static Magnetic Fields*, Springer, 2017.
- [43] L. Zhang, J. Wang, H. Wang et al., "Moderate and strong static magnetic fields directly affect EGFR kinase domain orientation to inhibit cancer cell proliferation," *Oncotarget*, vol. 7, no. 27, pp. 41527–41539, 2016.
- [44] L. Zhang, Y. Hou, Z. Li et al., "27 T ultra-high static magnetic field changes orientation and morphology of mitotic spindles in human cells," *eLife*, vol. 6, article e22911, 2017.
- [45] X. Yang, Z. Li, T. Polyakova, A. Dejneka, V. Zablotskii, and X. Zhang, "Effect of static magnetic field on DNA synthesis: the interplay between DNA chirality and magnetic field left-right asymmetry," *FASEB BioAdvances*, vol. 2, no. 4, pp. 254–263, 2020.
- [46] S. Tofani, D. Barone, S. Peano, P. Ossola, and M. Cintorino, "Anticancer activity by magnetic fields: inhibition of metastatic spread and growth in a breast cancer model," *IEEE Transactions on Plasma Science*, vol. 30, no. 4, pp. 1552–1557, 2003.
- [47] A. M. Sommer, A. K. Bitz, J. Streckert, V. W. Hansen, and A. Lerchl, "Lymphoma development in mice chronically exposed to UMTS-modulated radiofrequency electromagnetic fields," *Radiation Research*, vol. 168, no. 1, pp. 72–80, 2007.
- [48] V. V. Novikov, G. V. Novikov, and E. E. Fesenko, "Effect of weak combined static and extremely low-frequency alternating magnetic fields on tumor growth in mice inoculated with the Ehrlich ascites carcinoma," *Bioelectromagnetics*, vol. 30, no. 5, pp. 343–351, 2009.
- [49] Y. Nie, L. du, Y. Mou et al., "Effect of low frequency magnetic fields on melanoma: tumor inhibition and immune modulation," *BMC Cancer*, vol. 13, no. 1, p. 582, 2013.
- [50] W. C. Mo, Z. J. Zhang, D. L. Wang, Y. Liu, P. F. Bartlett, and R. Q. He, "Shielding of the geomagnetic field alters actin assembly and inhibits cell motility in human neuroblastoma cells," *Scientific Reports*, vol. 6, no. 1, p. 22624, 2016.

## Research Article

# Exploration of Redox-Related Molecular Patterns and the Redox Score for Prostate Cancer

Yue Wu,<sup>1,2</sup> Xi Zhang,<sup>3</sup> Huan Feng,<sup>1,2</sup> Bintao Hu,<sup>1,2</sup> Zhiyao Deng,<sup>1,2</sup> Chengwei Wang,<sup>1,2</sup> Bo Liu,<sup>4</sup> Yang Luan,<sup>1,2</sup> Yajun Ruan,<sup>1,2</sup> Xiaming Liu,<sup>1,2</sup> Zhuo Liu,<sup>1,2</sup> Jihong Liu,<sup>1,2</sup> and Tao Wang<sup>1,2</sup> 

<sup>1</sup>Department of Urology, Tongji Hospital, Tongji Medical College, Huazhong University of Science and Technology, Wuhan, 430030 Hubei, China

<sup>2</sup>Institute of Urology, Tongji Hospital, Tongji Medical College, Huazhong University of Science and Technology, Wuhan, 430030 Hubei, China

<sup>3</sup>The First Clinical Medical College of Anhui Medical University, Hefei, 230001 Anhui, China

<sup>4</sup>Department of Oncology, Tongji Hospital, Tongji Medical College, Huazhong University of Science and Technology, Wuhan, 430030 Hubei, China

Correspondence should be addressed to Tao Wang; [tjhwt@126.com](mailto:tjhwt@126.com)

Received 10 August 2021; Revised 7 October 2021; Accepted 22 October 2021; Published 11 November 2021

Academic Editor: Bin Duan

Copyright © 2021 Yue Wu et al. This is an open access article distributed under the Creative Commons Attribution License, which permits unrestricted use, distribution, and reproduction in any medium, provided the original work is properly cited.

Redox homeostasis is the key to cell survival, and its imbalance can promote the occurrence and progression of tumors. However, it remains unclear whether these redox-related genes (RRGs) have potential roles in the tumor microenvironment, immunotherapy, and drug sensitivity. Here, we performed a systematic and comprehensive analysis of 489 prostate cancer (PC) samples from The Cancer Genome Atlas database and 214 PC samples from 8 datasets in the Gene Expression Omnibus database to determine redox modification patterns and the redox scoring system for PC. We identified two modification patterns (Redox\_A and Redox\_B) in PC using unsupervised consensus clustering based on 1410 differential expression RRGs. We then compared the prognostic value, tumor microenvironment characteristics, immune cell infiltration, and molecular characteristics of the two patterns. The Redox\_A pattern was significantly enriched in the carcinogenic activation signaling pathways and had a poor prognosis, while the Redox\_B pattern was mainly enriched in a variety of metabolic and redox pathways and had a good prognosis. Next, redox-related characteristic genes were extracted from these two patterns, and a scoring system (Redox\_score) was constructed to evaluate PC patients. Further analysis indicated that lower Redox\_score patients had a better prognosis, while higher Redox\_score patients had a higher tumor mutation burden, driver gene mutation rate, and immune checkpoint inhibitor gene expression. We also found that higher Redox\_score patients were more responsive to anti-PD-1 immunotherapy. Moreover, Redox\_score was determined to be significantly correlated with anticancer drug sensitivity and resistance. Our study provides a comprehensive analysis of redox modifications in PC and reveals new patterns of PC based on RRGs, which will provide insights into the complex mechanisms of PC and develop more effective individualized therapeutic strategies.

## 1. Introduction

Prostate cancer (PC) is the most common noncutaneous malignancy in men worldwide and the second leading cause of tumor-related death in men [1]. It was estimated that there were 191,930 new diagnoses and 33,330 deaths from PC in the United States in 2020 [1]. Distant metastasis occurs in approximately 20% of all PC patients and is the

leading cause of PC-related death [2]. And the 5-year survival rate for these patients dropped significantly, to nearly 30% [3, 4]. The most common site of distant metastasis from PC is the bone, followed by the lung, lymph nodes, and liver, which are the most deadly sites of metastasis [5]. Thus, a better understanding of the occurrence and progression of PC may contribute to effective early diagnosis and targeted therapy.

Redox homeostasis is the balance of the equivalent of reduction and oxidation and has a great importance in many physiological and pathological processes. The imbalance of redox homeostasis is mainly caused by changes in reactive oxygen species (ROS)/reactive nitrogen (RNS) or antioxidant protein levels [6]. ROS are present in the cell as free radicals ( $\text{OH}^-$ ), neutral molecules ( $\text{H}_2\text{O}_2$ ), or ions ( $\text{O}_2^-$ ), while cellular RNS are present in the form of peroxynitrite ( $\text{ONOO}^-$ ), nitric oxide (NO), and nitrogen dioxide ( $\text{NO}_2$ ) [7, 8]. Studies have shown that RNS and ROS are crosstalk and have obvious correlation [9]. Under physiological conditions, various biological processes such as cell proliferation, cell differentiation, and adaptive immunity, as well as a variety of proteins including kinases, receptors, transcription factors, and ion channels, are dependent on ROS regulation and modification [10, 11]. However, sustained increases in intracellular ROS levels can cause a variety of pathological processes, such as cardiovascular disease, neurodegeneration, immune system dysfunction, and cancer [12]. Therefore, it is necessary to study the redox state in tumor cells.

Currently, there are not enough indicators to diagnose PC at an early stage and to distinguish between those who need a prostatectomy and those who need tumor treatment. Even prostate-specific antigen (PSA) levels, the most common marker for PC development and progression, can remain within normal ranges or have false negative results [13]. To this end, several researchers have sought to identify specific biomarkers in the redox system to determine the severity of prostate cancer. For example, the Süle et al. [13] study found that patients with early stage PC had significantly lower levels of cytokines and growth factors than controls. Blázovics et al. [14] found that the results of binding formaldehyde, Zn-protoporphyrin, and free protoporphyrin in erythrocytes were significantly different in patients with metastatic, histologically negative, and histologically positive PC treated with taxane compared with healthy controls. These findings are closely related to the redox state [15]. However, the large number of redox regulatory factors makes it difficult for traditional research methods to reflect the macrolandscape of the redox state of individual tumors. Moreover, the occurrence and progression of tumors are highly coordinated interactions of multiple regulatory factors, so a more comprehensive and effective analysis of the characteristics of redox reactions in PC is required. Herein, we comprehensively evaluated genomic changes and redox patterns by integrating transcriptome data of 489 PC samples from The Cancer Genome Atlas (TCGA) database and 214 PC samples from 8 datasets in the Gene Expression Omnibus (GEO) database. Two PC subclasses, Redox\_A and Redox\_B, were identified based on redox-related genes (RRGs) and by the unsupervised clustering method. Further analysis showed that the two patterns were enriched in different biological pathways and showed different characteristics of the immune microenvironment. Next, we extracted the redox-associated characteristic genes from these two modification patterns and constructed a scoring scheme (Redox\_score) to quantify the redox patterns of individual tumors and evaluate its prognostic value, clinical characteristics, drug sensitivity, and immunotherapy.

## 2. Materials and Methods

**2.1. Collection and Pretreatment of PC Datasets.** Transcriptome data and corresponding clinical characteristics of PC patients were collected and collated from TCGA and GEO databases, respectively. Specifically, in the TCGA database, we mainly collected RNA sequencing data (FPKM format and read counts), somatic mutation data (MAF format), miRNA sequencing data, and clinical prognosis information of PC patients (<https://portal.gdc.cancer.gov/>). The FPKM format was then converted into transcripts per kilobase million (TPM) format for subsequent analysis. Next, we obtained 8 datasets from the GEO database (<https://www.ncbi.nlm.nih.gov/geo/>) that shared the same microarray sequencing platform (Affymetrix GPL570-HGU133 plus 2.0), including GSE69223 ( $n = 30$ ), GSE55945 ( $n = 19$ ), GSE46602 ( $n = 50$ ), GSE45016 ( $n = 11$ ), GSE26910 ( $n = 12$ ), GSE17951 ( $n = 154$ ), GSE17906 ( $n = 25$ ), and GSE3325 ( $n = 19$ ). Subsequently, background adjustment and quantile normalization were performed on the original “CEL” files of the above 8 datasets through the “RMA” algorithm of the “affy” R package. The batch effects of merging 8 datasets were then removed by using the “ComBat” approach of the “SVA” R package. Moreover, we directly downloaded the standardized sequencing data and corresponding clinical prognosis information of the GSE70769 dataset from the GEO database and were used for subsequent score validation.

**2.2. Differential Expression of RRGs and Identification of PC Subclasses.** In order to obtain all RRGs, we used “redox” as the key word to screen human genes related to redox from the OMIM database (<https://www.oncomine.org/resource/>), gene function module of the NCBI database (<https://www.ncbi.nlm.nih.gov/gene/>), GeneCards database (<https://www.genecards.org/>), and GSEA-MSigDB (<https://www.gseamsigdb.org/gsea/msigdb>), and finally, we got a total of 4087 RRGs. Subsequently, the differential expression RRGs were obtained through the “DESeq2” R package in TCGA-PRAD and GEO-PRAD cohorts based on the standard  $P < 0.05$ . 2616 differentially expressed RRGs were obtained from TCGA-PRAD and 1850 differentially expressed RRGs were obtained from GEO-PRAD. Finally, the same differentially expressed RRGs ( $n = 1410$ ) in TCGA-PRAD and GEO-PRAD cohorts were selected for subsequent analysis. Next, we used the  $k$ -means algorithm in the “Consensus-Clusterplus” R package to perform unsupervised consensus clustering for these RRGs and repeated it for 1000 times to ensure classification stability [16].

**2.3. Gene Set Variation Analysis (GSVA).** We first downloaded the “c2.cp.kegg.v7.2.symbols” gene set and “h.all.v7.4.symbols” gene set from MSigDB database. We performed GSVA analysis and differential analysis using the “GSVA” and “Limma” R packages, respectively, to explore the biological processes that significantly differed between redox patterns. In addition, we also utilized the “clusterProfiler” R package for functional annotation of these RRGs.

**2.4. Evaluation of Immune Cell Infiltration between PC Patterns.** The cell-type identification by estimating relative subsets of RNA transcripts (CIBERSORT) algorithm developed by Newman et al. [17] and its attached LM22 gene set were used to assess differences in immune cell infiltration between different PC patterns. Here, in order to make the results more reliable, 1000 permutation tests were performed, and the results were screened according to the  $P < 0.05$  criterion.

**2.5. Construction of the Redox\_Score to Evaluate Individual PC.** We developed a redox scoring scheme based on the genes most associated with prognosis to assess individual PC patients. Specifically, we performed differential expression analysis for PC patterns and screened the results based on  $|\log_2 \text{fold change (FC)}| > 1$  and adjusted  $P < 0.05$ . Next, univariate Cox regression analysis, least absolute shrinkage and selection operator (LASSO) regression analysis, and multivariate Cox regression analysis were performed to identify RRGs most associated with prognosis. Then, we used the regression coefficients obtained from the multivariate Cox analysis and calculated the redox score based on the following formula:  $\text{Redox\_score} = \sum_{i=1}^n \text{Exp}i\beta_i$ , where Exp represents the expression value of the gene and  $\beta$  represents the regression coefficient of the corresponding gene.

**2.6. miRNA-RRG Regulatory Network and PC Mutation Analysis.** miRNA expression data in PC were obtained from the TCGA database, and the differential expression miRNAs were identified between the normal group and the tumor group. We then conducted the coexpression analysis of these miRNAs and prognostic-related RRGs. miRNAs with  $|\text{Cor}| > 0.3$  and  $P < 0.001$  were considered to be correlated. Next, the “maftools” R package was used to analyze the somatic mutation data and calculate the tumor mutation burden (TMB). We further analyzed the difference of TMB expression in different risk groups and its correlation with Redox\_score. We also delineate the landscape of driving gene mutations between low- and high-risk groups.

**2.7. Benefit of Redox\_Score in Predicting Immunotherapy Reactivity.** We first compared the expression differences of different immune checkpoint inhibitor (ICI) genes between low- and high-risk groups and further investigated whether the Redox\_score still had an impact on the prognosis of patients when the expression of the ICI gene was considered. Then, based on available data for melanoma patients receiving immunotherapy, we analyzed the similarity of gene expression profiles between patients in different risk groups and melanoma patient groups by SubMap to indirectly predict the response of Redox\_score-based PC patients to immunotherapy [18]. Moreover, we obtained an open access immunotherapy cohort of patients with metastatic melanoma undergoing anti-PD-1 therapy and performed a Kaplan–Meier analysis of pretreatment patients based on the Redox\_score.

**2.8. Correlation Analysis between Redox\_Score and Drug Sensitivity.** We downloaded transcriptional data of tumor cell lines, IC50 values of antitumor drugs, and drug target-

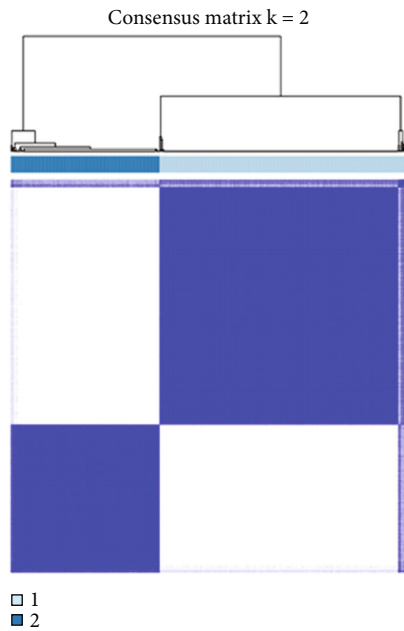
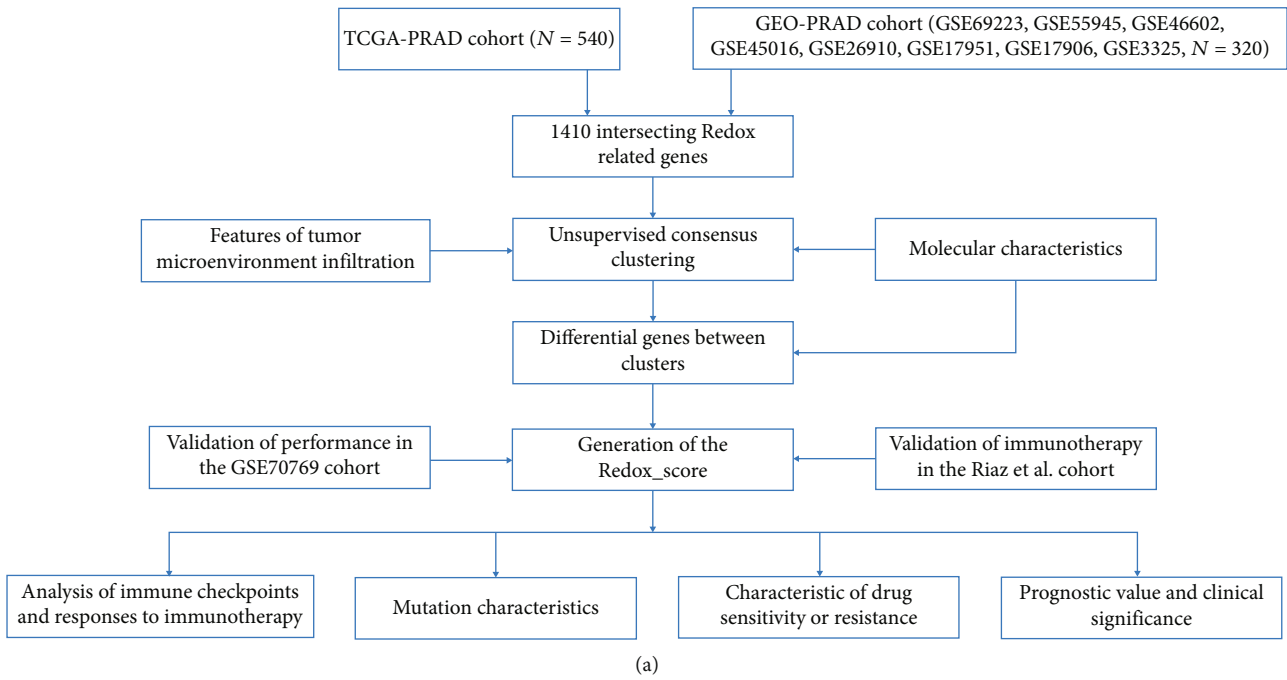
s/pathways from the Genomics of Drug Sensitivity in Cancer (GDSC, <https://www.cancerrxgene.org/>) database. Then, we did the Pearson correlation analysis between the Redox\_score and drug sensitivity and according to the  $P < 0.05$  and  $|\text{Rs}| > 0.15$  filtering results.

**2.9. Real-Time Quantitative Polymerase Chain Reaction (RT-QPCR) Verification.** We first used a TRIzol reagent (Beyotime, Jiangsu, China) to extract total RNA from various prostate cancer cells. These total RNA were then reversely transcribed into cDNA using the Hifair®III 1st Strand cDNA Synthesis SuperMix for qPCR (gDNA digester plus) (YEASEN, Shanghai, China), which was subsequently detected by qPCR using the Hieff® qPCR SYBR® Green Master Mix (Low Rox) (YEASEN, Shanghai, China) an ABI Prism 7300 system (Thermo Fisher Scientific). In this experiment, GAPDH was used as an internal reference gene, and all primer sequences are shown in Table S1.

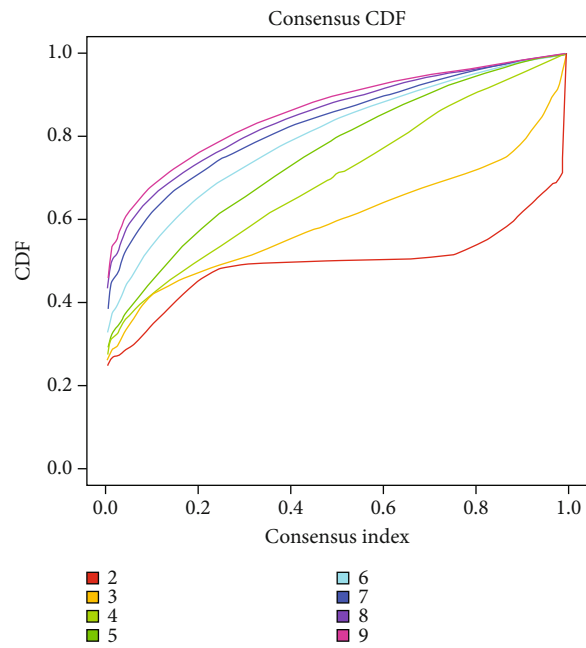
### 3. Results

**3.1. Identification of Core Differentially Expressed RRGs and Redox Patterns in PC.** Figure 1(a) shows the analysis flow chart of this study. After 4087 RRGs were obtained from the OMIM, NCBI, GeneCards, and GSEA-MSigDB databases, differential expression analysis was performed in TCGA-PRAD and GEO-PRAD cohorts. Then, we got 1410 overlapping RRGs from both cohorts. Next, we conducted unsupervised consensus clustering of PC samples in TCGA ( $n = 489$ ) and GEO ( $n = 214$ ) based on the 1410 RRGs. By calculating the cophenetic correlation coefficients of the two cohorts (delta area and CDF curve),  $k = 2$  was chosen as the optimal cluster number (Redox\_A and Redox\_B, Figures 1(b) and 1(c), Figure S1). When  $k = 2$ , the boundary between the heat maps of the consistency matrix remains clear, indicating that the sample classification was robust. 305 patients in the TCGA cohort were assigned to Redox\_A, and 184 were assigned to Redox\_B. In the GEO cohort, 103 patients were assigned to Redox\_A and 111 were assigned to Redox\_B. In order to further verify the subclass assignment, we also performed t-SNE dimension reduction, and the results showed that the t-SNE distribution was consistent with the subclass (Figure 1(d), Figure S1D). Here, we defined the biochemical relapse (BCR) in PC patients as an end point event and compared outcomes between subclasses in the TCGA cohort. Kaplan–Meier analysis revealed that Redox\_B had a significant survival advantage in BCR-free survival compared with Redox\_A ( $P = 0.009$ , Figure 1(e)). These results suggested that these RRGs presented two subclasses with different survival advantages in PC, which required further analysis.

**3.2. Molecular and Tumor Microenvironment Characteristics of Different Redox Patterns in PC.** In order to understand the biological process of redox patterns in PC, GSVA enrichment and pathway difference analyses were performed, and the results were filtered according to  $|\log_2 \text{FC}| > 0.15$  and adjusted  $P < 0.05$  (Figure 2(a)). The results showed that the Redox\_A pattern was significantly enriched in carcinogenic



(b)



(c)

FIGURE 1: Continued.

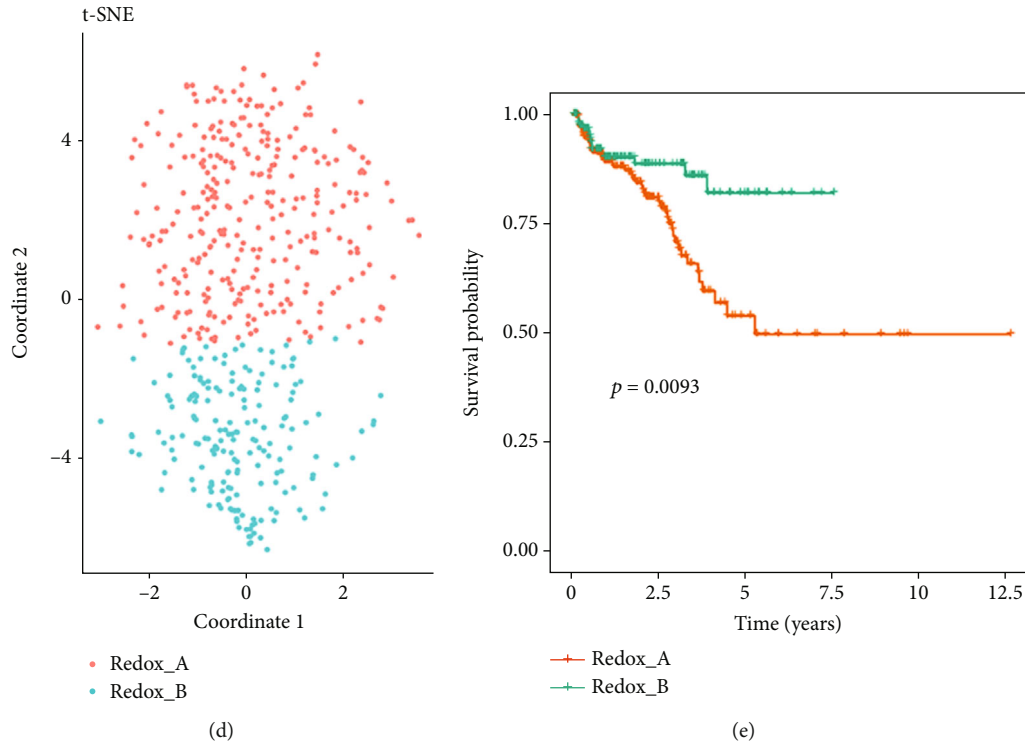


FIGURE 1: Identification of redox patterns in PC by unsupervised consensus clustering based on TCGA cohort. (a) The overall flow chart of this study. (b) Matrix heat map of  $k$ -means clustering based on 1410 differentially expressed RRGs. (c) CDF curve of  $k$ -means clustering. (d) The two-dimensional distribution of t-SNE at  $k = 2$ . (e) Kaplan-Meier survival curve of biochemical relapse (BCR) for PC patients in the TCGA cohort based on redox patterns.

activation signaling pathways, such as the JAK-STAT signaling pathway, TGF- $\beta$  signaling pathway, ECM receptor interaction, and NOD-like receptor signaling pathway, which also partly explained why Redox\_A has a shorter BCR-free survival time. The Redox\_B pattern was mainly enriched in various energy metabolism pathways, such as arginine and proline metabolism, glutathione metabolism, tyrosine metabolism, fatty acid metabolism, and oxidative phosphorylation. Then, we further applied GSEA enrichment analysis to identify the enrichment pathways in each subclass. The results showed that the Redox\_A pattern was significantly enriched in cell adhesion molecules, rap1 signaling pathway, NOD-like receptor signaling pathway, and transcriptional misregulation in cancer (Figure 2(b)), while the Redox\_B pattern was significantly enriched in the biosynthesis of amino acids, calcium signaling pathway, HIF-1 signaling pathway, MAPK signaling pathway, cGMP-PKG signaling pathway, and PPAR signaling pathway (Figure 2(c)).

Next, the differences in immune-related characteristics among the subtypes of PC revealed by the above analysis results prompted us to further explore the infiltrating characteristics of the tumor microenvironment. We first used the CIBERSORT algorithm to evaluate the abundance of infiltrated immune cells in each sample of different redox patterns in PC, and the results were shown in Figure 2(d). Specifically, the infiltration of M2 macrophages ( $P = 9.5e - 10$ ), memory B cells ( $P = 2.2e - 11$ ), CD8 T cells ( $P = 0.007$ ), M1 macrophages ( $P = 0.003$ ), naive B cells

( $P = 1.4e - 5$ ), activated dendritic cells ( $P = 0.029$ ), resting mast cells ( $P = 0.049$ ), T regulatory cells (Tregs) ( $P = 0.024$ ), and resting NK cells ( $P = 0.014$ ) was higher in Redox\_A, while the infiltration of plasma cells ( $P = 4.0e - 16$ ) was higher in Redox\_B. Moreover, we further evaluated the tumor microenvironment of each sample in different PC subclasses by the ESTIMATE algorithm to determine their stromal score, immune score, ESTIMATE score, and tumor purity. The results show that in pattern Redox\_A, immune score, stromal score, ESTIMATE score, and tumor purity were  $-274.825 \pm 188.801$  (Figure 2(e)),  $-400.188 \pm 139.841$  (Figure 2(f)),  $-675.013 \pm 290.894$  (Figure 2(g)), and  $0.874 \pm 0.021$  (Figure 2(h)), respectively, while in pattern Redox\_B, immune score, stromal score, ESTIMATE score, and tumor purity were  $-385.982 \pm 122.966$  (Figure 2(e)),  $-510.698 \pm 111.203$  (Figure 2(f)),  $-896.680 \pm 199.951$  (Figure 2(g)), and  $0.890 \pm 0.013$  (Figure 2(h)), respectively. Compared with pattern Redox\_B, the stromal cell and immune cell infiltration level in pattern Redox\_A was higher, but the tumor purity was decreased.

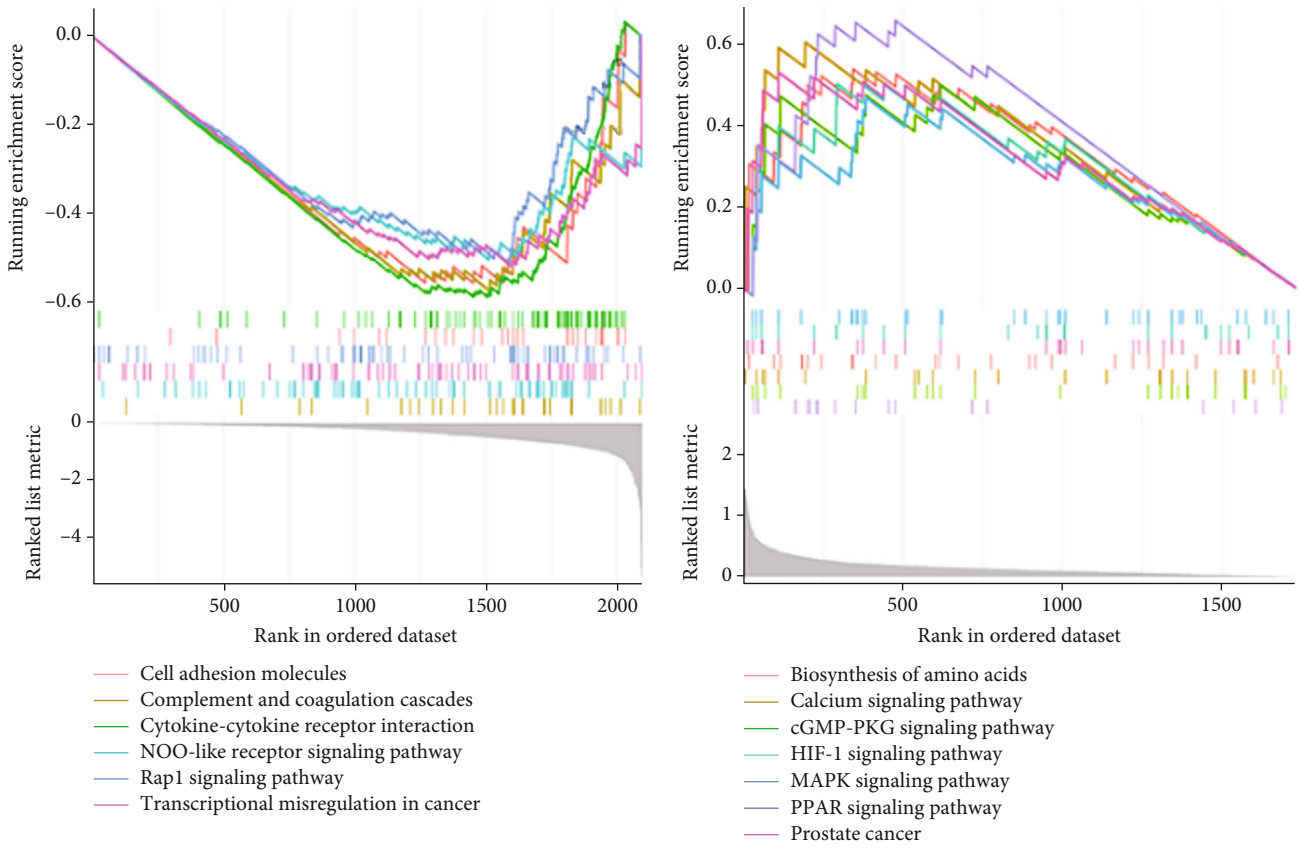
Studies have shown that the number of CD4<sup>+</sup>CD25<sup>+</sup>Foxp3<sup>+</sup> inhibitory regulatory T cells increases in peripheral blood of PC patients, and the ratio of CD4<sup>+</sup>/CD8<sup>+</sup>T cells is unbalanced, indicating that PC patients may be in a state of immunosuppression [19]. In addition, the previous analysis showed that M2 macrophages were associated with a higher Redox\_score, which also supported this conclusion. These results suggest that there may be infiltration of





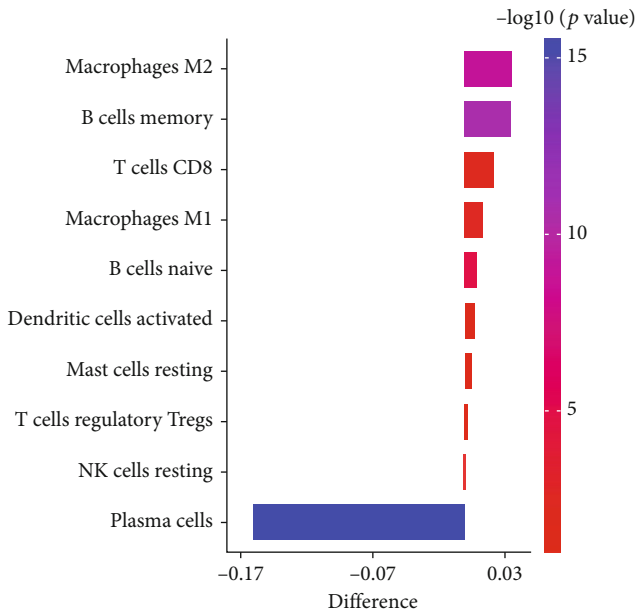
(a)

FIGURE 2: Continued.

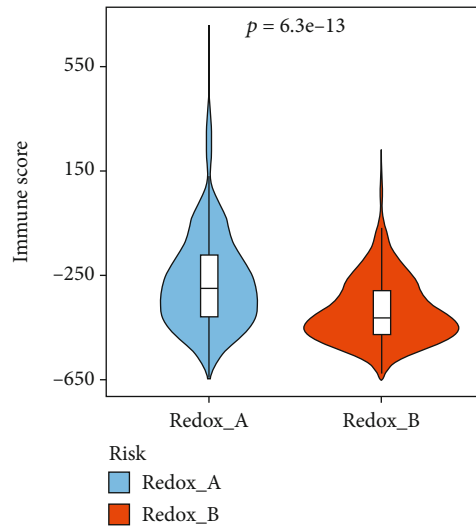


(b)

(c)



(d)



(e)

FIGURE 2: Continued.

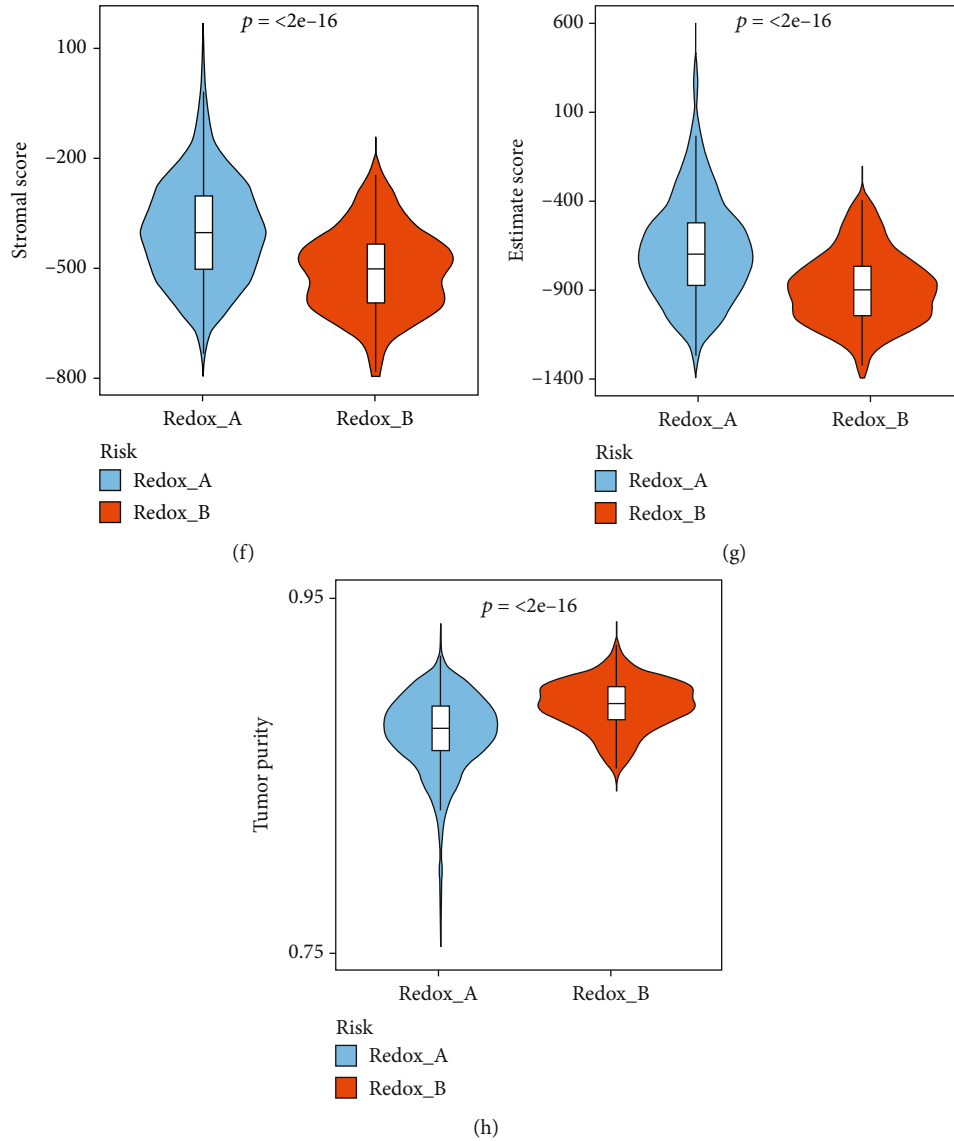


FIGURE 2: Molecular and tumor microenvironment characteristics of different PC subclasses. (a) Heat map of GSVA enrichment based on Hallmark and KEGG pathways from MSigDB in the redox patterns. (b) Heat map of GSEA enrichment of Redox\_A pattern in PC. (c) Heat map of GSEA enrichment of Redox\_B pattern in PC. (d) The distribution difference of immune infiltrating cells between redox patterns was analyzed by CIBERSORT algorithm. Differences  $> 0$  indicated that immune cells were enriched in Redox\_A pattern. The boxplot was the immune score (e), stromal score (f), ESTIMATE score (g), and tumor purity (h) of the redox patterns calculated by the ESTIMATE algorithm.

immunosuppressed myeloid cells in PC. Therefore, we further analyzed the correlation between myeloid markers (ITGAM, OLR1, CD84, CD33, CD14, and VSIR) and the Redox\_score. Figure S2A shows significant positive correlations between these myeloid marker molecules and between these molecules and the Redox\_score. At the same time, it was found that the expression levels of these myeloid marker molecules in the high-risk group were significantly higher than those in the low-risk group (Figure S2B, C, D, E, F, G). Further Kaplan–Meier survival analysis showed that patients in the high-risk group had a poor prognosis in both the high and low expression groups of these molecules (Figure S2H, I, J, K, L, M).

**3.3. Exploration Differential RRGs Associated with Redox Phenotype and Construction of a Redox\_Score.** Although the RRG-based unsupervised consensus clustering classified PC patients into two redox phenotypes, the potential genetic changes and expression disturbances in these phenotypes were not clear. Based on these doubts, we further explored possible changes in redox-related transcriptional expression in these two PC patterns. Differential expression analysis of the two redox patterns was performed through the “Limma” R package according to the screening criteria of  $|\log_2 FC| > 1$  and  $P < 0.05$ ; a total of 157 differentially expressed RRGs were obtained. Based on these RRGs, we conducted unsupervised consensus clustering analysis and finally selected  $k$

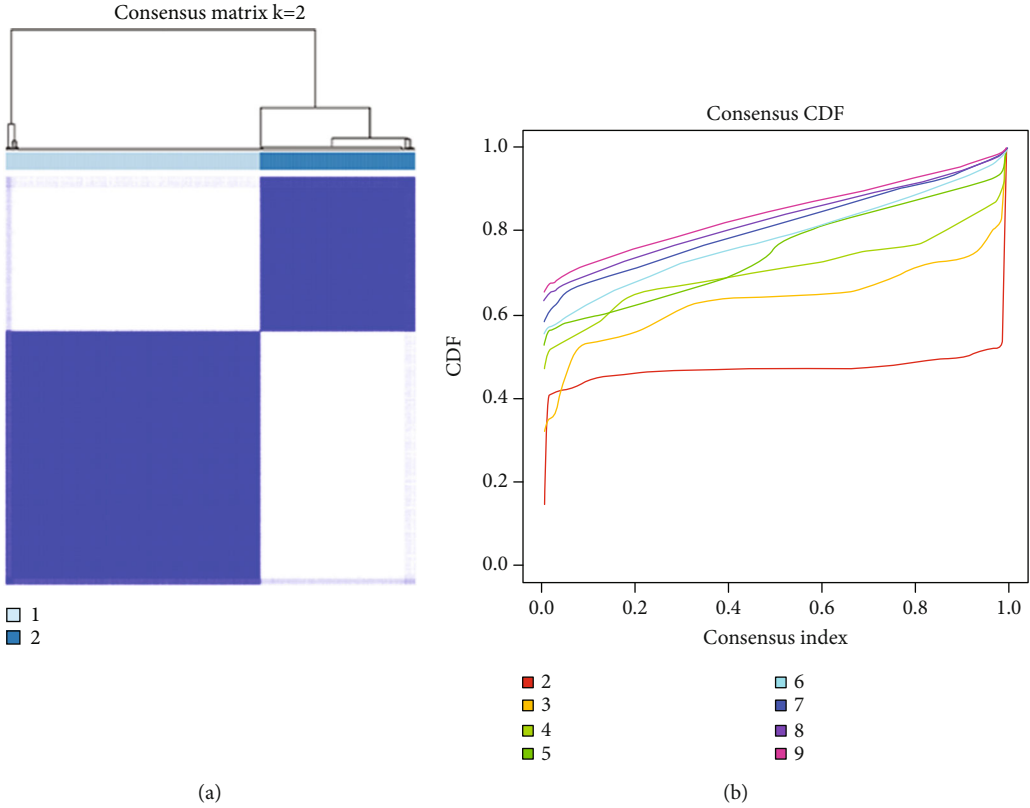


FIGURE 3: Continued.

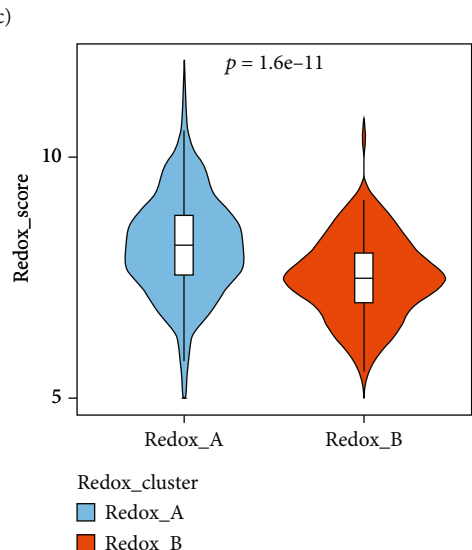
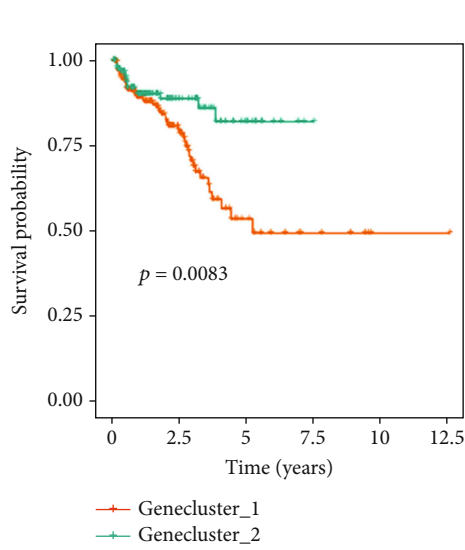
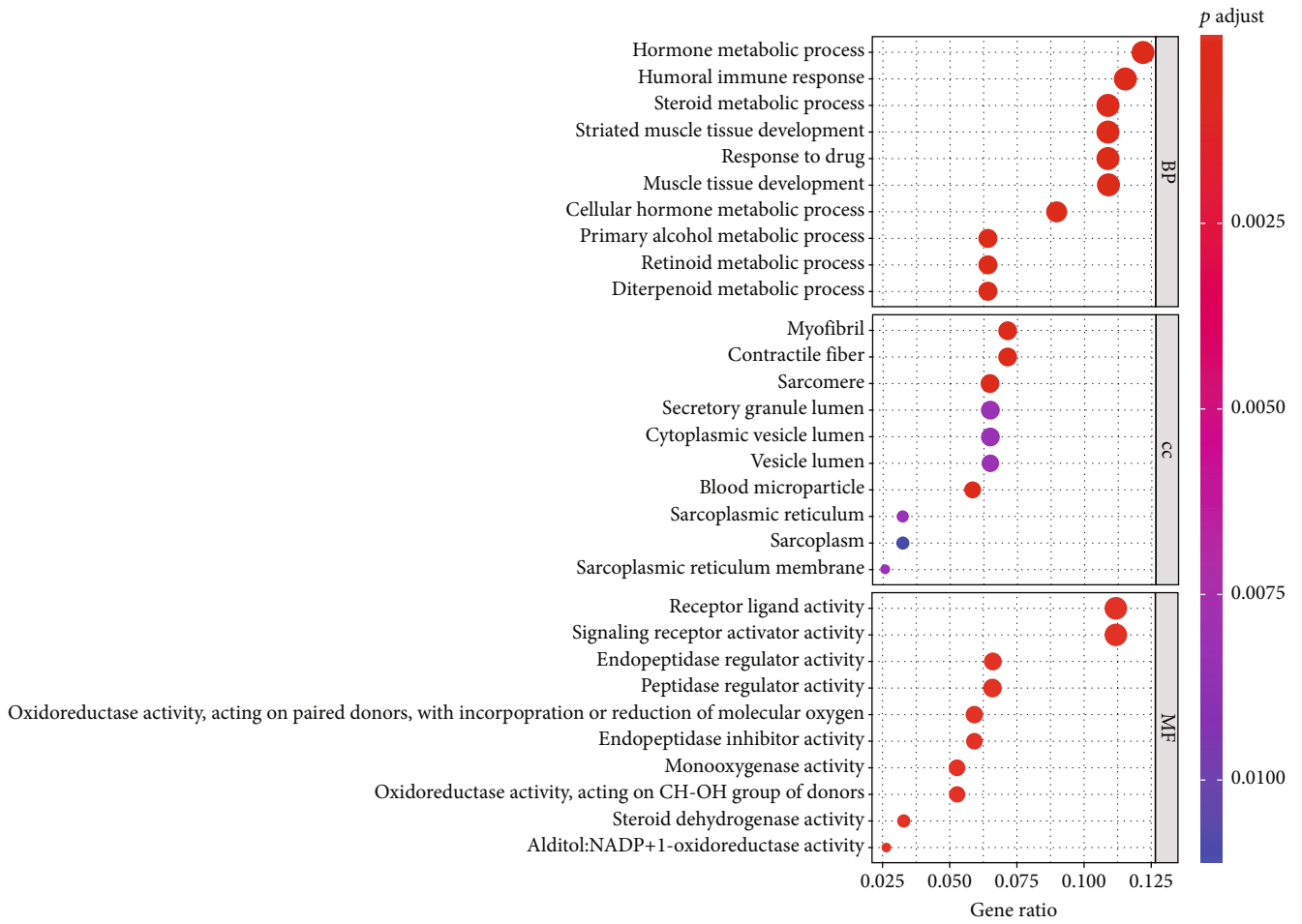


FIGURE 3: Continued.

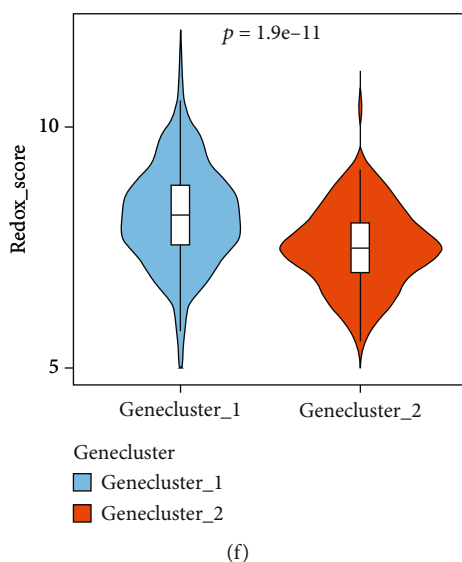


FIGURE 3: Identification of redox gene characteristic patterns in PC by unsupervised consensus clustering based on TCGA cohort. (a) Matrix heat map of  $k$ -means clustering based on 157 differentially expressed RRGs. (b) CDF curve of  $k$ -means clustering. (c) GO enrichment analysis of differentially expressed RRGs. (d) Kaplan-Meier survival curve of BCR for PC patients in the TCGA cohort based on gene characteristic patterns. The difference of Redox\_score between redox patterns (e) and gene characteristic patterns (f) in TCGA cohort.

= 2 as the optimal cluster number after comprehensive consideration and divided PC patients into two different redox gene characteristic subgroups (Genecluster\_1 and Genecluster\_2) (Figures 3(a) and 3(b)). Gene ontology analysis revealed that these RRGs were also mainly enriched in various metabolic and carcinogenic biological processes, indicating that these RRGs could be used as characteristics of redox-related genes (Figure 3(c)). We further conducted Kaplan-Meier survival analysis, and the results showed that the prognosis of PC patients in the two gene patterns was significantly different; specifically, Genecluster\_2 had a significant survival advantage in BCR-free survival ( $P = 0.008$ , Figure 3(d)).

Considering the heterogeneity and complexity of redox function in the tumor, we further screened the most prognostic redox characteristic RRGs to construct a score model to quantify the PC patients. We first performed univariate Cox regression analysis of these 157 RRGs and screened 46 prognostic RRGs. LASSO regression analysis was performed for these RRGs based on the “glmnet” R package, and the 11 most prognostic RRGs were identified. The trajectory changes of the 46 independent variable coefficients and the results of cross-validation are shown in Figure S3A, B. Subsequently, multiple stepwise Cox regression analysis was performed for these 11 RRGs and the optimal combinations were selected according to AIC (Figure S3C). Finally, 6 RRGs were obtained and a redox score (Redox\_score) was constructed based on the following formula:  $\text{Redox\_score} = (0.1713 \times \text{ExpAKR1C3}) + (0.3673 \times \text{ExpCOL1A1}) + (0.1393 \times \text{ExpCYP3A4}) + (0.2434 \times \text{ExpMYBL2}) + (0.0958 \times \text{ExpRALYL}) + (-0.3018 \times \text{ExpSCN4A})$ . We found that Redox\_A had a higher Redox\_score than Redox\_B ( $P = 1.6e - 11$ , Figure 3(e)). Similarly, Genecluster\_1 had a higher Redox\_score than Genecluster\_2 ( $P = 1.9e - 11$ , Figure 3(f)).

**3.4. Evaluation of Redox\_Score Performance.** We grouped PC patients in the TCGA cohort (low-risk group and high-risk group) according to the calculated median Redox\_score. Survival analysis revealed that the low-risk group had a significant survival advantage in BCR-free survival ( $P = 4.702e - 07$ , Figure 4(a)). The predicted area under the receiver operating characteristic (ROC) curve of Redox\_score was 0.786, 0.757, and 0.718 at 1, 3, and 5 years, respectively (Figure 4(e)). The results of the Kaplan-Meier survival analysis and ROC analysis based on the GSE46602 cohort were consistent with the above (Figures 4(b) and 4(f)). To investigate whether Redox\_score could independently predict patient outcomes, we included common clinical characteristics (including age, stage, Gleason score, and Redox\_score) for multivariate Cox analysis. The results showed that the Redox\_score was an independent and reliable prognostic factor for the prognosis of PC patients (HR = 0.380, 95% CI 0.210–0.700,  $P = 0.002$ , Figure 4(c)). We further used the GSE46602 cohort to verify the reliability of the Redox\_score (HR = 0.180, 95% CI 0.044–0.730,  $P = 0.016$ , Figure 4(d)). Additionally, we also used the GSE70769 cohort to verify the predictive performance of the Redox\_score, which was consistent with the above findings (Figures 4(g) and 4(h)). These results showed that the Redox\_score had great predictive potential.

**3.5. Exploration of the Redox\_Score's Clinical Relevance and miRNA-RRG Regulatory Networks.** Next, we first evaluated the relationship between Redox\_score and BCR. As shown in Figure 5(a), patients in the high-risk group had a higher rate of BCR than patients in the low-risk group (25.73% vs. 6.80%,  $P < 0.001$ ). Similarly, the higher the BCR rate, the higher the Redox\_score ( $P = 1.9e - 11$ , Figure 5(b)). Then, we stratified PC patients in the TCGA cohort with the Gleason score and T stage, and the results showed that low-risk

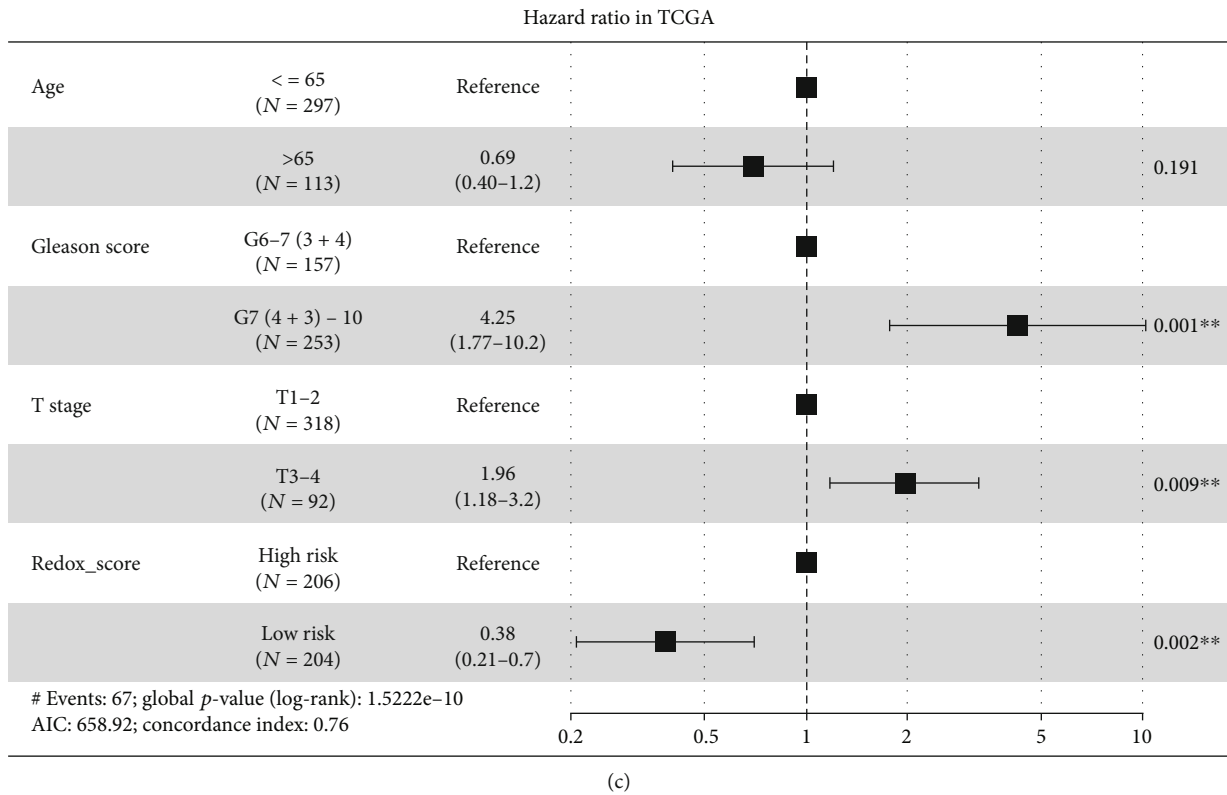
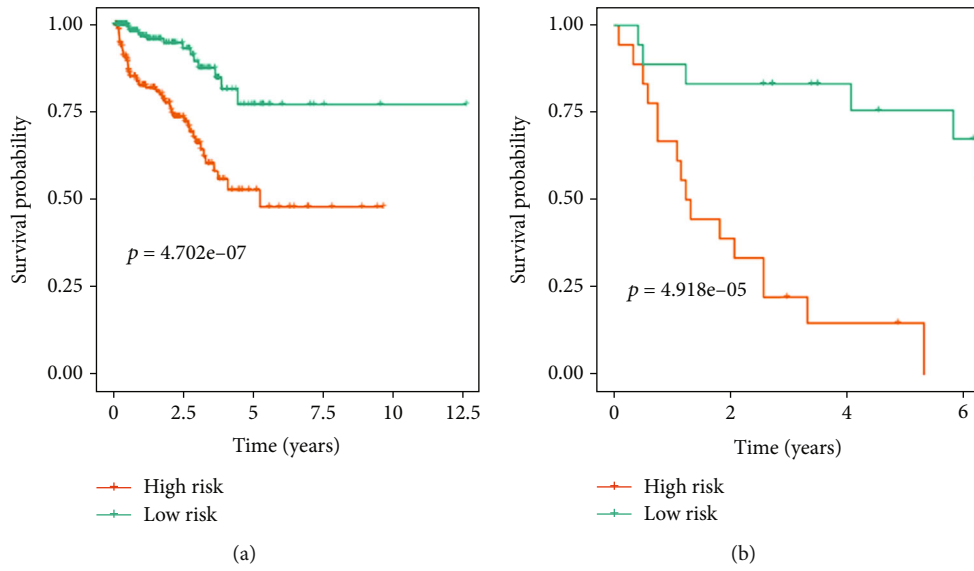
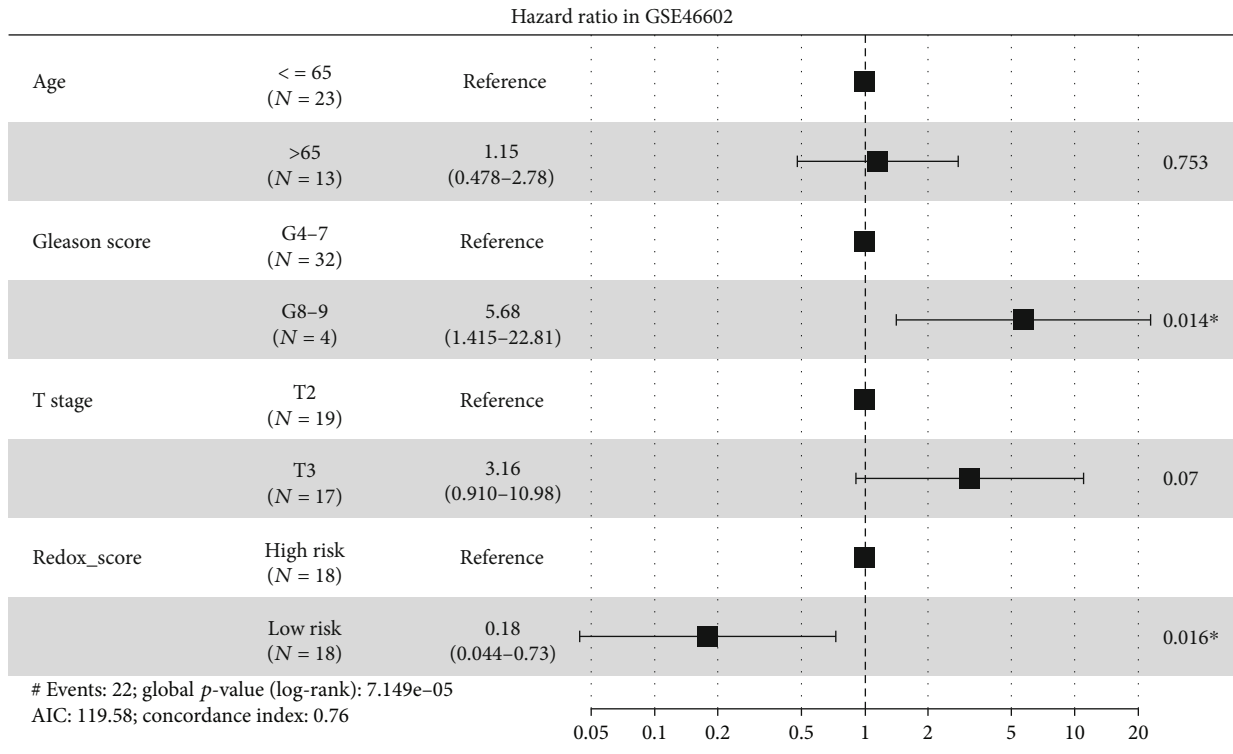
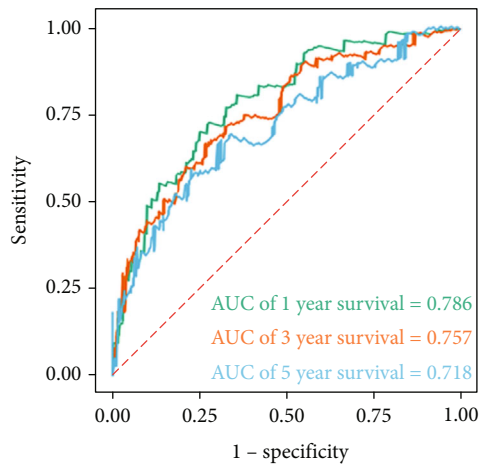


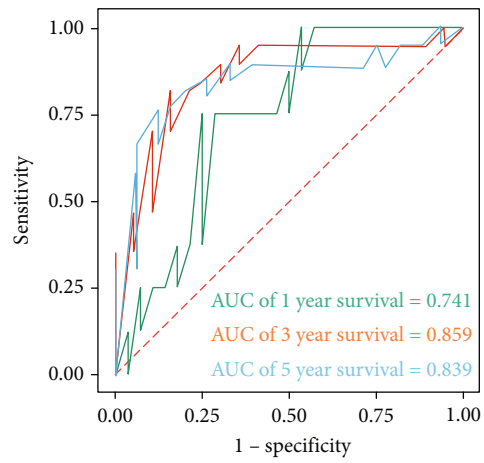
FIGURE 4: Continued.



(d)



(e)



(f)

FIGURE 4: Continued.



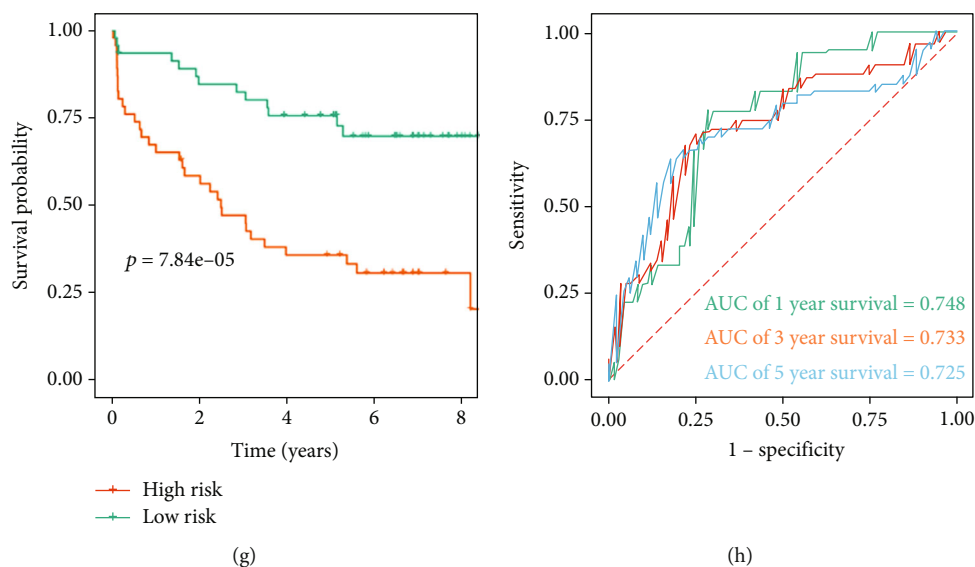


FIGURE 4: Evaluation of Redox\_score performance. (a) Kaplan-Meier survival curve of BCR between low- and high-risk groups in the TCGA cohort. (b) Kaplan-Meier survival curve of BCR between low- and high-risk groups in the GSE46602 cohort. (c) Multivariate Cox regression analysis of age, Gleason score, stage, and Redox\_score were included in the TCGA cohort. (d) Multivariate Cox regression analysis of age, Gleason score, stage, and Redox\_score were included in the GSE46602 cohort. (e) Redox\_score predicted AUC values at different time points in the TCGA cohort. (f) Redox\_score predicted AUC values at different time points in the GSE46602 cohort. (g) Kaplan-Meier survival curve of BCR between low- and high-risk groups in the GSE70769 cohort. (h) Redox\_score predicted AUC values at different time points in the GSE70769 cohort.

patients in each stratification had a higher survival advantage (Figures 5(c)–5(e)).

miRNAs are a class of important regulatory factors that significantly affect the genesis and progression of tumors by regulating the entire cell signaling network [20, 21]. Meanwhile, mRNAs also have a great importance in maintaining ROS homeostasis, and many studies focused on the regulatory interaction between miRNA and ROS [22]. For example, miR-21 can mediate ROS production by enhancing KRAS and epidermal growth factor receptor signaling, thereby promoting tumor development [23, 24]. Therefore, this study deserved further attention on the relationship between miRNAs and prognostic RRGs and to reveal the regulatory network of miRNAs-RRGs. We obtained miRNA expression data from the TCGA cohort, including 52 normal samples and 499 PC samples. A total of 76 downregulated miRNAs and 118 upregulated miRNAs were obtained after differential analysis. Figure 5(f) showed the heat map of differentially expressed miRNAs. Subsequently, we conducted the coexpression analysis of these 6 prognostic RRGs (the most prognostic redox characteristic RRGs) and these differential miRNAs and finally obtained 14 pairs of miRNA-RRG regulatory networks (Figure 5(g)). Here, all miRNAs were positively regulated corresponding RRGs. The specific regulatory relationship between these miRNAs and prognostic RRGs is shown in Table S2. Moreover, we further analyzed that the miRNAs related to the Redox\_score correlated with Redox\_A and Redox\_B by coexpression analysis according to suggestion. According to the criteria of  $\text{cor} > 0.3$  and  $P < 0.001$ , we found 11 miRNAs related to the Redox\_score correlated with Redox\_A. And according to the criteria of  $\text{cor} > 0.25$  and  $P < 0.001$ , we found 15

miRNAs related to the Redox\_score correlated with Redox\_B (Table S3).

**3.6. Correlation of the Redox\_Score with Mutations.** Tumor genomic patterns have been shown to be associated with antitumor immunity. The accumulation of somatic mutations is one of the main causes of tumorigenesis [25]. TMB is also considered a biomarker for predicting tumor behavior and immune response [26]. Higher TMB has been reported to be associated with better prognosis in patients with melanoma and non-small cell lung cancer [27]. In order to investigate whether there were differences in somatic mutations in Redox\_score and to observe the mutation patterns between Redox\_score, we analyzed the data of somatic mutations in the TCGA cohort. The results showed that TMB levels were higher in the high-risk group ( $P = 2.1e - 08$ , Figure 6(a)), and there was a significant positive correlation between the Redox\_score and TMB ( $R = 0.31$ ,  $P = 8.6e - 11$ , Figure 6(b)), indicating that TMB increased with the increase of the Redox\_score. We further investigated whether TMB was associated with survival advantage, and the analysis indicated that low TMB had a significant survival advantage in BCR-free survival ( $P = 0.005$ , Figure 6(c)). On this basis, we investigated whether the Redox\_score still had an impact on the prognosis of patients when the level of TMB was considered. The results showed that high TMB and low-risk patients had a significant survival advantage in BCR-free survival compared with the high TMB and high-risk patients, and the low TMB and low-risk patients had also a significant survival advantage in BCR-free survival compared with the low TMB and high-risk patients ( $P < 0.001$ , Figure 6(d)). Next,

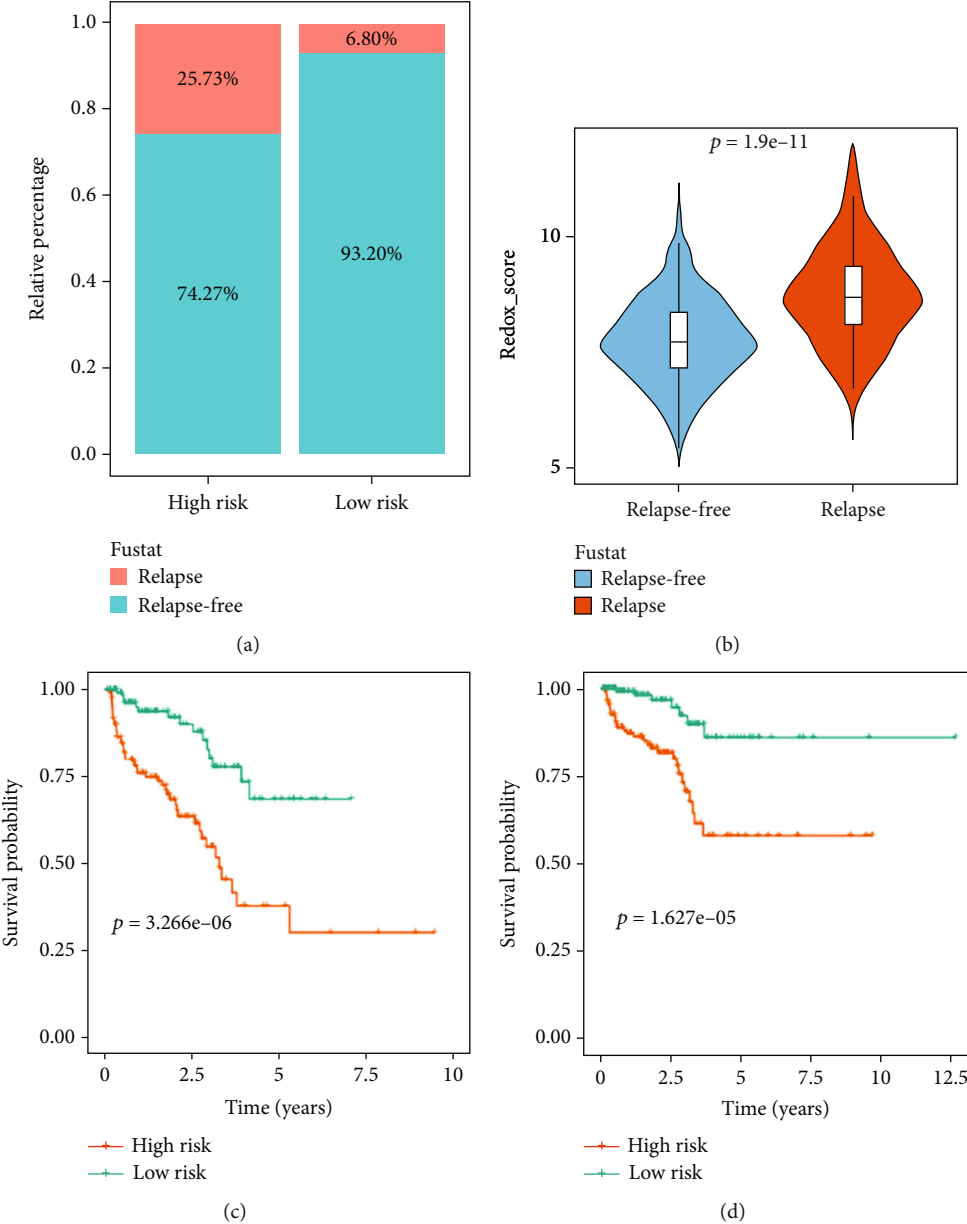


FIGURE 5: Continued.

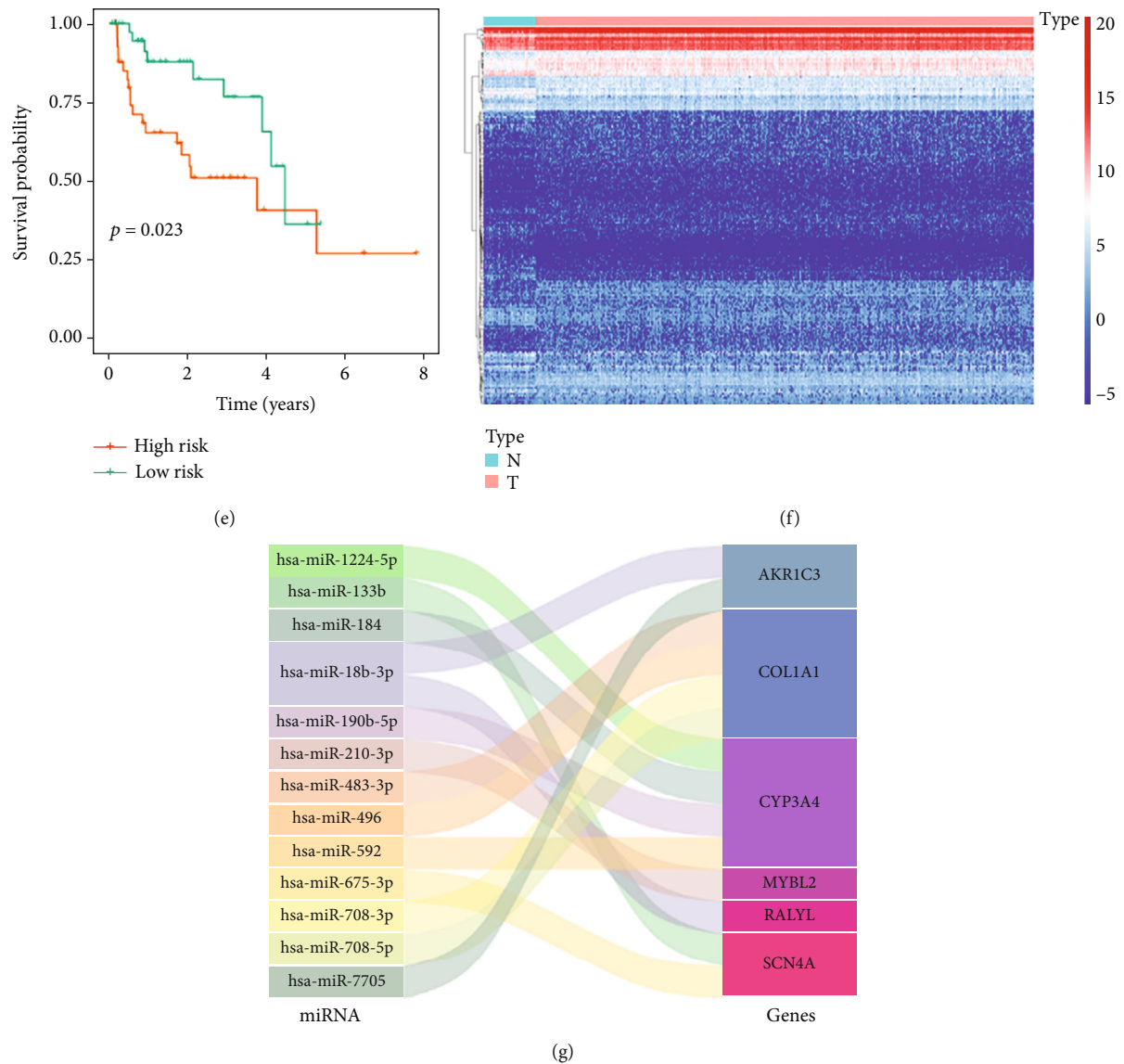


FIGURE 5: Exploration of the Redox\_score's clinical relevance and miRNA-RRG regulatory networks. (a) Differences in BCR between low- and high-risk groups in PC patients. (b) Differences in Redox\_score between patients with and without BCR. (c) Kaplan-Meier survival curve of BCR between low- and high-risk group G7(4+3)-10 patients in the TCGA cohort. (d) Kaplan-Meier survival curve of BCR between low- and high-risk group T stage 1-2 patients in the TCGA cohort. (e) Kaplan-Meier survival curve of BCR between low- and high-risk group T stage 3-4 patients in the TCGA cohort. (f) Expression heat map of differentially expressed miRNAs. N represents the normal group, and T represents the tumor group. (g) Sankey plot of differentially expressed miRNAs and prognostic RRG regulatory networks.

we showed the driver genes that were mutated in at least 3% of the samples in the low- and high-risk patients. The results indicated that there were more mutated driver genes in the high-risk patients (Figures 6(e) and 6(f)). We selected three driver genes (TP53, TTN, and SPOP) with high mutation rates and explored whether the Redox\_score still had an impact on the prognosis of patients when the expression of driver genes was considered. The results indicated that the TP53 mutation and low-risk patients had a significant survival advantage in BCR-free survival compared with the TP53 mutation and high-risk patients, and the TP53 wild and low-risk patients had also a significant survival advantage in BCR-free survival compared with the TP53

wild and high-risk patients ( $P < 0.001$ , Figure 6(g)). Consistent results were observed in other driver genes (Figures 6(h) and 6(i)). Considering that PTEN and AR mutations have important clinical significance for PC patients, we further analyzed whether Redox\_score still has an impact on the prognosis of patients when considering PTEN and AR mutations. We analyzed PTEN in the TCGA-PRAD dataset and AR in the metastatic PC dataset (Abida et al. PNAS 2019, cBioPortal, <https://www.cbioportal.org/>). The results of Kaplan-Meier analysis showed that the prognosis of high-risk patients was poor in both the AR (or PTEN) mutation group and the AR (or PTEN) wild group (Figure S4).

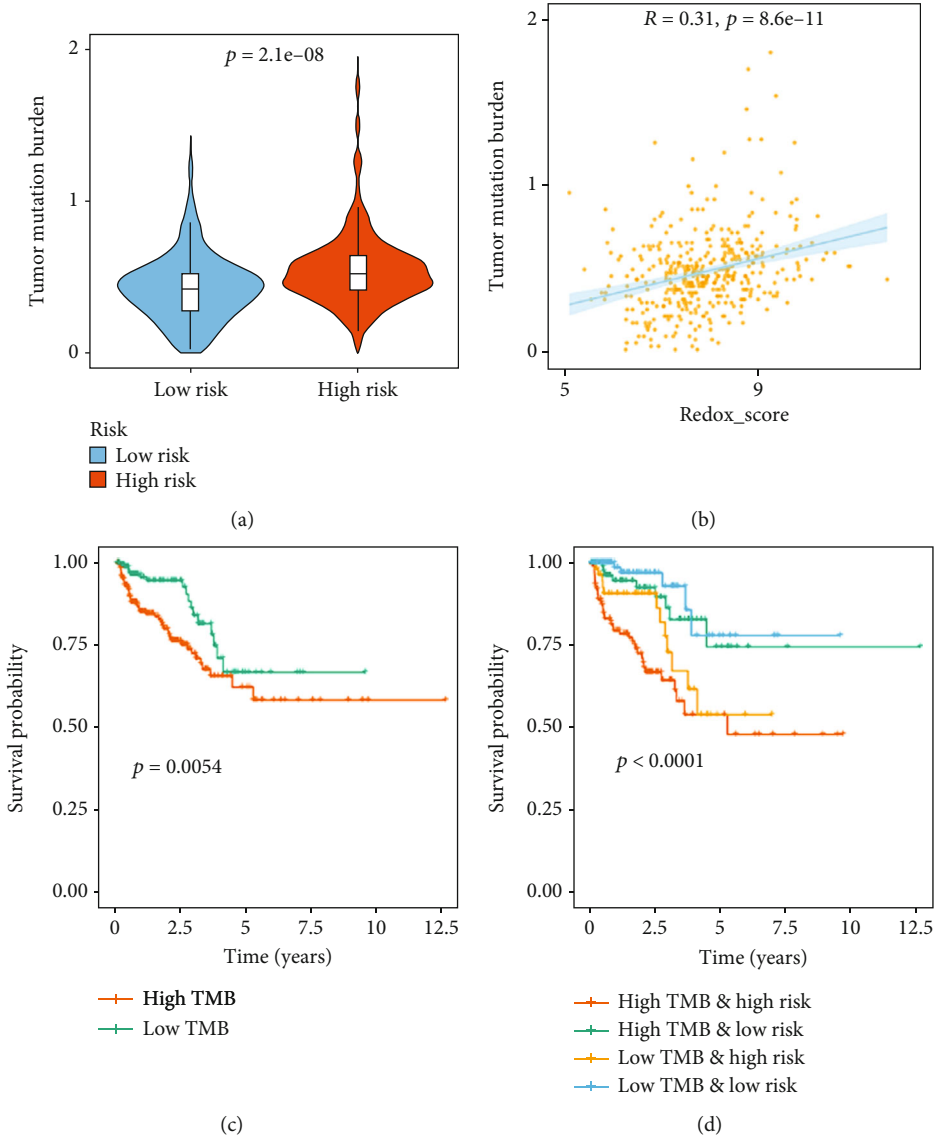
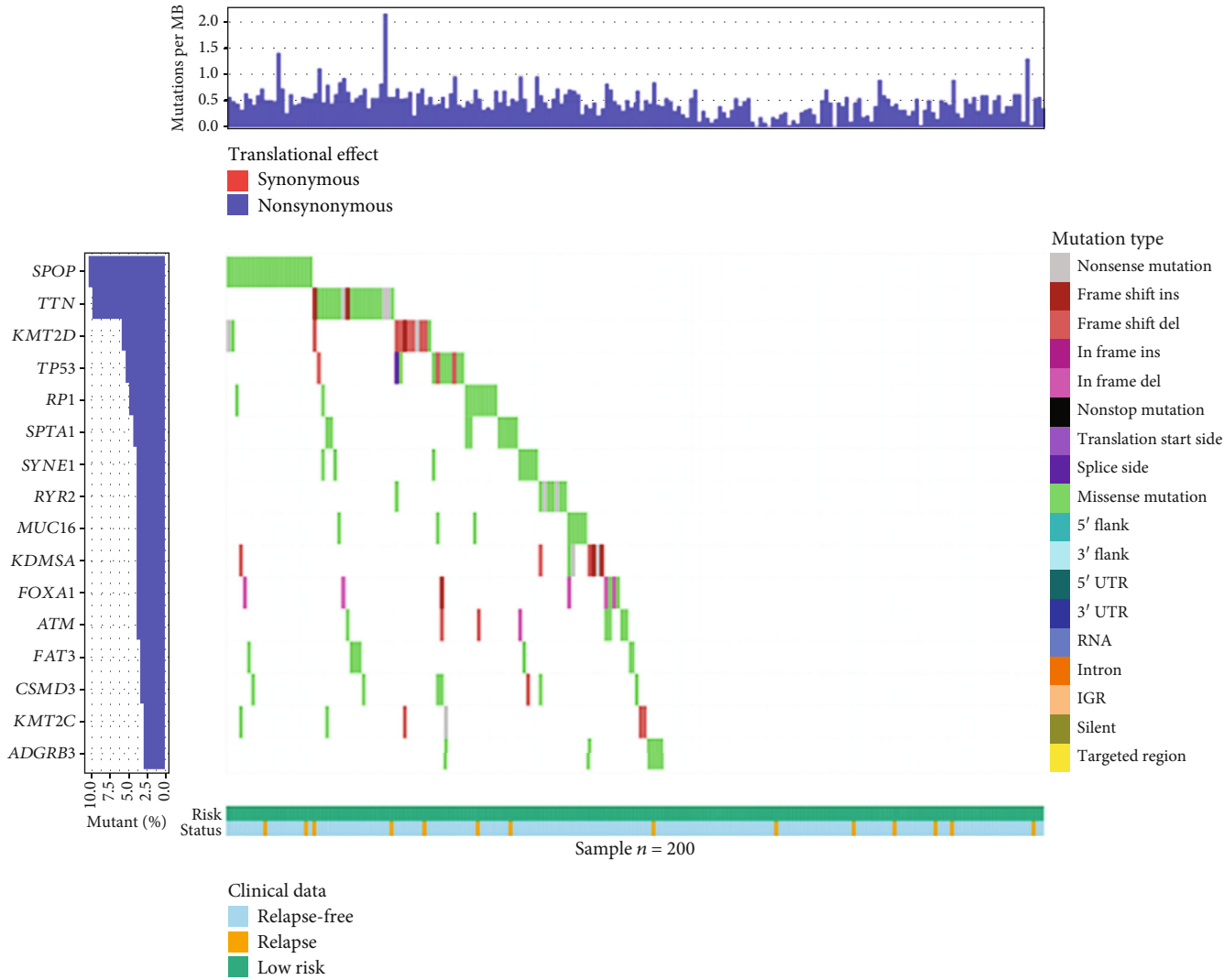
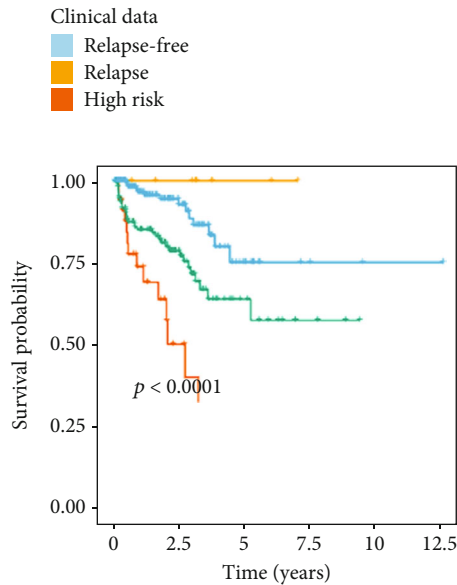
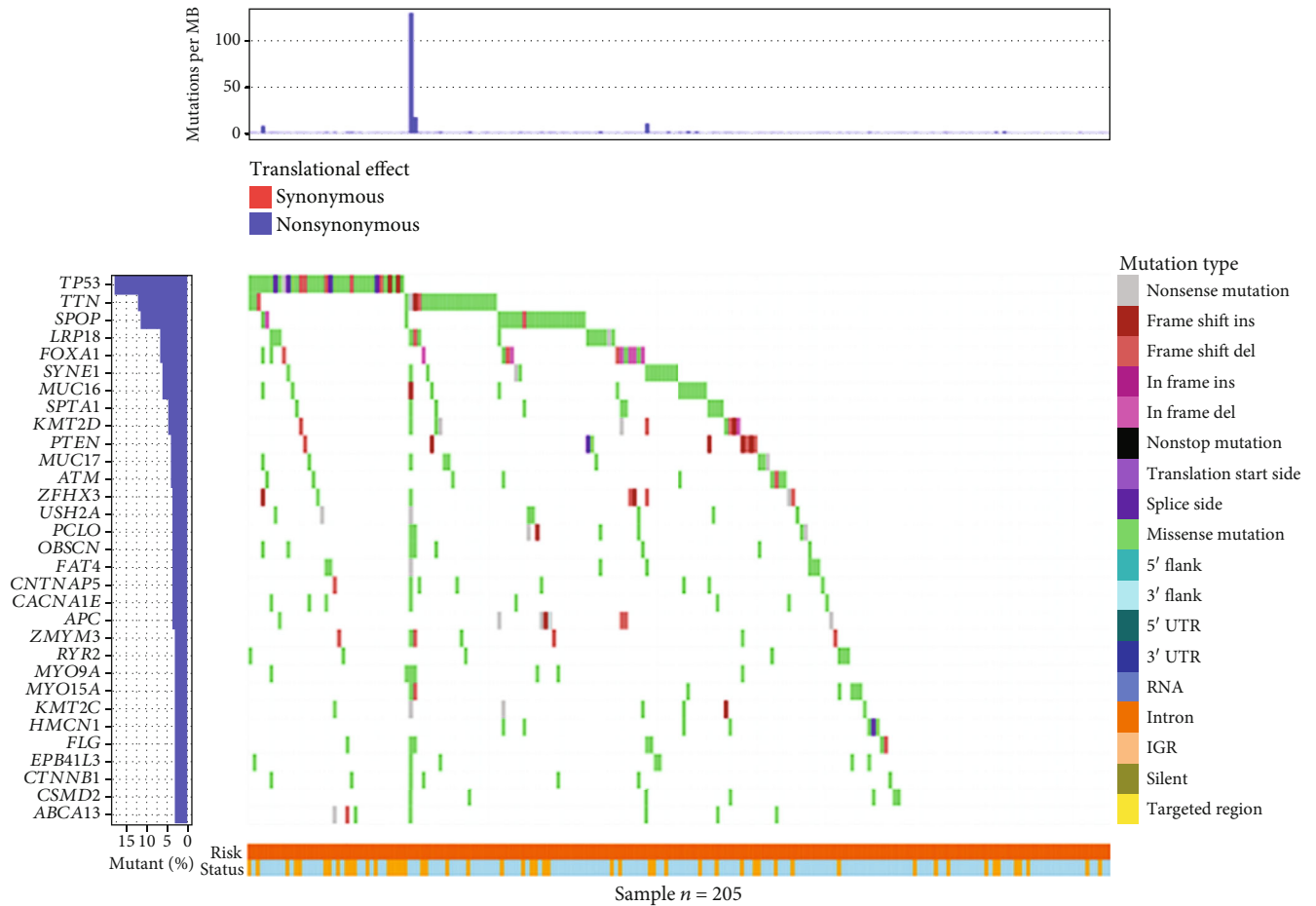


FIGURE 6: Continued.



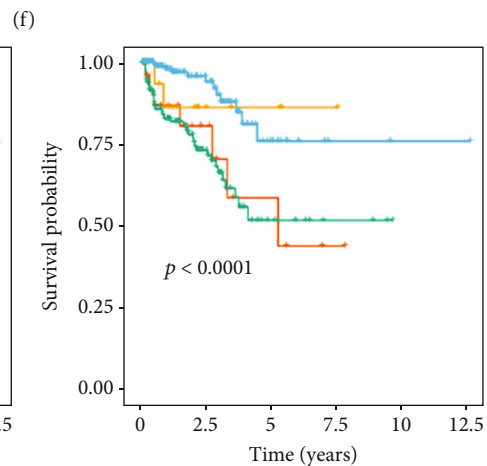
(e)

FIGURE 6: Continued.



- TP53 mutation & high risk
- TP53 wild & high risk
- TP53 mutation & low risk
- TP53 wild & low risk

(g)



- TTN mutation & high risk
- TTN wild & high risk
- TTN mutation & low risk
- TTN wild & low risk

(h)

FIGURE 6: Continued.

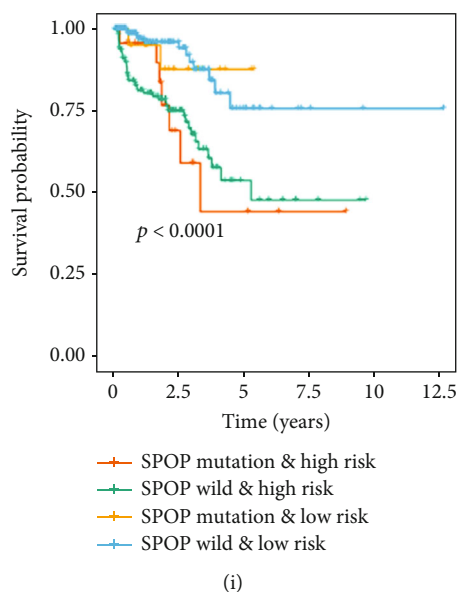


FIGURE 6: Correlation of the Redox\_score with mutations. (a) Differences in TMB between low- and high-risk groups in PC patients. (b) Correlation analysis between Redox\_score and TMB. (c) Kaplan-Meier survival curve of BCR between low- and high-TMB groups in the TCGA cohort. (d) Kaplan-Meier survival curve of BCR among four groups stratified by the Redox\_score and TMB. (e) Mutation waterfall plot of patients in the low-risk group. (f) Mutation waterfall plot of patients in the high-risk group. Kaplan-Meier survival curve of BCR among four groups stratified by the Redox\_score and TP53 (g), TTN (h), and SPOP (i).

**3.7. Benefit of Redox\_Score in Predicting Immunotherapy Reactivity.** Immunotherapy targeting ICI genes has been a major breakthrough in antitumor therapy in recent years [28]. In order to further study the complex interaction between ICI genes and Redox\_score, we first explored the expression of these genes (PD-1, PD-L2, CTLA-4, B7-H3, and B7-H4) in different patient groups of patients under stratification of the Redox\_score. The results indicated that compared with the low-risk patients, the expression levels of PD-1 ( $P = 0.014$ , Figure 7(a)), PD-L2 ( $P = 0.018$ , Figure 7(b)), CTLA-4 ( $P = 5e - 05$ , Figure 7(c)), B7-H3 ( $P = 1.9e - 05$ , Figure 7(d)), and B7-H4 ( $P = 0.001$ , Figure 7(e)) in the high-risk patients were significantly upregulated, which was similar to the result of Sun et al.'s [29] study that the expression level of the ICI gene was negatively correlated with the prognosis of patients. We also investigated whether the Redox\_score still had an impact on the prognosis of patients when the expression level of the ICI gene was considered. The results showed that the low-risk and high PD-1 expression patients had a significant survival advantage in BCR-free survival compared with the high-risk and high PD-1 expression patients, and the low-risk and low PD-1 expression patients had also a significant survival advantage in BCR-free survival compared with the high-risk and low PD-1 expression patients ( $P < 0.001$ , Figure 7(f)). Interestingly, when we stratified the Redox\_score based on the level of expression of the ICI gene, the results showed that the low-risk (or high-risk) and low PD-1 expression patients had no significant survival advantage in BCR-free survival compared with the low-risk (or high-risk) and high PD-1 expression patients. Similar results were found for other genes (Figures 7(g)–7(j)). These results suggested that the Redox\_score may be a potential marker

for predicting response to immunotherapy in patients with PC. By SubMap analysis, we further compared the expression data of Redox\_scores from the TCGA and GEO cohorts, with another available dataset of 47 melanoma patients receiving PD-1 or CTLA-4 immunotherapy. Both cohorts showed a significant correlation between the high-risk patients and the PD-1 response ( $P = 0.004$  and  $P = 0.037$ , Figures 7(k) and 7(l)), suggesting that patients with a higher Redox\_score were more responsive to PD-1 immunotherapy. Based on these results, we obtained an immunotherapy cohort of patients undergoing anti-PD-1 therapy for metastatic melanoma to further assess whether the Redox\_score could predict patient response to ICI. The results indicated that the low-risk patients had also a significant survival advantage in BCR-free survival ( $P = 0.012$ , Figure 7(m)). These results indicated that the Redox\_score was associated with response to immunotherapy and could further predict PC patient outcomes.

**3.8. Correlation Analysis between Redox\_Score and Drug Sensitivity.** To explore the effect of the Redox\_score on drug sensitivity of tumor cells, we further evaluated the correlation between the Redox\_score and the drug response in the GDSC database. We performed the Pearson correlation analysis between the Redox\_score and the drug response of cancer cell lines, and based on  $|R_s| > 0.15$  and  $P < 0.05$  screening criteria, 48 significant correlation pairs were identified (Figure 8(a)). Of these, 28 correlation pairs showed drug sensitivity associated with the Redox\_score. For example, A-443654 ( $R_s = -0.41$ ,  $P = 6.42e - 18$ ), FTI-277 ( $R_s = -0.41$ ,  $P = 8.03e - 18$ ), CGP-082996 ( $R_s = -0.38$ ,  $P = 1.79e - 15$ ), and GW843682X ( $R_s = -0.37$ ,  $P = 7.76e - 15$ ), and 20 correlation pairs showed drug resistance associated

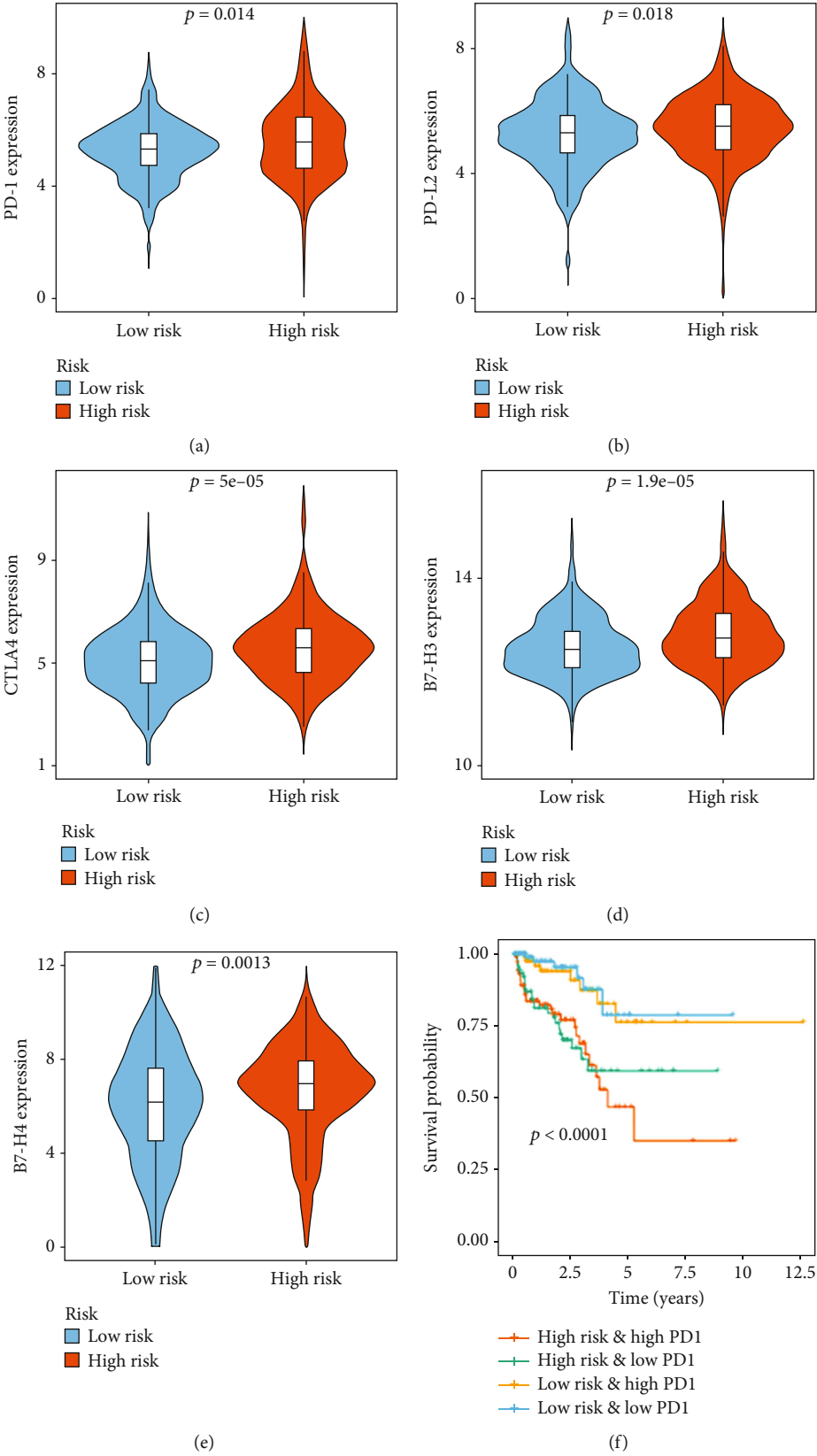


FIGURE 7: Continued.



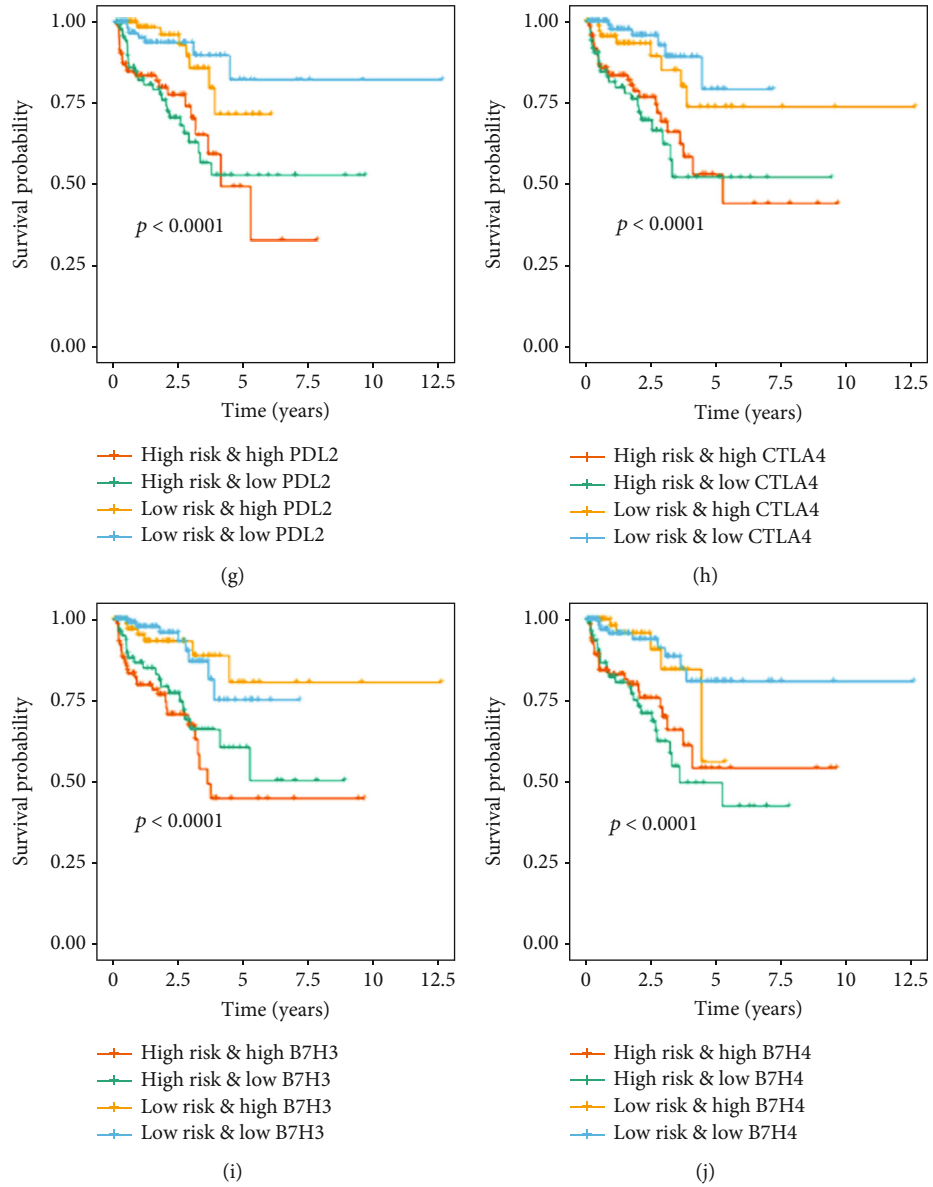


FIGURE 7: Continued.

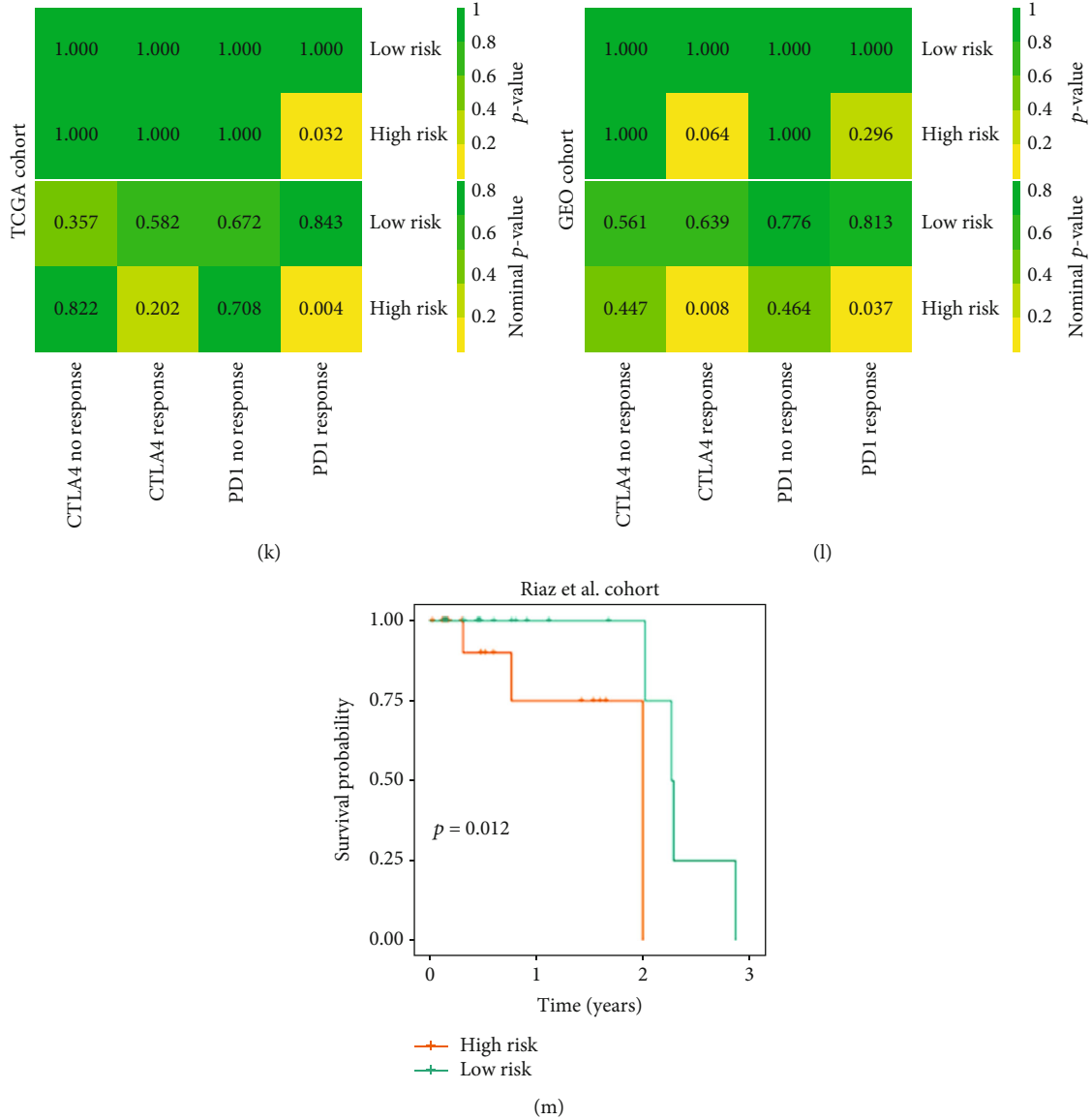


FIGURE 7: Benefit of Redox\_score in predicting immunotherapy reactivity. Differences in expression of PD-1 (a), PD-L2 (b), CTLA4 (c), B7-H3 (d), and B7-H4 (e) between low- and high-risk groups. Kaplan-Meier survival curve of BCR among four groups stratified by the Redox\_score and PD-1 (f), PD-L2 (g), CTLA4 (h), B7-H3 (i), and B7-H4 (j). (k) Similarity of gene expression profiles between redox patterns and ICI-treated melanoma patients in the TCGA cohort. (l) Similarity of gene expression profiles between redox patterns and ICI-treated melanoma patients in the GEO cohort. (m) Kaplan-Meier survival curve of BCR between low- and high-risk groups in the Riaz et al. cohort.

with the Redox\_score. For example, AG-014699 ( $R_s = 0.48$ ,  $P = 2.76e - 25$ ), JNJ-26854165 ( $R_s = 0.48$ ,  $P = 2.72e - 25$ ), CCT018159 ( $R_s = 0.43$ ,  $P = 2.60e - 20$ ), and EHT-1864 ( $R_s = 0.38$ ,  $P = 1.97e - 15$ ). We further analyzed the related signaling pathways of the drug-targeted genes mentioned above. The results indicated that the Redox\_score was related to drug sensitivity to targeted apoptosis regulation, cell cycle, DNA replication, and ERK MAPK signaling pathways, while the Redox\_score was related to drug resistance to targeted hormone-related, p53, and PI3K/MTOR signaling pathways (Figure 8(b)), indicating that higher Redox\_score patients may be more effective for drugs targeting apoptosis or the cycle pathway, while lower Redox\_score patients may be more effective for drugs targeting

hormone-related or p53 pathway. These results indicated that the Redox\_score was related to the sensitivity of tumor cells to drugs and could be used as a potential biomarker.

**3.9. RT-qPCR Verification.** To further evaluate the reliability of the Redox\_score, we detected the actual expression levels of these six redox characteristic genes in normal prostate epithelial cells (RWPE-1), hormone-dependent PC cells (LNCaP), and hormone-resistant PC cells (22RV1, DU-145, and PC-3) by RT-qPCR. The analysis results of the experiment are shown in Figure 9. AKR1C3 expression was significantly downregulated in LNCaP, DU-145, and PC-3 cells, while significantly upregulated in 22RV1 cells compared with RWPE-1 cells. Compared with RWPE-1 cells,

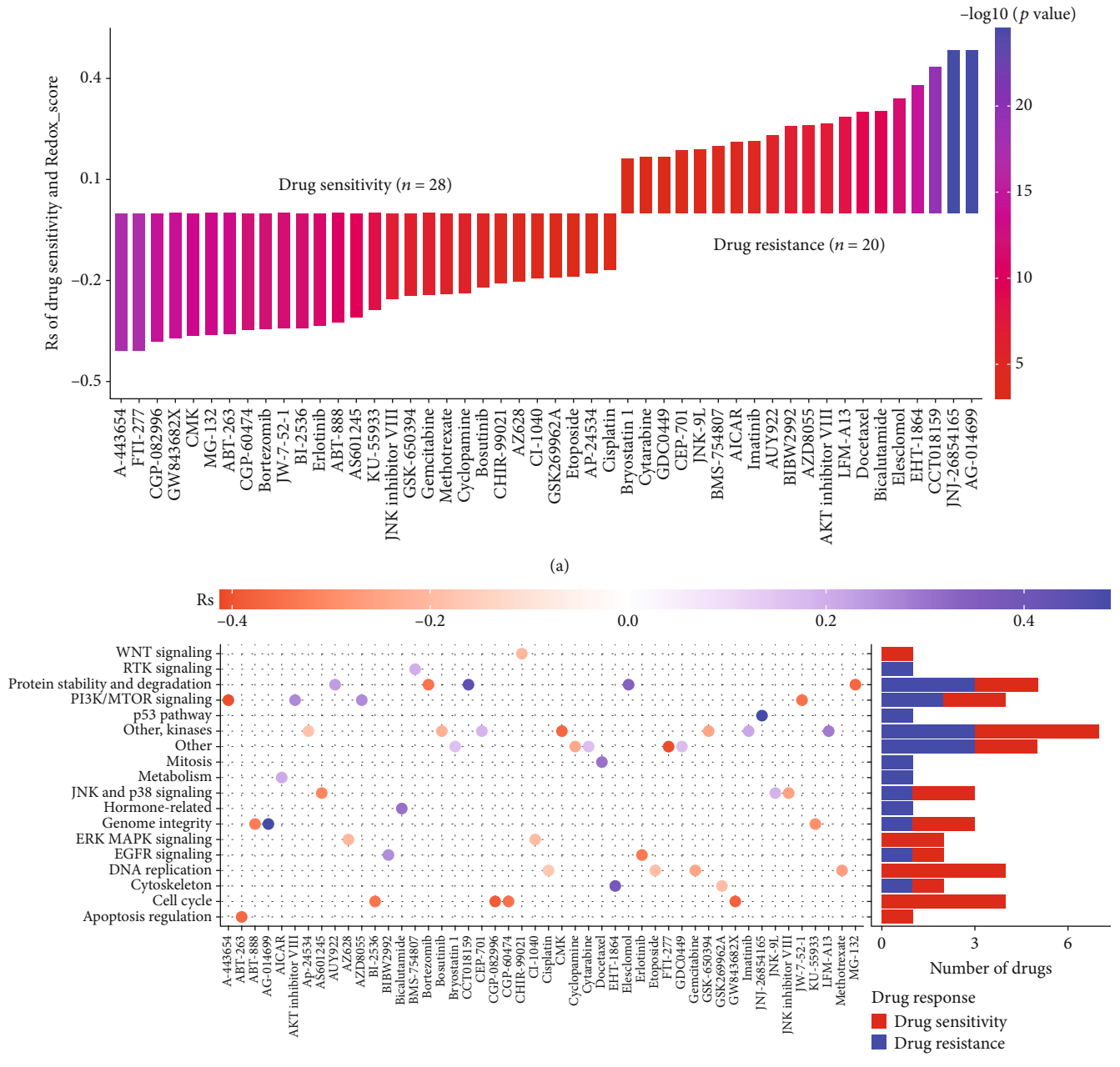


FIGURE 8: Correlation analysis between Redox\_score and drug sensitivity. (a) Pearson correlation analysis was used to evaluate the correlation between Redox\_score and drug sensitivity and drug resistance. (b) Related signaling pathways of drug-targeted genes associated with Redox\_score.

CYP3A4 expression was significantly downregulated in 22RV1 and DU-145 cells, while there was no significant difference in LNCaP and PC-3 cells. COL1A1 and MYBL2 were significantly downregulated in LNCaP, 22RV1, DU-145, and PC-3 cells compared with RWPE-1 cells. Compared with RWPE-1 cells, the RALYL expression was significantly upregulated in LNCaP cells and downregulated in DU-145 and PC-3 cells, while there was no significant difference in the RALYL expression in 22RV1 cells. Compared with RWPE-1 cells, SCN4A was significantly upregulated in LNCaP, 22RV1 and PC-3 cells, while downregulated in DU-145 cells.

#### 4. Discussion

Imbalance of redox homeostasis has been shown to be closely related to cancer genesis, proliferation, invasion, and vascularization [30, 31]. In addition, ROS components produced by a variety of inflammatory cells located in the tumor microenvironment, such as superoxide and hydrogen peroxide, can further affect the function of cancer cells and adjacent immune cells [30]. Although numerous studies have revealed the different roles of redox in numerous cancer-related processes, most current studies have only explored the function of a single redox gene; the overall

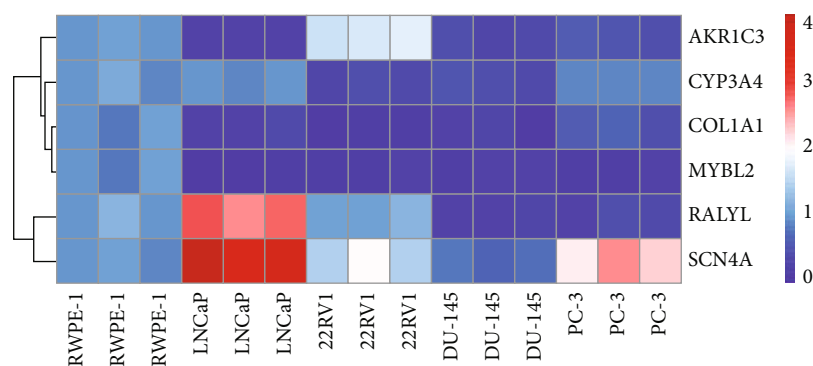


FIGURE 9: The expression heat map of prognostic redox characteristic RRGs in the normal prostate epithelial cells (RWPE-1), hormone-dependent prostate cancer cells (LNCaP), and hormone-resistant prostate cancer cells (22RV1, DU-145, and PC-3).

characteristics of cancer mediated by comprehensive redox genes, as well as their relationships and functions in cancer, have not yet been fully understood. Therefore, a comprehensive and effective analysis of redox modification patterns and characteristics in the PC tumor will contribute to a deeper understanding of the role of redox in the PC tumor and its interrelationship and promote more effective and precise treatment strategies. Here, we first identified two different redox modification patterns based on 1410 differentially expressed RRGs in TCGA and GEO cohorts. We analyzed the characteristics of the molecular and the tumor immune microenvironment of these two patterns. Next, we further identified two redox characteristic gene patterns through redox characteristic genes. Finally, we constructed a scoring system and assessed its benefit in predicting patient outcomes, responses to immunotherapy, and sensitivity or resistance to drug responses.

In this study, we identified two redox patterns based on differentially expressed RRGs. In these two patterns, the molecular characteristics of pattern A were significantly enriched in carcinogenic activation signaling pathways, for example, the JAK-STAT signaling pathway, TGF- $\beta$  signaling pathway, ECM receptor interaction, and NOD-like receptor signaling pathway, while pattern B was mainly enriched in metabolic- and redox-related pathways, for example, arginine and proline metabolism, glutathione metabolism, tyrosine metabolism, fatty acid metabolism, peroxisome, and oxidative phosphorylation. Activation of the TGF- $\beta$  signaling pathway regulates gene expression in a variety of cell biological processes, including cell proliferation, apoptosis, invasion, epithelial-mesenchymal transformation, and immune regulation [32]. Moreover, studies have shown that TGF- $\beta$  is closely related to the invasion and metastasis of advanced cancer cells [33]. In the case of PC, TGF- $\beta$ -regulated vimentin levels were significantly associated with patients' BCR, with TGF- $\beta$ 3 ligand being more able to control the metastatic behavior of cancer cells [34, 35]. Activation of the JAK-STAT signaling pathway is also a common event in multiple stages of carcinogenesis in PC [36]. Not surprisingly, patients with pattern A fared worse than those with pattern B. Pattern B enrichment in metabolic and redox signals suggested that these patients may benefit from metabolic therapy. Metabolic therapy, which targets certain

metabolic processes, offers alternative therapies for these patients. Given the complex interrelationship between redox homeostasis and metabolic pathways in cancer, multiple studies have focused on the treatment of cancer by targeting ROS with metabolic regulators. For instance, several studies have revealed that orlistat, as an antitumor drug, inhibits tumor growth in a variety of cancers, including prostate cancer, by inhibiting fatty acid synthase [37]. Biguanides (metformin and metformin) increase the AMP/ATP ratio mainly by inhibiting mitochondrial respiratory chain complex I, thus activating AMPK, further inducing catabolism process, increasing ATP level, reducing protein and lipid synthesis, and ultimately inhibiting tumor growth [38, 39]. This would provide new insights into metabolic therapy as an alternative therapy.

Next, we identified differentially expressed genes from the two patterns, which were significantly enriched in various metabolic pathways and immunoregulatory biological processes, and were considered to be gene characteristics associated with redox phenotypes. We also identified two gene patterns based on these redox signature genes and further constructed a scoring system (Redox\_score) based on the redox signature genes most associated with prognosis to more accurately guide the treatment strategies of individual patients. We found that the A pattern, characterized by stromal and carcinogenic activation pathways, had a higher Redox\_score, while the B pattern, characterized by metabolic and redox pathways, had a lower Redox\_score. Further analysis found that the Redox\_score independently predicted the prognosis of patients with PC in both the TCGA and GEO cohorts, suggesting that the Redox\_score had a high predictive potential in patients with PC.

The continuous accumulation of somatic mutations is one of the important causes of tumorigenesis and contributes to the production of new antigens [24]. Therefore, the evaluation of mutation-driving genes in human tumors is an important basis for cancer diagnosis and treatment formulation. Here, a significant positive correlation was found between Redox\_score and TMB. In addition, we found that SPOP was the most mutated driver gene in the low-risk patients, while TP53 was the most mutated driver gene in the high-risk patients. Several studies have revealed that SPOP inhibited the progression of PC by promoting the

degradation of various oncoproteins, such as androgen receptor [40], steroid receptor coactivator 3 [41], and Myc [42]. However, SPOP mutation rates have been reported to reach 6-15% in local and advanced PC [43], so SPOP mutations have been identified as an early event in the occurrence and progression of PC, partly due to genetic instability [44]. TP53 exerted the tumor inhibitory effect by regulating signaling pathways such as genomic stabilization and cell cycle arrest [45]. TP53 has a higher mutation frequency in patients with PC, affecting 50% of patients with metastatic PC [46]. Multiple studies have shown that TP53 levels have prognostic significance in castration-resistant PC and serve as a biomarker of adverse responses to novel hormone therapy [47].

The latest EAU guidelines indicated the currently approved ICI in PC target molecules CTLA4, PD-1, and PD-L1. Anti-CTLA-4 or anti-PD-1 monotherapy or combination immunotherapy was currently being rigorously tested in PC [48]. A phase II trial of 258 PC patients treated with pembrolizumab showed an objective response rate of about 4%, but these responses were long-lasting [49]. In our study, we also explored the expression relationship between common ICI genes (PD-1, PD-L2, CTLA4, B7-H3, and B7-H4) and the Redox\_score, and we found that compared with the low-risk patients, the expression levels of ICI genes in the high-risk patients were significantly upregulated. Immune checkpoint refers to a class of inhibitory or irritating molecules expressed mainly on tumor cells, antigen presenting cells, or immune cells. Immune checkpoint molecules expressed in antigen-presenting cells or immune cells mainly mediate the processes of the adaptive and innate immune systems. The immune checkpoint molecules expressed in different types of tumors play important roles in tumor cell biology, such as inducing epithelial-mesenchymal transformation, promoting tumor initiation, and promoting tumor metastasis, antiapoptosis, and antitumor drug resistance [50, 51]. Our results were consistent with previous findings that the expression level of the ICI gene was negatively correlated with the prognosis of patients [29, 50]. Moreover, SubMap analysis indicated that the high-risk patients were more responsive to ICI than the low-risk patients, which was consistent with the above results. We also further determined the potential value of the Redox\_score in predicting immunotherapy reactivity by analyzing the immunotherapy cohort of patients receiving PD-1 treatment for melanoma. We believed that our Redox\_score will be useful in assessing the benefit of patients receiving anti-CTLA-4 or anti-PD-1 immunotherapy. Therefore, accessible datasets of PC patients receiving immunotherapy were needed to further validate these results. Finally, the correlation between Redox\_score and drug sensitivity and drug resistance was also analyzed. We found that the drugs related to Redox\_score-high mostly targeted apoptosis regulation, cell cycle, DNA replication, and ERK MAPK signaling pathways, while the drugs related to Redox\_score-low mostly targeted hormone-related, p53, and PI3K/MTOR signaling pathways.

Overall, although we have analyzed the overall redox modification profile in PC and developed a scoring system

with prognostic potential, there are some limitations to this study. First, our study was based on retrospective datasets to determine redox modification patterns and Redox\_score, and prospective cohorts are needed to validate our results. Secondly, the specific biological functions and molecular mechanisms of RRGs affecting the prognosis of PC are still unclear, and further analysis is needed through experiments. Thirdly, the Redox\_score needs to be further validated in open-access expression data of cancer patients receiving antioxidant therapy. Finally, we used available immunotherapy cohorts for other tumor (melanoma) to validate the role of the Redox\_score, which needs further validation with available PC immunotherapy cohorts.

## 5. Conclusions

In our study, we systematically and comprehensively assessed the redox modification patterns of RRGs in PC, revealing their molecular mechanisms and immune micro-environment characteristics in PC. We also constructed a scoring system (Redox\_score) and identified its upstream regulatory network, prognostic value, benefit in predicting immunotherapeutic response, and drug sensitivity relationships in PC, which will help to develop individualized treatment strategies for PC patients.

## Abbreviations

|            |  |
|------------|--|
| PC:        | Prostate cancer  |
| ROS:       | Reactive oxygen species  |
| RNS:       | Reactive nitrogen  |
| TCGA:      | The Cancer Genome Atlas  |
| GEO:       | Gene Expression Omnibus  |
| RRGs:      | Redox-related genes  |
| GSA:       | Gene set variation analysis  |
| CIBERSORT: | Cell-type identification by estimating relative subsets of RNA transcripts |
| FC:        | Fold change  |
| LASSO:     | Least absolute shrinkage and selection operator                            |
| TMB:       | Tumor mutation burden  |
| ICI:       | Immune checkpoint inhibitor  |
| GDSC:      | Genomics of Drug Sensitivity in Cancer                                     |
| BCR:       | Biochemical relapse  |
| ROC:       | Receiver operating characteristic.   |

## Data Availability

The data and materials can be obtained by contacting the corresponding author.

## Conflicts of Interest

The authors declare that they have no competing interests.

## Authors' Contributions

Y.W. designed the study and performed the data analysis. X.Z., H.F., B.H., Z.D., C.W., and B.L. performed the data analysis. Y.L., Y.R., X.L., Z.L., and J.L. performed the data

analysis and revised the manuscript. T.W. designed the study and revised the manuscript. All authors read and approved the final manuscript.

## Acknowledgments

This work was supported by a grant from the National Natural Science Foundation of China (No. 81874165).

## Supplementary Materials

Supplemental Figure S1: identification of redox patterns in PC by unsupervised consensus clustering based on GEO cohort. Supplemental Figure S2: correlation analysis between myeloid marker molecules and the Redox\_score. Supplemental Figure S3: identification of prognosis-related RRGs. Supplemental Figure S4: correlation of the Redox\_score with PTEN and AR mutations. Supplemental Table S1: the sequences of primer RNA. Supplemental Table S2: miRNA and RRG regulatory networks. Supplemental Table S3: miRNAs related to which Redox\_score they correlated with Redox\_A and Redox\_B. (*Supplementary Materials*)

## References

- [1] R. L. Siegel, K. D. Miller, and A. Jemal, "Cancer statistics, 2020," *CA: a Cancer Journal for Clinicians*, vol. 70, no. 1, pp. 7–30, 2020.
- [2] C. G. Drake, "Visceral metastases and prostate cancer treatment: die hard, tough neighborhoods, or evil humors?," *Oncology (Williston Park, N.Y.)*, vol. 28, no. 11, pp. 974–980, 2014.
- [3] D. Bausch, S. Thomas, M. Mino-Kenudson et al., "Plectin-1 as a novel biomarker for pancreatic cancer," *Clinical Cancer Research*, vol. 17, no. 2, pp. 302–309, 2011.
- [4] J. E. Bekelman, R. B. Rumble, R. C. Chen et al., "Clinically localized prostate cancer: ASCO clinical practice guideline endorsement of an American Urological Association/American Society for Radiation Oncology/Society of Urologic Oncology Guideline," *Journal of Clinical Oncology*, vol. 36, no. 32, pp. 3251–3258, 2018.
- [5] J. E. Damber and G. Aus, "Prostate cancer," *Lancet*, vol. 371, no. 9625, pp. 1710–1721, 2008.
- [6] W. Zhong, H. L. Weiss, R. D. Jayswal et al., "Extracellular redox state shift: a novel approach to target prostate cancer invasion," *Free Radical Biology & Medicine*, vol. 117, pp. 99–109, 2018.
- [7] S. Parvez, M. J. C. Long, J. R. Poganik, and Y. Aye, "Redox signaling by reactive electrophiles and oxidants," *Chemical Reviews*, vol. 118, no. 18, pp. 8798–8888, 2018.
- [8] M. Calvani, A. Subbiani, M. Vignoli, and C. Favre, "Spotlight on ROS and  $\beta$ 3-adrenoreceptors fighting in cancer cells," *Oxidative Medicine and Cellular Longevity*, vol. 2019, Article ID 6346529, 2019.
- [9] C. C. Winterbourn, "The biological chemistry of hydrogen peroxide," *Methods in Enzymology*, vol. 528, pp. 3–25, 2013.
- [10] K. Brieger, S. Schiavone, F. J. Miller Jr., and K. H. Krause, "Reactive oxygen species: from health to disease," *Swiss Medical Weekly*, vol. 142, 2012.
- [11] L. B. Sullivan and N. S. Chandel, "Mitochondrial reactive oxygen species and cancer," *Cancer & Metabolism*, vol. 2, 2014.
- [12] C. Gorrini, I. S. Harris, and T. W. Mak, "Modulation of oxidative stress as an anticancer strategy," *Nature Reviews. Drug Discovery*, vol. 12, no. 12, pp. 931–947, 2013.
- [13] K. Süle, K. Szentmihályi, G. Szabó et al., "Metal- and redox homeostasis in prostate cancer with vitamin D<sub>3</sub> supplementation," *Biomedicine & Pharmacotherapy*, vol. 105, pp. 558–565, 2018.
- [14] A. Blázovics, P. Nyirády, G. Bekő et al., "Changes in erythrocyte transmethylation ability are predictive factors for tumor prognosis in prostate cancer," *Croatica Chemica Acta*, vol. 84, no. 2, pp. 127–131, 2011.
- [15] A. Blázovics, "Redox homeostasis, bioactive agents and transduction therapy," *Current Signal Transduction Therapy*, vol. 2, no. 3, pp. 226–239, 2007.
- [16] M. D. Wilkerson and N. D. Hayes, "ConsensusClusterPlus: a class discovery tool with confidence assessments and item tracking," *Bioinformatics*, vol. 26, no. 12, pp. 1572–1573, 2010.
- [17] A. M. Newman, C. L. Liu, M. R. Green et al., "Robust enumeration of cell subsets from tissue expression profiles," *Nature Methods*, vol. 12, no. 5, pp. 453–457, 2015.
- [18] W. Roh, P.-L. Chen, A. Reuben et al., "Integrated molecular analysis of tumor biopsies on sequential CTLA-4 and PD-1 blockade reveals markers of response and resistance," *Science Translational Medicine*, no. 9, 2017.
- [19] S. Sotosek, V. Sotosek Tokmadzic, I. Mrakovcic-Sutic et al., "Comparative study of frequency of different lymphocytes subpopulation in peripheral blood of patients with prostate cancer and benign prostatic hyperplasia," *Wiener Klinische Wochenschrift*, vol. 123, no. 23–24, pp. 718–725, 2011.
- [20] E. Anastasiadou, L. S. Jacob, and F. J. Slack, "Non-coding RNA networks in cancer," *Nature Reviews. Cancer*, vol. 18, no. 1, pp. 5–18, 2018.
- [21] M. Fan, R. Krutilina, J. Sun et al., "Comprehensive analysis of microRNA (miRNA) targets in breast cancer cells," *The Journal of Biological Chemistry*, vol. 288, no. 38, pp. 27480–27493, 2013.
- [22] J. Banerjee, S. Khanna, and A. Bhattacharya, "MicroRNA regulation of oxidative stress," *Oxidative Medicine and Cellular Longevity*, vol. 2017, Article ID 2872156, 2017.
- [23] M. E. Hatley, D. M. Patrick, M. R. Garcia et al., "Modulation of K-Ras-dependent lung tumorigenesis by microRNA-21," *Cancer Cell*, vol. 18, no. 3, pp. 282–293, 2010.
- [24] M. Seike, A. Goto, T. Okano et al., "miR-21 is an EGFR-regulated anti-apoptotic factor in lung cancer in never-smokers," *Proceedings of the National Academy of Sciences of the United States of America*, vol. 106, no. 29, pp. 12085–12090, 2009.
- [25] M. M. Gubin, M. N. Artyomov, E. R. Mardis, and R. D. Schreiber, "Tumor neoantigens: building a framework for personalized cancer immunotherapy," *The Journal of Clinical Investigation*, vol. 125, no. 9, pp. 3413–3421, 2015.
- [26] A. M. Goodman, S. Kato, L. Bazhenova et al., "Tumor mutational burden as an independent predictor of response to immunotherapy in diverse cancers," *Molecular Cancer Therapeutics*, vol. 16, no. 11, pp. 2598–2608, 2017.
- [27] H. Chen, W. Chong, Q. Wu, Y. Yao, M. Mao, and X. Wang, "Association of LRP1B mutation with tumor mutation burden and outcomes in melanoma and non-small cell lung cancer patients treated with immune check-point blockades," *Frontiers in Immunology*, vol. 10, 2019.

- [28] H. Chen, M. Yang, Q. Wang, F. Song, X. Li, and K. Chen, "The new identified biomarkers determine sensitivity to immune check-point blockade therapies in melanoma," *Oncoimmunology*, vol. 8, no. 8, 2019.
- [29] J. Sun, Z. Zhang, S. Bao et al., "Identification of tumor immune infiltration-associated lncRNAs for improving prognosis and immunotherapy response of patients with non-small cell lung cancer," *Journal for Immunotherapy of Cancer*, vol. 8, no. 1, article e000110, 2020.
- [30] C. Hegedűs, K. Kovács, Z. Polgár et al., "Redox control of cancer cell destruction," *Redox Biology*, vol. 16, pp. 59–74, 2018.
- [31] V. Helfinger and K. Schröder, "Redox control in cancer development and progression," *Molecular Aspects of Medicine*, vol. 63, pp. 88–98, 2018.
- [32] J. Massagué, "TGF $\beta$  in Cancer," *Cell*, vol. 134, no. 2, pp. 215–230, 2008.
- [33] D. Padua and J. Massagué, "Roles of TGF $\beta$  in metastasis," *Cell Research*, vol. 19, no. 1, pp. 89–102, 2009.
- [34] Q. Zhang, B. T. Helfand, T. L. Jang et al., "Nuclear factor-kappaB-mediated transforming growth factor-beta-induced expression of vimentin is an independent predictor of biochemical recurrence after radical prostatectomy," *Clinical Cancer Research*, vol. 15, no. 10, pp. 3557–3567, 2009.
- [35] L. Walker, A. C. Millena, N. Strong, and S. A. Khan, "Expression of TGF $\beta$ 3 and its effects on migratory and invasive behavior of prostate cancer cells: involvement of PI3-kinase/AKT signaling pathway," *Clinical & Experimental Metastasis*, vol. 30, no. 1, pp. 13–23, 2013.
- [36] R. Dhir, Z. Ni, W. Lou, F. DeMiguel, J. R. Grandis, and A. C. Gao, "Stat3 activation in prostatic carcinomas," *The Prostate*, vol. 51, no. 4, pp. 241–246, 2002.
- [37] H. Y. Chuang, Y. P. Lee, W. C. Lin, Y. H. Lin, and J. J. Hwang, "Fatty acid inhibition sensitizes androgen-dependent and -independent prostate cancer to radiotherapy via FASN/NF- $\kappa$ B pathway," *Scientific Reports*, vol. 9, no. 1, p. 13284, 2019.
- [38] C. Rubiño, D.-M. Alcalá, and B. Marchal, "Phenformin as an anticancer agent: challenges and prospects," *International Journal of Molecular Sciences*, vol. 20, no. 13, p. 3316, 2019.
- [39] D. G. Hardie, "AMPK: a target for drugs and natural products with effects on both diabetes and cancer," *Diabetes*, vol. 62, no. 7, pp. 2164–2172, 2013.
- [40] J. An, C. Wang, Y. Deng, L. Yu, and H. Huang, "Destruction of full-length androgen receptor by wild-type SPOP, but not prostate-cancer-associated mutants," *Cell Reports*, vol. 6, no. 4, pp. 657–669, 2014.
- [41] X. Dai, W. Gan, X. Li et al., "Prostate cancer-associated SPOP mutations confer resistance to BET inhibitors through stabilization of BRD4," *Nature Medicine*, vol. 23, no. 9, pp. 1063–1071, 2017.
- [42] C. Geng, S. Kaochar, M. Li et al., "SPOP regulates prostate epithelial cell proliferation and promotes ubiquitination and turnover of c-MYC oncoprotein," *Oncogene*, vol. 36, no. 33, pp. 4767–4777, 2017.
- [43] C. E. Barbieri, S. C. Baca, M. S. Lawrence et al., "Exome sequencing identifies recurrent *\_SPOP\_*, *\_FOXA1\_* and *\_MED12\_* mutations in prostate cancer," *Nature Genetics*, vol. 44, no. 6, pp. 685–689, 2012.
- [44] K. Hjorth-Jensen, A. Maya-Mendoza, N. Dalgaard et al., "SPOP promotes transcriptional expression of DNA repair and replication factors to prevent replication stress and genomic instability," *Nucleic Acids Research*, vol. 46, no. 18, pp. 9484–9495, 2018.
- [45] P. A. Muller and K. H. Vousden, "Mutant p53 in cancer: new functions and therapeutic opportunities," *Cancer Cell*, vol. 25, no. 3, pp. 304–317, 2014.
- [46] D. Robinson, E. M. Van Allen, Y.-M. Wu et al., "Integrative clinical genomics of advanced prostate cancer," *Cell*, vol. 161, no. 5, pp. 1215–1228, 2015.
- [47] A. A. Hamid, K. P. Gray, G. Shaw et al., "Compound genomic alterations of TP53, PTEN, and RB1 tumor suppressors in localized and metastatic prostate cancer," *European Urology*, vol. 76, no. 1, pp. 89–97, 2019.
- [48] P. Cornford, R. C. N. van den Bergh, E. Briers et al., "EAU-EANM-ESTRO-ESUR-SIOG guidelines on prostate cancer. Part II–2020 update: treatment of relapsing and metastatic prostate cancer," *European Urology*, vol. 79, no. 2, pp. 263–282, 2021.
- [49] E. S. Antonarakis, J. M. Piulats, M. Gross-Goupil et al., "Pembrolizumab for treatment-refractory metastatic castration-resistant prostate cancer: multicohort, open-label phase II KEYNOTE-199 study," *Journal of Clinical Oncology*, vol. 38, no. 5, pp. 395–405, 2020.
- [50] Y. Zhang and J. Zheng, "Functions of immune checkpoint molecules beyond immune evasion," *Advances in Experimental Medicine and Biology*, vol. 1248, pp. 201–226, 2020.
- [51] J. Wang, T. Yang, and J. Xu, "Therapeutic development of immune checkpoint inhibitors," *Advances in Experimental Medicine and Biology*, vol. 1248, pp. 619–649, 2020.

## Research Article

# A Ferroptosis-Related Prognostic Risk Score Model to Predict Clinical Significance and Immunogenic Characteristics in Glioblastoma Multiforme

Dongdong Xiao, Yujie Zhou , Xuan Wang , Hongyang Zhao , Chuansheng Nie ,  
and Xiaobing Jiang 

Department of Neurosurgery, Union Hospital, Tongji Medical College, Huazhong University of Science and Technology, Wuhan 430022, China

Correspondence should be addressed to Chuansheng Nie; 2017xh0116@hust.edu.cn and Xiaobing Jiang; jiangxbing@hotmail.com

Dongdong Xiao and Yujie Zhou contributed equally to this work.

Received 30 July 2021; Revised 4 October 2021; Accepted 12 October 2021; Published 9 November 2021

Academic Editor: Xiangpan Li

Copyright © 2021 Dongdong Xiao et al. This is an open access article distributed under the Creative Commons Attribution License, which permits unrestricted use, distribution, and reproduction in any medium, provided the original work is properly cited.

**Background.** Ferroptosis is a recently identified cell death pathway, and the susceptibility to ferroptosis inducers varies among cancer cell types. There have been recent attempts to clarify the mechanisms implicated in ferroptosis, glioma invasion, and the immune microenvironment but little is known about ferroptosis regulation in GBM. **Methods.** Screening ferroptosis-related genes from published reports and existing databases, we constructed an integrated model based on the RNA-sequencing data in GBM. The association of FRGPRS and overall survival is identified and validated across several different datasets. Genomic and clinical characteristics, immune infiltration, enriched pathways, pan-cancer, drug resistance, and immune checkpoint inhibitor therapy are compared among various FRGPRS subgroups. **Results.** We identified and confirmed the influences of five ferroptosis key hub genes in the FRGPRS model. The FRGPRS model could serve to predict overall survival and progression-free survival in GBM patients, and high FRGPRS was associated with comparatively stronger immunity, higher proportions of tumour tissue, and good cytolytic immune and chemotherapeutics response in GBM patients. **Conclusions.** The five ferroptosis key hub genes constituting the FRGPRS model could serve to predict overall survival and progression-free survival in patients with GBM and help guide timely and efficacious therapeutic strategies customised and optimised for each individual patient. This discovery may lay the foundation for the development and optimisation of other iterations of this model for the improved forecasting, detection, and treatment of other malignancies notorious for their drug resistance and immune escape.

## 1. Introduction

Glioblastoma multiforme (GBM) is a primary malignant brain tumour. Despite the fact that it is treated with multidisciplinary synthetic therapy, including surgical resection, radiotherapy, and chemotherapy, the patients' overall survival time is only approximately 15 months [1, 2]. Tumour necrosis is common in GBM, and it is positively correlated with tumour aggressiveness and poor outcome [3, 4]. Previous studies proposed that oxidative phosphorylation disorders and intracellular adenosine triphosphate (ATP) depletion lead to cell death

in chronic ischaemia microenvironments [5, 6]. Extensive tumour tissue hypoxia together with rapid tumour expansion triggers necrosis. Collectively, they comprise the fundamental stimuli of GBM stem cell progression [7]. Intense research efforts have elucidated the cell death pathways in other cancers. However, no such breakthrough has been made for GBM. Moreover, the mechanisms by which GBM escapes programmed cell death remain unclear [8–10]. Recent studies have demonstrated that targeting the cell death pathway is a promising therapeutic strategy for preventing the progression of GBM. For example, cell death-targeting drugs combined



with immunotherapy suppressed tumour growth in murine GBM models [11]. However, chemoradiotherapy resistance and immune evasion are extremely variable among GBM patients. Molecular alterations, such as isocitrate dehydrogenase1 (*IDH1*) mutation and tumour protein p53 (*TP53*) mutation, are widely utilised for the prognosis and treatment of GBM. Nevertheless, few of these strategies have been successful. Therefore, new, efficacious treatments for GBM are urgently required [12, 13].

Ferroptosis is a recently identified cell death pathway characterised by iron-dependent lipid peroxidation. It differs from apoptosis, necroptosis, and pyroptosis [14]. Overloading of intracellular iron ions leads to glutathione (GSH) depletion, reactive oxygen species (ROS) accumulation, and, ultimately, cell death [15, 16]. Chemotherapy-resistant GBM and other cancer cells, especially those that are mesenchymal and metastatic, are relatively more sensitive to ferroptosis induced by glutathione peroxidase-4 (GPX4) inhibition [17–19]. However, susceptibility to ferroptosis inducers varies among cancer cell types [20]. Despite the presence of continuous oxidative stress stimulation, ferroptosis is not always triggered during cancer progression [21]. There have been recent attempts to clarify the mechanisms implicated in ferroptosis, glioma invasion, and the immune microenvironment [22–25]. Unfortunately, these studies have not specifically focused on GBM, and little is known about ferroptosis regulation in GBM. Thus, ferroptosis-related prognosis and treatment indicators for GBM are promptly needed.

Now, the treatment of GBM has entered an era of the comprehensive treatment, therefore, identifying optimal biomarkers is the key to maximizing the comprehensive therapeutic effect. In the present study, we constructed a model which consists of 5 ferroptosis regulators and proposed it as a potential molecular classification for GBM, which could serve to predict overall survival and progression-free survival in patients with GBM and could identify distinct mutation pattern, immune infiltration, cytolytic immune response, and the drug resistance. This discovery may lay the foundation for the development and optimisation of other iterations of this model for the improved forecasting, detection, and treatment of other malignancies notorious for their drug resistance and immune escape.

## 2. Methods

**2.1. Patients and Datasets.** We download from cBioPortal database (<https://www.cbioportal.org/>) TCGA malignant glioblastoma (glioblastoma multiforme, GBM), genome sequencing data (whole exome sequencing, WES, 388 samples), copy number variation data (SNP6.0 chip data, HG19, 575 samples), transcriptome data (RNA-SEQ, 155 samples), and clinical information data (585 samples). The sample size of intersection of transcriptome data and clinical data was 155. Rna-seq data included RSEM standardized count and Z-score standardized expression profile. We download a set of validation set of data (GSE4412), including the transcriptome data and clinical data, from the GEO resource platform (<https://www.ncbi>

[.nlm.nih.gov/gds](https://www.ncbi.nlm.nih.gov/gds)). Microarray data of GPL96 transcriptome sequencing platform (Affymetrix Human Genome U133A Array) were selected, including 85 samples of right frontal, right frontal parietal, right frontal temporal, right parietal, right parietal occipital, right temporal, right temporal parietal, right anterior temporal, right cerebellum, left frontal, left frontal temporal, left parietal, left parietal occipital, left temporal, left temporal parietal, and thalamus. 74 patients were diagnosed with grade III ( $n = 24$ ) or grade IV ( $n = 50$ ) gliomas during the initial surgical treatment and were provided with fresh frozen materials for analysis as part of the study. Normal brain tissue RNA-sequencing expression data for 1,671 patients were obtained from the GTEx project (<https://gtexportal.org/home/>). RNA-sequencing data for 514 low-grade glioma (LGG) samples and 407 bladder urothelial carcinoma (BLCA) samples and their corresponding survival information were downloaded from the cBioportal database (<https://www.cbioportal.org/>) for pan-cancer analyses of ferroptosis-related risk factors. Clinical information and RNA-sequencing data for 298 patients with urothelial carcinoma being administered the PD-L1 inhibitor atezolizumab were extracted using the “IMvigor210CoreBiologies” package in R4.0.3 (R Core Team, Vienna, Austria). For patients with GBM, clinical data, including radiotherapy, race, and ethnicity, were downloaded from the Xena data resources ([https://xenabrowser.net/datapages/?cohort=GDC%20TCGA%20Glioblastoma%20\(GBM\)&removeHub=https%3A%2F%2Fxcna.treehouse.gi.ucsc.edu%3A443](https://xenabrowser.net/datapages/?cohort=GDC%20TCGA%20Glioblastoma%20(GBM)&removeHub=https%3A%2F%2Fxcna.treehouse.gi.ucsc.edu%3A443)). The intersection of the transcriptome and clinical data was 155. Data type and sample size information are summarised in Table 1.

Two hundred and sixty-nine ferroptosis genes were obtained from known studies and related databases. There were 259 in the FerrDb database (<http://www.zhounan.org/ferrdb/>), 60 in the study by Yee et al. [5], and 52 in the study by Liang et al. [26]. Data regarding the interactions among transcription factors (TF), mRNAs, miRNAs, and lncRNAs were downloaded from the Transfac (<http://gene-regulation.com/>), Chipbase (<http://rna.sysu.edu.cn/chipbase/>), miTarbase (<http://mirtarbase.cuhk.edu.cn/php/index.php>), Starbase (<http://starbase.info/>), and LncMAP (<http://www.biobigdata.com/LncMAP>) data (<http://2fxena.treehouse.gbases>). The protein–protein interaction (PPI) network of the coding genes was constructed using STRING (V11.0; <https://string-db.org/cgi/input.pl>). Clinical and phenotypic data for TCGA GBM samples matching the transcriptome data were sorted as shown in Table 2.

**2.2. Identification of Ferroptosis-Related Hub Genes.** For the RNA-sequencing data, genes not expressed in more than five samples were excluded. Log<sub>2</sub>-transformation was performed for both the control and validation groups, namely, 155 tumours (expression data) in TCGA database vs. 155 samples (expression data) in the GTEx. After gene overlap of the control and validation groups, expression levels were obtained for 13,762 genes in tumour and normal tissues. Batch effects were removed using the ComBat function in the “sva” package of R. A differentially expressed gene (DEG) analysis between the GBM and normal brain samples was performed using the “DESeq2” package in R. The false

TABLE 1: Basic information of the datasets included in this study.

| Dataset                 | Data type                                     | N    |
|-------------------------|---|------|
| TCGA GBM                | Expression                                    | 155  |
|                         | Mutation                                      | 388  |
|                         | Copy number                                   | 575  |
|                         | Clinical data                                 | 585  |
| GTEX brain              | Expression                                    | 1671 |
| GEO (GSE4412)           | Expression, survival                          | 85   |
| IMvigor210CoreBiologies | Expression, survival, drug response           | 298  |
| GDSC                    | Drug response, genomic markers of sensitivity | 155  |

TABLE 2: Summary of clinical information in TCGA-GBM dataset.

|                                  |            |
|----------------------------------|------------|
| Total patient ( <i>n</i> )       | 155        |
| Age at diagnosis (median, range) | 60 (21-89) |
| Gender                           |            |
| Male                             | 63         |
| Female                           | 43         |
| Unknown                          | 49         |
| Vital status                     |            |
| Alive                            | 32         |
| Dead                             | 122        |
| Unknown                          | 1          |
| Radiotherapy                     |            |
| Yes                              | 124        |
| No                               | 21         |
| Unknown                          | 10         |
| Ethnicity                        |            |
| Hispanic or Latino               | 3          |
| Not Hispanic or Latino           | 126        |
| Unknown                          | 26         |
| Race                             |            |
| Black or African American        | 10         |
| Asian                            | 5          |
| White                            | 138        |
| Unknown                          | 2          |

discovery rate- (FDR-) corrected threshold for statistical significance was  $p \leq 0.01$  (Benjamini and Hochberg method;  $FC \geq 2$  or  $FC \leq 1/2$ ). Instead of using  $\log_2 FC$ , we use  $FC$  directly to represent the threshold. Differential expression between tumour tissues and normal tissues was divided into two types: upregulation group ( $FC \geq 2$ ) and downregulation group ( $FC \leq 0.5$ ).

A Kyoto Encyclopedia of Genes and Genomes (KEGG) function enrichment analysis was performed on the DEGs using the “clusterProfiler” package in R to identify significantly ( $p \leq 0.01$ ) enriched pathways. Differentially ferroptosis-related (ferroptosis-DE) genes were selected among the DEGs and used in subsequent Gene Ontology (GO) functional and KEGG pathway enrichment analyses using MSigDB (V7.2) (<http://www.gsea-msigdb.org/gsea/msigdb>). The top 15 signifi-

cantly enriched GO terms and pathways were determined, and the related genes were extracted as Candidate-Ferroptosis-Geneset1 (cd-Ferr-Geneset1).

Ferroptosis-DE genes were screened out from among the DEGs. Consensus clustering analysis was performed using the “ConsensusClusterPlus” package in R to discover the ferroptosis-DE gene-based clusters in patients with GBM. Relative changes in the area under the cumulative distribution function (CDF) curve were evaluated for cluster number  $k$  in the range of two to ten. The optimal number of categories was determined to be four as the area under the CDF curve underwent the greatest changes between classes 4 and 5. The differences in survival among the four subcategories were evaluated using a log-rank test. The “survival” package in R was used to plot Kaplan–Meier (K–M) survival curves. For all GBM patients within the four categories, differential expression analyses were performed using the “DESeq2” package in R ( $FDR \leq 0.05$ ; Benjamini and Hochberg method;  $FC \geq 1.5$  or  $FC \leq 2/3$ ). The Candidate-Ferroptosis-Geneset2 (cd-Ferr-geneset2) was obtained by the intersection of DEGs among the four categories. The cd-Ferr-Geneset2 expression levels in the four categories were plotted with a heatmap using the “heatmap” package in R. A principal component analysis (PCA) was conducted using the “psych” package in R.

A weighted correlation network analysis (WGCNA) of the expression levels in the gene set collection was performed to screen for hub genes. Mean connectivity was used to select soft thresholds. A hierarchical cluster tree was plotted to reflect the significance levels of the hub genes and their associations with the clinical phenotypes. An association analysis was conducted to evaluate the correlations between the module genes and the clinical phenotypic data. The modules were identified, and their threshold values were  $\geq 0.7$  and  $\geq 0.2$  for gene significance (GS) and module membership (MM), respectively. Genes in the PPI networks with degree  $> 5$  were designated hub genes. The intersection of the key module and hub genes in the PPI network was designated as the ferroptosis-related disease hub gene dataset. Based on the regulatory factors of screened key hub genes, a multifactor regulatory network was constructed using the Cytoscape (<https://cytoscape.org/download.html>).

**2.3. Ferroptosis-Related Gene Prognostic Risk Score (FRGPRS) Construction and Validation.** Based on the

median expression values of the disease hub and known ferroptosis genes, the patients with GBM were separated into two groups. Thirteen prognosis-related core genes significantly influencing progression-free survival (PFS) were recognised with univariate Cox regression models ( $p \leq 0.01$ ; log-rank test) and screened and verified using least absolute shrinkage and selection operator- (Lasso-) logistic regression analysis. FRGPRS was constructed based on the prognostic gene expression levels using the regression coefficient from the multivariate Cox proportional hazards regression analysis. FRGPRS of the  $i^{\text{th}}$  sample was calculated as follows:

$$\text{Risk score}_i = \sum_{j=1}^n C_j * \exp_{ij}, \quad (1)$$

where  $C_j$  is the regression coefficient of the  $j^{\text{th}}$  prognostic factor in the Cox regression model, and  $\exp_{ij}$  is the expression level of the  $j^{\text{th}}$  prognostic factor in the  $i^{\text{th}}$  sample.

The patients with GBM were separated into two groups based on their median FRGPRS values. The relationship between FRGPRS and patients' overall survival (OS) was evaluated using log-rank test. ROC curves were plotted using the "timeROC" package of R and used to estimate the prognostic performance of the FRGPRS. GEO data (GSE4412) were used for validation analysis. Based on the FRGPRS, pan-cancer analyses were performed on TCGA GBM, GEO GBM, TCGA LGG, and TCGA BLCA.

**2.4. Comprehensive Analysis of Genomic, Clinical, and Immune Characteristics, Pan-Cancer, Drug Resistance, and Immune Checkpoint Inhibitor Therapy among Various FRGPRS Subgroups.** The relationships among FRGPRS level and clinical (gender, radiotherapy, and age) and genomic (*IDH1* mutation, *1p/19q* codeletion, and *TP53* mutation status) characteristics were examined. Moreover, the patients with GBM were divided into high-risk and low-risk groups based on their median FRGPRS values. Correlation analyses were performed on the immune characteristics and genome variants among the different groups. The immune subtypes come from previous studies on immune characteristics analysis of TCGA data [27]. For immune subtypes, gliomas involve only 3 subtypes, namely, C1, C4, and C5. The homologous recombination deficiency (HRD) scores, neoantigens, fractions altered, and mRNAsi indices were assessed according to previous analyses of the genomic characteristics of TCGA data [27, 28]. Nonsynonymous GBM tumour mutation burdens were calculated using the tumour mutational burden (TMB) analysis. Chromosomal instability was associated with HRD, and genomic DNA damage was assessed by loss-of-heterozygosity, large scale transition, and telomeric allelic imbalance (NtAI) [29]. The infiltration levels of 22 different immunocytes were determined with the "CIBERSORT" package in R [30]. The Wilcoxon rank-sum test compares significance between pairs, while the KW test is a nonparametric test that compares multiple groups. Based on the proportions of the stromal and cellular components, the immune, stromal, and ESTIMATE scores were evaluated using the "ESTIMATE" package in R [31]. Based

on GBM cell line and drug response data derived from the Genomics of Drug Sensitivity in Cancer website (<http://www.cancerrxgene.org/>), a drug sensitivity prediction model for the patients with GBM was constructed using ridge regression [32].

Survival analyses of FRGPRS groups were conducted to explore the predictive performance of FRGPRS in patients undergoing immune checkpoint inhibitor therapy. Based on their immunotherapy responses, the 298 aforementioned patients with urothelial carcinoma were divided into complete response (CR), partial response (PR), stable disease (SD), and progressive disease (PD) groups for validation analysis [33].

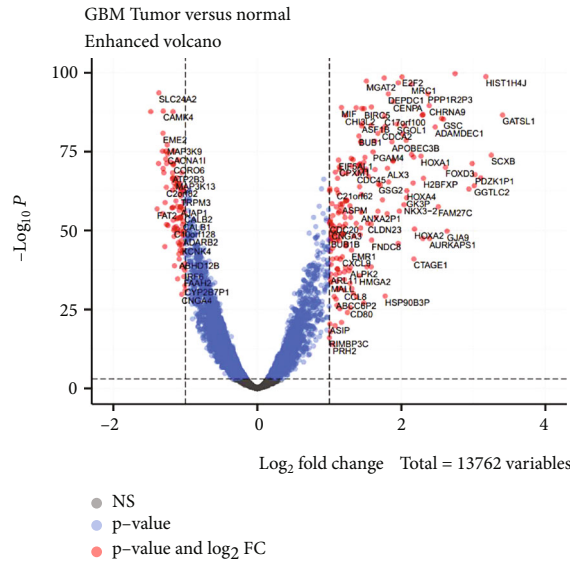
**2.5. Genomic Variant and Copy Number Variation Analyses.** To establish the differences in variation between low and high FRGPRS, mutation spectra were plotted using the "Maftools" package in R for the top 30 genes with highest frequency. The copy number alteration (CNA) frequency was calculated using the "copynumber" package in R. The log2CNA thresholds were set to  $\pm 0.3$ , namely,  $-0.3$  for loss and  $0.3$  for gain. A Wilcoxon test was used to plot the CNA frequency distribution graphs [34].

**2.6. Individualized Prognostic Prediction Models.** During the quantification of the risk on individuals in a clinical setting with the integration of multiple risk factors, the nomogram acts as a powerful tool in the assessment. A nomogram was constructed using the survival rate and "RMS" R package, and a correction curve was drawn to evaluate the consistency between the actual and predicted survival rates.

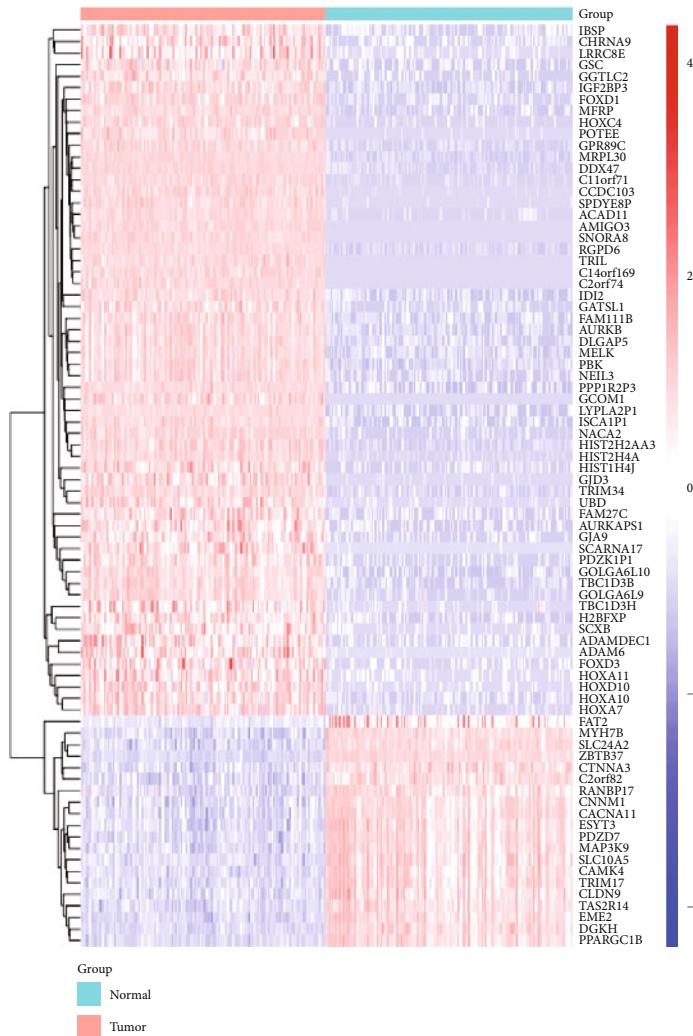
**2.7. Statistics.** A Wilcoxon rank-sum test was used to calculate the significance levels in pairs of groups. A Kruskal-Wallis test was used to compare the gene expression levels between two or more groups. The Benjamini and Hochberg method was used to correct the significance levels. Univariate and multivariate logistic regression models were applied to calculate the hazard ratios (HRs). Predictive performance of the model was evaluated by ROC curve analysis.  $p \leq 0.05$  was considered statistically significant.

### 3. Results

**3.1. Differential Expression Analysis between GBM and Normal Tissues.** We assessed the expression profiles of pre-processed GBM and normal brain tissue sample data downloaded from TCGA and GTEx. A differential expression analysis was performed using the "DEseq2" package in R, the screening threshold was  $\text{FDR} \leq 0.01$ , and the Benjamini and Hochberg correction significance level was  $\text{FC} \geq 2$  OR  $\text{FC} \leq 1/2$ . Three hundred and fifty-seven DEGs were identified. Of these, 266 were upregulated and 91 were downregulated (Table S1). A volcano map was plotted based on the foregoing results (Figure 1(a)). To display the gene expression levels in the tumour and normal brain tissues, we extracted 60 upregulated and 20 downregulated DEGs (Table S1) and used their expression levels to plot a standardized expression profile heat map (Figure 1(b)).

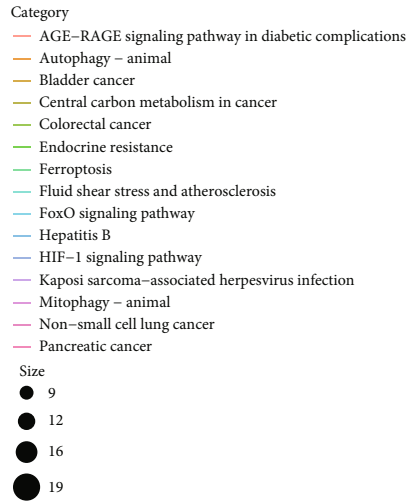
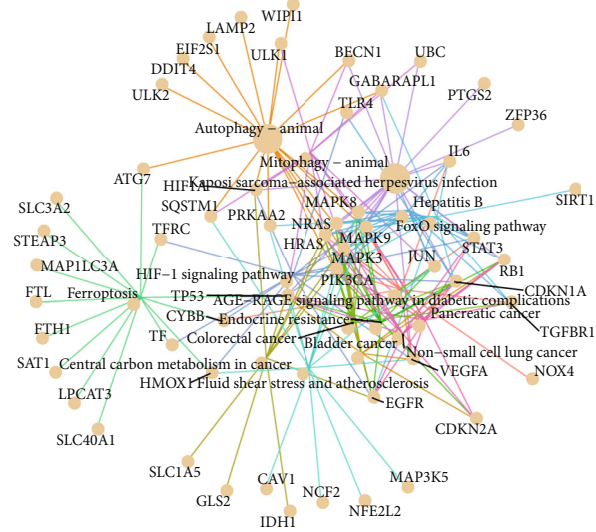


(a)

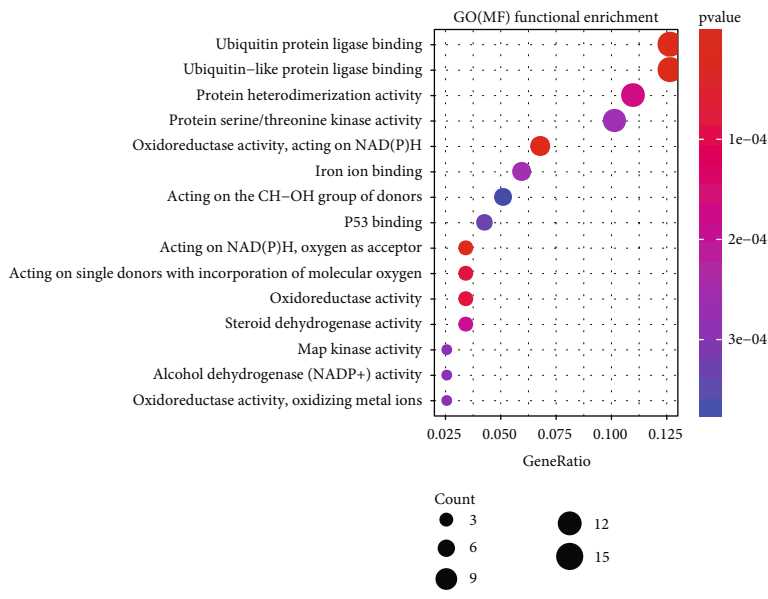


(b)

FIGURE 1: Differential expression analysis between GBM samples and normal brain tissue. (a) Volcano plot showing DEGs between GBM and normal brain tissue. (b) Heatmap showing differences in DEG expression patterns between GBM and normal brain tissue. Red, upregulated; blue, downregulated. GBM: glioblastoma multiforme; DEGs: differentially expressed genes.



(a)



(b)

FIGURE 2: Continued.

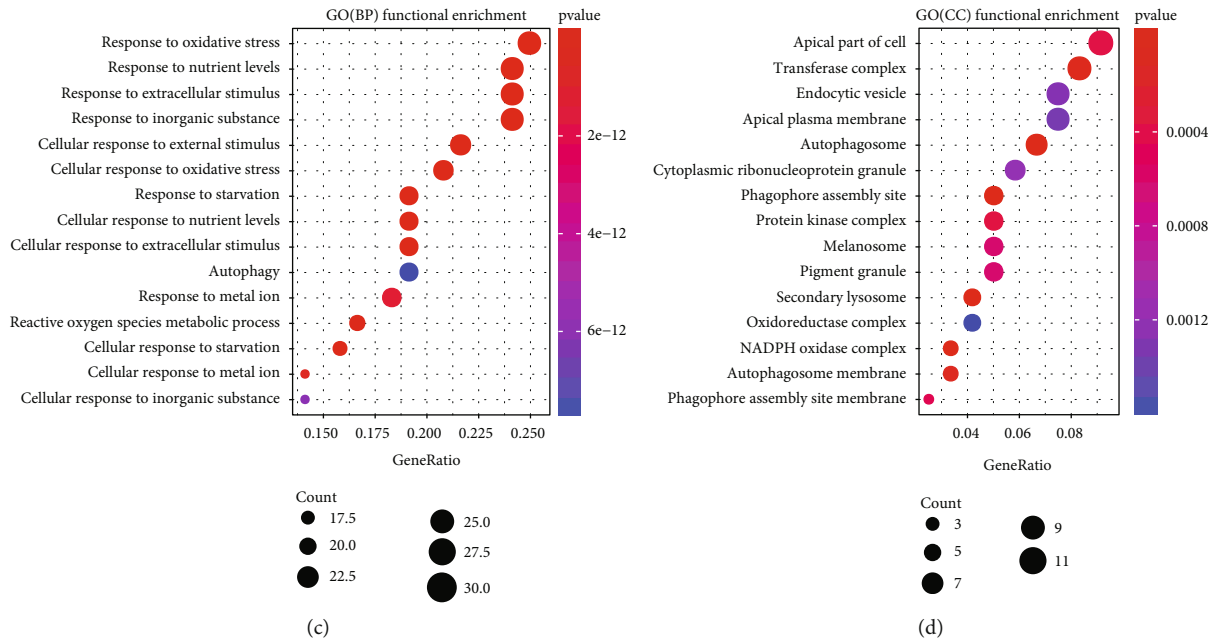


FIGURE 2: Functional enrichment analysis of ferroptosis-related DEGs in GBM samples. (a) KEGG pathway enrichment analysis network for ferroptosis-related DEGs. (b)–(d) GO enrichment analysis of MF, BP, and CC ranked by adjusted  $p$  value ( $p_{\text{adjust}} \leq 0.05$ ), respectively. DEGs: differentially expressed genes; KEGG: Kyoto Encyclopedia of Genes and Genomes; GBM: glioblastoma multiforme; GO: Gene Ontology; MF: molecular function; BP: biological process; CC: cellular component.

**3.2. Candidate Ferroptosis Geneset1 (*cd-Ferr-Geneset1*) Was Obtained Based on GO and KEGG Pathway Analyses of Ferroptosis-DE Genes.** A KEGG function enrichment analysis was performed on the DEGs identified in the GBM and normal brain tissue samples. We screened significantly enriched pathways (Figure S1). The DEGs were enriched in pathways related to cell growth and development, transcriptional regulation, and calcium signalling, such as “cell cycle,” “p53 signalling,” “Toll-like receptor signalling,” and “calcium signalling” (Figure S1). A GO enrichment analysis showed that the DEGs were not enriched in any iron-related function. Hence, 122 ferroptosis-DE genes were screened from among the DEGs for KEGG and GO enrichment analyses. According to the significance threshold, the top 15 significantly enriched pathways and GO terms were screened out for display. A KEGG functional enrichment analysis showed that the ferroptosis-DE genes were enriched in iron-related pathways, such as “ferroptosis” ( $p = 3.16E - 17$ ; Figure 2(a); Table S2). The GO enrichment analysis showed that the ferroptosis-DE genes were enriched in iron and oxygen consumption-related functions. For example, the GO functions in molecular function included “iron ion binding” ( $p = 2.53E - 04$ ; Figure 2(b); Table S3). The GO functions in biological process include “iron ion transport” ( $p = 5.15E - 08$ ), “iron ion homeostasis” ( $p = 1.97E - 08$ ), “cellular iron ion homeostasis” ( $p = 3.97E - 08$ ), “response to iron ion” ( $p = 7.07E - 07$ ), and “iron ion transmembrane transport” ( $p = 4.70E - 04$ ) (Figure 2(c); Table S4). In terms of cell components, however, no significant iron-related functions were found (Figure 2(d); Table S5). To obtain the *cd-Ferr-Geneset1* (Table S6), we downloaded all pathway and GO term genes from the

MSigDB (V7.2) database. Furthermore, from the KEGG and GO term analysis of ferroptosis-DE genes, we extracted genes as they were enriched in iron and oxygen consumption-related functions.

**3.3. Candidate Ferroptosis Geneset2 (*cd-Ferr-Geneset2*) Obtained Based on Cluster Analysis of Ferroptosis-DE Genes.** Based on the ferroptosis-DE gene expression levels, we used the consensus cluster analysis method on patients with GBM and explore the correlations between clustering category and patient survival time (Figures 3(a) and 3(b)). The optimal clustering effect was realised when the patients with GBM were divided into four subtypes (Figure 3(b)). A survival analysis showed that subtype 4 had relatively longer survival times than subtypes 1 and 3 ( $p = 0.031$  and  $p = 0.055$ , respectively) (Figure 3(c)). We used the “DEseq2” package in R for differential gene expression analysis and compared differential gene expression among the four subtypes. In all cases, the screening threshold was  $FDR \leq 0.05$ , and the Benjamini and Hochberg correction significance level was  $FC \geq 1.5$  OR  $FC \leq 2/3$ . Intersection of the DEGs identified in the four subtypes identified the ferroptosis-DE genes in the GBM samples. These 24 genes were then used as *cd-Ferr-Geneset2* (Table S7). A heatmap of the *cd-Ferr-Geneset2* expression levels in the four ferroptosis subtypes was plotted using the “pheatmap” package in R. The genes in the *cd-Ferr-Geneset2* were significantly differentially expressed among the four subtypes (Table S8–11). We used the “Psych” package in R to conduct a PCA based on the *cd-Ferr-Geneset2* expression levels in the four ferroptosis subtypes. We displayed the first two principal components (PC1 and PC2) contributing to the

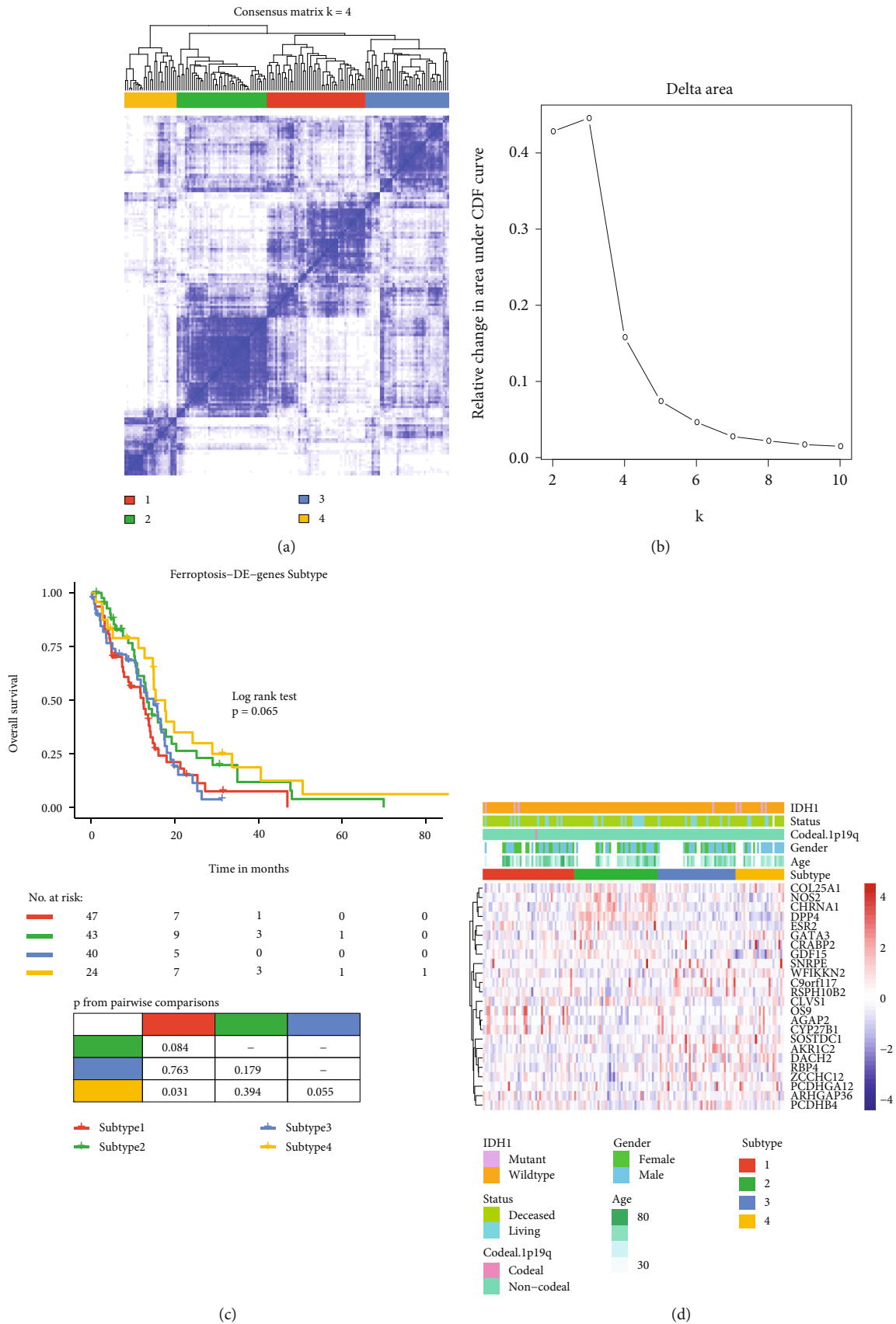


FIGURE 3: Continued.

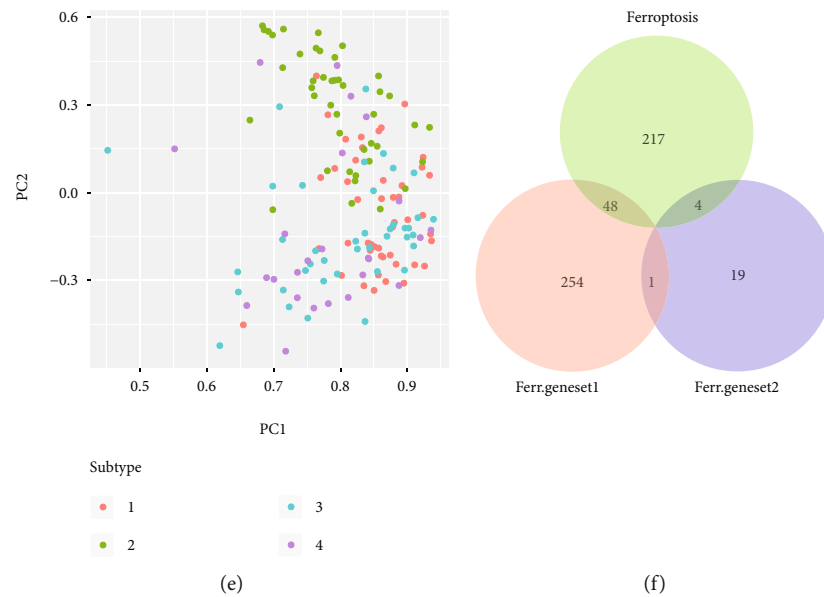


FIGURE 3: Identification of candidate ferroptosis genes in GBM samples. (a) Heatmap showing optimal consensus cluster effect (four subtypes), white (not clustered), and blue (clustered). (b) AUC of cumulative distribution function (c, d, and f). (c) Overall survival of patients among subtypes. (d) Heatmap showing DEG expression levels in four subtypes. (e) PCA showing expression levels in four subtypes. (f) Venn diagram of two categories of newly identified genes (cd-Ferr-Geneset1; cd-Ferr-Geneset2) and known ferroptosis genes. GBM: glioblastoma multiforme; AUC: area under curve; DEGs: differentially expressed genes; PCA: principal component analysis.

majority of the sample characteristics. The genes in the cd-Ferr-Geneset2 were localised mainly to PC1 for all four ferroptosis subtypes. Subtype 2 had a higher degree of discrimination than the other subtypes (Figure 3(e)). By combining cd-Ferr-Geneset1, cd-Ferr-Geneset2, and known ferroptosis genes (Table S12), we found that forty-eight genes intersected between ferroptosis genes and cd-Ferr-Geneset1, whereas four genes intersected between ferroptosis genes and cd-Ferr-Geneset2. Only one gene intersected between cd-Ferr-Geneset1 and cd-Ferr-Geneset2 (Figure 3(f)).

**3.4. Weighted Gene Coexpression Network Analysis (WGCNA) Based on Ferroptosis Geneset.** The union of known ferroptosis genes, cd-Ferr-Geneset1, and cd-Ferr-Geneset2 was plotted to generate a ferroptosis geneset consisting of 543 genes (Figure 3(f)). A weighted gene network was constructed by calculating Pearson's correlation coefficient between gene pairs. The soft threshold was calculated to the  $n^{\text{th}}$  power operation of Pearson's correlation coefficient. Based on the soft threshold distribution diagram and the mean connectivity, we obtained a power of five (Figure 4(a)). A hierarchical cluster dendrogram was plotted using the Pearson's correlation coefficients for gene pairs. Different colours and cluster tree branches represent different modules and gene modules, respectively. We divided the genes into 16 modules (Figures 4(b) and 4(c); Table 3). Based on their weighted Pearson's correlation coefficients, the genes were classified by expression pattern. Genes with similar patterns were grouped into a single module. We found that most of the modules had a significance level of approximately 0.1. The mean significance level of the green-yellow module was the highest (0.165) (Figure 4(c)).

A correlation analysis between the modules and clinical features revealed that the green-yellow module had the strongest positive correlation with the clinical feature age ( $r = 0.25$ ;  $p = 0.009$ ; Figure 4(d)). In the present study, then, the green-yellow module was selected for the subsequent downstream analysis. When we calculated the correlations between the green-yellow module and age separately, we identified significant positive correlations between both modules ( $r = 0.2$ ;  $p = 0.0011$ ; Figure 4(e)).

**3.5. Construction of a Multifactor Regulatory Network of Ferroptosis Key Hub Genes.** Twenty-nine genes were screened according to the threshold of the correlation coefficient of MM and GS. Based on the degrees of the known PPI interaction network and using degree  $\geq 5$  as the threshold, 194 hub genes were screened (Figure 5(a)). There were 26 intersections between the hub nodes genes and the key module genes (Figure S2). These intersections were regarded as the ferroptosis key hub genes in GBM. Regulatory relationship data for the TFs and noncoding RNAs (miRNAs and lncRNAs) on the mRNAs were downloaded from known databases to identify the regulatory factors of ferroptosis key hub genes in GBM. Cytoscape was used to construct a multifactor regulatory network of the ferroptosis key hub genes (Figure 5(b); Table S13).

**3.6. Univariate Cox Regression Analysis Screened Key Hub Genes Related to GBM Prognosis.** The patients with GBM were grouped according to the median expression levels of ferroptosis key hub genes and known ferroptosis genes. The relationships between the expression levels of the prognostic key genes and patient survival time were explored using the log-rank test. The analysis demonstrated that high



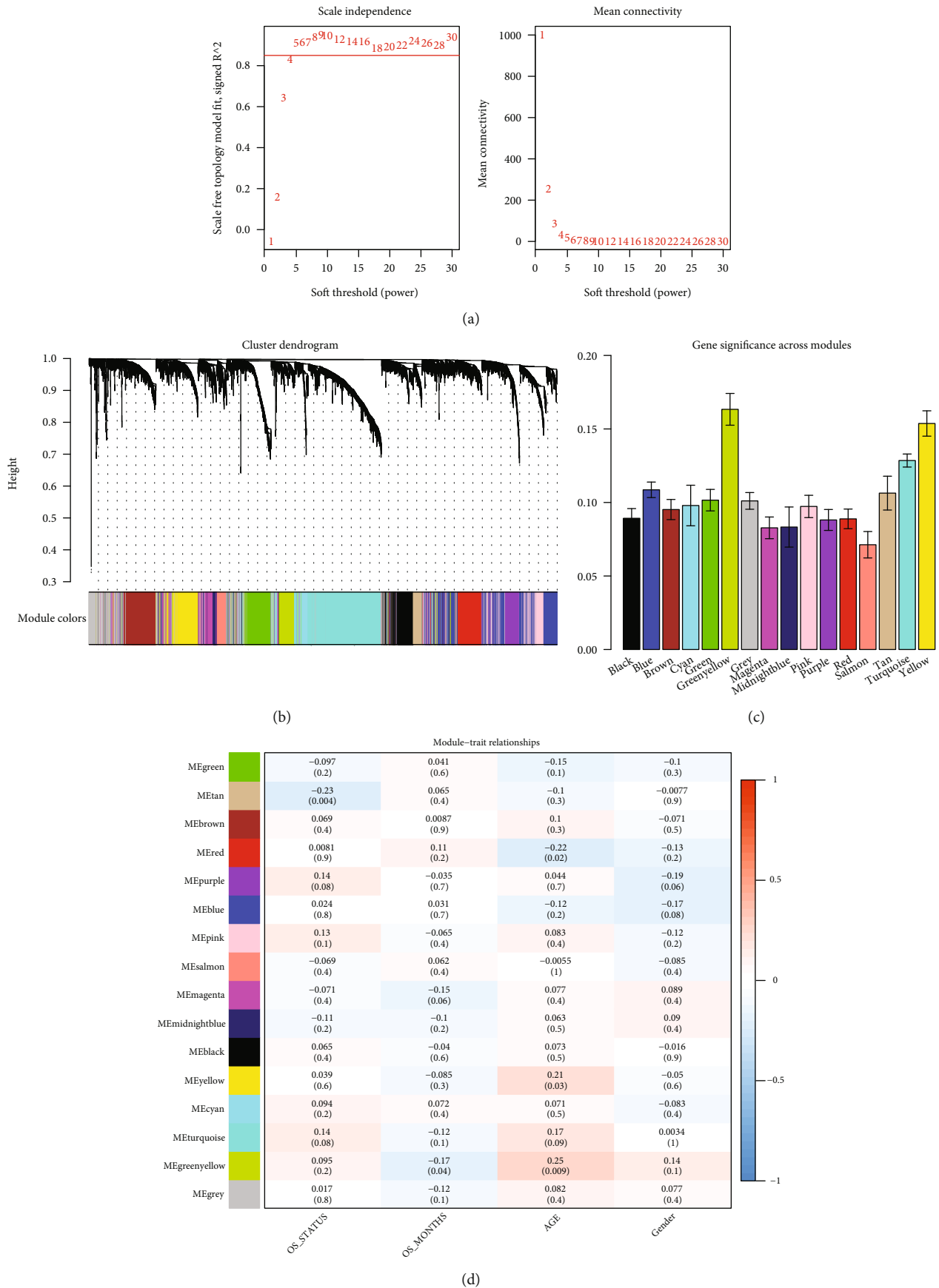


FIGURE 4: Continued.

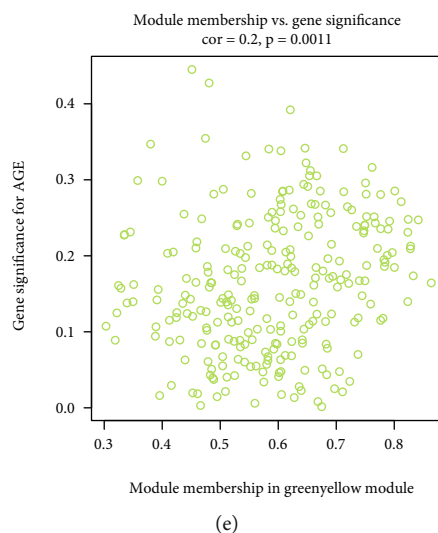


FIGURE 4: WGCNA of gene expression level in GBM. (a) Distribution diagram of soft threshold and mean connectivity. (b) Hierarchical cluster displaying various modules. Different colours represent genes in different modules; grey = unclassified genes. (c) Gene significance across modules. Average correlations among various module genes and clinical phenotypes. (d) Association analysis of module genes and clinical phenotypes; red (positive correlation), and blue (negative correlation). (e) Scattergram of correlations between green-yellow modules and the clinical age phenotypes. WGCNA: weighted gene coexpression network analysis; GBM: glioblastoma multiforme.

TABLE 3: Gene number of each module in WGCNA.

| Module type   | Number |
|---------------|--------|
| Black         | 361    |
| Blue          | 864    |
| Brown         | 433    |
| Cyan          | 99     |
| Green         | 378    |
| Green-yellow  | 265    |
| Grey          | 699    |
| Magenta       | 276    |
| Midnight blue | 85     |
| Pink          | 338    |
| Purple        | 273    |
| Red           | 362    |
| Yellow        | 402    |
| Turquoise     | 1,201  |
| Tan           | 183    |
| Salmon        | 131    |

expression levels of certain known ferroptosis-related genes and some of ferroptosis key hub genes are associated with significantly worse patient survival time (Figure 6). Other ferroptosis-related genes are listed in Figure S3. Thirteen prognosis-related genes were screened (Figure 7(a)).

**3.7. Construction of a Prognostic Risk Scoring Model for Ferroptosis Key Hub Genes.** A Lasso-logistic regression was used to screen for other prognostic factors and remove redundant ones. The model had optimal performance when

it included five prognostic factors (Figure 7(b)). Hence, they were selected for the subsequent analyses. A Cox regression analysis identified one protective factor (DUOX1) and four risk factors (CDKN1A, GSS, ALOX5, and SQSTM1) (Figure 7(c), Table S14).

**3.8. Evaluation of the Effectiveness of the Risk Scoring Model and Pan-Cancer Analysis.** To evaluate the overall influence of these prognostic factors on patient survival time, a scoring model was constructed based on their expression levels and Cox regression coefficients. We calculated the sample FRGPRS as well (Materials and Methods). The model was used to evaluate the predictive efficacy of TCGA GBM data and the validation dataset (GSE4412) (Table S15). For patient survival time (PFS) in TCGA, FRGPRS was ranked from low to high, and a median score of 0.551 was obtained (Figure 8(a)). The patients were grouped according to median score. Those in the FRGPRS group had significantly worse PFS ( $p = 5.4E - 03$ ; Figure 8(b)). When the scoring model was applied to the GEO dataset, the median FRGPRS was 0.384 (Figure 8(f)). Patients in the high-risk group had significantly worse OS; ( $p = 6.5E - 03$ ; Figure 8(g)). The patient survival status figure was drawn by the FRGPRS and ranked from small to large. Deceased patients had greater FRGPRS than living patients, especially in the TCGA GBM dataset (Figures 8(c) and 8(h)). Heatmaps of the prognostic factors were plotted on TCGA GBM data and GEO validation dataset. Patients with high CDKN1A, GSS, ALOX5, and SQSTM1 expression levels were relatively more likely to be enriched in FRGPRS. By contrast, the expression levels of the protective factor DUOX1 were negatively correlated with patient FRGPRS (Figures 8(d) and 8(i)). These findings



FIGURE 5: Identification of ferroptosis-related hub genes. (a) Screening of ferroptosis-related hub genes by PPI network; red (hub genes), purple (degree > five), and green (degree < five). (b) Multifactor regulatory network of ferroptosis-related hub genes in GBM; red (hub genes), green (lncRNA), purple (miRNA), and blue (TF). PPI: protein-protein interaction; TF: transcription factor.

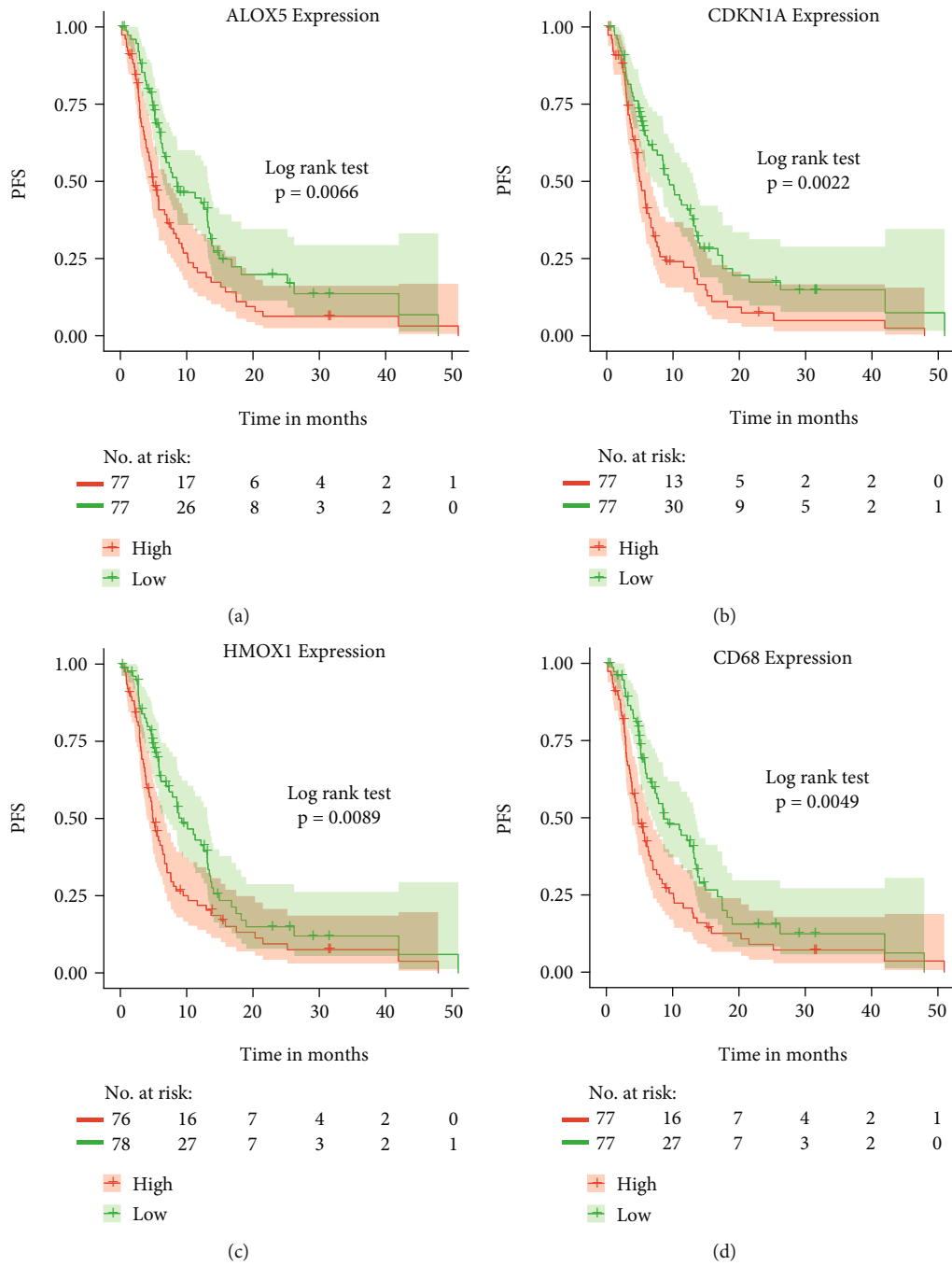


FIGURE 6: Continued.

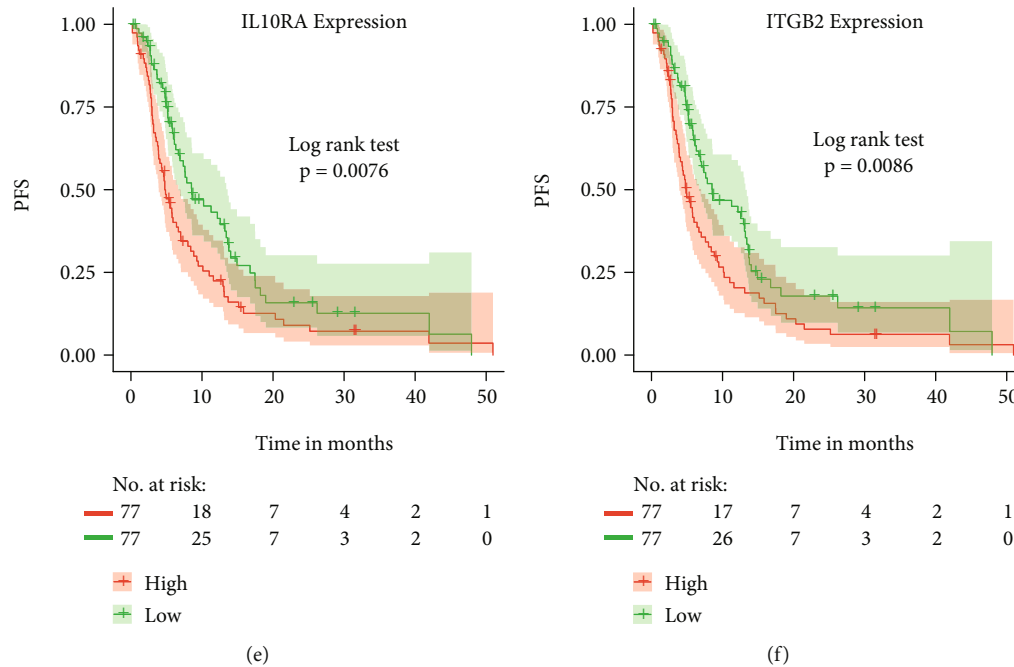


FIGURE 6: Identification of prognostic ferroptosis key hub genes. Prognostic ferroptosis key hub genes in GBM samples were screened using univariate Cox regression analysis and depicted by Kaplan-Meier survival analysis. (a)–(c) Known ferroptosis-related genes (AIOX5, CDKN1, and AHMOX1). Ferroptosis-related hub genes (CD68, IL10RA, and ITGB2) (d)–(f). GBM: glioblastoma multiforme.

were consistent with the effect of the expression level of a single gene on patient survival (Figures 6 and S3). We used the ROC curve to evaluate the prediction efficacy of the model. The areas under the curve (AUC) for one-year survival time were 0.69 (TCGA GBM dataset) and 0.68 (GEO validation data set) (Figures 8(e) and 8(j)). To characterise the prognostic efficacy of FRGPRS in pancreatic cancer, we downloaded multicentre data, including GBM (TCGA data, 155 samples; GEO data, 85 samples), LGG (514 samples), and BLCA (407 samples), calculated the FRGPRS, and explored the impact of the score on patient survival time (OS). Patients with high FRGPRS in TCGA LGG showed significantly worse OS ( $p = 0.0018$ ; log-rank test; Figure 7(d)). A Cox regression analysis demonstrated that FRGPRS was a significant risk factor, and it affected the OS of patients with LGG (HR = 1.11; 95% CI [1.05, 1.18];  $p = 2E - 04$ ; Figure 7(f)). FRGPRS also influenced the OS of patients with GEO GBM as a significant risk factor (HR = 1.1; 95% CI [1.01, 1.19];  $p = 0.019$ ; Figures 7(f) and 8(g)). However, FRGPRS was not correlated with patient OS for TCGA GBM or BLCA (Figures 7(e) and 7(f), and S4A). Compared with other models [1, 2, 17], our ferroptosis model had superior prognostic efficacy. The AUC of our model was 0.69, whereas those of previous models were 0.65 and 0.66, respectively (Figure S4B).

**3.9. Differential Analysis of FRGPRS in Grouping Genomic and Clinical Characteristics.** The genomic characteristics included IDH1 mutation, 1p/19q co-del, and TP53 mutation status. The clinical characteristics included gender, radiotherapy, and age. Patients with IDH1 mutation had significantly

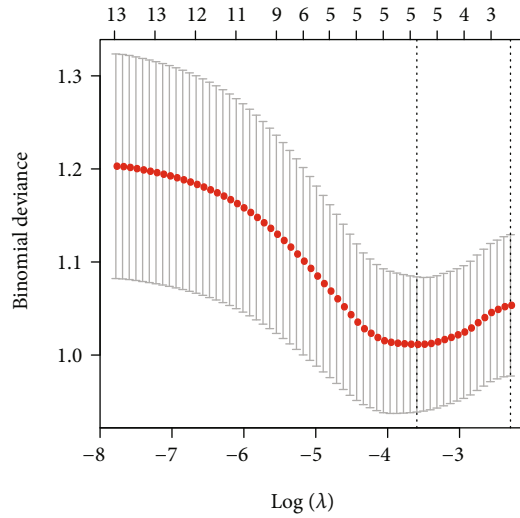
lower FRGPRS than those with wildtype IDH1 ( $p = 0.0069$ ; Wilcoxon rank-sum test; Figure 9(a)). Moreover, the patient with 1p/19q co-del had comparatively low FRGPRS. As there was only one patient of this type, an accurate significance level could not be calculated (Figure 9(b)). Patients with TP53 mutation had significantly lower FRGPRS ( $p = 6.3E - 04$ ; Figure 9(a)) than patients with wildtype TP53. Patients aged 60 years ( $p = 0.039$ ) or subjected to radiotherapy ( $p = 0.052$ ) had relatively reduced FRGPRS (Figures 9(d) and 9(e)). No correlation was found between gender and FRGPRS ( $p = 0.85$ ; Figure 9(f)). HRD scores, mutation and neoantigens loads, fractions altered, chromosome instability, and stemness indices (mRNAsi) were obtained from published studies. FRGPRS associated with genomic characteristics was reflected in Figure S5.

### 3.10. FRGPRS Tumour Immune Microenvironment Analysis.

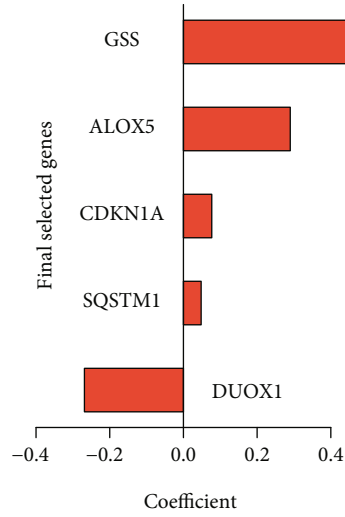
There were various overall immune cell infiltration scores among the high- and low-FRGPRS groups ( $p < 2.2E - 16$ ; Figure 10(a)). In addition, patients with high FRGPRS had higher infiltration scores for M0 macrophages ( $p < 0.05$ ), M2 macrophages ( $p < 0.01$ ), activated mast cells ( $p < 0.05$ ), and monocytes ( $p < 0.05$ ; Figure 10(a)). By contrast, patients with low FRGPRS had higher infiltration scores for resting mast cells ( $p < 0.01$ ), CD8<sup>+</sup> T cells ( $p < 0.05$ ), and follicular helper T cells ( $p < 0.01$ ; Figure 10(a)). We estimated the immune, stromal, and tumour purity (ESTIMATE) scores based on the stromal: immune cell ratios. Patients with high FRGPRS had significantly higher stromal cell ( $p = 7.1E - 10$ ; Figure 10(b)), immune cell ( $p = 2.9E - 12$ ; Figure 10(c)), and tumour purity ( $p = 4.9E - 12$ ; Figure 10(d)) scores than those with low FRGPRS.

| Factors  | Hazard ratio<br>(95% CI) | P value |
|----------|--------------------------|---------|
| DUOX1    | 0.787 (0.657–0.943)      | 0.0095  |
| IL6      | 1.146 (1.048–1.254)      | 0.003   |
| GDF15    | 1.16 (1.039–1.295)       | 0.0084  |
| ALOX5    | 1.27 (1.076–1.499)       | 0.0047  |
| CDKN1A   | 1.275 (1.102–1.474)      | 0.0011  |
| TLR2     | 1.279 (1.073–1.524)      | 0.0059  |
| SAT1     | 1.323 (1.097–1.595)      | 0.0033  |
| MAP1LC3A | 1.348 (1.087–1.672)      | 0.0065  |
| AIFM2    | 1.42 (1.112–1.813)       | 0.0049  |
| SQSTM1   | 1.43 (1.1–1.858)         | 0.0075  |
| CARS     | 1.522 (1.112–2.083)      | 0.0087  |
| SRXN1    | 1.541 (1.172–2.026)      | 0.002   |
| GSS      | 1.888 (1.286–2.773)      | 0.0012  |

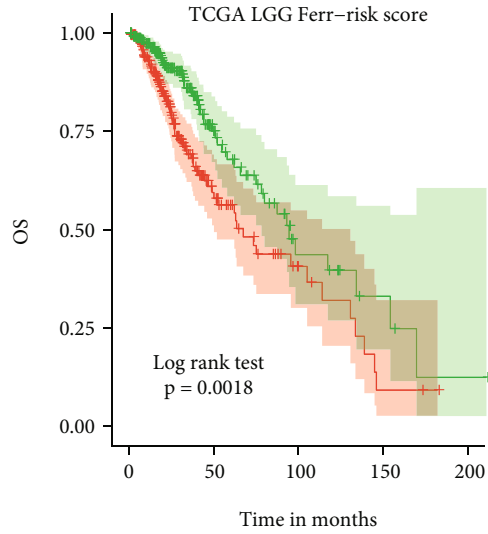
(a)



(b)



(c)



(d)

FIGURE 7: Continued.

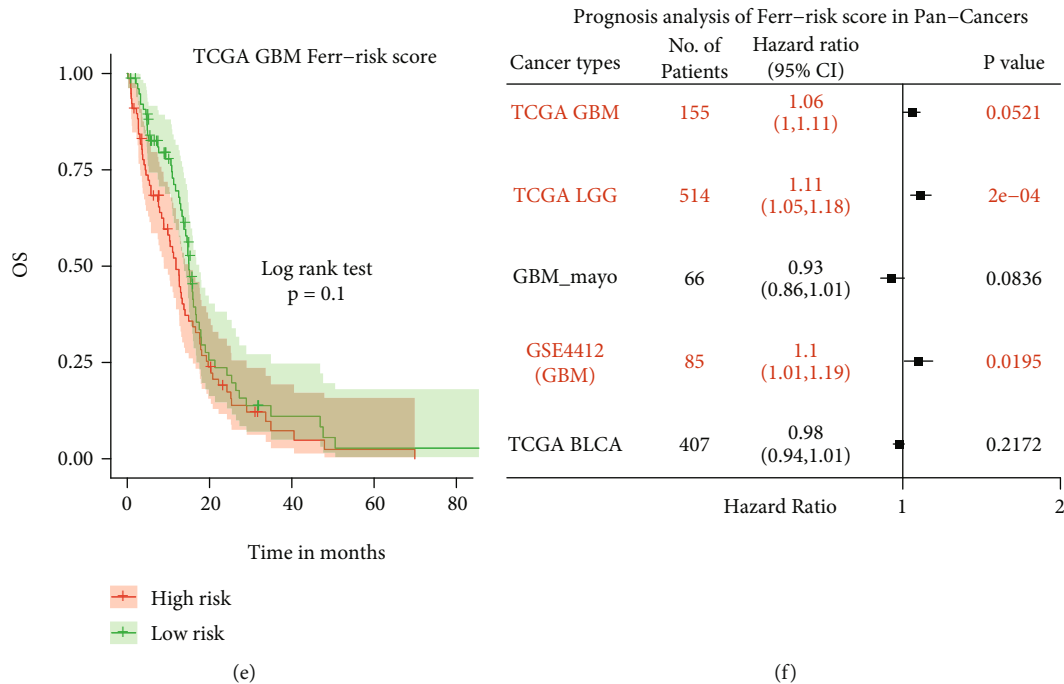


FIGURE 7: Construction of FRGPRS model for GBM. (a) Univariate Cox regression analysis. Forest plot of associations among 13 prognosis factors and GBM survival. Genes with  $HR > 1$  are risk factors, whereas genes with  $HR < 1$  are protective factors. (b) Identification of five-gene OS risk signature using Lasso-logistic regression analysis. (c) Lasso coefficient spectrum of five genes in GBM. (d)–(f) Prognostic analysis of FRGPRS in pan-cancers. (d) Kaplan-Meier survival analysis for TCGA LGG. (e) Kaplan-Meier survival analysis for TCGA GBM. (f) Cox regression analysis outcomes of pan-cancers. GBM: glioblastoma multiforme; OS: overall survival; Lasso: the least absolute shrinkage and selection operator.

**3.11. FRGPRS Genomic Mutation and CNA Analyses.** Silent mutations are removed while nonsynonymous mutations playing roles in protein-coding genes are retained. Thirty genes ranking from high- to low-mutation frequency were extracted and displayed using the “Maftools” package in R. PTEN (34%) had the highest mutation frequency. It included several mutations in GBM, including Nonsense\_Mutation, Frame\_Shift\_Del, and Missense\_Mutation (Figure 11(a)). PTEN is more likely to be mutated in the high-risk (41.6%) than in the low-risk (25.7%) patients. By contrast, for TP53 (34%), the major mutation type was Missense\_Mutation, and it was more likely to occur in low-risk patients. We also explored the relationship between edge disturbance characteristic subtypes and CNA frequency. We used the “copynumber” package in R to plot the CNA frequency for each subtype. This parameter differed between high- and low-risk groups (Figures 12(b) and 12(c);  $p < 2 \cdot 2E - 16$ ; Wilcoxon test).

**3.12. Association of FRGPRS with GBM Drug Resistance and Immunotherapy.** To determine whether FRGPRS could serve as an immunotherapy response marker, we extracted transcriptome and clinical data for urothelial carcinoma patients treated with the PD-L1 blocker atezolizumab. High FRGPRS was associated with poor patient outcome ( $p = 0.028$ ; log-rank test; Figure 12(a)). Patients in the high-risk group had comparatively lower atezolizumab response rates (CR/PR = 13.2%), whereas those in the low-risk group had relatively higher atezolizumab response

rates (CR/PR = 16.1%; Figure 12(b)). The atezolizumab response (CR/PR) and nonresponse (SD/PD) groups differed in terms of their FRGPRS ( $p = 0.0017$ ; Kruskal-Wallis test; Figure 12(c)). Patients with SD and PD had higher FRGPRS than patients with CR and PR. Ridge regression was used to predict drug sensitivity in patients based on cell line expression and drug response data downloaded from GDSC. We examined the correlations between the high- and low-risk groups and their drug response patterns. Low-risk GBM patients were comparatively more sensitive to temozolomide ( $p = 4.9E - 03$ ; Figure 12(d)), cisplatin ( $p = 2E - 05$ ), the PARP inhibitor olaparib ( $p = 0.025$ ), and anthracycline/taxanes. Low-risk GBM patients had significantly lower levels IC50 for doxorubicin ( $p = 0.013$ ) and docetaxel ( $p = 0.0049$ ). By contrast, high-risk GBM patients showed lower IC50 for imatinib ( $p = 4.9E - 10$ ) (Figure 12(d)). In addition, the response patterns of patients with low FRGPRS that were sensitive to zibotentan ( $p = 1.8E - 06$ ) and gemcitabine ( $p = 3.9E - 04$ ) were consistent with those for temozolomide (Figure 12(d)).

**3.13. Independent Prognostic Factor Analysis of FRGPRS.** FRGPRS was applied to TCGA GBM and GEO samples in univariate Cox analyses. FRGPRS ( $\log^2 HR = 0.15$ ; 95% CI [0.07, 0.23];  $p = 0.0024$ ; Figure 13(a)) and age ( $\log^2 HR = -0.03$ ; 95% CI [0, -0.05];  $p = 0.019$ ) were significant risk factors influencing GBM patient survival. Moreover, the radiotherapy status of patients with GBM positively affected

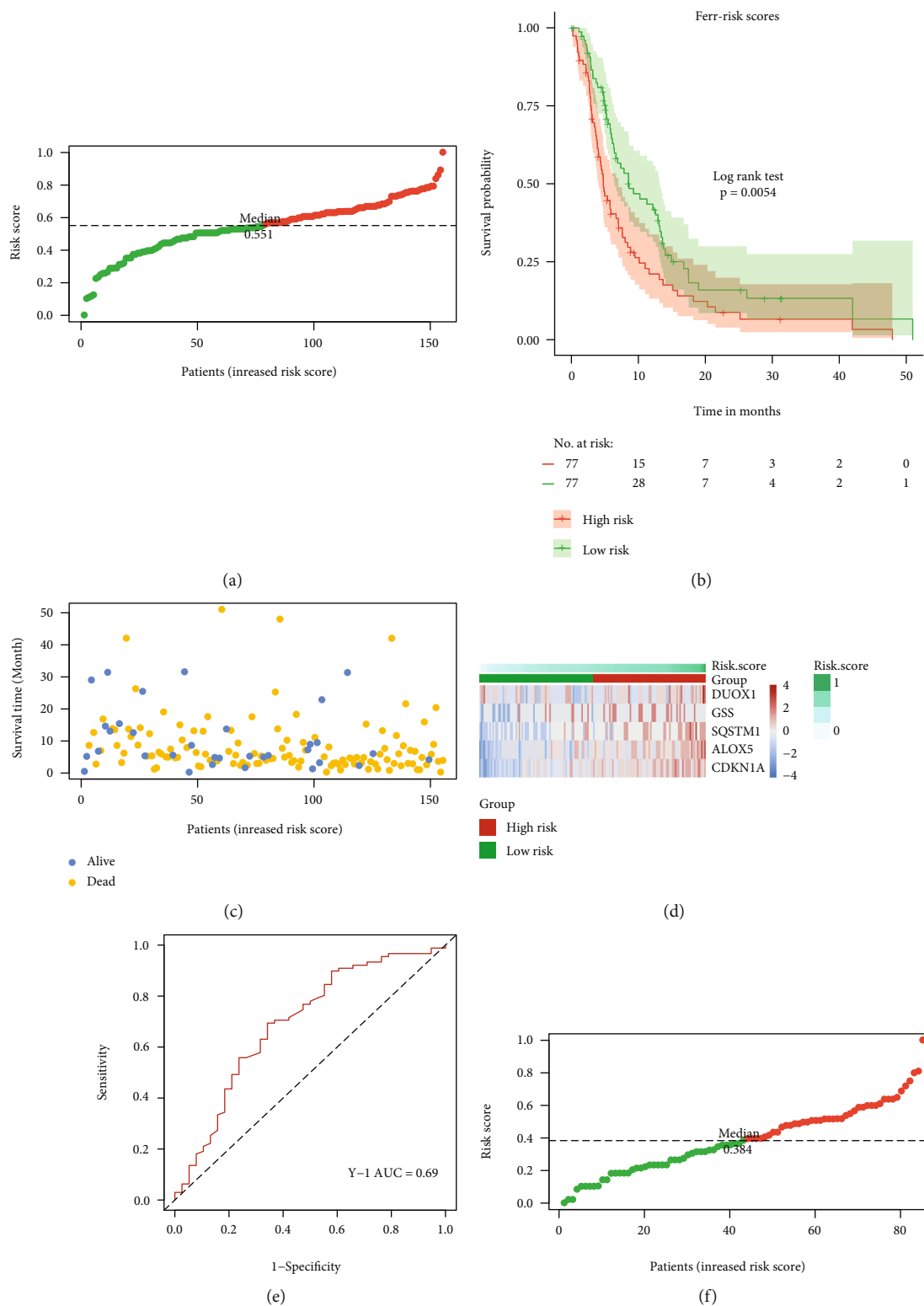


FIGURE 8: Continued.



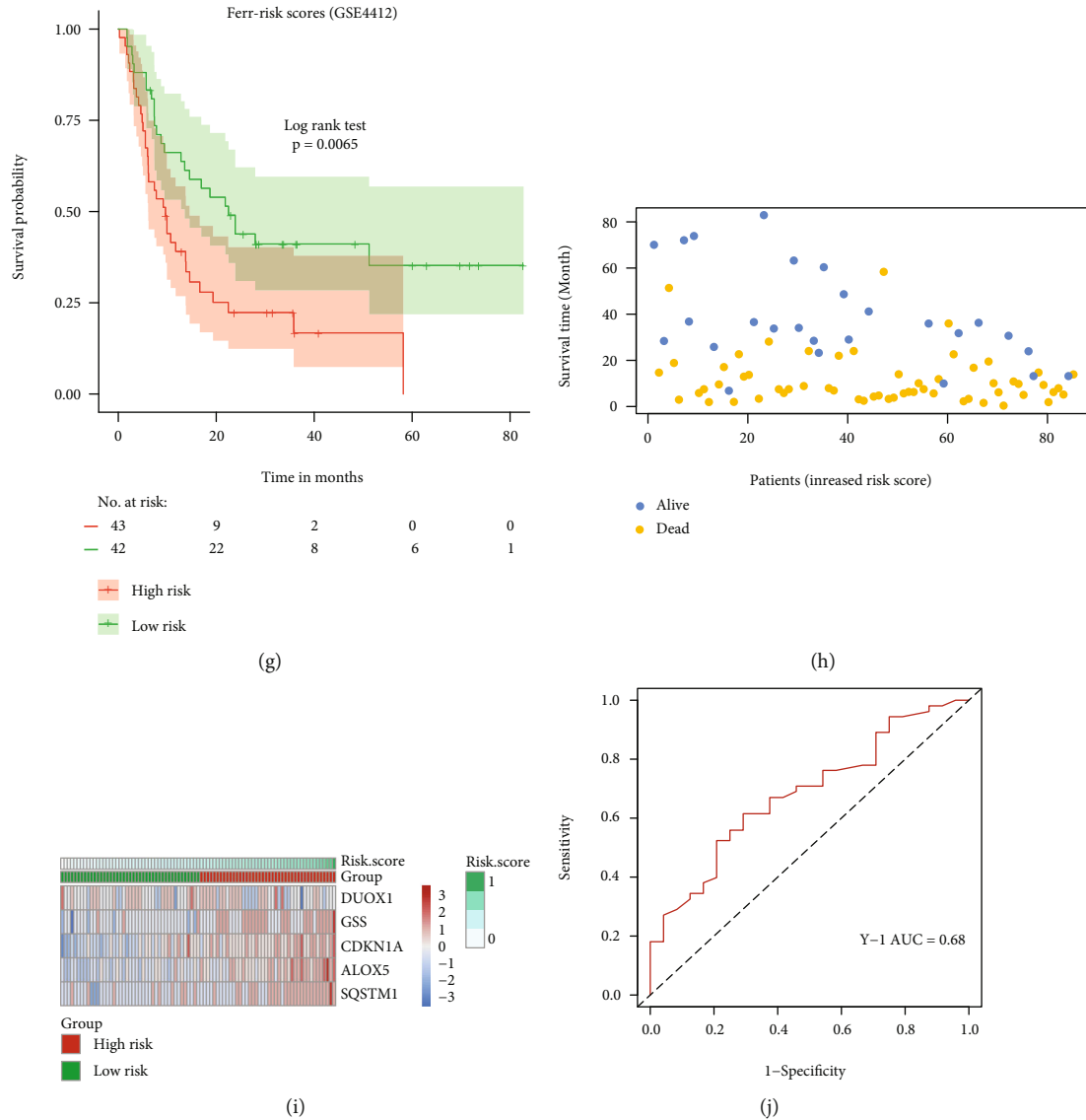


FIGURE 8: Efficiency evaluation of FRGPRS model for GBM. (a) and (e) Evaluation with TCGA GBM. (f) and (j) Evaluation with GEO validation set (GSE4412). (a) and (f) distribution diagram of two patient FRGPRS datasets. Groups higher than median are high-risk, whereas those lower than median are low-risk datasets. (b) and (g) Kaplan-Meier survival analysis of two patient FRGPRS datasets. (c) and (h) Distribution diagram of two survival FRGPRS datasets. (d) and (i) Expression levels of various prognostic factors in FRGPRS. (e) and (j) ROC curve of two survival FRGPRS datasets. GBM: glioblastoma multiforme; RCO: receiver operator characteristic.

patient survival ( $\log^2HR = -1.23$ ; 95% CI  $[-2.02, -0.44]$ ;  $p = 0.0024$ ; Figure 13(a)). After adjusting for age, sex, race, and radiotherapy status, a multivariate Cox regression analysis showed that FRGPRS was an independent risk prognostic factor influencing patient survival ( $HR = 1.13$ ; 95% CI  $[1.037, 1.23]$ ;  $p = 0.005$ ; Figure 13(b)). Radiotherapy status was also an independent protective prognostic factor ( $HR = 0.36$ ; 95% CI  $[0.143, 0.89]$ ;  $p = 0.027$ ). FRGPRS was applied to the validation set (GEO) and indicated to be a significant risk factor ( $\log^2HR = 0.14$ ; 95% CI  $[0.02, 0.25]$ ;  $p = 0.0195$ ; Figure 13(c)). Age, tumour grade, and GBM subtype were significant risk factors affecting patient survival (age:  $\log^2HR = 0.03$ ; 95% CI  $[0, 0.06]$ ;  $p = 0.028$ ; tumour grade:  $\log^2HR = 1.94$ ; 95% CI  $[0.97, 2.91]$ ;  $p = 1E - 04$ ;

GBM subtype:  $\log^2HR = 2.95$ ; 95% CI  $[1.87, 4.02]$ ;  $p < 0.0001$ ; Figure 13(c)). After correcting for age, tumour grade, and GBM subtype, however, the multivariate Cox regression analysis showed that the influence of FRGPRS was not significant ( $p = 0.48$ ; Figure 13(d)).

**3.14. FRGPRS Nomogram.** Using the FRGPRS, TP53/IDH1/EGFR mutation status, age, gender, and radiotherapy status data, a nomogram for the clinical analysis of patients with GBM was generated with the “RMS” package in R. In this study, the *c*-index calculated after 500 iterations is 0.683. For instance, if one patient had FRGPRS = 0.6 (points = 52), age = 50 (points = 43), TP53 mutation status = wildtype (points = 10), IDH1 mutation status = wildtype (points = 58),

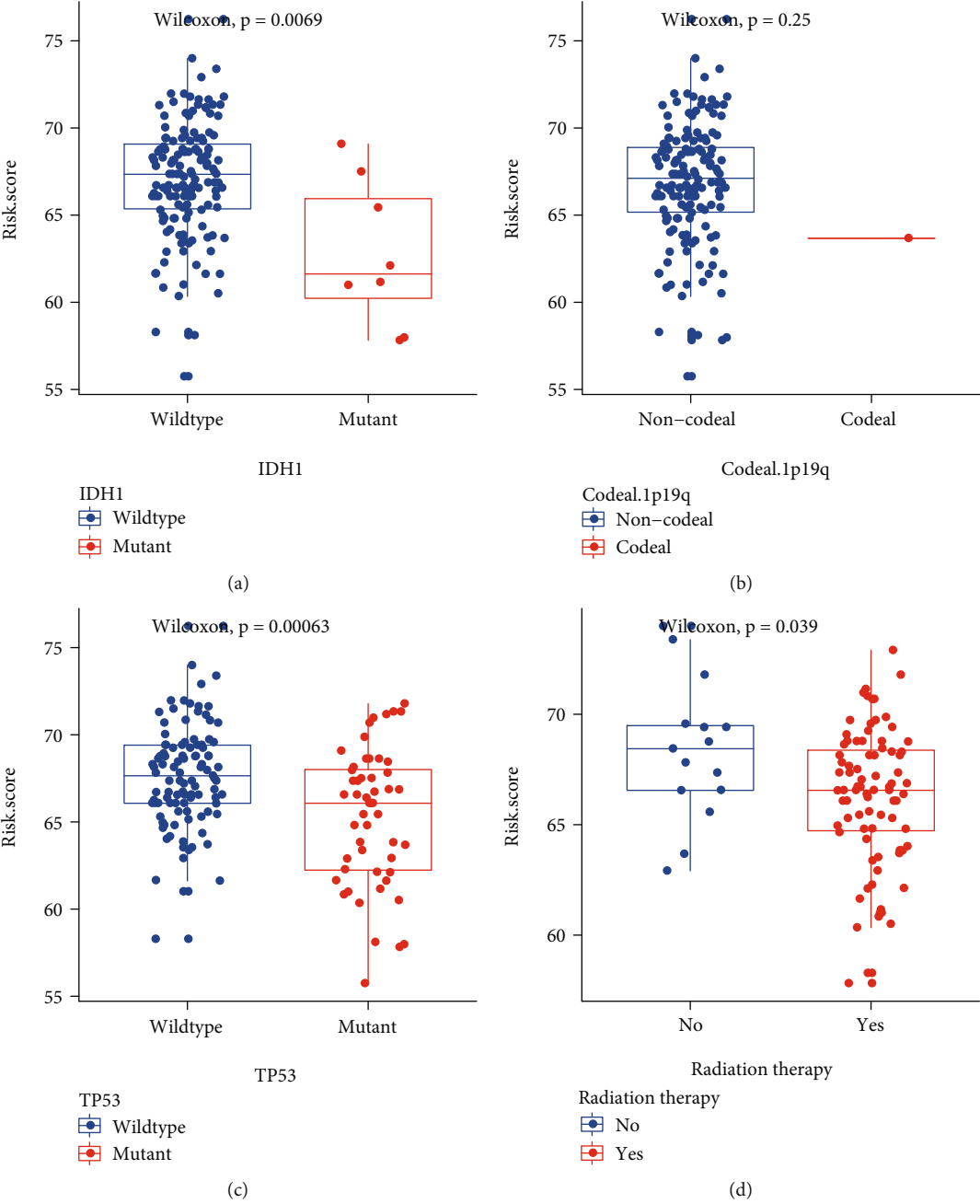


FIGURE 9: Continued.

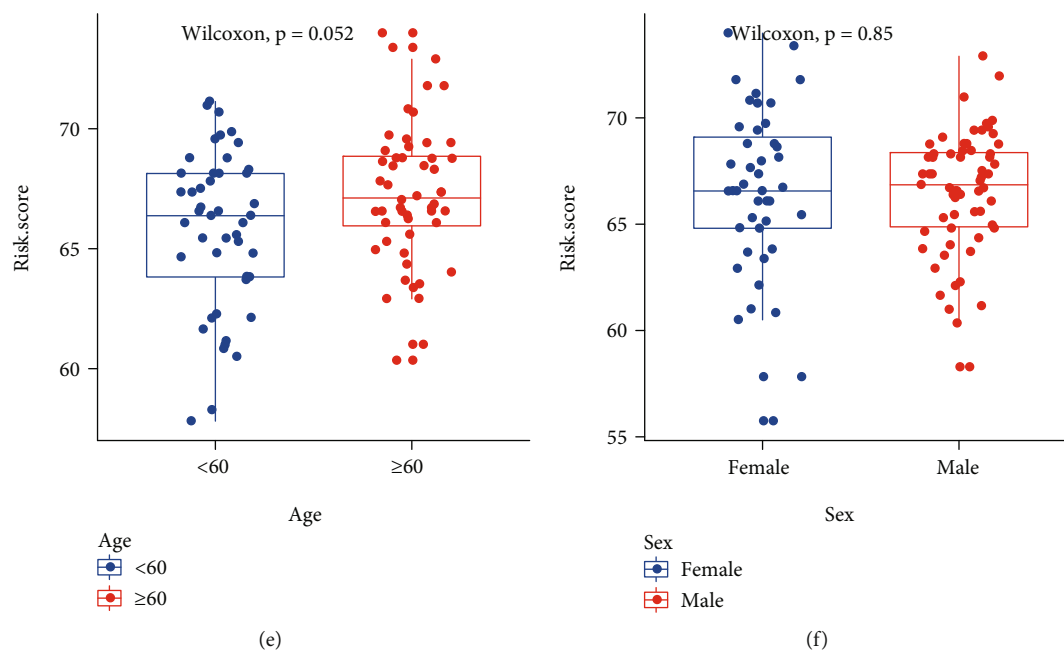


FIGURE 9: FRGPRS associated with genomic mutation and clinical characteristics. (a)–(c) Box plots depicting differences among patients with IDH1 mutation (a), 1p/19q co-del (b), and TP53 mutation (c). (d)–(f) Box plots depicting differences among patients according to radiotherapy (d), age (e), and sex (f). GBM: glioblastoma multiforme.

EGFR mutation status = wildtype (points = 12), and sex = female (points = 10), then points = 185. The 1.5-year, 2-year, and three-year survival rates would be 22%, 17%, and 15%, respectively (Figure 14). A calibration curve was plotted for the nomogram to compare between the actual and predicted risk at years one and a half, two, and three. The curves for years two and three approximated the ideal line (Figure 14(b)). A decision curve analysis was conducted based on the TP53 mutation state. The patient with wildtype TP53 had comparatively superior net benefit (Figure 14(c)). If we choose to diagnose and treat GBM with a predicted probability of 50%, then 5/100 patients with TP53 mutation will benefit from it without reducing the benefit to other patients. However, 7/100 patients with wildtype TP53 will benefit from it without decreasing the benefit to other patients (Figure 14(c)). Graphical abstract is for comprehensive characterization of FRGPRS groups in GBM (Figure 15).

#### 4. Discussion

In the present study, we comprehensively evaluated ferroptosis-related genes and their correlations with patient prognosis, drug resistance, immune infiltration, immunotherapy response, and gene mutation in GBM. As prognosis and survival are poor for GBM, concerted efforts have been made to improve quality of life and clinical benefit for GBM patients. To these ends, we constructed a prognostic risk model of five ferroptosis-related genes in patients with GBM. It was based on the PFS in TCGA chart and was validated with a GEO dataset. The calibration curve indicated that the prediction effect for years two and three was relatively good (Figure 14(b)). High-FRGPRS levels indicated

poor prognosis and insensitivity to first-line chemotherapy in GBM patients. Immunotherapy results revealed that the anti-PD-L1 response to urothelial cancer was comparatively more sensitive in low-risk patients. FRGPRS was significantly correlated with CAN and reflected the predictive power of gene mutation and immune infiltration, and these were closely related to clinical features, outcome, recurrence, and immune function.

There is growing evidence to suggest that ferroptosis is indispensable in eradicating cancer cells and that ferroptosis sensitivity differs among cancer types [35]. FRGPRS comprises five genes, namely, one protective factor (dual oxidase 1; DUOX1) and four risk factors (CDKN1A, GSS, ALOX5, and SQSTM1). DUOX1 is normally expressed in epithelial cells and plays an important role in the immune response [36]. DUOX1 silencing frequently occurs in epithelial-derived cancers and correlates with positive prognosis in certain tumours. However, DUOX1 expression levels in GBM are unknown [37–39]. Conditional DUOX1 overexpression could serve to evaluate the correlation between DUOX1 silencing and cancer progression or response to therapy [40]. Recent studies have revealed that DUOX1 suppression in cancer is driven mainly by hypermethylation of its promoter. Hence, DNA methyltransferase inhibition may be a promising approach toward recovering DUOX1 expression [37–39]. Defective cell cycle control is a common cause of tumorigenesis. CDKN1A is a prognostic marker for ferroptosis-related GBM [25]. CDKN1A is transcriptionally controlled by p53-dependent and p53-independent pathways and may regulate cell migration, DNA repair, and DNA reprogramming during induced pluripotent stem cell generation [40]. CDKN1A can act as a tumour suppressor or oncogene, depending on the cellular context [41]. The

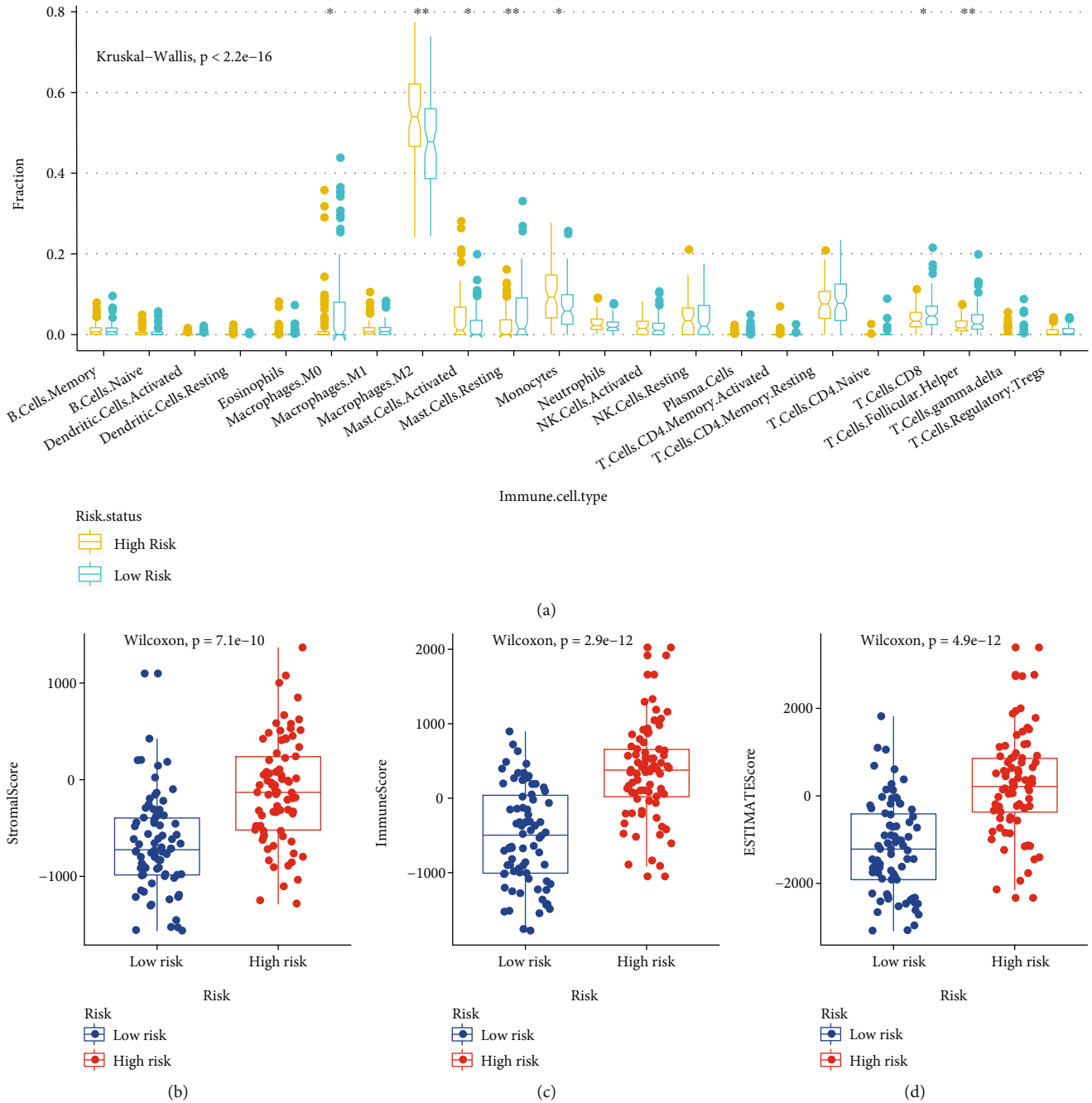


FIGURE 10: FRGPRS associated with TIME. (a) Infiltration abundance level distribution of 22 immune cell types in high- and low-risk groups ( $*p < 0.05$  and  $**p < 0.01$ ). (b)–(d) Box plots diagram showing differences in (c) stromal score, (d) immune score, and (e) tumour purity between high- and low-FRGPRS groups. TIME: tumour immune microenvironment.

GPX4-GSS/GSR-GGT axis is a crucial target of ammonium ferric citrate-induced ferroptosis. Interactions between the rapamycin kinase and GPX4 targets may regulate autophagy-dependent ferroptosis in cancer cells. GPX4 downregulation enhances sensitivity to chemotherapy by promoting ferroptotic cell death [42, 43]. Lipid peroxidation is positively regulated by ALOX5 and contributes to ferroptotic cell death. Here, differential ALOX5 expression was observed between the high- and low-FRGPRS groups. This discovery was consistent with a previous report [24]. Nrf2

and p62/SQSTM1 jointly contribute to mesenchymal transition and tumour infiltration in GBM [24]. The present study showed that high SQSTM1 expression indicated poor prognosis in GBM.

Significantly higher immune, stromal, and ESTIMATE scores were observed in the high-FRGPRS group than in the low-FRGPRS group. Patients in the former group had comparatively higher immune activity, greater proportions of tumour tissue, and favourable cytolytic immune response. Prior research emphasised the importance of tumour

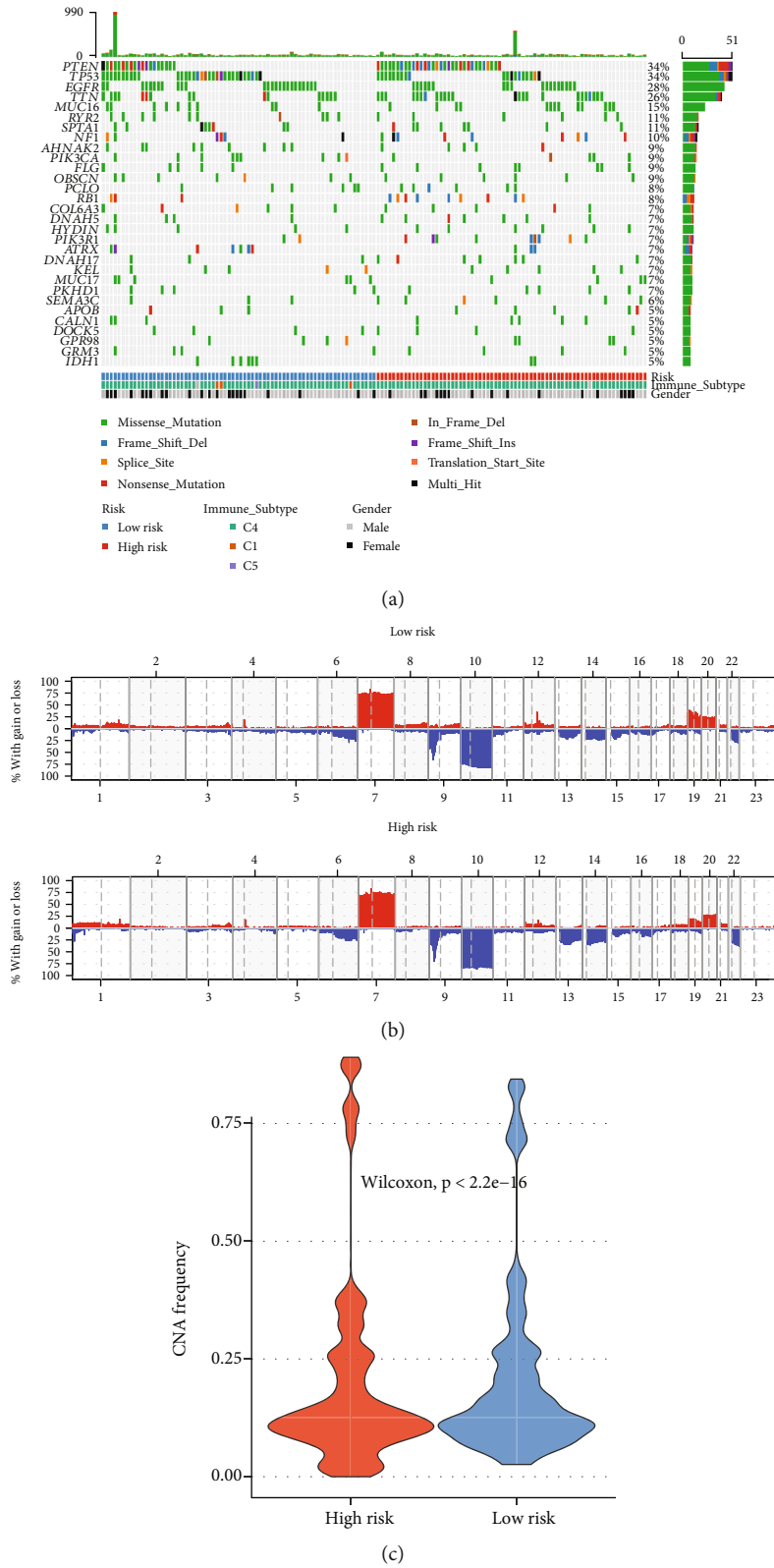


FIGURE 11: Analysis of genomic variation in FRGPRS. (a) OncoPrint diagram showing gene mutation distributions of high- and low-risk FRGPRS. (b) CNA distributions of high- and low-risk FRGPRS. (c) Violin plots depicting correlation analyses between CNA and FRGPRS. CNA: copy number alteration.

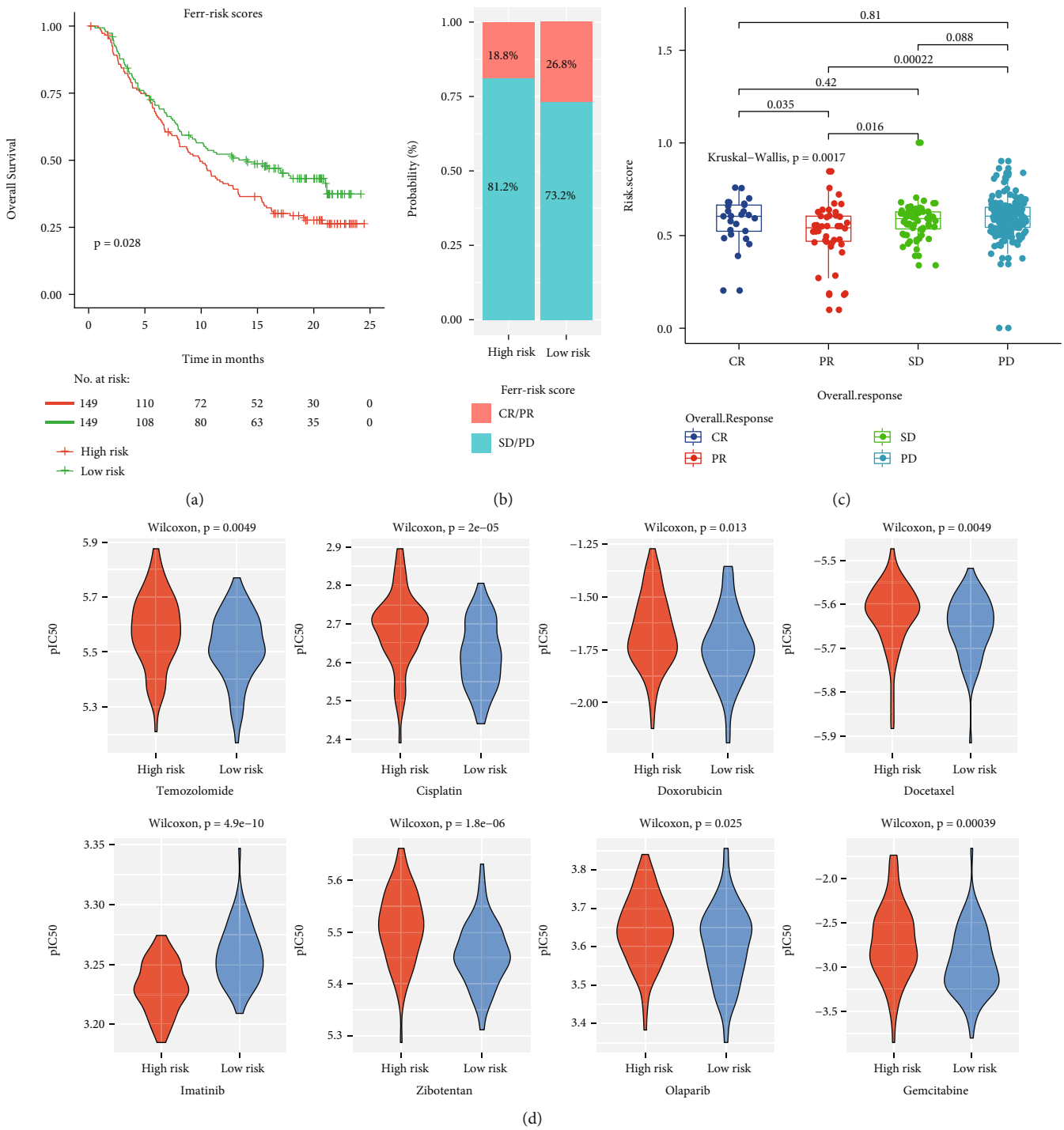
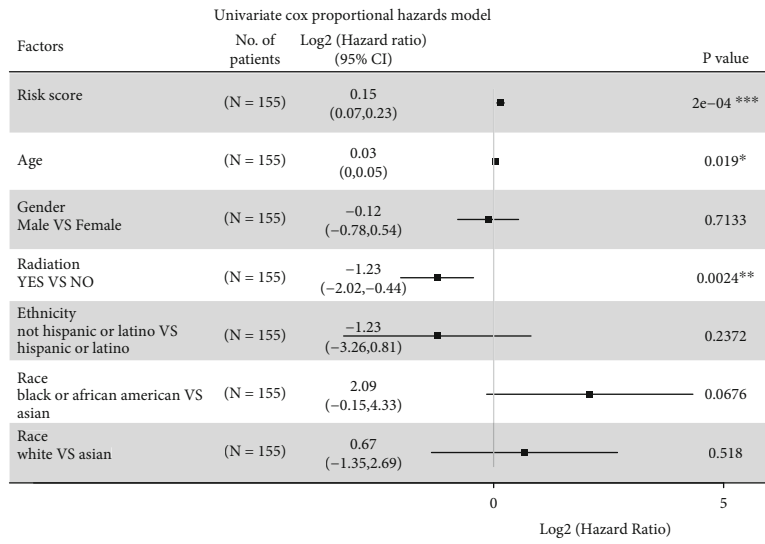


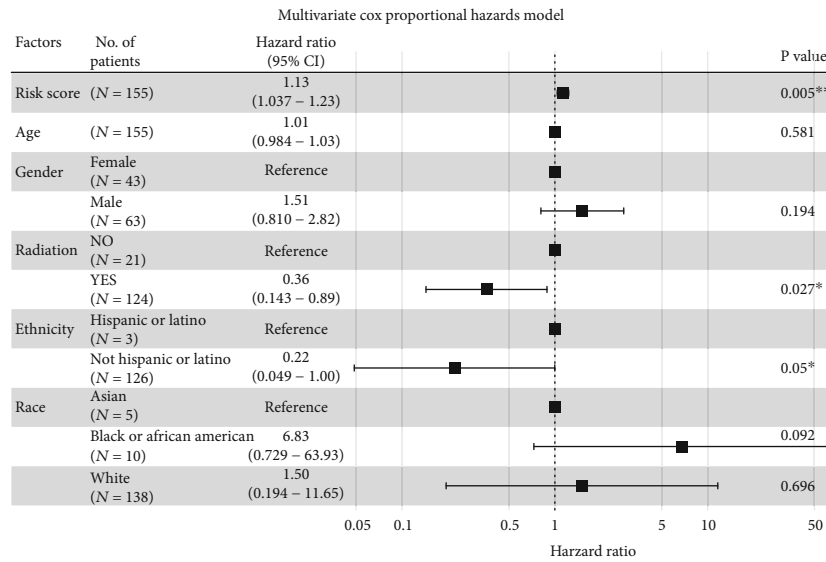
FIGURE 12: FRGPRS in prediction of immunotherapeutic benefits. (a) Kaplan–Meier curves and clinical responses to anti-PD-1 therapy in patients in IMvigor210 cohort with high- and low-FRGPRS. (b) Proportions of immunotherapy responses in high- and low-risk FRGPRS. (c) Box plots diagram depicting correlation analyses of overall response status and FRGPRS. (d) Violin plots depicting differences in estimated IC50 for temozolomide, cisplatin, doxorubicin, docetaxel, imatinib, zibotentan, olaparib, and gemcitabine between high- and low-FRGPRS groups. CR: complete response; PR: partial response; SD: stable disease; PD: progressive disease.

immune classification and the evaluation of local immunological biomarkers to make decisions regarding patient prognosis and prediction of treatment efficacy [44–46]. Ferroptosis may participate in cancer immune evasion. There

has been growing interest in clarifying the mechanisms regulating cancer cell sensitivity to ferroptosis [47]. PTGS2 upregulation and PGE2 release induce ferroptosis which may, in turn, modulate antitumor immunosuppression

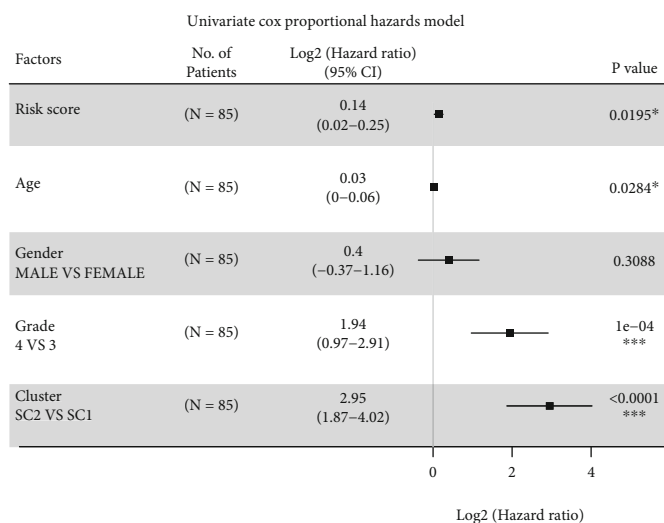


(a)

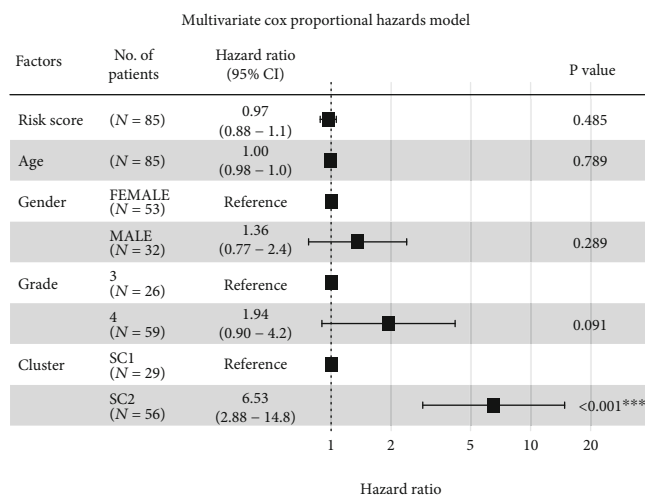


(b)

FIGURE 13: Continued.



(c)



(d)

FIGURE 13: Analysis of independent prognostic factors of FRGPRS. (a) and (b) Forest plots showing univariate Cox (a) and multifactor Cox (b) regression analyses of training dataset (TCGA GBM; progression-free survival). (c) and (d) Forest plots showing univariate Cox (c) and multifactor Cox (d) regression analyses of validation dataset GSE4412 GBM; overall survival.

[48, 49]. Further research is required to elucidate the immunomodulatory roles of ferroptosis in antitumor immunity [48, 49]. Elevated CD8+ and follicular helper T cell counts and infiltration in the low-FRGPRS group were indicative of antitumor efficacy. Immunotherapy promotes effector T cell function mainly by inducing cell death through the perforin-granzyme and Fas–Fas ligand pathways [50–52]. There is emerging evidence that ferroptosis is associated with various pathological scenarios. However, it is unclear whether, or how, ferroptosis is implicated in T cell immunity and cancer immunotherapy. CD8+ T cells secrete interferon gamma, regulate SLC3A2 and SLC7A11 expression, and promote cancer cell lipid peroxidation and ferroptosis [53]. Evidently, T cell-induced cancer ferroptosis is an antitumor mechanism that may serve as a novel approach toward GBM immunotherapy.

We assessed the differences in gene mutation between the low- and high-FRGPRS groups to clarify the mecha-

nisms of ferroptosis. Patients in the high-FRGPRS group showed significantly lower copy number variation frequencies than those in the low-FRGPRS group. Missense mutation and 1p19q codeletion furnish prognostically relevant information along with histological classification [54]. IDH1 mutation status was considered the basis for glioma diagnosis according to the 2016 WHO classification of CNS tumours. Gliomas with IDH1 mutations have relatively better outcomes and superior responses to therapy than those with the wildtype IDH1 gene. Nevertheless, the underlying mechanism has not been clarified [55]. A recent study revealed the roles of mutant IDH1 and 2-hydroxyglutarate in ferroptosis. The former reduces the GPX4 protein levels, thereby promoting the accumulating of lipid ROS and by extension ferroptosis [56]. Another study demonstrated that a TP53 gene variant plays a vital role in the functional interactions among thiol-based redox signalling, metabolism, and ferroptosis [57]. The low- and high-FRGPRS groups



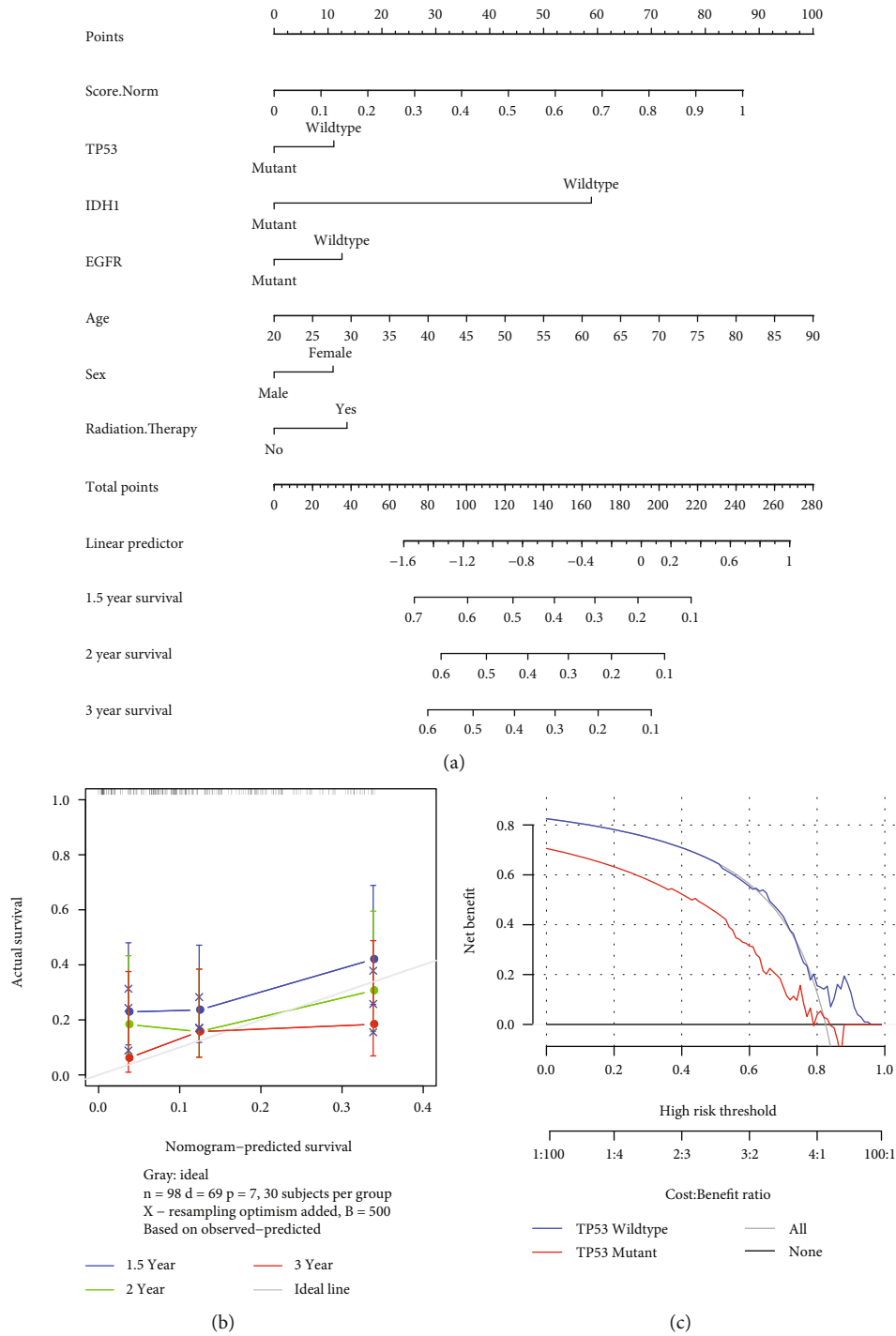


FIGURE 14: (a) Nomogram of FRGPRS in GBM patients. (b) Calibration maps were used to predict 1.5-year, 2-year, and 3-year survival. (c) Decision curve analysis of nomogram for TP53 mutation risk.

markedly differed in terms of their types of IDH1 and TP53 mutations. Overall, the wildtype forms were more abundant in the high-FRGPRS group. Hence, high FRGPRS is associated with a relatively greater risk of wildtype mutation and, therefore, worse prognosis. This finding was consistent with our survival results.

The present study revealed a significant association between FRGPRS and immunotherapy response in urothelial carcinoma patients treated with atezolizumab (anti-PD-

L1). The high-risk groups presented with worse survival after atezolizumab treatment. In general, PD-L1 (+) tumours respond better to anti-PD-1/PD-L1 therapy than PD-L1 (-) tumours [58, 59]. However, certain studies failed to show any significant correlation in this case possibly because of a lack of consistency in the measurements and variability of the threshold used to define PD-L1 positivity [60]. Therefore, further investigations are needed to establish the correlation between PD-L1 and GBM.

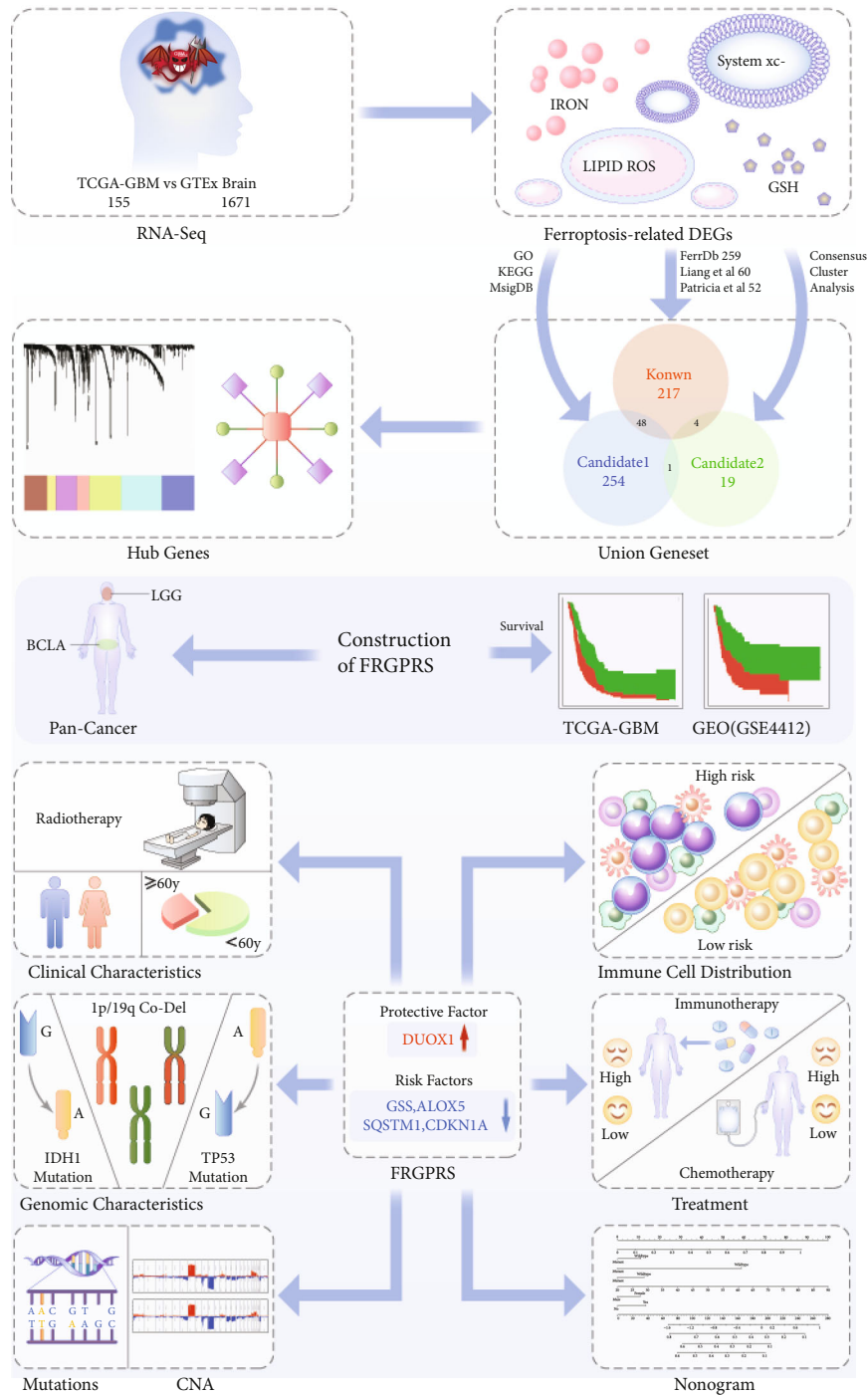


FIGURE 15: Graphical abstract for comprehensive characterization of FRGPRS groups in GBM. CNA: copy number alteration.

Drug resistance is a major hindrance in GBM therapy. Our research showed that low-FRGPRS patients were relatively more sensitive to temozolomide, cisplatin, and olaparib than high-FRGPRS patients. Liu et al. reported that TMZ-resistant glioma cells are more likely to undergo ferroptosis than normal glioma cells [24]. This finding was consistent with our research. The pathways regulating ferroptosis and inducing GBM TMZ resistance are complex, multifactorial processes that remain to be elucidated [18, 61–63]. A recent study demonstrated that ferroptosis plays

a vital role in cancer cell chemoresistance, and glioma-ferroptosis resistance is a putative TMZ resistance mechanism [64]. Iron is an important element in drug-resistant cancer cells. Iron-dependent ROS accumulation triggers ferroptosis [65]. Targeted ferroptosis-related pathways are promising strategies for reversing TMZ resistance.

The present study had certain limitations. As the survival time of GBM patient is short, we constructed a model based on PFS rather than OS. The independent prognostic risk factor FRGPRS was not significantly correlated with patient

survival according to a multivariate Cox regression, possibly because of sample size and other factors. Nevertheless, the training and validation sets showed that high FRGPRS significantly shortened patient survival and demonstrated the reliability of the model. The present study exclusively analysed GBM samples. Thus, it is unclear whether the FRGPRS model could be applied to any glioma sample from any genetic background. Moreover, the five-gene-based ferroptosis-related signature should be validated using larger samples. Future experiments should explore the potential mechanisms of the five genes in GBM ferroptosis and attempt to establish their correlations with immunotherapy and drug resistance.

## 5. Conclusions

In conclusion, the FRGPRS model is a powerful tool for predicting the survival and guiding the treatment of GBM. It might help distinguish immune and molecular characteristics, predict patient outcome, and stratify GBM patients benefiting from chemotherapy and immunotherapy. However, further research is required to identify and confirm the prognostic value of FRGPRS.

## Data Availability

All data are available on public repositories, which are listed in Table 1 and main context.

## Disclosure

The funders had a role in study design and data verification.

## Conflicts of Interest

The authors declare no potential conflicts of interest.

## Authors' Contributions

Dongdong Xiao did the conceptualization, data curation, project administration, resources, formal analysis, software, visualization, and writing original draft. Yujie Zhou did the conceptualization, data curation, project administration, resources, formal analysis, software, visualization, and writing original draft. Xuan Wang did the conceptualization, resources, investigation, and resources. Chuansheng Nie did the conceptualization, investigation, resources, supervision, and writing review and editing. Xiaobing Jiang did the methodology, validation, data curation, writing-original draft, writing review and editing, visualization, supervision, project administration, funding acquisition, resources, and data verification. Dongdong Xiao and Yujie Zhou have accessed verified the underlying data. All authors read and approved the final version of the manuscript. Dongdong Xiao and Yujie Zhou contributed equally to this work and share first authorship.

## Acknowledgments

This study has received funding from the National Natural Science Foundation of China (81974390)

## Supplementary Materials

*Supplementary 1.* Figure S1: Kyoto Encyclopedia of Genes and Genomes (KEGG) pathway analysis of differentially expressed genes (DEGs) ( $p < 0.05$ ). Figure S2: Venn diagram of ferroptosis key hub genes. Figure S3: prognostic ferroptosis key hub genes in GBM samples were screened using univariate Cox regression analysis and depicted by K-M curve. (a) DUOX1 ( $p = 0.026$ ), (b) SAT1 ( $p = 0.0042$ ), MUC1 ( $p = 0.0027$ ), (d) RB1 ( $p = 0.0016$ ), (e) HSPA5 ( $p = 0.0095$ ), and (f) HSPB1 ( $p = 0.0047$ ). Figure S4: (a) K-M curve of two patient FRGPRS in The Cancer Genome Atlas (TCGA) Bladder Urothelial Carcinoma (BLCA), (b) ROC curve analysis of FRGPRS model and known models. Figure S5: FRGPRS associated with genomic characteristics. (a) HRD score. (b) TMB. (c) Neoantigens. (d) Fractions altered. (e)–(g) Chromosome instability. (h) Stemness index (mRNAsi). HRD: homologous recombination deficiency; TMB: tumour mutational burden.

*Supplementary 2.* Table S1: DEGs between GBM and normal brain tissue. Table S2: KEGG pathways enriched in ferroptosis-related genes. Table S3: GO enrichment analysis of molecular function (MF). Table S4: GO enrichment analysis of biological process (BP). Table S5: GO enrichment analysis of cellular component (CC). Table S6: cd-Ferr-Geneset1. Table S7: cd-Ferr-geneset2. Table S8: DEG.Subtype1. Table S9: DEG.Subtype2. Table S10: DEG.Subtype3. Table S11: DEG.Subtype4. Table S12: known ferroptosis genes. Table S13: a multifactor regulatory network of the ferroptosis key hub genes. Table S14: Lasso-logistic regression analysis of prognosis factors. Table S15: FRGPRS model applied for TCGA GBM and GSE4412 GBM dataset.

## References

- [1] E. van Meir, C. G. Hadjipanayis, A. D. Norden, H. K. Shu, P. Y. Wen, and J. J. Olson, "Exciting new advances in neuro-oncology: the avenue to a cure for malignant glioma," *CA: A Cancer Journal for Clinicians*, vol. 60, no. 166–193, p. 3, 2010.
- [2] S. Osuka and E. G. Van Meir, "Overcoming therapeutic resistance in glioblastoma: the way forward," *Journal of Clinical Investigation*, vol. 127, no. 2, pp. 415–426, 2017.
- [3] M. A. Hammoud, R. Sawaya, W. Shi, P. F. Thall, and N. E. Leeds, "Prognostic significance of preoperative MRI scans in glioblastoma multiforme," *Journal of Neuro-Oncology*, vol. 27, pp. 65–73, 1996.
- [4] F. G. Barker, R. L. Davis, S. M. Chang, and M. D. Prados, "Necrosis as a prognostic factor in glioblastoma multiforme," *Cancer*, vol. 77, pp. 1161–1166, 1996.
- [5] P. P. Yee, Y. Wei, S.-Y. Kim et al., "Neutrophil-induced ferroptosis promotes tumor necrosis in glioblastoma progression," *Nature communications*, vol. 11, no. 1, p. 5424, 2020.
- [6] M. Chen, Z. Chen, Y. Wang et al., "Mitophagy receptor FUNDC1 regulates mitochondrial dynamics and mitophagy," *Autophagy*, vol. 12, no. 4, pp. 689–702, 2016.

- [7] M. Papale, M. Buccarelli, C. Mollinari et al., “Hypoxia, Inflammation and Necrosis as Determinants of Glioblastoma Cancer Stem Cells Progression,” *International journal of molecular sciences*, vol. 21, no. 8, p. 2660, 2020.
- [8] D. E. Swinson, J. L. Jones, D. Richardson, G. Cox, J. G. Edwards, and K. J. O’Byrne, “Tumour necrosis is an independent prognostic marker in non-small cell lung cancer: correlation with biological variables,” *Lung Cancer*, vol. 37, no. 3, pp. 235–240, 2002.
- [9] J. G. Edwards, D. E. B. Swinson, J. L. Jones, S. Muller, D. A. Waller, and K. J. O’Byrne, “Tumor Necrosis Correlates With Angiogenesis and Is a Predictor of Poor Prognosis in Malignant Mesothelioma,” *Chest*, vol. 124, no. 5, pp. 1916–1923, 2003.
- [10] J. C. Cheville, C. M. Lohse, H. Zincke, A. L. Weaver, and M. L. Blute, “Comparisons of outcome and prognostic features among histologic subtypes of renal cell carcinoma,” *The American Journal of Surgical Pathology*, vol. 27, no. 5, pp. 612–624, 2003.
- [11] S. T. Beug, C. E. Beaugard, C. Healy et al., “Smac mimetics synergize with immune checkpoint inhibitors to promote tumour immunity against glioblastoma,” *Nature Communications*, vol. 8, no. 1, 2017.
- [12] G. Reifenberger, H.-G. Wirsching, C. B. Knobbe-Thomsen, and M. Weller, “Advances in the molecular genetics of gliomas – implications for classification and therapy,” *Nature Reviews Clinical Oncology*, vol. 14, no. 7, pp. 434–452, 2017.
- [13] T. Komori, Y. Muragaki, and M. F. Chernov, “Pathology and genetics of gliomas,” *Progress in Neurological Surgery*, vol. 31, pp. 1–37, 2018.
- [14] S. Dixon, K. Lemberg, M. Lamprecht et al., “Ferroptosis: an iron-dependent form of nonapoptotic cell death,” *Cell*, vol. 149, no. 5, pp. 1060–1072, 2012.
- [15] G. Kroemer, L. Galluzzi, P. Vandenabeele et al., “Classification of cell death: recommendations of the Nomenclature Committee on Cell Death 2009,” *Cell Death & Differentiation*, vol. 16, no. 1, pp. 3–11, 2009.
- [16] L. Galluzzi, I. Vitale, J. M. Abrams et al., “Molecular definitions of cell death subroutines: recommendations of the Nomenclature Committee on Cell Death 2012,” *Cell Death & Differentiation*, vol. 19, no. 1, pp. 107–120, 2012.
- [17] V. S. Viswanathan, M. J. Ryan, H. D. Dhruv et al., “Dependency of a therapy-resistant state of cancer cells on a lipid peroxidase pathway,” *Nature*, vol. 547, no. 7664, pp. 453–457, 2017.
- [18] H. D. Dhruv, M. E. Berens, S. L. Schreiber, F. McCormick, and M. T. McManus, “Drug-tolerant persister cancer cells are vulnerable to GPX4 inhibition,” *Nature*, vol. 551, pp. 247–250, 2017.
- [19] J. Li, F. Cao, H. L. Yin et al., “Ferroptosis: past, present and future,” *Cell Death & Disease*, vol. 11, article 88, no. 2, 2020.
- [20] N. Verma, Y. Vinik, A. Saroha et al., “Synthetic lethal combination targeting BET uncovered intrinsic susceptibility of TNBC to ferroptosis,” *Science Advances*, vol. 6, no. 34, p. 34, 2020.
- [21] Y. Mou, J. Wang, J. Wu et al., “Ferroptosis, a new form of cell death: opportunities and challenges in cancer,” *Journal of hematology & oncology*, vol. 12, no. 1, pp. 1–6, 2019.
- [22] D. Chen, Z. Fan, M. Rauh, M. Buchfelder, I. Y. Eyupoglu, and N. Savaskan, “ATF4 promotes angiogenesis and neuronal cell death and confers ferroptosis in a xCT-dependent manner,” *Oncogene*, vol. 36, no. 40, pp. 5593–5608, 2017.
- [23] J. Cheng et al., “ACSL4 suppresses glioma cells proliferation via activating ferroptosis,” *Oncology reports*, vol. 43, no. 1, pp. 147–158, 2019.
- [24] H.-J. Liu, H.-m. Hu, G.-z. Li et al., “Ferroptosis-Related Gene Signature Predicts Glioma Cell Death and Glioma Patient Progression,” *Frontiers in cell and developmental biology*, vol. 8, p. 538, 2020.
- [25] S. Zhuo, Z. Chen, Y. Yang, J. Zhang, J. Tang, and K. Yang, “Clinical and Biological Significances of a Ferroptosis-Related Gene Signature in Glioma,” *Frontiers in oncology*, vol. 10, p. 590861, 2020.
- [26] J. Y. Liang, D. S. Wang, H. C. Lin et al., “A Novel Ferroptosis-related Gene Signature for Overall Survival Prediction in Patients with Hepatocellular Carcinoma,” *International journal of biological sciences*, vol. 16, no. 13, pp. 2430–2441, 2020.
- [27] V. Thorsson, D. L. Gibbs, S. D. Brown et al., “The Immune Landscape of Cancer,” *Immunity*, vol. 48, no. 4, pp. 812–830.e14, 2018.
- [28] T. M. Malta, A. Sokolov, A. J. Gentles et al., “Machine Learning Identifies Stemness Features Associated with Oncogenic Dedifferentiation,” *Cell*, vol. 173, no. 2, pp. 338–354.e15, 2018.
- [29] A. M. Marquard, A. C. Eklund, T. Joshi et al., “Pan-cancer analysis of genomic scar signatures associated with homologous recombination deficiency suggests novel indications for existing cancer drugs,” *Biomarker research*, vol. 3, no. 1, 2015.
- [30] A. M. Newman, C. B. Steen, C. L. Liu et al., “Determining cell type abundance and expression from bulk tissues with digital cytometry,” *Nature biotechnology*, vol. 37, no. 7, pp. 773–782, 2019.
- [31] K. Yoshihara, M. Shahmoradgoli, E. Martínez et al., “Inferring tumour purity and stromal and immune cell admixture from expression data,” *Nature communications*, vol. 4, no. 1, p. 2612, 2013.
- [32] P. Geeleher, N. J. Cox, and R. Huang, “Clinical drug response can be predicted using baseline gene expression levels and in vitro drug sensitivity in cell lines,” *Genome biology*, vol. 15, no. 3, p. R47, 2014.
- [33] S. Mariathasan, S. J. Turley, D. Nickles et al., “TGF $\beta$  attenuates tumour response to PD-L1 blockade by contributing to exclusion of T cells,” *Nature*, vol. 554, no. 7693, pp. 544–548, 2018.
- [34] The Cancer Genome Atlas Research Network, J. N. Weinstein, E. A. Collisson et al., “The Cancer Genome Atlas Pan-Cancer analysis project,” *Nature genetics*, vol. 45, no. 10, pp. 1113–1120, 2013.
- [35] T. Xu, W. Ding, X. Ji et al., “Molecular mechanisms of ferroptosis and its role in cancer therapy,” *Journal of Cellular and Molecular Medicine*, vol. 23, no. 8, pp. 4900–4912, 2019.
- [36] A. C. Little, A. Sulovari, K. Danyal, D. E. Heppner, D. J. Seward, and A. van der Vliet, “Paradoxical roles of dual oxidases in cancer biology,” *Free radical biology & medicine*, vol. 110, pp. 117–132, 2017.
- [37] S. Luxen, S. A. Belinsky, and U. G. Knaus, “Silencing of DUOX NADPH oxidases by promoter hypermethylation in lung cancer,” *Cancer Research*, vol. 68, no. 4, pp. 1037–1045, 2008.
- [38] C. Cheadle, M. P. Vawter, W. J. Freed, and K. G. Becker, “Analysis of Microarray Data Using Z Score Transformation,” *The Journal of molecular diagnostics*, vol. 5, no. 2, pp. 73–81, 2003.

- [39] A. C. Little, D. Sham, M. Hristova et al., “DUOX1 silencing in lung cancer promotes EMT, cancer stem cell characteristics and invasive properties,” *Oncogenesis*, vol. 5, no. 10, p. e261, 2016.
- [40] N. N. Kreis, F. Louwen, and J. Yuan, “The Multifaceted p21 (Cip1/Waf1/CDKN1A) in Cell Differentiation, Migration and Cancer Therapy,” *Cancers*, vol. 11, no. 9, p. 1220, 2019.
- [41] A. Santangelo, M. Rossato, G. Lombardi et al., “A molecular signature associated with prolonged survival in glioblastoma patients treated with regorafenib,” *Neuro-oncology*, vol. 23, no. 2, pp. 264–276, 2021.
- [42] Y. Liu, Y. Wang, J. Liu, R. Kang, and D. Tang, “Interplay between MTOR and GPX4 signaling modulates autophagy-dependent ferroptotic cancer cell death,” *Cancer gene therapy*, vol. 28, no. 1-2, pp. 55–63, 2021.
- [43] W. Wu, Z. Geng, H. Bai, T. Liu, and B. Zhang, “Ammonium Ferric Citrate induced Ferroptosis in Non-Small-Cell Lung Carcinoma through the inhibition of GPX4-GSS/GSR-GGT axis activity,” *International journal of medical sciences*, vol. 18, no. 8, pp. 1899–1909, 2021.
- [44] J. Galon, F. Pagès, F. M. Marincola et al., “The immune score as a new possible approach for the classification of cancer,” *Journal of translational medicine*, vol. 10, p. 1, 2012.
- [45] G. Bindea, B. Mlecnik, W. H. Fridman, F. Pagès, and J. Galon, “Natural immunity to cancer in humans,” *Current opinion in immunology*, vol. 22, no. 2, pp. 215–222, 2010.
- [46] F. Pages, J. Galon, M. C. Dieu-Nosjean, E. Tartour, C. Sautes-Fridman, and W. H. Fridman, “Immune infiltration in human tumors: a prognostic factor that should not be ignored,” *Oncogene*, vol. 29, no. 8, pp. 1093–1102, 2010.
- [47] J. P. Angeli, R. Shah, D. A. Pratt, and M. Conrad, “Ferroptosis Inhibition: Mechanisms and Opportunities,” *Trends in pharmacological sciences*, vol. 38, no. 5, pp. 489–498, 2017.
- [48] W. S. Yang, R. SriRamaratnam, M. E. Welsch et al., “Regulation of ferroptotic cancer cell death by GPX4,” *Cell*, vol. 156, no. 1-2, pp. 317–331, 2014.
- [49] D. Wang and R. N. DuBois, “The Role of Prostaglandin E(2) in Tumor-Associated Immunosuppression,” *Trends in molecular medicine*, vol. 22, no. 1, pp. 1–3, 2016.
- [50] D. N. Khalil, E. L. Smith, R. J. Brentjens, and J. D. Wolchok, “The future of cancer treatment: immunomodulation, CARs and combination immunotherapy,” *Nature reviews. Clinical oncology*, vol. 13, no. 5, pp. 273–290, 2016.
- [51] M. Barry and R. C. Bleackley, “Cytotoxic T lymphocytes: all roads lead to death,” *Nature reviews. Immunology*, vol. 2, no. 6, pp. 401–409, 2002.
- [52] P. Golstein and G. M. Griffiths, “An early history of T cell-mediated cytotoxicity,” *Nature reviews. Immunology*, vol. 18, no. 8, pp. 527–535, 2018.
- [53] W. Wang, M. Green, J. E. Choi et al., “CD8+ T cells regulate tumour ferroptosis during cancer immunotherapy,” *Nature*, vol. 569, no. 7755, pp. 270–274, 2019.
- [54] M. Weller, R. G. Weber, E. Willscher et al., “Molecular classification of diffuse cerebral WHO grade II/III gliomas using genome- and transcriptome-wide profiling improves stratification of prognostically distinct patient groups,” *Acta Neuropathologica*, vol. 129, no. 5, pp. 679–693, 2015.
- [55] H. Yan, D. W. Parsons, G. Jin et al., “IDH1 and IDH2 mutations in gliomas,” *The New England journal of medicine* vol., vol. 360, no. 8, pp. 765–773, 2009.
- [56] T. X. Wang, J. Y. Liang, C. Zhang, Y. Xiong, K. L. Guan, and H. X. Yuan, “The oncometabolite 2-hydroxyglutarate produced by mutant IDH1 sensitizes cells to ferroptosis,” *Cell death & disease*, vol. 10, no. 10, p. 755, 2019.
- [57] I. Julia, J. Leu, M. E. Murphy, and D. L. George, “Functional interplay among thiol-based redox signaling, metabolism, and ferroptosis unveiled by a genetic variant of TP53,” *Proceedings of the National Academy of Sciences of the United States of America*, vol. 117, no. 43, pp. 26804–26811, 2020.
- [58] A. R. Hansen and L. L. Siu, “PD-L1 Testing in Cancer: Challenges in Companion Diagnostic Development,” *JAMA oncology*, vol. 2, no. 1, pp. 15–16, 2016.
- [59] M. Oliva, A. Spreafico, M. Taberna et al., “Immune biomarkers of response to immune-checkpoint inhibitors in head and neck squamous cell carcinoma,” *Annals of oncology*, vol. 30, no. 1, pp. 57–67, 2019.
- [60] R. L. Ferris, G. Blumenschein, J. Fayette et al., “Nivolumab vs investigator's choice in recurrent or metastatic squamous cell carcinoma of the head and neck: 2-year long-term survival update of CheckMate 141 with analyses by tumor PD-L1 expression,” *Oral Oncology*, vol. 81, pp. 45–51, 2018.
- [61] W. S. Yang, K. J. Kim, M. M. Gaschler, M. Patel, M. S. Shchepinov, and B. R. Stockwell, “Peroxyoxidation of polyunsaturated fatty acids by lipoxygenases drives ferroptosis,” *Proceedings of the National Academy of Sciences of the United States of America*, vol. 113, no. 34, pp. E4966–E4975, 2016.
- [62] P. Ye, J. Mimura, T. Okada et al., “Nrf2- and ATF4-dependent upregulation of xCT modulates the sensitivity of T24 bladder carcinoma cells to proteasome inhibition,” *Molecular and Cellular Biology*, vol. 34, no. 18, pp. 3421–3434, 2014.
- [63] S. W. Lee, H. K. Kim, N. H. Lee et al., “The synergistic effect of combination temozolomide and chloroquine treatment is dependent on autophagy formation and p53 status in glioma cells,” *Cancer Letters*, vol. 360, no. 2, pp. 195–204, 2015.
- [64] Z. Hu, Y. Mi, H. Qian et al., “A Potential Mechanism of Temozolomide Resistance in Glioma-Ferroptosis,” *Frontiers in oncology*, vol. 10, no. 897, 2020.
- [65] X. Sui, R. Zhang, S. Liu et al., “RSL3 Drives Ferroptosis Through GPX4 Inactivation and ROS Production in Colorectal Cancer,” *Frontiers in pharmacology*, vol. 9, p. 1371, 2018.

## Research Article

# System Analysis of ROS-Related Genes in the Prognosis, Immune Infiltration, and Drug Sensitivity in Hepatocellular Carcinoma

Jun Hui Xu <sup>1,2,3</sup>, Yong Jun Guan,<sup>1</sup> Zhen Dong Qiu,<sup>1</sup> Xin Zhang <sup>1</sup>, Liu Liu Zi <sup>1</sup>,  
Yu Zhou,<sup>1</sup> Chen Chen,<sup>1</sup> Jia Yu,<sup>1</sup> Yi Chao Zhang <sup>1</sup>, and Wei Xing Wang <sup>1</sup>

<sup>1</sup>Department of Hepatobiliary Surgery, Renmin Hospital of Wuhan University, Wuhan, China

<sup>2</sup>Central Laboratory, Renmin Hospital of Wuhan University, Wuhan, China

<sup>3</sup>Hubei Key Laboratory of Digestive System Disease, Wuhan, China

Correspondence should be addressed to Yi Chao Zhang; 409849352@qq.com and Wei Xing Wang; sate.llite@163.com

Received 21 July 2021; Revised 22 September 2021; Accepted 29 September 2021; Published 8 November 2021

Academic Editor: Alessandro Poggi

Copyright © 2021 Jun Hui Xu et al. This is an open access article distributed under the Creative Commons Attribution License, which permits unrestricted use, distribution, and reproduction in any medium, provided the original work is properly cited.

Hepatocellular carcinoma (HCC) is an aggressive malignant tumor with a poor prognosis. Reactive oxygen species (ROS) play an important role in tumors; however, the role of ROS-related genes is still unclear in HCC. Therefore, we analyzed the role of ROS-related genes in HCC via bioinformatics methods. Firstly, a prognosis model was constructed using LASSO Cox regression and multivariate analyses. We also investigated the potential function of the ROS-related genes and the correlation with immune infiltration, tumor stemness, and drug sensitivity. ICGC database was used for validation. Secondly, we further analyzed the role of 11 ROS-related genes in HCC. As a member of ROS gene family, the role of STK25 has remained unclear in HCC. We explored the biological function of STK25 using *in vitro* experiments. The present study was the first to construct a ROS-related prognostic model in HCC. The correlation of ROS-related genes with immune infiltration, tumor stemness, and drug sensitivity was dissected. Furthermore, we demonstrated that STK25 knockdown could increase the proliferation, migration, and invasion capacity of HCC cells.

## 1. Introduction

Hepatocellular carcinoma (HCC) is the primary pathological type of liver cancer and is one of the most common malignancies worldwide [1, 2]. Liver cancer ranks the second leading cause of cancer-related death due to lack of effective treatment [3]. Currently, the mainstay treatment of HCC is surgical excision, liver transplantation, interventional, chemoradiotherapy, and targeted drug therapy. The early diagnosis of HCC is difficult, and hence, the majority of HCC patients suffer from a poor prognosis with a high recurrence rate. Therefore, it remains clinically essential to identify the novel and effective diagnostic markers for HCC. Chronic liver diseases, such as hepatitis B virus, liver cirrhosis, alcoholic liver disease, and nonalcoholic fatty liver disease, are the major risk factor for HCC [4]. HCC is a highly heterogeneous disease, and its mechanism of HCC is still not

completely understood. Abnormal expression and mutation of genes contribute to the progression of HCC [5]. However, the underlying mechanisms of HCC development and the key driving factors of carcinogenesis are still unclear, which impedes the development of targeted treatment [6].

Reactive oxygen species (ROS) are regarded as reactive oxygen metabolites and oxygen-containing materials, including superoxide anion ( $O_2^-$ ) and hydroxyl radical ( $OH\cdot$ ) as well as nonradical molecules, such as hydrogen peroxide ( $H_2O_2$ ) [7]. At normal concentrations, ROS serves as the second message that participates in a diversity of signal transduction and regulates cell growth, differentiation, and proliferation. Nevertheless, oxidative stress is the consequence of the imbalanced redox state accompanied by ROS production exceeds cell capacity for ROS scavenging that has been implicated in HCC occurrence [8]. Previous studies have indicated that ROS play a vital role in the progression

of HCC through the induction of autophagy [7]. However, a comprehensive analysis of the role of ROS-related genes in HCC has not been reported.

Serine/threonine-protein kinase 25 (SK25), also known as YSK1 or SOK1, plays important roles in different biological processes, such as the regulation of cell migration and modulation of Golgi morphology [9–12]. Some studies have shown that SOK1 can be activated by chemical anoxia induction, which is dependent upon the generation of ROS [13, 14]. In addition, a previous research has indicated that SOK1 promotes the apoptotic response to ROS with marked ROS production and severe ATP depletion [12]. However, as an ROS-related gene, the role of STK25 in liver cancer has not been reported.

In the present study, we systematically investigated the expression and clinicopathological characteristics of ROS-related genes and constructed ROS-related gene prognostic model in HCC patients. We further demonstrated the relationship between ROS-related genes and tumor-infiltrating immune cells. An ROS-related gene risk model can be used as a prognostic biomarker to predict immune microenvironment in HCC patients. Moreover, focusing on the clinicopathological and immunological characteristics of ROS-related genes in HCC may optimise tumor immunotherapy.

## 2. Materials and Methods

**2.1. Public mRNA Expression Datasets.** The mRNA expression of 371 HCC patients and the clinicopathological information of HCC samples were extracted from TCGA (<https://portal.gdc.cancer.gov/>) and ICGC (<https://dcc.icgc.org>) databases. In TCGA database, among the 371 patients, six patients were excluded due to lack of survival time, and 365 patients were eventually included in the study (Table 1). All the raw count data were analyzed to identify differential expression genes (DEGs) in HCC samples and matched noncancerous samples by the package “limma” of the R software.  $|\log 2FC| = 0$  and  $P < 0.05$  were set as the cut-off point. The mRNA data and clinical information of 231 liver cancer samples were downloaded from the ICGC database (<http://dcc.icgc.org/projects/LIRI-JP>). Then, we summarized 49 ROS-related genes from the Molecular Signatures Database (MSigDB) v7.2 (<https://www.gsea-msigdb.org/gsea/msigdb/index.jsp>) [15] for further analysis. They were listed in Supplementary Table S1. 38 detailed immune checkpoint genes are listed in the Supplementary Table S2.

**2.2. Construction of a ROS-Related Gene-Based Signature.** All the raw data were analyzed by the “limma” package in the R software and identified the DEGs between HCC tissues and noncancerous tissues. Univariate regression analysis of OS was conducted to screen ROS-related prognostic genes. Benjamini & Hochberg (BH) correction was used to adjust the  $P$  value. Then, the STRING database (version11.0) was used for constructing overlapping differential prognostic gene interaction networks [16]. In order to minimize the risk of overfitting, LASSO-penalized Cox regression analysis was used to develop the prognosis model [17, 18]. The LASSO algorithm was used for variable selection, combined with

TABLE 1: Clinical features of the hepatocellular carcinoma patients in this work.

|                         | TCGA cohort |
|-------------------------|-------------|
| No. of patients         | 365         |
| Age (median, range)     | 61(16-90)   |
| Gender (%)              |             |
| Male                    | 246(67.4%)  |
| Female                  | 119(32.6%)  |
| Stage (%)               |             |
| I                       | 170(46.6%)  |
| II                      | 84(23%)     |
| III                     | 83(22.7%)   |
| IV                      | 4(1.1%)     |
| unknown                 | 24(6.6%)    |
| Survival status (%)     |             |
| Living                  | 235(64.4%)  |
| Death                   | 130(35.6%)  |
| OS days (median, range) | 594(1-3675) |

“glmnet” R package for shrinkage. In the regression model, we took the normalized expression matrix of the candidate differential prognostic genes as the independent variable and the overall survival and state of the patients in TCGA cohort as the response variable. The penalty parameter (model parameter) of the model is calculated by ten ties cross-validation according to the minimum standard. The risk score was calculated based on the normalized expression level of each gene and its corresponding regression coefficient. The coefficient of each gene is listed in Supplementary Table S3. The formula was built as follows:  $\text{score} = e^{\text{sum}}$  (each gene’s expression  $\times$  corresponding coefficient). Patients were classified into high-risk and low-risk groups depending on the median risk score. Principal component (PCA) analysis was performed using “PRCOMP” function of “stats” R package based on the expression of gene signature. In addition, the “Rtsen” R package was adopted for t-distributed stochastic neighbour embedding (t-SNE) analysis to investigate the distribution of diverse groups. Kaplan-Meier curves were utilized to estimate the differences in OS between the two groups. The time-dependent ROC curve was plotted to illustrate the sensitivity and predictive ability of gene signature based on the “survival valroc” R package.

**2.3. The Construction of Nomograms.** Nomogram models were constructed based on the expression of ROS-related prognostic genes by using the “rms” and “survival” packages in R [19]. Then, calibration curves were plotted to estimate the consistency between actual and predicted survival.

**2.4. Functional Enrichment Analysis.** To explore the potential functional features of ROS-related genes in HCC, we performed Kyoto Encyclopedia of Genes and Genomes (KEGG) and Gene Ontology (GO) analyses based on ROS-related DEGs ( $|\log 2FC| \geq 1$ ,  $FDR < 0.05$ ) between different risk groups via the “clusterProfiler” R package.

**2.5. Immune Infiltration Analysis.** Then, we adopted the “gsva” R package to investigate single-sample gene set enrichment analysis (ssGSEA) and to calculate the relationship between risk score and 16 immune-infiltrating cells and 13 immune-related pathways. We further explored the connection between ROS-related DEGs and tumor purity and immune-infiltrating cells by the TIMER and TISIDB databases based on a previously published statistical deconvolution method from gene expression profiles. Tumor Immune Estimation Resource (TIMER) (<http://cistrome.org/TIMER/>) [20] is an ideal resource that contains 10897 samples across 32 cancer types from TCGA, and it can be adopted to comprehensively analyze immune infiltration levels of diverse cancer types. TISIDB (<http://cis.hku.hk/TISIDB/>) is also an online web with different types of data which can be used to explore the relationship between the tumor and immune infiltration [21].

**2.6. The GEPIA.** GEPIA (Gene Expression Profiling Interactive Analysis) (<http://gepia.cancer-pku.cn/>) has been a valuable and highly cited resource for gene expression analysis based on tumor and normal samples from TCGA and the GTEx databases [22]. GEPIA2021 is a standalone extension with multiple deconvolution-based analyses for GEPIA. They deconvolute each sample tool by TCGA/GTEx with the bioinformatics tools CIBERSORT, EPIC, and quanTIseq [19].

**2.7. The UALCAN Analysis.** UALCAN is a comprehensive, user-friendly, and interactive web resource for analyzing cancer OMICS data. It is built on PERL-CGI with high-quality graphics using JavaScript and CSS [23]. UALCAN can be used to explore the expression profile and patient survival information for genes and to evaluate epigenetic regulation of gene expression by promoter methylation.

**2.8. The Kaplan-Meier Plotter Analysis.** The Kaplan-Meier plotter can be used to estimate the effect of 54k genes on survival in 21 cancer types including liver cancer ( $n = 365$ ) [19, 24]. Sources for databases are from GEO, TCGA, and EGA.

**2.9. Clinical Sample Collection.** Nine HCC tissues and paired noncancerous tissues were collected from HCC patients who underwent liver resection in Renmin Hospital of Wuhan University (Wuhan, China) from October 2019 through October 2020. The collected tissues were stored at  $-80^{\circ}\text{C}$  for subsequent use. All patients were given informed consent before surgery treatment, and the study was approved by the Ethics Committee of Wuhan University.

**2.10. Cell Culture and Transfection.** HepG2 and SMMC-7721 cells were purchased from ATCC. HepG2 cells were cultured in DMEM high glucose medium (Servicebio), and SMMC-7721 cells were cultured in 1640 medium (Servicebio), all containing 10% Foetal Bovine Serum (FBS) and 1% penicillin and streptomycin (Servicebio). Short hairpin (sh)RNAs sh-STK25 were obtained from miaolingbio.lnc, Wuhan, China. HepG2 and SMMC-7721 cells were cultured in 6-well plates ( $5 \times 10^5$ /well) and transfected with  $2.4 \mu\text{g}$  siRNA using Attractance Transfection Reagent (Cat. No. 301005, QIAGEN, China).

**2.11. Immunohistochemical Staining (IHC).** This part of the operation refers to a previous study [25]. Paraffin-embedded liver cancer and corresponding noncancerous tissues were sliced and dewaxed, then treated with 3%  $\text{H}_2\text{O}_2$  for 10 min to inactivate endogenous peroxidase, and treated with 0.01% mol/L sodium citrate buffer in boiling water for antigen repair. Goat serum was dropped for a block for 20 min, and STK25 antibody (1:50) was dropped for overnight incubation at  $4^{\circ}\text{C}$  and washed with PBS three times. Then, DAB chromogen was added. Hematoxylin was redyed, and neutral gum was sealed. The primary antibody is as follows: anti-STK25 mouse monoclonal antibody (1:100; Cat. No. sc-271196; Santa Cruz Biotechnology, Inc.). The sections were observed under light microscopy, and five randomized microscopic views of 200-fold magnification of each section were observed and scored.

**2.12. Cell Proliferation Assay.** The treated cells (HepG2 and SMMC-7721) were collected, and 2000 cells/well were inoculated in 96-well plates. After incubation for 24, 48, and 72 hours,  $10 \mu\text{l}$  CCK8 solutions were added to each well. Then, the cells were incubated at  $37^{\circ}\text{C}$  for 1 h in the dark room, and the absorbance value (OD450) of each well at 450 nm was detected by a microplate analyzer.

**2.13. Cell Migration Assay.** HepG2 and SMMC-7721 cells were seeded in 6-well plates and transfected with control plasmid and shRNA-STK25 plasmid, respectively. When the cells have grown and fused to about 90%, a sterile  $200 \mu\text{l}$  pipette tip was used to create an artificial wound. Then, the cells were washed three times with 1X PBS buffer to remove floating cells and replaced with a serum-free medium. Photos were taken at 0 and 24 hours under a light microscope (magnification,  $\times 40$ ). The results of cell migration were analyzed by the Image J software.

**2.14. Cell Invasion Assay.** The transfected HepG2 and SMMC-7721 cells were collected, resuspended in  $100 \mu\text{l}$  serum-free medium, and  $5 \times 10^4$  cells were seeded into 24-well upper transwell chamber ( $8 \mu\text{m}$  pore size) with Matrigel (BD, USA). The lower part of the chamber was full of a medium containing 10% FBS. Invasion culture periods were about 24 h.

Cells on the top surface of the filters were wiped off using a cotton swab. The cells on the lower surface of the filter were fixed with 4% paraformaldehyde and stained with 0.1% crystal violet at  $37^{\circ}\text{C}$  for 30 min. The numbers of invading cells were counted using a light microscope with  $\times 200$  magnification.

**2.15. Flow Cytometry Analysis.** After transfection for 72 h, HCC cells were collected and washed three times with cold PBS solution. According to the instructions, HCC cells were resuspended with  $500 \mu\text{l}$  Annexin V binding buffer with adding  $5 \mu\text{l}$  Annexin V-FITC and  $5 \mu\text{l}$  PI, following incubation at room temperature for 30 min, and flow cytometer was performed to analyze apoptosis.

**2.16. EdU Assay.** HepG2 and SMMC-7721 cells with appropriate concentrations were added to the 6-well plates with  $2.4 \mu\text{g}$  plasmids (empty vector and shRNA-STK25). EdU



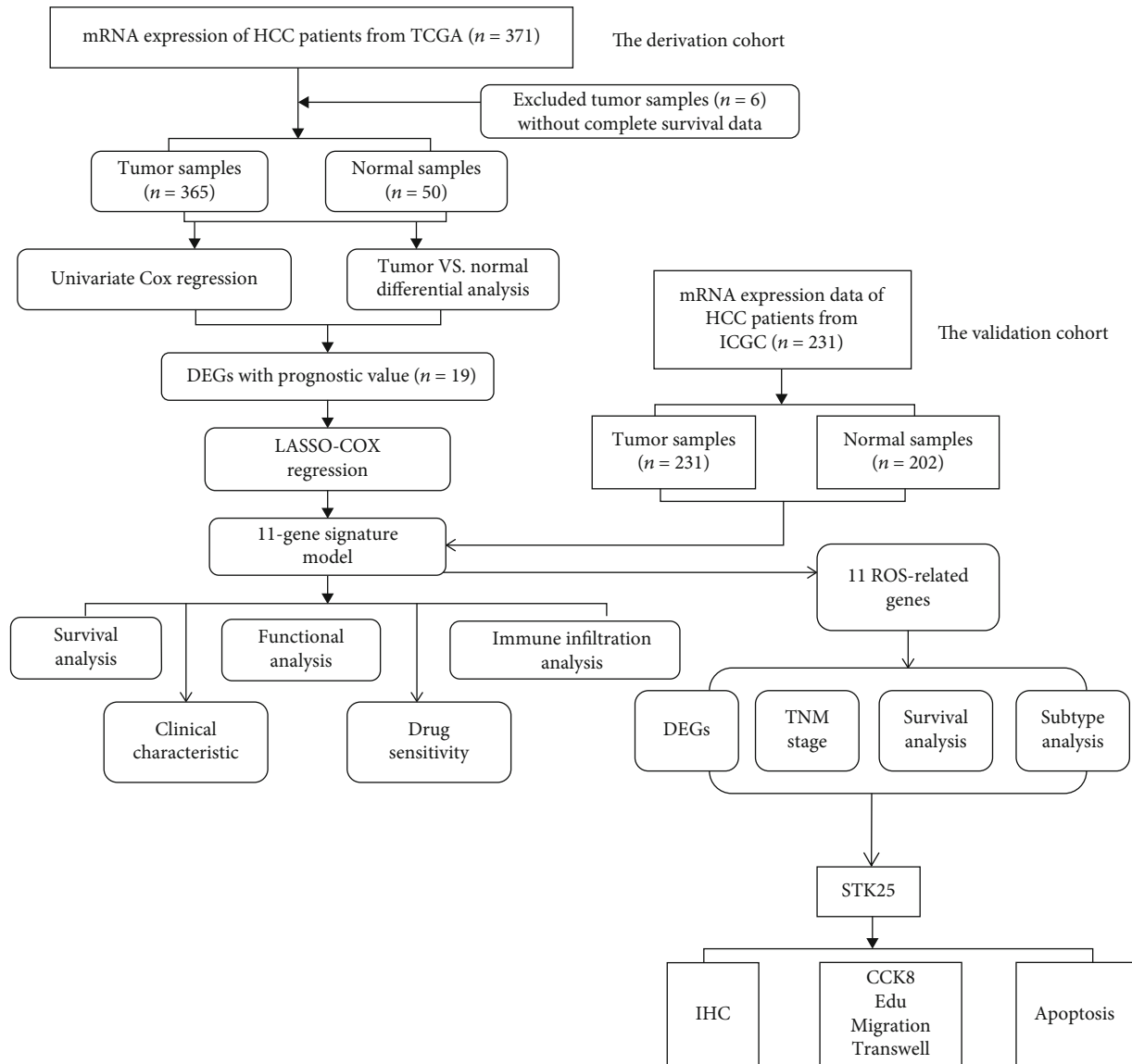


FIGURE 1: The workflow of the present study.

working solution (10  $\mu$ M) was added into cells in 6-well plates and incubated for 2 hours. After that, the culture medium was removed, and 1 ml 4% paraformaldehyde was added to each well at room temperature for 15 min. Then, the cells were washed with a washing solution (PBS solution containing 3% bovine serum albumin (BSA)) three times. The permeability solution (0.3% Triton X-100 solution) was added and incubated for 15 min at room temperature. Then, 0.5 ml Click reaction solution was added to each well and incubated for 30 min in the dark room. Finally, 1 ml 1X Hoechst33342 solution was added to 6-well plates and incubated for 10 min in the dark room. The staining was observed under a microscope.

### 3. Statistical Analysis

Student's *t*-test was employed to compare gene expression between HCC tissues and noncancerous tissues. Chi-square test was used to compare proportions between the high-

risk group and the low-risk group. The Mann-Whitney test was applied to compare the ssGSEA score of immune cells or pathways among different risk groups. The OS in different groups was performed by Kaplan-Meier (KM) survival analysis with a log-rank test. Univariate and multivariate analyses were used to evaluate independent risk factors for OS. The association of immune checkpoint genes with the risk score was performed by R. *F*-test (one-way ANOVA) was utilized to identify the expression of 11 ROS-related genes in immune cells between tumor tissues and normal tissues. All statistical analyses were conducted using R software 3.4.2 and SPSS 23.0 software, and  $P < 0.05$  was considered statistically significant.

### 4. Results

The workflow of the present study is shown in Figure 1. mRNA and clinical data of 371 patients with HCC were

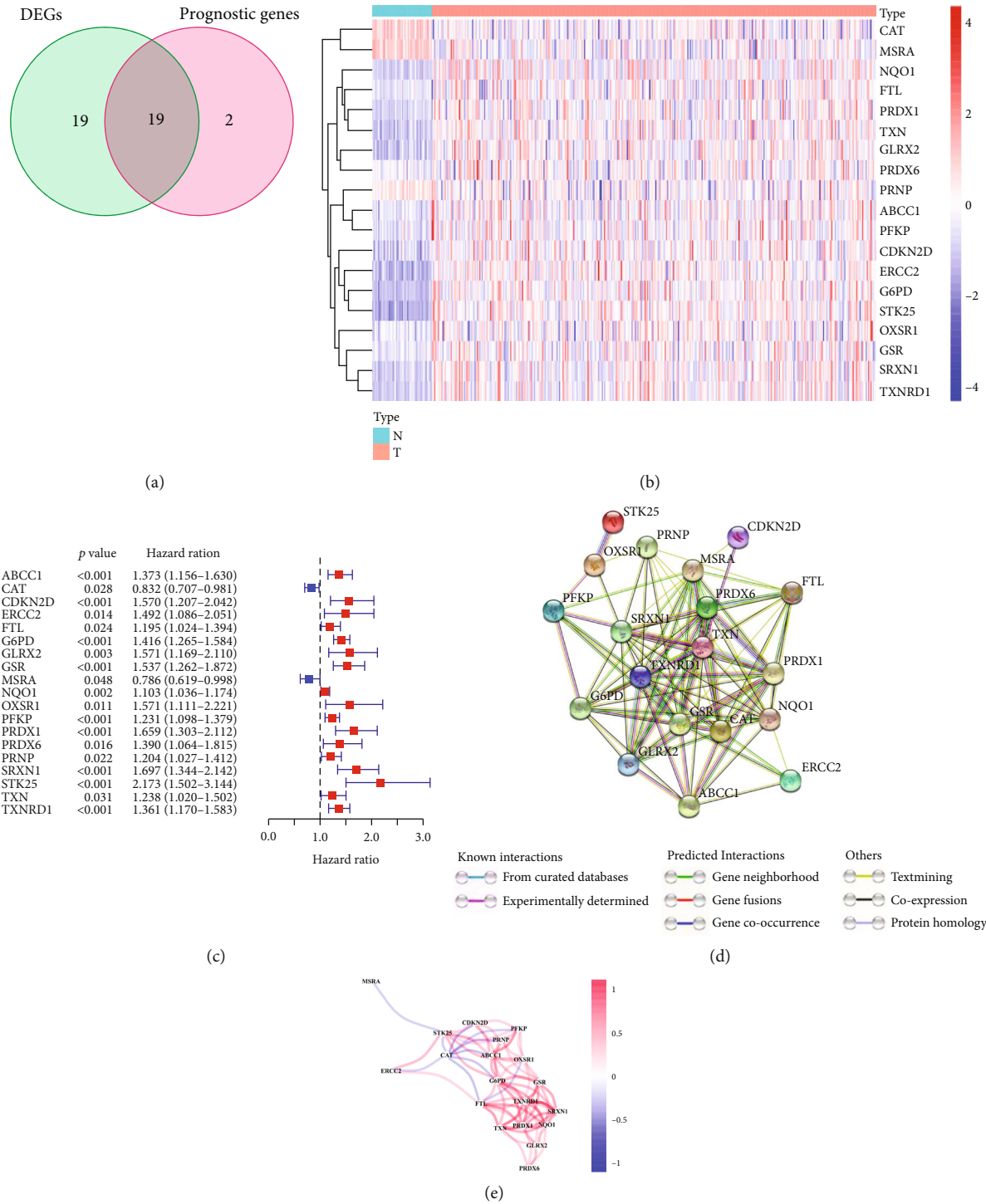


FIGURE 2: Identification of the candidate ROS-related genes in TCGA database. (a) Identification of differentially expressed genes in HCC tissues and paired noncancerous tissues that were related to OS. (b) 19 Overlapping genes were overexpressed in HCC tissues. (c) Forest plots indicating the results of the univariate Cox regression analysis between OS and gene expression. (d) The PPI network downloaded from the STRING database revealed the interactions among the DEGs. (e) The correlation network of DEGs. The correlation coefficients are denoted by different colors.

downloaded from TCGA. A total of 365 HCC patients had complete survival data. 49 ROS-related genes (Supplementary Table S1) were extracted from the MSigDB database v7.2. DEG screening analysis found that 38 ROS-related genes were differentially expressed between HCC tissues and

paired noncancerous tissues. We identified 19 differentially prognostic genes by performing univariate analysis for OS. Using LASSO Cox regression and multivariate analysis, 11 ROS-related genes were identified. Data downloaded from the ICGC database were used to verify the accuracy of the

model. We further conducted functional enrichment and immune infiltrating analyses. Differential expression analysis and survival analyses were performed on 11 ROS-related genes, and the relationship between the expression of the genes and TNM stages was calculated. In addition, we explored the expression of 11 ROS-related genes among different molecular and immune subtypes. Finally, only G6PD and STK25 were retained with  $P < 0.05$ . Although, the role of G6PD has been reported in HCC, the role of STK25 has remained unclear. *In vitro* experiments were carried out to explore the role of STK25 in liver cancer.

**4.1. Identification of Prognostic ROS-Related DEGs in TCGA Datasets.** 49 ROS-related genes listed in Supplementary Table S1 were drawn from the MSigDB database. 38 ROS-related genes were differentially expressed between HCC tissues and paired noncancerous tissues by DEG screening analysis based on the “limma” package in the R software. In addition, based on TCGA database, we identified 19 differentially prognostic genes by performing univariate analysis for OS. The results of univariate regression analysis are shown in Figures 2(a)–2(c) ( $P < 0.05$ ). The genes included are CAT, MSRA, NQO1, FTL, PRDX1, TXN, GLRX2, PRDX6, PRNP, ABCC1, PFKP, CDKN2D, ERCC2, G6PD, STK25, OXSR1, GSR, SRXN1, and TXNRD1. Based on the result of univariate analysis, a protein-protein interaction (PPI) network was built to analyze the association between 19 ROS-related genes, and the finding revealed that STK25 is one of the hub genes (Figures 2(d) and 2(e)).

**4.2. Constructing a ROS-Related DEG Prediction Model in TCGA Datasets.** LASSO Cox regression was performed to construct a prognostic model, and based on TCGA database, 11 ROS-related genes were retained by the coefficient values, which include CDKN2D, G6PD, GLRX2, GSR, MSRA, OXSR1, PFKP, PRDX1, PRDX6, SRXN1, and STK25. Patients were dichotomized into high and low groups based on the median cut-off value. Patients in the high-risk group were linked to tumor grade ( $P < 0.001$ ) (Table 2). Next, we performed PCA and t-SNE to explore the distribution of patients with different risk scores. The results showed that patients were grouped into two directions, and the high-risk group had a shorter survival time than the low-risk group ( $P < 0.05$ ) (Figures 3(a)–3(d)). This was supported by the results of Kaplan-Meier analysis, which showed that the OS time was shorter in the high-risk group compared with the low-risk group ( $P = 2.319e - 06$ ) (Figure 3(e)). Furthermore, ROC further demonstrated the possibility and accuracy of OS prediction based on the risk score. The AUC values of 1-year survival, 3-year survival, and 5-year were 0.793, 0.713, and 0.684, respectively (Figure 3(f)). Next, based on the ICGC database, we performed LASSO Cox regression, PCA, t-SNE, survival analysis, and ROC curve to demonstrate the aforementioned results. Our findings indicated that the high-risk group had a shorter survival time than the low-risk group, and the low-risk group had a longer survival time than the high-risk group ( $P < 0.05$ ) (Figures 4(a)–4(d)). Survival analysis revealed the high-risk

TABLE 2: Basic data of patients between different risk groups.

| Characteristics     | TCGA-LIHC cohort |            | P value |
|---------------------|------------------|------------|---------|
|                     | High risk        | Low risk   |         |
| Gender (%)          |                  |            | 0.063   |
| Female              | 51(28.0%)        | 68(37.2%)  |         |
| Male                | 131(72.0%)       | 115(62.8%) |         |
| Age (%)             |                  |            | 0.783   |
| <65y                | 109(59.9%)       | 107(58.5%) |         |
| ≥65y                | 73(40.1%)        | 76(41.5%)  |         |
| TNM stage (%)       |                  |            | 0.408   |
| I+II                | 121(66.5%)       | 133(72.7%) |         |
| III+IV              | 47(25.8%)        | 40(21.9%)  |         |
| unknown             | 14(7.7%)         | 10(5.5%)   |         |
| Grade (%)           |                  |            | <0.001  |
| G1+G2               | 96(52.7%)        | 134(73.2%) |         |
| G3+G4               | 83(45.6%)        | 47(25.7%)  |         |
| unknown             | 3(1.6%)          | 2(1.1%)    |         |
| Survival status (%) |                  |            | <0.001  |
| Living              | 101(55.5%)       | 134(73.2%) |         |
| Death               | 81(44.5%)        | 49(26.8%)  |         |

group had a shorter OS time than the low-risk group ( $P < 0.05$ ) (Figure 4(e)). The results of ROC manifested that the AUC values of 1-year survival, 2-year survival, and 3-year survival were 0.793, 0.713, and 0.704, respectively (Figure 4(f)). In the ICGC database, only a few liver cancer patients showed 5-year survival, and no results were obtained with R analysis. The ROC of 1, 2, and 3 years was performed to confirm the diagnostic value of the model.

**4.3. Prognostic Significance of the 11-Gene Signature in HCC.** Patients were grouped into two groups (high-risk and low-risk) based on the median risk value. According to the univariate and multivariate Cox regression analyses of TCGA database, the 11-gene signature was an independent prognostic factor for OS. The risk scores of univariate regression and multivariate analyses of OS were HR = 3.448 (2.479-4.796) ( $P < 0.001$ ) and HR = 3.145 (2.179-4.296) ( $P < 0.001$ ) (Figures 5(a) and 5(b)). Then, we performed the univariate and multivariate Cox regression analyses based on the ICGC cohort. The results also verified that the 11-gene signature was an independent prognostic factor for OS. The risk scores of univariate and multivariate analyses of OS were HR = 2.755 (1.714-4.431) ( $P < 0.001$ ) and HR = 2.225 (1.432-4.632) ( $P < 0.001$ ) (Figures 5(c) and 5(d)).

**4.4. Validation of the Prognostic Value of ROS-Related DEGs in HCC Based on Nomograms.** To further confirm the prognostic value of ROS-related DEGs in HCC, we constructed nomograms to predict 1-year OS, 3-year OS, and 5-year OS based on the above DEGs and calculated 1-, 3-, and 5-year OS of HCC patients (Figure 6(a)). The calibration curves fitted the data well. The C-index of a nomogram for OS prediction was 0.697 (95% CI: 0.674-0.721) (Figures 6(b)–6(d)).

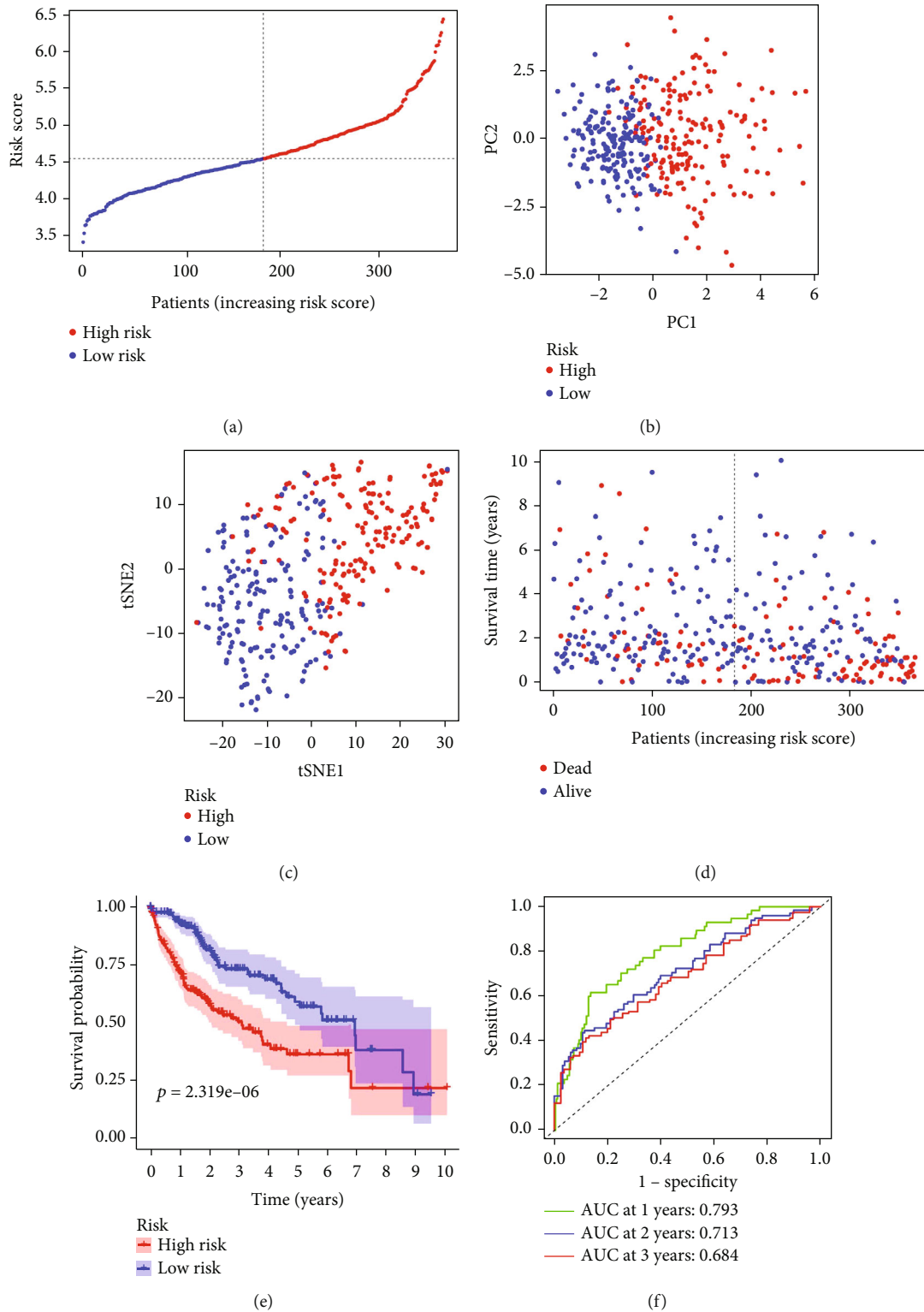


FIGURE 3: Prognostic analysis of 11-gene signature models in TCGA database. (a) The distribution and median value of the risk score in TCGA database. (b) PCA plot of TCGA database. (c) t-SNE analysis of TCGA database. (d) The distribution of OS status, OS, and risk score in TCGA database. (e) The OS of HCC patients between the high-risk group and low-risk group were analyzed by Kaplan-Meier curves. (f) AUC of time-dependent ROC curves confirmed the prognostic value of the risk score in TCGA database.

4.5. *Functional Analysis in HCC.* In addition, we determined the potential mechanisms of 11 ROS-related genes in HCC based on TCGA and ICGC databases. The “clusterProfiler”

R package was adopted to conduct GO and KEGG enrichment analyses. GO analysis indicated that B cell-mediated immunity, lymphocyte-mediated immunity, immunoglobulin-

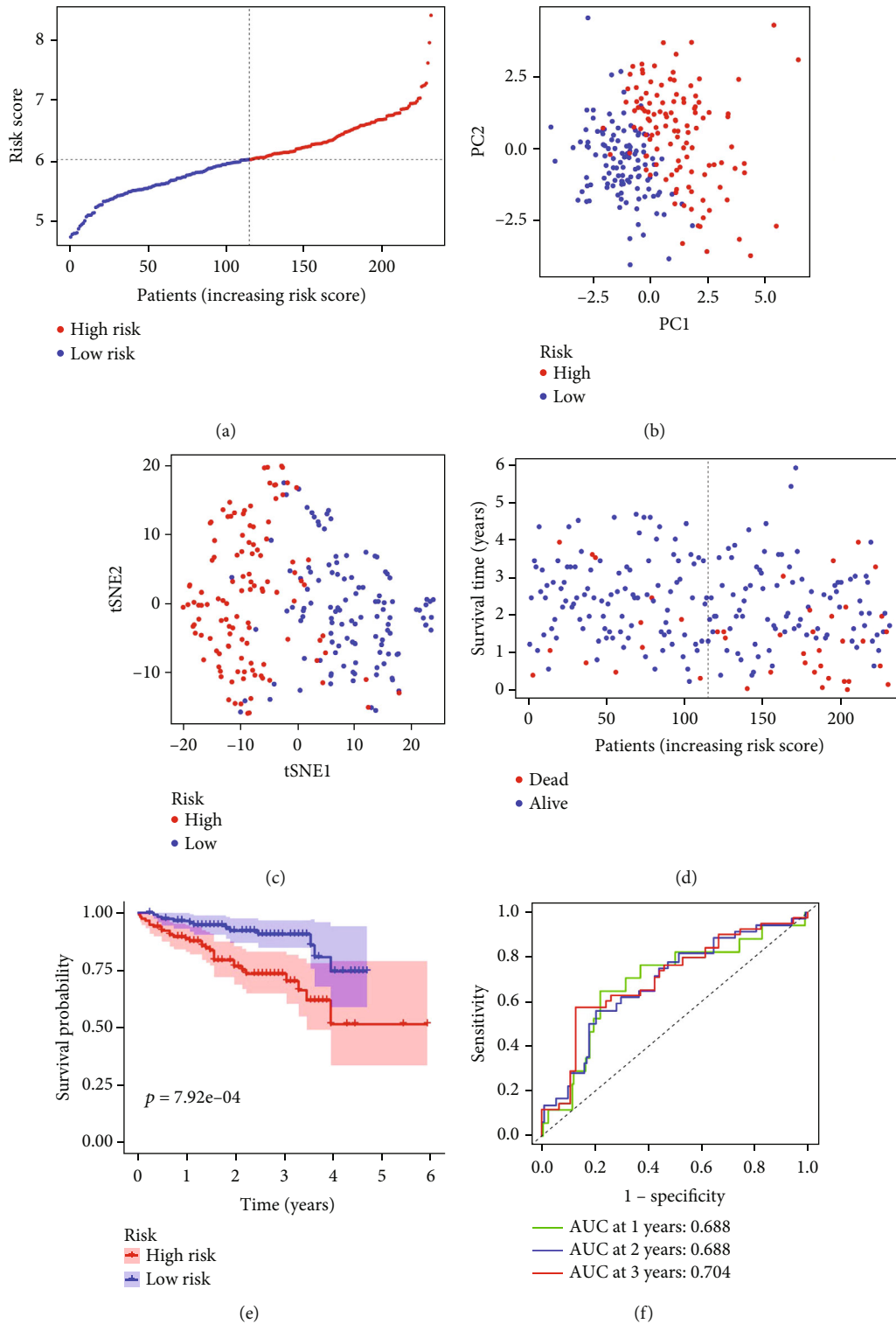


FIGURE 4: Prognostic analysis of 11-gene signature models in the ICGC database. (a) The distribution and median value of the risk score in the ICGC database. (b) PCA plot of the ICGC database. (c) t-SNE analysis of the ICGC database. (d) The distribution of OS status, OS, and risk score in the ICGC database. (e) The OS of HCC patients between the high-risk group and low-risk group was analyzed by Kaplan-Meier curves. (f) AUC of time-dependent ROC curves confirmed the prognostic value of the risk score in the ICGC database.

mediated immune response, histocompatibility complex (MHC) class II receptor activity, and major MHC protein complex binding were enriched. KEGG analysis showed that

the chemokine signaling pathway and cytokine-cytokine receptor interaction were enriched (Figures 7(a)–7(d)). Next, we also explored the relationship between risk score and

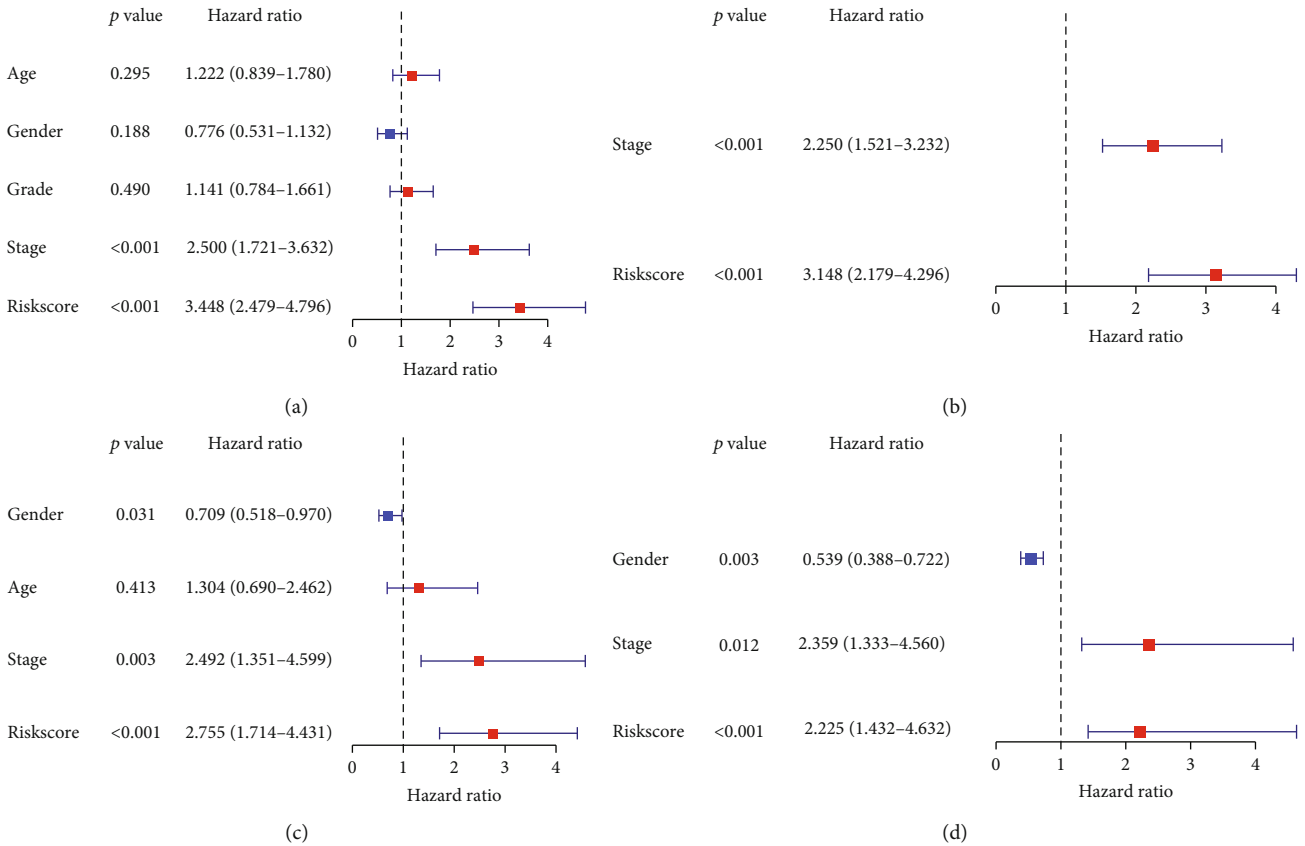


FIGURE 5: Results of the univariate and multivariate Cox regression analyses regarding OS. (a) The result of univariate Cox regression in TCGA database. (b) The result of multivariate Cox regression in TCGA database. (c) The result of univariate Cox regression in the ICGC database. (d) The result of multivariate Cox regression in the ICGC database.

immune status, and ssGSEA was used to quantify enrichment score for different subsets of immune cells as well as related functions and pathways. Our results also showed that the scores of aDCs, iDCs, macrophages, Tfh, Th1\_cells, Th2\_cells, and Treg in the high-risk group were higher compared with the low-risk group (Figure 8(a)). Immune infiltration of HCC with 11 ROS-related DEGs and the scores of APC\_co\_stimulation, CCR, checkpoint, HLA, and parainflammation were higher in the high-risk group than that in the low-risk group. The scores of type\_I\_IFN\_response and type\_II\_IFN\_response were lower in the high-risk group than that in the low-risk group (Figure 8(b)). Consistent with the aforementioned results, the association between risk score and immune status was investigated using the ICGC database. Our findings indicated that the scores of DCs, macrophages, and Th2\_cells were higher in the high-risk group than in the low-risk group (Figure 8(c)). The score of MHC\_class\_I was higher, and that of type\_II\_IFN\_response was lower in the high-risk group than in the low-risk group (Figure 8(d)).

**4.6. Correlation of Risk Score with the Expression of Immune Checkpoint Genes for Liver Cancer.** Currently, several genes are involved in the immune response, which are considered immune checkpoint genes. We investigated the expression of 38 immune checkpoint genes (listed in Supplementary

Table S2) in the high and low-risk groups of the model and performed survival analysis of differentially expressed genes (DEGs). Our results showed that 31 immune checkpoint genes were DEGs ( $P < 0.05$ ) (Figure 9(a)). Furthermore, survival analysis indicated that high expression of CD80, LDHA, TNFRSF4, and YTHDF1 was associated with poorer OS in the high-risk group compared with the low-risk group ( $P < 0.05$ ) (Figures 9(b)–9(e)). These findings suggested that the genes in the model possibly regulate tumor immune response by modulating immune checkpoint activity, thus providing a potential target for immunotherapy.

**4.7. Immune Infiltration Analyses.** We further analyzed the correlation between 11 ROS-related genes and immune infiltration cells based on the TIMER online database. Our findings have shown that OXSR1, PFKP, and STK25 associate with tumor purity (all  $P < 0.05$ ), CDKN2D correlates with B cell ( $\text{cor} = 0.419, P = 5.06e - 16$ ), CD8+ T cells ( $\text{cor} = 0.363, P = 4.17e - 12$ ), CD4+ T cells ( $\text{cor} = 0.419, P = 4.78e - 16$ ), macrophage ( $\text{cor} = 0.369, P = 2.07e - 20$ ), neutrophil ( $\text{cor} = 0.369, P = 1.46e - 12$ ), and dendritic cells ( $\text{cor} = 0.478, P = 7.74e - 21$ ), G6PD correlates with B cell ( $\text{cor} = 0.407, P = 3.95e - 15$ ), CD8+ T cells ( $\text{cor} = 0.321, P = 1.16e - 09$ ), CD4+ T cells ( $\text{cor} = 0.32, P = 1.25e - 09$ ), macrophage ( $\text{cor} = 0.522, P = 3.51e - 25$ ), neutrophil ( $\text{cor} = 0.419, P = 4.12e - 16$ ), and dendritic cells ( $\text{cor} = 0.432, P = 6.68e - 17$ ),

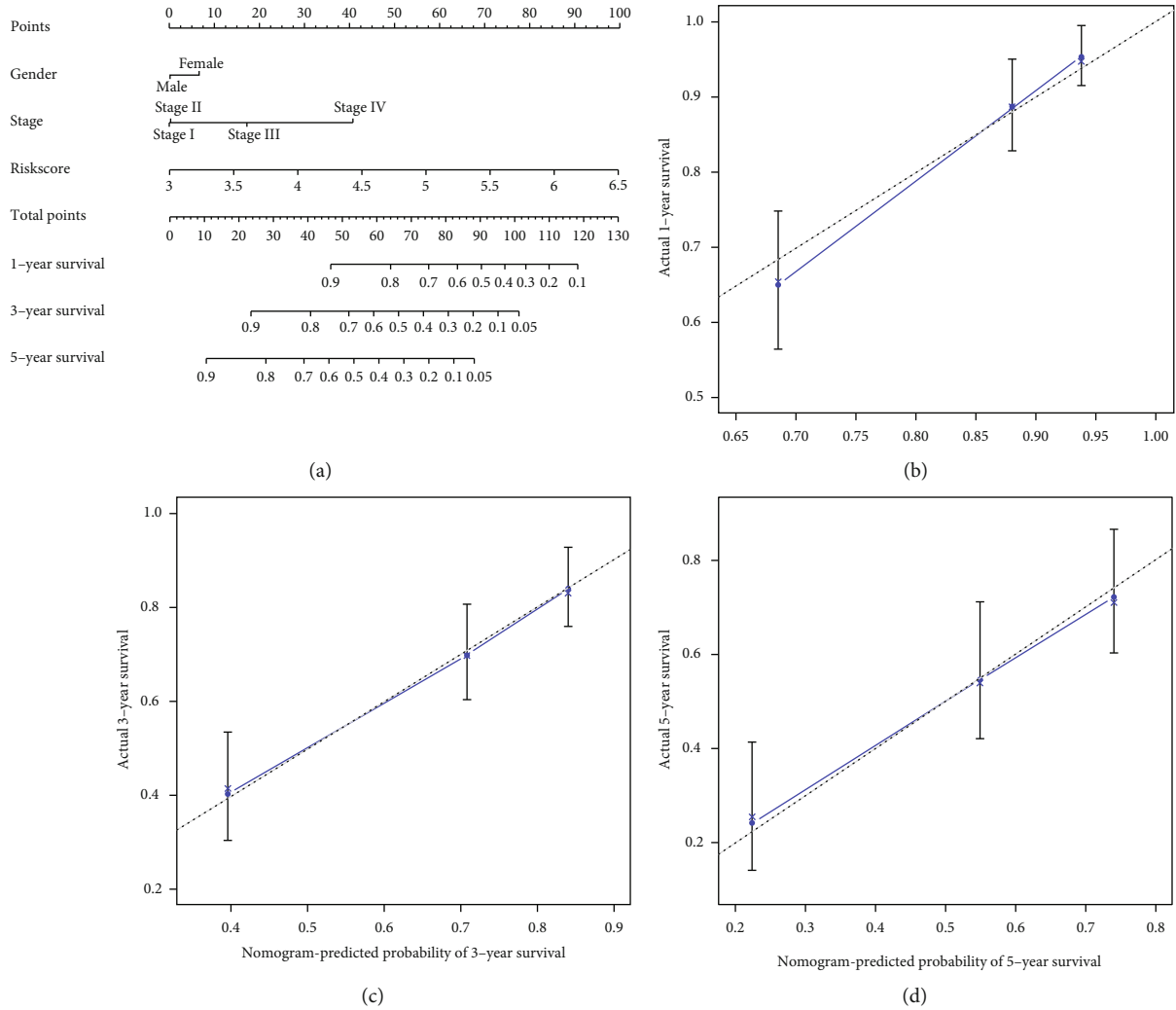
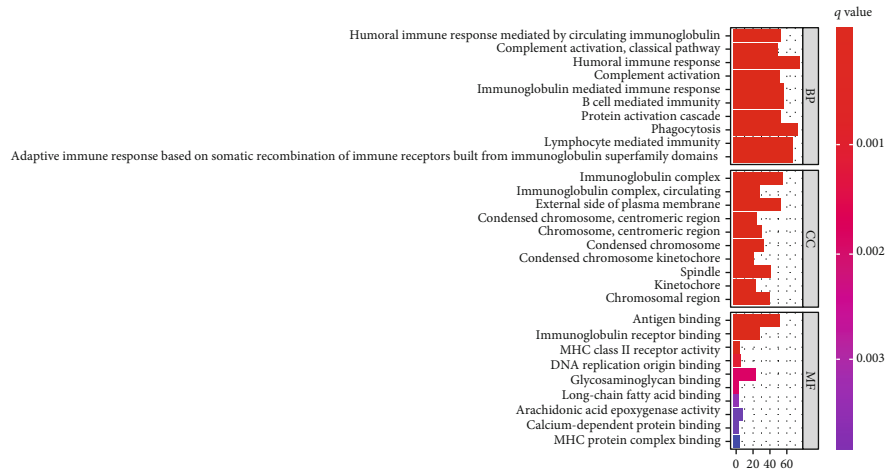


FIGURE 6: The prognostic value of nomograms for patients with HCC was based on TCGC database. (a) The calibration curve of nomograms for predicting overall survival (OS) at (b) 1 year, (c) 3 years, and (d) 5 years. The x-axis represents the possible OS, and the y-axis represents the actual OS.

GLRX2 associates with CD8+ T cells ( $cor = 0.145, P = 7.38e - 03$ ) and dendritic cells ( $cor = -0.109, P = 4.39e - 02$ ), GSR associates with B cell ( $cor = 0.203, P = 1.44e - 04$ ), CD8+ T cells ( $cor = 0.218, P = 4.79e - 05$ ), CD4+ T cells ( $cor = 0.237, P = 8.40e - 06$ ), macrophage ( $cor = 0.369, P = 1.82e - 12$ ), neutrophil ( $cor = 0.506, P = 8.13e - 24$ ), and dendritic cells ( $cor = 0.304, P = 1.11e - 08$ ), MSRA associates with CD4+ T cells ( $cor = -0.169, P = 1.67e - 03$ ) and macrophage ( $cor = -0.165, P = 2.28e - 03$ ), OXSR1 correlates with B cell ( $cor = 0.23, P = 1.71e - 05$ ), CD8+ T cells ( $cor = 0.2, P = 1.98e - 04$ ), CD4+ T cells ( $cor = 0.345, P = 4.79e - 11$ ), macrophage ( $cor = 0.381, P = 3.17e - 13$ ), neutrophil ( $cor = 0.441, P = 7.21e - 18$ ), and dendritic cells ( $cor = 0.337, P = 1.86e - 10$ ), PFKP correlates with B cell ( $cor = 0.307, P = 1.41e - 10$ ), CD8+ T cells ( $cor = 0.379, P = 3.78e - 13$ ), CD4+ T cells ( $cor = 0.416, P = 8.30e - 16$ ), macrophage ( $cor = 0.537, P = 1.50e - 27$ ), neutrophil ( $cor = 0.48, P = 3.07e - 21$ ), and dendritic cells ( $cor = 0.482, P = 3.76e - 21$ ), PRDX1 correlates with B cells ( $cor = 0.165, P = 2.14e - 03$ ), CD4+ T cells

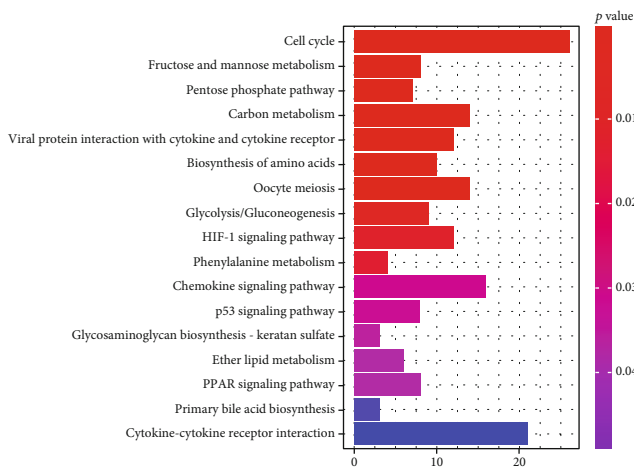
( $cor = 0.119, P = 2.84e - 02$ ), macrophage ( $cor = 0.164, P = 2.24e - 03$ ), and neutrophil ( $cor = 0.191, P = 3.99e - 04$ ), PRDX6 correlates with CD4+ T cells ( $cor = -0.222, P = 3.24e - 05$ ) and macrophage ( $cor = -0.127, P = 1.87e - 02$ ), SRXN1 correlates with B cells ( $cor = 0.162, P = 2.51e - 03$ ), macrophage ( $cor = 0.159, P = 3.19e - 03$ ), and neutrophil ( $cor = 0.216, P = 5.35e - 05$ ), and STK25 correlates with B cell ( $cor = 0.347, P = 3.71e - 11$ ), CD8+ T cells ( $cor = 0.223, P = 3.07e - 05$ ), CD4+ T cells ( $cor = 0.388, P = 8.08e - 14$ ), macrophage ( $cor = 0.413, P = 1.72e - 15$ ), neutrophil ( $cor = 0.283, P = 8.73e - 08$ ), and dendritic cells ( $cor = 0.391, P = 7.40e - 14$ ) (Figures 10(a)–10(k)). Furthermore, we demonstrated the relationship between ROS-related genes with immune filtering cells, and we observed that CDKN2D correlates with B cell ( $r = 0.228, P = 9.13e - 06$ ), CD4 T cells ( $r = 0.343, P = 1.39e - 11$ ), CD8 T cells ( $r = 0.388, P = 6.13e - 15$ ), dendritic cells ( $r = 0.208, P = 5.47e - 05$ ), macrophages ( $r = 0.298, P = 5.34e - 09$ ), and neutrophils ( $r = 0.174, P = 0.000735$ ), G6PD correlates with CD4 T cells



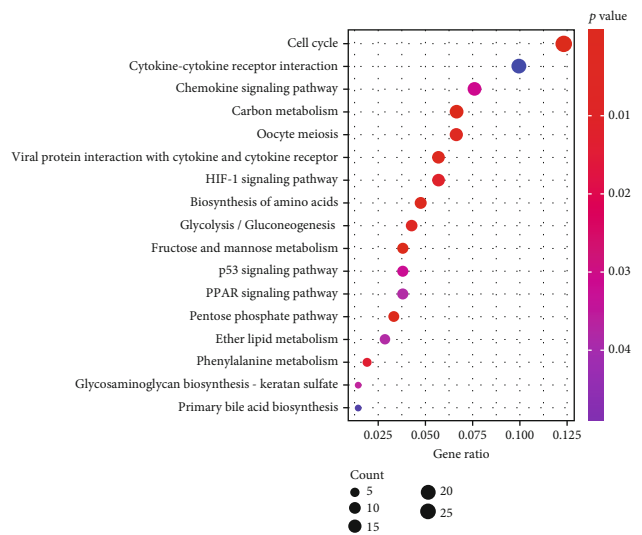
(a)



(b)



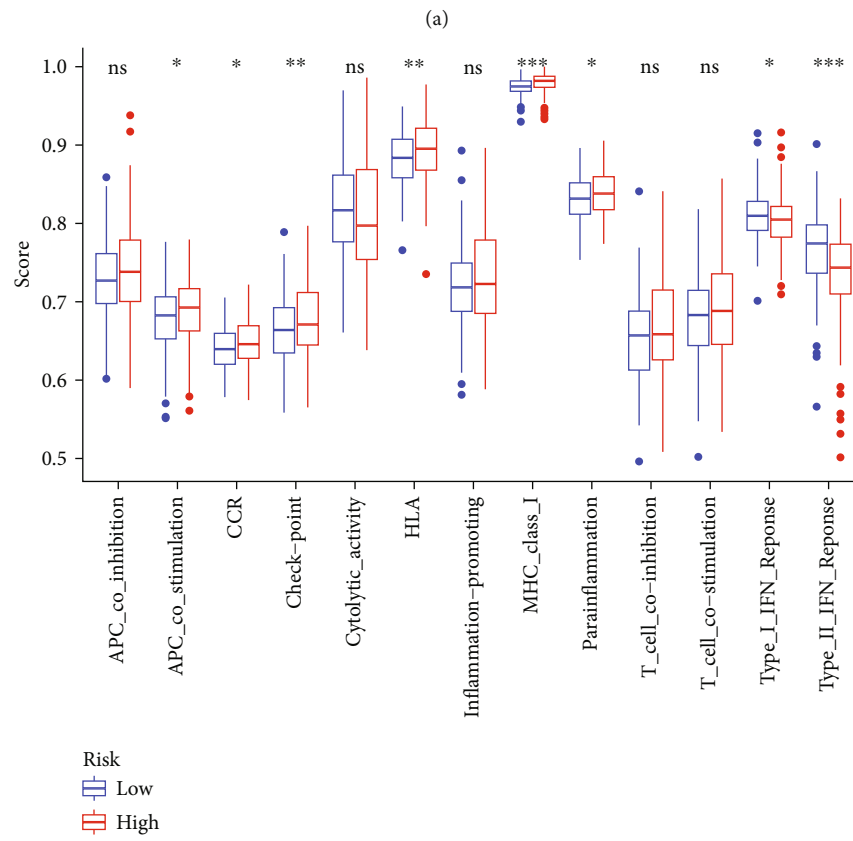
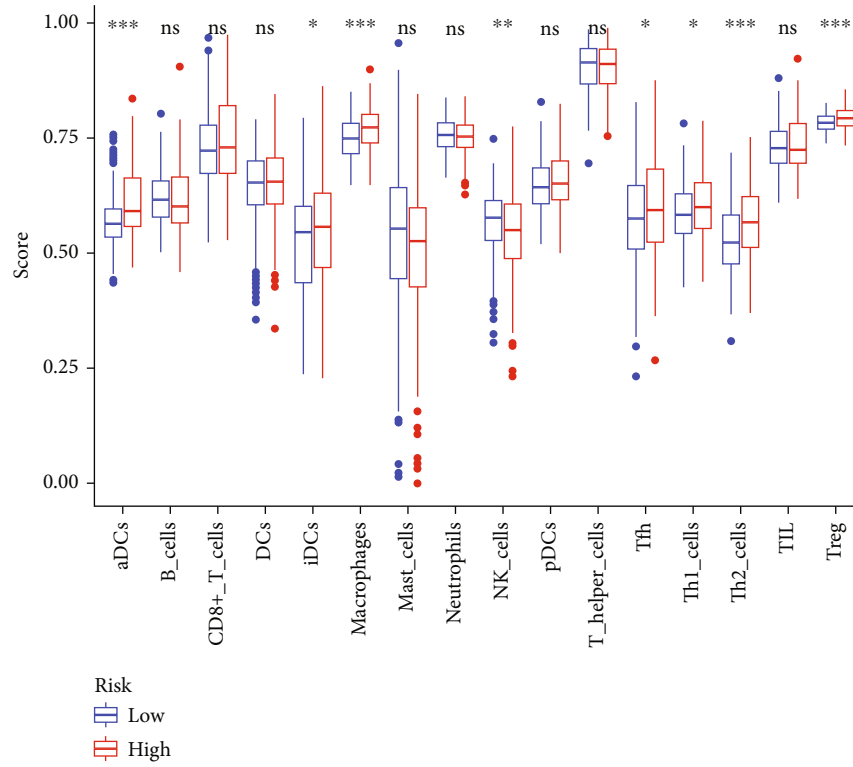
(c)



(d)

FIGURE 7: GO and KEGG analyses. (a, b) The results of GO enrichment analyses. (c, d) The result of KEGG enrichment analyses.





(b)

FIGURE 8: Continued.

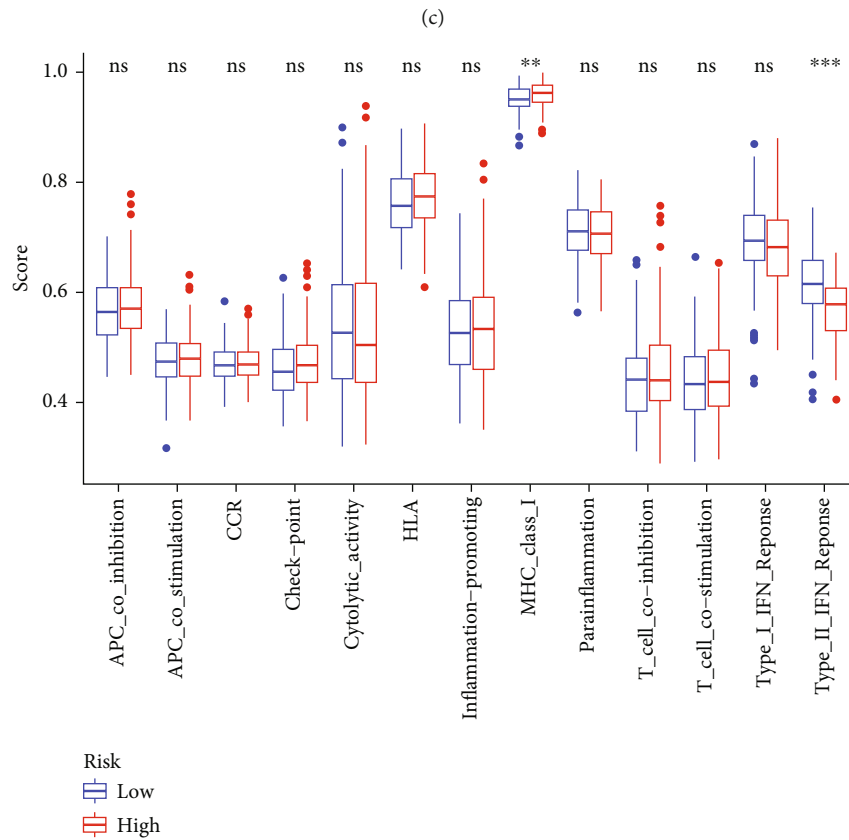
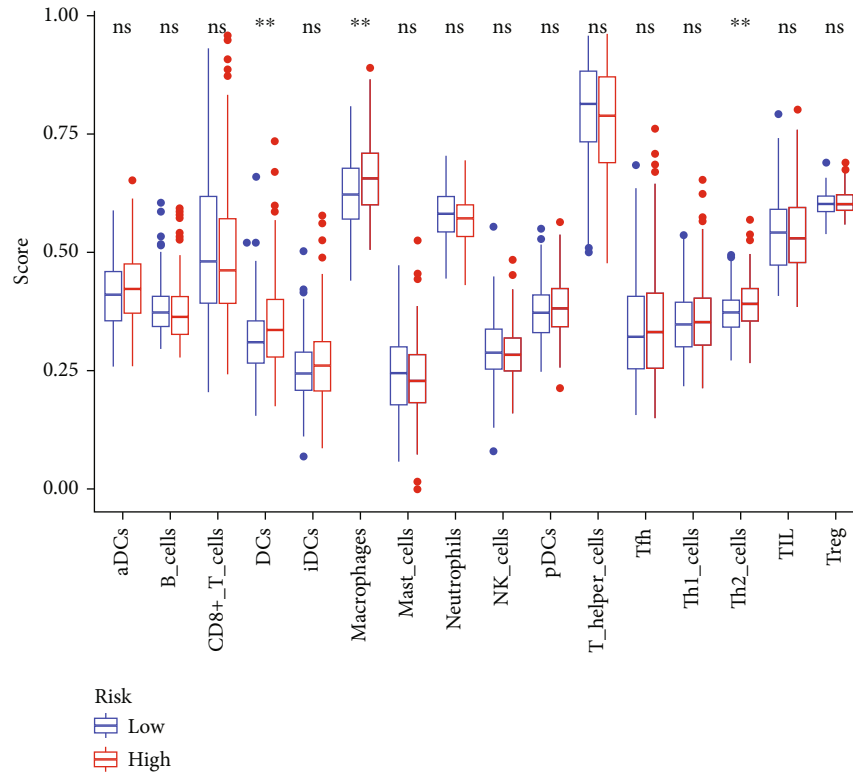


FIGURE 8: Comparison of ssGSEA score between different risk groups in the public database. (a) The score of 16 immune cells in TCGA database. (b) 13 immune-related functions are showed in boxplots. CCR: cytokine-cytokine receptor in TCGA database. (c) The score of 16 immune cells in the ICGC database. (d) 13 immune-related functions are showed in boxplots. CCR: cytokine-cytokine receptor in the ICGC database. Adjusted  $P$  values were displayed as follows: ns: not significant;  $*P < 0.05$ ;  $**P < 0.01$ ;  $***P < 0.001$ .

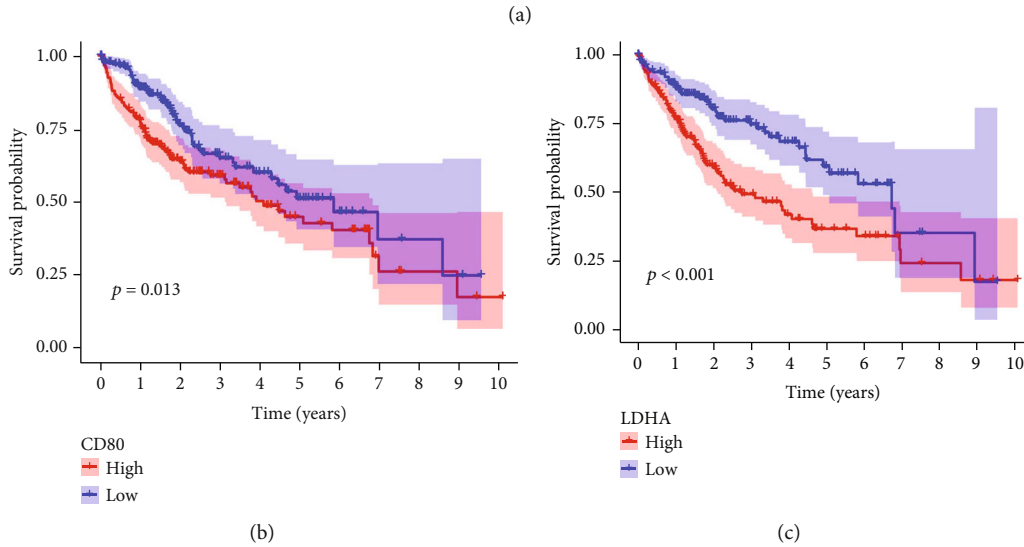
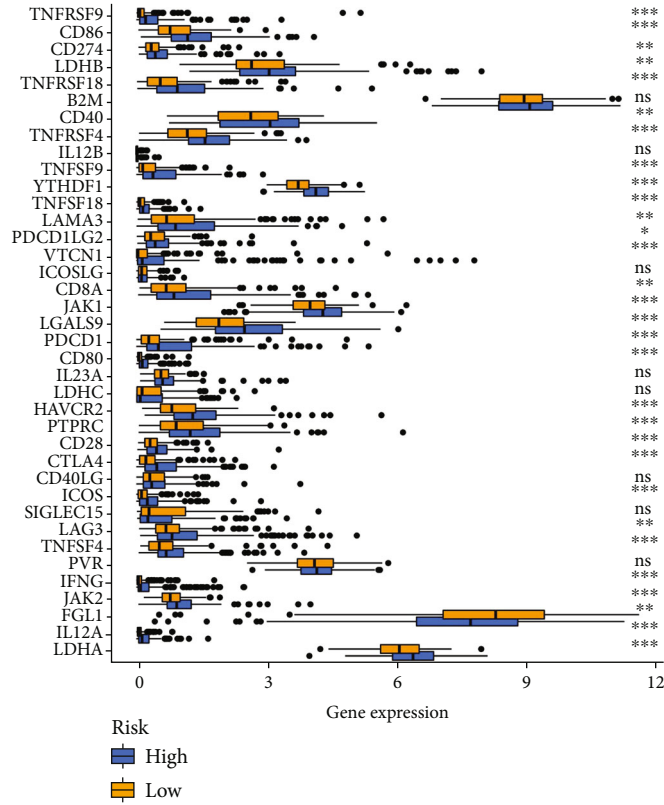


FIGURE 9: Continued.

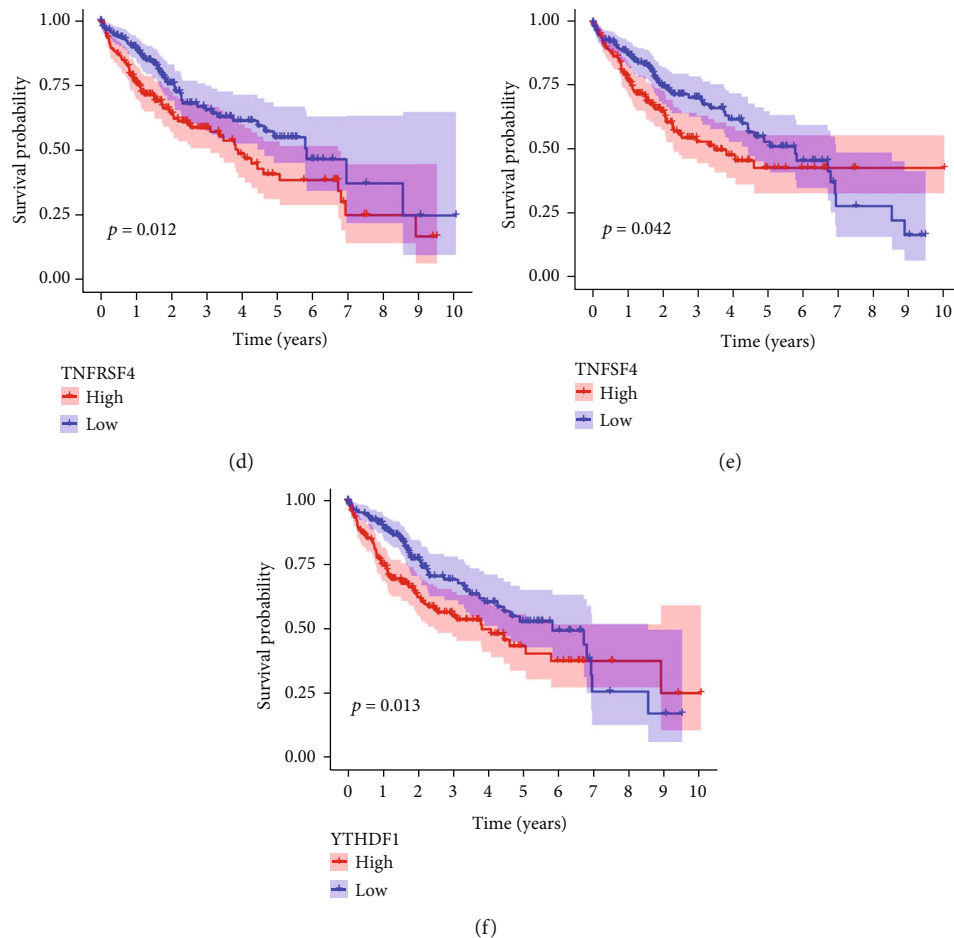


FIGURE 9: The analysis of immune checkpoint genes in HCC. (a) The expression of 38 immune checkpoint genes between the high-risk and low-risk groups. (b) Survival analysis of CD80. (c) Survival analysis of LDHA. (d) Survival analysis of TNFRSF4. (e) Survival analysis of TNFSF4. (f) Survival analysis of YTHDF1.

( $r = 0.406$ ,  $P < 2.2e - 16$ ), CD8 T cells ( $r = 0.188$ ,  $P = 0.00273$ ), dendritic cells ( $r = 0.3$ ,  $P = 4.2e - 09$ ), and macrophages ( $r = 0.126$ ,  $P = 0.0153$ ), GLRX2 associates with B cells ( $r = -0.192$ ,  $P = 0.000196$ ), CD4 T cells ( $r = 0.258$ ,  $P = 4.99e - 07$ ), and CD8 T cells ( $r = 0.116$ ,  $P = 0.249$ ), GSR associates with CD4 T cells ( $r = 0.196$ ,  $P = 0.000144$ ), CD8 T cells ( $r = -0.219$ ,  $P = 2.06e - 05$ ), dendritic cells ( $r = 0.247$ ,  $P = 1.47e - 06$ ), and neutrophils ( $r = 0.107$ ,  $P = 0.0394$ ), MSRA associates with CD4 T cells ( $r = -0.287$ ,  $P = 1.93e - 08$ ), CD8 T cells ( $r = 0.211$ ,  $P = 4.17e - 05$ ), macrophages ( $r = 0.114$ ,  $P = 0.0283$ ), and neutrophils ( $r = 0.102$ ,  $P = 0.0489$ ), OXSR1 correlates with B cell ( $r = -0.277$ ,  $P = 6.18e - 08$ ), CD8 T cells ( $r = -0.395$ ,  $P = 1.35e - 15$ ), dendritic cells ( $r = -0.254$ ,  $P = 7.49e - 07$ ), macrophages ( $r = -0.388$ ,  $P = 6.84e - 15$ ), and neutrophils ( $r = -0.244$ ,  $P = 1.96e - 06$ ), PFKP correlates with B cells ( $r = 0.37$ ,  $P = 1.94e - 13$ ), CD4 T cells ( $r = 0.306$ ,  $P = 1.83e - 09$ ), CD8 T cells ( $r = 0.233$ ,  $P = 5.7e - 06$ ), dendritic cells ( $r = 0.48$ ,  $P < 2.2e - 16$ ), macrophages ( $r = 0.427$ ,  $P < 2.2e - 16$ ), and neutrophils ( $r = 0.306$ ,  $P = 1.82e - 09$ ), PRDX1 correlates with CD8 T cells ( $r = 0.277$ ,  $P = 6.45e - 08$ ), dendritic cells ( $r = 0.215$ ,  $P = 2.85e - 05$ ), and macrophages ( $r = 0.134$ ,  $P = 0.00986$ ), PRDX6 correlates with B cells ( $r = -0.142$ ,  $P = 0.00609$ ), CD4 T cells ( $r = -0.258$ ,  $P = 4.81e - 07$ ), and CD8 T cells

( $r = 0.134$ ,  $P = 0.00952$ ), SRXN1 correlates with dendritic cells ( $r = 0.241$ ,  $P = 2.75e - 06$ ), STK25 correlates with B cells ( $r = -0.189$ ,  $P = 0.000253$ ), dendritic cells ( $r = -0.223$ ,  $P = 1.4e - 05$ ), macrophages ( $r = -0.243$ ,  $P = 2.28e - 06$ ), and neutrophils ( $r = -0.291$ ,  $P = 1.26e - 08$ ) (Figure S1).

**4.8. The Expression of 11 ROS-Related Genes in Different Immune Cells between Tumor Tissues and Matched Adjacent Tissues.** Since the expression of ROS-related genes was significantly correlated with immune-infiltrating cells, we speculated whether the levels of ROS-related gene expression were different in diverse immune cells in HCC tissues and corresponding adjacent tissues. By analyzing the GEPIA database, the findings indicated that the expression of 11 ROS-related genes was a statistical difference in HCC tissues (Figure 11(a)) ( $P < 0.05$ ). At the same time, we also explored the expression of 11 ROS-related genes in different immune cells between HCC tissues and paired noncancerous tissues, and our results revealed that the levels of 11 ROS-related gene expressions were significantly different in B naive cells, macrophage M0, and neutrophils (Figure 11(b)) ( $P < 0.05$ ). The above findings further demonstrated that ROS-related genes are related to tumor immunity.

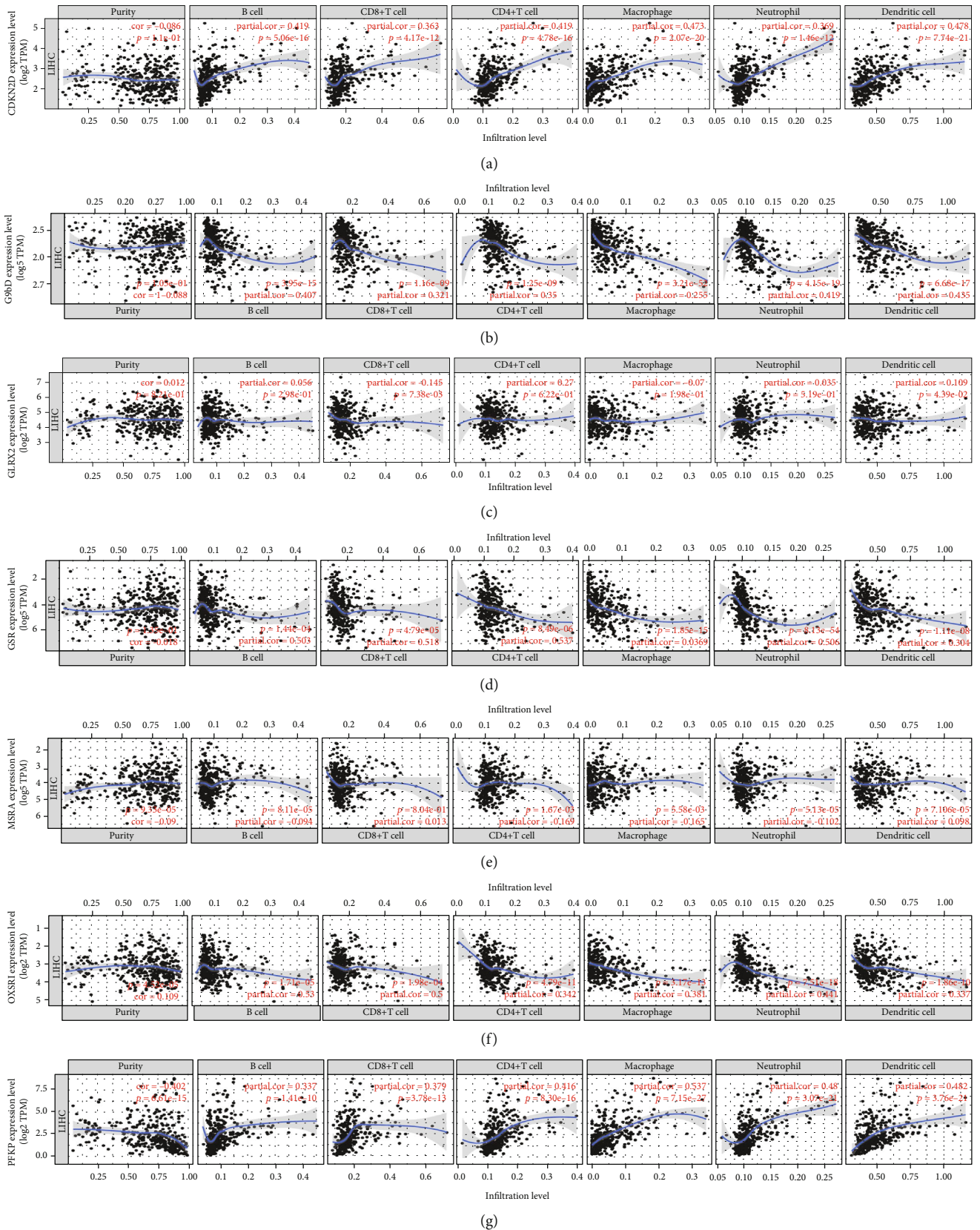


FIGURE 10: Continued.

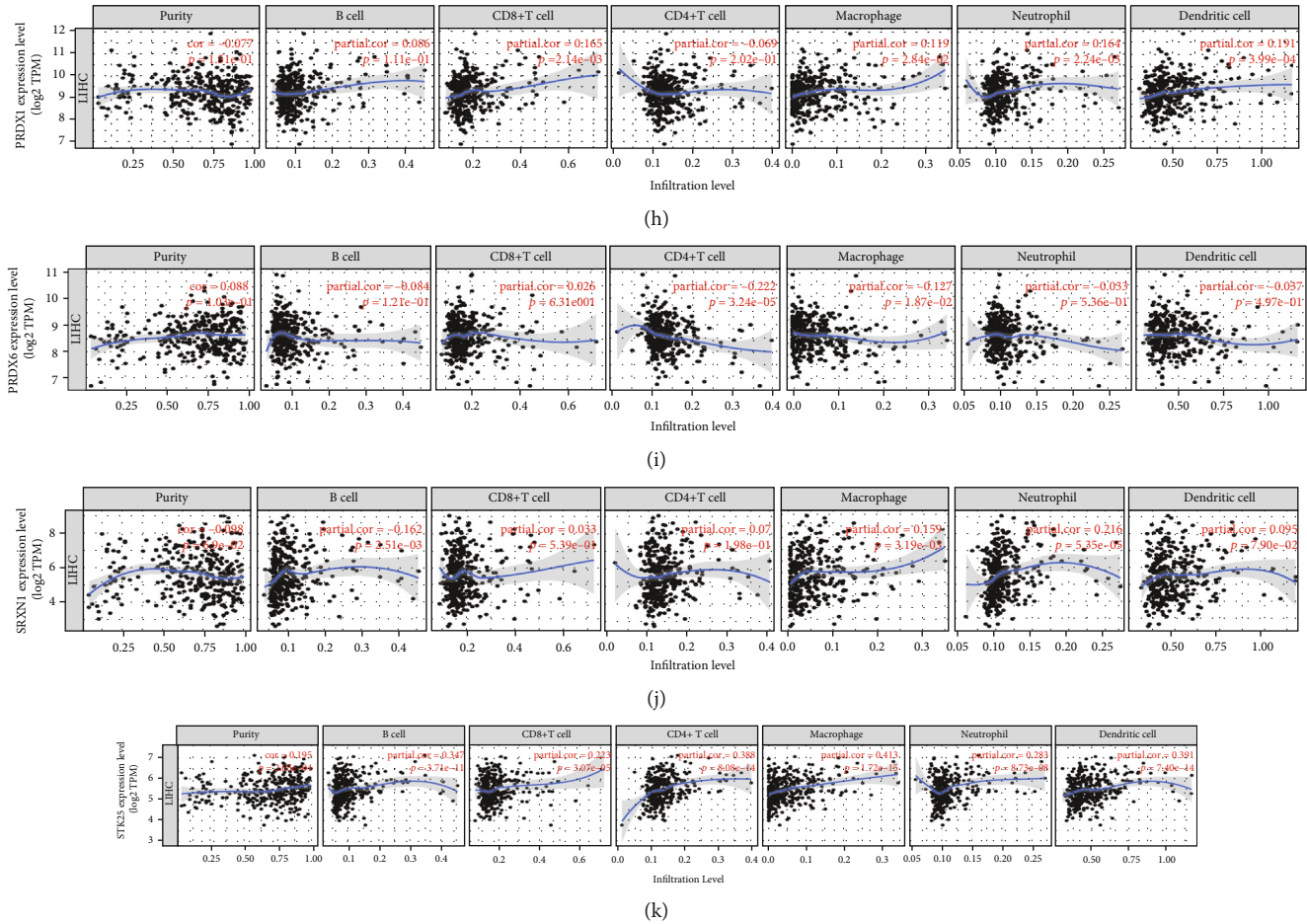


FIGURE 10: Immune infiltration analyses. (a) CDKN2D, (b) G6PD, (c) GLRX2, (d) GSR, (e) MSRA, (f) OXSRI, (g) PFKP, (h) PRDX1, (i) PRDX6, (j) SRXN1, and (k) STK25.

**4.9. The Correlation between the Copy Number Alterations of ROS-Related Genes and Immune-Infiltrating Cells.** Due to somatic copy number alterations (SCNAs) which are closely correlated with different cancers, circulating tumor DNA can be used to establish genome-wide profiles of SCNAs [26, 27]. Some studies confirmed correlations between CNA signatures and cancer characteristics [28, 29]. Therefore, we investigated the copy number alterations of ROS-related genes and the relationship of CNAs with immune-infiltrating cells. Our findings manifested that the majority of genes had CNA mutations (Figure 12(a)) ( $P < 0.05$ ), and the CNAs of G6PD, GLRX2, PFKP, PRDX1, PRDX6, and STK25 were related to immune-infiltrating cells, especially in B cells, CD8+ T cells, macrophages, neutrophils, and dendritic cells (Figures 12(b)–12(l)) ( $P < 0.05$ ).

**4.10. 11 ROS-Related Genes Are Correlated with Tumor Stemness, TME, and Drug Sensitivity.** Stemness represents the self-renewal, dedifferentiation with the ability to form other cell types in certain specific tissues [30]. A previous study indicated that tumor progression was not only affected by genetic changes, but also by tumor microenvironment [31]. Stemness index is associated with components of

TME, and genetic variations in tumor cells can interfere with antitumor immunotherapy [32]. Our results demonstrated that the expression of CDKN2D ( $R = 0.1$ ,  $P = 0.048$ ), G6PD ( $R = 0.26$ ,  $P = 6.8e - 07$ ), GLRX2 ( $R = 0.26$ ,  $P = 4e - 07$ ), MSRA ( $R = -0.11$ ,  $P = 0.036$ ), PFKP ( $R = -0.33$ ,  $P = 1.9e - 10$ ), PRDX1 ( $R = 0.37$ ,  $P = 3.3e - 13$ ), PRDX6 ( $R = 0.29$ ,  $P = 1.3e - 08$ ), and STK25 ( $R = 0.2$ ,  $P = 8.5e - 05$ ) was related to RNAss scores, and the expression of GLRX2 ( $R = 0.14$ ,  $P = 0.0081$ ), PFKP ( $R = -0.32$ ,  $P = 6.3e - 10$ ), and PRDX1 ( $R = 0.31$ ,  $P = 1.3e - 09$ ) was correlated with DNAss scores (Figures 13(a) and 13(b)). Then, we further analyzed the correlation of ROS-related genes with tumor immune microenvironment, and we found that the expression of CDKN2D ( $R = 0.11$ ,  $P = 0.031$ ), GLRX2 ( $R = -0.14$ ,  $P = 0.0063$ ), MSRA ( $R = 0.14$ ,  $P = 0.0054$ ), OXSRI ( $R = -0.13$ ,  $P = 0.014$ ), PFKP ( $R = 0.42$ ,  $P < 2.2e - 16$ ), PRDX6 ( $R = -0.13$ ,  $P = 0.016$ ), and STK25 ( $R = -0.25$ ,  $P = 1.3e - 06$ ) was correlated with stromal scores, the expression of CDKN2D ( $R = 0.32$ ,  $P = 2.9e - 10$ ), G6PD ( $R = 0.22$ ,  $P = 1.5e - 05$ ), OXSRI ( $R = -0.21$ ,  $P = 5.3e - 05$ ), PFKP ( $R = 0.41$ ,  $P < 2.2e - 16$ ), PRDX1 ( $R = 0.15$ ,  $P = 0.0041$ ), and STK25 ( $R = -0.12$ ,  $P = 0.024$ ) was associated with immune scores, and the expression of CDKN2D ( $R = 0.25$ ,  $P = 1.2e - 06$ ),

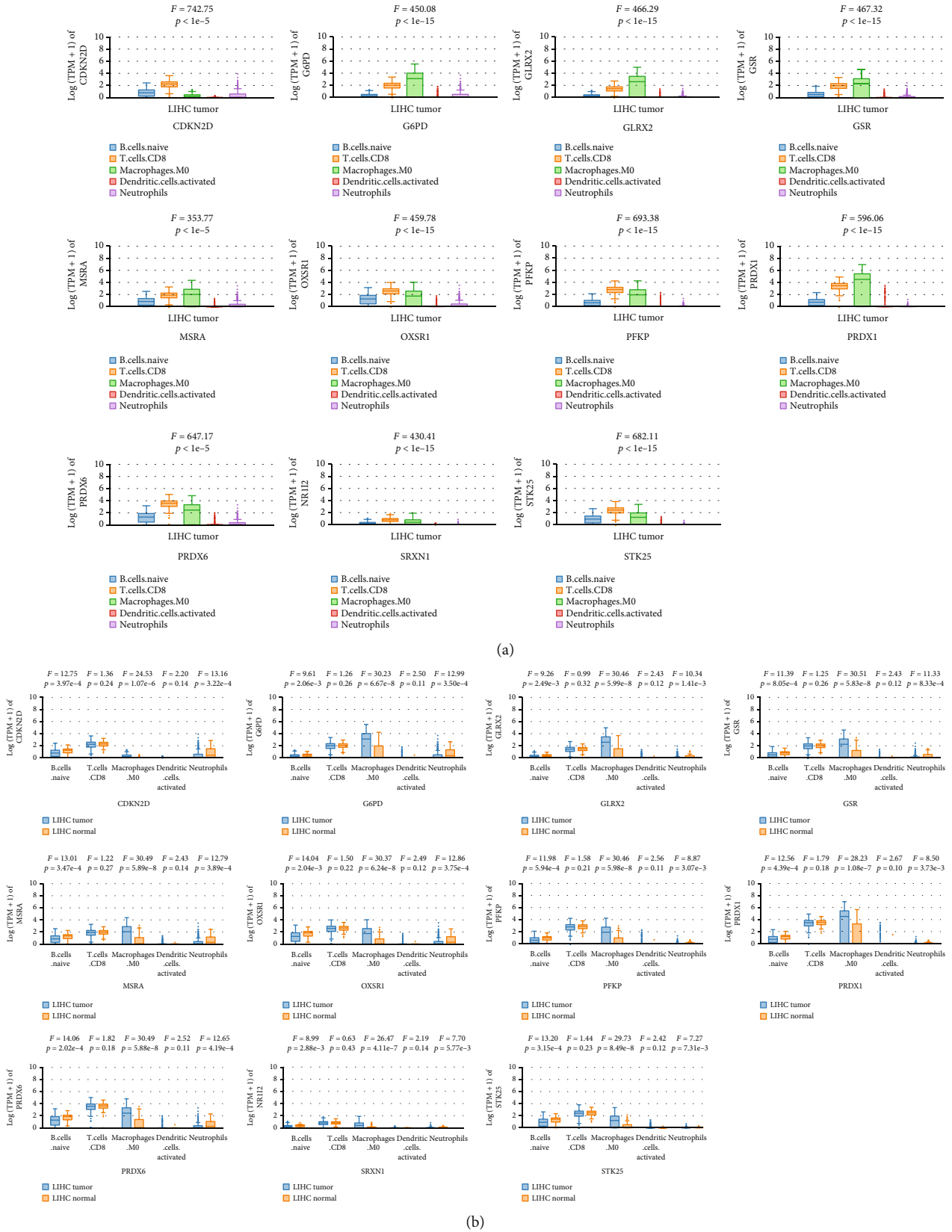
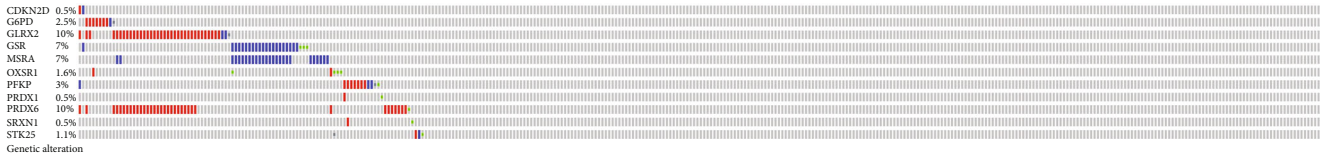
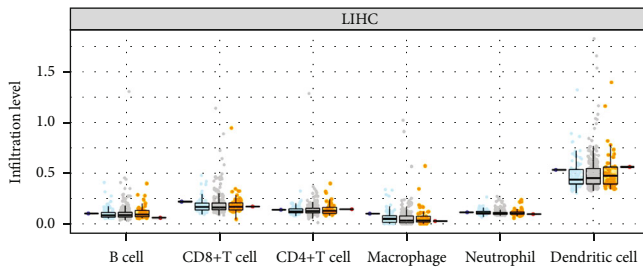


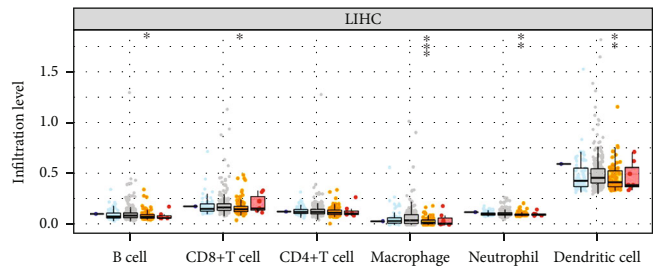
FIGURE 11: Comparison of the expression of 11 ROS-related genes in immune cells in HCC tissues and paired noncancerous tissues. (a) The expression of 11 ROS-related genes in diverse immune cells in HCC tissues. (b) The expression of 11 ROS-related genes in diverse immune cells between HCC tissues and corresponding normal tissues.



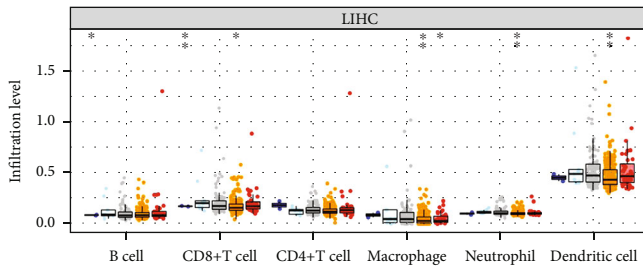
(a)



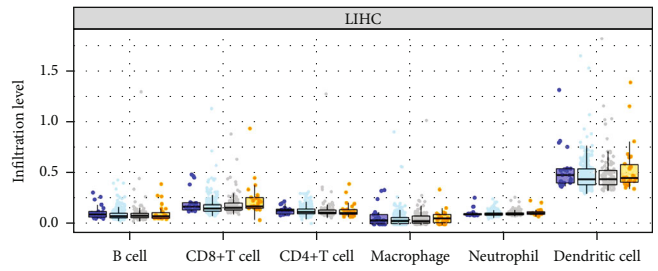
(b)



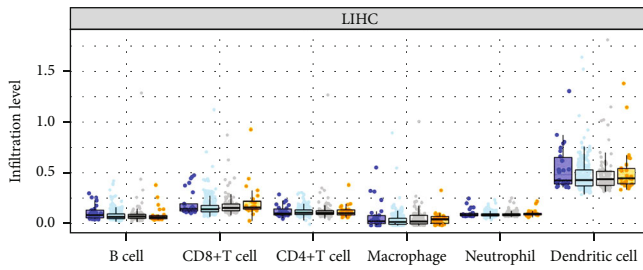
(c)



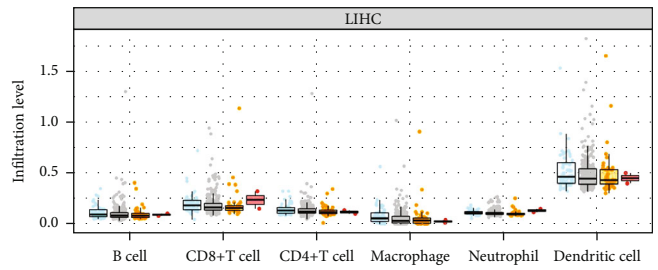
(d)



(e)



(f)



(g)

FIGURE 12: Continued.



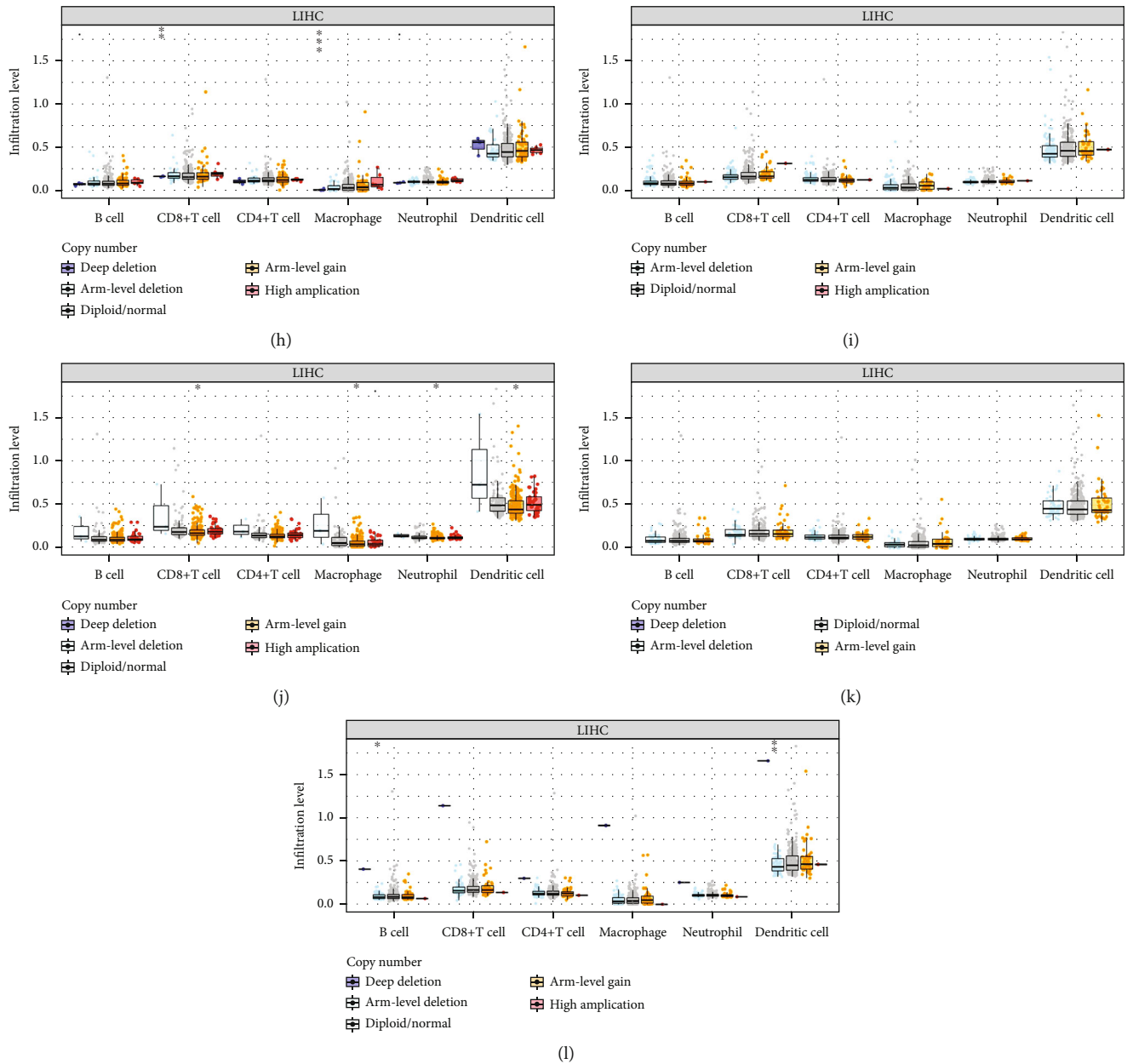


FIGURE 12: Copy number variation and immune infiltration correlated with 11 ROS-related gene expressions in HCC. (a) Copy number variation of 11 ROS-related gene expressions. (b) The relationship between copy number alterations of CDKN2D and immune infiltration. (c) The association between copy number alterations of G6PD and immune infiltration. (d) The relationship between copy number alterations of GLRK2 and immune infiltration. (e) The relationship between copy number alterations of GSR and immune infiltration. (f) The association between copy number alterations of MSRA and immune infiltration. (g) The relationship between copy number alterations of GXSR1 and immune infiltration. (h) The correlation between copy number alterations of PFKP and immune infiltration. (i) The relationship between copy number alterations of PRDX1 and immune infiltration. (j) The association between copy number alterations of PRDX6 and immune infiltration. (k) The relationship between copy number alterations of SRXN1 and immune infiltration. (l) The correlation between copy number alterations of STK25 and immune infiltration.

G6PD ( $R = 0.1$ ,  $P = 0.047$ ), MSRA ( $R = 0.11$ ,  $P = 0.028$ ), OXSR1 ( $R = -0.19$ ,  $P = 0.00029$ ), PFKP ( $R = 0.46$ ,  $P < 2.2e - 16$ ), and STK25 ( $R = -0.18$ ,  $P = 0.00036$ ) was connected with estimate scores (Figures 13(c)–13(e)). In addition, some studies indicated there was a relationship between the level of ROS and multidrug resistance in cancer [33–35]. Therefore,

we investigated the association of 11 ROS-related gene expressions with chemotherapy drugs. As shown in Figure 13(f) (we took STK25 as an example), STK25 expression was correlated with clofarabine ( $cor = 0.392$ ,  $P = 0.002$ ), Actinomycin D ( $cor = -0.325$ ,  $P = 0.011$ ), 5-fluoro deoxy uridine ( $cor = 0.334$ ,  $P = 0.009$ ), Vinorelbine ( $cor = 0.339$ ,  $P = 0.008$ ), Dolastain

Cancer: LIHC

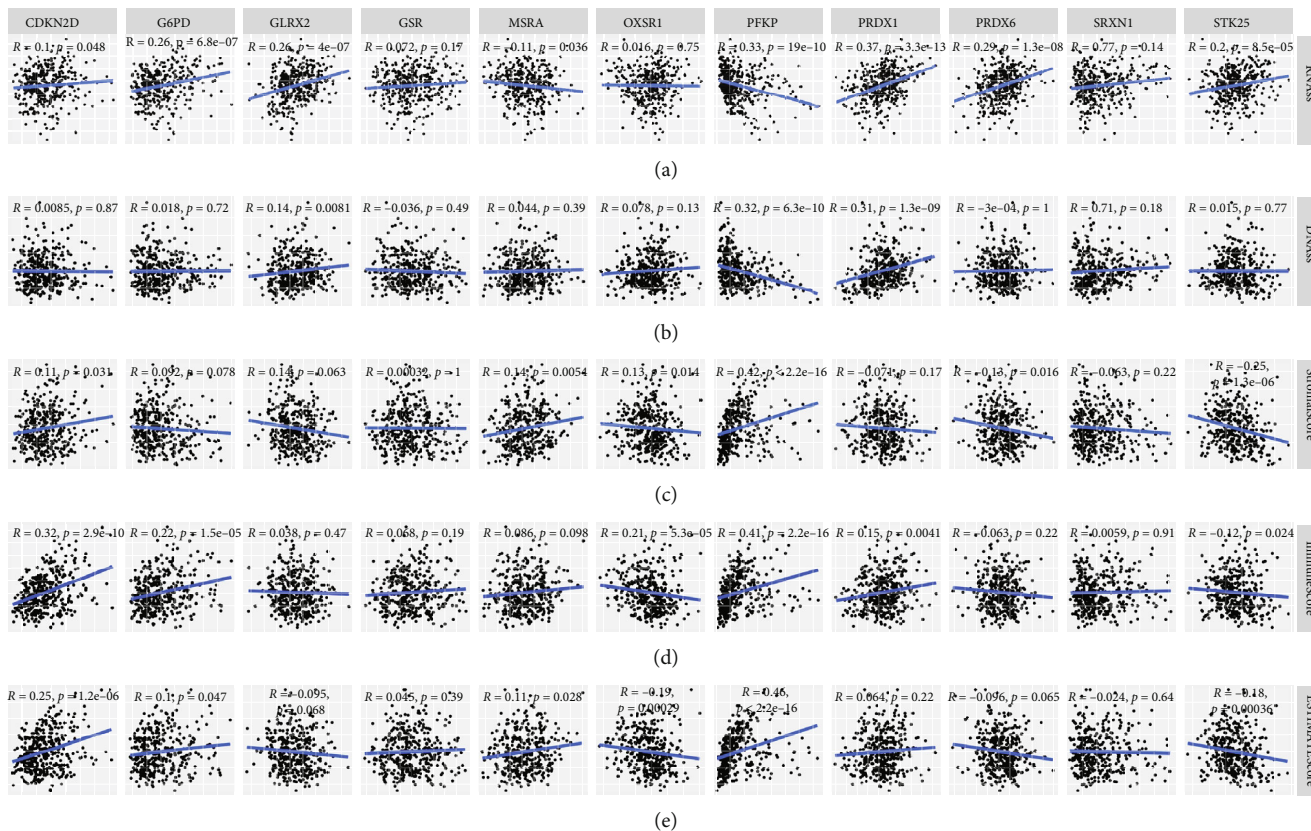


FIGURE 13: Continued.



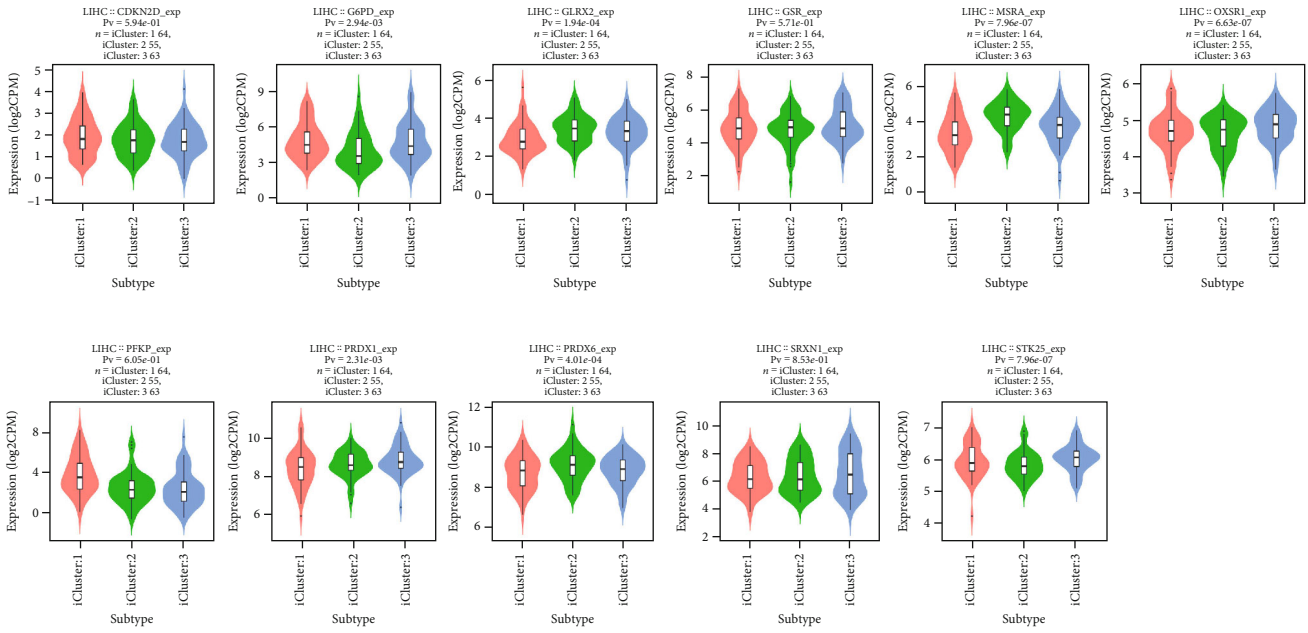
FIGURE 13: Correlation of 11 ROS-related gene expressions with tumor stemness, TME, and drug sensitivity. (a) Correlation of 11 ROS-related gene expressions with RNAss. (b) Correlation of 11 ROS-related gene expressions with DNAss. (c) Association of 11 ROS-related gene expressions with stromal score. (d) Association of 11 ROS-related gene expressions with immune score. (e) Association of 11 ROS-related gene expressions with estimate score. (f) Correlation of 11 ROS-related gene expressions with multidrug sensitivity.

10 ( $cor = -0.357$ ,  $P = 0.005$ ), Cladribine ( $cor = -0.392$ ,  $P = 0.002$ ), and Fludarabine ( $cor = 0.404$ ,  $P = 0.001$ ). Collectively, the above findings indicated that ROS-related genes might be as effective targets to reduce tumor drug resistance.

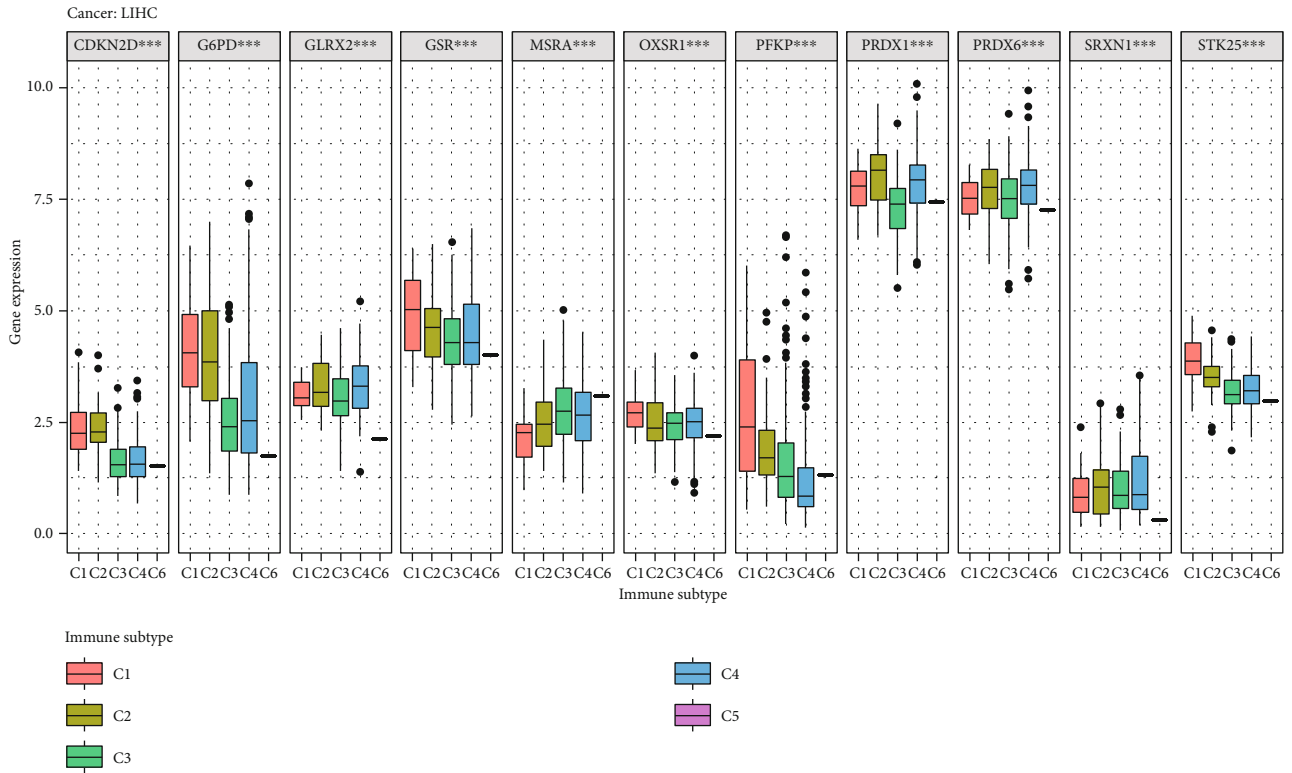
**4.11. Relationship between 11 ROS-Related Gene Expressions and Tumor Subtypes in HCC.** To further dissect the role of ROS-related genes in liver cancer, we divided liver cancer patients into three kinds of molecular subtypes based on TCGA database, namely, iCluster:1, iCluster:2, and iCluster:3, and five types of immune subtypes, namely, C1, C2, C3, C4, and C6. We explored whether the expression of ROS-related genes was a statistical difference among different subtypes. Our findings showed that the expression of G6PD, GLRX2, MSRA, PFKF, PRDX1, PRDX6, and STK25 was significantly different in three molecular subtypes ( $P < 0.05$ ) (Figure 14(a)). We also found that the expression of CDKN2D, G6PD, GLRX2, MSRA, PFKF, PRDX1, PRDX6, and STK25 was a significant difference

among five immune subtypes ( $P < 0.05$ ) (Figure 14(b)). The above results further confirmed that ROS-related genes were involved in the occurrence and development of liver cancer.

**4.12. 11 ROS-Related Gene Expressions and Survival Analysis in HCC.** The aforementioned results have shown that the model can predict the survival and prognosis of liver cancer patients, and it is closely related to tumor-infiltrating cells, TME, and immune checkpoints. To further study the role of 11 ROS-related genes in liver cancer, based on the UALCAN database, we found that CDKN2D, G6PD, GLRX, GSPPFKP, PRDX1, PRDX6, SRXN, and STK25 expression was higher in liver cancer tissues than that in adjacent normal tissues, and MSRA and OXSR1 expression was lower in liver cancer tissues compared with paired noncancerous tissues ( $P < 0.05$ ) (Figure 15(a)). Then, we also explored the correlation between the expression of 11 ROS-related genes and TNM stages in liver cancer, and the findings



(a)



(b)

FIGURE 14: The relationship between 11 ROS-related gene expressions and subtypes of HCC. (a) The correlation of 11 ROS-related gene expressions with molecular subtypes in HCC. (b) The association of 11 ROS-related gene expressions with immune subtypes in HCC.

showed that the expression of CDKN2D, G6PD, MSRA, OXSRI, PFKP, and STK25 was connected with TNM stages ( $P < 0.05$ ) (Figure 15(b)). Finally, survival analysis was performed based on the GEPIA and Kaplan-Meier plotter data-

bases. The results indicated that high expression of CDKN2D ( $P = 0.0014$ ), G6PD ( $P = 9.7e-05$ ), GLRX2 ( $P = 0.0016$ ), GSR ( $P = 0.0067$ ), PFKP ( $P = 0.0032$ ), PRDX1 ( $P = 0.00051$ ), PRDX6 ( $P = 0.0072$ ), and STK25 ( $P = 0.0051$ )

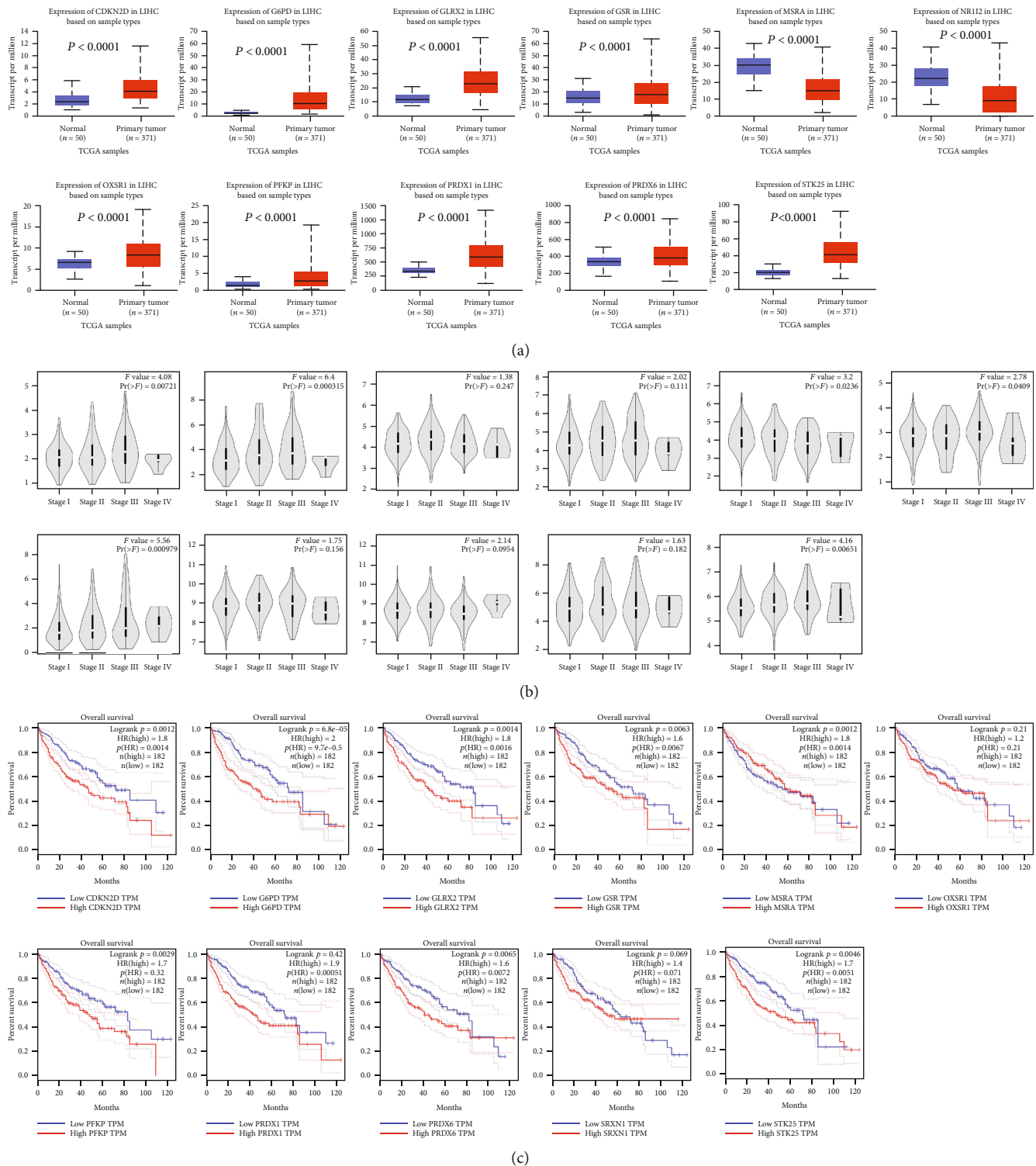


FIGURE 15: 11 ROS-related gene expressions in HCC. (a) The expression of 11 ROS-related genes between HCC tissues and corresponding normal tissues. (b) Correlation of 11 ROS-related gene expressions with TNM stages in HCC. (c) Survival analysis of 11 ROS-related genes.

was associated with poor overall survival (OS) via the analysis of GEPIA cohort (Figure 15(c)). Then, we further demonstrated the relationship between the expression of 11 ROS-related genes and survival of liver cancer patients based on the Kaplan-Meier plotter database, and the findings revealed

that overexpression of CDKN2D ( $P = 0.0099$ ), G6PD ( $P = 1.1e - 07$ ), GSR ( $P = 0.00019$ ), MSRA ( $P = 0.0013$ ), PFKP ( $P = 0.00016$ ), PRDX1 ( $P = 0.025$ ), SRXN1 ( $P = 0.00054$ ), and STK25 ( $P = 0.004$ ) was correlated with short overall survival time (Figure S2).

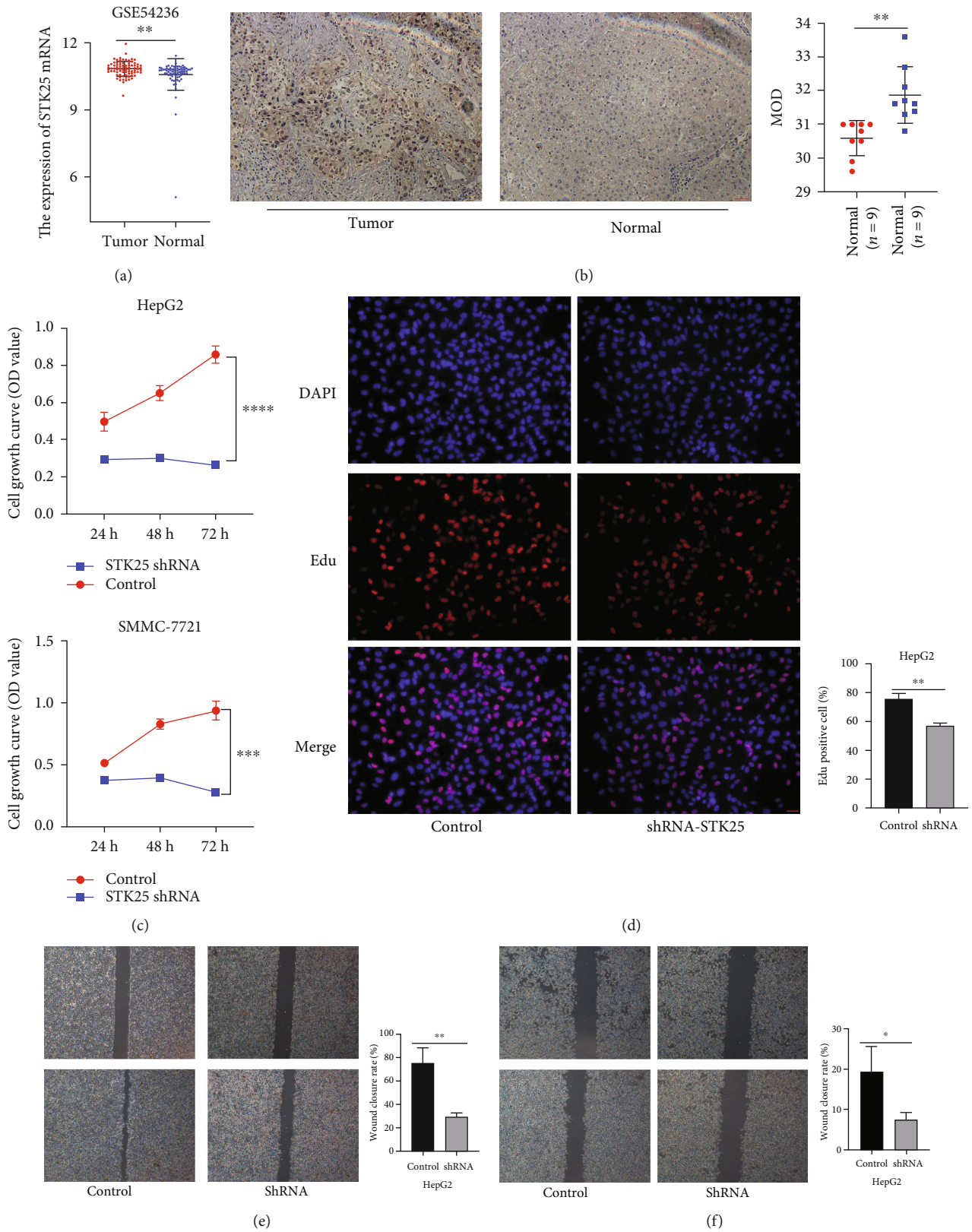
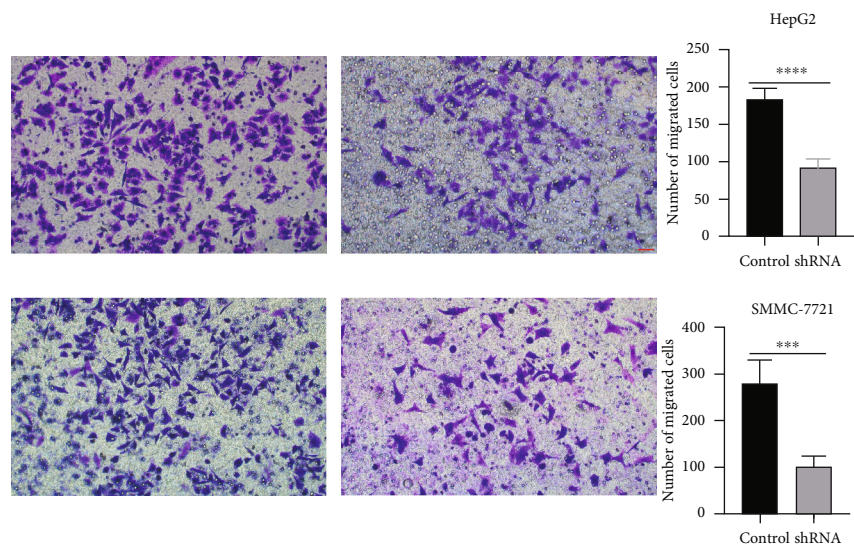
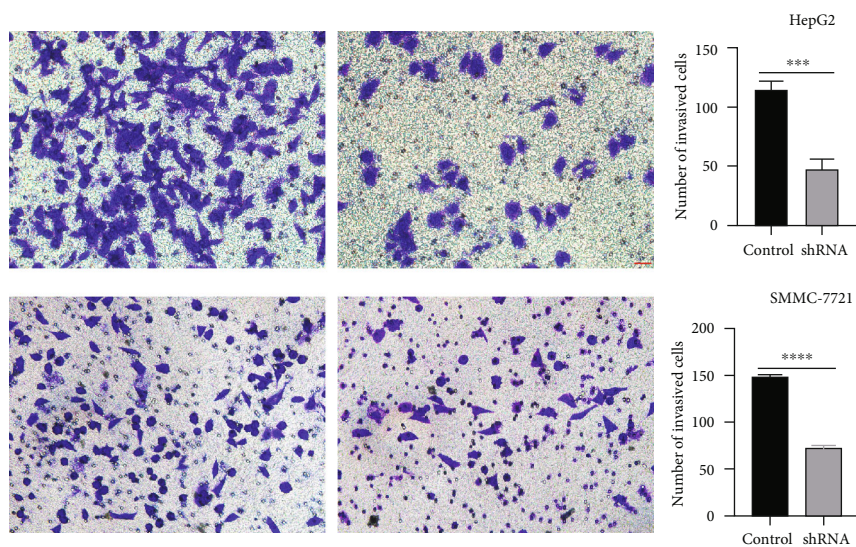


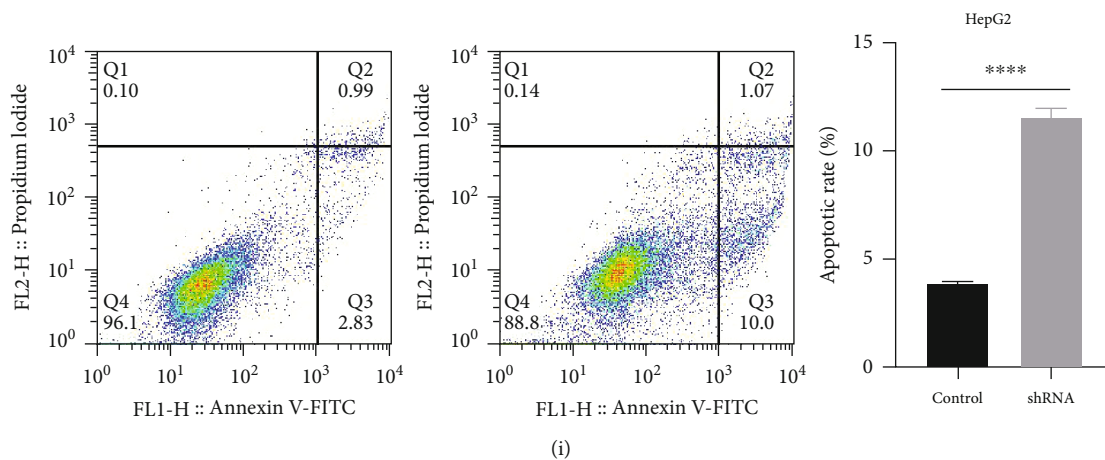
FIGURE 16: Continued.



(g)



(h)



(i)

FIGURE 16: Continued.

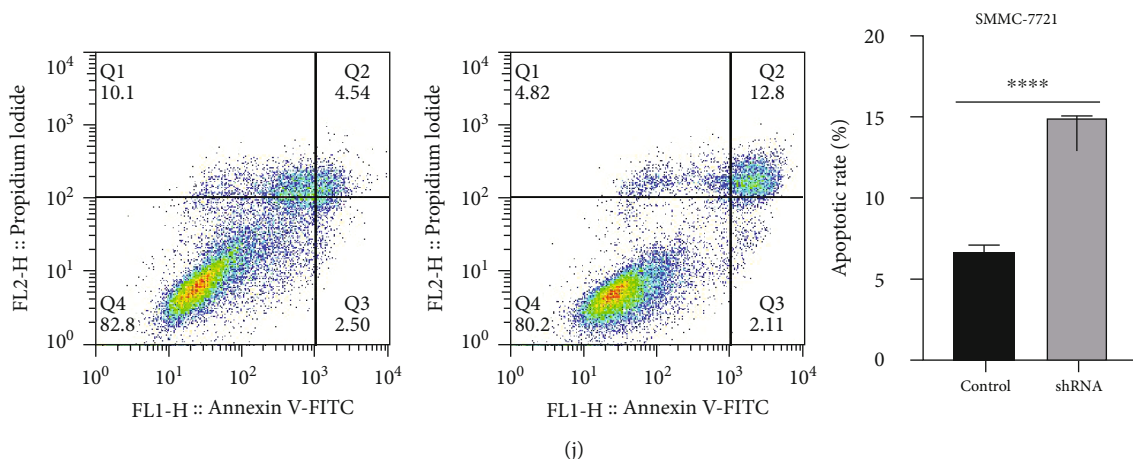


FIGURE 16: The expression and biological behavior of STK25 in liver cancer. (a) The level of STK25 expression was confirmed by GEO. (b) The protein level of STK25 expression was verified by IHC in liver cancer. Magnification,  $\times 200$ . Scale bar:  $50 \mu\text{m}$ . (c) STK25 knockdown inhibited the proliferation capacity of HepG2 cells and SMMC-7721 via CCK8 assays. (d) STK25 knockdown suppressed the proliferation capacity of HepG2 cells via EdU assays. Magnification,  $\times 200$ . Scale bar:  $50 \mu\text{m}$ . (e) STK25 knockdown suppressed the migration capacity of HepG2 cells via wound healing assays. Magnification,  $\times 40$ . Scale bar:  $200 \mu\text{m}$ . (f) STK25 knockdown suppressed the migration capacity of SMMC-7721 cells via wound healing assays. Magnification,  $\times 40$ . Scale bar:  $200 \mu\text{m}$ . (g) STK25 knockdown decreased the invasion capacity of liver cancer cells (HepG2 and SMMC-7721) via transwell invasive assays. Magnification,  $\times 200$ . Scale bar:  $50 \mu\text{m}$ . (h) STK25 knockdown decreased the migration capacity of liver cancer cells (HepG2 and SMMC-7721) via transwell migration assays. Magnification,  $\times 200$ . Scale bar:  $50 \mu\text{m}$ . (i) STK25 knockdown increased the apoptosis of HepG2 cells. (j) STK25 knockdown promoted the apoptosis of SMMC-7721 cells.

**4.13. Comparison of the Protein Level of STK25 in the Tumor and Paired Noncancerous Samples.** To further verify the expression of STK25 in liver cancer tissues and paracancerous tissues by the GEO database and clinical specimens, the expression of STK25 was confirmed based on the GEO database. The results showed that STK25 expression was higher in liver cancer tissues compared with paired noncancerous tissues (Figure 16(a)). Consistent with the results of TCGA and GEO databases, we detected STK25 expression in 9 pair tissues by performing IHC assays. Our findings revealed that the expression of STK25 was higher in the liver cancer tissues compared with the paracancerous tissues (Figure 16(b)).

**4.14. STK25 Knockdown Promoted Apoptosis and Inhibited the Proliferation, Migration, and Invasion Capacity of Liver Cancer Cells.** The analysis of public database data showed that STK25 was correlated with survival and prognosis of patients with liver cancer. We further demonstrated the role of STK25 in liver cancer by performing *in vitro* experiments. CCK8 assay revealed that STK25 knockdown significantly suppressed the proliferation of liver cancer cells (Figure 16(c)). In line with the result of CCK8 assay, EdU assays indicated that STK25 knockdown markedly decreased the proliferation capacity of liver cancer cells (Figure 16(d)). Wound healing assay and transwell migration assays were utilized to test cell migration. We observed that STK25 knockdown dramatically suppressed the migration capacity of liver cancer cells (Figures 16(e)–16(g)). In addition, transwell invasion assays were performed to estimate the invasion ability of cells, and the findings showed that STK25 knockdown significantly inhibited the invasion capacity of liver cancer cells (Figure 16(h)). A previous study demonstrated that the dysregulation of the balance between apoptosis and

proliferation of cells can lead to hepatocarcinogenesis [36]. We found that STK25 knockdown significantly increased the apoptosis of liver cancer cells (Figures 16(i) and 16(j)). These results confirm that STK25 has a significant role in the progression of liver cancer.

## 5. Discussion

With advances in high-throughput sequencing technology, increasing number of prognostic biomarkers and therapeutic target are being identified. However, immune-related prognostic biomarkers of HCC are still limited. Some studies have reported that the elevated levels of ROS correlate with tumorigenesis [37, 38]. To further clarify the role of ROS-related genes in HCC, we firstly constructed a prognostic model based on ROS-related DEGs. This is the first research to explore the prognostic value of 49 ROS-related genes in HCC. Next, a prognostic model, consisting of 11 ROS-related DEGs developed through multivariate regression and LASSO Cox regression analyses. Functional enrichment analysis indicated that immune-related pathways were enriched.

ROS are by-products of cellular metabolism, including hydroxyl radicals, superoxide anions, singlet oxygen, and hydrogen peroxides [38]. Several studies have demonstrated that ROS are related to tumors [37, 39]. An increased level of ROS can impair DNA, protein, and lipids and cause genetic instability and tumorigenesis [40, 41]. Furthermore, the elevation of ROS levels can activate prosurvival signaling pathways, decrease the activation of tumor suppressor pathways, enhance glucose metabolism, and lead to tumor mutations [7, 42]. A study has reported that ROS impair mitochondrial function and oxidative stress, which led to DNA damage and hepatocarcinogenesis [43].



ROS are not only related to tumorigenesis but they also correlated with immune checkpoint inhibitors. Some studies showed that ROS-induced PD-L1 expression by regulating the JAK/STAT3 pathway [44, 45], and ROS inducers also increased the level of PD-L1 expression in tumor cells [46]. Our results also verified that most of immune checkpoint genes were differentially expressed between the high- and low-risk groups, and the overexpression of CD80, LDHA, TNFRSF4, and YTHDF1 had a shorter survival time in the high-risk group compared with the low-risk group. In addition, ROS were able to regulate immune function, cell proliferation, and epithelial-mesenchymal transition by activating profibrotic transforming growth factor- $\beta$  (TGF- $\beta$ ), and they participated in the progression of fibrosis, tumor, and abnormal vascular function [47, 48].

To further elucidate the underlying mechanism of ROS-related genes in HCC, we conducted GO and KEGG analyses. GO analysis revealed that B cell-mediated immunity, lymphocyte-mediated immunity, immunoglobulin-mediated immune response, MHC class II receptor activity, and MHC protein complex binding were enriched. KEGG analysis indicated that the chemokine signaling pathway and cytokine-cytokine receptor interaction were enriched. Moreover, the ablation of CD20+ B cells contributed to senescence-mediated fibre regression and suppressed the TNF  $\alpha$ /NF- $\kappa$ B pathway in *Mdr2*-knockout mice [49]. In addition, this study demonstrated that the degree of B cell infiltration positively correlated with the degree of malignancy, and a high degree B cell infiltration causes a reducing in the disease-free survival rate of patients [48]. Tumor-infiltrating cytotoxic CD8+ T cells specifically suppress tumor growth and express a high level of PD1 in HCC [50]. A study also reported that PD1 exhausted CD8+ T cells in HCC [51].

Furthermore, some bioinformatics analyses were carried out to investigate 11 ROS-related genes in the model, and our results revealed that the expression of CDKN2D, G6PD, MSRA, OXSR1, and STK25 was significantly different at different stages. Survival analysis, based on the GEPIA cohort, indicated that high expression of CDKN2D, G6PD, GLRX2, GSR, PFKP, PRDX1, PRDX6, and STK25 was associated with poor OS. Additionally, our findings showed that the expression of G6PD, GLRX2, MSRA, PFKP, PRDX1, PRDX6, and STK25 was significantly different among three molecular subtypes. We also found that the expression of CDKN2D, G6PD, GLRX2, MSRA, PFKP, PRDX1, PRDX6, and STK25 was significantly different among five immune subtypes. Interestingly, the findings indicated that only G6PD and STK25 showed statistical significance. While the role of G6PD in the HCC has been investigated [52–54], the role of STK25 in liver cancer is still unclear.

STK25, as a member of the ROS family genes, is involved in lipid metabolism and tumor progression [55, 56]. In this study, the role of STK25 in liver cancer was determined through *in vitro* experiments. The findings manifested that STK25 knockdown significantly inhibited the proliferation, migration, and invasion capacity of liver cancer cells. In addition, STK25 knockdown increased the apoptosis of the cells. These results indicated that STK25, as a member of ROS family genes, played a crucial role in the progression of liver cancer.

Herein, we firstly constructed a prognostic model of ROS-related genes in HCC, and the role of STK25 in liver cancer was investigated using *in vitro* experiments. Some limitations were still in the present study. Firstly, data from public databases were not verified by our clinical samples. Secondly, all the genes involved in the study were confined to ROS-related genes, and because tumor microenvironment is highly heterogeneous, there were some limitations to the model. Finally, we did not perform *in vivo* experiments to verify the results.

In conclusion, this was the first and most comprehensive investigation of the expression of ROS-related genes and clinical characteristics in liver cancer. We firstly constructed a ROS-related prognostic model in liver cancer and confirmed the correlation of ROS-related genes with immune infiltration and immune checkpoint genes. In addition, we preliminarily investigated the role of STK25 in liver cancer. It could provide a screening instrument for HCC diagnosis and prognosis and offer a way for us to dissect the association between HCC and immunity.

## Data Availability

All the data of this work are available from the corresponding authors upon reasonable request.

## Ethical Approval

The study was approved by the Ethics Committee of Wuhan University.

## Consent

The consent was approved by the participants.

## Conflicts of Interest

The authors declare that they have no conflict of interest.

## Authors' Contributions

XJH, ZYC, and WWX designed the research; XJH, ZYC, CYJ, ZX, and ZLL conducted to review and editing; XJH and WWX wrote the paper. All authors read and approved the final manuscript. XJH and GYJ shared the first author and contributed equally. WWX and ZYC shared the co-corresponding author.

## Acknowledgments

This work was supported by the Natural Science Foundation of China (NSFC Grants 81870442).

## Supplementary Materials

*Supplementary 1.* Figure S1: correlation of 11 ROS-related gene expressions with immune-infiltrating cells based on the TISIDB. (A) CDKN2D, (B) G6PD, (C) GLRX2, (D) GSR, (E) MSRA, (F) OXSR1, (G) PFKP, (H) PRDX1, (I) PRDX6, (J) SRXN1, and (K) STK25.

*Supplementary 2.* Figure S2: survival analysis of 11 ROS-related genes based on the Kaplan-Meier plotter. (A) CDKN2D, (B)

G6PD, (C) GLRX2, (D) GSR, (E) MSRA, (F) OXSR1, (G) PFKP, (H) PRDX1, (I) PRDX6, (J) SRXN1, and (K) STK25.

*Supplementary 3.* Table S1: the list of 49 ROS-related genes.

*Supplementary 4.* Table S2: the list of 38 immune checkpoint genes.

*Supplementary 5.* Table S3: the value of the coefficient of 11 ROS-related genes.

## References

- [1] J. D. S. Yang and J. K. Heimbach, "New advances in the diagnosis and management of hepatocellular carcinoma," *BMJ*, vol. 26, no. 371, article m3544, 2020.
- [2] T. Akinyemiju, S. Abera, M. Ahmed et al., "The burden of primary liver cancer and underlying etiologies from 1990 to 2015 at the global, regional, and national level: results from the global burden of disease study 2015," *JAMA Oncology*, vol. 3, no. 12, pp. 1683–1691, 2017.
- [3] S. Xia, Y. Pan, Y. L. Liang, J. Xu, and X. Cai, "The microenvironmental and metabolic aspects of sorafenib resistance in hepatocellular carcinoma," *eBioMedicine*, vol. 51, article 102610, 2020.
- [4] L. Li, Q. S. Lei, S. J. Zhang, L. Kong, and B. Qin, "Screening and identification of key biomarkers in hepatocellular carcinoma: evidence from bioinformatic analysis," *Oncology Reports*, vol. 38, no. 5, pp. 2607–2618, 2017.
- [5] K. S. Jeng, C. F. Chang, W. J. Jeng, I. S. Sheen, and C. J. Jeng, "Heterogeneity of hepatocellular carcinoma contributes to cancer progression," *Critical Reviews in Oncology/Hematology*, vol. 94, no. 3, pp. 337–347, 2015.
- [6] J. C. Nault and J. Zucman-Rossi, "Genetics of hepatocellular carcinoma: the next generation," *Journal of Hepatology*, vol. 60, no. 1, pp. 224–226, 2014.
- [7] X. Yuan, B. Y. Wang, L. Yang, and Y. Zhang, "The role of ROS-induced autophagy in hepatocellular carcinoma," *Clinics and Research in Hepatology and Gastroenterology*, vol. 42, no. 4, pp. 306–312, 2018.
- [8] A. Glasauer and N. S. Chandel, "Targeting antioxidants for cancer therapy," *Biochemical Pharmacology*, vol. 92, no. 1, pp. 90–101, 2014.
- [9] T. Matsuki, J. Chen, and B. W. Howell, "Acute inactivation of the serine-threonine kinase Stk25 disrupts neuronal migration," *Neural Development*, vol. 8, no. 1, p. 21, 2013.
- [10] X. D. Chen and C. Y. Cho, "Downregulation of SOK1 promotes the migration of MCF-7 cells," *Biochemical and Biophysical Research Communications*, vol. 407, no. 2, pp. 389–392, 2011.
- [11] C. Preisinger, B. Short, V. de Corte et al., "YSK1 is activated by the Golgi matrix protein GM130 and plays a role in cell migration through its substrate 14-3-3zeta," *The Journal of Cell Biology*, vol. 164, no. 7, pp. 1009–1020, 2004.
- [12] E. Nogueira, M. Fidalgo, A. Molnar et al., "SOK1 translocates from the Golgi to the nucleus upon chemical anoxia and induces apoptotic cell death," *The Journal of Biological Chemistry*, vol. 283, no. 23, pp. 16248–16258, 2008.
- [13] C. M. Pombo, T. Tsujita, J. M. Kyriakis, J. V. Bonventre, and T. Force, "Activation of the Ste20-like Oxidant Stress Response Kinase-1 during the Initial Stages of Chemical Anoxia-induced Necrotic Cell Death," *Journal of Biological Chemistry*, vol. 272, no. 46, pp. 29372–29379, 1997.
- [14] C. M. Pombo, J. V. Bonventre, A. Molnar, J. Kyriakis, and T. Force, "Activation of a human Ste20-like kinase by oxidant stress defines a novel stress response pathway," *The EMBO Journal*, vol. 15, no. 17, pp. 4537–4546, 1996.
- [15] A. Subramanian, P. Tamayo, V. K. Mootha et al., "Gene set enrichment analysis: a knowledge-based approach for interpreting genome-wide expression profiles," *Proceedings of the National Academy of Sciences of the United States of America*, vol. 102, no. 43, pp. 15545–15550, 2005.
- [16] D. Szklarczyk, A. L. Gable, D. Lyon et al., "STRING v11: protein-protein association networks with increased coverage, supporting functional discovery in genome-wide experimental datasets," *Nucleic Acids Research*, vol. 47, no. D1, pp. D607–D613, 2019.
- [17] N. Simon, J. Friedman, T. Hastie, and R. Tibshirani, "Regularization paths for Cox's proportional hazards model via coordinate descent," *Journal of Statistical Software*, vol. 39, no. 5, pp. 1–13, 2011.
- [18] R. Tibshirani, "The lasso method for variable selection in the Cox model," *Statistics in Medicine*, vol. 16, no. 4, pp. 385–395, 1997.
- [19] J. H. Xu, Y. J. Guan, Y. C. Zhang et al., "ADAM15 correlates with prognosis, immune infiltration and apoptosis in hepatocellular carcinoma," *Aging-US*, vol. 13, no. 16, pp. 20395–20417, 2021.
- [20] B. Li, E. Severson, J. C. Pignon et al., "Comprehensive analyses of tumor immunity: implications for cancer immunotherapy," *Genome Biology*, vol. 17, no. 1, p. 174, 2016.
- [21] R. Beibei, C. N. Wong, and Y. Tong, "TISIDB: an integrated repository portal for tumor-immune system interactions," *Bioinformatics*, vol. 35, no. 20, pp. 4200–4202, 2019.
- [22] Z. Tang, C. W. Li, B. X. Kang, G. Gao, C. Li, and Z. Zhang, "GEPIA: a web server for cancer and normal gene expression profiling and interactive analyses," *Nucleic Acids Research*, vol. 45, no. W1, pp. W98–W102, 2017.
- [23] D. S. Chandrashekar, B. Bashel, S. A. H. Balasubramanya et al., "UALCAN: a portal for facilitating tumor subgroup gene expression and survival analyses," *Neoplasia*, vol. 19, no. 8, pp. 649–658, 2017.
- [24] A. Nagy, G. Munkácsy, and B. Györfy, "Pancancer survival analysis of cancer hallmark genes," *Scientific Reports*, vol. 11, no. 1, p. 6047, 2021.
- [25] Y. P. Hong, W. H. Deng, W. Y. Guo et al., "Inhibition of endoplasmic reticulum stress by 4-phenylbutyric acid prevents vital organ injury in rat acute pancreatitis," *American Journal of Physiology. Gastrointestinal and Liver Physiology*, vol. 315, no. 5, pp. G838–G847, 2018.
- [26] E. Heitzer, P. Ulz, J. B. Geigl, and M. R. Speicher, "Non-invasive detection of genome-wide somatic copy number alterations by liquid biopsies," *Molecular Oncology*, vol. 10, no. 3, pp. 494–502, 2016.
- [27] H. Hieronymus, R. Murali, A. Tin et al., "Tumor copy number alteration burden is a pan-cancer prognostic factor associated with recurrence and death," *eLife*, vol. 7, article e37294, 2018.
- [28] J. L. Williams, P. A. Greer, and J. A. Squire, "Recurrent copy number alterations in prostate cancer: an in silico meta-analysis of publicly available genomic data," *Cancer Genetics*, vol. 207, no. 10–12, pp. 474–488, 2014.
- [29] B. S. Taylor, N. Schultz, H. Hieronymus et al., "Integrative genomic profiling of human prostate cancer," *Cancer Cell*, vol. 18, no. 1, pp. 11–22, 2010.

- [30] H. Zeng, J. R. Ji, X. D. Song et al., "Stemness related genes revealed by network analysis associated with tumor immune microenvironment and the clinical outcome in lung adenocarcinoma," *Frontiers in Genetics*, vol. 11, article 549213, 2020.
- [31] W. Liu, H. Ye, Y. Liu et al., "Transcriptome-derived stromal and immune scores infer clinical outcomes of patients with cancer," *Oncology Letters*, vol. 15, no. 4, pp. 4351–4357, 2018.
- [32] T. M. Malta, A. Sokolov, A. J. Gentles et al., "Machine learning identifies stemness features associated with oncogenic dedifferentiation," *Cell*, vol. 173, no. 338, pp. e15–354.e15, 2018.
- [33] Q. Cui, J. Q. Wang, Y. G. Assaraf et al., "Modulating ROS to overcome multidrug resistance in cancer," *Drug Resistance Updates*, vol. 41, pp. 1–25, 2018.
- [34] E. Singer, J. Judkins, N. Salomonis et al., "Reactive oxygen species-mediated therapeutic response and resistance in glioblastoma," *Cell Death & Disease*, vol. 6, no. 1, article e1601, 2015.
- [35] W. Wu, M. Chen, T. Luo et al., "ROS and GSH-responsive S-nitrosoglutathione functionalized polymeric nanoparticles to overcome multidrug resistance in cancer," *Acta Biomaterialia*, vol. 103, pp. 259–271, 2020.
- [36] F. Isabel, R. César, and F. Margarita, "Survival and apoptosis: a dysregulated balance in liver cancer," *Liver International*, vol. 27, no. 2, pp. 155–162, 2007.
- [37] G. Y. Liou and P. Storz, "Reactive oxygen species in cancer," *Free Radical Research*, vol. 44, no. 5, pp. 479–496, 2010.
- [38] J. N. Moloney and T. G. Cotter, "ROS signalling in the biology of cancer," *Seminars in Cell & Developmental Biology*, vol. 80, pp. 50–64, 2018.
- [39] E. Panieri and M. M. Santoro, "ROS homeostasis and metabolism: a dangerous liaison in cancer cells," *Cell Death & Disease*, vol. 7, no. 6, article e2253, 2016.
- [40] J. Stanicka, E. G. Russell, J. F. Woolley, and T. G. Cotter, "NADPH oxidase-generated hydrogen peroxide induces DNA damage in mutant FLT3-expressing leukemia cells," *The Journal of Biological Chemistry*, vol. 290, no. 15, pp. 9348–9361, 2015.
- [41] S. S. Sabharwal and P. T. Schumacker, "Mitochondrial ROS in cancer: initiators, amplifiers or an Achilles' heel?," *Nature Reviews. Cancer*, vol. 14, no. 11, pp. 709–721, 2014.
- [42] H. M. Vander, L. C. Cantley, and C. B. Thompson, "Understanding the Warburg effect: the metabolic requirements of cell proliferation," *Science*, vol. 324, no. 5930, pp. 1029–1033, 2009.
- [43] A. Charras, P. Arvaniti, C. le Dantec et al., "JAK inhibitors and oxidative stress control," *Frontiers in Immunology*, vol. 10, p. 2814, 2019.
- [44] N. Wang, L. L. Song, Y. Xu et al., "Loss of Scribble confers cisplatin resistance during NSCLC chemotherapy via Nox2/ROS and Nrf2/PD-L1 signaling," *eBioMedicine*, vol. 47, pp. 65–77, 2019.
- [45] C. Roux, S. M. Jafari, R. Shinde et al., "Reactive oxygen species modulate macrophage immunosuppressive phenotype through the up-regulation of PD-L1," *Proceedings of the National Academy of Sciences of the United States of America*, vol. 116, no. 10, pp. 4326–4335, 2019.
- [46] M. J. Goumans and D. P. Ten, "TGF-beta signaling in control of cardiovascular function," *Cold Spring Harbor Perspectives in Biology*, vol. 10, no. 2, 2018.
- [47] M. Ruizortega, J. Rodriguezvita, E. Sanchezlopez, G. Carvajal, and J. Egido, "TGF- $\beta$  signaling in vascular fibrosis," *Cardiovascular Research*, vol. 74, no. 2, pp. 196–206, 2007.
- [48] J. Chen, J. Zhou, H. Fu, X. Ni, and Y. Shan, "Upregulation of oxidative stress-responsive 1(OXSR1) predicts poor prognosis and promotes hepatocellular carcinoma progression," *Bioengineered*, vol. 11, no. 1, pp. 958–971, 2020.
- [49] J. Ma, B. H. Zheng, S. Goswami et al., "PD1 (Hi) CD8(+) T cells correlate with exhausted signature and poor clinical outcome in hepatocellular carcinoma," *Journal for Immunotherapy of Cancer*, vol. 7, no. 1, p. 331, 2019.
- [50] H. D. Kim, G. W. Song, S. Park et al., "Association between expression level of PD1 by tumor-infiltrating CD8(+) T cells and features of hepatocellular carcinoma," *Gastroenterology*, vol. 155, no. 6, pp. 1936–1950.e17, 2018.
- [51] K. Wu, I. Kryczek, L. Chen, W. Zou, and T. H. Welling, "Kupffer cell suppression of CD8+ T cells in human hepatocellular carcinoma is mediated by B7-H1/programmed death-1 interactions," *Cancer Research*, vol. 69, no. 20, pp. 8067–8075, 2009.
- [52] J. M. Barajas, R. Reyes, M. J. Guerrero, S. T. Jacob, T. Motiwala, and K. Ghoshal, "The role of miR-122 in the dysregulation of glucose-6-phosphate dehydrogenase (G6PD) expression in hepatocellular cancer," *Scientific Reports*, vol. 8, no. 1, p. 9105, 2018.
- [53] H. Hu, X. Ding, Y. Yang et al., "Changes in glucose-6-phosphate dehydrogenase expression results in altered behavior of HBV-associated liver cancer cells," *American Journal of Physiology. Gastrointestinal and Liver Physiology*, vol. 307, no. 6, pp. G611–G622, 2014.
- [54] A. Wang, B. Chen, S. Jian, W. Cai, M. Xiao, and G. du, "miR-206-G6PD axis regulates lipogenesis and cell growth in hepatocellular carcinoma cell," *Anti-Cancer Drugs*, vol. 32, no. 5, pp. 508–516, 2021.
- [55] F. Wu, P. Gao, W. Wu et al., "STK25-induced inhibition of aerobic glycolysis via GOLPH3-mTOR pathway suppresses cell proliferation in colorectal cancer," *Journal of Experimental & Clinical Cancer Research*, vol. 37, no. 1, p. 144, 2018.
- [56] M. Amrutkar, M. Kern, E. Nuñez-Durán et al., "Protein kinase STK25 controls lipid partitioning in hepatocytes and correlates with liver fat content in humans," *Diabetologia*, vol. 59, no. 2, pp. 341–353, 2016.

## Research Article

# Downregulation of the Proton-Activated Cl<sup>-</sup> Channel TMEM206 Inhibits Malignant Properties of Human Osteosarcoma Cells

Fei Peng , Haohuan Li, Jianping Li, and Zhe Wang

Department of Orthopedics, Renmin Hospital of Wuhan University, Wuhan, Hubei 430060, China

Correspondence should be addressed to Fei Peng; pengf\_wuhu@sina.com

Received 1 September 2021; Accepted 25 October 2021; Published 5 November 2021

Academic Editor: Dragan Hrnčić

Copyright © 2021 Fei Peng et al. This is an open access article distributed under the Creative Commons Attribution License, which permits unrestricted use, distribution, and reproduction in any medium, provided the original work is properly cited.

Transmembrane protein 206 (TMEM206), a proton-activated chloride channel, has been implicated in various biochemical processes, including bone metabolism, and has emerged as a novel cancer-related protein in multiple tumor types. However, its role in primary malignant bone tumors, particularly in osteosarcoma (OS), remains unclear. This study is aimed at exploring the effects of TMEM206 gene silencing on the proliferation, migration, invasion, and metastasis of human OS cells *in vitro* and *in vivo* using an shRNA-knockdown strategy. We found that TMEM206 is frequently overexpressed and that high levels of TMEM206 correlated with clinical stage and pulmonary metastasis in patients with OS. We provided evidence that TMEM206-silenced OS cancer cells exhibit decreased proliferation, migration, and invasion *in vitro*. Mechanistically, we identified  $\beta$ -catenin, a key member of Wnt/ $\beta$ -catenin signaling, as a downstream effector of TMEM206. TMEM206 silencing inhibits the Wnt/ $\beta$ -catenin signaling pathway in expression rescue experiments, confirming that TMEM206 silencing attenuates OS cell tumorigenic behavior, at least in part, via the  $\beta$ -catenin mediated downregulation of Wnt/ $\beta$ -catenin signaling. More importantly, TMEM206 knockdown-related phenotype changes were replicated in a xenograft nude mouse model where pulmonary metastases of OS cells were suppressed. Together, our results demonstrate that silencing TMEM206 negatively modulates the Wnt/ $\beta$ -catenin signaling pathway via  $\beta$ -catenin to suppress proliferation, migration, invasion, and metastasis in OS carcinogenesis, suggesting TMEM206 as a potential oncogenic biomarker and a potential target for OS treatment.

## 1. Introduction

Osteosarcoma (OS) is the most common primary aggressive and malignant tumor of the bone, with high morbidity and metastatic potential. Approximately 75% of OS patients are between 15 and 25 years of age, which heavily threatens the health of adolescents [1]. Although significant progress has been made in diagnostic and therapeutic methods, the primary treatment for OS mainly depends on surgery combined with adjuvant chemotherapy; however, the clinical outcome is unsatisfactory [2]. The five-year survival rate of osteosarcoma without metastasis is only 60-70% [3]. The poor outcome of OS therapy is mostly due to the high incidence of recurrence and metastasis. Metastasis is common in OS, and approximately 85% of metastases are located in lungs [4], which contributes to most patients' death. Thus, exploring efficient diagnostic biomarkers and therapeutic targets for HCC treat-

ment could lead to novel intervention strategies for improving OS clinical outcomes.

Proliferation, invasion, and metastasis are the essential biological characteristics of OS [5] and are the root causes of tumor recurrence. When metastasis occurs, OS cells enter the peripheral vascular or lymphatic vascular system through normal tissues, invade the vascular system, stay in the target organ, and proliferate to form new lesions in the target organ, which fully demonstrates OS oncological characteristics [6]. Genetic changes are involved in tumor invasion and metastasis. Changes in these genes at the transcriptional and epigenetic levels are prerequisites for maintaining the malignant phenotype of tumor cells [6, 7]. Studying the potential role and molecular mechanism of these genes will help clarify the characteristics of tumor invasion and metastasis and provide new targets for antitumor therapy.

Ion-activated chloride channels (IACC) are members of the transmembrane (TMEM) chloride channel family and are widely distributed in human tissues, including bone [8, 9]. The TMEM family plays a vital role in the formation and osteoclastic processes of bone tissue [10, 11]. At the same time, abnormal expression of the TMEM family plays an important role in the occurrence and development of various tumors, such as gastric cancer [12], breast cancer [13], head and neck cancer [14], and OS [15]. TMEM206, also known as PAC or PACC1, encodes the proton-activated chloride (Cl<sup>-</sup>) channel, and although it has been implicated in some tumors, its role in OS has not been explored [16, 17]. A high incidence of OS during adolescence is accompanied by intensive bone development and bone remodeling, a continuous process that includes bone degradation, which depends on hydrogen ion translocation to solubilize bone minerals [18]. This hydrogen redistribution is supported by the parallel actions of a proton ATPase, and a chloride channel located in the osteoclast ruffled membrane [19]. These considerations hint that TMEM206 may also be closely related to OS occurrence, and its underlying mechanisms need to be explored.

In this study, we collected OS patient tissue samples to investigate whether TMEM206 was dysregulated in OS patients and correlated with prognosis. TMEM206 loss-of-function experiments in well characterized OS cell lines were then performed *in vitro* and tumor growth *in vivo* to confirm clinical observations. Our findings provide novel insights into the role of TMEM206 in OS cell proliferation, migration, invasion, and metastasis while shedding light on the potential molecular mechanisms.

## 2. Materials and Methods

**2.1. Sample Collection.** Human OS tissue samples were collected from Renmin Hospital of Wuhan University, from November 2017 to June 2019, from patients aged 7-33 years (median, 18 years). There were 33 adjacent nontumor tissues and 48 OS samples. Grade of OS tissues were distinguished on the basis of Enneking staging system during pathological examination. All participants have signed an informed consent form and been informed of all the surgery and experiment details in advance. Histologic sections were reviewed by two expert pathologists to verify the histologic diagnosis. We obtained written informed consent from all patients. The Ethics Committee of Renmin Hospital of Wuhan University approved the study protocol. Eighteen male BABL/c nude mice (6-8 weeks old) were purchased from the Wuhan University experimental animal center (Wuhan, China). All experimental procedures involving animals were strictly followed in accordance with the Guide for the Care and Use of Laboratory Animals and approved by Animal Care and Use Committee of Renmin Hospital of Wuhan University. The human fetal osteoblastic cell line hFOB1.19 and human OS cell lines SAOS2, U2OS, and MG63 were purchased from the Cell Bank of the Chinese Academy of Sciences (Shanghai, China). All cell lines were cultured in Dulbecco's Modified Eagle Medium DMEM (Gibco, Carlsbad, CA, USA), and 10% fetal bovine serum (Invitrogen, Carlsbad, CA, USA), 100 U/mL penicillin, and 100 mg/mL streptomycin (Gibco, Grand Island, NY, USA)

were added. Cells were cultured at 37°C with 5% CO<sub>2</sub> in an incubator (Thermo Fisher Scientific, Waltham, MA, USA).

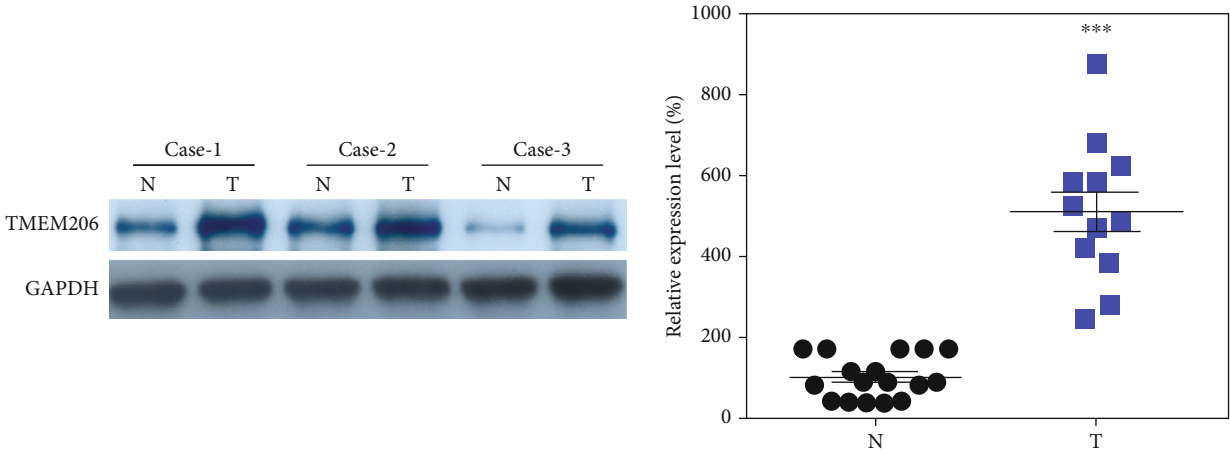
**2.2. Western Blot Assay.** RIPA lysis buffer (Beyotime, PRC) was adopted to abstract the overall proteins as per supplier's guideline. Immunoblotting was used to identify the protein expressing levels herein as per the guideline provided in the previous study. Primary antibodies against TMEM206 (1:300, ab99055, Abcam, MA, USA),  $\beta$ -catenin (1:200, ab32572, Abcam), c-Myc (1:500, ab32072, Abcam), CyclinD1 (1:400, ab16663, Abcam), MMP7 (1:400, ab207299, Abcam), MMP9 (1:200, ab76003, Abcam), and GAPDH (1:500, ab9485, Abcam) were purchased as primary antibodies. HRP-predicted sheep anti-rabbit second antisubstances (1:5000) were acquired as well. Eventually, the visualization of the protein bands were realized via an ECL system, and grayscale results were determined via Image J soft.

**2.3. Cell Transfection.** For knockdown of TMEM206, lentiviruses containing TMEM206 short hairpin (sh) RNAs/scramble controls (SC) were produced in HEK-293T cells with packaging vectors from ObiO (Shanghai, China). The medium supernatants were collected and concentrated by PEG-it virus precipitation solution (SBI, System Biosciences, Palo Alto, CA, USA). The obtained viruses were then used to infect U2OS and MG63 cells. Transient transfections of plasmids TMEM206-shRNA and SC-shRNA (Genechem, Shanghai, China) were performed with Lipofectamine 3000 (Invitrogen, Life Technologies, Carlsbad, CA, USA). Approximately  $2.5 \times 10^6$  cells were transfected with 2.5  $\mu$ g of plasmid using 3.75  $\mu$ L based on manufacturer's protocol.

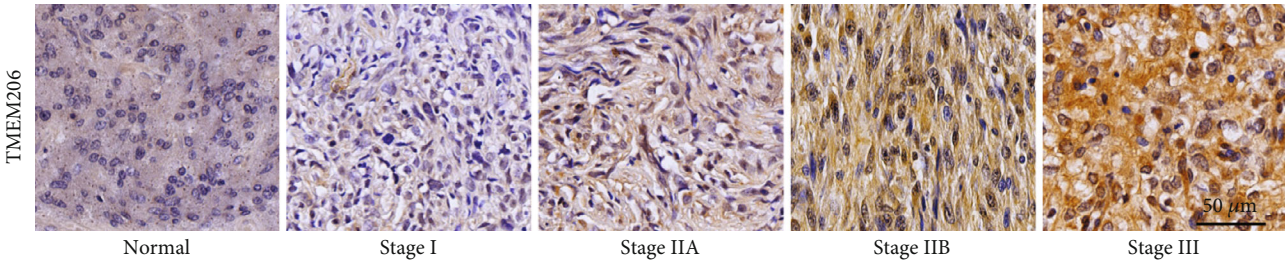
**2.4. Immunofluorescent Staining.** The transfected U2OS cells were fixed with 4% paraformaldehyde for 30 min and rinsed thrice with PBS and. The cells were then permeabilized with PBS containing 0.5% Triton X-100 for 15 min. The TMEM206 antibody (HPA008540, Sigma, USA) was applied to the coverslip and incubated in a wet box overnight at 4°C. After washing three times with PBS, the fluorescent secondary antibody (1:500, Invitrogen, USA) was added and incubated for 1 h in the wet box at 25°C. Following three additional washes with PBS, the DAPI mounting solution (Vector, USA) was added to stain the nuclear compartment. The immunoreactive cultured cells were observed using a fluorescence microscope (Olympus, Japan).

**2.5. CCK-8 Assay.** CCK-8 detection (Bimake, Shanghai, China) uses a similar method, as described earlier. Transfected cells were inoculated into 96-well plates and incubated overnight. Add CCK-8 reagent 10 mL to each well and incubate at 37°C for 2 hours. The absorption value was measured at 450 nm with a microplate analyzer (Bio-Tek Instruments Inc., USA).

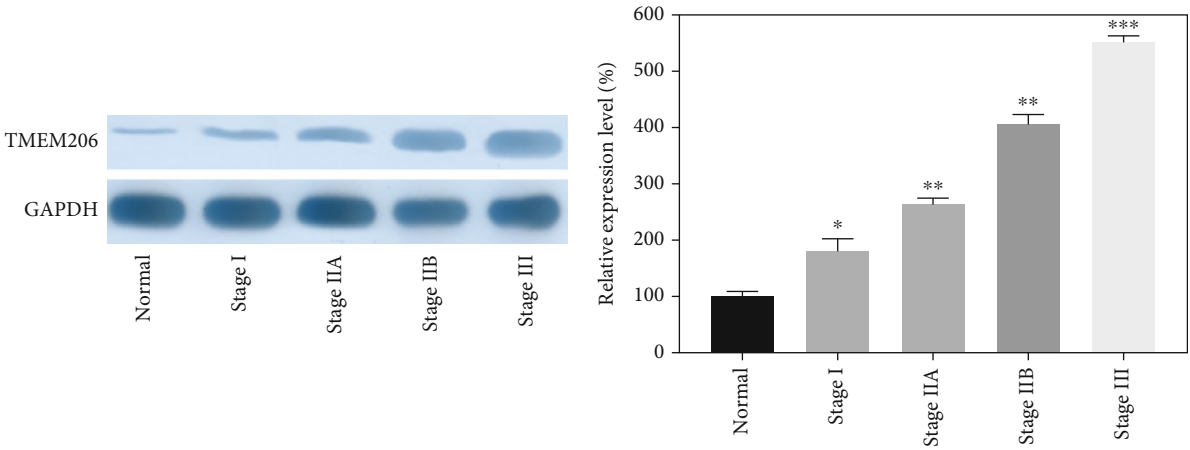
**2.6. 5-Ethynyl-2'-Deoxyuridine (EdU) Staining Assay.** U2OS and MG63 cells ( $6 \times 10^5$ ) were inoculated into 96-well plates, and cell proliferation was assayed using an EdU kit (Roche, Basel, Switzerland) according to manufacturer's instructions. Hoechst 33342 was added to stain the nuclei. After a 30-



(a)



(b)



(c)

FIGURE 1: Continued.

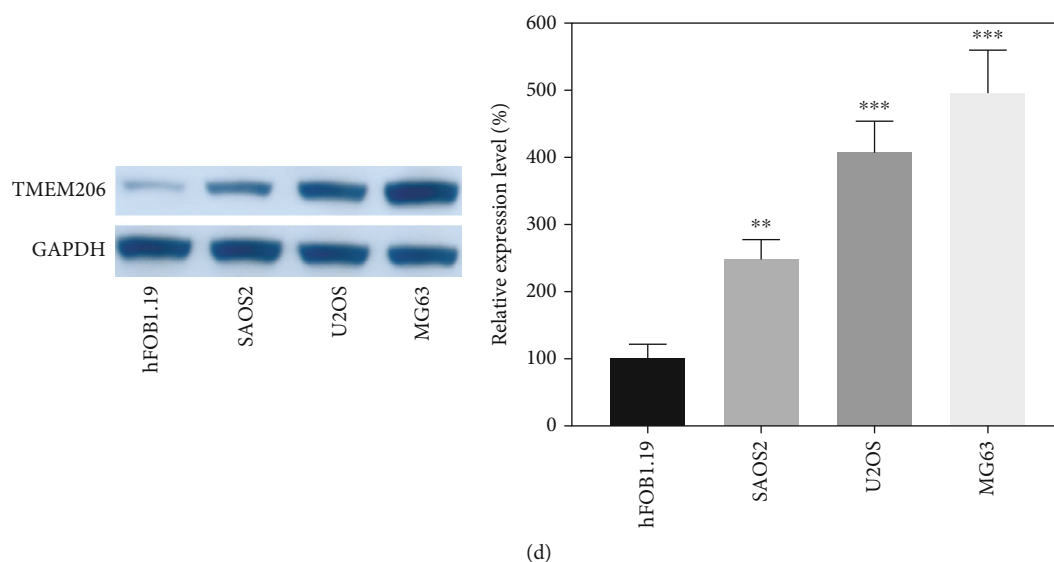


FIGURE 1: TMEM206 is overexpressed in OC tissues and cell lines. (a) The protein expression of TMEM206 in osteosarcoma tissues and paired para-tumor tissues were determined by using of WB ( $n = 10$ ). (b, c) IHC and WB results indicated TMEM206 expression was significantly elevated in patients with advanced stage ( $*P < 0.05$ ,  $**P < 0.01$ ,  $***P < 0.001$ , as comparing with para-tumor tissue group, respectively). (d) The expression of TMEM206 in osteosarcoma cell lines contrasted to hFOB 1.19 ( $***P < 0.001$ , as comparing with hFOB 1.19 group,  $**P < 0.01$ , as comparing with SAOS2 group). GAPDH was used as an internal control. The data are represented as means  $\pm$  SEM in (a, c) and represented as means  $\pm$  SD in (d).

minute incubation in the dark, the cells were observed under a fluorescence microscope (Olympus, Japan).

**2.7. Colony Formation Experiment.** Cells were collected during the exponential growth period, reinoculated on the plate, and cultured at  $37^{\circ}\text{C}$  for 6 days. After 6 days, the cells were washed with PBS, fixed with methanol, stained with crystal violet, and observed under the microscope.

**2.8. Migration and Invasion Assays.** Invasion assay was carried out using 24-well plates with the Matrigel coating (BD Bioscience, Franklin Lakes, NJ, USA) as previously described [20]. The migration assay was carried out without the Matrigel coating. Transfected cells were seeded in the upper chamber of a Transwell (BD Bioscience, USA) containing serum-free medium. DMEM or MEM medium containing 10% FBS was placed in the lower chamber. After incubation for 48 hr, migrated or invaded cells were fixed with 4% paraformaldehyde for 15 min and stained with 0.1% crystal violet for 20 min. Cells were imaged with a fluorescence microscope (Olympus, Japan).

**2.9. Luciferase Reporter Assay.** Reporter assays were performed with U2OS and MG63 cells, which were transfected with either wild type or mutant reporter plasmids containing the putative  $\beta$ -catenin binding site and cotransfected with the control (pcDNA-Con) or TMEM206 overexpression (pcDNA-TMEM206) plasmid. The resulting Firefly and Renilla luciferase activity were measured 48 h post-transfection using the Dual-Glo<sup>TM</sup> Luciferase Assay System, according to manufacturer's instructions (Promega, Wisconsin, USA).

**2.10. Xenograft Mode.** MG63 cells stably transfected with TMEM206-shRNA or SC-shRNA ( $6 \times 10^6$  cells) were inoculated subcutaneously into the nude mice. Tumor volumes were measured every 7 days. After 21 days, mice were sacrificed, and tissues were collected for further analyses.

**2.11. Statistical Analysis.** Statistical analysis and graph making were performed using SPSS Software version 22.0 (IBM, USA) and GraphPad Prism Software version 7.01 (GraphPad Software Inc., USA), respectively. All data were expressed as mean  $\pm$  standard deviation (SD) or mean  $\pm$  standard error means (SEM). Comparison between two groups was determined by unpaired  $t$  test or one-way ANOVA test.  $P$  value  $< 0.05$  was considered as statistically significant, which was displayed as  $*P < 0.05$ ,  $**P < 0.01$ ,  $***P < 0.001$ , while the  $P$  value  $> 0.05$  was displayed as not significant in all figures.

### 3. Results

**3.1. TMEM206 Is Highly Expressed in Human OS Tissues and Cell Lines and Predicts a Poor Prognosis.** We first set to explore whether TMEM206 was aberrantly expressed in OS tissues. Compared to paired adjacent normal tissues, the protein expression of TMEM206 was dramatically higher in tumor tissues (Figure 1(a),  $P < 0.001$ ). The IHC results indicated that TMEM206 was aberrantly expressed in the advanced Ennekin stage (Figure 1(b)), and WB results further confirmed this observation (Figure 1(c),  $P < 0.05$ ). We then analyzed the endogenous expression of TMEM206 in a panel of human OS cell lines (SaOS2, U2OS, and MG63). As shown in Figure 1(d), although all OS cell lines expressed more TMEM206 than the human fetal osteoblastic cell line hFOB1.19, interestingly, expression

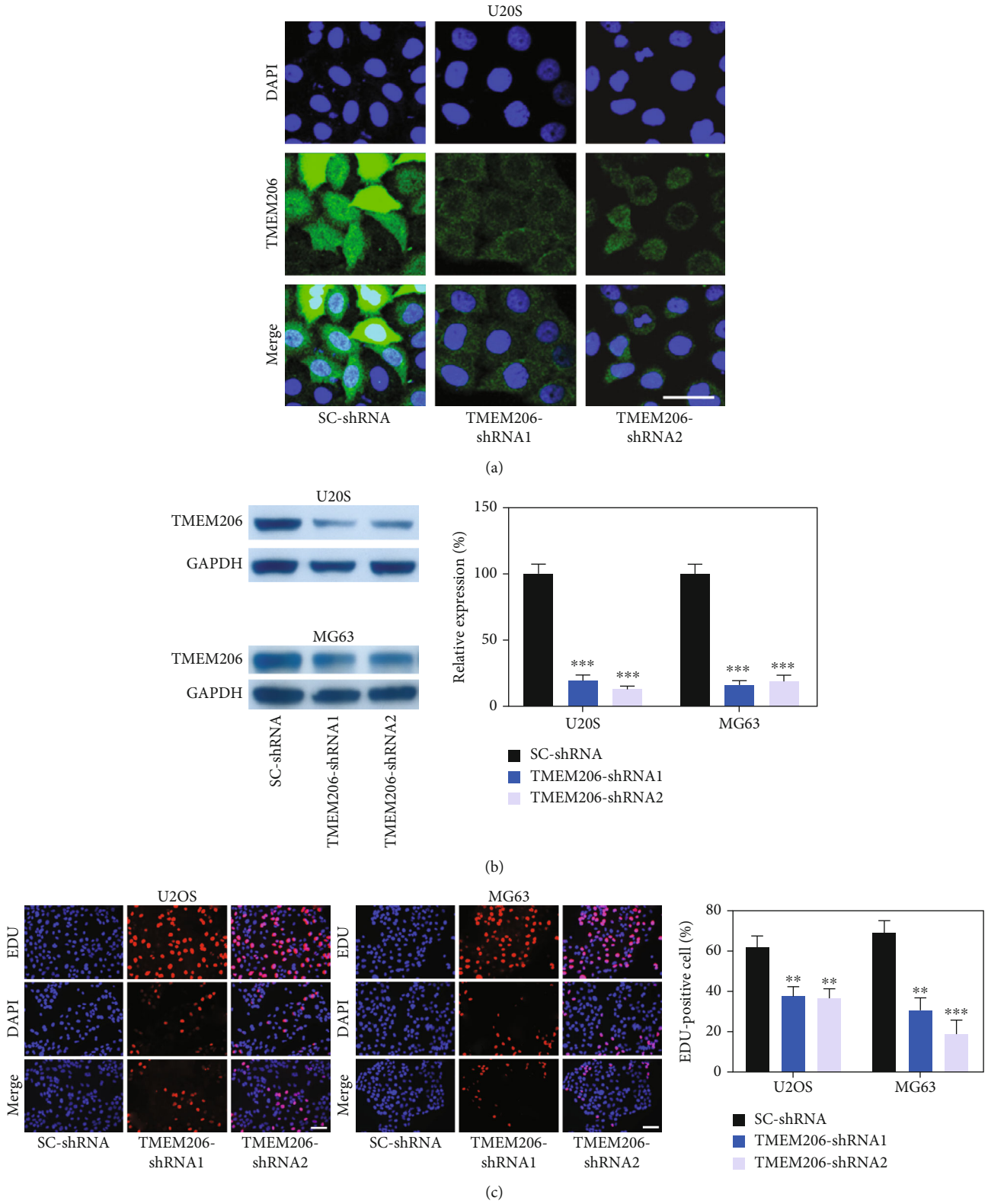
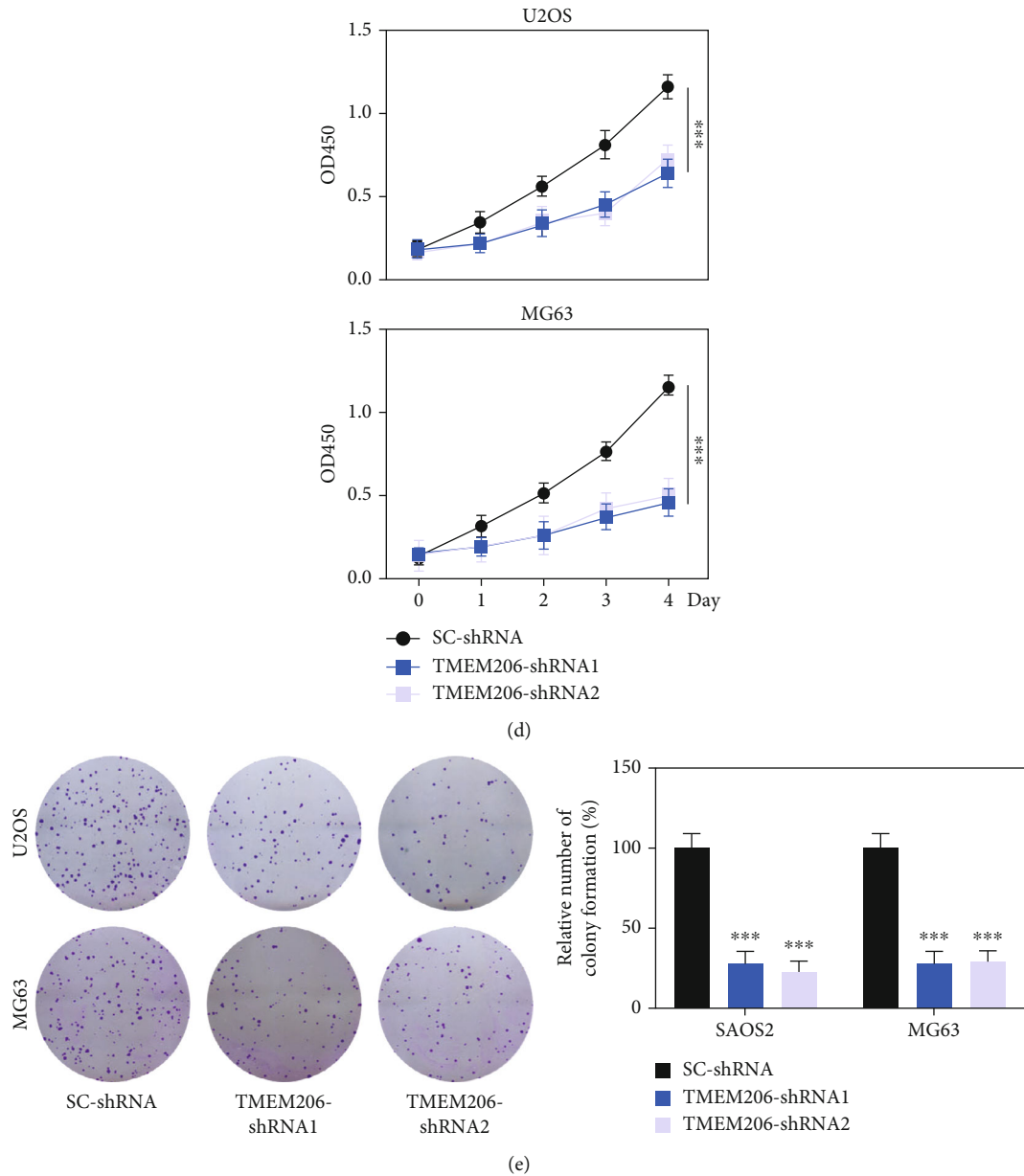


FIGURE 2: Continued.





**FIGURE 2: TMEM206 downregulation inhibits OS cell proliferation.** (a) The expression of TMEM206 in U2OS cell line were detected by fluorescence staining. Scale bar: 20  $\mu\text{m}$ . (b) The expression of TMEM206 in U2OS and MG63 cells were detected by western blot analysis ( $***P < 0.001$ , as comparing with SC-shRNA group, respectively). (c) EdU staining assays were performed to determine the growth of TMEM206-shRNA-transfected U2OS and MG63 cells ( $**P < 0.01$ ,  $***P < 0.001$ , as comparing with SC-shRNA group, respectively). (d) CCK-8 assay showed that downregulation of TMEM206 influence the proliferation rates in U2OS and MG63 cells measured at 1, 2, 3, and 4 day after transfection ( $***P < 0.001$ , as comparing with SC-shRNA group, respectively). (e) Colony formation assay showed that knockdown TMEM206 inhibited cell colony formation ( $***P < 0.001$ , as comparing with SC-shRNA group, respectively). GAPDH was used as an internal control. The data are represented as means  $\pm$  SD from 3 replicate experiments.

of TMEM206 was more apparent in lines with higher xenogenic tumor growth potential, such as MG 63, compared to lines with less tumorigenic capacity, such as SaOS2 (Figure 1(d),  $P < 0.01$ ).

**3.2. Silencing TMEM206 Inhibits Cell Proliferation and Colony Formation.** To elucidate the role of TMEM206 in OS, U2OS and MG63 cells were transfected with control scrambled shRNA or TMEM206-shRNA. Immunofluorescence staining indicated that TMEM206 expression was

reduced after TMEM206-shRNA transfection (Figure 2(a)), and this knockdown strategy resulted in a significant decrease in TMEM206 protein expression both in U2OS and MG63 cells (Figure 2(b),  $P < 0.001$ ). Next, we investigated whether TMEM206 regulates cell proliferation. EDU-staining and CCK-8 assays were used to evaluate the effects of silencing TMEM206 on cell proliferation. When TMEM206 was downregulated in OS cells, a significant decrease in proliferation rates was observed compared with SC-shRNA transfection

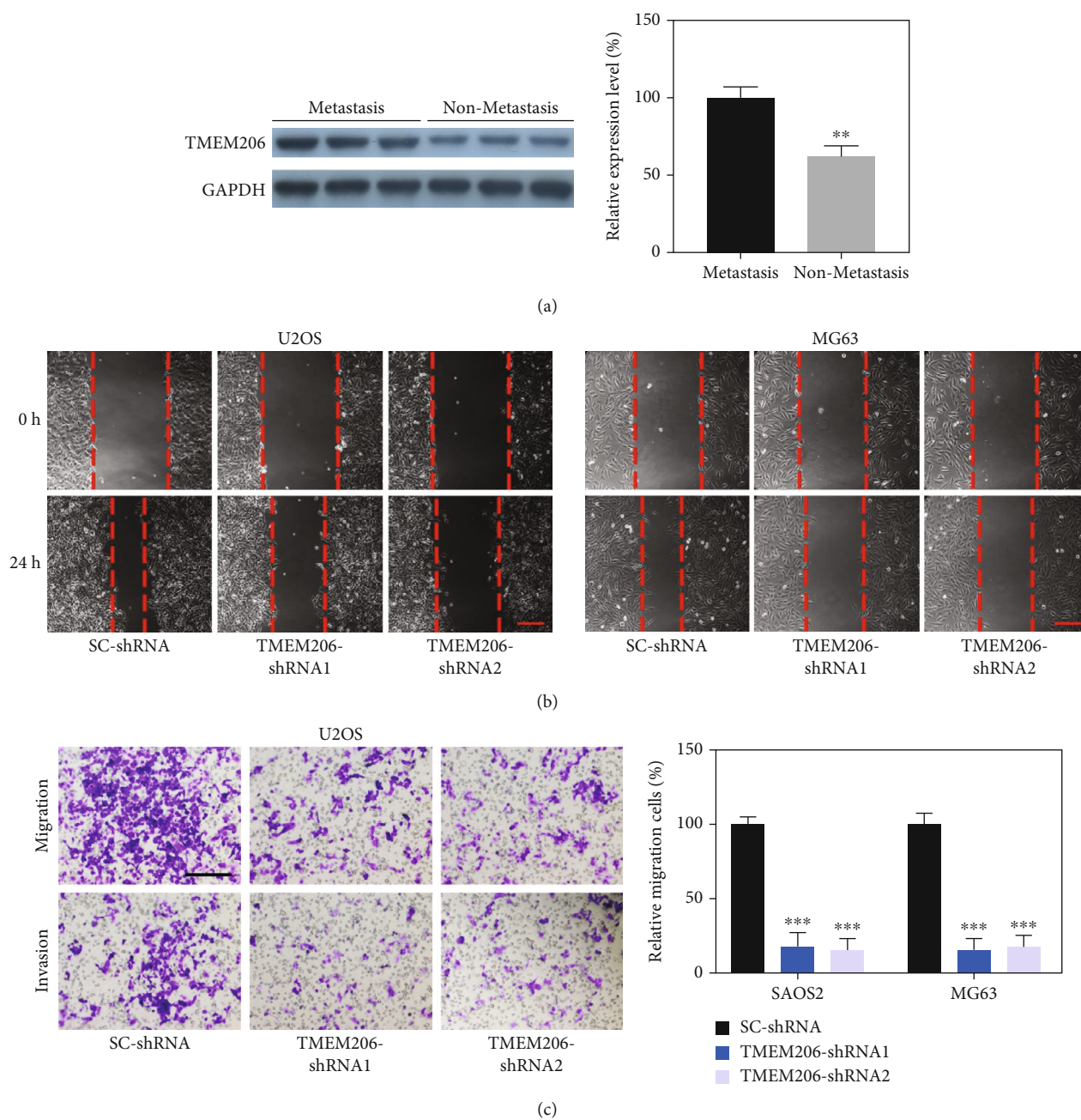


FIGURE 3: Continued.

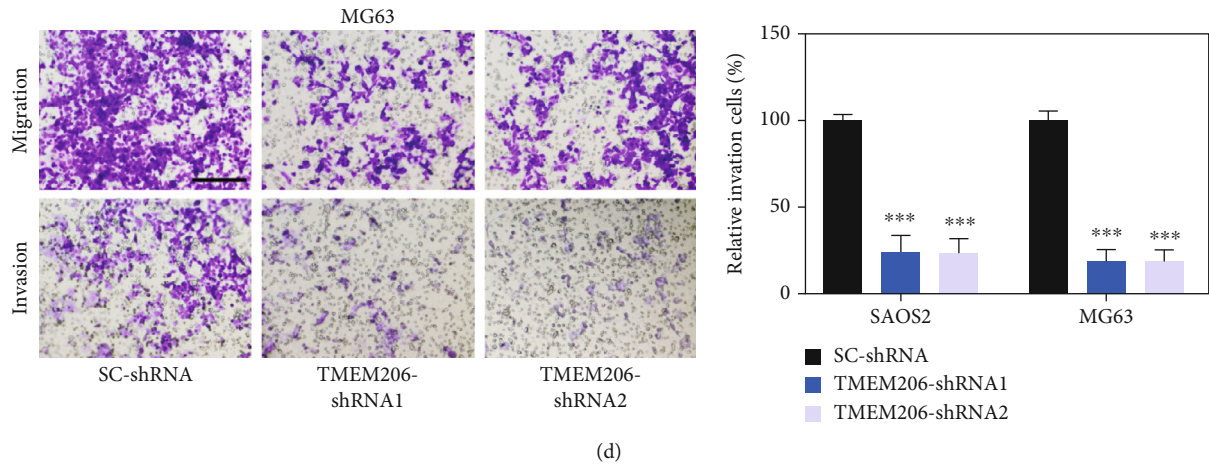


FIGURE 3: TMEM206 implicated in OS cell migration and invasion. (a) Relative expression of TMEM206 in OS tissues of patients with metastasis compared with OS patients without metastasis (\*\* $P < 0.01$ ,  $n = 8$  pair). (b) Cell migration was analyzed by the wound healing assay upon TMEM206 silencing. Scale bar:  $200 \mu\text{m}$ . (c, d) Representative images and the relative number of migration or invasion cells in the Transwell chamber coated without or with Matrigel for 24 h (\*\* $P < 0.001$ , as comparing with SC-shRNA group, respectively). Scale bar:  $100 \mu\text{m}$ . GAPDH was used as an internal control. The data are represented as means  $\pm$  SEM in (a) and represented as means  $\pm$  SD in (c, d).

(Figures 2(c) and 2(d),  $P < 0.01$ ). The colony formation assay showed that TMEM206-shRNA-transfection displayed significantly fewer colonies than SC-shRNA-transfected U2OS and MG63 cells (Figure 2(e),  $P < 0.001$ ). Collectively, these data suggest that TMEM206 plays an important role in OS cell growth *in vitro*.

**3.3. TMEM206 Involved in the Regulation of OS Cell Migration and Invasion.** Given that TMEM206 expression correlates with tumor stage, we investigated whether TMEM206 regulates OS cell migration and invasion, two critical features of malignant cell behavior. First, we analyzed the human OS tissues and found that the OS patients with metastasis showed much higher TMEM206 expression than the primary tumors without metastasis (Figure 3(a),  $P < 0.01$ ). We then examined the role of TMEM206 in U2OS and MG63 cells on cell migration using a wound scratch assay. As illustrated in Figure 3(b), decreased expression of TMEM206 significantly inhibited wound closure compared with that in U2OS and MG63 cells transfected with SC-shRNA vector. To further identify these observations, we examined the effects of TMEM206 on OS cell migration and invasion using Transwell chambers with or without Matrigel. Consistently, OS cells derived from TMEM206-shRNA-transfection displayed a significantly lower migration and invasion ability than that derived from SC-shRNA-transfected cells (Figures 3(c) and 3(d),  $P < 0.001$ ). Collectively, these data demonstrate that TMEM206 is involved in OS tumor metastasis *in vivo* and cell migration and invasion *in vitro*.

**3.4. Wnt/ $\beta$ -Catenin Signaling Upregulated in OS and Interacted with TMEM206.** Considering that Wnt/ $\beta$ -catenin signaling plays a critical role in the progression of tumor disease, we sought to determine the expression pattern of Wnt/ $\beta$ -catenin signaling in OS tissues. The IHC results indicated that  $\beta$ -catenin was aberrant increasingly expressed with advanced Ennekin stage (Figure 4(a)), and WB results further confirmed

this observation (Figure 4(b),  $P < 0.05$ ). The correlation between the TMEM206 and  $\beta$ -catenin reminds us that there is an interaction mechanism among them.

A dual-luciferase reporter analysis was performed to prove the interaction between TMEM206 and  $\beta$ -catenin. The results showed that overexpression of TMEM206 significantly promoted the activity of firefly luciferase that carried wild-type but not mutant TCF-binding sites both in U2OS and MG63 cells (Figure 4(c),  $P < 0.01$ ), which indicated that  $\beta$ -catenin is indeed a downstream target of TMEM206. In addition, by using immunofluorescence staining, we also observed that upregulation of TMEM206 expression noticeably promoted the  $\beta$ -catenin accumulation in MG63 cells (Figure 4(d)).

Consistently, upregulation of TMEM206 remarkably increased the protein level of  $\beta$ -catenin in MG63 cells (Figure 4(e)).

**3.5. Silencing TMEM206 Attenuates the Wnt/ $\beta$ -Catenin Signaling Pathway in OS Cell Lines.** To further confirm the underlying mechanisms by which TMEM206 interacted with  $\beta$ -catenin in OS, U2OS and MG63 cells transfected with SC-shRNA or TMEM206-targeting shRNAs. Intriguingly, silencing TMEM206 caused decreased  $\beta$ -catenin staining intensity in both U2OS and MG63 cells (Figure 5(a)). Wnt/ $\beta$ -catenin signaling pathway-related genes ( $\beta$ -catenin, c-Myc, cyclinD1, MMP7, and MMP9) were further confirmed by Western blotting. As shown in Figure 5(b), upon silencing of TMEM206, the protein levels of  $\beta$ -catenin, c-Myc, cyclinD1, MMP7, and MMP9, which are all key signaling intermediates of the Wnt/ $\beta$ -catenin signaling pathway, were all significantly decreased in both U2OS and MG63 cells (Figures 5(c)–5(g),  $P < 0.001$ ).

**3.6. Silencing TMEM206 Attenuates the OS Cell Migration and Invasion at Least in Part via the  $\beta$ -Catenin-Mediated Downregulation of Wnt/ $\beta$ -Catenin Signaling.** To determine

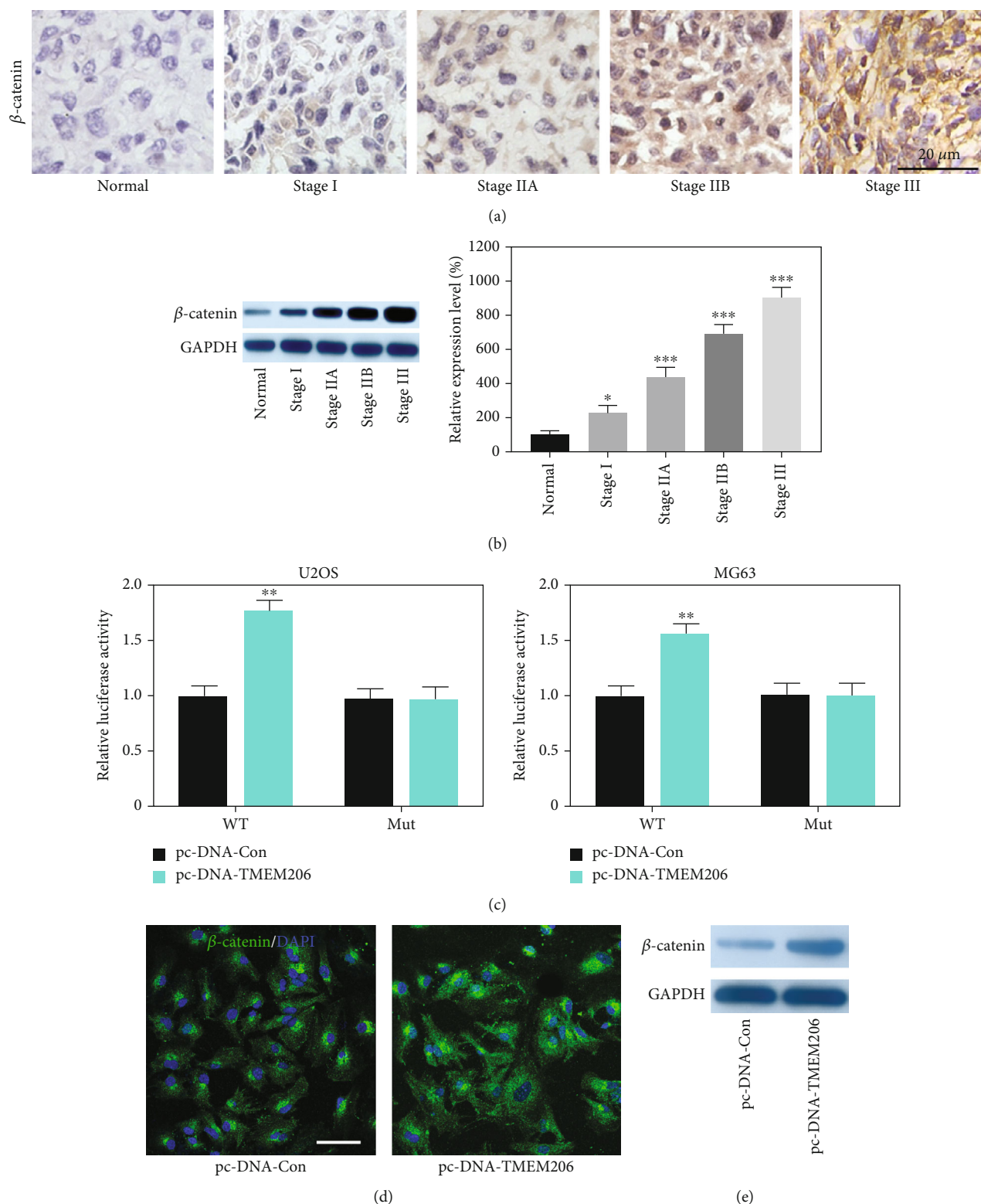
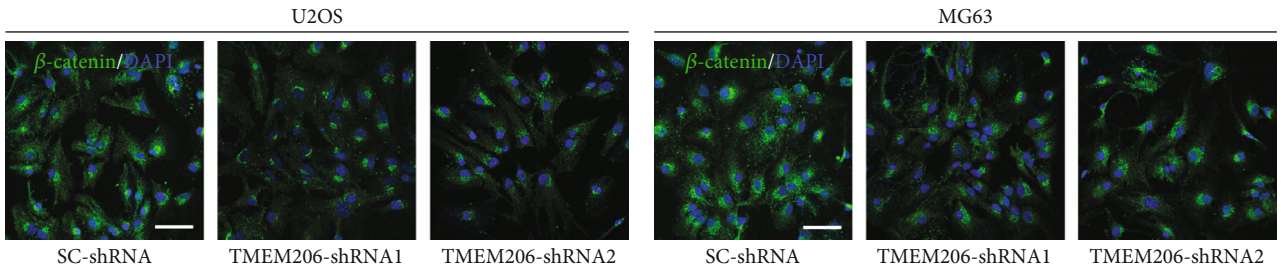
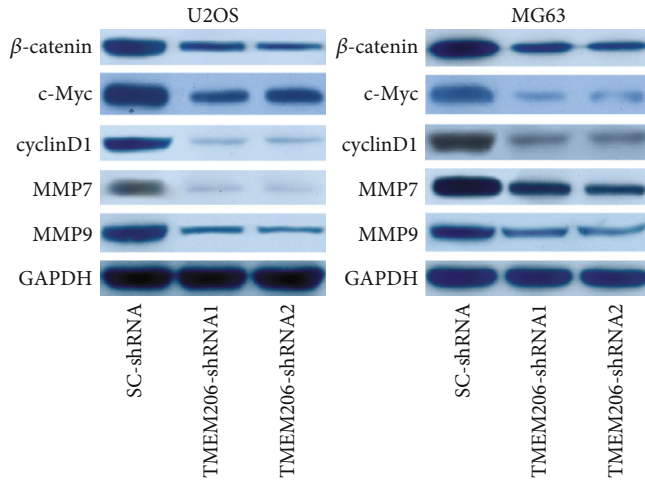


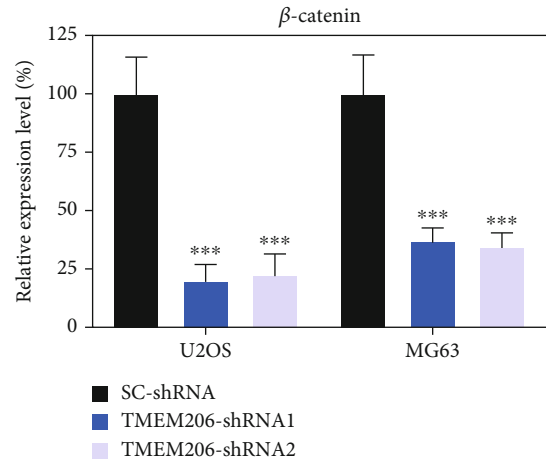
**FIGURE 4:** Upregulation of TMEM206 promotes the expression of  $\beta$ -catenin. (A) IHC results of the expression of  $\beta$ -catenin in osteosarcoma tissues and paired para-tumor tissues. Scale bar: 50  $\mu$ m. (b) WB results indicated  $\beta$ -catenin expression was significantly elevated in patients with advanced stage (\* $P < 0.05$ , \*\* $P < 0.01$ , \*\*\* $P < 0.001$ , as comparing with para-tumor tissue group, respectively). (c) U2OS and MG63 cells were conducted with a firefly luciferase reporter assay, and the firefly luciferase activity of each sample was normalized to the Renilla luciferase activity (\*\* $P < 0.001$ , as comparing with pcDNA-Con group, respectively). (d) Upregulation of TMEM206 enhanced the  $\beta$ -catenin stain intensity in MG63 cells. Scale bar: 50  $\mu$ m. (e) Upregulation of TMEM206 enhanced the expression level of  $\beta$ -catenin protein. GAPDH was used as an internal control. The data are represented as means  $\pm$  SEM in (b) and represented as means  $\pm$  SD in (c).



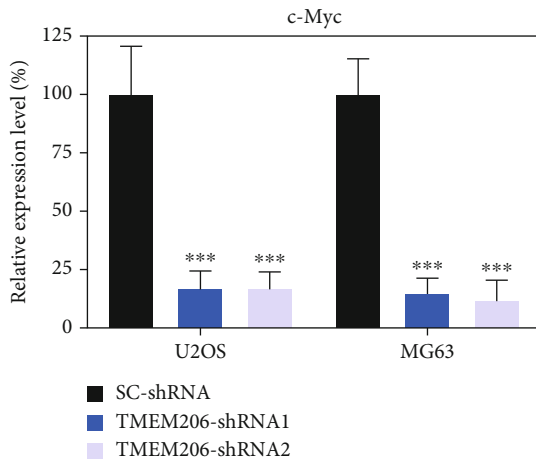
(a)



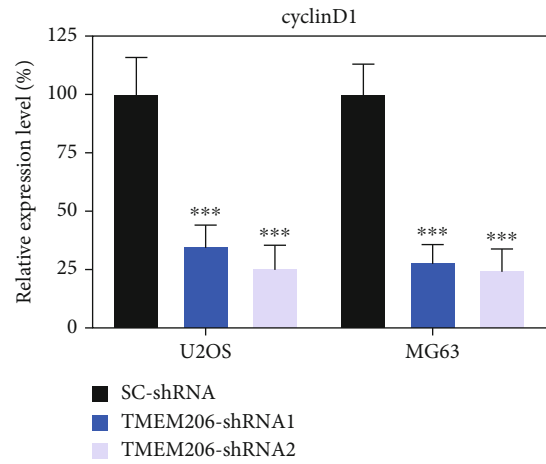
(b)



(c)



(d)



(e)

FIGURE 5: Continued.

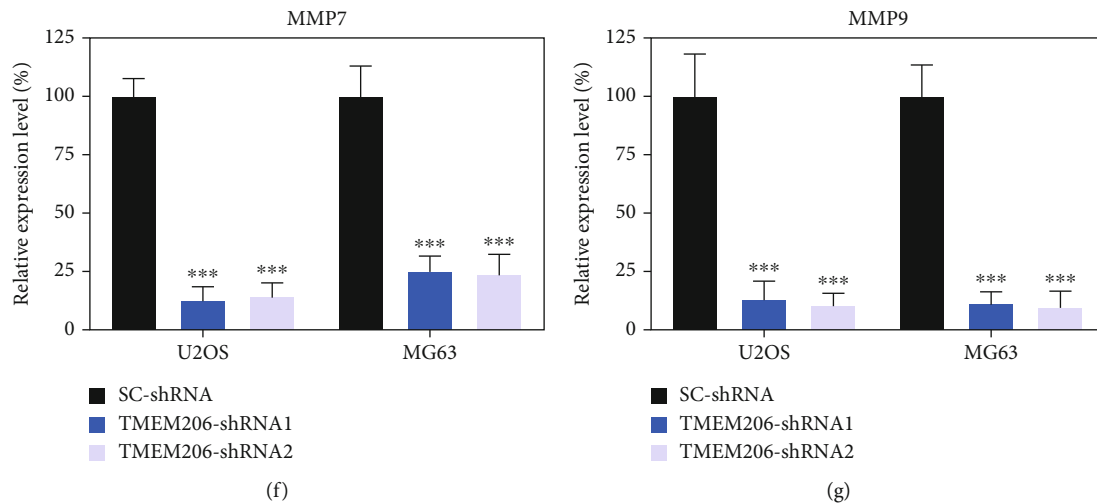


FIGURE 5: TMEM206 knockdown attenuates the Wnt/ $\beta$ -catenin signaling pathway. Wnt/ $\beta$ -catenin signaling pathway protein level was dramatically reduced in TMEM206-shRNA-transfected U2OS and MG63 cells ( $***P < 0.001$ , as comparing with SC-shRNA group, respectively). GAPDH was used as an internal control. The data are represented as means  $\pm$  SD in (b–f).

whether  $\beta$ -catenin is required for the observed phenotypes induced by TMEM206 knockdown in OS cells, we then conducted the following rescue experiments: first, the Wnt/ $\beta$ -catenin signaling activator lithium chloride (LiCl) was added to the TMEM206-shRNA-transfected U2OS and MG63 cells to rescue the function of Wnt/ $\beta$ -catenin signaling. As expected, the decreased migration and invasion of MG63 cells transfected with TMEM206-shRNA was reupregulated after LiCl administration (Figure 6(a),  $P < 0.001$ ). To further confirm our hypothesis, we constructed TMEM206 overexpressing MG63 cells, and the  $\beta$ -catenin inhibitor IWP-2 was added to observe its effect. Transfection of the plasmid containing TMEM206 promoted the migration and invasion of MG63 cells, and this promotive effect was abolished by IWP-2 treatment (Figure 6(b),  $P < 0.001$ ). Taken together, these data revealed that the defects in proliferation and migration induced by TMEM206 knockdown in OS cells were at least in part via the  $\beta$ -catenin-mediated downregulation of the Wnt/ $\beta$ -catenin signaling pathway.

**3.7. Silencing TMEM206 Inhibits OS Tumor Growth and Metastasis.** Previous results have shown that silencing TMEM206 inhibits OS cell metastasis *in vitro*. In this study, a xenograft model in nude mice injected with TMEM206-shRNA-transfected MG63 was used to determine the effect of silencing TMEM206 on OS tumor growth *in vivo*. Decreasing the expression of TMEM206 remarkably suppressed tumor growth, as reflected by tumor volume, compared with the SC-shRNA vector-transfected control cells (Figures 7(a) and 7(b),  $P < 0.001$ ). The decrease in cell proliferation in the xenograft model was also validated by immunohistochemical staining of TMEM206 and  $\beta$ -catenin (Figure 7(c)); these results are in line with *in vitro* results. To further investigate the effect of silencing TMEM206 *in vivo*, metastasis to the lungs was monitored. Fewer metastatic foci in the lungs were detected in mice injected with MG63 cells transfected with TMEM206-shRNA transfected with the SC-shRNA group (Figure 7(d),  $P < 0.001$ ). Taken together, silencing TMEM206

negatively regulated the proliferation and migration of OS cells *in vivo* and *in vitro* (Figure 7(e)).

#### 4. Discussion

Osteosarcoma (OS), the most common malignant bone tumor in children and adolescents, is characterized by a high degree of malignancy and high occurrence of lung metastasis [2]. The lack of efficient intervention approaches contributes to OS unsatisfactory clinical outcomes, which is a leading cause of cancer mortality worldwide. Exploring the molecular mechanisms and identifying therapeutic targets of OS has always been a hot topic in OS research. Although a growing body of evidence suggests that the TMEM family plays crucial roles in tumorigenesis and the progression of various malignant tumors, its role in OS cancer development is not fully understood. In the current report, we present evidence to demonstrate TMEM206 role in OS development and its potential regulatory pathway.

Taking advantage of clinical specimens and well-characterized OS cell lines, we sought to establish whether TMEM206 is associated with OS pathogenesis. TMEM206 was consistently found to be upregulated in clinical tumor samples and OS cell lines, and the levels of TMEM206 positively correlated with clinical stages in OS patients, which demonstrates that TMEM206 overexpression might drive OS progression. Similar to our results, the expression of TMEM206 positively correlated with the prognosis of HCC [17] and promoted colorectal cancer malignancy [21]. Consistently, our findings showed that TMEM206 expression is upregulated in highly malignant invasive OS cell lines, such as MG63, suggesting a link between the molecular levels of TMEM206 and OS clinical outcomes. We further constructed shRNA vectors and utilized a set of well-characterized OS cell lines to elucidate the role of TMEM206 in cell proliferation, migration, invasion, and metastasis.

Tumor biological functional experiments in OS cells showed that TMEM206 downregulation influences OS cell

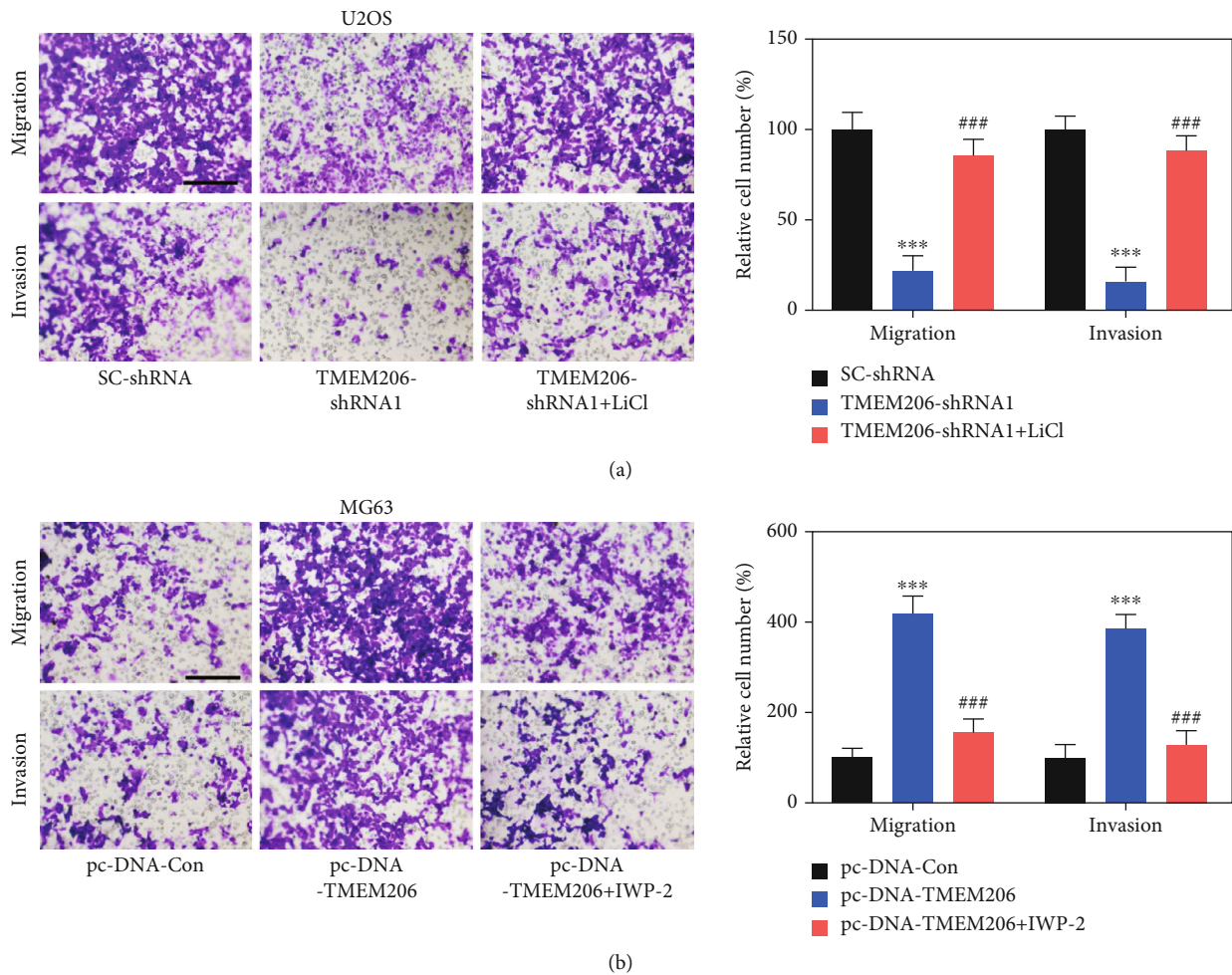
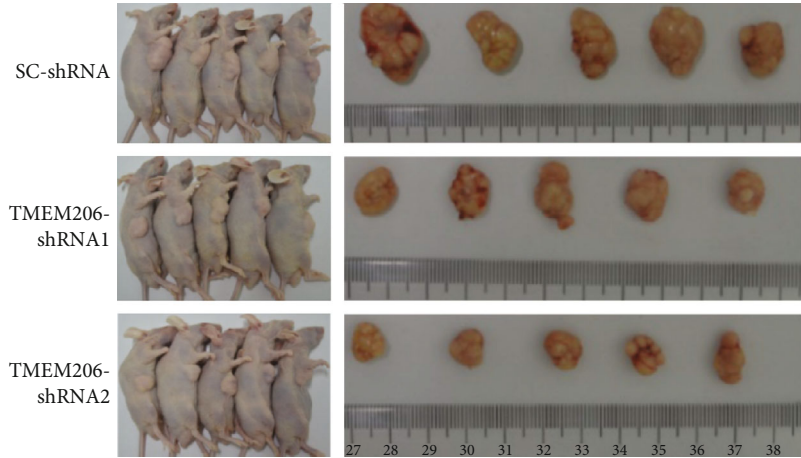


FIGURE 6: Wnt/ $\beta$ -catenin signaling is involved in TMEM206-mediated OS-metabolic properties. (a) Treatment with Wnt/ $\beta$ -catenin signaling activator LiCl rescued the effect of TMEM206-shRNA in OS cell migration and invasion ( $***P < 0.001$  compared with SC-shRNA,  $***P < 0.001$  compared with TMEM206-shRNA, respectively). Scale bar:  $100 \mu\text{m}$ . (b) Treatment with Wnt/ $\beta$ -catenin signaling pathway inhibitor IWP-2 reversed the TMEM206-overexpression mediated migration and invasion promotion ( $***P < 0.001$  compared with pcDNA-Con,  $***P < 0.001$  compared with pcDNA-TMEM206, respectively). Scale bar:  $100 \mu\text{m}$ . The data are represented as means  $\pm$  SD from 3 replicate experiments.

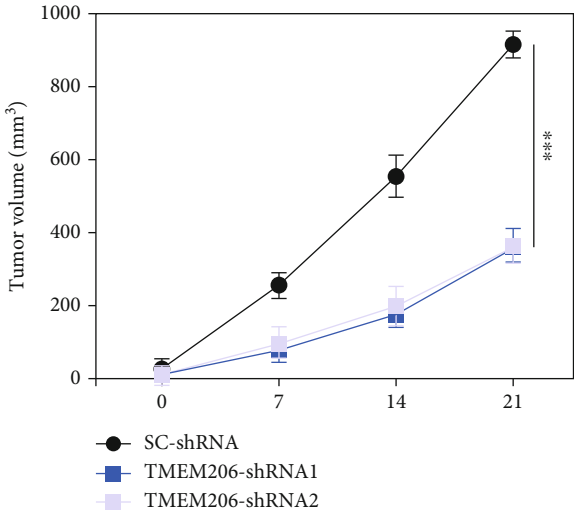
proliferation, colony formation, migration, and invasive capacity, the most important features of malignant cell behavior. Consistent with our present data, Zhao et al. found that knockdown or upregulation silencing of TMEM206 inhibited or promoted the proliferation of colorectal cancer cells [21], which supports our hypothesis that TMEM206 is an oncogenic gene and may be a promising therapeutic target. The underlying mechanism of TMEM206 involvement in OS tumorigenicity remains elusive. We then attempted to elucidate the underlying mechanisms by which TMEM206 functions in OS. Zhao et al. found that TMEM206 regulates the phosphorylation of AKT and its downstream signaling pathway [21]. In the present study, the Wnt/ $\beta$ -catenin signaling pathway was regulated by TMEM206 in OS cells. TMEM206 knockdown significantly altered the expression levels of Wnt/ $\beta$ -catenin signaling pathway markers in OS cells dual-luciferase reporter analysis showing that TMEM206 could directly interact with  $\beta$ -catenin. The results of rescue experiments further proved that the defects in proliferation and migration induced by

TMEM206 knockdown in OS cells were, at least partly, due to the downregulation of the Wnt/ $\beta$ -catenin signaling pathway. Along the same line of arguments, Jiang et al. reported that TMEM48 could promote cervical cancer invasion and metastasis *in vitro* and *in vivo* via activating the Wnt/ $\beta$ -catenin pathway [22]. Moreover, TMEM168 knockdown could also inhibit glioblastoma cell proliferation via suppression of the Wnt/ $\beta$ -catenin pathway [23]. The canonical Wnt/ $\beta$ -catenin pathway is crucial for bone morphogenesis and bone regeneration [24], and various Wnt antagonists have been tested to suppress the proliferation of OS cells *in vitro* and OS tumor growth *in vivo* [25]. TMEM206 knockdown mechanism of action on OS inhibition was determined by inhibiting the activation of the Wnt signaling pathway.

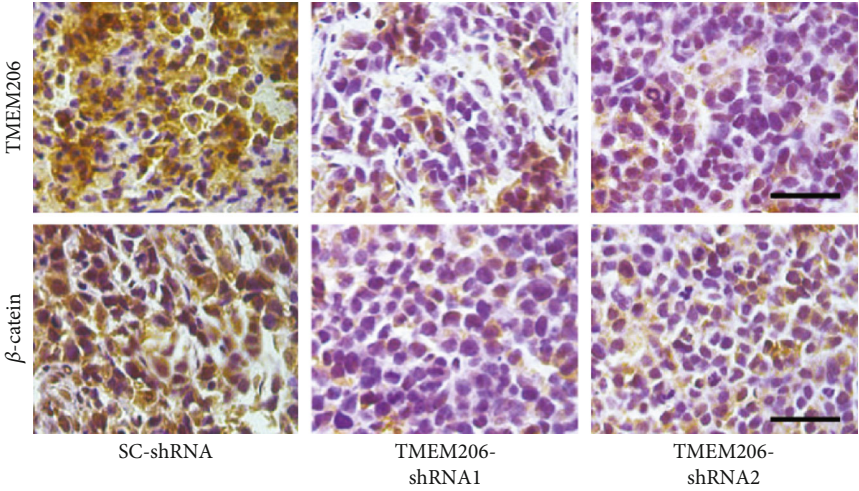
Based on the above evidence, we speculate that targeting TMEM206 might be a useful approach to repress the proliferation, migration, and metastasis of OS *in vivo*. Therefore, we utilized a xenograft model to determine the effect of silencing TMEM206 on OS tumor growth *in vivo*. Inhibition



(a)



(b)



(c)

FIGURE 7: Continued.



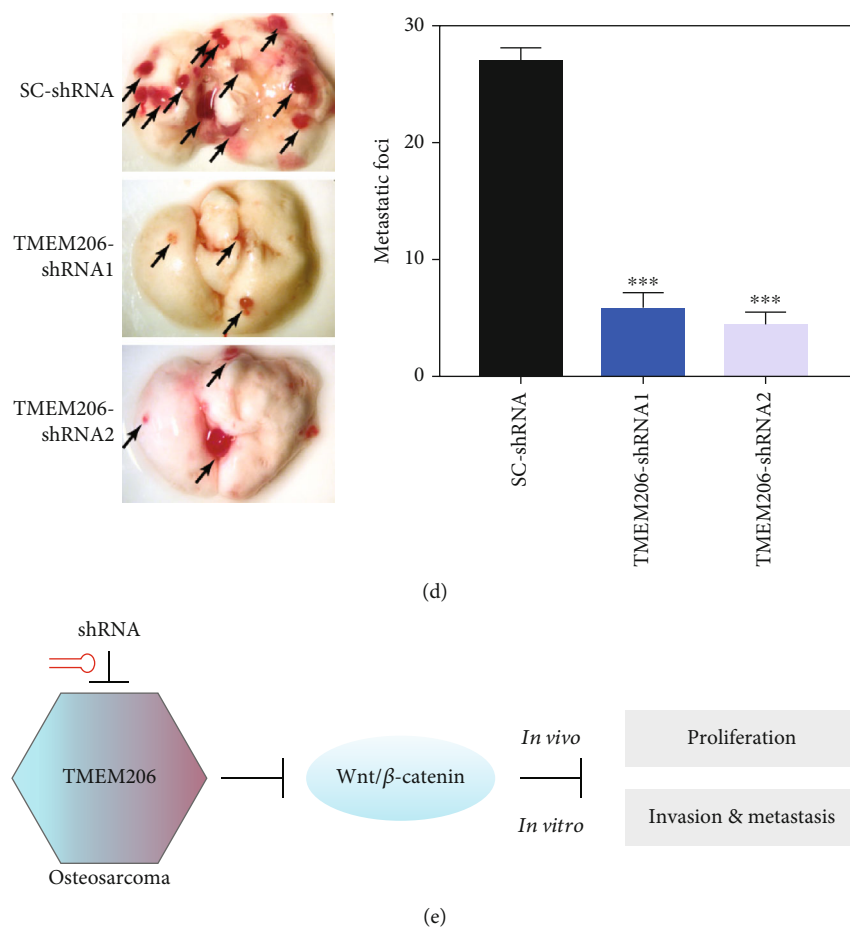


FIGURE 7: Effects of silencing TMEM206 on OS metastasis in vivo. (a, b) Silencing TMEM206 inhibited the tumor growth in the xenograft nude mice. Nude mice were subcutaneously injected with MG63 cells transfected with TMEM206-shRNA by lentivirus infection. Tumor sizes were measured every 7 days, and the mice were sacrificed on day 21, and the tumors were excised for analysis ( $n = 6$ ,  $***P < 0.001$ , as comparing with SC-shRNA group, respectively). (c) Representative immunohistochemical staining with TMEM206 and  $\beta$ -catenin antibody of the xenograft tumor. Scale bar:  $50 \mu\text{m}$ . (d) Representative images of whole lungs from nude mice inoculated with MG63 cells and the statistical analysis showed the metastatic foci of the lung ( $***P < 0.001$ , as comparing with SC-shRNA group, respectively). Black arrowhead represent the metastatic foci in the lung. (e) Schematic diagram of the mechanism that TMEM206 regulating OS. The data are represented as means  $\pm$  SEM from 3 replicate experiments.

expression of TMEM206 remarkably suppressed tumor growth, as reflected by the tumor volume accompanied by decreased immunohistochemical reactivity of Ki-67 and CD31. The lung is the most common site of distant metastasis of OS [26]. Our patient results showed that there was more TMEM206 expression in these patients with lung metastasis. Interestingly, after silencing the TMEM206 of the tumor in situ, significantly fewer metastatic foci in the lungs were observed. OS invasion and metastasis require complicated biological processes involving various molecules. The Wnt/ $\beta$ -catenin pathways, MMP7 and MMP9, have been regarded as metastasis-related genes, which play a critical role in OS invasion, metastasis, and tumor cell angiogenesis [27, 28]. The decreased tumor growth and metastasis *in vivo* could be explained by the inhibition of the Wnt/ $\beta$ -catenin pathway. Taken together, our results collectively indicate that blocking the TMEM206 could inhibit OS. Nevertheless, although the results are inspiring, the antitumor effects of the TMEM206 target should be investigated in patients in future clinical studies.

In summary, our findings are the first to show that TMEM206 is increased in human OS tissues and may represent a novel biomarker of OS. Silencing TMEM206 impedes the proliferation and invasion of OS cells *in vitro* and *in vivo* by downregulating Wnt/ $\beta$ -catenin signaling. These findings provide sufficient *in vitro* and *in vivo* evidence of the anti-cancer effects and tumor inhibitory role of TMEM206 inhibition in OS and confirm TMEM206 as a key regulator of Wnt/ $\beta$ -catenin signaling. Our study highlights a critical role for the TMEM206/Wnt/ $\beta$ -catenin signaling axis in OS progression and suggests that TMEM206 is a potential therapeutic target for OS diagnosis and therapy.

## Data Availability

The datasets used and/or analyzed during the current study are available from the corresponding author on reasonable request.

## Ethical Approval

The study was conducted according to the World Medical Association Declaration of Helsinki. The study was approved by the Ethics Committee of Renmin Hospital of Wuhan University.

## Consent

Informed consent was obtained from each patient before participating in this study

## Conflicts of Interest

The authors declare that they have no competing interests.

## Authors' Contributions

FP conceived and designed the present study. ZW, HHL, and JPL performed the experiments and analyzed the data. ZW and FP interpreted the data and wrote the manuscript. All authors read and approved the final manuscript.

## Acknowledgments

This study is supported by the National Natural Science Foundation of China (grant no. 61308110).

## References

- [1] K. Lu, R. Lin, J. Yang, W. Yang, R. Reiter, and S. Yang, "Molecular and cellular mechanisms of melatonin in osteosarcoma," *Cell*, vol. 8, no. 12, p. 1618, 2019.
- [2] D. Gianferante, L. Mirabello, and S. Savage, "Germline and somatic genetics of osteosarcoma – connecting aetiology, biology and therapy," *Nature Reviews Endocrinology*, vol. 13, no. 8, pp. 480–491, 2017.
- [3] Q. Gu, Y. Luo, C. Chen, D. Jiang, Q. Huang, and X. Wang, "GREM1 overexpression inhibits proliferation, migration and angiogenesis of osteosarcoma," *Experimental Cell Research*, vol. 384, no. 1, p. 111619, 2019.
- [4] D. Rasalkar, W. Chu, V. Lee, B. Paunipagar, F. Cheng, and C. Li, "Pulmonary metastases in children with osteosarcoma: characteristics and impact on patient survival," *Pediatric Radiology*, vol. 41, no. 2, pp. 227–236, 2011.
- [5] Z. Zhou, Y. Li, M. Kuang et al., "The CD24<sup>+</sup> cell subset promotes invasion and metastasis in human osteosarcoma," *eBioMedicine*, vol. 51, p. 102598, 2020.
- [6] S. Parashar, D. Cheishvili, A. Arakelian et al., "S-adenosylmethionine blocks osteosarcoma cells proliferation and invasion *in vitro* and tumor metastasis *in vivo*: therapeutic and diagnostic clinical applications," *Cancer Medicine*, vol. 4, no. 5, pp. 732–744, 2015.
- [7] R. Garva, C. Thepmalee, U. Yasamut et al., "Sirtuin family members selectively regulate autophagy in osteosarcoma and mesothelioma cells in response to cellular stress," *Frontiers in Oncology*, vol. 9, 2019.
- [8] R. Tao, C. Lau, H. Tse, and G. Li, "Regulation of cell proliferation by intermediate-conductance Ca<sup>2+</sup>-activated potassium and volume-sensitive chloride channels in mouse mesenchymal stem cells," *American journal of physiology Cell physiology*, vol. 295, no. 5, pp. C1409–C1416, 2008.
- [9] H. Yamamura, Y. Suzuki, and Y. Imaizumi, "Physiological and pathological functions of Cl channels in chondrocytes," *Biological & Pharmaceutical Bulletin*, vol. 41, no. 8, pp. 1145–1151, 2018.
- [10] C. Le Henaff, E. Hay, F. Velard et al., "Enhanced F508del-CFTR channel activity ameliorates bone pathology in murine cystic fibrosis," *The American Journal of Pathology*, vol. 184, no. 4, pp. 1132–1141, 2014.
- [11] P. Abeyrathne, M. Chami, and H. Stahlberg, "Biochemical and biophysical approaches to study the structure and function of the chloride channel (ClC) family of proteins," *Biochimie*, vol. 128–129, pp. 154–162, 2016.
- [12] Y. Wei, X. Shen, L. Li et al., "TM4SF1 inhibits apoptosis and promotes proliferation, migration and invasion in human gastric cancer cells," *Oncology Letters*, vol. 16, no. 5, pp. 6081–6088, 2018.
- [13] K. Liu, F. Dong, H. Gao et al., "Promoter hypermethylation of the CFTR gene as a novel diagnostic and prognostic marker of breast cancer," *Cell Biology International*, vol. 44, no. 2, pp. 603–609, 2020.
- [14] Y. Shin, M. Kim, J. Won et al., "Epigenetic modification of CFTR in head and neck cancer," *Journal of clinical medicine*, vol. 9, no. 3, p. 734, 2020.
- [15] Y. Li, W. Guo, S. Liu et al., "Silencing transmembrane protein 45B (TNEM45B) inhibits proliferation, invasion, and tumorigenesis in osteosarcoma cells," *Oncology Research*, vol. 25, no. 6, pp. 1021–1026, 2017.
- [16] J. Yang, J. Chen, V. M. Del Carmen et al., "PAC, an evolutionarily conserved membrane protein, is a proton-activated chloride channel," *Science*, vol. 364, no. 6438, pp. 395–399, 2019.
- [17] L. Zhang, S. Liu, X. Yang, Y. Wang, and Y. Cheng, "TMEM206 is a potential prognostic marker of hepatocellular carcinoma," *Oncology Letters*, vol. 20, no. 5, p. 1, 2020.
- [18] H. Lambert, L. Frassetto, J. Moore et al., "The effect of supplementation with alkaline potassium salts on bone metabolism: a meta-analysis," *Osteoporosis international: a journal established as result of cooperation between the European Foundation for Osteoporosis and the National Osteoporosis Foundation of the USA*, vol. 26, no. 4, pp. 1311–1318, 2015.
- [19] X. Bai, Y. Gao, M. Zhang et al., "Carboxylated gold nanoparticles inhibit bone erosion by disturbing the acidification of an osteoclast absorption microenvironment," *Nanoscale*, vol. 12, no. 6, pp. 3871–3878, 2020.
- [20] L. Li-Man, C. Chang, R. Ruo-Xi et al., "Corrigendum: Loss of TARBP2 drives the progression of hepatocellular carcinoma via miR-145-SERPINE1 axis," *Frontiers in Oncology*, vol. 11, 2021.
- [21] J. Zhao, D. Zhu, X. Zhang, Y. Zhang, J. Zhou, and M. Dong, "TMEM206 promotes the malignancy of colorectal cancer cells by interacting with AKT and extracellular signal-regulated kinase signaling pathways," *Journal of Cellular Physiology*, vol. 234, no. 7, pp. 10888–10898, 2019.
- [22] X. Jiang, L. Wang, Z. Liu, W. Song, M. Zhou, and L. Xi, "TMEM48 promotes cell proliferation and invasion in cervical cancer via activation of the Wnt/ $\beta$ -catenin pathway," *Journal of Receptor and Signal Transduction Research*, vol. 41, no. 4, pp. 371–377, 2021.
- [23] J. Xu, Z. Su, Q. Ding et al., "Inhibition of proliferation by knockdown of transmembrane (TMEM) 168 in glioblastoma cells via suppression of Wnt/ $\beta$ -catenin pathway," *Oncology Research*, vol. 27, no. 7, pp. 819–826, 2019.

- [24] M. Greenblatt, D. Shin, H. Oh et al., “MEKK2 mediates an alternative  $\beta$ -catenin pathway that promotes bone formation,” *Proceedings of the National Academy of Sciences of the United States of America*, vol. 113, no. 9, pp. E1226–E1235, 2016.
- [25] G. Danieau, S. Morice, F. Rédini, F. Verrecchia, and B. Royer, “New insights about the Wnt/ $\beta$ -catenin signaling pathway in primary bone tumors and their microenvironment: a promising target to develop therapeutic strategies?,” *International journal of molecular sciences*, vol. 20, no. 15, p. 3751, 2019.
- [26] A. Gross, H. Cam, D. Phelps et al., “IL-6 and CXCL8 mediate osteosarcoma-lung interactions critical to metastasis,” *JCI insight*, vol. 3, no. 16, 2018.
- [27] Y. Lv, H. Dai, G. Yan, G. Meng, X. Zhang, and Q. Guo, “Down-regulation of tumor suppressing STF cDNA 3 promotes epithelial-mesenchymal transition and tumor metastasis of osteosarcoma by the Wnt/GSK-3 $\beta$ / $\beta$ -catenin/snail signaling pathway,” *Cancer Letters*, vol. 373, no. 2, pp. 164–173, 2016.
- [28] M. Wang, T. Liu, X. Hu, A. Yin, J. Liu, and X. Wang, “EMP1 promotes the malignant progression of osteosarcoma through the IRX2/MMP9 axis,” *Panminerva Medica*, vol. 62, no. 3, pp. 150–154, 2020.

## Review Article

# ROS Pleiotropy in Melanoma and Local Therapy with Physical Modalities

Sanjeev Kumar Sagwal  and Sander Bekeschus 

ZIK Plasmatis, Leibniz Institute for Plasma Science and Technology (INP), Felix-Hausdorff-Str. 2, 17489 Greifswald, Germany

Correspondence should be addressed to Sander Bekeschus; [sander.bekeschus@inp-greifswald.de](mailto:sander.bekeschus@inp-greifswald.de)

Received 21 July 2021; Revised 6 September 2021; Accepted 11 October 2021; Published 3 November 2021

Academic Editor: Bin Duan

Copyright © 2021 Sanjeev Kumar Sagwal and Sander Bekeschus. This is an open access article distributed under the Creative Commons Attribution License, which permits unrestricted use, distribution, and reproduction in any medium, provided the original work is properly cited.

Metabolic energy production naturally generates unwanted products such as reactive oxygen species (ROS), causing oxidative damage. Oxidative damage has been linked to several pathologies, including diabetes, premature aging, neurodegenerative diseases, and cancer. ROS were therefore originally anticipated as an imperative evil, a product of an imperfect system. More recently, however, the role of ROS in signaling and tumor treatment is increasingly acknowledged. This review addresses the main types, sources, and pathways of ROS in melanoma by linking their pleiotropic roles in antioxidant and oxidant regulation, hypoxia, metabolism, and cell death. In addition, the implications of ROS in various physical therapy modalities targeting melanoma, such as radiotherapy, electrochemotherapy, hyperthermia, photodynamic therapy, and medical gas plasma, are also discussed. By including ROS in the main picture of melanoma skin cancer and as an integral part of cancer therapies, a greater understanding of melanoma cell biology is presented, which ultimately may elucidate additional clues on targeting therapy resistance of this most deadly form of skin cancer.

## 1. Introduction

Reactive oxygen species (ROS) are a consequence of imperfect aerobic metabolism. ROS are formed as a byproduct of electron transfer reactions from enzymatic and nonenzymatic sources [1]. This review also uses the term ROS to cover reactive nitrogen species (RNS) as many contain (reactive) oxygen. Oxidative stress is caused by the increased ROS or decrease in the activity of antioxidant systems in the cell. Slightly or detrimentally higher ROS levels have been coined oxidative eustress and oxidative distress, respectively [2]. The former relates to lower concentrations of ROS that amplify physiological processes such as proliferation and wound healing [3]. The latter covers exceedingly high levels of oxidative stress-provoking damage and cell death. Oxidative stress has been involved in several pathophysiological conditions, including cancer, by damaging lipids, proteins, and DNA [4–8]. ROS interaction with proteins impacts several signaling pathways by oxidizing redox-reactive cysteine and tyrosine residues within or nearby active sites [9, 10]. The effects of ROS vary from reversible to irreversible

depending on the ROS levels and antioxidant machinery efficiency in the cells. Milder effects of protein modifications are reversible and promote cellular signaling through a change in protein activity [7]. For example, while irreversible modification of cysteine residues in proteins can lead to permanent loss of protein function, reversible modification can be protective from excessive ROS [5]. Adaption to ROS elevation through protein modifications plays a prominent role in ROS metabolism either by activating antioxidant pathways (e.g., Kelch-like ECH-associated protein 1 (KEAP1)) through cysteine residue modification or metabolic pathways (e.g., pyruvate kinase isoenzyme type M2 (PMK2)) [9]. Other reversible modifications, including glutathionylation, S-sulfonation, CoAlation, nitrosylation, and disulfides, can modify proteins by protecting them from terminal oxidation and alter their functions to adapt to oxidative stress [5]. Subsequently, ROS-dependent signaling modulates the activation of transcription factors such as NF- $\kappa$ B (nuclear factor kappa-light-chain-enhancer of activated B-cells) and AP-1 (activator protein 1) [11–13]. Numerous mechanisms through which melanoma cells limit ROS exposure have

been described. For instance, NRF2 (nuclear factor erythroid 2-related factor 2) is the most ubiquitous transcription factor that regulates genes involved in antioxidant defense [14]. Hypoxia and activation of oncogenes can induce NRF2, with evidence that this response is mandatory for melanoma development [15, 16]. Thus, the influence of ROS on cellular process is complex and they have dual role of pro- and antitumorigenic effects depending on their regulation.

Based on the work done by several groups, melanoma is a ROS-operated tumor [17]. The contribution of ROS to melanoma therapy is multifaceted. In melanoma prevention studies, antioxidants failed to show any beneficial effects. In some instances, an increase in cancer development was even observed under antioxidant supplementation [18, 19]. Many studies have shown that increased oxidative stress results in increased sensitivity of cells to therapy-induced cell death [20]. Survival of cells under the burden of oxidative stress depends on activating ROS scavenging pathways that are not needed in normal cells, deducing that interference with these antioxidant pathways or additional ROS burden may selectively kill melanoma cells [20, 21]. Impressively, several commonly used chemotherapeutic agents and physical modalities effectively induce ROS as part of their mechanism of action [21–23]. Conversely, ROS may also affect the outcome of immunotherapy [24]. For instance, chimeric antigen receptor (CAR) T cells are prone to hostile inflammatory conditions [25]. Hence, appropriate combinatorial approaches are essential to overcome therapy resistance and achieve better efficacy in melanoma therapy. This review discusses the origin and types of ROS. Further, their signaling and damaging effects in melanoma initiation and progression are described. Moreover, several physical treatment modalities are summarized that contribute to local ROS production and subsequent antimelanoma efficacy

## 2. ROS: Types, Sources, and Regulation

ROS are molecules and free radicals involved in the transfer of electrons from reactive oxygen. There are various tools for indirectly measuring ROS in cells and tissues while measuring ROS directly is still deficient. A selection of ROS is described hereafter, which are relevant in both physiology and pathology, including cancer.

**2.1. ROS Types.** The primary production site of superoxide is mitochondria (Figure 1). During the leakage of electrons at several respiratory chain respiratory complexes, especially complex I and III, molecular oxygen is reduced by one electron to produce superoxide anion ( $O_2^-$ ).  $O_2^-$  is a moderately reactive short-lived species that dismutates spontaneously or by superoxide dismutases (SOD) (Figure 2) to  $H_2O_2$  [26]. This type of ROS is generated by the autoxidation of various small molecules such as dopamine, flavins, and hydroquinones (Figure 3). It is produced nonenzymatically when prosthetic groups or reduced coenzymes directly transfer a single electron to oxygen. Enzymatically, NADPH oxidases (NOXs) reside on the cell membrane of many cell types to produce extracellular superoxide [27]. Superoxide releases

iron by targeting iron-sulfur (Fe-S) clusters or react with nitric oxide (NO $\cdot$ ) to form peroxynitrite (ONOO $^-$ ) [26]. ONOO $^-$  is a strong oxidant that indiscriminately reacts with DNA to generate double-strand breaks, oxidation of amino acids in proteins and induces lipid peroxidation by reacting with lipids.

Hydrogen peroxide ( $H_2O_2$ ) plays a role as a second messenger in several pathways [28] by oxidizing the thiol group (-SH) on cysteine residues, resulting in the transduction of extracellular and intracellular signals and control of the gene expression [29]. Cysteine residues exist as thiolate anion (Cys-S $^-$ ) at physiological pH and are more susceptible to oxidation compared with the protonated cysteine thiol (Cys-SH) [9]. Reversible modifications like sulfenic species are generated after enzyme-mediated oxidation of cysteine residues by  $H_2O_2$  and can be returned to reduced states by the action of thioredoxin (TRX) and glutaredoxin reductases (GRX) [30]. However, advanced oxidation to sulfinic acid and irreversible oxidation to sulfonic acid results in permanent damage of protein function [30]. Cells have professional enzymes directed to prevent the buildup of intracellular  $H_2O_2$ , primarily peroxiredoxins (PRDXs) and glutathione peroxidases (GPXs) [30]. To decrease  $O_2^-$ -mediated ONOO $^-$  formation (Figure 2), SOD1 (located in the cytoplasm and mitochondria) and SOD2 (located in the mitochondrial matrix) convert  $O_2^-$  generated by mitochondria and NOXs into  $H_2O_2$  [30].  $H_2O_2$  diffuses freely to other sites in or outside the cell. When present in peroxisomes, catalase (CAT) can react with  $H_2O_2$  to form water and oxygen. The endoplasmic reticulum is another primary source of  $H_2O_2$  that is generated by the combined action of protein disulfide isomerase (PDI) and ER oxidoreductin 1 (Ero 1) during the formation of disulfide bonds [31]. It is noticeable that the concentration of  $H_2O_2$  defines its role as a signaling molecule (1–10 nM) regulating kinases and phosphatase-driven pathways or causes oxidative stress (>100 nM) [28].

Hydroxyl radicals (OH $\cdot$ ) are the most reactive type of ROS. It is generated in the Fenton reaction with  $H_2O_2$  [32], instigating lipid peroxidation and commencing lipid radicals and lipid peroxy radicals [33]. These short-lived radicals initiate lipid peroxidation by reacting with hydrogen atoms of polyunsaturated fatty acids, which are highly reactive because of the double bonds between carbon atoms in those fatty acids. Lipid peroxidation and GPX4 regulate an iron-dependent cell death known as ferroptosis, relevant to normal and pathological processes [34]. Several other transition metal ions can also react with  $H_2O_2$  to produce peroxy and alkoxy radicals [32]. The reduction of Fe $^{3+}$  to Fe $^{2+}$  by superoxide ion also leads to OH $\cdot$  under specific conditions [35].

**2.2. ROS Sources.** There exist several sites inside a cell that generates ROS. A large share of intracellular ROS is produced in the electron transport chain (ETC) [9]. ROS generated by the ETC into the mitochondria can be delivered into the cytoplasm through the permeability transition pore (PTP) [29]. The opening of PTP leads to a decrease in the concentrations of ATP and Ca $^{2+}$  to release cytochrome c [36–38]. This fuels the collapse of the membrane potential

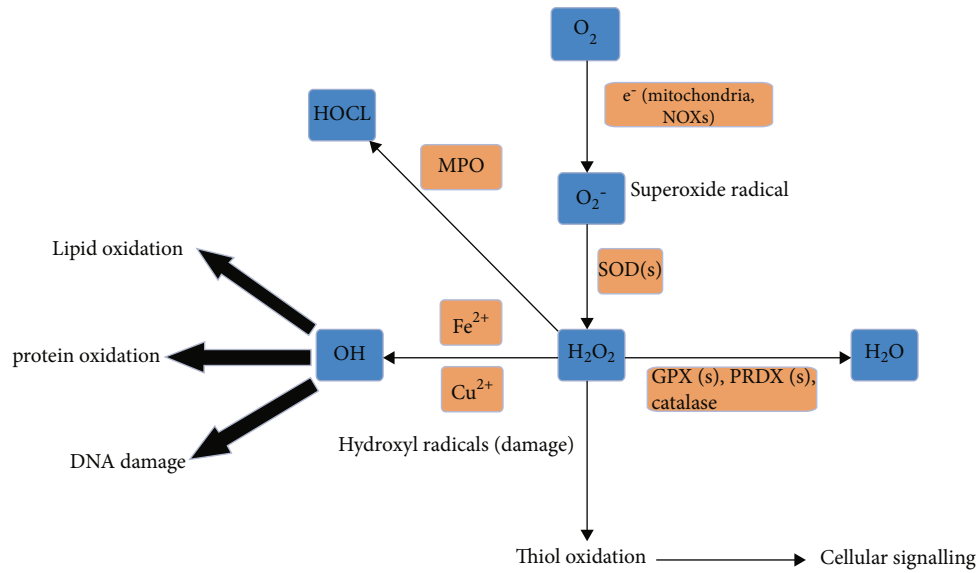


FIGURE 1: ROS types and generation.  $H_2O_2$  and  $O_2^-$  are released by mitochondria into the cytosol. SODs convert  $O_2^-$  in the cytosol to  $H_2O_2$ . NADPH oxidases (NOXs) also generate  $O_2^-$  in the cytosol.  $H_2O_2$  is converted to  $H_2O$  by GPXs and PRDXs. The reaction of ferrous or cuprous ions with  $H_2O_2$  forms  $OH\cdot$  radicals, subsequently damaging lipids, proteins, and DNA.  $H_2O_2$  affects signaling through oxidations of protein thiols. Abbreviations: GPXs: glutathione peroxidases; PRDXs: peroxiredoxins; SODs: superoxide dismutases. Created with <http://biorender.com>.

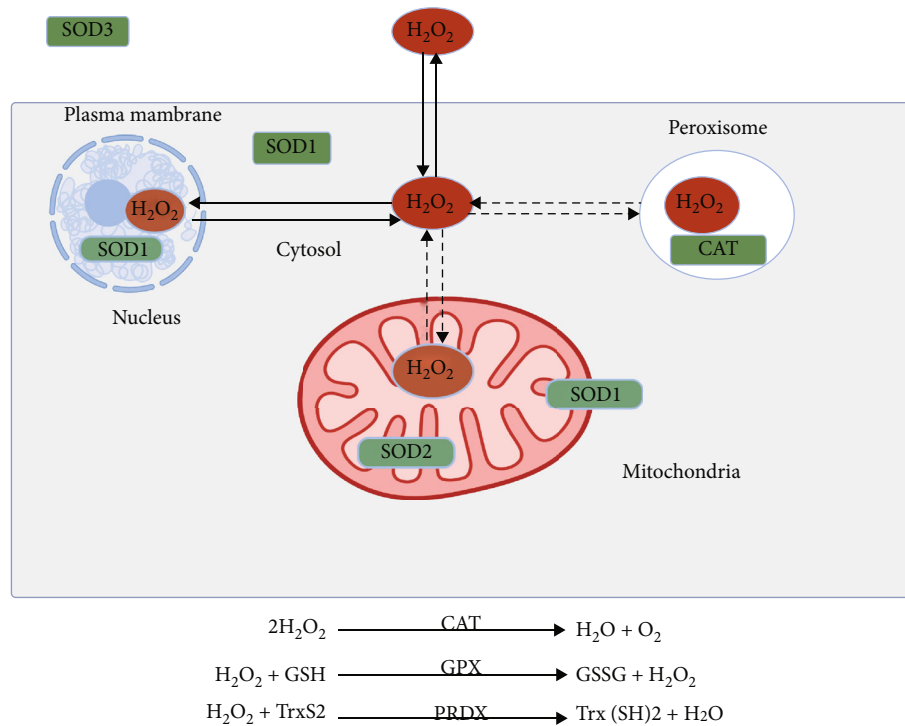


FIGURE 2: ROS detoxification. The cell is equipped with defense mechanisms to scavenge ROS. Detoxification enzymes like CAT react with  $H_2O_2$  to catalyze the formation of  $H_2O$  and  $O_2$ . GPX and PRDX reduce  $H_2O_2$ . Abbreviations: CAT: catalase; GPX: glutathione peroxidase; PRDX: peroxiredoxins; GSSG: glutathione disulfide, oxidized; GSH: glutathione, reduced. Created with <http://biorender.com>.

of mitochondria and a sudden increase in ROS generation by ETC [39]. It has been affirmed that this results in autophagy and apoptosis or necrosis, depending upon the extent of organelle damage. Hence, mitochondria are a major site for

ROS production, especially complexes I and III [40, 41]. In addition to mitochondria, peroxisomes and the endoplasmic reticulum produce ROS. Peroxisomes contain several  $H_2O_2$  generating enzymes, and catalase (CAT) in this organelle

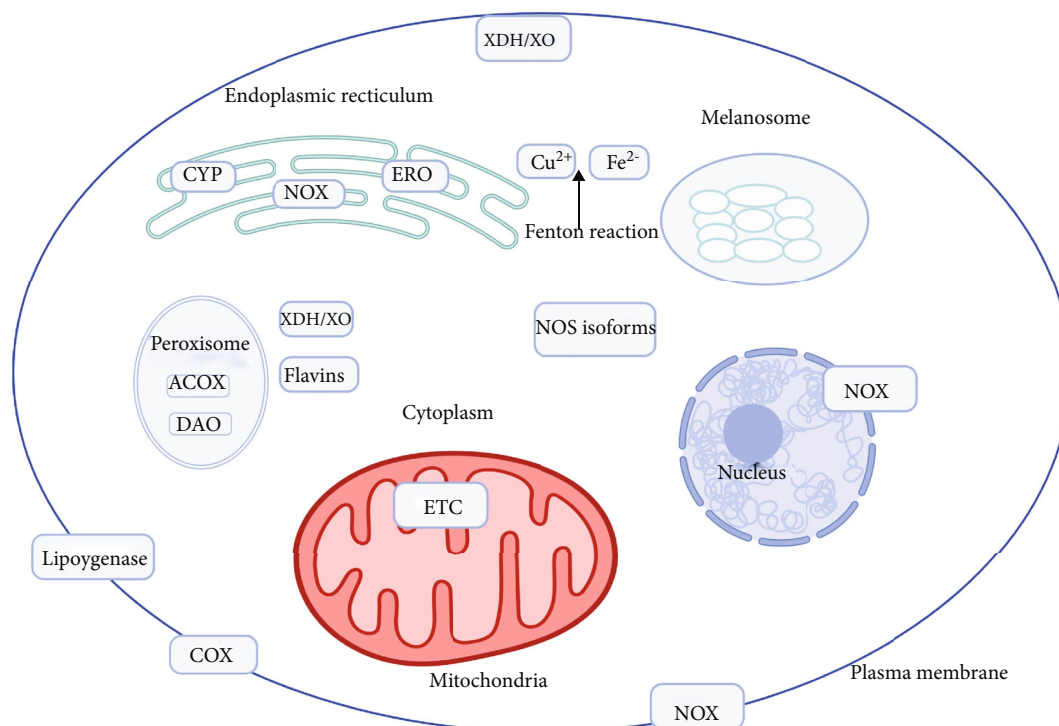


FIGURE 3: Sources of cellular ROS production. Prominently, melanosomes, mitochondria, and NOXs and NOS uncoupling generate ROS. Primarily, NOXs are localized in the plasma membrane, although they can be found on other membranes as well, including the endoplasmic reticulum and mitochondria. Cytosolic enzymes such as XO, XDH, and soluble components like flavin contribute to intracellular ROS production. Oxidative protein folding by ERO1 and enzymes like CYP in the endoplasmic reticulum and lipoygenase and cyclooxygenase in the plasma membrane also generate intracellular ROS. Peroxisomes containing DAO and ACOX generate ROS, too. Abbreviations: XO: xanthine oxidase; XDH: xanthine dehydrogenase; ERO1: endoplasmic reticulum oxidoreductin; CYP: cytochrome P450-dependent monooxygenases; DAO: D-amino oxidase; ACOX: acyl-CoA oxidase. Created with <http://biorender.com>.

detoxifies several substrates and toxic molecules (Figure 2). Other ROS-generating enzymes include xanthine oxidase,  $\alpha$ -ketoglutarate dehydrogenase complex, and NOXs [42]. Apart from phagocytes, NOXs are also found in nonphagocytic cells that regulate cellular growth responses [42]. It has been noticed that ROS produced by NOXs enhances melanoma cell proliferation through activation of NF- $\kappa$ B [43]. The oxidase components are expressed by both melanoma cells and melanocytes [43]. In primary and metastatic melanoma cells, higher levels of NOX and oxidative have been found compared to normal human melanocytes [44]. ONOO<sup>-</sup>, a species generated by the interaction of NO<sup>•</sup> with NOX-generated O<sub>2</sub><sup>-</sup>, is highly reactive toward redox-sensitive amino acid residues, including cysteine and tyrosine [42]. Enzymes like NO<sup>•</sup> synthases (NOS), xanthine oxidoreductase, and cytochrome c oxidase can be involved in NO<sup>•</sup> production [45].

**2.3. ROS Regulation.** To prevent ROS overload in the cytosol and ER, cells have antioxidant defense mechanisms in place tightly regulating ROS levels and maintaining the reduced state of critical biomolecules (Figure 4). Reduced glutathione (GSH) is the prolific reducing agent in the cytosol and ER, though the ratio of reduced to oxidized (GSSG) glutathione (GSH: GSSG) varies in these two compartments [46]. GSH diffuses from the production site to distant sites by passing

through the membranes and plays a prominent role in the ROS detoxification in cancer cells [47]. GSH is a glutamate, glycine, and cysteine tripeptide, synthesized by two enzymatic steps catalyzed by glutamate-cysteine ligase (GCLC) and GSH synthetase (GSS) to form the tripeptide. GSH is used by GSH peroxidases (GPXs) and GSH S-transferases (GSTs) for the elimination of ROS [48]. In addition to GSH-dependent antioxidant systems, there is another less abundant small protein antioxidant system consisting of PRDXs, having a high catalytic activity toward H<sub>2</sub>O<sub>2</sub> and being rejuvenated by thioredoxin (TXN) and sulfaredoxin (SRX) networks [49]. The oxidized forms of TXN and GSH are rejuvenated by TXN reductases [50] and GSH reductases (GR), respectively, using NADPH as an electron donor [51]. Oxidative stress develops when the production of ROS outpaces the scavenging ability of the cellular defense system made up of redox enzymes and several other antioxidant molecules [52]. Oxidative stress promotes the expression of enzymes involved in TXN and GSH systems, implying that they work in accord to buffer the stress induced by ROS molecules [53]. TXN is less significant as an antioxidant due to its lower concentration in cells ( $\mu$ M compared to mM range of GSH), controlling the redox state of specific factors by performing rapid oxidation-reduction reactions kinases and transcription factors [53]. In addition, GSH can reverse modifications such as sulfonylation

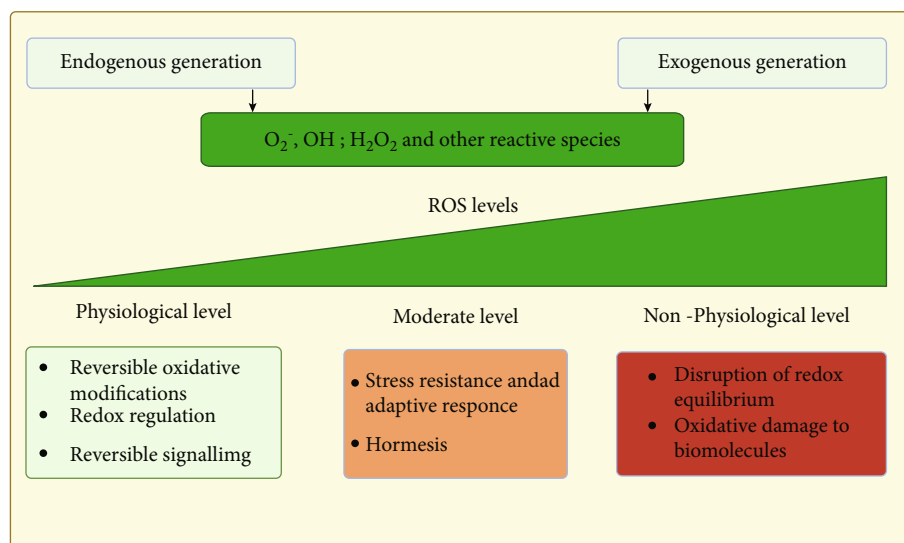


FIGURE 4: Cellular responses to endogenous and exogenous ROS. The response gradient will vary with the cell type, the location of ROS source inside the cells, and the activity of detoxifying enzymes. Blue and red colors represent predominantly beneficial or deleterious responses to ROS levels. Created with <http://biorender.com>.

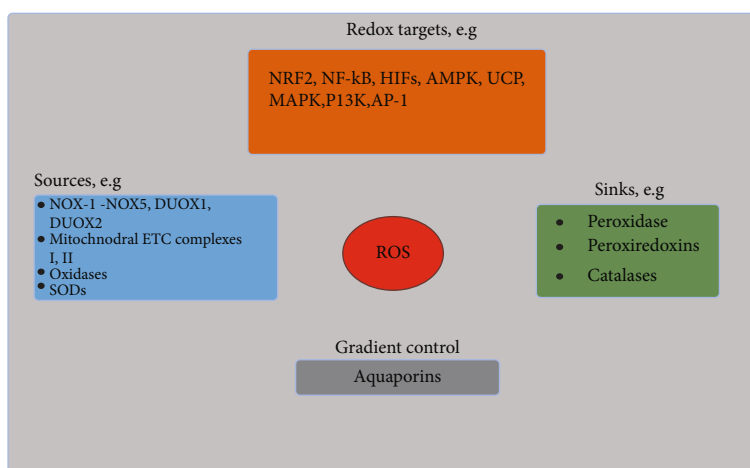


FIGURE 5: Targets and modulators of ROS. Sources of ROS (blue), its targets (orange), aquaporins (grey), and sinks (purple) are shown. Redox targets serve as the center point to support biological functions. SODs serve as a source for ROS and as a sink for the O<sub>2</sub><sup>-</sup>. Under homeostatic conditions, moderate or low levels of ROS induce the activation and inactivation of transcription factors. These transcription factors regulate stress adaptation (including antioxidant response), inflammatory response, hypoxic response, metabolic adaptation, and cell death. Abbreviations: SODs: superoxide dismutases.

mediated by ROS. In summary, several ROS sources affect redox targets and are additionally controlled by ROS sinks, while melanoma cells showed altered expression among all those steps (Figure 5).

### 3. Pleiotropic Roles of ROS in Melanoma Biology

Melanocytes are sensitive to oxidative stress induced by an imbalance of ROS. In normal melanocytes, melanin acts as an antioxidant and suppresses H<sub>2</sub>O<sub>2</sub>, O<sub>2</sub><sup>-</sup>, and singlet oxygen [54]. However, melanogenesis in melanoma cells itself is a source of ROS and oxidative stress [55]. O<sub>2</sub><sup>-</sup> and diffusible H<sub>2</sub>O<sub>2</sub> produced by the mitochondria and NOXs play an

important role in melanocyte malignant transformation [27]. Such Oxidative stress can cause an imbalance of homeostasis in melanocytes, jeopardizing their survival or leading to malignant transformation. In melanoma, NOX4 is highly expressed as compared to the low levels in melanocytes [56]. Overexpression of NOX1, uncoupled eNOS, and NOX4 produced ROS in melanoma, linked to the epithelial-mesenchymal transition [56, 57]. Uncoupled eNOS contributes to superoxide production during malignant transformation [57]. NOS-dependent superoxide formation has a prominent role in melanoma genesis [57]. Furthermore, these data show that superoxide production by eNOS plays a prominent role in melanoma cells' survival and melanocyte malignant transformation. In addition to



that, melanoma cells require NADPH generating enzymes to promote distant metastasis.  $H_2O_2$ ,  $O_2^-$ , and singlet oxygen are involved in various stages of melanomagenesis and tumor microenvironment (TME) quality, including hypoxia, metabolic profiles, immune responses, biosynthesis of melanin, metastasis, and oxidative profiles. ROS increases the toxicity of RNS dramatically begins melanomagenesis that attributes to the leakage of melanosome contents. Several findings suggested that worsen oxidative stress leads to the mutation in several melanoma-associated genes. For example, the somatic BRAF V600E mutation in melanoma can be induced by oxidative stress [58] and loss of p16 results in elevated ROS and mitochondrial biogenesis of human melanocytes [59]. In addition, melanoma progression is associated with depletion of PTEN and the resulting increase in  $O_2^-$  [60]. Hence, oxidative stress is a driver of melanomagenesis.

**3.1. Antioxidant Network.** The role of antioxidant systems is dual in melanoma initiation, progression, and metastasis. The misbalanced activation of the antioxidant transcription factor NRF2 leads to the promotion of melanoma [61]. This transcription factor is entangled in transcribing several GSH and TXN antioxidant pathways genes under various physiological and pathophysiological conditions [62]. In basal conditions, the level of NRF2 is under control by its association with KEAP1, which promotes its degradation via the ubiquitin-proteasome pathway. Increased ROS levels lead to oxidative stress modifications of cysteine residues of KEAP1, leading to flawed NRF2 ubiquitination and NRF2 accumulation [61]. Several mechanisms exist for NRF2 accumulation, such as mutations in the KEAP1 and NRF2 genes, carcinogen-induced DNA damage, and inactivation of KEAP1 due to methylation of its promoter [63]. The role of NRF2 is convoluted and tissue dependent. Loss of NRF2 bolsters epithelial-mesenchymal transition through ROS to promote migration and invasion to support invasion and diaporesis of cancer cells [64, 65]. In contrast, NRF2 can uphold migration and invasion through the BACH1 (BTB domain and CNC homolog 1) transcription factor [66]. Therefore, the role of ROS and NRF2 is complex at different tumor stages. Other agents involved in antioxidant defense and  $H_2O_2$  removal include GPXs, PRDXs, and CAT [12]. The antioxidant capacity of melanoma differs from normal melanocytes and that of other skin cancers. The expression and activity of the antioxidant enzymes catalases, Mn-SOD2, and Cu/Zn-SOD1 are higher in melanoma than in basal cell carcinoma and squamous cell carcinoma [67]. This explains that increased oxidative stress is an important marker in melanoma development. Furthermore, the GSH:GSSG ratio is also higher in melanoma compared with the other skin tumors. This suggests that in melanoma, the increased levels of GSH can readily scavenge ROS and that the subsequently formed GSSH is efficiently reduced to GSH. Collectively, these data imply that melanoma has a better antioxidant status than other skin tumors. The increased resistance of melanoma cells to oxidative stress is not observed in melanocytes [68], suggesting that acquiring an elevated antioxidant network is critical for melanoma development. In primary melanoma, Mn-SOD2, Cu/Zn-

SOD1, and CAT expression are elevated compared with normal skin and melanocytic nevi [67]. In addition, melanoma metastases show improved resistance to oxidative stress and display high levels of ferritin expression compared with their corresponding primary melanomas [69]. Ferritin binds to and prevents iron from being reduced in the Fenton reaction, thereby averting OH $\cdot$ -induced lipid peroxidation and apoptosis [69]. Summative, these findings indicate that primary and metastatic melanomas are highly resistant to oxidative stress through the increased activity of several antioxidative mechanisms. In other words, inhibition of ROS by antioxidants does not have a predictable outcome on cell function since the role of ROS changes under differing environmental conditions. For future aspects, it will be essential to identify specific molecular targets of ROS under different conditions to modulate pathways downstream of ROS that increase adaptation to stress to increase therapeutic efficacy.

**3.2. Apoptosis.** In response to ROS, melanoma cells can, in principal, succumb to regulated cell death. However, in approximately half of the sporadic melanomas, Protein kinase B, also known as AKT, is hyperactivated because of gene amplification and decreased PTEN (phosphatase and tensin homolog) activity [70]. Activated AKT can subsequently phosphorylate and thereby inhibit the activity of the proapoptotic factors BAD (Bcl-xL/Bcl-2-associated death promoter), caspase (cysteinyI-aspartate specific protease) 9, forkhead transcription factor, GSK3 (glycogen synthase kinase-3), and IKK (inhibitor of NF- $\kappa$ B). AKT stabilizes cells with extensive mitochondrial damage, which can generate surplus ROS [60]. Furthermore, AKT induces the expression of the ROS-generating enzyme NOX4 in melanoma cells and growth melanoma cells in mice [60]. In addition, the RAS/BRAF/MEK/ERK mitogen-activated protein kinase pathway is constitutively activated in melanoma via an activating mutation in BRAF or autocrine growth factor stimulation [71] and is a crucial modulator of melanoma initiation and progression [72]. Mitogen-activated protein kinases regulate ROS production by melanoma cells and cooperate with antiapoptotic proteins to maintain melanoma cell viability [73]. ROS constitutively activate NF- $\kappa$ B [74], a transcription factor critically involved in cell survival [75]. The activation of NF- $\kappa$ B has been proposed as an event that promotes melanoma tumor progression [76]. Transcription activation of NF- $\kappa$ B-regulated chemokines enhances melanoma progression through autocrine and paracrine loops, resulting in autonomous growth and invasion of melanoma cells [77]. Furthermore, ROS can activate AP-1 [78], a transcription factor critically involved in RAS-induced oncogenic transformation [79]. Furthermore, ROS regulate the expression of matrix metalloproteinase (MMP)1, MMP2, and urokinase plasminogen activator (uPA) [80, 81]. These proteinases are highly expressed in melanoma [82] and contribute to their migratory capacity. Recently, ROS-induced apoptosis of melanoma cells was shown to contribute to vasculogenic mimicry [83]. This process mimics the activity of endothelial cells and results in the formation of a fluid-conducting, matrix-rich meshwork [84]

that contributes to melanoma progression [85, 86]. As such, the proapoptotic activity of ROS contributes to melanoma progression. ROS' proapoptotic and antiapoptotic effects in melanoma cells appear to be a driving force of melanoma development.

**3.3. Hypoxia.** The role of mitochondrial ROS in apoptosis and hypoxia-induced gene transcription has been elucidated recently [15]. The well-established role of mitochondrial ROS for the stabilization of hypoxia-inducible transcription factors (HIFs) under hypoxia leads to angiogenesis through the upregulation of vascular endothelial growth factor (VEGF) expression [87]. The epidermal component of normal skin in which melanocytes reside is a mildly hypoxic environment, predicted due to the distance between the skin and superficial blood vessels [88]. To counteract the adverse effects of low oxygen levels, HIFs activate gene expression regulating multiple biological processes, including metabolism, proliferation, apoptosis, and migration [89]. HIF-1 regulates most of the hypoxia-responsive genes [90]. The transcription factor consists of a constitutively expressed  $\beta$ -subunit and an oxygen-monitored  $\alpha$ -subunit. Hence, HIF-1 is the master activator for dozens of target genes transcribed by cells in response to low oxygen concentrations [91]. HIF-1 activation is also required for the AKT-mediated transformation of melanocytes, hence regulating apoptosis [88].

Studies have identified increased HIF-1 expression and activity in melanoma under normoxia mediated by ROS and NF- $\kappa$ B [92, 93]. Under normoxic conditions in nonmalignant cells, HIF-1 is rapidly degraded by the ubiquitin-proteasome system, and it is upregulated in a hypoxic microenvironment [94]. However, it has been recently reported that HIF-1 can be upregulated under normoxia in response to growth factors, hormones, cytokines, UV irradiation, and metal ions [95–97]. In addition, several HIF target genes are strongly expressed in melanoma already under normoxic conditions, and elevated HIF-1 activity was found in melanoma cell lines under normoxic conditions in contrast to other types of tumors. Immunohistochemistry of malignant melanoma showed focal expression of HIF-1 in cancer tissue independent of regional hypoxia [15, 89]. Furthermore, several studies have demonstrated that part of the normoxic expression of VEGF and AngPTL4 depended on HIF-1 [98]. Interestingly, incubation of melanoma cells under reduced oxygen tension did not lead to a more substantial upregulation otherwise found in nonmelanoma cells, supporting the high basal expression of HIF-1 under normoxia [98, 99].

Melanocytes are more prone to oncogenic transformation when grown in a hypoxic environment. The cells' primary function is delivering melanin in melanosomes to keratinocytes resulting in protection against the harmful effects of UV radiation [88]. Within the melanocytes, the synthesis of melanin results in the generation of H<sub>2</sub>O<sub>2</sub> and, if inappropriately processed, OH $\cdot$  and other ROS [73]. In particular, melanosomes within melanoma cells are characteristically abnormal, with fragmented melanin and disrupted membranes. The disruption of melanosomal melanin is an early event in the etiology and progression of

melanoma, leading to increased oxidative stress, ROS production, and DNA mutation [4, 6, 83]. Several studies revealed that such ROS are responsible for the increased HIF activity under normoxia in melanoma. The activity and protein level of HIF are strictly controlled by the quenching of ROS or inducing reagents. The crucial redox-sensitive transcription factors in mammalian cells are NF- $\kappa$ B, NRF2, and AP-1 [74, 76]. ROS can activate the transcription factor NF- $\kappa$ B that is constitutively activated in melanoma cells [74, 76]. NF- $\kappa$ B, in turn, can induce HIF-1 expression and NF- $\kappa$ B-HIF-1 interaction contributes to breast cancer metastatic capacity [88, 100]. Studies confirmed the regulation of NF- $\kappa$ B through ROS in malignant melanoma and showed that the inhibition of NF- $\kappa$ B by the adenoviral overexpression of the IKK led to the attenuation of the HIF activity [101]. These data support the concept of transcriptional regulation of HIF-1 by NF- $\kappa$ B under normoxic conditions.

Besides the described ROS-dependent regulation, HIF-1 is translationally regulated by the mammalian target of rapamycin (mTOR). The mechanism of regulation of HIF by mTOR is poorly understood. It appears that under hypoxia, mTOR is inactivated, which led to the conclusion that mTOR signaling to HIF is oxygen independently regulated [102]. Under severe hypoxia, no influence of mTOR inhibitors was observed; thus, the stimulation of HIF-1 by mTOR is relevant under mild hypoxia or even normoxia only [102]. Several studies confirmed this hypothesis, as rapamycin reduced the HIF activity and protein expression under normoxia. One study showed that rapamycin, in contrast to ROS and NF- $\kappa$ B, does not influence HIF-1 mRNA expression, suggesting posttranscriptional regulation. Recently, Aprelikova and colleagues described a novel role for the cancer-testis antigen melanoma antigen-11 (MAGE11) as an inhibitor of prolyl hydroxylase (PHD2) in hypoxic responses [103]. Strong expression of MAGE-11 has been seen in different melanoma cell lines, which led to HIF stabilization under normoxia [104]. The finding that the regulation of protein abundance and the transcriptional regulatory network is crucial in controlling HIF-1 levels in melanoma and other tumor types opens new therapeutic options in modulating HIF-1 activity.

**3.4. Melanin Biosynthesis.** Exposure to UV is suggested to be a significant risk factor for developing melanoma, especially during childhood [105, 106]. However, this only refers to the sun-induced type of melanoma and not other types of melanoma that were never exposed to the sun [107]. About 90%–95% of the solar UV radiation that reaches the earth is UVA. Due to its high penetration capacity, UVA can irradiate melanocytes even through clothes and windows [106]. In response to the direct mutagenic effect of UV radiation, melanin synthesis by melanocytes is induced. Although melanin is initially necessary for protection from UV, it can turn into a prooxidant under oxidative stress because of inflammation, UV exposure, or higher metabolic processes, thus regulating epidermal homeostasis and affecting melanoma behavior [108]. UV-induced melanin biosynthesis results in an increased cellular concentration of its reactive

precursors. The initial reaction in melanin formation is the enzymatic oxidation of L-tyrosine to dopaquinone [109]. This reactive precursor is either converted into monomers that polymerize into black/brown eumelanin or reacts with a -SH group of cysteine to form 5-S-cysteinyl-dopa, ultimately forming the basic monomers for red/light brown pheomelanin. Cysteine is a necessary amino acid for pheomelanin production, even though it is also a part of the GSH molecule, which acts as a part of the defense system against intracellular ROS [110]. When cysteine is used for increased UV-induced production of pheomelanin, less GSH is produced, and oxidative stress may be more likely. Oxidative stress, in turn, releases iron from its intracellular storages into the cytosol of mammalian cells [111]. In the presence of large amounts of iron, which is frequently observed in melanoma and its precursor stages but not in normal melanocytes [110], pheomelanin and 5-S-cysteinyl-dopa become prooxidants [110]. Oxidized melanin reacts with  $O_2$  to form  $H_2O_2$ ,  $O_2^-$ , and other radicals [104] and adversely affects ROS homeostasis. During the biosynthesis of pheomelanin, 5-S-cysteinyl-dopa can disturb redox homeostasis directly through its ROS production in the presence of iron and indirectly through depletion of the GSH antioxidant buffer system. Their independent actions or dependent interaction play a role in UV-dependent or -independent melanomagenesis and progression and in drug resistance, as melanocytes and melanoma have higher ROS levels that seem to coevolve with enhanced antioxidant defense systems [112]. Thus, melanin and melanogenesis play a dual role in melanoma. They protect the melanocytes against insults, such as oxidative stress and UV radiation, but accelerate melanoma progression and weaken the effects of chemotherapy and radiation therapy [109, 113].

**3.5. Metabolic Profile.** Tumor cells are metabolically hyperactive, so it requires high ATP levels to enable cell proliferation. In melanoma, ATP is predominantly generated through aerobic glycolytic metabolic pathways and lactic acid production, which leads to several advantages for melanoma cells [114]. This includes, for instance, higher proliferation of tumor stem cell populations, increased hypoxia, elevated M2 macrophage polarization, lower intratumoral T cell activation, additional NADPH for ROS detoxification, and metastasis via MMP production. An in-depth analysis of adaptive redox homeostasis in melanoma and energy metabolism has been provided recently [115, 116], and the reader is referred to these and complementing views on oxidative phosphorylation [117].

**3.6. Metastasis.** Over the recent years, it has become evident that early inflammatory and angiogenic response and remodeling of the extracellular proteins are key factors (i.e., type I collagen) in creating a microenvironment that sustains tumor growth and metastasis [118]. Metastasis is a hallmark of most malignant tumors and the primary cause of mortality and morbidity in patients with melanoma [119]. The entry of tumor cells into the circulation is the critical rate-limiting step in metastasis that requires MMP expression [119], uroplasinogen activation, epidermal

growth factor receptor-driven polarity changes and migration, interaction with integrins [120], and other mechanisms all tightly linked to ROS. The cytoplasmic TRX is a ubiquitous thiol-reducing system implicated in cancer progression of melanoma [121]. TRX can be bound by the endogenous inhibitor thioredoxin-interacting protein (TXNIP), which negatively regulates TRX [121]. Importantly, inhibition of TRX activity promotes the transendothelial migration (TEM) of melanoma cells in vitro through endothelial injury and the loss of VE-cadherin-mediated endothelial cell-cell adhesion [122]. Overexpression of TRX inhibits both the baseline and ROS-induced TEM. Therefore, ROS enhance the TEM of melanoma cells during intravasation, and XNIP and inhibition of TRX activity could trigger this mechanism. It has also been observed that hypoxia in melanoma xenografts induces a higher metastatic frequency by increasing the expression of hypoxia-inducible genes promoting metastasis in a radiated transplant animal melanoma model [122]. However, the regulation of intravasation in vivo is not simply a matter of high or low intracellular concentrations of ROS. It requires the coordinate expression and activity of, for example, IL-8-mediated chemotaxis and CD9 and the integrin-mediated adhesion of melanoma cells to vascular endothelial cells [122]. The expression of the genes that promote melanoma metastasis is upregulated after subcurative melanoma irradiation [122]. Intriguingly, antioxidant supplementation in vivo was observed to spur rather than inhibit melanoma metastasis in mice inoculated with melanoma cells individually isolated from patients [123]. The authors found that blood and viscera are especially impinging strong oxidative stress in melanoma cells, forming a natural barrier against cancer metastasis. Antioxidants hampered this barrier and thus allow melanoma cells that had migrated to the circulation to survive better, subsequently forming more metastasis. These results were reiterated in a parallel in vivo study using the antioxidant N-acetyl-cysteine (NAC) [124].

**3.7. ROS and Different Cell Types in the Tumor Microenvironment.** The production of ROS by tumor cells plays a prominent role in driving tumorigenesis by shaping the tumor microenvironment (TME) [125, 126]. In addition, ROS generated by nontumor cells infiltrating the TME collectively decide the overall oxidative state of local TME. The TME consists of cancer cells, stromal cells, and immune cells. Immune cells infiltrate the environment of cutaneous melanoma during its early onset and throughout tumor development [127]. During inflammation, the migration of myeloid cells such as neutrophils, monocytes, eosinophils, and tissue-resident macrophages, dendritic cells, and mast cells play a role in cancer development [128].

Macrophages are of central importance in melanoma initiation and progression, especially tumor-associated macrophages (TAM) [129]. These cells fuel tumor growth by creating an immunosuppressive micro milieu via the production of chemokines, cytokines, and other mediators. Intriguingly, TAM polarization in the TME is associated with ROS and oxidative stress [130]. TAM, in turn, autoamplify ROS production via aberrant activation of NOX and

NOS. The released species react to form ONOO<sup>-</sup>, a mutagenic agent that inhibits T cell activity [131]. This will affect cells nearby, their integrity, and the composition of the TME, such as matrix remodeling and angiogenesis [132]. In addition, this exerts selective pressure on the development of genetically adapted tumor cells with high resistance to oxidative stress pressure, affecting melanoma therapy [128]. It is also well established that ROS leads to metabolic reprogramming of different cell types in the TME [133, 134].

ROS-mediated metabolic reprogramming also changes the energy requirements of T cells in the TME [135, 136]. Effector T cells ( $T_{\text{eff}}$ ) are less oxidative and have more metabolic activity than naive T cells ( $T_{\text{n}}$ ). Naive T cells keep in check the ROS levels by persistently synthesizing antioxidant molecules to avoid excessive ROS, which otherwise would initiate cell death and introduce a constant prooxidative state in cancer cells [20, 137]. Activation of T cells is escorted by increases in glucose uptake and mitochondrial activity fueled by glutaminolysis [138, 139]. Studies have shown that low ROS levels generated by mitochondria are pivotal for NFAT (nuclear factor of activated T cells) activation and IL-2 production by T cells [140, 141]. By contradiction, ROS can selectively suppress the DNA-binding capacities of NF- $\kappa$ B and NFAT, resulting in the downregulation of IL-2 transcription [142]. ROS being generated upon TCR engagement regulate ERK proliferative pathways and CD95/CD95L proapoptotic pathways, critical for normal T cell responses [143]. Hence, uncontrolled surplus ROS generation in the melanoma TME leads to nonfunctional T cells and failure to develop  $T_{\text{eff}}$  or  $T_{\text{m}}$  responses. Henceforth, ROS levels must be buffered in a safe range for clonal expansion and differentiation of an activated T cell through metabolic reprogramming. This is a daunting task, as antioxidants would improve T cell activity while at the same time also fueling melanoma growth.

In contrast to normal fibroblasts, which are responsible for the turnover of extracellular matrix (ECM), ROS-activated cancer-associated fibroblasts (CAFs) can be found at the edge of tumors or infiltrating the tumor [144–146]. These cells are a potent source of ROS, adding to the already hostile micro milieu [147]. Another considerable role of CAFs is to enhance tumorigenesis by activating specific signaling pathways crucial for promoting tumor growth. For instance, this is done through AKT in epithelial cells and the secretion of soluble factors like CXCL12 [148]. The domination of CAFs within cancer tissues is correlated with poor prognosis, elevated infiltration of tumor-associated macrophages, epithelial to mesenchymal transition, and ROS-driven hypoxia [149]. Hypoxia created by desmoplasia, in turn, stimulates the production of mitochondrial ROS, which can influence CAF function [150]. CAFs expressing smooth-muscle  $\alpha$ -actin ( $\alpha$ -SMA) are called myofibroblasts. The role of ROS in transition from fibroblasts to myofibroblasts is well reported, and this transition is driven by factors such as transforming growth factor beta1 (TGF- $\beta$ 1) and stromal cell-derived factor 1 (SDF-1) in a ROS-dependent manner [151]. Moreover, chronic oxidative stress also leads to the differentiation of fibroblasts to myofibroblasts. These ROS effects can be reversed with prolonged exogenous anti-

oxidants in fibroblasts isolated from mouse models of oxidative stress that lack prominent antioxidant transcription factors [152]. In addition, antioxidant enzymes such as GPX3 and thioredoxin reductase I upregulation within fibroblasts inhibit differentiation into myofibroblasts. The conclusion of these observations establishes that ROS can enhance specific fibroblast subtypes, including the predominant myofibroblast differentiation in human tumors [153]. ROS produced by fibroblast can also augment tumorigenesis [154]. Numerous studies focused on the role of H<sub>2</sub>O<sub>2</sub> in TME and stroma [155]. The H<sub>2</sub>O<sub>2</sub> is produced by tumor epithelial cells and can diffuse to adjacent cells, inducing a more protumorigenic environment. This effect can be abrogated with the addition of CAT [155].

ROS levels are the prominent factor in deciding its role as a signaling molecule or oxidative stress-causing agent, leading to activation of various defense mechanisms or cell death [156]. ROS can regulate autophagy through LC3-associated autophagosomes or AMP-activated protein kinase (AMPK) and the regulation of gene transcription factor activity like NF- $\kappa$ B inducing autophagy gene expression (BECLIN1/ATG6 or SQSTM1/p62) and unfolded protein response (UPR) during hypoxia [157]. Autophagy plays a complex role in the initiation of cancer [158]. Fibroblasts have p21<sup>Ras</sup>-independent ROS generating enzymatic systems which set up extracellular H<sub>2</sub>O<sub>2</sub> in response to TGF- $\beta$ 1 [159]. In addition, an enzyme similar to 15-LOX in fibroblasts has been shown to procreate substantial amounts of O<sub>2</sub><sup>-</sup> that developed without flavoenzyme activity [160]. These modifications have a crucial impact on the proteins' signaling and functional role, augment genome instability, prevent inflammation, and make cancer cells survive under hypoxia and starvation [15]. In addition, elevation in autophagy is associated with metastasis and poor prognosis in melanoma patients [161].

#### 4. ROS in Melanoma Therapy with Physical Modalities

The pillars of oncology are surgery, chemotherapy, radiotherapy, and immunotherapy. Especially, the latter three involve the generation of ROS as a byproduct or as a targeted approach to eliminate melanoma. Besides, several physical modalities have emerged throughout the past three decades that come with therapeutic ROS production. A comprehensive review on all present and experimental therapeutic chemotherapeutic, biological, and immunological modalities for melanoma treatment is out of scope of this review. All these approaches are systemic treatments where local control of ROS production may be challenging. Instead, we here focus on local treatments of physical modalities reported to come with augmented ROS production (Figure 6).

**4.1. Radiotherapy.** Radiotherapy is one of the key therapeutic options in oncology. Radiotherapy produces radiation-induced ROS. For instance, OH $\cdot$  is formed directly by the radiolysis of water molecules or indirectly by the formation of secondary ROS [162]. These molecules indiscriminately attack nearby molecules such as DNA and target membranes

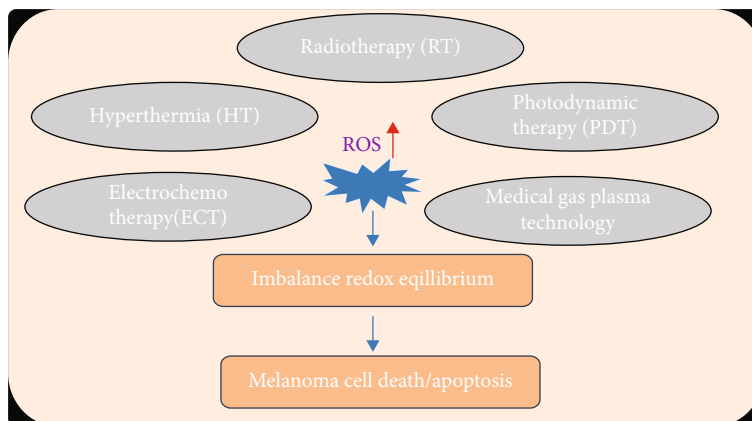


FIGURE 6: Physical therapy modalities exploiting supraphysiological ROS for melanoma treatment. Several treatments exploit ROS-based effects, including radiotherapy, photodynamic therapy, cryoablation, hyperthermia, and gas plasma technology. ROS induced by these therapies lead to an imbalance in redox equilibrium and subsequently promote melanoma cell death.

of cells and organelles, leading to cell cycle arrest and apoptosis [163]. ROS induced by radiation can induce cell death through necrosis, autophagy, mitotic cell death, and cell cycle arrest [163]. The mechanism varies by cell- and tissue-specific factors. ROS generated by radiation triggers DNA damage and apoptosis [162, 163]. Radiotherapy may cause damage to normal tissues alongside tumor. Resistance or sensitivity of tumor cells to radiotherapy depends on cell cycle phase, endogenous antioxidant levels, oxygen availability, and gene expression. Many tumors divide slowly due to their long duration time in the S-phase/interphase of the cell cycle. Therefore, they get more time to repair the damaged DNA, which results in radiation resistance [164]. Several studies showed that mitotic cells with the lowest SH-AOs (SH-containing groups) are most radiosensitive than S-phase cells, which have the highest levels of these compounds [164, 165]. Henceforth, synchronization of the cell cycle under these two sensitive cell cycle phases supports tumor eradication [166]. Moreover, rapidly dividing tumors are more prone to ROS-induced oxidative damage than slowly dividing tumors [165, 167]. In addition, MAPK activation and VEGF release after radiation result in reduced tumor cell response, as shown by several experimental studies [168]. ROS-regulated MAPK determines whether tumor cells proliferate or undergo cell cycle arrest or apoptosis. Lastly, the DNA damage ability of ionizing radiation can be reduced by the antioxidant molecules inside the cells [165]. Several studies have shown that depletion of GSH and its synergistic effects with thioredoxin could increase the radiosensitivity of squamous cell carcinoma cell lines [169]. Intriguingly, depletion of ROS scavengers in cancer stem cells (CSCs) rapidly decreases their clonogenicity and consequence in radiosensitization [170].

The role of NRF2 in radioresistance is well described by recent studies [171, 172]. Aberration of NRF2 activation due to decreased KEAP1-NRF2 interaction and loss of mutations of KEAP1 leads to radiotherapy resistance [172]. In the presence of certain antioxidants, resistant tumor cells respond to radiation-induced killing mostly via ROS-mediated apoptosis [162, 165, 168, 172]. However, there is limited evidence

for definitive radiation therapy in melanoma, besides palliation [173]. However, retrospective and phase II studies have divulged that adjuvant radiotherapy can significantly improve the local-regional control rate in a specific clinical setting [174]. Adjuvant radiotherapy is offered to patients who are at high risk of recurrence [175]. Dose and fractionation schedules depend upon the melanoma site, even though the optimal radiation fractionation schedule remains controversial and convenient for patients with low survival expectations. ROS production is a well-recognized mechanism in radiotherapy [176, 177]. This occurs during the tumor treatment and after that, as ROS are being released by stressed and dying cells in the TME due to uncoupled ETC and subsequent superoxide production. Accordingly, antioxidants were found to dampen the efficacy of radiotherapy in preclinical cancer models [178]. Moreover, hypoxic tumors were found to show enhanced radioresistant, and combination treatment with ROS-promoting therapies has been hypothesized to overcome this limitation [179].

**4.2. Cryoablation.** Cryoablation is an intrusive treatment that uses nitrogen or argon gas to create extreme cold to freeze and destroy tumors. The therapy induces tumor cell death by necrosis, hyperosmosis, and apoptosis [180]. Therefore, the treatment is not tightly entangled with the action of ROS [181], but since the therapy is an integral part of melanoma management, it is briefly outlined here nevertheless. The intracellular contents of cryoablation-damaged cells remain preserved for the immune system's recognition to initiate a tumor-specific immune response. Cryoablation slows down the rate of tumor spread and weakens tumor load by ablation of the primary site [182]. Cryoablation combined with distinct immunostimulants enhances the efficacy of cryoablation for the suppression of new tumor growth in metastatic mouse models [183, 184]. This combination can overcome the limitations of immunotherapy. The combination of cryoablation with various immunostimulants (including TLR9 and CPG) has suppressed new tumor growth in metastatic mouse models [184, 185]. In a recent study, cryoablation combined with a transarterial infusion

of pembrolizumab has shown promising clinical activity in managing melanoma liver metastasis. However, the efficacy of the therapy needs to be confirmed with a controlled trial in the future [186]. ROS production can be anticipated with this destructive modality, but the therapeutic relevance for cryoablation-related ROS in melanoma remains limited as of now.

**4.3. Electrochemotherapy.** Electrochemotherapy (ECT) is a technique that involves the harmonious use of high-intensity electric pulses to the tumor to increase the cytotoxicity of anticancer drugs, bleomycin and cisplatin, via electroporation [187]. The therapeutic efficacy of electroporation itself without drug application is negligible [188]. The cytotoxicity of drugs such as cisplatin and bleomycin increases by a factor of 100-1000 by electroporation of cell membranes [189]. ECT results demonstrate to be effective for treating cutaneous and subcutaneous malignant melanoma nodules [190]. No major negative AEs were observed [191]. ROS production is a byproduct of the pulsed electric field treatment and plays a role in its efficacy [192] as it can be prevented by antioxidants [193, 194]. ROS production and oxidative stress were also observed in electroporated melanoma cells in vitro [195]. Novel ECT approaches involve calcium electroporation with promising clinical results [196]. The treatment engages antitumor immunity to promote systemic attack of metastasis distant to the treatment site [197]. A case report showing such an abscopal effect in a melanoma patient has been published [198]. The calcium treatment locally elevates ROS that contributes to this effect [199, 200] and modulates the tumor vasculature [201]. Hence, this physical treatment modality might be a promising approach for treating therapy-resistant melanoma metastasis, as well as releasing tumor antigen for immunotherapies. A study protocol for a randomized clinical trial in this regard for skin cancer treatment was recently published [202].

**4.4. Hyperthermia.** Hyperthermia is described as the use of exogenous heat sources that directly kill tumor cells or intensify the efficacy of other therapeutic means (e.g., radiotherapy, chemotherapy, and immunotherapies) against various cancer types. Mild hyperthermia as an adjuvant has shown improved antitumor immune response in preclinical and clinical data [203–205]. Hyperthermia generates heat-shock proteins, induces the activation and migration of dendritic cells (DCs), increases the efficacy of tumor antigen presentation, and releases chemo attractants to tumor sites for leukocyte immigration and activation [206]. In vitro studies have shown that hyperthermia inhibits the mobility and proliferative ability of B16F10 cells in a temperature-dependent manner and regulates the TGF- $\beta$ 1 protein expression in mouse malignant melanoma B16F10 cells both in vivo and in vitro [207]. In a metastatic mouse model, hyperthermia has significantly extended survival in an animal model. In addition, hyperthermia enhances the therapeutic effectiveness of drugs by activating caspase-8 and caspase-9 to trigger apoptotic responses [208]. The imperative role of ROS in hyperthermia therapy has been thor-

oughly described [209]. Mechanistically, hyperthermia elevates the levels of transition metal ions, which leads to enhanced production of H<sub>2</sub>O<sub>2</sub> and OH<sup>-</sup> by mediating mitochondrial damage. This can be controlled by the amount and duration of heat applied. In doing so, the heat shock also promotes autophagy and local apoptosis [210] while preserving the ability to mount antitumor immunity. Therefore, hyperthermia is well suited to be combined with, e.g., checkpoint therapy. The hyperthermic treatment will generate controlled melanoma cell destruction ROS-dependent and locally restricted without any debulking or therapeutic intent. The tumor antigens subsequently released may then augment antitumor immunity that, in combination with checkpoint therapy, will promote the systemic targeting of melanoma metastasis [211]. This ROS and stress-based heat therapy also show great promise in combination with targeted and nontargeted chemotherapy [208]. Clinical research on hyperthermia in melanoma therapy exists [212], but only a few centers work with techniques so far.

**4.5. Medical Gas Plasma Technology.** Along similar lines, gas plasma technology may be usefully combined with existing oncotherapies [213]. In contrast to hyperthermia, where heat and ROS are generated within the melanoma tissues at sufficient depths, gas plasma technology generates exogenous ROS applied topically to the treatment target [214]. Therefore, it might be well suited in the palliative setting for ulcerating melanoma lesions not covered by skin [215]. Gas plasma technology is unique in generating a plethora of ROS simultaneously with dozens of different agents [216]. The concentration of the ROS can be tuned by changing the ionization variables and the target exposure time [217], while the ambient air condition was found to have a lower impact [218]. As a mechanism of action, gas plasma-derived ROS modulate the expression of redox-regulating enzymes and pathways [219–221] and was found to show combinatorial effects with chemotherapy [222–224], radiotherapy [225–227], and antibody [228] and topical immunotherapy [229]. We have recently also reported for the first time apoptotic effects in patient-derived melanoma tissues [230] and that ROS-derived oxidative posttranslational protein modifications (oxPTMs) generated with gas plasma technology have immunogenic properties and protect from melanoma growth in vivo [231]. Such an approach would be entirely novel in upgrading antitumor vaccines [232] used, for instance, for autologous DC vaccination. Intriguingly, we were also the first to report an abscopal effect in a model of breast cancer where the tumor size of an untreated murine flank decreased in parallel to that of the treated flank, suggesting engagement of antitumor immunity using gas plasma-derived therapeutic ROS [233], as suggested before using human NK cell-mediated melanoma killing in vitro [234]. Gas plasma technology is safe and virtually free of side effects [235–237]. Several devices are marketed in Europe based on accreditation as medical device class IIa [238]. Clinical experience shows promising results in treating actinic keratosis [239–241] and locally advanced head and neck cancer in palliative patients [242–244], and more clinical research is heavily awaited.

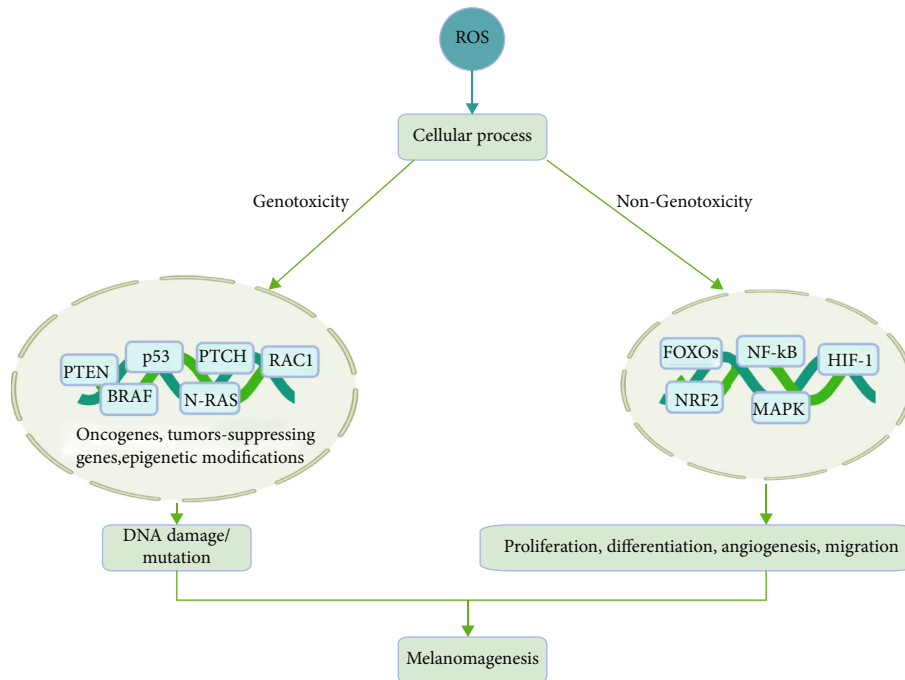


FIGURE 7: ROS role in melanomagenesis. High ROS levels activate protooncogenes, inactivate tumor suppressor genes, and cause genetic modifications. This leads to DNA damage and mutations and involves cellular signaling that blunts DNA repair and cell death and drives melanomagenesis. Conversely, signaling pathways less involved in DNA repair, such as MAPK, NF- $\kappa$ B, PI3K/AKT/mTOR, and NRF2 spur melanoma cells' proliferation, angiogenesis, and metastasis. Together, these processes cause the occurrence of melanoma. Created with <http://biorender.com>.

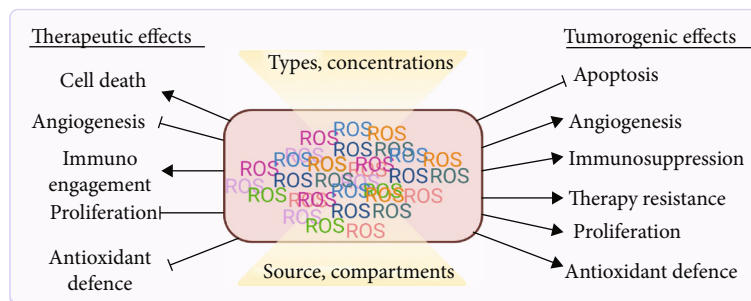


FIGURE 8: Pleiotropic roles of ROS in melanoma. ROS have pleiotropic roles in melanoma therapy and tumorigenesis depending on their source, concentration, location, and types. Created with <http://biorender.com>.

**4.6. Photodynamic Therapy.** Photodynamic therapy (PDT) has a long-standing application in the clinic already. This light-based and minimally invasive therapy is promising and effective in various types of cancers including nonmelanoma and melanoma skin cancer, for patients with stage III/IV cutaneous metastatic melanomas [245]. PDT is a minimally invasive procedure [246] that requires a photosensitizer (PS) molecule which, upon excitation by the specific wavelength of light, reacts with oxygen and causes oxidant species in target tissues, leading to increased ROS production, redox signaling, and cell death [247]. The advantage of PDT is its low systemic toxicity and its ability to destroy tumors selectively [246]. ROS, especially singlet oxygen, unleash irreversible damage to tumor cells and tumor-associated blood vessels, also activating antitumor immunity via inflammatory responses [248]. The limited penetration

of light restricts the clinical use of PDT. For better efficacy of PDT in melanoma, overcoming protective mechanisms such as pigmentation and oxidative stress resistance is necessary to treat intracutaneous lesions [249]. The concepts and challenges of oxidative stress and PDT in skin cancer have been elegantly reported recently [250]. Clinically, PDT can be used along with other procedures, such as surgery, radiotherapy, or chemotherapy [251, 252]. Combined therapies have been studied to overcome melanoma resistance. The combination of PDT and chemotherapy (dacarbazine) was an efficient treatment to overcome the internal resistance in metastatic melanoma [253]. Most ongoing trials for cancer are using the photosensitizers that are approved for clinical use, mainly ALA (aminolevulinic acid) and photofrin (porfimer sodium) [254]. Combining PDT with immunoadjuvants to stimulate the antitumor immunity was more

efficient and safer for treating melanoma than the monotherapies strategy [255], but still needs more clinical studies to elaborate efficacy and safety.

## 5. Conclusion

Following a review of ROS' divergent biological processes, some generalizations regarding the induction and function of ROS can be made. Importantly, ROS are generally induced by cell stress, starvation, hypoxia, and growth factor stimulation. Mild ROS induction promotes adaptation to ROS stress via HIF activation under hypoxia, inflammatory cytokine production in tissue damage, and differentiation in receptor-dependent stimulation, conjointly promoting cell survival (Figure 7). Although ROS have been recognized as important second messengers in cell biology, they have only recently gained attention concerning melanoma biology. At higher levels, ROS are detrimental, and several physical modalities directly or indirectly exploit such damaging functions for the treatment of skin cancer (Figure 8), including melanoma. As primary and metastatic melanoma provides high dynamic and plasticity in the TME, specifically targeting ROS is challenging as melanoma cells adapt to altered redox environments.

Even though the failure of dietary antioxidants in several clinical trials resulted in the emergence of alternative anti-melanoma therapeutic approaches, there is still considerable controversy as to whether the use of either antioxidant supplementation or inhibition of ROS modulation is detrimental or beneficial for melanoma treatment. The effect of ROS is predominantly near the site of ROS production. Therefore, the use of inhibitors or antioxidants may prevent melanomagenesis. In addition to that, prooxidant melanoma therapy, through which scavenging of ROS is decreased or production of ROS is increased, or both, is a pioneering approach to exploit the higher levels of ROS in cancer cells to elicit cell death selectively. The eminent role of ROS modulation in antimelanoma therapies like ROS-inducing drugs and physical modalities, such as radiotherapy and photodynamic therapy, is well reported. It follows that combination therapies, e.g., checkpoint inhibition and ROS-generating therapies, might constitute novel avenues for targeting melanoma. While more preclinical and clinical research is excitingly awaited, the data known to date are encouraging that understanding, targeting, and utilizing ROS in melanoma treatment might be an effective adjuvant treatment in patient therapy in the future.

## Abbreviations

|       |                               |
|-------|-------------------------------|
| CAFs: | Cancer-associated fibroblasts |
| CAT:  | Catalase                      |
| ECM:  | Extracellular matrix          |
| ECT:  | Electrochemotherapy           |
| ETC:  | Electron transport chain      |
| GPX:  | Glutathione peroxidase        |
| GSH:  | Glutathione                   |
| GSS:  | Glutathione synthetase        |
| GSSG: | Oxidized glutathione          |

|                                 |  |
|---------------------------------|--|
| H <sub>2</sub> O <sub>2</sub> : | Hydrogen peroxide  |
| HIF:                            | Hypoxia-inducible factor                                       |
| IL:                             | Interleukin  |
| KEAP1:                          | Kelch-like ECH-associated protein 1                            |
| MMP:                            | Matrix metalloproteinases                                      |
| NADPH:                          | Nicotinamide adenine dinucleotide phosphate                    |
| NF-κB:                          | Nuclear factor kappa-light-chain-enhancer of activated B cells |
| NOS:                            | Nitric oxide synthase  |
| NOX:                            | NADPH oxidase  |
| NRF2:                           | Nuclear factor erythroid 2-related factor 2                    |
| O <sub>2</sub> <sup>-</sup> :   | Superoxide ion   |
| OH <sup>·</sup> :               | Hydroxyl radical   |
| PDT:                            | Photodynamic therapy   |
| PRDX:                           | peroxiredoxins   |
| ROS:                            | Reactive oxygen species  |
| SOD:                            | Superoxide dismutase.  |

## Conflicts of Interest

The authors declare no conflict of interest.

## Acknowledgments

The work of SB is supported by the German Federal Ministry of Education and Research (BMBF, grant number 03Z22DN11), the European Social Fund ("ONKOTHER-H," ESF/14-BM-A55-0006/18), and the Ministry of Education, Science and Culture of Mecklenburg-Vorpommern, Germany.

## References

- [1] J. R. Henderson, H. Swalwell, S. Boulton, P. Manning, C. J. McNeil, and M. A. Birch-Machin, "Direct, real-time monitoring of superoxide generation in isolated mitochondria," *Free Radical Research*, vol. 43, no. 9, pp. 796–802, 2009.
- [2] H. Sies, C. Berndt, and D. P. Jones, "Oxidative stress," *Annual Review of Biochemistry*, vol. 86, no. 1, pp. 715–748, 2017.
- [3] A. Schmidt and S. Bekeschus, "Redox for repair: cold physical plasmas and Nrf2 signaling promoting wound healing," *Antioxidants*, vol. 7, no. 10, p. 146, 2018.
- [4] K. V. Donkena, C. Y. Young, and D. J. Tindall, "Oxidative stress and DNA methylation in prostate cancer," *Obstetrics and Gynecology International*, vol. 2010, Article ID 302051, 14 pages, 2010.
- [5] T. Finkel, "Oxygen radicals and signaling," *Current Opinion in Cell Biology*, vol. 10, no. 2, pp. 248–253, 1998.
- [6] T. Gao, B. T. Joyce, L. Liu et al., "DNA methylation of oxidative stress genes and cancer risk in the normative aging study," *American Journal of Cancer Research*, vol. 6, pp. 553–561, 2016.
- [7] A. M. Gorman, "Neuronal cell death in neurodegenerative diseases: recurring themes around protein handling," *Journal of Cellular and Molecular Medicine*, vol. 12, no. 6a, pp. 2263–2280, 2008.
- [8] D. Harman, "Aging: a theory based on free radical and radiation chemistry," *Journal of Gerontology*, vol. 11, no. 3, pp. 298–300, 1956.



- [9] S. G. Rhee, Y. S. Bae, S. R. Lee, and J. Kwon, "Hydrogen peroxide: a key messenger that modulates protein phosphorylation through cysteine oxidation," *Science Signaling*, vol. 2000, no. 53, 2000.
- [10] H. Sies and D. P. Jones, "Reactive oxygen species (ROS) as pleiotropic physiological signalling agents," *Nature Reviews Molecular Cell Biology*, vol. 21, no. 7, pp. 363–383, 2020.
- [11] C. Espinosa-Diez, V. Miguel, D. Mennerich et al., "Antioxidant responses and cellular adjustments to oxidative stress," *Redox Biology*, vol. 6, pp. 183–197, 2015.
- [12] L. A. Sena and N. S. Chandel, "Physiological roles of mitochondrial reactive oxygen species," *Molecular Cell*, vol. 48, no. 2, pp. 158–167, 2012.
- [13] N. Brandes, S. Schmitt, and U. Jakob, "Thiol-based redox switches in eukaryotic proteins," *Antioxidants & Redox Signaling*, vol. 11, no. 5, pp. 997–1014, 2009.
- [14] C. R. Rocha, G. S. Kajitani, A. Quinet, R. S. Fortunato, and C. F. Menck, "Nrf2 and glutathione are key resistance mediators to temozolomide in glioma and melanoma cells," *Oncotarget*, vol. 7, no. 30, pp. 48081–48092, 2016.
- [15] K. Balamurugan, "HIF-1 at the crossroads of hypoxia, inflammation, and cancer," *International Journal of Cancer*, vol. 138, no. 5, pp. 1058–1066, 2016.
- [16] N. S. Chandel, M. G. Vander Heiden, C. B. Thompson, and P. T. Schumacker, "Redox regulation of p53 during hypoxia," *Oncogene*, vol. 19, no. 34, pp. 3840–3848, 2000.
- [17] A. Tramutola, S. Falcucci, U. Brocco et al., "Protein oxidative damage in uv-related skin cancer and dysplastic lesions contributes to neoplastic promotion and progression," *Cancers*, vol. 12, no. 1, p. 110, 2020.
- [18] J. Blumberg and G. Block, "The alpha-tocopherol, beta-carotene cancer prevention study in finland," *Nutrition Reviews*, vol. 52, no. 7, pp. 242–245, 1994.
- [19] E. A. Klein, I. M. Thompson Jr., C. M. Tangen et al., "Vitamin e and the risk of prostate cancer," *JAMA*, vol. 306, no. 14, pp. 1549–1556, 2011.
- [20] C. Gorrini, I. S. Harris, and T. W. Mak, "Modulation of oxidative stress as an anticancer strategy," *Nature Reviews Drug Discovery*, vol. 12, no. 12, pp. 931–947, 2013.
- [21] N. S. Chandel and D. A. Tuveson, "The promise and perils of antioxidants for cancer patients," *The New England Journal of Medicine*, vol. 371, no. 2, pp. 177–178, 2014.
- [22] S. A. Del Prete, L. H. Maurer, J. O'Donnell, R. J. Forcier, and P. LeMarbre, "Combination chemotherapy with cisplatin, carmustine, dacarbazine, and tamoxifen in metastatic melanoma," *Cancer Treatment Reports*, vol. 68, pp. 1403–1405, 1984.
- [23] V. Monge-Fuentes, L. A. Muehlmann, J. P. Longo et al., "Photodynamic therapy mediated by acai oil (*Euterpe oleracea* Martius) in nanoemulsion: A potential treatment for melanoma," *Journal of Photochemistry and Photobiology B: Biology*, vol. 166, pp. 301–310, 2017.
- [24] F. V. Almeida, S. M. Douglass, M. E. Fane, and A. T. Weeraratna, "Bad company: microenvironmentally mediated resistance to targeted therapy in melanoma," *Pigment Cell & Melanoma Research*, vol. 32, no. 2, pp. 237–247, 2019.
- [25] D. G. Franchina, C. Dostert, and D. Brenner, "Reactive oxygen species: involvement in t cell signaling and metabolism," *Trends in Immunology*, vol. 39, no. 6, pp. 489–502, 2018.
- [26] K. Keyer and J. A. Inlay, "Superoxide accelerates DNA damage by elevating free-iron levels," *Proceedings of the National Academy of Sciences of the United States of America*, vol. 93, no. 24, pp. 13635–13640, 1996.
- [27] K. Bedard and K. H. Krause, "The nox family of ros-generating nadph oxidases: physiology and pathophysiology," *Physiological Reviews*, vol. 87, no. 1, pp. 245–313, 2007.
- [28] H. Sies, "Hydrogen peroxide as a central redox signaling molecule in physiological oxidative stress: oxidative eustress," *Redox Biology*, vol. 11, pp. 613–619, 2017.
- [29] K. S. Echtay, M. P. Murphy, R. A. Smith, D. A. Talbot, and M. D. Brand, "Superoxide Activates Mitochondrial Uncoupling Protein 2 from the Matrix Side," *Journal of Biological Chemistry*, vol. 277, no. 49, pp. 47129–47135, 2002.
- [30] M. Sattler, T. Winkler, S. Verma et al., "Hematopoietic growth factors signal through the formation of reactive oxygen species," *Blood*, vol. 93, no. 9, pp. 2928–2935, 1999.
- [31] B. P. Tu and J. S. Weissman, "The FAD- and O<sub>2</sub>-Dependent Reaction Cycle of Ero1-Mediated Oxidative Protein Folding in the Endoplasmic Reticulum," *Molecular Cell*, vol. 10, no. 5, pp. 983–994, 2002.
- [32] C. C. Winterbourn, "Toxicity of iron and hydrogen peroxide: the fenton reaction," *Toxicology Letters*, vol. 82–83, pp. 969–974, 1995.
- [33] A. Ayala, M. F. Munoz, and S. Arguelles, "Lipid peroxidation: production, metabolism, and signaling mechanisms of malondialdehyde and 4-hydroxy-2-nonenal," *Oxidative Medicine and Cellular Longevity*, vol. 2014, Article ID 360438, 31 pages, 2014.
- [34] B. R. Stockwell, J. P. Friedmann Angeli, H. Bayir et al., "Ferroptosis: a regulated cell death nexus linking metabolism, redox biology, and disease," *Cell*, vol. 171, no. 2, pp. 273–285, 2017.
- [35] K. L. Fong, P. B. McCay, J. L. Poyer, H. P. Misra, and B. B. Keele, "Evidence for superoxide-dependent reduction of fe<sup>3+</sup> and its role in enzyme-generated hydroxyl radical formation," *Chemico-Biological Interactions*, vol. 15, no. 1, pp. 77–89, 1976.
- [36] H. R. Stennicke, Q. L. Deveraux, E. W. Humke, J. C. Reed, V. M. Dixit, and G. S. Salvesen, "Caspase-9 Can Be Activated without Proteolytic Processing," *Journal of Biological Chemistry*, vol. 274, no. 13, pp. 8359–8362, 1999.
- [37] S. H. Kaufmann and W. C. Earnshaw, "Induction of apoptosis by cancer chemotherapy," *Experimental Cell Research*, vol. 256, no. 1, pp. 42–49, 2000.
- [38] V. E. Kagan, V. A. Tyurin, J. Jiang et al., "Cytochrome c acts as a cardiolipin oxygenase required for release of proapoptotic factors," *Nature Chemical Biology*, vol. 1, no. 4, pp. 223–232, 2005.
- [39] G. Paradies, G. Petrosillo, M. Pistolesse, N. Di Venosa, A. Federici, and F. M. Ruggiero, "Decrease in mitochondrial complex i activity in ischemic/reperfused rat heart," *Circulation Research*, vol. 94, no. 1, pp. 53–59, 2004.
- [40] M. D. Brand, "The sites and topology of mitochondrial superoxide production," *Experimental Gerontology*, vol. 45, no. 7–8, pp. 466–472, 2010.
- [41] F. L. Muller, Y. Liu, and H. Van Remmen, "Complex III Releases Superoxide to Both Sides of the Inner Mitochondrial Membrane," *Journal of Biological Chemistry*, vol. 279, no. 47, pp. 49064–49073, 2004.
- [42] J. D. Lambeth, G. Cheng, R. S. Arnold, and W. A. Edens, "Novel homologs of gp91 *phox*," *Trends in Biochemical Sciences*, vol. 25, no. 10, pp. 459–461, 2000.

- [43] S. S. Brar, T. P. Kennedy, A. R. Whorton et al., "Reactive oxygen species from nad(p)h:quinone oxidoreductase constitutively activate NF- $\kappa$ B in malignant melanoma cells," *American Journal of Physiology-Cell Physiology*, vol. 280, no. 3, pp. C659–C676, 2001.
- [44] F. Liu, A. M. Gomez Garcia, and F. L. Meyskens Jr., "Nadph oxidase 1 overexpression enhances invasion via matrix metalloproteinase-2 and epithelial-mesenchymal transition in melanoma cells," *Journal of Investigative Dermatology*, vol. 132, no. 8, pp. 2033–2041, 2012.
- [45] M. G. Espey, D. D. Thomas, K. M. Miranda, and D. A. Wink, "Focusing of nitric oxide mediated nitrosation and oxidative nitrosylation as a consequence of reaction with superoxide," *Proceedings of the National Academy of Sciences of the United States of America*, vol. 99, no. 17, pp. 11127–11132, 2002.
- [46] S. C. Albrecht, A. G. Barata, J. Grosshans, A. A. Teleman, and T. P. Dick, "In vivo mapping of hydrogen peroxide and oxidized glutathione reveals chemical and regional specificity of redox homeostasis," *Cell Metabolism*, vol. 14, no. 6, pp. 819–829, 2011.
- [47] I. Hirono, "Mechanism of natural and acquired resistance to methyl-bis-(beta-chlorethyl)-amine n-oxide in ascites tumors," *Gan*, vol. 52, pp. 39–48, 1961.
- [48] S. C. Lu, "Regulation of glutathione synthesis," *Molecular Aspects of Medicine*, vol. 30, no. 1-2, pp. 42–59, 2009.
- [49] D. W. Nebert and V. Vasiliou, "Analysis of the glutathione s-transferase (gst) gene family," *Human Genomics*, vol. 1, no. 6, pp. 460–464, 2004.
- [50] A. Holmgren and M. Bjornstedt, "[21] Thioredoxin and thioredoxin reductase," *Methods in Enzymology*, vol. 252, pp. 199–208, 1995.
- [51] S. C. Lu, "Glutathione synthesis," *Biochimica et Biophysica Acta (BBA) - General Subjects*, vol. 1830, no. 5, pp. 3143–3153, 2013.
- [52] C. C. Winterbourn and M. B. Hampton, "Thiol chemistry and specificity in redox signaling," *Free Radical Biology & Medicine*, vol. 45, no. 5, pp. 549–561, 2008.
- [53] J. Lu and A. Holmgren, "The thioredoxin antioxidant system," *Free Radical Biology & Medicine*, vol. 66, pp. 75–87, 2014.
- [54] S. Gidanian, M. Mentelle, F. L. Meyskens Jr., and P. J. Farmer, "Melanosomal damage in normal human melanocytes induced by uvb and metal uptake—a basis for the pro-oxidant state of melanoma," *Photochemistry and Photobiology*, vol. 84, no. 3, pp. 556–564, 2008.
- [55] R. Sarangarajan and S. P. Apte, "The polymerization of melanin: a poorly understood phenomenon with egregious biological implications," *Melanoma Research*, vol. 16, no. 1, pp. 3–10, 2006.
- [56] L. C. Godoy, C. T. Anderson, R. Chowdhury, L. J. Trudel, and G. N. Wogan, "Endogenously produced nitric oxide mitigates sensitivity of melanoma cells to cisplatin," *Proceedings of the National Academy of Sciences of the United States of America*, vol. 109, no. 50, pp. 20373–20378, 2012.
- [57] F. H. Melo, F. Molognoni, A. S. Morais et al., "Endothelial nitric oxide synthase uncoupling as a key mediator of melanocyte malignant transformation associated with sustained stress conditions," *Free Radical Biology & Medicine*, vol. 50, no. 10, pp. 1263–1273, 2011.
- [58] M. T. Landi, J. Bauer, R. M. Pfeiffer et al., "MC1R Germline variants confer risk for BRAF-Mutant melanoma," *Science*, vol. 313, no. 5786, pp. 521–522, 2006.
- [59] N. C. Jenkins, T. Liu, P. Cassidy et al., "The p16<sup>INK4A</sup> tumor suppressor regulates cellular oxidative stress," *Oncogene*, vol. 30, no. 3, pp. 265–274, 2011.
- [60] B. Govindarajan, J. E. Sligh, B. J. Vincent et al., "Overexpression of akt converts radial growth melanoma to vertical growth melanoma," *Journal of Clinical Investigation*, vol. 117, no. 3, pp. 719–729, 2007.
- [61] K. Itoh, N. Wakabayashi, Y. Katoh et al., "Keap1 represses nuclear activation of antioxidant responsive elements by Nrf2 through binding to the amino-terminal Neh2 domain," *Genes & Development*, vol. 13, no. 1, pp. 76–86, 1999.
- [62] J. D. Hayes and M. McMahon, "NRF2 and KEAP1 mutations: permanent activation of an adaptive response in cancer," *Trends in Biochemical Sciences*, vol. 34, no. 4, pp. 176–188, 2009.
- [63] R. Wang, J. An, F. Ji, H. Jiao, H. Sun, and D. Zhou, "Hypermethylation of the *\_Keap1\_* gene in human lung cancer cell lines and lung cancer tissues," *Biochemical and Biophysical Research Communications*, vol. 373, no. 1, pp. 151–154, 2008.
- [64] H. Zhu, Z. Jia, M. A. Trush, and Y. R. Li, "Nrf2 deficiency promotes melanoma growth and lung metastasis," *Reactive Oxygen Species*, vol. 2, pp. 308–314, 2016.
- [65] E. V. Knatko, M. Higgins, J. W. Fahey, and A. T. Dinkova-Kostova, "Loss of Nrf2 abrogates the protective effect of Keap1 downregulation in a preclinical model of cutaneous squamous cell carcinoma," *Scientific Reports*, vol. 6, no. 1, article 25804, 2016.
- [66] C. Wiel, K. Le Gal, M. X. Ibrahim et al., "Bach1 stabilization by antioxidants stimulates lung cancer metastasis," *Cell*, vol. 178, no. 2, pp. 330–345.e22, 2019.
- [67] C. S. Sander, H. Chang, F. Hamm, P. Elsner, and J. J. Thiele, "Role of oxidative stress and the antioxidant network in cutaneous carcinogenesis," *International Journal of Dermatology*, vol. 43, no. 5, pp. 326–335, 2004.
- [68] D. T. Lincoln, E. M. Ali Emadi, K. F. Tonissen, and F. M. Clarke, "The thioredoxin-thioredoxin reductase system: over-expression in human cancer," *Anticancer Research*, vol. 23, pp. 2425–2433, 2003.
- [69] A. Baldi, D. Lombardi, P. Russo et al., "Ferritin contributes to melanoma progression by modulating cell growth and sensitivity to oxidative stress," *Clinical Cancer Research*, vol. 11, no. 9, pp. 3175–3183, 2005.
- [70] J. M. Stahl, A. Sharma, M. Cheung et al., "Deregulated Akt3 activity promotes development of malignant melanoma," *Cancer Research*, vol. 64, no. 19, pp. 7002–7010, 2004.
- [71] J. Liu, K. G. Suresh Kumar, D. Yu et al., "Oncogenic BRAF regulates  $\beta$ -Trcp expression and NF- $\kappa$ B activity in human melanoma cells," *Oncogene*, vol. 26, no. 13, pp. 1954–1958, 2007.
- [72] K. S. Smalley, "A pivotal role for erk in the oncogenic behaviour of malignant melanoma?," *International Journal of Cancer*, vol. 104, no. 5, pp. 527–532, 2003.
- [73] M. Verhaegen, J. A. Bauer, C. Martín de la Vega et al., "A novel bh3 mimetic reveals a mitogen-activated protein kinase-dependent mechanism of melanoma cell death controlled by p53 and reactive oxygen species," *Cancer Research*, vol. 66, no. 23, pp. 11348–11359, 2006.
- [74] G. Gloire, S. Legrand-Poels, and J. Piette, "NF- $\kappa$ B activation by reactive oxygen species: Fifteen years later," *Biochemical Pharmacology*, vol. 72, no. 11, pp. 1493–1505, 2006.
- [75] M. Karin, "Nuclear factor- $\kappa$ B in cancer development and progression," *Nature*, vol. 441, no. 7092, pp. 431–436, 2006.

- [76] Y. Ueda and A. Richmond, "NF-kappa activation in melanoma," *Pigment Cell Research*, vol. 19, no. 2, pp. 112–124, 2006.
- [77] A. S. Payne and L. A. Cornelius, "The role of chemokines in melanoma tumor growth and metastasis," *Journal of Investigative Dermatology*, vol. 118, no. 6, pp. 915–922, 2002.
- [78] S. Xanthoudakis, G. Miao, F. Wang, Y. C. E. Pan, and T. Curran, "Redox activation of Fos-Jun DNA binding activity is mediated by a DNA repair enzyme," *The EMBO Journal*, vol. 11, no. 9, pp. 3323–3335, 1992.
- [79] T. Smeal, B. Binetruy, D. A. Mercola, M. Birrer, and M. Karin, "Oncogenic and transcriptional cooperation with Ha-Ras requires phosphorylation of *c-Jun* on serines 63 and 73," *Nature*, vol. 354, no. 6353, pp. 494–496, 1991.
- [80] J. Westermarck, J. Lohi, J. Kesioja, and V. M. Kahari, "Okadaic acid-elicited transcriptional activation of collagenase gene-expression in HT-1080 fibrosarcoma cells is mediated by JunB," *Cell Growth and Differentiation*, vol. 5, pp. 1205–1213, 1994.
- [81] M. H. Kim, H. S. Cho, M. Jung et al., "Extracellular signal-regulated kinase and AP-1 pathways are involved in reactive oxygen species-induced urokinase plasminogen activator receptor expression in human gastric cancer cells," *International Journal of Oncology*, vol. 26, pp. 1669–1674, 2005.
- [82] N. J. de Wit, G. N. van Muijen, and D. J. Ruiter, "Immunohistochemistry in melanocytic proliferative lesions," *Histopathology*, vol. 44, no. 6, pp. 517–541, 2004.
- [83] A. Vartanian and A. Y. Baryshnikov, "Crosstalk between apoptosis and antioxidants in melanoma vasculogenic mimicry," *Advances in Experimental Medicine and Biology*, vol. 601, pp. 145–153, 2007.
- [84] R. Clarijs, D. J. Ruiter, and R. M. W. de Waal, "Pathophysiological implications of stroma pattern formation in uveal melanoma," *Journal of Cellular Physiology*, vol. 194, no. 3, pp. 267–271, 2003.
- [85] M. J. Hendrix, E. A. Seftor, A. R. Hess, and R. E. Seftor, "Vasculogenic mimicry and tumour-cell plasticity: lessons from melanoma," *Nature Reviews Cancer*, vol. 3, no. 6, pp. 411–421, 2003.
- [86] L. M. Postovit, E. A. Seftor, R. E. Seftor, and M. J. Hendrix, "Influence of the microenvironment on melanoma cell fate determination and Phenotype: Figure 1," *Cancer Research*, vol. 66, no. 16, pp. 7833–7836, 2006.
- [87] M. R. Abid, K. C. Spokes, S. C. Shih, and W. C. Aird, "NADPH oxidase activity selectively modulates vascular endothelial growth factor signaling pathways," *Journal of Biological Chemistry*, vol. 282, no. 48, pp. 35373–35385, 2007.
- [88] B. Bedogni, S. M. Welford, D. S. Cassarino, B. J. Nickoloff, A. J. Giaccia, and M. B. Powell, "The hypoxic microenvironment of the skin contributes to akt-mediated melanocyte transformation," *Cancer Cell*, vol. 8, no. 6, pp. 443–454, 2005.
- [89] A. L. Harris, "Hypoxia – a key regulatory factor in tumour growth," *Nature Reviews Cancer*, vol. 2, no. 1, pp. 38–47, 2002.
- [90] S. Moniz, J. Biddlestone, and S. Rocha, "Grow(2): the HIF system, energy homeostasis and the cell cycle," *Histology and Histopathology*, vol. 29, pp. 589–600, 2014.
- [91] J. Fandrey, T. A. Gorr, and M. Gassmann, "Regulating cellular oxygen sensing by hydroxylation," *Cardiovascular Research*, vol. 71, no. 4, pp. 642–651, 2006.
- [92] D. A. Kirschmann, E. A. Seftor, S. F. Fong et al., "A molecular role for lysyl oxidase in breast cancer invasion," *Cancer Research*, vol. 62, pp. 4478–4483, 2002.
- [93] M. Callapina, J. Zhou, T. Schmid, R. Kohl, and B. Brune, "NO restores HIF-1 $\alpha$  hydroxylation during hypoxia: Role of reactive oxygen species," *Free Radical Biology & Medicine*, vol. 39, no. 7, pp. 925–936, 2005.
- [94] Z. Li, D. Wang, E. M. Messing, and G. Wu, "VHL protein-interacting deubiquitinating enzyme 2 deubiquitinates and stabilizes HIF-1 $\alpha$ ," *EMBO Reports*, vol. 6, no. 4, pp. 373–378, 2005.
- [95] G. L. Wang and G. L. Semenza, "Desferrioxamine induces erythropoietin gene expression and hypoxia-inducible factor 1 DNA-binding activity: implications for models of hypoxia signal transduction," *Blood*, vol. 82, no. 12, pp. 3610–3615, 1993.
- [96] Y. Yuan, G. Hilliard, T. Ferguson, and D. E. Millhorn, "Cobalt Inhibits the Interaction between Hypoxia-inducible Factor- $\alpha$  and von Hippel-Lindau Protein by Direct Binding to Hypoxia-inducible Factor- $\alpha$ ," *Journal of Biological Chemistry*, vol. 278, no. 18, pp. 15911–15916, 2003.
- [97] K. Salmikow, S. P. Donald, R. K. Bruick, A. Zhitkovich, J. M. Phang, and K. S. Kasprzak, "Depletion of Intracellular Ascorbate by the Carcinogenic Metals Nickel and Cobalt Results in the Induction of Hypoxic Stress," *Journal of Biological Chemistry*, vol. 279, no. 39, pp. 40337–40344, 2004.
- [98] N. Ferrara, "Vascular endothelial growth factor," *Arteriosclerosis, Thrombosis, and Vascular Biology*, vol. 29, no. 6, pp. 789–791, 2009.
- [99] J. A. Forsythe, B. H. Jiang, N. V. Iyer et al., "Activation of vascular endothelial growth factor gene transcription by hypoxia-inducible factor 1," *Molecular and Cellular Biology*, vol. 16, no. 9, pp. 4604–4613, 1996.
- [100] N. S. Chandel, W. C. Trzyna, D. S. McClintock, and P. T. Schumacker, "Role of oxidants in NF- $\kappa$ B activation and TNF- $\alpha$  gene transcription induced by hypoxia and endotoxin," *The Journal of Immunology*, vol. 165, no. 2, pp. 1013–1021, 2000.
- [101] S. Kuphal, S. Wallner, and A. K. Bosserhoff, "Impact of LIF (leukemia inhibitory factor) expression in malignant melanoma," *Experimental and Molecular Pathology*, vol. 95, no. 2, pp. 156–165, 2013.
- [102] J. P. Dutcher, "Mammalian target of rapamycin inhibition," *Clinical Cancer Research*, vol. 10, no. 18, pp. 6382S–6387S, 2004.
- [103] O. Aprelikova, S. Pandolfi, S. Tackett et al., "Melanoma antigen-11 inhibits the hypoxia-inducible factor prolyl hydroxylase 2 and activates hypoxic response," *Cancer Research*, vol. 69, no. 2, pp. 616–624, 2009.
- [104] S. Kuphal, A. Winklmeier, C. Warnecke, and A. K. Bosserhoff, "Constitutive HIF-1 activity in malignant melanoma," *European Journal of Cancer*, vol. 46, no. 6, pp. 1159–1169, 2010.
- [105] Y. Chudnovsky, P. A. Khavari, and A. E. Adams, "Melanoma genetics and the development of rational therapeutics," *Journal of Clinical Investigation*, vol. 115, no. 4, pp. 813–824, 2005.
- [106] R. M. MacKie, "Long-term health risk to the skin of ultraviolet radiation," *Progress in Biophysics and Molecular Biology*, vol. 92, no. 1, pp. 92–96, 2006.

- [107] J. A. Curtin, J. Fridlyand, T. Kageshita et al., "Distinct sets of genetic alterations in melanoma," *The New England Journal of Medicine*, vol. 353, no. 20, pp. 2135–2147, 2005.
- [108] F. L. Meyskens Jr., P. J. Farmer, and H. Anton-Culver, "Etiologic pathogenesis of melanoma: Fig. 1," *Clinical Cancer Research*, vol. 10, no. 8, pp. 2581–2583, 2004.
- [109] A. Slominski, M. A. Zmijewski, and J. Pawelek, "L-tyrosine and l-dihydroxyphenylalanine as hormone-like regulators of melanocyte functions," *Pigment Cell & Melanoma Research*, vol. 25, no. 1, pp. 14–27, 2012.
- [110] S. Pavel, F. van Nieuwpoort, H. van der Meulen et al., "Disturbed melanin synthesis and chronic oxidative stress in dysplastic naevi," *European Journal of Cancer*, vol. 40, no. 9, pp. 1423–1430, 2004.
- [111] J. M. McCord, "Iron, free radicals, and oxidative injury," *Seminars in Hematology*, vol. 35, pp. 5–12, 1998.
- [112] F. Liu-Smith, R. Dellinger, and F. L. Meyskens Jr., "Updates of reactive oxygen species in melanoma etiology and progression," *Archives of Biochemistry and Biophysics*, vol. 563, pp. 51–55, 2014.
- [113] A. T. Slominski and J. A. Carlson, "Melanoma resistance: a bright future for academicians and a challenge for patient advocates," *Mayo Clinic Proceedings*, vol. 89, no. 4, pp. 429–433, 2014.
- [114] Y. Kamenisch, I. Ivanova, K. Drexler, and M. Berneburg, "UVA, metabolism and melanoma: UVA makes melanoma hungry for metastasis," *Experimental Dermatology*, vol. 27, no. 9, pp. 941–949, 2018.
- [115] L. R. Arslanbaeva and M. M. Santoro, "Adaptive redox homeostasis in cutaneous melanoma," *Redox Biology*, vol. 37, article 101753, 2020.
- [116] M. Hosseini, Z. Kasraian, and H. R. Rezvani, "Energy metabolism in skin cancers: a therapeutic perspective," *Biochimica et Biophysica Acta (BBA) - Bioenergetics*, vol. 1858, no. 8, pp. 712–722, 2017.
- [117] P. R. Kumar, J. A. Moore, K. M. Bowles, S. A. Rushworth, and M. D. Moncrieff, "Mitochondrial oxidative phosphorylation in cutaneous melanoma," *British Journal of Cancer*, vol. 124, no. 1, pp. 115–123, 2021.
- [118] L. C. van Kempen, G. N. van Muijen, and D. J. Ruiter, "Stromal responses in human primary melanoma of the skin," *Frontiers in Bioscience*, vol. 10, no. 1-3, pp. 2922–2931, 2005.
- [119] J. B. Wyckoff, J. G. Jones, J. S. Condeelis, and J. E. Segall, "A critical step in metastasis: in vivo analysis of intravasation at the primary tumor," *Cancer Research*, vol. 60, pp. 2504–2511, 2000.
- [120] T. Ota, M. Maeda, M. Tanino, and M. Tatsuka, "Functional suppression of integrin beta 4-mediated adhesion caused by in vivo sequential selection for cancer cell intravasation," *Anticancer Research*, vol. 21, pp. 205–211, 2001.
- [121] J. Raffle, A. K. Bhattacharyya, A. Gallegos et al., "Increased expression of thioredoxin-1 in human colorectal cancer is associated with decreased patient survival," *Journal of Laboratory and Clinical Medicine*, vol. 142, no. 1, pp. 46–51, 2003.
- [122] G. C. Cheng, P. C. Schulze, R. T. Lee, J. Sylvan, B. R. Zetter, and H. Huang, "Oxidative stress and thioredoxin-interacting protein promote intravasation of melanoma cells," *Experimental Cell Research*, vol. 300, no. 2, pp. 297–307, 2004.
- [123] E. Piskounova, M. Agathocleous, M. M. Murphy et al., "Oxidative stress inhibits distant metastasis by human melanoma cells," *Nature*, vol. 527, no. 7577, pp. 186–191, 2015.
- [124] K. Le Gal, M. X. Ibrahim, C. Wiel et al., "Antioxidants can increase melanoma metastasis in mice," *Science Translational Medicine*, vol. 7, 2015.
- [125] R. A. Cairns, I. S. Harris, and T. W. Mak, "Regulation of cancer cell metabolism," *Nature Reviews Cancer*, vol. 11, no. 2, pp. 85–95, 2011.
- [126] A. Glasauer and N. S. Chandel, "Targeting antioxidants for cancer therapy," *Biochemical Pharmacology*, vol. 92, no. 1, pp. 90–101, 2014.
- [127] P. Allavena, C. Garlanda, M. G. Borrello, A. Sica, and A. Mantovani, "Pathways connecting inflammation and cancer," *Current Opinion in Genetics & Development*, vol. 18, no. 1, pp. 3–10, 2008.
- [128] L. M. Coussens and Z. Werb, "Inflammation and cancer," *Nature*, vol. 420, no. 6917, pp. 860–867, 2002.
- [129] M. Pieniazek, R. Matkowski, and P. Donizy, "Macrophages in skin melanoma—the key element in melanomagenesis (Review)," *Oncology Letters*, vol. 15, pp. 5399–5404, 2018.
- [130] C. Ceci, M. G. Atzori, P. M. Lical, and G. Graziani, "Targeting tumor-associated macrophages to increase the efficacy of immune checkpoint inhibitors: a glimpse into novel therapeutic approaches for metastatic melanoma," *Cancers*, vol. 12, no. 11, p. 3401, 2020.
- [131] H. Maeda and T. Akaike, "Nitric oxide and oxygen radicals in infection, inflammation, and cancer," *Biochemistry*, vol. 63, pp. 854–865, 1998.
- [132] L. C. van Kempen, K. E. de Visser, and L. M. Coussens, "Inflammation, proteases and cancer," *European Journal of Cancer*, vol. 42, no. 6, pp. 728–734, 2006.
- [133] I. Bohme and A. Bosserhoff, "Extracellular acidosis triggers a senescence-like phenotype in human melanoma cells," *Pigment Cell & Melanoma Research*, vol. 33, no. 1, pp. 41–51, 2020.
- [134] A. Indini, F. Grossi, M. Mandala, D. Taverna, and V. Audrito, "Metabolic interplay between the immune system and melanoma cells: therapeutic implications," *Biomedicine*, vol. 9, no. 6, p. 607, 2021.
- [135] B. A. Olenchock, J. C. Rathmell, and M. G. Vander Heiden, "Biochemical underpinnings of immune cell metabolic phenotypes," *Immunity*, vol. 46, no. 5, pp. 703–713, 2017.
- [136] M. D. Buck, R. T. Sowell, S. M. Kaech, and E. L. Pearce, "Metabolic instruction of immunity," *Cell*, vol. 169, no. 4, pp. 570–586, 2017.
- [137] D. Brenner and T. W. Mak, "Mitochondrial cell death effectors," *Current Opinion in Cell Biology*, vol. 21, no. 6, pp. 871–877, 2009.
- [138] S. R. Jacobs, C. E. Herman, N. J. Maciver et al., "Glucose uptake is limiting in t cell activation and requires CD28-mediated akt-dependent and independent pathways," *The Journal of Immunology*, vol. 180, no. 7, pp. 4476–4486, 2008.
- [139] E. L. Carr, A. Kelman, G. S. Wu et al., "Glutamine uptake and metabolism are coordinately regulated by erk/mapk during t lymphocyte activation," *The Journal of Immunology*, vol. 185, no. 2, pp. 1037–1044, 2010.
- [140] L. A. Sena, S. Li, A. Jairaman et al., "Mitochondria are required for antigen-specific t cell activation through reactive oxygen species signaling," *Immunity*, vol. 38, no. 2, pp. 225–236, 2013.
- [141] A. Quintana, C. Schwindling, A. S. Wenning et al., "T cell activation requires mitochondrial translocation to the immunological synapse," *Proceedings of the National Academy of Sciences*, vol. 116, no. 12, pp. 5845–5850, 2019.

- Sciences of the United States of America*, vol. 104, no. 36, pp. 14418–14423, 2007.
- [142] E. Flescher, J. A. Ledbetter, G. L. Schieven et al., “Longitudinal exposure of human t lymphocytes to weak oxidative stress suppresses transmembrane and nuclear signal transduction,” *The Journal of Immunology*, vol. 153, pp. 4880–4889, 1994.
- [143] S. Devadas, L. Zaritskaya, S. G. Rhee, L. Oberley, and M. S. Williams, “Discrete generation of superoxide and hydrogen peroxide by t cell receptor stimulation,” *Journal of Experimental Medicine*, vol. 195, no. 1, pp. 59–70, 2002.
- [144] K. M. Holmstrom and T. Finkel, “Cellular mechanisms and physiological consequences of redox-dependent signalling,” *Nature Reviews Molecular Cell Biology*, vol. 15, no. 6, pp. 411–421, 2014.
- [145] D. Hanahan and L. M. Coussens, “Accessories to the crime: functions of cells recruited to the tumor microenvironment,” *Cancer Cell*, vol. 21, no. 3, pp. 309–322, 2012.
- [146] J. A. Joyce and J. W. Pollard, “Microenvironmental regulation of metastasis,” *Nature Reviews Cancer*, vol. 9, no. 4, pp. 239–252, 2009.
- [147] J. S. Chan, M. J. Tan, M. K. Sng et al., “Cancer-associated fibroblasts enact field cancerization by promoting extratumoral oxidative stress,” *Cell Death & Disease*, vol. 8, article e2562, 2018.
- [148] C. Kuperwasser, T. Chavarria, M. Wu et al., “From The Cover: Reconstruction of functionally normal and malignant human breast tissues in mice,” *Proceedings of the National Academy of Sciences of the United States of America*, vol. 101, no. 14, pp. 4966–4971, 2004.
- [149] P. Gascard and T. D. Tlsty, “Carcinoma-associated fibroblasts: orchestrating the composition of malignancy,” *Genes & Development*, vol. 30, no. 9, pp. 1002–1019, 2016.
- [150] V. P. Chauhan, Y. Boucher, C. R. Ferrone et al., “Compression of pancreatic tumor blood vessels by hyaluronan is caused by solid stress and not interstitial fluid pressure,” *Cancer Cell*, vol. 26, no. 1, pp. 14–15, 2014.
- [151] Y. Kojima, A. Acar, E. N. Eaton et al., “Autocrine TGF- and stromal cell-derived factor-1 (SDF-1) signaling drives the evolution of tumor-promoting mammary stromal myofibroblasts,” *Proceedings of the National Academy of Sciences of the United States of America*, vol. 107, no. 46, pp. 20009–20014, 2010.
- [152] A. Toullec, D. Gerald, G. Despouy et al., “Oxidative stress promotes myofibroblast differentiation and tumour spreading,” *EMBO Molecular Medicine*, vol. 2, no. 6, pp. 211–230, 2010.
- [153] E. Artaud-Macari, D. Goven, S. Brayer et al., “Nuclear factor erythroid 2-related factor 2 nuclear translocation induces myofibroblastic dedifferentiation in idiopathic pulmonary fibrosis,” *Antioxidants & Redox Signaling*, vol. 18, no. 1, pp. 66–79, 2013.
- [154] A. Costa, A. Scholer-Dahirel, and F. Mechta-Grigoriou, “The role of reactive oxygen species and metabolism on cancer cells and their microenvironment,” *Seminars in Cancer Biology*, vol. 25, pp. 23–32, 2014.
- [155] U. E. Martinez-Outschoorn, Z. Lin, C. Trimmer et al., “Cancer cells metabolically “fertilize” the tumor microenvironment with hydrogen peroxide, driving the warburg effect,” *Cell Cycle*, vol. 10, no. 15, pp. 2504–2520, 2011.
- [156] A. L. Levonen, B. G. Hill, E. Kansanen, J. Zhang, and V. M. Darley-Usmar, “Redox regulation of antioxidants, autophagy, and the response to stress: implications for electrophile therapeutics,” *Free Radical Biology & Medicine*, vol. 71, pp. 196–207, 2014.
- [157] S. Arico, A. Petiot, C. Bauvy et al., “The Tumor Suppressor PTEN Positively Regulates Macroautophagy by Inhibiting the Phosphatidylinositol 3-Kinase/Protein Kinase B Pathway,” *Journal of Biological Chemistry*, vol. 276, no. 38, pp. 35243–35246, 2001.
- [158] S. Demirsoy, S. Martin, H. Maes, and P. Agostinis, “Adapt, recycle, and move on: proteostasis and trafficking mechanisms in melanoma,” *Frontiers in Oncology*, vol. 6, p. 240, 2016.
- [159] R. M. Liu and L. P. Desai, “Reciprocal regulation of TGF- $\beta$  and reactive oxygen species: A perverse cycle for fibrosis,” *Redox Biology*, vol. 6, pp. 565–577, 2015.
- [160] K. Richter and T. Kietzmann, “Reactive oxygen species and fibrosis: further evidence of a significant liaison,” *Cell and Tissue Research*, vol. 365, no. 3, pp. 591–605, 2016.
- [161] M. Ren, C. Y. Wei, L. Wang, X. Y. Deng, N. H. Lu, and J. Y. Gu, “Integration of individual prediction index based on autophagy-related genes and clinical phenomes in melanoma patients,” *Clinical and Translational Medicine*, vol. 10, no. 4, article e132, 2020.
- [162] C. Borek, “Antioxidants and radiation therapy,” *The Journal of Nutrition*, vol. 134, no. 11, pp. 3207S–3209S, 2004.
- [163] G. Loo, “Redox-sensitive mechanisms of phytochemical-mediated inhibition of cancer cell proliferation<sup>1</sup> (review),” *The Journal of Nutritional Biochemistry*, vol. 14, no. 2, pp. 64–73, 2003.
- [164] A. Affolter, M. Drigotas, K. Fruth et al., “Increased radioresistance via G12S K-RAS by compensatory upregulation of MAPK and PI3K pathways in epithelial cancer,” *Head & Neck*, vol. 35, no. 2, pp. 220–228, 2013.
- [165] K. N. Prasad, W. C. Cole, B. Kumar, and K. Che Prasad, “Pros and cons of antioxidant use during radiation therapy,” *Cancer Treatment Reviews*, vol. 28, no. 2, pp. 79–91, 2002.
- [166] S. U. Mertens-Talcott and S. S. Percival, “Ellagic acid and quercetin interact synergistically with resveratrol in the induction of apoptosis and cause transient cell cycle arrest in human leukemia cells,” *Cancer Letters*, vol. 218, no. 2, pp. 141–151, 2005.
- [167] W. K. Sinclair, “Cysteamine: Differential x-ray protective effect on chinese hamster cells during the cell cycle,” *Science*, vol. 159, no. 3813, pp. 442–444, 1968.
- [168] M. Drigotas, A. Affolter, W. J. Mann, and J. Brieger, “Reactive oxygen species activation of mapk pathway results in VEGF upregulation as an undesired irradiation response,” *Journal of Oral Pathology & Medicine*, vol. 42, no. 8, pp. 612–619, 2013.
- [169] J. H. Cho, H. J. Lee, H. J. Ko et al., “The tlr7 agonist imiquimod induces anti-cancer effects via autophagic cell death and enhances anti-tumoral and systemic immunity during radiotherapy for melanoma,” *Oncotarget*, vol. 8, no. 15, pp. 24932–24948, 2017.
- [170] M. Diehn, R. W. Cho, N. A. Lobo et al., “Association of reactive oxygen species levels and radioresistance in cancer stem cells,” *Nature*, vol. 458, no. 7239, pp. 780–783, 2009.
- [171] H. Wang, S. Bouzakoura, S. de Mey et al., “Auranofin radiosensitizes tumor cells through targeting thioredoxin reductase and resulting overproduction of reactive oxygen species,” *Oncotarget*, vol. 8, no. 22, pp. 35728–35742, 2017.

- [172] S. Zhou, W. Ye, Q. Shao, M. Zhang, and J. Liang, "Nrf2 is a potential therapeutic target in radioresistance in human cancer," *Critical Reviews in Oncology/Hematology*, vol. 88, no. 3, pp. 706–715, 2013.
- [173] A. Mahadevan, V. L. Patel, and N. Dagoglu, "Radiation therapy in the management of malignant melanoma," *Oncology*, vol. 29, pp. 743–751, 2015.
- [174] J. French, C. McGahan, G. Duncan, S. Lengoc, J. Soo, and J. Cannon, "How gender, age, and geography influence the utilization of radiation therapy in the management of malignant melanoma," *International Journal of Radiation Oncology • Biology • Physics*, vol. 66, no. 4, pp. 1056–1063, 2006.
- [175] E. Fenig, E. Eidelevich, E. Njuguna et al., "Role of radiation therapy in the management of cutaneous malignant melanoma," *American Journal of Clinical Oncology*, vol. 22, no. 2, pp. 184–186, 1999.
- [176] Q. Xie, G. Lan, Y. Zhou et al., "Strategy to enhance the anticancer efficacy of x-ray radiotherapy in melanoma cells by platinum complexes, the role of ros-mediated signaling pathways," *Cancer Letters*, vol. 354, no. 1, pp. 58–67, 2014.
- [177] H. H. W. Chen and M. T. Kuo, "Improving radiotherapy in cancer treatment: promises and challenges," *Oncotarget*, vol. 8, no. 37, pp. 62742–62758, 2017.
- [178] D. F. Meng, L. L. Guo, L. X. Peng et al., "Antioxidants suppress radiation-induced apoptosis via inhibiting mapk pathway in nasopharyngeal carcinoma cells," *Biochemical and Biophysical Research Communications*, vol. 527, no. 3, pp. 770–777, 2020.
- [179] H. Wang, H. Jiang, M. Van De Gucht, and M. De Ridder, "Hypoxic radioresistance: can ROS be the key to overcome it?," *Cancers*, vol. 11, no. 1, p. 112, 2019.
- [180] B. M. Aarts, E. G. Klompenhouwer, S. L. Rice et al., "Cryoablation and immunotherapy: an overview of evidence on its synergy," *Insights Imaging*, vol. 10, no. 1, p. 53, 2019.
- [181] R. L. Manthe, S. P. Foy, N. Krishnamurthy, B. Sharma, and V. Labhasetwar, "Tumor ablation and nanotechnology," *Molecular Pharmaceutics*, vol. 7, no. 6, pp. 1880–1898, 2010.
- [182] J. J. Joosten, G. N. P. Muijen, T. Wobbes, and T. J. Ruers, "In Vivo Destruction of Tumor Tissue by Cryoablation Can Induce Inhibition of Secondary Tumor Growth: An Experimental Study," *Cryobiology*, vol. 42, no. 1, pp. 49–58, 2001.
- [183] M. H. den Brok, R. P. Suttmuller, S. Nierkens et al., "Efficient loading of dendritic cells following cryo and radiofrequency ablation in combination with immune modulation induces anti-tumour immunity," *British Journal of Cancer*, vol. 95, no. 7, pp. 896–905, 2006.
- [184] C. Kudo-Saito, T. Fuwa, and Y. Kawakami, "Targeting ALCAM in the cryo-treated tumour microenvironment successfully induces systemic anti-tumour immunity," *European Journal of Cancer*, vol. 62, pp. 54–61, 2016.
- [185] S. Nierkens, M. H. den Brok, R. P. Suttmuller et al., "In vivo Colocalization of antigen and cpG within dendritic cells is associated with the efficacy of cancer immunotherapy," *Cancer Research*, vol. 68, no. 13, pp. 5390–5396, 2008.
- [186] L. Shen, H. Qi, S. Chen et al., "Cryoablation combined with transarterial infusion of pembrolizumab (catap) for liver metastases of melanoma: an ambispective, proof-of-concept cohort study," *Cancer Immunology, Immunotherapy*, vol. 69, no. 9, pp. 1713–1724, 2020.
- [187] M. Fiorentzis, H. Kalirai, P. Katopodis, B. Seitz, A. Viestenz, and S. E. Coupland, "Electrochemotherapy with bleomycin and cisplatin enhances cytotoxicity in primary and metastatic uveal melanoma cell lines in vitro," *Neoplasma*, vol. 65, no. 2, pp. 210–215, 2018.
- [188] C. M. Wolff, A. Steuer, I. Stoffels et al., "Combination of cold plasma and pulsed electric fields - A rationale for cancer patients in palliative care," *Clinical Plasma Medicine*, vol. 16, article 100096, 2019.
- [189] M. A. O'Brien, D. G. Power, A. J. Clover, B. Bird, D. M. Soden, and P. F. Forde, "Local tumour ablative therapies: opportunities for maximising immune engagement and activation," *Biochimica et Biophysica Acta (BBA) - Reviews on Cancer*, vol. 2014, pp. 510–523, 2014.
- [190] N. Mozzillo, C. Caraco, S. Mori et al., "Use of neoadjuvant electrochemotherapy to treat a large metastatic lesion of the cheek in a patient with melanoma," *Journal of Translational Medicine*, vol. 10, no. 1, p. 131, 2012.
- [191] G. Sersa, B. Stabuc, M. Cemazar, D. Miklavcic, and Z. Rudolf, "Electrochemotherapy with cisplatin: clinical experience in malignant melanoma patients," *Clinical Cancer Research*, vol. 6, pp. 863–867, 2000.
- [192] R. M. Brock, N. Beitel-White, R. V. Davalos, and I. C. Allen, "Starting a fire without flame: the induction of cell death and inflammation in electroporation-based tumor ablation strategies," *Frontiers in Oncology*, vol. 10, p. 1235, 2020.
- [193] G. Sersa, J. Teissie, M. Cemazar et al., "Electrochemotherapy of tumors as in situ vaccination boosted by immunogene electrotransfer," *Cancer Immunology, Immunotherapy*, vol. 64, no. 10, pp. 1315–1327, 2015.
- [194] C. M. Wolff, J. F. Kolb, K. D. Weltmann, T. von Woedtke, and S. Bekeschus, "Combination treatment with cold physical plasma and pulsed electric fields augments ros production and cytotoxicity in lymphoma," *Cancers*, vol. 12, no. 4, p. 845, 2020.
- [195] W. Szlasa, A. Kielbik, A. Szewczyk et al., "Oxidative effects during irreversible electroporation of melanoma cells-in vitro study," *Molecules*, vol. 26, 2021.
- [196] D. Agoston, E. Baltas, H. Ocsai et al., "Evaluation of calcium electroporation for the treatment of cutaneous metastases: a double blinded randomised controlled phase II trial," *Cancers*, vol. 12, no. 1, p. 179, 2020.
- [197] H. Falk, P. F. Forde, M. L. Bay et al., "Calcium electroporation induces tumor eradication, long-lasting immunity and cytokine responses in the CT26 colon cancer mouse model," *Oncoimmunology*, vol. 6, no. 5, article e1301332, 2017.
- [198] H. Falk, S. Lambaa, H. H. Johannesen, G. Wooler, A. Venzo, and J. Gehl, "Electrochemotherapy and calcium electroporation inducing a systemic immune response with local and distant remission of tumors in a patient with malignant melanoma - a case report," *Acta Oncologica*, vol. 56, no. 8, pp. 1126–1131, 2017.
- [199] S. K. Frandsen and J. Gehl, "A review on differences in effects on normal and malignant cells and tissues to electroporation-based therapies: a focus on calcium electroporation," *Technology in Cancer Research & Treatment*, vol. 17, 2018.
- [200] K. L. Hoejholt, T. Muzic, S. D. Jensen et al., "Calcium electroporation and electrochemotherapy for cancer treatment: Importance of cell membrane composition investigated by lipidomics, calorimetry and in vitro efficacy," *Scientific Reports*, vol. 9, no. 1, p. 4758, 2019.
- [201] B. Staresinic, T. Jesenko, U. Kamensek et al., "Effect of calcium electroporation on tumour vasculature," *Scientific Reports*, vol. 8, no. 1, p. 9412, 2018.

- [202] M. Vissing, J. Ploen, M. Pervan et al., "Study protocol designed to investigate tumour response to calcium electro- poration in cancers affecting the skin: a non-randomised phase ii clinical trial," *BMJ Open*, vol. 11, no. 6, article e046779, 2021.
- [203] J. J. Skitzki, E. A. Repasky, and S. S. Evans, "Hyperthermia as an immunotherapy strategy for cancer," *Current Opinion in Investigational Drugs*, vol. 10, pp. 550–558, 2009.
- [204] M. Nishikawa, S. Takemoto, and Y. Takakura, "Heat shock protein derivatives for delivery of antigens to antigen present- ing cells," *International Journal of Pharmaceutics*, vol. 354, no. 1–2, pp. 23–27, 2008.
- [205] T. Takeda, K. Fukunaga, K. Miyazawa et al., "Hyperthermic immuno-cellular therapy-basic and clinical study," *Gan To Kagaku Ryoho*, vol. 35, pp. 2244–2246, 2008.
- [206] Y. Tamura, N. Tsuboi, N. Sato, and K. Kikuchi, "70 kDa heat shock cognate protein is a transformation-associated antigen and a possible target for the host's anti-tumor immunity," *Journal of Immunology*, vol. 151, pp. 5516–5524, 1993.
- [207] H. Jin, X. Xie, B. Hu et al., "Hyperthermia inhibits the prolifer- ation and invasive ability of mouse malignant melanoma through TGF- $\beta$ 1," *Oncology Reports*, vol. 29, no. 2, pp. 725– 734, 2013.
- [208] T. Mantso, S. Vasileiadis, I. Anestopoulos et al., "Hyperther- mia induces therapeutic effectiveness and potentiates adju- vant therapy with non-targeted and targeted drugs in an *in vitro* model of human malignant melanoma," *Scientific Reports*, vol. 8, no. 1, article 10724, 2018.
- [209] I. Belhadj Slimen, T. Najar, A. Ghram, H. Dabbebi, M. Ben Mrad, and M. Abdrabbah, "Reactive oxygen species, heat stress and oxidative-induced mitochondrial damage. A review," *International Journal of Hyperthermia*, vol. 30, no. 7, pp. 513–523, 2014.
- [210] S. Kassis, M. Grondin, and D. A. Averill-Bates, "Heat shock increases levels of reactive oxygen species, autophagy and apoptosis," *Biochimica et Biophysica Acta (BBA) - Molecular Cell Research*, vol. 1868, no. 3, article 118924, 2021.
- [211] M. D. Hurwitz, "Hyperthermia and immunotherapy: clinical opportunities," *International Journal of Hyperthermia*, vol. 36, no. sup1, pp. 4–9, 2019.
- [212] K. Engin, L. Tupchong, D. Phil et al., "Hyperthermia and radiation in advanced malignant melanoma," *International Journal of Radiation Oncology • Biology • Physics*, vol. 25, no. 1, pp. 87–94, 1993.
- [213] H. R. Metelmann, C. Seebauer, R. Rutkowski, M. Schuster, S. Bekechus, and P. Metelmann, "Treating cancer with cold physical plasma: on the way to evidence-based medicine," *Con- tributions to Plasma Physics*, vol. 58, no. 5, pp. 415–419, 2018.
- [214] A. Privat-Maldonado, A. Schmidt, A. Lin et al., "ROS from physical plasmas: redox chemistry for biomedical therapy," *Oxidative Medicine and Cellular Longevity*, vol. 2019, Article ID 9062098, 29 pages, 2019.
- [215] G. Pasqual-Melo, R. K. Gandhirajan, I. Stoffels, and S. Bekechus, "Targeting malignant melanoma with physical plasmas," *Clinical Plasma Medicine*, vol. 10, pp. 1–8, 2018.
- [216] K. Wende, T. von Woedtke, K. D. Weltmann, and S. Bekechus, "Chemistry and biochemistry of cold physical plasma derived reactive species in liquids," *Biological Chemis- try*, vol. 400, pp. 19–38, 2019.
- [217] S. Bekechus, A. Schmidt, F. Niessner, T. Gerling, K. D. Welt- mann, and K. Wende, "Basic research in plasma medicine - a throughput approach from liquids to cells," *Journal of Visual- ized Experiments*, no. 129, article e56331, 2017.
- [218] S. Hasse, T. Meder, E. Freund, T. von Woedtke, and S. Bekechus, "Plasma treatment limits human melanoma spheroid growth and metastasis independent of the ambient gas composition," *Cancers*, vol. 12, no. 9, p. 2570, 2020.
- [219] S. Bekechus, S. Eisenmann, S. K. Sagwal et al., "xCT (SLC7A11) expression confers intrinsic resistance to physical plasma treatment in tumor cells," *Redox Biology*, vol. 30, article 101423, 2020.
- [220] R. K. Gandhirajan, D. Meyer, S. K. Sagwal, K. D. Weltmann, T. von Woedtke, and S. Bekechus, "The amino acid metabo- lism is essential for evading physical plasma-induced tumour cell death," *British Journal of Cancer*, vol. 124, no. 11, pp. 1854–1863, 2021.
- [221] S. Bekechus, R. Clemen, L. Haralambiev et al., "The plasma- induced leukemia cell death is dictated by the ROS chemistry and the HO-1/CXCL8 axis," *IEEE Transactions on Radiation and Plasma Medical Sciences*, vol. 5, no. 3, pp. 398–411, 2021.
- [222] L. Brulle, M. Vandamme, D. Ries et al., "Effects of a non ther- mal plasma treatment alone or in combination with gemcita- bine in a MIA PaCa2-luc orthotopic pancreatic carcinoma model," *PLoS One*, vol. 7, no. 12, article e52653, 2012.
- [223] S. K. Sagwal, G. Pasqual-Melo, Y. Bodnar, R. K. Gandhirajan, and S. Bekechus, "Combination of chemotherapy and phys- ical plasma elicits melanoma cell death via upregulation of SLC22A16," *Cell Death & Disease*, vol. 9, no. 12, p. 1179, 2018.
- [224] P. Shaw, N. Kumar, A. Privat-Maldonado, E. Smits, and A. Bogaerts, "Cold atmospheric plasma increases temozolo- mide sensitivity of three-dimensional glioblastoma spheroids via oxidative stress-mediated DNA damage," *Cancers*, vol. 13, no. 8, p. 1780, 2021.
- [225] J. Lafontaine, J. S. Boisvert, A. Glory, S. Coulombe, and P. Wong, "Synergy between non-thermal plasma with radi- ation therapy and olaparib in a panel of breast cancer cell lines," *Cancers*, vol. 12, no. 2, p. 348, 2020.
- [226] G. Pasqual-Melo, S. K. Sagwal, E. Freund et al., "Combination of gas plasma and radiotherapy has immunostimulatory potential and additive toxicity in murine melanoma cells *in vitro*," *International Journal of Molecular Sciences*, vol. 21, no. 4, p. 1379, 2020.
- [227] J.-S. Boisvert, J. Lafontaine, A. Glory, S. Coulombe, and P. Wong, "Comparison of three radio-frequency discharge modes on the treatment of breast cancer Cells *in vitro*," *IEEE Transactions on Radiation and Plasma Medical Sciences*, vol. 4, no. 5, pp. 644–654, 2020.
- [228] G. Chen, Z. Chen, D. Wen et al., "Transdermal cold atmo- spheric plasma-mediated immune checkpoint blockade ther- apy," *Proceedings of the National Academy of Sciences of the United States of America*, vol. 117, no. 7, pp. 3687–3692, 2020.
- [229] S. Bekechus, R. Clemen, F. Niessner, S. K. Sagwal, E. Freund, and A. Schmidt, "Medical gas plasma jet technology targets murine melanoma in an immunogenic fashion," *Advanced Science*, vol. 7, no. 10, article 1903438, 2020.
- [230] S. Bekechus, J. Moritz, I. Helfrich et al., "Ex vivo exposure of human melanoma tissue to cold physical plasma elicits apo- ptosis and modulates inflammation," *Applied Sciences*, vol. 10, no. 6, p. 1971, 2020.
- [231] R. Clemen, E. Freund, D. Mrochen et al., "Gas plasma tech- nology augments ovalbumin immunogenicity and OT-II t

- cell activation conferring tumor protection in mice,” *Advanced Science*, vol. 8, no. 10, article 2003395, 2021.
- [232] R. Clemen and S. Bekeschus, “Ros cocktails as an adjuvant for personalized antitumor vaccination?,” *Vaccines*, vol. 9, no. 5, p. 527, 2021.
- [233] H. Mahdikia, F. Saadati, E. Freund et al., “Gas plasma irradiation of breast cancers promotes immunogenicity, tumor reduction, and an abscopal effect in vivo,” *Oncoimmunology*, vol. 10, article 1859731, 2021.
- [234] R. Clemen, P. Heirman, A. Lin, A. Bogaerts, and S. Bekeschus, “Physical plasma-treated skin cancer cells amplify tumor cytotoxicity of human natural killer (NK) cells,” *Cancers*, vol. 12, no. 12, p. 3575, 2020.
- [235] S. Bekeschus, A. Schmidt, A. Kramer et al., “High throughput image cytometry micronucleus assay to investigate the presence or absence of mutagenic effects of cold physical plasma,” *Environmental and Molecular Mutagenesis*, vol. 59, no. 4, pp. 268–277, 2018.
- [236] L. Miebach, E. Freund, S. Horn et al., “Tumor cytotoxicity and immunogenicity of a novel V-jet neon plasma source compared to the kINPen,” *Scientific Reports*, vol. 11, no. 1, p. 136, 2021.
- [237] R. Rutkowski, G. Daeschlein, T. von Woedtke, R. Smeets, M. Gosau, and H. R. Metelmann, “Long-term risk assessment for medical application of cold atmospheric pressure plasma,” *Diagnostics*, vol. 10, no. 4, p. 210, 2020.
- [238] S. Bekeschus, T. von Woedtke, S. Emmert, and A. Schmidt, “Medical gas plasma-stimulated wound healing: evidence and mechanisms,” *Redox Biology*, vol. 46, p. 102116, 2021.
- [239] M. Arisi, S. Soglia, E. Guasco Pisani et al., “Cold atmospheric plasma (CAP) for the treatment of actinic keratosis and skin field cancerization: clinical and high-frequency ultrasound evaluation,” *Dermatology and Therapy*, vol. 11, no. 3, pp. 855–866, 2021.
- [240] G. Daeschlein, A. Arnold, S. Lutze et al., “Treatment of recalcitrant actinic keratosis (AK) of the scalp by cold atmospheric plasma,” *Cogent Medicine*, vol. 4, no. 1, article 1412903, 2017.
- [241] P. C. Friedman, V. Miller, G. Fridman, A. Lin, and A. Fridman, “Successful treatment of actinic keratoses using nonthermal atmospheric pressure plasma: a case series,” *Journal of the American Academy of Dermatology*, vol. 76, no. 2, pp. 349–350, 2017.
- [242] H.-R. Metelmann, D. S. Nedrelov, C. Seebauer et al., “Head and neck cancer treatment and physical plasma,” *Clinical Plasma Medicine*, vol. 3, no. 1, pp. 17–23, 2015.
- [243] H.-R. Metelmann, C. Seebauer, V. Miller et al., “Clinical experience with cold plasma in the treatment of locally advanced head and neck cancer,” *Clinical Plasma Medicine*, vol. 9, pp. 6–13, 2018.
- [244] M. Schuster, C. Seebauer, R. Rutkowski et al., “Visible tumor surface response to physical plasma and apoptotic cell kill in head and neck cancer,” *Journal of the American Academy of Dermatology*, vol. 44, no. 9, pp. 1445–1452, 2016.
- [245] E. Buytaert, M. Dewaele, and P. Agostinis, “Molecular effectors of multiple cell death pathways initiated by photodynamic therapy,” *Journal of Cranio-Maxillofacial Surgery*, vol. 2007, pp. 86–107, 2007.
- [246] T. J. Dougherty, C. J. Gomer, B. W. Henderson et al., “Photodynamic therapy,” *Journal of the National Cancer Institute*, vol. 90, no. 12, pp. 889–905, 1998.
- [247] P. Mroz, A. Yaroslavsky, G. B. Kharkwal, and M. R. Hamblin, “Cell death pathways in photodynamic therapy of cancer,” *Cancers*, vol. 3, no. 2, pp. 2516–2539, 2011.
- [248] R. Falk-Mahapatra and S. O. Gollnick, “Photodynamic therapy and immunity: an update,” *Photochemistry and Photobiology*, vol. 96, no. 3, pp. 550–559, 2020.
- [249] Y. Y. Huang, D. Vecchio, P. Avci, R. Yin, M. Garcia-Diaz, and M. R. Hamblin, “Melanoma resistance to photodynamic therapy: new insights,” *Biological Chemistry*, vol. 394, no. 2, pp. 239–250, 2013.
- [250] A. Allegra, G. Pioggia, A. Tonacci, C. Musolino, and S. Gangemi, “Oxidative stress and photodynamic therapy of skin cancers: mechanisms, challenges and promising developments,” *Antioxidants*, vol. 9, no. 5, p. 448, 2020.
- [251] J. Xu, J. Q. Gao, and Q. C. Wei, “Combination of photodynamic therapy with radiotherapy for cancer treatment,” *Journal of Nanomaterials*, vol. 2016, Article ID 8507924, 7 pages, 2016.
- [252] M. Wachowska, A. Muchowicz, and J. Golab, “Targeting epigenetic processes in photodynamic therapy-induced anticancer immunity,” *Frontiers in Oncology*, vol. 5, p. 176, 2015.
- [253] F. N. Biteghe and L. M. Davids, “A combination of photodynamic therapy and chemotherapy displays a differential cytotoxic effect on human metastatic melanoma cells,” *Journal of Photochemistry and Photobiology B: Biology*, vol. 166, pp. 18–27, 2017.
- [254] S. M. Gondivkar, A. R. Gadail, M. G. Choudhary, P. R. Vedpathak, and M. S. Likhitkar, “Photodynamic treatment outcomes of potentially-malignant lesions and malignancies of the head and neck region: a systematic review,” *Journal of Investigative and Clinical Dentistry*, vol. 9, no. 1, article e12270, 2018.
- [255] H. S. Hwang, H. Shin, J. Han, and K. Na, “Combination of photodynamic therapy (PDT) and anti-tumor immunity in cancer therapy,” *Journal of Pharmaceutical Investigation*, vol. 48, no. 2, pp. 143–151, 2018.



## Review Article

# Interplay between Mitochondrial Metabolism and Cellular Redox State Dictates Cancer Cell Survival

**Brittney Joy-Anne Foo,<sup>1</sup> Jie Qing Eu,<sup>1,2</sup> Jayshree L. Hirpara,<sup>2</sup> and Shazib Pervaiz<sup>1,3,4,5,6,7</sup>** 

<sup>1</sup>Department of Physiology, Yong Loo Lin School of Medicine, National University of Singapore (NUS), Singapore, Singapore

<sup>2</sup>Cancer Science Institute, NUS, Singapore, Singapore

<sup>3</sup>NUS Center for Cancer Research (N2CR), Yong Loo Lin School of Medicine, NUS, Singapore, Singapore

<sup>4</sup>NUS Medicine Healthy Longevity Program, Yong Loo Lin School of Medicine, NUS, Singapore, Singapore

<sup>5</sup>Integrative Sciences and Engineering Program, NUS Graduate School, NUS, Singapore, Singapore

<sup>6</sup>National University Cancer Institute, National University Health System, Singapore, Singapore

<sup>7</sup>Faculté de Médecine, Université de Paris, Paris, France

Correspondence should be addressed to Shazib Pervaiz; phssp@nus.edu.sg

Received 22 August 2021; Revised 30 September 2021; Accepted 4 October 2021; Published 3 November 2021

Academic Editor: Qiang Tong

Copyright © 2021 Brittney Joy-Anne Foo et al. This is an open access article distributed under the Creative Commons Attribution License, which permits unrestricted use, distribution, and reproduction in any medium, provided the original work is properly cited.

Mitochondria are the main powerhouse of the cell, generating ATP through the tricarboxylic acid cycle (TCA) and oxidative phosphorylation (OXPHOS), which drives myriad cellular processes. In addition to their role in maintaining bioenergetic homeostasis, changes in mitochondrial metabolism, permeability, and morphology are critical in cell fate decisions and determination. Notably, mitochondrial respiration coupled with the passage of electrons through the electron transport chain (ETC) set up a potential source of reactive oxygen species (ROS). While low to moderate increase in intracellular ROS serves as secondary messenger, an overwhelming increase as a result of either increased production and/or deficient antioxidant defenses is detrimental to biomolecules, cells, and tissues. Since ROS and mitochondria both regulate cell fate, attention has been drawn to their involvement in the various processes of carcinogenesis. To that end, the link between a prooxidant milieu and cell survival and proliferation as well as a switch to mitochondrial OXPHOS associated with recalcitrant cancers provide testimony for the remarkable metabolic plasticity as an important hallmark of cancers. In this review, the regulation of cell redox status by mitochondrial metabolism and its implications for cancer cell fate will be discussed followed by the significance of mitochondria-targeted therapies for cancer.

## 1. Introduction

The mitochondrion is a double-membraned organelle that was hypothesized to have evolved from a prokaryote to endosymbionts within eukaryotes [1]. The inner membrane folds on itself to form cristae, enclosing the granular matrix [2]. The significance of the resultant intermembrane space (IMS) is highlighted in its role in the production of cellular energy (ATP) through glycolysis, the tricarboxylic acid (TCA) cycle, and oxidative phosphorylation (OXPHOS). Cancer is characterized by the accumulation of multiple genetic alterations that give rise to multiple mutations, resulting in uncontrolled cell proliferation that requires high

energy production and macromolecule synthesis. As such, cancer cells rely on processes such as glycolysis and TCA metabolism for cell survival.

The TCA cycle comprises of a series of biochemical reactions that contribute to energy production and macromolecule synthesis in the mitochondrial matrix. Under normal physiological conditions, the TCA cycle can be divided into two stages. First, citrate is converted into succinyl-CoA through a series of reactions that leads to decarboxylation, releasing two CO<sub>2</sub> molecules and conversion of NAD<sup>+</sup> to NADH + H<sup>+</sup> in the process. Second, succinate is converted to oxaloacetate through successive oxidation steps [3]. Intriguingly, tumor cells have been reported to harbor

genetic alterations in enzymes involved in the TCA cycle such as succinate dehydrogenase (SDH) and fumarate hydratase (FH) [4, 5]. Loss of SDH and FH leads to the accumulation of ROS which, in turn, leads to DNA damage and altered cellular processes that contribute to oncogenesis.

Otto Warburg postulated that cancer cells rely on aerobic glycolysis, a term now known as Warburg effect. As such, the role of mitochondrial metabolism in tumorigenesis has been often overlooked until recent years where several evidences point to a reliance on mitochondrial respiration in some cancers. Hence, in this review, we discuss the regulation of mitochondrial metabolism and redox balance in tumorigenesis and evaluate therapeutic strategies designed to target these pathways in cancer.

## 2. Mitochondrial Metabolism Regulates Cellular Redox Status

*2.1. Mitochondria as a Major Cellular Source of ROS.* ROS are molecules that contain oxygen that is derived from incomplete reduction of  $O_2$ . Some ROS molecules include superoxide ( $O_2^{\bullet-}$ ), hydrogen peroxide ( $H_2O_2$ ), and hydroxyl radical ( $OH^{\bullet}$ ) [6]. ROS production could be attributed to nonmitochondrial ROS-producing enzymes such as NADPH oxidase (NOX) and xanthine oxidase (XO) or as a result of electron leakage at the mitochondrial ETC. XO catalyzes the oxidation of xanthine and hypoxanthine in purine metabolism, which leads to the formation of  $O_2^{\bullet-}$  and  $H_2O_2$ . NOX has also been reported to promote XO-dependent  $O_2^{\bullet-}$  production [7]. NOX family members are transmembrane proteins that generate ROS through the transport of electrons across biological membranes, leading to reduction of oxygen to  $O_2^{\bullet-}$ . There are seven isoforms of NOX (NOX1-5, DUOX1-2) that have been identified, each localized in different cell types. For example, NOX1 is commonly found in endothelial cells, neurons, and microglia; NOX2 is found in phagocytes and microvascular endothelial cells while NOX3 is found in renal cells [8, 9]. Interestingly, the interaction between mitochondria and NOX, termed “ROS-induced ROS release” has been highlighted in glucose withdrawal-induced phospho-tyrosine signaling in glioblastoma (GBM) cell lines [10] and is suggested as a mechanism of ROS accumulation to sustain redox activation [11].

The aerobic nature of cellular respiration in the mitochondria makes ROS an inevitable by-product of the redox reactions. The dogmatic view is that excessive production of ROS could be detrimental to subcellular biomolecules, impair cellular processes, and trigger cell damage and death. Electron leakage in the mitochondrial ETC contributes largely to mitochondrial ROS accumulation. Complex I is the largest complex of the ETC and has been observed to be a major source of ROS under pathological conditions. This is due to mutations in the complex I subunits found in approximately 40% of mitochondrial disorders including diabetes and cancer [12, 13]. The Q-cycle is the mechanism of  $O_2^{\bullet-}$  production in complex III, another complex in the ETC. Complex III transfers the electrons from complexes I and II to cytochrome c, and in the process, protons translocate into the inner mitochondrial membrane (IMM). As a

result, electrons leak and interact with  $O_2$ , producing  $O_2^{\bullet-}$  in the IMM and mitochondrial matrix [14]. In the cancer context, overexpression of complex III subunits such as UQCR2 and UQCRH has been observed to induce tumorigenesis in colorectal cancer [15], lung carcinoma, and hepatocarcinoma [16] in a ROS-dependent manner. This highlights the role of mitochondrial metabolism in maintaining the redox balance and tumorigenesis.

*2.2. Cellular Antioxidant Defense Systems.* In most cellular processes, homeostatic balance is important in maintaining normal functioning of cells. The production of ROS is countered by antioxidant systems [17], which scavenge harmful ROS that can cause oxidative damage resulting in DNA point mutations [18, 19], disrupted lipid membranes [20], and altered protein function [21–23]. Amongst the many enzymatic antioxidant defenses are the various superoxide dismutase (SOD) and the glutathione (GSH) system. SOD is a family of enzymes that catalyzes the conversion of  $O_2^{\bullet-}$  to  $H_2O_2$ . In mammals, there are three SODs: cytoplasmic SOD1 (Cu/ZnSOD), extracellular SOD3 (ecSOD) [24, 25], and mitochondrial manganese-dependent SOD2 (MnSOD) [26]. MnSOD is shown to be downregulated in several cancers including lung carcinomas [27, 28]. Intriguingly, MnSOD was observed to be increased in tumor tissues and is associated with drug resistance [29, 30]. Furthermore, MnSOD expression is reportedly increased in aggressive breast cancer and influences epithelial-mesenchymal transition (EMT) in breast cancer [31, 32]. The glutathione peroxidase family (GPx) utilizes reduced GSH as the cofactor in reducing  $H_2O_2$  into harmless  $H_2O$ . During the reduction of  $H_2O_2$ , cofactor GSH is oxidized and disulphide bonded into a GS-SG dimer. Glutathione reductase is then responsible for reducing the GS-SG dimer, replenishing the GSH cofactor for further antioxidant activity [33]. Modified GPx expression has been observed in several cancers such as breast cancer [34], gastric cancer [35, 36], and thyroid cancer [37].

## 3. Dichotomy of Redox Signaling in Cancer Cell Fate Decisions

Depending on the type and concentration, ROS can impact cell fate signaling. As a matter of fact, cellular redox status serves as a double-edged sword from the standpoint of carcinogenesis and its progression, as summarized in Figure 1. At moderate but sublethal concentrations, a mild oxidative stress milieu can have prosurvival/proliferation properties. Coupled with the ability of cells to mount sufficiently effective antioxidant defenses, an association between a “pro-oxidant” environment and processes that favor tumor progression such as metastasis has been strongly suggested [38, 39].

*3.1. Conventional Dogma: ROS are Onco-Suppressors.* Conventionally, increased ROS levels have also been implicated in tumor cell growth inhibition. Interestingly, the reactive intermediates damage biomolecules such as membrane lipid bilayer, leading to lipid peroxidation;  $OH^{\bullet}$  radical has been

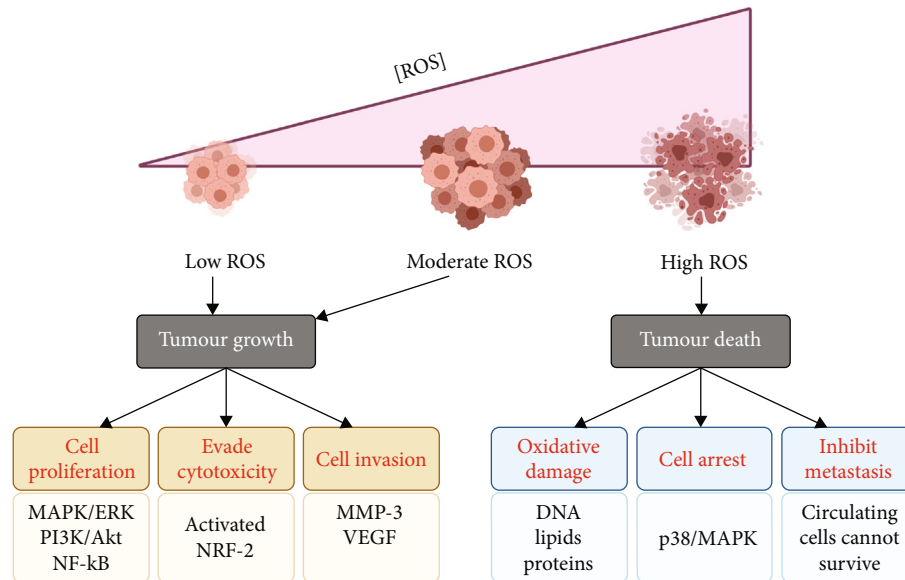


FIGURE 1: Regulation of carcinogenesis by ROS. At different ROS levels, cells experience a dichotomous fate. Moderate and low ROS levels tend to promote cell growth and uncontrolled proliferation, thus, promoting carcinogenesis and/or its progression. On the other end of the spectrum, high ROS levels tip the balance to cell death, preventing further growth of the tumor. Figure created with biorender.com.

shown to attack unsaturated lipids, generating lipid hydroperoxides [40]. A notable by-product of lipid peroxidation is 4-hydroxynonenal (4-HNE) that is found to exert cytotoxic and genotoxic effects [41]. Moreover, low levels of 4-HNE reportedly inhibit c-Myc expression and cell proliferation in leukemia cell lines [42, 43], suggesting an association between ROS-induced lipid peroxidation and inhibition of cancer progression. Furthermore, 4-HNE has been shown to activate both the intrinsic and extrinsic apoptotic pathways [44] as high peroxidation rates overwhelm natural antioxidant systems causing the cells to undergo programmed cell death, thus, highlighting the role of ROS in inhibiting tumor cell growth.

Metastasis can similarly be limited upon exposure to an oxidizing stimulus. Increased oxidative stress inhibits proliferation and survival of circulating cancer cells [45]. In an *in vivo* study conducted by Piskounova et al., NSG mice were subcutaneously transplanted with metastasizing melanoma cells and treated with antioxidant N-acetyl-cysteine (NAC). Interestingly, NAC treated mice were observed to have greater frequency of circulating melanoma cells and increased metastatic disease burden, thereby suggesting that oxidative stress limits the metastatic capacity of melanoma cells [45].

Low dose of ROS activates p53, a tumor suppressor that regulates cellular apoptosis, DNA repair, and cell cycle arrest. Upon ROS activation, p53 in turn downregulates prosurvival proteins such as Bcl-2 and Bcl-xL while activating proapoptotic genes such as Bax, PUMA, and NOXA transcriptionally [46]. Datta et al. showed that in the presence of  $H_2O_2$ , p53 expression and cell apoptosis were induced. Furthermore,  $H_2O_2$ -induced apoptosis was abrogated in the presence of p53 antisense oligonucleotides. Similarly, p53-null U373MG cells are resistant to  $H_2O_2$ -induced apoptosis [47]. The role of p53 in mediating  $H_2O_2$ -induced

apoptosis is supported by Kitamura et al. where they demonstrated an increase in p53 expression as well as Bak, p21WAF1/CIP1 proteins upon  $H_2O_2$  treatment [48]. Interestingly, mutant p53 in turn induces ROS accumulation and enhances ROS level through regulation of ROS-related transcription factors such as PGC1- $\alpha$  [49, 50]. ROS levels were also seen elevated in p53-induced senescent and apoptotic cells along with decrease in GSH levels in prostate cancer cells [50].

Intriguingly, ROS has been implicated in senescence-induced tumor suppression in several cellular senescence studies. It is noteworthy that ROS-induced oxidative damage is a signal for irreversible cell cycle arrest or senescence [51]. In particular, telomeres are observed to be sensitive to increase in ROS [52], supporting the view that mtROS results in telomere dysfunction and therefore premature senescence [53]. ROS can also serve as secondary messengers in senescence-inducing pathways such as p53/p21<sup>WAF1</sup> [54], p16<sup>INK-4a</sup> [55], and p38<sup>MAPK</sup> [56, 57]. Senescence is closely associated with p16<sup>INK-4a</sup>, and Takahashi et al. demonstrated that ROS determines irreversibility of senescence-induced cell cycle arrest and treatment with NAC rescued cells and reinitiates cell proliferation, suggesting a role of ROS in regulating tumor suppression through senescence [58].

**3.2. Flip Side of the Coin: ROS are Oncogenic.** Interestingly, while ROS has been shown to affect cell fate and signaling in cancer, in a rapidly proliferating cell, such as a cancer cell, increased metabolic activity in turn leads to high levels of ROS.

**3.2.1. ROS Regulation of Keap1/Nrf2 Complex.** As a protective measure, reinforcement of antioxidant defenses such as the Nrf2 pathway provides cells with the ability to adapt, thereby evading oxidative stress-mediated cytotoxicity and

tissue damage. Nrf2 is a transcription factor that controls nuclear antioxidant response elements (ARE) in the promoter region of target genes [59], such as those utilized by oncogenes K-Ras<sup>G12D</sup> and B-Raf<sup>V619E</sup> in human pancreatic cancer cells *in vivo* [60] and *in vitro* [61]. Further supporting that, Nrf2-knockout mice exhibit increased oxidative stress and predilection for carcinogenesis [62, 63]. Aside from the direct effect of Nrf2 on antioxidant defense reinforcement, increased oxidative stress also promotes stability of Nrf2 via oxidative modification of its regulator Keap1, which promotes Nrf2 proteasomal degradation by polyubiquitination [64]. Keap1 has redox-sensitive cysteine thiols that are prone to modification by H<sub>2</sub>O<sub>2</sub>, altering the Keap1/Nrf2 complex and ultimately inhibiting Nrf2 degradation [65]. Other antioxidant systems like glutathione and thioredoxin have also been shown to promote breast tumor progression in a synergistic manner [66]. However, in other cancer types such as lung [67] and prostate [68], SOD2 levels have been found suppressed, hence, suggesting that the regulation of intracellular antioxidants depends on the primary tumor.

**3.2.2. Oncogenic Mutations Tilt the Balance of ROS.** ROS levels could also be affected by oncogene mutations arising from chromosomal translocations. The fusion protein BCR/ABL in the Philadelphia chromosome is characteristic of predominantly chronic myeloid leukemia (CML) and acute lymphoblastic leukemia (ALL) [69]. This hybrid protein has constitutive tyrosine kinase signaling properties that allow uncontrolled cell cycle progression [70]. Increased H<sub>2</sub>O<sub>2</sub> levels have been found in BCR/ABL-activated cell lines [71–73], followed by a decrease of BCR/ABL activity in the presence of antioxidants [73]. Additionally, ROS from BCR/ABL activation can further mutate the fusion BCR/ABL gene to confer therapeutic resistance against specific tyrosine kinase inhibitors [74]. Another chromosomal translocation is NPM/ALK, which also displays upregulated tyrosine kinase activity in anaplastic large-cell lymphoma (ALCL) [75]. The mutation leads to downstream ROS production via the lipoxygenase enzyme family [76], where ROS can act as secondary messengers to activate pathways implicated in tumorigenesis such as MAPK for metastasis [77].

**3.2.3. ROS-Mediated Genome Instability.** As genomic instability is a hallmark of cancer [78], ROS-mediated DNA damage hints to cancer formation. Under oxidative stress, ROS oxidizes DNA bases. The most common oxidation is guanine to 8-oxo-dG due to it having the lowest reduction potential amongst the other bases [79–82]. 8-oxo-dG is a DNA lesion and can lead to permanent mutations which modify gene expression. In 1990, the association between 8-oxo-dG and carcinogenesis was established [83] although the direct link has not been found. Notably, DNA changes such as base substitutions occur in cells with artificially added 8-oxo-dG [84]. A common mutation is the transversion of oxidized guanine to thymine [85, 86]. As a matter of fact, 8-oxo-dG has been proposed as a marker of neoplastic transformation, thus, linking oxidation-induced DNA damage to carcinogenesis [87].

Genomic instability is promoted by the loss of tumor suppressors that control cell cycle progression and DNA damage repair process, such as the master transcription factor, p53, which is mutated in more than 50% of human solid tumors [88, 89]. At moderate sublethal ROS, p53 upregulates antioxidants to evade oxidative stress [90–92]; however, in the face of cytotoxic ROS levels, p53 downregulates antioxidants to tip the cell towards apoptosis [93, 94]. As such, the dual role of p53 in regulating cellular redox state switches the pendulum from survival to death execution [95]. Mechanistically, loss-of-functional of p53 increases ROS levels via the TP53-inducible glycolysis and apoptosis regulator (TIGAR). TIGAR normally shifts carbon from glycolysis to the pentose phosphate pathway (PPP) by degrading the allosteric activator of phosphofructokinase-1 (PFK1) and NADPH generated from PPP can fuel antioxidant processes by glutathione [92, 96]. Reduced GSH can then convert H<sub>2</sub>O<sub>2</sub> to water, reducing ROS levels. Without functional p53, ROS levels are no longer regulated by the TIGAR-dependent process. Besides the downstream ROS effects of p53, it is worthy to mention that p53 itself contains conserved cysteine residues that are susceptible to redox modification [97].

**3.2.4. Effect of ROS on Signaling Pathways.** ROS can also damage functional proteins directly by oxidizing susceptible catalytic thiol groups in enzymes [19, 22, 98]. In this regard, ROS can activate signaling pathways that promote cell proliferation and survival as a secondary messenger [99]. A large body of evidence appears to implicate intracellular H<sub>2</sub>O<sub>2</sub>, due to its diffusion efficiency and ubiquitous nature in most cells, as the major ROS involved in most physiological redox signaling [100]. The mechanism of ROS signaling is via its oxidation of thiol “switches” [101] in redox-sensitive substrates that have conserved cysteine residues [102, 103]. To that end, increased ROS has been shown to activate PI3K/Akt pathway to drive cell survival via inactivation of its regulator protein, phosphatase and tensin homolog (PTEN) [22, 104]; exogenously added H<sub>2</sub>O<sub>2</sub> can directly oxidize cysteine residues on PTEN, thereby compromising its PI3K/Akt-regulating activity [19, 22, 105] (Figure 2). Interestingly, constitutively activated PI3K/Akt pathway results also results in an increase in intracellular O<sub>2</sub><sup>•-</sup> production as a side-product from the generation of prostaglandin by COX enzymes with peroxidase activity [106, 107]. The involvement of NOX family of oxidase has also been shown in Akt-induced O<sub>2</sub><sup>•-</sup> production [108], which has been associated with mutation(s) of RAS, an oncogene that is constitutively activated in approximately 20–30% of human cancers [109]. RAS is a GTPase protein that is activated downstream of growth factor receptor tyrosine kinase (e.g., EGFR) which then activates PI3K by phosphorylation. Although NOX-mediated ROS production is mainly recognized for phagocytic respiratory burst, and its significance in tumor angiogenesis and metastasis is not dismissed [110]. Direct pathway components can also increase ROS levels, such as the catalytic subunit of PI3K (encoded by PIK3CA), which are found to be mutated in most solid tumors [111–113]. Mutated PIK3CA cell lines were

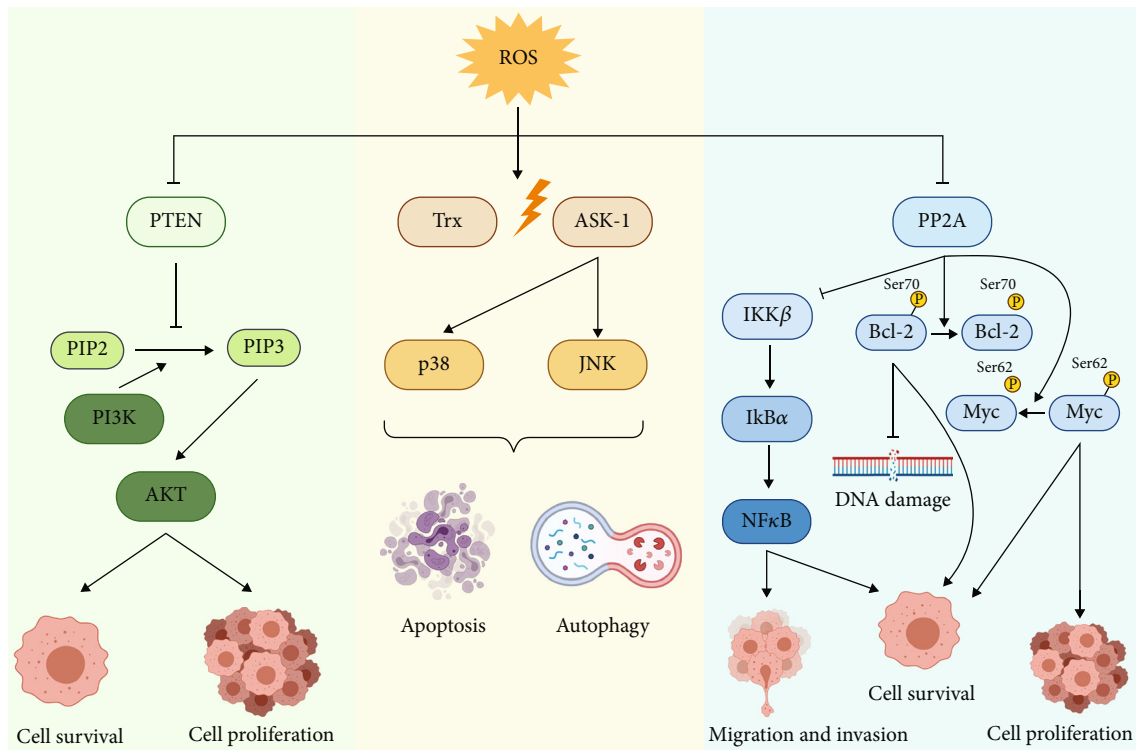


FIGURE 2: ROS regulation of signaling pathways in cancer. ROS has been demonstrated to regulate signaling pathways in cancer. Increase in ROS such as  $H_2O_2$  activates PI3K/Akt signaling pathway through the inhibition of PTEN, resulting in constitutive activation of PI3K/Akt that contributes to cell survival and proliferation in cancer. Similarly, ASK-1, a kinase in the MAPK signaling cascade, is displaced from Trx-ASK1 complex under oxidative stress. ASK-1 subsequently activates downstream p38 and JNK, leading to apoptosis and autophagy. Redox-mediated inactivation of PP2A was reported to sustain NF- $\kappa$ B activation, Bcl-2 phosphorylation at Ser70, and Myc phosphorylation at Ser62, leading to cell migration and invasion, inhibition of DNA damage and cell proliferation, respectively. Figure created with biorender.com.

observed to display raised  $\alpha$ -KGDH activity, a source of ROS [114]. Further corroborating this, negative regulators of the PI3K pathway, such as PTEN, are tumor suppressors that can be modulated by ROS.

Similarly, signaling pathways like the mitogen-activated protein kinase (MAPK/ERK) have demonstrated mediation by ROS, and other studies conversely demonstrate the ability of antioxidants to alleviate MAPK activation [77]. Oxidative stress upon exposure to exogenously added  $H_2O_2$  also correlated with MAPK activation [115, 116]. For example, apoptosis signal-regulating kinase-1 (ASK-1), a kinase in the MAPK signaling cascade, is displaced from antioxidant protein, thioredoxin, under oxidative stress, and oligomerizes to activate downstream p38 and c-jun N-terminal kinase (JNK) [117]. Moreover, ASK-1 expression has been associated with gastric cancer progression, where cell proliferation decreased in ASK-1 knockdown gastric cancer cells [118]. Since oxidative stress is reportedly the most common activator of ASK-1, this highlights the prominent role of oxidative stress in carcinogenesis through the regulation of signaling pathways (Figure 2).

**3.2.5. Oxidative Stress-induced Metastasis, Angiogenesis and Cell Death Inhibition.** Oxidative stress is also able to drive hallmarks involving cell motility and invasion such as

metastasis and angiogenesis. Kundu et al. demonstrated that exposure to sublethal exogenous  $H_2O_2$  in murine cancer cells increased rates of metastasis and anchorage-independent survival while reducing tumor cell adhesion to ECM [119].  $H_2O_2$  has been shown to regulate the expression of matrix metalloproteases (MMPs) that disrupt the ECM to facilitate cancer cell invasion [120]. Along similar lines, MMP-3 was shown to increase oxidative stress and induce EMT in murine mammary epithelial cells [121]. Moreover,  $H_2O_2$ -associated EGFR signaling is also vital for tumor metastasis [122], where murine metastatic melanoma colonies had greater EGFR expression [123]. Oxidative stress has been shown to stabilize HIF-1 $\alpha$  and allow the initiation of VEGF expression, which leads to the induction of angiogenesis [124], thus, supplying oxygen and nutrients to hypoxic tumors [125]. Furthermore, the NF- $\kappa$ B pathway associated with processes involved in carcinogenesis such as inflammation, cell survival, migration, and invasion is activated by  $H_2O_2$  via IKK-dependent mechanism [126] as well as by redox-mediated inactivation of the phosphatase PP2A [127], which regulates phosphorylation-dependent degradation of I $\kappa$ B $\alpha$ , further corroborating the involvement of ROS in processes associated with metastasis. Likewise, redox-mediated inactivation of PP2A has also been associated with phospho-stability of the antiapoptotic protein

Bcl-2 (pS70) and oncogene c-Myc (pS62), specifically implicating  $O_2^{\bullet-}$ -mediated ONOO<sup>-</sup> induced tyrosine nitration [128, 129]. Sustained pS70 of Bcl-2 in turn blocks oxidative stress-induced DNA damage to promote cancer cell survival [130]. Similarly, death receptor inhibitory protein, cFLIP, was shown to be upregulated upon an increase in intracellular  $O_2^{\bullet-}$ , thereby blunting death receptor signaling [131].

#### 4. Redox Dysregulation and Mitochondrial Metabolism in Cancer

**4.1. Warburg and Reverse Warburg Effects.** Mitochondrial ROS can impact mitochondrial function, which can ignite further imbalance in redox homeostasis. The main mitochondrial function is the metabolism of organic substrates such as glucose, lipids, amino acids, and nucleic acids. In terms of energy production from cellular respiration, the metabolism of glucose for ATP has been observed to be dysregulated in cancer cells that are actively proliferating. As mentioned earlier, the Warburg effect postulated that cancer cells rely on aerobic glycolysis to rapidly produce energy for proliferation due to mitochondria dysfunction and suppression of OXPHOS. Pyruvate is an end-product of glycolysis that exerts antioxidant effect and protects the mitochondria from oxidative damage [132]. Wang et al. reported that pyruvate is able to inhibit  $O_2^{\bullet-}$  production in the presence of mitochondrial complex inhibitors and inhibits mitochondrial ROS generation to a greater extent compared to intracellular ROS levels [132]. Moreover, it was observed that intracellular increase in ROS levels leads to inhibition of pyruvate kinase M2 isoform (PKM2), a glycolytic enzyme that plays a vital role in catalyzing the conversion of phosphoenolpyruvate to pyruvate [133]. PKM2 has also been reported to serve as a metabolic sensor under glucose-starved conditions, as inhibition of PKM2 was observed to enhance metabolic activity and protect against apoptotic cell death [134].

However, this milestone discovery is challenged by studies demonstrating that glycolysis accounted for less than half of the ATP produced in multiple malignant cell lines [135]; OXPHOS still contributed the majority of ATP during normoxia and lesser than 50% during hypoxia in malignant breast and cervical cell lines [136, 137]. The effectively coined “Reverse Warburg Effect” has brought attention to the tumor microenvironment (TME), where stromal cells such as cancer-associated fibroblasts (CAFs) could be responsible for allowing malignant cells to produce ATP while reducing reliance on OXPHOS [138, 139]. Oxygen becomes a limiting factor when proliferation is uncontrolled, producing ROS such as  $H_2O_2$  to initiate CAF production of high energy metabolites such as pyruvate and lactate. These products are then transported to the tumor cells to be funneled into OXPHOS to produce a significant amount of ATP [140], demonstrating altered metabolism within tumor mitochondria. In fact, OXPHOS has been shown to be upregulated in ovarian cancer stem cells [141] as well as drug-resistant cancers [142–144] which give rise to an emerging number of studies on targeting OXPHOS in cancer therapy.

**4.2. ROS and Nuclear-Encoded Mitochondrial Proteins.** Nuclear-encoded mitochondria genes are susceptible to oxidative damage (Figure 3). Some of the protein products of nuclear-encoded mitochondrial genes include *SDH* [4, 5] and *FH* [5]. Inactivation of these enzymes by  $H_2O_2$  [145] or by somatic mutations in the enzymatic subunits [5] could reduce the rate of ATP and ROS production during OXPHOS. The inactivation of these enzymes could trigger cellular transformation, as evidenced by the association of *SDH* subunit mutations with paraganglioma [146, 147]. *SDH*, also known as complex II of the mitochondrial ETC, is an important ROS-producing site, which either generates ROS directly from the release of electrons from the conversion of FAD to  $FADH_2$  under low succinate concentration condition, or indirectly through reverse electron transfer (RET) in the presence of high concentration of succinate, forcing electrons through complex I [148]. Loss of function mutations in *SDH* reported in HPGL/PCC cancer could lead to an accumulation of succinate and ROS which leads to further oxidative stress and DNA hypermutations [149].

Similarly, altered FH activity has been implicated in renal cell carcinoma and uterine leiomyoma [150–152]. Patients with germline mutations in *FH* were also observed to have a higher risk in cancers such as renal cell cancer, breast, and bladder cancer [134]. As FH catalyzes the conversion of fumarate to malate, loss-of-function mutations of *FH* lead to fumarate build up, which can activate Nrf2 by inhibiting Keap1 [153]. The protective effect of the genes regulated by Nrf2 downstream of the ARE, such as heme oxygenase 1 (*HMOX1*), promote tumorigenesis by alleviating oxidative stress [154, 155].

In addition, nuclear-encoded *Suppressor of Var1 (SUV3)* RNA helicase is responsible for mitochondria DNA (mtDNA) replication and murine haploinsufficiency of *SUV3* allele predisposes to tumorigenesis *in vivo* [156], indicating its role as a tumor suppressor. Furthermore, complete knockdown of *SUV3* results in a decrease in mtDNA copy number and, subsequently, together with an increase in  $O_2^{\bullet-}$  formation and enhanced tumorigenesis [157]. *SUV3* knockdown also observed change in mitochondrial morphology and eventual senescence [156].

**4.3. ROS and Mitochondria-Encoded Proteins.** Since mitochondria are an important source of ROS, mtDNA is highly vulnerable to oxidative stress-induced damage in the prooxidant milieu of cancer cells, as mtDNA is not protected by histone proteins [158]. The mitochondrial genome encodes for 13 OXPHOS subunits, 22 tRNAs, and 2 rRNAs [159], including cytochrome proteins that are critical for optimal functioning of the ETC (Figure 3).

**4.3.1. Cytochrome c Oxidase (COX).** In particular, mitochondria-encoded COX displays antioxidant activity to lower ROS levels, which prevents further oxidative damage [160]. Furthermore, studies have also reported a decrease in COX activity and expression, associated with increased ROS production in human colon adenocarcinoma [161, 162] and murine hepatoma cells [163].

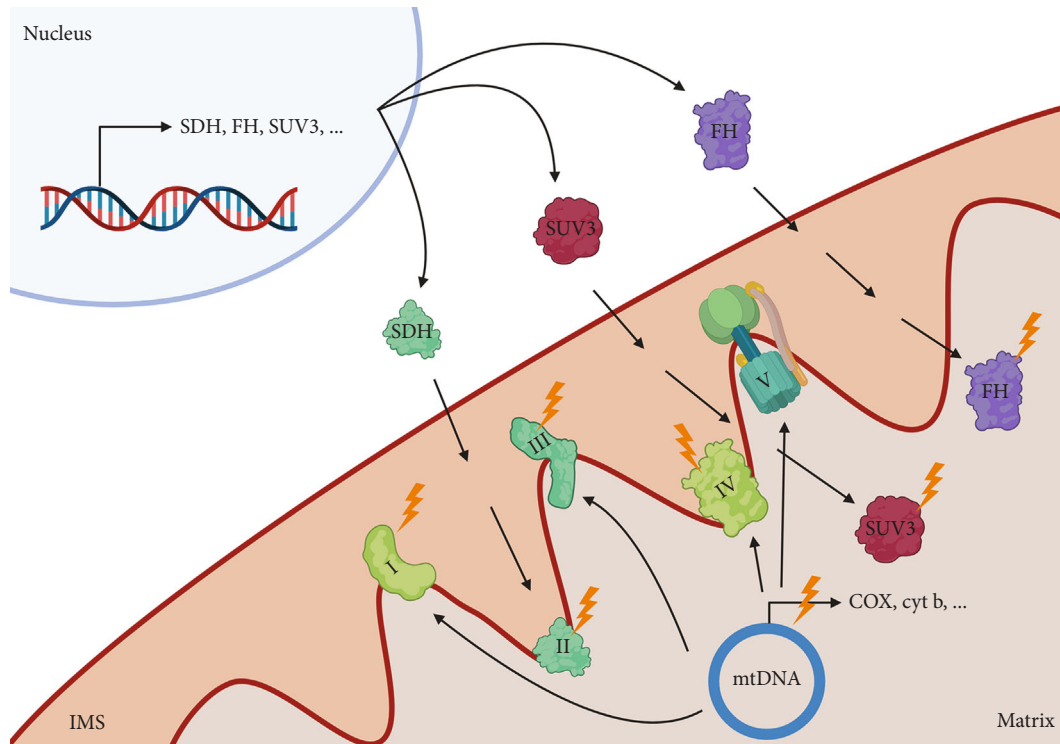


FIGURE 3: Nuclear-encoded and mitochondrial-encoded mitochondria regulatory genes are susceptible to oxidative damage. Nuclear-encoded mitochondrial genes such as SDH, which makes up complex II of the ETC, are assembled and transported into the mitochondria and susceptible to inactivation by ROS such as  $H_2O_2$ . In addition, FH generates energy for the cells by converting fumarate into malate in the TCA cycle, and SUV3 is a nuclear-encoded ATP-dependent DNA/RNA helicase and function as a tumor suppressor. The mtDNA encodes for subunits of the ETC and regulatory proteins that are important for the assembly and function of the ETC. The mtDNA is highly susceptible to oxidative stress-induced damage, leading to OXPHOS dysregulation. Figure created with biorender.com.

**4.3.2. Cytochrome *b*.** MtDNA also codes for *cytochrome b*, which is the only component of complex III encoded by the mtDNA. Cytochrome *b* is found to be mutated in bladder cancer, which leads to increased ROS production coupled with amplified NF- $\kappa$ B signaling and tumor cell growth. Overexpression of *mtCYB* was associated with increased tumor growth and invasion *in vivo*. Interestingly, inhibition of ROS inhibited cell proliferation driven by NF- $\kappa$ B, thus, suggesting that increase in ROS upon *cytochrome b* mutation is involved in mediating cell proliferation in bladder cancer [164].

**4.3.3. Mitochondrial-Encoded Complex I.** The mtDNA codes for 7 subunits of the complex I—ND1, ND2, ND3, ND4, ND4L, ND5, and ND6. Mutations in mtDNA most commonly affect complex I genes and induce feedback induction of Warburg effect and AMPK activation. Iommarini et al. also demonstrated that different degrees of complex I dysfunction induced differential oxidative stress. Severe mutations lead to complex I disassembly, inhibiting the transfer of electrons to ROS-generating complexes leading to inhibition of ROS generation [165].

**4.3.4. ATP Synthase.** mtDNA codes for 2 subunits of ATP synthase—MT-ATP6 and MT-ATP8. Mutations occur at two amino acid positions 8993T>G and 8993T>C, which

has reportedly caused 90% and 70% deficit, respectively, in ATP synthase function due to inefficient assembly and stability of the subunit [166]. Mutations in ATP6 and ATP8 genes were observed in breast cancer although functional effect of the mutation has yet to be studied widely in the model [167].

**4.4. Effect of Aberrant ROS Signaling on Mitochondrial Apoptotic Pathway.** Altered redox metabolism also regulates mitochondrial (intrinsic) apoptotic signaling. Singh et al. demonstrated that  $H_2O_2$  induces Bax expression with a reciprocal decrease in antiapoptotic protein Bcl-xL in HeLa cells, which triggered cytochrome *c* release from mitochondria [168]. This is supported by several studies demonstrating the importance of  $H_2O_2$  as a signaling molecule for apoptosis induction [169–171]. On the other hand,  $H_2O_2$  was observed to inhibit drug-induced apoptosis through the depletion of cellular energy (ATP) by activation of PARP [172, 173], hence, suggesting a dual role of  $H_2O_2$  in regulating apoptotic signaling. Other redox-sensitive proteins such as VDAC and ANT can stimulate MOMP and cytochrome *c* release upon exposure to  $H_2O_2$  or  $O_2^{\bullet -}$  [169, 174, 175]. Furthermore, increased  $H_2O_2$  levels coincide with increased FADD intermembrane translocation and FasL, which activate initiator caspase-8 in the extrinsic apoptotic pathway,

whereas decreasing  $O_2^{\bullet -}$  sensitizes Bcl-2 overexpressing cancer cells to receptor or drug-induced apoptosis [176, 177]. Collectively, these findings highlight the critical role of an altered redox state in mitochondria-dependent apoptotic execution.

## 5. Targeting Mitochondria as a Therapeutic Strategy

Since cancer cells harness ROS at a level that stimulates proliferative and survival signaling without being cytotoxic, therapeutics aim to create oxidative stress to drive transformed cells towards apoptotic clearance. Here, we compare several compounds developed to target mitochondria and ROS production in cancer (Table 1, Figure 4). The oxidative burden generated can also confer sensitivity to other anti-cancer drugs.

**5.1. Complex I Inhibitors.** Although metformin was developed as a diabetic drug, there is an increasing interest in its anticancer properties through inhibition of complex I of the ETC, which disrupts ATP production by OXPHOS. Metformin was also reported to indirectly reduce mitogenic insulin growth factors when controlling blood glucose and preventing PI3K activation of cell proliferation [178]. Metformin exerts antioxidant properties through inhibition of protein kinase C activity and, in turn, leading to decreased ROS production [179]. The clinical efficacy was reflected in the phase III randomized trial breast cancer patients where the compound displayed increased progression-free survival (NCT01101438). In addition, the efficacy of metformin in combination with chemotherapy such as gemcitabine as well as targeted therapies such as erlotinib such as tyrosine kinase inhibitors (TKI) has been evaluated in phase II clinical trials in pancreatic cancer patients (NCT01210911), although more studies need to be conducted to evaluate the safety and efficacy of combination therapies with metformin.

Small molecule inhibitor IACS-010759 also attacks complex I, displaying *in vitro* benefits in both AML and CLL. AML cells were sensitive to IACS-010759 treatment where cell viability and oxygen consumption rate were decreased [180]. In CLL, tumor cells exposed to IACS-010759 had lower OXPHOS rates but adapted by relying on glycolysis for survival, highlighting that maximum IACS efficacy can be achieved by inhibiting both glycolysis and OXPHOS [181]. A recent phase I trial also pointed out the antitumor potential of IACS-010759 in pancreatic cancer, triple-negative breast cancer, and SWI/SNF-related tumors (NCT03291938) [182]. Combination therapy of complex I inhibitor IACs-010759 with vinorelbine was shown to have a synergistic effect in primary cells of AML patients [183]. Currently, IACS-010759 is also in phase I study in relapsed/refractory AML (NCT02882321) and variety of solid tumors (NCT03291938) as well as BCL2 inhibitor venetoclax (ABT-199). Dual therapy of IACS-010759 with venetoclax has shown elimination of leukemic cells in *in vitro* and *in vivo* AML models by inhibiting mitochondrial respiration and BCL2/VDAC interaction [184]. IACS-010759 has also shown prolonged survival effect in PD-1 resistant NSCLC

in combination with radiation therapy and anti-PD1 by inhibiting RT-induced immunosuppression [185].

OPB-51602 (OPB) is another novel complex I inhibitor that has shown high specificity and produced antitumor effects in drug-resistant cancer cell lines [143]. A previous phase I trial on OPB's clinical effectiveness showcased preliminary benefits of OPB in TKI-resistant cancers [186]. Although known to restrict respiration by interfering with STAT3 signaling [187], Hirpara et al. have demonstrated that OPB specifically inhibits complex I due to increase in  $O_2^{\bullet -}$  production and reduction in  $NAD^+/NADH$  ratio, an indicator of complex I inhibition. Furthermore, OPB proved effective in patients with TKI-resistant EGFR mutation NSCLC, by reducing tumor burden significantly [143]. OPB was also shown to have significant sensitizing effect with TKI in variety of cancer cells [186].

**5.2. ATP Synthase Inhibitor.** The final OXPHOS step can also be targeted by ATP synthase inhibitors such as oligomycin [188]. The disruption of ATP production similarly causes  $O_2^{\bullet -}$  formation from resultant electron leaks in the ETC. Oligomycin is found to specifically inhibit membrane-bound  $F_o$  region of ATPase [189]. Recent studies demonstrate how oligomycin helps resensitize leukemic cells to TKI treatment [190]. The treated leukemic cells were subsequently responsive to Bcr/Abl inhibition, where they had decreased ATP production and increased superoxide production and apoptosis occurrences [190].

A novel ATP synthase inhibitor that has similar effects to oligomycin is positively charged Gboxin, which interacts with the ETC complexes I, II, IV, and ATP synthase to restrict ATP synthase activity in glioblastoma (GBM) [191]. Gboxin-sensitive GBM cells lacked expression of mitochondrial permeability transition pore (mPTP) that could prevent ROS accumulation in the mitochondria, hence, making them susceptible to Gboxin. Gboxin significantly increased mitochondrial membrane potential, with contrast to complex I and III poisons (rotenone and antimycin respectively) which reduced the membrane potential [191]. Gboxin analogue (S-Gboxin) for *in vivo* studies also demonstrated inhibited GBM growth, indicating promising antitumor potential [191].

**5.3. Mitochondria Biogenesis Targeting Compounds.** On top of direct inhibition of the mitochondrial ETC complex activity, there is an emerging interest in targeting mitochondria biogenesis, which is a process defined by an increase in mitochondria mass through the increase in size and number of mitochondria in cells. Mitochondria alleviate oxidative stress through the regulation of several processes including the biogenesis of new mitochondria and mitochondria fusion/fission processes [192]. Although mitochondria biogenesis is regulated by several key factors including PPAR gamma coactivator-1 $\alpha$  (PGC-1 $\alpha$ ), Nrf1, Nrf2, and mitochondria transcription factor A (TFAM), direct inhibitors to these regulators have yet to be developed. Nevertheless, several drugs have been reported to show a direct impact on mitochondria biogenesis.



TABLE 1: Summary of the various mitochondrial-related therapeutics in targeting tumor progression.

| Category                                    | Drug name  | Mechanism   | References   |
|---|--|---|--|
| Complex I inhibitors                        | Metformin  | Inhibits complex I, disrupting ATP production by OXPHOS.  | [170]  |
|   | IACS-010759                                      |   | [171–173]  |
|   | OPB-51602  |   | [174, 175]   |
| ATP synthase inhibitors                     | Oligomycin                                       | Restricts ATP synthase, increases mitochondria membrane potential.  | [178, 179]   |
|   | Gboxin   |   | [180]  |
| Mitochondria biogenesis targeting compounds | Gamitinib  | Specifically inhibits tumor mitochondrial HSP90 and induces mitochondria apoptosis.   | [182–185]  |
|   | Doxycycline                                      | Inhibits mitochondrial biogenesis in bacterial and mammalian cells and reduces mitochondrial translation.                           | [187, 188]   |
|   |  |   |  |
| Inhibitors of mitochondria dynamics         | Mitochondrial division inhibitor (e.g., Mdivi 1) | Inhibits mitochondrial fission which prevents cell cycle progression and hence suppresses tumor growth.                             | [191–194]  |
|   | Manganese porphyrins (e.g., MnTnHex 2 PyP5+)     | Mimics MnSOD activity; increases cellular ROS levels, and ultimately induces cell death. Also inhibits cell migration and invasion. | [198, 199]   |
| SOD mimetics                                | Nitroxides (e.g., Mito TEMPOL)                   | Antioxidative function; induces DNA damage, apoptosis, and mitochondrial distress in tumors.  | [200, 201]   |
| Bcl-2 inhibitors                            | ABT-263 (Navitoclax)                             | BH3 mimetic that targets antiapoptotic Bcl-2 and Bcl-xL.  | [206, 207]   |
|   | ABT-737  |   |  |
|   | ABT-199 (Venetoclax)                             |   | BH3 mimetic that has affinity for antiapoptotic Bcl-2. |

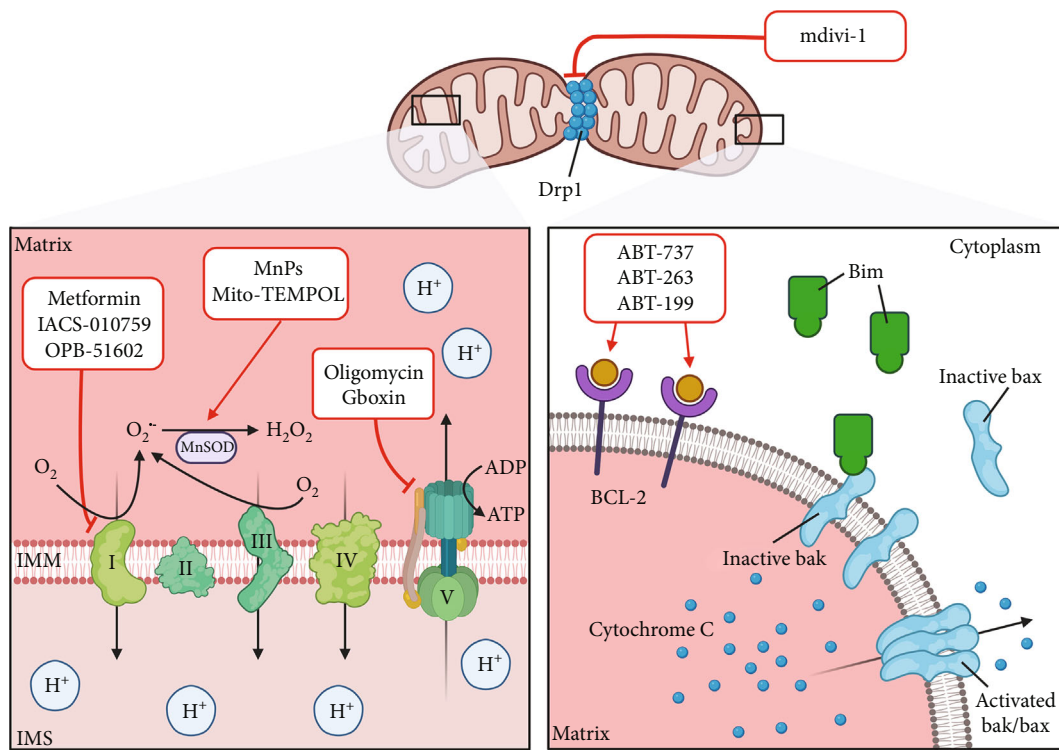


FIGURE 4: Mitochondrial-directed therapeutic strategies. For drugs that target the mitochondrial matrix, components of the electron transport chain and MnSOD are mainly affected, whereas drugs targeting cytosolic regulatory proteins/factors such as the balance between the pro- and antiapoptotic members of the Bcl-2 family affect apoptotic execution. Figure created with biorender.com.

Gamitrinib is a small molecule mitochondrial HSP90 inhibitor that has shown promising antitumor effects in various cancer types including glioblastoma [193, 194] and prostate cancer [195]. Unlike other general HSP90 antagonists, gamitrinib selectively targets tumor mitochondria and does not affect the HSP90 homeostasis in other cellular compartments other than the mitochondria and does not induce toxicity to normal cells. Gamitrinib was observed to induce mitochondria apoptosis and a loss of inner membrane potential, which leads to the release of mitochondrial cytochrome c [196]. Gamitrinib has also been reported to lead to a decrease in mtDNA copy number, mitochondria mass, and respiration in melanoma cells, which is indicative of an inhibition of mitochondria biogenesis. Pretreatment with gamitrinib was able to sensitize vemurafenib-resistant A375 cells to vemurafenib treatment through inhibition of mitochondria biogenesis and activity [197].

Doxycycline is an FDA-approved antibiotic used in the treatment of various infections through targeting bacterial mitochondria. In cancer, doxycycline was observed to limit self-renewal ability of cancer stem cells (CSCs) in several types of cancers [198]. In addition to bacterial mitochondria, doxycycline was shown to inhibit mitochondrial biogenesis in mammalian cells; doxycycline treatment decreased mtDNA copy number and mitochondrial translation, eventually leading to cell death [199].

**5.4. Inhibition of Mitochondria Dynamics.** Mitochondria dynamics refer to the balance between fusion and fission that maintain mitochondria morphology and number in mammalian cells. Mitochondria fission is elevated under stress conditions, which induces mitochondrial fragmentation [200]. Impairment of mitochondria fusion and fission results in structural changes, cellular dysfunction, and damage [201]. Mitochondrial division inhibitor (mdivi-1) was reported to inhibit Drp1-dependent mitochondria fission and oxidative metabolism and impair cell proliferation in lung cancer [202]. Mdivi-1 was also reported to inhibit complex I function and modulate intracellular  $\text{Ca}^{2+}$  signaling [203]. The inhibition of mitochondria fission by mdivi-1 reduces tumor growth through prevention of cell cycle progression [204] and cell migration [205], suggesting mitochondrial dynamics as one of the targets and its inhibition as a way to suppress cancer cell growth.

**5.5. SOD Mimetics.** MnSOD (SOD2) is shown to be frequently dysregulated in several cancers, and thus, there is an emerging interest in complexes that mimic MnSOD (MnSOD mimetics) as therapeutic agents against cancers with suppressed MnSOD activity. SOD mimetics are modulators of cellular redox environment, and several compounds have been examined and reviewed in detail by Vincent et al., Batinic-Haberle et al., and Miriyala et al. [206–208]. In this section, we aim to evaluate the reported antitumor properties of some promising therapeutic MnSOD mimetics.

Manganese porphyrins (MnP) are Mn-based SOD mimetics and have been identified as potential therapeutics due to their high SOD-like activity. In addition, MnP have

been shown to regulate signaling pathways, which in turn modulate cellular processes such as apoptosis and proliferation. With excellent bioavailability and specificity for targeting mitochondria, MnTnHex-2-PyP<sup>5+</sup> is considered one of the most promising therapeutic SOD mimics. Treatment with MnTnHex-2-PyP<sup>5+</sup> increases cellular ROS levels and induces cell death in human renal cancer cells, 786-O [209]. Furthermore, MnTnHex-2-PyP<sup>5+</sup> was shown to inhibit cell migration, chemotaxis, and invasion in doxorubicin-treated breast cancer, demonstrating therapeutic potential in several cancer models [210]. Interestingly, another MnSOD mimic, MnTnBuOE-2-PyP<sup>5+</sup> (MnBuOE/BMX-001) has been reported to enhance carbenoxolone- (CBX-) mediated tumor necrosis factor-related apoptosis-inducing ligand- (TRAIL-) induced apoptosis in GBM cells. MnBuOE also demonstrated an enhanced mitochondrial over cytosolic accumulation [211]. BMX-001 is currently in two Phase II studies—one in combination with radiation therapy and tamazolamide in glioblastoma and high-grade glioma and another in patients with multiple brain metastases (MBM) undergoing whole brain radiation therapy. In addition, the safety and tolerability of BMX-001 are currently being evaluated in two Phase I/II studies using a combination approach of BMX-001, standard radiation therapy (RT), and cisplatin in head and neck cancer patients to reduce radiation-induced mucositis and xerostomia, and in combination with 5-FU in anal squamous cell carcinoma (ASCC) (ClinicalTrials: NCT02655601, NCT02990468, NCT03386500, NCT03608020) [212].

Nitroxides are weak SOD mimetics which have been used as an antioxidant both *in vivo* and *in vitro*. Mito-TEMPOL is a mitochondria-targeted derivative of TEMPOL, which catalyzes the dismutation of  $\text{O}_2^{\bullet}$  [213]. Mito-TEMPOL possesses a triphenylphosphonium group which enhances its accumulation in the mitochondria. In a study by Dickey et al., Mito-TEMPOL treatment led to a reduction in tumor size as a single agent and enhanced the antitumor effect of doxorubicin in a murine syngeneic breast cancer model. Furthermore, Mito-TEMPOL was also observed to induce DNA damage, apoptosis, and mitochondrial distress in the tumors [214], highlighting its potential as a therapeutic antioxidant in cancer.

**5.6. Bcl-2 Inhibitors.** Antiapoptotic proteins like Bcl-2 are implicated in the intrinsic apoptotic pathway. The proteins prevent the oligomerization of effector Bax/Bak proteins into a membrane pore, disallowing the release of cytochrome c [215] and modulate ROS production through regulation of mitochondria respiration [128, 216]. Cytochrome c is responsible for the activation of downstream caspase 3 and 8 which result in apoptosis [217]. BH3-only proteins (e.g., Bim, tBid, and PUMA) naturally induce apoptosis by inhibiting Bcl-2 proteins directly, facilitating MOMP for cytochrome c release [218]. The role that Bcl-2 plays in apoptosis makes it an attractive drug target for novel inhibitors that aim to induce apoptosis in tumor cells. BH3 mimetics such as ABT-263 (Navitoclax) and ABT-737 targets both the main antiapoptotic proteins, Bcl-2 and Bcl-xL [219]. ABT-737 displayed antitumor potential in animal hematological cancer models, while a more stable ABT-263

has been tested in phase I and II trials for human hematological cancers too [220].

However, thrombocytopenia is a significant toxicity that challenges the effectiveness of ABT-263 and ABT-737 [220, 221]. To combat this toxicity, a recently approved BH3 mimetic called ABT-199 (venetoclax) is proving to be specific for Bcl-2, possessing subnanomolecular affinity for Bcl-2, while not targeting Bcl-xL [222]. ABT-199 was shown to display a significant response rate in a phase I trial with CLL patients, with common side effects like diarrhea and neutropenia [223]. Phase II trials for ABT-199 on high-risk relapsed and refractory AML patients demonstrated promising clinical benefits with tolerable safety profile [224]. ABT-199 was also effective in acute leukemia for both in vitro [225] and in vivo mouse studies [226]. BH3 mimetics displace BH3-only sensitizers such as Bim from binding with Bcl-2, directly inhibiting Bcl-2 and allowing free Bim to activate Bax/Bak for cytochrome release [227, 228]. However, a recent publication posits that BH3-only proteins can interact with Bax/Bak but is not needed for apoptosis [229], which is consistent with an alternative BH3-only indirect activation model [230]. Although the exact mechanism for BH3 mimetics is unclear, the clinical benefits make them attractive antitumor mitochondrial therapies.

## 6. Concluding Remarks

A multitude of biological responses and signaling pathways impacted by altered cellular redox state is a testament to the crucial role that oxidative metabolism plays in cancer cell fate determination. Outstanding contributions over the past couple of decades have clearly highlighted the dichotomy of redox-mediated responses and their effect(s) on myriad processes associated with carcinogenesis and its progression, such as regulation of gene expression, genome instability and mutagenesis, structural and functional modifications of proteins, cell growth and proliferation, cell cycle progression, cellular senescence, and apoptosis execution and resistance. To that end, an intricate crosstalk between altered redox state (and mitochondrial metabolism) and oncogenic or tumor suppressor proteins has been elegantly demonstrated using various model systems. This has seen the emergence of a new paradigm in which cellular redox metabolism appears to dictate cancer cell fate decisions and as such a highly attractive target for novel anticancer drug design and development. The latter include therapeutics to specifically target mitochondrial metabolism, which is a potent source of intracellular ROS. Some of these strategies are already undergoing clinical evaluation such as the Mitocans and MnSOD mimetics. Despite these encouraging developments, there also remain important unresolved issues, such as the design of specific probes for the temporal and spatial detection *in vivo* of various reactive oxygen intermediates, the development of more effective oxidants/anti-oxidants with good therapeutic indices, and the selective delivery of mitochondria-targeted agents. Surely, the intricate interplay between mitochondria and cellular redox state in cancer cell fate is beginning to be realized and exploited for the design of ROS-targeted therapies.

## Abbreviations

|           |   |
|-----------|---|
| 4-HNE:    | 4-Hydroxynonenal                              |
| 8-oxo-dG: | 8-Oxo-2'-deoxyguanosine                       |
| a-KG:     | Alpha-ketoglutarate                           |
| a-KGDH:   | Alpha ketoglutarate dehydrogenase             |
| ADP:      | Adenosine diphosphate                         |
| Akt:      | Protein kinase B                              |
| ALCL:     | Anaplastic large cell lymphoma                |
| ALL:      | Acute lymphocytic leukemia                    |
| AML:      | Acute myeloid leukemia                        |
| AMP:      | Adenosine monophosphate                       |
| AMPK:     | AMP-activated protein kinase                  |
| ANT:      | Adenine nucleotide translocase                |
| ARE:      | Antioxidant response element                  |
| ASK-1:    | Apoptosis signal-regulating kinase 1          |
| ATP:      | Adenosine triphosphate                        |
| Bak:      | BCL-2 associated X protein                    |
| Bax:      | BCL-2 homologous antagonist killer            |
| BCL-2:    | B-cell lymphoma 2                             |
| BCL-XL:   | BCL- extra large                              |
| Bcr/Abl:  | Breakpoint cluster/Abelson                    |
| BH3:      | BCL-2 homology 3 region                       |
| Bim:      | BCL-2-like protein 11                         |
| CAFs:     | Cancer-associated fibroblasts                 |
| c-FLIP:   | CASP8 and FADD-like apoptosis regulator       |
| CKI:      | Cyclin-dependent kinase inhibitor             |
| CML:      | Chronic myelogenous leukemia                  |
| CoQ:      | Coenzyme Q                                    |
| COX:      | Cyclooxygenase                                |
| DDR:      | DNA damage response                           |
| DNA:      | Deoxyribonucleic acid                         |
| dNTPs:    | Nucleoside triphosphate                       |
| ECM:      | Extracellular matrix                          |
| EGFR:     | Epidermal growth factor receptor              |
| EMT:      | Epithelial-mesenchymal transition             |
| ERK:      | Extracellular-signal regulated kinase         |
| ETC:      | Electron transport chain                      |
| FAD:      | Flavin adenine dinucleotide                   |
| FADD:     | Fas-associated death domain protein           |
| FasL:     | Fas ligand                                    |
| FH:       | Fumarate hydratase                            |
| FMN:      | Flavin mononucleotide                         |
| GBM:      | Glioblastoma                                  |
| GSH:      | Glutathione                                   |
| GTPase:   | Guanosine trisphosphate hydrolase             |
| HIF-1:    | Hypoxia-inducible factor 1                    |
| HMOX-1:   | Haem oxygenase 1                              |
| IKK:      | I $\kappa$ B kinase                           |
| IL-1:     | Interleukin 1                                 |
| IL-6:     | Interleukin 6                                 |
| IMS:      | Intermembrane space                           |
| JNK:      | c-Jun N-terminal kinase                       |
| Keap:     | Kelch-like ECH-associated protein 1           |
| MAPK:     | Mitogen-activated protein kinase              |
| MMPs:     | Matrix metalloproteases                       |
| MOMP:     | Mitochondrial outer membrane permeabilization |
| mPTP:     | Mitochondrial permeability transition pore    |
| mTOR:     | Mammalian target of rapamycin                 |

|                    |  |
|--------------------|--|
| NAD:               | Nicotinamide adenine dinucleotide                              |
| NADPH:             | Nicotinamide adenine dinucleotide phosphate hydrogen           |
| NF- $\kappa$ B:    | Nuclear factor kappa-light-chain-enhancer of activated B cells |
| NOX:               | NAPH oxidase   |
| Nrf2:              | Nuclear factor erythroid 2-related factor 2                    |
| NSCLC:             | Nonsmall cell lung cancer                                      |
| OCT:               | Organic cation transporter                                     |
| OIS:               | Oncogene-induced senescence                                    |
| OXPPOS:            | Oxidative phosphorylation                                      |
| PFK-1:             | Phosphofructokinase 1  |
| PI3K:              | Phosphoinositide 3-kinase                                      |
| PIP <sub>3</sub> : | Phosphatidylinositol (3,4,5)-triphosphate                      |
| PPP:               | Pentose phosphate pathway                                      |
| PTEN:              | Phosphatase and tensin homolog                                 |
| PUMA:              | p53 upregulated modulator of apoptosis                         |
| RNA:               | Ribonucleic acid   |
| ROS:               | Reactive oxygen species  |
| SASP:              | Senescence-associated secretory phenotype                      |
| SIPS:              | Stress-induced premature senescence                            |
| SOD:               | Superoxide dismutase   |
| SUV:               | Suppressor of Var1   |
| tBid:              | Truncated BH3-interacting domain death agonist                 |
| TCA:               | Tricarboxylic acid cycle                                       |
| TIGAR:             | TP53-induced glycolysis and apoptosis regulator                |
| TKI:               | Tyrosine kinase inhibitor                                      |
| VDAC:              | Voltage-dependent anion channel                                |
| VEGF:              | Vascular endothelial growth factor.                            |

## Data Availability

It is a review paper and no data is included.

## Conflicts of Interest

The authors declare that they have no conflicts of interest.

## Authors' Contributions

Brittney Joy-Anne Foo and Jie Qing Eu contributed equally as first authors.

## Acknowledgments

The authors wish to acknowledge the contributions of those whose work might have been inadvertently overlooked. Shazib Pervaiz (SP) is supported by the National Medical Research Council of Singapore (NMRC CIRG/1433/2015 and OFIRG/0041/2017), and a USPC-NUS 2021 award.

## References

- [1] L. Margulis and D. Sagan, *Origins of Sex: Three Billion Years of Genetic Recombination*, Yale University Press, 1990.
- [2] L. Griparic and A. M. van der Blik, "The many shapes of mitochondrial membranes," *Traffic*, vol. 2, no. 4, pp. 235–244, 2001.
- [3] S. Cardaci and M. R. Ciriolo, "TCA cycle defects and cancer: when metabolism tunes redox state," *International Journal of Cell Biology*, vol. 2012, Article ID 161837, 9 pages, 2012.
- [4] M. W. van Gisbergen, A. M. Voets, M. H. Starmans et al., "How do changes in the mtDNA and mitochondrial dysfunction influence cancer and cancer therapy? Challenges, opportunities and models," *Mutation Research/Reviews in Mutation Research*, vol. 764, pp. 16–30, 2015.
- [5] A. King, M. A. Selak, and E. Gottlieb, "Succinate dehydrogenase and fumarate hydratase: linking mitochondrial dysfunction and cancer," *Oncogene*, vol. 25, no. 34, pp. 4675–4682, 2006.
- [6] J. F. Turrens, "Mitochondrial formation of reactive oxygen species," *The Journal of physiology*, vol. 552, no. 2, pp. 335–344, 2003.
- [7] U. Landmesser, D. G. Harrison, and H. Drexler, "Oxidant stress—a major cause of reduced endothelial nitric oxide availability in cardiovascular disease," *European Journal of Clinical Pharmacology*, vol. 62, no. S1, pp. 13–19, 2006.
- [8] A. Panday, M. K. Sahoo, D. Osorio, and S. Batra, "NADPH oxidases: an overview from structure to innate immunity-associated pathologies," *Cellular & molecular immunology*, vol. 12, no. 1, pp. 5–23, 2015.
- [9] K. Bedard and K. H. Krause, "The NOX family of ROS-generating NADPH oxidases: physiology and pathophysiology," *Physiological reviews*, vol. 87, no. 1, pp. 245–313, 2007.
- [10] N. A. Graham, M. Tahmasian, B. Kohli et al., "Glucose deprivation activates a metabolic and signaling amplification loop leading to cell death," *Molecular systems biology*, vol. 8, no. 1, p. 589, 2012.
- [11] T. Fukai and M. Ushio-Fukai, "Cross-talk between NADPH oxidase and mitochondria: role in ROS signaling and angiogenesis," *Cells*, vol. 9, no. 8, p. 1849, 2020.
- [12] J. Smeitink, L. van den Heuvel, and S. DiMauro, "The genetics and pathology of oxidative phosphorylation," *Nature Reviews Genetics*, vol. 2, no. 5, pp. 342–352, 2001.
- [13] L. Iommarini, M. A. Calvaruso, I. Kurelac, G. Gasparre, and A. M. Porcelli, "Complex I impairment in mitochondrial diseases and cancer: parallel roads leading to different outcomes," *The international journal of biochemistry & cell biology*, vol. 45, no. 1, pp. 47–63, 2013.
- [14] V. Raimondi, F. Ciccarese, and V. Ciminale, "Oncogenic pathways and the electron transport chain: a dangerROS liaison," *British journal of cancer*, vol. 122, no. 2, pp. 168–181, 2020.
- [15] Y. Shang, F. Zhang, D. Li et al., "Overexpression of UQCRC2 is correlated with tumor progression and poor prognosis in colorectal cancer," *Pathology-Research and Practice*, vol. 214, no. 10, pp. 1613–1620, 2018.
- [16] F. Gao, Q. Liu, G. Li et al., "Identification of ubiquinol cytochrome c reductase hinge (UQCRH) as a potential diagnostic biomarker for lung adenocarcinoma," *Open biology*, vol. 6, no. 6, 2016.
- [17] D. E. Handy and J. Loscalzo, "Redox regulation of mitochondrial function," *Antioxidants & redox signaling*, vol. 16, no. 11, pp. 1323–1367, 2012.
- [18] M. Ogrunc, R. di Micco, M. Lontos et al., "Oncogene-induced reactive oxygen species fuel hyperproliferation and DNA damage response activation," *Cell Death & Differentiation*, vol. 21, no. 6, pp. 998–1012, 2014.

- [19] S. R. Lee, K. S. Yang, J. Kwon, C. Lee, W. Jeong, and S. G. Rhee, "Reversible Inactivation of the Tumor Suppressor PTEN by H<sub>2</sub>O<sub>2</sub>," *Journal of Biological Chemistry*, vol. 277, no. 23, pp. 20336–20342, 2002.
- [20] B. Halliwell and S. Chirico, "Lipid peroxidation: its mechanism, measurement, and significance," *The American journal of clinical nutrition*, vol. 57, no. 5, pp. 715S–725S, 1993.
- [21] S. P. LeDoux, W. J. Driggers, B. S. Hollensworth, and G. L. Wilson, "Repair of alkylation and oxidative damage in mitochondrial DNA," *Mutation research. DNA repair*, vol. 434, no. 3, pp. 149–159, 1999.
- [22] J. Kwon, S. R. Lee, K. S. Yang et al., "Reversible oxidation and inactivation of the tumor suppressor PTEN in cells stimulated with peptide growth factors," *Proceedings of the National Academy of Sciences*, vol. 101, no. 47, pp. 16419–16424, 2004.
- [23] P. Gao, H. Zhang, R. Dinavahi et al., "HIF-dependent antitumorogenic effect of antioxidants in vivo," *Cancer cell*, vol. 12, no. 3, pp. 230–238, 2007.
- [24] J. Richardson, K. A. Thomas, B. H. Rubin, and D. C. Richardson, "Crystal structure of bovine Cu, Zn superoxide dismutase at 3 Å resolution: chain tracing and metal ligands," *Proceedings of the National Academy of Sciences*, vol. 72, no. 4, pp. 1349–1353, 1975.
- [25] J. A. Tainer, E. D. Getzoff, J. S. Richardson, and D. C. Richardson, "Structure and mechanism of copper, zinc superoxide dismutase," *Nature*, vol. 306, no. 5940, pp. 284–287, 1983.
- [26] G. E. Borgstahl, H. E. Parge, M. J. Hickey, W. F. Beyer Jr., R. A. Hallewell, and J. A. Tainer, "The structure of human mitochondrial manganese superoxide dismutase reveals a novel tetrameric interface of two 4-helix bundles," *Cell*, vol. 71, no. 1, pp. 107–118, 1992.
- [27] M. L. Teoh-Fitzgerald, M. P. Fitzgerald, T. J. Jensen, B. W. Futscher, and F. E. Domann, "Genetic and epigenetic inactivation of extracellular superoxide dismutase promotes an invasive phenotype in human lung cancer by disrupting ECM homeostasis," *Molecular Cancer Research*, vol. 10, no. 1, pp. 40–51, 2012.
- [28] S. M. Tsai, M. F. Hou, S. H. Wu et al., "Expression of manganese superoxide dismutase in patients with breast cancer," *The Kaohsiung journal of medical sciences*, vol. 27, no. 5, pp. 167–172, 2011.
- [29] A. Fu, S. Ma, N. Wei, B. X. Xuan Tan, E. Y. Tan, and K. Q. Luo, "High expression of MnSOD promotes survival of circulating breast cancer cells and increases their resistance to doxorubicin," *Oncotarget*, vol. 7, no. 31, pp. 50239–50257, 2016.
- [30] Y. Hu, D. G. Rosen, Y. Zhou et al., "Mitochondrial Manganese-Superoxide Dismutase Expression in Ovarian Cancer," *Journal of Biological Chemistry*, vol. 280, no. 47, pp. 39485–39492, 2005.
- [31] A. P. Kumar, S. Y. Loo, S. W. Shin et al., "Manganese superoxide dismutase is a promising target for enhancing chemosensitivity of basal-like breast carcinoma," *Antioxidants & redox signaling*, vol. 20, no. 15, pp. 2326–2346, 2014.
- [32] S. Y. Loo, J. L. Hirpara, V. Pandey et al., "Manganese superoxide dismutase expression regulates the switch between an epithelial and a mesenchymal-like phenotype in breast carcinoma," *Antioxidants & redox signaling*, vol. 25, no. 6, pp. 283–299, 2016.
- [33] K. P. Bhabak and G. Mughesh, "Functional mimics of glutathione peroxidase: bioinspired synthetic antioxidants," *Accounts of chemical research*, vol. 43, no. 11, pp. 1408–1419, 2010.
- [34] E. Jablonska, J. Gromadzinska, B. Peplonska et al., "Lipid peroxidation and glutathione peroxidase activity relationship in breast cancer depends on functional polymorphism of GPX1," *BMC cancer*, vol. 15, no. 1, p. 657, 2015.
- [35] Z. Chen, T. Hu, S. Zhu, K. Mukaisho, W. El-Rifai, and D. F. Peng, "Glutathione peroxidase 7 suppresses cancer cell growth and is hypermethylated in gastric cancer," *Oncotarget*, vol. 8, no. 33, pp. 54345–54356, 2017.
- [36] S. Y. Min, H. S. Kim, E. J. Jung, E. J. Jung, C. D. Jee, and W. H. Kim, "Prognostic significance of glutathione peroxidase 1 (GPX1) down-regulation and correlation with aberrant promoter methylation in human gastric cancer," *Anticancer research*, vol. 32, no. 8, pp. 3169–3175, 2012.
- [37] A. Metere, F. Frezzotti, C. E. Graves et al., "A possible role for selenoprotein glutathione peroxidase (GPx1) and thioredoxin reductases (TrxR1) in thyroid cancer: our experience in thyroid surgery," *Cancer cell international*, vol. 18, no. 1, p. 7, 2018.
- [38] S. Kumari, A. K. Badana, M. M. G. S. G., and R. Malla, "Reactive oxygen species: a key constituent in cancer survival," *Biomarker insights*, vol. 13, 2018.
- [39] M. V. Clément and S. Pervaiz, "Intracellular superoxide and hydrogen peroxide concentrations: a critical balance that determines survival or death," *Redox Report*, vol. 6, no. 4, pp. 211–214, 2001.
- [40] H. Yin, L. Xu, and N. A. Porter, "Free radical lipid peroxidation: mechanisms and analysis," *Chemical reviews*, vol. 111, no. 10, pp. 5944–5972, 2011.
- [41] G. Brambilla, L. Sciabà, P. Faggini et al., "Cytotoxicity, DNA fragmentation and sister-chromatid exchange in Chinese hamster ovary cells exposed to the lipid peroxidation product 4-hydroxynonenal and homologous aldehydes," *Mutation Research/Genetic Toxicology*, vol. 171, no. 2-3, pp. 169–176, 1986.
- [42] G. Barrera, R. Muraca, S. Pizzimenti et al., "Inhibition of c-myc expression induced by 4-hydroxynonenal, a product of lipid peroxidation, in the HL-60 human leukemic cell line," *Biochemical and Biophysical Research Communications*, vol. 203, no. 1, pp. 553–561, 1994.
- [43] V. M. Fazio, G. Barrera, S. Martinotti et al., "4-Hydroxynonenal, a product of cellular lipid peroxidation, which modulates c-myc and globin gene expression in K562 erythroleukemic cells," *Cancer Research*, vol. 52, no. 18, pp. 4866–4871, 1992.
- [44] S. Dalleau, M. Baradat, F. Gueraud, and L. Huc, "Cell death and diseases related to oxidative stress: 4-hydroxynonenal (HNE) in the balance," *Cell Death & Differentiation*, vol. 20, no. 12, pp. 1615–1630, 2013.
- [45] E. Piskounova, M. Agathocleous, M. M. Murphy et al., "Oxidative stress inhibits distant metastasis by human melanoma cells," *Nature*, vol. 527, no. 7577, pp. 186–191, 2015.
- [46] M. Redza-Dutordoir and D. A. Averill-Bates, "Activation of apoptosis signalling pathways by reactive oxygen species," *Biochimica et Biophysica Acta (BBA)-Molecular Cell Research*, vol. 1863, no. 12, pp. 2977–2992, 2016.
- [47] K. Datta, P. Babbar, T. Srivastava, S. Sinha, and P. Chattopadhyay, "p53 dependent apoptosis in glioma cell

- lines in response to hydrogen peroxide induced oxidative stress," *The international journal of biochemistry & cell biology*, vol. 34, no. 2, pp. 148–157, 2002.
- [48] Y. Kitamura, T. Ota, Y. Matsuoka et al., "Hydrogen peroxide-induced apoptosis mediated by p53 protein in glial cells," *Glia*, vol. 25, no. 2, pp. 154–164, 1999.
- [49] M. Cordani, G. Butera, R. Pacchiana et al., "Mutant p53-associated molecular mechanisms of ROS regulation in cancer cells," *Biomolecules*, vol. 10, no. 3, p. 361, 2020.
- [50] S. Macip, M. Igarashi, P. Berggren, J. Yu, S. W. Lee, and S. A. Aaronson, "Influence of induced reactive oxygen species in p53-mediated cell fate decisions," *Molecular and cellular biology*, vol. 23, no. 23, pp. 8576–8585, 2003.
- [51] N. Y. L. Ngoi, A. Q. X. Liew, S. J. F. Chong, M. S. Davids, M.-V. Clement, and S. Pervaiz, "The redox-senescence axis and its therapeutic targeting," *Redox Biology*, vol. 45, article 102032, 2021.
- [52] G. Hewitt, D. Jurk, F. D. Marques et al., "Telomeres are favoured targets of a persistent DNA damage response in ageing and stress-induced senescence," *Nature communications*, vol. 3, no. 1, p. 708, 2012.
- [53] J. F. Passos, G. Saretzki, S. Ahmed et al., "Mitochondrial dysfunction accounts for the stochastic heterogeneity in telomere-dependent senescence," *PLoS biology*, vol. 5, no. 5, article e110, 2007.
- [54] Q. M. Chen, J. C. Bartholomew, J. Campisi, M. Acosta, J. D. Reagan, and B. N. Ames, "Molecular analysis of H<sub>2</sub>O<sub>2</sub>-induced senescent-like growth arrest in normal human fibroblasts: p53 and Rb control G1 arrest but not cell replication," *Biochemical Journal*, vol. 332, no. 1, pp. 43–50, 1998.
- [55] M. Serrano, A. W. Lin, M. E. McCurrach, D. Beach, and S. W. Lowe, "Oncogenic *ras* Provokes Premature Cell Senescence Associated with Accumulation of p53 and p16<sup>INK4a</sup>," *Cell*, vol. 88, no. 5, pp. 593–602, 1997.
- [56] P. Sun, N. Yoshizuka, L. New et al., "PRAK Is Essential for *ras*-Induced Senescence and Tumor Suppression," *Cell*, vol. 128, no. 2, pp. 295–308, 2007.
- [57] Q. Deng, R. Liao, B. L. Wu, and P. Sun, "High Intensity *ras* Signaling Induces Premature Senescence by Activating p38 Pathway in Primary Human Fibroblasts," *Journal of Biological Chemistry*, vol. 279, no. 2, pp. 1050–1059, 2004.
- [58] A. Takahashi, N. Ohtani, K. Yamakoshi et al., "Mitogenic signalling and the p16<sup>INK4a</sup>-Rb pathway cooperate to enforce irreversible cellular senescence," *Nature cell biology*, vol. 8, no. 11, pp. 1291–1297, 2006.
- [59] Q. Ma, "Role of *nrf2* in oxidative stress and toxicity," *Annual review of pharmacology and toxicology*, vol. 53, no. 1, pp. 401–426, 2013.
- [60] G. M. DeNicola, F. A. Karreth, T. J. Humpton et al., "Oncogene-induced *Nrf2* transcription promotes ROS detoxification and tumorigenesis," *Nature*, vol. 475, no. 7354, pp. 106–109, 2011.
- [61] T. D. Oberley, W. Zhong, L. I. Szweda, and L. W. Oberley, "Localization of antioxidant enzymes and oxidative damage products in normal and malignant prostate epithelium," *Prostate*, vol. 44, no. 2, pp. 144–155, 2000.
- [62] T. O. Khor, M. T. Huang, A. Prawan et al., "Increased susceptibility of *Nrf2* knockout mice to colitis-associated colorectal cancer," *Cancer prevention research*, vol. 1, no. 3, pp. 187–191, 2008.
- [63] L. Becks, M. Prince, H. Burson et al., "Aggressive mammary carcinoma progression in *Nrf2* knockout mice treated with 7,12-dimethylbenz[a]anthracene," *BMC Cancer*, vol. 10, no. 1, p. 540, 2010.
- [64] K. Taguchi, H. Motohashi, and M. Yamamoto, "Molecular mechanisms of the Keap1-Nrf2 pathway in stress response and cancer evolution," *Genes to cells*, vol. 16, no. 2, pp. 123–140, 2011.
- [65] E. Kansanen, S. M. Kuosmanen, H. Leinonen, and A. L. Levenonen, "The Keap1-Nrf2 pathway: mechanisms of activation and dysregulation in cancer," *Redox biology*, vol. 1, no. 1, pp. 45–49, 2013.
- [66] I. S. Harris, A. E. Treloar, S. Inoue et al., "Glutathione and thioredoxin antioxidant pathways synergize to drive cancer initiation and progression," *Cancer cell*, vol. 27, no. 2, pp. 211–222, 2015.
- [67] D. B. Coursin, H. P. Cihla, J. Sempf, T. D. Oberley, and L. W. Oberley, "An immunohistochemical analysis of antioxidant and glutathione S-transferase enzyme levels in normal and neoplastic human lung," *Histology and histopathology*, vol. 11, no. 4, pp. 851–860, 1996.
- [68] D. G. Bostwick, E. E. Alexander, R. Singh et al., "Antioxidant enzyme expression and reactive oxygen species damage in prostatic intraepithelial neoplasia and cancer," *Cancer*, vol. 89, no. 1, pp. 123–134, 2000.
- [69] R. Kurzrock, H. M. Kantarjian, B. J. Druker, and M. Talpaz, "Philadelphia chromosome-positive leukemias: from basic mechanisms to molecular therapeutics," *Annals of internal medicine*, vol. 138, no. 10, pp. 819–830, 2003.
- [70] S. Salesse and C. M. Verfaillie, "BCR/ABL: from molecular mechanisms of leukemia induction to treatment of chronic myelogenous leukemia," *Oncogene*, vol. 21, no. 56, pp. 8547–8559, 2002.
- [71] D. Trachootham, Y. Zhou, H. Zhang et al., "Selective killing of oncogenically transformed cells through a ROS-mediated mechanism by  $\beta$ -phenylethyl isothiocyanate," *Cancer Cell*, vol. 10, no. 3, pp. 241–252, 2006.
- [72] J. H. Kim, S. C. Chu, J. L. Gramlich et al., "Activation of the PI3K/mTOR pathway by BCR-ABL contributes to increased production of reactive oxygen species," *Blood*, vol. 105, no. 4, pp. 1717–1723, 2005.
- [73] M. Sattler, S. Verma, G. Shrikhande et al., "The BCR/ABL Tyrosine Kinase Induces Production of Reactive Oxygen Species in Hematopoietic Cells," *Journal of Biological Chemistry*, vol. 275, no. 32, pp. 24273–24278, 2000.
- [74] M. Koptyra, R. Falinski, M. O. Nowicki et al., "BCR/ABL kinase induces self-mutagenesis via reactive oxygen species to encode imatinib resistance," *Blood*, vol. 108, no. 1, pp. 319–327, 2006.
- [75] H. M. Amin and R. Lai, "Pathobiology of ALK+ anaplastic large-cell lymphoma," *Blood*, vol. 110, no. 7, pp. 2259–2267, 2007.
- [76] K. Thornber, A. Colomba, L. Ceccato, G. Delsol, B. Payrastre, and F. Gaits-Iacovoni, "Reactive oxygen species and lipoxigenases regulate the oncogenicity of NPM- ALK-positive anaplastic large cell lymphomas," *Oncogene*, vol. 28, no. 29, pp. 2690–2696, 2009.
- [77] J. A. McCubrey, M. M. LaHair, and R. A. Franklin, "Reactive oxygen species-induced activation of the MAP kinase signaling pathways," *Antioxidants & redox signaling*, vol. 8, no. 9–10, pp. 1775–1789, 2006.

- [78] D. Hanahan and R. A. Weinberg, "Hallmarks of cancer: the next generation," *Cell*, vol. 144, no. 5, pp. 646–674, 2011.
- [79] H. Kasai and S. Nishimura, "Hydroxylation of deoxyguanosine at the C-8 position by ascorbic acid and other reducing agents," *Nucleic acids research*, vol. 12, no. 4, pp. 2137–2145, 1984.
- [80] H. Kasai, P. F. Crain, Y. Kuchino, S. Nishimura, A. Ootsuyama, and H. Tanooka, "Formation of 8-hydroxyguanine moiety in cellular DNA by agents producing oxygen radicals and evidence for its repair," *Carcinogenesis*, vol. 7, no. 11, pp. 1849–1851, 1986.
- [81] C. J. Burrows and J. G. Muller, "Oxidative nucleobase modifications leading to strand scission," *Chemical Reviews*, vol. 98, no. 3, pp. 1109–1152, 1998.
- [82] J. Cadet and J. R. Wagner, "DNA base damage by reactive oxygen species, oxidizing agents, and UV radiation," *Cold Spring Harbor perspectives in biology*, vol. 5, no. 2, 2013.
- [83] R. A. Floyd, "Role of oxygen free radicals in carcinogenesis and brain ischemia," *The FASEB journal*, vol. 4, no. 9, pp. 2587–2597, 1990.
- [84] T. Suzuki and H. Kamiya, "Mutations induced by 8-hydroxyguanine (8-oxo-7,8-dihydroguanine), a representative oxidized base, in mammalian cells," *Genes and Environment*, vol. 39, no. 1, p. 2, 2017.
- [85] H. Kamiya, N. Murata-Kamiya, S. Koizume, H. Inoue, S. Nishimura, and E. Ohtsuka, "8-Hydroxyguanine (7,8-dihydro-8-oxoguanine) in hot spots of the c-Ha-ras gene: effects of sequence contexts on mutation spectra," *Carcinogenesis*, vol. 16, no. 4, pp. 883–889, 1995.
- [86] H. Kamiya, K. Miura, H. Ishikawa, H. Inoue, S. Nishimura, and E. Ohtsuka, "c-Ha-ras containing 8-hydroxyguanine at codon 12 induces point mutations at the modified and adjacent positions," *Cancer research*, vol. 52, no. 12, pp. 3483–3485, 1992.
- [87] S. Borrego, A. Vazquez, F. Dasí et al., "Oxidative stress and DNA damage in human gastric carcinoma: 8-oxo-7,8-dihydro-2'-deoxyguanosine (8-oxo-dG) as a possible tumor marker," *International Journal of Molecular Sciences*, vol. 14, no. 2, pp. 3467–3486, 2013.
- [88] M. Olivier, M. Hollstein, and P. Hainaut, "TP53 mutations in human cancers: origins, consequences, and clinical use," *Cold Spring Harbor perspectives in biology*, vol. 2, no. 1, article a001008, 2010.
- [89] B. Vogelstein, D. Lane, and A. J. Levine, "Surfing the p53 network," *Nature*, vol. 408, no. 6810, pp. 307–310, 2000.
- [90] C. Wanka, J. P. Steinbach, and J. Rieger, "Tp53-induced Glycolysis and Apoptosis Regulator (TIGAR) Protects Glioma Cells from Starvation-induced Cell Death by Up-regulating Respiration and Improving Cellular Redox Homeostasis," *Journal of Biological Chemistry*, vol. 287, no. 40, pp. 33436–33446, 2012.
- [91] A. A. Sablina, A. V. Budanov, G. V. Ilyinskaya, L. S. Agapova, J. E. Kravchenko, and P. M. Chumakov, "The antioxidant function of the p53 tumor suppressor," *Nature medicine*, vol. 11, no. 12, pp. 1306–1313, 2005.
- [92] K. Bensaad, A. Tsuruta, M. A. Selak et al., "TIGAR, a p53-inducible regulator of glycolysis and apoptosis," *Cell*, vol. 126, no. 1, pp. 107–120, 2006.
- [93] R. Faraonio, P. Vergara, D. di Marzo et al., "p53 Suppresses the Nrf2-dependent Transcription of Antioxidant Response Genes," *Journal of Biological Chemistry*, vol. 281, no. 52, pp. 39776–39784, 2006.
- [94] P. Drane, A. Bravard, V. Bouvard, and E. May, "Reciprocal down-regulation of p53 and SOD2 gene expression -implication in p53 mediated apoptosis," *Oncogene*, vol. 20, no. 4, pp. 430–439, 2001.
- [95] U. S. Srinivas, B. W. Q. Tan, B. A. Vellayappan, and A. D. Jeyasekharan, "ROS and the DNA damage response in cancer," *Redox biology*, vol. 25, article 101084, 2019.
- [96] K. Bensaad, E. C. Cheung, and K. H. Vousden, "Modulation of intracellular ROS levels by TIGAR controls autophagy," *The EMBO journal*, vol. 28, no. 19, pp. 3015–3026, 2009.
- [97] A. Maillet and S. Pervaiz, "Redox regulation of p53, redox effectors regulated by p53: a subtle balance," *Antioxidants & redox signaling*, vol. 16, no. 11, pp. 1285–1294, 2012.
- [98] I. R. Indran, M. P. Hande, and S. Pervaiz, "hTERT overexpression alleviates intracellular ROS production, improves mitochondrial function, and inhibits ROS-mediated apoptosis in cancer cells," *Cancer research*, vol. 71, no. 1, pp. 266–276, 2011.
- [99] A. C. Newton, M. D. Bootman, and J. D. Scott, "Second messengers," *Cold Spring Harbor perspectives in biology*, vol. 8, no. 8, 2016.
- [100] B. Chance, H. Sies, and A. Boveris, "Hydroperoxide metabolism in mammalian organs," *Physiological reviews*, vol. 59, no. 3, pp. 527–605, 1979.
- [101] H. J. Forman, M. Maiorino, and F. Ursini, "Signaling functions of reactive oxygen species," *Biochemistry*, vol. 49, no. 5, pp. 835–842, 2010.
- [102] H. Miki and Y. Funato, "Regulation of intracellular signalling through cysteine oxidation by reactive oxygen species," *The Journal of Biochemistry*, vol. 151, no. 3, pp. 255–261, 2012.
- [103] H. E. Marshall, K. Merchant, and J. S. Stamler, "Nitrosation and oxidation in the regulation of gene expression," *The FASEB Journal*, vol. 14, no. 13, pp. 1889–1900, 2000.
- [104] T. W. Poh and S. Pervaiz, "LY294002 and LY303511 sensitize tumor cells to drug-induced apoptosis via intracellular hydrogen peroxide production independent of the phosphoinositide 3-kinase-Akt pathway," *Cancer research*, vol. 65, no. 14, pp. 6264–6274, 2005.
- [105] K. H. Kang, G. Lemke, and J. W. Kim, "The PI3K-PTEN tug-of-war, oxidative stress and retinal degeneration," *Trends in molecular medicine*, vol. 15, no. 5, pp. 191–198, 2009.
- [106] R. C. Kukreja, H. A. Kontos, M. L. Hess, and E. F. Ellis, "PGH synthase and lipoxygenase generate superoxide in the presence of NADH or NADPH," *Circulation research*, vol. 59, no. 6, pp. 612–619, 1986.
- [107] A. Bhattacharyya, R. Chattopadhyay, S. Mitra, and S. E. Crowe, "Oxidative stress: an essential factor in the pathogenesis of gastrointestinal mucosal diseases," *Physiological reviews*, vol. 94, no. 2, pp. 329–354, 2014.
- [108] S. Chatterjee, E. A. Browning, N. Hong et al., "Membrane depolarization is the trigger for PI3K/Akt activation and leads to the generation of ROS," *American Journal of Physiology-Heart and Circulatory Physiology*, vol. 302, no. 1, pp. H105–H114, 2012.
- [109] J. Downward, "Targeting RAS signalling pathways in cancer therapy," *Nature reviews cancer*, vol. 3, no. 1, pp. 11–22, 2003.
- [110] J. L. Meitzler, S. Antony, Y. Wu et al., "NADPH oxidases: a perspective on reactive oxygen species production in tumor

- biology," *Antioxidants & redox signaling*, vol. 20, no. 17, pp. 2873–2889, 2014.
- [111] Y. Samuels and T. Waldman, "Oncogenic mutations of PIK3CA in human cancers," *Current Topics in Microbiology and Immunology*, vol. 347, pp. 21–41, 2010.
- [112] R. R. Madsen, B. Vanhaesebroeck, and R. K. Semple, "Cancer-Associated PIK3CA Mutations in Overgrowth Disorders," *Trends in molecular medicine*, vol. 24, no. 10, pp. 856–870, 2018.
- [113] T. Shimoi, A. Hamada, M. Yamagishi et al., "PIK3CA mutation profiling in patients with breast cancer, using a highly sensitive detection system," *Cancer science*, vol. 109, no. 8, pp. 2558–2566, 2018.
- [114] N. Ilic, K. Birsoy, A. J. Aguirre et al., "PIK3CA mutant tumors depend on oxoglutarate dehydrogenase," *Proceedings of the National Academy of Sciences*, vol. 114, no. 17, pp. E3434–E3443, 2017.
- [115] J. Ruffels, M. Griffin, and J. M. Dickenson, "Activation of ERK1/2, JNK and PKB by hydrogen peroxide in human SH-SY5Y neuroblastoma cells: role of ERK1/2 in H<sub>2</sub>O<sub>2</sub>-induced cell death," *European journal of pharmacology*, vol. 483, no. 2-3, pp. 163–173, 2004.
- [116] C. H. Wong, K. B. Iskandar, S. K. Yadav, J. L. Hirpara, T. Loh, and S. Pervaiz, "Simultaneous induction of non-canonical autophagy and apoptosis in cancer cells by ROS-dependent ERK and JNK activation," *PLoS One*, vol. 5, no. 4, article e9996, 2010.
- [117] H. Nagai, T. Noguchi, K. Takeda, and H. Ichijo, "Pathophysiological roles of ASK1-MAP kinase signaling pathways," *BMB Reports*, vol. 40, no. 1, pp. 1–6, 2007.
- [118] Y. Hayakawa, Y. Hirata, H. Nakagawa et al., "Apoptosis signal-regulating kinase 1 and cyclin D1 compose a positive feedback loop contributing to tumor growth in gastric cancer," *Proceedings of the National Academy of Sciences*, vol. 108, no. 2, pp. 780–785, 2011.
- [119] N. Kundu, S. Zhang, and A. M. Fulton, "Sublethal oxidative stress inhibits tumor cell adhesion and enhances experimental metastasis of murine mammary carcinoma," *Clinical & experimental metastasis*, vol. 13, no. 1, pp. 16–22, 1995.
- [120] A. Belkhir, C. Richards, M. Whaley, S. A. McQueen, and F. W. Orr, "Increased expression of activated matrix metalloproteinase-2 by human endothelial cells after sublethal H<sub>2</sub>O<sub>2</sub> exposure," *Laboratory investigation; a journal of technical methods and pathology*, vol. 77, no. 5, pp. 533–539, 1997.
- [121] D. C. Radisky, D. D. Levy, L. E. Littlepage et al., "Rac1b and reactive oxygen species mediate MMP-3-induced EMT and genomic instability," *Nature*, vol. 436, no. 7047, pp. 123–127, 2005.
- [122] D. S. Salomon, R. Brandt, F. Ciardiello, and N. Normanno, "Epidermal growth factor-related peptides and their receptors in human malignancies," *Critical reviews in oncology/hematology*, vol. 19, no. 3, pp. 183–232, 1995.
- [123] K. Hyoudou, M. Nishikawa, Y. Kobayashi, Y. Umeyama, F. Yamashita, and M. Hashida, "PEGylated catalase prevents metastatic tumor growth aggravated by tumor removal," *Free Radical Biology and Medicine*, vol. 41, no. 9, pp. 1449–1458, 2006.
- [124] L. F. Brown, M. Detmar, K. Claffey et al., "Vascular permeability factor/vascular endothelial growth factor: a multifunctional angiogenic cytokine," *Regulation of angiogenesis*, vol. 79, pp. 233–269, 1997.
- [125] J. A. Bertout, S. A. Patel, and M. C. Simon, "The impact of O<sub>2</sub> availability on human cancer," *Nature Reviews Cancer*, vol. 8, no. 12, pp. 967–975, 2008.
- [126] P. Storz, H. Doppler, and A. Toker, "Protein kinase Cdelta selectively regulates protein kinase D-dependent activation of NF-kappaB in oxidative stress signaling," *Molecular and cellular biology*, vol. 24, no. 7, pp. 2614–2626, 2004.
- [127] Y. H. Yee, S. J. F. Chong, L. R. Kong, B. C. Goh, and S. Pervaiz, "Sustained IKKβ phosphorylation and NF-κB activation by superoxide-induced peroxynitrite-mediated nitrotyrosine modification of B56γ3 and PP2A inactivation," *Redox biology*, vol. 41, article 101834, 2021.
- [128] I. C. Low, Z. X. Chen, and S. Pervaiz, "Bcl-2 modulates resveratrol-induced ROS production by regulating mitochondrial respiration in tumor cells," *Antioxidants & redox signaling*, vol. 13, no. 6, pp. 807–819, 2010.
- [129] D. Raman, S. J. F. Chong, K. Iskandar, J. L. Hirpara, and S. Pervaiz, "Peroxyntitrite promotes serine-62 phosphorylation-dependent stabilization of the oncoprotein c-Myc," *Redox biology*, vol. 34, article 101587, 2020.
- [130] S. J. F. Chong, K. Iskandar, J. X. H. Lai et al., "Serine-70 phosphorylated Bcl-2 prevents oxidative stress-induced DNA damage by modulating the mitochondrial redox metabolism," *Nucleic acids research*, vol. 48, no. 22, article 12727, 45 pages, 2020.
- [131] J. L. Hirpara, K. Subramaniam, G. Bellot et al., "Superoxide induced inhibition of death receptor signaling is mediated via induced expression of apoptosis inhibitory protein cFLIP," *Redox biology*, vol. 30, article 101403, 2020.
- [132] S. Desagher, J. Glowinski, and J. Premont, "Pyruvate protects neurons against hydrogen peroxide-induced toxicity," *Journal of Neuroscience*, vol. 17, no. 23, pp. 9060–9067, 1997.
- [133] D. Anastasiou, G. Poulgiannis, J. M. Asara et al., "Inhibition of pyruvate kinase M2 by reactive oxygen species contributes to cellular antioxidant responses," *Science*, vol. 334, no. 6060, pp. 1278–1283, 2011.
- [134] G. A. Spoden, U. Rostek, S. Lechner, M. Mitterberger, S. Mazurek, and W. Zwerschke, "Pyruvate kinase isoenzyme M2 is a glycolytic sensor differentially regulating cell proliferation, cell size and apoptotic cell death dependent on glucose supply," *Experimental cell research*, vol. 315, no. 16, pp. 2765–2774, 2009.
- [135] X. L. Zu and M. Guppy, "Cancer metabolism: facts, fantasy, and fiction," *Biochemical and biophysical research communications*, vol. 313, no. 3, pp. 459–465, 2004.
- [136] S. Rodríguez-Enríquez, L. Carreño-Fuentes, J. C. Gallardo-Pérez et al., "Oxidative phosphorylation is impaired by prolonged hypoxia in breast and possibly in cervix carcinoma," *The international journal of biochemistry & cell biology*, vol. 42, no. 10, pp. 1744–1751, 2010.
- [137] I. Hernández-Reséndiz, A. Román-Rosales, E. García-Villa et al., "Dual regulation of energy metabolism by p53 in human cervix and breast cancer cells," *Biochimica et Biophysica Acta (BBA)-Molecular Cell Research*, vol. 1853, no. 12, pp. 3266–3278, 2015.
- [138] G. Migneco, D. Whitaker-Menezes, B. Chiavarina et al., "Glycolytic cancer associated fibroblasts promote breast cancer tumor growth, without a measurable increase in



- angiogenesis: evidence for stromal-epithelial metabolic coupling," *Cell Cycle*, vol. 9, no. 12, pp. 2412–2422, 2010.
- [139] A. Orimo, P. B. Gupta, D. C. Sgroi et al., "Stromal fibroblasts present in invasive human breast carcinomas promote tumor growth and angiogenesis through elevated SDF-1/CXCL12 secretion," *Cell*, vol. 121, no. 3, pp. 335–348, 2005.
- [140] S. Pavlides, D. Whitaker-Menezes, R. Castello-Cros et al., "The reverse Warburg effect: aerobic glycolysis in cancer associated fibroblasts and the tumor stroma," *Cell Cycle*, vol. 8, no. 23, pp. 3984–4001, 2009.
- [141] A. Pastò, C. Bellio, G. Pilotto et al., "Cancer stem cells from epithelial ovarian cancer patients privilege oxidative phosphorylation, and resist glucose deprivation," *Oncotarget*, vol. 5, no. 12, pp. 4305–4319, 2014.
- [142] V. de Rosa, F. Iommelli, M. Monti et al., "Reversal of Warburg effect and reactivation of oxidative phosphorylation by differential inhibition of EGFR signaling pathways in non-small cell lung cancer," *Clinical Cancer Research*, vol. 21, no. 22, pp. 5110–5120, 2015.
- [143] J. Hirpara, J. Q. Eu, J. K. M. Tan et al., "Metabolic reprogramming of oncogene-addicted cancer cells to OXPHOS as a mechanism of drug resistance," *Redox biology*, vol. 25, article 101076, 2019.
- [144] D. S. Matassa, M. R. Amoroso, H. Lu et al., "Oxidative metabolism drives inflammation-induced platinum resistance in human ovarian cancer," *Cell Death & Differentiation*, vol. 23, no. 9, pp. 1542–1554, 2016.
- [145] A. C. Nulton-Persson and L. I. Szweda, "Modulation of Mitochondrial Function by Hydrogen Peroxide," *Journal of Biological Chemistry*, vol. 276, no. 26, pp. 23357–23361, 2001.
- [146] B. E. Baysal, R. E. Ferrell, J. E. Willett-Brozick et al., "Mutations in SDHD, a mitochondrial complex II gene, in hereditary paraganglioma," *Science*, vol. 287, no. 5454, pp. 848–851, 2000.
- [147] S. Niemann and U. Muller, "Mutations in *SDHC* cause autosomal dominant paraganglioma, type 3," *Nature genetics*, vol. 26, no. 3, pp. 268–270, 2000.
- [148] K. Hadrava Vanova, M. Kraus, J. Neuzil, and J. Rohlena, "Mitochondrial complex II and reactive oxygen species in disease and therapy," *Redox Report*, vol. 25, no. 1, pp. 26–32, 2020.
- [149] C. Bardella, P. J. Pollard, and I. Tomlinson, "SDH mutations in cancer," *Biochimica et Biophysica Acta (BBA)-Bioenergetics*, vol. 1807, no. 11, pp. 1432–1443, 2011.
- [150] S. Picaud, K. L. Kavanagh, W. W. Yue et al., "Structural basis of fumarate hydratase deficiency," *Journal of inherited metabolic disease*, vol. 34, no. 3, pp. 671–676, 2011.
- [151] R. Lehtonen, M. Kiuru, S. Vanharanta et al., "Biallelic Inactivation of *Fumarate Hydratase*(FH) Occurs in Nonsyndromic Uterine Leiomyomas but Is Rare in Other Tumors," *The American journal of pathology*, vol. 164, no. 1, pp. 17–22, 2004.
- [152] I. P. Tomlinson, N. A. Alam, A. J. Rowan et al., "Germline mutations in *FH* predispose to dominantly inherited uterine fibroids, skin leiomyomata and papillary renal cell cancer," *Nature genetics*, vol. 30, no. 4, pp. 406–410, 2002.
- [153] J. Adam, E. Hatipoglu, L. O'Flaherty et al., "Renal cyst formation in *Fh1*-deficient mice is independent of the Hif/Phd pathway: roles for fumarate in KEAP1 succination and Nrf2 signaling," *Cancer Cell*, vol. 20, no. 4, pp. 524–537, 2011.
- [154] M. Escoll, D. Lastra, M. Pajares et al., "Transcription factor NRF2 uses the Hippo pathway effector TAZ to induce tumorigenesis in glioblastomas," *Redox Biology*, vol. 30, article 101425, 2020.
- [155] C. Frezza, L. Zheng, O. Folger et al., "Haem oxygenase is synthetically lethal with the tumour suppressor fumarate hydratase," *Nature*, vol. 477, no. 7363, pp. 225–228, 2011.
- [156] P. L. Chen, C. F. Chen, Y. Chen et al., "Mitochondrial genome instability resulting from SUV3 haploinsufficiency leads to tumorigenesis and shortened lifespan," *Oncogene*, vol. 32, no. 9, pp. 1193–1201, 2013.
- [157] L. Khidr, G. Wu, A. Davila, V. Procaccio, D. Wallace, and W. H. Lee, "Role of SUV3 Helicase in Maintaining Mitochondrial Homeostasis in Human Cells," *Journal of Biological Chemistry*, vol. 283, no. 40, pp. 27064–27073, 2008.
- [158] M. Alexeyev, I. Shokolenko, G. Wilson, and S. LeDoux, "The maintenance of mitochondrial DNA integrity—critical analysis and update," *Cold Spring Harbor perspectives in biology*, vol. 5, no. 5, article a012641, 2013.
- [159] S. Anderson, A. T. Bankier, B. G. Barrell et al., "Sequence and organization of the human mitochondrial genome," *Nature*, vol. 290, no. 5806, pp. 457–465, 1981.
- [160] A. Chatterjee, E. Mambo, and D. Sidransky, "Mitochondrial DNA mutations in human cancer," *Oncogene*, vol. 25, no. 34, pp. 4663–4674, 2006.
- [161] A. S. Sun, K. Sepkowitz, and S. A. Geller, "A study of some mitochondrial and peroxisomal enzymes in human colonic adenocarcinoma," *Laboratory investigation; a journal of technical methods and pathology*, vol. 44, no. 1, pp. 13–17, 1981.
- [162] B. G. Heerdt, H. K. Halsey, M. Lipkin, and L. H. Augenlicht, "Expression of mitochondrial cytochrome c oxidase in human colonic cell differentiation, transformation, and risk for colonic cancer," *Cancer research*, vol. 50, no. 5, pp. 1596–1600, 1990.
- [163] A. S. Sun and A. I. Cederbaum, "Oxidoreductase activities in normal rat liver, tumor-bearing rat liver, and hepatoma HC-252," *Cancer Research*, vol. 40, no. 12, pp. 4677–4681, 1980.
- [164] S. Dasgupta, M. O. Hoque, S. Upadhyay, and D. Sidransky, "Mitochondrial cytochrome B gene mutation promotes tumor growth in bladder cancer," *Cancer research*, vol. 68, no. 3, pp. 700–706, 2008.
- [165] L. Iommarini, I. Kurelac, M. Capristo et al., "Different mtDNA mutations modify tumor progression in dependence of the degree of respiratory complex I impairment," *Human molecular genetics*, vol. 23, no. 6, pp. 1453–1466, 2014.
- [166] A. Dautant, T. Meier, A. Hahn, D. Tribouillard-Tanvier, J. P. di Rago, and R. Kucharczyk, "ATP synthase diseases of mitochondrial genetic origin," *Frontiers in physiology*, vol. 9, p. 329, 2018.
- [167] L. Grzybowska-Szatkowska, B. Slaska, J. Rzymowska, A. Brzozowska, and B. Florianczyk, "Novel mitochondrial mutations in the ATP6 and ATP8 genes in patients with breast cancer," *Molecular medicine reports*, vol. 10, no. 4, pp. 1772–1778, 2014.
- [168] M. Singh, H. Sharma, and N. Singh, "Hydrogen peroxide induces apoptosis in HeLa cells through mitochondrial pathway," *Mitochondrion*, vol. 7, no. 6, pp. 367–373, 2007.
- [169] K. A. Ahmad, K. B. Iskandar, J. L. Hirpara, M. V. Clement, and S. Pervaiz, "Hydrogen peroxide-mediated cytosolic acidification is a signal for mitochondrial translocation of Bax







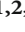


- during drug-induced apoptosis of tumor cells,” *Cancer research*, vol. 64, no. 21, pp. 7867–7878, 2004.
- [170] M. V. Clement, A. Ponton, and S. Pervaiz, “Apoptosis induced by hydrogen peroxide is mediated by decreased superoxide anion concentration and reduction of intracellular milieu,” *FEBS letters*, vol. 440, no. 1-2, pp. 13–18, 1998.
- [171] S. Teramoto, T. Tomita, H. Matsui, E. Ohga, T. Matsuse, and Y. Ouchi, “Hydrogen peroxide-induced apoptosis and necrosis in human lung fibroblasts: protective roles of glutathione,” *The Japanese Journal of Pharmacology*, vol. 79, no. 1, pp. 33–40, 1999.
- [172] Y. J. Lee and E. Shacter, “Hydrogen peroxide inhibits activation, not activity, of cellular caspase-3 *in vivo*,” *Free Radical Biology and Medicine*, vol. 29, no. 7, pp. 684–692, 2000.
- [173] Y. J. Lee and E. Shacter, “Oxidative Stress Inhibits Apoptosis in Human Lymphoma Cells,” *Journal of Biological Chemistry*, vol. 274, no. 28, pp. 19792–19798, 1999.
- [174] M. L. Circu and T. Y. Aw, “Glutathione and modulation of cell apoptosis,” *Biochimica et Biophysica Acta (BBA)-Molecular Cell Research*, vol. 1823, no. 10, pp. 1767–1777, 2012.
- [175] M. L. Circu and T. Y. Aw, “Reactive oxygen species, cellular redox systems, and apoptosis,” *Free Radical Biology and Medicine*, vol. 48, no. 6, pp. 749–762, 2010.
- [176] P. Palapati and D. Averill-Bates, “Mild thermotolerance induced at 40 °C increases antioxidants and protects HeLa cells against mitochondrial apoptosis induced by hydrogen peroxide: Role of p53,” *Archives of biochemistry and biophysics*, vol. 495, no. 2, pp. 97–111, 2010.
- [177] M. V. Clément, J. L. Hirpara, and S. Pervaiz, “Decrease in intracellular superoxide sensitizes Bcl-2-overexpressing tumor cells to receptor and drug-induced apoptosis independent of the mitochondria,” *Cell Death & Differentiation*, vol. 10, no. 11, pp. 1273–1285, 2003.
- [178] M. Pollak, “The insulin and insulin-like growth factor receptor family in neoplasia: an update,” *Nature Reviews Cancer*, vol. 12, no. 3, pp. 159–169, 2012.
- [179] K. Marycz, K. A. Tomaszewski, K. Kornicka et al., “Metformin decreases reactive oxygen species, enhances osteogenic properties of adipose-derived multipotent mesenchymal stem cells *in vitro*, and increases bone density *in vivo*,” *Oxidative medicine and cellular longevity*, vol. 2016, Article ID 9785890, 19 pages, 2016.
- [180] J. R. Molina, Y. Sun, M. Protopopova et al., “An inhibitor of oxidative phosphorylation exploits cancer vulnerability,” *Nature medicine*, vol. 24, no. 7, pp. 1036–1046, 2018.
- [181] H. V. Vangapandu, B. Alston, J. Morse et al., “Biological and metabolic effects of IACS-010759, an OxPhos inhibitor, on chronic lymphocytic leukemia cells,” *Oncotarget*, vol. 9, no. 38, pp. 24980–24991, 2018.
- [182] T. A. Yap, J. Rodon Ahnert, S. A. Piha-Paul et al., “Phase I trial of IACS-010759 (IACS), a potent, selective inhibitor of complex I of the mitochondrial electron transport chain, in patients (pts) with advanced solid tumors,” *Journal of Clinical Oncology*, vol. 37, 15 supplement, p. 3014, 2019.
- [183] S. B. Panina, J. Pei, N. Baran, M. Konopleva, and N. V. Kirienko, “Utilizing synergistic potential of mitochondria-targeting drugs for leukemia therapy,” *Frontiers in oncology*, vol. 10, p. 435, 2020.
- [184] Q. Zhang, A. Lodi, S. R. Sweeney et al., “Inhibiting mitochondria function by Bcl-2 inhibitor venetoclax and complex I inhibitor Iacs-010759 eliminate leukemia cells in pre-clinical AML models,” *Blood*, vol. 134, Supplement\_1, p. 3927, 2019.
- [185] D. Chen, H. B. Barsoumian, G. Fischer et al., “Combination treatment with radiotherapy and a novel oxidative phosphorylation inhibitor overcomes PD-1 resistance and enhances antitumor immunity,” *Journal for immunotherapy of cancer*, vol. 8, no. 1, article e000289, 2020.
- [186] A. L. Wong, R. A. Soo, D. S. Tan et al., “Phase I and biomarker study of OPB-51602, a novel signal transducer and activator of transcription (STAT) 3 inhibitor, in patients with refractory solid malignancies,” *Annals of Oncology*, vol. 26, no. 5, pp. 998–1005, 2015.
- [187] D. Genini, L. Brambilla, E. Laurini et al., “Mitochondrial dysfunction induced by a SH2 domain-targeting STAT3 inhibitor leads to metabolic synthetic lethality in cancer cells,” *Proceedings of the National Academy of Sciences*, vol. 114, no. 25, pp. E4924–E4933, 2017.
- [188] F. Huijing and E. C. Slater, “The use of oligomycin as an inhibitor of oxidative phosphorylation,” *The Journal of Biochemistry*, vol. 49, no. 6, pp. 493–501, 1961.
- [189] D. S. Perlin, L. R. Latchney, and A. E. Senior, “Inhibition of *Escherichia coli* H<sup>+</sup>-ATPase by venturicidin, oligomycin and ossamycin,” *Biochimica et Biophysica Acta (BBA)-Bioenergetics*, vol. 807, no. 3, pp. 238–244, 1985.
- [190] F. Alvarez-Calderon, M. A. Gregory, C. Pham-Danis et al., “Tyrosine kinase inhibition in leukemia induces an altered metabolic state sensitive to mitochondrial perturbations,” *Clinical Cancer Research*, vol. 21, no. 6, pp. 1360–1372, 2015.
- [191] Y. Shi, S. K. Lim, Q. Liang et al., “Gboxin is an oxidative phosphorylation inhibitor that targets glioblastoma,” *Nature*, vol. 567, no. 7748, pp. 341–346, 2019.
- [192] R. M. Whitaker, D. Corum, C. C. Beeson, and R. G. Schnellmann, “Mitochondrial biogenesis as a pharmacological target: a new approach to acute and chronic diseases,” *Annual review of pharmacology and toxicology*, vol. 56, no. 1, pp. 229–249, 2016.
- [193] M. D. Siegelin, T. Dohi, C. M. Raskett et al., “Exploiting the mitochondrial unfolded protein response for cancer therapy in mice and human cells,” *The Journal of clinical investigation*, vol. 121, no. 4, pp. 1349–1360, 2011.
- [194] J. C. Ghosh, M. D. Siegelin, V. Vaira et al., “Adaptive mitochondrial reprogramming and resistance to PI3K therapy,” *JNCI: Journal of the National Cancer Institute*, vol. 107, no. 3, 2015.
- [195] B. H. Kang, M. D. Siegelin, J. Plescia et al., “Preclinical characterization of mitochondria-targeted small molecule hsp90 inhibitors, gamitrinibs, in advanced prostate cancer,” *Clinical Cancer Research*, vol. 16, no. 19, pp. 4779–4788, 2010.
- [196] B. H. Kang, J. Plescia, H. Y. Song et al., “Combinatorial drug design targeting multiple cancer signaling networks controlled by mitochondrial Hsp90,” *The Journal of clinical investigation*, vol. 119, no. 3, pp. 454–464, 2009.
- [197] G. Zhang, D. T. Frederick, L. Wu et al., “Targeting mitochondrial biogenesis to overcome drug resistance to MAPK inhibitors,” *The Journal of clinical investigation*, vol. 126, no. 5, pp. 1834–1856, 2016.
- [198] C. C. Lin, M. C. Lo, R. R. Moody, N. O. Stevers, S. L. Tinsley, and D. Sun, “Doxycycline targets aldehyde dehydrogenase-positive breast cancer stem cells,” *Oncology reports*, vol. 39, no. 6, pp. 3041–3047, 2018.

- [199] S. N. Dijk, M. Protasoni, M. Elpidorou, A. M. Kroon, and J.-W. Taanman, "Mitochondria as target to inhibit proliferation and induce apoptosis of cancer cells: the effects of doxycycline and gemcitabine," *Scientific Reports*, vol. 10, no. 1, p. 4363, 2020.
- [200] S. Iqbal and D. A. Hood, "Oxidative stress-induced mitochondrial fragmentation and movement in skeletal muscle myoblasts," *American Journal of Physiology-Cell Physiology*, vol. 306, no. 12, pp. C1176–C1183, 2014.
- [201] P. H. Reddy, "Inhibitors of mitochondrial fission as a therapeutic strategy for diseases with oxidative stress and mitochondrial dysfunction," *Journal of Alzheimer's Disease*, vol. 40, no. 2, pp. 245–256, 2014.
- [202] W. Dai, G. Wang, J. Chwa et al., "Mitochondrial division inhibitor (mdivi-1) decreases oxidative metabolism in cancer," *British journal of cancer*, vol. 122, no. 9, pp. 1288–1297, 2020.
- [203] C. Duan, L. Wang, J. Zhang et al., "Mdivi-1 attenuates oxidative stress and exerts vascular protection in ischemic/hypoxic injury by a mechanism independent of Drp1 GTPase activity," *Redox biology*, vol. 37, article 101706, 2020.
- [204] J. Rehman, H. J. Zhang, P. T. Toth et al., "Inhibition of mitochondrial fission prevents cell cycle progression in lung cancer," *The FASEB Journal*, vol. 26, no. 5, pp. 2175–2186, 2012.
- [205] A. Ferreira-da-Silva, C. Valacca, E. Rios et al., "Mitochondrial dynamics protein Drp1 is overexpressed in oncogenic thyroid tumors and regulates cancer cell migration," *PLoS One*, vol. 10, no. 3, article e0122308, 2015.
- [206] A. Vincent, M. Thauvin, E. Quévrain et al., "Evaluation of the compounds commonly known as superoxide dismutase and catalase mimics in cellular models," *Journal of inorganic biochemistry*, vol. 219, article 111431, 2021.
- [207] S. Miriyala, I. Spasojevic, A. Tovmasyan et al., "Manganese superoxide dismutase, MnSOD and its mimics," *Biochimica et Biophysica Acta (BBA)-Molecular Basis of Disease*, vol. 1822, no. 5, pp. 794–814, 2012.
- [208] I. Batinic-Haberle, A. Tovmasyan, E. R. H. Roberts, Z. Vujaskovic, K. W. Leong, and I. Spasojevic, "SOD therapeutics: latest insights into their structure-activity relationships and impact on the cellular redox-based signaling pathways," *Antioxidants & redox signaling*, vol. 20, no. 15, pp. 2372–2415, 2014.
- [209] J. G. Costa, N. Saraiva, I. Batinic-Haberle, M. Castro, N. G. Oliveira, and A. S. Fernandes, "The SOD Mimic MnTnHex-2-PyP<sup>5+</sup> reduces the viability and migration of 786-O human renal cancer cells," *Antioxidants (Basel)*, vol. 8, no. 10, p. 490, 2019.
- [210] A. Flórido, N. Saraiva, S. Cerqueira et al., "The manganese(III) porphyrin MnTnHex-2-PyP<sup>5+</sup> modulates intracellular ROS and breast cancer cell migration: Impact on doxorubicin-treated cells," *Redox biology*, vol. 20, pp. 367–378, 2019.
- [211] Y. Yulyana, A. Tovmasyan, I. A. W. Ho et al., "Redox-active Mn porphyrin-based potent SOD mimic, MnTnBuOE-2-PyP<sup>5+</sup>, enhances carbenoxolone-mediated TRAIL-induced apoptosis in glioblastoma multiforme," *Stem cell reviews and reports*, vol. 12, no. 1, pp. 140–155, 2016.
- [212] S. L. Schlichte, E. J. Pekas, T. J. Bruett et al., "Sympathoinhibition and vasodilation contribute to the acute hypotensive response of the superoxide dismutase mimic, MnTnBuOE-2-PyP<sup>5+</sup>, in hypertensive animals," *Advances in Redox Research*, vol. 3, article 100016, 2021.
- [213] J. Trnka, F. H. Blaikie, A. Logan, R. A. Smith, and M. P. Murphy, "Antioxidant properties of MitoTEMPO and its hydroxylamine," *Free radical research*, vol. 43, no. 1, pp. 4–12, 2009.
- [214] J. S. Dickey, Y. Gonzalez, B. Aryal et al., "Mito-tempol and dexrazoxane exhibit cardioprotective and chemotherapeutic effects through specific protein oxidation and autophagy in a syngeneic breast tumor preclinical model," *PLoS one*, vol. 8, no. 8, article e70575, 2013.
- [215] J. E. Chipuk and D. R. Green, "How do BCL-2 proteins induce mitochondrial outer membrane permeabilization?," *Trends in cell biology*, vol. 18, no. 4, pp. 157–164, 2008.
- [216] Z. X. Chen and S. Pervaiz, "Bcl-2 induces pro-oxidant state by engaging mitochondrial respiration in tumor cells," *Cell Death & Differentiation*, vol. 14, no. 9, pp. 1617–1627, 2007.
- [217] X. Jiang and X. Wang, "Cytochrome C-Mediated apoptosis," *Annual review of biochemistry*, vol. 73, no. 1, pp. 87–106, 2004.
- [218] R. J. Youle and A. Strasser, "The BCL-2 protein family: opposing activities that mediate cell death," *Nature reviews Molecular cell biology*, vol. 9, no. 1, pp. 47–59, 2008.
- [219] C. M. Park, M. Bruncko, J. Adickes et al., "Discovery of an orally bioavailable small molecule inhibitor of prosurvival B-cell lymphoma 2 proteins," *Journal of medicinal chemistry*, vol. 51, no. 21, pp. 6902–6915, 2008.
- [220] G. Wierda, P. Roberts, R. Brown et al., "Pharmacokinetics, safety and anti-tumor activity of ABT-263 in patients with relapsed or refractory chronic lymphocytic leukemia/small lymphocytic lymphoma," *Haematologica-The Hematology Journal*, vol. 94, p. 138, 2009.
- [221] K. D. Mason, M. R. Carpinelli, J. I. Fletcher et al., "Programmed anuclear cell death delimits platelet life span," *Cell*, vol. 128, no. 6, pp. 1173–1186, 2007.
- [222] A. J. Souers, J. D. Levenson, E. R. Boghaert et al., "ABT-199, a potent and selective BCL-2 inhibitor, achieves antitumor activity while sparing platelets," *Nature medicine*, vol. 19, no. 2, pp. 202–208, 2013.
- [223] J. F. Seymour, M. S. Davids, J. M. Pagel et al., "ABT-199 (GDC-0199) in relapsed/refractory (R/R) chronic lymphocytic leukemia (CLL) and small lymphocytic lymphoma (SLL): High complete-response rate and durable disease control," *American Society of Clinical Oncology*, vol. 32, 15 supplement, p. 7015, 2014.
- [224] M. Konopleva, D. A. Pollyea, J. Potluri et al., "A phase 2 study of ABT-199 (GDC-0199) in patients with acute myelogenous leukemia (AML)," *Blood*, vol. 124, no. 21, p. 118, 2014.
- [225] R. Pan, L. J. Hogdal, J. M. Benito et al., "Selective BCL-2 inhibition by ABT-199 causes on-target cell death in acute myeloid leukemia," *Cancer discovery*, vol. 4, no. 3, pp. 362–375, 2014.
- [226] S. Peirs, F. Matthijssens, S. Goossens et al., "ABT-199 mediated inhibition of BCL-2 as a novel therapeutic strategy in T-cell acute lymphoblastic leukemia," *Blood*, vol. 124, no. 25, pp. 3738–3747, 2014.
- [227] J. F. Lovell, L. P. Billen, S. Bindner et al., "Membrane binding by tBid initiates an ordered series of events culminating in membrane permeabilization by Bax," *Cell*, vol. 135, no. 6, pp. 1074–1084, 2009.

- [228] P. E. Czabotar, D. Westphal, G. Dewson et al., “Bax crystal structures reveal how BH3 domains activate Bax and nucleate its oligomerization to induce apoptosis,” *Cell*, vol. 152, no. 3, pp. 519–531, 2013.
- [229] K. Huang, K. L. O’Neill, J. Li et al., “BH3-only proteins target BCL-xL/MCL-1, not BAX/BAK, to initiate apoptosis,” *Cell research*, vol. 29, no. 11, pp. 942–952, 2019.
- [230] S. N. Willis, J. I. Fletcher, T. Kaufmann et al., “Apoptosis initiated when BH3 ligands engage multiple Bcl-2 homologs, not Bax or Bak,” *Science*, vol. 315, no. 5813, pp. 856–859, 2007.

## Research Article

# Comprehensive Analysis of Ferroptosis-Related Markers for the Clinical and Biological Value in Gastric Cancer

Yanfei Shao <sup>1,2,3</sup> Hongtao Jia <sup>1,2,3</sup> Shuchun Li <sup>1,2</sup> Ling Huang <sup>1,2,3</sup>  
Batuer Aikemu <sup>1,2</sup> Guang Yang <sup>1,2</sup> Sen Zhang <sup>1,2,3</sup> Jing Sun <sup>1,2</sup>  
and Minhua Zheng <sup>1,2</sup>

<sup>1</sup>Department of General Surgery, Ruijin Hospital, Shanghai Jiao Tong University School of Medicine, Shanghai, China

<sup>2</sup>Shanghai Minimally Invasive Surgery Center, Ruijin Hospital, Shanghai Jiao Tong University School of Medicine, Shanghai, China

<sup>3</sup>Shanghai Institute of Digestive Surgery, Ruijin Hospital, Shanghai Jiao Tong University School of Medicine, Shanghai, China

Correspondence should be addressed to Sen Zhang; [zs01d43@rjh.com.cn](mailto:zs01d43@rjh.com.cn) and Jing Sun; [sj11788@rjh.com.cn](mailto:sj11788@rjh.com.cn)

Received 9 August 2021; Revised 10 September 2021; Accepted 15 September 2021; Published 27 October 2021

Academic Editor: Peichao CHEN

Copyright © 2021 Yanfei Shao et al. This is an open access article distributed under the Creative Commons Attribution License, which permits unrestricted use, distribution, and reproduction in any medium, provided the original work is properly cited.

Gastric cancer is a highly malignant tumor with poor survival rate. Ferroptosis, a newly defined regulated cell death, is closely related to several tumors. Introduction of ferroptosis is promising for cancer treatments. However, the predictive role of ferroptosis in GC remains elusive. In this study, we screened the ferroptosis-related genes which were differentially expressed between normal and GC tissues. Then, based on these differentially expressed genes (DEGs), the least absolute shrinkage and selection operator (LASSO) and multivariate Cox regressions were applied to construct the 10-gene prognostic signature (*SPI1*, *MYB*, *ALDH3A2*, *KEAP1*, *AIFM2*, *ITGB4*, *TGFBRI*, *MAP1LC3B*, *NOX4*, and *ZFP36*) in TCGA training dataset. Based on the median risk score, all GC patients in TCGA training dataset and GSE84437 testing dataset were classified into a high- or low-risk group. GC patients in the low-risk group showed significantly higher survival possibilities than those in the high-risk group ( $P < 0.001$ ). Combined with the clinical characteristics, the risk score was proven as an independent factor for predicting the OS of GC patients. Besides, the GC patients in the high- or low-risk group showed significantly different GO and KEGG functional enrichments, somatic mutation, fractions of immune cells, and immunotherapy response. Then, the expression levels of these genes in signature were further verified in the GC cell lines and our own GC samples (30-paired tumor/normal tissues). Furthermore, the effects of ferroptosis inducer Erastin on these 10 ferroptosis-related genes in GC cell lines were also explored in our study. In conclusion, our study constructed a prognostic signature of 10 ferroptosis-related genes, which could well predict the prognosis and immunotherapy for GC patients.

## 1. Introduction

Gastric cancer (GC) is one of the most common malignant tumors in the world, ranking fifth for incidence (1,089,103 cases) and fourth for mortality (768,793 cases) globally in 2020 [1]. Besides, the incidence rate of GC is the highest in digestive malignant tumors in China [2]. Due to the comprehensive treatments in the last few decades, including curative surgery, chemoradiotherapy, targeted therapy, and immunotherapy, the prognosis of GC patients has improved a lot. However, most patients are diagnosed at advanced stages; the overall survival (OS) rate of 5 years remains less than 40% [3]. Currently, the prognosis of GC patients was based

on the TNM staging system; nevertheless, the patients at the same stage could show obviously different prognosis. Therefore, it is necessary to identify novel and reliable biomarkers to accurately predict prognosis, to find potential therapeutic targets, and finally to improve the outcomes of GC patients.

Distinct from apoptosis, ferroptosis is a newly defined form of programmed cell death characterized by iron-dependent peroxide lipid accumulation, inducing reactive oxygen species (ROS) production and subsequent cell death [4]. Emerging evidence has demonstrated that ferroptosis plays a critical role in the redox status, cell metabolism, and multiple diseases, such as ischemia-reperfusion injury, neurodegenerative and neuropsychiatric diseases, and

diverse kidney diseases [4–6]. More importantly, ferroptosis dysfunction has been implicated in the process of various tumors, including glioma [7], lung cancer [8], breast cancer [9], renal cell carcinoma [10], colorectal cancer [11], and gastric cancer [12]. Ferroptosis is inhibited in various tumors, resulting in uncontrolled proliferation of tumor cells, and is also involved in immunotherapy and drug sensitivity. Therefore, ferroptosis can serve as a promising interventional target to induce tumor cell death. Recent studies also identified some key ferroptosis-related gene signature, such as glutathione peroxidase 4 (*GPX4*), solute carrier family 7 member 11 (*SLC7A11*), nuclear respiratory factor 2 (*NRF2*), and cysteine dioxygenase type 1 (*CDO1*), which are closely related to cancer progression and patients' prognosis [13–16]. However, only few studies to date focused on the role of ferroptosis in GC, and whether ferroptosis-related genes are related to patients' prognosis and clinical treatments still needs to be fully elucidated.

In this study, we constructed and validated a ferroptosis-related gene signature, which could well predict the prognosis of GC patients. We further performed pathway and functional enrichment analysis to study the underlying mechanisms. The clinical value of the risk model based on this ferroptosis-related gene signature was also explored in immune microenvironment and tumor mutation burden of GC. In addition, the effects of ferroptosis inducer Erastin on these 10 ferroptosis-related genes in GC cell lines were also explored in our study.

## 2. Materials and Methods

**2.1. Collection of Data.** The RNA sequencing (RNA-seq) data and corresponding clinical characteristics and molecular information of gastric cancer (GC) samples (normal: 32, tumor: 375) in training cohort (TCGA-STAD) were downloaded from The Cancer Genome Atlas (TCGA) database by the “TCGAbiolinks” R package in February 2021. Similarly, the RNA-seq data of 174 normal human stomach samples in the Genotype-Tissue Expression (GTEx) database was downloaded from the University of California Santa Cruz (UCSC, <https://xenabrowser.net/datapages/>). Besides, the gene expression data and corresponding clinical information of the external validation cohort (GSE84437,  $n = 433$ ; GSE29272,  $n = 268$ ; normal: 134, tumor: 134) were downloaded from the Gene Expression Omnibus (GEO) database (<https://www.ncbi.nlm.nih.gov/>). Furthermore, the somatic mutation data of the TCGA-STAD was downloaded from the websites (<https://portal.gdc.cancer.gov/>). The 261 ferroptosis-related genes were downloaded from the FerrDb website (<http://www.zhounan.org/ferrdb/>), updating on 10 March 2021 [17].

**2.2. Screening of Candidate Gene.** The RNA-seq data of TCGA and GTEx datasets was normalized into the transcripts per million (TPM) data. And the scale function in the dplyr R package was employed to further normalize the RNA-seq data (TPM normalized). Batch correction was performed using the sva R package. Then, the RNA-seq data of the 261 ferroptosis-related genes was extracted to perform

subsequent difference analysis. Differentially expressed gene (DEG) analysis between the normal and tumor tissues was performed by limma R package, screening out the ferroptosis-related differentially expressed genes (FDEGs). And the results of the FDEGs were visualized by ggplot2 R package. Then, univariate Cox regression analysis was performed to screen out the overall survival- (OS-) associated FDEGs which were identified as the candidate genes for subsequent establishment of prognostic ferroptosis-related gene signature.

**2.3. Establishment and Validation of a Prognostic Ferroptosis-Related Gene Signature.** In order to minimize the risk of overfitting, the least absolute shrinkage and selection operator (LASSO) regression was utilized to establish a gene prognostic signature and further screen the 10 potential hub genes from the FDEGs by the glmnet R package. Then, the protein-protein interaction (PPI) network was conducted to reveal the interaction of proteins among the protein coding between the 10 genes by the STRING database (<http://www.string-db.org/>). In order to explore the connection of the transcriptional level among these 10 candidate genes, the igraph and reshape2 R packages were utilized to construct correlation network of these 10 candidate genes. The multivariate Cox regression analysis based on these 10 genes was utilized to establish the prognostic ferroptosis-related gene signature. The regression coefficients of genes and their corresponding mRNA expressions were utilized to calculate the risk scores of patients. The formula of risk score was established as follows:  $\text{score} = \sum(\text{corresponding mRNA expressions} \times \text{regression coefficients})$ . The median value of risk scores was utilized as the cutoff value to divide GC patients into the high- and low-risk subgroups. To test the distribution of different groups, the principal component analysis (PCA) was performed by the Rtsne and ggplot2 R packages. The survival curves were performed to analyze the prognostic status between the high- and low-risk groups by the survminer R package. And the time-dependent receiver operating characteristic curve (ROC) was performed to evaluate the predictive value of the prognostic signature by the survival and timeROC R package. Besides, the univariate and multivariate Cox regression analysis was also performed to evaluate the independent prognostic value of the prognostic signature. Furthermore, nomograms of the training and testing groups were constructed to predict the survival probability of GC patients in 1, 2, and 3 years, and their corresponding nomogram calibration curves were also constructed based on the multivariate Cox regression analysis by the rms R package.

**2.4. Functional Enrichment Analysis.** The OmicShare tools, a free online platform for data analysis (<https://www.omicshare.com/tools>), was employed to perform Gene Ontology (GO) and Kyoto Encyclopedia of Genes and Genomes (KEGG) analysis with  $P < 0.05$  and normalized enrichment score  $> 1$  based on the DEGs between the high- and low-risk groups. The Gene Set Enrichment Analysis (GSEA) software (<https://www.gsea-msigdb.org/gsea/login.jsp/>) was also utilized to further reveal the significantly enriched pathways

of these DEGs. Furthermore, the *maftools* R package was utilized to explore and visualize the MAF files of somatic mutation data and also calculate the tumor mutation burden (TMB) scores of patients in the training group.

**2.5. Immunotherapy Targets and Immune Infiltration Analysis.** To explore the potential relationship between the 10-gene signature and the immune cell infiltration, Tumor Immune Estimation Resource (TIMER) which is a platform for analyzing the abundance of the six immune infiltration cells (macrophages, dendritic cells, neutrophils, CD4<sup>+</sup> T cells, CD8<sup>+</sup> T cells, and B cells) in malignant tumors was applied to evaluate the associations between the 10 hub genes and the infiltrating immune cells by Pearson correlation analysis and Student's *t*-test. And the *estimate* R package was utilized to explore the relationship between the risk scores and immune cell infiltration. Besides, considering the significant roles of more immune cells in the tumor microenvironment, the abundance of 22 infiltrating immune cell types in each tumor sample was calculated by CIBERSORT. Furthermore, the expression of the target genes which have been reported to be related to the immunotherapy was compared between different risk groups.

**2.6. Expression Verification of the 10 FDEGs in the Datasets, Cell Lines, and Gastric Cancer Specimen.** The differential expression levels of the 10 FDEGs between the normal and tumor stomach tissues in the training and testing groups were compared by the Wilcoxon rank-sum test. Besides, the results of the differential expression levels of the 10 FDEGs were verified by Gene Expression Profiling Interactive Analysis (GEPIA) tools (<http://gepia.cancer-pku.cn/detail.php>). Furthermore, a total of 30-paired normal/tumor GC specimens were recruited from Ruijin Hospital (Shanghai, China) following the guidelines set by the Ethical Committee of Ruijin Hospital. The tumor and adjacent normal stomach tissues were fixed by 10% formalin and embedded by paraffin. The optimum sections of tissue specimens were selected and deparaffinized, and immunohistochemistry (IHC) was implemented as the following antibodies: SP1 (Abcam, ab124804), NOX4 (Abcam, ab109225), AIFM2 (Proteintech, 20886-1-AP), and TFAP2C (Proteintech, 60027-1-ig). Finally, GES1, HGC-27, and MGC-803 cell lines were also applied to verify the expression of all the 10 FDEGs using real-time PCR.

**2.7. Gastric Cancer Cell Lines and Cell Culture.** GES1, HGC-27, and MGC-803 cell lines were obtained from the American Type Culture Collection (ATCC, Manassas, VA) and stored at the Shanghai Institute of Digestive Surgery. All the three cell lines were cultured in RPMI-1640 medium (Meilunbio, China) supplemented with 10% fetal bovine serum (Sunrise, Uruguay) in a humidified atmosphere at 37°C with 5% CO<sub>2</sub>.

**2.8. Cytotoxicity Assay.** For cytotoxicity assay, HGC-27 and MGC-803 cells were seeded in 96-well plates at a density of 5000/well and cultured in a humidified atmosphere at 37°C with 5% CO<sub>2</sub> for 12 h. The ferroptosis inducer Erastin (Selleck, USA) was dissolved in dimethyl sulfoxide (DMSO) to a total concentration of 40 mM. The working concentra-

tions were diluted to 0, 0.75, 1.5, 3, 6, 12, 25, and 50 μM, and six wells were applied for each concentration. Cell proliferation was assessed using the Cell Counting Kit-8 (CCK-8; Meilunbio, China). The optical density (OD) values were measured at the 450 nm absorbance using a microplate reader. Then, the half maximal inhibitory concentration (IC<sub>50</sub>) values of each cell line were calculated, and the inhibition curve was plotted by *ggplot2* R package.

**2.9. Reactive Oxygen Species (ROS) Measurement.** HGC-27 and MGC-803 cells were cultured in 6-well and 12-well plates for 24 h. Firstly, different working concentrations of Erastin (5, 10, and 20 μM) were added to each well and treated for another 48 h. Then, these cells were washed twice with PBS and incubated with fresh RPMI-1640 medium containing 10 μM 2',7'-dichlorofluorescein diacetate (DCF; Sigma, D6883, USA) at 37°C with 5% CO<sub>2</sub> for 30 min. The cells in 12-well plates were washed twice with PBS, and then, the different ROS fluorescence intensity of these cells was compared by the fluorescence microscope. In addition, the cells in 6-well plates were also washed twice with PBS and trypsinized (Meilunbio, China). The harvested cells were resuspended in PBS at 10<sup>6</sup>-10<sup>7</sup> cells/ml, and their ROS levels were measured using flow cytometry with emission at 515-545 nm and excitation at 488 nm.

**2.10. RNA Isolation and Real-Time PCR.** Total RNA was extracted from culture cells using RNA isolator (Vazyme, China). 1 μg of total RNA was reverse transcribed into complementary DNA (cDNA) using HiScript III RT SuperMix for qPCR with gDNA wiper (Vazyme, China). Then, real-time PCR was performed using ChamQ™ Universal SYBR qPCR Master Mix (Vazyme, China). The cyclor protocol was 5 min at 95°C, 40 cycles of 15 s at 95°C, 60 s at 60°C, and 5 min at 72°C [18]. All primers were synthesized by Tsingke (Beijing, China) and listed in Table 1. The mRNA expression levels of the 10 candidate genes were calculated using the 2<sup>-ΔΔCt</sup> method and normalized against that of GAPDH.

**2.11. Western Blot.** Cells were washed twice with PBS and then lysed with RIPA buffer containing 1% PMSF on ice for 30 min and transferred to the centrifuge tubes for centrifugation at 12000 rpm for 20 min at 4°C. The BCA assay (Beyotime, China) was used to quantify the proteins, and the equal amounts of protein were separated by 10% SDS-PAGE, transferred onto the PVDF membranes, and incubated with appropriate antibodies (SP1: Abcam, ab124804, 1:1000; NOX4: Abcam, ab109225, 1:1000; AIFM2: Proteintech, 20886-1-AP, 1:1000; and TFAP2C: Proteintech, 60027-1-ig, 1:1000) overnight at 4°C. Then, samples were incubated with anti-horseradish peroxidase-linked IgG secondary antibody (Proteintech, SA00001-1 and SA00001-2, 1:5000) at room temperature for 1 h and detected using chemiluminescence detection system (Tanon, China). Immunoreactive bands were measured using the sensitive ECL kit (Meilunbio, China).

**2.12. Statistical Analysis.** All the statistical analysis was conducted by the R software (version: 3.6.3) in this article. All P

TABLE 1: Real-time PCR primer sequences.

| Gene     | Sequence                               |
|----------|--|
| SP1      | Forward primer: TGCCTTTTCACAGGCTCGAA   |
|          | Reversed primer: TTGTGTGGCTGTGAGGTCAG  |
| MAP1LC3B | Forward primer: TTCGAGAGCAGCATCCAACC   |
|          | Reversed primer: GATTGGTGTGGAGACGCTGA  |
| KEAP1    | Forward primer: ACGGGACAAACCGCCTTAAT   |
|          | Reversed primer: GTCCAGGAACGTGTGACCAT  |
| AIFM2    | Forward primer: TGCACCGGCATCAAGATCAA   |
|          | Reversed primer: AATGGCGTAGACGTTGCTGT  |
| MYB      | Forward primer: GATCCTGGCTCCCTACCTGA   |
|          | Reversed primer: CCAGTGGTGTGAGCAGAAGA  |
| ALDH3A2  | Forward primer: GGGATGGGAGCTTATCACGG   |
|          | Reversed primer: CACAGCGGCTACAATACCCA  |
| ITGB4    | Forward primer: TGTCCATCCCCATCATCCCT   |
|          | Reversed primer: CCCGATGGAGAGCGTAGAAC  |
| TGFBF1   | Forward primer: GTGACAGATGGGCTCTGCTT   |
|          | Reversed primer: AAGGGCCAGTAGTTGGAAGT  |
| NOX4     | Forward primer: AGCTGCCCACTTGGTGAACGC  |
|          | Reversed primer: TCAGGCCCGGAACAGTTGTGA |
| ZFP36    | Forward primer: CCACCCCAAATACAAGACGGA  |
|          | Reversed primer: CAGGTCTTCGCTAGGGTTGT  |
| GAPDH    | Forward primer: TGAAGGTCGGAGTCAACGG    |
|          | Reversed primer: CCTGGAAGATGGTGATGGG   |

values of statistical data were based on two-sided statistical tests.  $P < 0.05$  was considered to be statistically significant.

### 3. Results

**3.1. Identification of the FDEGs.** Firstly, the batch effect between the GTEx and TCGA cohorts had been corrected and the results are shown in Figures 1(a) and 1(b). Then, a total of 166 ferroptosis-related genes were proven to differentially express between the 206 normal and 375 tumor stomach samples ( $|\log_2FC| > 0.5$  and false discovery rate (FDR)  $< 0.01$ ). The volcano and heat map plots were drawn to show the different expressions of ferroptosis-related genes between the normal and tumor samples based on  $|\log_2FC|$  and FDR (Figures 1(c) and 1(d)).

**3.2. Establishment of Ferroptosis-Related Prognostic Signature.** 36 samples without complete OS or OS time information in TCGA training group and 136 samples whose OS time over 9 years were eliminated. Then, 29 ferroptosis-related genes were correlated with OS by the univariate Cox analysis ( $P < 0.05$ ) in the training group and 18 of them were differentially expressed between normal and tumor tissues (Figures 2(a) and 2(b)). LASSO Cox regression analysis was utilized to construct a prognostic signature using the expression value of the 18 prognostic FDEGs mentioned above. Then, a 10-gene signature (*SP1*, *MYB*, *ALDH3A2*, *KEAP1*, *AIFM2*, *ITGB4*, *TGFBF1*, *MAP1LC3B*, *NOX4*, and *ZFP36*) was filtered out by the minimum value of lambda ( $\lambda$ ) (Figure 2(c)). The coefficients of these genes

are shown in Figure 2(d). And the full names, function, and coefficients of these 10 genes are shown in Table S1. According to the value of coefficients and hazard ratio (HR), the genes *TGFBF1*, *MAP1LC3B*, *NOX4*, and *ZFP36* were considered as the risk genes, while the genes *SP1*, *MYB*, *ALDH3A2*, *KEAP1*, *AIFM2*, and *ITGB4* as the protective genes. The protein interaction network among these 10 genes indicated that *NOX4*, *SP1*, and *KEAP1* were the hub genes (Figure 2(e)). The gene correlation among them is shown in Figure 2(f). Besides, the risk scores of the signature were applied to predict prognosis in GC patients and median risk score was utilized to classify patients into the high- or low-risk groups, which was calculated as follows: risk score =  $(-0.181) \times$  expression of *SP1* +  $(-0.085) \times$  expression of *MYB* +  $(-0.076) \times$  expression of *ALDH3A2* +  $(-0.075) \times$  expression of *KEAP1* +  $(-0.031) \times$  expression of *AIFM2* +  $(-0.026) \times$  expression of *ITGB4* +  $(0.072) \times$  expression of *TGFBF1* +  $(0.138) \times$  expression of *MAP1LC3B* +  $(0.148) \times$  expression of *NOX4* +  $(0.345) \times$  expression of *ZFP36*.

**3.3. Evaluation and Validation of Ferroptosis-Related Gene Signature.** As shown in Figure S1, PCA of the training and testing groups revealed that the patients in different risk groups could be distributed in two discrete directions. The high-risk GC patients were more likely to die earlier than low-risk patients from the results of the scatterplots (Figure 3(a)) and heat maps (Figure 3(b)). Besides, the Kaplan-Meier survival curve (Figure 3(c)) indicated that patients with low-risk scores may have a better prognosis than patients with high-risk scores in the training group. The sensitivity and specificity of the risk scores to predict prognostic features were determined from the time-dependent ROC curves by calculating the areas under the curve (AUC). And the risk scores presented the potential ability of predicting the OS status (1-year AUC = 0.722, 2-year AUC = 0.704, and 3-year AUC = 0.680) in Figure 3(d). In order to avoid the contingency of TCGA results, patients in the testing group were also classified into the low- and high-risk groups based on the median risk score. Similar to all the results above, patients with high-risk scores had a higher probability to encounter death earlier and had worse overall survival outcome than those with low-risk scores (Figures 3(e)–3(h)).

**3.4. Analysis of Independent Prognostic Factors.** The univariate and multivariate Cox regression analysis was applied to evaluate whether the risk score was the independent prognostic factor of GC patients. Firstly, in the training group, the results of the univariate Cox regression analysis showed that the risk score ( $P < 0.001$ , HR = 3.154, 95%CI = 2.104 – 4.728) and other clinical parameters, including T stage ( $P = 0.044$ , HR = 1.634, 95%CI = 1.014 – 2.633), N stage ( $P = 0.025$ , HR = 1.648, 95%CI = 1.065 – 2.548), and TNM stage ( $P < 0.001$ , HR = 1.515, 95%CI = 1.207 – 1.902), were significantly associated with OS (Figure 4(a)). Then, the multivariate Cox regression analysis indicated that the risk score ( $P < 0.001$ , HR = 3.626, 95%CI = 2.362 – 5.566) and TNM stage ( $P = 0.005$ , HR = 1.622, 95%CI = 1.155 – 2.277) were the independent prognostic factors of the OS



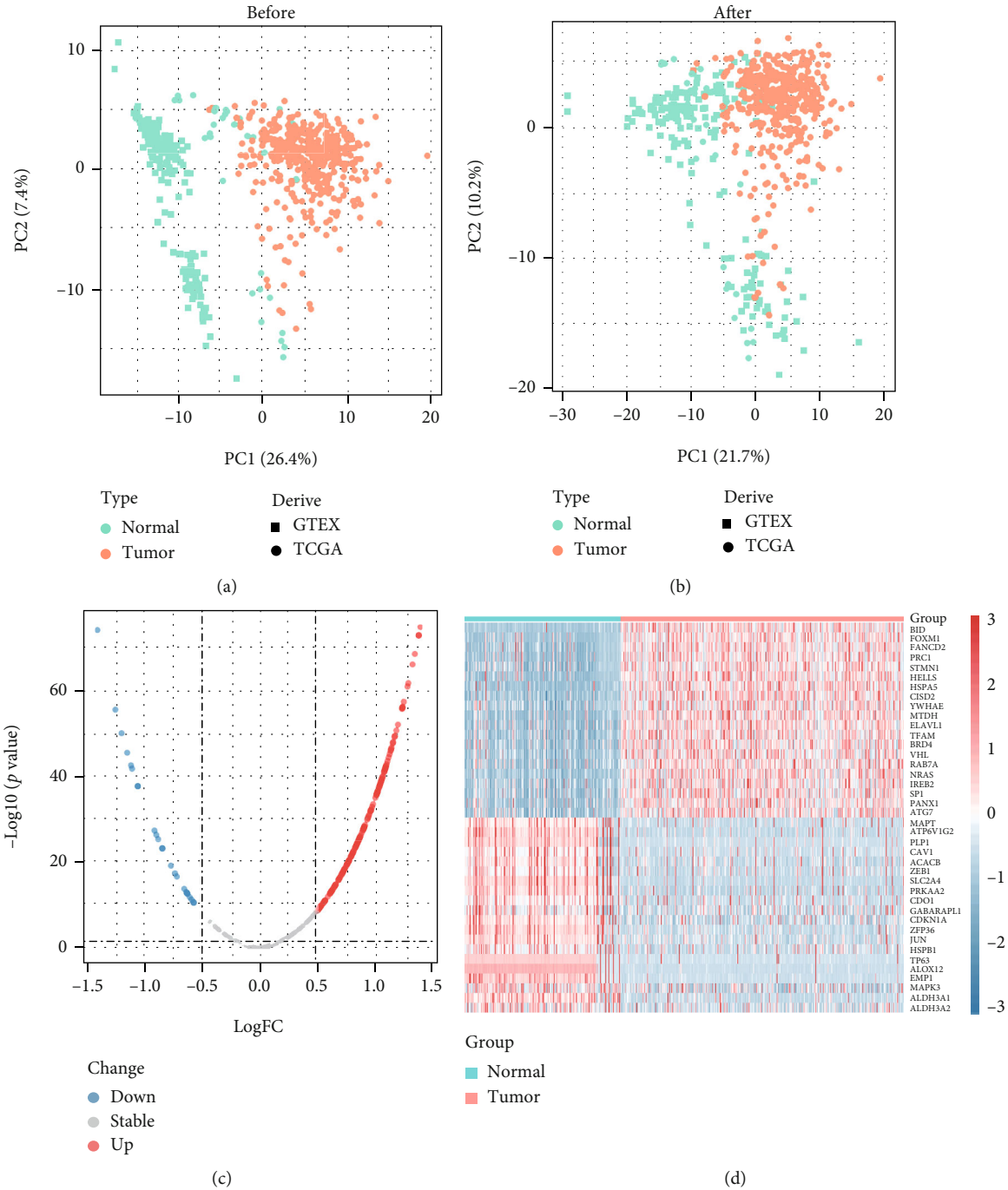


FIGURE 1: (a, b) PCA plots show batch correction between GTEX and TCGA-STAD datasets. (c) Volcano plot and (d) heat map of the FDEGs between the normal and tumor tissues from the GTEX and TCGA datasets.

(Figure 4(b)). Similar to the results above, in the testing group, the risk score was also verified to be the independent prognostic factors of the OS (Figures 4(c) and 4(d)).

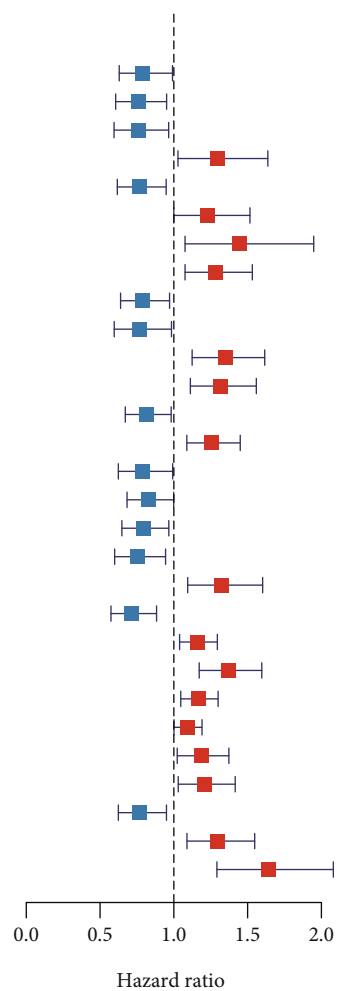
**3.5. Construction and Validation of the Nomogram Prediction Model.** In order to predict the survival probability of GC patients at 1, 2, and 3 years, the clinicopathological characteristics, including grade, N stage, T stage, TNM stage, and risk score, were applied to construct the nomogram prediction model in the training group (Figure 4(e)). The

corresponding calibration curves were shown to perform the good prediction in the observations in 1-3 years (Figure 4(f)). Thus, the nomogram incorporating clinical features and the risk score was stable and accurate and may be applied in the clinical evaluation of GC patients.

**3.6. Analysis of Functional Enrichment.** In order to further explore the signature-related downstream molecular biological functions and pathways, the GO enrichment and KEGG pathway analyses were performed by the DEGs between the

|           | <i>p</i> value | Hazard ratio        |
|-----------|----------------|---------------------|
| AIFM1     | 0.042          | 0.790 (0.630–0.991) |
| AIFM2     | 0.017          | 0.759 (0.606–0.951) |
| ALDH3A2   | 0.024          | 0.758 (0.595–0.965) |
| ATF3      | 0.028          | 1.297 (1.028–1.637) |
| ATG4D     | 0.014          | 0.765 (0.617–0.948) |
| ATP6V1G2  | 0.050          | 1.231 (1.000–1.516) |
| CBS       | 0.014          | 1.448 (1.076–1.948) |
| CDO1      | 0.006          | 1.284 (1.076–1.532) |
| CHAC1     | 0.025          | 0.788 (0.639–0.971) |
| FANCD2    | 0.037          | 0.766 (0.596–0.984) |
| GABARAPL1 | 0.001          | 1.348 (1.124–1.616) |
| GABARAPL2 | 0.001          | 1.317 (1.112–1.559) |
| GOT1      | 0.031          | 0.812 (0.671–0.982) |
| HBA1      | 0.002          | 1.256 (1.088–1.450) |
| HELLS     | 0.042          | 0.787 (0.624–0.992) |
| HNF4A     | 0.049          | 0.826 (0.683–0.999) |
| ITGB4     | 0.021          | 0.791 (0.648–0.966) |
| KEAP1     | 0.014          | 0.752 (0.599–0.944) |
| MAP1LC3B  | 0.004          | 1.324 (1.094–1.602) |
| MYB       | 0.002          | 0.712 (0.574–0.883) |
| NOX3      | 0.008          | 1.160 (1.039–1.295) |
| NOX4      | < 0.001        | 1.368 (1.172–1.596) |
| NOX5      | 0.005          | 1.167 (1.047–1.300) |
| PAX3      | 0.048          | 1.092 (1.001–1.191) |
| PLIN2     | 0.024          | 1.185 (1.023–1.373) |
| S MPD1    | 0.020          | 1.208 (1.030–1.416) |
| SP 1      | 0.015          | 0.770 (0.624–0.950) |
| TGFBR1    | 0.004          | 1.298 (1.089–1.548) |
| ZFP36     | < 0.001        | 1.640 (1.292–2.081) |

(a)



(b)

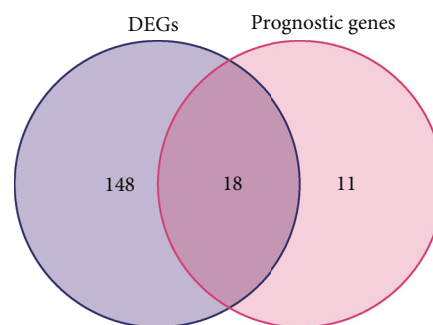


FIGURE 2: Continued.

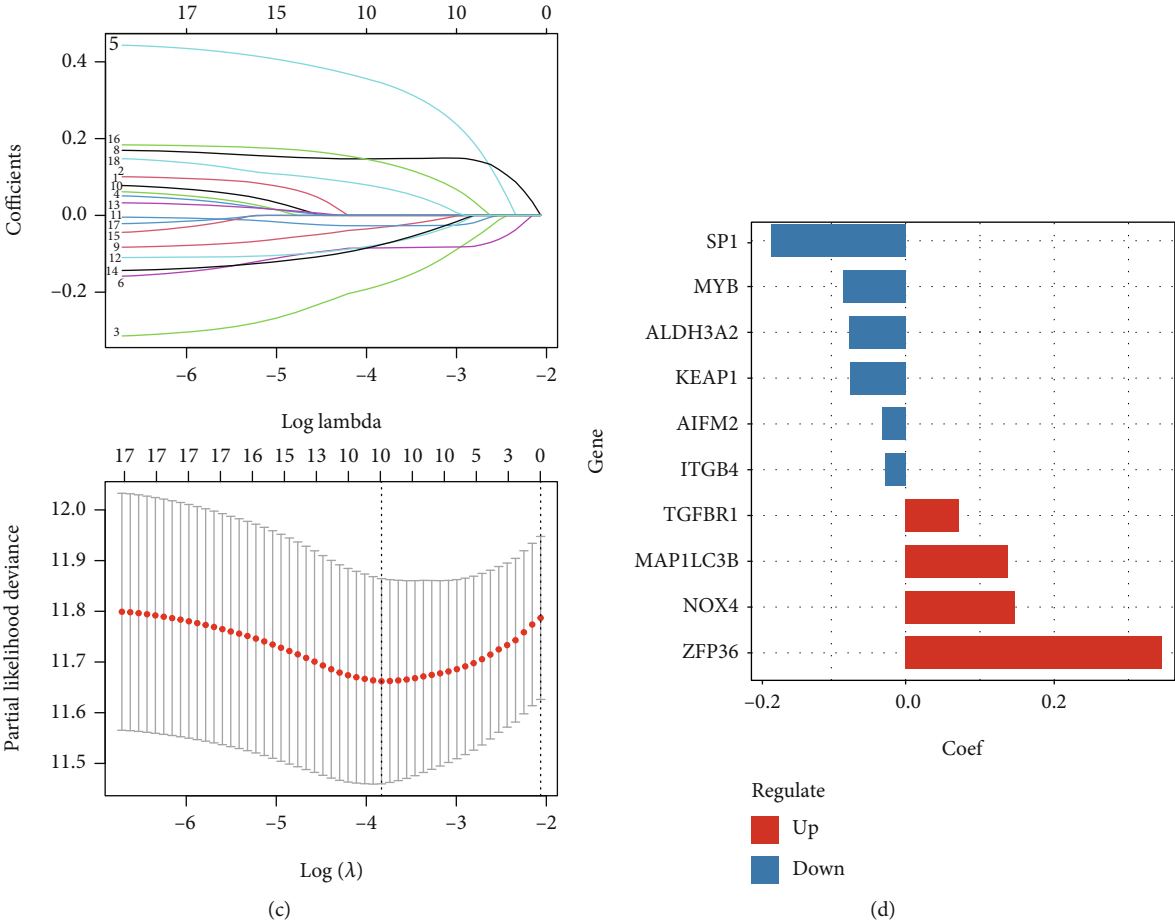


FIGURE 2: Continued.

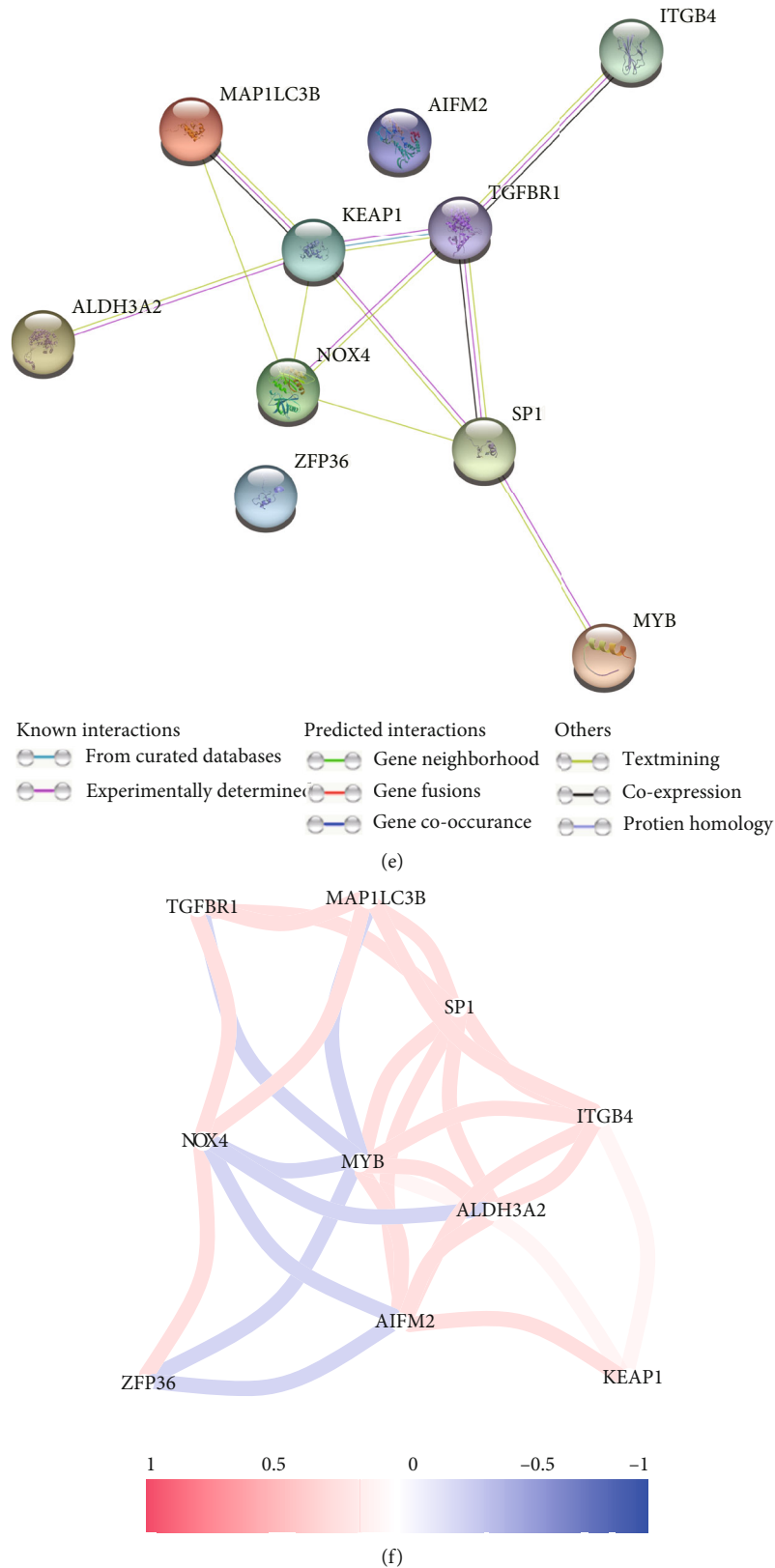


FIGURE 2: (a) Forest plot shows the results of the univariate Cox regression analysis between the expression and prognosis of ferroptosis-related genes in the training group. (b) Venn plot identifies the FDEGs that were correlated with prognosis. (c) The log lambda value and the 10 prognostic ferroptosis-related genes with nonzero coefficient. (d) Bar plot shows the coefficient of each gene. (e) PPI network constructed by STRING to indicate the interactions among these 10 genes. (f) The network plot shows the correlation among these 10 genes.

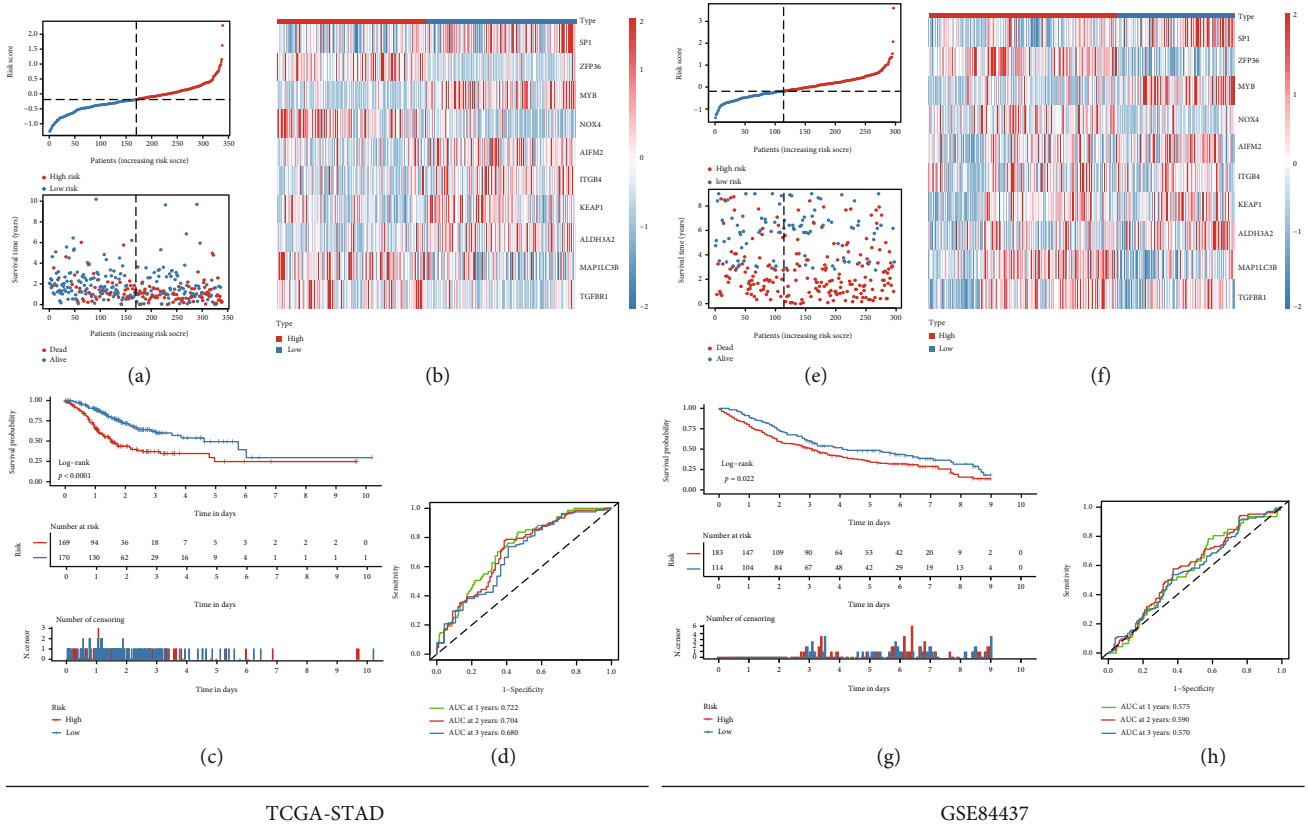


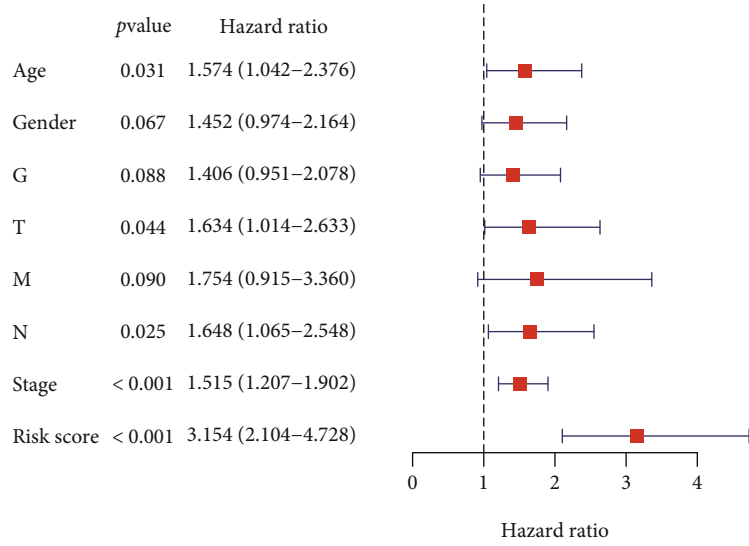
FIGURE 3: (a) The OS status and OS risk score plots of these 10 genes in the TCGA-STAD training dataset. (b) The heat map of these 10 genes between the high- and low-risk groups in the TCGA-STAD training dataset. (c) Kaplan-Meier survival curves for the OS between the high- and low-risk groups in the TCGA-STAD training dataset. (d) AUC of time-dependent ROC curve for the risk score in the TCGA-STAD training dataset. (e) The OS status and OS risk score plots of these 10 genes in the GSE84437 testing dataset. (f) The heat map of these 10 genes between the high- and low-risk groups in the GSE84437 testing dataset. (g) Kaplan-Meier survival curve for the OS between the high- and low-risk groups in the GSE84437 testing dataset. (h) AUC of time-dependent ROC curve for the risk score in the GSE84437 testing dataset.

high- and low-risk groups in the training and testing group. The results of GO enrichment analysis indicated that DEGs could be enriched in several tumorigenesis-related molecular functions, such as cell junction, metabolic process, immune system process, and catalytic activity in both the training and testing groups (Figures 5(a) and 5(b)). Similarly, several tumorigenesis-related pathways were also enriched based on KEGG pathway analysis, including cell cycle, regulation of actin cytoskeleton, DNA replication, ECM-receptor interaction, and focal adhesion (Figures 5(c) and 5(d)). Meanwhile, cell cycle, focal adhesion, and ECM-receptor interaction were enriched by the GSEA software and shown in Figures 5(e) and 5(f). In summary, all results of the functional enrichment analysis indicated that the risk score of the ferroptosis-related gene signature was significantly related to tumorigenesis of GC.

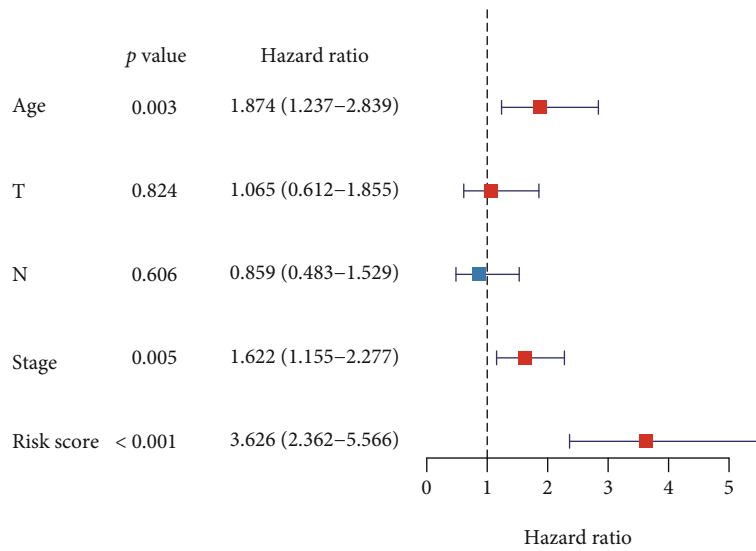
**3.7. Analysis of Somatic Mutation.** Somatic mutations were closely related to the tumorigenesis of gastric cancer. To further explore the relationship between somatic mutation and risk score, simple nucleotide variation data of the high- and low-risk groups in TCGA cohort was downloaded and analyzed. The gene mutation information of the GC patients

was shown in the bar and waterfall plots. Titin (*TTN*) (47%), tumor protein P53 (*TP53*) (43%), and LDL receptor-related protein 1B (*LRP1B*) (25%) were the top three genes with the highest mutation frequencies in the high-risk group and *TTN* (58%), *TP53* (49%), and mucin 16, cell surface-associated (*MUC16*) (36%) in the low-risk group (Figures 6(a) and 6(b)), while TP53 was relatively high mutated in the low-risk group (Figures 6(c) and 6(d)). The forest plot was drawn to show the difference of gene mutation distributions between the high- and low-risk groups (Figure 6(e)). Besides, tumor mutation burden (TMB) was calculated and analyzed in both groups, indicating that TMB level was significantly higher in the low-risk group (Figure 6(f)).

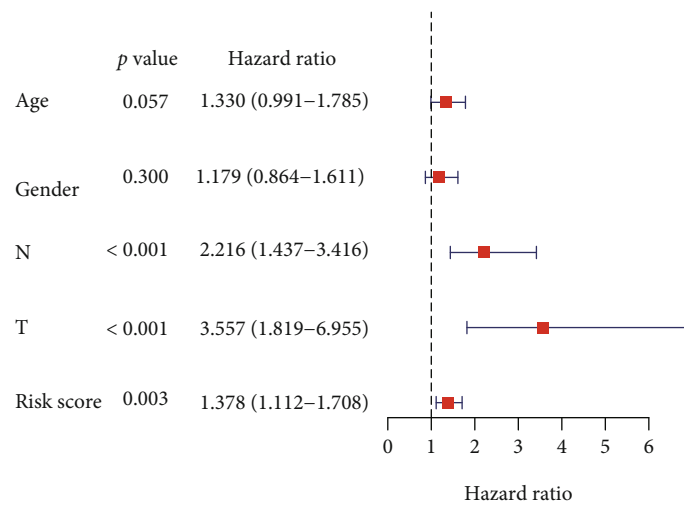
**3.8. Analysis of Tumor Microenvironment and Immunotherapy Response.** According to the results of the functional enrichment analysis, immune process was significantly different between the high- and low-risk GC patients (Figure S2). Thus, TIMER and CIBERSORT analysis was utilized to further explore the relationship between risk score and tumor microenvironment. Firstly, the results of TIMER analysis indicated that the 10 FDEGs were associated with all 6 immune infiltration cells (purity, B



(a)



(b)



(c)

FIGURE 4: Continued.

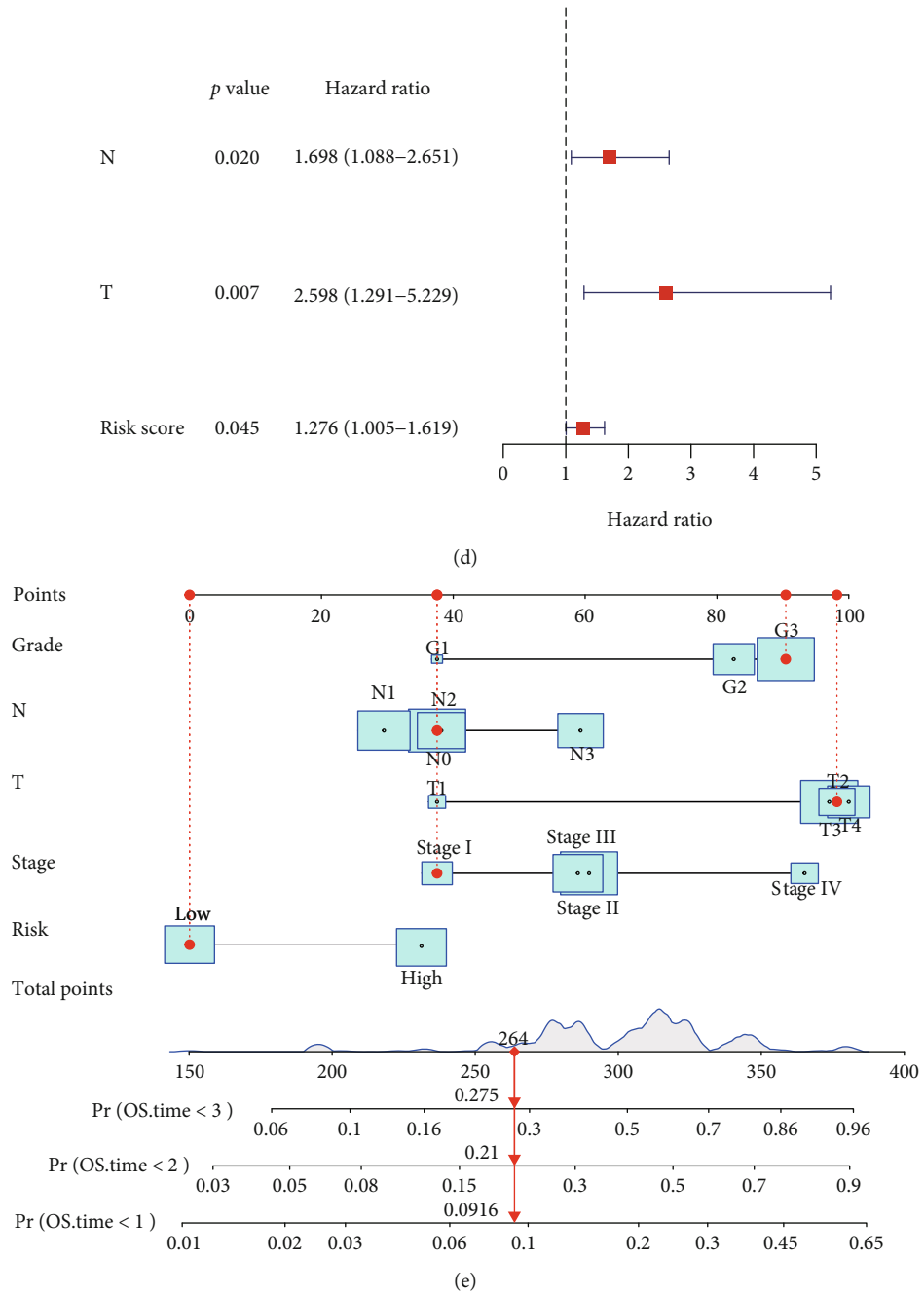


FIGURE 4: Continued.

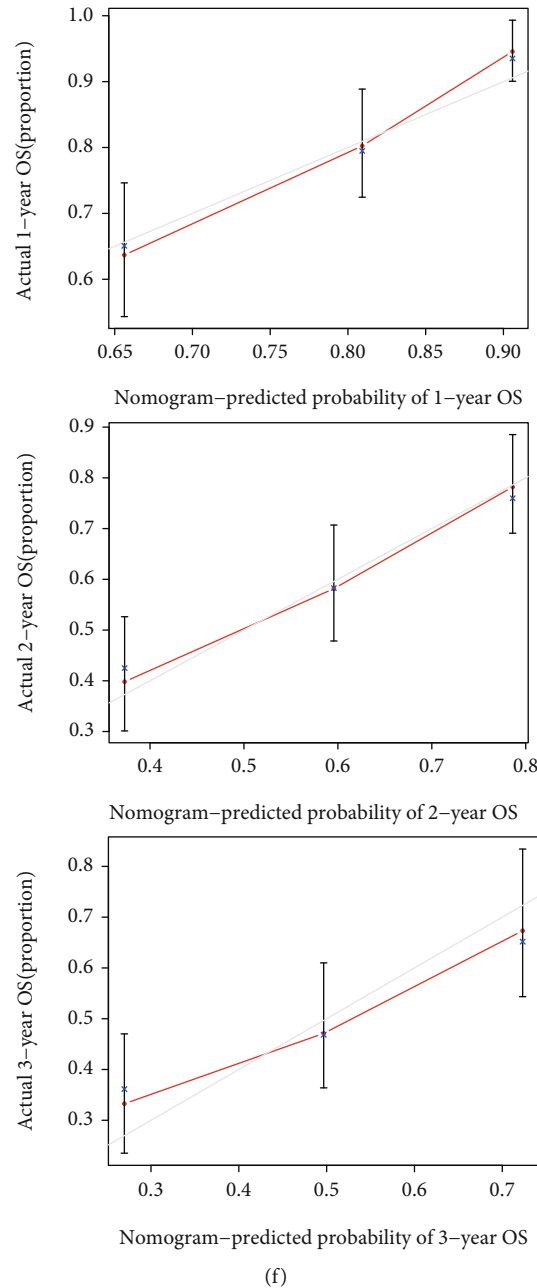


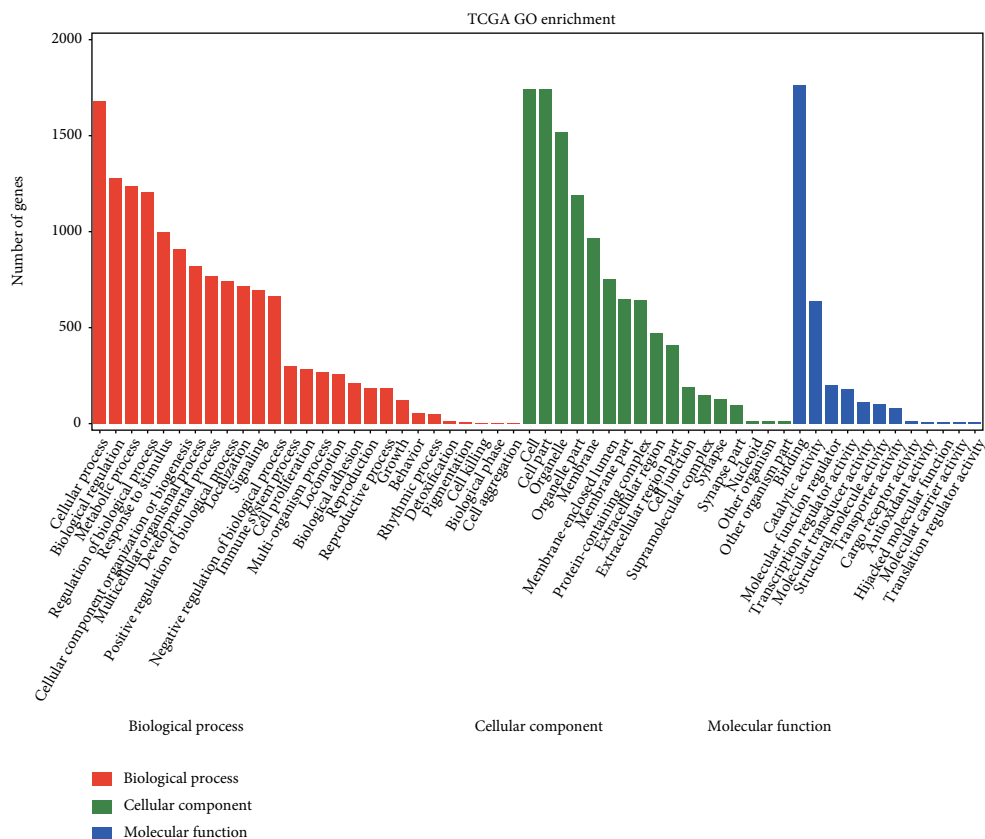
FIGURE 4: The forest plots show the results of the univariate and multivariate Cox regression analysis regarding OS in (a, b) the TCGA-STAD training and (c, d) the GSE84437 testing datasets. (e) Nomograms for predicting 3-year survival in the TCGA-STAD training dataset. (f) Calibration curves for the nomogram predicting 1- to 3-year survival in the TCGA-STAD training dataset.

cell, CD8<sup>+</sup> T cell, CD4<sup>+</sup> T cell, macrophage, neutrophil, and dendritic cell), especially for *NOX4*, *AIFM2*, and *SP1* genes (Figure S3). Meanwhile, CIBERSORT was also applied to estimate the different infiltration abundance of 22 immune cells between the high- and low-risk groups in the training group. The results showed that mast cells resting, B cells naive, dendritic cells resting, and monocytes were downregulated in the low-risk groups, while NK cells resting, macrophages M0, and T cells follicular helper were significantly upregulated ( $P < 0.05$ , Figures 7(a)–7(c)). Besides, the correlation analysis of risk score with common

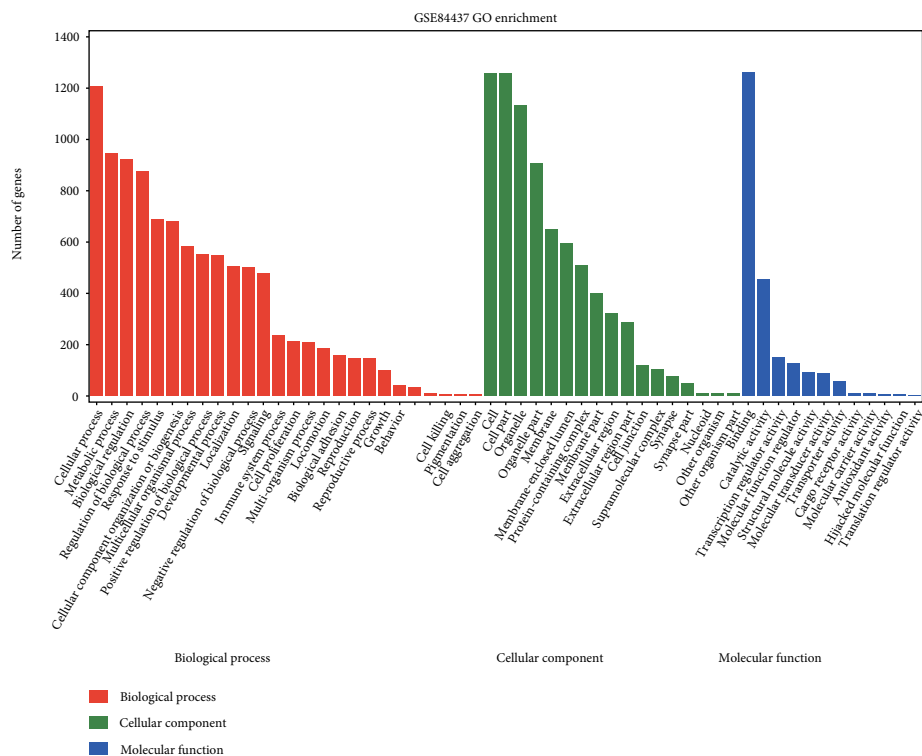
immune checkpoints (ICPs), including cytotoxic T lymphocyte-associated protein 4 (*CTLA4*), programmed cell death 1 (*PDCD1*) (PD1), *CD274* (PD-L1), hepatitis A virus cellular receptor 2 (*HAVCR2*), and lymphocyte-activating 3 (*LAG3*), was performed to estimate the immunotherapy responses through the 10-gene signature. As expected, the gene expression levels of most ICPs were significantly upregulated in the high-risk group (Figure 7(d)).

**3.9. Validation of the Expression Levels of the 10 Ferroptosis-Related Genes.** Compared to normal tissues, the expression



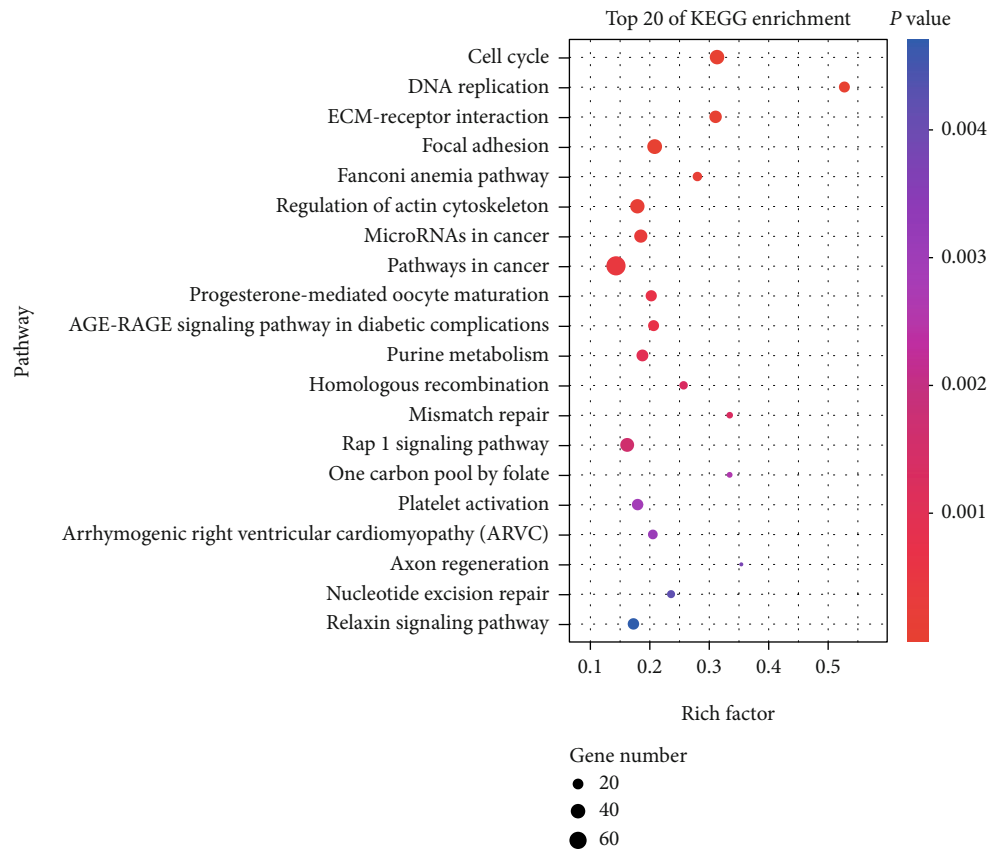


(a)



(b)

FIGURE 5: Continued.



(c)

FIGURE 5: Continued.

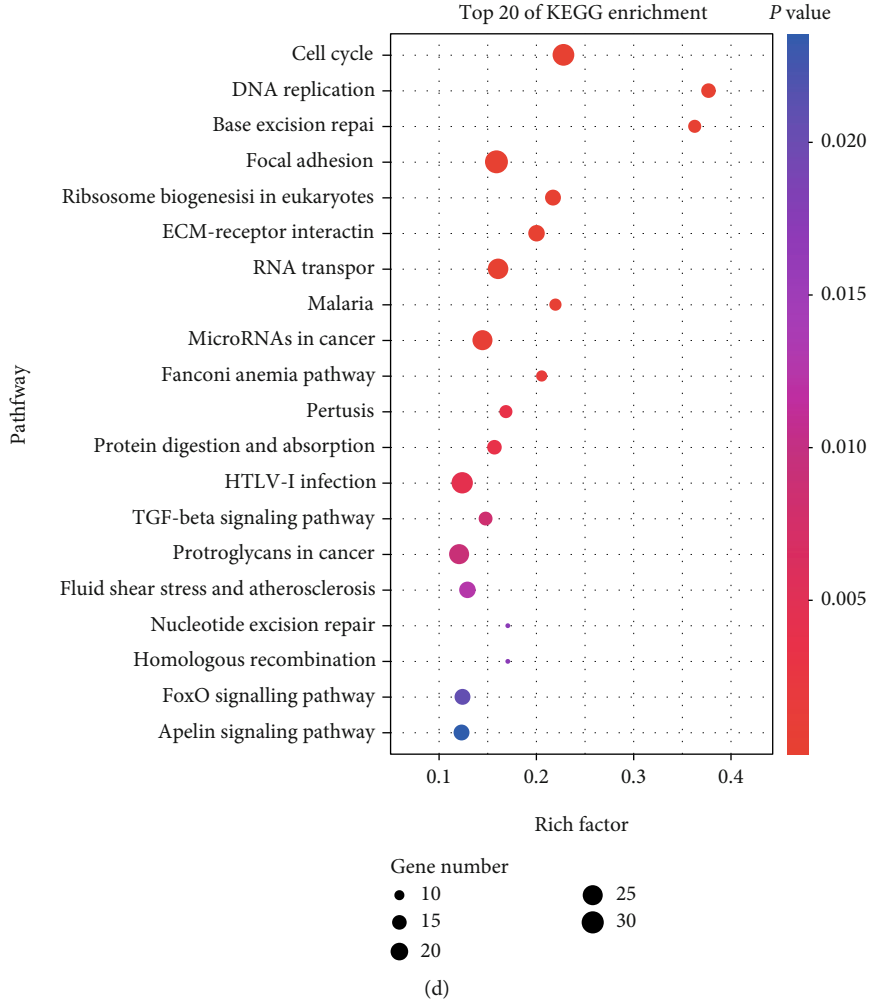
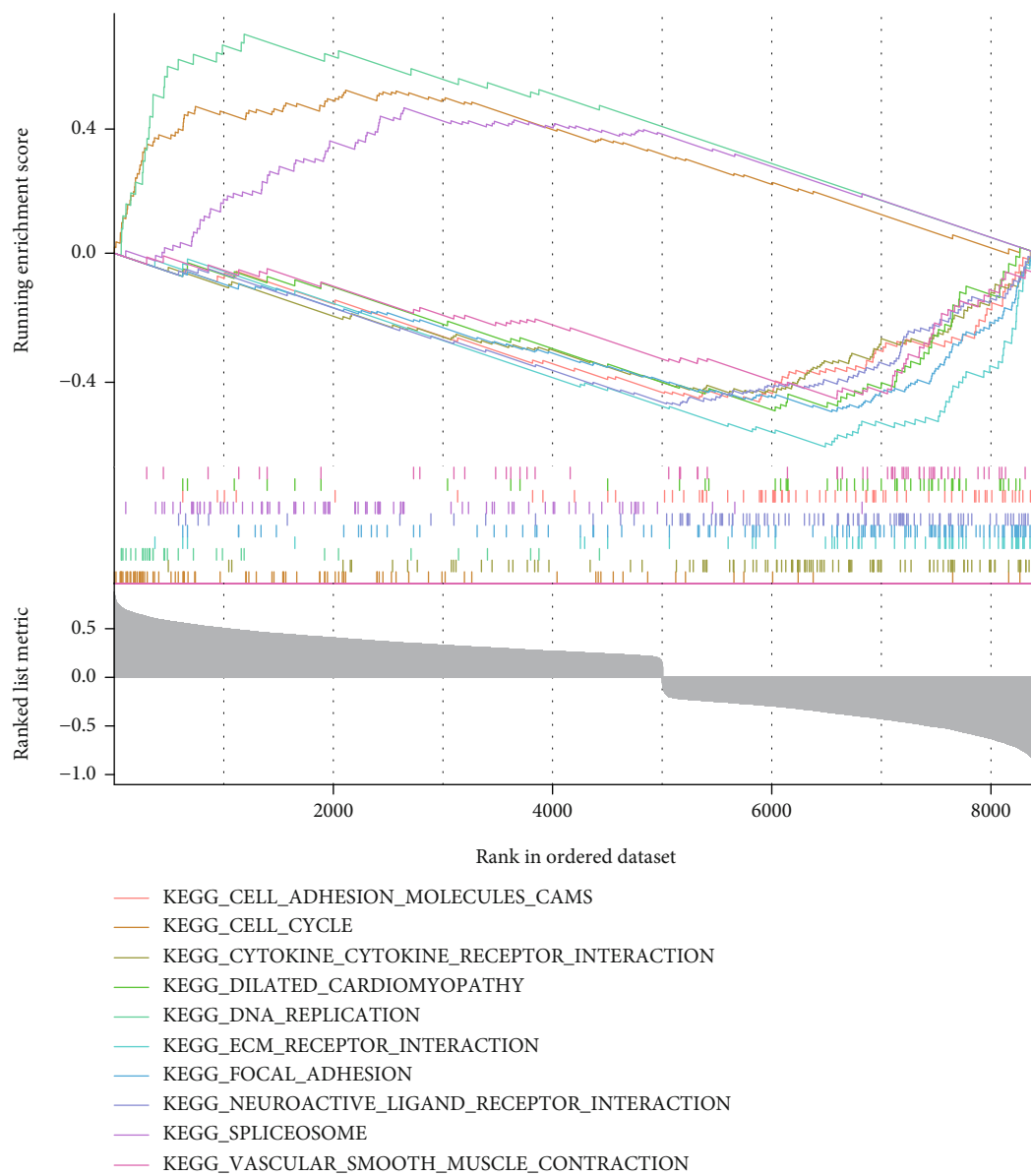
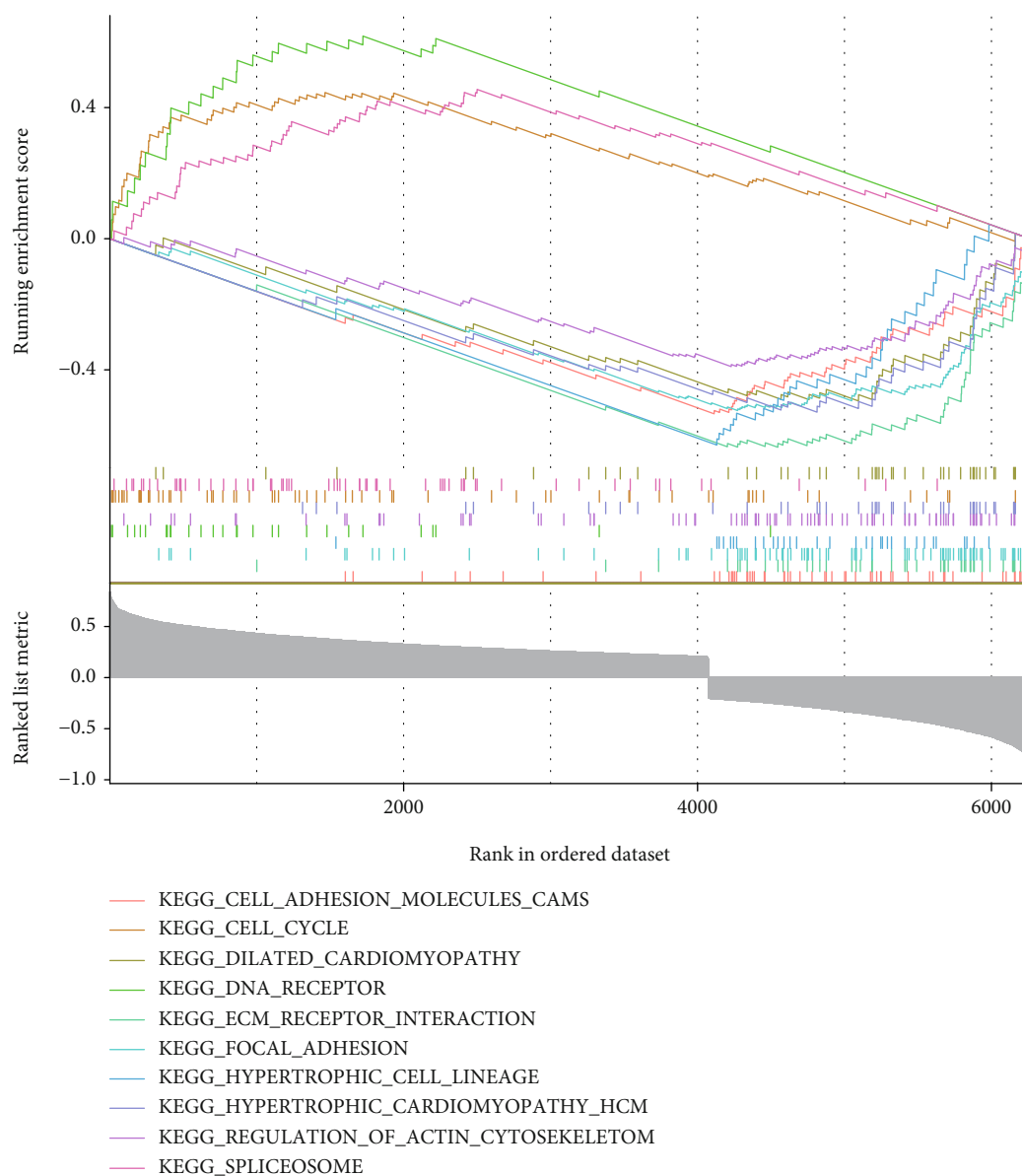


FIGURE 5: Continued.



(e)

FIGURE 5: Continued.



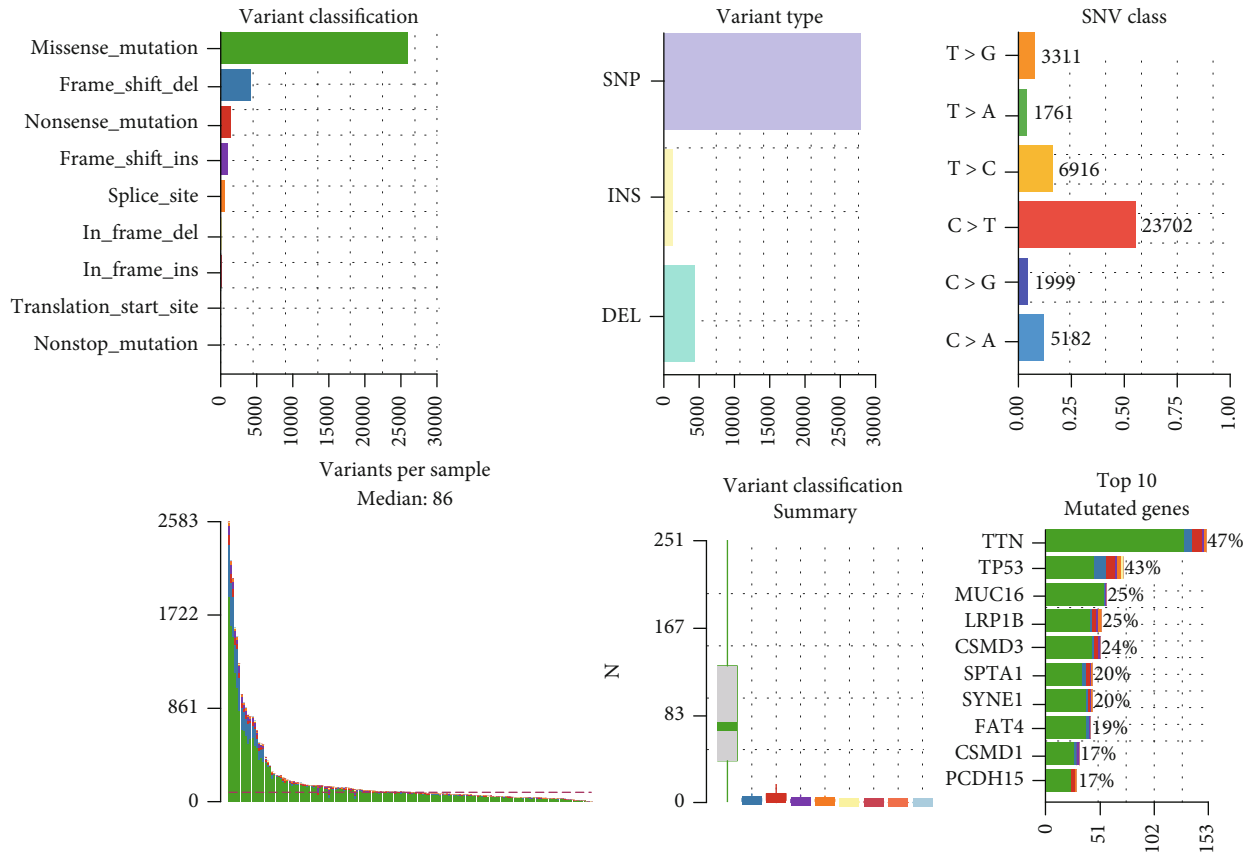
(f)

FIGURE 5: GO, KEGG, and GSEA analysis of the DEGs between the high- and low-risk groups in the (a, c, e) TCGA-STAD training and (b, d, f) GSE84437 testing datasets.

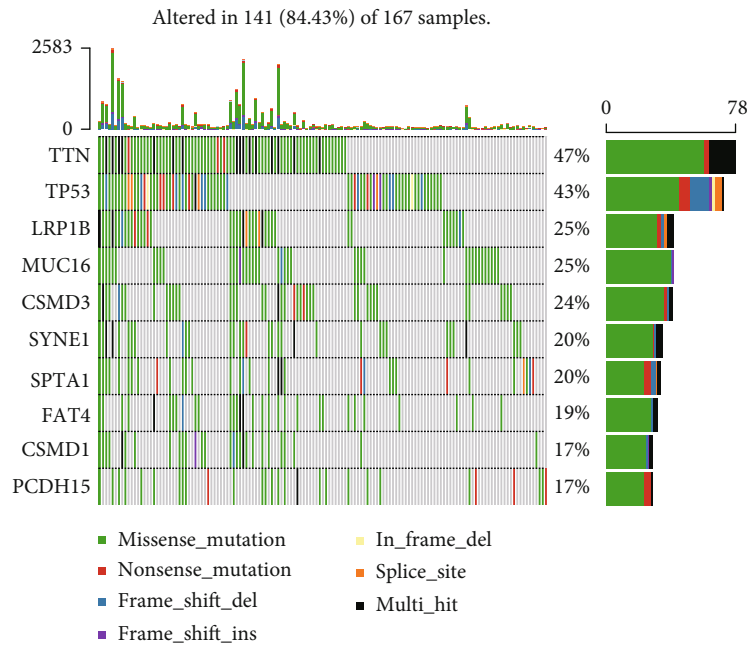
levels of *SP1*, *MYB*, *KEAP1*, *AIFM2*, *ITGB4*, *TGFBR1*, *MAP1LC3B*, and *NOX4* were significantly upregulated, while the expression of *ALDH3A2* and *ZFP36* was downregulated in GC tumor tissues in the training group (Figure 8(a)). The same results were also verified by GEPIA (Figure 8(b)). Similarly, compared to the normal gastric cell GES1, most of these 10 genes were also differentially expressed in GC cell lines (HGC-27 and MGC-803) using real-time PCR (Figure 8(c)). Besides, we further validated the mRNA or protein expression of these 10 genes in GSE29272 and Human Protein Atlas (HPA) datasets in Figure S4. Furthermore, the expression levels of hub genes *SP1*, *KEAP1*, *AIFM2*, and *NOX4* were further verified in our GC samples. The results showed that the expression of *SP1*, *KEAP1*, *AIFM2*, and *NOX4* all increased in tumor tissues (Figure 8(d)).

### 3.10. Analysis of the Effects of Ferroptosis Inducer Erastin on the 10 Ferroptosis-Related Genes in Gastric Cancer Cell Lines.

To explore the effects of the 10 ferroptosis-related genes, gastric cancer cell lines HGC-27 and MGC-803 were treated by different working concentrations of Erastin. The results of cell cytotoxicity assay indicated that Erastin could significantly inhibit the cell proliferation of HGC-27 and MGC-803 in a dose-dependent manner. The  $IC_{50}$  value of them was all around  $10 \mu\text{M}$  (Figures 9(a) and 9(d)). Then, according to their  $IC_{50}$ , different concentrations of Erastin (5, 10, and  $20 \mu\text{M}$ ) significantly increased the ROS both in HGC-27 and MGC-803 cell lines (Figures 9(b), 9(c), 9(e), and 9(f)). In addition, after  $10 \mu\text{M}$  concentration of Erastin treatment for 48 h, the mRNA expression levels of these 10 genes in HGC-27 and MGC-803 cell lines were all investigated by

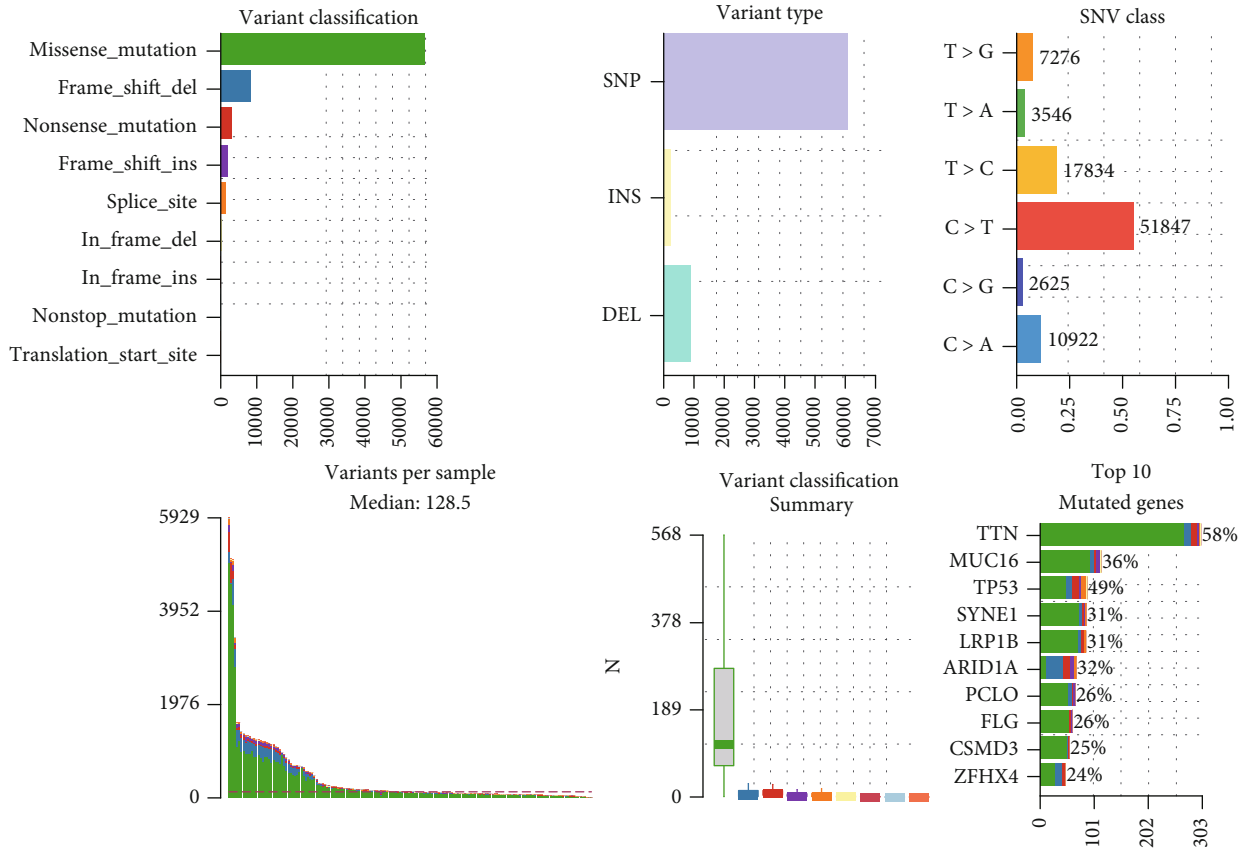


(a)

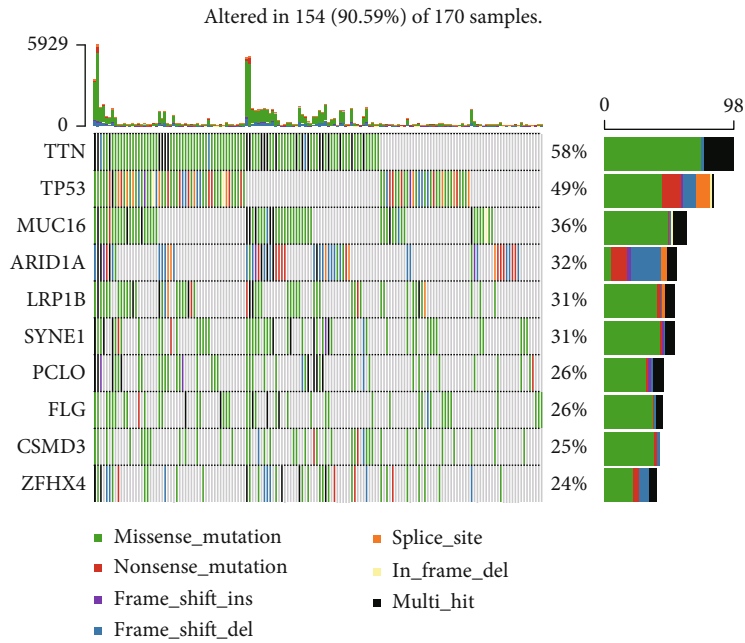


(b)

FIGURE 6: Continued.



(c)



(d)

FIGURE 6: Continued.

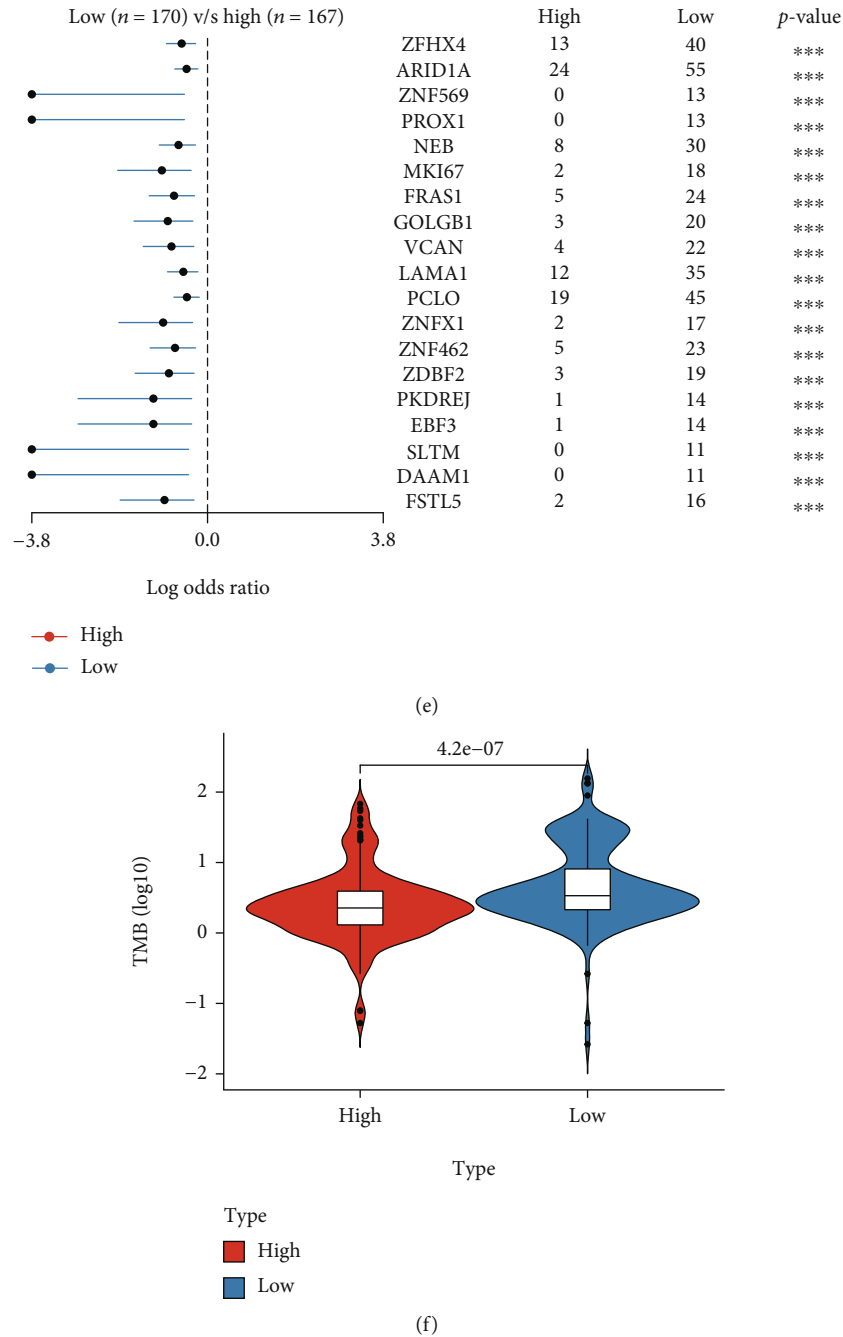


FIGURE 6: Somatic mutation summary plots and oncoplots between the (a, b) high- and (c, d) low-risk groups in the TCGA-STAD training dataset. (e) Forest plot for the differentially somatic mutation and (f) the violin plot for the TMB scores between the high- and low-risk groups in the TCGA-STAD training dataset.

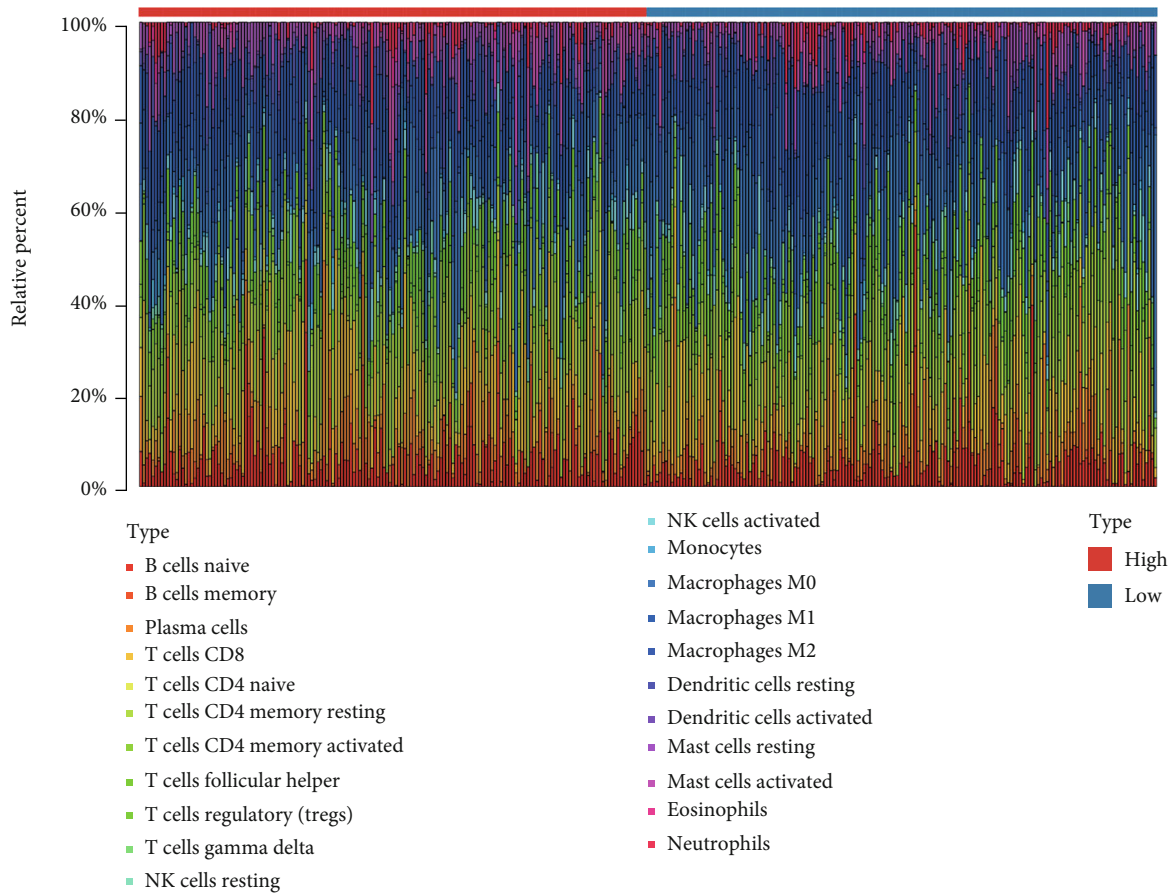
real-time PCR. The results indicated that the mRNA expression levels of eight genes (*AIFM2*, *ALDH3A2*, *KEAP1*, *MAP1LC3B*, *MYB*, *NOX4*, *SP1*, and *TGFBR1*) were decreased and two genes (*ITGB4* and *ZFP36*) were increased after being treated with Erastin. However, in the HGC-27 cell line, there was no statistical difference in the mRNA expression level of SP1. *ITGB4* and *MAP1LC3B* genes were also not statistically different in MGC803-Erastin cell line (Figures 9(g) and 9(h)). In addition, similar to the mRNA expression results, the different protein expression levels of

the hub genes (*AIFM2*, *KEAP1*, *NOX4*, and *SP1*) were further confirmed by western blot except *AIFM2* and *SP1* in the HGC-27 cell line (Figure 9(i)). In summary, the potential roles of these 10 ferroptosis-related gene markers could also be verified in cell line experiment.

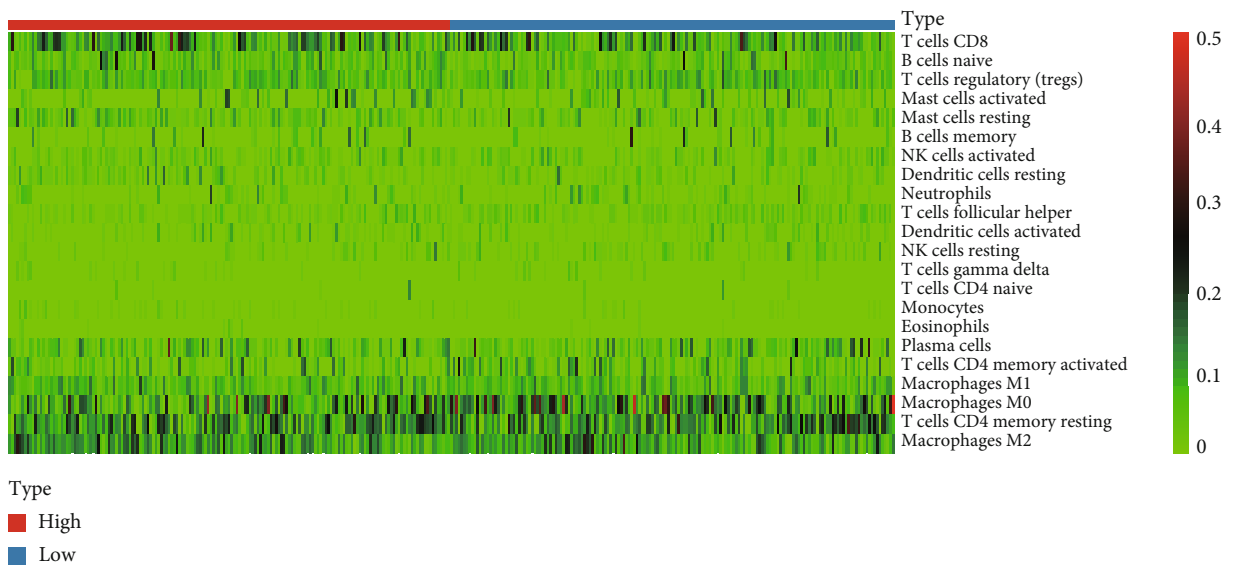
#### 4. Discussion

In this study, the expression level of the ferroptosis-related genes in GC tumor and normal tissues and their associations



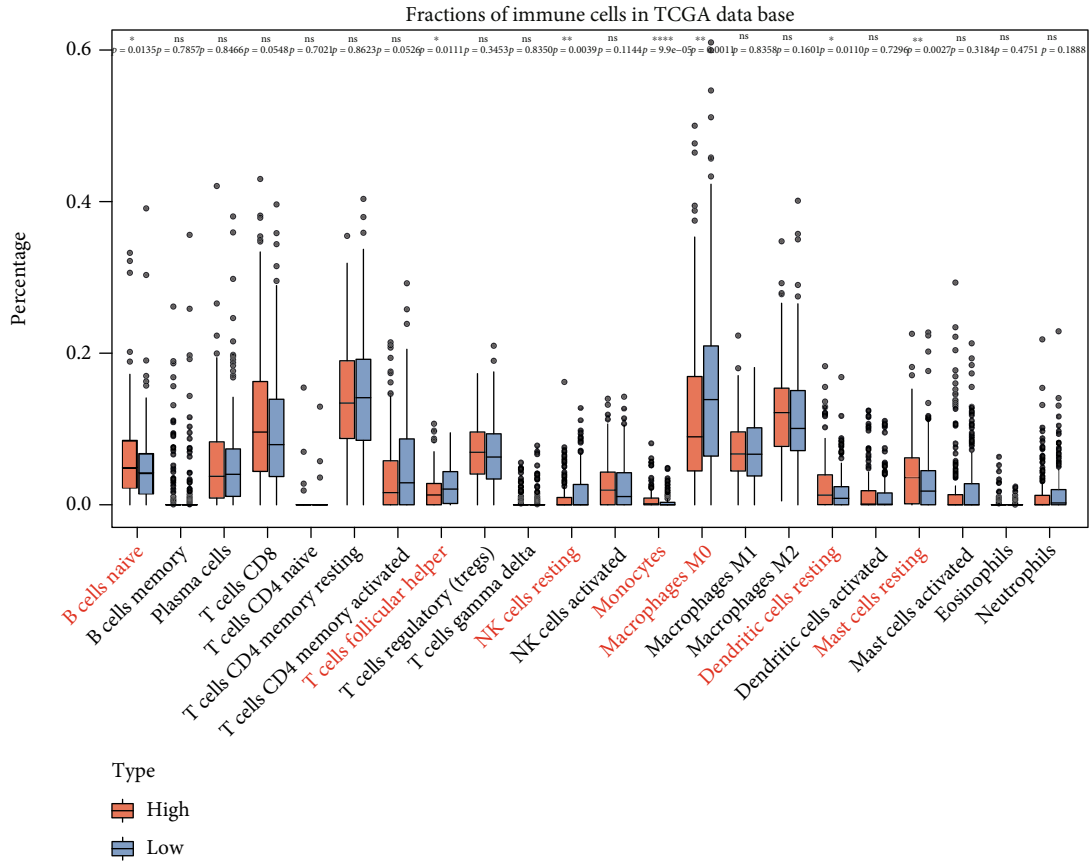


(a)

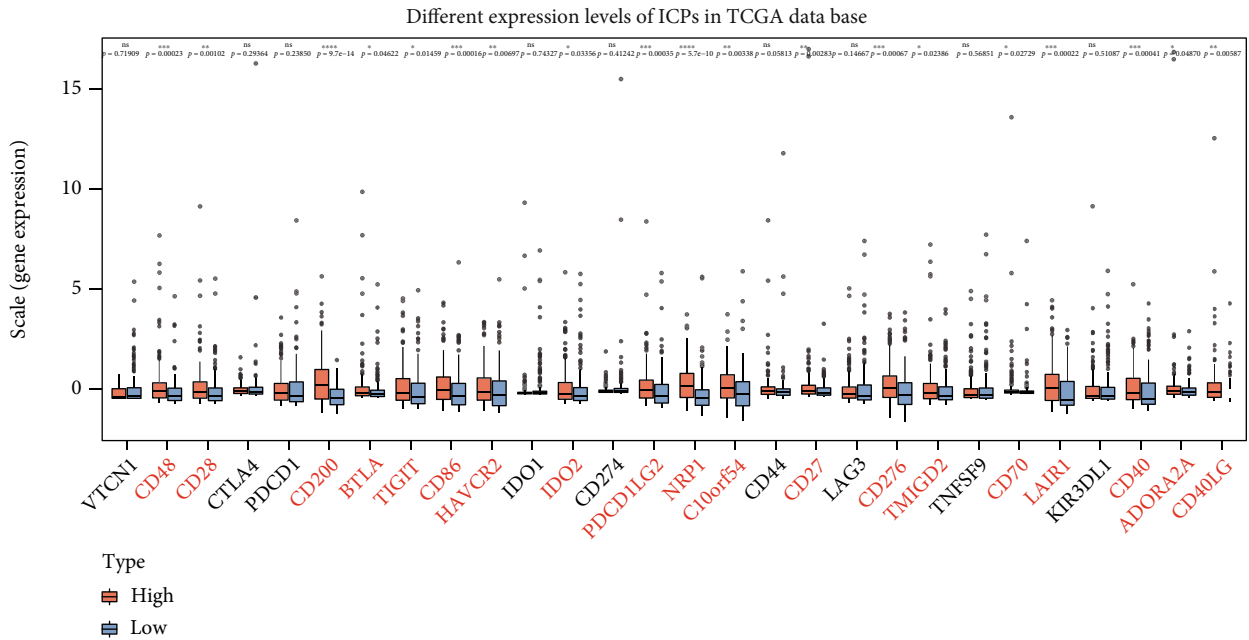


(b)

FIGURE 7: Continued.



(c)



(d)

FIGURE 7: (a) Bar plot shows the proportion of 22 tumor-infiltrating immune cells (TICs) between the high- and low-risk groups in the TCGA-STAD training dataset. (b) Heat map shows the correlation between 22 TICs in the TCGA-STAD training dataset. (c) The boxplot shows the ratio differentiation of the 22 immune cells between the high- and low-risk groups in the TCGA-STAD training dataset. (d) The boxplot shows the results of the different expression levels of ICPs between the high- and low-risk groups in the TCGA-STAD training dataset. \* $P < 0.05$ , \*\* $P < 0.01$ , \*\*\* $P < 0.001$ , and \*\*\*\* $P < 0.0001$ .

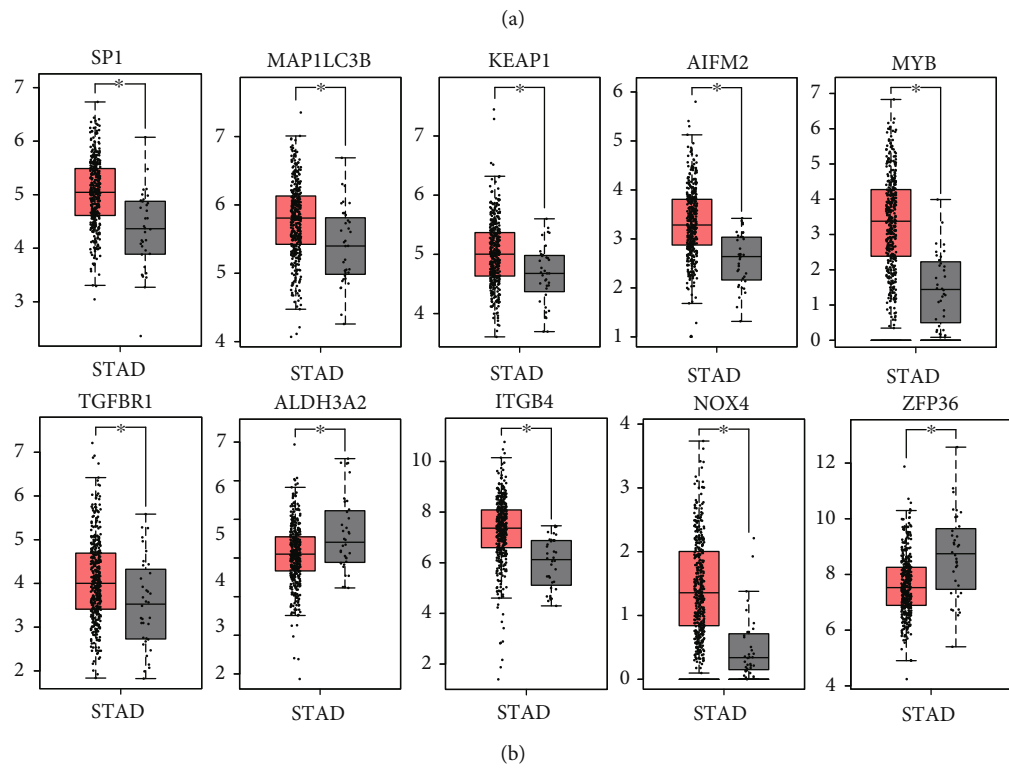
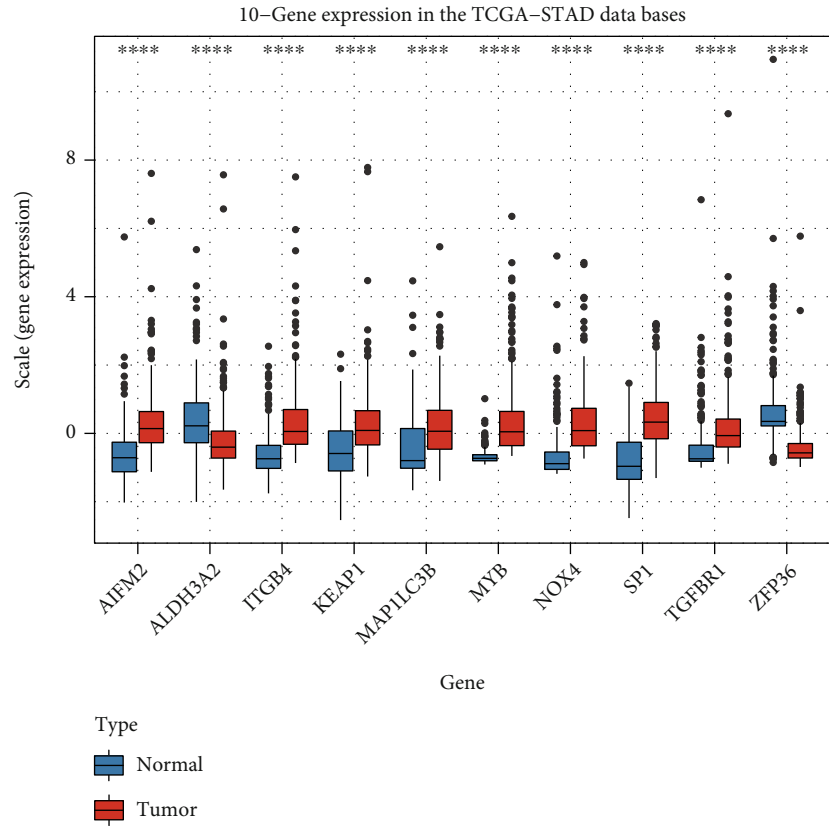
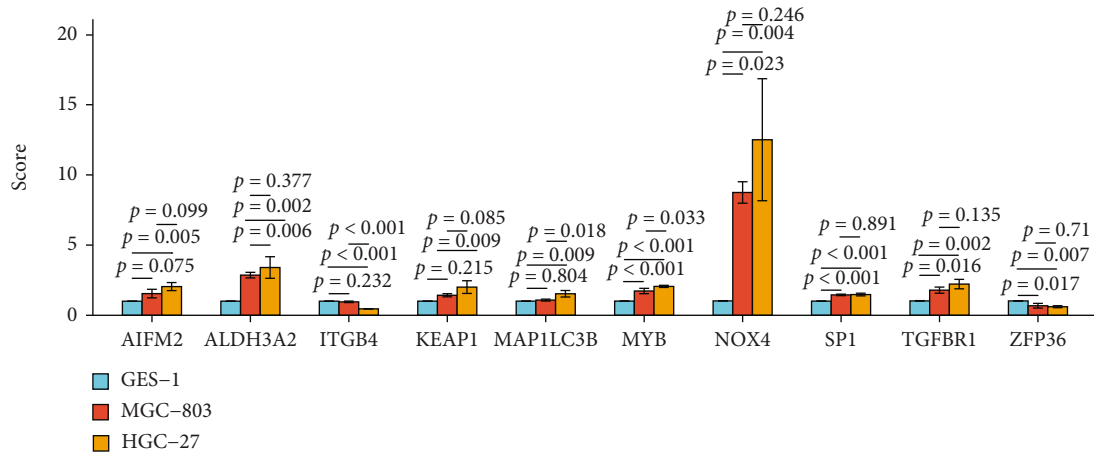
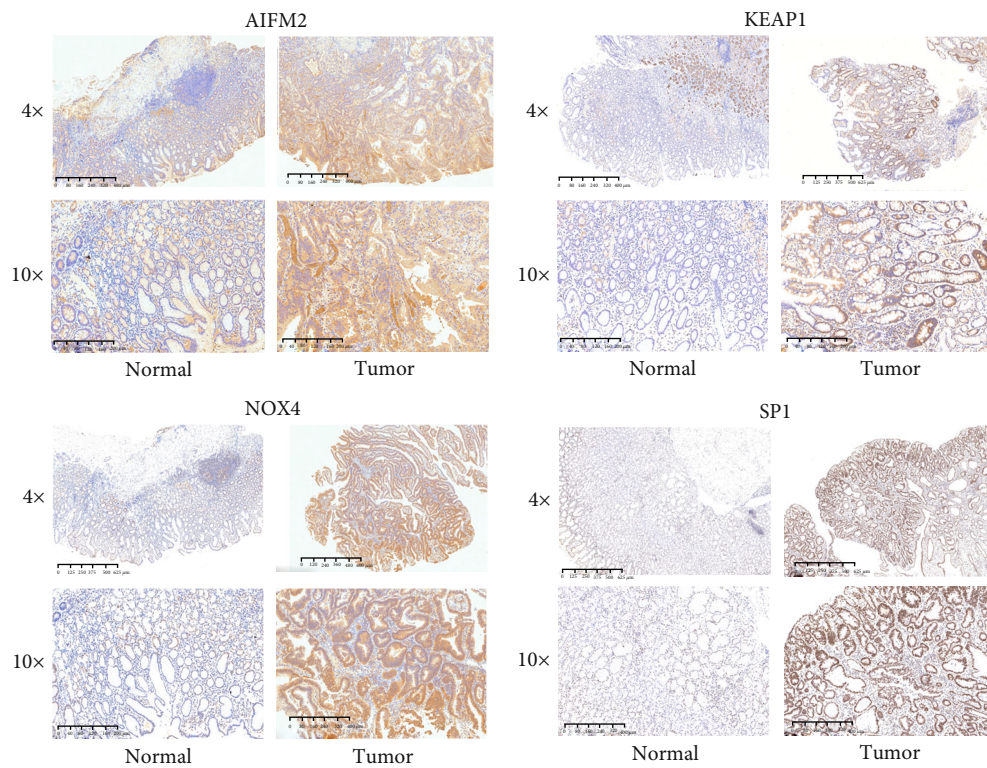


FIGURE 8: Continued.



(c)



(d)

FIGURE 8: (a) The boxplot shows the expression levels of the 10 FDEGs between the normal and tumor tissues in TCGA datasets. (b) The boxplots from the GEPIA dataset verify the expression levels of the 10 FDEGs in GC patients. (c) The boxplot indicates the different expression levels of these 10 FDEGs in GC cell lines by real-time PCR. (d) Representative immunohistochemistry images of AIFM2, KEAP1, NOX4, and SP1 in GC tissues and corresponding normal tissues. \* $P < 0.05$ , \*\* $P < 0.01$ , \*\*\* $P < 0.001$ , and \*\*\*\* $P < 0.0001$ .

with OS were systematically investigated. A novel prognostic gene signature was established and validated in an external cohort. The independent prognostic factor, functional enrichment, somatic mutation, tumor microenvironment, and immunotherapy response analysis were performed and indicated that the ferroptosis-related gene signature can effectively predict the prognosis and clinical status for GC patients.

Ferroptosis is involved in various diseases, especially in malignant tumors [19]. Recently, several studies [12, 20–22] have proven that some ferroptosis-related genes play

key roles in the process of tumorigenesis and progression of GC, but whether ferroptosis could predict the prognosis and clinical status of GC patients remains largely unknown. Usually, TNM stage system or some serum biomarkers, including CEA, CA19-9, and CA125, are used to monitor the progress and predict the prognosis of GC patients. However, these approaches are not satisfactory with low accuracy and high nonspecificity; especially, there is higher heterogeneity in GC patients. Meanwhile, with the impressive progress of bioinformatics and RNA-seq, many scholars around the

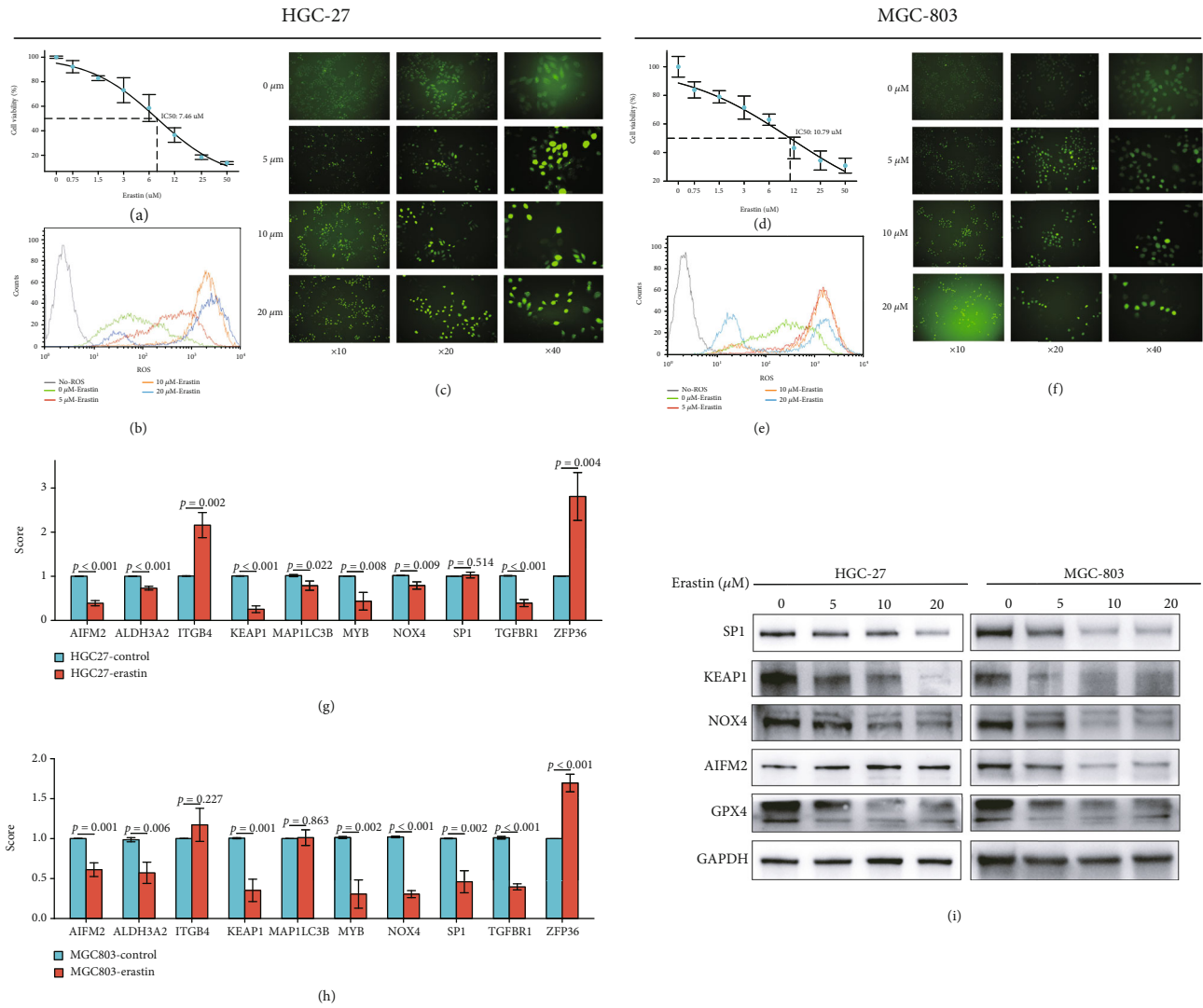


FIGURE 9: The IC<sub>50</sub> curve shows the cytotoxicity assay of (a) HGC-27 and (d) MGC-803 cell lines treated with Erastin. The flow cytometry and fluorescence microscope plots verify the different ROS levels of (b, c) HGC-27 and (e, f) MGC-803 cell lines treated with Erastin. The boxplots indicate the different mRNA expression levels of these 10 FDEGs in (g) HGC-27 and (h) MGC-803 after being treated with 10 μM Erastin by real-time PCR. (i) The plot detects the different protein expression levels of hub FDEGs (SP1, KEAP1, NOX4, AIFM2, and GPX4) in HGC-27 and MGC-803 after being treated with 10 μM Erastin by western blot. \**P* < 0.05, \*\**P* < 0.01, \*\*\**P* < 0.001, and \*\*\*\**P* < 0.0001.

world have constructed some ferroptosis-related gene signature by public databases to further explore key molecular markers and better methods to accurately predict the prognosis and drug sensitivity in several malignant tumors, including uveal melanoma, lung cancer, hepatocellular carcinoma, pancreatic cancer, and glioma [23–26]. However, few studies on gene signature had been constructed in gastric cancer.

In this study, we first screened the key ferroptosis-related DEGs in GC from the public databases. As expected, more than half of the ferroptosis-related genes were differentially expressed between adjacent nontumorous and tumor tissues in GC patients, suggesting ferroptosis plays a significant role in GC. Then, 29 of them were proven related to OS by the univariate Cox analysis, indicating that constructing a prognostic signature with these FDEGs is feasible and reasonable. Using the LASSO Cox analysis, the novel prognostic signa-

ture integrating 10 ferroptosis-related genes was identified, including *SP1*, *MYB*, *ALDH3A2*, *KEAP1*, *AIFM2*, *ITGB4*, *TGFBR1*, *MAP1LC3B*, *NOX4*, and *ZFP36*. To further explore the role of these genes in GC, we summarized their main molecular functions based on the results of this study and previous studies.

SP1, a key member of the transcription factor SP family, plays important roles in tissue development, cell differentiation, and tumor molecular biology [27]. SP1 can directly positively regulate glutathione peroxidase 4 (GPX4), which is able to significantly influence the level of lipid peroxidation and inhibit ferroptosis [28]. AIFM2 belongs to the anti-ferroptotic genes and is renamed as ferroptosis suppressor protein 1 (FSP1). Recent studies indicated that AIFM2 plays a significant role in ferroptosis and can act parallel to GPX4 to inhibit ferroptosis [29, 30]. ALDH3A2 is involved in preventing cellular oxidative damage by oxidizing long-chain

aliphatic aldehydes. A recent study showed that ALDH3A2 can protect progenitor and leukemic stem cells from ferroptosis. Inhibiting GPX4 expression can further enhance the ferroptosis-inducing influence of ALDH3A2 depletion [31]. Different from other types of tumors, the expression of GPX4 is positively correlated with the prognosis of GC patients [12]. Thus, the potential role of SP1 and FSP1 during the process of ferroptosis in GC patients remains to be further explored. MYB has also been reported as an important transcription factor in solid tumors, which can regulate ferroptosis expression, iron-related cellular activities, and tumor cell growth by modulating myeloid zinc-finger 1 [32]. Notably, a specific study indicated that MYB could inhibit Erastin-induced ferroptosis which was restrained through interacting with CDO1 in GC cells [13]. KEAP1 interacts with nuclear factor erythroid 2-related factor 2 (NRF2) in a redox-sensitive manner, and the interaction can promote the expression of gamma-glutamylcysteine synthetase [33]. In recent study, the NRF2-KEAP1 pathway is activated and upregulates SLC7A11 to inhibit ferroptosis when the expression of KEAP1 is downregulated [34]. ITGB4, a member of the integrin family, mediates cell-cell adhesion or cell growth and plays a significant role in the biology of invasive carcinoma by associating with integrin alpha 6 (ITGA6) subunit [35]. Besides, it has been reported that the induction of ferroptosis depends on cell clustering in matrix-detached cells that lack ITGB4 and ITGA6 expression [36]. TGFBR1, also known as the activin receptor-like kinase (ALK4/5), is involved in oxidative stress responses [37]. In renal proximal tubular epithelial cells, the ALK4/5 signaling pathway has been proven to be correlated with ferroptosis and blockade of the ALK4/5 signaling pathway can suppress ferroptosis [38]. Recent evidences demonstrated that autophagy facilitates ferroptosis by degrading anti-ferroptosis factors [39]. MAP1LC3B [40] and ZFP36 [41], key proteins of autophagy, have been considered to be correlated with ferroptosis. NOX4 is the core enzyme in mediating lipid peroxidation and promoting ferroptosis, and inhibition of NOX4 can significantly block ferroptosis [42, 43]. In summary, although these 10 genes were all correlated with ferroptosis, few studies were performed to explore their molecular functions during the process of ferroptosis in GC. Thus, to make these results more scientific, we also choose the 4 hub genes (SP1, KEAP1, AIFM2, and NOX4) of these 10 genes to further verify their expression levels in the GC cell lines and our 30-paired GC tissues by real-time PCR and immunohistochemistry. In summary, similar to the gene expression level of public databases and related studies, the expression level of them was also upregulated in GC cell lines and tissues.

Based on risk score of the 10-gene signature, GC patients can be divided into the low- and high-risk groups. Low-risk GC patients were proven to have the better prognosis and significantly longer OS than high-risk patients in both the training and testing groups. Furthermore, a series of analysis was applied to further explore the prognostic value of the signature; the results showed that the risk score was the independent prognostic factor of the OS in GC patients. Accurate nomogram prediction models can also be con-

structed based on the risk score. In summary, these results reveal a favorable predictive efficacy of the signature in both the training and testing groups. Meanwhile, we performed GO, KEGG, and GSEA analysis to identify the enriched biological process and pathway based on the DEGs in the high- and low-risk patients. The results showed that the cell cycle, ECM-receptor interaction, PI3K-Akt signaling pathway, and tumorigenesis-related pathways were significantly enriched both in the training and testing groups. Consistent with our results, recently, Lin et al. [44] reported that dihydroartemisinin can cause cell cycle arrest in head and neck carcinoma (HNC) cells by inducing ferroptosis. Some studies [45, 46] also demonstrated that epigenetic reprogramming of EMT promotes ferroptosis in HNC cells and gambogin acid-induced ferroptosis inhibits the EMT in melanoma cells. Yi et al. [47] found that mutation of PI3K-Akt signaling could protect cancer cells from oxidative stress and ferroptosis.

Recent studies [48, 49] have proven that somatic mutation and tumor immune microenvironment significantly correlate with tumorigenesis, tumor progress, and drug resistance in GC patients. Wang et al. demonstrated that IFN $\gamma$  released by CD8<sup>+</sup> T cells could inhibit expression of glutamate-cystine antiporter system xc<sup>-</sup>, then induce tumor cell lipid peroxidation and ferroptosis, and finally improve antitumor efficacy of immunotherapy [50]. Besides, Hung et al. reported that tyrosine-protein kinase receptor TYRO3 (TYRO3) overexpression elicited anti-PD-1/PD-L1 resistance through protecting tumor cells from immunotherapy-induced ferroptosis [51]. However, the specific mechanisms of ferroptosis in tumor immunotherapy are largely unknown. In order to explore the potential mechanism of this signature, we further performed somatic mutation, tumor microenvironment, and immunotherapy response analysis. To our surprise, the somatic mutation frequency of the low-risk GC patients was higher than that of the high-risk patients and the TMB level was significantly higher in the low-risk group indicating that low-risk GC patients may be more sensitive to immunotherapy and can benefit from the immunotherapy. Based on the TMB results, we also confirmed that there were significant differences in the signature and immune checkpoints between the high- and low-risk groups. Low-risk patients had a better response to immunotherapy, suggesting that the signature has the potential to predict the immunotherapy response in GC patients. Meanwhile, the infiltration abundance of immune cells was significantly different between the low- and high-risk groups in this study. Most of the immune cells were highly infiltrated in the high-risk patients, while the abundance of NK cells was higher in the low-risk group. Previous reports indicated that increased abundance of NK cells can bring better immunotherapy efficacy [52], further suggesting the low-risk GC patients have a better response to immunotherapy. In fact, the relationship between ferroptosis and cancer immunotherapy has been reported in 2019 [50, 53], showing the sensitivity of tumor cells to ferroptosis is parallel to immune functions, which may be the reasonable explanation for the better response to immunotherapy in low-risk patients. But the exact mechanisms of how these 10 ferroptosis-related genes interact to

affect tumorigenesis and immune process are still unclear and further studies are demanded.

With the gradual understanding of the role of ferroptosis in various cancers, different ferroptosis inducers have been developed as anticancer therapies, such as sulfasalazine, sorafenib, and Erastin [54, 55]. Erastin, first identified as killing tumor cells expressing oncogenic RAS, is a classical agent to induce ferroptosis by suppressing cystine/glutamate antiporter (xCT) and leading to decreased cysteine and then inhibiting the function of glutathione peroxidase 4 (GPX4) [4]. To evaluate whether these key genes play key roles in ferroptosis of GC, we applied Erastin to trigger ferroptosis in two GC cell lines, HGC-27 and MGC-803. Using CCK-8 assay, we detected significant lethal toxicity to both GC cell lines by Erastin at low concentration, showing  $IC_{50}$  value was 7.46 and 10.79  $\mu M$ , for HGC-27 and MGC-803, respectively. Increased ROS level is one of the features for ferroptosis. After treatment with Erastin, both cell lines showed obvious increased ROS signal by flow cytometry and fluorescence microscope, indicating Erastin-induced cell death could be attributed to ferroptosis. Besides, we also explored whether the expression of these key ferroptosis-related genes was regulated by Erastin during ferroptosis. Not surprisingly, most of the genes were dysregulated at mRNA or protein expression level, while the underlying mechanism was still not clear. Therefore, these ferroptosis-related gene could be targeted to induce cancer cell ferroptosis for future personalized therapy.

## 5. Conclusion

Ferroptosis has great potential clinical value in tumor treatments. However, the relationship between ferroptosis and tumors such as GC remains largely unclear. Thus, we systemically explored the key ferroptosis biomarkers in GC and constructed a novel ferroptosis-related gene signature which could effectively predict the prognosis of GC patients. Besides, we also further explored the signature-related downstream molecular biology functions and pathways, demonstrating the potential clinical value of this signature in somatic mutation and immunotherapy. In addition, all results had been verified by various external datasets and expression of 4 hub genes was verified in our own clinical samples. Finally, the novel prognostic signature constructed in this study needs further validation and the underlying mechanisms of ferroptosis in GC should be explored in future studies.

## Data Availability

The RNA sequencing (RNA-seq) data and corresponding clinical characteristics and molecular information of gastric cancer samples in training cohort (TCGA-STAD) were downloaded from The Cancer Genome Atlas (TCGA) database by the “TCGAbiolinks” R package in February 2021. The RNA-seq data of normal human stomach samples in GTEx database was downloaded from the University of California Santa Cruz (UCSC, <https://xenabrowser.net/datapages/>). Besides, the gene expression data and corre-

sponding clinical information of the external validation cohorts (GSE84437, GSE29272) were downloaded from the GEO database (<https://www.ncbi.nlm.nih.gov/>). Furthermore, the somatic mutation data of the TCGA-STAD was downloaded from the websites (<https://portal.gdc.cancer.gov/>). The 261 ferroptosis-related genes were downloaded from the FerrDb website (<http://www.zhounan.org/ferrdb/>), updating on 10 March 2021.

## Ethical Approval

The study was conducted according to the guidelines of the Declaration of Helsinki, approved by the Ethical Committee of Ruijin Hospital (Shanghai, China).

## Conflicts of Interest

The authors declare no conflict of interest.

## Authors' Contributions

S.Z. and J.S. were responsible for conceptualization; Y.S. and S.Z. were responsible for methodology; Y.S. and S.L. were responsible for software; H.J. and L.H. were responsible for validation; B.A. was responsible for resources; G.Y. was responsible for data curation; Y.S. and S.Z. were responsible for writing—original draft preparation; J.S. and M.Z. were responsible for writing—review and editing; J.S. was responsible for supervision; S.Z. and J.S. were responsible for funding acquisition. All authors have read and agreed to the published version of the manuscript. Yanfei Shao, Hongtao Jia, and Shuchun Li contributed equally to this work.

## Acknowledgments

We thank Dr. Jianming Zeng (University of Macau) and Dr. Xinyi Liu (Shanghai Jiao Tong University School of Medicine), and all the members of their bioinformatics teams, for generously sharing their experience and codes. This research was funded by the National Nature Science Foundation of China (NSFC) (Grant Nos. 8210111994 and 81871984), the Shanghai Science and Technology Commission Science and Technology Innovation Action Clinical Innovation Field (Grant No. 18411953200), the Youth Science and Technology Innovation Studio of Shanghai Jiao Tong University School of Medicine, and the Youth Cultivation Project of Ruijin Hospital (Grant No. KY2021611).

## Supplementary Materials

Figure S1: PCA plots of the TCGA-STAD training and GSE84437 testing datasets. Figure S2: KEGG circular and pathway annotation plots of the TCGA-STAD training and GSE84437 testing datasets. Figure S3: the diagrams of the correlation analysis between these 10 FDEGs and the immune infiltration level in TCGA dataset by TIMER. Figure S4: validation of the mRNA or protein expression of these 10 genes in GSE29272 (except *AIFM2*) and HPA (except *NOX4*) datasets. Table S1: full names, function, and coefficients of the 10 genes. (*Supplementary Materials*)

## References

- [1] H. Sung, J. Ferlay, R. L. Siegel et al., "Global cancer statistics 2020: GLOBOCAN estimates of incidence and mortality worldwide for 36 cancers in 185 countries," *CA: a Cancer Journal for Clinicians*, vol. 71, no. 3, pp. 209–249, 2021.
- [2] M. Cao, L. Li, and D. Sun, "Epidemiological trend analysis of gastric cancer in China from 2000 to 2019," *Chin J Dig Surg*, vol. 20, no. 1, pp. 102–109, 2021.
- [3] S. Zheng, Z. Zhang, N. Ding et al., "Identification of the angiogenesis related genes for predicting prognosis of patients with gastric cancer," *BMC Gastroenterology*, vol. 21, no. 1, p. 146, 2021.
- [4] S. J. Dixon, K. M. Lemberg, M. R. Lamprecht et al., "Ferroptosis: an iron-dependent form of nonapoptotic cell death," *Cell*, vol. 149, no. 5, pp. 1060–1072, 2012.
- [5] T. Hirschhorn and B. R. Stockwell, "The development of the concept of ferroptosis," *Free Radical Biology & Medicine*, vol. 133, pp. 130–143, 2019.
- [6] H. Wang, Y. Cheng, C. Mao et al., "Emerging mechanisms and targeted therapy of ferroptosis in cancer," *Molecular Therapy*, vol. 29, no. 7, pp. 2185–2208, 2021.
- [7] S. Zhuo, Z. Chen, Y. Yang, J. Zhang, J. Tang, and K. Yang, "Clinical and biological significances of a ferroptosis-related gene signature in glioma," *Frontiers in Oncology*, vol. 10, p. 590861, 2020.
- [8] Y. Lai, Z. Zhang, J. Li et al., "STYK1/NOK correlates with ferroptosis in non-small cell lung carcinoma," *Biochemical and Biophysical Research Communications*, vol. 519, no. 4, pp. 659–666, 2019.
- [9] Y. Ding, X. Chen, C. Liu et al., "Identification of a small molecule as inducer of ferroptosis and apoptosis through ubiquitination of GPX4 in triple negative breast cancer cells," *Journal of Hematology & Oncology*, vol. 14, no. 1, p. 19, 2021.
- [10] W. H. Yang, C. C. Ding, T. Sun et al., "The hippo pathway effector TAZ regulates ferroptosis in renal cell carcinoma," *Cell Reports*, vol. 28, no. 10, pp. 2501–2508.e4, 2019, e4.
- [11] P. Chen, X. Li, R. Zhang et al., "Combinative treatment of  $\beta$ -elemene and cetuximab is sensitive to KRAS mutant colorectal cancer cells by inducing ferroptosis and inhibiting epithelial-mesenchymal transformation," *Theranostics*, vol. 10, no. 11, pp. 5107–5119, 2020.
- [12] L. Zhao, Y. Peng, S. He et al., "Apatinib induced ferroptosis by lipid peroxidation in gastric cancer," *Gastric Cancer*, vol. 24, no. 3, pp. 642–654, 2021.
- [13] S. Hao, J. Yu, W. He et al., "Cysteine dioxygenase 1 mediates erastin-induced ferroptosis in human gastric cancer cells," *Neoplasia*, vol. 19, no. 12, pp. 1022–1032, 2017.
- [14] T. Liu, L. Jiang, O. Tavana, and W. Gu, "The deubiquitylase OTUB1 mediates ferroptosis via stabilization of SLC7A11," *Cancer Research*, vol. 79, no. 8, pp. 1913–1924, 2019.
- [15] Y. Liu, X. Zhang, J. Zhang, J. Tan, J. Li, and Z. Song, "Development and validation of a combined ferroptosis and immune prognostic classifier for hepatocellular carcinoma," *Frontiers in Cell and Development Biology*, vol. 8, p. 596679, 2020.
- [16] Y. Wei, H. Lv, A. B. Shaikh et al., "Directly targeting glutathione peroxidase 4 may be more effective than disrupting glutathione on ferroptosis-based cancer therapy," *Biochimica et Biophysica Acta - General Subjects*, vol. 1864, no. 4, article 129539, 2020.
- [17] N. Zhou and J. Bao, "FerrDb: a manually curated resource for regulators and markers of ferroptosis and ferroptosis-disease associations," *Database*, vol. 2020, article baaa021, 2020.
- [18] S. Zhang, C. Yu, X. Yang et al., "N-myc downstream-regulated gene 1 inhibits the proliferation of colorectal cancer through emulative antagonizing NEDD4-mediated ubiquitylation of p 21," *Journal of Experimental & Clinical Cancer Research*, vol. 38, no. 1, p. 490, 2019.
- [19] M. Tang, Z. Chen, D. Wu, and L. Chen, "Ferritinophagy/ferroptosis: iron-related newcomers in human diseases," *Journal of Cellular Physiology*, vol. 233, no. 12, pp. 9179–9190, 2018.
- [20] C. Li, Y. Tian, Y. Liang, and Q. Li, "Retracted article: Circ\_0008035 contributes to cell proliferation and inhibits apoptosis and ferroptosis in gastric cancer via miR-599/EIF4A1 axis," *Cancer Cell International*, vol. 20, no. 1, p. 84, 2020.
- [21] H. Zhang, T. Deng, R. Liu et al., "CAF secreted miR-522 suppresses ferroptosis and promotes acquired chemo-resistance in gastric cancer," *Molecular Cancer*, vol. 19, no. 1, p. 43, 2020.
- [22] X. Sun, S. Yang, X. Feng et al., "The modification of ferroptosis and abnormal lipometabolism through overexpression and knockdown of potential prognostic biomarker perilipin 2 in gastric carcinoma," *Gastric Cancer*, vol. 23, no. 2, pp. 241–259, 2020.
- [23] X. Gao, M. Tang, S. Tian, J. Li, and W. Liu, "A ferroptosis-related gene signature predicts overall survival in patients with lung adenocarcinoma," *Future Oncology*, vol. 17, no. 12, pp. 1533–1544, 2021.
- [24] X. Du and Y. Zhang, "Integrated analysis of immunity- and ferroptosis-related biomarker signatures to improve the prognosis prediction of hepatocellular carcinoma," *Frontiers in Genetics*, vol. 11, p. 614888, 2020.
- [25] S. W. Kim, Y. Kim, S. E. Kim, and J. Y. An, "Ferroptosis-related genes in neurodevelopment and central nervous system," *Biology (Basel)*, vol. 10, no. 1, p. 35, 2021.
- [26] B. Tang, J. Zhu, J. Li et al., "The ferroptosis and iron-metabolism signature robustly predicts clinical diagnosis, prognosis and immune microenvironment for hepatocellular carcinoma," *Cell Communication and Signaling: CCS*, vol. 18, no. 1, p. 174, 2020.
- [27] T. Hirose and H. R. Horvitz, "An Sp1 transcription factor coordinates caspase-dependent and -independent apoptotic pathways," *Nature*, vol. 500, no. 7462, pp. 354–358, 2013.
- [28] G. C. Forcina and S. J. Dixon, "GPX4 at the crossroads of lipid homeostasis and ferroptosis," *Proteomics*, vol. 19, no. 18, article e1800311, 2019.
- [29] S. Doll, F. P. Freitas, R. Shah et al., "FSP1 is a glutathione-independent ferroptosis suppressor," *Nature*, vol. 575, no. 7784, pp. 693–698, 2019.
- [30] K. Bersuker, J. M. Hendricks, Z. Li et al., "The CoQ oxidoreductase FSP1 acts parallel to GPX4 to inhibit ferroptosis," *Nature*, vol. 575, no. 7784, pp. 688–692, 2019.
- [31] R. Z. Yusuf, B. Saez, A. Sharda et al., "Aldehyde dehydrogenase 3a2 protects AML cells from oxidative death and the synthetic lethality of ferroptosis inducers," *Blood*, vol. 136, no. 11, pp. 1303–1316, 2020.
- [32] Y. Chen, Z. Zhang, K. Yang, J. du, Y. Xu, and S. Liu, "Myeloid zinc-finger 1 (MZF-1) suppresses prostate tumor growth through enforcing ferroportin-conducted iron egress," *Oncogene*, vol. 34, no. 29, pp. 3839–3847, 2015.
- [33] J. J. Qin, X. D. Cheng, J. Zhang, and W. D. Zhang, "Dual roles and therapeutic potential of Keap1-Nrf2 pathway in



- pancreatic cancer: a systematic review,” *Cell Communication and Signaling: CCS*, vol. 17, no. 1, p. 121, 2019.
- [34] Z. Fan, A. K. Wirth, D. Chen et al., “Nrf2-Keap1 pathway promotes cell proliferation and diminishes ferroptosis,” *Oncogene*, vol. 6, no. 8, article e371, 2017.
- [35] J. S. Sung, C. W. Kang, S. Kang et al., “ITGB4-mediated metabolic reprogramming of cancer-associated fibroblasts,” *Oncogene*, vol. 39, no. 3, pp. 664–676, 2020.
- [36] C. W. Brown, J. J. Amante, and A. M. Mercurio, “Cell clustering mediated by the adhesion protein PVRL4 is necessary for  $\alpha 6 \beta 4$  integrin-promoted ferroptosis resistance in matrix-detached cells,” *The Journal of Biological Chemistry*, vol. 293, no. 33, pp. 12741–12748, 2018.
- [37] R. Derynck and Y. E. Zhang, “Smad-dependent and Smad-independent pathways in TGF- $\beta$  family signalling,” *Nature*, vol. 425, no. 6958, pp. 577–584, 2003.
- [38] K. Fujiki, H. Inamura, T. Sugaya, and M. Matsuoka, “Blockade of ALK4/5 signaling suppresses cadmium- and erastin-induced cell death in renal proximal tubular epithelial cells via distinct signaling mechanisms,” *Cell Death and Differentiation*, vol. 26, no. 11, pp. 2371–2385, 2019.
- [39] X. Qin, J. Zhang, B. Wang et al., “Ferritinophagy is involved in the zinc oxide nanoparticles-induced ferroptosis of vascular endothelial cells,” *Autophagy*, pp. 1–20, 2021.
- [40] J. Li, J. Liu, Y. Xu et al., “Tumor heterogeneity in autophagy-dependent ferroptosis,” *Autophagy*, pp. 1–14, 2021.
- [41] Z. Zhang, M. Guo, Y. Li et al., “RNA-binding protein ZFP36/TTP protects against ferroptosis by regulating autophagy signaling pathway in hepatic stellate cells,” *Autophagy*, vol. 16, no. 8, pp. 1482–1505, 2020.
- [42] I. Poursaitidis, X. Wang, T. Crighton et al., “Oncogene-selective sensitivity to synchronous cell death following modulation of the amino acid nutrient cystine,” *Cell Reports*, vol. 18, no. 11, pp. 2547–2556, 2017.
- [43] M. W. Park, H. W. Cha, J. Kim et al., “NOX4 promotes ferroptosis of astrocytes by oxidative stress-induced lipid peroxidation via the impairment of mitochondrial metabolism in Alzheimer’s diseases,” *Redox Biology*, vol. 41, p. 101947, 2021.
- [44] R. Lin, Z. Zhang, L. Chen et al., “Dihydroartemisinin (DHA) induces ferroptosis and causes cell cycle arrest in head and neck carcinoma cells,” *Cancer Letters*, vol. 381, no. 1, pp. 165–175, 2016.
- [45] J. Lee, J. H. You, M. S. Kim, and J. L. Roh, “Epigenetic reprogramming of epithelial-mesenchymal transition promotes ferroptosis of head and neck cancer,” *Redox Biology*, vol. 37, p. 101697, 2020.
- [46] M. Wang, S. Li, Y. Wang, H. Cheng, J. Su, and Q. Li, “Gambogic acid induces ferroptosis in melanoma cells undergoing epithelial- to-mesenchymal transition,” *Toxicology and Applied Pharmacology*, vol. 401, p. 115110, 2020.
- [47] J. Yi, J. Zhu, J. Wu, C. B. Thompson, and X. Jiang, “Oncogenic activation of PI3K-AKT-mTOR signaling suppresses ferroptosis via SREBP-mediated lipogenesis,” *Proceedings of the National Academy of Sciences of the United States of America*, vol. 117, no. 49, pp. 31189–31197, 2020.
- [48] G. Corso, J. Carvalho, D. Marrelli et al., “Somatic mutations and deletions of the E-cadherin gene predict poor survival of patients with gastric cancer,” *Journal of Clinical Oncology*, vol. 31, no. 7, pp. 868–875, 2013.
- [49] S. Kumagai, Y. Togashi, C. Sakai et al., “An oncogenic alteration creates a microenvironment that promotes tumor progression by conferring a metabolic advantage to regulatory T cells,” *Immunity*, vol. 53, no. 1, pp. 187–203.e8, 2020, e8.
- [50] W. Wang, M. Green, J. E. Choi et al., “CD8<sup>+</sup> T cells regulate tumour ferroptosis during cancer immunotherapy,” *Nature*, vol. 569, no. 7755, pp. 270–274, 2019.
- [51] Z. Jiang, S. O. Lim, M. Yan et al., “TYRO3 induces anti-PD-1/PD-L1 therapy resistance by limiting innate immunity and tumoral ferroptosis,” *The Journal of Clinical Investigation*, vol. 131, no. 8, article e139434, 2021.
- [52] L. C. Cutmore and J. F. Marshall, “Current perspectives on the use of off the shelf CAR-T/NK cells for the treatment of cancer,” *Cancers (Basel)*, vol. 13, no. 8, p. 1926, 2021.
- [53] Y. Ye, Q. Dai, S. Li, J. He, and H. Qi, “A novel defined risk signature of the ferroptosis-related genes for predicting the prognosis of ovarian cancer,” *Frontiers in Molecular Biosciences*, vol. 8, p. 645845, 2021.
- [54] S. Dolma, S. L. Lessnick, W. C. Hahn, and B. R. Stockwell, “Identification of genotype-selective antitumor agents using synthetic lethal chemical screening in engineered human tumor cells,” *Cancer Cell*, vol. 3, no. 3, pp. 285–296, 2003.
- [55] O. S. Kwon, E. J. Kwon, H. J. Kong et al., “Systematic identification of a nuclear receptor-enriched predictive signature for erastin-induced ferroptosis,” *Redox Biology*, vol. 37, p. 101719, 2020.

## Research Article

# A Novel Systematic Oxidative Stress Score Predicts the Prognosis of Patients with Operable Breast Cancer

Kaiming Zhang,<sup>1</sup> Liqin Ping,<sup>2</sup> Tian Du,<sup>1</sup> Yan Wang,<sup>1</sup> Ya Sun,<sup>1</sup> Gehao Liang,<sup>1</sup> Xi Wang,<sup>1</sup> Xiaoming Xie,<sup>1</sup> Weidong Wei,<sup>1</sup> Xiangsheng Xiao <sup>1</sup> and Jun Tang <sup>1</sup>

<sup>1</sup>Department of Breast Oncology, Sun Yat-sen University Cancer Center, State Key Laboratory of Oncology in South China, Collaborative Innovation Center for Cancer Medicine, Guangzhou, Guangdong, China

<sup>2</sup>Department of Medical Oncology, Sun Yat-sen University Cancer Center, State Key Laboratory of Oncology in South China, Collaborative Innovation Center for Cancer Medicine, Guangzhou, Guangdong, China

Correspondence should be addressed to Xiangsheng Xiao; [xiaoxsh@sysucc.org.cn](mailto:xiaoxsh@sysucc.org.cn) and Jun Tang; [tangjun@sysucc.org.cn](mailto:tangjun@sysucc.org.cn)

Received 9 August 2021; Accepted 21 September 2021; Published 7 October 2021

Academic Editor: Guoku Hu

Copyright © 2021 Kaiming Zhang et al. This is an open access article distributed under the Creative Commons Attribution License, which permits unrestricted use, distribution, and reproduction in any medium, provided the original work is properly cited.

**Background.** Breast cancer was associated with imbalance between oxidation and antioxidation. Local oxidative stress in tumors is closely related to the occurrence and development of breast cancer. However, the relationship between systematic oxidative stress and breast cancer remains unclear. This study is aimed at exploring the prognostic value of systematic oxidative stress in patients with operable breast cancer. **Methods.** A total of 1583 operable female breast cancer patients were randomly assigned into the training set and validation set. The relationship between systematic oxidative stress biomarkers and prognosis were analyzed in the training and validation sets. **Results.** The systematic oxidative stress score (SOS) was established based on five systematic oxidative stress biomarkers including serum creatinine (CRE), serum albumin (ALB), total bilirubin (TBIL), lactate dehydrogenase (LDH), and blood urea nitrogen (BUN). SOS was an independent prognostic factor for operable breast cancer patients. A nomogram based on SOS and clinical characteristics could accurately predict the prognosis of operable breast cancer patients, and the area under the curve (AUC) of the nomogram was 0.823 in the training set and 0.872 in the validation set, which was much higher than the traditional prognostic indicators. **Conclusions.** SOS is an independent prognostic indicator for operable breast cancer patients. A prediction model based on SOS could accurately predict the outcome of operable breast cancer patients.

## 1. Background

Breast cancer is a malignancy with the highest incidence and the highest mortality rate among female population [1]. The heterogeneity of breast cancer is strong, and the prognosis of patients with the same American Joint Committee on Cancer (AJCC) stage and immunohistochemical subtype is greatly different [2, 3], suggesting that there are still subtle factors affecting the outcome of patients despite known risk factors such as AJCC stage and immunohistochemical subtype.

Reactive oxygen species (ROS) are important mediators for the body's defense and killing cancer cells. However, excessive ROS could induce DNA damage and genomic

instability, leading to the loss of cell integrity, function, and viability [4]. Breast cancer cells have a higher level of ROS, and DNA damage induced by ROS is closely related to the occurrence and development of breast cancer [5–7].

At present, the important role of local ROS in tumor tissue has been reported by many studies [8–10], but the relationship between systematic oxidative stress and prognosis of breast cancer patients is still unclear. In a systematic oxidative stress mouse model, total bilirubin (TBIL), lactate dehydrogenase (LDH), creatinine (CRE), and blood urea nitrogen (BUN) were significantly increased [11]. At the same time, in critically ill polytrauma patients, there were significant statistical differences in TBIL, serum albumin (ALB), LDH, and C-reactive protein (CRP) of patients

TABLE 1: Clinical characteristics in the training set and validation set.

| Variables          | Total ( <i>n</i> = 1583) |      | Training set<br>( <i>n</i> = 1187) |      | Validation set<br>( <i>n</i> = 396) |      | <i>P</i> value |
|--------------------|--------------------------|------|------------------------------------|------|-------------------------------------|------|----------------|
|                    | No.                      | %    | No.                                | %    | No.                                 | %    |                |
| Age                |                          |      |                                    |      |                                     |      | 0.252          |
| ≤60                | 1347                     | 85.1 | 1003                               | 84.5 | 344                                 | 86.9 |                |
| >60                | 236                      | 14.9 | 184                                | 15.5 | 52                                  | 13.1 |                |
| Multifocality      |                          |      |                                    |      |                                     |      | 0.927          |
| Yes                | 39                       | 2.5  | 29                                 | 2.4  | 10                                  | 2.5  |                |
| No                 | 1544                     | 97.5 | 1158                               | 97.6 | 386                                 | 97.5 |                |
| Histological grade |                          |      |                                    |      |                                     |      | 0.180          |
| I                  | 108                      | 6.8  | 89                                 | 7.5  | 19                                  | 4.8  |                |
| II                 | 903                      | 57.0 | 671                                | 56.5 | 232                                 | 58.6 |                |
| III                | 572                      | 36.2 | 427                                | 36.0 | 145                                 | 36.6 |                |
| VCE                |                          |      |                                    |      |                                     |      | 0.307          |
| Yes                | 558                      | 35.2 | 410                                | 34.5 | 148                                 | 37.4 |                |
| No                 | 1025                     | 64.8 | 777                                | 65.5 | 248                                 | 62.6 |                |
| T stage            |                          |      |                                    |      |                                     |      | 0.371          |
| T1                 | 717                      | 45.3 | 549                                | 46.2 | 168                                 | 42.4 |                |
| T2                 | 760                      | 48.0 | 555                                | 46.8 | 205                                 | 51.8 |                |
| T3                 | 60                       | 3.8  | 47                                 | 4.0  | 13                                  | 3.3  |                |
| T4                 | 46                       | 2.9  | 36                                 | 3.0  | 10                                  | 2.5  |                |
| N stage            |                          |      |                                    |      |                                     |      | 0.248          |
| N0                 | 828                      | 52.3 | 630                                | 53.1 | 198                                 | 50.0 |                |
| N1                 | 402                      | 25.4 | 298                                | 25.1 | 104                                 | 26.3 |                |
| N2                 | 207                      | 13.1 | 145                                | 12.2 | 62                                  | 15.7 |                |
| N3                 | 146                      | 9.2  | 114                                | 9.6  | 32                                  | 8.0  |                |
| TNM stage          |                          |      |                                    |      |                                     |      | 0.263          |
| Stage I            | 438                      | 27.7 | 341                                | 28.7 | 97                                  | 24.5 |                |
| Stage II           | 744                      | 47.0 | 549                                | 46.3 | 195                                 | 49.2 |                |
| Stage III          | 401                      | 25.3 | 297                                | 25.0 | 104                                 | 26.3 |                |
| IHC subtype        |                          |      |                                    |      |                                     |      | 0.155          |
| Luminal A          | 328                      | 20.7 | 252                                | 21.3 | 76                                  | 19.2 |                |
| Luminal B          | 883                      | 55.8 | 645                                | 54.3 | 238                                 | 60.1 |                |
| HER2+              | 184                      | 11.6 | 139                                | 11.7 | 45                                  | 11.4 |                |
| TNBC               | 188                      | 11.9 | 151                                | 12.7 | 37                                  | 9.3  |                |
| CRE (μmol/L)       |                          |      |                                    |      |                                     |      | 0.544          |
| <59.30             | 963                      | 60.8 | 717                                | 60.4 | 246                                 | 62.1 |                |
| ≥59.30             | 620                      | 39.2 | 470                                | 39.6 | 150                                 | 37.9 |                |
| DBIL (μmol/L)      |                          |      |                                    |      |                                     |      | 0.326          |
| <2.20              | 393                      | 24.8 | 302                                | 25.4 | 91                                  | 23.0 |                |
| ≥2.20              | 1190                     | 75.2 | 885                                | 74.6 | 305                                 | 77.0 |                |
| TBIL (μmol/L)      |                          |      |                                    |      |                                     |      | 0.262          |
| <13.80             | 1270                     | 80.2 | 960                                | 80.9 | 310                                 | 78.3 |                |
| ≥13.80             | 313                      | 19.8 | 227                                | 19.1 | 86                                  | 21.7 |                |
| LDH (U/L)          |                          |      |                                    |      |                                     |      | 0.732          |
| <205.70            | 1424                     | 90.0 | 1066                               | 89.8 | 358                                 | 90.4 |                |
| ≥205.70            | 159                      | 10.0 | 121                                | 10.2 | 38                                  | 9.6  |                |
| UA (μmol/L)        |                          |      |                                    |      |                                     |      | 0.357          |
| <255.20            | 408                      | 25.8 | 299                                | 25.2 | 109                                 | 27.5 |                |
| ≥255.20            | 1175                     | 74.2 | 888                                | 74.8 | 287                                 | 72.5 |                |

TABLE 1: Continued.

| Variables    | Total ( <i>n</i> = 1583) |      | Training set ( <i>n</i> = 1187) |      | Validation set ( <i>n</i> = 396) |      | <i>P</i> value |
|--------------|--------------------------|------|---------------------------------|------|----------------------------------|------|----------------|
|              | No.                      | %    | No.                             | %    | No.                              | %    |                |
| BUN (mmol/L) |                          |      |                                 |      |                                  |      | 0.466          |
| <6.29        | 1424                     | 90.0 | 1064                            | 89.6 | 360                              | 90.9 |                |
| ≥6.29        | 159                      | 10.0 | 123                             | 10.4 | 36                               | 9.1  |                |
| ALB (g/L)    |                          |      |                                 |      |                                  |      | 0.966          |
| <43.00       | 830                      | 52.4 | 622                             | 52.4 | 208                              | 52.5 |                |
| ≥43.00       | 753                      | 47.6 | 565                             | 47.6 | 188                              | 47.5 |                |
| CRP (mg/L)   |                          |      |                                 |      |                                  |      | 0.807          |
| <3.78        | 1361                     | 86.0 | 1022                            | 86.1 | 339                              | 85.6 |                |
| ≥3.78        | 222                      | 14.0 | 165                             | 13.9 | 57                               | 14.4 |                |

with antioxidant treatment compared with those without [12]. It was suggested that these biochemical indicators may be biomarkers of systematic oxidative stress of the whole body.

This study is aimed at exploring the relationship between systematic oxidative stress and prognosis of breast cancer patients based on biochemical oxidative indicators. Furthermore, a novel systematic oxidative stress score (SOS) was established based on biochemical indicators of systematic oxidative stress. Finally, a prognostic nomogram was created by combining SOS with other clinical variables for predicting the prognosis of breast cancer patients.

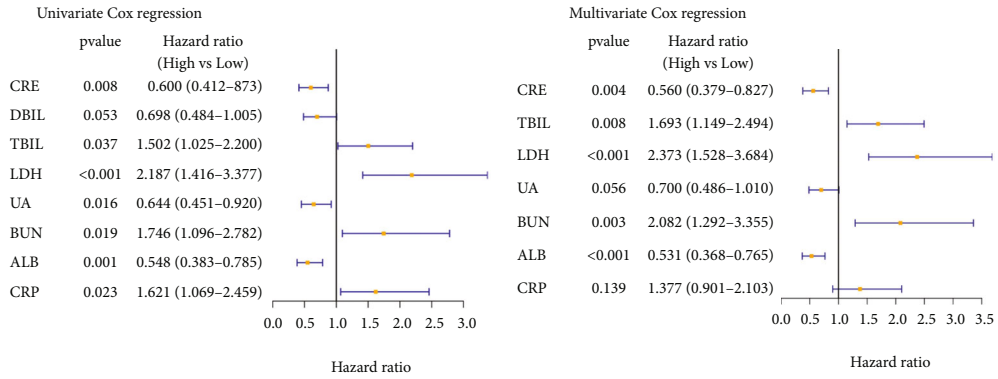
## 2. Methods

**2.1. Patients and Study Design.** This study included female breast cancer patients who received breast conserving surgery or modified radical mastectomy at Sun Yat-sen University Cancer Center (SYSUCC) from August 2012 to December 2015. Inclusion criteria included the following: (1) diagnosed as invasive breast cancer by histopathology, (2) received breast conserving surgery or modified radical mastectomy at SYSUCC, (3) no distant metastasis before surgery, (4) complete preoperative biochemical examination and clinical information, and (5) normal liver and kidney function. Exclusion criteria included the following: (1) received preoperative chemotherapy or other antitumor therapy before surgery, (2) complicated with other uncured malignant tumors, and (3) renal or liver dysfunction. A total of 1583 female breast cancer patients were enrolled in the study and randomly assigned to the training set (*n* = 1187) or validation set (*n* = 396). Prognostic models were established in the training set and the accuracy of the prediction model was subsequently verified in the validation set. The study was approved by the SYSUCC Ethics Committee (identifier: 81372133), and all patients signed an informed consent form. The study complied with the Helsinki Declaration and the Ethics Committee.

**2.2. Data Collection and Treatment.** We collected the information about age, gender, history of disease, immunohistochemical (IHC) subtype of breast cancer, number of primary lesions, tumor size and T stage, lymph node metas-

tasis and N stage, AJCC stage and vessel carcinoma embolus (VCE) of breast cancer patients from SYSUCC hospital information system. CRE, TBIL, direct bilirubin (DBIL), LDH, uric acid (UA), BUN, ALB, and CRP were obtained 3 days before operation. The biochemical indicators were measured by automatic biochemical analyzer (Hitachi Ltd. 7600 Serial, Tokyo, Japan). According to the receiver operating characteristic (ROC) curve analysis, the best cut-off values of these biochemical indicators were as follows: CRE 59.3  $\mu$ mol/L, DBIL 2.2  $\mu$ mol/L, TBIL 13.8  $\mu$ mol/L, LDH 205.7 U/L, UA 255.2  $\mu$ mol/L, BUN 6.29 mmol/L, ALB 43 g/L, and CRP 3.37 mg/L. And the status of these biochemical indicators was defined as high if it was greater than the cut-off, and low if not. Age was defined as the age of the patient at the time of surgery. The sex is the biological sex. Complicated with other uncured tumors refers to the occurrence of other malignancies within 5 years (excluding curable carcinoma in situ). Pathological diagnosis of enrolled patients was reviewed by an experienced pathologist at SYSUCC, and patients were pathologically analyzed based on IHC and/or fluorescence in situ hybridization (FISH) detection of estrogen receptor (ER), progesterone receptor (PR), human epidermal growth factor receptor-2 (HER-2), and Ki-67 status. The size of the tumor was the longest diameter of the tumor tissue reported by pathology. The number of lymph node metastasis was determined by postoperative histopathological examination. Distant metastases preoperatively were identified by radiographic examination. The AJCC staging of patients is based on the Eighth Edition of the AJCC Staging Systems. Most patients received standard postoperative adjuvant chemotherapy, anti-HER2 therapy, postoperative adjuvant radiotherapy, or postoperative adjuvant endocrine therapy. They were followed up and received physical check every three months after surgery, every six months after two years, and every year after five years. The overall survival (OS) of patients who died was defined as the time from surgical treatment to death, and the OS of patients who are still alive was defined as the time from surgery to the last follow-up. The last follow-up of patients enrolled in this study was in December 2020.

**2.3. Statistical Analysis.** R software version 4.0.2 (R Statistical Computing Foundation, Vienna, Austria) and SPSS 24.0

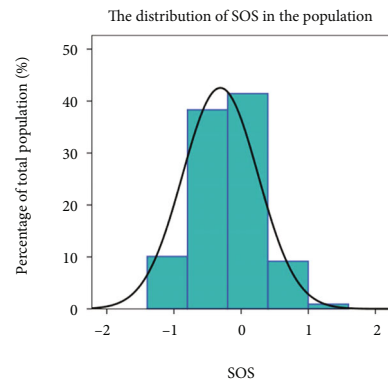


(a)

(b)

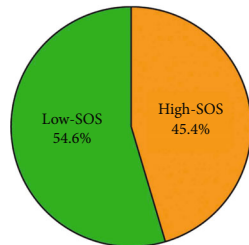
Formula of SOS based on multivariate Cox regression analysis:

$$SOS = -0.64^* CRE + 0.56^* TBIL + 0.86^* LDH + 0.70^* BUN - 0.68^* ALB$$

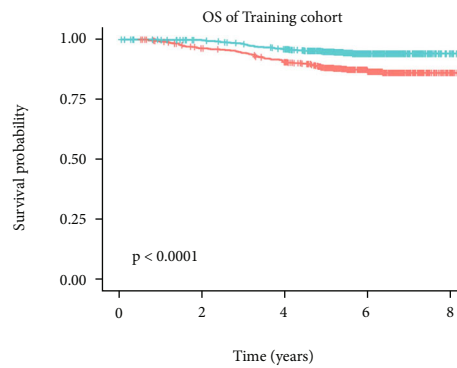


(d)

The distribution of SOS in the population



(e)



(f)

|               | Number at risk |     |     |     |   |
|---------------|----------------|-----|-----|-----|---|
|               | 0              | 2   | 4   | 6   | 8 |
| —+ SOS = High | 539            | 505 | 468 | 210 | 6 |
| —+ SOS = Low  | 648            | 629 | 594 | 209 | 4 |

FIGURE 1: Continued.

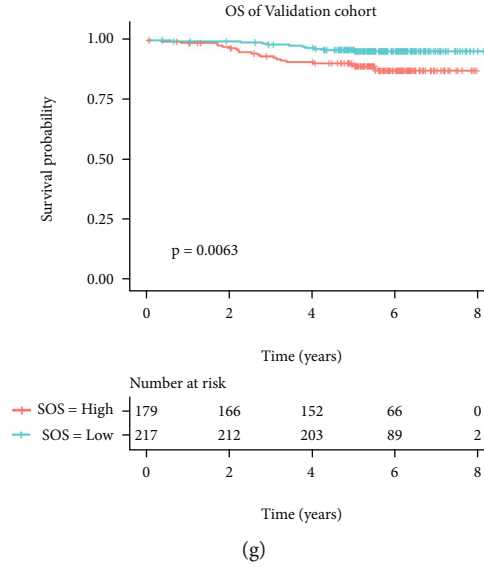


FIGURE 1: SOS is related with OS of breast cancer patients. (a, b) Systematic oxidative stress indicators were included in the univariate Cox regression analysis and multivariate Cox regression analysis in the training set. (c) The specific calculation formula of SOS. (d, e) The distribution of SOS in breast cancer patients. (f) Kaplan-Meier curves showed that the OS of high-SOS patients was longer than that of low-SOS patients in the training set. (g) Kaplan-Meier curves showed that the OS of high-SOS patients was longer than that of low-SOS patients in the validation set.

TABLE 2: Multivariate Cox regression analysis of candidate indicators for SOS.

| Factors | Coef  | HR (95% CI)         | P value  |
|---------|-------|---------------------|----------|
| CRE     | -0.64 | 0.525 (0.358-0.769) | 0.000966 |
| TBIL    | 0.56  | 1.756 (1.194-2.582) | 0.004186 |
| LDH     | 0.86  | 2.365 (1.527-3.663) | 0.000114 |
| BUN     | 0.7   | 2.017 (1.256-3.240) | 0.003678 |
| ALB     | -0.68 | 0.506 (0.353-0.726) | 0.000221 |

(IBM, Armonk, NY, USA) were used to perform the analysis of this research. Chi-squared test was used to analyze the differences in proportions of clinical variables. The independent prognostic indicators of OS were identified through univariate Cox regression analysis and multivariate Cox regression analysis. Then, five optimal biochemical indicators, such as CRE, ALB, TBIL, LDH, and BUN, were identified for calculating systematic oxidative stress score (SOS), which was based on the lowest Akaike information criterion (AIC) value [13]. The SOS of each patient was calculated by the status of biochemical indicators, which below the cut-off value was defined as 0, and above the cut-off value was defined as 1. The corresponding regression coefficient of each biochemical indicator was identified based on multivariate Cox regression analysis. The formula of SOS was as follows:  $SOS = \sum (\text{corresponding regression coefficient} \times \text{status of biochemical indicator})$ . Patients were separated into low-SOS and high-SOS groups based on the median value of the SOS. 'rms' package of R software was used to construct a nomogram combining SOS with other clinical variables. The predictive performance of the nomo-

gram was analyzed through calibration plots. The time-dependent ROC curve was used to evaluate the predictive accuracy of nomogram.  $P$  value  $< 0.05$  in two-tailed test was considered statistically significant.

### 3. Results

**3.1. Clinical Characteristics of Patients.** A total of 1583 female breast cancer patients were enrolled in this study, of whom 1187 (75%) patients were randomly assigned to the training set, and 396 (25%) patients were assigned to the validation set. The clinical characteristics as well as the pre-operative biochemical oxidative stress markers of breast cancer patients in the training set and validation set were shown in Table 1. There were no statistical differences in clinical characteristics and systematic oxidative stress indicators between the two sets.

**3.2. Systematic Oxidative Stress Score (SOS) Was Established Based on Systematic Oxidative Stress Indicators.** To explore the prognostic value of systematic oxidative stress indicators, the systematic oxidative stress indicators were transformed into dichotomous variables according to the cut-off determined by ROC. In univariate Cox regression analysis, CRE, TBIL, LDH, UA, BUN, ALB, and CRP were correlated with the OS of breast cancer patients, while there is no statistical relationship between DBIL and OS (Figure 1(a)). In multivariate Cox regression analysis, elevated CRE and ALB were associated with better OS, while elevated TBIL, LDH, and BUN predicted worse prognosis (Figure 1(b)). To simplify the calculation, the status of systematic oxidative stress indicator was defined as 1 if it was greater than the cut-off, and 0 if not. Then, the systematic oxidative stress score (SOS) was

TABLE 3: Relationship between SOS and clinical characteristics in the training set.

| Variables          | Total (n = 1187) |      | SOS high (n = 539) |      | SOS low (n = 648) |      | P value |
|--------------------|------------------|------|--------------------|------|-------------------|------|---------|
|                    | No.              | %    | No.                | %    | No.               | %    |         |
| Age                |                  |      |                    |      |                   |      | 0.002   |
| ≤60                | 1003             | 84.5 | 436                | 80.9 | 567               | 87.5 |         |
| >60                | 184              | 15.5 | 103                | 19.1 | 81                | 12.5 |         |
| Multifocality      |                  |      |                    |      |                   |      | 0.115   |
| Yes                | 29               | 2.4  | 9                  | 1.7  | 20                | 3.1  |         |
| No                 | 1158             | 97.6 | 530                | 98.3 | 628               | 96.9 |         |
| Histological grade |                  |      |                    |      |                   |      | 0.611   |
| I                  | 89               | 7.5  | 36                 | 6.7  | 53                | 8.2  |         |
| II                 | 671              | 56.5 | 306                | 56.8 | 365               | 56.3 |         |
| III                | 427              | 36.0 | 197                | 36.5 | 230               | 35.5 |         |
| VCE                |                  |      |                    |      |                   |      | 0.790   |
| Yes                | 410              | 34.5 | 184                | 34.1 | 226               | 34.9 |         |
| No                 | 777              | 65.5 | 355                | 65.9 | 422               | 65.1 |         |
| T stage            |                  |      |                    |      |                   |      | 0.038   |
| T1                 | 549              | 46.2 | 225                | 41.7 | 324               | 50.0 |         |
| T2                 | 555              | 46.8 | 275                | 51.0 | 280               | 43.2 |         |
| T3                 | 47               | 4.0  | 23                 | 4.3  | 24                | 3.7  |         |
| T4                 | 36               | 3.0  | 16                 | 3.0  | 20                | 3.1  |         |
| N stage            |                  |      |                    |      |                   |      | 0.059   |
| N0                 | 630              | 53.1 | 264                | 49.1 | 366               | 56.5 |         |
| N1                 | 298              | 25.1 | 142                | 26.3 | 156               | 24.0 |         |
| N2                 | 145              | 12.2 | 74                 | 13.7 | 71                | 11.0 |         |
| N3                 | 114              | 9.6  | 59                 | 10.9 | 55                | 8.5  |         |
| IHC subtype        |                  |      |                    |      |                   |      | 0.466   |
| Luminal A          | 252              | 21.1 | 104                | 19.3 | 148               | 22.8 |         |
| Luminal B          | 645              | 54.3 | 296                | 54.9 | 349               | 53.9 |         |
| HER2+              | 139              | 11.7 | 67                 | 12.4 | 72                | 11.1 |         |
| TNBC               | 151              | 11.9 | 72                 | 13.4 | 79                | 12.2 |         |

established based on multivariate Cox regression analysis and the lowest value of AIC (Table 2). Finally, the formula of SOS was as follows:  $SOS = -0.64 \times CRE + 0.56 \times TBIL + 0.86 \times LDH + 0.7 \times BUN - 0.68 \times ALB$  (Figure 1(c)). The distribution of SOS in breast cancer patients was shown in Figure 1(d). The value of SOS was between -1.32 and 1.56, and the median SOS was -0.12. Based on the median SOS, breast cancer patients were divided into the high-SOS group (45.4%) and low-SOS group (56.6%) (Figure 1(e)). Patients with higher SOS had worse prognosis in the training set (Figure 1(f)), and the same result was observed in the validation set (Figure 1(g)).

**3.3. The Relationship between Systematic Oxidative Stress Score (SOS) and Clinical Characteristics.** The relationship between SOS and clinical characteristics was shown in Table 3, and we could find that elder or advanced T stage patients tended to have higher SOS. Then, subgroup analysis was performed in breast cancer patients with different clinical characteristics. In patients with stage II and III breast

cancer, there was a statistical difference in OS between the low-SOS and high-SOS groups (Figures 2(b) and 2(c)). However, no statistical difference was observed in stage I breast cancer patients (Figure 2(a)). In terms of immunohistochemical subtypes, the higher SOS in patients with non-triple-negative breast cancer predicted a worse prognosis (Figure 2(d)). But there was no statistical difference in prognosis between the high-SOS and low-SOS patients with triple-negative breast cancer (Figure 2(e)).

**3.4. SOS Was an Independent Prognostic Indicator of OS for Breast Cancer Patients.** Univariate and multivariate Cox regression analyses were performed to determine the independent prognostic value of SOS. The result of univariate Cox regression analysis showed that age, SOS, histological grade, VCE, T stage, N stage, and IHC subtype were prognostic indexes for OS. Subsequently, these indexes were included in the multivariate Cox regression analysis, and the results showed that age, SOS, T stage, N stage, and IHC subtype were independent prognostic indicators (Table 4). In general, SOS

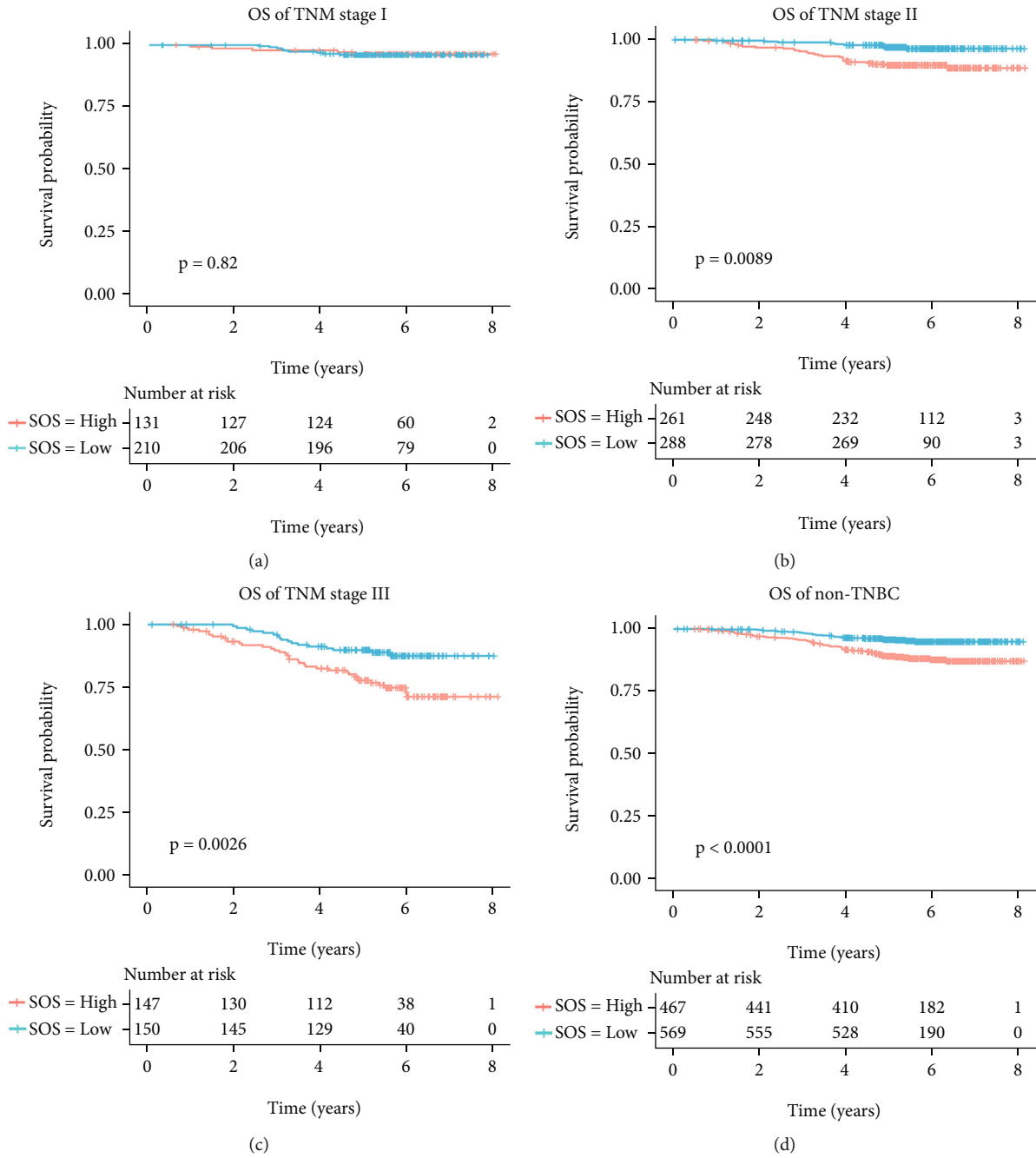


FIGURE 2: Continued.



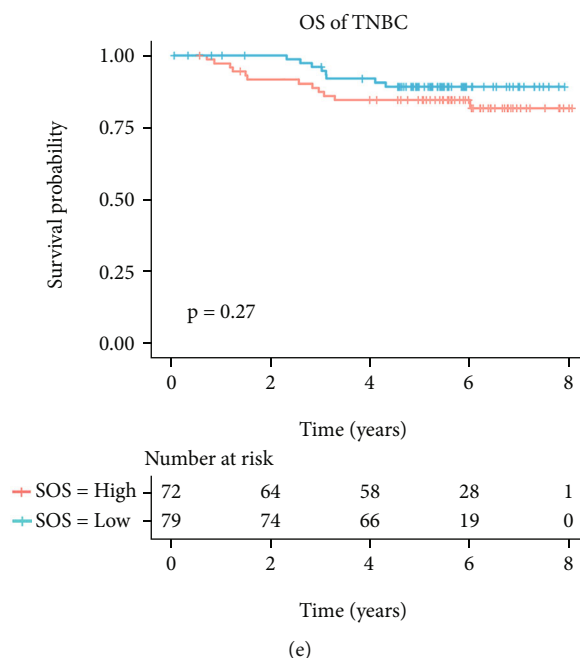


FIGURE 2: Subgroup-based survival analysis for patients with breast cancer. (a) Kaplan-Meier analysis for the OS of patients with AJCC staging I breast cancer. (b) Kaplan-Meier analysis for the OS of patients with AJCC staging II breast cancer. (c) Kaplan-Meier analysis for the OS of patients with AJCC staging III breast cancer. (d) Kaplan-Meier analysis for the OS of patients with nontriple-negative breast cancer. (e) Kaplan-Meier analysis for the OS of patients with triple-negative breast cancer.

was an independent prognostic indicator of OS for breast cancer patients.

**3.5. Construction and Verification of a Nomogram.** All independent prognostic indexes identified through multivariate Cox regression analysis were included to build a nomogram (Figure 3(a)). The consistency of this nomogram was analyzed by calibration plots, showing the strong consistency between prediction and observation in predicting OS (Figures 3(b)–3(e)). And the predictive accuracy was estimated by time-dependent ROC curve analysis, showing that the area under the curve (AUC) of the nomogram in predicting 2-year, 3-year, and 5-year survival rates were 0.823, 0.780, and 0.761, respectively, in the training set and were 0.872, 0.808 and 0.786, respectively, in the validation set (Figures 4(a) and 4(b)). In order to compare the predictive capacity between this nomogram and traditional prognostic indicators, such as age, AJCC staging, and IHC subtype, the ROC curve analysis was conducted. And the results showed that the AUC of the nomogram was much higher than that of these traditional prognostic indicators (Figures 4(c)–4(h)), suggesting that the nomogram owned a higher accuracy in predicting OS than these traditional prognostic indicators.

## 4. Discussion

This study is the first to explore the significance of systematic oxidative stress status for the prognosis of breast cancer and the first to establish a prognostic model including SOS. In this study, biochemical indicators of systematic oxidative

stress were analyzed to explore the relationship between systematic oxidative stress and prognosis in breast cancer patients. According to univariate and multivariate Cox regression analyses, elevated CRE and ALB were associated with better OS, while elevated TBIL, LDH, and BUN predicted poorer prognosis. In order to combine these factors, SOS was established based on these five indicators. SOS was an independent prognostic indicator for breast cancer patients, and higher SOS was related with poorer survival. Then, a nomogram based on SOS and clinical characteristics was built, which could provide higher accuracy in predicting OS than traditional prognostic indicators.

The imbalance between oxidation and antioxidation is related to the occurrence and development of breast cancer. The high-risk factors of breast cancer, such as age increasing, obesity, alcohol consumption, smoking, estrogen, BRCA gene mutation, and ionizing radiation, are all related to oxides and oxidative stress [14]. As an important tumor suppressor gene, BRCA1 gene is involved in the upregulation of gene expression of protective antioxidant response and antioxidant response transcription factors. Its products can downregulate the level of ROS in cells and protect cells from DNA oxidative damage [5]. On the contrary, estrogen can lead to DNA damage and the occurrence of breast cancer by inducing the generation of ROS [7].

Studies on the prevention of breast cancer have shown that dietary intake of high antioxidant foods was associated with a lower risk of breast cancer [15]. The increased intake of vegetable-fruit-soybean diet in postmenopausal women was associated with a dose-dependent decrease in breast cancer risk [16]. Oxidative stress promotes the formation

TABLE 4: Results of the univariate and multivariate Cox regression analyses for OS among the clinical characteristics and SOS.

| Variables          | Univariate Cox analysis |         | Multivariate Cox analysis |         |
|--------------------|-------------------------|---------|---------------------------|---------|
|                    | HR (95% CI)             | P value | HR (95% CI)               | P value |
| Age                |                         | 0.002   |                           | 0.003   |
| ≤60                | Reference               |         | Reference -               |         |
| >60                | 1.435 (1.155-1.783)     |         | 1.943 (1.247-3.027)       |         |
| SOS                |                         | <0.001  |                           | <0.001  |
| Low                | Reference               |         | Reference                 |         |
| High               | 2.389 (1.589-3.592)     |         | 2.096 (1.385-3.170)       |         |
| Multifocality      |                         | 0.786   |                           |         |
| No                 | Reference               |         |                           |         |
| Yes                | 1.177 (0.373-3.712)     |         |                           |         |
| Histological grade |                         | 0.019   |                           | 0.430   |
| I                  | Reference               |         | Reference                 |         |
| II                 | 1.704 (0.616-4.716)     | 0.305   | 1.411 (0.495-4.023)       | 0.520   |
| III                | 2.719 (0.980-7.542)     | 0.055   | 1.749 (0.602-5.082)       | 0.304   |
| VCE                |                         | <0.001  |                           | 0.055   |
| No                 | Reference               |         | Reference                 |         |
| Yes                | 2.295 (1.558-3.380)     |         | 1.518 (0.992-2.322)       |         |
| T stage            |                         | <0.001  |                           | <0.001  |
| T1                 | Reference               |         | Reference                 |         |
| T2                 | 2.076 (1.310-3.290)     | 0.002   | 1.409 (0.876-2.265)       | 0.157   |
| T3                 | 4.812 (2.328-9.945)     | <0.001  | 2.558 (1.190-5.497)       | 0.016   |
| T4                 | 7.158 (3.548-14.442)    | <0.001  | 4.528 (2.150-9.540)       | <0.001  |
| N stage            |                         | <0.001  |                           | <0.001  |
| N0                 | Reference               |         | Reference                 |         |
| N1                 | 1.680 (0.999-2.825)     | 0.050   | 1.567 (0.911-2.693)       | 0.104   |
| N2                 | 2.211 (1.217-4.017)     | 0.009   | 1.634 (0.856-3.121)       | 0.137   |
| N3                 | 5.911 (3.586-9.741)     | <0.001  | 3.612 (2.056-6.346)       | <0.001  |
| IHC subtype        |                         | <0.001  |                           | 0.032   |
| Luminal A          | 0.185 (0.078-0.439)     | <0.001  | 0.261 (0.107-0.642)       | 0.003   |
| Luminal B          | 0.684 (0.414-1.131)     | 0.139   | 0.618 (0.362-1.056)       | 0.078   |
| HER2+              | 0.683 (0.340-1.373)     | 0.284   | 0.625 (0.305-1.283)       | 0.201   |
| TNBC               | Reference               |         | Reference                 |         |

of breast cancer, but the relationship between the level of systematic oxidative stress and the prognosis of breast cancer patients remains unclear. Some studies reported that antioxidants can reduce the effectiveness of treatment and even contribute to the progression of breast cancer. Tamoxifen (TAM) induced apoptosis in MCF-7 cells by inducing the increase of ROS and the release of proapoptotic factors in mitochondria. However, vitamin C, an antioxidant, can protect cancer cells from TAM-induced oxidation, thereby inhibiting MCF-7 cell death [17]. Meanwhile, vitamin E, another antioxidant, could significantly reduce the production of ROS and the expression of p53 to promote the proliferation of MCF-7 cells [18]. It was suggested that the relationship between oxidative stress and breast cancer was complex. Before tumor formation, excessive oxidants can lead to DNA damage and increase the incidence of cancer. However, once the tumor was formed, the reduced oxidation level caused by antioxidants may reduce the ability of killing

cancer cells, leading to the progression of cancer and the decrease of therapeutic efficacy.

Bilirubin is the end product of heme metabolism and is considered an anticancer factor due to its antioxidant function, but the relationship between bilirubin and prognosis of cancers is adverse. Evidence showed increased bilirubin indicated poorer prognosis in advanced non-small-lung cancer, cholangiocarcinoma, and rectal cancer patients [19–21]. In patients with metastatic breast cancer, higher bilirubin levels are associated with decreased survival [22]. In this study, elevated total bilirubin was associated with worse prognosis for breast cancer patients. In muscle, creatine is formed into CRE and released into the blood through an irreversible nonenzymatic dehydration reaction. Endogenous CRE is a product of muscle metabolism in the human body. BUN is the main end product of protein metabolism in human body. Both CRE and BUN are excreted by the kidneys, but systematic oxidative stress reduces the ability of the

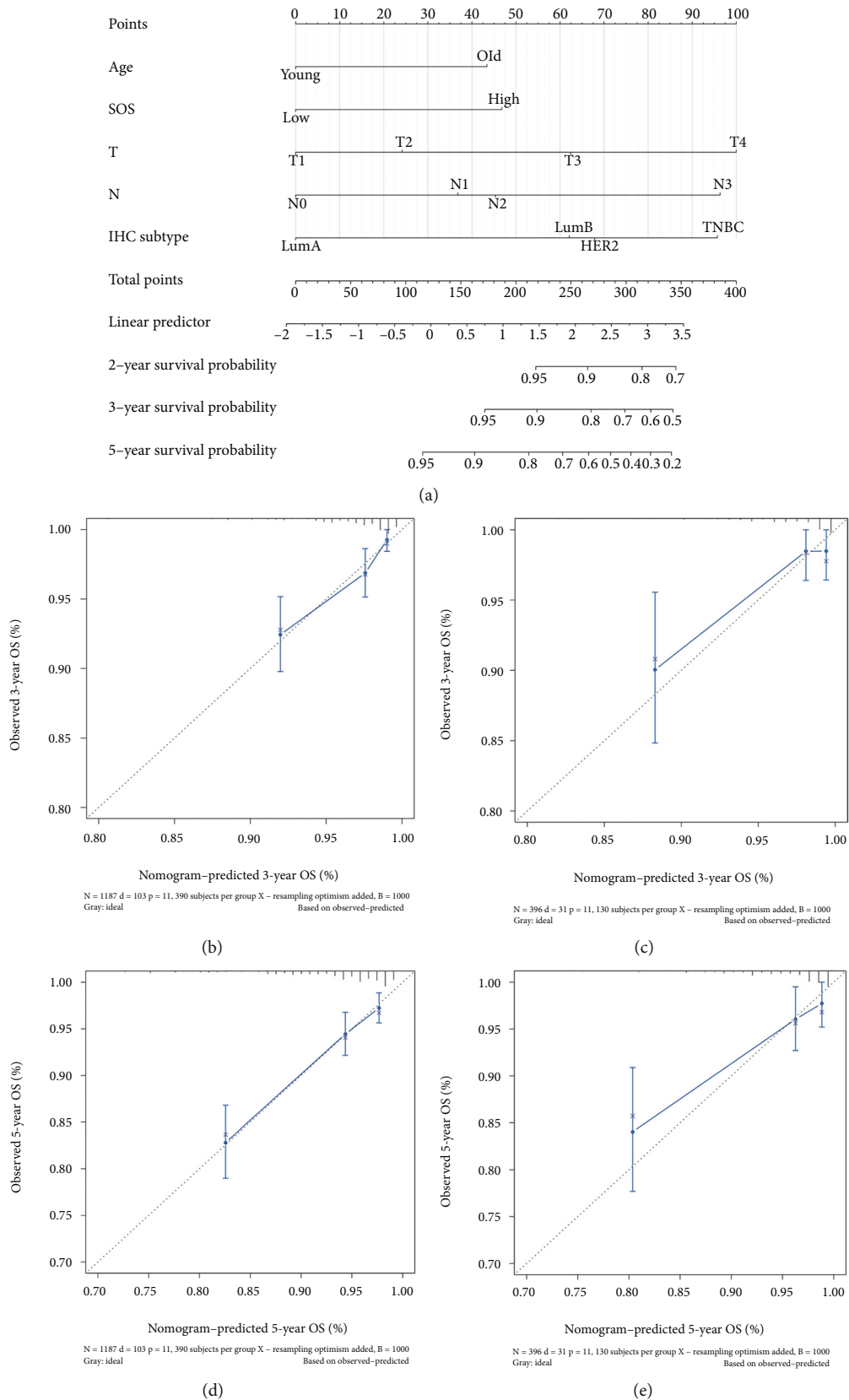


FIGURE 3: Nomogram could predict the OS of breast cancer patients. (a) Nomogram for predicting the OS of patients with breast cancer. (b) Calibration plot of the nomogram for 3-year overall survival in the training cohort. (c) Calibration plot of the nomogram for 3-year overall survival in the validation cohort. (d) Calibration plot of the nomogram for 5-year overall survival in the training cohort. (e) Calibration plot of the nomogram for 5-year overall survival in the validation cohort.

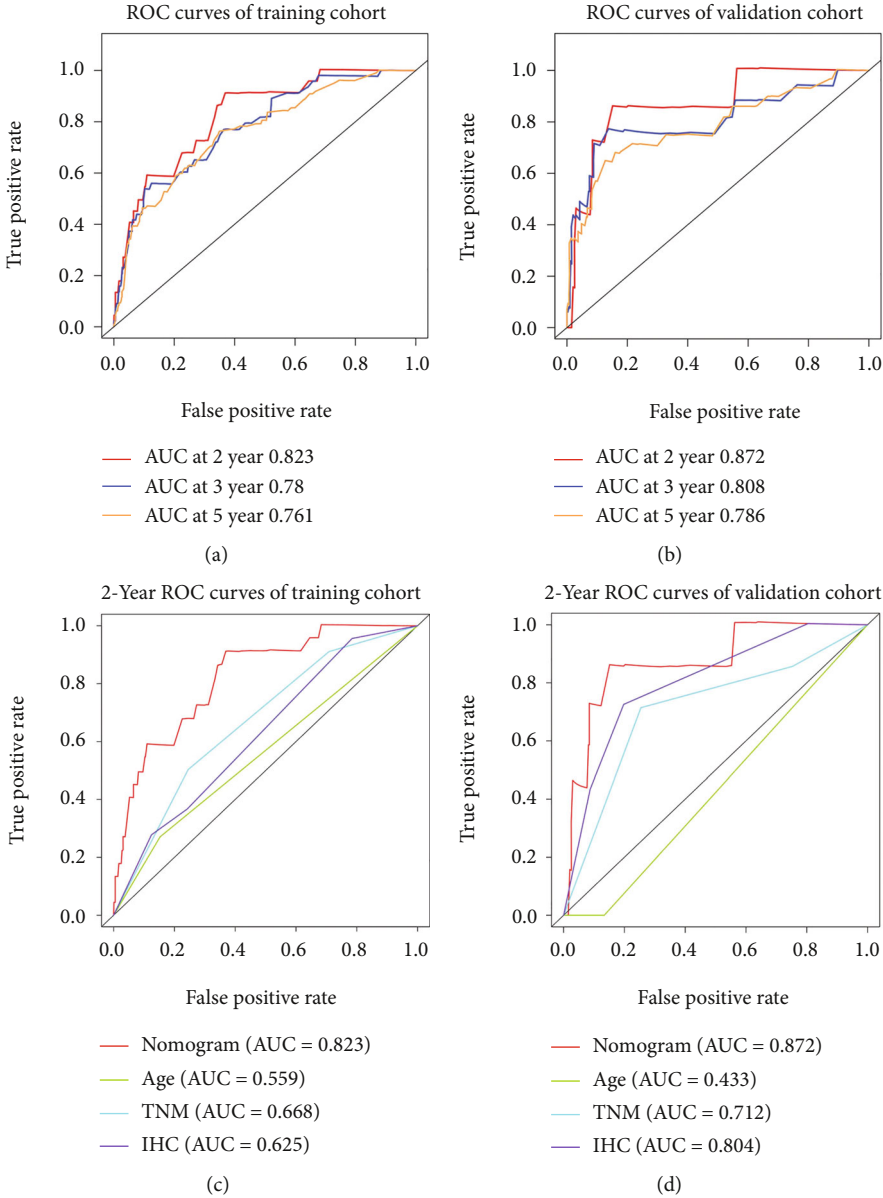


FIGURE 4: Continued.

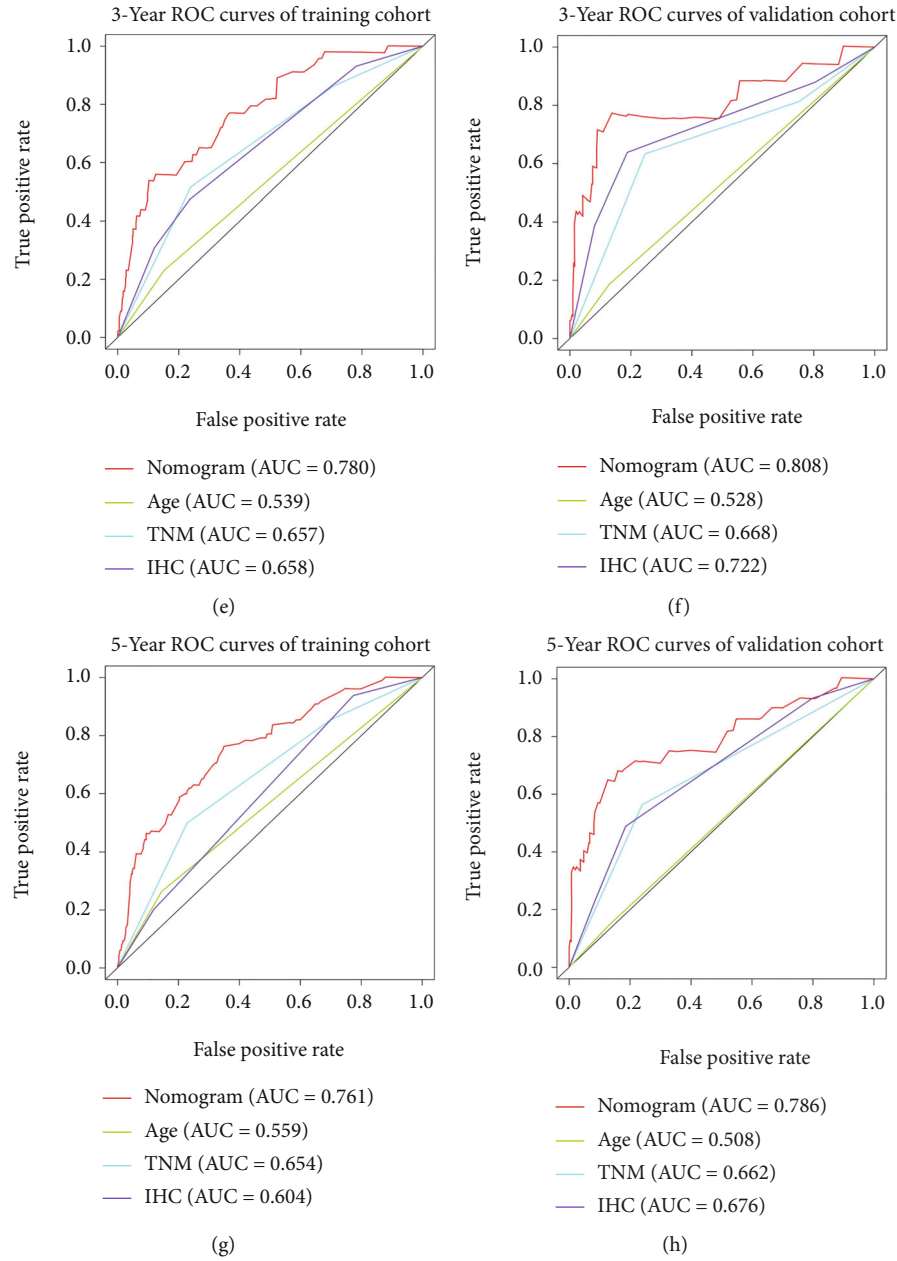


FIGURE 4: The predictive accuracy of our nomogram is much better than that of previous prognostic indicators. (a). Time-dependent ROC curves were used to determine the prognostic value of the nomogram in the training set. (b) Time-dependent ROC curves were used to determine the prognostic value of the nomogram in the validation set. (c–h) Area under the ROC curves was used to compare the prognostic value of the nomogram and previous prognostic indicators for predicting 2-year overall survival, 3-year overall survival, or 5-year overall survival in the training set and validation set.

kidneys to excrete urea and creatinine, leading to increases of CRE and BUN in blood, which decrease after antioxidant treatment [23]. Therefore, CRE and BUN could reflect the status of systematic oxidative stress. It has been proved that antioxidant compounds could activate the antioxidant transcription factor Nrf2 and reduce CRE level [24, 25]. On the other hand, the synthesis of BUN is the main way to reduce ammonia. If the synthesis of BUN is blocked, it will lead to the increase of ammonia, which could promote the production of ROS and oxidative stress [26]. In this study, increased CRE and decreased BUN were associated with longer OS in

breast cancer patients. ALB is an important protein produced by the liver and can reflect the nutritional status and inflammatory response status of the human body [27]. In addition, ALB has antioxidant function and enzymatic activity [28]. Higher ALB levels are associated with longer OS in patients with a number of cancers, including breast cancer [29]. It is consistent with the results of our study. Lactate dehydrogenase A (LDHA) provides energy for tumor metabolism by promoting glycolysis to transform pyruvate into lactic acid. LDHA produces  $\alpha$ -hydroxybutyrate and triggers hypermethylation of histone H3K79, which activates

the antioxidant reaction [30]. Decrease of LDHA translation or inhibition of LDHA function can reduce ATP production, increase ROS production, and induce significant oxidative stress and cell death [31]. In our study, decreased LDH was associated with longer OS in breast cancer patients.

To our knowledge, all reported biochemical markers associated with oxidative stress were included in this study, including CRE, TBIL, LDH, UA, BUN, ALB, and CRP. After univariate and multivariate analyses, we identified five independent systematic oxidative stress indicators (TBIL, BUN, CRE, ALB, and BUN) to calculate SOS, which is an independent prognostic factor for breast cancer patients. This study reported the relationship between systematic oxidative stress indexes and breast cancer prognosis for the first time and established the prediction model, of which the AUC could reach 0.872.

Oxidative stress is involved in the formation and development of tumors, but there are few reports on its effect on prognosis. SOS can provide prognostic information for patients from systematic oxidative stress status. This study could help clinicians identify patients with poor outcomes, allowing more aggressive treatment regimens for high-risk patients, and increasing the frequency of postoperative follow-up. In addition, the results of this study are beneficial to the subsequent studies on the relationship between oxidative stress and tumor prognosis and provide reference for the development of therapeutic targets for oxidative stress. However, our study was a single-center retrospective study, and the causal relationship between the included indicators and oxidative stress as well as the mechanism is still unclear, which still needs to be confirmed by multicenter prospective studies and more basic research in the future.

## 5. Conclusion

SOS can predict the prognosis of patients with breast cancer based on the status of oxidative stress, and the SOS-based nomogram has a good accuracy in predicting the prognosis of patients with operable breast cancer. In addition, SOS provides a new idea for the establishment of prognosis model of breast cancer.

## Data Availability

These data are available by individual application to the corresponding authors.

## Ethical Approval

Our study was approved by the Ethics Committee of Sun-Yat-Sen University Cancer Center Health Authority (identifier: 81372133).

## Conflicts of Interest

The authors declare that there is no conflict of interest.

## Authors' Contributions

All authors participated in this research, including conception and design (ZKM, PLQ, XXS, TJ), data acquisition (ZKM, PLQ, WY, SY, DT, LGH, WX, XXM, WWD, XXS, TJ), data analysis and interpretation (ZKM, PLQ), material support (PLQ, XXS, TJ), study supervision (ZKM, PLQ, XXS, TJ), and drafting the article or critically revising (ZKM, PLQ, DT, XXS, TJ). The final version was ensured and approved by all authors. Kaiming Zhang, Liqin Ping, and Tian Du contributed equally to this work and share first authorship.

## Acknowledgments

This study was supported by the National Natural Science Foundation of China (81372133).

## References

- [1] H. Sung, J. Ferlay, R. L. Siegel et al., "Global cancer statistics 2020: GLOBOCAN estimates of incidence and mortality worldwide for 36 cancers in 185 countries," *CA: a Cancer Journal for Clinicians*, vol. 71, no. 3, pp. 209–249, 2021.
- [2] O. Yersal and S. Barutca, "Biological subtypes of breast cancer: prognostic and therapeutic implications," *World Journal of Clinical Oncology*, vol. 5, no. 3, pp. 412–424, 2014.
- [3] V. Zelli, C. Compagnoni, R. Capelli et al., "Circulating micro-RNAs as prognostic and therapeutic biomarkers in breast cancer molecular subtypes," *Journal of Personalized Medicine*, vol. 10, no. 3, p. 98, 2020.
- [4] M. Dizdaroglu, "Oxidatively induced DNA damage and its repair in cancer," *Mutation Research, Reviews in Mutation Research*, vol. 763, pp. 212–245, 2015.
- [5] H. J. Kang, Y. B. Hong, H. J. Kim, A. Wang, and I. Bae, "Bioactive food components prevent carcinogenic stress via Nrf2 activation in BRCA1 deficient breast epithelial cells," *Toxicology Letters*, vol. 209, no. 2, pp. 154–160, 2012.
- [6] A. Matsui, T. Ikeda, K. Enomoto et al., "Increased formation of oxidative DNA damage, 8-hydroxy-2'-deoxyguanosine, in human breast cancer tissue and its relationship to GSTP1 and COMT genotypes," *Cancer Letters*, vol. 151, no. 1, pp. 87–95, 2000.
- [7] V. Okoh, A. Deoraj, and D. Roy, "Estrogen-induced reactive oxygen species-mediated signalings contribute to breast cancer," *Biochimica et Biophysica Acta*, vol. 1815, no. 1, pp. 115–133, 2011.
- [8] A. Toullec, D. Gerald, G. Despouy et al., "Oxidative stress promotes myofibroblast differentiation and tumour spreading," *EMBO Molecular Medicine*, vol. 2, no. 6, pp. 211–230, 2010.
- [9] H. N. Xu, S. Nioka, B. Chance, and L. Z. Li, "3-D high-resolution mapping of the heterogeneity in mitochondrial redox state of human breast tumor xenografts," *Advances in Experimental Medicine and Biology*, vol. 737, pp. 169–174, 2012.
- [10] H. N. Xu, J. Tchou, B. Chance, and L. Z. Li, "Imaging the redox states of human breast cancer core biopsies," *Advances in Experimental Medicine and Biology*, vol. 765, pp. 343–349, 2013.
- [11] S. Periasamy, D. Z. Hsu, Y. H. Fu, and M. Y. Liu, "Sleep deprivation-induced multi-organ injury: role of oxidative

- stress and inflammation,” *Excli Journal*, vol. 14, pp. 672–683, 2015.
- [12] M. Sandesc, A. F. Rogobete, O. H. Bedreag et al., “Analysis of oxidative stress-related markers in critically ill polytrauma patients: an observational prospective single-center study,” *Bosnian Journal of Basic Medical Sciences*, vol. 18, no. 2, pp. 191–197, 2018.
- [13] S. I. Vrieze, “Model selection and psychological theory: a discussion of the differences between the Akaike information criterion (AIC) and the Bayesian information criterion (BIC),” *Psychological Methods*, vol. 17, no. 2, pp. 228–243, 2012.
- [14] H. Gurer-Orhan, E. Ince, D. Konyar, L. Saso, and S. Suzen, “The role of oxidative stress modulators in breast cancer,” *Current Medicinal Chemistry*, vol. 25, no. 33, pp. 4084–4101, 2018.
- [15] A. Pantavos, R. Ruiter, E. F. Feskens et al., “Total dietary antioxidant capacity, individual antioxidant intake and breast cancer risk: the Rotterdam study,” *International Journal of Cancer*, vol. 136, no. 9, pp. 2178–2186, 2015.
- [16] L. M. Butler, A. H. Wu, R. Wang, W. P. Koh, J. M. Yuan, and M. C. Yu, “A vegetable-fruit-soy dietary pattern protects against breast cancer among postmenopausal Singapore Chinese women,” *The American Journal of Clinical Nutrition*, vol. 91, no. 4, pp. 1013–1019, 2010.
- [17] T. Subramani, S. K. Yeap, W. Y. Ho et al., “Vitamin C suppresses cell death in MCF-7 human breast cancer cells induced by tamoxifen,” *Journal of Cellular and Molecular Medicine*, vol. 18, no. 2, pp. 305–313, 2014.
- [18] Q. X. Diao, J. Z. Zhang, T. Zhao et al., “Vitamin E promotes breast cancer cell proliferation by reducing ROS production and p53 expression,” *European Review for Medical and Pharmacological Sciences*, vol. 20, no. 12, pp. 2710–2717, 2016.
- [19] J. Bridgewater, A. Lopes, H. Wasan et al., “Prognostic factors for progression-free and overall survival in advanced biliary tract cancer,” *Annals of Oncology*, vol. 27, no. 1, pp. 134–140, 2016.
- [20] C. Gao, L. Fang, J. T. Li, and H. C. Zhao, “Significance and prognostic value of increased serum direct bilirubin level for lymph node metastasis in Chinese rectal cancer patients,” *World Journal of Gastroenterology*, vol. 22, no. 8, pp. 2576–2584, 2016.
- [21] Y. Zhang, J. Xu, Y. Lou et al., “Pretreatment direct bilirubin and total cholesterol are significant predictors of overall survival in advanced non-small-cell lung cancer patients with EGFR mutations,” *International Journal of Cancer*, vol. 140, no. 7, pp. 1645–1652, 2017.
- [22] J. Alexandre, P. Bleuzen, J. Bonneterre et al., “Factors predicting for efficacy and safety of docetaxel in a compassionate-use cohort of 825 heavily pretreated advanced breast cancer patients,” *Journal of Clinical Oncology*, vol. 18, no. 3, pp. 562–573, 2000.
- [23] D. M. Okamura and S. Pennathur, “The balance of powers: redox regulation of fibrogenic pathways in kidney injury,” *Redox Biology*, vol. 6, pp. 495–504, 2015.
- [24] B. H. Ali, S. Al-Salam, Y. Al Suleimani et al., “Curcumin ameliorates kidney function and oxidative stress in experimental chronic kidney disease,” *Basic & Clinical Pharmacology & Toxicology*, vol. 122, no. 1, pp. 65–73, 2018.
- [25] X. Chen, W. Wei, Y. Li, J. Huang, and X. Ci, “Hesperetin relieves cisplatin-induced acute kidney injury by mitigating oxidative stress, inflammation and apoptosis,” *Chemico-Biological Interactions*, vol. 308, pp. 269–278, 2019.
- [26] Y. Li, J. Zhang, P. Xu et al., “Acute liver failure impairs function and expression of breast cancer-resistant protein (BCRP) at rat blood-brain barrier partly via ammonia-ROS-ERK1/2 activation,” *Journal of Neurochemistry*, vol. 138, no. 2, pp. 282–294, 2016.
- [27] Y. Chang, H. An, L. Xu et al., “Systemic inflammation score predicts postoperative prognosis of patients with clear-cell renal cell carcinoma,” *British Journal of Cancer*, vol. 113, no. 4, pp. 626–633, 2015.
- [28] G. J. Quinlan, G. S. Martin, and T. W. Evans, “Albumin: biochemical properties and therapeutic potential,” *Hepatology*, vol. 41, no. 6, pp. 1211–1219, 2005.
- [29] T. Kühn, D. Sookthai, M. E. Graf et al., “Albumin, bilirubin, uric acid and cancer risk: results from a prospective population-based study,” *British Journal of Cancer*, vol. 117, no. 10, pp. 1572–1579, 2017.
- [30] Y. Liu, J. Z. Guo, Y. Liu et al., “Nuclear lactate dehydrogenase A senses ROS to produce  $\alpha$ -hydroxybutyrate for HPV-induced cervical tumor growth,” *Nature Communications*, vol. 9, no. 1, p. 4429, 2018.
- [31] A. Le, C. R. Cooper, A. M. Gouw et al., “Inhibition of lactate dehydrogenase A induces oxidative stress and inhibits tumor progression,” *Proceedings of the National Academy of Sciences of the United States of America*, vol. 107, no. 5, pp. 2037–2042, 2010.

## Research Article

# ***Lactobacillus plantarum* and *Lactobacillus brevis* Alleviate Intestinal Inflammation and Microbial Disorder Induced by ETEC in a Murine Model**

Xuebing Han, Sujuan Ding , Yong Ma, Jun Fang , Hongmei Jiang, Yi Li, and Gang Liu 

College of Bioscience and Biotechnology, Hunan Agricultural University, Hunan Provincial Engineering Research Center of Applied Microbial Resources Development for Livestock and Poultry, Changsha, Hunan 410125, China

Correspondence should be addressed to Jun Fang; [fangjun1973@hunau.edu.cn](mailto:fangjun1973@hunau.edu.cn) and Gang Liu; [gangle.liu@gmail.com](mailto:gangle.liu@gmail.com)

Received 10 July 2021; Accepted 20 August 2021; Published 21 September 2021

Academic Editor: Guoku Hu

Copyright © 2021 Xuebing Han et al. This is an open access article distributed under the Creative Commons Attribution License, which permits unrestricted use, distribution, and reproduction in any medium, provided the original work is properly cited.

The purpose of this research is to explore the positive effects of *Lactobacillus plantarum* and *Lactobacillus brevis* on the tissue damage and microbial community in mice challenged by Enterotoxigenic *Escherichia coli* (ETEC). Twenty-four mice were divided into four groups randomly: the CON group, ETEC group, LP-ETEC group and LB-ETEC group. Our results demonstrated that, compared with the ETEC group, the LP-ETEC and LB-ETEC groups experienced less weight loss and morphological damage of the jejunum. We measured proinflammatory factors of colonic tissue and found that *L. plantarum* and *L. brevis* inhibited the expression of proinflammatory factors such as IL- $\beta$ , TNF- $\alpha$ , and IL-6 and promoted that of the tight junction protein such as claudin-1, occludin, and ZO-1. Additionally, *L. plantarum* and *L. brevis* altered the impact of ETEC on the intestinal microbial community of mice, significantly increased the abundance of probiotics such as *Lactobacillus*, and reduced that of pathogenic bacteria such as *Proteobacteria*, *Clostridia*, *Epsilonproteobacteria*, and *Helicobacter*. Therefore, we believe that *L. plantarum* and *L. brevis* can stabilize the intestinal microbiota and inhibit the growth of pathogenic bacteria, thus protecting mice from the gut inflammation induced by ETEC.

## 1. Introduction

Diarrhea induced by Enterotoxigenic *Escherichia coli* (ETEC) is a major challenge to newborn piglets and weaned piglets. The condition increases occurrences of morbidity and mortality, which results in huge economic losses in the global swine industry [1]. ETEC can colonize in the small intestine, increase the expression of proinflammatory factors, cause intestinal barrier damage, and eventually lead to the development of intestinal inflammation [2–4]. Previous studies have proven that probiotics are vital to prevent and treat cancer [5], inflammatory bowel disease (IBD) [6], irritable bowel syndrome [7], and other diseases. In addition, probiotics can counteract the inflammation caused by ETEC [8, 9]. Most notably, probiotics are considered the only effective feed additives that protect against pathogens. In view of the injury and economic losses caused by intestinal inflammation such as diarrhea, colorectal cancer, and IBD, it is neces-

sary to study probiotics, which are used as feed additives to inhibit pathogens and promote intestinal health.

Lactic acid bacteria, a kind of probiotic that exists in human and animal intestines, can enhance the immune system by inhibiting the expression of proinflammatory cytokines or promoting that of anti-inflammatory cytokines [10, 11]. *Lactobacillus plantarum* is a major species of lactic acid bacteria, with a variety of probiotic characteristics, gastrointestinal transport tolerance, and anti-inflammatory properties [12]. Previous studies have shown that the supplementation of *L. plantarum* in the diet can promote the gastrointestinal health of weaned piglets [13] and improve the antioxidant status and growth performance of piglets [14]. It is worth noting that studies on the effect of *L. plantarum* on various cancers are also being actively carried out [15, 16]. As a close relative of *L. plantarum*, *L. brevis* also has a variety of probiotic characteristics, including tolerance to acid and bile, adhesion to intestinal cells, and the ability to



survive through the gastrointestinal tract [17, 18]. These characteristics of *L. brevis* enable it to maintain the homeostasis of the intestine, improve the barrier function of intestinal epithelium under oxidative stress, and reduce intestinal inflammation in the mouse model [19, 20].

In this study, ETEC was used to induce intestinal inflammation in a mouse model. And we explored the protective effects of *L. plantarum* and *L. brevis* on the injury induced by ETEC in the murine model, observed the changes in the amounts of cytokines and tight junction proteins, and determined the effects of these two probiotics on intestinal flora.

## 2. Materials and Methods

**2.1. Bacteria.** The strains *Lactobacillus plantarum* GL17, *Lactobacillus brevis* AY858, and Enterotoxigenic *Escherichia coli* used in this study were stored in Hunan Agricultural University (Changsha, China). *L. plantarum* GL17 and *L. brevis* AY858 were cultured in MRS broth at 37°C for 24 hours, while ETEC was cultured in a Luria-Bertani liquid medium at 37°C for the same time. To quantify the colonies, the cultured bacterial fluid was transferred to the corresponding solid medium and incubated at 37°C for 24 hours. Then, the bacterial samples of both probiotics and ETEC were centrifuged and suspended in sterile normal saline solution at  $5 \times 10^{10}$  CFU/mL and  $1 \times 10^8$  CFU/mL, respectively.

**2.2. Animals and Experimental Design.** The experiment was approved by the Animal Care and Use Committee of Hunan Agricultural University. Twenty-four eight-week-old ICR mice from the Shanghai Laboratory Animal Central (Changsha, China) were housed in a pathogen-free environment for seven days of adaptation. Then, the mice were divided into four groups randomly: the control group (CON), the ETEC group (ETEC), the *L. plantarum* GL17 treatment group (LP-ETEC), and the *L. brevis* AY858 treatment group (LB-ETEC). There were six mice in each group, and the basic diet and water for all mice were not limited. The experiment lasted for 21 days (Figure 1(a)). During the first 14 days of the experiment, the LP-ETEC group and the LB-ETEC group were given *L. plantarum* GL17 and *L. brevis* AY858, respectively, by gavage every day, while the control group and the ETEC group were given sterile saline every day. From the 15th day of the experiment, the ETEC group, LP-ETEC group, and LB-ETEC group were given ETEC by gavage until the end of the experiment. On the 21st day, all mice were killed, and a part of the jejunum was fixed in paraformaldehyde for histomorphological analysis, while the contents of the colon were collected and frozen in liquid nitrogen for the determination of microbial diversity.

**2.3. Jejunum Histopathology.** The jejunum samples fixed in the paraformaldehyde were dehydrated using ethanol gradient and embedded in paraffin. The samples were then stained with hematoxylin and eosin and observed under a microscope. The specific process is in accordance with methods used in previous research [21].

**2.4. qPCR.** The total RNA of frozen colonic tissue was extracted by TRIzol (Invitrogen, USA) according to the instruction. To determine the concentration of the extracted RNA, DNase I was used to treat RNA, and then, the concentration was determined by spectrophotometer at 260 nm. The primers used in the experiment are shown in Table 1, and the specific methods refer to a previous experiment [22]. Finally, the amplification reaction was carried out, and the calculation formula used to determine gene expression level refers to Ma et al. [23].

**2.5. 16S Ribosomal RNA Amplicon Sequencing.** To determine the diversity of microorganisms in the colonic contents, the microbial genomic DNA of colon contents was extracted by using the QIAamp DNA Stool Mini Kit firstly. Then, the concentration and purity of DNA were detected on 1% agarose gel, and the primers 357F (5'-ACTCCTACGGRAGGCAGCAG-3') and 806R (5'-GGACTACHVGGGTWTCTAAT-3') were used to amplify the V3-V4 region of 16S rDNA. After recovery and purification of PCR products, the library was prepared for sequencing analysis. Finally, the quality of off-machine data was controlled and optimized, and the composition of microbial communities was determined by OTU clustering. Moreover, the  $\alpha$  diversity analysis was performed by mothur (Version 1.33.3).

**2.6. Data Analysis.** All of the data in the experiment are expressed as mean  $\pm$  standard deviation (SD) and analyzed by one-way ANOVA and Tukey's multiple comparison test to compare the differences between the four groups (SPSS 21 software). *P* value < 0.05 was regarded as a significant difference.

## 3. Results

**3.1. *L. plantarum* and *L. brevis* Inhibit the Weight Loss Induced by ETEC.** The results of weight are shown in Figure 1(b). Compared with the CON group, ETEC reduced the weight of mice significantly ( $P < 0.05$ ). When treated with *L. plantarum* GL17 and *L. brevis* AY858, the weight of mice increased significantly ( $P < 0.05$ ). The results showed that these two probiotics reduced weight loss in the mice.

**3.2. *L. plantarum* and *L. brevis* Inhibit the Development of Intestinal Injury Induced by ETEC.** The results of histologic examination (Figure 2) showed that the height of jejunal villi decreased significantly ( $P < 0.05$ ) and the crypt depth increased significantly ( $P < 0.05$ ) after ETEC attack. Compared with the ETEC group, the mice in the LP-ETEC group had increased villus heights and reduced crypt depth significantly ( $P < 0.05$ ). Similar results were observed in the LB-ETEC group, with a slight increase in villus heights and a significant decrease in crypt depth ( $P < 0.05$ ). These results indicated that both of those two probiotics can reduce the intestinal damage caused by ETEC, especially *L. plantarum* GL17, which made the LP-ETEC group return to the same level as the CON group.

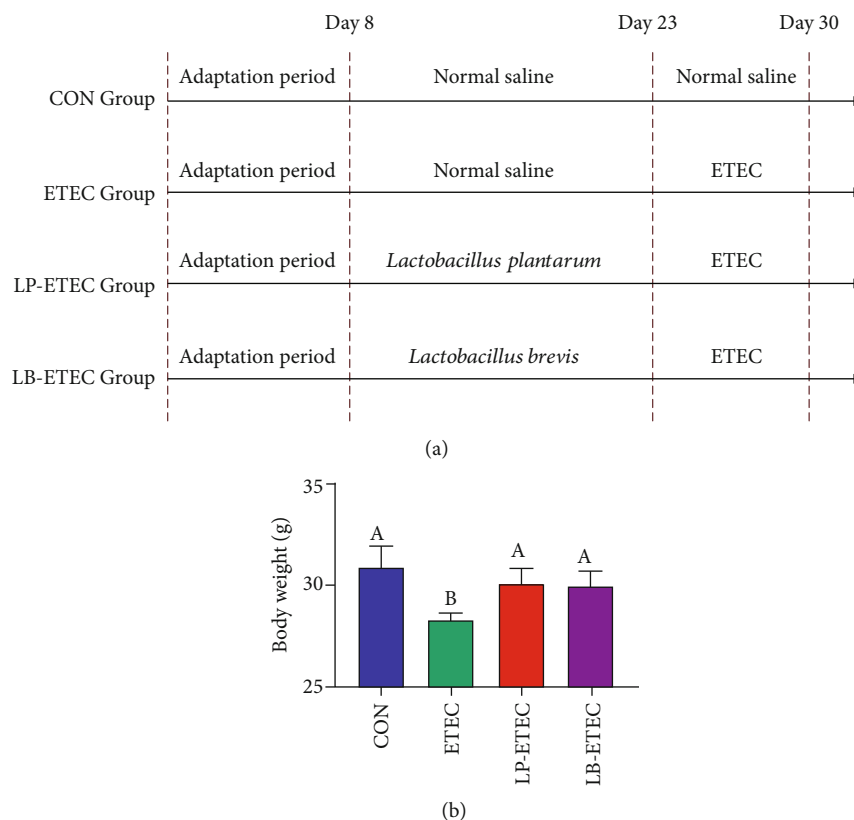


FIGURE 1: Impact of *Lactobacillus plantarum* and *Lactobacillus brevis* on body weight. The experimental process (a) and body weight (b). Data are mean  $\pm$  SD ( $n = 6$ ). Without a common letter mark indicates significant differences ( $P < 0.05$ ).

TABLE 1: The primers for this study.

| Primer        | Name             | 5'→3' sequence               |
|---------------|------------------|------------------------------|
| IL-1 $\beta$  | IL-1 $\beta$ _F  | ATGAAAGACGGCACACCCAC         |
|               | IL-1 $\beta$ _R  | GCTTGTGCTCTGCTTGTGAG         |
| TNF- $\alpha$ | TNF- $\alpha$ _F | ACCCTGGTATGAGCCCATATAC       |
|               | TNF- $\alpha$ _R | ACACCCATTCCCTTCACAGAG        |
| IL-6          | IL-6_F           | GAGGATACCACTCCCAACAGACC      |
|               | IL-6_R           | AAGTGCATCATCGTTGTTTCATACA    |
| Claudin-1     | Claudin-1_F      | GGGGACAACATCGTGACCG          |
|               | Claudin-1_R      | AGGAGTCGAAGACTTTGCACT        |
| Occludin      | Occludin_F       | TTGAAAGTCCACCTCCTTACAGA      |
|               | Occludin_R       | CCGGATAAAAAGAGTACGCTGG       |
| ZO-1          | ZO-1_F           | GATCCCTGTAAGTCACCCAGA        |
|               | ZO-1_R           | CTCCCTGCTTGCACTCCTATC        |
| Lysozyme      | Lysozyme_F       | GCCAAGGTCTAACAATCGTTGTGAGTTG |
|               | Lysozyme_R       | CAGTCAGCCAGCTTGACACCACG      |
| Cryptidin     | Cryptidin_F      | TCAAGAGGCTGCAAAGGAAGAGAAC    |
|               | Cryptidin_R      | TGGTCTCCATGTTTCAGCGACAGC     |
| A20           | A20_F            | AAACCAATGGTGATGGAAACTG       |
|               | A20_R            | GTTGTCCCATTTCGTCATTCC        |

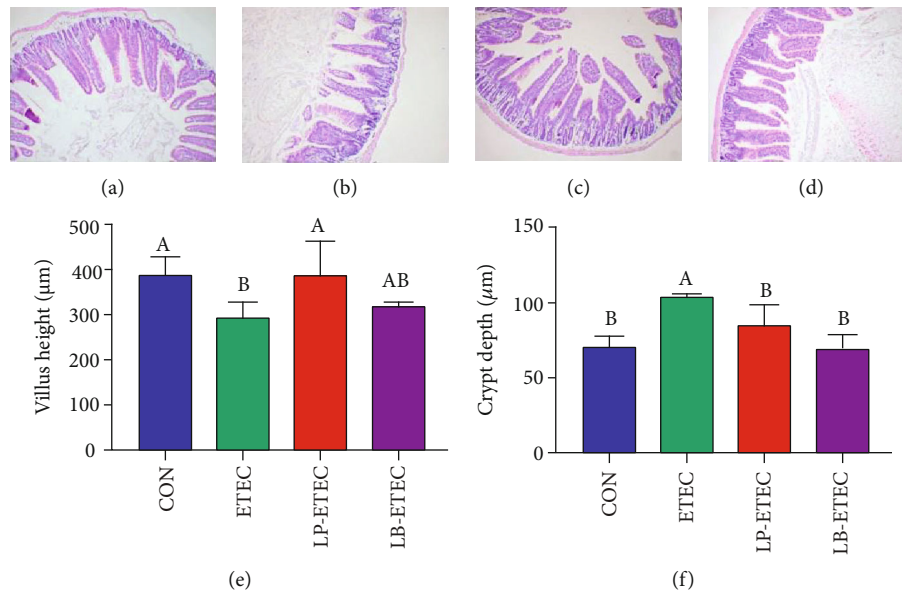


FIGURE 2: Impact of *Lactobacillus plantarum* and *Lactobacillus brevis* on jejunum tissue damage induced by ETEC. Images of jejunal tissue in the CON (a), ETEC (b), LP-ETEC (c), and LB-ETEC (d) groups; villus height (e); and crypt depth (f) in the four groups. Data are mean  $\pm$  SD ( $n = 6$ ). Without a common letter mark indicates significant differences ( $P < 0.05$ ).

**3.3. *L. plantarum* and *L. brevis* Affect Inflammation and Intestinal Barrier.** The expressions of cytokines in the colonic tissues were measured (Figures 3(a)–3(f)). Compared with the CON group, lysozyme and cryptidin in the ETEC group decreased significantly ( $P < 0.05$ ), while no significant difference was observed in that of IL-1 $\beta$ , TNF- $\alpha$ , IL-6, and A20. When treated with *L. plantarum* GL17, lysozyme and cryptidin increased significantly ( $P < 0.05$ ). Similarly, after the treatment of *L. brevis* AY858, a significant increase in lysozyme and cryptidin ( $P < 0.05$ ) and a significant decrease in IL-6 ( $P < 0.05$ ) were observed.

The expression of tight junction proteins is shown in Figures 3(g)–3(i). When attacked by ETEC, claudin-1 and occludin decreased significantly ( $P < 0.05$ ), while ZO-1 remained almost unchanged. *L. plantarum* GL17 increased claudin-1 and occludin slightly, but there was no significant difference compared with the ETEC group. Similarly, no significant difference was observed in occludin between the LB-ETEC group and the ETEC group. However, compared with the ETEC group, claudin-1 in the LB-ETEC group increased significantly ( $P < 0.05$ ).

**3.4. *L. plantarum* and *L. brevis* Regulate Intestinal Microbes in Mice.** The results of intestinal microorganism diversity are shown in Figure 4. After the ETEC challenge, the Sobs index, Shannon index, Simpson index, and PD-whole-tree index decreased significantly ( $P < 0.05$ ). After the treatment of *L. plantarum* GL17 and *L. brevis* AY858, these indexes increased and returned to normal level, especially the Sobs index and Simpson index, which were significantly different from those of the ETEC group ( $P < 0.05$ ). Furthermore, the Shannon index in the LB-ETEC group and the PD-whole-tree index in the LP-ETEC group were significantly different from those in the ETEC group ( $P < 0.05$ ). Therefore, both of these two probiotics have obvious protective effects on

ETEC-induced decline of intestinal microbial diversity in mice.

At the phylum level, there are nine kinds of microorganisms in each of four groups, of which *Bacteroidetes*, *Firmicutes*, and *Proteobacteria* accounted for more than 86% of all microorganisms (Figure 5(a)). The abundance of *Bacteroidetes* in the CON, ETEC, LP-ETEC, and LB-ETEC groups was 62.1485%, 42.3336%, 43.6535%, and 53.8593%, respectively. *Firmicutes* accounted for 26.6949%, 40.0591%, 46.6572%, and 33.6746%, respectively. The *Proteobacteria* abundance was 8.4628%, 14.4314%, 6.6691%, and 8.7466%, respectively. After being challenged by ETEC, *Bacteroidetes* in mice decreased significantly ( $P < 0.05$ ). In contrast, the abundance of *Proteobacteria* showed the opposite trend, which was significantly higher than that of the CON group ( $P < 0.05$ ) (Figures 5(b) and 5(c)). However, when treated with *L. plantarum* GL17 and *L. brevis* AY858, *Proteobacteria* in mice decreased significantly ( $P < 0.05$ ).

The abundance of *Bacteroidia*, *Clostridia*, and *Bacilli* accounted for more than 80% of all microorganisms in the class level (Figure 6(a)). The abundance of *Bacteroidia* in the CON, ETEC, LP-ETEC, and LB-ETEC groups was 52.562%, 49.0004%, 52.9771%, and 51.7049%, respectively. *Clostridia* accounted for 16.7878%, 23.7975%, 14.2299%, and 14.7012%, respectively. The *Bacilli* abundance was 11.3105%, 10.0499%, 17.1775%, and 16.7497%, respectively. After being attacked by ETEC, the abundance of *Clostridia* and *Epsilonproteobacteria* increased, especially *Epsilonproteobacteria*, which increased significantly ( $P < 0.05$ ) (Figures 6(b) and 6(c)). However, both *L. plantarum* GL17 and *L. brevis* AY858 significantly reduced the abundance of *Clostridia* and *Epsilonproteobacteria* ( $P < 0.05$ ).

As for the order level, the abundance of *Bacteroidales*, *Clostridiales*, and *Lactobacillales* was the highest in the CON, LP-ETEC, and LB-ETEC groups (Figure 7(a)). The

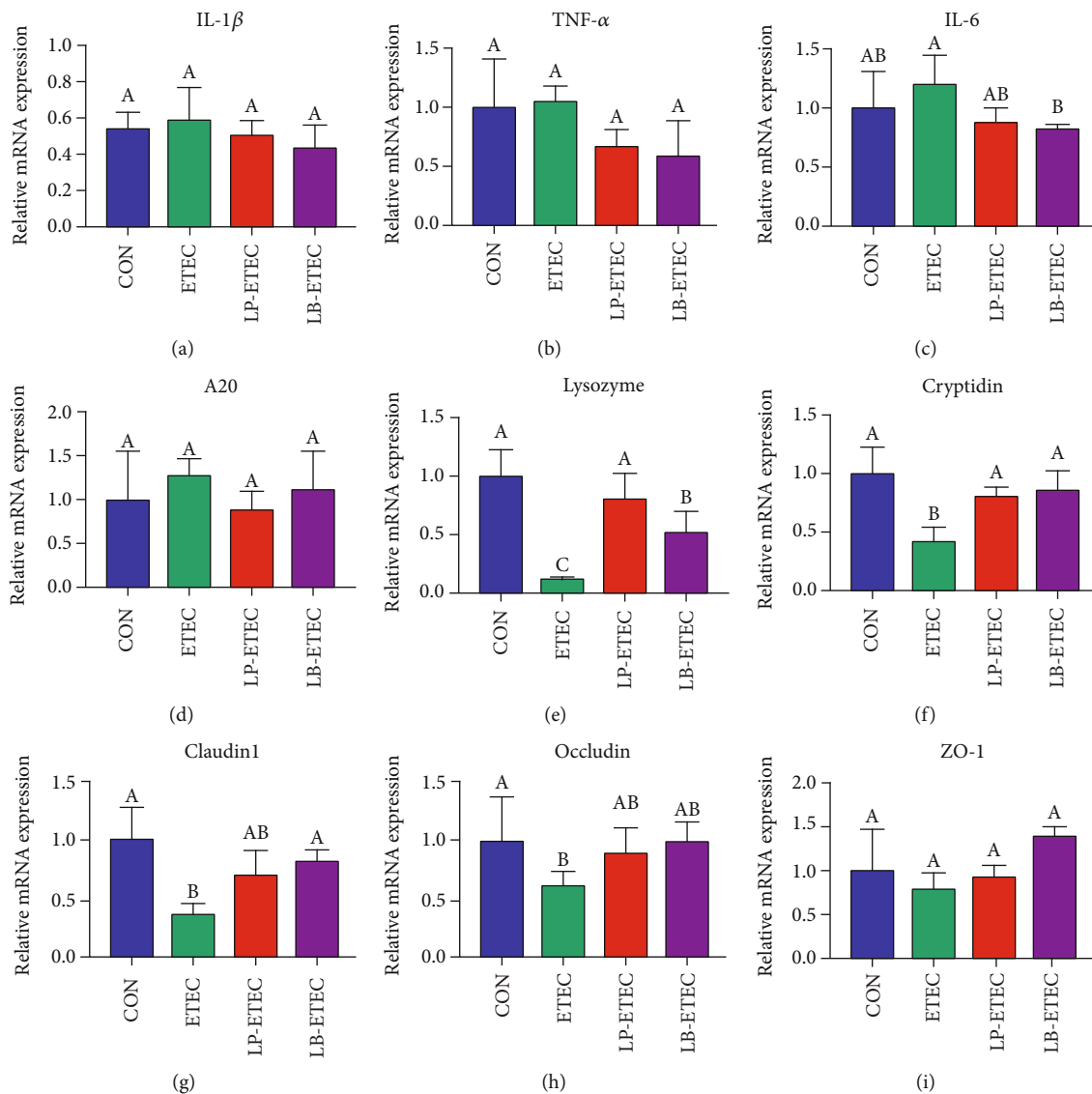


FIGURE 3: Impact of *Lactobacillus plantarum* and *Lactobacillus brevis* treatment on the expressions of cytokines and tight junction protein. 1The relative gene expression level determined by qPCR of (a) IL-1 $\beta$ , (b) TNF- $\alpha$ , (c) IL-6, (d) A20, (e) lysozyme, (f) cryptidin, (g) claudin-1, (h) occludin, and (i) ZO-1. Data are mean  $\pm$  SD ( $n = 6$ ). Without a common letter mark indicates significant differences ( $P < 0.05$ ).

abundance of *Bacteroidales* in the CON, LP-ETEC, and LB-ETEC groups was 50.562%, 39.1805%, and 39.7049%, respectively. *Clostridiales* accounted for 17.1168%, 14.2299%, and 16.8516%, respectively. The abundance of *Lactobacillales* was 17.2176%, 22.0299%, and 21.248%, respectively. However, the top three most abundant microorganisms at the order level in ETEC group were *Bacteroidales*, *Clostridiales*, and *Campylobacterales*, accounting for 49.0004%, 25.221%, and 7.6303%, respectively. *Clostridiales* in the ETEC group increased significantly ( $P < 0.05$ ) and *Lactobacillales* in the ETEC group decreased significantly ( $P < 0.05$ ) compared with those in the CON group (Figures 7(b) and 7(c)). After the treatment of *L. plantarum* GL17 and *L. brevis* AY858, the abundance of *Clostridiales* and *Lactobacillales* had changed significantly ( $P < 0.05$ ).

Eight representative microbial genera in the four groups were selected and analyzed (Figure 8(a)). In the genus of

microorganisms that have been classified, *Lactobacillus*, *Bacteroides*, and *Helicobacter* were the three main microorganisms among the groups of CON, LP-ETEC, and LB-ETEC. The abundance of *Lactobacillus* in the CON, LP-ETEC, and LB-ETEC groups was 26.08%, 33.5332%, and 27.7802%, respectively. *Bacteroides* accounted for 7.4573%, 23.1571%, and 9.449%, respectively. The abundance of *Helicobacter* was 1.486%, 2.9112%, and 3.2437%, respectively. However, the top three most abundant microbial genera in the ETEC group were *Bacteroides*, *Helicobacter*, and *Alloprevotella*, accounting for 5.9428%, 8.0295%, and 4.6711%, respectively. After being challenged by ETEC, the abundance of *Lactobacillus* reduced significantly ( $P < 0.05$ ), while that of *Helicobacter* increased significantly ( $P < 0.05$ ) (Figures 8(b) and 8(c)). However, when treated with *L. plantarum* GL17 and *L. brevis* AY858, the abundance of *Lactobacillus* and *Helicobacter* changed significantly ( $P < 0.05$ ) and returned to the normal level.

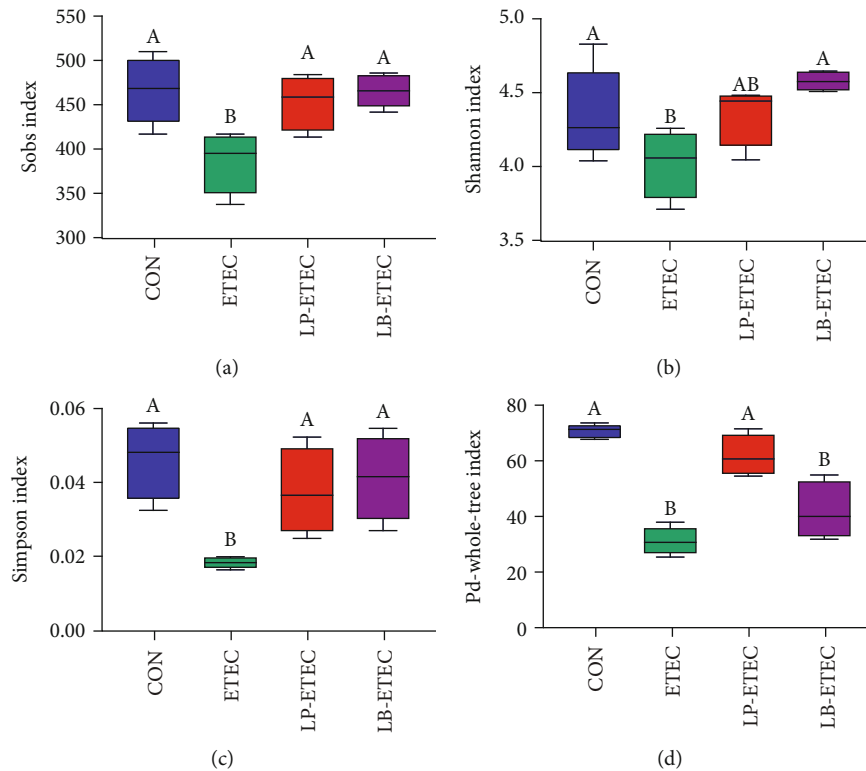


FIGURE 4: Impact of *Lactobacillus plantarum* and *Lactobacillus brevis* treatment on intestinal microbial diversity. (a) Sobs index; (b) Shannon index; (c) Simpson index; (d) PD-whole-tree index. Data are mean  $\pm$  SD ( $n = 6$ ). Without a common letter mark indicates significant differences ( $P < 0.05$ ).

#### 4. Discussion

The protective effects of *L. plantarum* GL17 and *L. brevis* AY858 on the injury induced by ETEC were explored in this study. The results showed that both probiotics reduced the weight loss and morphological damage of the jejunum significantly. The expression of cytokines decreased, while that of the tight junction protein increased in mice treated with *L. plantarum* GL17 and *L. brevis* AY858. Meanwhile, *L. plantarum* GL17 and *L. brevis* AY858 restored the colonic microbial diversity to the normal level in mice challenged by ETEC and increased the relative abundance of *Lactobacillus*. In contrast, *L. plantarum* GL17 and *L. brevis* AY858 reduced the relative abundance of *Proteobacteria*, *Clostridia*, *Epsilonproteobacteria*, and *Helicobacter* in the colon after ETEC challenge.

The surface of intestinal mucosa, which is the largest surface of the human body, contacts with the external environment continuously [24]. Columnar epithelial cells are arranged into the intestinal epithelium and folded into crypts or concave [25]. These fully differentiated epithelial cells protect the body from potentially harmful microorganisms and viruses in the intestinal microenvironment [26]. Intestinal villi are critical components of the intestine that can increase the absorption area and promote the absorption of nutrients [27]. Endotoxin produced by ETEC can cause a variety of morphological changes of the intestinal tract, such as the increase of mucosal crypt depth, decrease of villus height, and submucosal edema [28]. Probiotics can reduce

the morphological damage caused by the endotoxin, which can increase the height of villi and promote the growth of piglets [29, 30]. A previous study has shown that piglets fed with *L. plantarum* displayed higher villus height and lower crypt depth in the jejunum [1]. The same results were obtained in this experiment. *L. plantarum* and *L. brevis* protected the structural integrity of the jejunum, as well as the ability of absorbing nutrients. However, the protective effect of these two probiotics on villi is slightly different; *L. plantarum* is better than *L. brevis* at restoring the height of intestinal villi.

ETEC produces heat-labile enterotoxin (LT), and the LTA subunit of it, together with ADP-ribosylation factor, can induce the ribosylation of Gs $\alpha$  [31]. At that time, the adenylate cyclase of the target cell is uncontrolled, converting ATP to cAMP continuously. The increase of cAMP will not only activate the NF- $\kappa$ B signaling pathway and produce a large number of inflammatory factors [32] but also activate the MAPK signaling pathway, resulting in the dislocation of tight junction proteins and impairment of intestinal barrier function [33]. The increase of proinflammatory factors, including IL-1 $\beta$ , TNF- $\alpha$ , and IL-6, will aggravate intestinal inflammation and promote the occurrence of colorectal cancer. In this experiment, although the difference was insignificant, the proinflammatory factors showed an upward trend after ETEC challenge, which indicated that ETEC increased intestinal inflammation in mice. Probiotics can reduce the inflammatory response by reducing the level of cytokines [12, 34, 35], which is also proven by our research. Although

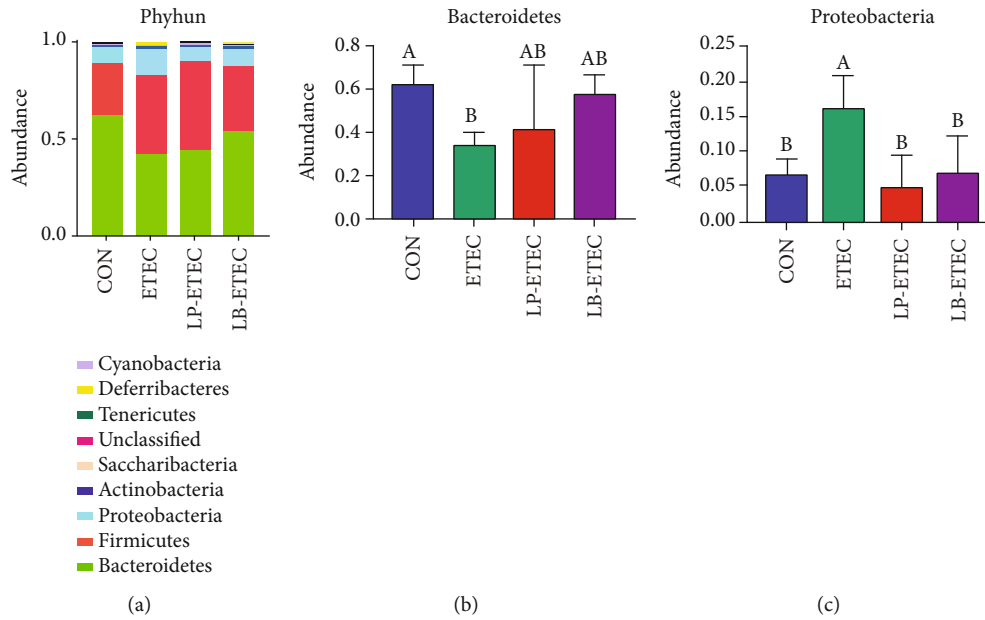


FIGURE 5: Impact of *Lactobacillus plantarum* and *Lactobacillus brevis* treatment on the microorganisms at the phylum level. (a) Relative abundance of microorganisms in the four groups at the phylum level; (b) abundance of *Bacteroidetes* in each of four groups; (c) abundance of *Proteobacteria* in each of four groups. Data are mean  $\pm$  SD ( $n = 6$ ). Without a common letter mark indicates significant differences ( $P < 0.05$ ).

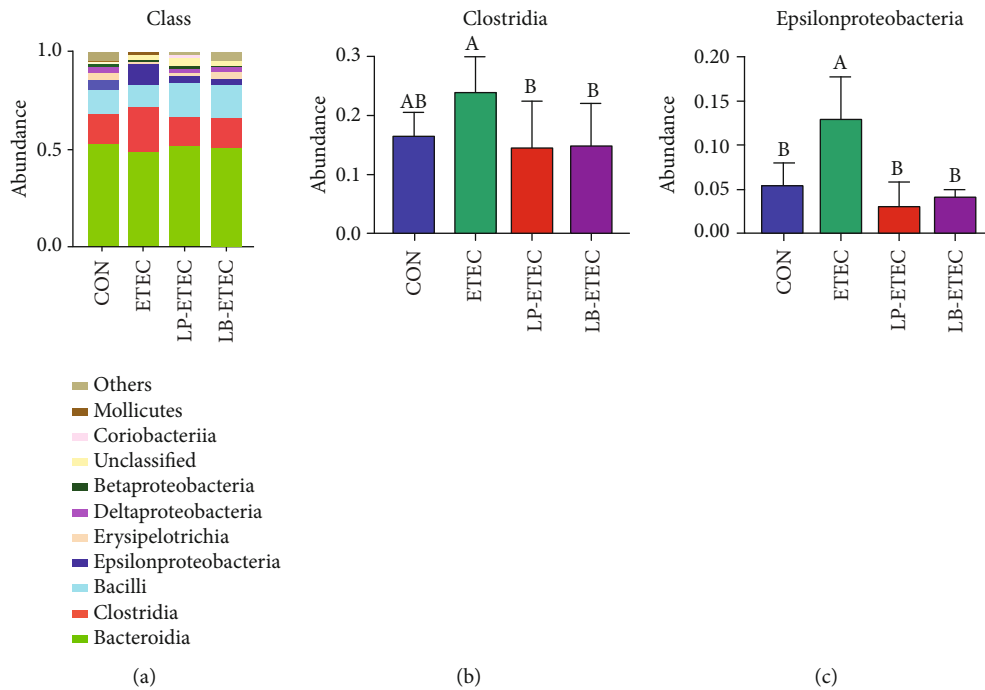


FIGURE 6: Impact of *Lactobacillus plantarum* and *Lactobacillus brevis* treatment on the microorganisms at the class level. (a) Relative abundance of microorganisms in the four groups at the class level; (b) abundance of *Clostridia* in each of four groups; (c) abundance of *Epsilonproteobacteria* in each of four groups. Data are mean  $\pm$  SD ( $n = 6$ ). Without a common letter mark indicates significant differences ( $P < 0.05$ ).

the difference was not significant, the proinflammatory factors in mice treated with *L. plantarum* and *L. brevis* showed a decreasing trend. Previous researches conducted *in vitro* have shown that ETEC can reduce the amounts of occludin in Small Intestinal Epithelial Cell Line- (IPEC-) 1 entero-

cytes of piglets [36], the permeability of tight junctions in IPEC-J2 enterocytes of piglets [37], and dislocation of ZO-1 Caco-2 cells of human [38]. However, probiotics increased the expression of tight junction proteins such as ZO-1, claudin-1, and occludin to protect cells [36, 39]. In this

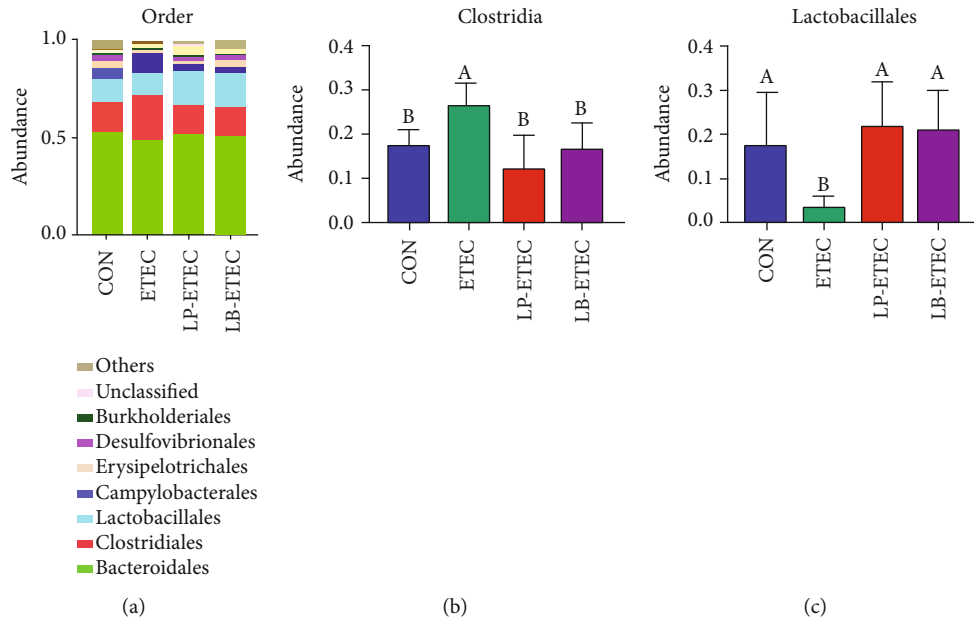


FIGURE 7: Impact of *Lactobacillus plantarum* and *Lactobacillus brevis* treatment on the microorganisms at the order level. (a) Relative abundance of microorganisms in the four groups at the order level; (b) abundance of *Clostridiales* in each of four groups; (c) abundance of *Lactobacillales* in each of four groups. Data are mean  $\pm$  SD ( $n = 6$ ). Without a common letter mark indicates significant differences ( $P < 0.05$ ).

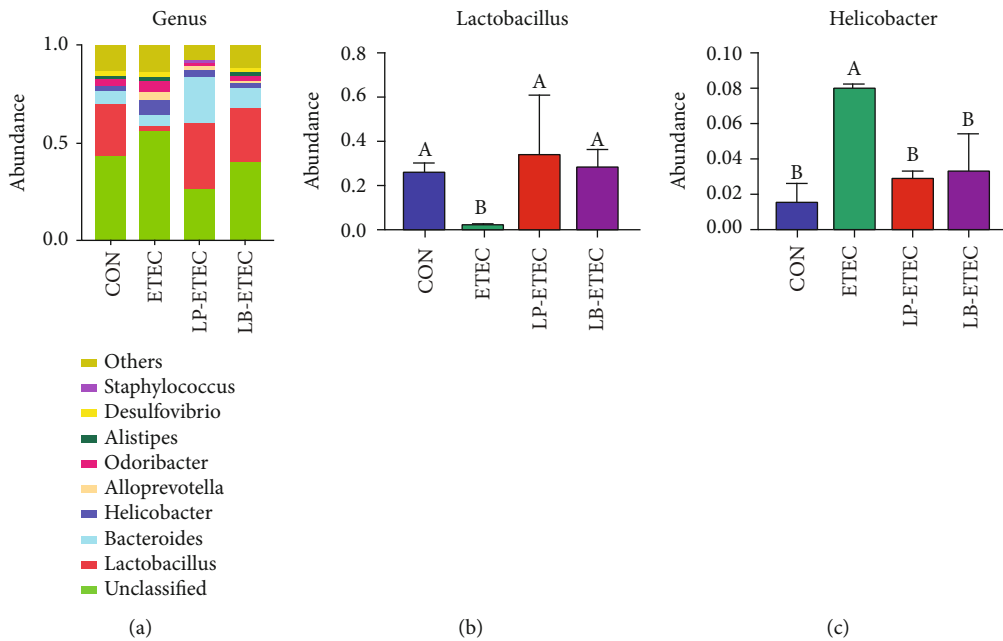


FIGURE 8: Impact of *Lactobacillus plantarum* and *Lactobacillus brevis* treatment on the microorganisms at the genus level. (a) Relative abundance of microorganism in the four groups at the genus level; (b) abundance of *Lactobacillus* in each of four groups; (c) abundance of *Helicobacter* in each of four groups. Data are mean  $\pm$  SD ( $n = 6$ ). Without a common letter mark indicates significant differences ( $P < 0.05$ ).

experiment, claudin-1 and occludin decreased significantly after ETEC challenge, while ZO-1 also showed a decreasing trend in mice, indicating that ETEC destroyed the intestinal barrier in mice. In contrast, *L. plantarum* and *L. brevis* increased the expression of the tight junction protein in mice challenged by ETEC. And the protective effect of *L. brevis* on the barrier function of mice was slightly higher than that of

*L. plantarum*. Lysozyme is a critical bacteriostatic protein that strongly inhibits gram-positive bacteria [40], and cryptidin has a significant therapeutic effect on mice infected with *Salmonella Typhimurium* [41]. Therefore, the increase of these two substances in mice treated with *L. plantarum* and *L. brevis* may inhibit the growth of pathogenic bacteria and protect the health of mice.

There are lots of microbiota in the intestinal ecosystem, which play a significant role in host immunity and disease prevention. Therefore, unstable intestinal ecology may cause many diseases, such as ulcerative colitis and chronic diarrhea [42, 43]. ETEC reduced the intestinal microbial diversity of mice, while *L. plantarum* and *L. brevis* restored it to the normal level. The PD-whole-tree index of mice treated with *L. plantarum* was significantly higher than that of mice only challenged by ETEC, but there was no significant difference in the Shannon index. However, the results of mice treated with *L. brevis* showed the opposite results. This indicates that these two probiotics have almost the same effect on the recovery of intestinal microbial diversity in mice.

*Proteobacteria* is known to be the most disease-related intestinal microorganism, causing metabolic diseases and intestinal inflammation [44–46]. In this phylum, most microorganisms are human pathogens. Our study found that both *L. plantarum* and *L. brevis* inhibited the increase of *Proteobacteria* caused by ETEC significantly and made it return to the normal level, thus reducing the risk of intestinal inflammation in mice. Both *Clostridia* and *Epsilonproteobacteria* are pernicious bacteria that can cause digestive tract diseases in children. Tissue infection and intestinal diseases are often caused when those two bacteria enter the body of humans and other animals [47, 48]. *Clostridia* is involved in the development of necrotizing enterocolitis, which is a digestive tract disease that can threaten the life of preterm neonates [47]. In this study, mice treated with *L. plantarum* and *L. brevis* decreased the abundance of *Clostridia* and *Epsilonproteobacteria*, as well as a lower risk of digestive tract disease. As we all know, *Lactobacillus* is a probiotic with the function of preventing infection, reducing incidences of diarrhea, and improving production performance [49]. Some microorganisms of this genus, such as *Lactobacillus rhamnosus* and *Lactobacillus reuteri*, can protect the tight junctional protein after infection and contribute to the gut barrier function [50, 51]. In this experiment, both *L. plantarum* and *L. brevis* increased the abundance of *Lactobacillus* significantly, which may contribute to the gut barrier function and protection against inflammation. *Helicobacter* is the most common source of infection in the world, and it is the main risk factor of gastric cancer. Due to the ability to adapt to extreme acidic environment, *Helicobacter* can establish persistent infection and relieve the regulatory function of the host, leading to the pathogenesis and cancer of the digestive tract [52]. *L. plantarum* and *L. brevis* inhibited the growth of such pathogenic bacteria significantly and reduced the risk of canceration in tissue. It can be seen from the results that there is no significant difference between *L. plantarum* and *L. brevis* in promoting the abundance of probiotics and inhibiting that of pathogenic bacteria, indicating that they have almost the same effects on inhibiting intestinal inflammation and canceration.

## 5. Conclusion

The results in this experiment showed that *L. plantarum* and *L. brevis* can prevent the weight loss and intestinal injury caused by ETEC effectively, reduce the production of inflam-

matory factors, and strengthen the intestinal barrier function. Moreover, both of these two probiotics can stabilize the microbial community structure of intestine in mice, increase the abundance of probiotics such as *Lactobacillus*, and reduce the abundance of pathogenic bacteria such as *Proteobacteria*, *Clostridia*, *Epsilonproteobacteria*, and *Helicobacter*. Therefore, *L. plantarum* and *L. brevis* showed similarly effective inhibition on intestinal injury induced by ETEC and the ability to improve immune function. In summary, the feasibility and effectiveness of *L. plantarum* and *L. brevis* in the treatment of intestinal inflammation are demonstrated in our study, which provides a basis for further study of these two probiotics and their impact on intestinal inflammation such as diarrhea and colon cancer.

## Data Availability

The data of this study is available from the correspondence authors upon reasonable request.

## Conflicts of Interest

The authors declare that the research was conducted in the absence of any commercial or financial relationships that could be construed as a potential conflict of interest.

## Acknowledgments

This research was supported by the National Natural Science Foundation of China (Nos. 31772642, 31672457, and 41807135), Local Science and Technology Development Project Guided by the Central Government (YDZX2018 4300002303), Hunan Provincial Science and Technology Department (2019TP2004, 2018WK4025, 2020NK2004, 2020ZL2004, 2016NK2101, 2016TP2005, and 2018CT5002), China Postdoctoral Science Foundation (2018M632963 and 2019T120705), Scientific Research Fund of Hunan Provincial Education Department (2020JGYB112 and 18B107), Double First-Class Construction Project of Hunan Agricultural University (SYL201802003, YB2018007, and CX20190497), and Natural Science Foundation of Hunan Province, China (No. 2019JJ50220).

## References

- [1] K. M. Yang, Z. Y. Jiang, C. T. Zheng, L. Wang, and X. F. Yang, "Effect of *Lactobacillus plantarum* on diarrhea and intestinal barrier function of young piglets challenged with enterotoxigenic *Escherichia coli* K88," *Journal of Animal Science*, vol. 92, no. 4, pp. 1496–1503, 2014.
- [2] J. M. Fairbrother, E. Nadeau, and C. L. Gyles, "Escherichia coli in postweaning diarrhea in pigs: an update on bacterial types, pathogenesis, and prevention strategies," *Animal Health Research Reviews*, vol. 6, no. 1, pp. 17–39, 2005.
- [3] J. Guignot, C. Chaplais, M. H. Coconnier-Polter, and A. L. Servin, "The secreted autotransporter toxin, sat, functions as a virulence factor in Afa/Dr diffusely adhering *Escherichia coli* by promoting lesions in tight junction of polarized epithelial cells," *Cellular Microbiology*, vol. 9, no. 1, pp. 204–221, 2007.



- [4] J. A. Guttman, Y. Li, M. E. Wickham, W. Deng, A. W. Vogl, and B. B. Finlay, "Attaching and effacing pathogen-induced tight junction disruption in vivo," *Cellular Microbiology*, vol. 8, no. 4, pp. 634–645, 2006.
- [5] S. H. Kwak, Y. M. Cho, G. M. Noh, and A. S. Om, "Cancer preventive potential of kimchi lactic acid bacteria (*Weissella cibaria*, *Lactobacillus plantarum*)," *Journal of cancer prevention*, vol. 19, no. 4, pp. 253–258, 2014.
- [6] B. Le and S. H. Yang, "Efficacy of *Lactobacillus plantarum* in prevention of inflammatory bowel disease," *Toxicology Reports*, vol. 5, pp. 314–317, 2018.
- [7] C. Stevenson, R. Blaauw, E. Fredericks, J. Visser, and S. Roux, "Randomized clinical trial: Effect of *Lactobacillus plantarum* 299 v on symptoms of irritable bowel syndrome," *Nutrition*, vol. 30, no. 10, pp. 1151–1157, 2014.
- [8] P. Trevisi, R. Latorre, D. Priori et al., "Effect of feed supplementation with live yeast on the intestinal transcriptome profile of weaning pigs orally challenged with *Escherichia coli* F4," *Animal: an international journal of animal bioscience*, vol. 11, no. 1, pp. 33–44, 2017.
- [9] G. Y. Yang, Y. H. Zhu, W. Zhang, D. Zhou, C. C. Zhai, and J. F. Wang, "Influence of orally fed a select mixture of *Bacillus* probiotics on intestinal T-cell migration in weaned MUC4 resistant pigs following *Escherichia coli* challenge," *Veterinary Research*, vol. 47, no. 1, p. 71, 2016.
- [10] J. Villena, E. Chiba, M. G. Vizoso-Pinto et al., "Immunobiotic *Lactobacillus rhamnosus* strains differentially modulate antiviral immune response in porcine intestinal epithelial and antigen presenting cells," *BMC Microbiology*, vol. 14, no. 1, p. 126, 2014.
- [11] O. Farkas, G. Mátis, E. Pászti-Gere et al., "Effects of *Lactobacillus plantarum* 2142 and sodium n-butyrate in lipopolysaccharide-triggered inflammation: comparison of a porcine intestinal epithelial cell line and primary hepatocyte monocultures with a porcine enterohepatic co-culture system," *Journal of Animal Science*, vol. 92, no. 9, pp. 3835–3845, 2014.
- [12] P. Yu, C. Ke, J. Guo, X. Zhang, and B. Li, "*Lactobacillus plantarum* L15 alleviates colitis by inhibiting LPS-mediated NF- $\kappa$ B activation and ameliorates DSS-induced gut microbiota dysbiosis," *Frontiers in Immunology*, vol. 11, p. 575173, 2020.
- [13] R. Pieper, P. Janczyk, V. Uruschurov, U. Korn, B. Pieper, and W. B. Souffrant, "Effect of a single oral administration of *Lactobacillus plantarum* DSMZ 8862/8866 before and at the time point of weaning on intestinal microbial communities in piglets," *International Journal of Food Microbiology*, vol. 130, no. 3, pp. 227–232, 2009.
- [14] J. Wang, H. F. Ji, S. X. Wang et al., "*Lactobacillus plantarum* ZLP001: in vitro assessment of antioxidant capacity and effect on growth performance and antioxidant status in weaning piglets," *Asian-Australasian Journal of Animal Sciences*, vol. 25, no. 8, pp. 1153–1158, 2012.
- [15] M. Kassayová, N. Bobrov, L. Strojny et al., "Anticancer and immunomodulatory effects of *Lactobacillus plantarum* LS/07, inulin and melatonin in NMU-induced rat model of breast cancer," *Anticancer Research*, vol. 36, no. 6, pp. 2719–2728, 2016.
- [16] L. O. Chuah, H. L. Foo, T. C. Loh et al., "Postbiotic metabolites produced by *Lactobacillus plantarum* strains exert selective cytotoxicity effects on cancer cells," *BMC Complementary and Alternative Medicine*, vol. 19, no. 1, p. 114, 2019.
- [17] E. Rönkä, E. Malinen, M. Saarela, M. Rinta-Koski, J. Aarnikunnas, and A. Palva, "Probiotic and milk technological properties of *Lactobacillus brevis*," *International Journal of Food Microbiology*, vol. 83, no. 1, pp. 63–74, 2003.
- [18] R. Kant, J. Blom, A. Palva, R. J. Siezen, and W. M. de Vos, "Comparative genomics of *Lactobacillus*," *Microbial Biotechnology*, vol. 4, no. 3, pp. 323–332, 2011.
- [19] N. Fuke, T. Takagi, Y. Higashimura et al., "*Lactobacillus brevis* KB290 with vitamin a ameliorates murine intestinal inflammation associated with the increase of CD11c+ macrophage/CD103- dendritic cell ratio," *Inflammatory Bowel Diseases*, vol. 24, no. 2, pp. 317–331, 2018.
- [20] N. Ueno, M. Fujiya, S. Segawa et al., "Heat-killed body of *Lactobacillus brevis* SBC8803 ameliorates intestinal injury in a murine model of colitis by enhancing the intestinal barrier function," *Inflammatory Bowel Diseases*, vol. 17, no. 11, pp. 2235–2250, 2011.
- [21] Y. Ma, C. Hu, W. Yan, H. Jiang, and G. Liu, "*Lactobacillus pentosus* increases the abundance of *Akkermansia* and affects the serum metabolome to alleviate DSS-induced colitis in a murine model," *Frontiers in cell and developmental biology*, vol. 8, p. 591408, 2020.
- [22] W. Ren, J. Yin, M. Wu et al., "Serum amino acids profile and the beneficial effects of L-arginine or L-glutamine supplementation in dextran sulfate sodium colitis," *PLoS One*, vol. 9, no. 2, article e88335, 2014.
- [23] Y. Ma, H. Jiang, J. Fang, and G. Liu, "IRW and IQW reduce colitis-associated cancer risk by alleviating DSS-induced colonic inflammation," *BioMed Research International*, vol. 2019, Article ID 6429845, 9 pages, 2019.
- [24] V. Liévin-Le Moal, "Dysfunctions at human intestinal barrier by water-borne protozoan parasites: lessons from cultured human fully differentiated colon cancer cell lines," *Cellular Microbiology*, vol. 15, no. 6, pp. 860–869, 2013.
- [25] S. Ding, Y. Ma, G. Liu, W. Yan, H. Jiang, and J. Fang, "*Lactobacillus brevis* alleviates DSS-induced colitis by reprogramming intestinal microbiota and influencing serum metabolome in murine model," *Frontiers in Physiology*, vol. 10, p. 1152, 2019.
- [26] V. Liévin-Le Moal and A. L. Servin, "The front line of enteric host defense against unwelcome intrusion of harmful microorganisms: mucins, antimicrobial peptides, and microbiota," *Clinical Microbiology Reviews*, vol. 19, no. 2, pp. 315–337, 2006.
- [27] Y. Ma, G. Liu, M. Tang, J. Fang, and H. Jiang, "Epigallocatechin gallate can protect mice from acute stress induced by LPS while stabilizing gut microbes and serum metabolites levels," *Frontiers in Immunology*, vol. 12, p. 640305, 2021.
- [28] Y. Hou, L. Wang, W. Zhang et al., "Protective effects of N-acetylcysteine on intestinal functions of piglets challenged with lipopolysaccharide," *Amino Acids*, vol. 43, no. 3, pp. 1233–1242, 2012.
- [29] H. Liu, J. Zhang, S. Zhang et al., "Oral administration of *Lactobacillus fermentum* I5007 favors intestinal development and alters the intestinal microbiota in formula-fed piglets," *Journal of Agricultural and Food Chemistry*, vol. 62, no. 4, pp. 860–866, 2014.
- [30] C. Suo, Y. Yin, X. Wang et al., "Effects of *Lactobacillus plantarum* ZJ316 on pig growth and pork quality," *BMC Veterinary Research*, vol. 8, no. 1, p. 89, 2012.
- [31] S. C. Tsai, M. Noda, R. Adamik, J. Moss, and M. Vaughan, "Enhancement of cholera toxin ADP-ribosyltransferase activities

- by guanyl nucleotides and a 19-kDa membrane protein,” *Proceedings of the National Academy of Sciences of the United States of America*, vol. 84, no. 15, pp. 5139–5142, 1987.
- [32] X. Wang, X. Gao, and P. R. Hardwidge, “Heat-labile enterotoxin-induced activation of NF- $\kappa$ B and MAPK pathways in intestinal epithelial cells impacts enterotoxigenic *Escherichia coli* (ETEC) adherence,” *Cellular Microbiology*, vol. 14, no. 8, pp. 1231–1241, 2012.
- [33] L. Petecchia, F. Sabatini, C. Usai, E. Caci, L. Varesio, and G. A. Rossi, “Cytokines induce tight junction disassembly in airway cells via an EGFR-dependent MAPK/ERK1/2-pathway,” *Laboratory investigation; a journal of technical methods and pathology*, vol. 92, no. 8, pp. 1140–1148, 2012.
- [34] L. Huang, Z. Zhao, C. Duan et al., “*Lactobacillus plantarum* C88 protects against aflatoxin B1-induced liver injury in mice via inhibition of NF- $\kappa$ B-mediated inflammatory responses and excessive apoptosis,” *BMC Microbiology*, vol. 19, no. 1, p. 170, 2019.
- [35] T. Lahteinen, A. Lindholm, T. Rintila et al., “Effect of *Lactobacillus brevis*\_ ATCC 8287 as a feeding supplement on the performance and immune function of piglets,” *Veterinary Immunology and Immunopathology*, vol. 158, no. 1-2, pp. 14–25, 2014.
- [36] M. Roselli, A. Finamore, M. S. Britti et al., “The novel porcine *Lactobacillus sobrius* strain protects intestinal cells from enterotoxigenic *Escherichia coli* K88 infection and prevents membrane barrier damage,” *The Journal of Nutrition*, vol. 137, no. 12, pp. 2709–2716, 2007.
- [37] A. M. Johnson, R. S. Kaushik, and P. R. Hardwidge, “Disruption of transepithelial resistance by enterotoxigenic *Escherichia coli*,” *Veterinary Microbiology*, vol. 141, no. 1-2, pp. 115–119, 2010.
- [38] M. Roselli, A. Finamore, I. Garaguso, M. S. Britti, and E. Mengheri, “Zinc oxide protects cultured enterocytes from the damage induced by *Escherichia coli*,” *The Journal of Nutrition*, vol. 133, no. 12, pp. 4077–4082, 2003.
- [39] Y. Wu, C. Zhu, Z. Chen et al., “Protective effects of *Lactobacillus plantarum*\_ on epithelial barrier disruption caused by enterotoxigenic *Escherichia coli*\_ in intestinal porcine epithelial cells,” *Veterinary Immunology and Immunopathology*, vol. 172, pp. 55–63, 2016.
- [40] T. Wu, Q. Jiang, D. Wu et al., “What is new in lysozyme research and its application in food industry? A review,” *Food Chemistry*, vol. 274, pp. 698–709, 2019.
- [41] P. Rishi, A. Bhogal, S. Arora, S. K. Pandey, I. Verma, and I. P. Kaur, “Improved oral therapeutic potential of nanoencapsulated cryptdin formulation against *Salmonella* infection,” *European Journal of Pharmaceutical Sciences: Official Journal of the European Federation for Pharmaceutical Sciences*, vol. 72, pp. 27–33, 2015.
- [42] R. C. Vemuri, R. Gundamaraju, T. Shinde, and R. Eri, “Therapeutic interventions for gut dysbiosis and related disorders in the elderly: antibiotics, probiotics or faecal microbiota transplantation?,” *Beneficial Microbes*, vol. 8, no. 2, pp. 179–192, 2017.
- [43] I. Garcia-Mantrana, M. Selma-Royo, C. Alcantara, and M. C. Collado, “Shifts on gut microbiota associated to Mediterranean diet adherence and specific dietary intakes on general adult population,” *Frontiers in Microbiology*, vol. 9, p. 890, 2018.
- [44] N. R. Shin, T. W. Whon, and J. W. Bae, “Proteobacteria: microbial signature of dysbiosis in gut microbiota,” *Trends in Biotechnology*, vol. 33, no. 9, pp. 496–503, 2015.
- [45] D. N. Frank, A. L. St Amand, R. A. Feldman, E. C. Boedeker, N. Harpaz, and N. R. Pace, “Molecular-phylogenetic characterization of microbial community imbalances in human inflammatory bowel diseases,” *Proceedings of the National Academy of Sciences of the United States of America*, vol. 104, no. 34, pp. 13780–13785, 2007.
- [46] R. B. Sartor, “Microbial influences in inflammatory bowel diseases,” *Gastroenterology*, vol. 134, no. 2, pp. 577–594, 2008.
- [47] S. Schonherr-Hellec and J. Aires, “Clostridia and necrotizing enterocolitis in preterm neonates,” *Anaerobe*, vol. 58, pp. 6–12, 2019.
- [48] O. Vandenberg, A. J. Cornelius, H. Souayah et al., “The role of Epsilonproteobacteria in children with gastroenteritis,” *The Pediatric Infectious Disease Journal*, vol. 32, no. 10, pp. 1140–1142, 2013.
- [49] J. F. Koninkx and J. J. Malago, “The protective potency of probiotic bacteria and their microbial products against enteric infections-review,” *Folia Microbiologica*, vol. 53, no. 3, pp. 189–194, 2008.
- [50] B. P. Blackwood, C. Y. Yuan, D. R. Wood, J. D. Nicolas, J. S. Grothaus, and C. J. Hunter, “Probiotic *Lactobacillus* species strengthen intestinal barrier function and tight junction integrity in experimental necrotizing Enterocolitis,” *Journal of probiotics & health*, vol. 5, no. 1, 2017.
- [51] F. Yang, A. Wang, X. Zeng, C. Hou, H. Liu, and S. Qiao, “*Lactobacillus reuteri* I5007 modulates tight junction protein expression in IPEC-J2 cells with LPS stimulation and in newborn piglets under normal conditions,” *BMC Microbiology*, vol. 15, no. 1, p. 32, 2015.
- [52] V. Camilo, T. Sugiyama, and E. Touati, “Pathogenesis of *Helicobacter pylori* infection,” *Helicobacter*, vol. 22, Supplement 1, 2017.

## Review Article

# Targeting Reactive Oxygen Species Capacity of Tumor Cells with Repurposed Drug as an Anticancer Therapy

Jiabing Wang <sup>1</sup>, Dongsheng Sun <sup>2</sup>, Lili Huang <sup>3</sup>, Shijian Wang <sup>1</sup>, and Yong Jin <sup>1</sup>

<sup>1</sup>Municipal Hospital Affiliated to Taizhou University, Taizhou 318000, China

<sup>2</sup>Taizhou University Hospital, Taizhou University, Taizhou, Zhejiang 318000, China

<sup>3</sup>Lihuli Hospital Affiliated to Ningbo University, Ningbo, Zhejiang 315100, China

Correspondence should be addressed to Jiabing Wang; wangjiabing@tzc.edu.cn and Yong Jin; tzmhsjwk@163.com

Received 6 July 2021; Accepted 16 August 2021; Published 8 September 2021

Academic Editor: Peichao Chen

Copyright © 2021 Jiabing Wang et al. This is an open access article distributed under the Creative Commons Attribution License, which permits unrestricted use, distribution, and reproduction in any medium, provided the original work is properly cited.

Accumulating evidence shows that elevated levels of reactive oxygen species (ROS) are associated with cancer initiation, growth, and response to therapies. As concentrations increase, ROS influence cancer development in a paradoxical way, either triggering tumorigenesis and supporting the proliferation of cancer cells at moderate levels of ROS or causing cancer cell death at high levels of ROS. Thus, ROS can be considered an attractive target for therapy of cancer and two apparently contradictory but virtually complementary therapeutic strategies for the regulation of ROS to treat cancer. Despite tremendous resources being invested in prevention and treatment for cancer, cancer remains a leading cause of human deaths and brings a heavy burden to humans worldwide. Chemotherapy remains the key treatment for cancer therapy, but it produces harmful side effects. Meanwhile, the process of de novo development of new anticancer drugs generally needs increasing cost, long development cycle, and high risk of failure. The use of ROS-based repurposed drugs may be one of the promising ways to overcome current cancer treatment challenges. In this review, we briefly introduce the source and regulation of ROS and then focus on the status of repurposed drugs based on ROS regulation for cancer therapy and propose the challenges and direction of ROS-mediated cancer treatment.

## 1. Introduction

As a common and frequently occurring disease worldwide, cancers increasingly continue to produce serious clinical and socioeconomic issues [1, 2]. Reducing cancer mortality is the primary challenge globally, and the study on cancer treatment has increasingly been a hot spot in the field of scientific research [1, 2]. Despite the progress made in cancer therapy, the growing burden of the most common cancers in low-income and middle-income countries remains to be a major challenge [3]. More importantly, global cancer mortality is not much decreased compared with those in the past decades, though many new anticancer drugs have been approved for tumor prevention or treatment [4]. Unfortunately, the commonly used chemotherapeutics are accompanied with severe adverse effects [5]. Extensive efforts have been made to develop novel and highly efficacious tumor-targeting agents [6]. However, it is not only the frequent

appearance of resistance concomitant with targeted therapies but also the higher budgets of targeted drugs that account for the limited use clinically, which lead to the classical cytotoxic drugs to remain the first choice for patients [7, 8]. Therefore, there is still a need to develop more effective and less toxic anticancer drugs worldwide to prevent and treat cancer.

Over the past few decades, the challenges of drug discovery facing the global pharmaceutical industry are multifold and stagnant, including the escalating cost and length of time required for new drug development and high risk of research and development failure [9, 10]. Currently, the cost of discovering and developing a drug from scratch is traditionally about 2.5 billion US dollars on average, and it takes about 10 to 15 years to enter the market and the success rate is only 2% [11, 12]. Few new anticancer drugs are approved by the FDA annually (Figure 1), though more than 10,000 clinical trials have been completed to evaluate cancer drug

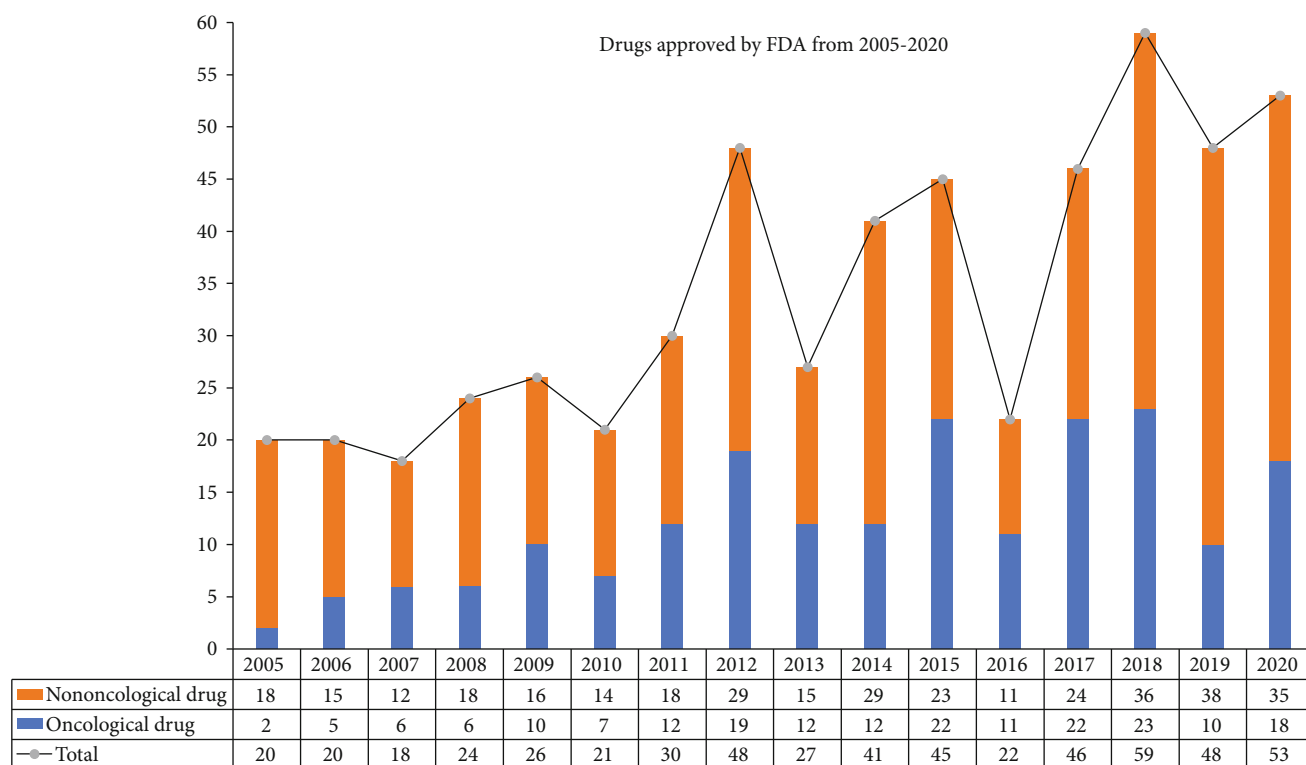


FIGURE 1: The number of the FDA approved drugs for oncology from 2005 to 2020.

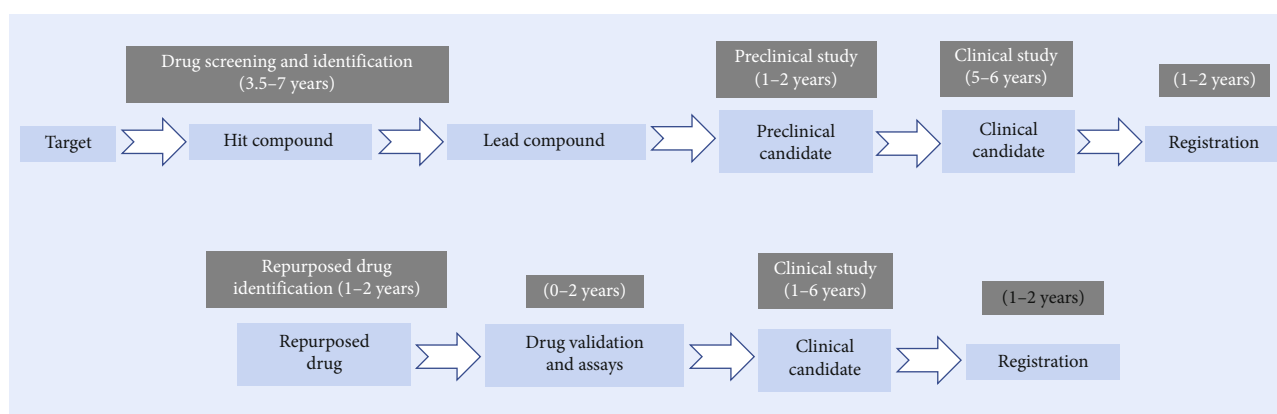


FIGURE 2: A comparison of the estimated time and main steps in de novo drug development and drug repurposing tactics.

interventions [13]. Hence, alternative approaches to drug development are direly needed.

In light of these challenges, drug repurposing may be an alternative approach to overcome obstructions and has gained much attention and momentum in recent years. Drug repurposing is the practice of discovering novel effects or targets of the approved drugs beyond their initial approval, which can expand the indications for marketed drugs [14]. Drug repurposing has many advantages over developing an entirely new drug for a specific indication. For example, repurposed drugs have been found to be safe enough in preclinical models and humans; it is unlikely to fail in early-stage trials and subsequent efficacy trials based on the safety standpoint [15]. Additionally, the time frame and investment for drug development can be reduced; that

is, the return on investment in the development of repurposed drugs for new uses is more rapid (Figure 2) [15]. Finally, repurposed drugs may reveal new anticancer targets and pathways that can be further developed [15]. Historically, drug repurposing was largely discovered by accident by researchers [15]. Once it is discovered that repurposed drugs have off-target effects or newly discovered target effects, they will be developed commercially [15]. The most dramatic examples of repurposed drug are thalidomide and sildenafil citrate. Thalidomide was initially used to treat morning sickness, but it was found to cause severe skeletal birth defects in newborns [16]. However, it was successfully repositioned for use in erythema nodosum leprosum and multiple myeloma therapy [17]. Sildenafil citrate was originally developed as an antihypertension drug, but when

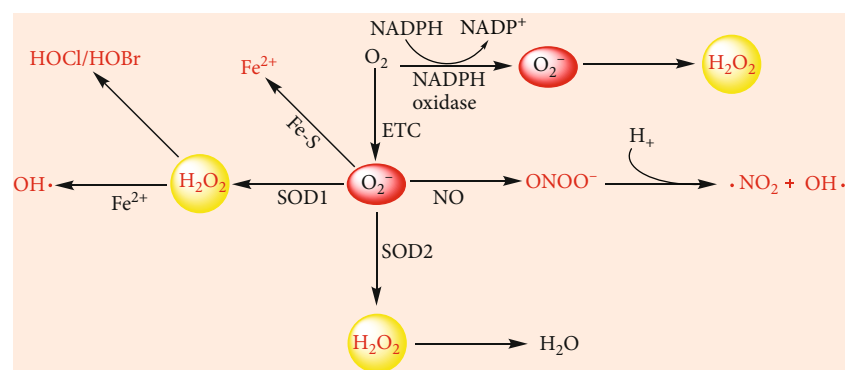


FIGURE 3: General scheme for ROS production by cellular enzymes and electron transport chain. The major sources of intracellular ROS include the mitochondrial ETC and NADPH oxidases. SOD1 and SOD2 can convert  $O_2^-$  into  $H_2O_2$ ; then  $H_2O_2$  can be converted into  $H_2O$ . Meanwhile,  $H_2O_2$  can also be converted into  $OH^\cdot$ , HOCl, and HOBr by  $Fe^{2+}$  and myeloperoxidase, respectively. NO is responsible for the conversion of  $O_2^-$  into  $ONOO^-$  and  $OH^\cdot$ .

Pfizer reintroduced it to treat erectile dysfunction and marketed it as Viagra [18]. Surprisingly, it captured vast majority of the erectile dysfunction drug market [15]. Such successes have encouraged the global pharmaceutical industry and drug researchers to identify repurposed drugs. Indeed, there is no systematic approach to predict which drugs can be used as repurposed drugs. The strategies towards identifying drug repurposing opportunities based on a number of promising candidate drugs roughly include computational and experimental approaches [15, 19]. A full account of the comprehensive strategies used for drug repurposing is beyond the scope of this review, and readers are directed elsewhere [15, 19].

## 2. Overview Biological Characteristics of Reactive Oxygen Species (ROS)

**2.1. The Types and Sources of ROS.** In recent years, the understanding of tumor pathophysiology and pathogenesis has witnessed an unprecedented explosion. A large number of pleiotropic physiological signaling pathway factors regulating tumor occurrence and development have been emerged. Reactive oxygen species (ROS), the inevitable product of cell metabolism in aerobic life, are broadly defined as oxygen-containing chemical species with reactive properties, and they can be divided into nonradical and free radical [20, 21]. ROS are constantly produced by both enzymatic reaction and the mitochondrial electron transport chain (ETC) from molecular oxygen [20–22]. Complexes I, II, and III of mitochondrial ETC account for a great amount of the intracellular ROS production [23]. The enzyme-catalyzed reactions involve NADPH oxidase (NOX), xanthine oxidase, uncoupled endothelial nitric oxide synthase (eNOS), arachidonic acid, and metabolic enzymes such as the cytochrome P450 enzymes, lipoxygenase, and cyclooxygenase; indeed, NOX has primarily evolved to produce ROS [22, 24]. During the process of aerobic respiration and cellular metabolism, superoxide ( $O_2^-$ ) is generated either intracellularly by  $1 e^-$  transfer to  $O_2$  from the ETC or extracellularly by NOX. In the mitochondria,  $O_2^-$  damages iron-sulfur (Fe-S) clusters to release iron ( $Fe^{2+}$ ) into

the extracellular matrix and reduces ferric iron ( $Fe^{3+}$ ) to ferrous iron ( $Fe^{2+}$ ), which leads to inactivation of protein function [25, 26]. The  $O_2^-$  is dismutated to hydrogen peroxide ( $H_2O_2$ ) in a buffer or catalyzed by superoxide dismutases (SOD1 and SOD2) [22]. Moreover,  $H_2O_2$  is also generated by various other oxidases present in subcellular localizations, prominently including the endoplasmic reticulum (ER) lumen [27, 28]. Meanwhile,  $O_2^-$  is converted into peroxynitrite ( $ONOO^-$ ) and hydroxyl radical ( $OH^\cdot$ ) through a reaction with nitric oxide (NO) [29].  $OH^\cdot$  is generated by a ferrous iron-mediated reduction of  $H_2O_2$  and the decomposition of  $ONOO^-$  [29]. Additionally,  $H_2O_2$  can be converted into hypochlorous acid and hypobromous acid (HOCl and HOBr) through myeloperoxidase in the phagocytic vacuole in neutrophils for pathogen defense [22, 30, 31] (Figure 3). Meanwhile, biologically relevant ROS are also derived from the exogenous environment, which includes air pollutants, stress, ultraviolet rays, toxicants, tumor chemotherapy, and radiotherapy [24, 32–35]. However, these exposures are highly variable; it is challenging to measure ROS directly in cells and tissues.

**2.2. The Impact and Damage Outcomes of ROS.** Among the radical and nonradical oxygen species,  $H_2O_2$  is recognized as the key redox signaling agent in redox regulation of biological activities, and a total of 37  $H_2O_2$ -generating enzymes have been found [36, 37]. It is now clear that  $H_2O_2$  plays a fundamental role in physiology as a functional signaling entity [38].  $H_2O_2$  first occurred at low homeostasis levels in normally breathing eukaryotic cells, and it was the primary ROS responsible for protein oxidation [39]. Generally, the generation of  $H_2O_2$  was constantly stimulated by metabolic cues or various stressors intracellularly, and the concentration of  $H_2O_2$  is maintained in the low nanomolar range, which is important for signaling by redox signaling via oxidation and called “oxidative eustress” [40, 41]. The overall cellular concentration of the  $O_2^-$  is maintained at about  $10^{-11}$  M, which is much lower than the  $10^{-8}$  M of  $H_2O_2$  [42]. Diffusible  $H_2O_2$  contributes to orchestration of various processes including cell proliferation, differentiation, and angiogenesis through oxidation of sulfur

(thiolate groups) in target proteins and further activates stress responsive survival pathways [43, 44]. Meanwhile,  $H_2O_2$  acts as signal transduction molecules that induce proinflammatory cytokines and the nuclear factor- $\kappa$ B (NF- $\kappa$ B) pathway [45, 46].

In contrast to low levels of  $H_2O_2$ , supraphysiological concentrations of  $H_2O_2$  cause “oxidative distress,” which can induce a plethora of irreversible damaging effects to proteins, DNA, and lipids and ultimately cause cell death [47]. At the cellular level, oxidation of proteins by ROS is more common than that of DNA and lipids [48]. When proteins are exposed to ROS, amino acid side chains are modified, and consequently, the protein structure is altered [48]. ROS can cleave peptide bonds through  $\alpha$ -amidation, diamidation, proline residue oxidation, glutamine residue oxidation, and aspartyl residue oxidation [49]. ROS-induced protein oxidation may contribute to the following: (1) hydroxylation of aromatic groups and aliphatic amino acid side chains, nitration of aromatic amino acid residues, nitrosation of sulfhydryl groups, and sulfonation of methionine residues; (2) polypeptide chain breaking to form cross-linked protein aggregates; and (3) the functional groups of proteins reacting with oxidation products of polyunsaturated fatty acids or carbohydrate derivatives, which affects normal physiological function [48, 49]. It is equally well known that sustained exposure to high ROS levels can damage DNA through single strand break, point mutations, mis-coding, and abnormal amplification [48]. DNA is complexed as chromatin with histones; ROS can further affect the oxidation and reduction of adduct radicals of DNA [48]. Besides, toxic concentrations of ROS also induce mitochondrial DNA mutations [48, 50]. Lipids have the functions of energy storage, signal transduction, transport, and cell membrane composition in cells, and many types of lipids are easily oxidized by ROS [48, 51]. The reaction of ROS with lipid molecules can activate the lipid peroxidation free radical cascade, which is generally very fast [48]. The hydrogen atom abstraction forms a methylene carbon of a polyunsaturated fatty acid by a lipid hydroperoxyl radical, forming a new carbon centered radical that propagates the peroxidative chain reaction and a hydroperoxide [52]. Moreover, the more double bonds in the lipid, the easier it is for hydrogen atoms to be taken away [53]. Excessive ROS can cause lipid peroxidation in biofilms, which would result in loss of fluidity, abnormal membrane potential, and rupture and leakage of cell contents [54]. Therefore, it is challenging and important to determine the precise role and maintain a safe cellular ROS gradient and regulate redox signaling pathways.

**2.3. Intracellular Clearance of ROS.** Excess ROS production induces a plethora of damaging effects to cellular biomacromolecules. Hence, supraphysiological gradients of ROS are showcased as harmful species, and buffering ROS to maintain redox homeostasis is required. In order to prevent the unrestricted accumulation of ROS, a series of antioxidant defense systems have been discovered and can act independently or synergistically to neutralize ROS. Antioxidants can be divided into two groups, that is, noncatalytic small molecules and catalytic antioxidants [29]. Glutathione

(GSH) is the most abundant nonenzymatic antioxidant molecule and is essential for cell survival and redox homeostasis [55]. GSH is a tripeptide that synthesis catalyzed by glutamate-cysteine ligase (GCL) and GSH synthetase (GSS), and it is used as a cofactor by GSH S-transferases (GSTs) and GSH peroxidases (GPxs) to eliminate ROS [56]. Besides, endogenously synthesized bilirubin, melatonin,  $\alpha$ -lipoic acid, and uric acid are other nonenzymatic antioxidant molecules that mitigate the excess level of ROS produced in cells [29, 57]. Enzymatic antioxidants include SOD, catalase (CAT), peroxiredoxins (PRxs, also called PRxs), glutathione peroxidases (GPxs), thioredoxin reductases (TrxRs), and thioredoxins (Trxs) [29]. Enzymatic antioxidants with high catalytic activity are uncovered as handling ROS levels in cells [29]. SODs are a family of metalloenzymes catalyzing the dismutation of  $O_2^-$  to  $H_2O_2$ , which utilizes metal ions, including copper ( $Cu^{2+}$ ), ferrous iron ( $Fe^{2+}$ ), manganese ( $Mn^{2+}$ ), and zinc ( $Zn^{2+}$ ) as cofactors [58]. CAT is primarily localized in the cytosol and cell organelles called the peroxisome, which can convert  $H_2O_2$  into  $O_2$  and  $H_2O$  [59]. In addition, Trxs promote PRDX-mediated  $H_2O_2$  detoxification and reduction of lipid by GPx requires GSH [56]. More importantly, GSH and Trxs generate oxidized forms through detoxification of ROS [56]. Oxidized GSH and Trxs are both regenerated by GSH reductase (GSR) and Trxs reductase 1 using NADPH as a cofactor, respectively [60]. GSH and Trxs, and TrxRs are noncatalytic and catalytic antioxidants, which are critically involved in different stages of cancers [61–63].

In addition, it is established that many transcription factors, including nuclear factor erythroid 2-related factor 2 (NRF2), the forkhead box O (FOXO), hypoxia-inducible factor (HIF), NF- $\kappa$ B, and tumor protein p53 (TP53 or Trp53 in mice), are activated by ROS and regulate intracellular redox environment of cells [64]. NRF2 is the most important transcription factor for the activation of a number of genes that have antioxidant functions within the cell [65, 66]. However, under resting conditions, NRF2 is degraded through interacting with Kelch-like ECH-associated protein 1- (KEAP1-) Cullin 3 (CUL3) E3 ligase complex. Under conditions of oxidative stress or electrophilic addition, cysteine residues on KEAP1 are modified, thus blocking NRF2 interaction and subsequent degradation [67]. Then, NRF2 translocated into the nucleus, where it serves as a transcription factor for expression of the antioxidant responsive element-(ARE-) driven genes, including hemeoxygenase-1 (HO-1), NAD(P)H quinone oxidoreductase 1 (NQO1), glutathione S-transferases (GSTs), and UDP-glucuronosyltransferases (UGTs) [67]. In addition, sestrins (SESN1, 2, and 3) exert indirect antioxidant activity, in part by activation of transcription factor NRF2 [68, 69]. The FOXO family of transcription factors contributes to the maintenance of cellular and organismal homeostasis in various ways [70]. For example, FOXO improves mitochondrial redox, suppresses the levels of free transition metal ions, and promotes antioxidant defense system [71]. Hypoxia has been associated with an increase in  $O_2^-$  and  $H_2O_2$  generation through inhibition of the mitochondrial ETC [72]. HIF is a transcription factor that serves as the master regulator of transcriptional

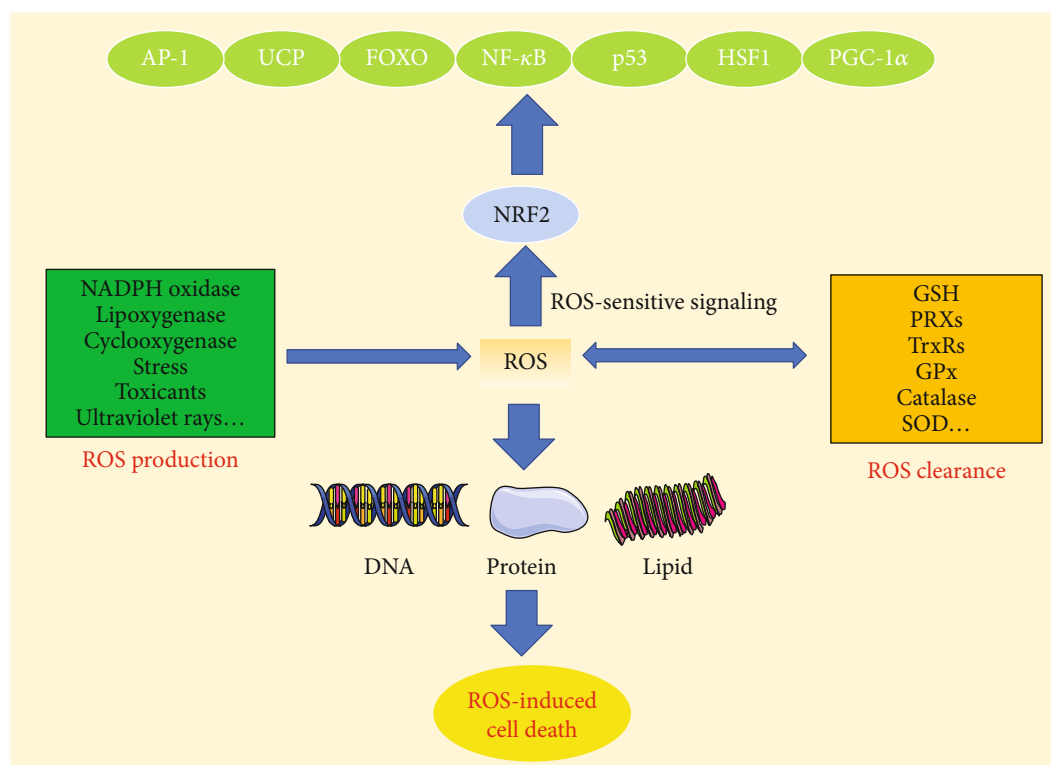


FIGURE 4: ROS balance and their roles in regulating transcription factors and cell death. ROS can be produced by NADPH oxidases, lipoxygenase, cyclooxygenase, stress, toxicants, and ultraviolet rays. On the other hand, ROS can be eliminated via activation of the GSH, PRXs, TrxRs, GPx, catalase, and SOD. Extremely high levels of ROS are dangerous for the DNA, protein, and lipid and eventually cause cell death. Cells first adapt to the increase in ROS by activating NRF2 and then trigger other members of the antioxidant transcription factor when the excess levels of ROS that are not countered by the NRF2-directed defenses.

responses to hypoxia [73]. Oxidants can stabilize HIF during hypoxia, thereby helping to increase the hypoxia response [73]. NF- $\kappa$ B serves as a master switch of inflammation, which is associated with extensive  $H_2O_2$  production [74]. In different context,  $H_2O_2$  has different roles in NF- $\kappa$ B function [74].  $H_2O_2$  activates NF- $\kappa$ B pathway and then negatively controls the stability of I $\kappa$ B in the cytosol [75], while  $H_2O_2$  also directly modulates NF- $\kappa$ B due to the presence of oxidizable cysteines in the DNA-binding region of NF- $\kappa$ B [76]. The tumor suppressor protein p53 was considered the transcription factor that has a major role in regulating antioxidant gene expression [77, 78]. Under the control of  $H_2O_2$ , it regulates the selective transcription activation of p53 target genes through the oxidation of p53 cysteine residues. Reciprocally, p53 regulates the expression of antioxidant genes to maintain cellular redox balance [79]. Other transcription factors, such as AMP-activated protein kinase (AMPK), activator protein 1 (AP-1), heat shock factor 1 (HSF1), peroxisome proliferator-activated receptor  $\gamma$  coactivator-1 $\alpha$  (PGC-1 $\alpha$ ), uncoupling protein (UCP), and protein-tyrosine phosphatase 1B (PTP1B), also contribute to redox status [80–85].

However, the extents to which individual members of the above network of antioxidant transcription factors are differentially activated by oxidative stress are uncertain, although it is improbable that all of them are activated simultaneously. However, different transcription factors

may respond to distinct threshold levels of ROS. When cells suffered from moderate levels of ROS, NRF2 first was activated, and then a series of genes encoding detoxification enzymes were further induced, which provided a floodgate to protect against ROS [20]. When cells further adapt to sustained exposure to high ROS levels, which causes activation of Krüppel-like transcription factor 9 (KLF9) and downregulation of NRF2, the NRF2-induced defense cannot counteract the excess ROS, then triggering additional redox switches that activate other members of the antioxidant transcription factor network [20] (Figure 4). Therefore, intracellular ROS regulation is closely related to the above complex processes, and there is no constant boundary between prooxidants and antioxidants in the regulation of ROS.

### 3. ROS Paradox and Contradictory Strategies Based on ROS for Cancer Treatment

Under normal physiological conditions, the redox system is in good coordination and well-balanced. However, in the presence of obvious stimuli, the balance would be disrupted, triggering oxidative stress and in turn increasing ROS levels, implicated in various human diseases including cancer. Interestingly, oxidative stress can activate cell survival or death mechanisms depending on the severity and exposure time of ROS excess. In general, ROS act as mitogens to induce proliferation and differentiation of normal and

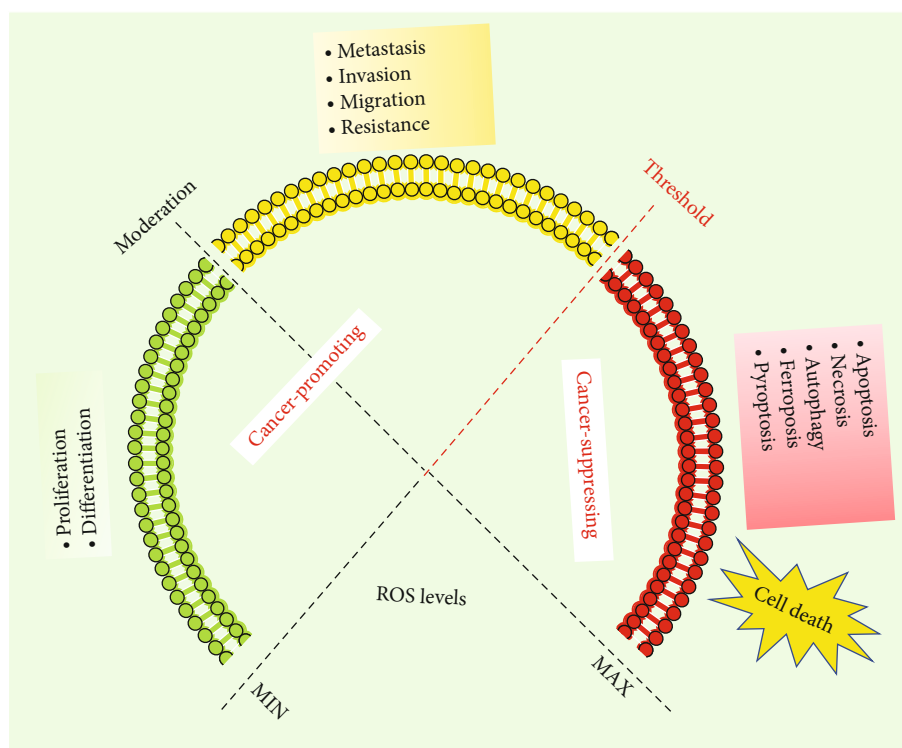


FIGURE 5: The cancer-promoting activities and cancer-suppressing activities of ROS in cancer. Low ROS (green) is the basic need to maintain normal cellular proliferation, and differentiation. Moderate ROS (yellow) is the signal for the increased cellular metastasis, invasion and migration, and resistance. When the ROS level exceeds threshold (red), ROS can induce cancer cell death via the activation of cell apoptosis, necrosis, autophagy, ferroptosis, and pyroptosis.

cancer cells at low concentrations (usually submicromolar concentrations) [48]. At moderate concentrations, ROS have been implicated in tumor initiation and progression, malignant conversion, and resistance to chemotherapy. The higher concentrations of ROS result in damage cellular biomolecules and cause gene mutations, thus promoting canceration of normal cells or inducing cancer cell apoptosis, necrosis, autophagy, ferroptosis, and pyroptosis [48, 86] (Figure 5). Therefore, the roles of ROS are complicated, and ROS operate as a diversified biochemical entity in cancer progression.

Because the influence of ROS on cancer development is contradictory, reducing or increasing intracellular ROS levels would be a potential strategy to prevent or treat cancer [87]. Namely, reducing the intracellular ROS content by inhibiting ROS production pathway and using exogenous supplementation of antioxidants is an effective strategy, and it could effectively prevent the early stage of tumor occurrence. Cancer cells are more sensitive to enhanced intracellular ROS than normal cells; thus, cancer cells can be preferentially killed by enhancing the cellular ROS levels, which might be another puissant strategy to selectively kill cancer cells. Moreover, the expression level of antioxidant enzymes and oxidative stress environment in drug-resistant tumor cells are usually higher; ROS-modulating drugs may have a better therapeutic effect on the intervention of drug-resistant tumor cells. The use of small molecules to increase the production of ROS or/and inhibit the antioxi-

dant defense system is one of the most effective anticancer methods [87]. In recent years, several clinical trials have been made in the research of therapeutic drugs targeting ROS regulation in cancer cells [88]. Moreover, small molecules regulating ROS homeostasis for cancer therapy have been comprehensively reviewed [24, 87]. However, most small molecules described in the literature or on the clinical development stages have not entered into clinical treatment for cancer. Several FDA-approved drugs based on ROS regulation have led to repurposing of cancer indications, which may be considered a novel and valid cancer therapeutics [89]. Therefore, in this paper, we will focus on repurposed drugs for cancer therapy by the regulation of ROS homeostasis.

#### 4. Repurposed Drug-Regulated ROS Homeostasis as a Novel Cancer Therapeutics in Oncology

**4.1. Repurposed Drugs as a ROS Scavenger in Cancer.** ROS accumulation is one of the initiating factors in the early stage of the neoplastic process. To this extent, ROS can lead to more metabolic adaptations and more levels of DNA damage and genetic instability in normal cells, consequently promoting the cancer cell proliferation and growth [90, 91]. Numerous epidemiological data and preclinical/clinical studies suggest that small molecule ROS inhibitors can



TABLE 1: Repurposed clinical candidates for cancer.

| Drug               | Original indication | Clinical trials  |
|--------------------|---------------------|--|
| Vitamin C          | Antioxidant         | <p>(1) Effect of vitamin C and E in breast cancer patients undergoing chemotherapy (nct04463459)</p> <p>(2) Preoperative IMRT with concurrent high-dose vitamin C and mFOLFOX6 in locally advanced rectal cancer (nct04801511)</p> <p>(3) Intravenous (IV) vitamin C with chemotherapy for cisplatin-ineligible bladder cancer patients (nct04046094)</p> <p>(4) Intravenous ascorbic acid supplementation in neoadjuvant chemotherapy for breast cancer (nct03175341)</p> <p>(5) Ph 2 trial of vitamin C &amp; G-FLIP (low doses of gemcitabine, 5FU, leucovorin, irinotecan, and oxaliplatin) for pancreatic cancer (nct01905150)</p> <p>(6) Other clinical trials are available at <a href="http://clinicaltrials.gov">clinicaltrials.gov</a></p> |
| Vitamin E          | Antioxidant         | <p>(1) Vitamin E supplements in preventing cancer in patients at risk of prostate cancer or who have prostate cancer (nct00895115)</p> <p>(2) Vitamin E supplements in treating patients undergoing surgery for colorectal cancer (nct00905918)</p> <p>(3) Selenium and vitamin E in preventing cancer progression and recurrence in patients with early-stage bladder cancer (nct00553345)</p> <p>(4) S0000 selenium and vitamin E in preventing prostate cancer (nct00006392)</p> <p>(5) A pilot clinical trial with tocotrienol on breast cancer (nct01157026)</p> <p>(6) Other clinical trials are available at <a href="http://clinicaltrials.gov">clinicaltrials.gov</a></p>   |
| Tigecycline        | Antibacterial       | <p>(1) Personalized treatment of urogenital cancers depends on the microbiome (nct03962920)</p> <p>(2) Safety study evaluating intravenous infusions of tigecycline to treat acute myeloid leukemia (nct01332786)</p> <p>(3) In vitro study of tigecycline to treat chronic myeloid leukemia (nct02883036)</p>   |
| Doxycycline        | Antibacterial       | <p>(1) Metformin hydrochloride and doxycycline in treating patients with localized breast or uterine cancer (nct02874430)</p> <p>(2) Doxycycline for the treatment of cutaneous T-cell lymphoma (nct02341209)</p> <p>(3) Combining doxycycline with bone-targeted therapy in patients with metastatic breast cancer (nct01847976)</p> <p>(4) Doxycycline in lymphangioliomyomatosis (lam) (nct00989742)</p> <p>(5) Doxycycline, temozolomide, and ipilimumab in melanoma (nct01590082)</p> <p>(6) A phase II study of doxycycline in relapsed NHL (nct02086591)</p>  |
| Clarithromycin     | Antibacterial       | <p>(1) Is clarithromycin a potential treatment for cachexia in people with lung cancer? (nct02416570)</p> <p>(2) A trial with metronomic low-dose treosulfan, pioglitazone, and clarithromycin versus standard treatment in NSCLC (nct02852083)</p> <p>(3) Chemoprevention therapy in treating patients at high risk of developing multiple myeloma (nct00006219)</p> <p>(4) Clarithromycin in multiple myeloma induction therapy (nct02573935)</p> <p>(5) Clinical trial of clarithromycin, lenalidomide, and dexamethasone in the treatment of the first relapsed multiple myeloma (nct04063189)</p> <p>(6) Other clinical trials are available at <a href="http://clinicaltrials.gov">clinicaltrials.gov</a></p>                                  |
| Nicosamide         | Antiparasitic       | <p>(1) A study of nicosamide in patients with resectable colon cancer (nct02687009)</p> <p>(2) Drug trial to investigate the safety and efficacy of nicosamide tablets in patients with metastases of a colorectal cancer progressing after therapy (nct02519582)</p> <p>(3) Enzalutamide and nicosamide in treating patients with recurrent or metastatic castration-resistant prostate cancer (nct03123978)</p> <p>(4) Nicosamide and enzalutamide in treating patients with castration-resistant, metastatic prostate cancer (nct02532114)</p> <p>(5) Abiraterone acetate, nicosamide, and prednisone in treating patients with hormone-resistant prostate cancer (nct02807805)</p>   |
| Hydroxychloroquine | Antimalarial        | <p>(1) Phase I/II study of hydroxychloroquine with itraconazole with biochemically recurrent prostate cancer (nct03513211)</p> <p>(2) Hydroxychloroquine in previously treated patients with metastatic pancreatic cancer (nct01273805)</p> <p>(3) Hydroxychloroquine to increase tumor suppressor par-4 levels in oligometastatic prostate cancer (nct04011410)</p>   |

TABLE 1: Continued.

| Drug         | Original indication | Clinical trials   |
|--------------|---------------------|---|
| Simvastatin  | Antihyperlipidemic  | (4) Hydroxychloroquine in metastatic estrogen receptor-positive breast cancer progressing on hormonal therapy (nct02414776)                   |
|              |                     | (5) Hydroxychloroquine and gefitinib to treat lung cancer (nct00809237)   |
|              |                     | (6) Other clinical trials are available at <a href="http://clinicaltrials.gov">clinicaltrials.gov</a>   |
|              |                     | (1) Simvastatin plus dual anti-HER2 therapy for metastatic breast cancer (nct03324425)  |
|              |                     | (2) Trial of xp (capecitabine/cddp) simvastatin in advanced gastric cancer patients (nct0109908)  |
|              |                     | (3) Simvastatin in preventing a new breast cancer in women at high risk for a new breast cancer (nct00334542)                                 |
| Digoxin      | Antiheart failure   | (4) Metformin and simvastatin use in bladder cancer (nct02360618)   |
|              |                     | (5) A phase I study of high-dose simvastatin in patients with gastrointestinal tract cancer who failed to standard chemotherapy (nct03086291) |
|              |                     | (6) Other clinical trials are available at <a href="http://clinicaltrials.gov">clinicaltrials.gov</a>   |
|              |                     | (1) Potentiation of cisplatin-based chemotherapy by digoxin in advanced unresectable head and neck cancer patients (nct02906800)              |
|              |                     | (2) Digoxin for recurrent prostate cancer (nct01162135)   |
|              |                     | (3) Capecitabine with digoxin for metastatic breast cancer (nct01887288)  |
| Fluphenazine | Antipsychotics      | (4) Phase IB metformin, digoxin, and simvastatin in solid tumors (nct03889795)  |
|              |                     | (5) Phase II multicenter study of digoxin per os in classic or endemic Kaposi's sarcoma (nct02212639)   |
|              |                     | (6) Other clinical trials are available at <a href="http://clinicaltrials.gov">clinicaltrials.gov</a>   |
|              |                     | (1) Fluphenazine in treating patients with refractory advanced multiple myeloma (nct00335647)   |
|              |                     | (2) Study of fluphenazine in relapsed or relapsed-and-refractory multiple myeloma (nct00821301)   |

effectively prevent tumorigenesis. Therefore, repurposed drugs that act as ROS scavengers have the potential to modulate levels of ROS for therapeutic benefit in cancer.

**4.1.1. Vitamin C.** Vitamin C, known as ascorbic acid, is an antioxidant converted from glucose, which is abundant in fresh fruits and vegetables [92]. At physiological concentrations, vitamin C prevents gene mutations caused by peroxidation by removing ROS, and it also blocks oxidative modification of amino acids to maintain protein integrity and protects lipids from peroxidation [93]. In a cohort study, Wright et al. analyzed the comprehensive intake of individual selenium, flavonoids, vitamin C, and carotenoids to predict the risk of lung cancer. They proved that integration of dietary antioxidants can significantly reduce lung cancer incidence in male smokers [94]. However, it has been nearly half of a century since the beginning of researches of anticancer mechanism of vitamin C, and its role was challenged and verified repeatedly. Moreover, the controversy about the anticancer efficiency of vitamin C may depend on the administration ways (oral or intravenous), which can result in different concentrations in the plasma of cancer subjects [92]. High-dose vitamin C alone or in combination can inhibit tumor growth in various cancer models through regulation the level of ROS [95–97]. Furthermore, high-dose intravenous vitamin C in cancer patients has led to increased quality of life with minimal side effects [98, 99]. Several excellent reviews have recently described that vitamin C is used for cancer chemoprevention and clarified that the anticancer mechanism of high doses of vitamin C is targeting excessive ROS generation and/or epigenetic regulators

and/or hypoxia-inducible factor 1 (HIF-1) [92, 100, 101]. Moreover, vitamin C has also been extensively tested in clinical trials of cancer for many years (Table 1).

**4.1.2. Vitamin E.** Vitamin E is a hydrophobic fat-soluble compound that exists in a variety of food sources, and it in nature occurs as 8 isoforms (tocopherols and tocotrienols, both as  $\alpha$ ,  $\beta$ ,  $\gamma$ , and  $\delta$  forms); however, only  $\alpha$ -tocopherol is considered to be essential for human [102, 103]. Vitamin E protects cells from cell damage caused by ROS, thereby attenuating DNA damage and cancer development [102]. Vitamin E has been extensively studied, and much data indicates that it has a role in cancer prevention [103]. For example, it is found that vitamin E can interfere phosphatidylinositol-3-kinase/protein kinase B (PI3K/PKB) and protein kinase C (PKC) signaling pathways by scavenging ROS, which may be one of the antitumor mechanisms [102, 104–106]. Moreover, clinical trials of vitamin E in cancer treatment have been detailed in some review and research articles [107, 108], although it was found that the development and metastasis of lung tumors were increased in vitamin E-treated mouse models [109].

**4.2. Repurposed Drugs as a ROS Inducer in Cancer.** Interestingly, repurposed drugs are more likely to act as ROS inducers in the treatment or prevention of cancer. ROS-inducing repurposed drugs by mechanisms of inhibiting intracellular antioxidant systems and/or producing ROS generation in cells were reported to selectively kill cancer phenotypes. Several reviews on the small molecules regulating ROS homeostasis for cancer therapy have been

published [24, 87, 89]. In the review, we will classify and describe repurposed drugs that induce the excessive production of ROS in the cancer cells to exert antitumor effects.

#### 4.2.1. Antibacterial

(1) *Tigecycline*. Tigecycline is a broad-spectrum antibiotic approved by the FDA for the treatment of multidrug-resistant bacterial infections, complicated intra-abdominal infections, complicated skin structure infections, and community-acquired pneumonia [110]. Its antibacterial mechanism involves killing bacteria by binding to the 30S bacterial ribosomal subunit, thereby preventing tRNA and its codons from linking to the A site of the ribosomal complex, which result in inhibiting protein synthesis [111, 112]. Recent studies have found that tigecycline is identified as one of the effective anticancer agents by enhancing the levels ROS. For example, tigecycline inhibited mitochondrial respiration, mitochondrial membrane potential, and adenosine triphosphate (ATP) levels and caused an increase in intracellular ROS in a dose-dependent manner, which induced death of non-small-cell lung cancer cells [113]. Additionally, tigecycline was found to selectively kill leukemic stem and progenitor cells by inhibiting mitochondrial translation [114]. Besides, tigecycline significantly enhanced conventional cisplatin activity against human hepatocellular carcinoma through inducing mitochondrial dysfunction and increasing the levels of mitochondrial superoxide, hydrogen peroxide, and ROS levels [115]. More importantly, a phase I clinical trial evaluating the safety and biologic activity of intravenous infusions of tigecycline to treat acute myeloid leukemia was completed (NCT01332786) (Table 1).

(2) *Levofloxacin*. Levofloxacin is a third-generation fluoroquinolone antibacterial drug, which can kill bacterial through preventing DNA replication [116]. It is often used clinically for some moderate and severe infections caused by sensitive bacteria [116]. With the further study, repurposed antibiotic levofloxacin is an attractive candidate for cancer treatment. It was found that levofloxacin effectively inhibited lung cancer cell proliferation and induces apoptosis [117]. Mechanistically, levofloxacin inhibited the activity of the mitochondrial electron transport chain complex, which in turn blocked mitochondrial respiration, reduced ATP production, and increased the levels of ROS, mitochondrial superoxide, and hydrogen peroxide [117]. Moreover, levofloxacin effectively targeted breast cancer cells and acted synergistically with 5-fluorouracil through inhibiting mitochondrial biogenesis and was accompanied by the deactivation of PI3K/PKB/mammalian target of rapamycin (mTOR) and mitogen-activated protein kinase/extracellular signal-regulated kinase (MAPK/ERK) signaling pathways [118].

(3) *Doxycycline*. Doxycycline (DOXY), a derivative of tetracycline, is a broad-spectrum antibiotic that exhibits many therapeutic activities in addition to its antibacterial properties [116, 119]. Doxycycline has recently carved out a role in cancer therapy. It was found that doxycycline triggered cell death in different cancer cells, including cervical, breast,

lung, and prostate cancer cells [120]. A further study found that doxycycline was effective in targeting glioblastoma through inducing mitochondrial dysfunctions and oxidative stress [121]. Moreover, the ROS-apoptosis signal regulating kinase 1- (ASK1-) Jun N-terminal kinase (JNK) pathway is involved in doxycycline-induced melanoma cell death [122]. Amplification of tumor-associated ROS has been used as a boosting strategy to improve tumor therapy. A recent study has shown that prodrug chlorin e6 (Ce6) and zoledronic acid (ZA)/mesoporous silica nanoparticles (MSN)/doxorubicin- (DOX-) thioketal- (TK-) DOXY can be used for the chemodynamic therapy of osteosarcoma [123]. Upon laser irradiation, the loaded Ce6 produced in situ ROS and subsequently resulted in DOX/DOXY release. The released DOXY promoted ROS production and further induced ROS burst, which increased the sensitivity of the osteosarcoma to chemotherapy and resulted in enhancing tumor cell inhibition and apoptosis [123]. Furthermore, some clinical trials are ongoing, including a phase II trial study of how well metformin hydrochloride works together with doxycycline in treating patients with localized breast or uterine cancer (NCT02874430) and a study of doxycycline for the treatment of cutaneous T-cell lymphoma (NCT02341209) (Table 1).

(4) *Clarithromycin*. Clarithromycin belongs to a family of 14-membered ring macrolide antibiotics, but several clinical investigations showed that clarithromycin was highly efficient for multiple myeloma (MM) when used in combination with conventional chemotherapy since 1997 [124]. This finding highlights the importance of clarithromycin on the treatment of MM and offers a new regimen for the relapsed/refractory MM patients. Moreover, the results of Zhou et al. showed that clarithromycin plus cisplatin had a synergetic effect against ovarian cancer cell viability and induced the apoptosis rate, which was linked to the increase of ROS levels *in vitro* and *in vivo* [125]. This result proved that clarithromycin augmented cisplatin response via a ROS-mediated synergistic effect. However, no clinical trials have investigated the activity of clarithromycin against ovarian cancer. Indeed, a phase II clinical trial evaluating clarithromycin treatment for cachexia (the loss of muscle mass) in people with non-small-cell lung cancer was terminated due to having not enough participants (NCT02416570) (Table 1).

#### 4.2.2. Anthelmintic

(1) *Niclosamide*. Niclosamide, an FDA-approved oral agent, belongs to the antiparasitic disease drug and has been used in the clinical treatment of intestinal parasitic infections for nearly 50 years [126]. In recent studies, it had been documented that niclosamide had antitumor effects and can increase the sensitivity of tumor cells to chemotherapy and radiotherapy through regulating redox homeostasis. For example, niclosamide inhibited the NF- $\kappa$ B pathway and increased ROS levels to induce apoptosis in acute myelogenous leukemia cells [127]. Niclosamide also suppressed renal cell carcinoma by inhibiting Wnt/beta-catenin and inducing

mitochondrial dysfunctions [128]. Moreover, niclosamide was found to sensitize the responsiveness of cervical cancer cells to paclitaxel via ROS-mediated mTOR inhibition [129]. Also, niclosamide was chosen based on a cell-based high-throughput viability screen and it had a radiosensitizing effect on H1299 human lung cancer cells [130]. A further study had demonstrated that niclosamide plus gamma-ionizing radiation can produce ROS and promote c-Jun and its phosphorylation [130]. Moreover, niclosamide also acted as a potent radiosensitizer through inhibiting signal transducer and activator of transcription 3 (STAT3) and B-cell lymphoma-2 (Bcl-2) and increasing ROS generation in triple-negative breast cancer cells [131]. The therapeutic effect of combination valproic acid and niclosamide was investigated on human lung cancer cell line [132]. The results showed that combination therapy caused a dramatic decrease in cell viability by inducing the extrinsic apoptotic pathway and stimulating endoplasmic reticulum stress and mitochondrial membrane potential loss associated with increased ROS levels [132]. Based on these encouraging results, the evaluation of niclosamide in several clinical trials has been investigated (Table 1).

(2) *Albendazole*. Albendazole is a broad-spectrum, low-toxic antiparasitic drug that kills susceptible parasites by reducing the glycogen stores and the formation of ATP [133]. There are several evidences supporting albendazole repositioning for cancer therapy against tumor cell lines [133]. Further studies have shown that oxidative stress was one of anticancer mechanisms that mediated albendazole. Castro et al. had demonstrated that albendazole treatment could trigger apoptosis and induce MCF-7 cell death through ROS generation, which was related to depletion of reduced glutathione levels, augmented important oxidative biomarkers, and increased the activity of antioxidant enzymes [134]. It was found that ROS can induce p38 MAPK activation in U937 cells treated with albendazole. Pretreatment with SB202190 (p38 MAPK inhibitor) increased the activity of cells treated with albendazole, indicating that ROS-induced P38 MAPK activation was associated with albendazole-mediated cell death [135]. However, no clinical trials have been conducted to investigate the antitumor effects of the albendazole.

#### 4.2.3. Antimalarial

(1) *Artemisinin*. Artemisinin and its derivatives are natural synthetic antimalarial drugs [136]. With the deepening of research, artemisinin not only has strong antimalarial activity but also has obvious antitumor effects. Artemisinin harbors an endoperoxide bridge whose cleavage results in the generation of ROS and/or artemisinin carbon-centered free radicals, further promoting cell apoptosis, inhibiting cell proliferation and damaging DNA, cell membrane, protein, and organelles to play an antitumor effect [137]. The ROS-mediated antitumor properties of artemisinin on numerous cancer types have been reported [138–142]. Compared with traditional chemotherapeutic drugs, artemisinin has the advantages of broad antitumor spectrum, less toxicity, and

side effects, so it can be identified as an intriguing candidate for repurposing. However, there are no clinical trials investigating the antiproliferative effects of artemisinin; an additional study is necessary for optimal clinical efficacy.

(2) *Hydroxychloroquine*. Hydroxychloroquine, a chloroquine derivative, is originally developed to treat patients with malaria, but it has been further investigated because of its antiproliferative effects on different types of tumors [143]. In general, hydroxychloroquine has a better oral bioavailability and safety profile than chloroquine, which makes it a suitable candidate to evaluate its potential therapeutic applications in cancer [143]. Hence, hydroxychloroquine was under investigation in cell level, animal models, and clinical trials for a variety of cancers. Many studies found that hydroxychloroquine was capable of killing tumor cells by different pathways accompanied by the massive production of ROS. In-depth evaluation of hydroxychloroquine, it revealed that it could be considered an effective autophagy inhibitor [144]. Autophagy is a self-degrading intracellular process involving tumor suppression and promotion [145]. However, inhibition of autophagy with hydroxychloroquine can not only hinder the autophagic protective effect but also increase dysfunctional mitochondria and ROS production, and a further study found that ROS was the main mechanism of enhanced cytotoxicity with autophagy inhibition [144]. Moreover, hydroxychloroquine exhibited a good synergism with microtubule polymerization inhibitor CYT997 on the induction of ROS-associated apoptosis in human head and neck squamous cell carcinoma [146]. In addition, breast cancer cell apoptosis induced by hydroxychloroquine was related to the inhibition of the autophagic flux and accumulation of damaged mitochondria and ROS [147]. Hence, the inhibition of autophagy is, at least partially, responsible for hydroxychloroquine-mediated upregulation of ROS in cancer cell death.

#### 4.2.4. Cardiovascular

(1) *Simvastatin*. Simvastatin is an antihigh cholesterol drug widely used in the prevention and treatment of cardiovascular diseases by inhibiting the 3-hydroxy-3-methylglutaryl-coenzyme a (Hmg-CoA) reductase in the mevalonate pathway and blocking the formation of intermediary products in the biosynthesis of cholesterol [148]. Simvastatin has recently been considered a potential sensitizer to chemotherapy and radiotherapy and exhibits inhibitory effects on amounts of types of cancer [149]. For example, simvastatin alone or in combination with doxorubicin significantly increased ROS levels and suppressed breast cancer MCF-7 cell proliferation [150]. Moreover, a combined therapy of simvastatin and pentoxifylline effectively activated ERK/AKT, upregulated ROS levels, downregulated p-p38, and inhibited NF- $\kappa$ B signaling pathway, thereby promoting triple-negative breast cancer cell apoptosis [150]. Additionally, simvastatin administration alone also could induce ROS formation in the KKV-100 cells [151]. Due to the excellent antitumor effect of simvastatin *in vitro*, a large number of clinical studies have been conducted (Table 1).

(2) *Digoxin*. Digoxin, an inhibitor of  $\text{Na}^+/\text{K}^+$  ATPase, is widely used to treat heart failure. The clinical tests of digoxin as an anticancer drug, alone or in combination with chemotherapeutic drug, were reported [152]. Anticancer effects of digoxin involve various mechanisms. For example, Wang et al. reported that digoxin inhibited p53 synthesis by activating Src/MAPK signaling pathways and suppresses tumor growth [153]. In addition, digoxin induced apoptosis and cell cycle arrest and had antitumor effects on Burkitt lymphoma cells *in vitro* and *in vivo* [154]. Many studies also reported that digoxin promoted ROS generation via inhibiting hypoxia-inducible factor-1 $\alpha$  (HIF-1 $\alpha$ ), a key regulator of angiogenesis, to block cell growth in a multiple tumor model [155–157]. Moreover, digoxin was found to inhibit activity of the NRF2-ARE luciferase reporter gene in A549-ARE cells, which suggested that digoxin may be a potent NRF2 inhibitor [158]. Zhou et al. found that digoxin could reverse drug resistance of gemcitabine in SW1990/Gem and Panc-1/Gem cells [159]. Mechanistically, digoxin inhibited the activity of NRF2 by suppressing PI3K/Akt signaling pathway in gemcitabine-resistant pancreatic cancer cells [159]. To date, digoxin has been investigated in clinical trials for cancer therapy (Table 1).

#### 4.2.5. Antipsychotics

(1) *Fluphenazine*. Fluphenazine is a phenothiazine antipsychotic drug, which is an antagonist of dopamine D1 and D2 receptors and has a high affinity with 5-HT receptors [160]. It is used in the treatment of schizophrenia and bipolar disorder [160]. Studies have shown an overall decreased cancer incidence in schizophrenic patients using antipsychotics, implying that antipsychotics may have anticancer potentials [161]. As expected, research found that fluphenazine may play an important role in the treatment of cancer [161]. It was found that the ROS levels in triple negative breast cancer cells were significantly increased after fluphenazine treatment, which could impair the mitochondria membrane integrity and further induce cancer cell death [162]. Moreover, HeLa cancer cells treated with fluphenazine in combination with UVA light demonstrated a consistent ROS production in a clearly concentration-dependent manner, indicating a significant photodynamic mechanism involved in the photocytotoxic effect of fluphenazine [163]. Moreover, a clinical trial of fluphenazine in treating patients with refractory advanced multiple myeloma was completed (NCT00335647) (Table 1).

(2) *Pimozide*. Pimozide is an FDA-approved antipsychotic, and it is used to treat clinical Tourette syndrome and schizophrenia [164]. In 1979, pimozide was first found to act as a dopamine antagonist with antimelanoma cancer effect [165]. After that, pimozide had been investigated in a number of cancer cells, and a further study found that pimozide inhibited the cancer cells through the generation of ROS [166]. For example, pimozide induced ROS generation by downregulating the expression of the antioxidant enzyme catalase to suppress osteosarcoma and prostate cancer [166, 167]. Moreover, recently, the ability of ROS generation

to suppress hepatocellular carcinoma cells has been reported [168]. However, to date, pimozide has not been investigated in clinical trials to clarify the antitumor activity.

## 5. Research Perspectives and Discussion

Despite the fact that traditional approaches of looking for differences in the transcriptome or the proteome in cancer have many benefits, much attention has been focused on significant changes in function, such as regulating ROS level, which may be an effective anticancer strategy [169, 170]. Certainly, many clinical chemotherapeutic drugs, such as doxorubicin, daunorubicin, and epirubicin, can kill cancer cells by enhancing ROS production. However, the uses of these drugs are accompanied by indiscriminate cytotoxicity and adverse events and chemoresistance. Repurposed drugs with established safety profiles that are developed based on clearing ROS generation or increasing ROS production may be a novel strategy for the treatment of cancers. However, repurposed drugs may be the lack of specificity for cancer. Moreover, ROS are considered a double-edged sword in cancer. The molecular action of ROS is multidirectional, which in turn produces many uncertainties. There are still some key issues that need to be resolved in the development of ROS-related repurposed drugs.

It is necessary to first understand whether repurposed drugs based on ROS regulation can really be used clinically to treat cancer. The benefits of antioxidant drugs for early cancer therapies by reducing ROS level have been widely recognized. However, several studies have demonstrated antioxidant drugs produced the paradoxical results. Long-term supplementation with the antioxidants N-acetylcysteine and vitamin E promotes KRAS-driven lung cancer metastasis [109]. In addition, it has been shown that the administration of antioxidants, such as N-acetylcysteine, accelerates the progression of lung cancers and melanomas [171]. Thus, whether antioxidants inhibit or promote tumors needs further support by solid trials performed on a large scale. Meanwhile, raising ROS to cytotoxic levels can kill cancer cells; this strategy may inevitably damage normal cells. Since the dose of chemotherapy drugs clinically is much higher than the dose required for the original effect of the repurposed drugs, it may be difficult to obtain an effective and safe dose clinically. Repurposed drugs may produce ultrahigh ROS levels that the human body cannot tolerate when administered rapidly and at a high concentration, which can significantly induce systemic toxicity to cancer patients. In this regard, ROS-related repurposed drugs are more suitable for use as chemotherapy sensitizers or adjuvant drugs in tumor treatment, which may lead to unexpected response. Moreover, further elucidation of ROS-related cysteine modifications and their functional consequences will be the basis for improving our understanding of the selective effects of ROS on cancer and normal cells.

Another major challenge is increasing the selectivity of ROS-related repurposed drugs as therapeutic drugs. Cancer cells thrive on levels of ROS that are moderately higher than those in their normal counterparts; this feature renders ROS-responsive photodynamic therapy can reach good results. Up to now, new ROS-responsive prodrugs, probes,

theranostic prodrugs, and nanotheranostics that allow for the monitoring of ROS with temporal and spatial specificity have been developed for the targeted treatment and precise diagnosis of cancer and selectively killing tumor cells [172, 173]. In fact, ROS-responsive prodrug strategies have been successfully used to modify clinically platinum-based drugs, showing enhanced therapeutic efficacy and reduced side effects [174, 175]. Therefore, the development of repurposed drugs inspired ROS-responsive groups/probes/nanoparticles would be a significant improvement in cancer treatment selectively.

In future research, before adopting the treatment method, there should be advanced inspection and real-time monitoring of the ROS status in the body, and ROS-related repurposed drugs should be taken appropriately to increase or decrease the ROS level in the body, so as to obtain a better treatment effect.

### Ethical Approval

This review article does not contain any original studies with animals or human participants.

### Conflicts of Interest

All authors declare that they have no conflict of interest.

### Authors' Contributions

Jiabing Wang and Dongsheng Sun contributed equally to this work.

### Acknowledgments

The work was supported by the National Natural Science Foundation of China (No. 81903074), the Medical Health Science and Technology Project of Health Commission of Zhejiang Province (Nos. 2020KY366 and 2021KY399), the Hospital Pharmacy Program of Zhejiang Pharmaceutical Association (No. 2019ZYY43), and the Science and Technology Plan Project of Taizhou (No. 1901ky48).

### References

- [1] R. L. Siegel, K. D. Miller, H. E. Fuchs, and A. Jemal, "Cancer statistics, 2021," *CA: a Cancer Journal for Clinicians*, vol. 71, no. 1, pp. 7–33, 2021.
- [2] E. Koren and Y. Fuchs, "Modes of regulated cell death in cancer," *Cancer Discovery*, vol. 11, no. 2, pp. 245–265, 2021.
- [3] A. Gonzalez-Fierro and A. Duenas-Gonzalez, "Drug repurposing for cancer therapy, easier said than done," *Seminars in Cancer Biology*, vol. 68, pp. 123–131, 2021.
- [4] F. Bray, J. Ferlay, I. Soerjomataram et al., "GLOBOCAN estimates of incidence and mortality worldwide for 36 cancers in 185 countries," *CA: a Cancer Journal for Clinicians*, vol. 2018, no. 68, pp. 394–424, 2018.
- [5] A. S. Brown and C. J. Patel, "A standard database for drug repositioning," *Scientific data*, vol. 4, no. 1, p. 170029, 2017.
- [6] S. L. Wood, M. Pernemalm, P. A. Crosbie, and A. D. Whetton, "Molecular histology of lung cancer: from targets to treatments," *Cancer Treatment Reviews*, vol. 41, no. 4, pp. 361–375, 2015.
- [7] A. Hill, D. Gotham, J. Fortunak et al., "Target prices for mass production of tyrosine kinase inhibitors for global cancer treatment," *BMJ Open*, vol. 6, no. 1, p. e009586, 2016.
- [8] P. L. Bedard, D. M. Hyman, M. S. Davids, and L. L. Siu, "Small molecules, big impact: 20 years of targeted therapy in oncology," *Lancet*, vol. 395, no. 10229, pp. 1078–1088, 2020.
- [9] F. Pammolli, L. Magazzini, and M. Riccaboni, "The productivity crisis in pharmaceutical R&D," *Nature Reviews. Drug Discovery*, vol. 10, no. 6, pp. 428–438, 2011.
- [10] M. J. Waring, J. Arrowsmith, A. R. Leach et al., "An analysis of the attrition of drug candidates from four major pharmaceutical companies," *Nature Reviews. Drug Discovery*, vol. 14, no. 7, pp. 475–486, 2015.
- [11] S. Hanash and A. Taguchi, "The grand challenge to decipher the cancer proteome," *Nature Reviews Cancer*, vol. 10, no. 9, pp. 652–660, 2010.
- [12] N. Nosengo, "Can you teach old drugs new tricks?," *Nature*, vol. 534, no. 7607, pp. 314–316, 2016.
- [13] M. Hay, D. W. Thomas, J. L. Craighead, C. Economides, and J. Rosenthal, "Clinical development success rates for investigational drugs," *Nature Biotechnology*, vol. 32, no. 1, pp. 40–51, 2014.
- [14] T. T. Ashburn and K. B. Thor, "Drug repositioning: identifying and developing new uses for existing drugs," *Nature Reviews Drug Discovery*, vol. 3, no. 8, pp. 673–683, 2004.
- [15] S. Pushpakom, F. Iorio, P. A. Eyers et al., "Drug repurposing: progress, challenges and recommendations," *Nature Reviews. Drug Discovery*, vol. 18, no. 1, pp. 41–58, 2019.
- [16] A. Kirtonia, K. Gala, S. G. Fernandes et al., "Repurposing of drugs: an attractive pharmacological strategy for cancer therapeutics," *Seminars in Cancer Biology*, vol. 68, pp. 258–278, 2021.
- [17] S. Singhal, J. Mehta, R. Desikan et al., "Antitumor activity of thalidomide in refractory multiple myeloma," *The New England Journal of Medicine*, vol. 341, no. 21, pp. 1565–1571, 1999.
- [18] T. G. Sivasankaran, R. Udayakumar, C. Elanchezhian, and S. Sabhanayakam, "Effect of sildenafil citrate (Viagra) and ethanol on the albino rat testis: a scanning electron microscopic approach," *Cell Biology International*, vol. 32, no. 2, pp. 293–297, 2008.
- [19] B. Turanli, O. Altay, J. Boren et al., "Systems biology based drug repositioning for development of cancer therapy," *Seminars in cancer biology*, vol. 68, 2019.
- [20] J. D. Hayes, A. T. Dinkova-Kostova, and K. D. Tew, "Oxidative stress in cancer," *Cancer Cell*, vol. 38, no. 2, pp. 167–197, 2020.
- [21] C. Gorrini, I. S. Harris, and T. W. Mak, "Modulation of oxidative stress as an anticancer strategy," *Nature Reviews. Drug Discovery*, vol. 12, no. 12, pp. 931–947, 2013.
- [22] A. T. Dharmaraja, "Role of reactive oxygen species (ROS) in therapeutics and drug resistance in cancer and bacteria," *Journal of Medicinal Chemistry*, vol. 60, no. 8, pp. 3221–3240, 2017.
- [23] J. S. Sousa, E. D'Imprima, and J. Vonck, "Mitochondrial respiratory chain complexes," *Subcellular Biochemistry*, vol. 87, pp. 167–227, 2018.

- [24] Y. Wang, H. Qi, Y. Liu et al., "The double-edged roles of ROS in cancer prevention and therapy," *Theranostics*, vol. 11, no. 10, pp. 4839–4857, 2021.
- [25] I. Fridovich, "Superoxide radical: an endogenous toxicant," *Annual Review of Pharmacology and Toxicology*, vol. 23, no. 1, pp. 239–257, 1983.
- [26] J. A. Imlay, "The molecular mechanisms and physiological consequences of oxidative stress: lessons from a model bacterium," *Nature Reviews. Microbiology*, vol. 11, no. 7, pp. 443–454, 2013.
- [27] L. A. Del Rio and E. Lopez-Huertas, "ROS generation in peroxisomes and its role in cell signaling," *Plant & Cell Physiology*, vol. 57, no. 7, pp. 1364–1376, 2016.
- [28] E. D. Yoboue, R. Sitia, and T. Simmen, "Redox crosstalk at endoplasmic reticulum (ER) membrane contact sites (MCS) uses toxic waste to deliver messages," *Cell Death & Disease*, vol. 9, no. 3, p. 331, 2018.
- [29] H. Sies and D. P. Jones, "Reactive oxygen species (ROS) as pleiotropic physiological signalling agents," *Nature Reviews. Molecular Cell Biology*, vol. 21, no. 7, pp. 363–383, 2020.
- [30] C. C. Winterbourn, A. J. Kettle, and M. B. Hampton, "Reactive oxygen species and neutrophil function," *Annual Review of Biochemistry*, vol. 85, pp. 765–792, 2016.
- [31] B. C. Dickinson and C. J. Chang, "Chemistry and biology of reactive oxygen species in signaling or stress responses," *Nature Chemical Biology*, vol. 7, no. 8, pp. 504–511, 2011.
- [32] L. Urso, I. Cavallari, E. Sharova, F. Ciccarese, G. Pasello, and V. Ciminale, "Metabolic rewiring and redox alterations in malignant pleural mesothelioma," *British Journal of Cancer*, vol. 122, no. 1, pp. 52–61, 2020.
- [33] T. L. de Jager, A. E. Cockrell, and S. S. Du Plessis, "Ultraviolet light induced generation of reactive oxygen species," *Advances in Experimental Medicine and Biology*, vol. 996, pp. 15–23, 2017.
- [34] S. Kumari, A. K. Badana, and R. Malla, "Reactive oxygen species: a key constituent in cancer survival," *Biomarker Insights*, vol. 13, pp. 1–9, 2018.
- [35] M. Inoue, E. F. Sato, M. Nishikawa et al., "Mitochondrial generation of reactive oxygen species and its role in aerobic life," *Current Medicinal Chemistry*, vol. 10, no. 23, pp. 2495–2505, 2003.
- [36] S. G. Rhee, "Redox signaling: hydrogen peroxide as intracellular messenger," *Experimental & Molecular Medicine*, vol. 31, no. 2, pp. 53–59, 1999.
- [37] J. R. Stone and S. Yang, "Hydrogen peroxide: a signaling messenger," *Antioxidants & Redox Signaling*, vol. 8, no. 3–4, pp. 243–270, 2006.
- [38] Y. M. Go, J. D. Chandler, and D. P. Jones, "The cysteine proteome," *Free Radical Biology & Medicine*, vol. 84, pp. 227–245, 2015.
- [39] F. Ursini, M. Maiorino, and H. J. Forman, "Redox homeostasis: the golden mean of healthy living," *Redox Biology*, vol. 8, pp. 205–215, 2016.
- [40] E. Niki, "Oxidative stress and antioxidants: Distress or eustress?," *Archives of Biochemistry and Biophysics*, vol. 595, pp. 19–24, 2016.
- [41] H. Sies, "Hydrogen peroxide as a central redox signaling molecule in physiological oxidative stress: oxidative eustress," *Redox Biology*, vol. 11, pp. 613–619, 2017.
- [42] B. Chance, H. Sies, and A. Boveris, "Hydroperoxide metabolism in mammalian organs," *Physiological Reviews*, vol. 59, no. 3, pp. 527–605, 1979.
- [43] A. Zeida, M. Trujillo, G. Ferrer-Sueta, A. Denicola, D. A. Estrin, and R. Radi, "Catalysis of peroxide reduction by fast reacting protein thiols," *Chemical Reviews*, vol. 119, no. 19, pp. 10829–10855, 2019.
- [44] L. B. Poole, "The basics of thiols and cysteines in redox biology and chemistry," *Free Radical Biology & Medicine*, vol. 80, pp. 148–157, 2015.
- [45] E. Naik and V. M. Dixit, "Mitochondrial reactive oxygen species drive proinflammatory cytokine production," *The Journal of Experimental Medicine*, vol. 208, no. 3, pp. 417–420, 2011.
- [46] G. Gloire, S. Legrand-Poels, and J. Piette, "NF- $\kappa$ B activation by reactive oxygen species: Fifteen years later," *Biochemical Pharmacology*, vol. 72, no. 11, pp. 1493–1505, 2006.
- [47] B. Halliwell, "Biochemistry of oxidative stress," *Biochemical Society Transactions*, vol. 35, no. 5, pp. 1147–1150, 2007.
- [48] Q. Cui, J. Q. Wang, Y. G. Assaraf et al., "Modulating ROS to overcome multidrug resistance in cancer," *Drug Resistance Updates*, vol. 41, pp. 1–25, 2018.
- [49] E. R. Stadtman and R. L. Levine, "Free radical-mediated oxidation of free amino acids and amino acid residues in proteins," *Amino Acids*, vol. 25, no. 3–4, pp. 207–218, 2003.
- [50] K. Ishikawa, K. Takenaga, M. Akimoto et al., "ROS-generating mitochondrial DNA mutations can regulate tumor cell metastasis," *Science*, vol. 320, no. 5876, pp. 661–664, 2008.
- [51] V. Brovkovich, A. Aldrich, N. Li, G. E. Atilla-Gokcumen, and J. Frasier, "Removal of serum lipids and lipid-derived metabolites to investigate breast cancer cell biology," *Proteomics*, vol. 19, 2019.
- [52] M. M. Gaschler and B. R. Stockwell, "Lipid peroxidation in cell death," *Biochemical and Biophysical Research Communications*, vol. 482, no. 3, pp. 419–425, 2017.
- [53] A. Ayala, M. F. Munoz, and S. Arguelles, "Lipid peroxidation: production, metabolism, and signaling mechanisms of malondialdehyde and 4-hydroxy-2-nonenal," *Oxidative Medicine and Cellular Longevity*, vol. 2014, Article ID 360438, 31 pages, 2014.
- [54] M. Maiorino, M. Conrad, and F. Ursini, "GPx4, lipid peroxidation, and cell death: discoveries, rediscoveries, and open issues," *Antioxidants & Redox Signaling*, vol. 29, no. 1, pp. 61–74, 2018.
- [55] M. P. Gamcsik, M. S. Kasibhatla, S. D. Teeter, and O. M. Colvin, "Glutathione levels in human tumors," *Biomarkers*, vol. 17, no. 8, pp. 671–691, 2012.
- [56] I. S. Harris and G. M. DeNicola, "The complex interplay between antioxidants and ROS in cancer," *Trends in Cell Biology*, vol. 30, no. 6, pp. 440–451, 2020.
- [57] O. I. Aruoma, M. Grootveld, and T. Bahorun, "Free radicals in biology and medicine: from inflammation to biotechnology," *BioFactors*, vol. 27, no. 1–4, pp. 1–3, 2006.
- [58] N. H. Nguyen, G. B. Tran, and C. T. Nguyen, "Anti-oxidative effects of superoxide dismutase 3 on inflammatory diseases," *Journal of Molecular Medicine*, vol. 98, no. 1, pp. 59–69, 2020.
- [59] H. N. Kirkman and G. F. Gaetani, "Mammalian catalase: a venerable enzyme with new mysteries," *Trends in Biochemical Sciences*, vol. 32, no. 1, pp. 44–50, 2007.
- [60] N. Couto, J. Wood, and J. Barber, "The role of glutathione reductase and related enzymes on cellular redox

- homeostasis network," *Free Radical Biology & Medicine*, vol. 95, pp. 27–42, 2016.
- [61] M. Bian, R. Fan, S. Zhao, and W. Liu, "Targeting the thioredoxin system as a strategy for cancer therapy," *Journal of Medicinal Chemistry*, vol. 62, no. 16, pp. 7309–7321, 2019.
- [62] J. Zhang, X. Li, X. Han, R. Liu, and J. Fang, "Targeting the thioredoxin system for cancer therapy," *Trends in Pharmacological Sciences*, vol. 38, no. 9, pp. 794–808, 2017.
- [63] I. S. Harris, A. E. Treloar, S. Inoue et al., "Glutathione and thioredoxin antioxidant pathways synergize to drive cancer initiation and progression," *Cancer Cell*, vol. 27, no. 2, pp. 211–222, 2015.
- [64] H. S. Marinho, C. Real, L. Cyrne, H. Soares, and F. Antunes, "Hydrogen peroxide sensing, signaling and regulation of transcription factors," *Redox Biology*, vol. 2, pp. 535–562, 2014.
- [65] J. D. Hayes and A. T. Dinkova-Kostova, "The Nrf2 regulatory network provides an interface between redox and intermediary metabolism," *Trends in Biochemical Sciences*, vol. 39, no. 4, pp. 199–218, 2014.
- [66] H. Sies, C. Berndt, and D. P. Jones, "Oxidative Stress," *Annual Review of Biochemistry*, vol. 86, no. 1, pp. 715–748, 2017.
- [67] P. Deshmukh, S. Unni, G. Krishnappa, and B. Padmanabhan, "The Keap1-Nrf2 pathway: promising therapeutic target to counteract ROS-mediated damage in cancers and neurodegenerative diseases," *Biophysical Reviews*, vol. 9, no. 1, pp. 41–56, 2017.
- [68] M. Sánchez-Álvarez, R. Strippoli, M. Donadelli, A. V. Bazhin, and M. Cordani, "Sestrins as a therapeutic bridge between ROS and autophagy in cancer," *Cancers*, vol. 11, 2019.
- [69] S. G. Rhee and S. H. Bae, "The antioxidant function of sestrins is mediated by promotion of autophagic degradation of Keap1 and Nrf2 activation and by inhibition of mTORC1," *Free Radical Biology & Medicine*, vol. 88, Part B, pp. 205–211, 2015.
- [70] A. Eijkelenboom and B. M. Burgering, "FOXOs: signalling integrators for homeostasis maintenance," *Nature Reviews. Molecular Cell Biology*, vol. 14, no. 2, pp. 83–97, 2013.
- [71] L. O. Klotz, C. Sanchez-Ramos, I. Prieto-Arroyo, P. Urbanek, H. Steinbrenner, and M. Monsalve, "Redox regulation of FoxO transcription factors," *Redox Biology*, vol. 6, pp. 51–72, 2015.
- [72] P. Hernansanz-Agustin, E. Ramos, E. Navarro et al., "Mitochondrial complex I deactivation is related to superoxide production in acute hypoxia," *Redox Biology*, vol. 12, pp. 1040–1051, 2017.
- [73] W. G. Kaelin Jr. and P. J. Ratcliffe, "Oxygen sensing by metalloproteins: the central role of the HIF hydroxylase pathway," *Molecular Cell*, vol. 30, no. 4, pp. 393–402, 2008.
- [74] V. Oliveira-Marques, H. S. Marinho, L. Cyrne, and F. Antunes, "Role of hydrogen peroxide in NF- $\kappa$ B activation: from inducer to modulator," *Antioxidants & Redox Signaling*, vol. 11, no. 9, pp. 2223–2243, 2009.
- [75] R. Schreck, P. Rieber, and P. A. Baeuerle, "Reactive oxygen intermediates as apparently widely used messengers in the activation of the NF- $\kappa$ B transcription factor and HIV-1," *The EMBO Journal*, vol. 10, no. 8, pp. 2247–2258, 1991.
- [76] P. J. Halvey, J. M. Hansen, J. M. Johnson, Y. M. Go, A. Samali, and D. P. Jones, "Selective oxidative stress in cell nuclei by nuclear-targeted D-amino acid oxidase," *Antioxidants & Redox Signaling*, vol. 9, no. 7, pp. 807–816, 2007.
- [77] A. Maillet and S. Pervaiz, "Redox regulation of p53, redox effectors regulated by p53: a subtle balance," *Antioxidants & Redox Signaling*, vol. 16, no. 11, pp. 1285–1294, 2012.
- [78] T. T. Nguyen, S. A. Grimm, P. R. Bushel et al., "Revealing a human p53 universe," *Nucleic Acids Research*, vol. 46, no. 16, pp. 8153–8167, 2018.
- [79] B. Liu, Y. Chen, and D. K. St. Clair, "ROS and p53: a versatile partnership," *Free Radical Biology & Medicine*, vol. 44, no. 8, pp. 1529–1535, 2008.
- [80] S. Herzig and R. J. Shaw, "AMPK: guardian of metabolism and mitochondrial homeostasis," *Nature Reviews. Molecular Cell Biology*, vol. 19, no. 2, pp. 121–135, 2018.
- [81] F. X. Soriano, P. Baxter, L. M. Murray, M. B. Sporn, T. H. Gillingwater, and G. E. Hardingham, "Transcriptional regulation of the AP-1 and Nrf2 target gene sulfiredoxin," *Molecules and Cells*, vol. 27, no. 3, pp. 279–282, 2009.
- [82] D. Kovacs, T. Sigmond, B. Hotzi et al., "HSF1Base: a comprehensive database of HSF1 (heat shock factor 1) target genes," *International Journal of Molecular Sciences*, vol. 20, no. 22, p. 5815, 2019.
- [83] J. St-Pierre, S. Drori, M. Uldry et al., "Suppression of reactive oxygen species and neurodegeneration by the PGC-1 transcriptional coactivators," *Cell*, vol. 127, no. 2, pp. 397–408, 2006.
- [84] K. S. Echtay, D. Roussel, J. St-Pierre et al., "Superoxide activates mitochondrial uncoupling proteins," *Nature*, vol. 415, no. 6867, pp. 96–99, 2002.
- [85] A. D. Londhe, A. Bergeron, S. M. Curley et al., "Regulation of PTP1B activation through disruption of redox-complex formation," *Nature Chemical Biology*, vol. 16, no. 2, pp. 122–125, 2020.
- [86] H. An, J. S. Heo, P. Kim et al., "Tetraarsenic hexoxide enhances generation of mitochondrial ROS to promote pyroptosis by inducing the activation of caspase-3/GSDME in triple-negative breast cancer cells," *Cell Death & Disease*, vol. 12, no. 2, p. 159, 2021.
- [87] A. Kirtonia, G. Sethi, and M. Garg, "The multifaceted role of reactive oxygen species in tumorigenesis," *Cellular and Molecular Life Sciences*, vol. 77, no. 22, pp. 4459–4483, 2020.
- [88] D. L. Kirkpatrick and G. Powis, "Clinically evaluated cancer drugs inhibiting redox signaling," *Antioxidants & Redox Signaling*, vol. 26, no. 6, pp. 262–273, 2017.
- [89] S. J. Ralph, S. Nozuhur, R. A. ALHulais, S. Rodríguez-Enríquez, and R. Moreno-Sánchez, "Repurposing drugs as pro-oxidant redox modifiers to eliminate cancer stem cells and improve the treatment of advanced stage cancers," *Medicinal Research Reviews*, vol. 39, no. 6, pp. 2397–2426, 2019.
- [90] E. Sasseti, M. H. Clausen, and L. Laraia, "Small-molecule inhibitors of reactive oxygen species production," *Journal of Medicinal Chemistry*, vol. 64, no. 9, pp. 5252–5275, 2021.
- [91] G. Bridge, S. Rashid, and S. Martin, "DNA mismatch repair and oxidative DNA damage: implications for cancer biology and treatment," *Cancers*, vol. 6, pp. 1597–1614, 2014.
- [92] L. Pauling, "Vitamin C therapy of advanced cancer," *The New England Journal of Medicine*, vol. 302, pp. 694–695, 1980.
- [93] Q. Chen, M. G. Espey, A. Y. Sun et al., "Ascorbate in pharmacologic concentrations selectively generates ascorbate radical and hydrogen peroxide in extracellular fluid in vivo," *Proceedings of the National Academy of Sciences of the United States of America*, vol. 104, pp. 8749–8754, 2007.



- [94] M. E. Wright, S. T. Mayne, R. Z. Stolzenberg-Solomon et al., "Development of a comprehensive dietary antioxidant index and application to lung cancer risk in a cohort of male smokers," *American Journal of Epidemiology*, vol. 160, pp. 68–76, 2004.
- [95] J. Du, S. M. Martin, M. Levine et al., "Mechanisms of ascorbate-induced cytotoxicity in pancreatic cancer," *Clinical Cancer Research*, vol. 16, pp. 509–520, 2010.
- [96] M. G. Espey, P. Chen, B. Chalmers et al., "Pharmacologic ascorbate synergizes with gemcitabine in preclinical models of pancreatic cancer," *Free Radical Biology & Medicine*, vol. 50, pp. 1610–1619, 2011.
- [97] C. M. Stephenson, R. D. Levin, T. Spector, and C. G. Lis, "Phase I clinical trial to evaluate the safety, tolerability, and pharmacokinetics of high-dose intravenous ascorbic acid in patients with advanced cancer," *Cancer Chemotherapy and Pharmacology*, vol. 72, pp. 139–146, 2013.
- [98] G. Banhegyi, A. Benedetti, E. Margittai et al., "Subcellular compartmentation of ascorbate and its variation in disease states," *Biochimica et Biophysica Acta*, vol. 1843, pp. 1909–1916, 2014.
- [99] K. A. Naidu, "Vitamin C in human health and disease is still a mystery? An overview," *Nutrition Journal*, vol. 2, no. 1, p. 7, 2003.
- [100] A. Zasowska-Nowak, P. J. Nowak, and A. Cialkowska-Rysz, "High-dose vitamin C in advanced-stage cancer patients," *Nutrients*, vol. 13, no. 3, p. 735, 2021.
- [101] J. Kazmierczak-Baranska, K. Boguszewska, A. Adamus-Grabicka, and B. T. Karwowski, "Two faces of vitamin C-antioxidative and pro-oxidative agent," *Nutrients*, vol. 12, no. 5, p. 1501, 2020.
- [102] J. M. Zingg, "Vitamin E: regulatory role on signal transduction," *IUBMB Life*, vol. 71, no. 4, pp. 456–478, 2019.
- [103] A. Azzi, "Many tocopherols, one vitamin E," *Molecular Aspects of Medicine*, vol. 61, pp. 92–103, 2018.
- [104] R. Ricciarelli and A. Azzi, "Regulation of Recombinant PKC $\alpha$  Activity by Protein Phosphatase 1 and Protein Phosphatase 2A," *Archives of Biochemistry and Biophysics*, vol. 355, no. 2, pp. 197–200, 1998.
- [105] V. Nogueira, Y. Park, C. C. Chen et al., "Akt determines replicative senescence and oxidative or oncogenic premature senescence and sensitizes cells to oxidative apoptosis," *Cancer Cell*, vol. 14, no. 6, pp. 458–470, 2008.
- [106] P. H. Huang, H. C. Chuang, C. C. Chou et al., "Vitamin E facilitates the inactivation of the kinase Akt by the phosphatase PHLPP1," *Science Signaling*, vol. 6, 2013.
- [107] A. Ungurianu, A. Zanfrescu, G. Nițulescu, and D. Margină, "Vitamin E beyond its antioxidant label," *Antioxidants*, vol. 10, 2021.
- [108] E. Cardenas and R. Ghosh, "Vitamin E: a dark horse at the crossroad of cancer management," *Biochemical Pharmacology*, vol. 86, no. 7, pp. 845–852, 2013.
- [109] C. Wiel, K. Le Gal, M. X. Ibrahim et al., "BACH1 stabilization by antioxidants stimulates lung cancer metastasis," *Cell*, vol. 178, no. 2, pp. 330–345.e22, 2019, e22.
- [110] E. Tasina, A. B. Haidich, S. Kokkali, and M. Arvanitidou, "Efficacy and safety of tigecycline for the treatment of infectious diseases: a meta-analysis," *The Lancet Infectious Diseases*, vol. 11, no. 11, pp. 834–844, 2011.
- [111] G. E. Stein and T. Babinchak, "Tigecycline: an update," *Diagnostic Microbiology and Infectious Disease*, vol. 75, no. 4, pp. 331–336, 2013.
- [112] Y. Cai, N. Bai, X. Liu, B. Liang, J. Wang, and R. Wang, "Tigecycline: alone or in combination?," *Infectious Diseases*, vol. 48, no. 7, pp. 491–502, 2016.
- [113] X. Jia, Z. Gu, W. Chen, and J. Jiao, "Tigecycline targets non-small cell lung cancer through inhibition of mitochondrial function," *Fundamental & Clinical Pharmacology*, vol. 30, no. 4, pp. 297–306, 2016.
- [114] M. Skrtic, S. Sriskanthadevan, B. Jhas et al., "Inhibition of mitochondrial translation as a therapeutic strategy for human acute myeloid leukemia," *Cancer Cell*, vol. 20, pp. 674–688, 2011.
- [115] J. Tan, M. Song, M. Zhou, and Y. Hu, "Antibiotic tigecycline enhances cisplatin activity against human hepatocellular carcinoma through inducing mitochondrial dysfunction and oxidative damage," *Biochemical and Biophysical Research Communications*, vol. 483, no. 1, pp. 17–23, 2017.
- [116] A. Bahuguna and D. S. Rawat, "An overview of new anti-tubercular drugs, drug candidates, and their targets," *Medicinal Research Reviews*, vol. 40, no. 1, pp. 263–292, 2020.
- [117] M. Song, H. Wu, S. Wu et al., "Antibiotic drug levofloxacin inhibits proliferation and induces apoptosis of lung cancer cells through inducing mitochondrial dysfunction and oxidative damage," *Biomedicine & Pharmacotherapy*, vol. 84, pp. 1137–1143, 2016.
- [118] M. Yu, R. Li, and J. Zhang, "Repositioning of antibiotic levofloxacin as a mitochondrial biogenesis inhibitor to target breast cancer," *Biochemical and Biophysical Research Communications*, vol. 471, no. 4, pp. 639–645, 2016.
- [119] M. Henahan, M. Montuno, and A. De Benedetto, "Doxycycline as an anti-inflammatory agent: updates in dermatology," *Journal of the European Academy of Dermatology and Venereology*, vol. 31, pp. 1800–1808, 2017.
- [120] A. Markowska, J. Kaysiewicz, J. Markowska, and A. Huczynski, "Doxycycline, salinomycin, monensin and ivermectin repositioned as cancer drugs," *Bioorganic & Medicinal Chemistry Letters*, vol. 29, no. 13, pp. 1549–1554, 2019.
- [121] Q. Tan, X. Yan, L. Song et al., "Induction of mitochondrial dysfunction and oxidative damage by antibiotic drug doxycycline enhances the responsiveness of glioblastoma to chemotherapy," *Medical Science Monitor*, vol. 23, pp. 4117–4125, 2017.
- [122] J. M. Shieh, T. F. Huang, C. F. Hung, K. H. Chou, Y. J. Tsai, and W. B. Wu, "Activation of c-Jun N-terminal kinase is essential for mitochondrial membrane potential change and apoptosis induced by doxycycline in melanoma cells," *British Journal of Pharmacology*, vol. 160, no. 5, pp. 1171–1184, 2010.
- [123] F. Tong, Y. Ye, B. Chen et al., "Bone-targeting prodrug mesoporous silica-based nanoreactor with reactive oxygen species burst for enhanced chemotherapy," *ACS Applied Materials & Interfaces*, vol. 12, no. 31, pp. 34630–34642, 2020.
- [124] T. M. Mark and M. Coleman, "It's time to take clarithromycin seriously in multiple myeloma," *Acta Haematologica*, vol. 135, no. 2, pp. 101–102, 2016.
- [125] B. Zhou, M. Xia, B. Wang et al., "Clarithromycin synergizes with cisplatin to inhibit ovarian cancer growth in vitro and in vivo," *Journal of Ovarian Research*, vol. 12, no. 1, p. 107, 2019.

- [126] J. Xu, P. Y. Shi, H. Li, and J. Zhou, "Broad spectrum antiviral agent niclosamide and its therapeutic potential," *ACS Infectious Diseases*, vol. 6, no. 5, pp. 909–915, 2020.
- [127] Y. Jin, Z. Lu, K. Ding et al., "Antineoplastic mechanisms of niclosamide in acute myelogenous leukemia stem cells: inactivation of the NF- $\kappa$ B pathway and generation of reactive oxygen species," *Cancer Research*, vol. 70, no. 6, pp. 2516–2527, 2010.
- [128] J. Zhao, Q. He, Z. Gong, S. Chen, and L. Cui, "Niclosamide suppresses renal cell carcinoma by inhibiting Wnt/ $\beta$ -catenin and inducing mitochondrial dysfunctions," *Springerplus*, vol. 5, no. 1, p. 1436, 2016.
- [129] L. Chen, L. Wang, H. Shen, H. Lin, and D. Li, "Anthelmintic drug niclosamide sensitizes the responsiveness of cervical cancer cells to paclitaxel via oxidative stress-mediated mTOR inhibition," *Biochemical and Biophysical Research Communications*, vol. 484, no. 2, pp. 416–421, 2017.
- [130] S. L. Lee, A. R. Son, J. Ahn, and J. Y. Song, "Niclosamide enhances ROS-mediated cell death through c-Jun activation," *Biomedicine & Pharmacotherapy*, vol. 68, no. 5, pp. 619–624, 2014.
- [131] L. Lu, J. Dong, L. Wang et al., "Activation of STAT3 and Bcl-2 and reduction of reactive oxygen species (ROS) promote radioresistance in breast cancer and overcome of radioresistance with niclosamide," *Oncogene*, vol. 37, no. 39, pp. 5292–5304, 2018.
- [132] O. Akgun, M. Erkiş, and F. Ari, "Effective and new potent drug combination: histone deacetylase and Wnt/ $\beta$ -catenin pathway inhibitors in lung carcinoma cells," *Journal of Cellular Biochemistry*, vol. 120, no. 9, pp. 15467–15482, 2019.
- [133] J. Nath, R. Paul, S. K. Ghosh, J. Paul, B. Singha, and N. Debnath, "Drug repurposing and relabeling for cancer therapy: emerging benzimidazole antihelmintics with potent anticancer effects," *Life Sciences*, vol. 258, 2020.
- [134] L. S. Castro, M. R. Kwiecinski, F. Ourique et al., "Albendazole as a promising molecule for tumor control," *Redox Biology*, vol. 10, pp. 90–99, 2016.
- [135] L. J. Wang, Y. C. Lee, C. H. Huang et al., "Non-mitotic effect of albendazole triggers apoptosis of human leukemia cells via SIRT3/ROS/p38 MAPK/TTP axis-mediated TNF- $\alpha$  upregulation," *Biochemical Pharmacology*, vol. 162, pp. 154–168, 2019.
- [136] O. P. S. Patel, R. M. Beteck, and L. J. Legoabe, "Exploration of artemisinin derivatives and synthetic peroxides in antimalarial drug discovery research," *European Journal of Medicinal Chemistry*, vol. 213, 2021.
- [137] D. H. J. Cheong, D. W. S. Tan, F. W. S. Wong, and T. Tran, "Anti-malarial drug, artemisinin and its derivatives for the treatment of respiratory diseases," *Pharmacological Research*, vol. 158, 2020.
- [138] F. L. Xiao, W. J. Gao, C. Y. Liu, X. P. Wang, and T. S. Chen, "Artemisinin induces caspase-8/9-mediated and Bax/Bak-independent apoptosis in human lung adenocarcinoma (ASTC-a-1) cells," *Journal of X-Ray Science and Technology*, vol. 19, no. 4, pp. 545–555, 2011.
- [139] P. Li, S. Yang, M. Dou, Y. Chen, J. Zhang, and X. Zhao, "Synergic effects of artemisinin and resveratrol in cancer cells," *Journal of Cancer Research and Clinical Oncology*, vol. 140, no. 12, pp. 2065–2075, 2014.
- [140] S. Noori, Z. M. Hassan, and V. Farsam, "Artemisinin as a Chinese medicine, selectively induces apoptosis in pancreatic tumor cell line," *Chinese Journal of Integrative Medicine*, vol. 20, no. 8, pp. 618–623, 2014.
- [141] J. M. Fox, J. R. Moynihan, B. T. Mott et al., "Artemisinin-derived dimer ART-838 potentially inhibited human acute leukemias, persisted in vivo, and synergized with antileukemic drugs," *Oncotarget*, vol. 7, no. 6, pp. 7268–7279, 2016.
- [142] J. Jia, Y. Qin, L. Zhang et al., "Artemisinin inhibits gallbladder cancer cell lines through triggering cell cycle arrest and apoptosis," *Molecular Medicine Reports*, vol. 13, no. 5, pp. 4461–4468, 2016.
- [143] V. E. Gomez, E. Giovannetti, and G. J. Peters, "Unraveling the complexity of autophagy: potential therapeutic applications in pancreatic ductal adenocarcinoma," *Seminars in Cancer Biology*, vol. 35, pp. 11–19, 2015.
- [144] A. Saleem, D. Dvorzhinski, U. Santanam et al., "Effect of dual inhibition of apoptosis and autophagy in prostate cancer," *Prostate*, vol. 72, no. 12, pp. 1374–1381, 2012.
- [145] H. Xia, D. R. Green, and W. Zou, "Autophagy in tumour immunity and therapy," *Nature Reviews. Cancer*, vol. 21, no. 5, pp. 281–297, 2021.
- [146] L. Gao, X. Zhao, L. Lang, C. Shay, W. Andrew Yeudall, and Y. Teng, "Autophagy blockade sensitizes human head and neck squamous cell carcinoma towards CYT997 through enhancing excessively high reactive oxygen species-induced apoptosis," *Journal of Molecular Medicine (Berlin, Germany)*, vol. 96, no. 9, pp. 929–938, 2018.
- [147] L. Vera-Ramirez, S. K. Vodnala, R. Nini, K. W. Hunter, and J. E. Green, "Autophagy promotes the survival of dormant breast cancer cells and metastatic tumor recurrence," *Nature Communications*, vol. 9, no. 1, p. 1944, 2018.
- [148] E. Di Bello, C. Zwergel, A. Mai, and S. Valente, "The innovative potential of statins in cancer: new targets for new therapies," *Frontiers in Chemistry*, vol. 8, p. 516, 2020.
- [149] C. A. Sánchez, E. Rodríguez, E. Varela et al., "Statin-induced inhibition of MCF-7 breast cancer cell proliferation is related to cell cycle arrest and apoptotic and necrotic cell death mediated by an enhanced oxidative stress," *Cancer Investigation*, vol. 26, no. 7, pp. 698–707, 2008.
- [150] Y. C. Castellanos-Esparza, S. Wu, L. Huang et al., "Synergistic promoting effects of pentoxifylline and simvastatin on the apoptosis of triple-negative MDA-MB-231 breast cancer cells," *International Journal of Oncology*, vol. 52, no. 4, pp. 1246–1254, 2018.
- [151] B. Buranrat, L. Senggunprai, A. Prawan, and V. Kukongviriyapan, "Simvastatin and atorvastatin as inhibitors of proliferation and inducers of apoptosis in human cholangiocarcinoma cells," *Life Sciences*, vol. 153, pp. 41–49, 2016.
- [152] K. Alevizopoulos, T. Calogeropoulou, F. Lang, and C. Stournaras, "Na<sup>+</sup>/K<sup>+</sup> ATPase inhibitors in cancer," *Current Drug Targets*, vol. 15, no. 10, pp. 988–1000, 2014.
- [153] Z. Wang, M. Zheng, Z. Li et al., "Cardiac glycosides inhibit p53 synthesis by a mechanism relieved by Src or MAPK inhibition," *Cancer Research*, vol. 69, no. 16, pp. 6556–6564, 2009.
- [154] T. Wang, P. Xu, F. Wang et al., "Effects of digoxin on cell cycle, apoptosis and NF- $\kappa$ B pathway in Burkitt's lymphoma cells and animal model," *Leukemia & Lymphoma*, vol. 58, 2017.
- [155] D. Wei, J. J. Peng, H. Gao et al., "Digoxin downregulates NDRG1 and VEGF through the inhibition of HIF-1 $\alpha$  under hypoxic conditions in human lung adenocarcinoma A549

- cells," *International Journal of Molecular Sciences*, vol. 14, no. 4, pp. 7273–7285, 2013.
- [156] B. A. Gayed, K. J. O'Malley, J. Pilch, and Z. Wang, "Digoxin inhibits blood vessel density and HIF-1 $\alpha$  expression in castration-resistant C4-2 xenograft prostate tumors," *Clinical and Translational Science*, vol. 5, no. 1, pp. 39–42, 2012.
- [157] M. Abu-Remaileh, A. Khalaileh, E. Pikarsky, and R. I. Aqeilan, "WWOX controls hepatic HIF1 $\alpha$  to suppress hepatocyte proliferation and neoplasia," *Cell Death & Disease*, vol. 9, no. 5, p. 511, 2018.
- [158] E. J. Choi, B. J. Jung, S. H. Lee et al., "A clinical drug library screen identifies clobetasol propionate as an NRF2 inhibitor with potential therapeutic efficacy in KEAP1 mutant lung cancer," *Oncogene*, vol. 36, no. 37, pp. 5285–5295, 2017.
- [159] Y. Zhou, Y. Zhou, M. Yang et al., "Digoxin sensitizes gemcitabine-resistant pancreatic cancer cells to gemcitabine via inhibiting Nrf2 signaling pathway," *Redox Biology*, vol. 22, 2019.
- [160] N. Hendouei, F. Saghafi, F. Shadfar, and S. J. Hosseini-mehr, "Molecular mechanisms of anti-psychotic drugs for improvement of cancer treatment," *European Journal of Pharmacology*, vol. 856, 2019.
- [161] M. Otreba and L. Kosmider, "In vitro anticancer activity of fluphenazine, perphenazine and prochlorperazine. A review," *Journal of Applied Toxicology*, vol. 41, no. 1, pp. 82–94, 2021.
- [162] F. Xu, Y. Xia, Z. Feng et al., "Repositioning antipsychotic fluphenazine hydrochloride for treating triple negative breast cancer with brain metastases and lung metastases," *American Journal of Cancer Research*, vol. 9, no. 3, pp. 459–478, 2019.
- [163] L. Menilli, A. N. Garcia-Argaez, L. Dalla Via, and G. Miolo, "The neuroleptic drug fluphenazine induces a significant UVA-mediated cytotoxic effect on three human cancer cell lines through apoptosis," *Photochemical & Photobiological Sciences*, vol. 18, no. 9, pp. 2232–2239, 2019.
- [164] M. Mothi and S. Sampson, "Pimozide for schizophrenia or related psychoses," *Cochrane Database of Systematic Reviews*, vol. 13, 2013.
- [165] R. N. Taub and M. A. Baker, "Treatment of metastatic malignant melanoma with pimozide," *The Lancet*, vol. 313, no. 8116, p. 605, 1979.
- [166] U. Kim, C. Y. Kim, J. M. Lee et al., "Pimozide inhibits the human prostate cancer cells through the generation of reactive oxygen species," *Frontiers in Pharmacology*, vol. 10, 2020.
- [167] N. Cai, W. Zhou, L. L. Ye et al., "The STAT3 inhibitor pimozide impedes cell proliferation and induces ROS generation in human osteosarcoma by suppressing catalase expression," *American Journal of Translational Research*, vol. 9, no. 8, pp. 3853–3866, 2017.
- [168] J. J. Chen, L. N. Zhang, N. Cai, Z. Zhang, and K. Ji, "Antipsychotic agent pimozide promotes reversible proliferative suppression by inducing cellular quiescence in liver cancer," *Oncology Reports*, vol. 42, no. 3, pp. 1101–1109, 2019.
- [169] R. Moreno-Sanchez, E. Saavedra, J. C. Gallardo-Perez, F. D. Rumjanek, and S. Rodriguez-Enriquez, "Understanding the cancer cell phenotype beyond the limitations of current omics analyses," *The FEBS Journal*, vol. 283, no. 1, pp. 54–73, 2016.
- [170] S. J. Ralph, R. Pritchard, S. Rodríguez-Enriquez, R. Moreno-Sánchez, and R. Ralph, "Hitting the bull's-eye in metastatic cancers-NSAIDs elevate ROS in mitochondria, inducing malignant cell death," *Pharmaceuticals*, vol. 8, no. 1, pp. 62–106, 2015.
- [171] R. Kodama, M. Kato, S. Furuta et al., "ROS-generating oxidases Nox1 and Nox4 contribute to oncogenic Ras-induced premature senescence," *Genes to Cells*, vol. 18, no. 1, pp. 32–41, 2013.
- [172] P. Wang, Q. Gong, J. Hu, X. Li, and X. Zhang, "Reactive oxygen species (ROS)-responsive prodrugs, probes, and therapeutic prodrugs: applications in the ROS-related diseases," *Journal of Medicinal Chemistry*, vol. 64, no. 1, pp. 298–325, 2021.
- [173] Y. Li, J. Yang, and X. Sun, "Reactive oxygen species-based nanomaterials for cancer therapy," *Frontiers in Chemistry*, vol. 9, 2021.
- [174] S. Dilruba and G. V. Kalayda, "Platinum-based drugs: past, present and future," *Cancer Chemotherapy and Pharmacology*, vol. 77, no. 6, pp. 1103–1124, 2016.
- [175] N. J. Wheate, S. Walker, G. E. Craig, and R. Oun, "The status of platinum anticancer drugs in the clinic and in clinical trials," *Dalton Transactions*, vol. 39, no. 35, pp. 8113–8127, 2010.